

NASA Conference Publication 2303

Frontiers of Remote Sensing of the Oceans and Troposphere From Air and Space Platforms

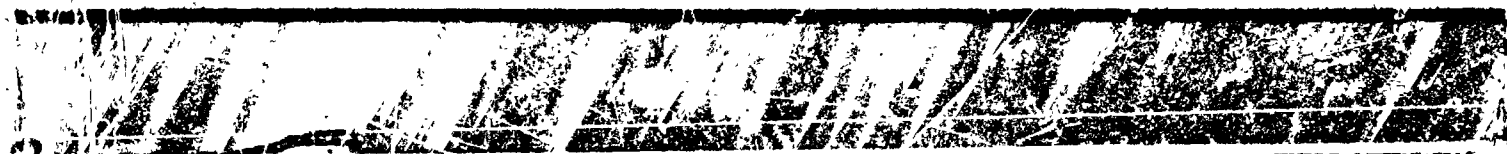
(NASA-CP-2303) FRONTIERS OF REMOTE SENSING
OF THE OCEANS AND TROPOSPHERE FROM AIR AND
SPACE PLATFORMS (NASA) 615 p HC 199/MF A01
CSCL 08C

N84-27262
THRU
N84-27318
Unclass
G3/43 17268

*Proceedings of the URSI Commission F
symposium and workshop
held in Sharmah Israel
May 14-20, 1984*



NASA



NASA Conference Publication 2303

Frontiers of Remote Sensing of the Oceans and Troposphere From Air and Space Platforms

Proceedings of the URSI Commission F
symposium and workshop cosponsored by the
National Aeronautics and Space Administration
and the Israel Academy of Sciences and Humanities
and held in Shresh, Israel
May 14-23, 1984

NASA

National Aeronautics
and Space Administration

Scientific and Technical
Information Branch

1984

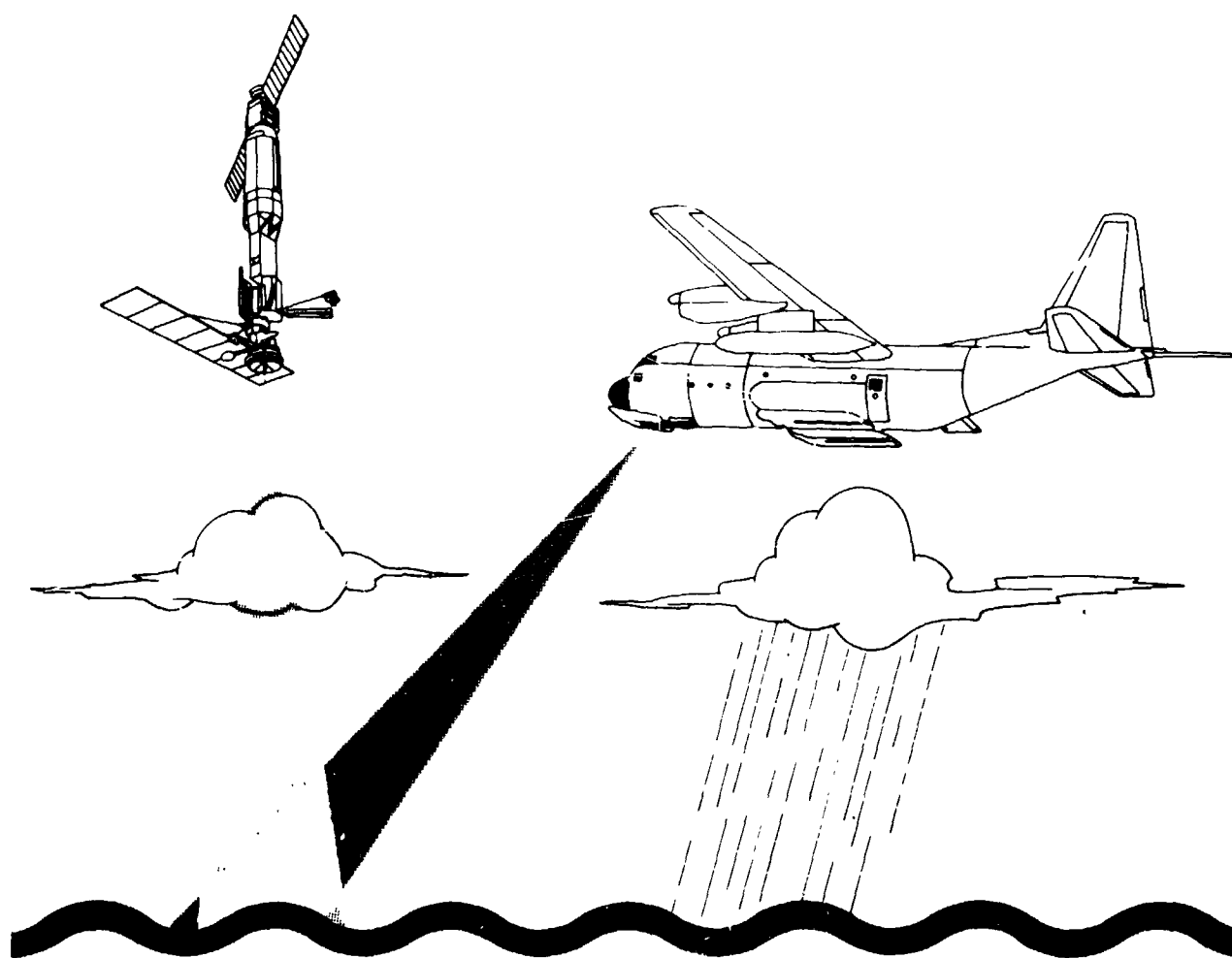


NASA

National Aeronautics and Space Administration

George C. Marshall Space Flight Center
Marshall Space Flight Center, Alabama 35812
AG 205-453 0034

Proceedings Of COMMISSION F SYMPOSIUM on Frontiers of Remote Sensing of the Oceans and Troposphere from Air and Space Platforms



URSI Commission F
Symposium and Workshop
ISRAEL, MAY 14-23, 1984

A Note From The Chairman

The theme of this Meeting is to bring to light new concepts dealing with emerging technology, theory, and applications associated with remote sensing of the oceans and troposphere from space and air platforms.

This URSI Symposium and Workshop brings together radio scientists, atmospheric scientists, and oceanographers for purposes of shedding light on where we have been, where we are at present, and where we are going in the near and distant future. This mixture of investigators we believe to be consistent with the spirit of the IUCRM (The Inter Union Commission of Radio Meteorology) whose aim it was to unite both the geophysical and radio science communities.

The major theme for the Workshop is to attempt to answer the questions:

1. What are the existing methods and techniques?
2. How do we propose to improve upon these existing methods?

These questions apply to geophysical, instrumental, and system related concepts associated with the remote sensing of the oceans and troposphere.

Much appreciation is expressed to Dr. Dag Gjessing, Chairman of the International Commission F of URSI who originally conceived and set into machinery the organization of this meeting. We are deeply indebted to Dr. John S. Theon, Chief of the Atmospheric Dynamics and Radiation Branch of NASA for agreeing to have NASA's cosponsorship and subsequent publishing of this Proceedings. In particular, we are grateful to Dr. Joseph Shapira, President of the URSI Organization within Israel and to the Israel Academy of Sciences and Humanities for extending their kind invitation to support and host this meeting. Many thanks are expressed to the Division of Atmospheric Sciences of The National Science Foundation who supported air travel to this Meeting for a selected number of scientists.

Finally, I would like to thank Isadore Katz, Dr. David Atlas, and Dr. Joseph Shapira, my colleagues and co-organizers, without whose help this meeting would not have taken place.

Julius Goldhirsh, Chairman
International Commission F
Meeting on Remote Sensing

Contents

A Note From the Chairman	ii
<u>Session A</u> <u>FUTURE SATELLITE SYSTEMS</u>	
Remote Sensing for Oceanography: Past, Present, Future L.F. McGoldrick	1
ESA Activities in the Use of Microwaves For The Remote Sensing of the Earth D. Maccoll	11
Spectrasat: A Concept for the Collection of Global Directional Wave Spectra R.C. Beal	19
High Resolution Observations of Low Contrast Phenomena from an Advanced Geosynchronous Platform (AGP) M.S. Maxwell	29
<u>Session B</u> <u>AIR-SEA INTERACTION/WIND</u>	
Remote Sensing of Air-Sea Interaction D. Atlas and E. Mollo-Christensen	41
Scatterometer Capabilities in Remotely Sensing Geophysical Parameters Over the Ocean: The Status and Possibilities R. A. Brown	51
A New Parameterization of an Empirical Model for Wind/Ocean Scatterometry P.M. Woiceshyn et al	57
Does the Scatterometer See Wind Speed or Friction Velocity? M.A. Donelan and W.J. Pierson	75
Scanning Wind-Vector Scatterometers with Two Pencil Beams T. Kirimoto and R.K. Moore	89
New Algorithms for Microwave Measurements of Ocean Winds F.J. Wentz and S. Peteherych	105
Ocean Wind Field Measurement Performance of the ERS-1 Scatterometer P. Hans and H. Schuessler	115

Contents

Session C OCEAN WAVES AND SPECTRA/SAR

Theory and Measure of Certain Image Norms in SAR R. K. Raney	123
Synthetic Aperture Radar Images of Ocean Waves: Theories of Imaging Physics and Experimental Tests J.F. Vesecky et al	137
Optimum Backscatter Cross Section of the Ocean as Measured by Synthetic Aperture Radars E. Bahar et al	149
Tracking Ocean Wave Spectrum from SAR Images A. D. Goldfinger et al	159
SAR Imagery of Ocean-Wave Swell Traveling in an Arbitrary Direction C.L. Rufenach et al	169

Session D OCEAN WAVES AND SPECTRA/OTHER REMOTE SENSORS

Ocean Waves and Turbulence as Observed with an Adaptive Coherent Multifrequency Radar D.T. Gjessing and J. Hjelmstad	179
The Dual-Frequency Scatterometer Re-Examined W.J. Plant and A.B. Reeves	193
An Improved Dual-Frequency Technique for the Remote Sensing of Ocean Currents and Wave Spectra D.L. Schuler and W.P. Eng	199
Measurements of Ocean Wave Spectra and Modulation Transfer Function with the Airborne Two Frequency Scatterometer D.E. Weissman and J.W. Johnson	215
Some Case Studies of Ocean Wave Physical Processes Utilizing the GSFC Airborne Radar Ocean Wave Spectrometer F.C. Jackson	233
Non-Gaussian Statistical Models of Surface Wave Fields for Remote Sensing Applications N.E. Huang	247
A Tentative Unified Sea Model for Scattering and Emission A. Guissard and P. Sobieski	257

Contents

<u>Session E</u>	<u>ATMOSPHERIC MEASUREMENTS/PARTICULATES AND WATER VAPOR RELATED</u>	
Applications of Airborne Remote Sensing in Atmospheric Sciences Research R.J. Serafin et al		259
Evaluation of Meteorological Airborne Doppler Radar P.H. Hildebrand and C.K. Mueller		271
Microwave Remote Sensing of Ocean Surface Wind Speed and Rain Rates Over Tropical Storms C.T. Swift et al		281
Altimeter Height Measurement Errors Introduced by the Presence of Variable Cloud and Rain Attenuation F.M. Monaldo et al		287
Improved Resolution Rain Measurements from Spaceborne Radar Altimeters J. Goldhirsh and F.M. Monaldo		297
Observing Atmospheric Water in Storms with the NIMBUS 7 Scanning Multichannel Microwave Radiometer K.B. Katsaros and R.M. Lewis		307
Temperature and Humidity Profiles in the Atmosphere from Space Borne Lasers H. Grassl and P. Schlusser		317
A New Technique for Monitoring the Water Vapor in the Atmosphere H.D. Black and A. Eisner		327
<u>Session F</u>	<u>ATMOSPHERIC MEASUREMENTS/SYNOPTIC AND WEATHER FORECASTING</u>	
Case Studies of NOAA 6/FIROS N Data Impact on Numerical Weather Forecasts L.M. D'uyan et al		337
The Impact of Satellite Temperature Soundings on the Forecasts of a Small National Meteorological Service N. Wolfson et al		345

Contents

The Variability of the Surface Wind Field in the Equatorial Pacific Ocean: Criteria for Satellite Measurements D. Halpern	357
Recent Advances in Multispectral Sensing of Ocean Surface Temperature From Space E.P. McClain	367
<u>Session G</u> <u>TOPOGRAPHY, BATHYMETRY, AND CURRENTS</u>	
Satellite Techniques for Determining the Geopotential for Sea-Surface Elevations V.L. Pisacane	377
The Satellite Altimeter as a Platform for Observation of the Oceanic Mesoscale J.L. Mitchell	389
The Evolutionary Trend in Airborne and Satellite Radar Altimeters L.S. Fedor and E.J. Walsh	391
On the Detection of Underwater Bottom Topography by Imaging Radars W. Alpers	403
Modeling of SAR Signatures of Shallow Water Ocean Topography R.A. Shuchman et al	415
Coastal Bathymetry and Currents from Landsat Data N. Rosenberg	431
On the Response to Ocean Surface Currents in Synthetic Aperture Radar Imagery O.M. Phillips	433
Variations in Surface Current off the Coasts of Canada as Inferred from Satellite Imagery W.J. Emery et al	453
The Depiction of the Alboran Sea Gyre During Donde VA? Using Remote Sensing and Conventional Data P.E. La Violette	479
Somali Current Studied from Seasat Altimetry C. Perigaud et al	497

Contents

Session H SEA ICE

Satellite Remote Sensing Over Ice R.H. Thomas	501
Radar Altimetry Over Sea Ice H. Powell	513
Method to Estimate Drag Coefficient at the Air-Ice Interface From Drifting Open Pack Ice from Remotely Sensed Data U. Feldman	515
Observations of Sea Ice and Icebergs from Satellite Radar Altimeters C.G. Rapley	527

Session I IMPACT OF REMOTE SENSING ON SYNOPTIC ANALYSIS/FORECASTING

Simulation and Assimilation of Satellite Altimeter Data at the Oceanic Mesoscale P. De Mey and A.R. Robinson	537
Vector Wind, Horizontal Divergence, Wind Stress and Wind Stress Curl from Seasat-SASS at a One Degree Resolution W.J. Pierson et al	557
The Impact of Scatterometer Wind Data on Global Weather Forecasting R. Atlas et al	567
First Global Analysis of Seasat Scatterometer Winds and Potential for Meteorological Research S. Petehterych et al	575
The Importance of Altimeter and Scatterometer Data for Ocean Prediction H.E. Hurlburt	587
Sampling Strategies and Four-Dimensional Assimilation of Altimetric Data for Ocean Monitoring and Prediction J.C. Kindle et al	601
The Influence of Actual and Apparent Geoid Error on Ocean Analysis and Prediction J.D. Thompson	613

Contents

Appendix A Author Index	615
Appendix B List of First Authors and Affiliations	617

Publication Coordinated by
Atmospheric Sciences Division
NASA-Marshall Space Flight Center

N84 27263

REMOTE SENSING FOR OCEANOGRAPHY: PAST, PRESENT, FUTURE

L. F. McGoldrick
The Johns Hopkins University
Applied Physics Laboratory
Johns Hopkins Road
Laurel, Maryland 20707

ABSTRACT

Oceanic dynamics has traditionally been investigated by sampling from instruments in situ, yielding quantitative measurements that are intermittent in both space and time; the ocean is undersampled. The need to obtain proper sampling of the averaged quantities treated in our analytical and numerical models is at present the most significant limitation on advances in physical oceanography. Within the past decade, many electromagnetic techniques for the study of the earth and planets have been applied to the study of the ocean. Now satellites promise nearly total coverage of the world's oceans using only a few days to a few weeks of observations. This paper presents both a review of the early and present techniques applied to satellite oceanography and a description of some future systems to be launched into orbit during the remainder of this century. Both scientific and technologic capabilities are discussed.

INTRODUCTION

Oceanic processes have traditionally been investigated by sampling from instruments in situ, yielding quantitative measurements that are intermittent in both space and time. The past two decades have seen the development of new observing systems such as the STD, current meters, and SOFAR floats. These devices give continuous records in one dimension, either instantaneously in the vertical, or at a fixed point, or approximately moving with a water parcel. Arrays of these instruments have greatly increased our awareness of the space-time variability in the oceans, be it due to internal waves, mesoscale eddies, or fluctuations in the general circulation itself. The need to obtain proper sampling of the averaged quantities treated in our analytical and numerical models is at present probably the most significant limitation on advances in physical oceanography.

In principle, space-based techniques can offer substantial information important to this four-dimensional jigsaw puzzle. Global coverage of broad scale surface features such as wind stress, sea level, surface waves and currents, and temperature at time intervals which are short enough to be effectively continuous gives an enormous potential advantage over shipborne techniques. High resolution images of temperature or color or microwave emissivity allow unique visualization of near-surface processes such as internal waves and eddy formation. Such visualizations can greatly extend the interpretation of conventional measurements, and allow considerable economics and a new kind of strategic planning of ship operations, which

are rapidly becoming intolerably expensive. Communications with sensors on fixed and drifting buoys, and the location of non-fixed systems through satellites make possible all sorts of composite subsurface measurement systems which would otherwise be quite impracticable.

Remote sensors operating from the vantage point of space will never replace direct measurements and acoustic remote sensing, because the ocean is essentially opaque to electromagnetic radiation, but satellite remote sensing observing and data relay and platform location techniques should play a substantial role that needs to be systematically recognized and exploited in future programs of ocean sciences research.

Such exploitation requires a developing synergism between specific space-based techniques and missions, on the one hand, with research experiments on important oceanographic problems that benefit from those techniques, on the other. The uncertainties associated with inference from remote sensing, and the difficulties of reconstructing the overall picture from observations in situ imply that the acceptance of new information will come only after a painstaking program of observing system intercomparisons and confidence building case studies. These will require long-range commitment by leading oceanographic scientists and satellite instrument specialists.

Recent experience with sensors on Skylab, GEOS-3, Nimbus-7, and Seasat designed for ocean observation underline the need to include from the beginning explicit planning for validation/control observations, and a substantial data collection, archiving, and distribution effort. To do otherwise would risk not extracting the full advantage of the very large investment in the satellite portion of the system.

New observing tools can transform the basic perception of old problems, but only after their interpretation has been established, necessary corrections have been applied, and calibrations and error estimates are known. There are few applicable standards for "surface truth". Indeed, the space-derived information has fundamentally new characteristics, such as horizontal averaging over larger regions and the feasibility of averaging over longer times (through repeat observations), so that it is attractive as a unique complement to information derived from direct observations. The orderly evolution of composite systems also needs long-range vision and stability of institutional arrangements which transcend the traditional boundaries of funding agencies. The process of assimilation and adjustment to these new opportunities will be a long and sometimes painful one.

The following descriptions of possible research activities are not ordered according to priority, but illustrate a range of important and challenging scientific applications. Many such research objectives could be met by a few satellite flight programs, and there are many ways in which observing systems may be combined on any particular flight. No attempt is made here to discuss such matters.

WIND STRESS

The wind stress at the surface is one of the major driving forces of oceanic circulation. There are no systematic observations with which to test the performance of various models of ocean circulation and ocean response to the atmosphere. Ship observations of wind provide some coverage in regions served by commercial shipping; ship observations, however, are noisy (i.e., may contain undetectable errors) and uncalibrated (e.g., for ship effects) and must be processed carefully before use.

Remote sensing systems mounted on polar orbiting satellites can rapidly and frequently sample nearly the entire earth's surface. Although numerous satellite-borne active and passive systems (altimeters, radiometers, and scatterometers) have been used to measure wind speed, microwave scatterometers have demonstrated a decided advantage due to their ability to measure the vector winds (speed and direction) needed as inputs for oceanographic and meteorological studies.

The use of active microwave systems for the measurement of oceanic winds resulted from the World War II development of radar systems for air defense. Research into the causes of "sea clutter" was conducted in the U.S. and U.K. following the end of that war. Experimental studies in the 1950's and 1960's established an apparent correlation between backscatter at moderate incidence angles and surface wind speed. Extensive series of airborne radar measurements by the Naval Research Laboratory utilizing a four-frequency pencil-beam scatterometer, and NASA/JSC utilizing an airborne fan-beam scatterometer at Ku-band frequencies established an approximate power-law dependence of normalized radar cross section (NRCS) on wind speed. In the early 1970's, NASA developed an improved pencil-beam aircraft scatterometer (AAFE RADSCAT) that was stable and demonstrated good absolute calibration. Field experiments improved and refined the approximate power-law relationship between the NRCS and the wind speed at incidence angles from 20° to 70° . In addition, by obtaining data from circle flights, the relationship between the NRCS and azimuth angle relative to the wind was examined. The amplitude of the NRCS varied with both wind speed and azimuth angle, and the nearly harmonic variation with azimuth angle made it possible to determine wind direction by radar measurements of the same spot of the ocean at two azimuth angles.

A pencil-beam radiometer/scatterometer was flown aboard the Skylab missions SL-2, SL-3, and SL-4 in 1973-77. Since the scatterometer was a single beam, only a single measurement of the NRCS at one value of azimuth angle was obtained from each portion of the sea surface. Nonetheless, these experiments demonstrated that wind speed scatterometry was feasible.

The Seasat-A Scatterometer System (SASS), a four antenna fan-beam dual polarized Ku band system was flown aboard Seasat from June to October 1978. NRCS measurements from the fore and aft beams were combined to give estimates of wind speed with up to four possible directions (unfortunately called "aliases"). This was a major accomplishment. Using SASS data, the first global nearly synoptic maps of

wind speed and direction have been constructed by P. Woiceshyn and others at JPL.

In 1988, the U.S. Navy plans to fly NROSS, an oceanographic satellite which will carry NSCATT, a NASA scatterometer. An additional antenna on each side of the spacecraft (making six in all) will reduce the "alias problem" to an ambiguity of 180° for about 95% of the measurements. The NRCS will be measured with a spatial resolution of 25 km. In the opinion of scientists who are trying to develop better models of the ocean circulation, one of the greatest needs, at present, is a coherent, calibrated long-term data set of surface stress or wind over at least the tropical zone, and preferably over the globe. The Seasat data processing effort and the experience with the validation program indicate what explicit measurements must be made in situ to facilitate the use of the basic observations. The Seasat data offer an enticing glimpse of future routine wind stress/wind velocity observations globally. But can satellite techniques really supply the information with enough ancillary data for its interpretation? Many special studies will be needed to improve the interpretation of scatterometer observations (i.e., to translate the radar backscatter cross section of capillary waves into stress/speed) and also to identify situations in which there might be other physical or biological factors contributing to the backscattered signal, i.e., to identify reliably the various surface effects that influence the backscatter, and to make adequate corrections.

For example, the return signal from a scatterometer depends on the presence of surface structures with scales in the centimeter range; the usefulness of the scatterometer in measuring wind speed depends upon variations in the intensity and density of these structures as a function of wind speed. One kind of structure involves groups or trains of capillary-gravity waves at these scales, generated directly by the wind stress and perhaps to some extent by weak resonant wave-wave interactions from larger components. At low wind speeds, the local amplitude of these waves trains may not vary strongly with wind speed -- they may reach a local saturation quite quickly -- but the fraction of total area covered by them will surely increase with the wind stress. Also at these scales will be found harmonics of longer, short gravity waves which can be relatively sharp-crested and rich in harmonics. Finally, at these scales also will be found Fourier components associated with the deformed profiles of short, breaking waves as well as the parasitic capillary waves on short gravity waves with relatively sharp crests.

Not much is known in detail about the distribution of these structures and the way that this varies with wind stress. Although our knowledge is sketchy, certain simple properties are reasonably well established. First, the density of microscale breaking waves (wavelengths on the order of 10 cm) increases with wind stress but the amplitude at breaking decreases with wind stress. These profiles are substantially deformed during microscale breaking and contain harmonics at the scales responsible for backscattering. The time scales for generation and decay of wave trains at this scale are short, seconds or tens of seconds at most. Short gravity waves, on the other hand, have growth and decay times longer than this so that (as is usual in the ocean) if they are accompanied by a dominant

longer gravity wave these short waves will be substantially modulated in amplitude and also in wave number by the dominant wave. Short gravity waves are pushed close to saturation near dominant wave crests and this results in a substantially increased density of microscale breaking, parasitic capillary waves, and harmonics of the short gravity waves themselves. On the other hand, in the troughs of the dominant wave, the desaturation of the short gravity waves reduces these. These modulations provide the basis of operation for the scatterometer radar. It is this melange of structures that provides the back-scattered return. The return is clearly a function of wind stress (more properly, u_*^2/c , where u_* is the friction velocity and c is a representative phase speed of the structures) but observational results still give a great deal of scatter. Enough is known about these structures to be confident that they are also influenced strongly by the slope of the dominant wave present, ak , or Huang's "significant slope" parameter. This dependence is not taken into account in analysis of scatterometer results in which its influence is ignored.

It is evident that there is a considerable need for further research in this area to establish better the characteristics of these small-scale structures, their distribution on the ocean surface, their appearance in response to short-wave/long wave interactions, and so forth. Experiments and observations are difficult. Conventional probe measurements give very restricted information and are extremely difficult to interpret because of the Doppler shifting produced by the orbital velocities of longer waves. Instantaneous spatial definition of the water surface, even in a restricted region, is a tricky problem.

MESOSCALE VARIABILITY

The most energetic mesoscale oceanic eddies are found in the vicinity of strong currents and probably have their source in instabilities. Over most of the ocean, the level of eddy energy is lower; recent studies have concluded that these eddies could be attributed to direct forcing by the variable winds. Their conclusions require some assumptions about the nature of wind spectra. Scatterometer data will go a long way toward replacing these assumptions with solid data, but some field work will also be necessary to extend spectra to finer time and space scales than a scatterometer will provide.

It has also recently been suggested that a significant part of the eddy field of the open ocean away from strong boundary currents is directly forced by fluctuations in the curl of the atmospheric wind-stress. This conclusion was based admittedly on a few observations which show a significant coherent between a seasonal modulation of atmospheric and oceanic fields and on a theoretical evaluation of the oceanic response to forcing by a fluctuating wind-stress field. The theoretical estimate used a model wind-stress spectrum which extrapolated the observed spectral slope at scales on the order of 1,000 km down to scales on the order of 100 km.

To substantiate these suggestions it is extremely important to determine accurately the space-time structure of the wind-stress over the ocean on eddy scales. This would require a spatial resolu-

tion of approximately 50 km and a time resolution of approximately three days.

OBSERVATIONS OF SEA LEVEL (RADAR ALTIMETRY)

One satellite-based effort that has been under discussion for some time has been a topographical experiment (TOPEX). The radar altimeters on the GEOS-3 and Seasat satellites have proven that observations of the distance between the sea surface and a satellite can be obtained to a useful precision, and that a wide variety of important oceanographic and geophysical information can be derived from such observations. Accurate knowledge of the satellite orbital quantities and of the earth's gravity field is necessary to extract the maximum information from the satellite altimeter observations. These matters, as well as the scientific problems to be addressed by TOPEX, are discussed in detail in the report Satellite Altimetric Measurements of the Oceans, prepared by the TOPEX Working Group, published by the Jet Propulsion Laboratory (March, 1981).

The Seasat altimeter showed a precision of about 10 cm in the measurement of the distance between the instantaneous sea surface and the satellite. It is estimated that this precision has to be increased to something like 2 cm to meet the majority of the scientific goals of TOPEX.

A feature of the altimeter is its ability to provide very important and reliable information on the statistics of ocean waves, in particular the significant wave height, $H_{1/3}$. This ocean surface variable is very important for practical purposes, e.g., for marine operations, and also for the study of the development, propagation, and effects of such ocean events as major storm surges.

The radar altimetry could also provide useful information on the topography of the great continental ice sheets of Greenland and Antarctica, which is difficult to obtain by conventional geodetic leveling.

COLOR SCANNER OBSERVATIONS

The Coastal Zone Color Scanner (CZCS) operating on Nimbus-7 is providing a most intriguing new data set. The CZCS instrument was planned primarily for biological investigation, but there is evidence from the data set now available that the patterns seen in the images also trace dynamic oceanic features of great interest.

The intended purpose is to depict, using several bands in the visible (and bands in the red and infrared for correction purposes), the distribution of biological and other scattering agents (chlorophyll, and organic and inorganic suspended materials). It has been realized that, in addition, important information is made available on oceanic structures, sea-surface temperatures, and gross aerosol distribution.

Global and selected regional assessment of living marine resources is the ultimate objective of satellite ocean color sensors. It is abundantly clear from years of shipboard experience that ocean

areas with the most biota of interest are also areas that are dynamically the most complex and variable. As a consequence, the accurate assessment of living marine resources can benefit significantly from synoptic data that are impractical, or virtually impossible, to obtain from ships alone.

Chlorophyll in the ocean, as an index of phytoplankton biomass, is a fundamental quantity that can be estimated using aircraft and satellite remote sensors. To date, no ecologically significant biological quantity other than chlorophyll has been shown to be quantitatively estimatable by satellite.

Synoptic estimates of chlorophyll are important because phytoplankton variability in space and time is a ubiquitous and important feature of the marine environment. [Phytoplankton variability includes not only the density of organisms but also the number of species present (species abundance) and the distribution of individuals among these species (species equitability), but observations of these factors are hardly accessible to shipboard sensing and are inaccessible to remote sensing.] This variability influences both practical problems associated with sampling and estimating abundance within the environment and theoretical considerations related to the structure and dynamics of phytoplankton ecology. Also, the variability of phytoplankton communities is thought to hold a key to understanding the relative importance of physical and biological factors in structuring the marine food web. In addition, there is evidence that the successful modeling of phytoplankton dynamics, and the predictive linkage of phytoplankton production to higher trophic levels, has so far been limited by a lack of synoptic data and limited sampling strategies.

A fundamental problem in marine ecology is to establish both the spatial and the temporal scales in which fundamental physical and biological processes occur and to sample the environment accordingly. Ships, aircraft, and satellites provide alternative, and complementary, strategies for sampling the environment. For example, if chlorophyll concentration, as an index of phytoplankton biomass, is the variable under investigation then ship, aircraft, and satellite "platforms" offer the opportunity to obtain diverse, and often mutually exclusive, experimental information. Shipboard data provide continuity with conventional oceanographic research techniques, can be relatively accurate, can include both vertical and horizontal measurements, but are comparatively limited in both space and time. Chlorophyll data from aircraft systems provide rapid spatial coverage of regional areas, can include both vertical and long-track measurements, can be relatively precise (however, accuracies are the subject of ongoing research), but are limited by the logistics of aircraft, and provide linear (as distinct from areal) coverage. Satellite chlorophyll imagery can provide worldwide coverage of cloud-free areas, can provide repeated routine coverage of regional areas (including those areas that are far from our oceanographic research institutions), but are relatively less accurate without concurrent ship or aircraft data, are limited by cloud coverage, and require more complex image and data processing. The key point is that the living marine resources are unlikely to be assessed adequately without the synoptic perspective, the quantitative areal data, and the quasi-

continuous temporal coverage provided by remote sensors.

Some early use of the Nimbus-7 color images has shown very promising application to the studies of the food web and to illuminating the relationships between the planktonic distribution and the development of young fish. For example, off the California coast, such information has been used effectively to study plankton distribution and the distribution of anchovy spawning. More detailed studies of these kinds would clearly be important contributions to biological oceanography.

DATA COLLECTION AND LOCATION SYSTEMS (DCLS)

A DCLS (Argos) was implemented on the NOAA operational satellites for the Global Weather Experiment, 1979, in cooperation with French colleagues who supplied the hardware and undertook the data processing. This joint arrangement is expected to continue through at least the mid-1980's. It must be remembered that the Argos system was designed primarily to track constant-level balloons accurately for the Global Weather Experiment, 1979; its applicability to other moving platforms was a most useful bonus, but the Argos system has some limitations with respect to other platforms that make it desirable to consider what improvements might increase its support to ocean sciences direct and remote sensing programs. For example, the DCLS for ocean sciences must be able to view a larger number of platforms that Argos does, up to many hundreds of platforms simultaneously, or else some regional projects being considered will not be able to use sufficient numbers of observing sites. The data rate should be increased, but not at the price of more power, so that considerable stored data can be relayed over one pass. Finally, it would be most useful for extensive oceanographic observations if the DCLS design could permit a relatively simple and inexpensive electronic package on the platform, to reduce the unit cost and thus encourage use of larger numbers of observing platforms.

Underwater telemetry can usually be accomplished by relatively low-power acoustic transmission, but long ranges impose severe constraints on batteries, weight, and overall system lifetime. Staging to satellites through a surface intermediary at a known location is an attractive alternative to present techniques, but only provided that a reliable and available satellite link is assured for the foreseeable future. The practicability of large-scale deployment and the scientific utility of drifting buoys was demonstrated in the Global Weather Experiment (GWE), 1979. The buoy program for the GWE was invented and implemented for meteorological purposes. The data fields, however, are also useful per se to define some of the oceanic circulation. The success of the program has stimulated new technical efforts to develop drifters of several types into instruments of broader oceanographic use -- better sensors, reliable thermister chains to obtain temperature profiles, subsurface flotation with tracking and data relay via the sound channel.

An exciting research prospect, feasible in the second half of the 1980s, is exploration of ocean circulation on a global basis using drifters both as tracers of horizontal advection and as platforms from which scalar properties are measured. The objective of

this exploration would be development of worldwide maps of statistical indicators of the general circulation, such a mean flow, eddy energy, and reynolds stress, and of lateral mixing as indicated by drifter dispersion. Eventually, it will be necessary to map variability in various frequency bands at various depths on a global basis. Nearly continuous satellite positioning and data telemetry permit intensive measurement of the upper ocean on a global basis at a reasonable level of effort. Present methods of communicating with drifters at depth are more costly than is ultimately desirable. This will probably limit the use of very frequently positioned subsurface drifters to regional studies in the near future. However, for describing the mean general circulation, including lateral eddy dispersion, the use of satellite-positioned drifters may permit global coverage at a reasonable level of effort.

Assuming that buoy development will proceed as planned (a substantial project is now under way that is supported by NASA, NOAA, and ONR, and that involves collaboration by a group of researchers as well as sensor and buoy engineers) and assuming that a suitable DCLS is available, a substantial program would be feasible to produce worldwide maps of statistics of ocean circulation for four frequency bands: band (i), one cycle per two to 40 days, which is a spectral band containing the results of direct atmospheric forcing; band (ii), one cycle per 40-150 days, the temporal mesoscale; band (iii), one cycle per 150 days to the length of a feasible program, say three to five years, which contains the secular climatic variability scale; and band (iv), the long term mean, representative of the general circulation. All buoys would include sensors for temperature and pressure, and surface drifters could profile down to 100-200 m. Drifters would be distributed at the surface, in the thermocline, and at an abyssal level, say 3,000-4,000 m. Satellite DCLS or acoustic relay, or a combination, would be used.

SUMMARY

Satellite-borne observing and communication systems offer a variety of techniques to observe and map qualitatively, with high resolution, many oceanic features of importance, and to make measurements that are the basis of quantitative information. These techniques, however, are limited essentially to surface manifestations, and hence there will continue to be a strong need for direct measurements using ships, buoys, moorings, etc., as well as for subsurface remote sensing by acoustic methods.

There are several large scale national and international experiments being planned in the context of the World Climate Research Program (WCRP) for which satellite techniques offer valuable and in some cases unique capability: a large scale study of the heat budget in the North Atlantic; a tropical ocean-atmosphere experiment (TOGA) with emphasis on the Southern Oscillation; and a World Ocean Circulation Experiment (WOCE) for which TOPEX and extensive use of satellite tracked drifters would offer unique contributions.

For any large scale ocean circulation study, it is imperative that we obtain both the global surface wind stress field and the global dynamic topography field: these fields are the necessary

boundary conditions for any ocean general circulation models that may be developed in the near future. TOPEX, NROSS, and the European Space Agency's ERS-1 seem to be the ripest satellite techniques for early implementation.

For the decade of the 1990's, NASA is conducting a study for a comprehensive Earth Observation System (EOS, formerly called System-2). EOS will consist of four parts:

- 1) A set of instruments in low, sun-synchronous Earth orbits dedicated to long term remote sensing of various global phenomena of land, ocean, and atmosphere,
- 2) A global set of land, ocean, and atmosphere in situ instruments to complement the orbiting instruments,
- 3) An international community of scientists who perform the research by analyzing the information gathered by 1) and 2) and controlling their operation, and
- 4) A data communication/computation network that collects the data from 1) and 2) and any required data from other sources (such as operational Earth sensing satellites), operates on these data to increase its information content, stores this information in various data bases and archives, and distributes the information to 3).

The intent of this system is to be interdisciplinary since most geophysical processes involve exchanges occurring at the atmosphere-ocean or atmosphere-solid earth interfaces.

During the past decade, remote sensing of the oceans has been demonstrated to be feasible. It is now time to implement routine satellite observations during the remainder of this century. The processes will be difficult, but the rewards enormous.

N84 27264

ESA ACTIVITIES IN THE USE OF MICROWAVES
FOR THE REMOTE SENSING OF THE EARTH

D. Maccoll
European Space & Technology Centre (ESTEC)
Noordwijk, The Netherlands

ABSTRACT

This paper discusses the programme of activities under way in the European Space Agency (ESA) directed towards Remote Sensing of the oceans and troposphere. The initial project is the launch of a satellite named ERS-1 with a primary payload of microwave values in the C- and Ku-bands. This payload is discussed in depth. The secondary payload include precision location experiments and an instrument to measure sea surface temperature, which are described. The important topic of calibration is extensively discussed, and the paper continues with a review of activities directed towards improvements to the instruments for future satellites. Some discussion of the impact of the instrument payload on the spacecraft design follows and the paper concludes by emphasizing the commitment of ESA to the provision of a service of value to the ultimate user.

1. INTRODUCTION

The European Space Agency has initiated a Remote Sensing programme with several elements. The major element is the launch of a satellite dedicated to remote sensing of the oceans (ERS-1) in 1987. It is planned to follow this launch two years later with a second (ERS-2) which will be similar to the first. Later satellites in the 1990 decade will be considerably larger and likely dedicated to Land Observation. In parallel with the satellite programme there is an existing data dissemination network Earthnet which currently handles Landsat data but has also disseminated Seasat data and will of course be used for the ERS-1 data. There is also planned a series of campaigns, on-ground and aircraft which will be used to confirm the models and assumptions behind the instrument design, to aid the in flight calibration of the instruments and to promote user interest and understanding.

2. ERS-1 PAYLOAD

The payload comprises three primary instruments: a Synthetic Aperture Radar (SAR), a Scatterometer, and a Radar Altimeter (R.A.). The first two are combined in a single microwave package operating in C-band with three operation modes; full SAR imaging, small area SAR imaging (wave mode), and scatterometer. This C-band package is known as the Active Microwave Instrument (AMI).

2.1 AMI

The AMI comprises four antennas, one SAR antenna and three wind scatterometer antennas, a high power transmitter and low noise receiver common to all modes, and various low frequency, low power components exploit commonality between modes as far as possible. The SAR antenna is 10m x 1m, and the two fore and aft looking scatterometer antennas are 4m x .35m. The central scatterometer antenna is not deployed and is 2.3m x .35m. The high power amplifier is a pulsed tube with 4.8kW peak power, with an average power varied by changing the pulse length and repetition frequency.

In the full SAR imaging mode this instrument will have a swath width of 80 km, and will have a ground resolution of 100m and radiometric resolution of 1dB at -18dB backscatter coefficient. It will be possible to produce images with 30m spatial resolution, but the radiometric resolution will be degraded since there will be few "looks" available. This mode will only be used when the spacecraft is within sight of a ground station since the data rate (100 Mb/s) is too high for onboard storage to be feasible. Also the D.C. power requirements in this mode are too high for continuous operation throughout the orbit. The D.C. available will allow approximately 10% operation which is compatible with the visibility from the planned ERS-1 ground stations, but much of that time the SAR will be imaging land.

Over the oceans the SAR will be used in a low power mode (100W average R.F.). This wave mode will be interleaved with the wind mode which is discussed later. In the wave mode the SAR is operated with a reduced pulse length at the full peak power, thus the energy per pulse and the average RF power are reduced while operating the power amplifier at its optimum peak power. The wave mode is operated for approximately 1.4 seconds every 14 seconds which allows imaging of a 5 km strip each 100 km. The radar returns are sampled over a short part of the total return sufficient to image 5km out of the available 80km swath. Thus only the data from a 5km square patch is retained, and the data rate is sufficiently reduced for storage on a tape recorder, and global coverage of the oceans can be achieved. The objective of this so called wave mode is to measure ocean wave spectra, but the specifications have been expressed in terms of image spectra. It is clear that peaks in the two dimensional spectra correspond to ocean wave and swell patterns, however the modulation transfer function between ocean wave and image spectrum is not well developed so the ocean characteristics cannot make a sound foundation for the instrument specification. In particular there is some doubt whether wave trains in certain directions or under certain wind conditions will appear at all on the image spectrum.

The wind mode is far better understood, the basic concept having been proven on SEASAT. ERS-1 however works at C-band where though the backscatter coefficient is higher than at Ku band, the modulation by wind speed and direction is less. The principle of operation is based on the fact that the backscatter coefficient from a wind disturbed sea is dependant on both wind speed and direction with respect to the radar beam. Since there are two parameters to be measured two measurements must be made and this is done by looking at the same patch of ocean from two different parts of the orbit. Unfortunately the experience of SEASAT showed that there are ambiguities in the extraction of the wind speed and direction from the two measured backscatter coefficients, due to the inherently noisy measurement and the shape of the modulation curve which has bigger change between up-wind and cross-wind than between up-wind and down-wind. In order to help resolve these ambiguities the ERS-1 instrument includes a third measurement. Two measurements are made looking at 45° forwards and 45° aft, and the third measurement is made looking abeam.

The selection of these three look directions was made after extensive analysis and simulation taking account of noise, speckle, model uncertainties, and the range of incidence angles. The choice of one beam looking directly sideways lead to another change in implementation with respect to SEASAT: the doppler filterbank approach of SEASAT clearly will not work on the side looking beam since this beam looks almost exactly down the zero doppler line. The alternative approach of range gating had been under consideration and the need for a side-looking beam confirmed the choice of range gating. Since these measurements require both high accuracy and good calibration between beams the possibility of using a mixed system of two doppler and one range gated beam was not considered. In order to ease the on-board frequency tracking and also to ensure the full wind swath of 400 km can be imaged the satellite will be steered in yaw to keep the side looking beam on the zero doppler line including the effect of earth rotation.

2.2 Radar Altimeter

The ERS-1 Radar Altimeter is designed to have the same performance over the oceans as the SEASAT Altimeter. However there are improvements in two important areas: the instrument is fully redundant within approximately the same mass and power envelope, and the acquisition and tracking loops have been improved.

A trade-off peak power requirement and chirped pulse length taken together with an investment in surface acoustic wave (SAW) technology has allowed the use of a power amplifier with a peak power of 50W. Since the mass of both the tube and the power conditioner are closely linked to the peak power this relatively low peak power has effected a substantial reduction in mass and therefore a redundant system can be used. Additionally an existing space qualified tube and power conditioner can be used with some small modifications thus saving the cost and problems of space qualifying a new amplifier. Associated with this power level is a long pulse of 20 ms. SAW technology development has resulted in a single component generating the wideband (330 MHz) long pulse with a time bandwidth product of 6600.

The acquisition and tracking are both done using digital technology taking advantage of more powerful microprocessing (8086) and other processing elements than were available in the mid 1970's when the SEASAT instrument was designed. In the tracking mode the level, the position and the slope of the leading edge are followed and the backscatter coefficient, the altitude and the significant wave height can thus be estimated. The instrument uses a deramp technique in which the signal return is mixed with a delayed replica of the transmitted signal, and differences in height are converted to a frequency shift. The deramped output is then filtered using a digital Fourier transform to give the return signal profile. This profile is averaged over fifty pulses and used to provide the inputs to the tracking loops. In the acquisition mode the transmitted pulse is unmodulated, and the leading edge of the return is detected with sufficient accuracy to be able to switch to a modulated pulse form. The possibility of detection of 95% is achieved after 50ms which is significantly better than SEASAT which could take 5s to reacquire after losing lock, and over some sloping surfaces even longer.

Over the oceans the results from the SEASAT altimeter were good though occasionally it lost lock (probably over severe weather systems). The ERS-1 RA should equal this performance. Over ice the SEASAT RA often lost lock and it is expected that the improvements in the acquisition and tracking of the ERS-1 instrument will permit a more consistent coverage.

2.3 ERS-1 Secondary Instruments

ERS-1 will also carry three other instruments which will support the altimeter, namely a Laser Retro Reflector (LRR), an Along Track Scanning Radiometer with two nadir pointing microwave channels (ATSR/M), and a Precision Range and Range Rate Experiment (PRARE). The LRR is entirely passive and will be used in conjunction with ground based laser tracking stations for accurate (10 cm) orbit measurement, and thus enhance the ability of the R.A. to measure mesoscale sea eddies. The ATSR/M is principally designed for sea surface temperature measurements, but the microwave channels will be used for atmospheric water vapour corrections to the altimeter measurement. The PRARE is a two frequency (S- and X-band) transponder system which in conjunction with a network of ground stations will be used for precision location experiments. The second frequency allows to correct for ionospheric effects. As with the LRR this experiment will also enhance the R.A. capability.

2.4 Calibration

The instruments described above will all certainly produce results: images, wind fields or profiles. It is an important aspect of the ERS-1 programme that these results will be properly calibrated in the sense that there is an assurance that the product meet certain minima in accuracy and resolution. The calibration approach of the AMI modes are the most developed, of the R.A. less so.

ORIGINAL PAGE 19
OF POOR QUALITY

The final requirement is for calibration of the geophysical product, for example wind speed or significant wave height; but an important intermediate step is the calibration of the engineering product, backscatter coefficient or output from the slope tracking loop respectively. To achieve this engineering calibration all instruments are designed with internal calibration loops which, bypassing only the antenna and some of the passive output networks, provide an accurate measurement of the levels and gains of the onboard components. To include the impact of the antenna some ground sites will be provided with artificial targets which will permit calibration of the complete instrument. For the SAR modes these targets may be passive corner reflectors which can be positioned in an area of low backscatter coefficient and sized so as not to overload the receiver. For the scatterometer mode a passive target would have to be enormous to stand out against the fixed area of $25 \times 10^8 \text{m}^2$. Therefore an active target is being developed which amplifies the received radar signal and retransmits it with a frequency shift. The reason for the frequency shift is to separate the artificial return from the natural return of the surroundings, and thus to establish the proper level at the input to the radar receiver.

For the Radar Altimeter the problem of creating an artificial target is more difficult, since the RA will have to acquire and track, but the target will only be in the beam a few tenths of a second. Some work is being done on a "Return Signal Simulator" which will be used for on ground testing prior to launch. This will accept as input a radar pulse and generate a return with the shape, duration and spectral content that would be expected from a sea surface. As stated above this is being developed for on ground use prior to launch but it could form the nucleus of an artificial target for use in flight.

The geophysical calibration starts when the engineering calibration is complete. Essentially it will comprise campaigns of ground truth measurements possibly coordinated with aircraft underflights. In advance of this campaigns are planned to develop and verify models and information extraction algorithms. The first of these took place in 1981 using an aircraft SAR at X, L, and C bands. A large number of users participated but the main interest of ESA was the calibration exercise using corner reflector arrays at two sites. The next will be specifically dedicated to C-band scatterometer measurements and will take place early in 1984. Preliminary results tend to conform the models that have been used in defining the AMI instrument.

3. INSTRUMENTS FOR FUTURE MISSIONS

The instruments for ERS-1 are now well developed and receive substantial resources from industry and ESA to build, test and fly. However there are areas in which improvements can be conceived, and the ESA activities include basic technology development for next generation instruments. For the SAR the primary limitation in performance due to the instrument is the swath width. To achieve full equatorial coverage requires five hundred orbits or almost exactly one month.

The evolution of many oceanic and climate processes occurs in days so a monthly report cycle is too long to follow the developments of these processes. Of course a complete global coverage at a resolution of 30 or 100 m would swamp most users with data, nonetheless the ability to image particular areas frequently is highly desirable and some substantial improvements may be made by investigating the possibility of overcoming the ambiguity constraints. The first step is a study of the possibilities including antenna modifications, multibeam transmit and receive, squint beams, and novel pulse modulation techniques. Following this evaluation the more promising techniques will be subject to a detailed analysis and possibly breadboarding.

The scatterometer and altimeter are both required to operate over the whole oceans which cover about 70% of the earth surface. Minimising the power consumption is thus highly desirable. One technique which has been proposed for the scatterometer is to abandon the fixed fan beam concept and use a scanned beam, and a very elegant way of scanning the beam is by changing the frequency of a frequency sensitive antenna. The bandwidth of the scatterometer signal is very small, a few hundred kilohertz including the doppler shift. By suitable design of the antennas the beam may be scanned over the full 40° range with frequency shifts of several megahertz. By switching the full beam at the required pixel there is a significant saving in required transmitted power. Additionally the shape of the antennas, which using the conventional technique are long and narrow, became nearly circular which can relax the accommodation position. This topic is the subject of future work which should lead to a more economic scatterometer design for future missions.

The radar altimeter is characterised by a very low duty cycle (2%). Thus a power amplifier capable of delivering 50W rf power is used to deliver one watt average. It is planned to do some technology work on long pulse systems, at both instrument and component level with the objective of designing an altimeter with a peak power low enough to use solid state amplifiers. As far as solid state devices are concerned a pulse length of 20 μ s is the same as c.w. since the device thermal time constants are much shorter than this. Currently it is just within the state of the art of FET technology to produce 1 watt rf power, and exploiting this level in next generation altimeters is expected to simplify the front end design considerably.

The primary instruments of ERS-1 are active radars: the only passive microwave instrument is the radiometer in the ATSR/M, which has been included as an aid to the altimeter. Passive microwave radiometers can produce results which have an autonomous value. An Imaging Microwave Radiometer was studied to Phase A level as a candidate instrument for ERS-1 but was not included. Like other microwave instruments it has a great importance for all weather, night and day synoptic global coverage. This type of instrument is not particularly demanding in terms of microwave technology: it is big! Future work by ESA will include developing compact technology for the microwave receivers and developing instrument and antenna concepts suitable for large antennas, up to 10m diameter, and pushbroom systems.

ORIGINAL PAGE IS
OF POOR QUALITY

The topics of this symposium include the troposphere: the instruments described so far are directed towards measurements of the oceans and cryosphere, and the intervening atmosphere is an embarrassment! The imaging microwave radiometer does contain higher frequency channels whose main objective is to allow corrections to the low frequency measurement errors which are due to the atmosphere. In the inversion process useful information about the atmosphere is also extracted. Recognising the value of atmospheric research ESA is also doing technology development for higher frequencies in the millimeter and submillimeter wave bands. The latter is mainly driven by astronomy needs, but the millimeter wave work is driven by the needs of atmospheric research.

4. SPACECRAFT REQUIREMENTS

As stated before the spacecraft resources required to support the various instruments are large. Since all these instruments are complementary each supporting the others in their contribution to earth and atmospheric observation, there is a pressure to include as many as possible. The SPOT platform used for ERS-1 has very little growth capability: the additional resources required by just one more instrument would require such modifications that there would be in effect a wholly new platform.

ESA has been studying in house the possible configurations of a large platform. This conceptual platform for an Advanced Earth Research Satellite (AERS) should exploit the full capability of the ARIANE 4 launcher. It would have accommodation for double sided SAR with a total payload mass of 2 tonnes and end of life d.c. power of 7.6 kw from the solar arrays giving a possible 5 kw available to the instruments. A topic rarely mentioned is the problem of data dissemination: the ERS-1 SAR is as much constrained by the 100 Mb/s data rate limit as by any other resource limitation. Future AERS will need a data rate in the region of 500 Mb/s and will require also a data relay capability in order to ensure the worldwide availability of the data. Data relay experiments are planned between two ESA platforms, EURECA and OLYMPUS, which may lead to the implementation of data relay on AERS.

CONCLUSION

This paper has addressed the activities under way in ESA in the field of Remote Sensing of the Oceans and Atmosphere, and attempted to demonstrate the commitment of ESA to providing the instruments required to explore this field form space. This is a complete programme including the satellite and its instruments and ground support, and the data dissemination as the nucleus but also including supporting campaigns of ground and aircraft experiment, and studies for follow-on missions with advanced spacecraft and a range of advanced instruments. While ESA does not undertake scientific and applications analysis of the data products, ESA is very concerned that the product is of maximum value to the user community, and therefore has from the inception of the project involved the users in the definition of the programme and the instruments. This involvement will continue through the development, manufacture and launch of ERS-1 and it is hoped that this cooperation will result in the product supplied being of maximum value to the oceanographic and atmospheric user communities.

SPECTRASAT: A CONCEPT FOR THE COLLECTION
OF GLOBAL DIRECTIONAL WAVE SPECTRA

Robert C. Beal
The Johns Hopkins University
Applied Physics Laboratory
Johns Hopkins Road
Laurel, Maryland 20707

ABSTRACT

The synthetic aperture radar (SAR) imagery from Seasat revealed a rich tapestry of backscatter patterns from the surface of the ocean. Although still far from being fully understood, these patterns occurred on nearly all spatial scales accessible to the SAR, that is, from its spatial resolution of 25 m to its full swath width of 100 km. Furthermore, the backscatter signatures appear to reveal a large variety of atmospheric and oceanic processes that occur above, at, and below the ocean surface. Proper interpretation of these signatures of varying scales with respect to their underlying geophysical causes is a major objective of SAR ocean research. Even now, however, it is clear that SAR offers a unique means to monitor wind and waves over global scales. A properly designed, configured, and complimented orbiting SAR system should yield substantial improvements in operational forecasts vital to marine activities. Since wind and wave information can be optimally extracted in the spectral domain, the name "Spectrasat" is proposed for this global collection scheme.

1. GEOPHYSICAL SIGNATURES IN SAR OCEAN IMAGERY

1.1 Background

Any geophysical process which directly or indirectly influences the short 30 cm waves on the ocean surface will produce a signature in SAR imagery (Beal, DeLeonibus, and Katz, 1981; Fu and Holt, 1982). Figure 1 is a particularly vivid illustration of the variety of signatures evident in a single 2 minute SAR pass (pass 1339, 28 September 1978). Some of these effects are easily visible in the spatial domain; others are much more obvious in the spectral domain. Moreover, some signatures are instantaneous expressions of the wind field, while others are the results of winds occurring many days previously and thousands of kilometers distant.

1.2 A Seasat Data Base

Figure 1a, derived from an examination of Seasat scatterometer wind fields over a several day period, shows the spatial and temporal locations of two separate storm systems as they evolved during the days just prior to SAR pass 1339. Both of these storms spawned wave systems emanating from their centers, and propagating generally toward the west, i.e., toward the SAR overpass region (Beal, Monaldo, and Tilley, 1983). The southernmost "primary" storm was the more intense of the two, and reached peak winds in excess of 20 m/s and peak

ORIGINAL PAGE 19
POOR QUALITY

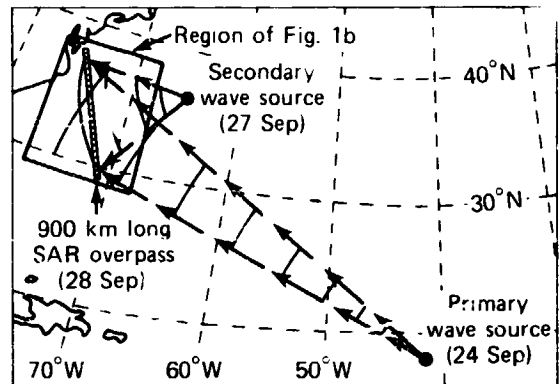


Fig. 1a Sources of wave energy in the North Atlantic, 28 Sep, 1978.

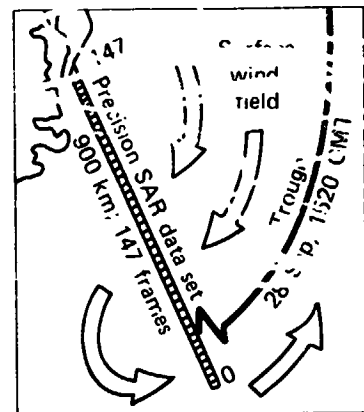


Fig. 1b Location of 900 km long SAR pass, divided into 147 6.4 km squares.

Fig. 1d SAR imagery at the shelf edge.

Fig. 1c Northernmost 300 km of SAR imagery.

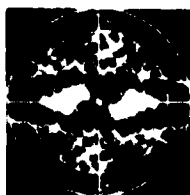


Fig. 1e Typical wave spectrum. Outer ring corresponds to 50 m wavelength.

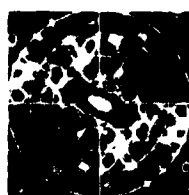


Fig. 1f Typical wind spectrum. Outer ring corresponds to 400 m wavelength.

Fig. 1 Various types of signatures in SAR imagery.

(significant) wave heights of about 6 m (as measured by the Seasat altimeter) before subsiding. As this wave system approached the East Coast of the United States, the average wavelength was ~ 200 m, and the wave height had diminished to about 0.75 m.

Meanwhile, also from an examination of previous scatterometer wind fields, a somewhat weaker, but spatially and temporally more proximate "secondary" storm had developed about 1000 km from the impending 900 km long SAR overpass. This wind field barely reached 15 m/s, and spawned waves of height 2 to 3 meters. Since the secondary wave source was so much closer to the SAR overpass, however, the resulting wave field experienced rapid spatial evolution.

Figure 1b illustrates the area in the immediate vicinity of the SAR overpass, which occurred as waves from both sources were propagating through the region. Figure 1c shows the northern third of the SAR overpass. The displayed imagery is only 40 km wide by about 300 km long, and was collected in less than 1 minute, but contains much information on wind, waves, and currents.

1.3 Surface Current Boundaries

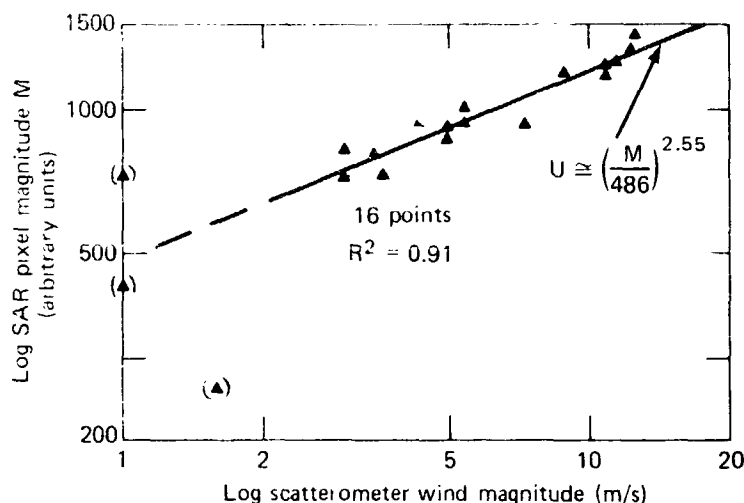
The Gulf Stream North Wall, as well as a number of mesoscale eddies, are apparent as quasi-linear features just above the center of the imagery. These small eddies are shown in greater detail in Figure 1d. Current shear boundaries apparently excite the 30 cm waves to provide a high contrast signature in the SAR imagery, particularly at lower (2-5 m/s) wind speeds.

1.4 Surface Wind Magnitude

The overall brightness of the SAR image is generally correlated with the amplitude of the 30 cm surface waves, which in turn responds directly to the local wind. This relationship is most clearly evident at very low wind speeds, where the 30 cm waves are effectively extinguished. Although the amplitude of these waves may not continue to increase indefinitely with wind magnitude, there is good evidence (from simultaneous aircraft and scatterometer measurements) that the local average brightness (or radar backscatter) of Figure 1c is strongly correlated with surface wind magnitude up to 13 m/s. Figure 2 shows the correlation between scatterometer-deduced winds and SAR backscatter over an entire 900 km pass length, of which Figure 1c represents the northern third.

1.5 Surface Wave Fields

For long (50-500 m) surface waves, there is an apparent periodic spatial modulation of the local wind-generated 30 cm waves. The modulation may be much less than the noise on the scale of a single 25 m resolution element, but the spatial spectrum of the wave field is generally well-behaved and homogeneous over tens and even hundreds of kilometers. Extensive averaging over both wavenumber and space, therefore, can reduce a very noisy background by as much as a factor of 20 or 30, revealing extremely subtle modulations of only a few percent. For example, Figure 1e illustrates the extensively



ORIGINAL PAGE IS
OF POOR QUALITY

Fig. 2 SAR backscatter magnitude versus scatterometer winds.

spatially and spectrally smoothed spectrum of a portion of Figure 1d. The noise has been reduced to the point where the primary (200 m wavelength) and secondary (100 m wavelength) systems are clearly distinguishable, even though the significant waveheight of each system was under 1 m in this portion of the pass. With appropriate (and, in the future, perhaps adaptable) filtering, the spatial evolution of the dominant vector wavenumber can be tracked with mean residuals of only a few percent. Figure 3a shows the result of near-optimal tracking of the primary wavenumber over 900 km, clearly showing deep-water dispersion, refraction in the Gulf Stream, and shallow water wavelength shortening. Moreover, Figure 3b shows subtle perturbations of the wavenumber in shallow water which reveal the presence of subsurface mounts and depressions. The angular evolution of the wavenumber accurately locates the (previous) position of the wave generation sources.

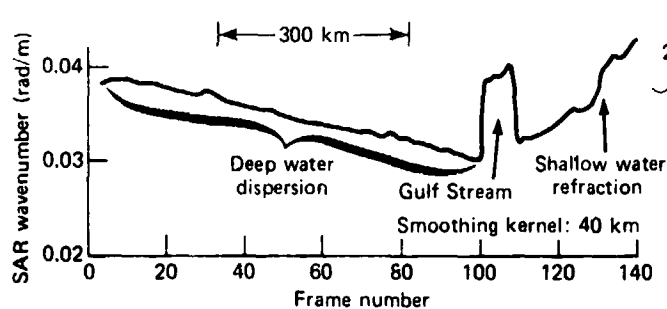


Fig. 3a Entire 900 km pass

Fig. 3 SAR wavenumber refraction in the presence of currents and bottom topography for pass 1339.

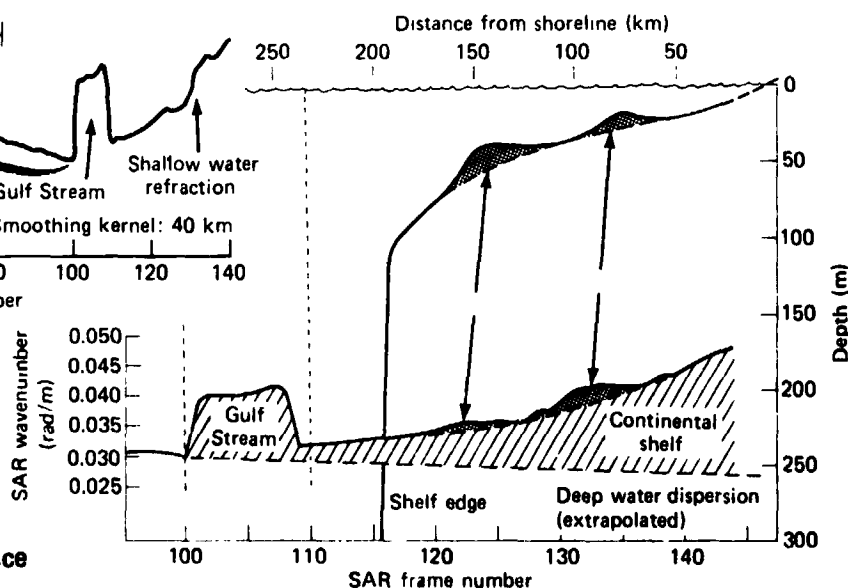


Fig. 3b Northernmost 300 km

1.6 Surface Wind Direction

The horizontal wind field at the surface of the ocean is neither temporally nor spatially homogeneous. In particular, as the horizontal component of the wind stresses the surface, it produces large streaks of higher backscatter, aligned with the local wind direction, and having spatial scales of a few hundred meters to a few km. At the higher wind speeds, and when the water surface temperature exceeds that of the air, elongated atmospheric convection cells can be established, with their long axes aligned with the wind. Both phenomena exhibit asymmetric spatial spectra which can reveal the direction of the local wind, when properly processed. A typical example of such a wind direction signature is illustrated by the asymmetric shape of the spectral energy bundle about the origin of Figure 1e, or its higher wavenumber resolution equivalent in Figure 1f. In both cases, the minor axis is closely aligned with the best estimate of the local wind direction from the scatterometer. Figure 4 summarizes the accuracy of this technique for wind direction estimation with respect to scatterometer estimates. On this pass at least, the residual directional deviations from a smoothed estimate of the local wind field are approximately equal when determined from either the scatterometer or the SAR. Moreover, the SAR may be yielding an estimate of the fine scale spatial spectrum of the wind field, which could be useful in the understanding of scatterometer wind field estimates.

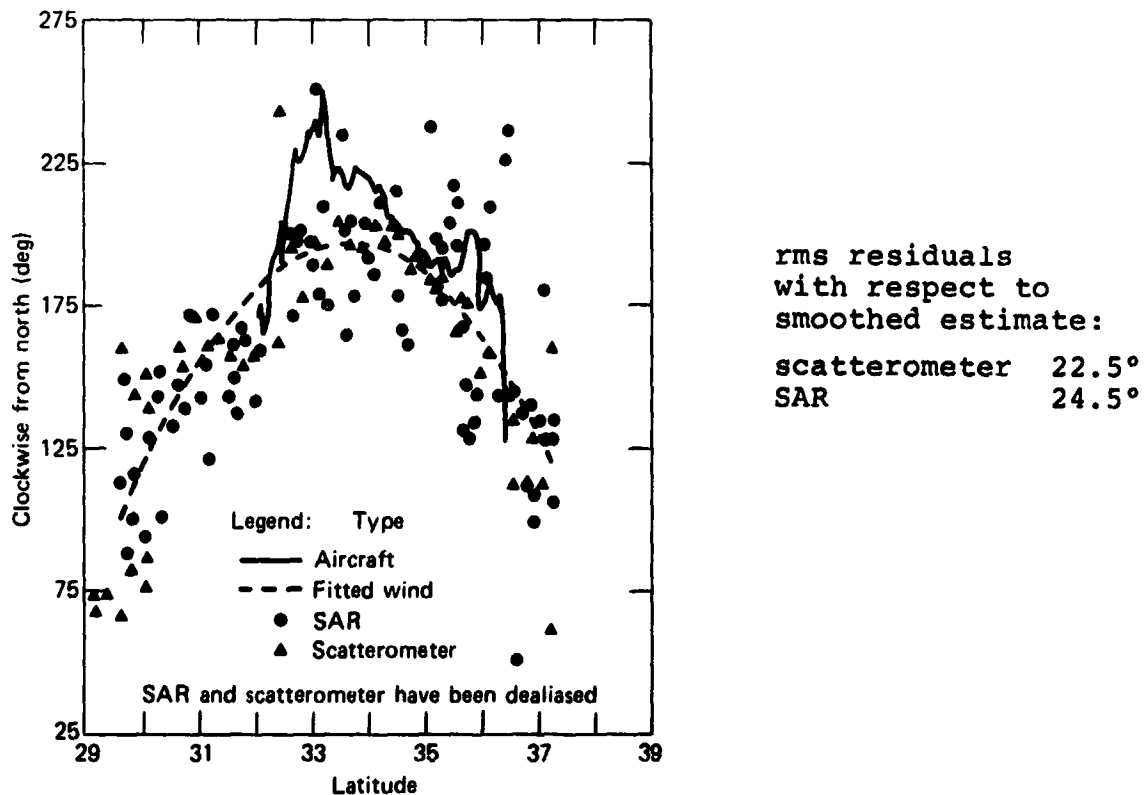


Fig. 4 Various wind direction estimates.

2. SOME PRACTICAL PROBLEMS AND CAVEATS

2.1 General Comments

As the above evidence clearly demonstrates, spaceborne SAR possesses a fascinating ability to reveal current boundaries, spatially evolving directional wave spectra, and even the magnitude and direction of the local wind field. Prior to Seasat, there existed no satisfactory theory which would have predicted these results; indeed, even now the experimental evidence is forcing the theoretical advances. In spite of these encouraging results, however, we must still admit to a number of fundamental limitations in our present state of knowledge.

2.2 Doppler Smear

One of the more controversial aspects of SAR concerns its limitations for imaging moving ocean waves (see, for example, the Journal of Geophysical Research Special Issue on MARSEN, 1983). Being a Doppler measuring device which implicitly assumes a stationary target for precise focusing and location, a randomly moving ocean wave presents a particular challenge. In view of the results shown in Figure 3, however, this limitation is not necessarily devastating. The Doppler motion is most severe for short waves travelling in the direction of the spacecraft; these waves are effectively smeared, or filtered, in the SAR spectrum. The effect can be seen quite clearly in Figure 1e as an absence of energy at the higher spatial wave-numbers. Fortunately, in the pass discussed above, both the primary and secondary wave systems are within the "azimuth passband" of the SAR.

In future SAR systems, the only practical way of increasing the azimuth passband (which is narrowest at high sea states) is to reduce the altitude of the spacecraft. A factor of four reduction over the Seasat altitude of 800 km may be feasible with active drag compensation; such a reduction could effectively eliminate the azimuth smear problem. The upcoming Shuttle Imaging Radar experiment (SIR-B) will offer an excellent opportunity to check this hypothesis.

2.3 Spatial and Temporal Coverage

Data rates from spaceborne SAR can be many hundreds of megabits per second; the problem is particularly aggravated by requirements for wide swaths and high resolution. Construction of a synthetic aperture in real time, on board the satellite, has been consequently frustrated by both the overwhelming data rates and the required size of the processing and storage arrays. Yet, for both wind and wave spectra, especially in deep water, the actual information rate is trivial - perhaps a kilobit per second. Moreover, there is good evidence that reliable wind and wave spectra can be generated over spatial dimensions of under 10 km. One might therefore envision a SAR system sampling the global wave field very much as the Seasat scatterometer sampled the global wind field, that is, with 500 km equatorial spacings between tracks, and repetitive coverage every three days. Although such coverage is less than ideal for detailed storm tracking, it is at least consistent with the scatterometer coverage,

and is probably the best that can be expected with a single satellite.

2.4 Auxiliary Data Sources

Probably the primary rationale for orbiting a narrow swath SAR would be for the collection of global wave spectra. By themselves, these spectra would be of little value, but as a supplement and periodic update to a global wind-wave forecast model, the impact of actual measurements of directional spectra could be revolutionary. For example, present wave generation models in operation around the world are in gross disagreement with respect to the directional properties of waves generated from even the simplest wind fields (c.f., the Sea Wave Modelling Project "SWAMP", in press). There are no good data on the large scale directional evolution of wind-driven waves, and therefore no valid criteria for the acceptance or rejection of particular models.

This dilemma could be solved if there existed a comprehensive set of evolving winds, together with their resultant evolving (directional) waves. The SAR, although capable of precisely tracking the magnitude and direction of the dominant wavenumber, has generally proven elusive with respect to an estimate of the total wave energy. The problem is aggravated both by the Doppler smear effect present in existing data, and by the absence of accurate and comprehensive independent estimates of wave energy. Concurrent altimeter estimates of significant wave height will probably be of value in calibrating the SAR relative directional spectra in an operational configuration.

3. SPECTRASAT: ITS MAJOR CHARACTERISTICS

3.1 Motivation for Proposal

"Spectrasat" is an initial attempt to define the major properties of a SAR satellite specifically designed for the global collection of ocean wave spectra. Although the initial version of Spectrasat can be quite explicit, many of the design parameters are tentative, pending an analysis of SIR-B results in 1985 and 1986. Nevertheless, it is important even now to define a "strawman" version of Spectrasat, both to stimulate debate, and to aid in the design and analysis of future SAR ocean experiments.

3.2 General Characteristics

Spectrasat should be a low (200-250 km) altitude satellite, with active drag compensation. The instantaneous ground swath need be sufficient only for a statistically reliable transform, probably of order 10 km or less. This small swath will allow a greatly reduced (with respect to Seasat) along-track antenna dimension, probably only 1 to 2 m. The potentially overwhelming data rate problem is consequently alleviated, not only by the reduction in swath, but also possibly by sparse sampling of the spectra, similar to the scheme planned for the European Remote Sensing Satellite ERS-1 in its sampled Wave Mode. Global sampling strategies will depend mainly on the scale size of storms in the open ocean, and on whether oceanographic significance can be attached to the observed fine scale (<50 km) evolution of the dominant wave vector.

An adaptive sampling strategy, built around an onboard buffer storage and electronically steerable antenna beams, could allow increased sampling in the vicinity of developing storms, and a commensurate decrease in the more benign regions. Spectrasat, or an experimental precursor, should operate in the presence of NROSS (Navy Remote Ocean Satellite System), ERS-1, or some similar global wind measuring system, so that its directional wave spectra may be interpreted in the context of a simultaneously developing global wave forecast model. Indeed, the ultimate test of Spectrasat will be to significantly improve the wave forecast model through the addition of actual directional wave measurements. Figure 5 illustrates the basic geometry of the proposed satellite.

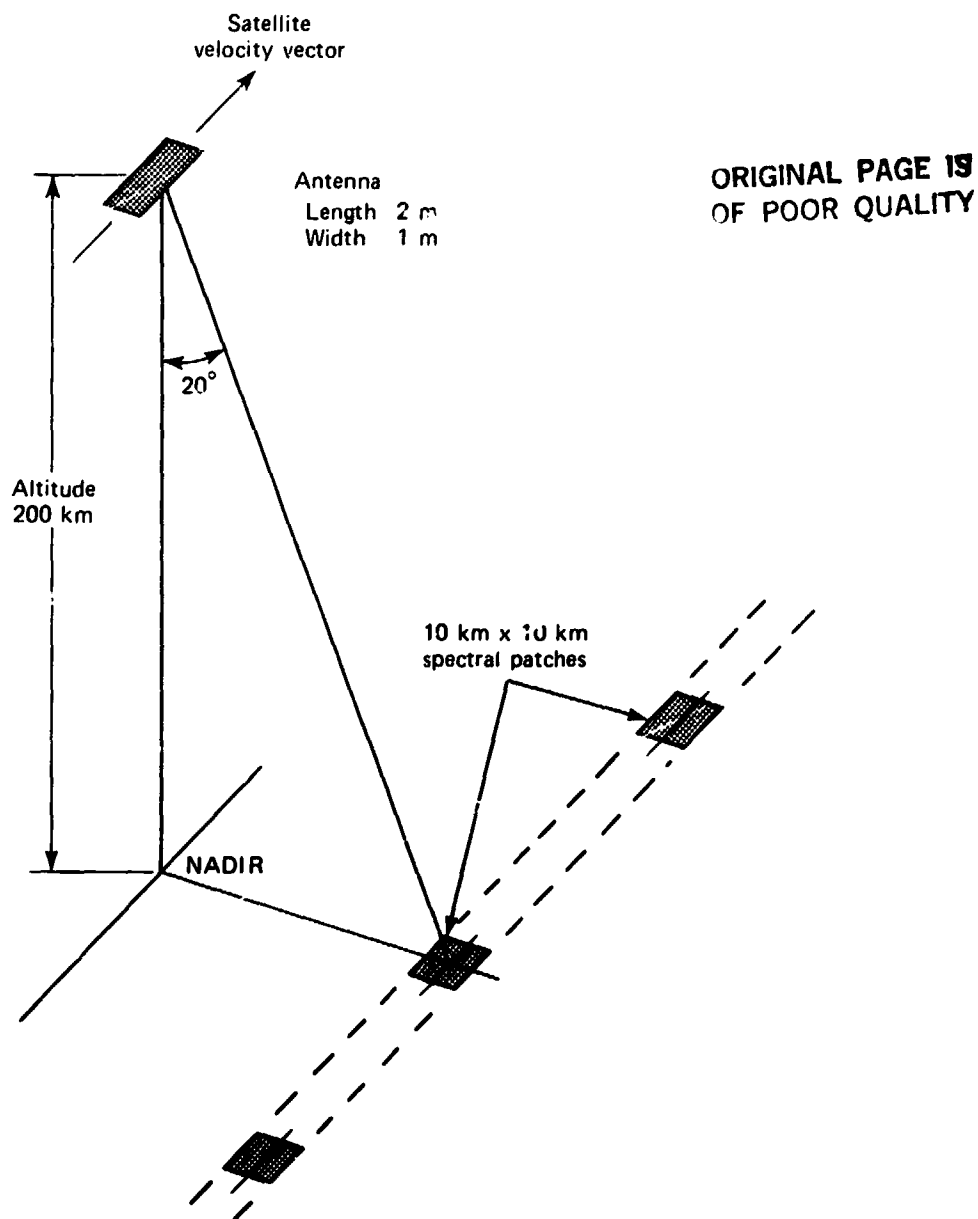


Fig. 5 Spectrasat basic configuration.

3.3 Some Questions to be Resolved

Determination of the major system characteristics of Spectrasat will naturally require a detailed design study. Of particular importance will be

1. the type and complexity of active drag compensation, necessary because of the very low altitude,
2. the required transmitter power, considering the smaller swath, smaller antenna, smaller range, the possibility of operating at a shorter wavelength (C-band), and the fact that substantial spectral and spatial averaging should be possible, and
3. the feasibility of on-board processing, given the smaller swath; the reduced azimuth compression ratio resulting from both the shorter transmitter wavelength and the possibility of presuming; and the insignificant range curvature resulting from the smaller swath.

Of equal importance is the question of Doppler smear, which in Seasat resulted in a lack of response to azimuth-travelling waves. Since theoretical models have not been very impressive in predicting the quality of SAR wave imagery, we should await the results of a decisive experiment, such as SIR-B, to verify that the lower altitude will indeed restore the necessary azimuth response.

Finally, it should be emphasized that many of the quantitative results summarized here are necessarily tentative, since they are based on an analysis of only one data set from Seasat. A comparable analysis of several data sets should be a prerequisite for extending the results more generally.

4. CONCLUSIONS

Analysis and interpretation of precision processed SAR wave imagery from Seasat over the past five years demonstrates a unique ability of SAR to monitor the large scale spatial evolution of the directional wave spectrum, directional properties of the wind field, and locations of current boundaries. Moreover, the geometry of Seasat (particularly its relatively high altitude and large swath) was not optimally chosen for the collection of global wave spectra. Many of the limitations of the Seasat SAR, therefore, were very likely not fundamental to the Doppler technique, but rather peculiar to the Seasat SAR parameters.

It is now appropriate to consider a dedicated SAR mission, not dictated by altimeter, scatterometer, or even SAR imagery requirements, but optimized solely for the acquisition of SAR ocean spectra. Such a system will be much simpler than Seasat, orbit at a much lower altitude, cover a much narrower swath, require less antenna area, consume less transmitted power, and permit an on-board, near-real-time processing capability.

Although such a mission should be unconstrained by other instrument requirements, it must nevertheless operate in the presence of a simultaneous altimeter and scatterometer mission. For only by synergistically combining the outputs of each of these sensors will we make significant progress in the global wave forecasting problem.

5. ACKNOWLEDGEMENTS

Results from the Seasat SAR analysis of Pass 1339, described in the first portion of this paper, are a collective effort of many of my colleagues at the Applied Physics Laboratory, particularly F. M. Monaldo, D. G. Tilley, T. W. Gerling, A. D. Goldfinger, and D. E. Irvine. We were also fortunate to have concurrent aircraft data supplied by D. B. Ross of the National Oceanic and Atmospheric Administration.

The Seasat SAR data analysis and interpretation is sponsored by the Office of Naval Research and the National Aeronautics and Space Administration. Conceptual design of Spectrasat is supported by Internal Research and Development funds.

6. REFERENCES

- Beal, R.C., P.S. DeLeonibus and I. Katz (eds.): Spaceborne synthetic aperture radar for oceanography. The Johns Hopkins University Press, 1981, 215 pages.
- Beal, R.C., D.G. Tilley and F.M. Monaldo, 1983: Large and small-scale spatial evolution of digitally processed ocean wave spectra from Seasat synthetic aperture radar. J. of Geophys. Res., Vol. 88, No. C3, pp. 1761-1778, February 28.
- Fu, L.L. and B. Holt, 1982: Seasat views ocean and sea ice with synthetic aperture radar. Publication 81-120, Jet Propulsion Laboratory, Pasadena, California.
- Series of papers on MARSEN. Journal of Geophysical Research, 1983, Vol. 88, pp. 9745-9882.
- Sea Wave Modelling Project (SWAMP), (in press), Part I: Principal results and conclusions, from Wave Dynamics and Radio Probing of the Sea Surface, Miami, Florida, USA, ed. O.M. Phillips and K. Hasselmann.

HIGH RESOLUTION OBSERVATIONS OF LOW CONTRAST PHENOMENA FROM AN
ADVANCED GEOSYNCHRONOUS PLATFORM (AGP)

Marvin S. Maxwell
NASA/Goddard Space Flight Center
Greenbelt, Maryland, 20771
USA

1. ABSTRACT

Present technology allows radiometric monitoring of the earth ocean and atmosphere from a geosynchronous platform with good spatial, spectral and temporal resolution. The proposed system could provide a capability for multispectral remote sensing with a 50 m nadir spatial resolution in the visible bands, 250 m in the 4 μ m band and 1 km in the 11 μ m thermal infrared band. The diffraction limited telescope has a 1 m aperture, a 10 m focal length (with a shorter focal length in the infrared) and linear and area arrays of detectors. The diffraction limited resolution applies to scenes of any brightness but for a dark low contrast scenes, the good signal-to-noise ratio of the system contribute to the observation capability. The capabilities of the AGP system are assessed for quantitative observations of ocean scenes. Instrument and ground system configuration are presented and projected sensor capabilities are analyzed.

2. INTRODUCTION

An advanced Geosynchronous Platform, called AGP in the rest of this paper, can provide significant new observation capabilities in the Visible and Infrared spectral region for studying the oceans, land and atmosphere (Otterman, 1983). A satellite at an altitude of 35,870 km in an equatorial orbit will move in synchronism with the earth's rotation and thus appear to hover over a fixed point at the equator. The primary advantages that result from geostationary observations occur because the earth appears to be stationary under the satellite. The unique capabilities that result are:

- observation, on demand, of approximately one-fourth of the world
- observation of short lived events
- observation of diurnal variations
- high spectral resolution, when desired
- high signal to noise
- interactive data acquisition
- constant off nadir viewing

The primary limitations result from the high altitude required for geostationary observations (35,878 km) and the fact that the satellite can only hover above the equator. Even using a very large sensor with a 1 meter aperture, a realistic AGP can provide only modest spatial resolution and because of diffraction effects

the resolution is wavelength dependent, as indicated below:

<u>Spectral Band</u>	<u>Instantaneous Field of View (IFOV)</u>
0.4 to 1.0 μm	50 - 100 Meters
1.0 to 2.4 μm	100 - 200 Meters
3.5 to 4.2 μm	400 Meters
10.5 to 12.5 μm	1,000 Meters

The major advantages an AGP may offer for ocean observations will derive from its capabilities to: observe desired areas on demand with optimized observation intervals (from minutes to days); interactive observation, i.e. the experimenter can modify observations based on the results of prior observations, optimization of spectral band selection; and optimization of dynamic range and signal-to-noise ratio.

2.1 Geometric Observation Considerations

The constant location above the equator will lead to observation with oblique, but constant, view angle (nadir angle). This also leads to an increase in the Instantaneous Field of View (IFOV) which corresponds to a reduction in resolution as indicated in the following table.

<u>NADIR ANGLE</u> <u>DEGREES</u>	<u>DISTANCE FROM NADIR</u> <u>KM</u>	<u>+ LAT/LONG.</u> <u>DEGREES</u>	<u>INCREASE IN IFOV</u> <u>%</u>
10	930	8	2
30	2,800	25	15
40	3,800	34	30
50	4,800	43	50
60	5,800	52	100

2.2 Microwave Observations

Passive microwave observations are not likely to be very useful for ocean observations from an AGP because of the diffraction limited resolution that can be achieved with real apertures as indicated by the following table:

<u>Wavelength (cm)</u>	<u>Frequency (GHz)</u>	<u>Aperture</u>	
		<u>4m</u>	<u>15m</u>
		<u>IFOV in km</u>	<u>IFOV in km</u>
21	1.4	2,300	600
5	6	540	145
1.5	20	150	40

Synthesized passive apertures to achieve reasonable resolution will be very difficult to achieve and active microwave sensing, such as with a synthetic aperture radar is exceedingly difficult to do at a range of 36,000 km. Therefore, there will be no further consideration of microwave sensing from an AGP in this paper.

3. SYSTEM CONSIDERATIONS

Present launch vehicles can deliver a very limited payload to geosynchronous orbit. The AGP will require a high performance, heavy, three axis stabilized space craft carrying a large earth viewing telescope as its primary sensor. A well designed three mirror system can provide the desired field of view with diffraction limited performance over the spectral range of 500 nm to 13 micrometers.

3.1 Sensor Configuration

The weight of a telescope tends to grow as the cube of the aperture diameter. The diffraction limited performance grows linearly with the aperture. The cost of a large diffraction limited moderate field of view instrument grows very rapidly with aperture. All of these considerations tend to limit the maximum aperture to something on the order of 1.6 meters (Perkin-Elmer, 1975, Itek, 1975). In an effort to keep the probable cost of an AGP for ocean observation to moderate levels this paper will concentrate on a sensor with a 1 meter aperture and selectable focal lengths of 3, 5 and 10 meters depending upon the detectors used and the spatial resolution desired. Figure 1 shows a simplified profile view of the sensor.

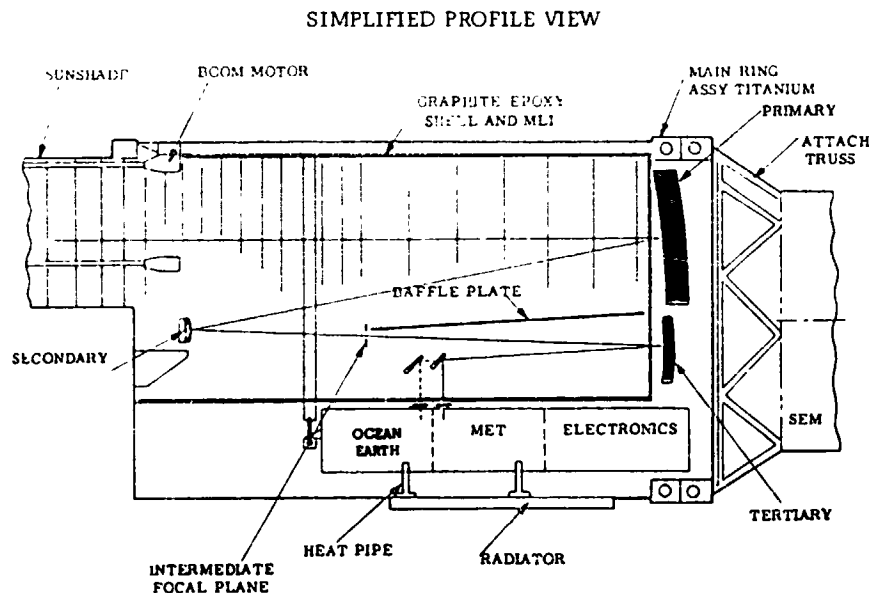


Figure 1

3.2 Diffraction and Modulation Transfer Function Considerations

The sensor design is dominated by diffraction considerations. An imaging radiometer must have a high Modulation Transfer Function (MTF) if it is to produce accurate measurements of the scene radiance. MTF is a measure of the relative response of the system to a sine wave modulated input radiance at various spatial frequencies to that at very low spatial frequencies (almost DC). Figure 2 shows how the diffraction limited MTF varies with the spatial frequency of

objects in the scene in angular units of λ/D per cycle, where λ is the wavelength of the light and D is the diameter of the sensor aperture. The central obscuration is the blockage in the center of some telescope designs. The design proposed for the ACP has zero blockage.

In this paper diffraction limited performance is generally defined to occur when the IFOV = $2.44 \lambda/D$. That corresponds to a diffraction MTF of 0.73 and is shown at a value of 4.88 Angular Units on Figure 2. Figure 3 shows the diffraction limited resolution as a function of wavelength and clear aperture diameter.

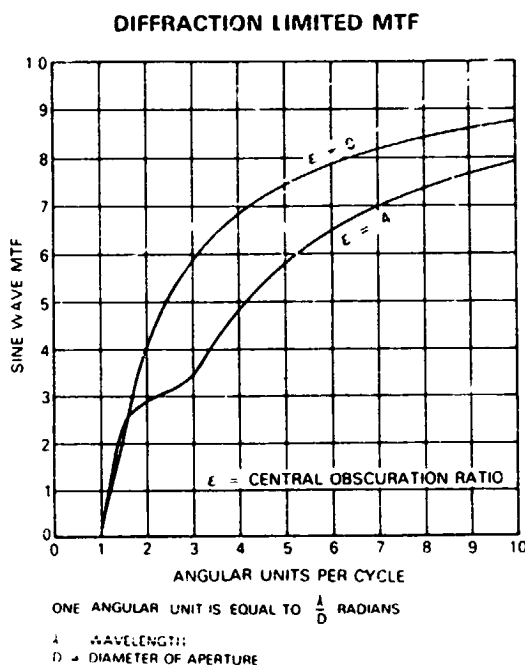


Figure 2

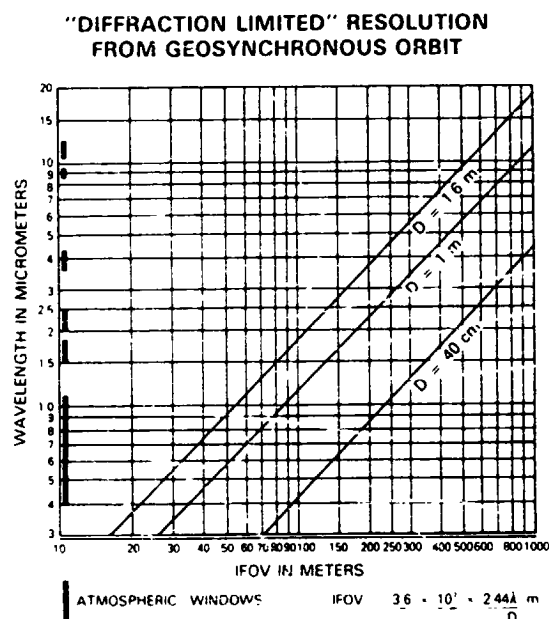


Figure 3

The overall or system MTF is the product of all the elements in the imaging chain and includes the following elements. The value given for each element refers to the response to a signal with 1/2 cycle equal to the IFOV, often referred to as the Nyquist frequency.

- Diffraction--0.73
- Detector size--0.64
- Smear--0.85, due to detector motion during integration time
- Diffusion--0.95, due to cross talk in the detectors
- Optical Quality--0.9, due to aberrations and optical imperfections

The system MTF is the product of all terms and equals 0.33 at the Nyquist frequency. This is a value that will allow radiometric measurements to be made of objects larger than 3 to 4 IFOV's. In orbit the effective MTF is further reduced by the atmospheric adjacency effects in which the atmosphere, especially aerosols, scatter light into the signal path and thus reduce the contrast and in turn the MTF.

3.3 Multispectral Linear Array Approach

The scene radiance in the focal plane of the optics will be selected by dichroic beam splitters and selection mirrors to transfer the desired spectral channel to the appropriate detectors. Reimaging optics will be used to reduce the effective focal length to 3 or 5 meters to optimize the performance in chosen spectral regions or to provide a desired field of view. Silicon linear array detectors which can cover the visible to near IR (VIS/NIR) spectral region from 400 nm to 1,000 nm are in production with dimensions of 15 micrometers or less and with array lengths of from 1,000 to 4,000 detectors. These detectors will provide an IFOV of 50 m in the visible using a 10 meter focal length telescope. Using arrays with multiple lines of detectors on a single chip plus beam splitters will allow the scene to be observed in 12 or more spectral bands in the VIS/NIR region. The number of detectors in the total array will determine the field of view of the system. Total array lengths of from 4,000 to 10,000 detectors are reasonable and will provide a field of view of from 200 km to 500 km. Imaging these arrays thru the 5 m focal length optics would provide an IFOV of 100m and a FOV of from 400 km to 1,000 km. The line of detectors would be arrayed in an east west direction and the spacecraft would scan north and south at the appropriate rate to acquire the full scene. As is discussed in a later section the scan rate will be selected so as to achieve the required signal-to-noise ratio.

Detectors are under development in the Short Wave IR (SWIR) region, between 1 and 2.5 micrometers, with dimensions of 30 micrometers and array lengths of 512 detectors on a chip. These detectors can provide 100 m IFOV using the 10 m focal length telescope and 200 m IFOV using the 5m focal length. Using from 2,000 to 5,000 detectors in a line is reasonable and will provide a FOV which is the same as that provided by the silicon detectors. A variety of detector systems are under development for this spectral region. Paladium Silicide, Indium Antimonide and Mercury-Cadmium-Telluride are all under development. Use of beam splitters and spectral filters on the chips should allow 6 to 10 spectral bands to be obtained in this region.

The 4 micrometer Mid IR (MIR) spectral region can be covered by detectors produced from Platinum Silicide, Indium Antimonide or Mercury-Cadmium-Telluride. Detectors in this spectral region will probably be larger, on the order of 50 micrometers on a side, and can provide a 400 meter IFOV. It should be feasible to divide the 3.5 to 4.5 micrometer region into 2 bands if desired. The FOV could match that of the other bands. The use of this band in daylight is complicated by the fact that the reflected sunlight is similar in intensity to the thermal flux emitted by the scene.

The Thermal IR (TIR) spectral region between 8 and 12 micrometers can be covered by Mercury-Cadmium-Telluride detectors and will probably be about 100 micrometers on a side. This will provide an IFOV of 1000 meters with the 3 meter focal length telescope and a FOV similar to the other bands. It should be reasonable to include 4 to 6 bands in this region.

The following Table shows FOV, IFOV and Data Rate considerations for the MLA System.

Field of View		Number of Detectors/Band					Data Rate* KB/SEC				
		Spectral Region					Spectral Region				
		IFOV (M)					IFOV (M)				
KM	Degrees	VIS/NIR 50	SWIR 100	SWIR 200	MIR 400	TIR 1,000	VIS/NIR 50	SWIR 100	SWIR 200	MIR 400	TIR 1,000
200	+ 0.16	4,000	2,000	1,000	500	200	2,000	500	125	50	4
500	+ 0.4	10,000	5,000	2,500	1,250	500	5,000	1,250	312	125	10

* SCAN VELOCITY = 2.5 km/sec and 10 bits/Pixel.

3.4 Alternative Focal Plane Systems

There are other techniques to provide the multispectral sensing required for ocean observations. The preferred approach depends upon the desired spatial resolution, spectral resolution, number of bands, and field of view.

--Imaging Spectrometer

If a large number of moderately high spectral resolution bands are desired, especially in the range from 400 nm to 2.5 micrometers at relatively low spatial resolution, i.e. 200 to 400 meters and modest FOV, i.e. 100km, then an imaging spectrometer may be the preferred approach. Using this technique the VIS/NIR region can be partitioned into 60 bands of 10 nm spectral bands width each and the SWIR region into 60 bands of 20 nm spectral band width each. In this technique the scene is first imaged on a slit. The image passing through the slit is collimated, dispersed by a prism or a grating, and then reimaged onto rectangular arrays of detectors in which one dimension of the array is spatial and the other is spectral. The required reimaging and spectral dispersing systems are large and heavy and thus will be limited to applications with moderate spatial resolution requirements.

--Area Arrays

If very high spectral resolution is desired, i.e. less than 10 nanometers, but a moderate number of spectral bands are desired, a simpler technique is available. The scene is imaged onto an area array of detectors through a spectral defining filter mounted on a filter wheel selection device. This approach provides good geometry to determine the relative position of objects and thus simplifies determining relative motions of clouds and water. Its major virtue is that since an entire scene is imaged at one time very long integration times can be used which allows the use of correspondingly narrow spectral intervals. Silicon arrays covering the VIS/NIR region are presently available with 256 x 256 detectors on 30 micrometer centers, and it is reasonable to project that arrays of 1024 by 1024 detectors will be available in the near future. It is reasonable to project the development of arrays of 256 x 256 in the SWIR band and 128 x 128 in the 4 micrometer band.

The following table gives a feel for the IFOV's, FOV's and data rates that such area arrays could provide in the AGP sensor.

Spectral Region (m)	Array Size	Detector Size (m)	Focal Length (m)	IFOV (m)	FOV (km)	Data Rate MB/S
.4 - 1.0	1024 x 1024	30	10	100	100	21
			5	200	200	21
			3	360	370	21
.4 - 1.0	512 x 512	30	10	100	50	5.2
			5	200	100	5.2
			3	360	185	5.2
1.0 - 2.5	256 x 256	50	5	350	90	1.3
			3	580	140	1.3
3.5 - 4.2	128 x 128	50	5	350	45	.3
			3	580	75	.3

*AT 10 BITS/PIXEL, READOUT PERIOD OF 500 ms

3.5 Signal-to-Noise Ratio Considerations

An AGP can provide an excellent signal-to-noise ratio in narrow spectral bands over a wide range of illumination conditions. This can be done by controlling the time a detector look at a given area (IFOV) so as to build up an adequate signal level which is then digitized and sent to the ground. In the VIS/NIR and SWIR bands the detectors can be considered photon counting devices (with the appropriate quantum efficiency) and the preamplifier and dark current noises are small, typically under 100 electrons. The dominant noise component for signal-to-noise values greater than 100 to 1 is the shot noise or random fluctuation of the signal flux during the integration time which varies as the square root of the number of signal electrons.

There is a maximum number of signal electrons that can be measured at any pixel in a scene for a given detector system before the data saturates or becomes too nonlinear to calibrate. Linear arrays often have a maximum capacity of about 200,000 electrons and a noise level in the order of 100 electrons. Area arrays often have a maximum of 300,000 electrons and a noise level of 200 to 300 electrons, or more.

The analog-to-digital converter is another source of noise in the system. The quantizing noise is equal to the quantizing step size divided by the square root of 12. The quantizing step size is equal to the full scale signal divided by 2 to the nth power, where n is the number of bits in the analog-to-digital converter. Another, harder to quantify, source of noise is due to calibration errors and is discussed in another section. The noise contributors combine as the square root of the sum of the square of the noise sources.

The following table gives some typical values for the systems.

Se Number of Signal Electrons	<u>Signal to Noise Ratio</u>				<u>Quantizing Noise (Electrons)</u>		
					Full Scale = Se		
	<u>Number of Noise Electrons (Ne)</u>				<u>Number of Bits in A/D</u>		
	<u>100</u>	<u>200</u>	<u>300</u>	<u>500</u>	<u>8</u>	<u>10</u>	<u>12</u>
500,000	700	680	650	580	560	140	35
300,000	550	530	500	420	340	85	21
100,000	300	270	230	170	110	28	7
50,000	200	170	130	90	56	14	4
30,000	150	120	100	60	34	9	2
10,000	70	45	30	20	11	3	-
5,000	40	24	16	10	5	2	-
3,000	27	15	10	6	3	1	-
1,000	9	4	3	2	-	-	-

The Number of Signal Electrons (Se) can be estimated using the following relationships:

$$Se = \frac{(S \cdot Ta \cdot \cos Z + Na) \cdot R \cdot Tas + Np}{\pi} \cdot \frac{\pi \cdot To \cdot Fb \cdot Tf \cdot Qd \cdot Ad \cdot It}{4(f\#)^2} \quad (1)$$

$$Ns = \frac{(S \cdot Ta \cdot \cos Z + Na) \cdot R \cdot Tas}{\pi} \quad (2)$$

All of the variables may vary with the wavelength, λ , of the radiation with the exception of the solar zenith angle.

- S Solar irradiance in number of photons/sec/cm²/nm at top of atmosphere
- Ta Transmission of the atmosphere to the surface
- Z Zenith angle of sun
- Na Atmospheric radiance, number of photons/sec/cm²/sr/nm scattered onto the surface from the atmosphere
- R Reflectivity of target
- Tas Transmission through the atmosphere from the surface to the sensor
- Np Radiance added by the atmosphere to the signal in photons/sec/cm²/sr/nm
- To Transmission of the optics
- f# f number of optics = focal length/aperture
- Fb Bandwidth in nm of spectral defining filter
- Tf Transmission of the spectral filter
- Qd Quantum efficiency of the detector
- Ad area of the detector in cm²
- It Integration time in seconds
- Ns Surface radiance in photons/sec/cm²/sr/nm above the atmosphere

There is a complex interrelationship between many of the atmospheric terms, especially the atmospheric path radiance, which is a function of wavelength, sun angle, angle to sensor, target and surround reflectivity, and the state of the atmosphere.

ORIGINAL PAGE IS
OF POOR QUALITY

The following table gives representative value for some of these parameters.

Sample calculation of Signal-to-Noise Ratio (S/N) and Noise Equivalent Delta Reflectivity (NEDR)

λ μm	S $\times 10^{13}$	Ta	Z	Na $\times 10^{13}$	R	Tas	Ns $\times 10^{13}$	Np $\times 10^{13}$	f#	Fb	Qd	Ad $\times 10^{-6}$	It $\times 10^{-3}$	Se $\times 10^3$	S/N	NEDR %
.45	44	.7	30	3	.1	.7	.8	3	10	20	.7	2.2	40	110	315	.15
.45	44	.6	60	2.5	.1	.7	.47	3	10	20	.7	2.2	40	100	301	.25
.55	47	.8	30	2	.05	.8	.49	2	10	20	.8	2.2	40	80	265	.1
.55	47	.6	70	1.5	.05	.8	.18	2	10	20	.8	2.2	40	75	260	.2
.65	50	.8	30	1.	.05	.8	.48	1.	10	20	.8	2.2	40	50	205	.08
.65	50	.8	30	1.	.	.8	4.8	1.	10	20	.8	2.2	40	130	425	.14
.75	47	.9	60	.7	.05	.9	.34	.5	10	20	.8	2.2	40	30	150	.08
.85	41	.9	60	.5	.05	.9	.29	.3	5	20	.5	2.2	80	90	285	.04
1.2	28	1	30	.2	.2	1	1.6	.2	10	20	.2	9	80	120	335	.07
1.6	19	1	30	.1	.2	1	1.1	.1	10	40	.15	9	80	120	335	.07
2.2	9	1	30	0	.2	1	.50	0	5	40	.05	9	160	135	355	.06

Note, $T_0 = 0.5$, $T_f = 0.6$ for all λ for these calculation
100 noise electrons assumed for S/N calculation

It should be noted that for a given set of scene conditions the items that can be selected to provide the needed signal to noise ratio are primarily the optics f number, detector size, spectral bandwidth and integration time. The geostationary orbit is unique in that it allows adjustment of the integration time to allow the required signal-to-noise to be obtained. In a low altitude orbiting satellite the integration time must be less than the dwell time (IFOV/velocity) and for a system with an IFOV of 50 m and a sub-point velocity of 7km/sec the maximum integration time is 7 milliseconds. In geostationary orbit the integration time is fundamentally limited by the stability of the spacecraft and the maximum signal that the detector can accommodate. The need to cover a given area in the observation time allowed is also an operational limitation.

The Noise Equivalent Delta Reflectivity (NEDR) is that change in reflectance which produces a change in the signal level just equal to the RMS noise of the system. A large object (say 6 x 6 IFOV's) with a change in reflectivity equal to the NEDR would be detectable, but the precise locations of its boundary would be hard to determine because the peak-to-peak noise is about 6 times the RMS noise. To reliably observe a small object (say 2 x 2 IFOV's) would require an NEDR 4 to 6 times smaller than the reflectivity difference between the object and the background. The relationship between Signal/Noise and NEDR is given by the following formulas using the notation from the previous table.

$$\text{NEDR} = \frac{R(N_s + N_p)}{N_s \cdot \text{S/N}}, \quad \text{S/N} = \frac{R(N_s + N_p)}{N_s \cdot \text{NEDR}} \quad (3)$$

Note that in the absence of any path radiance the Noise Equivalent Delta Reflectivity equals the reflectivity divided by the signal-to-noise ratio.

3.6 Calibration Considerations

Calibration of the detectors may limit the ultimate signal to noise ratio that can be achieved in the AGP system. A system that uses many detectors in each spectral band exhibits stripes or banding in images due to imperfect calibration. A sensing system that uses only one detector per spectral band can have calibration errors that lead to radiometric errors in the data but all of the data in a given band will be uniformly in error at any radiance level. In a system with many detectors in a given band, calibration errors lead to pixel to pixel variations in output even if the input radiances are identical. For many applications of the AGP very good signal to noise performance is required, often in excess of several hundred to one. As is indicated in the section on Signal-to-Noise Ratio, achieving such performance is feasible with the AGP because of the freedom to select the integration time however calibration errors may provide the ultimate limit.

Preflight calibration is essential to provide information on the spectral band-pass of the detectors and their absolute radiometric sensitivity. Variations with time and launch induced effects must be measured while the instrument is in orbit. Many approaches to inflight calibration are available, but there are no techniques that are fully satisfactory in providing the very precise detector to detector calibration required to destripe the data and to provide the band to band calibration or absolute calibration required for interpretation of the data.

One of the best calibration techniques is to fill the aperture with diffuse radiation of known intensity. This can be done by deploying a diffuse reflector in front of the telescope and reflecting sunlight from it into the sensor. The primary problem with this technique is related to the problem of knowing how the reflectance characteristics change with time. There now exist "Absolute Detectors" whose calibration should be stable with time to measure the input radiance, but it is difficult to apportion that among the spectral bands. There are also engineering difficulties in reliably putting a reflector in front of 1 meter aperture. The AGP may use such a calibration scheme, but it would be used only occasionally, perhaps every few weeks and the reflector would be enclosed at all other times to minimize its reflectivity changes during the life of the mission.

The moon offers the possibility of a good transfer calibration standard. It will be possible to observe a fully illuminated moon every month and it seems reasonable to assume that the moons' reflectivity changes only very slowly with time so that changes observed during the mission can be attributed to sensor changes.

The short term detector to detector calibration will require internal calibration systems using lamps or mirrors to inject a controlled radiance onto the detectors. The fundamental problem in all of these approaches is to assure the uniformity, or knowledge of the variation, of the detector irradiance to one part in a few hundred and to be able to vary the irradiance levels and know their values to a fraction of a percent.

4. APPLICATION CONSIDERATIONS

4.1 Ocean Color

Many ocean parameters can be acquired by observation of the surface color and its change with time. The AGP can acquire data on the ocean color in the spectral regions from 400 nm to 1,000 nm with spatial resolution of 50 to 100 meters, spectral resolution of 20 nm or less and with a signal to noise of better than several hundred to one. Observation of diurnal and tidal changes will be easy from the AGP. Such observations can provide information on water pollution, upwellings and ocean nutrients. Sun glint can be either a problem or a source of information of surface roughness from which surface winds can be deduced.

4.2 Ocean Temperature

The AGP can provide ocean temperature data with a Noise Equivalent Delta Temperature of less than 0.5 degrees Celcius with some capability of correction for atmosphere effects by using two or more bands in the 10 to 12 micron region and by use of the 4 micron band at night. The ability to observe on demand will increase the probability of getting data when the atmosphere is clear. The constant view angles will make change detection easier, but the large view angles may limit data usefulness at distances greater than 4,000 km from the nadir location of the AGP.

4.3 Atmospheric Interactions

The good spatial, spectral, and temporal resolution of the AGP combined with its high signal to noise will offer a unique capability to observe the dynamics and diurnal interaction of the ocean and atmosphere. Selected test areas can be observed hourly for many days coincident with ship and aircraft observations and used to extend these observations to a much larger area. The real time nature of the observation will allow using the AGP data to direct surface and air observers to regions of maximum interest.

The AGP will allow the detection of small clouds as they are being formed and to observe how they change and move to provide information on atmospheric wind fields and other important parameters. Low level clouds are sensitive to heat, moisture and other energy interchanges between the ocean surface and the atmosphere. There is the possibility of learning more about these interactions by detailed observations of these clouds. Thin small clouds are difficult to detect because they present a small reflectance change against a dark ocean background. The ability to optimize the integration time to build up the signal will allow the AGP to provide the necessary performance even when the sun is within 20 degrees of the local horizon.

5. GROUND SYSTEM

The AGP system will consist of the satellite, a central ground command, control and preprocessing system and the experimenters or users of the data at locations convenient to their facilities or experimental test sites. These user facilities will interconnect to a central site via telephone lines or satellite communications as appropriate. A communication link of between 50 kb/s and a few million bits per second will suffice for transmitting the data to almost all experimenters. A possible scenario of the operations follows. Low resolution images of all of the current test sites would be distributed to the appropriate experimenters every few hours. Short range meteorological forecasts would also be distributed to aid in the experimenters scheduling their data requests. These acquisition requests would be sent to the central facility by a computer-to-computer link.

The control center would establish the planned observation sequence for the next few hours, inform the experimenters of the schedule and control the spacecraft so as to acquire the data. The data would be received at the central facility, calibrated, geometrically located, and the desired data sent to the requesting investigators. All data would be archived in a form to allow recalibration without loss of any data quality. In most cases the processing and data distribution would be done in near real time so that the data would be available to the experimenter within a few minutes of acquisition. It would be routine for an experimenter to request a minor modification of the operation plans, such as spectral band selection, integration time adjustment, etc. as a result of one observation in time to affect his next observation. Some experiments that require large area coverage of high resolution data will not be able to receive the data over a moderate bandwidth link. In these cases the experiment plan can call for distributing subsampled or averaged data in near real time and sending the full resolution data at a slow rate or via mail. There will also be capabilities to support guest investigators at the central facility who will be able to use the more powerful computing and display systems that could be located there.

6. REFERENCES

- Itek, 1975: Requirements and Concept Design for Large Earth Survey Telescope for SEOS. Final Report, 1975. Itek Optical Systems/RCA Astro-Electronics Division.
- Ottermann, J., V. Salomonson, D. Atlas, W. Shenk, M. Maxwell, and D. Pitts, 1983: A Case for GOHREM: Geosynchronous Orbit High Resolution Earth Monitoring. Seventeenth International Symposium on Remote Sensing of Environment, Ann Arbor, Michigan, May, 1983.
- Perkin-Elmer, 1975: Russo, John J. and Robert S. Rowley, Perkin-Elmer Corporation. Synchronous Earth Observatory Satellite/Large Earth Survey Telescope. Vol. 1 - Executive overview, December 1975.

REMOTE SENSING OF AIR-SEA INTERACTION.

David Atlas and Erik Mollo-Christensen
Goddard Laboratory for Atmospheric Sciences
NASA/Goddard Space Flight Center
Greenbelt, Maryland 20771

ABSTRACT

We set out a number of preliminary concepts for the measurement or inference of fluxes across the air-sea interface through remote sensing. All the methods are achievable from aircraft with state-of-the-art technology. Only one is now ready for space implementation. The focus is on cold outbreaks. It is possible to infer sensible (latent) heat flux from the difference between initial surface air temperature (vapor mixing ratio) and the downwind SST (and corresponding saturation mixing ratio). The downwind growth rate of the PBL as measured by lidar also provides estimates of surface heating and the cross-inversion entrainment velocity. The lidar also provides a measure of the depth of the inversion and its penetration by surface-forced convection; this permits estimates of the surface heat flux. Lidar and radiometric measurements of cloud top height and temperature provide means of deducing the temperature sounding downstream so that heating may be computed with the aid of a known sounding upstream. Vapor fluxes are measurable by differencing total precipitable water at two ends of a path measured by either IR or microwave radiometers. All the methods suffer from deficiencies; these are discussed.

1. INTRODUCTION

This work attempts to advance our understanding of possible methods for the measurement or inference of fluxes across the air-sea interface through remote sensing. We are concerned mainly with measurements from space; however, the concepts are generally applicable to aircraft platforms as well. The problem is a difficult one for which there are no straightforward solutions. Much of the work in this realm is therefore of a preliminary nature (Gautier, 1980) or deals with methods which are applicable under restricted conditions (Chou and Atlas, 1982). This paper is an extension of that of Chou and Atlas. It is also a synthesis of relatively recent findings and developments and a variety of untested concepts. Thus, the discussion is speculative.

The bulk of the sensible and latent heat fluxes over the globe occur over the warm western boundary currents during winter. For this reason, we focus on the phenomenon of the cold air outbreak. Indeed, we shall see that flux measurements and inferences are more readily made under such conditions.

2. METHODS OF ESTIMATING SEA SURFACE HEAT AND MOISTURE FLUXES

2.1 Downstream Horizontal Gradients of Surface Properties

We start from the premise that no remote sensing technique can sense potential temperature (θ) or vapor density (q) in the lower few tens of meters of the atmosphere. As a result, it is not possible to use the conventional bulk formulas for the fluxes, such as an expression of the form for the flux of the property x

$$F = \mu C [x(z) - x(0)] \quad (1)$$

Here, u is the wind speed at "anemometer height" (usually at 10 m), C is a constant transfer coefficient, and x represents either θ or q . However, in cold outbreaks, Chou and Atlas (1982), (hereafter referred to as I), developed a method based on the planetary boundary layer model of Stage and Businger (1981, a,b). They show that the vertical gradient in the bulk formula can be parameterized in terms of the downstream horizontal gradient. The resultant total heating of an air column over the distance of travel from the upwind shore is expressed by Eqs. (2) and (3) for sensible and latent heat.

$$S = \rho C_p \chi^{-1} \int_0^\infty C_T (\theta_0 - \theta) dx \quad (2) \quad E = \rho L \chi^{-1} \int_0^\infty C_q (q_0 - q) dx \quad (3)$$

Using the model of Stage and Businger, I showed that S and E are essentially linear with $(\theta_0 - \theta_1)$ and $(q_0 - q_1)$, respectively. Here θ_1 and q_1 are the values of θ and q at the upwind shore (or the upwind end) of the path. Thus, given these values, a measurement of the SST any place upstream of the cloud edge determines the sensible heating S . The presence of clouds invalidates the results thus constraining the method to the cloud-free region near shore. Similarly, since the SST determines the saturation mixing ratio at the sea surface, knowledge of q_1 at the shore determines the moisture and latent heat flux.

Fig. 1 is a nomogram for column sensible heating. The abscissa, labeled "cloud free distance" may be replaced simply by downstream distance provided it does not extend beyond the upstream edge of the clouds. There is a similar nomogram for latent heating. In order to convert the column heating to a flux one must multiply by the wind speed. Wind speed can be sensed remotely by one of the well known methods. Note that the sensitivity to downstream distance is small. For most realistic cases, the SST (θ_0) varies with fetch so that the SST implicitly includes the effect of distance. In any case, S may be estimated to better than $\pm 25\%$ independent of downstream distance.

2.2 Downstream Growth of Boundary Layer

One of the problems with the Chou-Atlas method is its dependence upon the lapse rate at the shore end. However, for accuracies of $\sim 10\%$ the lapse rate is not important. For greater accuracy they suggest that one use the downwind derivative of the square of the boundary layer depth Z_B as a proxy for lapse rate. This would be a convenient way if Z_B could be observed by lidar. As a good approximation for non-divergent conditions, we may write

$$dZ_B^2/dx \approx 2(1 + A_0) C_T (\theta_0 - \theta_1) / \Gamma_\theta \quad (4)$$

where A_0 is the entrainment coefficient, the ratio of the flux entrained across the PBL inversion to the surface flux. Eq. (4) is plotted in Fig. 2. As can be seen from Fig. 1 the column sensible heating is most sensitive to the temperature

constrast ($\theta_0 - \theta_1$). Accordingly, to a good approximation, the curves of ($\theta_0 - \theta_1$) in Fig. 2 may be replaced by isopleths of S. As a result, the quantity (dZ_B/dx) becomes a more direct measure of sensible heating. More precisely, following I

$$S = \rho C_p \chi^{-1} \int_0^x [0.5 \Gamma_\theta / (1 + 2A_\theta)] [dZ_B^2/dx] dx \quad (5)$$

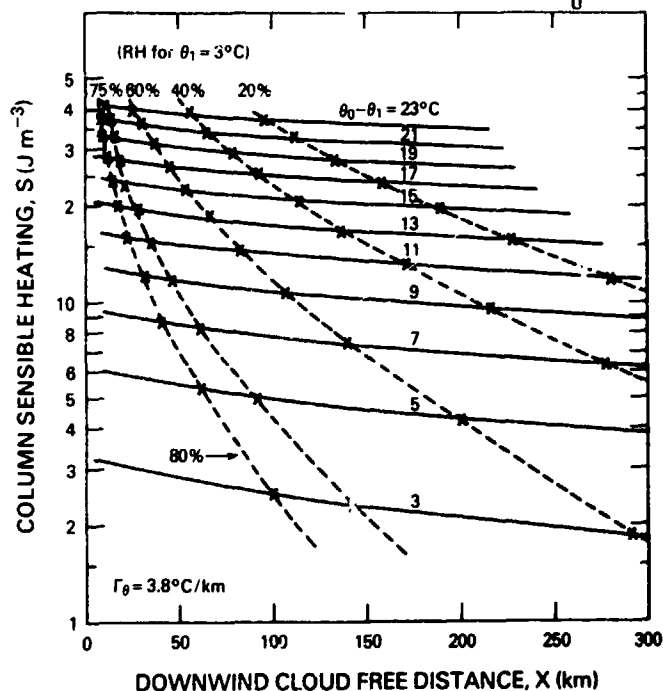


Fig. 1. Mean column sensible heating (S) between shore and downwind cloud free distance (x) versus x for various land air-sea surface temperature differences ($\theta_0 - \theta_1$) under non-divergent conditions and initial potential temperature lapse rate of $3.8^\circ\text{C km}^{-1}$ (solid lines). Dashed lines correspond to the cloud-free paths for various surface relative humidities (RH) and initial shore surface air temperature (θ_1) of 3°C . Each cross indicates a numerical experiment (after Chou and Atlas, 1982).

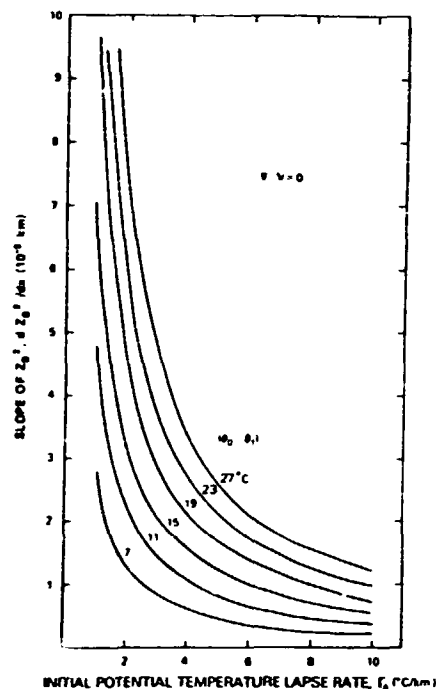


Fig. 2. Slope of Z_B^2 versus the initial potential temperature lapse rate (Γ_0) for various ($\theta_0 - \theta_1$) under non-divergent conditions. ($\theta_0 - \theta_1$) may be replaced approximately by S the column sensible heating.

Column sensible heating is thus directly proportional to the average values of (dZ_B^2/dx). We assume that Z_B is measured by lidar. Note that these results pertain to cloud-free regions.

2.3 The depth of the entrainment zone.

An interesting feature of the unstable marine boundary layer is the roughness at the inversion and the depth of penetration of the buoyant elements into the stable layer. Deardorff et al. (1980) have shown that these characteristics carry significant information.

Fig. 3 shows the structure of the clear air portion of a convective PBL observed by airborne lidar during a cold outbreak off the NE coast of the United States (Melfi et al., 1983). The convection is made visible by the sea salt aerosols. In this case, the turrets do not appear to grow with distance because the flight is parallel to

shore and the section is normal to the wind. The organized structure is remarkable. The turret tops correspond closely to the top of the inversion; the troughs to the bottom as shown in Fig. 4.

Following Deardorff et al. (1980), Melfi et al. (1983) have computed the parameters \bar{h} , h_0 , h_2 , and Δh as shown in Fig. 4. The quantity h_0 , corresponding to the altitude attained by more than 96% of the turrets, represents the top of the well mixed layer at the base of the density inversion; the height h_2 , attained by 4% of the turrets, is the top of the inversion. \bar{h} is the median height; Δh is the depth of the entrainment zone and the inversion. Melfi et al. (1983), show that

$$[(\bar{h}/h_0) - 1] = [(\omega'\theta')_{\bar{h}}/(\omega'\theta')_s] = A_0 \quad (6)$$

With lidar data of the quality shown in Fig. 3, it is now possible to compute the value of A_0 , rather than assume it.

Assuming zero divergence, one can set

$$dz_B/dx = \omega_e/\mu \quad (7)$$

where w_e is the entrainment velocity and u is the wind speed in the mixed layer. Melfi et al. (1983), analyzed the laboratory data of Deardorff et al. (1980), and showed that

$$(\Delta h/h_0) \approx 3(\omega_e/\omega_s)^{0.5} \quad (8)$$

If this laboratory experiment simulates the atmosphere, then lidar observations of $(\Delta h/h_0)$ and (dz_B/dx) should permit the estimation of both the entrainment velocity, w_e , and the turbulent vertical velocity scale w_* defined by

$$\omega_* = [(g/\bar{\theta})(\omega'\theta')_s \bar{h}]^{1/3} \quad (9)$$

We see that w_* is a function of the surface flux $(\omega'\theta')_s$ and the height \bar{h} . Clearly high resolution lidar observations tell us much about the unstable PBL and fluxes. Since both the lidar schemes assume zero divergence, the results should be considered only as approximations.

BOUNDARY LAYER LIDAR

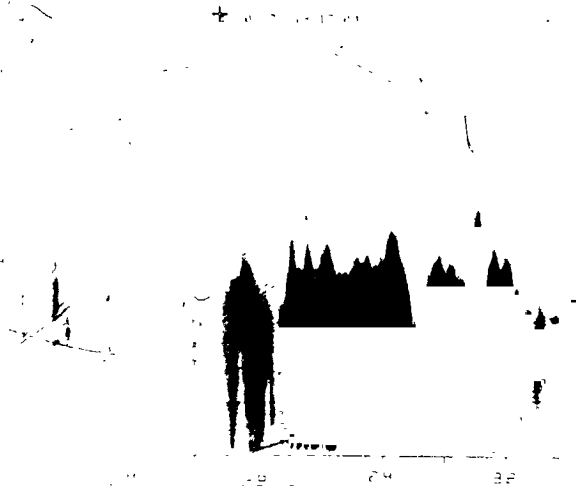


Fig. 3. West-east vertical cross section of convective streets made visible to airborne down-looking lidar (0.53 μ m wavelength) by scatter from sea salt aerosols on January 20, 1983. It took 5.3 min to fly from left to right (after Melfi et al., 1983).

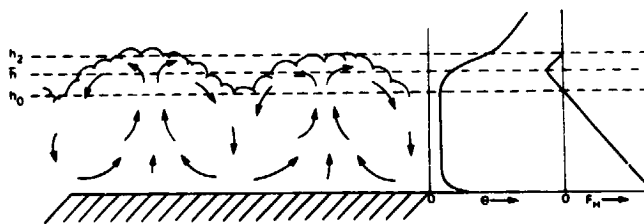


Fig. 4. Schematic showing the flow in the PBL and the vertical profiles of potential temperature and heat flux.; see text (after Melfi et al., 1983).

2.4 Measurements of water vapor (latent) heat flux.

The measurement of water vapor flux is done by measuring the vertical integrals of vapor at both the upwind and downwind ends of the path over the ocean; the difference is the integrated flux from below. Let the integrals over the column be Q_1 and Q_2 . The flux is then

$$F_q = \mu(Q_2 - Q_1)\lambda^{-1} \quad (10)$$

There are at least two basic schemes of measuring the total burden of water vapor (Q) in a beam extending from a satellite instrument to the surface. One operates in the IR; the other in the microwave band. Prabhakara et al. (1979) have used the 8 m to 9 m spectral window as observed by the Nimbus 4 Infrared Interferometer Spectrometer (IRIS) to measure the precipitable water over the oceans. They report an accuracy of about $\pm 15\%$ ($\sim 0.45 \text{ g cm}^{-2}$) rms and a measurement threshold of 1 g cm^{-2} as compared to radiosonde data. Prabhakara et al. (1982) have also shown that the difference in microwave brightness temperature between the 19 and 21 GHz channels on the Nimbus 7 Scanning Multichannel Microwave Radiometer (SMMR) also provides a measure of Q . The latter method yields an rms error of 0.25 g cm^{-2} and a threshold of about 0.5 g cm^{-2} . Gloersen et al. (1983) have used this approach to map the global distribution of mean seasonal integrated vapor

Recent developments have stimulated the move to the 183 GHz water vapor absorption line as a means of profiling water vapor radiometrically (Wang et al., 1983). Because of the strength of this line, it is believed that such a radiometer will provide especially high accuracy and an exceedingly small Q threshold. At this time, however, no quantitative estimates can be given.

For climatic purposes it is generally accepted that a precision of 10 to 15 watts m^{-2} would be useful over times of a few weeks to discern significant changes. To achieve a precision of 10 watts m^{-2} in the latent heat flux over a time of 10^4 sec. and over a corresponding path would require a precision of about $4 \times 10^{-3} \text{ g cm}^{-2}$ in the measured difference in Q . This can not be done with existing methods. However, it is thought to be attainable with the sensitive 183 GHz system (T. T. Wilheit, private communication). The smallest significant value of water vapor worthy of detection is about 0.2 g cm^{-2} . This is below the detection thresholds of either the present methods, but it is probably achievable in the 183 GHz band. By and large the effects of most clouds may be neglected. Only the large high liquid water content clouds will contaminate the measurements.

In the case of cold outbreaks within a few hundred kilometers from shore, one may assume that the air above the PBL is very dry. Accordingly, any downstream difference in the column integral of vapor is attributable to flux from the ocean. In other situations, however, it is possible that advection across the direction of the surface wind at levels above the PBL may contribute to the observed changes in Q . In the absence of a high resolution water vapor profiling system such as the DIAL lidar (Wilkerson and Schwemmer, 1983) it may be impossible to make the needed corrections. The only reasonable alternative is to use a regional or global circulation model (GCM) which incorporates a parameterization of surface fluxes and permits one to compute advective fluxes above the PBL. Of course, the accuracy of the model calculations is subject to question. However, one may assume that they provide acceptable approximations if they simulate the essential atmospheric features.

2.5 Inferring temperature profiles from cloud features.

Another set of schemes to approximate the flux in cold air outbreaks are illustrated in Fig. 5. Here, the basic idea is to deduce the change in the air column as it moves from near shore out over the ocean. This is what Henry and Thompson (1976) did over the Gulf of Mexico. But they used actual radiosonde data. In our case, there is no sounding available at the downwind end of the path. Accordingly, the sounding must be made by remote sensing methods.

For this purpose, one may use the upwind cloud edge position. We assume that all the changes in the temperature and humidity profiles occur in the PBL. Radiometric measurements may be made of the cloud top temperature near the upwind end of the cloud streets. Since the air in the PBL is well mixed, one assumes an adiabatic profile from the surface to the cloud top as in sounding B in Fig. 5. One can neglect the unstable profile in the immediate surface layer. The difference between the measured temperature profile at the shore and that deduced at the cloud edge is proportional to the total heat flux from the water. One can improve the accuracy by taking account of the entrainment across the inversion layer by increasing the estimate by about 20%. Henry and Thompson (1976) neglected this effect.

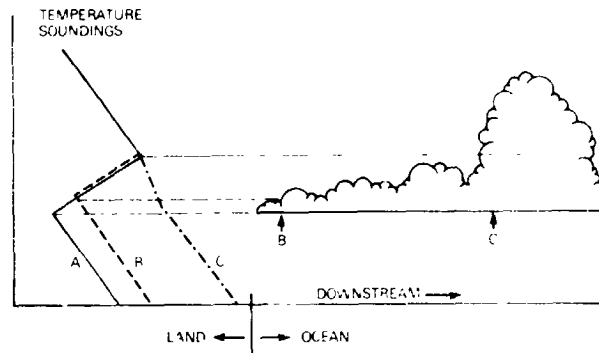


Fig. 5. Schematic of downstream growth of cloud streets in cold outbreak. Sounding A is measured at shore; B and C are inferred. B is near upwind cloud edge; C where clouds suddenly penetrate inversion.

A serious problem is that the clouds at the upwind end of the cloud streets do not usually fill the 1 km field-of-view of an instrument such as the TIROS-N Advanced Very High Resolution Radiometer (AVHRR). Hopefully, a future satellite will have better IR resolution. At present, the approach is usable only from aircraft. The resolution problem decreases as clouds grow larger downwind. But one then has to estimate the temperature profile assuming a wet adiabatic profile from cloud base to cloud top, and a dry adiabat in the PBL below cloud base. This requires knowledge of the cloud base height as obtainable from a model.

When the surface heating has produced a potential temperature in the PBL which exceeds the maximum temperature in the inversion, then the clouds will suddenly break through the inversion as shown at point C in Fig. 5. The downwind position of this event marks the point at which the equivalent potential temperature in the PBL is equal to that at the top of the inversion. The temperature profile there is then known at least approximately.

The latter approach assumes that there is no change in the temperature profile above the PBL from that measured at the shore line. Since this assumption is not always valid, the use of a lidar and a high resolution radiometer would provide the height and temperature coordinates from which soundings may be extrapolated downwards. We may assume that we have some measure of SST from prior measurements in clear air or from microwave observations. The SST provides an upper bound to the surface air temperature.

Our problems should be alleviated in the future through the use of lidar sounding techniques in the absence of clouds (Korb and Weng, 1982; Wilkerson and Schwemmer, 1982). Unlike passive methods, active sensors should be capable of giving vertical resolutions of 1 km for temperature and humidity from spacecraft and better resolution from aircraft. (Much higher resolution is achievable in measuring boundaries of clouds and aerosol layers.) The present spacecraft design studies consider instrument systems that require considerable time integration. This in turn, limits the horizontal spatial resolution to some 200 km. At this scale, the appearance of significant cloud cover anywhere along the path would contaminate the measurements. Unfortunately, we do not anticipate a lidar capability for the measurement of vertical profiles of temperature in the lowest few tens of meters.

2.6 Measurements of wind stress at sea surface.

For wind stress observations scatterometry has been proven to work under a range of wind conditions. However, work is needed to find optimal algorithms during cold outbreaks. Such conditions involve high winds, often above 20 m/s, and rapidly developing wave fields and boundary layers. Not only is there convective overturning in both the air and the water, but the mechanism of generation of turbulence in both media depend upon the waves, so that the mechanism is different from the turbulence generating process in the boundary layer of a rigid surface. This was reported by Donelan et al. (1983) and Kitaigorodskii (1983). One should therefore expect that one would have to take both the wave field and the wind into consideration when one attempts a parameterization of stress. Fortunately, under most conditions, the winds and the waves are related; thus a single parameter representation may be sufficient. But it may be inadequate under strongly developing waves where wind and waves are far from equilibrium, such as during cold outbreaks.

Breaking waves also create streamwise vorticity in the water, and the orbital velocity field of the waves stretch and compress this vorticity, causing turbulence production through vortex breakdown and shear instability. The measurements of Cavalieri under cold outbreak conditions in the Northern Adriatic (personal communication) shows that the shear stresses in the water can reach five to ten times the value given by conventional parameterizations based on wind speed.

Added to this is the fact that waves carry momentum. So the wind stress on the water surface will be found partly in the mean velocity field in the water boundary layer and partly in the wave field. Waves transport momentum at group velocity, so that momentum introduced into the water by wind stress can be converted to mean current far away from where the stress was put in. Scatterometry may still be a good method for measuring wind stress, since the short waves that the scatterometer observes are generated locally, although, of course, they may be affected by wave breaking and water turbulence.

2.7 Possible inferences of ocean effects.

Cold outbreaks cause cooling of the water, equal in heat to the heating of the atmosphere, and the overturning may reach to great depths. Horizontal variations in cooling lead to mean density gradients and thus to currents. After a particularly cold winter the effects may be dramatic; for example, after the winter of 1976-77 in the eastern U.S., Worthington (1977) showed that the speed of the Gulf Stream had reached an all time high.

However, few of the oceanographic consequences of cold outbreaks will be observable from satellites. It is therefore especially important to make the most out of the atmospheric observations so that one can relate total heat transfer, total evaporation and wind stress to changes in oceanic stratification and excitation of oceanic motions. This will have to be done through numerical modeling.

3. CONCLUDING REMARKS

We have attempted to gather a variety of concepts for the measurement or inference of the energy and vapor fluxes across the air-sea interface under conditions of unstable cold outbreaks. These proposed methods are summarized in the abstract. By and large, the techniques permit us to infer fluxes through the observation of the effects of the transports on the atmosphere such as the progressive downstream heating, moistening, and growth of the planetary boundary layer and associated cloud formation. The observed evolution of the PBL is related to the fluxes through the use of numerical and analytical models. The measurables include surface wind speed, SST, the downstream slope of the PBL as observed by lidar, the roughness and depth of the PBL inversion also observed by lidar, and precipitable water vapor as observed by either IR or microwave radiometry.

None of the concepts has been demonstrated and so the paper is necessarily speculative. Individually, the methods are subject to serious constraints; as a group, however, they complement each other and appear promising in providing reasonable estimates of the fluxes of heat and vapor.

4. ACKNOWLEDGEMENTS

The authors are indebted to Drs. S. H. Chou, S. H. Melfi, P. Cuddapah, T. T. Wilheit, and P. Gloersen for valuable discussions and the use of data from their papers. We also greatly appreciate the insight provided by Dr. Mark Helfand and the general assistance of Mr. Earl Kreins and Mrs. Tracy Pepin. All are members of our Laboratory.

5. REFERENCES

Chou, S. H. and D. Atlas, 1982: Satellite estimates of ocean-air heat fluxes during cold air outbreaks. *Mon. Wea. Rev.*, 110, 1434-1450.

Deardorff, J. W., G. E. Willis, and B. H. Stockton, 1980: Laboratory studies of the entrainment zone of a convectively mixed layer, *J. Fluid Mech.*, 100, 41 pp.

Donelan, M. A., S. A. Kitaigorodskii, J. L. Lumley, and E. A. Terray, 1983: A case study of wave-turbulence interactions in the marine surface layer. Talk given at the Sixth Symposium on Turbulence and Diffusion of American Meteorological Society, March 22-25, 1983.

Gautier, C., 1981: Proc. Workshop of Applications of Existing Satellite Data to the Study of the Ocean Surface Energetics, 19-21 November 1980. Rep. NASW-57380, University of Wisconsin Press, Madison, 237 pp.

Gloersen, P., D. J. Cavalieri, A. T. C. Chang, T. T. Wilheit, W. J. Campbell, K. F. Kunzi, R. O. Ramseier, D. B. Ross, D. Staelin, E. P. L. Windsor, F. T. Barath, P. Gudmandsen, O. M. Johannesen and E. Langham, (1984): A summary of results from the first Nimbus 7 SMMR observations. *J. Geophys. Res.* (in press).

ORIGINAL PAGE 19
OF POOR QUALITY

Henry, W. K. and A. H. Thompson, 1976: An example of polar air modification over the Gulf of Mexico. *Mon. Wea. Rev.*, 104, 1324-1327.

Kitaigorodskii, S. A., 1983: The equilibrium range in the spectrum of wind generated waves. Talk given at Sixth Symposium on Turbulence and Diffusion of American Meteorological Society, March 22-25, 1983.

Korb, C. L. and C. Y. Weng, 1982: A theoretical study of a two wavelength lidar technique for the measurement of atmospheric temperature profiles. *J. Appl. Meteor.*, 21, 1346-1355.

Melfi, S. H., J. D. Spinhirne, S. H. Chou, and S. Palm, 1983: Lidar observations of vertically organized convection in the planetary boundary layer over the ocean. *J. Clim. Appl. Meteor.* (to be submitted).

Prabhakara, C., H. D. Chang, and A. T. C. Chang, 1982: Remote sensing of precipitable water over the oceans from Nimbus 7 microwave measurements. *J. Appl. Meteor.*, 21, 59-68.

Prabhakara, C., G. Dalu, R. C. Lo, and N. R. Nath, 1979: Remote sensing of seasonal distribution of precipitable water vapor over the oceans and the inference of boundary-layer structure. *Mon. Wea. Rev.*, 107, 1388-1401.

Sanders, F. and J. R. Gyakum, 1980: Synoptic-dynamic climatology of the "bomb". *Mon. Wea. Rev.*, 108, 1589-1606.

Stage, S. A. and J. A. Businger, 1981a: A model for entrainment into a cloud-topped marine boundary layer -- Part I: Model description and application to a cold air outbreak episode. *J. Atmos. Sci.*, 38, 2213-2229.

Stage, S. A. and J. A. Businger, 1981b: A model for entrainment into a cloud-topped marine boundary layer -- Part II: Discussion of model behavior and comparison with other models. *J. Atmos. Sci.*, 38, 2230-2242.

Wang, J. R., J. L. King, T. T. Wilheit, G. Szejwach, L. H. Gesell, R. A. Nieman, D. S. Niver, B. M. Krupp, and J. A. Gagliano, 1983: Profiling atmospheric water vapor by microwave radiometry. *J. Appl. Meteor.*, 22, 779-788.

Wilkerson, T. D. and G. K. Schwemmer, 1982: Lidar techniques for humidity and temperature measurements, *Opt. Eng.*, 21, 1022-1024.

Worthington, L. V., 1977: Intensification of the Gulf Stream after the winter of 1976-77. *Nature*, 270, 415-417.

N84 27268

SCATTEROMETER CAPABILITIES IN REMOTELY SENSING GEOPHYSICAL
PARAMETERS OVER THE OCEAN: THE STATUS AND THE POSSIBILITIES

R. A. Brown

University of Washington
Department of Atmospheric Sciences

In accordance with a venerable remote sensing, and personal, tradition, this discussion will oscillate between the real and the speculative.... between the verified capability and the likely operational possibilities for the microwave sensors. I doubt that there exist simple relations between a single microwave return and a geophysical parameter for all practical conditions, e. g. between the scatterometer (SCATT) brightness and wind vectors or radiometers and Sea Surface Temperature. In fact, each fails in special circumstances due to increasing importance of some additional geophysical variable. However, this is no absolute limitation---the number of independent geophysical parameters is finite, even small. It may mean that a combination of sensors will be sufficient to define an operational set of geophysical parameters. Or perhaps simply an occasional buoy measurement will be needed to establish an absolute value.

If the desired geophysical parameters were linked in direct proportion, then only one sensor would be needed. For instance, the oceanic surface stress would give the mixed layer flow in the ocean, the air-sea fluxes and the wind profile in the atmospheric boundary layer. Indeed, the wind generated surface roughness in the 1-6 cm wavelength; the longer waves comprising the steady "sea state"; and the SST are all sufficiently interrelated that microwave brightness has been accurate to some degree in relating to each. Still, any dynamic oceanographer or atmospheric scientist can rattle off a dozen reasons why the capillary scale ocean waves are not uniquely related to the wind in the Planetary Boundary Layer (PBL). Nevertheless, verification experiments have shown that successful simple linear correlations do exist. I have been involved in studying the verification and physical mechanisms of the SCATT relation to wind or stress, so the following is from this perspective. Perhaps similar problems beset all electromagnetic remote sensing relations.

The SEASAT Scatterometer (SASS) fortunately had two surface wind verification experiments, the Gulf of Alaska Experiment (GOASEX) and the serendipitous Joint Air Sea Action Experiment (JASIN) in the North Atlantic. Detailed analysis of these two experiments indicated two unexpected things to me: (1) SASS determines winds on a large scale average to ± 2 m/s and has the potential to determine the direction to ± 20 deg. (2) The

surface verification capability is only marginally better than this. Thus, the routine operational capability for determining winds over the ocean conventionally is considerably less than the SCATT potential. So we have the problem that the complete capability of a satellite microwave sensor is not discernable by the surface measurements. Yet the empirical correlations between sensor signal and measured geophysical parameter, which makes up the sensor algorithm, is established using these insufficient measurements. One way around this lack of point by point verification is to look for integrated effects.

We can amass many points by creating surface windfields from conventional data (National Weather Service (NWS) pressure charts; ship and buoy data...) and build up statistical comparisons with SCATT data. This has been done for the base experiments, and is summarized in figure 1. Since derived windfields from conventional data without dedicated scientific ships and buoys is significantly worse, this verification product is essentially completed. Further information is being sought from comparing different sensors with a careful eye to the limitations of each. There are other papers summarizing these efforts. We have directed our efforts toward seeking implied verification from investigating the sensor ability to discern singular features, such as fronts in particular, but also tight cyclones, low or high pressure centers. If we assume that the SCATT footprint individual values are accurate, then features with variability on the scale of 20-50 km would be discernable. The first indications, from a weak front in JASIN, were encouraging (Brown, 1982). The characteristic of the brightness signal and the correlated multiple wind vector plots showed change along a line which more clearly defined the frontal location than did conventional analysis. In this respect, we are looking at sensor capabilities beyond wind sensing. Since sensor wind measurement accuracies cannot be evaluated with direct surface measurements, some measure of theory is needed to guide the empirical parameterization process, i. e. the algorithm development. There exists a mixture of relevant theoretical developments and observational facts which may help in understanding the physics involved and suggest some new operational capabilities for the SCATT.

1) The wind field over the ocean and the corresponding bulk flux coefficients, $C_D = \tau / \rho U^2$, $C_H = H_0 / \rho \Theta_* U$ (where τ and H_0 are surface stress and heat fluxes, ρ is density, Θ_* is a temperature parameter and U is wind, usually at 10 m), are not constant with respect to variation in wind, PBL stratification or humidity effects. The state of the art variation of the drag coefficient with these variables is shown and discussed.

2) Wind momentum obviously goes into long wave production. This must be related in a fairly constant way to the short wave energy for the linear algorithm to work. In some cases, such as behind fronts, the long wave steady state may not be attained. From the Storms Response Experiment (STREX) some data is shown to illustrate this effect.

In other cases, spurious swell may intrude. In this case, the relation to short waves is not understood and we had better hope that the effect is small. One can note that the short waves must result from a dynamic wind shear instability at or near the surface with wavelength rather independent of stratification. Also, the common observation of windrows, wherein convergence zones exhibit short wave suppression, suggests that surface tension is a factor. Here is a link between momentum transfer and SST effects on the resulting wave structure which has yet to be sorted out.

3) The flow in the PBL has distinctly different regimes. For $U > 7$ m/s, instabilities and large scale coherent structures exist in the flow, modifying the fluxes. This may be related to a discontinuity observed in the linear wind versus SASS brightness relations. It is possible that this fact led to the consternation at the SEASAT II workshop where one algorithm fit the linear relation below critical wind velocities and the other above. A single linear relation is inadequate to fit the two disparate regimes. There probably exist similar problems in other algorithms.

While the final parameterization scheme may evolve to two patched linear segments by itself, the theoretical knowledge may facilitate things, and offers physical justification.

4) When the complete, multivector plot of possible SASS wind vectors is examined, distinct changes in character occur in association with corresponding mesoscale wind and ocean wave phenomena, such as fronts and local storm activity. Some specific examples have been identified and are shown in figure 3. The accuracies and abilities of Scatt compared to conventional analyses in locating fronts is evident from this figure.

5) When the Scatt windfield---with its current verified accuracy--- is used as input to the state of art PBL model--- with its current verified accuracy---a geostrophic windfield, with error bars, is produced. The corresponding barotropic surface pressure map can be constructed. A comparison between this and conventional

weather service maps over the ocean can be made.

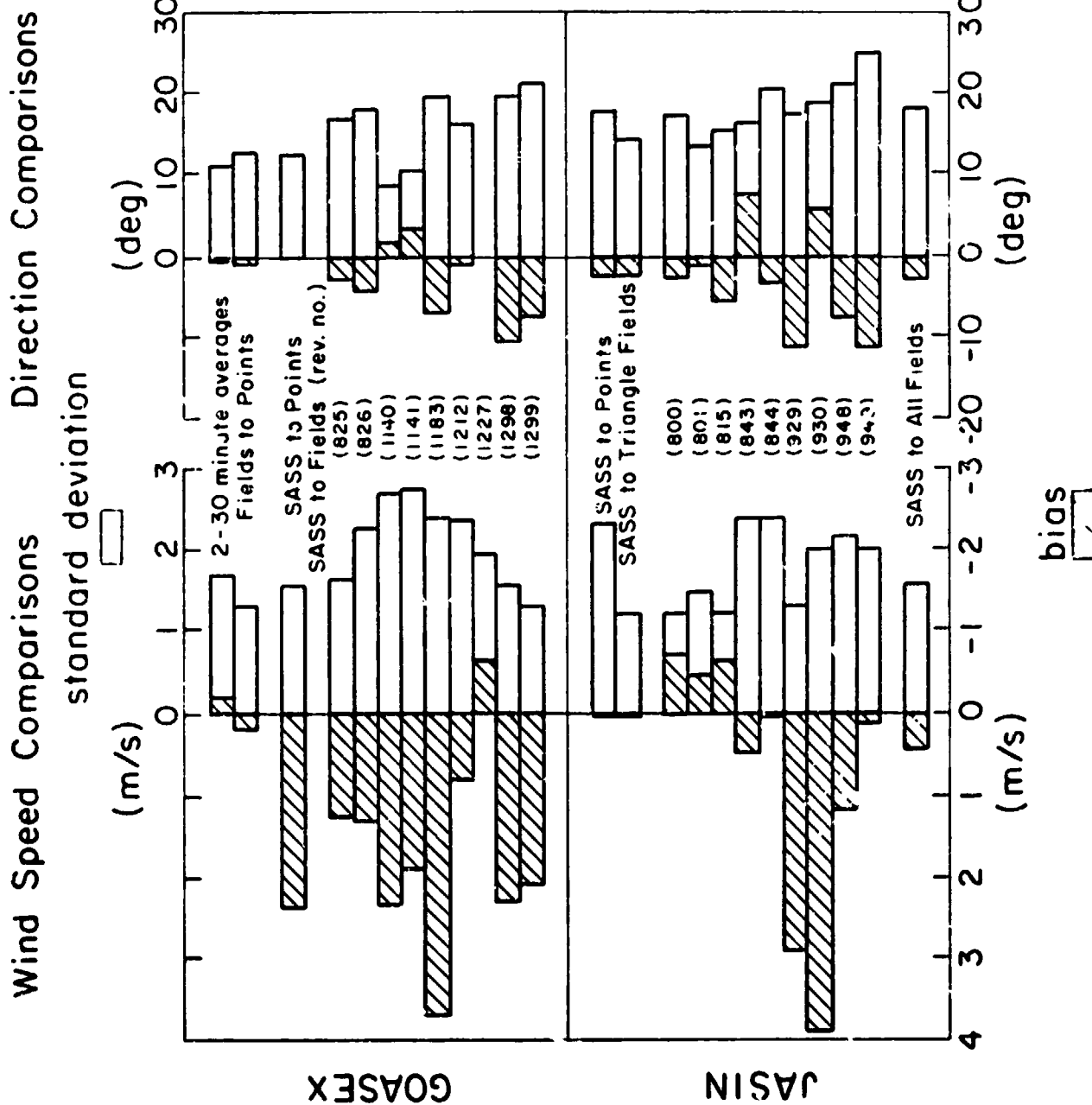
6) Specific storm fronts were flown through by the NOAA P-3 aircraft in or near the PBL during STREX. Some unexpected indications of strong wind and stress variation in the vicinity of a front were found.

In this experiment, comparison between the P-3, the NCAR Electra and the NASA Convair 990 Scatt measurements were made in very high winds. Scatt versus aircraft stress and winds are summarized. Variations and measurement errors in both terms were significant. However, it is clear that the variation of fluxes (heat and momentum) across a front is significant on the Scatt resolution.

In summary, extensive comparison between surface measurements and satellite Scatt signal and predicted winds show successful wind and weather analysis comparable with conventional weather service analyses. However, in regions often of the most interest, e. g. fronts and local storms, inadequacies in the latter fields leaves an inability to establish the satellite sensor capabilities. Thus, comparisons must be made between wind detecting measurements and other satellite measurements of clouds, moisture, waves or any other parameter which responds to sharp gradients in the wind.

The ability of the sensors to distinguish dynamic regions in the wind and stress fields is a separate capability, of practical use in supplementing conventional analyses right now.

It seems likely, at least for the windfields and the derived surface pressure field analysis, that occasional surface measurements are required to anchor and monitor the satellite analyses. These should be permanent, calibrated high accuracy point measurements. Their averaging times must be made compatible with the satellite sensor measurement. Careful attention must be paid to the complex fields which contain many scales of turbulence and coherent structures affecting the averaging process. It also seems likely that the satellite microwave system is capable of replacing the conventional point observational/numerical analysis for the ocean weather.



N84 27269

A NEW PARAMETERIZATION OF AN EMPIRICAL MODEL FOR
WIND/OCEAN SCATTEROMETRY

Peter M. Woiceshyn
Jet Propulsion Laboratory, California Institute of Technology,
Pasadena, CA, USA
Morton G. Wurtele
Department of Atmospheric Sciences, UCLA, Los Angeles, CA, USA
Dale H. Boggs
dB Systems, Ltd., La Canada-Flintridge, CA, USA
Lawrence F. McGoldrick
Applied Physics Laboratory, Johns Hopkins University, Laurel, MD, USA
Steven Peteherych
Atmospheric Environment Service, Downsview, Ont., Canada

1. ABSTRACT

This study reveals that the power-law form of the Seasat A Scatterometer System (SASS) empirical backscatter-to-wind model function does not uniformly meet the instrument performance specification requirements; viz., error in derived wind speed $< \max(2 \text{ ms}^{-1}, 10 \text{ percent})$, over the range 4 to 24 ms^{-1} . Analysis indicates that the horizontal-polarization (H-Pol) and vertical-polarization (V-Pol) components of the benchmark SASS1 model function (Schroeder, et al 1982b) yield self-consistent results only for a small mid-range of speeds at larger incidence angles, and for a somewhat larger range of speeds at smaller incidence angles. The present approach differs from previous calibration studies (e.g., Jones et al., 1982): here the model's internal V-Pol vs. H-Pol consistency is examined by the use of a set of pair-wise collocated SASS-produced winds, where one member of a wind pair derives from only V-Pol backscatter measurements and the other from only H-Pol measurements. This data set was created by extracting all pairs of SASS GDR (Boggs, 1982) winds of the form (U_{VV}, U_{HH}) such that U_{VV} and U_{HH} are contemporaneous and are separated by no more than 50 km, and contains 377,289 such pairs.

Comparison of SASS1 to in situ data over the Gulf of Alaska region further underscores the shortcomings of the power-law form. We find that the slope of the V-Pol-backscatter-measurement vs. wind-speed relationship for speeds greater than 10 ms^{-1} is less than that given by SASS1. Taken together, this in situ comparison and the SASS1 V-H self-consistency study indicate that H-Pol-backscatter vs. wind-speed slope is greater than V-Pol-backscatter slope for speeds above 10 ms^{-1} , with the reverse holding for speeds under 10 ms^{-1} . Thus H-Pol backscatter shows greater sensitivity to wind speed variation at higher winds, and less at lower winds, than does V-Pol backscatter.

Finally, a physically-based empirical SASS model is proposed which corrects some of the deficiencies of power-law models like SASS1. The new model allows the mutual determination of sea surface wind stress and wind speed in a consistent manner from SASS backscatter measurements. In contrast, the SASS1 model only determines the wind speed.

ORIGINAL PAGE IS
OF POOR QUALITY

1. INTRODUCTION:

The oceans cover 70 percent of the Earth's surface, and the paucity of weather observations over these huge areas has always been a great handicap to wind and wave forecasting. This condition was alleviated for the short three summer months in 1978 when NASA flew the Seasat satellite, which carried three wind measuring instruments (Hinds and Wilson, 1983); only one of which we are concerned with here.

The Seasat A Scatterometer System (SASS) was a 14.6 GHz (2.1 cm) active microwave radar designed to permit inference of the ocean surface wind from precise measurements of the backscatter of emitted radiation by gravity-capillary waves on the sea surface. The received return, expressed as the normalized radar cross section (NRCS or σ^0), from the four dual-polarized, x-oriented antennae may be directly related to the surface wind speed through a geophysical "model function", constructed by means of a combination of theory and experiment (Schroeder et al., 1982b). The wind direction, however, is not uniquely determined (Wurtele et al., 1982; Peteherych et al., these Proceedings). This paper will not be concerned with the multiple wind-direction ambiguity (i.e., the "alias") problem.

The fundamental validations of SASS are contained in the articles by Jones et al. (1982), Schroeder et al. (1982a and 1982b), Wurtele et al. (1982), Brown (1983), reporting on the large cooperative Gulf of Alaska Seasat Experiment (GOASEX) and Joint Air-Sea Interaction Experiment (JASIN) workshops, out of which came the benchmark SASS1 "model function". The SASS1 relates the NRCS to the wind field parameters, speed and direction, relative to: the incidence angle (θ) of the radar radiation arriving at the sea surface, the azimuth angle (χ) of the wind direction relative to the radar beam illumination at the surface, and the polarization type (ϵ) of the incident radar radiation: i.e., vertical polarization (V-POL or V-POLE) or horizontal polarization (H-POL or H-POLE). A review of the history of the relationship between NRCS and wind speed at microwave frequencies is given by Moore and Fung (1979), Boggs (1981), and Schroeder et al. (1982b). The basic assumptions are that the relationship between the NRCS and the wind speed is a power law (described below), and that there is no dependence on sea surface parameters such as temperature, viscosity, and surface tension. The constants of the power law were evaluated by "tuning" the model to a "surface truth" comparison wind data set in JASIN, where the sea surface temperature was constant (about 12°C) and the wind speed range was small (4 - 16 ms⁻¹, Boggs, (1981)). The Seasat specifications for the SASS were: wind speed measurement range of 4 to 24 ms⁻¹ with an accuracy of ± 2 ms⁻¹ or 10%, whichever is greater; and wind direction of 0 to 360 to within 20 degrees (Jones et al., 1982). Jones et al. claim that the SASS model function, SASS1 (Schroeder et al., 1982b) yield accuracies better than the Seasat specifications over the 0 to 16 ms⁻¹ range of winds observed during JASIN. This paper outlines problems with the above assumptions in the SASS model function, particularly at larger wind speeds and incidence angles. The results here will begin to show that SASS did not uniformly meet its performance specifications over the

ORIGINAL PAGE IS
OF POOR QUALITY

wind speed range placed by the Seasat Project, and that a small fraction of the 16 million SASS observations may be in error by more than the performance specifications allowed. In spite of this, the study by Peteherych et al. (1984, these Proceedings) clearly shows that the scatterometer system "works" in defining and locating the weather patterns. Therefore, the SASS data record derived using SASS1 is eminently qualified for many meteorological and oceanographic purposes.

The presentation of our results to date is organized into three parts:

- (1) The first part is a restriction to aspects of the SASS1 model function that can be treated without reference to surface truth. Here we use various checks in order to test the internal consistency of the model function, both quantitatively and in its form. The data set used for this study consists of 377,289 pairs of SASS wind speeds of the form (U_{VV}, U_{HH}) , where each member of the pair is derived separately from V-Pol and H-Pol NRCS's such that U_{VV} and U_{HH} are located within 50 km of each other. This data set is an extraction of all such pairs of SASS/SASS1 derived wind speeds from the complete Seasat mission data set resident on the Pilot Ocean Data System (PODS) at JPL.
- (2) The second study makes some comparisons of wind speeds from in situ wind fields derived from ships and buoy reports, to SASS1 and other scatterometer model functions.
- (3) A new model is then hypothesized to reduce or eliminate some of the discrepancies shown by the studies cited above. This model differs in form from previous models, including SASS1, but should be considered as a modification of these, rather than as a construction from first principles.

3. INTERNAL CONSISTENCY CHECK OF THE SASS1 MODEL

The SASS operated in any one of 8 modes of antenna/polarization combinations during which a four antenna-beam/polarization sequence was cycled through. The principal operational mode was mode 1. This resulted in sequencing the four antennas through vertical polarization on both sides of the spacecraft. The present study, however, is based exclusively on data taken during modes 3 and 4. These two modes generated vertical and horizontal polarization sequencing on the left side of the spacecraft only (mode 3) or on the right side only (mode 4). This resulted in the determination of SASS winds derived from either V-Pol NRCS data or H-Pol NRCS data in nearby locations.

Figure 1 illustrates samples of SASS wind fields in the form of direction ambiguity "aliases" (the X's with noted speeds in meters per

second) derived with the SASS1 model function. The wind solutions in the left panel are computed from V-Pol-only data, and in the right panel from H-Pol-only data. These measurements were taken during a single SASS pass on the morning of September 17, 1978 in the vicinity of the HMS Ark Royal aircraft carrier (marked A) and the NATO fleet operating in the southern Norwegian Sea (Fett and Bohan (1981)). The flag symbol at A notes that the Ark Royal reported winds of 55 knots (about 28 meters per second) in magnitude by the anemometer mounted 18 meters above the ocean surface. Besides the near agreement between Ark Royal and the H-Pol winds (U_{HH} , at 19.5 m elevation), note the large disagreement between the V-Pol winds (U_{VV} , at 19.5 m elevation) and U_{HH} . We also discovered similar disagreements between U_{VV} and U_{HH} for the high winds in the SASS passes over the storm which damaged the Queen Elizabeth II luxury liner on September 11, 1978.

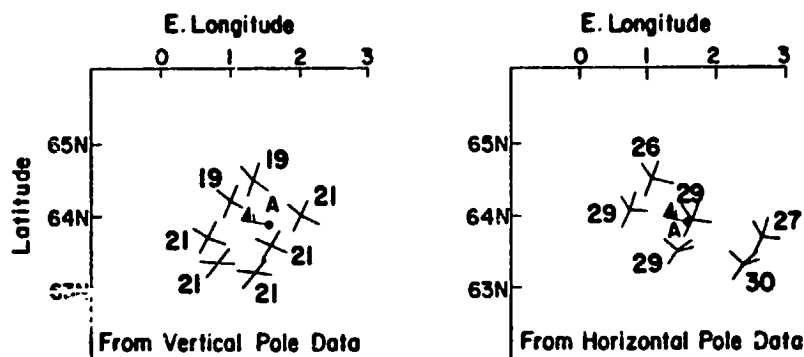


Figure 1. Wind speed comparisons between the HMS Ark Royal (at position A) and winds determined from (1) V-Pol SASS NRCS measurements (left plot), and (2) winds determined from H-Pol SASS NRCS measurements (right plot); during the same Seasat overflight (pass) on Sept 17, 1978.

Having concluded from these specific examples that serious polarization inconsistencies exist in SASS1, we turn to a more systematic and fundamental approach. We first note that the SASS1 model function relates the NRCS intensity to the surface marine wind field by a power law:

$$\text{NRCS} = g(\theta, \chi, \epsilon) U^H(\theta, \chi, \epsilon) \quad (1)$$

Since the NRCS is usually expressed in decibel (dB) units, Equation (1) is written in its logarithmic form:

$$\sigma^\circ = \text{NRCS (dB)} = 10 \{ G(\theta, \chi, \epsilon) + H(\theta, \chi, \epsilon) \log_{10} U \} \quad (2)$$

where $G = \log_{10} g$. The parameters θ , χ , and ϵ are defined above. It is important to observe that this power-law relationship is an established conventional formulation which seems to have arisen (e.g.,

ORIGINAL PAGE IS
OF POOR QUALITY

Valenzuela et al, 1971) as a convenient curve-fitting technique, without any particular physical rationale. The official SASS1 model function is in the form of tables of G and H functions for two-degree intervals of incidence angle (Θ) and ten-degree intervals of azimuth angle (χ) for both V-Pol and H-Pol NRCS (Schroeder et al. 1982b, table 2). As remarked above, these table values were tuned to the high-quality JASIN surface wind fields data set. The total data set was derived from about 700 wind measurements with an upper bound of 16 ms^{-1} , 66 of which are in the low-speed interval 0 to 6 ms^{-1} . Insofar as wind speed is concerned, it is fair to say that SASS1 was tuned to a very limited data set.

If we take $\Theta = 38$ degrees and $\chi = 0$ degrees as typical values, we find in Schroeder et al. (1982b) the table entries for SASS1:

		G	H
ϵ	= V-Pol:	-2.953	1.690
ϵ	= H-Pol:	-3.368	1.823

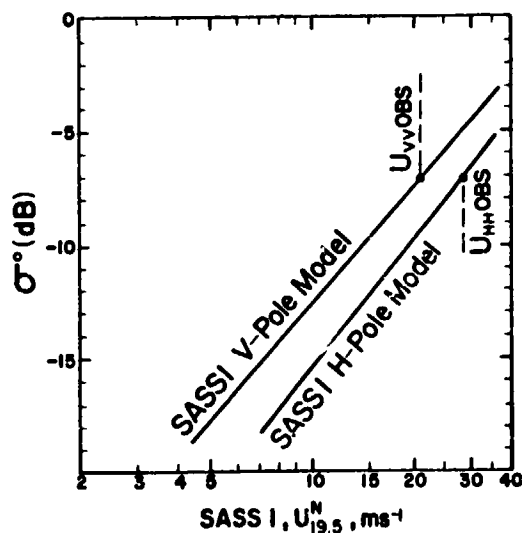


Figure 2. A graphical depiction of SASS1 power-law function, Eq.(2), for the conditions $\Theta = 38$, $\chi = 0$, for both V-Pol and H-Pol NRCS (σ^0). Shown also are representative values from Fig. 1. The superscript N on U (the windspeed) denotes winds corrected to neutral stratification conditions for the atmospheric surface layer. The subscript 19.5 on U indicates the reference height for U above sea level. Both subscripts and superscripts have been dropped elsewhere in the figures and text.

Thus, on a σ^0 vs $\log U$ diagram the H-Pol plot will be below the V-Pol plot, with a slightly greater slope, as seen in Figure 2. Referring to Figure 1, we may take the mean H-Pol wind speed as 29 ms^{-1} and the V-Pol as 21 ms^{-1} . If these two speeds are mapped into NRCS values via the SASS1 table entries -- indicated by the points $U_{V OBS}$ and $U_{H OBS}$ in Figure 2 -- we see that the resulting H-pol and V-pol NRCS's are approximately equal ($\sim -7\text{dB}$). These results at high winds have been anticipated. Valenzuela (1968) reported that "for very rough seas the cross-sections for horizontal polarization become comparable to, or greater, by a few decibels, than those for vertical polarizations; while for calm and moderate sea conditions, the cross sections for vertical polarization are always greater".

The discrepancy noted in the Ark Royal case is characteristic of the higher wind-speed range, as can be seen from the statistical presentation of Figure 3. Here the set of pair-

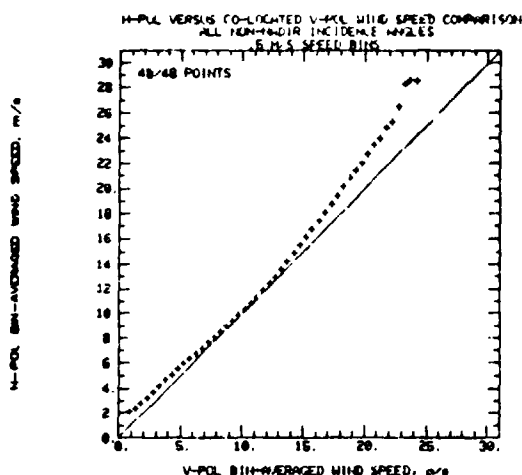


Figure 3. Statistical comparison of winds derived from the SASS1 V-Pol and H-Pol power law. 377,289 pairs of V-Pol and H-Pol wind data were sorted in one-half meter per second V-Pol wind bins.

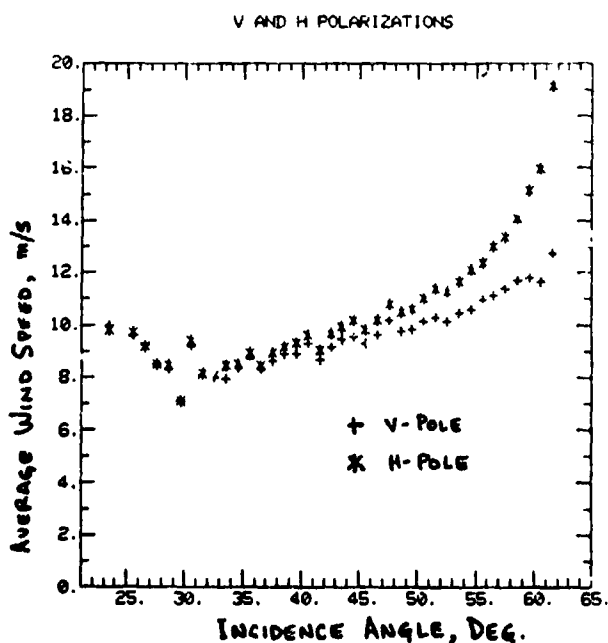


Figure 4. Consistency between winds derived from the SASS1 V-Pol and H-pol power law, Eq. (2), as a function of incidence angle. 377,289 pairs of V-Pol and H-Pol wind data were sorted in one degree incidence angle bands.

wise concurrent SASS V and H pol winds described above is examined in a V vs. H sense. The 377,289 V/H pairs were first sorted by V value into forty-eight 0.5 m/s V-pol wind speed bands along the abscissa. Each ordinate point shown is then the mean speed of all the H values falling within a particular band. Note that this comparison does not depend on the quality of *in situ* data (except for the model-tuning JASIN data itself), but constitutes an internal consistency check on the SASS1 model function.

Figure 4 examines the incidence angle. This study shows differences and sensitivities of the mean wind speeds (grouped in one-degree incidence angle "bands") as a function of incidence angle. The trend in difference between V-Pol and H-Pol winds as a function of Θ , and the general dip of both VV and HH mean wind speeds as a function of Θ beg explanation. If the SASS1 were correctly specified, we would then expect constant and identical mean wind speeds as a function of Θ .

An examination of the sensitivity of SASS1 to wind speed, polarization, and incidence angle, is better displayed in Figure 5, which shows the bivariate frequency distribution of U_{VV} and U_{HH} in three-dimensional form as a function of incidence angle (noted to the right of each of the three distribution plots).

ORIGINAL PAGE IS
OF POOR QUALITY

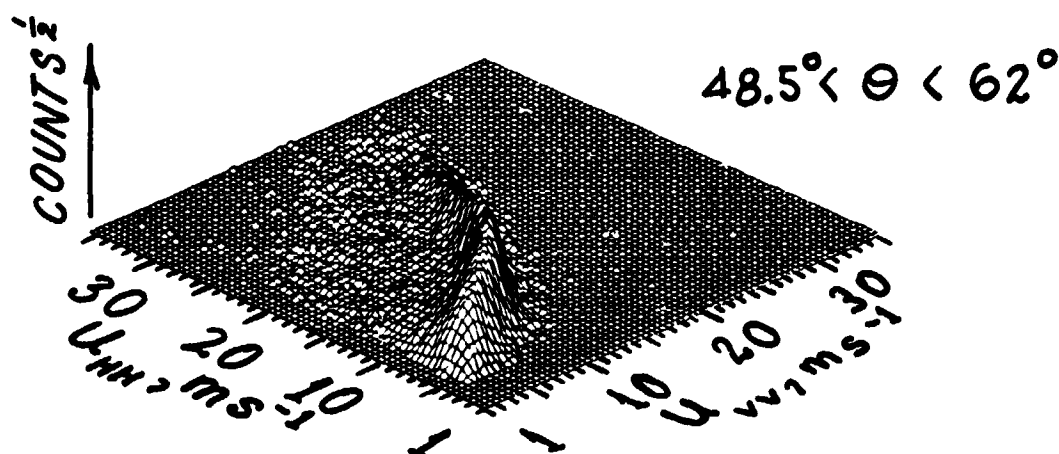
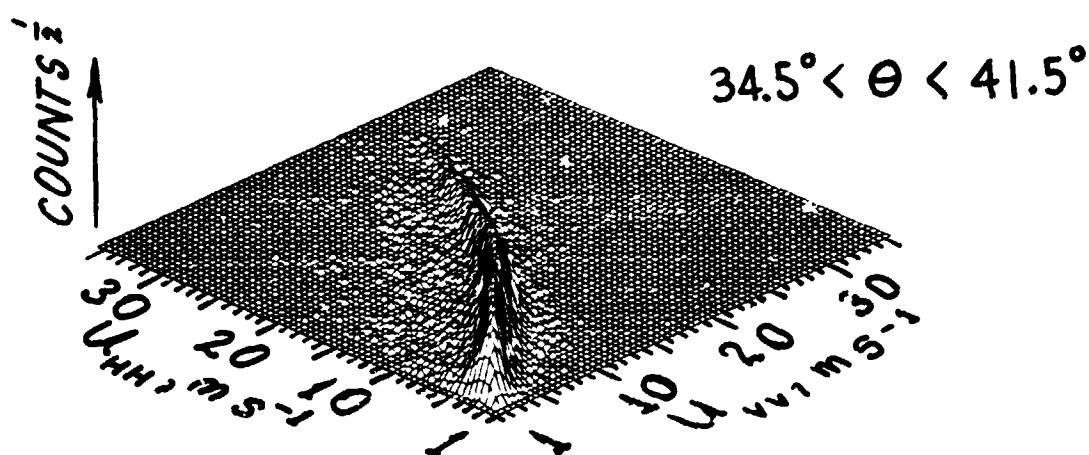
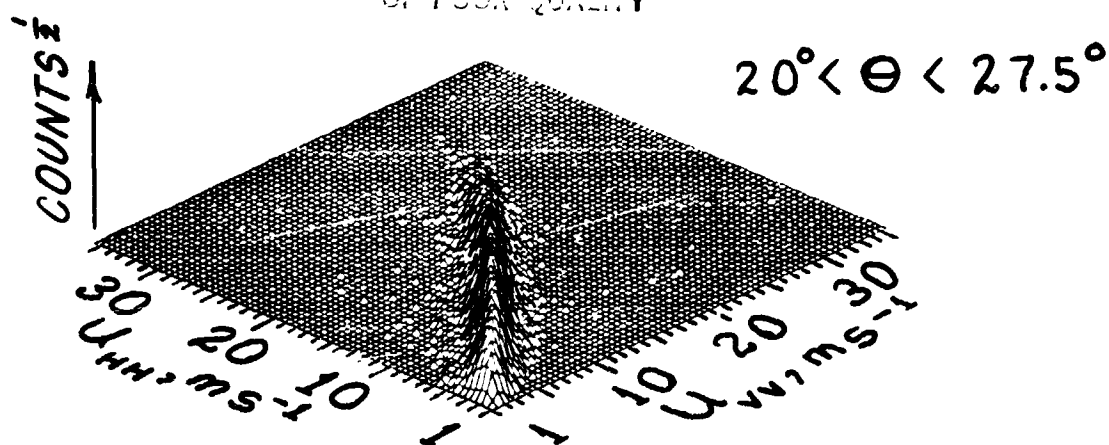


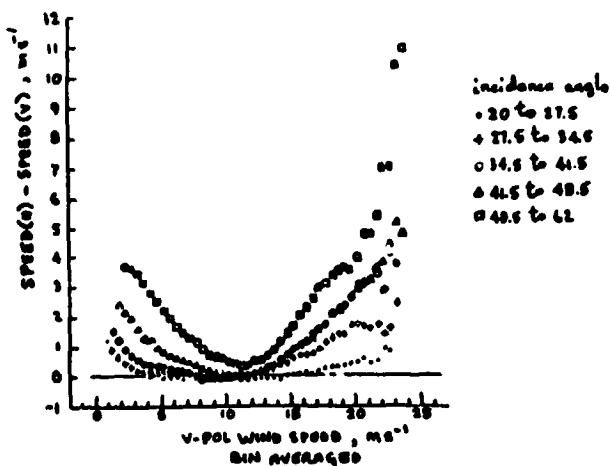
Figure 3. A 3-dimensional display of the characteristics of the bivariate frequency distribution (vertical scale) of collocated (within 50 KM) U_{VV} (right horizontal scale) and U_{HH} (left horizontal scale) derived from SASSI for 3 different incidence angle (Θ) bands. The vertical scale is to the one-half power for ease of display of the characteristics. The wind data are sorted in one-half by one-half meter per second windspeed bins.

ORIGINAL PAGE IS
OF POOR QUALITY

The paired U_{VV} and U_{HH} data set was sub-divided into one-half meter per second wind speed bins in U_{VV} and U_{HH} . These bins were further segregated into 5 incidence angle bands of about 75,000 pairs of measurements in each band. This incidence angle band breakdown is sufficient to indicate the trend of the data. The vertical scale is the square root of the number of pairs (counts) in each one-half by one-half meter per second bin to make the lower frequency counts visible and to ease analysis of the characteristics. The range of wind speeds shown is from one to 35 ms^{-1} for both U_{VV} and U_{HH} ; the grid is one-half ms^{-1} . The data shows the best agreement between U_{VV} and U_{HH} for the lowest range of incidence angles (top panel), except at small winds where U_{HH} is greater than U_{VV} (data lying along the vertical diagonal would indicate exact agreement). The poorest agreement between U_{HH} and U_{VV} evidently is at the largest range of incidence angles. Here, U_{HH} is greater in magnitude for both the lowest and highest winds. In a small interval of midrange wind speeds, the agreement appears satisfactory.

A quantitative estimate of the differences in wind speeds between U_{VV} and U_{HH} as a function of incidence angle is better illustrated by the two plots of Figure 6. In the left plot the data are sorted into one ms^{-1} U_{VV} wind-speed bins on the abscissa, and then averaged over the corresponding ordinate values. Shown is the difference between the mean value of U_{HH} and the mean value of U_{VV} for each U_{VV} bin. In the right plot, the data are sorted into one ms^{-1} U_{HH} wind speed bins.

(H-POL - V-POL) VS Co-LOCATED H-and-V-pol
WIND SPEED COMPARISON
AS A FUNCTION OF INCIDENCE ANGLE



(H-POL - V-POL) VS Co-LOCATED H-and-V-pol
WIND SPEED COMPARISON
AS A FUNCTION OF INCIDENCE ANGLE

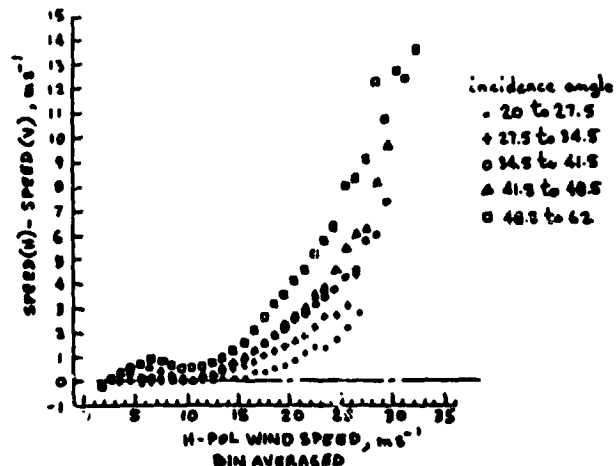


Figure 6. Comparisons of differences between mean values of U_{HH} and U_{VV} as a function of either U_{VV} sorted data (left plot) or U_{HH} sorted data (right plot) for the five different incidence angle bands noted by the symbols at the right of each plot.

ORIGINAL PAGE 13
OF 20

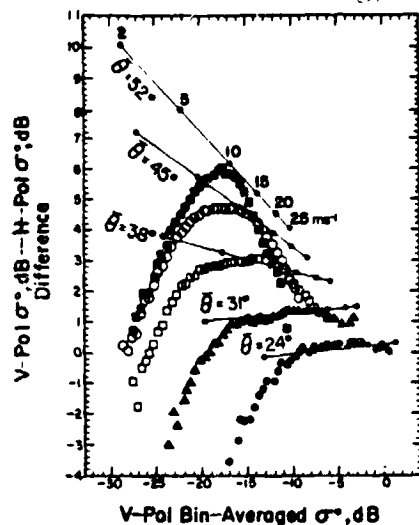


Figure 7. Comparison of differences between mean values of σ_{VV} and σ_{HH} as a function of bin averaged σ_{VV} , all rederived from SASS1 and all the 377,289 pairs of the U_{VV} and U_{HH} data, for the five incidence angle bands centered at Θ values shown. The lines represent the corresponding SASS1 model differences in σ_{VV} and σ_{HH} as a function of σ_{VV} for the five incidence angles. The wind speeds determined from the V-Pole SASS1 model are noted on the top line for a reference.

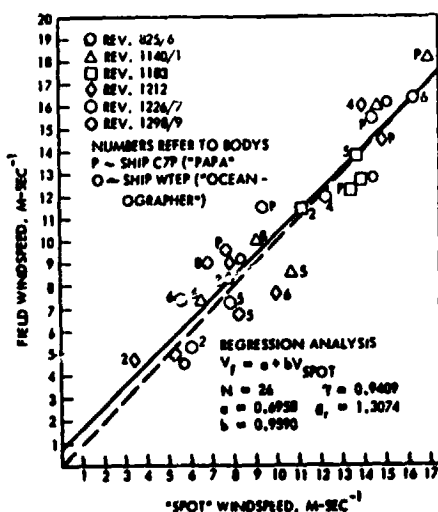


Figure 8. Calibration of the BOASEX-region windfield speeds derived from surface pressure fields to collocated high-quality observations of wind speed from buoys (numbers), research vessels at PAPA (P), and the research ship Oceanographer (O).

The data points are further sorted into incidence angle bands as noted on the plots by coded symbols. Here, all five incidence angle bands are displayed. The best agreements between U_{VV} and U_{HH} for all incidence angles for both binning methods occurs near 10 ms^{-1} , the mid-range of the JASIN wind speed data used to "tune" the SASS1 model function. This data illustrates the lack of consistency between U_{VV} and U_{HH} and shows V-H differences greater than specifications allowed in the error of either polarization type, particularly at the higher winds and larger incidence angles. The differences in both plots for wind speeds less than 10 ms^{-1} , can be partially reconciled by examining the three-dimensional distributions of the U_{HH} and U_{VV} data in Figure 5. The left plot of Figure 6 appears to be more indicative of the trend in the U_{VV}/U_{HH} bivariate distribution mean (approximately given by the ridge top) than is the right plot at lower wind speeds.

Now, is it possible that a minor correction can bring SASS1 into internal conformity? To test this hypothesis, we present the statistical data in a different format. Consider the difference $\sigma_{VV} - \sigma_{HH}$. According to the power law formulation, this difference must have the form:

$$\alpha + \beta \log_{10} U \quad (3)$$

This logarithmic form is seen in the straight lines on Figure 7 plotted according to SASS1 for five incidence angles. The data points corresponding to these incidence angle categories are also plotted as recomputed (i.e. mapped back to units using SASS1 at mid-band incidence angles and the arbitrarily chosen value $\chi = 0$ (upwind) for the azimuth) $\sigma_{VV} - \sigma_{HH}$ versus the bin-averaged V-Pole σ_{VV} . The conclusions of the previous paragraphs are confirmed: the consistency of SASS1 is

ORIGINAL PAGE 13
OF POOR QUALITY

validated only for a small mid-range of speeds for the larger incidence angles, and for a somewhat larger range of speeds for the smaller incidence angles. Altogether, the shapes of the data-curves in Figure 7 strongly suggest that the power law relationship of Equation (1) is not an adequate representation.

4. COMPARISONS OF SASS1 AND OTHER MODEL PREDICTED WINDS WITH IN SITU WINDS

This section will use in situ data to reinforce the conclusions of the previous section: the power law relationship (1) between NRCS and wind speed requires revision.

The primary in situ winds used in this study came from wind fields analyzed for the GOASEX workshops (Barrick et al, 1980, and Brown et al, 1982). Figure 8 illustrates the relatively good quality of the winds from the wind fields when calibrated to buoys in the Gulf of Alaska (the numbers refer to the last digit of the buoy identification number; e.g. "2" refers to buoy 46002) and the research vessels: Oceanographer ("O") and either the Quadra or Vancouver which were located at ocean station "Papa" ("P") at that time. The symbols indicate the SASS Rev numbers at the time of the Seasat overflights of the in situ buoy and ship measurements used in these comparisons. The abscissa, noted in the figure as the "spot" wind field, represents the values of these in situ measurements, while the ordinate represents those from the GOASEX wind fields.

Plotted in Figure 9a (upper left plot) are the wind speed comparisons of the winds from SASS (the ordinate) estimated by the Wentz2 model function (one of the ancestors of SASS1, Barrick et al., 1980), versus the winds from the GOASEX wind fields (the abscissa). Each data point represents a bin of 100 independent pairs of measurements which were sorted along the abscissa, and which were co-located in space and time within 3 hours of the Seasat overpass. The bars represent one sample standard deviation for both parameters in each 100 sample-size bin. Barrick et al. (1980) noted that the G-H table for Wentz2 was based solely on aircraft-scatterometer/wind-"truth" measurements. Thus the computed SASS winds in this plot, derived from a power-law model, were independent of the influence of any SASS/wind-"truth" calibrations. Note that estimations of the SASS/Wentz2 wind speeds are generally higher than those from the GOASEX wind fields. Agreement between these two independent wind data sets occurs near 18 ms^{-1} where the diagonal (which would represent perfect agreement) appears to intercept the data.

The data points in Figure 9b (upper right plot) represent the same data set as in the upper left plot, except the ordinate values have been transformed back to NRCS V-Pol values with Wentz2 using

ORIGINAL PAGE 19
OF POOR QUALITY

$\Theta = 38$ and $\chi = 0$. For the latter specification, the Wentz22 table value for G is -3.524, and for H is 2.074 (F. J. Wentz, personal communication). For comparison, the SASS1 V-Pol model is plotted (the dashed line through the data points), also for $\Theta = 38$ and $\chi = 0$.

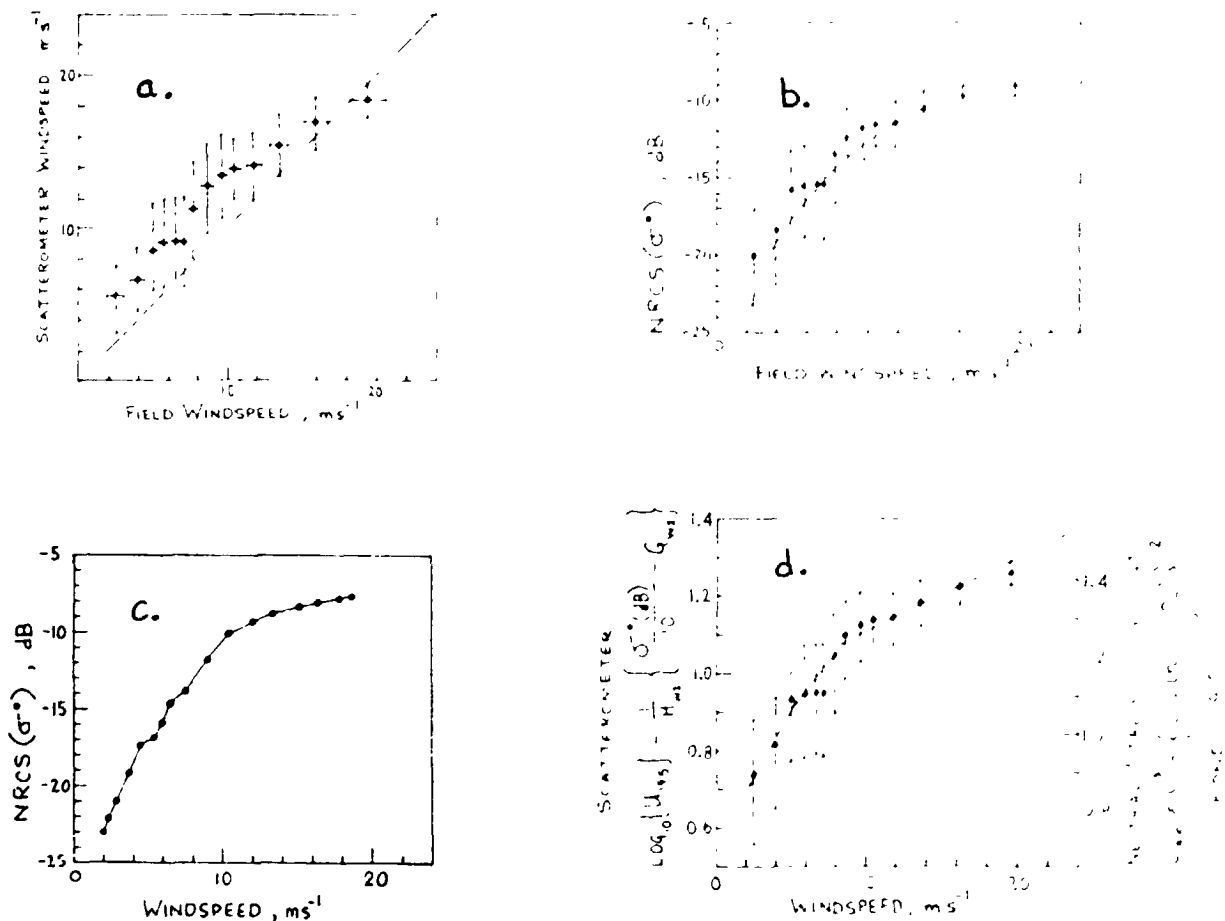


Figure 9. Four plots that essentially compare V-Pol scatterometer-related data (left ordinate), and collocated in situ "truth" data (abscissa): a) The upper left plot compares the results from the GOASEX region to Wentz22 (an ancestor of SASS1) model-derived results. Perfect agreement would be along the diagonal. b) The upper right plot compares results (data points) from the GOASEX region to the SASS1 (dashed line through the data points). c) The lower left plot shows replotted data from Duncan et al. (1974). d) The lower right plot shows comparisons between SASS data (left ordinate vs. abscissa) and Kondo's (1975) empirical model which relates the measurements of the rms heights of the high frequency ocean waves (wavelengths from about 0.8 cm to 62 cm) via the aerodynamic roughness length, L_0 , further related to the bulk momentum transfer coefficient, $10^3 C_{10.5}$ (right ordinate), to measured windspeeds.

As previously noted, SASS1 was calibrated to the JASIN wind field data set. The abscissa in Figure 9b thus represents wind values from GOASEX (data points) as well as wind values from JASIN (the SASS1 curve). The horizontal error bars for the GOASEX winds have been left off for clarity. These errors are shown in the upper left plot. However, because of the new scale for the ordinate, the vertical error bars from Figure 9a have been transformed. A comparison of Figures 9a and 9b shows that there is considerable improvement in model fit to the data by the JASIN-calibrated SASS1 over its ancestor.

Wentz2. Although much of the model bias has been removed for the lower wind speeds, SASS1 would appear to underestimate the higher winds. The data of Figure 1, as well as some other case studies (e.g. Jones et al, 1982, Figure 14), appear to confirm the poorer estimates of U_{VV} at higher speeds when a power-law function empirical model is calibrated to fit only the lower wind speed regime (i.e., wind speeds $< 16 \text{ ms}^{-1}$).

We now examine the tendencies of the data obtained during the GOASEX period which are displayed in Figure 9b. The mean values of the distributions appear to be rather smoothly varying over the entire range of values with the possible exception of the mean wind speeds located near 7 ms^{-1} . It seems that an empirical model function determined with two, or possibly three, disjoint linear regressions yielding a broken line through the mean wind speeds of the distributions would give better estimates of U_{VV} for both the lower and higher wind speed regimes. It could also be argued that one of the breakpoints connecting the linear fits would occur near 10 ms^{-1} , and perhaps a second near 5 ms^{-1} . Such a model would obviously deviate from a power-law function attempting to cover the entire wind speed regime. In addition, the trend of the mean values suggests that this hypothesized empirical model would result in a σ° vs. wind-speed slope less than predicted by SASS1 for wind speeds greater than 10 ms^{-1} .

The two- or three-regime type scatterometer model function speculated on here could also be suggested for the data shown in Figure 9c (the lower left plot). However, the data shown by the points in this plot resulted from a wind-wave tank experiment reported by Duncan et al. (1974), which included measurements by an X-band (frequency of 9.375 GHz, wavelength of 3.2 cm) scatterometer in the vertical polarization mode. The data in Duncan et al. (their Figure 13) was replotted here with a logarithmic scale in dB for σ° . The authors noted that a "second break point is easily discernible in the data at a wind speed of about 10 m sec^{-1} ", apparently confirming our view that the form of the model function for the vertically polarized SASS data should be other than a single power function over the entire wind speed regime.

The evidence presented thus far at least suggests that the form of the model function relating σ° and U_{VV} might be more convex in shape than SASS1, and thus departs somewhat from SASS1 and its ancestors. As seen in Figure 9b, however, SASS1 gives a fair empirical representation of the rate of change of σ° to U over the wind speed range available for its calibration. The perceived inadequacies of SASS1 are probably not due to a lack of quality of the calibration in situ JASIN data used (inasmuch as the JASIN data was the best possibly available), but are perhaps due to the limited quantity and range of environmental conditions available for its calibration. Other shortcomings are noted in Schroeder et al. (1982b., p 3335). A new model, which would correct some of the difficulties with SASS1, is proposed in the following section.

5. AN EMPIRICAL MODEL RELATING SCATTEROMETER NRCS TO BOTH WIND AND WIND STRESS

The four plots of Figure 9 form a group of related data. A discussion of Figure 9d will involve the proffering of a new empirical scatterometer-model-function parameterization --- the topic of this section. The new aspects of this parameterization are: (a) the departure from an empirical model based on a power-law function, and (b) the estimation of both wind and wind stress from the NRCS. Previous models only resulted in either an estimation of wind, or an estimation of wind stress (Jones and Schroeder, 1978).

The theoretical basis for the parameterization of air-sea interaction is a complex and controversial subject that cannot be entered into here. In our view, however, the best treatment of the theory and the most appropriate ocean measurements are those of Kondo (1975) and Kondo et al. (1973). His analysis relates the bulk momentum transfer coefficient C_{10} (since his observations were taken at 10 meters) to the aerodynamic roughness length of the sea surface Z_0 , which he describes as related to the rms height of the "sea surface irregularities associated with the high frequency ocean waves" with wavelengths from about 0.8 cm to 62 cm. This relationship, of course, derives from the logarithmic wind profile in the surface layer, an assumption commonly accepted over the ocean surface. From his experiments, Kondo then determines C_{10} from the roughness length and relates the drag to the wind speed according to an approximate linear formula. Since our wind data are referred to at a 19.5 meter elevation, we convert Kondo's results to:

$$10^3 C_{19.5} = A + BU = C_{**} \quad (4)$$

Kondo (1975) presents constants for four wind-speed regimes, and also gives formulas for converting to arbitrary C_z . Thus, the following set of constants are calculated entirely from his work, with no assumptions of our own:

U, ms^{-1} (at 19.5 m)	A	B
2.3 - 5.3	0.71	0.069
5.3 - 8.5	0.80	0.052
8.5 - 26.8	1.08	0.019

We now, however, allow ourselves one adjustable additive constant, S_p , which will then be a function of incidence angle, azimuth angle, and polarization. Then the model function (2) takes the new form:

$$\sigma^\circ(\text{dB}) = 10 \left\{ G(\theta, \chi, \epsilon) + H(\theta, \chi, \epsilon) \left[C_{**} - S_p(\theta, \chi, \epsilon) \right] \right\} \quad (5)$$

The adjustable constant S_p was chosen to produce a best fit to the SASS data points of Figure 9d. The results appear in Figure 9d, where the solid line - composed of three segments - is calculated from equation (5) with $S_p = 0.157$.

There are two features to note about Figure 9d. First, owing to the different structures of the three wind-speed regimes, as observed by Kondo (and others), the low and high wind-speed regimes are fit by (5) better than by SASS1, as seen in Figure 9b. Second, because the formulation of Kondo has a physical basis in the similarity theory of the surface layer, it results in the determination of the stress on the sea surface

$$\tau = \rho C_z U_z^2 \quad (6)$$

consistent with, and at the same time as, the wind speed U_z . The appropriateness of this formulation was long ago recognized by Munk (1955), who emphasized that the form drag is essentially determined by the high frequency portion of the ocean wave spectrum owing to the contribution thereof to the mean-squared surface slope.

6. DISCUSSION AND CONCLUSIONS

The stroke of perspicacity resulting in the design of dual-polarization modes for each SASS antenna permitted the possibility of an internal calibration of the SASS1 model function, as demonstrated above. Our study of comparisons between collocated U_{VV} and U_{HH} strongly suggests that the power-law relationship of equation (1) is not an adequate representation. But, if the proper function for determining U_{VV} or U_{HH} becomes known, the other could be defined. The results at the higher wind range were anticipated by Valenzuela (1968). Wright (1966, and 1968), from his comparative studies of σ_{VV}^0 and σ_{HH}^0 , suggested that the major behavioral differences between σ_{VV}^0 and σ_{HH}^0 as a function of incidence angle and wind speed could be explained by the much stronger dependence of σ_{HH}^0 than σ_{VV}^0 on sea slope. In addition, Wright showed that this characteristic difference leads to an estimate of the mean-squared slope of the sea surface.

The data analysis performed in Section 3, i.e., the comparisons between SASS1 and other model-predicted winds with in situ winds, reinforce the results of Section 2. Further, the evidence provided by the data at least shows that the model relating σ_{VV}^0 to U_{VV} is more convex in form than the SASS1 form, a result which could be anticipated by the experimental data of Duncan et al (1974). This observation about the σ_{VV}^0 vs U_{VV} form, plus that about the relative change of σ_{VV}^0 with σ_{HH}^0 , Figure 7, leads to the conclusion that H-Pol backscatter shows greater sensitivity to wind speed variation at higher winds, and less at lower winds, than does V-Pol backscatter.

ORIGINAL PAGE
OF POOR QUALITY

The data analysis in Section 2 and 3 above clearly suggests that further SASS1 model function adjustments are still required if the Seasat scatterometer wind specifications are to be met over the entire range of wind speeds (4 to 24 ms^{-1}), particularly for winds greater than 16 ms^{-1} . The GOASEX winds, although of less quality than those from JASIN, proved to be beneficial in this evaluation and in the formulation of the proposed new model (Section 4) because of the larger dynamic range of environmental conditions available, and because of the larger statistical sample. Our new model fits the data better than SASS1, particularly for the higher wind speed range.

The understanding of the physics of the NRCS and its interaction with the ocean surface is an air-sea interaction problem - a complex and controversial subject. In addition, meteorologists are largely interested in the marine winds, while oceanographers are largely interested in the wind stress. Previous SASS models only led to the computation of one of these geophysical parameters. For SASS1, the output was the marine wind speed. Herein, both the meteorologists and oceanographers are presented a consistent formulation, Equations (4), (5), and (6), of a model function that results in the estimation of both the wind speed and wind stress from SASS measurements.

The new empirical model has a more physical basis for its development and formulation than its predecessor, SASS1. In our formulation, the NRCS is related to the aerodynamic roughness length through the bulk momentum transfer coefficient (right scale of Figure 9d). The aerodynamic roughness lengths, as noted by Kondo (1975), are based on measurements of the rms height of the amplitude of ocean waves between about 0.6 to 62 cm in wavelength. These were then correlated to measured winds by Kondo through the bulk momentum transfer coefficient. Scattering theory shows that the NRCS is a measure of the mean-squared amplitude of the Bragg resonant scattered ocean waves (Wright and Keller, 1971). For SASS, these Bragg resonant waves are between about 1 to 3 cm in wavelength (for incidence angles 60 to 20 degrees, respectively). It therefore may not be surprising that the rate of change of the NRCS with wind speed and the rate of change of the bulk momentum transfer coefficient of Kondo (1975) with wind speed is strongly correlated (correlation coefficient of 0.99). Whether Kondo's empirical parameterization adequately represents the wind stress is a matter for future verification. Even so, Garratt (1977) noted that the bulk momentum transfer coefficient of Kondo "based on high-frequency wave amplitude data, agrees well with the collected C_{DN} data".

The ocean wavelength regimes discussed above neatly straddle the capillary-gravity wavelength range. In the theories of capillary-gravity wave propagation, viscosity and surface tension play an important role and should be taken into consideration for future scatterometers as well as for SASS. Over a global ocean surface temperature range of 25C the viscosity of sea water varies by a factor of two: this variation affects the short wave structure and thence possibly the backscatter which is sensitive to these waves. Our continuing work on the parameterization of the model function includes the incorporation of both viscosity and surface tension.

ORIGINAL PAGE IS
OF POOR QUALITY

Spaceborne scatterometer systems are now being considered necessary by NASA and the Navy for future satellites. ESA (European Space Agency) has already approved a spaceborne mission which includes a scatterometer. Our research, which includes studies to characterize the errors as well as the important scatterometer-related physics, are potentially important to the design, implementation, and utilization of future spaceborne scatterometers, and to an understanding of the role of scatterometry in global meteorological and oceanographic research, applications, and predictions.

7. ACKNOWLEDGEMENTS

The following offered their advice and time freely in our sometimes detailed and vigorous discussions: Willard Pierson, Richard Moore, Sergei Kitaigorodski, Joost Businger, Mark Donelan, Kristina Katsaros, Robert Brown, Larry Bliven, Steve Long, Norden Huang, Fred Jackson, Robert Beal, Jeff Hawkins, Vince Noble, Dale Schuler, Gus Valenzuela, William Plant, William Keller, Emideo Bracalente, William Grantham, Jimmy Johnson, Cliff Schroeder, Linwood Jones, Philip Callahan, Timothy Liu and the many others who participated in the Seasat Project. Glenn Cunningham and Greg Pihos participated in the production of the comparison data sets as well as in the discussions. We wish to thank Shehenaz Bhanji for typing this manuscript. We also wish to thank Mimi Archie for some of the graphics.

The authors would like to express their gratitude to John Theon, Robert Curran, and Jack Fanselow for continued encouragement and counsel.

This research was supported by the Atmospheric and Oceanic Branches at NASA Headquarters, and was partly conducted at the Jet Propulsion Laboratory, California Institute of Technology, Pasadena, CA, under NASA Contract NAS7-918.

8. REFERENCES

- Barrick, D. E., P. M. Woiceshyn, J. C. Wilkerson, G. H. Born and D. B. Lame, 1980: SEASAT Gulf of Alaska workshop II report. JPL Int. Doc. 622-107, Jet Propulsion Laboratory, Pasadena, CA.
- Boggs, D. H., 1981: The Seasat scatterometer model function: the genesis of SASS1. JPL Int. Doc. 622-230, Jet Propulsion Laboratory, Pasadena, CA.
- Boggs, D. H., 1982: Geophysical data record (GDR) users handbook. JPL Int. Doc. 622-232, Jet Propulsion Laboratory, Pasadena, CA.
- Brown, R. A., 1983: On a satellite scatterometer as an anemometer. J. Geophys. Res., 88, 1663-1673.

- Duncan, J. R., W. C. Keller, and J. W. Wright, 1974: Fetch and wind speed dependence of Doppler Spectra. *Radio Science*, 9, 809-819.
- Fett, R. W. and W. A. Bohan, 1981: Navy tactical applications guide, vol. 3. NEPRF Tech. Report 80-07, Naval Environmental Prediction Research Facility, Monterey, CA
- Garratt, J. R., 1977: Review of drag coefficients over oceans and continents. *Mon. Wed. Rev.*, 105, 915-929.
- Hibbs, A. R., and W. S. Wilson, 1983: Satellite map of the oceans. *IEEE Spectrum*, 20, No. 11, 46-53.
- Jones W. L. and L. C. Schroeder, 1978: Radar backscatter from the ocean: dependence on surface friction velocity. *Bound.-Layer Meteor.*, 13, 133-149.
- Jones, W. L. and L. C. Schroeder, D. H. Boggs, E. M. Bracalente, R. A. Brown, G. J. Dome, W J. Pierson and F. J. Wentz 1982: The SEASAT-A satellite scatterometer: the geophysical evaluation of remotely sensed wind vectors over the ocean. *J. Geophys. Res.*, 87, 3297-3317.
- Kondo, J., Y. Fujinawa and G. Naito, 1983: High-frequency components of ocean waves and their relation to the aerodynamic roughness. *J. Phys. Ocean.*, 3, 197-202.
- Kondo, J., 1975: Air-sea bulk transfer coefficients in diabatic conditions. *Bound.-Layer Meteor.*, 9, 91-112.
- Moore, R. K. and A. K. Fung, 1979: Radar determination of winds at sea. *Proc. of IEEE*, 67, 1504-1521.
- Schroeder, L. C., W. L. Grantham, J. L. Mitchell and J. L. Sweet, 1982a: SASS measurements of the Ku-band radar signature of the ocean. *IEEE J. Oceanic Eng.*, OE-7, 3-14.
- Schroeder, L. C., D. H. Boggs, G. J. Dome, I. M. Halberstam, W. L. Jones, W. J. Pierson and F. J. Wentz, 1982b: The relationship between wind vector and normalized radar cross section used to derive SEASAT-A satellite scatterometer winds. *J. Geophys. Res.*, 87, 3318-3336.
- Peteherych, S., M. G. Wurtele, P. M. Woiceshyn, D. H. Boggs and R. Atlas, 1984: First global analysis of SEASAT scatterometer winds and potential for meteorological research. *These proceedings*.
- Valenzuela, G. R., 1968: Scattering of electromagnetic waves from a tilted slightly rough surface. *Radio Science*, 3, 1057-1066.
- Valenzuela, G. R., M. B. Laing, and J. C. Daley, 1971: Ocean spectra for the high-frequency waves as determined from airborne radar measurements. *J. Marine Res.*, 29, 69-84.
- Wright, J. W., 1966: Backscattering from capillary waves with

application to sea clutter. IEEE Trans. on Ant. and Prop., AP-14, 749-754.

Wright, J. W., 1968: A new model for sea clutter. IEEE Trans. on Ant. and Prop., AP-16, 217-223.

Wurtele, M. G., P. M. Woiceshyn, S. Pateherych, M. Borowki and W. S. Appleby, 1982: Wind direction alias removal studies of SEASAT scatterometer-derived wind fields. J. Geophys. Res., 87, 3365-3377.

Wright, J. W. and W. C. Keller, 1971: Doppler spectra in microwave scattering from wind waves. The Physics of Fluids, 14, 466-474.

DOES THE SCATTEROMETER SEE WIND SPEED OR FRICTION VELOCITY?

By

Mark A. Donelan⁺ and Willard J. Pierson Jr.^{*}

⁺Canada Centre for Inland Waters. ^{*}The City College of N.Y.

ABSTRACT

Studies of radar backscatter from the sea surface are referred either to the wind speed, U , or friction velocity, u_* . Bragg scattering theory suggests that these variations in backscatter are directly related to the height of the capillary-gravity waves modulated by the larger waves in tilt and by straining of the short wave field. The question then arises as to what characteristic of the wind field is most probably correlated with the wave number spectrum of the capillary-gravity waves. This study reviews the justification for selecting U as the appropriate meteorological parameter to be associated with backscatter from L-band to K_u-band. Both theoretical reasons and experimental evidence are used to demonstrate that the dominant parameter is $U/C(\lambda)$ where U is the wind speed at a height of about $\lambda/2$ for waves having a phase speed of $C(\lambda)$.

HISTORICAL REVIEW

The steps that lead to the development of the SEASAT-SASS go back to the early theories of radar backscatter from the sea surface and to measurements of the high frequency part of the spectrum of wind generated waves in wind wave flumes. Programs of the Advanced Applications Experiment Office of NASA were initiated in the middle 1960's to measure the normalized radar backscattering cross section from aircraft as reported by Moore and Bradley (1969). Measurements of the high frequency waves in wind-wave flumes as in Pierson and Stacy (1973) and Mitsuyasu and Honda (1974) were made in attempts to relate the water waves to the radar waves by means of various versions of Bragg scattering theory, as in Rice (1951), and others. There were other contending theories of backscatter that depended on the entire wave number spectrum as in Chia (1968). The full spectrum is still, in a sense, needed to correct Bragg theory and to account for low incidence angles.

To connect aircraft measurements at 500 m, or lower, to wind-wave flume measurements in flumes several meters high requires knowledge of the variation of the time averaged wind with height. Experiments in wind wave flumes usually provided the quantities, u_* and z_0 , and aircraft measurements provided a mean wind at flight altitude or were made near some surface platform to obtain wind speed and direction, air temperature, sea temperature and, perhaps, relative humidity at some height above the sea surface.

The available theory for connecting wind wave flume measurements to free atmosphere measurements is that of Monin Obukhov (1954), which requires the empirical determination of the function, $\phi(z/L)$, where L is the stability length and of either a relationship between z_0 and u_* or the neutral drag coefficient, C_{DN} , defined by

$$C_{DN} = u_*^2 / (\overline{UN}_{10})^2 \quad (1)$$

The generally accepted function for $\phi(z/L)$ is presently the Businger-Dyer function but there are no generally accepted functions for either $C_{DN}(\overline{UN}_{10})$ or $z_0 = z_0(u_*)$. It is, however, generally agreed that the neutral drag coefficient is not a constant.

ORIGINAL PAGE 19
OF POOR QUALITY

The details on the development of the SEASAT-SASS can be found in the Skylab EREP Investigations Summary (NASA SP-399), the special issue in Science (Vol. 204, June 1979), the IEEE Journal of Oceanic Engineering (Vol. OE-5, April 1980) and two Journal of Geophysical Research special issues (Vol. 87 No. C5 April 1982 and Vol. 88, No. C3 Feb. 1983) and in the papers cited therein. It will be necessary to search rather diligently to find out which, of many, closure relations was used either to relate wind-wave flux data to the free atmosphere or to refer the wind to some constant height above the sea surface. It will also be difficult to find the rationale for the decision to relate backscatter to the mean wind speed and direction at a height of 19.5 m above the sea surface.

THE PRESENT SITUATION

The situation becomes even more confusing when one reads Jones, et al. (1977), Jones and Schroeder (1978), Ross and Jones (1978), Liu and Large (1981), O'Brien, et al. (1982), Brown (1983) and Pierson (1983). The 1977 reference finds a power law (to be defined later) relationship between σ^0 (NRCS) and wind speed for up wind, downwind and crosswind and gives forms for σ^0 versus x for fixed $|V|$ and θ . Jones and Schroeder (1978) use a z_0 versus u_* relationship given by Cardone (1970) and find a power law relationship for u_* . Ross and Jones (1978) measured backscatter, both polarizations, UN_{10} , u_* and z_0 inferred from aircraft data at 150 m over a fetch from zero to 34 km and found essentially constant backscatter, wind speed, and u_* values for UN_{10} equal to 13.0 m/s and 9.0 m/s. The gravity waves increased in height over the fetch, but none of the other parameters changed by more than what would be expected as a result of mesoscale turbulence. Liu and Large (1981) tried to relate JASIN measurements of u_* to σ^0 and found "no significant difference between the correlation of σ^0 versus U_N and σ^0 versus u_* " (see also Pierson (1983)). The S³ group (O'Brien, et al. (1982)) believe that the vector wind stress, τ , is the primary quantity needed to study wind driven ocean currents but do not address either the relationship between the wind and the wind stress or the mechanism by which the wind actually generates ocean currents. Brown (1983) writes that "Since the establishment of good parameterizations between scatterometer signal and surface winds in regions of rapid change and strong air-sea interaction are hampered by lack of good wind data, the rationalization for wind rather than surface stress algorithms is not so strong. As an appropriate consort to the surface reflectivity, we might as well accept u_* rather than its ersatz companion, the wind. In regions where air-sea temperature differences are available, there is no difference, as [(1)] accurately relates $U(z)$ to u_* . However, in dynamic regions, such as an intense cyclone with resultant large air-sea temperature difference, u_* can be expected to provide better correlations with the scatterometer". Pierson (1983) identifies the problem and argues that the wind is the more basic parameter and should be the quantity correlated with backscatter. An experiment to help clarify the problem is outlined for some future scatterometer such as NROSS.

STATEMENT OF PROBLEM

The various paper cited above document a variety of opinions on the relative importance of various parameters and measurements of the dependence of radar backscatter or some property of the atmosphere in motion. To do so, it is first necessary to state the problem according to our present understanding of it.

The primary quantity of meteorology is the air itself. It has mass, or density, and a wide variation in its ability to hold water vapor.

Air in motion is the wind, so wind is a secondary quantity. The speeds and directions of the winds are highly variable quantities near the Earth's surface, and even more so at the higher elevations of the atmosphere. For synoptic scale meteorological applications, the winds in a time averaged sense are not measured very accurately by presently available conventional and remotely sensed meteorological methods (with the possible exception of the SASS) as shown by Pierson (1983) and others.

Air in motion, the wind, is turbulent. For the study of turbulence, a tertiary quantity is the downward flux of turbulent momentum toward the sea surface in the planetary boundary layer as defined by (2).

$$u_*^2 = \tau/\rho = -\langle u' w' \rangle \quad (2)$$

The quantity, u_*^2 , is not routinely measured over the oceans. The quantity indicated by (2) is in essence the cospectrum of the fluctuations about some mean value of U as in $U = \bar{U} + u'$ averaged over an appropriate time interval at some reasonable height above the sea surface and the fluctuations in the vertical velocity, which are usually taken to have a zero mean. This cospectrum is shown by Large and Pond (1981) and high quality data on (2) can be found in Large's Thesis, Large and Pond (1981) and Smith (1980), among others. Near the sea surface for a height somewhere above the waves up to some higher elevation (2) is assumed to be a slowly varying quantity with time but more or less independent of height.

There are other ways that the wind affects the sea surface other than the downward flux of momentum implied by $\langle u' w' \rangle$. One of the most important is the variable dynamic pressures applied to the moving water surface and the phase and magnitude of these varying pressures relative to the waves that are present. Fluxes of heat and water vapor are also involved as eddy quantities, each having problems associated with their bulk parameterization.

Somehow or other, air in turbulent motion over the ocean generates waves. These waves are more or less random as a time history at a point, short crested, and variable as to their properties as a function of the motion of the air over them, distance over which the air has moved and the time duration of the velocity of movement. These waves are described ultimately by non-linear equations, but present theories are at best third order approximations.

Within a linear theory, the spectrum of the waves generated by the moving air covers about three orders of magnitude in frequency and five, or so, in wave number. For waves shorter than about 5 cm, surface tension becomes important. Since the radar wavelength of the SASS on SEASAT is 2 cm, capillary waves near 2 cm in length are important in backscattering theories. Capillary waves have rounded crests and sharper troughs that point down into the water. According to Crapper (1957) the limiting form of pure periodic capillary waves produces waves with a very strange profile that can be as high as they are long.

The SEASAT-SASS estimated the power of the electromagnetic radiation back-scattered from the sea surface. Actually the received power plus the noise in the system was estimated and then an estimate of the noise was subtracted. For low signal ($\sim 10^{-15}$ to 10^{-16} watts) to noise ratios (~ -10 to -15 db), it was quite possible to obtain a negative estimate of the received power, which, unfortunately, was ignored in further data processing.

Pierson and Stacy (1973) showed that capillary waves are not generated in a

wind-wave flume for winds corresponding to friction velocities up to about 12 cm/sec, which yields a wind of about 4 m/s at 19.5 m. Liu and Lin (1982) have used laser methods to estimate the frequency spectrum of capillary waves. Their results differ from earlier studies, but still suggest that the spectrum increases more rapidly at higher frequencies than at lower frequencies in the capillary range. Since wavenumbers and not frequencies are the appropriate quantities in backscatter theories capillary waves advected forward and backward by the longer gravity waves may have their frequencies Doppler shifted so that the frequency spectrum cannot be simply transformed to the wavenumber spectrum.

The SEASAT-SASS (and by extension any other scatterometer) measures the roughness of the sea surface, including, perhaps, flying spray, and the sharp corners at the crests of gravity waves, and the Bragg scattering from a surface tilted by gravity waves and related to the capillary vector wave number spectrum. A scatterometer measures neither the wind nor u_* , or by extension, $\tau = \rho u_*$. The connection between the sea surface roughened by the moving air and the estimates of the normalized radar backscattering cross section measured by a scatterometer is thus built on a chain of theoretical and experimental results that depend on the true nature of the moving air in the planetary boundary layer and on how waves are generated. Neither the effective neutral wind at 19.5 m above the mean sea surface nor u_* may prove to be most directly related to backscatter measurements.

THE SASS-1 MODEL FUNCTION

The design of the experiments to determine the relationship between backscatter and moving air began several years before the launch of SEASAT. The worst case design was predicated on being able to determine a wind of 4 m/s within plus or minus 2 m/s based on the aircraft data of Jones, et al. (1977) and on Pierson and Stacy (1973). There were several dozens of published relationships for $C_{DN} = C_{DN}(U_{10})$, or variants thereof relating z_0 and u_* . It was impossible to pick one and prohibitively expensive to measure u_* over a wide enough range of wind speeds during the anticipated lifetime of SEASAT.

The choice of the effective neutral wind at 19.5 m was based on two considerations. They were that anemometers on transient ships are at heights considerably in excess of 10 meters and that winds corrected to this height by means of Monin-Obukhov theory were relatively insensitive to which choice, of many, was made for equation (1) even after correction for stability effects.

Consider, the simplified situation for which the drag coefficient is constant and might equal 10^{-3} , or perhaps $2 \cdot 10^{-3}$ or perhaps $3 \cdot 10^{-3}$. The mean wind at 40 m can be referred to the wind at 19.5 m for neutral stability by

$$\bar{U}(19.5) = \frac{\bar{U}(40)(1 + 1.63 C_{DN}^{1/2})}{(1 + 3.38 C_{DN}^{1/2})} \quad (3)$$

and the wind at 5 m can be referred to 19.5 m by

$$\bar{U}(19.5) = \frac{\bar{U}(5)(1 + 1.63 C_{DN}^{1/2})}{(1 - 1.69 C_{DN}^{1/2})} \quad (4)$$

The wind stress computed for a mean wind at 40 m is given by

$$\tau = \rho C_{DN} \bar{U}_{40}^2 (1 + 3.38 C_{DN}^{1/2})^{-2} \quad (5)$$

and for 5 m by

$$\tau = \rho C_{DN} \bar{U}_5^2 (1 - 1.69 C_{DN}^{1/2})^{-2} \quad (6)$$

For the same wind at 10 m, the stress varies by a factor of 3 and u_* varies by 73% under these assumptions. With these equations, and their obvious extensions, the wind measured at any height can be referred to 19.5 m. A wind for neutral stratification of 15 m/s at 40 m yields winds of 14.09, 13.77 and 13.52 m/s, for example, which for a factor of 3 in C_D produces a 56 cm/sec change in the wind at 19.5 m. Similarly a wind of 1 m/s at 5 m produces winds of 16.65, 17.4 and 18.00 m/s at 19.5 m for a 1.35 m/s change. Corrections for stability have roughly the same effect for a considerable variation in C_{DN} . The choices avoided a decision as to which of many drag coefficients should be used. However, it did not avoid the basic question of how the roughened sea surface is related to the turbulent moving air over the ocean.

When these decisions were made, the inherent difficulties of measuring the winds correctly by conventional meteorological means were not clearly in focus. The evolution of the understanding of the problem can be traced through the papers and special issues that have been cited above.

The SASS-1 model function is an attempt to relate the effective neutral wind speed at 19.5 m, which is (or was) the anemometer height on the British weather ships I and J, and wind direction, to backscatter, either vertically or horizontally polarized, by means of a relationship of the form

$$\sigma^0 = \sigma^0(|\vec{V}|, \chi, \theta) \quad (7)$$

where $|\vec{V}|$ is the magnitude of the wind vector, χ , is the wind direction relative to the pointing direction of the radar beam and θ is the incidence angle. The model for the model function was simplified to the form

$$\sigma^0 = K(\chi, \theta) V^M(\chi, \theta) \quad (8)$$

or to

$$\sigma_{db}^0 = 10 \log_{10} \sigma^0 = 10 \left[G(\chi, \theta) + H(\chi, \theta) \log_{10} V \right] \quad (9)$$

, hence the G-H tables of Schroeder, et al. (1983), and the concept, continued from earlier references, of a power law relation between wind and backscatter, which may or may not be correct. The objective is to find the vector wind, i.e. \vec{V} , given pairs of backscatter measurements 90° apart for two slightly different θ 's, and one really needs to find a best fit to

$$|\vec{V}| = V(\chi, \theta, \sigma^0) \quad (10)$$

if the data have random errors. The problem becomes trivial if (8) or (9) is used but non-trivial if a simple inverse of (7) to yield (10) is not available. The graph of σ^0 in db versus $\log_{10} V$ is a straight line for any θ and χ .

If the SASS-1 model function is correct, if a correct way to recover the wind given the backscatter measurements is used and if the function giving C_{DN} as a function of $\bar{U}(10)$ is known, then τ can be found (plus ambiguities or aliases). If C_{DN} is a constant for all winds speeds, equation (9) becomes trivial since it becomes (11) from (1) with a minor correction for the difference between 19.5 and 10 m

$$\begin{aligned}\sigma^0_{db} &= 10(G(\chi, \theta) + H(\chi, \theta) \log_{10}(u_* / C_{DN}^{1/2})) \\ &= 10(G(\chi, \theta) - \frac{H(\chi, \theta)}{2} \log_{10}(C_{DN}) + H(\chi, \theta) \log_{10} u_*)\end{aligned}\quad (11)$$

and a power law still results.

However, if for the higher wind speeds

$$C_{DN} = \alpha + \beta \bar{U}(10) \quad (12)$$

as in both Smith (1980) and Large and Pond (1981), then

$$u_*^2 = (\alpha + \beta \bar{U}(10))(\bar{U}(10))^2. \quad (13)$$

The value of u_* is then a rather complex function of $\bar{U}(10)$ and clearly a power law relation between u_* and σ^0 will not apply.

Conversely if the correct relation between backscatter and u_* was a power law as in

$$\sigma^0 = \alpha(\chi, \theta) (u_*^2)^{\beta(\chi, \theta)/2} \quad (14)$$

then

$$\begin{aligned}10 \log_{10} \sigma^0 &= 10(\log_{10} \alpha(\chi, \theta) + \beta(\chi, \theta) \log_{10} u_* + \beta(\chi, \theta) \log_{10} \bar{U}(10)) \\ &= 10(\log_{10} \alpha(\chi, \theta) + \frac{\beta(\chi, \theta)}{2} (\log_{10} (\alpha + \beta \bar{U}(10))(\bar{U}(10))^2))\end{aligned}\quad (15)$$

which is not a straight line on a σ^0_{db} versus $\log \bar{U}(10)$ plot.

Inevitably, then, it is necessary to return to the fundamental questions of the way moving turbulent air roughens the sea surface. These are questions of how the wind varies with height very close to the sea surface, of the relation between $\bar{U}(z)$, u_* , and other parameters and of the basic physical effects involved. The problem is in one sense trivial, given an accepted equation for $C_{DN}(\bar{U}_{10})$ and that SASS-1, or something very similar, is correct. In another sense, it is extremely complex, given that some of the theories and assumptions that have been used may be incorrect and that the study of the generation of waves by the wind, especially capillary waves, is a difficult subject.

THE ROUGHNESS OF SHORT WAVES

Given that scatterometers respond to the roughness of waves with wavelengths in the neighborhood of the incident Bragg wavelengths, the fundamental question posed in the title to this paper separates neatly into two parts:

- (a) the relationship between scattering cross-section and the vector wave number spectrum of the Bragg scatterers; and
- (b) the parameterization of the spectrum of the Bragg scatterers in terms of characteristics of the wind and of the entire wave spectrum. The traditional approach has been to lump the two parts into a single "model function" relating the measured backscatter to either wind speed or friction velocity. There are so many sources of error in this approach and so few comprehensive sets of surface comparative data that no consensus has emerged regarding the source of backscatter variations. In this section we employ some field observations of frequency spectra of short waves to attempt to throw some light on the second of the points listed above.

OCEANOGRAPHY OF POOL C

A complete answer to part (b), above, requires detailed knowledge of the wave number spectrum of the Bragg scatterers and its dependence on external forcing, dissipation and modulation by longer wave components. This is a great deal more than the experimental data will support, and we must content ourselves here with a look at the integral of the spectrum or the variance for particular bands of components. Thus, we would like to explore the dependence of the spectral density of the gravity-capillary or, at least the very short gravity waves, on appropriate indicators of external forcing.

However, the Doppler shift of observed frequencies of short waves due to longer waves and currents limits the range of short waves for which the observed frequency spectrum yields any useful information about the desired wave number spectrum. For waves at the gravity-capillary range of direct interest, the orbital velocities of the long waves are generally sufficient to reverse their propagation direction, thereby making it difficult to deduce the wave-number spectrum from the observed frequency spectrum. On the other hand, longer waves near the peak of the spectrum cannot be expected to behave in an analogous way to the very short Bragg scatterers, their spectral density being affected by advection and by non-linear effects.

The spectral density of wave components on the rear face of the spectrum, sufficiently far from the peak, is a consequence of a balance between wind input and dissipation. The energy flux from the wind to the wave components is brought about by both normal (pressure) and tangential (shear) stresses. However, both calculations (Brooke Benjamin, (1959) and Miles, 1962)) and experiment (Kendall (1970)) indicate that normal stresses dominate the energy flux. In a recent numerical study, Al-Zanaidi and Hui (1984), using a two-equation closure model for the boundary layer turbulence, have shown that the energy input from the wind, $\partial E / \partial t$, is related to the wind speed and the wave phase speed, C by:

$$\frac{\partial E}{\partial t} = \omega E \frac{\rho_a}{\rho_w} \beta \left(\frac{U_\lambda}{C} - 1 \right)^2 \quad (16)$$

where β is a parameter, weakly dependent on the aerodynamic condition of the surface - smooth, transitional or rough, ω in the radian frequency of the wave component receiving wind input and, λ is its wavelength and U_λ is a reference height for the calculation.

The expression (16), supported by laboratory measurements in the wind-wave tank at the Canada Centre for Inland Waters, has the character of wind input induced by form drag. Inasmuch as the sea surface is aerodynamically smooth only at the lowest wind speeds, much of the momentum and energy flux from the wind must necessarily involve correlations between surface slope and pressure brought about by the flow near the surface in relation to the wavelengths of the surface roughness; i.e. the wave components inducing and absorbing the energy flux. Thus, the appropriate wind speed is the speed at a height corresponding to the wavelength (16) or a fraction thereof. Some further ideas of the nature of marine surface drag are given by Stewart (1974).

In an actively wind forced sea the gravity waves suffer dissipation largely through intermittent breaking. Breaking occurs when the local vertical acceleration at the crest exceeds $g/2$. Since the height of waves of a particular wavelength varies irrationally in space and time, breaking is highly intermittent. However, the frequency of breaking events will clearly increase as the energy level in the spectrum increases. Thus the irracional rate of

dissipation per radian of waves at a particular frequency will depend on the spectral energy density $\phi(\omega)$ and the gravitational acceleration, g ,

$$\frac{1}{\omega E} \frac{\partial E}{\partial t} = \delta \left(-\frac{\omega^5 \phi(\omega)}{2g} \right)^n \quad (17)$$

where δ is a dimensionless constant and n , an exponent to be determined by experiment.

Of course the choice of a power law for the functional form of (17) is purely a matter of convenience. By suitable choice of n , the dissipation rate can be made more or less sensitive to spectral density.

On the plausible assumption that the short gravity waves strike a balance between direct wind input and dissipation through breaking, (16) and (17) may be equated to yield:

$$\phi(\omega) = \gamma \omega^{-5} g^2 \left(\frac{U\omega}{g} - 1 \right)^{2/n} \quad (18)$$

where the dispersion relation for small amplitude gravity waves has been used to replace C .

For many years the rear face of the spectrum was thought to follow an ω^{-5} power law corresponding to the "hard saturation" of Phillips (1958) theory. In (18) this frequency dependence implies $n = \infty$. Now it appears (Forristall (1981), Kahma, (1981), Donelan, et al. (1983), Kitaigorodskii, (1983)) that ω^{-4} provides a better description of the energy containing (and not severely Doppler shifted) waves on the rear face of the spectrum. This corresponds to $n = 2$ or relatively "soft saturation", i.e. the rate of dissipation is not extremely sharply dependent on the spectral density.

After correcting for Doppler shift distortions to the observed spectrum, the normalized spectral density $\phi(\omega) \omega^5/g^2$ may be compared with the various candidates taken to be representative of wind forcing. These are: (a) the neutral equivalent wind speed at ship anemometer height $U_{10.5}$, generally favoured by meteorologists and (b) the friction velocity u_{*} , the hope of most oceanographers, and (c), $((U\omega/g) - 1)$ which is suggested by the rough analysis above.

DATA

The data set consists of 52 observations on Lake Ontario each 20 minutes long in which the waves were sensed by a capacitance wire and sampled at 20 Hz and the wind speed and turbulent components were sensed by a Gill anemometer binnacle and sampled at 5 Hz. The average drag coefficient was estimated from the direct Reynolds flux using stresses averaged over 1 hour, or longer, if conditions were steady. The friction velocity was then computed from the 20 minute average wind speed using (1). The observed frequency of $\omega = 17.3 \text{ sec}^{-1}$ was selected because these waves were sufficiently far from the peak to allow the balance of wind input and dissipation and yet long enough ($\lambda = 20.7 \text{ cm}$) so that the Doppler distortion was tolerable. Each spectral estimate had 1916 degrees of freedom and the frequency of 17.3 sec^{-1} was the energy weighted centroid of the band analysed, based on an ω^{-4} spectrum.

Each spectral estimate was corrected for the effect of the Doppler shift of the longer waves using an ω^{-4} spectral slope and orbital velocities with a Gaussian distribution of standard deviation $\sigma_v = u_p \sigma_\eta$; where u_p is the peak frequency and σ_η^2 is the variance of the surface elevation. An ω^{-4} spectrum with sharp cut-off at ω_p yields $\sigma_v = \sqrt{3} \omega_p \sigma_\eta$. However, these generally short-

fetch spectra have most of the energy concentrated near the peak (Donelan, et al. (1983)); furthermore the attenuation of the velocities due to shorter waves and the increased spreading of wave energy of the shorter waves all tend to reduce the contribution of the waves above the peak to the root-mean-square Doppler shifting orbital velocities.

Observations of the bulk Richardson number were used to compute the Monin-Obukhov stability index (Donelan, et al. (1974)) and thus to compute the neutral equivalent wind speed at any height in the manner described by Large and Pond (1981).

RESULTS AND DISCUSSION

The Doppler shift corrected and normalized spectral estimates are compared with $\bar{U}(19.5)$, u_* and $((U(\lambda/2)\omega/g)-1)$ in Figures 1, 2 and 3 respectively. In each case there is some correlation of the spectral estimates with the wind forcing parameter.

The points of Figs. 1 and 2 are clearly stratified with respect to the parameter, U/C_p . Especially in Fig. 2, the spectral estimates corresponding to high U/C_p values are well below the other estimates. The explanation for this is probably that the friction velocity (or stress) receives contributions from the roughness due to the entire wave spectrum, while the spectral estimate reflects only the wind input to that part of the spectrum. For low values of U/C_p , most of the stress is carried by short waves (see for example, Kitaigorodskii and Volkov (1965) and Donelan (1982)) and therefore the spectral estimates on the rear face of the spectrum reflect the stress. On the other hand when U/C_p is large (small nondimensional fetch) a greater portion of the flux of momentum to the waves is absorbed directly by the waves near the peak of the spectrum. Under these conditions, the spectral levels on the rear face are poor indicators of the total stress. The equivalent neutral wind at an anemometer height, (say 19.5 m) is obtained from the usual logarithmic profile equation, $U_z = (u_* \ln(z/z_0))/\kappa$, where both u_* and z_0 are affected by the entire wave spectrum. The above comments regarding u_* consequently apply also to $\bar{U}(19.5)$.

When the spectral estimates are plotted in the context of (18) as in Fig. 3, the stratification U/C_p disappears although some scatter remains. Much of the scatter is probably due to inexact correction for Doppler shift and other more complex aspects of the modulation of short waves by long waves (Irvine (1983)). Nonetheless, the considerable improvement of the correlation in Fig. 3 over Figs. 1 and 2 suggests that, of the three choices explored, that given by (18) follows the data best. The least square regression line shown has been forced through the origin and has a slope of $4.66 \cdot 10^{-3}$, which is therefore the empirical value of γ in (18). A reasonable fit to the straight line in Fig. 3 implies $n = 2$ in (18). The choice of U at $\lambda/2$ is arbitrary and relatively insensitive to height within a wavelength, or so of the surface.

It might be argued that since the spectral estimates are related to u_* , except for high U/C_p , u_* may be inferred from backscatter at these wavelengths over most of the ocean much of the time where U/C_p is generally less than 2.0. Clearly this is unacceptable since during major storms the stress will be surely underestimated. Opposing swells complicate the situation even more.

The waves analysed here are an order of magnitude longer than those of the SASS. The response of 2 cm waves to some wind parameter is the question. Clearly these short waves are affected by other factors. However, the comments

ORIGINAL PAGE IS
OF POOR QUALITY

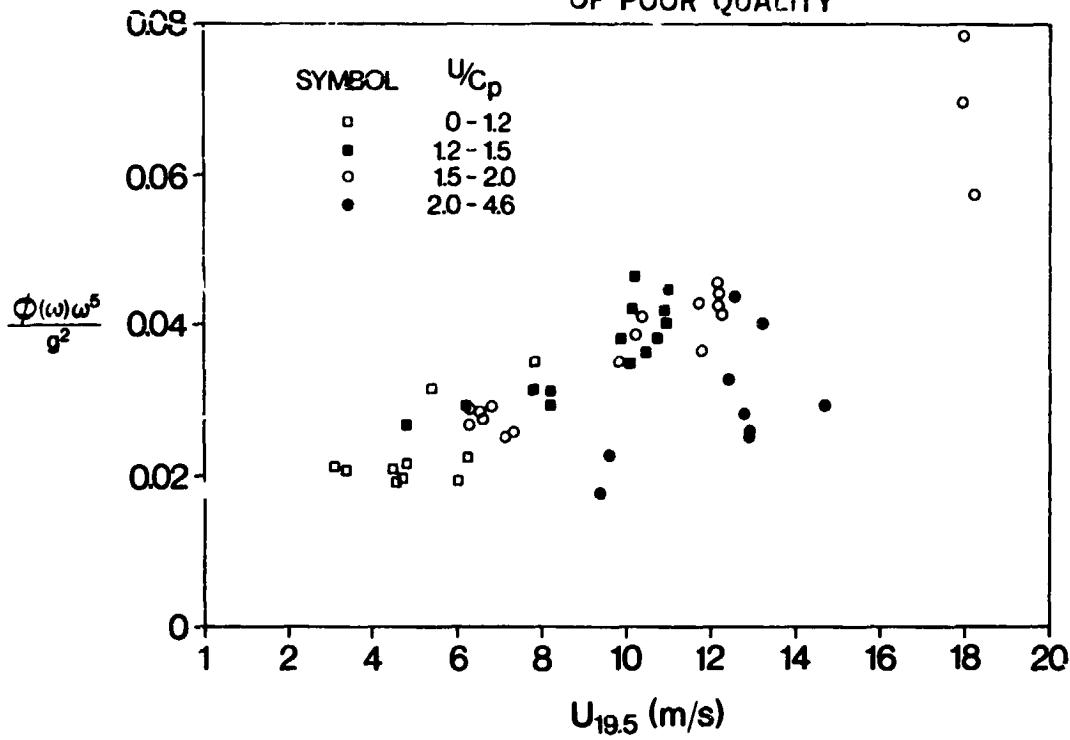


FIG. 1 Normalized Spectral Density at $\omega = 17.3 \text{ sec}^{-1}$ Versus $\bar{U}(19.5)$.

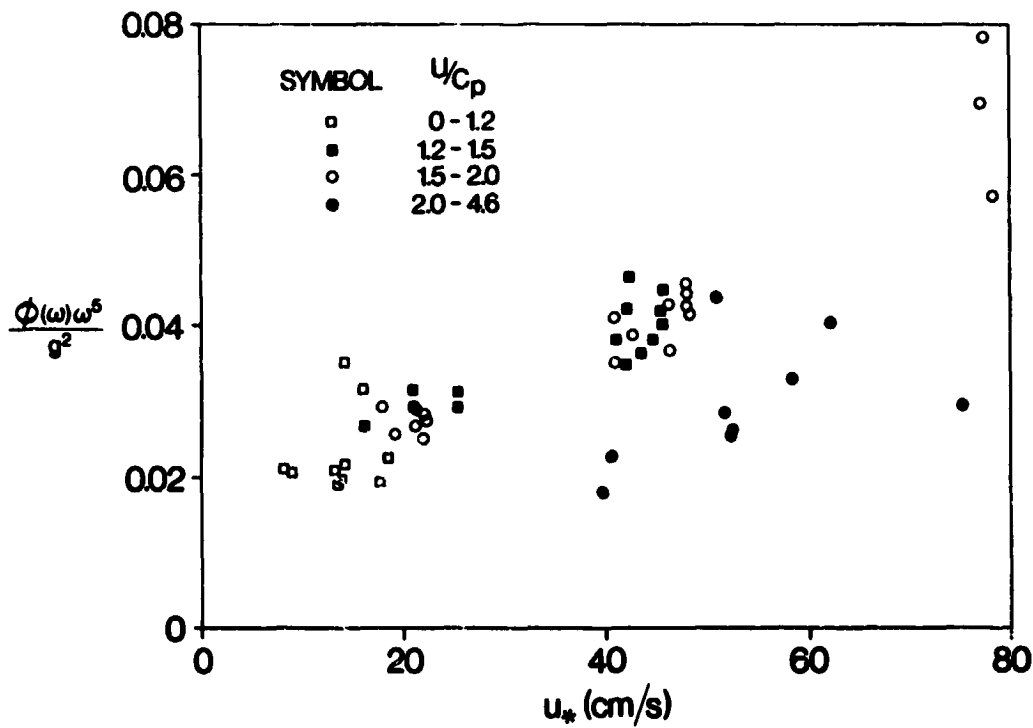


FIG. 2 Normalized Spectral Density Versus Friction Velocity.

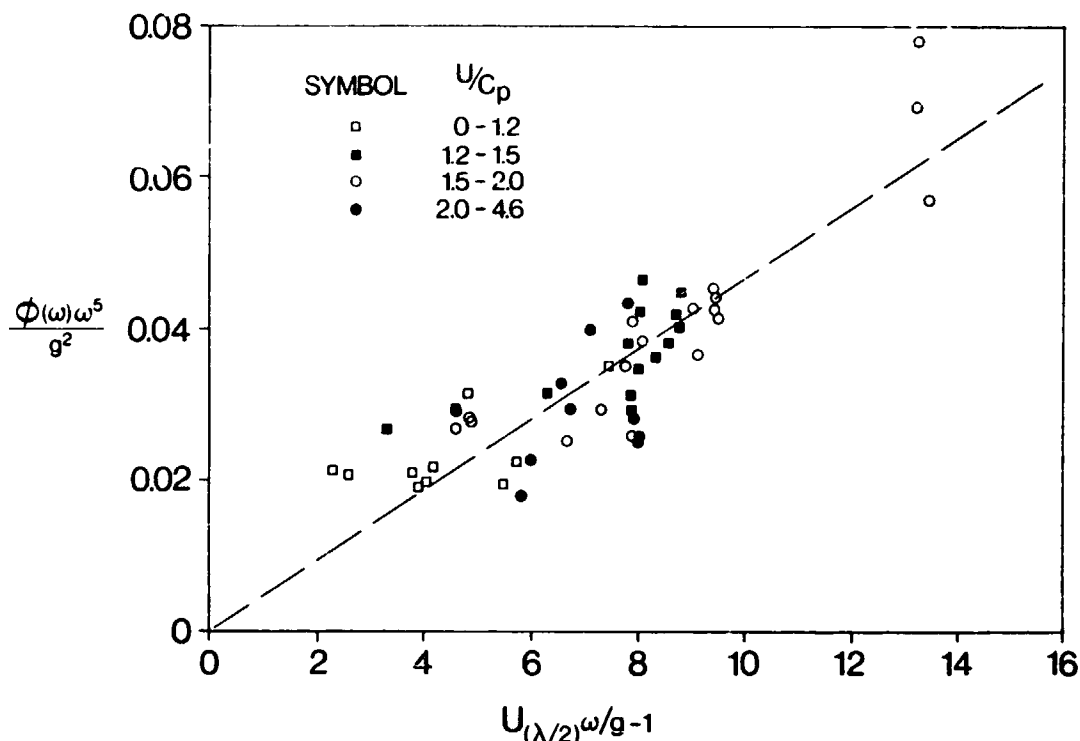


FIG 3 Normalized Spectral Density Versus $((U\omega/g)-1)$. (In these three figures, symbols correspond to various values of the ratio of the measured wind speed to the phase speed of the spectral peak.)

made above for longer waves might be expected to apply. Even though the spectral form may change, the relevant wind parameter will still be $((U/C(\lambda))-1)$ and not u_* .

CONCLUDING REMARKS

This complex problem has many facets, but we note that the wind profile near the surface is nearly neutral so that U at some height is not too illogical a starting point for improved models. Ultimately, though, it is to be expected that $U(z)$, u_* and z_0 will be related to the wave spectrum with perhaps a time lag and perhaps a dependence on high opposing swells and cross seas. Capillary waves for κ_u band will also be affected by surface tension and viscosity as well as possible breaking. That some sort of quasi-equilibrium exists over most of the ocean most of the time is demonstrated by the wind data from the SASS, but the reservations stated herein and the first sentence of the quotation from Brown (1983) must be kept in mind. There is, however, little hope that the tangential stress, u_* , will be more directly related to the waves than the normal stress (i.e. turbulent pressure variations). Direct measurements at sea of the vector wave number spectrum for waves from 20 to 1 cm in length will be needed to clarify these problems as well as more accurate data on the air sea temperature difference.

REFERENCES

- Al-Zanadi, M. A., and W. H. Hui (1984): Turbulent air flow over water waves a numerical study. Submitted to J. Fluid Mech.

- Brooke Benjamin, T. (1959): Shearing flow over a wavy boundary. J. Fluid Mech. Vol. 6. 161-205.
- Brown, R. A. (1983): On a satellite scatterometer as an anemometer. SEASAT II. Scientific Results. J. Geophys. Res. Vol. 88, No. C3. 1663-1673.
- Cardone, V. J. (1969): Specification of the wind field distribution in the marine boundary layer for wave forecasting. Rep. JR-69-1, Geophysics Science Lab., New York Univ.
- Chia, R. C. (1968): The theory of radar backscatter from the sea. PH. D. Thesis Univ. of Kansas. 120 pp.
- Crapper, G. D. (1957): An exact solution for progressive capillary waves of finite amplitude. J. Fluid Mech. Vol. 2, No. 6, 532-540.
- Donelan, M. A., J. Hamilton and W. H. Hui (1983): Directional spectra of wind generated waves. Internal Report Canada Centre for Inland Waters. Burlington, Ontario.
- Donelan, M. A. (1982): The dependence of the aerodynamic drag coefficient on wave parameters. First Internat. Conference on Meteorology and Air Sea Interaction of the Coastal Zone. 381-387. Amer. Meteor. Soc. Boston, Mass.
- Donelan, M.A., K.N. Birch and D.C. Beesley (1982): Generalized profiles of wind speed, temperature and humidity. Internat. Assoc. Great Lakes Res. Conf. Proc. 17, 369-388.
- Forristall, G. Z. (1981): Measurements of the saturated range in ocean wave spectra. J. Geophys. Res. Vol. 86, C9, 8075-8084.
- Irvine, D. (1983): The interaction of long waves and short waves in the presence of wind. PH. D. Dissertation. Johns Hopkins Univ. 114 pp.
- Jones, W. L., and L. C. Schroeder (1978): Radar backscatter from the ocean: Dependence on surface friction velocity. Boundary Layer Meteor. Vol. 13, 133-149.
- Jones, W. L., L. C. Schroeder and J. L. Mitchell (1977): Aircraft measurements of the microwave scattering signature of the ocean, IEEE J. Oceanic. Eng. Vol. OE-2, No. 1. 52-61.
- Kahma, K. K. (1981): A study of the growth of the wave spectrum with fetch. J. Phys. Ocean. Vol. 11. 1503-1515.
- Kendall, J. M. (1970): The turbulent boundary layer over a wall with progressive surface waves. J. Fluid Mech. Vol. 41. 259-281.
- Kitaigorodskii, S. A. (1983): On the theory of the equilibrium range in the spectrum of wind generated gravity waves. J. Phys. Ocean. Vol. 13, 816-827.
- Kitaigorodskii, S. A., and Yu A. Volkov (1965): On the roughness parameter of the sea surface and the calculation of momentum flux in the near water layer of the atmosphere. Izv, Atm. Ocean. Phys. Vol. 1. 973-988.
- Large, W. G., and S. Pond (1981): Open ocean momentum flux measurements in moderate to strong winds. J. Phys. Oceanogr. Vol. 11, 324-336.
- Liu, W. T., and W. G. Large (1981): Determination of surface stress by SEASAT-SASS. J. Phys. Oceanogr. Vol. 11, 1603-1611.

- Liu, H.-T. and J.-T. Lin (1982): On the spectra of high-frequency wind waves. J. Fluid Mech. Vol. 123. 165-185.
- Miles, J. W. (1962): On the generation of surface waves by shear flows. Part 4. J. Fluid Mech. 13, 433-448.
- Mitsuyasu, H., and T. Honda (1974): The high frequency spectrum of wind generated waves, J. Oceangr. Soc. Japan, Vol. 30, No. 4, 29-42.
- Monin, A. S., and A. M. Obukhov (1954): Basic laws of turbulent mixing in the ground layer of the atmosphere. Akademiia Nauk SSSR Leningrad Goefizicheskii, Institut Trudy No. 24 (151) 163-187.
- Moore, R. K., and G. Bradley (1969): Radar and oceanography in Microwave Observations of the Ocean Surface SP-152. Spacecraft Oceanography Project, Naval Oceanographic Office. 221-250.
- O'Brien, J. J. et al. (1982): Scientific opportunities using satellite wind stress measurements over the ocean. (Report of the Satellite Surface Stress Working Group) Nova Univ./N. Y. I. Y. Press. Ft. Lauderdale, Fla.
- Pierson, W. J. (1983): Highlights of the SEASAT-SASS Program: A Review. in Allan T. D. Satellite Microwave Remote Sensing. 69-86. John Wiley and Sons.
- Pierson, W. J., and R. A. Stacy (1973): The elevation slope, and curvature spectra of a wind roughened sea surface. NASA Contractor, Rep. CR-2646.
- Phillips, O. M. (1958): The equilibrium range in the spectrum of wind generated waves. J. Fluid Mech. Vol. 4. 426-434.
- Rice, S. O. (1951): Reflection of electromagnetic waves from slightly rough surfaces, Comm. Pure Appl. Math. Vol. 4, Mos 2/3. 361-378.
- Ross, D., and W. L. Jones (1978): On the relationship of radar backscatter to wind speed and fetch. Boundary Layer Meteorol. 13. Vol. 13. 133-149.
- Stewart, R. W. (1974): The air-sea momentum exchange. Boundary Layer Meteor. Vol. 6. 151-167.

ACKNOWLEDGEMENTS

The City College Contribution to this paper was supported by NASA contract NASA-266.

SCANNING WIND-VECTOR SCATTEROMETERS WITH TWO PENCIL BEAMS

T. Kirimoto and R.K. Moore
Remote Sensing Laboratory
University of Kansas Center for Research, Inc.
Lawrence, Kansas 66045-2969, U.S.A.

Abstract

A scanning pencil-beam scatterometer for ocean windvector determination has potential advantages over the fan-beam systems used and proposed heretofore. The pencil beam permits use of lower transmitter power, and at the same time allows concurrent use of the reflector by a radiometer to correct for atmospheric attenuation and other radiometers for other purposes. The use of dual beams based on the same scanning reflector permits four looks at each cell on the surface, thereby improving accuracy and allowing alias removal.

This paper describes simulation results for a spaceborne dual-beam scanning scatterometer with a 1-watt radiated power at an orbital altitude of 900 km. Two novel algorithms for removing the aliases in the windvector are described, in addition to an adaptation of the conventional maximum-likelihood algorithm. The new algorithms are more effective at alias removal than the conventional one. Measurement errors for the wind speed, assuming perfect alias removal, were found to be less than 10%.

1.0 INTRODUCTION

Plans for wind-vector measurement with spaceborne radar scatterometers often call for measurements with a radiometer on the same spacecraft. Although many of these measurements may be independent of the scatterometer, at least some of them should be used to correct errors in the measured backscatter due to atmospheric attenuation. In fact, a radiometer should always be used in conjunction with a scatterometer for this purpose.

A major problem with this correction occurs when the radiometer and scatterometer have different scan patterns and the radiometer has a larger footprint than the scatterometer [Moore, et al., 1983]. The problem exists because storm cells are often small compared with the size of a single radiometer footprint, so combining several radiometer measurements to correct a scatterometer measurement for a cell overlapping several radiometer cells results in significant errors in the "correction". The instrument configuration discussed here is intended to overcome this problem.

This arrangement calls for both instruments to have the same scan pattern and for the radiometer to have a footprint coincident with that of the scatterometer and, to the extent possible, a footprint of the same or smaller size. This is achieved by using the same scanning pencil-beam antenna for both scatterometer and radiometer. In addition, a second beam achieved by using an offset feed in the same antenna allows the scatterometer to have four rather than two azimuth angles (relative to the wind direction) for viewing each scatterometer cell.

The basic configuration is shown in Figure 1. Two circles at different distances from the suborbital track are shown, along with a line parallel to the track but displaced from it. The outer circle is the locus of scan positions for the radiometer and for scatterometer beam no.1, and the inner circle is the locus for scatterometer beam no. 2. The intersections of these circles with the

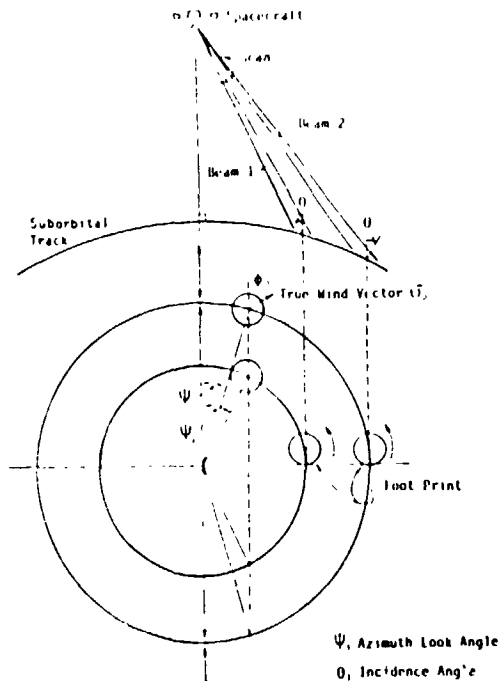


Fig. 1: Basic Configuration of Scanning Scatterometer

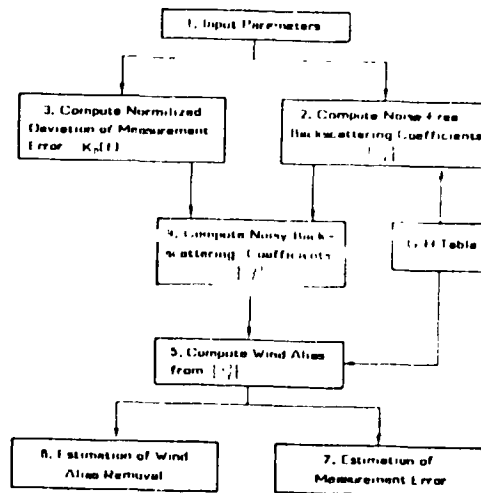


Fig. 2: Flow Chart for Simulation

displaced track line show the four different angles that are used by the scatterometer to view each cell on the surface. Use of only two look directions results in up to four "aliases" of the wind direction [Wurtele, et al., 1982]. Use of additional beams can reduce this alias problem and allow determination of the correct wind direction much of the time without use of collateral data or pattern recognition [Shanmugan, et al., 1982]. This paper presents simulations that illustrate how well the four-beam system solves the alias problem.

Advantages of this system include:

- (1) Only one antenna is needed for both radiometer and scatterometer.
- (2) Use of the relatively large aperture required for the radiometer allows the scatterometer power to be quite low (1 watt in these simulations).
- (3) Since all scatterometer measurements are at only two fixed angles of incidence, errors in modeling the incidence-angle variation of the scattering coefficient do not exist, and the data processing for the scatterometer need not have algorithms to handle incidence-angle variations.

The primary disadvantage of this system is that the look directions for the different cells are neither orthogonal (as on SEASAT) nor constant. On the other hand, the effect of the rotation of the earth on the SEASAT observations was to make the orthogonal beams on the spacecraft more difficult to handle than they would have been if they had been oriented relative to the ground track rather than relative to the orbit plane. Hence the complexity in the computations associated with non-orthogonal beams is at least partly cancelled by the complexity associated with correcting for earth-rotation effects in the orthogonal-beam system. For some angular combinations with the scanning beam the accuracy is less than with orthogonal looks, but these may be avoided at some sacrifice in swath width.

Here we treat two subjects associated with the scanning-beam system:

ORIGINAL FORM OF PCR QUALITY

algorithm development for determining wind vectors with the scanning four-beam scatterometer and measurement errors with such a system. The treatment is accomplished using Monte Carlo simulations. All simulations assume an effective transmitter average power of 1 watt at a spacecraft altitude of 900 km. Other parameters used are listed in Table 1. The algorithms used include a modification of the maximum-likelihood (or SOS) algorithm used for SEASAT [Jones, et al., 1982] and two simple pattern-recognition schemes based on comparison of results from nearby cells. The averages of norms between the true wind vectors and the simulated ones are computed to illustrate the errors.

2.0 SIMULATION METHOD

The major steps in the simulation of the scanning scatterometers are shown in Figure 2.

Step 1: Input of System Parameters: This step inputs all parameters that are needed in the following computation. The list of the parameters is shown in Table 1.

Step 2: Compute Noise-Free Backscattering Coefficients $\{\sigma_0\}$: This step computes a set of noise-free backscattering coefficients in equation (1).

$$\tilde{\sigma}_0^2 \text{ (dB)} = 10[G(\phi_0 - \psi_\ell - 180^\circ, \theta_\ell, \epsilon_\ell) + H(\phi_0 - \psi_\ell - 180^\circ, \theta_\ell, \epsilon_\ell) \log_{10} |\vec{U}_0|] \quad (1)$$

where:

- \vec{U}_0 = true wind vector
- $\vec{U}_0 = (|\vec{U}_0| \cos \phi_0, |\vec{U}_0| \sin \phi_0)$
- ϕ_0 = true wind direction relative to suborbital track (see Figure 1)
- ψ_ℓ = look angle relative to suborbital track (see Figure 1)
- ℓ = notation to distinguish looks
- θ_ℓ = incidence angle
- ϵ_ℓ = polarization (HH or VV)
- $G(\cdot), H(\cdot)$ = G-H Table [Schroeder, et al., 1982] describing the scattering model function

TABLE 1
PARAMETERS OF SIMULATION

Transmit Power (W)	1.0
Noise Temperature (°K)	273.0
System Loss (dB)	4.0
Noise Figure (dB)	4.0
Beamwidth-H (deg)	1.0
Beamwidth-V (deg)	1.0
Radiation Efficiency	0.8
Fraction of time to pass footprint k_I	0.1
Signal and Noise Integration Time Ratio k_N	10.0
Wavelength (MM)	22.0
Satellite Height (km)	900.0
Slant Range (km)	1127.6

ORIGINAL PAGE 12
OF POOR QUALITY

Step 3: Compute Normalized Standard Deviation of Measurement Error $K_p(\lambda)$ Due to Noise. This step computes the normalized standard deviation $K_p(\lambda)$ of measurement error [Grantham, et al.,] as

$$K_p^2(\lambda) = \frac{(1 + \text{SNR}^{-1})^2}{B_c T_I} + \frac{\text{SNR}^{-2}}{B_c T_I k_N} \quad (2)$$

where:

- SNR = signal-to-noise power ratio
- B_c = receiver bandwidth
- T_I = signal integration time
- k_N = noise-to-signal integration time ratio
- λ = notation to distinguish looks.

Note that only the receiver noise is taken account of in these simulations, although the measurements might also be noisy because of sampling variability.

Step 4: Compute Noisy Backscattering Coefficients $\{\sigma_l^0\}$. This step computes the set of noisy backscattering coefficients $\{\sigma_l^0\}$ in equation (3). It is assumed that $\{\sigma_l^0\}$ are distributed log-normally.

$$\ln \sigma_l^0 = \ln \tilde{\sigma}_l^0 + \Delta \sigma_l^0 \quad (3)$$

where:

- $\Delta \sigma_l^0$ = Gaussian random variable with 0 mean and $K_p(\lambda)$ deviation.
- p = notation to distinguish looks.

Step 5: Compute Wind Alias from $\{\sigma_l^0\}$. The maximum-likelihood method is applied as the algorithm for computation of the wind alias from $\{\sigma_l^0\}$. Thus, the wind vectors $\vec{U} = (|\vec{U}| \cos \phi, |\vec{U}| \sin \phi)$ at which the probability density function (PDF) of equation (4) have local maxima are computed [Jones, et al., 1982]

$$\text{PDF}(\vec{U} | \{\sigma_l^0\}) = \frac{\exp \left\{ - \sum_{l=1}^4 (\ln \sigma_l^0 - f(\vec{U}, l))^2 / 2K_p^2(\lambda) \right\}}{\int d\vec{U} \exp \left\{ - \sum_{l=1}^4 (\ln \sigma_l^0 - f(\vec{U}, l))^2 / 2K_p^2(\lambda) \right\}} \quad (4)$$

where:

$$f(\vec{U}, l) = (\ln 10) [G(\phi - \psi_l - 180^\circ, \theta_l, \epsilon_l) + H(\phi - \psi_l - 180^\circ, \theta_l, \epsilon_l)] \cdot \log_{10} |\vec{U}| \quad (5)$$

The procedures from Step 1 to Step 5 are iterated for several true wind vectors \vec{U}_0 , ground points, incidence angles and two polarizations, because these parameters seriously influence wind alias and wind measurement error. Other parameters are fixed at suitable values for spaceborne systems. Wind-alias removal and measurement error are estimated in Steps 6 and 7.

3.0 WIND-ALIAS REMOVAL

The PDF of equation (4) usually results in two or four local maxima of the wind direction, resulting in wind aliases. The local probability maximum for a wrong wind vector often has a larger value than the local maximum of the correct wind vector. Hence, it is important to remove wind aliases by other means.

Examples of the simulation results are shown in Figures 4-13. Parameters of the simulation are shown in these figures and in Table 1. In these figures

"ground-track" shows the direction of spacecraft motion and "AZ.Ang." shows forward azimuth look angles of each beam. (The reference axis is the ground-track). Aft azimuth look angles of each beam are given by subtracting forward look angles from 180°. The angle between the vector and "ground-track" shows the wind direction and the magnitude of the vector shows the wind speed.

Note that the type of "box" used for simulating the pattern recognition techniques is not completely realistic because it is based on the angles used for the simulations. The horizontal (j) dimension on the "chicken tracks" corresponds with along-track spacings for the satellite. The vertical (i) dimension on the "chicken tracks" corresponds to across-track spacings for the beam, but these dimensions are based on the angles selected for simulation rather than on uniform spacings. Figure 3 illustrates the dimensions of these boxes for different central angles chosen. A more realistic simulation would involve square boxes, but would mean repeating the simulations for these angles.

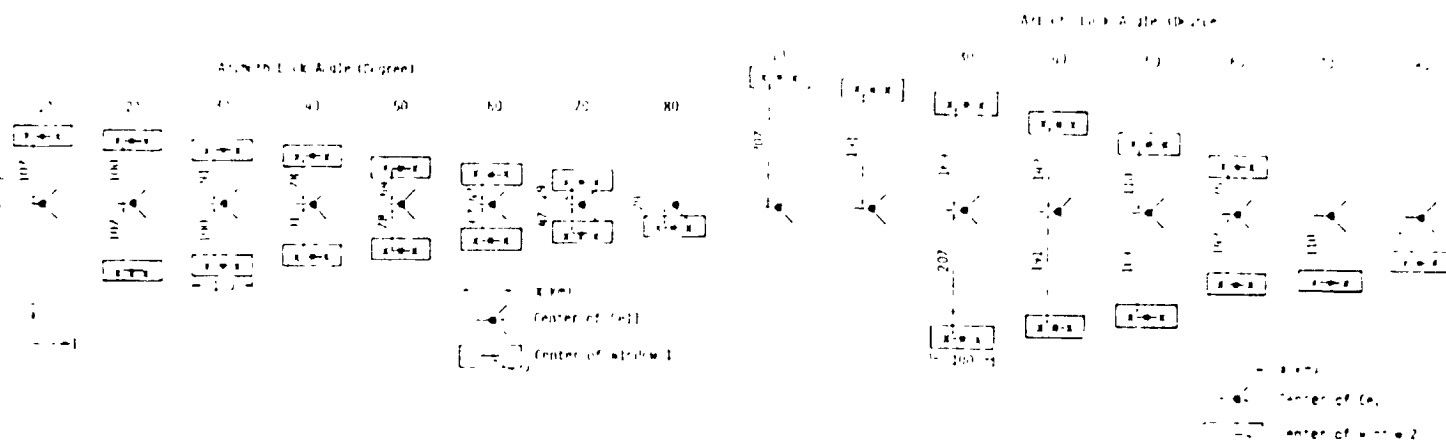


Fig. 3: Ground Spacings of Cells vs Azimuth Angle. (a) Outer Cells for Window 1; (b) Outer Cells for Window 2

The 4-vector plots ("sea chickens") shown in Figure 4a were prepared for each case studied, but only one example is presented here. These show the wind alias vectors, and ----X shows any wind alias whose normalized probability $P(K)$, is over 0.1, where

$$P(K) = \frac{\text{PDF}(K)}{\sum_{K=1}^{K_n} \text{PDF}(K)} \quad (6)$$

where:

PDF = probability density function in equation (4).

K = notation to distinguish aliases.

K_n = number of aliases.

The "Alias Removal" code shows the wind vectors which are selected by one of the following alias removal algorithms.

(1) Algorithm 1 - (Maximum Probability)

$$U(I, J, K_c) = \text{Max}_{K=K_c} [P(I, J, K)] \quad (7)$$

In this algorithm, the alias that has maximum normalized probability is selected as the correct wind vector. Where:

$\vec{U}(I,J,K)$ = wind alias,

I,J = notation to distinguish ground point (see Figures 3(a) and (b)),

K = notation to distinguish alias,

$P(I,J,K)$ = normalized probability of wind alias.

Figure 4b shows an example of the wind vectors obtained by selecting the alias in Figure 4a using Algorithm 1 for 4 m/sec winds with vertical polarization for the forward beam pointed in the upwind direction. Since the results with Algorithm 1 are generally inferior to those with the other algorithms, the results obtained with this algorithm are not repeated for the other examples shown.

(2) Algorithm 2 - (Pattern Recognition - 1)

$$\vec{U}(I,J,K_c) = \text{Min}_{K=K_c} \left[E_{ij} \left[\text{Min}_k \left[\left| \vec{U}(i,j,k) - \vec{U}(I,J,K) \right| / \left| \vec{U}(I,J,K) \right| \right] \right] \right] \quad (8)$$

In this algorithm, the wind alias which is satisfied with equation (8) is selected as the correct wind vector. There $E[\cdot]$ is the average over i and j and the ranges of i and j are as follows:

$$(i) \quad I-1 < i < I+1, \quad j = J-1, \quad j = J+1 \quad \text{-Window 1} \quad (9)$$

$$(ii) \quad I-1 < i < I+1, \quad j = J-2, \quad j = J+2 \quad \text{-Window 2} \quad (10)$$

(See Figure 3)

Window 1 uses adjacent cells in the pattern-recognition scheme, whereas Window 2 uses both adjacent cells and the next cell away in the cross-track direction. Thus, Window 1 uses 9 cells for alias removal, whereas Window 2 uses 15 cells. This is particularly important for the large azimuth angles, where the geometry of the simulation indicated in Figure 3 causes adjacent cross-track cells to be very close together. Of course, the assumption of uniform wind fields is more important in using Window 2.

Window 1 is used in Figures 4c and 5a to illustrate the use of Algorithm 2 (Pattern Recognition - 1). The other examples shown are for Algorithm 3 (Pattern Recognition - 2), since it gives better results.

(3) Algorithm 3 - (Pattern Recognition - 2)

$$\vec{U}(I,J,K_c) = \text{Min}_{K=K_c} \left[E_{ij} \left[\text{Min}_k \left[\left\{ -\ln \{ P(I,J,K) \cdot P(i,j,k) \} \right\} \cdot \left| \vec{U}(i,j,k) - \vec{U}(I,J,K) \right| / \left| \vec{U}(I,J,K) \right| \right] \right] \right] \quad (11)$$

In this algorithm, the wind alias which is selected by equation (11) is presumed to be the correct wind vector. The range of i,j is given by equation (9) or (10). This weighted algorithm gives generally better results than Algorithm 2. Therefore it is used in all of the examples following the initial ones that are shown in Figures 4 and 5 to illustrate the improvement of Algorithm 3 over Algorithm 2. Window 2 is used in Figures 6b, 7b, 10 and 13, since it gives significant improvement when the forward beam is in the crosswind (90°) direction.

The simulation results show the following:

- (1) Every algorithm is apt to select wrong wind vectors in the case of low wind speed. The error pattern of algorithm 1 seems to be random, but the error patterns of algorithm 2 and of algorithm 3 seem to be more consistent. Thus, algorithm 2 and algorithm 3 are apt to select wind vectors 180° from the correct direction. This error can easily be removed by examining the wind patterns.
- (2) Algorithm 2 is apt to select opposite wind vectors even in the case of high wind speed.
- (3) Window 2 improves the performance of Algorithm 2 and of Algorithm 3.
- (4) Algorithm 3 with window 2 will select correct wind vectors almost perfectly.

Note that the low-wind-speed errors might be reduced by use of higher power than the 1 watt assumed. They would also be smaller if the satellite were at a lower altitude than 900 km.

4.0 MEASUREMENT ERROR OF WIND VECTOR

In this section, the measurement error of the wind vector (after alias removal) is investigated. It is presumed that the alias-removal algorithm works perfectly. Scanning scatterometers with one beam (two look angles) are also investigated here.

The simulation results are shown in Figures 14-16. Parameters of the simulation are shown in Table 1 and in these figures. In these figures the horizontal axes show the forward look angle of the inner beam. The vertical axes show measurement error MC

$$MC = \frac{\sqrt{E[|\vec{U}| - |\vec{U}_0|^2]}}{|\vec{U}_0|} \quad (12)$$

where:

\vec{U}_0 = true wind vector.

\vec{U} = simulated wind vector.

Twenty-five noisy samples of wind vectors were simulated in look directions relative to the wind of 0°, 30°, 60° and 90°. Hence, one hundred samples are used in the average of equation (12). These figures show that vertical polarization, small incidence angle, and high wind speed reduce measurement error of scatterometers because they increase received power. Higher power at larger incidence angles might improve performance, but no such simulations were performed.

The averages of 2400 simulation samples as to three wind speeds (4.0 m/s, 12.0 m/s, 24 m/s), four wind directions (0°, 30°, 60°, 90°) and eight azimuth look angles (10°, 20°, 30°, 40°, 50°, 60°, 70°, 80°) are shown in Table 2. The rows of Table 2 show parameters (incidence angle and polarization) of the inner beam and the columns show parameters of the outer beam. Although a smaller incidence angle is better for scatterometers, scatterometers whose incidence angle is 50° for the outer beams were investigated because 50° is often used in radiometers, and because 50° gives a wider measurement swath. These figures and Table 2 obviously show the following:

- (1) Two-beam (four-look) scatterometers are better than one-beam (two-look) scatterometers.
- (2) Two-beam scatterometers give quite low measurement error over look angles from 20° to 80° off the surface track.

ORIGINAL PAGE IS
OF POOR QUALITY

- (3) The simulation results in the case of low wind speed are not good, but an increase (i.e., to two watts) in transmit power would resolve this problem easily.

TABLE 2

AVERAGE MEASUREMENT ERROR

2		35		40		45		50	
1		HH	VV	HH	VV	HH	VV	HH	VV
	HH	.088		.060		.062		.068	
35	VV		.064						
	HH			.114		.058	.093	.058	
40	VV				.069				.044
	HH					.161		.128	.090
45	VV						.087		.056
	HH							.255	
50	VV								.098

DIAGONAL - SINGLE-BEAM SCATTERDMETER

5.0 CONCLUSIONS

Wind alias removal and measurement error of wind vector in scanning two-beam scatterometers were estimated using computer simulation. In the estimation of wind alias removal, two novel algorithms using pattern recognition technique were introduced and simulation results showed these algorithms are more powerful than the conventional maximum-likelihood algorithm. Note that these algorithms would not be powerful in scatterometers with fixed fan beams like SEASAT SASS. In the estimation of measurement error of wind vector, simulation results showed the scanning scatterometers give low enough measurement error over an arc from 20° to the side of the spacecraft track to 80° to the side to be practical. The average of measurement error was under 10.0%.

Only receiver noise was taken account of as the primary factor of noise in this simulation. Other noise sources should be taken account of in future studies. Additional noise would increase K_p . However, it is possible to reduce K_p by increasing transmit power. Only 1-watt transmit power was used in this simulation. More detailed studies would make certain that the scanning scatterometers are very powerful spaceborne wind-vector-measurement systems.

REFERENCES

- Grantham, W.L., et al., "An Operational Satellite Scatterometer for Wind Vector Measurement Over the Ocean," NASA Tech Memo TMX-72672.
- Jones, W.L., et al., "The SEASAT-A Satellite Scatterometer: The Geophysical Evaluation of Remotely Sensed Wind Vector Over the Ocean," J. Geophys. Res., vol. 87, April 1982, pp. 3297-3317.
- Moore, R.K., A.H. Chaudhry and I.J. Birrer, "Errors in Scatterometer-Radiometer Wind Measurement Due to Rain," IEEE J. Ocean Engr., vol. OE-8, no. 1, January 1983, pp. 37-49.
- Schroeder, L.C., et al., "The Relationship Between Wind Vector and Normalized Radar Cross-Section Used to Derive SEASAT-A Satellite Scatterometer Winds," J. Geophys. Res., vol. 87, April 1982, pp. 3318-3336.
- Shanmugan, K.S., V. Narayanan and J. Stiles, "NOSS-SCAT Wind Direction Alias Removal," Remote Sensing Laboratory Technical Report 515-1, University of Kansas Center for Research, Inc., Lawrence, Kansas, January 1982.
- Wurtele, M.G., et al., "Wind Direction Alias Removal Studies of SEASAT Scatterometer-Driven Wind," J. Geophys. Res., vol. 87, April 1982, pp. 3365-3377.

WIND SPEED (M/S) = 4.0
WIND DIRECTION (DEG) = 0.0
BEAM NO. = 1
POLARIZATION = VV
INC. ANG. (DEG) = 40

TRUE WIND VECTOR

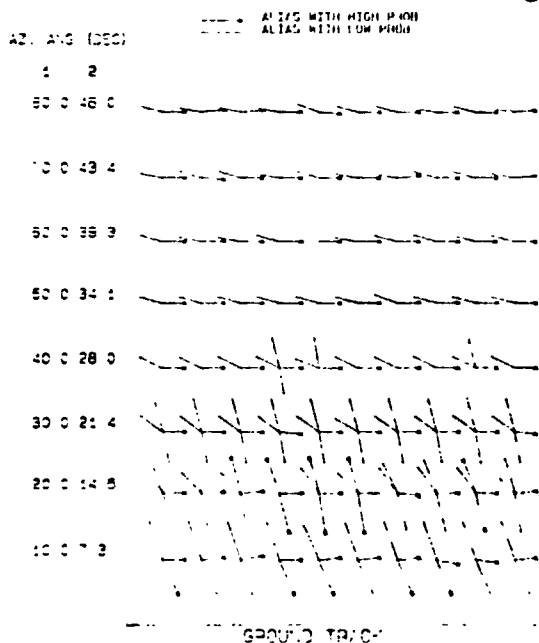
SEA CHICKEN

ORIGINAL PAGE IS
OF POOR QUALITY

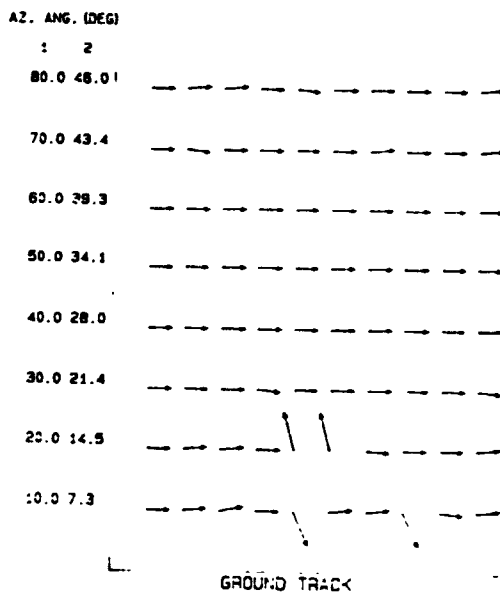
WIND SPEED (M/S) = 4.0
WIND DIRECTION (DEG) = 0.0
BEAM NO. = 1
POLARIZATION = VV
INC. ANG. (DEG) = 40

TRUE WIND VECTOR

ALIAS REMOVAL (MAX PROB.)



a

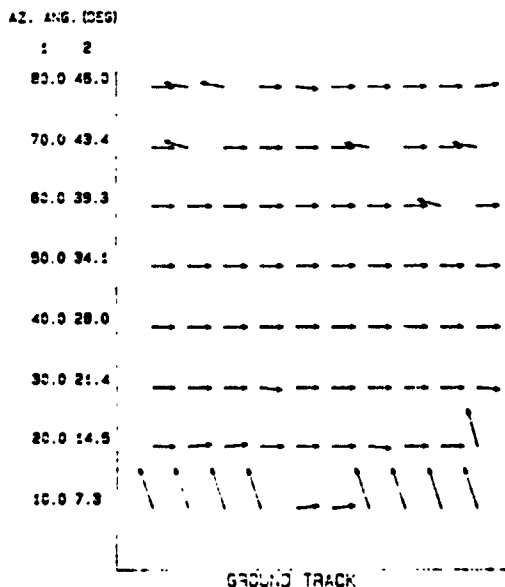


b

WIND SPEED (M/S) = 4.0
WIND DIRECTION (DEG) = 0.0
BEAM NO. = 1
POLARIZATION = VV
INC. ANG. (DEG) = 40

TRUE WIND VECTOR

ALIAS REMOVAL (PATTERN RECOG.-1)

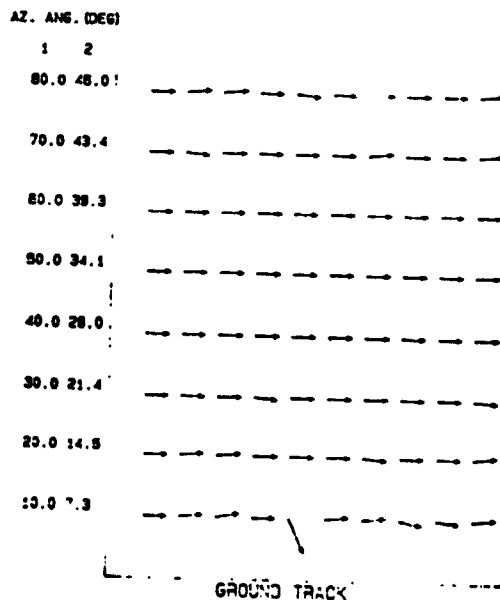


c

WIND SPEED (M/S) = 4.0
WIND DIRECTION (DEG) = 0.0
BEAM NO. = 1
POLARIZATION = VV
INC. ANG. (DEG) = 40

TRUE WIND VECTOR

ALIAS REMOVAL (PATTERN RECOG.-2)



d

Figure 4: Examples for Different Stages in Alias Removal. Wind Speed 4 m/sec. Look Angle 0° (Upwind for Forward Beam). Vertical polarization. (a) Result of basic algorithm, showing aliases; (b) Aliases with maximum probability on basic algorithm; (c) Aliases selected by algorithm 2; (d) Aliases selected by algorithm 3.

WIND SPEED (M/S) = 4.0
WIND DIRECTION (DEG) = 30.0
BEAM NO. = 1 2
POLARIZATION = VV VV
INC. ANG. (DEG) = 40 50

TRUE WIND VECTOR

ORIGINAL PAGE IS
OF POOR QUALITY

WIND SPEED (M/S) = 4.0
WIND DIRECTION (DEG) = 30.0
BEAM NO. = 1 2
POLARIZATION = VV VV
INC. ANG. (DEG) = 40 50

TRUE WIND VECTOR

ALIAS REMOVAL (PATTERN RECOG.-1)

ALIAS REMOVAL (PATTERN RECOG.-2)

AZ. ANG. (DEG)

AZ. ANG. (DEG)

1 2

1 2

80.0 48.0

80.0 48.0

70.0 43.4

70.0 43.4

60.0 39.3

60.0 39.3

50.0 34.1

50.0 34.1

40.0 29.0

40.0 29.0

30.0 24.4

30.0 24.4

20.0 14.5

20.0 14.5

10.0 7.3

10.0 7.3

GROUND TRACK

GROUND TRACK

Figure 5: Examples for Algorithms 2 and 3. Wind Speed 4 m/sec. Look Angle 30°. Vertical Polarization. (a) Algorithm 2; (b) Algorithm 3.

WIND SPEED (M/S) = 4.0
WIND DIRECTION (DEG) = 60.0
BEAM NO. = 1 2
POLARIZATION = VV VV
INC. ANG. (DEG) = 40 50

TRUE WIND VECTOR

ALIAS REMOVAL (PATTERN RECOG.-2)

WIND SPEED (M/S) = 4.0
WIND DIRECTION (DEG) = 60.0
BEAM NO. = 1 2
POLARIZATION = VV VV
INC. ANG. (DEG) = 40 50

TRUE WIND VECTOR

ALIAS REMOVAL (PATTERN RECOG.-2)

AZ. ANG. (DEG)

AZ. ANG. (DEG)

1 2

1 2

80.0 48.0

80.0 48.0

70.0 43.4

70.0 43.4

60.0 39.3

60.0 39.3

50.0 34.1

50.0 34.1

40.0 29.0

40.0 29.0

30.0 24.4

30.0 24.4

20.0 14.5

20.0 14.5

10.0 7.3

10.0 7.3

GROUND TRACK

GROUND TRACK

Figure 6: Examples for Algorithm 3, Windows 1 and 2. Wind Speed 4 m/sec. Look Angle 60°. Vertical Polarization. (a) Window 1; (b) Window 2.

WIND SPEED (M/S) = 4.0
WIND DIRECTION (DEG) = 90.0
BEAM NO. = 1 2
POLARIZATION = VV VV
INC. ANG. (DEG) = 40 50

TRUE WIND VECTOR

ORIGINAL PAGE IS
OF POOR QUALITY

WIND SPEED (M/S) = 4.0
WIND DIRECTION (DEG) = 90.0
BEAM NO. = 1 2
POLARIZATION = VV VV
INC. ANG. (DEG) = 40 50

TRUE WIND VECTOR

ALIAS REMOVAL (PATTERN RECOG.-2)

ALIAS REMOVAL (PATTERN RECOG.-2)

AZ. ANG. (DEG)

1 2

80.0 48.0

70.0 43.4

60.0 39.3

50.0 34.1

40.0 28.0

30.0 21.4

20.0 14.5

10.0 7.3

GROUND TRACK

AZ. ANG. (DEG)

1 2

80.0 48.0

70.0 43.4

60.0 39.3

50.0 34.1

40.0 28.0

30.0 21.4

20.0 14.5

10.0 7.3

GROUND TRACK

Figure 7: Examples for Algorithm 3, Windows 1 and 2. Wind Speed 4 m/sec. Look Angle 90°. Vertical Polarization. This look angle is always the worst case. (a) Window 1; (b) Window 2.

WIND SPEED (M/S) = 12.0
WIND DIRECTION (DEG) = 90.0
BEAM NO. = 1 2
POLARIZATION = HH HH
INC. ANG. (DEG) = 40 50

TRUE WIND VECTOR

ALIAS REMOVAL (PATTERN RECOG.-2)

AZ. ANG. (DEG)

1 2

80.0 48.0

70.0 43.4

60.0 39.3

50.0 34.1

40.0 28.0

30.0 21.4

20.0 14.5

10.0 7.3

GROUND TRACK

WIND SPEED (M/S) = 12.0
WIND DIRECTION (DEG) = 90.0
BEAM NO. = 1 2
POLARIZATION = HH HH
INC. ANG. (DEG) = 40 50

TRUE WIND VECTOR

ALIAS REMOVAL (PATTERN RECOG.-2)

AZ. ANG. (DEG)

1 2

80.0 48.0

70.0 43.4

60.0 39.3

50.0 34.1

40.0 28.0

30.0 21.4

20.0 14.5

10.0 7.3

GROUND TRACK

Figure 8: Example for Algorithm 3, Window 1. Wind Speed 12 m/s. Look Angle 0°. Horizontal Polarization.

Figure 9: Example for Algorithm 3, Window 1. Wind Speed 12 m/s. Look Angle 60°. Horizontal Polarization

WIND SPEED (M/S) = 12.0
WIND DIRECTION (DEG) = 90.0
BEAM NO. 1 2
POLARIZATION = HH HH
INC. ANG. (DEG) = 40 50

TRUE WIND VECTOR

ALIAS REMOVAL (PATTERN RECOG.-2)

AZ. ANG. (DEG)

1 2

80.0 48.0

70.0 43.4

60.0 39.3

50.0 34.1

40.0 28.0

30.0 21.4

20.0 14.5

10.0 7.3

GROUND TRACK

WIND SPEED (M/S) = 24.0
WIND DIRECTION (DEG) = 0.0
BEAM NO. 1 2
POLARIZATION = HH HH
INC. ANG. (DEG) = 40 50

TRUE WIND VECTOR

ALIAS REMOVAL (PATTERN RECOG.-2)

AZ. ANG. (DEG)

1 2

80.0 48.0

70.0 43.4

60.0 39.3

50.0 34.1

40.0 28.0

30.0 21.4

20.0 14.5

10.0 7.3

GROUND TRACK

Figure 10: Example for Algorithm 3, Window 2. Wind Speed 12 m/s. Look Angle 90°. Horizontal Polarization.

Figure 11: Example for Algorithm 3, Window 1. Wind Speed 24 m/s. Look Angle 0°. Horizontal Polarization.

WIND SPEED (M/S) = 24.0
WIND DIRECTION (DEG) = 60.0
BEAM NO. 1 2
POLARIZATION = HH HH
INC. ANG. (DEG) = 40 50

TRUE WIND VECTOR

ALIAS REMOVAL (PATTERN RECOG.-2)

AZ. ANG. (DEG)

1 2

80.0 48.0

70.0 43.4

60.0 39.3

50.0 34.1

40.0 28.0

30.0 21.4

20.0 14.5

10.0 7.3

GROUND TRACK

WIND SPEED (M/S) = 24.0
WIND DIRECTION (DEG) = 90.0
BEAM NO. 1 2
POLARIZATION = HH HH
INC. ANG. (DEG) = 40 50

TRUE WIND VECTOR

ALIAS REMOVAL (PATTERN RECOG.-2)

AZ. ANG. (DEG)

1 2

80.0 48.0

70.0 43.4

60.0 39.3

50.0 34.1

40.0 28.0

30.0 21.4

20.0 14.5

10.0 7.3

GROUND TRACK

Figure 12: Example for Algorithm 3, Window 1. Wind Speed 24 m/s. Look Angle 60°. Horizontal Polarization.

Figure 13: Example for Algorithm 3, Window 2. Wind Speed 24 m/s. Look Angle 90°. Horizontal Polarization.

2 BEAM SYSTEM $U_0=4.0$ (M/S)

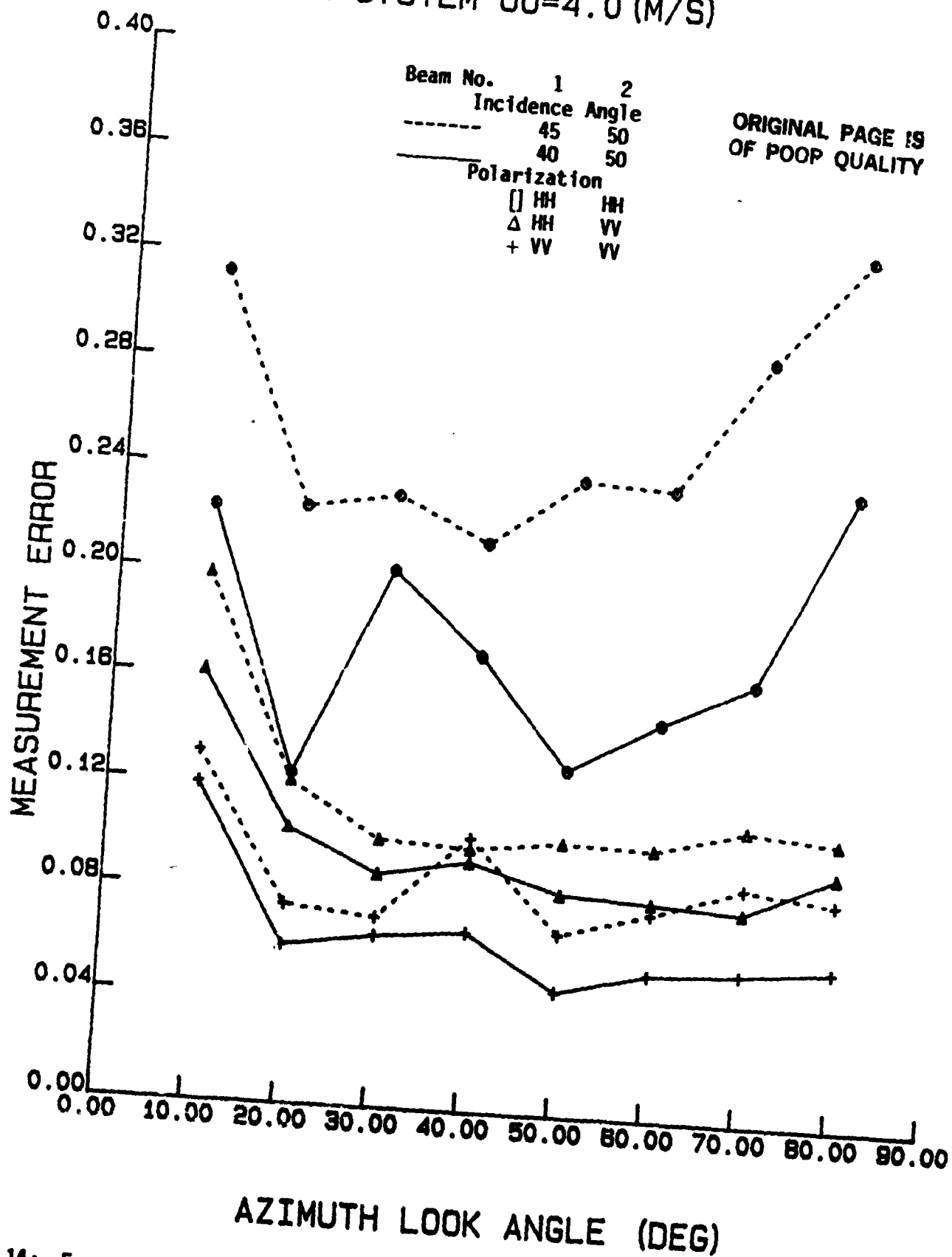


Figure 14: Errors for Wind Speed of 4 m/sec vs Azimuth Angle with Beam Incidence Angles and Polarizations as Parameters.

2 BEAM SYSTEM $U_0=12.0$ (M/S)

ORIGINAL PAGE 19
OF POOR QUALITY

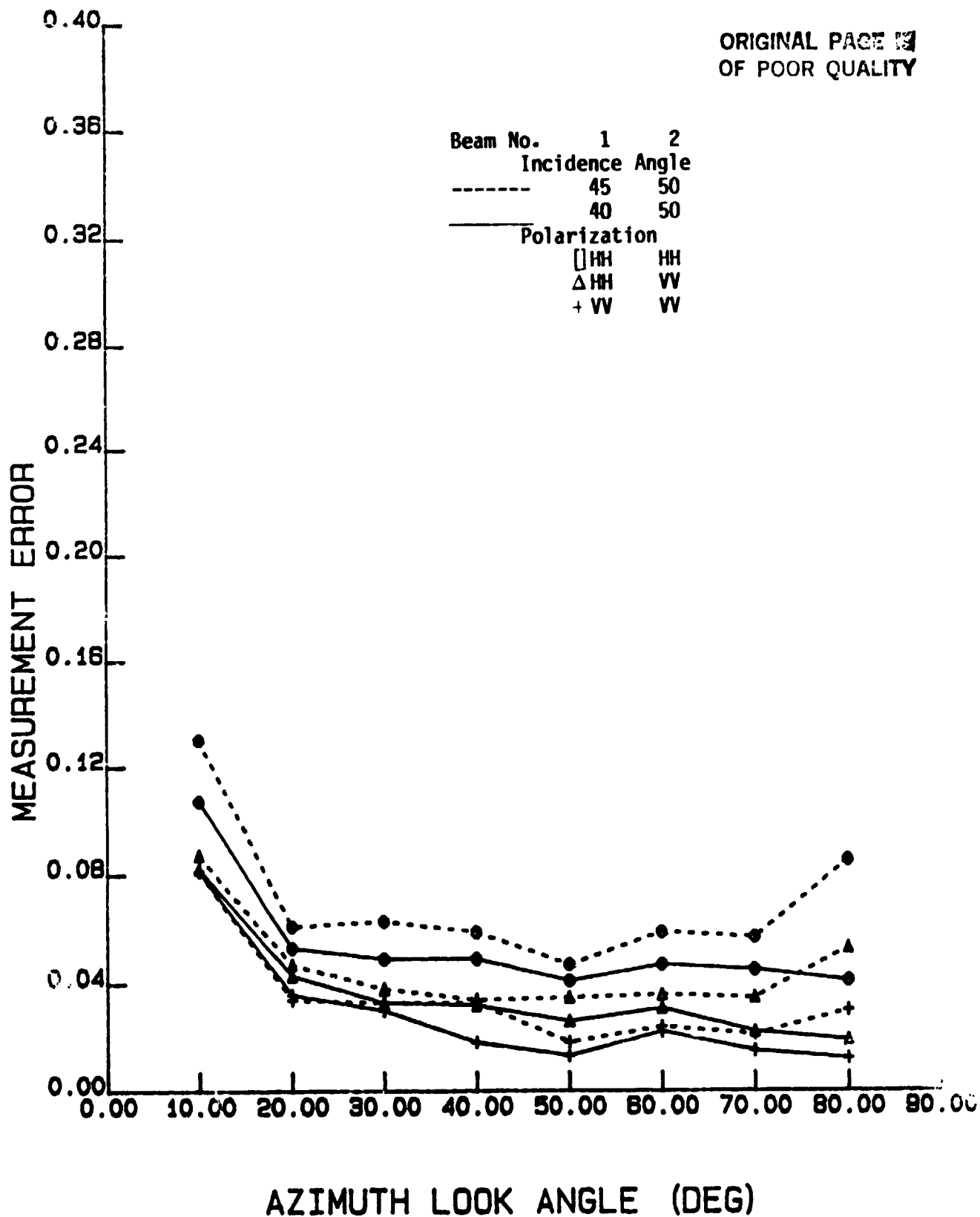


Figure 15: Errors for Wind Speed of 12 m/sec vs Azimuth Angle with Beam Incidence Angles and Polarizations as Parameters.

2 BEAM SYSTEM $U_0=24.0$ (M/S)

ORIGINAL PAGE IS
OF POOR QUALITY

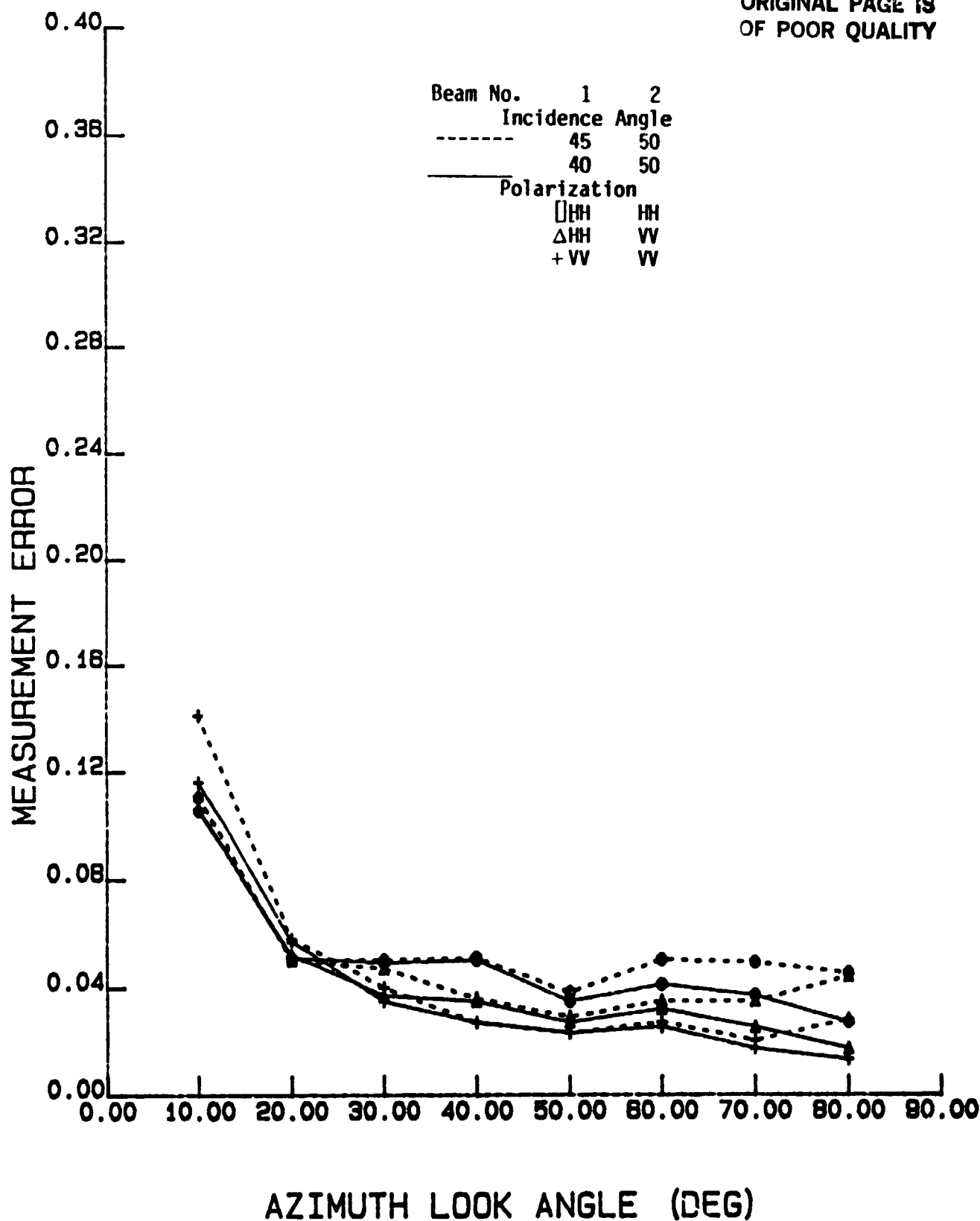


Figure 16: Errors for Wind Speed of 24 m/sec vs Azimuth Angle with Beam Incidence Angles and Polarizations as Parameters.

N84 27372

NEW ALGORITHMS FOR MICROWAVE MEASUREMENTS OF OCEAN WINDS

Frank J. Wentz
Remote Sensing Systems
475 Gate Five Rd., Sausalito, California 94965, USA

Steve Peteherych
Atmospheric Environment Service
4905 Dufferin Street, Downsview, Ontario M3H5T4, Canada

ABSTRACT

Improved second generation wind algorithms are used to process the three month SEASAT SMMR and SASS data sets. The new algorithms are derived without using in situ anemometer measurements. All known biases in the sensors' measurements are removed, and the algorithms' model functions are internally self-consistent. The computed SMMR and SASS winds are collocated and compared on a 150 km cell-by-cell basis, giving a total of 115444 wind comparisons. The comparisons are done using three different sets of SMMR channels. When the 6.6H SMMR channel is used for wind retrieval, the SMMR and SASS winds agree to within 1.3 m/s over the SASS primary swath. At nadir where the radar cross section is less sensitive to wind, the agreement degrades to 1.9 m/s. The agreement is very good for winds from 0 to 15 m/s. Above 15 m/s, the off-nadir SASS winds are consistently lower than the SMMR winds, while at nadir the high SASS winds are greater than SMMR's. When 10.7H is used for the SMMR wind channel, the SMMR/SASS wind comparisons are not quite as good. When the frequency of the wind channel is increased to 18 GHz, the SMMR/SASS agreement substantially degrades to about 5 m/s.

1. INTRODUCTION

Aircraft and satellite experiments have clearly demonstrated that the wind speed near the sea surface can be remotely sensed by microwave radiometers and scatterometers [Swift, 1977; Munn, 1978; Bernstein, 1982]. The passive radiometer collects the radiation that is naturally emitted by the sea surface and intervening atmosphere, whereas the active scatterometer measures the component of transmitted power that is backscattered from the sea surface. Both the emitted and backscattered radiation are directly affected by surface roughness, which is correlated with the near-surface wind speed. The correlation of roughness and wind speed is a complex, coupled phenomenon [Kinsman, 1965]. Ocean roughness is first generated by atmospheric pressure fluctuations and tangential wind shears. The newly generated waves then transfer energy to other ocean wavelengths, which in turn affect the wind flow.

The oceanographic satellite SEASAT carried a multi-frequency microwave radiometer SMMR and a 14.6 GHz scatterometer SASS [Weissman, 1980]. The wind speeds inferred by these two sensors agreed with in situ anemometer measurements to within about 2 m/s [Jones et al., 1982; Wentz et al., 1982]. Better agreement (1.4 m/s) was obtained when the SMMR winds were directly compared to the SASS winds. This good agreement for the SMMR/SASS comparisons indicated a high correlation exists between the types of roughness sensed by the two instruments.

These original SMMR/SASS wind comparisons were limited to a series of case studies over the Northeast Pacific and the North Atlantic during two weeks in

September 1978. The wind retrieval algorithms were carefully tuned for this time period and region, and the resulting wind comparisons looked very promising. However, when extending the comparisons to all oceans for the entire three month life of SEASAT, these first generation algorithms proved to be biased and overly complex. For example, the SMMR algorithm was plagued with temporal brightness temperature (T_B) drifts and with relative T_B biases that varied across the swath [Bernstein and Morris, 1983]. Also the algorithm attempted to use all the SMMR channels, even though not enough was known about the relative error statistics of the various channels. The SASS algorithm produced winds that had an artificial cross swath variation [Wentz et al., 1984]. Furthermore, the winds retrieved from the horizontal polarization radar cross section (σ^0) measurements did not agree with those coming from the vertical polarization σ^0 . Finally, σ^0 's corresponding to low winds were systematically filtered out, and as a result the winds below 6 m/s were biased high.

In this investigation, we use improved second generation wind algorithms to process the three month SMMR/SASS data set. A unique feature of these algorithms is that their derivations do not require in situ anemometer measurements. Thus the algorithm winds are a true satellite product, not affected by problematic conventional observations. In addition, the SMMR and SASS algorithms are developed independently of each other. All known biases in the T_B 's and σ^0 's are removed, and the algorithms' model functions are internally self-consistent. The resulting retrieval techniques are more accurate and simpler than their forerunners.

The computed SMMP and SASS winds are collocated and compared on a cell-by-cell basis. The cell resolution is 150 km, which corresponds to the SMMR footprint size for the lowest resolution 6.6 GHz channel. A total of 115444 wind comparisons are made over SEASAT's three months. These comparisons are stratified according to four swath positions going from nadir to the outer portion of the swath. To determine the wind sensing performance of various radiometer configurations, the comparisons are done using three different combinations of SMMR channels.

2. SMMR GEOPHYSICAL ALGORITHM

The retrieval of wind speed and other geophysical parameters from SMMR T_B measurements is accomplished by solving a set of simultaneous equations:

$$T_{Bi} = f_i(T_s, W, V, L) \quad (1)$$

where T_{Bi} is the SMMR measurement for the i th channel and $f_i(\dots)$ is the corresponding model function. The unknown variables are sea-surface temperature T_s (K), wind speed W (m/s), atmospheric water vapor V (g/cm²), and atmospheric liquid water L (g/cm²). The SMMR T_B model function was first derived by Wentz [1983a], and later the wind-induced emissivity term ΔE was modified [Wentz, 1984]. In the original model, ΔE came from 119 collocated SMMR T_B cells and SASS wind speeds for two SEASAT passes over the North Pacific. Because of the small size of this data set and problems with the earlier versions of the SASS winds, ΔE was rederived. The new derivation is based on 32213 SMMR T_B cells and is independent of SASS winds. In addition, no in situ anemometer measurements are required in the new derivation. The new ΔE 's are approximately the same as those obtained for the earlier model.

The original SEASAT SMMR geophysical algorithm [Wentz et al., 1982] used all ten SMMR channels. With ten observations and four unknowns, the system of equations (1) is over-determined, and a least-squares technique was used to find T_s , W ,

V, and L. Although the least-squares algorithm performed better than regression algorithms [Lipes and Born, 1981], there was a drawback. A weight must be assigned to each channel. This weight represents the inverse of the expected variance between the observation and the model function. In general, the lower frequency channels should be weighted more heavily than the higher frequencies. Unfortunately, not enough is currently known about the error statistics of the observations or model function to determine the correct weights. In view of this, we decided to simplify the inversion problem and deal with a deterministic set of equations.

A deterministic algorithm for finding T_s , W, V, and L consists of solving a set of four simultaneous model function equations. As explained below, a good choice for the four channels is 6.6V, 6.6H, 18V, and 21V (6.6V denotes 6.6 GHz, vertical polarization). The model function is quasi-linear in terms of T_s , W, V, and L, and a unique solution exists for the system of four equations. This solution is found by Newton's iterative method extended to four dimensions. Only two or three iterations are required for convergence. The performance of the four parameter algorithm was first tested by comparing the retrieved T_s with Reynolds' [1982] SST climatology. The rms difference was 1.58 C when the SST's for 31781 individual SMMR cells were compared to the climatology [Wentz, 1983b].

In this paper we are only interested the wind speed retrieval, not SST. To estimate the wind speed, we use a three channel algorithm (6.6H/18V/21V), rather than the four channel algorithm discussed above. The variable T_s is set equal to Reynolds' SST climatology, which is given on a one month by 1° latitude by 1° longitude grid. The climatology SST is interpolated to the center of the SMMR cell. Once T_s is specified, there are only three unknowns, and hence only three channels are required by the inversion algorithm. We select the three channel algorithm because it is simpler, requires fewer radiometer channels, and is as accurate as the four channel algorithm in determining W. Typically, the difference between the climatology SST and the true SST is about 1.5 C, which causes only a 0.6 m/s error in the retrieved wind. To verify this, we compare wind speeds coming from the 6.6H/18V/21V algorithm with those coming from the 6.6V/6.6H/18V/21V algorithm. The rms difference is 0.7 m/s. Furthermore, when compared to the SASS winds, the three channel algorithm shows slightly better agreement than the four channel algorithm (rms of 1.3 m/s compared to 1.4 m/s).

To minimize the retrieval error, the algorithm's three channels are selected such that a given channel has a high sensitivity to one variable and low sensitivity to the other two variables. In this way, the determinant for the system of equations is maximized. Horizontal polarization is used to infer wind speed because it is more sensitive to surface roughness than vertical polarization. Conversely, vertical polarization is used to determine V and L. The best frequency for wind speed determination is 6.6 GHz, which is least affected by atmospheric interference. Thus 6.6H is selected for the wind speed channel. The 18V channel is chosen for liquid water determination. This channel is better than the 37V channel because it does not saturate as fast with increasing L. Furthermore, 37 GHz is more susceptible to errors caused by variations in the rain drop size distribution and by rain cells that do not fill the SMMR footprint. Finally, the obvious selection for the water vapor channel is 21V, which is on the water vapor absorption line.

In addition to the 6.6H/18V/21V algorithm, we also analyze the performance of a 10.7H/18V/21V algorithm and a 18H/18V/21V algorithm. The purpose of changing the wind speed channel from 6.6H to 10.7H and 18H is to compare the performance of

different radiometer systems. For example, the microwave radiometer SSM/I to be launched in 1985 aboard the DMSP Block 5D-2 satellite operates at four frequencies: 19, 22, 37, and 85 GHz. Thus the performance of the 18H/18V/21V algorithm will provide some information on the SSM/I wind sensing capability.

3. SASS WIND ALGORITHM

The retrieval of wind speed from SASS σ^0 measurements is performed in a way analogous to that described in Section 2 for the SMMR. We solve a set of two simultaneous equations that equate the σ^0 measurement to the SASS model function. Wentz et al. [1984] derived the following function for the ocean radar cross section at the SASS frequency of 14.6 GHz:

$$\sigma^0 = A_0 + A_1 \cos(X - X_w) + A_2 \cos[2(X - X_w)] \quad (2)$$

The angles X_w and X are azimuth angles for the wind direction and σ^0 measurement, respectively. The A coefficients are known functions of the incidence angle and wind speed W . The derivation of A_0 and A_2 is based on the statistics of the SASS observations, and no in situ anemometer measurements are required. The A_1 coefficient comes from aircraft circle measurements of σ^0 . The statistically derived model is free of the incidence angle and polarization relative biases that occurred in the earlier version of the model function [Schroeder et al., 1982], which was tuned to the JASIN anemometer measurements.

In computing the SASS winds, we only use vertical polarization observations, which constitute 88% of all observations. Excluding horizontal polarization simplifies the retrieval problem and subsequent analysis. A collocation algorithm finds all SASS measurements that fall within a given SMMR 150 km cell. The SMMR swath is on the starboard side of the satellite subtrack. Except at nadir, the SASS measurements will come from either the forward starboard antenna (beam 1) or the aft starboard antenna (beam 2). The azimuth angles X for all measurements in a 150 km cell coming from the same beam are essentially the same, and the following averages are computed:

$$\langle \sigma^0 \rangle_i = \langle A_0 \rangle_i + \langle A_1 \rangle_i \cos(X_i - X_w) + \langle A_2 \rangle_i \cos[2(X_i - X_w)] \quad (3)$$

where $\langle \dots \rangle_i$ represents an average over the measurements coming from beam i , $i = 1$ or 2 , and X_i is the azimuth angle for beam i . For nadir observations, the SASS measurements come from all four antennas. Since A_1 and A_2 equal zero for the nadir σ^0 , these measurements are averaged together irrespective of beam number.

The preaveraging of σ^0 before retrieving wind speed increases the signal-to-noise ratio (SNR). In a 150 km cell in the middle of the SASS primary swath, there are typically 9 observations from each beam. Averaging these observations increases the SNR by a factor of 3. For light winds below 6 m/s, the SNR is poor, and the preaveraging helps considerably. In the original SASS algorithm [Jones et al., 1982], no preaveraging was done. The low SNR measurements were simply excluded from processing, which resulted in data gaps in low wind speed areas and a positive bias in the retrieved wind speeds for moderate wind speed areas.

Equation (3) represents two equations in two unknowns, W and X_w . The equations are solved by noting that the azimuth angles for the forward and aft antennas are nearly orthogonal ($X_2 = X_1 + 90^\circ \pm 1^\circ$). Using this orthogonality property, the second harmonic in the two equations is eliminated, giving

$$\langle A_2 \rangle_2 \langle \sigma^0 \rangle_1 + \langle A_2 \rangle_1 \langle \sigma^0 \rangle_2 = \langle A_2 \rangle_2 \langle A_0 \rangle_1 + \langle A_2 \rangle_1 \langle A_0 \rangle_2 + \varepsilon \quad (4)$$

$$\varepsilon = \langle A_2 \rangle_2 \langle A_1 \rangle_1 \cos(X_1 - X_w) - \langle A_2 \rangle_1 \langle A_1 \rangle_2 \sin(X_1 - X_w) \quad (5)$$

The term ε arises because there is a difference between an upwind and downwind measurement of σ^0 . If the upwind and downwind σ^0 were equal, then A_1 would be zero. For vertical polarization, which is used herein, the upwind-downwind difference is quite small, and ε can be treated as an error. Setting the term to zero gives

$$F(W) = \langle A_2 \rangle_2 \langle \sigma^0 \rangle_1 + \langle A_2 \rangle_1 \langle \sigma^0 \rangle_2 - \langle A_2 \rangle_2 \langle A_0 \rangle_1 - \langle A_2 \rangle_1 \langle A_0 \rangle_2 = 0 \quad (6)$$

The only unknown in the function $F(W)$ is wind speed W , which is found by Newton's iterative method. Only two or three iterations are required for convergence. The wind speed error introduced by neglecting ε is approximately

$$\Delta W = -\varepsilon / [\partial F(W) / \partial W] \quad (7)$$

For vertical polarization, $\Delta W / W$ is typically about 2%.

Once W is found, it can be substituted back into (3), and X_w can be calculated. The harmonic properties of (3) produce multiple solutions for X_w , which are called aliases. The number of these solutions is between 0 (no solution) and 4. This procedure gives a good estimate of the alias wind directions. However, to be exact, each alias has a slightly different wind speed solution because of the upwind-downwind term ε , and the wind speed coming from (6) cannot be applied to the individual aliases. Although the term ε is different for each alias, its average over the various aliases is nearly zero. Thus the average wind speed error ΔW is also zero, and the wind speed coming from (6) equals the average of the alias wind speeds. As such, it is the best estimate of wind speed that can be obtained if there is no additional dealiasing information, which is the case for this investigation. Fortunately, we are only interested in obtaining the wind speed and do not have to deal with the alias problem or the exact solution for X_w .

4. RESULTS

In this section, the collocated SMMR and SASS winds are compared. The SMMR and SASS swaths overlap on the starboard side of the satellite subtrack. The overlap area extends 600 km out from the subtrack and is divided into four 150 km square resolution cells. Beginning with the subtrack cell, these cells are numbered 1 through 4. The SMMR T_p measurements uniformly cover each cell, but the SASS σ^0 measurements do not. For cell 1, we only use the nadir SASS measurements that are restricted to a 40 km wide strip along the subtrack. The near-nadir SASS measurements at incidence angles of 4° and 8° are not used because they are relatively insensitive to wind speed. Cell 2 is also only partially filled with SASS observations. There is a gap in the SASS swath for incidence angles between 10° and 20° , and as a result the left half of cell 2 does not contain any SASS observations. The outer cells 3 and 4 are completely within the SASS primary swath and are uniformly filled with SASS measurements.

The SMMR antenna does a conical scan such that the incidence angle is a constant 49° . Thus the same physics and model function applies to cells 1 through 4. The only difference is that significant polarization coupling occurs in the edge cells 1 and 4. This polarization coupling makes the decoupled T_p values noisier for the edge cells. In contrast, the SASS antennas are fixed sticks, and each cell

corresponds to a different range of incidence angles. The SASS measurements in cell 1 are nadir observations for which σ^0 decreases with wind speed W approximately as $(1/W)^2$. For cell 2 the average incidence angle is about 25° , and σ^0 increases linearly with wind speed. For the two outer cells, σ^0 increases as the square of wind speed. Thus the SASS model function is quite different for the four cells. In view of this, the SMMR/SASS wind comparisons are stratified according to cell number. We expect that the best comparisons will occur for cell 3. For this cell, there is uniform coverage of both SMMR and SASS observations, the signal-to-noise ratio for SASS is the best, σ^0 is most sensitive to wind speed, and the polarization coupling for SMMR is a minimum.

For the 6.6H/18V/21V system, wind comparisons are done for the entire three month SEASAT mission. However, only nighttime observations are used because sea-surface sun glitter and Faraday rotation degrade the daytime SMMR data. Furthermore, the SMMR observations must be at least 800 km from land to avoid antenna sidelobe contamination. As a final filtering criteria, when the liquid water content L coming from the SMMR algorithm exceeds 50 mg/cm^2 , which corresponds to a 0.5 mm/hr rain, the observation is excluded. The same filtering criteria are used for the 10.7H/18V/21V and 18H/18V/21V systems, except that only data coming from the second half of the SEASAT mission are used because of a problem with the 18 GHz channels. In the middle of the mission, the 18H and 18V channels experienced a sudden 4 K to 5 K drop in the mean T_B level. This drop is probably due to an unexpected change in the transmissivity of a SMMR waveguide component. Since the two higher frequency systems are rather sensitive to errors in the 18 GHz channels, we choose to avoid the problem and only use observations occurring in the second half of the mission after the 18 GHz anomaly. The wind retrieval from the 6.6H/18V/21V system is less sensitive to errors in the 18V T_B , and we correct the problem, as much as possible, by adding a time step bias to the 18V T_B so that the entire mission can be processed. A small linear time-dependent bias is also added to the 6.6H T_B to compensate for an observed 1.5 K drift over the three months.

Table 1 shows the summary statistics for the wind comparisons for the three radiometer systems. For cells 1 through 4, the table gives the number of observations, the mean SASS wind, the mean SMMR wind, and the standard deviation of the SMMR wind minus the SASS wind. As expected the 6.6H/18V/21V system gives the best results. The agreement between the SMMR and SASS winds for cells 2 through 4 is between 1.3 and 1.4 m/s and degrades to 1.9 m/s for nadir cell 1. Averaged over the three months, the mean wind speed should be nearly the same for the four cells. This is the case except that the SASS cell 2 winds appear to be about 0.5 m/s high relative to the other three cells. Also the SMMR cell 1 winds seem to be running about 0.3 m/s too high. These small cross swath wind variations are probably due to residual biases in the observations and in the SASS model function. The results for the 10.7H/18V/21V system are about the same as for the 6.6H/18V/21V system except that the SMMR/SASS wind agreement is somewhat poorer, being about 1.7 m/s for the off-nadir cells and 2.5 m/s for cell 1. Also, the mean SMMR wind is about 0.8 m/s lower than that for the 6.6H/18V/21V system. A substantial degradation in performance occurs for the 18H/18V/21V system. The wind agreement for cells 2 through 4 worsen to about 5 m/s, and cell 1 shows a 7.1 m/s variation between SMMR and SASS. The large discrepancy for cell 1 may be due to the fact that this cell is particularly affected by polarization coupling.

Table 1. SMMR/SASS Wind Comparisons

6.6H/18V/21V System	Cell 1	Cell 2	Cell 3	Cell 4
Number of Observations	31320	28714	28043	27367
Mean SASS Wind (m/s)	7.5	7.9	7.4	7.3
Mean SMMR Wind (m/s)	7.8	7.5	7.4	7.4
Std. Dev. SMMR-SASS (m/s)	1.9	1.4	1.3	1.4
10.7H/18V/21V System	Cell 1	Cell 2	Cell 3	Cell 4
Number of Observations	15031	13605	13164	12643
Mean SASS Wind (m/s)	7.1	7.7	7.2	7.0
Mean SMMR Wind (m/s)	7.1	6.7	6.6	6.4
Std. Dev. SMMR-SASS (m/s)	2.5	1.7	1.7	1.8
18H/18V/21V System	Cell 1	Cell 2	Cell 3	Cell 4
Number of Observations	14904	13592	13158	12613
Mean SASS Wind (m/s)	7.1	7.7	7.2	7.0
Mean SMMR Wind (m/s)	7.8	7.2	7.3	7.8
Std. Dev. SMMR-SASS (m/s)	7.1	4.5	4.7	5.2

Figure 1 shows the SMMR/SASS wind comparisons for the three radiometer systems and the four cells. In generating these plots, the observations are stratified into 1 m/s SASS wind speed bins. For each bin the mean SASS wind, the mean SMMR wind, and the standard deviation of SMMR winds are computed. The error bars in the plots are centered on these mean wind values. The length of the error bars equals the \pm one standard deviation of SMMR winds. An error bar for moderate winds represents thousands of observations. For the extreme low and high winds, the number of observations for an error bar drops to between 5 and 100. For the 6.6H/18V/21V system, the agreement for low to moderate winds is quite good. However for winds above 15 m/s, the SASS winds are lower than the SMMR winds for the off-nadir cells and are higher than the SMMR winds for the nadir cell. There is no additional information to determine which is more correct, SMMR or SASS. However, in passing we note that the discrepancy at high winds cannot be corrected by simply adjusting the SMMR model function because the model and the physics are the same for cells 1 through 4. On the other hand, the SASS model function could be adjusted to remove the high wind discrepancy. At nadir, the sensitivity of σ^0 to high wind speeds could be increased, and off nadir the sensitivity could be decreased. Such an adjustment would be a departure from the constant power law model that is commonly used.

The 10.7H/18V/21V system shows the same trends as the 6.6H/18V/21V system except that the error bars are a little larger. However, going to the 18H/18V/21V system we see very large error bars. The apparent problem with the high frequency system is the difficulty in separating atmospheric effects from wind effects. The 18H wind channel is quite sensitive to atmospheric liquid water and water vapor.

ORIGINAL PAGE IS
OF POOR QUALITY

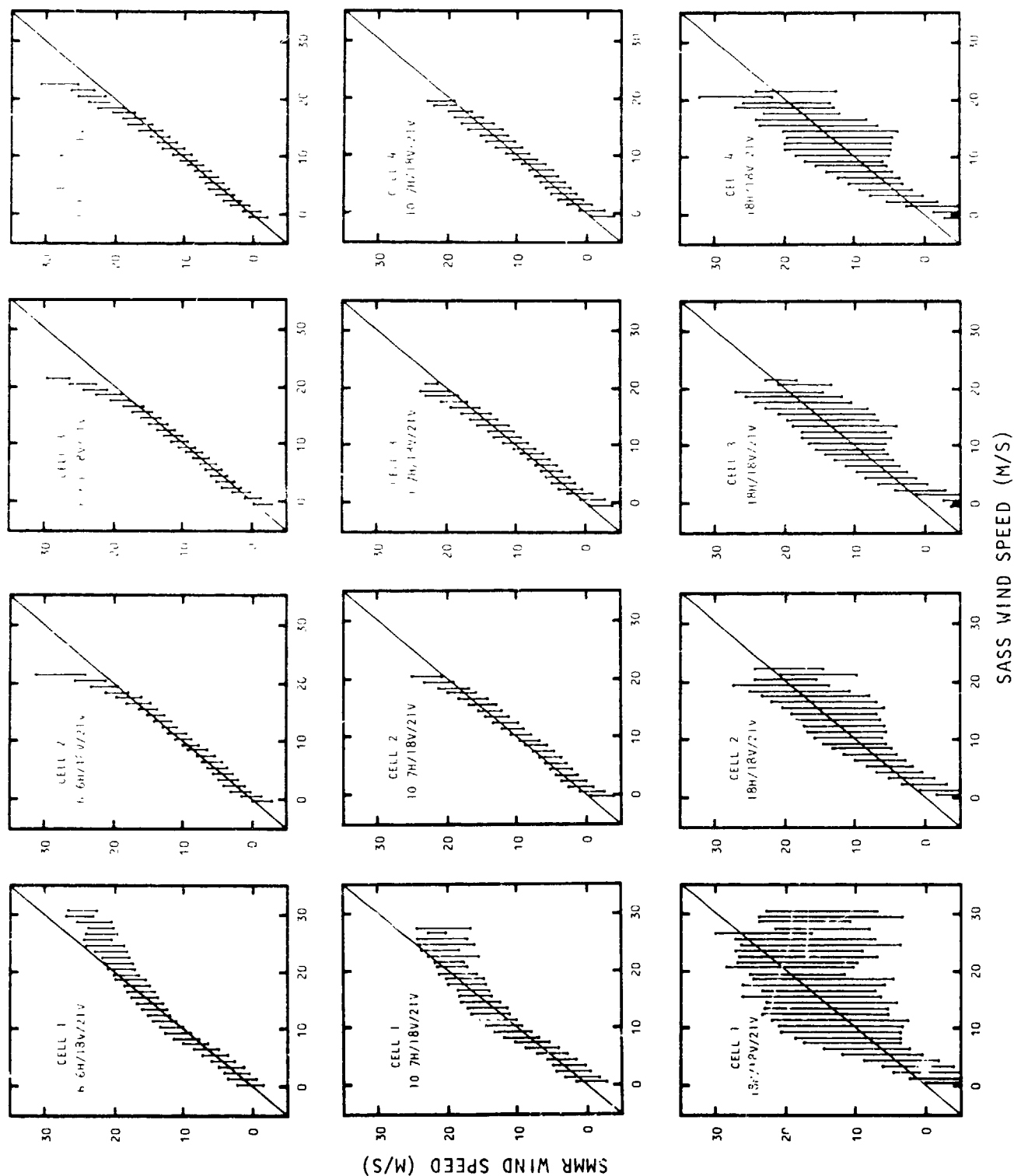


Fig. 1. A comparison of SMR and SASS winds for three radiometer systems. Each row of plots corresponds to a particular radiometer system. The four plots in a row correspond to the cell swath position. Cell 1 is along the satellite subtrack and Cell 4 is at the outer portion of the swath.

5. SUMMARY AND CONCLUSIONS

Improved second generation algorithms are used to compute wind speeds for the SMMR and SASS over the three month life of SEASAT. When 6.6H is used for the SMMR wind channel, the winds coming from the two sensors agree to within 1.3 m/s over the SASS primary swath. At nadir where the radar cross section is less sensitive to wind, the agreement degrades to 1.9 m/s. The agreement is very good for low and moderate winds (0 to 15 m/s), and it thus appears that the SMMR can accurately measure winds even when there is no whitecapping. For winds above 15 m/s, the off-nadir SASS winds are consistently lower than the SMMR winds, while at nadir the high SASS winds are greater than the SMMR winds.

The SMMR/SASS wind agreement degrades a little when 10.7H is used as the wind speed channel, rather than 6.6H. When the frequency of the wind channel is increased to 18 GHz, the agreement is much worse, being 5 m/s over the SASS primary swath. This poor agreement is due to the difficulty in separating wind effects from atmospheric effects at 18 GHz. This separability problem is due to the fact that wind speed and atmospheric liquid water have nearly the same polarization signature at 18 GHz. Recent results show that if 37 GHz is used, rather than 18 GHz, the wind sensing performance is substantially improved. For example, the winds coming from a 37H/37V/21V configuration show about a 2.5 m/s agreement when compared to the SASS winds. The microwave radiometer SSM/I to be launched in 1985 aboard the DMSP Block 5D-2 satellite will operate at 19, 22, 37, and 85 GHz. Our results indicate that a 37H/37V/21V SSM/I wind algorithm will perform much better than a 19H/19V/21V algorithm.

We emphasize that the good agreement obtained in the 6.6H SMMR versus SASS comparisons does not necessarily mean that the actual wind speed can be measured to a 1.3 m/s accuracy. Rather, the results indicate that there exists a high correlation between the sea-surface roughness characteristics that affect microwave brightness temperatures and radar cross sections. Unfortunately, these inter-sensor comparisons do not really address the complex boundary layer problem involving the correlation of near-surface winds and sea-surface roughness.

Based on the results of this study, a number of recommendations are made:

(1) We recommend that users of the SEASAT SMMR and SASS geophysical products obtain the new second generation data sets, which are a substantial improvement over the first generation products released in 1981.

(2) The new SEASAT winds should be compared with all available in situ anemometer measurements so that the correlation between wind speed and surface roughness can be better quantified. Previous comparisons of SEASAT winds with in situ were clouded by the fact that the wind algorithms, which had many degrees of freedom, were initially tuned to the in situ.

(3) Potential users need to understand the capabilities and limitations of SSM/I. More study is required to determine the wind sensing performance of this important new sensor.

(4) Two-scale scattering theory should be compared to the SMMR and SASS model functions. In derivation of the models, wind speed sensitivities as functions of frequency, polarization, and incidence angle are obtained from the statistics of the SMMR and SASS observations, rather than theory. The question to be answered is whether or not the two-scale theory is consistent with the model functions.

6. ACKNOWLEDGMENTS

This research was supported by NASA's Oceanic Processes Program under Contract NASW-3606. Additional support for investigating the SSM/I performance was provided by NORDA's Remote Sensing Branch under Contract N00014-83-C-0520. We are also grateful to the Canadian Atmospheric Environment Service for generously providing computer support. We thank L. McGoldrick of NASA Headquarters and J. Hawkins of NORDA for making this investigation possible.

7. REFERENCES

- Bernstein, R.L. (ed), 1982: Seasat Spec. Issue I, J. Geophys. Res., 87, 3173-3438.
- Bernstein, R.L. and J.H. Morris, 1983: Tropical and mid-latitude North Pacific sea surface temperature variability from the SEASAT SMMR. J. Geophys. Res., 88, 1877-1891.
- Jones, W.L., L.C. Schroeder, D.H. Boggs, E.M. Bracalente, R.A. Brown, G.J. Dome, W.J. Pierson, and F.J. Wentz, 1982: The SEASAT-A satellite scatterometer: the geophysical evaluation of remotely sensed wind vectors over the ocean. J. Geophys. Res., 87, 3297-3317.
- Kinsman, B., 1965: Wind Waves, 543-583, Prentice-Hall, New Jersey.
- Lipes, R.G. and G.H. Born (ed), 1981: SMMR Mini-Workshop IV, JPL Tech. Rept. 622-234, Jet Propulsion Laboratory, Pasadena, California.
- Munn, R.E. (ed), 1978: Boundary-Layer Meteorology, 13, 1-429.
- Reynolds, R.W., 1982: A monthly averaged climatology of sea surface temperature. NOAA Tech. Rep. NWS 31, National Weather Service, Silver Spring, Maryland.
- Schroeder, L.C., D.H. Boggs, G. Dome, I.M. Halberstam, W.L. Jones, W.J. Pierson, and F.J. Wentz, 1982: The relationship between wind vector and normalized radar cross section used to derive SEASAT-A satellite scatterometer winds. J. Geophys. Res., 87, 3318-3336.
- Swift, C.T. (ed), 1977: IEEE J. of Oceanic Engineering, OE-2, 1-159.
- Weissman, D.E. (ed), 1980: IEEE J. of Oceanic Engineering, OE-5, 71-182.
- Wentz, F.J., V.J. Cardone, and L.S. Fedor, 1982: Intercomparison of wind speeds inferred by the SASS, Altimeter, and SMMR. J. Geophys. Res., 87, 3378-3384.
- Wentz, F.J., 1983a: A model function for ocean microwave brightness temperatures. J. Geophys. Res., 88, 1892-1908.
- Wentz, F.J., 1983b: Comparison of sea surface temperature retrievals using 6.6 and 10.7 GHz, RSS Tech. Rept., Remote Sensing Systems, Sausalito, California.
- Wentz, F.J., 1984: Modifications to brightness temperature model function, RSS Tech. Rept., Remote Sensing Systems, Sausalito, California.
- Wentz, F.J., S. Peteherych, and L.A. Thomas, 1984: A model function for ocean radar cross sections at 14.6 GHz. To be published in J. Geophys. Res.

OCEAN WIND FIELD MEASUREMENT PERFORMANCE
OF THE ERS-1 SCATTEROMETER

P. Hans and H. Schuessler
SPACE PROGRAMME DEPARTMENT
Dornier System GmbH
P.O. Box 1360, 7990 Friedrichshafen, West Germany

ABSTRACT

In 1988, Europe will launch the next generation of its Earth Resources Satellites, the ESA Remote Sensing Satellite (ERS-1). The Active Microwave Instrumentation (AMI), which will be implemented on the ERS-1, is a 5.3 GHz multi-purpose radar for land surface imaging, ocean wave spectrum measurement and wind observations over oceans.

The imaging and wave measurements apply Synthetic Aperture Radar (SAR) techniques, while wind field detection is performed by the Scatterometer as part of the AMI.

At DORNIER SYSTEM, the Scatterometer system design has been developed and optimized with the aid of a Performance Simulator.

This paper is aimed at giving an overview about the

- ERS-1 Scatterometer system design
- Error budget
- Overall calibration concept.

1. INTRODUCTION

During the last decade, microwave Scatterometers have been shown to be sensitive to ocean surface wind speed and direction in various aircraft programs, the SKYLAB S-193 experiment and SEASAT.

At microwave frequencies, the ocean surface roughness, which is a function of actual wind condition, appears like a reflection grating. Thus, there is a functional dependence of the normalized radar cross section (σ^0) and the wind speed.

Moreover, the radar cross section is anisotropic with respect to the angle between wind vector and incident radar beam. With the aid of several σ^0 -measurements of the same area from different measurement directions, the actual wind vector in terms of speed and direction can be determined, using a specific mathematical model, which defines the relation between the radar cross section and wind speed, wind direction as well as incidence angle and antenna polarization.

Hence, spaceborne ocean wind field detection requires a microwave Scatterometer with multiple beams. The number of antenna configurations, which can be imagined, is nearly unlimited, 2, 3, 4 etc. beams with any combination of beam

ORIGINAL PAGE IS
OF POOR QUALITY

squint angle. However, when transmit power and mechanical limitations of a satellite platform are considered, the options reduce.

Furthermore, σ^0 -measurements of an ocean patch, from which the wind vector shall be derived are perturbed due to system noise, instrument calibration errors, atmospheric attenuation etc. The problem of ambiguous solutions for the wind speed arises, which sets the minimum bound for required σ^0 -samples and hence the beam number.

In order to identify the optimum beam configuration with regard to wind vector measurement accuracy, extensive analysis was performed by DORNIER SYSTEM GmbH in close cooperation with the European Space Agency (ESA) and the Max Planck Institute at Hamburg (Germany) which has led to a 3 beam configuration.

2. ERS-1 SCATTEROMETER SYSTEM DEFINITION

2.1 System Geometry and Measurement Sequence

The Scatterometer as part of the Active Microwave Instrumentation (Wind Mode operation) illuminates the sea surface sequentially for reflectivity measurements by RF pulses at a carrier frequency of 5.3 GHz from different direction by 3 antennas. The nominal look angles of the antennas are 45 fore and aft of broadside as well as broadside to the satellite velocity vector. The overall system geometry is shown in Fig. 2-1.

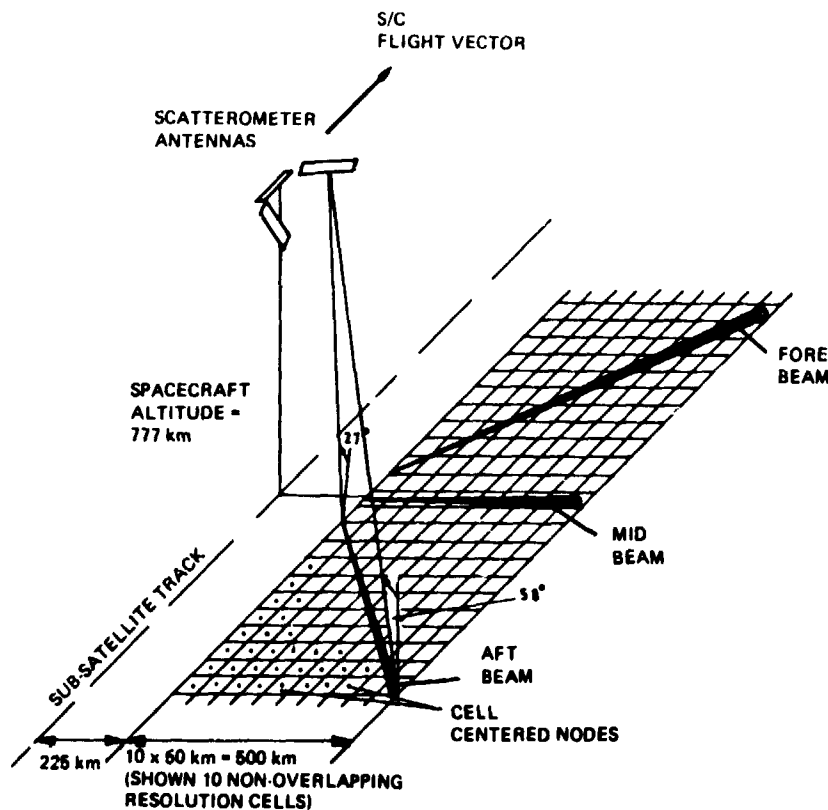


Fig. 2-1: Scatterometer Overall System Geometry

ORIGINAL PAGE 19
OF POOR QUALITY

Reflectivity data will be provided for a 500 km wide continuous swath along the satellite ground track to deduce wind speed and direction at nodes with 25 km separation along and across the Sub-Satellite track within the swath.

Each node is centered within a resolution cell of $50 \times 50 \text{ km}^2$, which is determined in range direction by appropriate range gating of the received echo signal and in azimuth by averaging of corresponding range gated echo signals of 256 RF pulses.

In order to achieve a correct illumination of nodes by all three beams, the total satellite will be steered in yaw-axis (compensation of earth rotation effects) such, that the spectrum of the received echo of a RF pulse transmitted by the mid beam antenna will not be shifted in frequency (Doppler).

The yaw angle variation throughout the orbit related to the spacecraft velocity vector is sinusoidal with max. deflections at the equator $\pm 3.91^\circ$ for a spacecraft altitude of 780 km.

2.2 Electrical Characteristics

The general processing flow of the AMI in Wind Mode operation (Scatterometer) is shown in Fig. 2-2.

A rectangular pulse at a carrier frequency of 123.4 MHz is generated, up-converted to 5.3 GHz and finally amplified to 4.8 kW peak transmit power before radiation via one of the three Scatterometer antennas. The pulselength will be different for the FWD/AFT-Beam and the Mid-Beam antenna and is determined by ground resolution requirements (50 km in range) and signal-to-noise ratio (SNR) optimization.

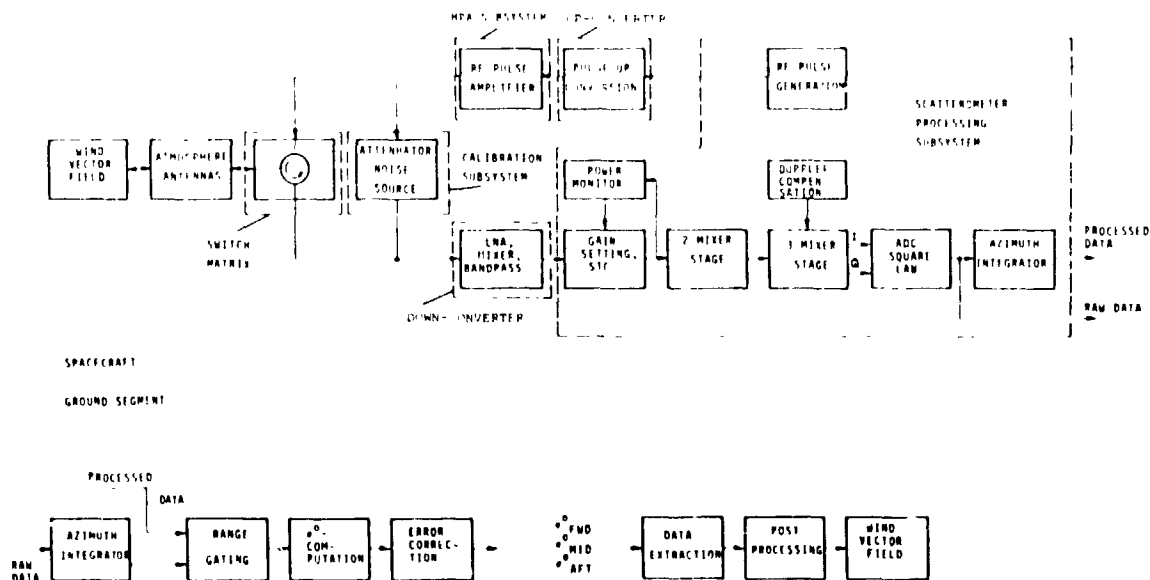


Fig. 2-3: Scatterometer Processing Flow

The received signal is amplified (LNA), down-converted and bandpass filtered. Within the next processing steps further down conversion to baseband including Doppler compensation for SNR maximization, low-pass filtering, A/D-conversion and square-law detection is performed.

The samples of one echo signal are either transferred directly to ground (raw data transmission mode) or stored temporarily in a memory. Here they are summed up with corresponding samples to successive echos for averaging (data reduction) before transmission to ground.

As an internal calibration routine, the first RF pulse of the operational sequence of one antenna (32 shots) is routed back via the calibration unit (where it is delayed and attenuated) to the receiver to identify gain/loss variation within the transmitter/receiver processing chain.

Within the ground segment, gated integration of the averaged echo signal of 256 RF pulses is performed according to ground resolution requirements to extract the average signal power for a specific resolution cell (node).

Finally, the radar cross section (σ^0) is derived from the received signal power value with the aid of appropriate conversion factors, which are determined by the nominal system transfer function as well as auxiliary data for error correction, provided by external and internal calibration routines.

Performing this for all beams, gives three σ^0 -values, which are passed to a data extraction algorithm for wind vector computation.

A summary of the main electrical system parameters of the ERS-1 Scatterometer is listed in Table 2-1.

2.3 Scatterometer Performance Evaluation

Two different error types contribute to the potential error in the measurement of the radar cross section σ^0 :

- bias errors (even and odd with regard to 3 scatterometer antennas)
- random errors.

Both types limit the absolute radiometric resolution of the Scatterometer.

The ESA geophysical requirements for the Scatterometer in terms of wind field measurement accuracy are listed below:

- wind speed measurement range:
 $4 \text{ m/sec} < v < 24 \text{ m/sec}^*$
- wind speed tolerance:
 $\pm 2 \text{ m/sec}$ or $\pm 10 \%$ whichever is larger

- wind direction measurement range:
 $0^\circ < \phi < 360^\circ$ *
- wind direction tolerance:
 $\pm 20^\circ$

*A priori probability of rank-1 solution of the data extraction algorithm (maximum likelihood estimator) being within the tolerance is 63 % (wind speed) and 55 %/75 % (wind direction) excl./including 180° ambiguity.

In order to fulfill the above geophysical requirements, the max. allowable errors in σ° -measurements amount to:

- even bias errors = ± 0.35 dB
- odd bias errors = ± 0.5 dB
- random errors = < 8.5 %
(standard deviation)

The above data were established by ESTEC with the aid of detailed Monte Carlo Simulation taking into account an empirical C-band σ° -reference model. This C-band model, which forms the basis for the ERS-1 Scatterometer system design, has been developed by A.E. Long (1981), based on σ° data obtained with an airborne multifrequency coherent pulse radar by the Naval Research Laboratories and further analysis by Moore (1970) and Jones and Schroeder (1978).

In this formulation σ° is given by

$$\sigma^\circ = a \cdot v^c (1 + b_1 \cos \phi + b_2 \cos 2\phi)$$

where

v = windspeed
 ϕ = wind direction
 a, c, b_1, b_2 = given in an empirical form as a function of incidence angle

The random error in the σ° -measurement (Gaussian distribution is assumed) is determined by the normalized standard deviation (k_p) of the received signal power, which is proportional to σ° .

It is calculated according to the formula

$$k_p^2 = \frac{1}{B \cdot T_{SN}} \left[\left(1 + \frac{1}{SNR}\right)^2 + \left(\frac{1}{SNR}\right)^2 \cdot \frac{T_{SN}}{T_N} \right]$$

and hence is a function of signal-to-noise ratio (SNR), system bandwidth (B) and the integration time of the signal + noise measurement (T_{SN}) and the noise only measurement (T_N).

The actual baseline of the system design concept leads to a normalized standard deviation of the received signal of < 9 % for worst case conditions (min. windspeed, crosswind).

Transmitter/Receiver:

- o Transmit signal frequency: 5.3 GHz
- o Transmit pulse length: 130 μ sec (F,A)*
70 μ sec (M)*
- o Pulse repetition interval: 4.878 msec (F,A)*
4.347 msec (M)*
- o Peak transmit power: 4 kW
- o RF average transmit power: 54 W
- o Receive signal bandwidth (3 dB)
 - before Doppler compensation: 350 kHz
 - after Doppler compensation: 9.2 kHz (F,A)*
17.3 kHz (M)*
- o ADC-resolution: 8 bit (I,Q)
- o Min. SNR: 0 dB

Antenna:

- o Beamwidth (3 dB)
 - Azimuth 0.8°(F,A)*, 1.3°(M)*
 - Elevation 26°(F,A)*, 24°(M)*
(shaped elevation gain pattern, figures represent swath coverage)

o Gain

$$(F,A)^* : > 31 \text{ dB} - \frac{9 \text{ dB}}{26^\circ} \theta, 0^\circ < \theta < 26^\circ$$

$$(M)^* : > 29 \text{ dB} - \frac{6 \text{ dB}}{24^\circ} \theta, 0^\circ < \theta < 24^\circ$$

θ = antenna elevation angle

*(F,A) = fore and aft beam antenna
(M) = mid beam antenna

Table 2-1: Summary of Electrical Characteristics

Odd bias errors (relative beams) impact directly the measurement accuracy in terms of wind direction, while even bias errors degrade the windspeed measurement accuracy. The main error sources which contribute to the above error types, are listed below:

- Antenna elevation pattern
 - prelaunch gain measurement error
 - distortion during launch
 - in-flight thermal distortion
- Antenna pointing error
- Propagation path (atmospheric attenuation etc.)
- Transmitter/receiver gain fluctuations
- Stability of internal calibration subsystem.

Each of the above error sources which contribute to bias errors may be subdivided into static and harmonic portions. The latter are slowly varying errors of the order of an orbit in period (caused through thermal effects etc.).

Generally static errors may be corrected by appropriate instrument internal and external calibration which will roughly be discussed in the following chapter.

Harmonic errors appear twice within the system error budget, i.e. during external calibration and during nominal Scatterometer operation.

At the time this paper was established, the system error budget was under development and hence not yet ready for publication. It is believed that the requirement of an odd bias error of < 0.5 dB may be achieved, while an max. allowable even bias error of < 0.35 dB will cause problems. The minimization of the even bias error is subject of actual Scatterometer system design work. First results and a preliminary system error budget will be presented during the symposium.

2.4 Scatterometer Calibration

The Scatterometer requires a calibration strategy which provides absolute radiometric accuracy across the entire swath.

With regard to the radar equation* which is solved for σ^0 (radar back-scattering coefficient) below, it becomes obvious, that absolute radiometric accuracy can only be achieved by a combination of external and internal (on-board) calibration methods.

$$\sigma^0 = (P_1 - P_2) \cdot \frac{(4\pi)^3 \cdot R^4}{\lambda^2} \cdot \frac{L_1}{v \cdot P_t} \cdot \frac{L_2}{G^2 \cdot A_{eff}}$$

(1)
(2)
(3)
(4)

* σ^0 calculation is an over simplification for clarity. In reality the illumination function must be taken into account

where

P_1 = Signal + Noise Measurement
 P_2 = Noise measurement only
 R = Slant range
 λ = RF wave length
 v = Receiver gain
 P_t = Peak transmit power
 L_1 = On-board loss (waveguide and circulator)
 L_2 = Atmospheric attenuation
 G = Antenna gain (one-way)
 A_{eff} = Effective illumination field

- (1) Signal + noise-measurement (P_1) and noise-only-measurement (P_2) are performed for noise subtraction
- (2) System parameters to be calculated
- (3) To be measured by internal calibration
- (4) To be measured by external calibration

2.4.1 Internal Calibration

The so called "ratio method" is applied. The RF transmit pulse at the output of the HPA is delayed, attenuated and routed back to the receiver via the calibration subsystem (programmable attenuator etc.). This method will allow the compensation of non-linear effects of the transmitter/receiver transfer function.

2.4.2 External Calibration

The baseline involves two sets of measurements. The first is the relative cross swath calibration over the Brazilian Rain Forest and the second is absolute calibration at three points within an extended swath against ground transponders.

The relative cross-swath calibration is performed by taking two sets of measurements, one taken with the satellite stepped in the roll direction with respects to the other. Comparison of both measurements leads to the relative across swath system gain curve, which can be related to the absolute measurements against transponders.

3. CONCLUSIONS

The design phase of the ERS-1 Scatterometer is nearly finished. The overall system error budget taking into account hardware component stabilities is still under development. It is believed that the wind direction measurement accuracy may be achieved. The performance requirements for windspeed may cause problems due to an required absolute radiometric accuracy of 0.35 dB.

Actually a comprehensive System Simulator, which models the overall baseline ERS-1 Scatterometer system is under development at Dornier System. It will enable the Scatterometer equipment components to be specified in terms of required performance and the effects of any degradation investigated. This will allow the realistic prediction of the Scatterometer measurement performance.

N84 27274

THEORY AND MEASURE OF CERTAIN IMAGE NORMS IN SAR

R. Keith Kane
RADARSAT
Canada Centre for Remote Sensing
Ottawa, Canada

ABSTRACT

This paper summarizes principal properties of SAR imagery of point and distributed objects. Against this background, the response of a SAR (Synthetic Aperture Radar) to the moving surface of the sea is considered. Certain conclusions are drawn as to the mechanism of interaction between microwaves and the sea surface.

It has been established for a "well-behaved" SAR (as for other radars) that a principle of conservation of energy is satisfied. This means that the energy of the response (in the image) is constant under conditions of changing phase of the signal. Phase errors may arise systematically, such as focus mis-match to parameters appropriate to a specular scattering centre, or randomly, as from complex motion of the sea surface. Of course, focus errors reduce the peak and spread the impulse response of the image of a point target. Focus errors do not, however, change the speckle spectrum of a truly random "uniform" Gaussian scene.

Focus and speckle spectral tests may be used on selected SAR imagery for areas of the ocean. When this is done, it is observed that the fine structure of the sea imagery is sensitive to processor focus and adjustment. Furthermore, there is frequently correlation between nominally statistically independent looks. Therefore, the ocean reflectivity mechanism must include point-like scatterers of sufficient radar cross-section to dominate the return from certain individual resolution elements. Furthermore, both specular and diffuse scattering mechanisms are observed together, to varying degree. The effect is sea state dependent, of course. This mechanism would explain the evident diversity of theoretical opinion on the subject of SAR wave response.

Several experiments are proposed based on imaging theory that could assist in the investigation of reflectivity mechanisms.

1. INTRODUCTION

It is a reasonable requirement of SAR (Synthetic Aperture Radar) ocean reflectivity theories that they be consistent in every regard with the facts of life of SAR image formation. To the knowledge of this author, there are no theories of ocean reflectivity that pass this test.

A SAR, even operating in a partially coherent mode, is a special kind of linear system. Several fundamental properties for such systems have been rigorously proven (Harger, 1970, Raney, 1983). The observation by the SAR of particular scenes, such as an ocean surface, cannot change these facts.

The purpose of this paper is two-fold. First, pertinent properties of SAR operation are presented and succinctly discussed. Whereas many of these properties have been known for some years, they seem not to have been fully apprehended by workers in the ocean reflectivity field. Second, there follow from the first discussion consequences of importance to the oceanographic application. Several of these are highlighted and discussed. Furthermore, it is possible to design certain data processing and field experiments that may be used to take advantage of these properties, and so to shed some light on the reflectivity mechanisms involved. Suggestions are made for such tests.

The major thrust of Raney (1983) is that for SAR (as for all radar systems) there exist fundamental properties such as conservation of energy. These properties, if suitably employed, can be helpful in deriving quantitative information about the reflectivity mechanism from the imagery. The matter is complicated by (1) the partial coherence of most radar systems, (2) non-linearities and temporal variations found in all practical radar systems, and (3) the presence of both specular and diffuse scatterers in the input scene. This work deals directly with (1), disregards (2), and makes some observations based on (3) that have direct impact on SAR reflectivity models of the ocean surface.

Following the introduction, Section 2 of the paper considers suitable model representation of a SAR. Basic properties are identified in signal processing considerations.

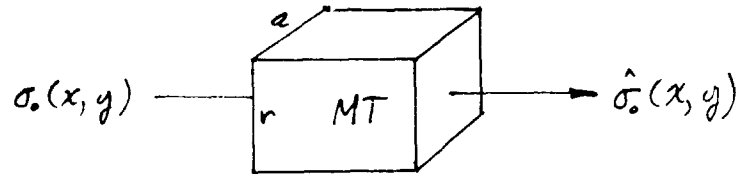
Section 3 considers the "impulse response" of a SAR, the way in which the system images an idealized point object. Section 4 reviews the way in which a SAR images an idealized uniform random distributed scene such as the classic wheat field. In each of these discussions, radar system parameters (such as nominal resolution and bandwidth) and processing system parameters (such as focus and multi-looking) are considered.

In Section 5 basic properties of speckle are reviewed. As is well known, radar speckle is an unwelcome but ever present characteristic of quasi-coherent imagery, and it, too, obeys certain well established principles.

In Section 6, the properties previously presented are revisited, with the objective of seeing them from the point of view of applications to the oceanic imaging problem, leading to a discussion of recommended experiments. The paper has a brief concluding section.

2. SAR MODEL

The basic objective of an imaging radar system is deceptively simple: we wish to derive an "image" which is a mapping of the reflectivity of a scene observed by microwave probing of the real world, expressed in photographic form. In model language, real world reflectivity $\sigma_o(x,y)$ is estimated as $\hat{\sigma}_o(x,y)$ through a microwave transducer (MT) thus



... and at the outset, complexities are apparent. Let us confine the discussion to synthetic aperture radar (SAR) systems. Then the following are true:

i) SAR systems "work" because of the different mechanisms used to form the azimuth (a) and the range (r) dimensions of the image (Harger, 1970). Range scanning is at one half the speed of light (thus in effect instantaneous) and continuous. Azimuth scanning is at the speed of the carrier vehicle (thus at velocities sensitive to possible changes in the scene itself) and is dependent on the pulsed nature of the radar. For the moment, we ignore these fundamental range and azimuth differences, and treat the two "channels" of a SAR in like manner, a satisfactory approximation for the first sections of this paper. The differences in time scale between these channels lie at the core of the SAR ocean imaging problem, however.

ii) The transducer "MT" is not perfect. That is, it is not able to image all of the detail inherent in the scene. This characteristic is typical of any imaging system: resolution (in range or azimuth) is a measure of this limitation. There is rather little subtlety in this consideration, except that...

iii) The microwave probe (transmitted signal of the SAR) is essentially monochromatic and coherent. There are many important implications that follow from this simple fact. It means that we do not measure the reflected energy density directly (as one might visualize, for example, using the polychromatic and non-coherent sun as an illumination source, deriving thus an analog of "reflectivity"). The monochromatic radar illumination makes the radar behave as an interferometer, whose input is a linear sum of complex amplitude signals, each of the form

$$|\sigma_o(x,y)|^2 e^{j\phi(x,y)} e^{j(2\pi ft + \theta)}$$

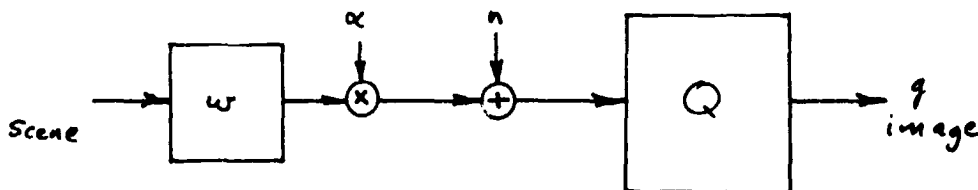
Thus the input includes the (square root of) reflectivity, but also the phase $\phi(x,y)$ of each reflecting element, which of course is directly affected by the (accidental) distance and aspect angle between that reflector and the radar. The phase is a mixed blessing, for it allows "synthetic aperture" resolution (Brown and Porcello, 1969) (beam sharpening) to occur; it also gives rise to "speckle" (described below).

iv) Whereas the probe of the scene is at complex (microwave) amplitude, the image is in terms of amplitude magnitude squared. Thus, in numerical terms, the image $\hat{\sigma}_0(x,y)$ is a real non-negative variable in contrast to the radar's observation in the scene, which is in terms of complex amplitude. (This seeming non-linear transformation is the key to the radar principles of "conservation of energy".)

v) A SAR works because the radar's motion imposes a structure on the phases of the received signals that can be used to "focus" the resulting imagery to a specific resolution (Brown and Porcello, 1969; Harger, 1970; Raney, 1983). Once this is accomplished, then the phase information becomes irrelevant, and now the disadvantages of the remaining phase structure (speckle) become important. Speckle can be reduced (at the expense of resolution - see below) in either of the two dimensions, range or azimuth, by one of two linear techniques, frequency domain filtering (subapertures) (Bennett and McConnell, 1980; Porcello, 1976) or by adjacent cell averaging (Zelenka, 1976). These two techniques, frequency domain and image domain, are mathematically equivalent for stationary inputs and SAR type systems (Raney, 1983), an important consideration for users who may have to deal with pre-formed imagery. (Non-linear speckle reduction techniques may also be employed, but are not of interest in this paper.)

vi) Finally, all of the above deals with systems that present imagery in $\hat{\sigma}_0(x,y)$ form, i.e., amplitude squared. There are systems, such as the MDA G-SAR processor, that (a) do a square-root or other amplitude mapping, and (b) perform a "most significant bit" or other automatic gain control function, both with the intent to improve image cosmetics or data volume compression. It is important to note that the considerations of this paper apply to the "unscaled amplitude square" image data format. For those wishing to pursue experiments in this area, either access to such data is essential, or suitable transformations are required.

Given all of the above, there exists a "model" of a SAR system that incorporates these characteristics, in terms of a generalized quadratic filter theory (Raney, 1983). In this language, a SAR is described (for either the range or the azimuth channel) as a simple sequence of operations



... in which the input is in complex amplitude, the range coding or azimuth Doppler modulation is represented by the pre-filter w , multiplicative random phase perturbation, additive (complex receiver) noise n enters, the data is focussed, amplitude squared, and speckle smoothed (Q) to arrive at the image g .

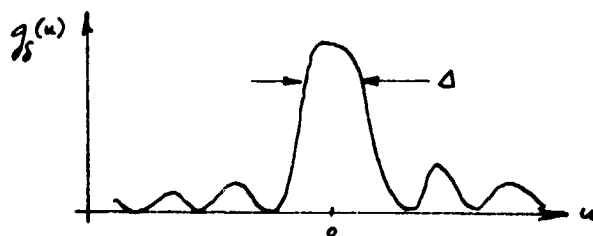
For the following, we assume that the system is "linear", but not "perfect". There may occur focus errors, or variations in the coherence of the processor (i.e. intentional speckle smoothing) or in the scene (unintentional, resulting from sea surface motion). We will be interested in measures of g (the image) as they relate to properties of the scene and the processor.

The system is linear in a special sense. A SAR, like other types of radars, includes filters linear in complex amplitude (pre-detection or coherent integration), square law detection, and image smoothing (post-detection or non-coherent integration, i.e., "multi-looking" in popular SAR terminology). For such partially coherent systems, the input/output relationship may be expressed in terms of a modulation transfer function (O'Neill, 1963) which is linear in intensity (spatial reflectivity density). This is valid, no matter the degree of partial coherence of the (radar) system or the scene (Raney, 1983).

3. IMPULSE RESPONSE

The response of a SAR to a small specular point scatterer such as a corner reflector gives rise to an image pattern that is of fundamental importance in system characterization, analogous to the "point-spread function" of non-coherent optics (O'Neill, 1963). The impulse response is the classic test signal for radars.

Let the impulse response be represented by $g_s(u)$, a non-negative function with units of voltage squared. A well behaved impulse response will be sharply peaked



.... has a width Δ at the half-power level, and has "reasonable" side lobes. The width Δ is (loosely) referred to as the resolution of the radar, in either the range or azimuth dimension.

The following properties may be proven for the impulse response:

i) The energy $\int g_s(u)du$ in the response is constant in the face of focus variations in the SAR (processor), random phase perturbations in the reflector, and for differing degrees of non-coherent integration (multi-looking). There is no coherent gain on the mean reflectivity of a point (coherent) target. This is the conservation of energy principle for point targets.

ii) The fully coherent correctly focussed impulse response has width Δ_1 , which is the minimum width obtainable from the system. The inverse width $(\Delta_1)^{-1}$ is a measure of the effective system bandwidth in the pertinent channel, suitably scaled from spatial coordinates to Hertz. Focus errors, or partial coherence in the point target, result in broadening of the impulse responses and reduction of its peak.

iii) For a given system differing amounts of non-coherent integration may be employed in the processor. Increased non-coherent integration degrades resolution. For N statistically independent looks, the corresponding impulse response width $\Delta_N = N\Delta_1$.

iv) It follows that for an N -look response, the peak is reduced N -fold. This occurs because specular scatterers maintain their coherence as the radar observes them, so that the coherent gain due to processor focus is reduced as less of the signal is used coherently. Note that the famous coherent gain of a SAR is applicable to the peak value of reflectivity of a single coherent scattering centre (in one resolution cell), and is dependent on scene and system coherence.

v) As an obvious but important generalization, it follows that for a specular scatterer, there is very high correlation of the response between any two looks of a multi-look set.

vi) In the event that there are deterministic phase perturbations on a point scatterer, azimuth shift (proportional to the linear phase term) and azimuth defocus (proportional to the quadratic phase error) plague the affected impulse response (Raney, 1971). The radar processor may be retuned to match these perturbations, but at the expense of becoming mis-matched to all other signals in the processed field. (It follows that if there are a variety of different shift and focus perturbations affecting various scatterers in the scene, they cannot all be optimally processed simultaneously.)

4. RESPONSE TO DISTRIBUTED SCENES

For many remote sensing applications, the response of a SAR to distributed scenes is of more interest than the point target response. One can show (Raney, 1983) that the input/output relationship is $\hat{\sigma}_0(x,y) = g_s(x,y) ** \sigma_0(x,y)$ where $**$ denotes convolution on the x and y coordinates respectively and $g_s(x,y)$ is the appropriate impulse response of the SAR. The following properties are satisfied:

i) The average value of the output, for nominally constant input, is a constant, independent of system focus, system coherence, or scene coherence, assuming that all available data is used in each case. This is the most fundamental feature of the system, the principle of conservation of energy. It means that there is no coherent gain by the radar or processor for the mean reflectivity of diffuse distributed scenes. Furthermore, between multi-look sets, relative gain can be normalized since total average response is not a function of the number of looks.

ii) From i) it follows that a SAR's response to a (Gaussian) distributed scene relative to receiver noise is not a function of processing. Thus, for a given radar and scene, the SNR is constant as processor focus and coherence are varied, assuming that all the available data is used.

iii) The two-dimensional Fourier transform of $g_s(x,y)$, written as $\tilde{g}_s(\omega,\lambda)$, is the modulation transfer function (MTF) of the system. If the system focus is incorrect, partial coherence is used in the processor, or if there is loss of temporal coherence in the scene, then the width of the MTF is reduced, thereby limiting the ability of the system to image scene detail (Raney, 1983, 1980). This is of central importance in the response of a SAR to distributed dynamic phenomena, such as ocean reflectivity. It has the heavy consequence that the appropriate impulse response for the SAR may not be the same for all parts of the image simultaneously.

5. SPECKLE CONSIDERATIONS

The output of the system is deeply modulated even for nominally constant input $\sigma_0(x,y)$. This phenomenon is known as speckle (Zelenka, 1976; Porcello, 1976; Bennett and McConnell, 1980), and is a natural consequence of coherent illumination by the radar of a Gaussian scene. (By definition, a Gaussian scene is one in which, for each (nominal) resolution cell, there are many effective scatterers of statistically independent amplitude and phase.)

i) To first and second order, speckle statistics (for a uniform Gaussian distributed scene) are not a function of system focus.

ii) Speckle statistics are not a function of scene temporal coherence. Thus, for Gaussian scattering, one cannot use speckle measures to estimate scene coherence.

iii) For a Gaussian random input, the several "looks" separated by a multi-look processor are largely uncorrelated. The correlation properties observed are a measure of the bandwidth and frequency weighting of the SAR/processor combination.

iv) One effective measure of speckle is its variance. The amount of non-coherent integration in the processor, that is, the effective number of statistically independent looks N , may be estimated by the ratio

$$N = \frac{|\text{mean value } \hat{\sigma}_0|^2}{\text{variance } \hat{\sigma}_0} = (VMS)^{-1}$$

for a nominally uniform region of a given scene.

v) As a consequence of the preceeding four properties, speckle can be used to estimate the potential resolution of a SAR/processor. The nominal impulse response of the radar is closely approximated by the square root of the speckle covariance function for correct focus and scene coherence. However, speckle cannot be used to estimate actual SAR performance against particular (possibly dynamic) objects unless focus and scene coherence can be (independently) ascertained as correct for the dynamics of those objects.

vi) There is evidently a direct trade-off between resolution (Δ_N proportional to N) and speckle reduction (variance inversely proportional to N). This can be stated as the principle of conservation of confusion

$$\int [R_g(x) - g^2] dx = \text{constant}$$

independent of the degree of partial coherence, where $R_g(x)$ is the spatial correlation function, under the assumption of uniform Gaussian input.

vii) In the event that the scene is not Gaussian at the nominal resolution cell level, then these properties do not necessarily hold. In particular, if there are dominant scattering centres, then image behavior will be described more appropriately by articles in Section 4 above, even if the so-called image resembles speckle in appearance.

6. OBSERVATIONS AND IMPLICATIONS

The properties of SAR imaging behavior introduced above should be incontrovertible. Any observation, theoretical or experimental, that purports to "explain" the content of SAR ocean imagery, or to go even further and to "explain" the scattering mechanism, must be consistent with these principles.

There seem to be two general issues in active discussion in the theory of SAR ocean wave imaging: Gaussian versus non-Gaussian scattering; and the causes (and possible remedy) of azimuth directional spectral narrowing (Hasselmann et al., 1984). Therefore, it would be helpful to organize the foregoing SAR facts of life accordingly.

Table 1 compares the response of Gaussian scatterers and a specular scatterer for eleven measurable SAR image properties. These properties in turn are organized into two groups, General Considerations, having to do with a nominally uniform average reflectivity (of which a wheat field is the classic example), and Two-scale Considerations, for which there is assumed a low (spatial) frequency modulation of the reflectivity, as by a swell or more fully developed sea. The Table is filled in under the assumption that the SAR azimuth response is of interest.

TABLE 1

COMPARISON OF IMAGE PROPERTIES

	GAUSSIAN SCATTERING	SPECULAR SCATTERER
<u>General Considerations</u>		
1. High correlation between looks (azimuth sub-aperture filtering)	No	Yes
2. Average image (intensity) dependent on N-look processing	No	No
3. Peak values of image (intensity) dependence on N	$N^{-1/2}$	N^{-1}
4. Focus sensitivity (uniform reflector)	No	Yes
5. Image sensitivity to scene coherence time	No	Yes
6. Fourier transform of "image" a measure of SAR/processor (<u>resolution</u>) ⁻¹	No	Yes
7. Fourier transform of "image" a measure of SAR/processor <u>bandwidth</u>	Yes	No
<u>Two-scale Considerations</u>		
8. Velocity bunching	Yes	Yes
9. Velocity spreading	Yes	No
10. Focus sensitivity	Weak	Strong
11. Coherence time limitation	Yes	Yes

The issue of Gaussian versus non-Gaussian scattering is an important one, both technically and philosophically. From a technical point of view, there is ample evidence that non-Gaussian scattering is characteristic of sea radar return (Trunk and George, 1970; Barkeshli and Moore, 1983), and indeed for many applications it is the reflectivity characteristic of central concern, as in target detection (Trunk and George, 1970), or in explaining the difference between airborne and tower based scatterometer results (Barkeshli and Moore, 1983). It seems well established that as the nominal resolution cell size decreases, the importance of "spikey" non-Gaussian reflectivity elements increases (Trunk, 1972, and especially Jakeman and Pusey, 1976).

There are various "explanations" for non-Gaussian scattering. Most of these explanations are based on statistics that are closely related to the expected result of a very small average number of effective scatterers per resolution cell, where this value ranges from 0.1 or less (Jakeman and Pusey, 1976) to (less than) 5, the accepted threshold for Rayleigh - hence Gaussian - scattering. For this reason, in Table 1 the non-Gaussian case is represented by a single (dominant) specular scattering centre in a resolution cell. There may or may not be such a scatterer in an adjacent cell in a typical situation, indeed usually not. Hence the point target properties of SAR response apply to such a case.

For Gaussian scattering, it is assumed that there are "many" effective scattering centres per resolution cell.

As an aside, it is important to note that for a SAR, the number of effective scatterers per resolution cell is the spatial scale of interest, not the instantaneous field of view (antenna width by pulse length) of the radar.

From a philosophical point of view, the existence of and differences between Gaussian and non-Gaussian scatterers is important in that agreement on the veracity or significance of theoretical or experimental results is impossible unless assumptions about the underlying scattering, either explicitly presented or implicitly employed, are clearly explored and consistently followed. From the point of view of this writer, most of the controversy in the "focus" area is potentially resolvable if first there would be agreement on the type of scattering being considered.

Finally, some remarks on the nature of "a specular scatterer". It is obvious that a solid corner reflector is an example of a specular scatterer, as is a facet whose plane is orthogonal to the radar range line. It is likely that instances of coherent specular reflection arise from such geometrics accidentally simulated by the sea surface. Likewise, point scattering by a cusp or other surface discontinuity could provide a source of specular reflection.

There is another source of "specular" reflection that seems to have been overlooked to date; Bragg scattering. Whereas Bragg scattering, the geometry in which the radar wavelength projected onto a wavy surface picks out preferentially the matching surface spatial frequency, is usually taken to be the epitome of Gaussian scattering (Hasselmann et al., 1984), it is by definition just the opposite! Bragg scattering, for one set of resonant scatterers in a local region, results in a coherent specular signal. It is only if there is an ensemble of many such Bragg scattering cells in one resolution cell that Gaussian statistics again apply. The modelling issue then reduces to representation of the expected size of a Bragg region as compared to a radar resolution cell.

Differentiation between these two specular reflection concepts should be possible experimentally as they are modulated by quite different portions of the ocean Doppler spectrum. The first typically move at nominal phase speed of the longer waves, whereas the second are dominated by orbital advection, hence much more slowly.

Irregardless of "the cause" of specular events in SAR ocean imagery, they do exist. Their observable properties are in many cases different from proper Gaussian scattering. Search for and observation of these features is worthwhile.

Turn now to the considerations of the Table. The first group (items 1-7) apply directly to a nominally idealized scene, and may be visualized as being analogous in the uniform Gaussian scattering case to determination of system response by white random noise or in the specular scatterer case to the optical "point spread function" (O'Neill, 1963).

It is of central importance to this discussion that unlike conventional imaging systems analysis using purely non-coherent illumination, for partially coherent systems there is not a one-to-one equivalence between frequency domain, and time domain norms. Independent measures of frequency structure (e.g., bandwidth) and temporal structure (e.g., coherence) are required. One purpose of the Table is to suggest approaches to this question. In this sense, the first seven items carry over directly and impact the final four items.

The Two-scale Considerations are meant to be those of first order relevance under the assumption that one is attempting to "image" azimuth waves, and thus to understand the azimuth wave spectral response of a SAR.

In order to get a bit more depth into the implications of the Table, consider an experiment using existing data. We need to have examples of SAR ocean imagery with different qualities of azimuth waves visible. There should also be available a control, an example of imagery (from the same radar and processor) that includes a large random field, and if possible at least one point reflector. The experimental procedure is to perform on both the control and the sea images the series of tests suggested in the Table. From the Control, general considerations 1,2,3,4,6 and 7 may be verified. The same measures should then be performed on the sea images, with the results used to classify regions of sea scattering as dominantly Gaussian or

specular.

For example, it has been observed that the apparent speckle in certain SEASAT scenes is elongated in azimuth by several resolution cells. This feature has been called "streakle"*, a most descriptive terminology. The occurrence of streakle seems to be correlated with reduction of the azimuth bandwidth of associated directional spectra. The streakle events should be processed according to the tests of Table 1. From this one may conclude whether or not they correspond to specular or Gaussian scattering.

Again, one may search for focus sensitivities. Certain investigators have reported finding focus dependence in SAR data. In the context of the Table, this corresponds to item 10, in which there is a value judgement required. The case may be strengthened, by subjecting the area in question to the test of item 1. for those areas in which both strong focus dependence is found and specular correlation between looks is satisfied, then more presumptive steps (such as wave height estimation) can be hazarded.

It is true that an ensemble of scatterers, or a point scatter, should they have a Doppler (linearly changing phase) component will suffer an azimuth position shift (item 8 in the Table). This is difficult to observe confidently on the ocean, however, due to the complexity of the full spectrum of motions present.

In the event that the sea spectrum is nearly pure swell, as is the case for ocean waves in a field of floating ice, and the problem of scattering coherence time is avoided, then the velocity bunching mechanism may be directly observed (Raney, 1981). There are interesting questions that have to do with identifying the cause of loss of azimuth wave sensitivity in a SAR. Perhaps the issue could be addressed by observation of a wave field as it propagates from open water into an ice covered region, progressively attenuating the higher frequency portion of the wave spectrum. Again, any experimental observations should be verified by a control frame of SAR data, and judicious use of the measureable norms of Table 1.

7. CONCLUSIONS

This paper has attempted to present and tabulate imaging properties of a SAR that are facts of life. These have been selectively explored as they apply to the ocean imaging problem.

It is suggested that most SAR ocean imagery has properties of both Gaussian and specular scattering. Existing theories and experimental observations are controversial largely due to inconsistencies in the assumed scattering mechanism. Logical approach to the problem requires that the rules of SAR image formation be utilized as guidance to localize and interpret ocean imagery phenomena. An experimental procedure is suggested to realize this goal.

* Dr. A. Goldfinger

REFERENCES

- Barkeshli, S. and R.K. Moore, 1983; "Interaction of the Radar Waves with the Capillary Wave on the Ocean", University of Kansas, Remote Sensing Laboratory Report RSL TR 419-1.
- Bennett, J.R. and P.R. McConnell, 1980; "Considerations in the Design of Optimal Multilook Processors for Image Quality", Proceedings of the 3rd SEASAT-SAR Workshop on SAR Image Quality, Frascati, Italy, (ESA SP-172) pp. 5-12.
- Brown, W.M. and L.J. Porcello, 1969; "An Introduction to Synthetic Aperture Radar", IEEE Spectrum 6, pp. 52-62.
- Hargreaves, R.O., 1970; Synthetic Aperture Radar Systems: Theory and Design. Academic Press, New York.
- Hasselman, K., et al., 1984; "Theory of SAR Ocean Wave Imaging, A Marsden View", Journal of Geophysical Research (in publication).
- Jakeman, E. and P.N. Pusey, 1976; "A Model for Non-Rayleigh Sea Echo", IEEE Trans. Antennas and Propagation, Vol. AP-24, No. 6.
- O'Neill, E.L., 1963; Introduction to Statistical Optics, Addison-Wesley, Reading, Mass.
- Porcello, L.J. et al., 1976; "Speckle Reduction in Synthetic Aperture Radars", Journal of Optical Society of America, Vol. 66, No. 11, pp. 1305-1311.
- Raney, R.K., 1971; "Synthetic Aperture Radar and Moving Targets", IEEE Trans. on Aerospace and Electronic Systems, AES-7, pp. 499-505.
- Raney, R.K., 1980; "SAR Response to Partially Coherent Phenomena", IEEE Transactions on Antennas and Propagation, Vol. AP-28, No. 6, pp. 777-787.
- Raney, R.K., 1981; "Wave Orbital Velocity, Fade, and SAR Response to Azimuth Waves", IEEE Journal of Oceanic Engineering, Vol. OE-6, No. 4.
- Raney, R.K., 1983; "Transfer Functions for Partially Coherent and SAR Systems", IEEE Transactions on Aerospace and Electronic Systems, 19, No. 5.
- Trunk, G.V. and S.F. George, 1970; "Detection of Targets in Non-Gaussian Sea Clutter", IEEE Trans. Aerospace and Electronic Systems, Vol. AES-6, No. 5, pp. 620-628.
- Trunk, G.V., 1972; "Radar Properties of Non-Rayleigh Sea Clutter", IEEE Trans. Aerospace and Electronic Systems, Vol. AES-8, No. 2, pp. 196-204.
- Zelenka, J.S., 1976; "A Comparison of Continuous and Discrete Mixed Integrator Processors", Journal of Optical Society of America, Vol. 66, No. 11, pp. 1295-1304.

SYNTHETIC APERTURE RADAR IMAGES OF OCEAN WAVES,
THEORIES OF IMAGING PHYSICS
AND EXPERIMENTAL TESTS

John F. Vesecky, Stephen L. Durden,
Martha P. Smith and David A. Napolitano
Stanford Center for Radar Astronomy
Durand Building, Stanford University
Stanford, CA 94305 USA

1. INTRODUCTION

Observation of ocean surface waves was one of the primary reasons for including the synthetic aperture radar (SAR) in the instrument complement of the SEASAT oceanography satellite. As a natural result, understanding SAR response to ocean waves has been a central issue in the interpretation of SAR ocean images. Although much research has been done and several models have emerged to explain the mechanism for SAR imaging of ocean waves, only limited agreement has been reached on a correct understanding of the mechanism. Understanding the physics of this imaging mechanism is important for two reasons. First, understanding the imaging mechanism would allow improved estimates of wave field characteristics. Second, knowledge of the imaging physics for ocean gravity waves would have significant application to SAR images of other ocean surface phenomena, such as internal waves, slicks, surface wind fields and sea surface temperature variations. Our approach to understanding SAR imaging mechanisms is straightforward. First, we develop from each candidate model a set of hypotheses which can be experimentally tested. Second, we test these statements using data sets of SAR images and corresponding in situ surface observations. Our primary source of data sets has been from the SEASAT mission and several large scale field experiments using aircraft SAR's. This paper will summarize initial research results and the conclusions that can be drawn from them.

2. CONTENDING MODELS

Here we discuss three major models which claim to contain the important physics of the SAR imaging mechanism for ocean gravity waves. We pick these models because they represent major, different and well known points of view. Much of the physics involved here is relevant to other areas of ocean remote sensing by radar. While there are other important contributions to this problem (e.g. Swift & Wilson, 1979; Valenzuela, 1980; Ivanov, 1982 & 1983; Plant, 1983; Rotherham, 1983), we focus on work by Alpers et al (1981), Alpers (1983), Harger (1981 & 1984) and Jain (1981).

Two basic mechanisms for radar wave scattering from a statistically rough surface have been treated analytically. For a surface which is only slightly rough ($|k\zeta\cos\theta| \ll 1$, where k is radar wavenumber, ζ height deviation and θ angle of incidence) a perturbation analysis can be used and the resulting backscatter mechanism is referred to as the Bragg mechanism because of the analogy with Bragg (resonant) scattering from a crystal lattice. Here the structure resonant with the radar waves is a collection of short (~ 10 's of cm) ocean waves. The other case is termed the quasi-specular mechanism since it evokes scattering from a statistical ensemble of facets, each scattering via specular reflection. This mechanism is valid for situations where ζ may be large, but the surface is gently undulating (radius of curvature \gg radar wavelength). In general Bragg scatter is more impor-

tant for $\theta \gtrsim 20^\circ$ while quasi-specular scatter dominates for $\theta \lesssim 20^\circ$. In understanding the models discussed below it is important to note the role played by each of these mechanisms. This is especially important for SEASAT SAR observations since $19^\circ < \theta < 26^\circ$ in that case. Fig. 1 shows the observational geometry for SAR ocean remote sensing.

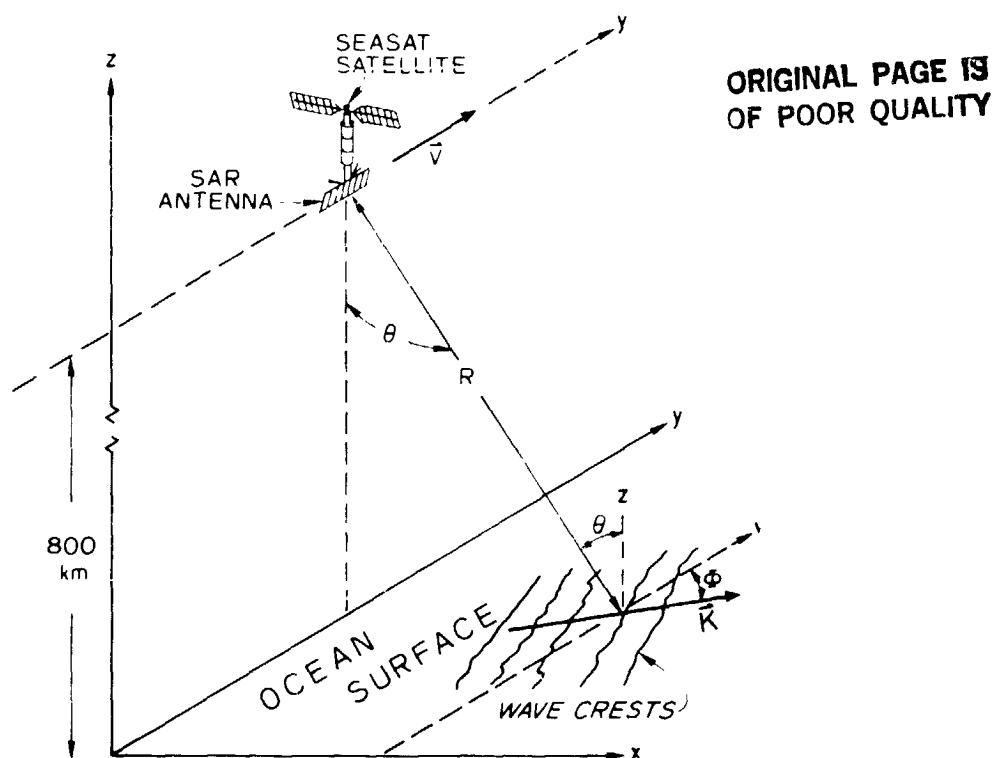


Fig. 1. Geometry for observation of the ocean surface by SEASAT (or aircraft) synthetic aperture radar. Here we define the geometry for SEASAT SAR observations of the ocean surface, (x,y) plane; in particular, observations of long gravity waves at a point (x,y) traveling at an angle ϕ with respect to the SAR flight path and having a wave vector K where $K = (2\pi/\Lambda)$ and Λ is the ocean wavelength.

Alpers, et al. (1981-1983)

This model contains perhaps the most straightforward and easily comprehended analysis of SAR imaging of ocean waves. In this (ARR) model small ($\gtrsim 10$ radar wavelengths) facets are treated as floating corks, each with its own Doppler shift and scattering properties. Each facet is statistically independent of surrounding facets and a two-scale scattering model is used to calculate the radar echoes which determine the SAR image. The facets constitute the small scale, while the long (~ 10 's to 100 's of m) ocean waves determine the large scale surface behavior. So each facet has its own position, orientation, surface roughness and velocity. These properties are governed by the large scale, long ocean wave behavior. Given a facet's position, ocean surface dynamics determine the latter three quantities. Then, knowing a facet's orientation, surface roughness and velocity, Alpers et al use SAR and scattering theory to calculate the backscattered power which the SAR would sense from each facet location. Facet orientation, surface roughness and velocity vary with position along the propagation direction of a wave and give rise to three mech-

anisms by which a long ocean wave modulates the power sensed by the SAR for a given position along the wave propagation direction. This modulation makes the waves visible in the SAR image. Facet orientation leads to the tilt modulation mechanism in which, for a given surface roughness, the radar backscatter is enhanced when the long ocean wave tilts a facet so that it is viewed at nearer normal incidence by the radar and visa-versa. Facet roughness leads to the hydrodynamic modulation mechanism in which, for a given orientation, the radar backscatter is enhanced for those portions of a wave (near the crest) where surface dynamics enhances small scale roughness. Finally, facet velocity along the radar propagation vector \hat{k} leads to the velocity bunching modulation mechanism in which, for a given tilt and surface roughness, the backscattered power sensed by the radar is systematically misplaced in the image due to the facet having a Doppler shift different from the mean for the large scale surface, i.e. Doppler misplacement bunches power in some image locations and disperses it from others. Alpers and Rufenach (1979), Alpers et al. (1981) and Alpers (1983a) apply this model to monochromatic sinusoidal waves while Alpers (1983b) uses a Monte Carlo calculation to make the application to a spectrum of waves. This model is relatively well developed and many quantitative statements which can be experimentally tested have been derived from it. Some of these statements are in terms of a modulation transfer function R defined by Alpers and Hasselmann (1979) as

$$\sigma = \sigma_0 + \delta\sigma = \sigma_0 [1 + \int (R(K) z(K) e^{i(Kx - \Omega t)} + c.c.) dK] \quad (1)$$

where σ is normalized radar cross section $z(K)$ is the Fourier transform of the surface height fluctuation associated with the long waves, K and Ω are the wave-number and radian frequency of the long waves and c.c. stands for complex conjugate. Equation (1) implies that R characterizes a linear process. This is an unwarranted, but apparently useful assumption. R is of course a function of observational and ocean parameters as well as K . Since R relates SAR and ocean surface observables it can be determined experimentally and this empirically determined R compared with theoretical expressions from the different models. The model also makes predictions regarding other quantities, for example image smearing (degraded resolution) and biases of SAR estimates of wave characteristics relative to surface measurements. Because of the relatively straightforward connection between assumptions and predictions of this model we have emphasized it here.

Harger (1980-1984)

Harger (1980, 1981, 1983, 1984) approaches the SAR wave imaging problem from a radar point of view and his extensive background in SAR (e.g., Harger, 1970). In this model the ocean surface is characterized as a continuous, dynamic surface having an 'effective reflectivity density' (g) which varies spatially and temporally in accordance with the surface dynamics. Thus this model uses a distributed radar scattering surface rather than the floating corks of Alpers et al. The key elements in the model are SAR imaging of time variant scenes, rough surface scattering and ocean surface hydrodynamics. Harger (1980) characterizes the SAR system as a series of transformations in which $g(x,y)$ of the ocean surface [Fig. 1 coordinates are used here] is transformed into $I(x,y)$ which is the SAR image output. Harger (1980, 1981, 1983) investigates how these transformations filter the wavenumber spectrum of g to yield the wavenumber spectrum of I . To obtain g Harger (1984) uses Phillips' (1981) hydrodynamic model for short ocean waves (small scale roughness) riding on long gravity waves (large scale structure), i.e. a two scale model. The large scale waves are simple sinusoids. For scattering from small scale roughness the Bragg scattering model is used. In this imaging model, Phillips' hydrodynamic model produces hydrodynamic modulation analogous to, but not the same as, the work of Alpers et al. above. Tilt modulation is produced by the large scale

sinusoidal waves. There are several major differences between the results of this model and those of Alpers et al. First, Harger finds no 'velocity bunching' modulation effects whereas Alpers et al. do. Second, Harger finds the long wave phase velocity to be important whereas this quantity does not directly enter the model of Alpers et al.

Jain (1981)

This model is less fully developed than the previous two, but raises some important questions. Jain's model uses a distributed radar scattering surface as does Harger. He makes provision for quasi-specular as well as Bragg scattering and for scattering features travelling at the long wave phase velocity. Further he questions the application of the two scale model used by both Alpers et al. and Harger. While tilt and hydrodynamic modulation are included in this model, Jain and Harger agree that velocity bunching modulation should not be present. Jain's model is less well developed and quantitative predictions which can be experimentally tested are fewer. One prediction is that ocean wave fields containing wave trains in multiple directions will in general exhibit different properties than a simple super-position of two wave-train images rotated with respect to one another. Further Jain contends that for SAR observations at $\theta \lesssim 20^\circ$ (including SEASAT SAR) quasi-specular scattering is important. We discuss this question further below.

Key Issues

Here we summarize the major issues which we think are the crux of the wave imaging problem.

1. Role of surface motion: Does a SAR sense radar scattering as having a Doppler shift associated with the orbital or with the phase velocity of an underlying long wavelength ocean wave? Is the velocity bunching mechanism valid?
2. Degradation of SAR resolution by ocean surface motion: Is the degradation related primarily to long wave orbital acceleration (Alpers et al.) or does the presence of more than one dominant wave component imply a degradation of resolution as claimed by Jain?
3. Relative importance of quasi-specular, Bragg or other mechanisms: Alpers et al. and Harger consider only Bragg resonant scatter. Is quasi-specular scattering also important as Jain claims? Within the Bragg mechanism what is the relative importance of the tilt, hydrodynamic and velocity bunching mechanisms?
4. Validity of the two-scale scattering model: Can the ocean surface be separated into two importance scale lengths, the long ocean waves and the short Bragg resonant waves, as Alpers et al. and Harger assume or are intermediate scales also important as Jain claims?

3. RELEVANT EXPERIMENTAL DATA

There is a large collection of SAR and surface data sets concerning ocean waves. Several large field experiments were conducted both preceeding SEASAT (1978) and after, e.g., Marineland in 1975, Westcoast in 1976, and MARSEN in 1979. In these experiments various aircraft SAR's were flown over wave fields also observed by buoys, pressure arrays, wave staffs, and ground wave radar. Particularly useful are the multiple direction flights which view waves from several aspects. During the Seasat mission 100,000,000 km² of SAR images were collected, most over the ocean. The Seasat data have the advantage of a consistent SAR system and very high quality digital imaging. Several good data sets of SEASAT SAR and surface wave observations were collected during the JASON, GOASEX, DUCKEX, and Atlantic Coast experiments in 1978. Besides simple wavefields observed during the SEASAT mission there are several cases of ship wake waves and waves near islands which bear upon

the SAR ocean waves imaging mechanism. Two other sources of important experimental data are tower experiments, such as those of Plant (1977), and scaled down laboratory experiments. An extensive tower experiment called TOWARD will begin in August 1985 using the NOSC tower off San Diego. It will involve tower mounted radars, aircraft SAR and the Shuttle Imaging Radar, SIR-B. Other relevant wave experiments are planned for SIR-B in August 1984, in particular SAR observations at varying incidence angles (θ).

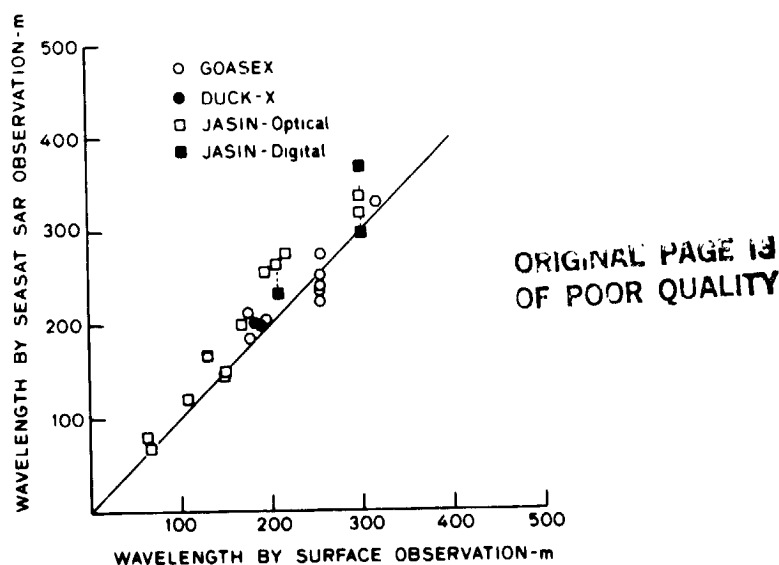
In bringing these data sets to bear on the SAR imaging problem two factors are of major importance. First, the SAR (or other radar) and surface and measurement data must test some critical hypothesis emerging from the contending models, i.e., the data set should address one of the critical issues listed above. Second, both the radar and surface data must be of sufficiently high quality to make a convincing test. In particular digitally imaged SAR data should be used whenever possible. Below we discuss some initial results using the aforementioned data sets to confront hypothesis derived from the models of section 2.

4. EXPERIMENTAL TESTS OF MODEL PREDICTIONS

Here we present initial results using data of section 3 to test the models of section 2. These results are limited both because this report is a brief one and because the research is still going on. The model of Alpers et al. receives somewhat more attention here because these authors have worked out a number of predictions which can be tested by available data in a straightforward manner.

Bias of SAR Estimates of Wave Properties Relative to Surface Measurements

One of the most straight forward comparisons of SAR estimates of wave properties with surface measurements is for the dominant wavelength of the ocean wave field being observed. Gonzalez et al. (1981) and Vesecky et al. (1983 and 1984) make such comparisons using SEASAT SAR data for several tens of cases.



Because the physical mechanism which allow SAR to image ocean waves are not well understood, first order estimates of ocean wave characteristics are based on a simple assumption, namely that intensity fluctuations, δI , in a SAR image of ocean waves are linearly proportional to fluctuations in ocean waveheight, $\delta \zeta$. Thus we let

$$F_I^2 = H^2 B^2 R^2 \Psi \quad (2)$$

where H is the transfer function related to the SAR system characteristics, B is related to oceanic background fluctuations not directly related to ocean waves, R is related to the physics of the wave imaging mechanism and $F_I(K, \Phi)$ is the Fourier transform of the image intensity $I(x, y)$ and K and Φ are polar coordinates in two-dimensional wavenumber space. The angle Φ is referenced to the velocity vector of the platform surface track and is positive clockwise when viewed from the platform. Thus $\Phi = 0$ is the azimuth or along track direction and $\Phi = 90$ is the range or cross track direction (see Fig. 1). The SAR wavelength estimates in Fig. 2 were made by computing F_I^2 from SAR images, letting B and R be unity and estimating the SAR system response H^2 according to Beal et al. (1983) for the JASIN digitally imaged data and according to Vesecky et al. (1984) for the JASIN optically processed data. For the GOASEX and DUCK-X optically processed data $H^2 = 1$. Thus biases due to SAR system response H^2 should be limited while biases due to the imaging mechanism R^2 remain. It is clear that the SAR estimates are biased slightly toward longer wavelengths. Monte Carlo simulations of SAR imaging of a spectrum of ocean waves by Alpers (1983) clearly predict such a bias (see Figs. 3, 7, 9, 10, 11, and 12). However, the parameters of these simulation do not match precisely the conditions of Fig. 2 (e.g., only the azimuthal component of the wave field is simulated). Hence, we can make only a semi-quantitative confirmation of this prediction of the Alpers et al. model. No analogous predictions for the Harger and Jain methods have been done so we can not evaluate them at this time.

Relative Importance of Bragg Resonance and Quasi Specular Scattering Mechanisms

It is well known (Bahar et al., 1983) that the relative importance of the Bragg resonance and quasi specular scattering mechanisms varies with angle of incidence (θ in Fig. 1). In section 2 we noted that both the Alpers et al. and Harger models take only Bragg scattering into account, while Jain contends that for the SEASAT SAR geometry specular scatter is also important. As a first step in sorting out this problem Vesecky et al. (1983) have calculated the variation of the modulation transfer function [R in eq. (1)] with incidence angle (θ). In this calculation only the tilt modulation mechanism was considered. In the calculation a SAR resolution wavenumber, $K_{sar} = \pi/(\text{resolution})$, is defined such that waves with $K < K_{sar}$ are imaged and waves with $K > K_{sar}$ are not. Waves that can be imaged are treated deterministically, while sub-resolution waves are treated statistically. Thus, the resolution cell is considered to be a random rough surface which is tilted by the deterministic long wave. To find the cross section in the resolution cell as a function of angle of incidence θ and the tilt angles, ψ and δ , a two-scale model is used. The height of the surface within the resolution cell is:

$$h = h_l + h_s \quad (3)$$

where h_s is for a small scale surface which scatters by the Bragg mechanism and h_l is for the large scale surface which scatters by the quasi specular mechanism. Here large scale refers to waves intermediate between the Bragg resonant wavelength (~ 30 cm) and the resolution cell size (~ 25 m). The waveheight spectrum for h is derived into three parts:

$$W(K) = \begin{cases} W_S(K) & K > K_d \\ W_1(K) & K_{SAR} < K < K_d \\ 0 & K < K_{SAR} \end{cases} \quad (4)$$

k_d is the wavenumber of transition between the large scale surfaces.

In Fig. 3 results are shown for three progressively complex model calculations. In the most simple case (dotted line) quasi specular is neglected as well as the tilting of h_s by h_l . This corresponds to the Alpers et al. model and is the same curve as Fig. 1 of Alpers et al. (1981). Next the tilting of h_s by h_l is included, but only Bragg scatter is considered. This corresponds, at least in part, to including the effects of surface height structure in between the small scale Bragg resonant waves (~30 cm) and the long ocean waves (~100's of m). These results corresponding to the dashed line go toward zero at small θ as one knows physically they should. Finally quasi-specular scatter is included (solid curve) and a peak in the modulation transfer function emerges at $\theta \sim 18^\circ$. Similar results have been obtained by Bahar et al. (1983).

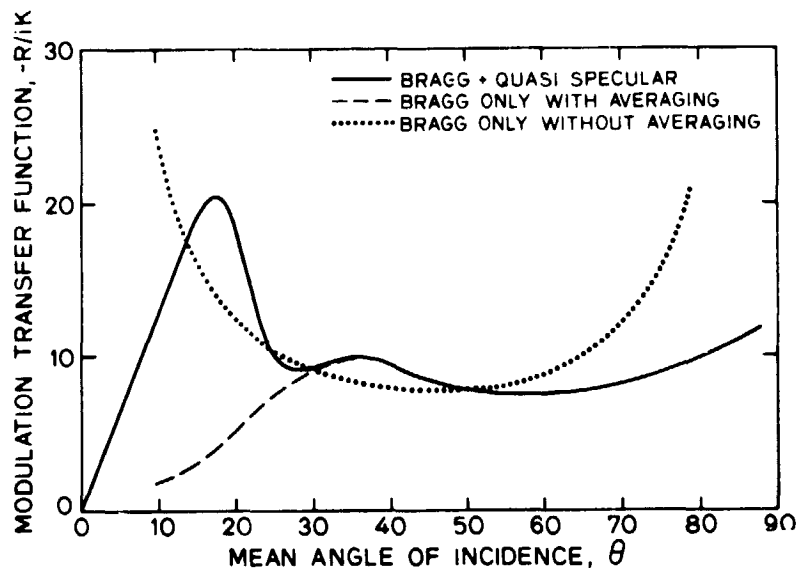


Fig. 3. Normalized modulation transfer function ($-R/ik$) taking into account various effects.

According to Fig. 3 one should observe a rather sharp decline in the visibility of waves in SAR images as θ increases from about 20° to 30° . SEASAT SAR observations over the JASIN experiment area off the west coast of Scotland provide an opportunity to test this implication of Fig. 3. On orbit 1044 300 m wavelength waves at $H_{1/3} \sim 3.5$ m traveling at about 40° relative to the satellite surface track ($\Phi = 229^\circ$ in Fig. 1) were imaged by SEASAT SAR. A scene about 40×40 km in size was digitally imaged at DFVLR Oberpfaffenhofen. This image was divided into 9 squares -- 3 in azimuth by 3 in range. Along the range direction θ varies over a little less than 2° . SAR estimates for Ψ were obtained as discussed above letting R^2 and B^2 go to unity in eq. (2). The relative values of the Ψ estimates at the dominant wavenumber k_p were compared to note the variation of SAR estimate of

$\Psi(k)$ with θ . If one assumes that the ocean wavefield is homogeneous over the 40×40 km square, that SAR system effects have been successfully removed, and that there are no relevant background contributions (e.g. from internal waves), then the variation must be due to R^2 in eq. (2), i.e. to the imaging mechanism. Over this 40×40 km area 300 m swell in deep water should be very nearly homogeneous even in the 11 m/s wind blowing at the time. Use of H^2 in eq. (2) as discussed above, plus the fact that we are considering wave sizes much smaller than the image size and that the digital imaging was carefully done convince us that the variation seen in Fig. 3 is not due to SAR or imaging artifacts. Further visual examination of the image reveals no significant background effects. Thus although this initial result must be confirmed from other data, we think it is indicative of a real variation of R^2 with θ and thus can be considered as experimental evidence confirming the existence of a rapid decrease of R^2 with θ for $20^\circ \lesssim \theta \lesssim 30^\circ$. Knowing the origin of Fig. 3 we thus have experimental evidence for the importance of quasi-specular scattering for SEASAT SAR images of ocean waves.

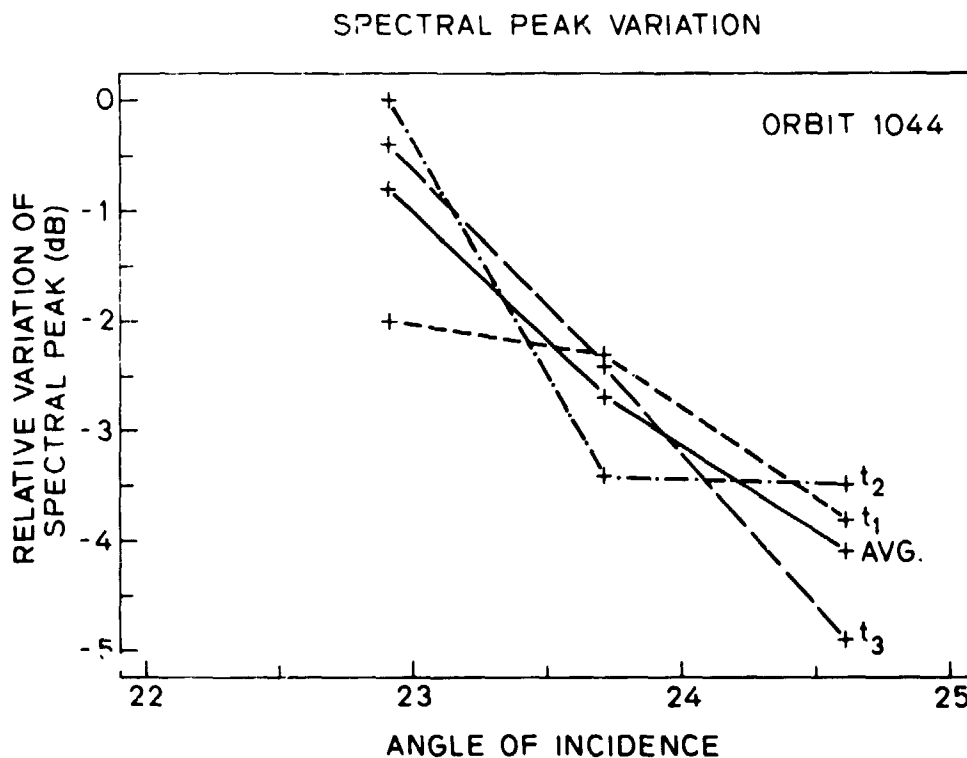


Fig. 4. Dependence of the SAR estimate of the directional wave spectrum Ψ (at the dominant wavenumber) on incidence angle θ . The data comes from a 40×40 km SEASAT SAR image collected on orbit 1044 over the JASIN experiment area 8 Sept. 1978, 0019 GMT. The three curves correspond to dividing the image into a 3×3 matrix and calculating the θ variation (along the range direction) at three locations along the azimuth direction. The mean curve for the three is also shown.

Ship Wakes

SAR images of ship wakes take many forms as shown by Fu & Holt (1982) and Vesecky & Stewart (1982). Those images are not useful here because there were no corresponding surface wave measurements. However, in Fig. 5 we show a splendid

SEASAT image of a classical Kelvin ship wake. Since we can clearly identify the SAR image as a Kelvin wake and since we know a good deal about Kelvin wakes (e.g. Lighthill, 1978, ch. 3), some useful information can be obtained. Aside from its form, a very convincing argument that the wake is indeed a Kelvin wake was pointed out to the authors by Brian Barber of the Remote Sensing Centre, RAE Farnborough, U.K. Noting the displacement of the ship from the wake and the SAR observational parameters a speed of about 11 m/s can be calculated for the ship. From wake theory we know that the transverse waves in the wake must have a phase velocity equal to the ship's velocity. We can calculate the required wavelength of the transverse waves in the image. The wavelength observed in the image is within 10% of the required value.

The important point here is that the ship is displaced from the wake by an amount which implies that the wake is virtually stationary on the sea surface. We make the analogy with the familiar 'train off the track' phenomena of SAR images in which the train's motion displaces it from the stationary track because the train and track have different Doppler shifts and SAR uses Doppler shift to locate objects along directions parallel to the SAR flight path. Thus the SAR observes these ~90 m waves of the ship wake as if they were stationary with respect to the sea surface (as assumed by Alpers et al.) rather than as if they were moving at the wave phase velocity. A similar point was noted by Keith Raney in his lecture at the Royal Society Meeting on Remote Sensing in Autumn, 1982.

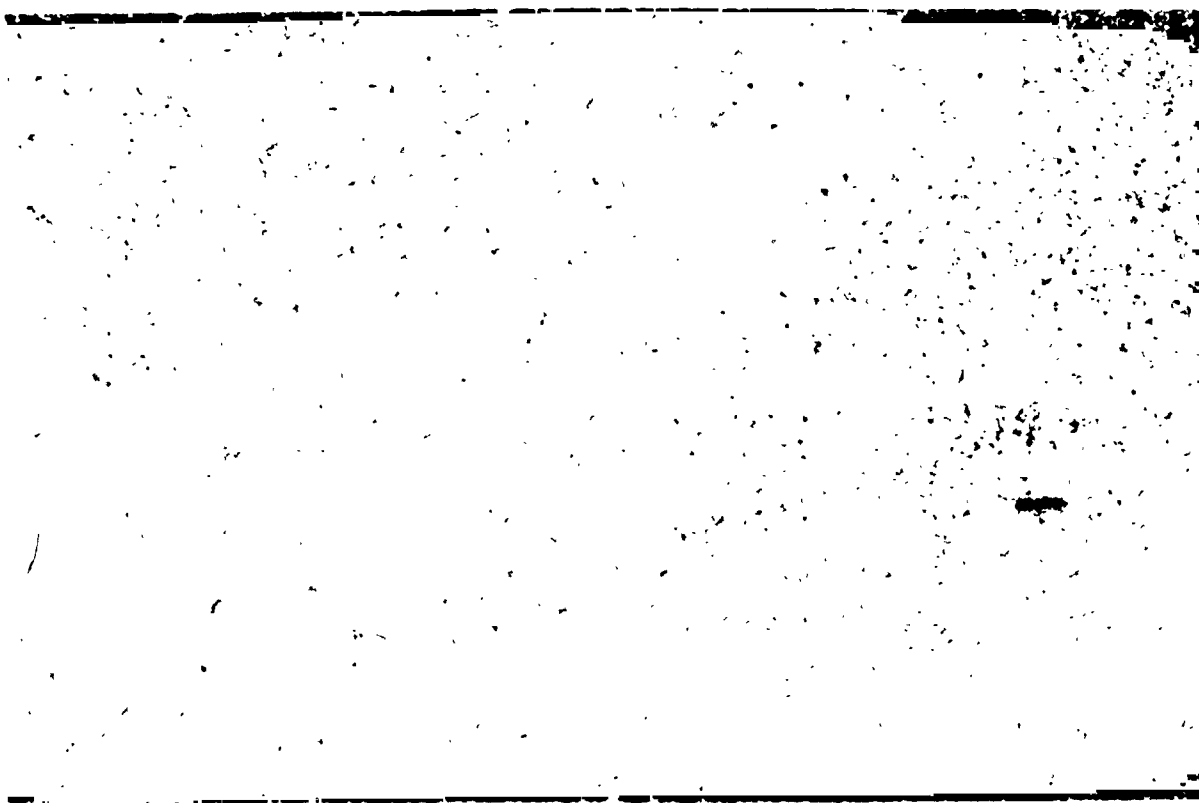


Fig. 5. SEASAT SAR image of a classical Kelvin wake generated by a ship in the English Channel. The image was collected on orbit 834, 24 August 1978, at 0727 GMT and digitally imaged at the Remote Sensing Center, RAE Farnborough, U.K.

Conclusions

We have discussed three major models for the mechanism by which SAR images ocean waves. From section 2 we conclude that there are significant fundamental differences between these models. These differences occur both in fundamental assumptions and in subsequent developments. Thus it is not surprising to find significant differences between predictions arising from these different models. In section 2 we list four key issues which need to be resolved in order to sort out the correct and incorrect features in the contending models. Although testing these models against experimental evidence is still in the initial stages, we draw several preliminary conclusions. For the most part these conclusions require further testing to confirm them.

1. SAR estimates of dominant ocean wavelength are biased slightly toward longer wavelengths when compared to surface measurements. The work of Alpers (1983) predicts just such a bias. However, we have not yet made detailed quantitative comparisons.

2. Inclusion of the quasi-specular scattering mechanism (Fig. 3) produces predictions which appear to agree with experimental evidence (Fig. 4) regarding the variation of the modulation transfer function with angle of incidence. Hence the quasi specular scattering mechanism is important for SEASAT SAR observations ($\theta \sim 22^\circ$) of ocean waves.

3. For the waves of the Kelvin ship wake of Fig. 5 the Doppler shift sensed by the SEASAT SAR is essentially that of the mean sea surface. Hence for these 90 m wavelength waves we conclude that wave orbital velocity is involved rather than wave phase velocity.

Future experiments using the Space Shuttle imaging radar (SIR-B) should be very helpful in resolving the key issues of section 2 both because observations will be made at multiple angle of incidence and because high quality digitally imaged data will be available. SIR-B observations during the TOWARD (instrumented sea tower) experiment off San Diego would be particularly useful.

ACKNOWLEDGEMENTS

The authors thank Dr. W.R. Alpers of University of Hamburg, Brian Barber of RAE Farnborough and DFVLR Oberpfaffenhofen for kindly providing images and information. We are also thankful to Sara Zientek and Corinne Kelsch for camera ready copy preparation. The Office of Naval Research (Coastal Sciences) and the National Aeronautics and Space Administration (Ocean Processes) have provided financial support (including an ONR scholarship). We thank them.

REFERENCES

- Allen, T.D. (ed.), 1983: Satellite Microwave Remote Sensing, Ellis Horwood, Chichester, U.K.
- Alpers, W.R., 1983a: Imaging ocean surface waves by synthetic aperture radar -- a review, 107-120, in Allen (1983).
- Alpers, W.R., 1983: Monte Carlo simulations for studying the relationship between ocean wave and synthetic aperture radar image spectra, J. Geophys. Res., **88**, 1745-1759.
- Alpers, W.R. and C.L. Rufenach, 1979: The effect of orbital motions on synthetic aperture radar imagery of ocean waves, IEEE Trans. Antennas and Propagat., **AP-27**, 685-690.

- Alpers, W.R., D.B. Ross, and C.L. Rufenach, 1981: On the detectability of ocean surface waves by real and synthetic aperture radar, J. Geophys. Res., 86, 6481-6498.
- Bahar, E., C.L. Rufenach, D.E. Barrick and M.A. Fitzwater, 1983: Scattering cross section modulation for arbitrarily oriented composite rough surfaces: Full wave approach, Radio Sci., 18, 675-690.
- Beal, R.C., D.G. Tilleg and F.M. Monaldo, 1983: Large- and small-scale spatial evolution of digitally processed ocean wave spectra from SEASAT synthetic aperture radar, J. Geophys. Res., 88, 1761-1778.
- Fu, L-L and B. Holt, 1982: Seasat Views Oceans and Sea Ice with Synthetic-Aperture Radar, JPL Publ. 81-120, Jet Propulsion Lab., Pasadena, CA.
- Gonzalez, F.I., R.A. Shuchman, D.B. Ross, C.L. Rufenach and J.F.R. Gower, 1981: Synthetic aperture radar observations during GOASEX, in Oceanography from Space, J.F.R. Gower (ed.), 459-468, Plenum Press, N.Y.
- Harger, R.O., 1983: A sea surface height estimator using synthetic aperture radar complex imagery, IEEE J. Oceanic Engr., OE-8, 71-78.
- Harger, R.O., 1981: Sar ocean imaging mechanisms, in Spaceborne Synthetic Aperture Radar for Oceanography (R.C. Beal et al., ed.), Johns Hopkins Press, Baltimore, 110-127.
- Harger, R.O., 1984: The SAR imaging of short gravity waves on a long gravity wave, Proceeding of the IUCRM Symposium on Wave Dynamics and Radio Probing of the Ocean Surface (O.M. Phillips, ed.) Plenum Press, N.Y. (in press).
- Harger, R.O., 1980: The synthetic aperture radar image of time-variant scenes, Radio Sci., 15, 749-756.
- Harger, R.O., 1970: Synthetic Aperture Radar Systems, Academic Press, N.Y.
- Ivanov, A.V., 1983: On the mechanism for imaging ocean waves by synthetic aperture radar, IEEE Trans. Ant. & Propagat., AP-31, 538-541.
- Ivanov, A.V., 1983: Reply to "Comments on 'On the synthetic aperture radar imaging of ocean surface waves'" by W.J. Plant, IEEE J. Ocean Engr., OE-8, 300.
- Ivanov, A.V., 1982: On the synthetic aperture radar imaging of ocean surface waves, IEEE J. Ocean Engr., OE-7, 96-102.
- Jain, A., 1981: SAR imaging of ocean waves: Theory, IEEE J. Ocean Engr., OE-6, 130-139.
- Lighthill, J.A., 1978: Waves in Fluids, Cambridge Univ. Press, Cambridge, U.K.
- Plant, W.J., 1983: Comments on "On the synthetic aperture radar imaging of ocean surface waves", IEEE J. Ocean Engr., OE-8, 300.
- Plant, W.J., 1977: Studies of backscattered sea return with CW dual-frequency X-band radar, IEEE Trans. Antennas and Propagat., AP-25, 28-36.
- Rotheram, S., 1983: Theory of SAR ocean wave imaging in Allen (1983), pp. 155-186.

- Swift, C.T. and L.R. Wilson, 1979: Synthetic aperture radar imaging of moving ocean waves, IEEE Trans. Ant. & Propagat., AP-27, 685-689.
- Valenzuela, G.R., 1980: An asymptotic formulation of the SAR images of the dynamical ocean surface, Radio Sci., 15, 105-114.
- Vesecky, J.F. and R.H. Stewart, 1982: The observation of ocean surface phenomena using imagery from the SEASAT synthetic aperture radar, J. Geophys. Res., 87, 3327-3430.
- Vesecky, J.F., H.M. Assal and R.H. Stewart, 1981: Remote sensing of the ocean wave height spectrum using synthetic-aperture-radar images, in Oceanography from Space (J.F.R. Gower, ed.) Plenum Press, N.Y., 449-568.
- Vesecky, J.F., S.L. Durden, D.A. Napolitano and M.P. Smith, 1983: Theory and practice of ocean wave measurement by synthetic aperture radar, Proceedings of Oceans '83, IEEE Press, N.Y.
- Vesecky, J.F., R.H. Stewart, R.A. Shuchman, H.M. Assal, E.R. Kasischke and J.D. Lyden, 1984: On the ability of synthetic aperture radar to measure ocean waves, Proceedings of IUCRM Symposium of Wave Dynamics and Radio Probing of the Ocean Surface, (O.M. Phillips, ed.) Plenum Press, N.Y. in press.

OPTIMUM BACKSCATTER CROSS SECTION OF THE OCEAN
AS MEASURED BY SYNTHETIC APERTURE RADARS

Ezekiel Bahar

Electrical Engineering Department
University of Nebraska-Lincoln, NE 68588-0511Clifford L. Rufenach and Donald E. Barrick
NOAA/ERL/Wave Propagation Laboratory, Boulder, CO 80303Mary Ann Fitzwater
Electrical Engineering Department
University of Nebraska-Lincoln, NE 68588-0511ABSTRACT

Microwave remote sensing of rough surfaces (both land and ocean), using moving platforms (aircraft and satellite), as well as ground based measurements has illustrated the need for a better understanding of the interaction of the radar signals with these surfaces. This interaction is particularly important for the ocean surface where the radar modulation can yield information about the long ocean wave field. Radar modulation measurements from fixed platforms have been made in wavetanks and the open oceans. The surfaces have been described in terms of two-scale models. The radar modulation is considered to be principally due to: (1) geometrical tilt due to the slope of the long ocean waves and (2) the straining of the short waves (by hydrodynamic interaction). For application to moving platforms, Synthetic Aperture Radar (SAR) and Side Looking Airborne Radar (SLAR), this modulation needs to be described in terms of a general geometry for both like- and cross-polarization since the long ocean waves, in general, travel in arbitrary directions. In the present work, the finite resolution of the radar is considered for tilt modulation with hydrodynamic effects neglected.

1. INTRODUCTION

The full wave approach is used to determine the modulation of the like- and cross-polarized scattering cross sections for composite models of rough surfaces illuminated by SAR. The full wave approach accounts for both specular point scattering and Bragg scattering in a self-consistent manner. Thus, the total scattering cross section is expressed as a weighted sum of two cross sections (Bahar et al., 1983). The first is the scattering cross section associated with the filtered surface consisting of the large-scale specular components of the illuminated rough surface area. The second is the cross section associated with the surface consisting of the small-scale spectral components that ride on the filtered surface.

Full wave solutions are derived for the scattering cross sections of a relatively small area or resolution cell of the rough surface that is effectively illuminated by SAR. The normal to an arbitrarily oriented mean plane associated with the illuminated cell is characterized by tilt angles Ω and τ in and perpendicular to a fixed reference plane of incidence. It is assumed that the lateral dimension of the resolution cell L_g is much larger than both the electromagnetic wavelength and the surface height correlation distance for the cell. As the SAR scans different portions of the rough surface S , the direction of the unit vector normal to the cell F fluctuates. In this paper the "modulations" of scattering cross sections are determined as the tilt angles Ω and τ fluctuate. In a recent study of "tilt modulation" by Alpers et al. (1981), first-order Bragg scatter due to capillary waves on a tilted plane is considered. It can be shown that if the large scale spectral components of the surface within the cell are ignored, the full wave solutions derived here for tilt modulation reduce to the results obtained by Alpers et al.

$$\bar{n} = \nabla f / |\nabla f| = (-h_x \bar{a}_x + \bar{a}_y - h_z \bar{a}_z) / (h_x^2 + h_z^2 + 1)^{1/2} \quad (7a)$$

where

$$f = y - h(x, z), \quad h_x = \partial h / \partial x, \quad h_z = \partial h / \partial z \quad (7b)$$

and

$$\bar{n}_s = \bar{v} / v. \quad (7c)$$

The expression for the physical optics (specular point) cross section for the large-scale surface h_s is

$$\langle \sigma_{\infty}^{PQ} \rangle = \frac{4k_o^2}{v_y^2} \left[\left| \frac{D^{PQ}}{\bar{n} \cdot \bar{a}_y} \right|^2 P_2(\bar{n}^f, \bar{n}^i | \bar{n}) p(\bar{n}) \right] \bar{n}_s \quad (8)$$

in which D^{PQ} depends on \bar{n}^i , \bar{n}^f , \bar{n} , the media of propagation above and below the rough surface $h(x, z)$ and the polarization of the incident and scattered waves (Bahar, 1981a, b). The shadow function P_2 is the probability that a point on the rough surface is both illuminated and visible, given the slopes $\bar{n}(h_x, h_z)$, at the point (Smith, 1967; Sancer, 1969). The probability density function for the slopes h_x and h_z is $p(\bar{n})$. The factor $\chi^S(v)$ that multiplies $\langle \sigma_{\infty}^{PQ} \rangle$ accounts for the degradation of the contributions from the specular points due to the superimposed small scale rough surface h_s .

Assuming a Gaussian probability density function for h_s , $\langle \sigma^{PQ} \rangle_s$ is given by the sum

$$\langle \sigma^{PQ} \rangle_s = \sum_{m=1}^{\infty} \langle \sigma^{PQ} \rangle_{sm} \quad (9)$$

where

$$\langle \sigma^{PQ} \rangle_{sm} = 4\pi k_o^2 \int \frac{|D^{PQ}|^2 P_2(\bar{n}^f, \bar{n}^i | \bar{n})}{\bar{n} \cdot \bar{a}_y} \cdot \exp(-v_{\bar{y}}^2 \langle h_s^2 \rangle) \left(\frac{v_{\bar{y}}^2}{2} \right)^{2m} \frac{W_m(v_{\bar{x}}, v_{\bar{z}})}{m!} p(h_x, h_z) dh_x dh_z \quad (10)$$

in which $\langle h_s^2 \rangle$ is the mean square of the surface height h_s and $v_{\bar{x}}, v_{\bar{y}}$ and $v_{\bar{z}}$ are the components of \bar{v} (6) in the local coordinate system (at each point on the large scale surface) associated with the unit vectors \bar{n}_1, \bar{n}_2 and \bar{n}_3 . Thus \bar{v} can also be expressed as

$$\bar{v} = v_{\bar{x}} \bar{n}_1 + v_{\bar{y}} \bar{n}_2 + v_{\bar{z}} \bar{n}_3 \quad (11)$$

where

$$\bar{n}_1 = (\bar{n} \times \bar{a}_z) / |\bar{n} \times \bar{a}_z|, \quad \bar{n}_2 = \bar{n}, \quad \bar{n}_3 = \bar{n}_1 \times \bar{n}. \quad (12)$$

The function $W_m(v_{\bar{x}}, v_{\bar{z}}) / 2^{2m}$ is the two-dimensional Fourier transform of $\langle h_s h_s' \rangle^m$.

For $\beta \ll 1$ and arbitrary $p(h_x, h_z)$ the first term in (9), $\langle \sigma^{PQ} \rangle_{s1}$ is also in agreement with Valenzuela's solutions that are "mostly based on physical considerations" (Valenzuela, 1968, Valenzuela et al., 1971). For small slopes $\bar{n} \approx \bar{a}_y$ and $\beta \ll 1$ the first term in (3) reduces to Brown's solution (1978) based on a combination of physical optics and perturbation theory. Since it is assumed (on deriving (3) from the full wave solutions for the scattered fields) that the surface h_s satisfies the radii of curvature criteria as well as the condition for deep phase modulation, it is necessary to choose $\beta = 4k_o^2 \langle h_s^2 \rangle \geq 1$ in order to assure that the weighted sum of cross sections (3) remains insensitive to variations in k_d , the wavenumber where spectral splitting is assumed to occur (Bahar et al., 1983).

In order to apply the full wave approach to SAR it is necessary to modify the results presented in this section (a) to account for the filtering of the very

For the illustrated examples presented, the scattering cross sections and their derivatives with respect to the tilt angles are evaluated for all angles of incidence. The modulation of the like cross sections near normal incidence is due primarily to fluctuations in specular point scattering while the modulation of the like cross section for near grazing angles is due primarily to fluctuations in Bragg scattering. Thus, for large angles of incidence the cross sections for the horizontally polarized waves are shown to be more strongly modulated than the cross sections for vertically polarized waves. The relative modulations of the like polarized backscatter cross sections are optimum for incident angles between 10° and 15° depending upon the lateral dimension of the resolution cell and the polarization.

2. FORMULATION OF THE PROBLEM

The full wave solutions for the normalized cross sections per unit area are summarized here for composite rough surfaces. The position vector to a point on the rough surface is expressed as follows:

$$\bar{r}_s = \bar{r}_\ell(x, h_\ell, z) + \bar{n}h_s \quad (1)$$

in which $y=h_\ell(x, z)$ is the filtered surface consisting of the large scale spectral components of the rough surface and h_s , the small scale surface height is measured in the direction of the normal (\bar{n}) to the large scale surface $y=h_\ell$. For a homogenous, isotropic surface height the spectral density function is the Fourier transform of the surface height autocorrelation function $\langle h(x, z), h'(x', z') \rangle$.

$$W(v_x, v_z) = \frac{1}{2} \int_{-\infty}^{\infty} \langle hh' \rangle \exp(iv_x x_d + iv_z z_d) dx_d dz_d \quad (2a)$$

where $\langle hh' \rangle$ is a function of distance $|\bar{r}_d| = (x_d^2 + z_d^2)^{1/2}$ and

$$x - x' = x_d \text{ and } z - z' = z_d. \quad (2b)$$

The surface $h_\ell(x, z)$ consists of the spectral components $k = (v_x^2 + v_z^2)^{1/2} \leq k_d$ and the remainder term $h_s(x, z)$ consists of the spectral components $k > k_d$. The full wave approach accounts for both specular point scattering and Bragg scattering in a self-consistent manner the total scattering cross section can be expressed as a weighted sum of the cross section $\langle \sigma^{PQ} \rangle_\ell$ for the filtered surface h_ℓ and the cross section $\langle \sigma^{PQ} \rangle_s$ for the surface h_s that rides on the large-scale surface h_ℓ (Bahar et al., 1983)

$$\langle \sigma^{PQ} \rangle = \langle \sigma^{PQ} \rangle_\ell + \langle \sigma^{PQ} \rangle_s. \quad (3)$$

The symbol $\langle \rangle$ denotes statistical average. The first superscript P corresponds to the polarization of the scattered wave while the second superscript Q corresponds to the polarization of the incident wave. To derive (3) using the full wave approach it is implicitly assumed that the large scale surface meets the radii of curvature criteria (associated with the Kirchhoff approximations for the surface fields) as well as the condition for deep phase modulation. Thus the first term in (3) is

$$\langle \sigma^{PQ} \rangle_\ell = |\chi^s(\bar{v} \cdot \bar{n}_s)|^2 \langle \sigma_\infty^{PQ} \rangle \quad (4)$$

in which χ^s is the characteristic function for the small scale surface

$$\chi^s(\bar{v} \cdot \bar{n}_s) = \chi^s(v) = \langle \exp i v h_s \rangle \quad (5)$$

and

$$\bar{v} = \bar{k}^f - \bar{k}^i = k_0(\bar{n}^f - \bar{n}^i), \quad v = |\bar{v}|. \quad (6)$$

The unit vectors \bar{n}^f and \bar{n}^i are in the directions of the scattered and incident wave normals respectively; thus for backscatter $\bar{n}^f = -\bar{n}^i$. The free space radio wavenumber is k_0 . An $\exp(i\omega t)$ time dependence is assumed. The vector \bar{n}_s is the value of the unit vector \bar{n} normal to the surface $h(x, z)$ at the specular points. Thus

large scale spectral component of the rough surface by the SAR that effectively illuminates a relatively small area of cell F of the rough surface S and (b) to account for the normal to a reference plane associated with the illuminated cell which is characterized by arbitrary tilt angles Ω and τ in and perpendicular to the reference plane of incidence. It is assumed here that the lateral dimension of the cell illuminated by the SAR is much larger than the surface height correlation distance for the cell and that as the SAR scans different portions of the rough surface S the direction of the unit vector normal to the cell F fluctuates. Our purpose is to determine the "modulation" of the backscatter cross sections $\langle \sigma^{PQ} \rangle$ (3) as the tilt angles (of the normal to the cell) in and perpendicular to the reference plane of incidence fluctuate.

3. SCATTERING CROSS SECTIONS FOR ARBITRARILY ORIENTED RESOLUTION CELLS OF THE ROUGH SURFACE

Let x, y, z be the reference coordinate system associated with the surface of the cell F that is illuminated by the SAR such that the mean surface of the cell is the $y=0$ plane. Furthermore, let x', y', z' be the fixed coordinate system associated with the large surface S such that the unit vector \bar{a}'_y is normal to the mean rough surface height $h(x', z')$. The unit vector $\bar{n}^i = -\bar{n}^f$ is expressed in terms of the unit vectors of the fixed coordinate system (x', y', z') :

$$\bar{n}^i = -\bar{n}^f = \sin\theta'_0 \bar{a}'_x - \cos\theta'_0 \bar{a}'_y. \quad (13)$$

The unit vector \bar{a}_y normal to the reference surface associated with the cell is expressed in terms of the tilt angles Ω and τ in and perpendicular to the fixed plane of incidence, the x', y' plane. Thus

$$\bar{a}_y = \sin\Omega \cos\tau \bar{a}'_x + \cos\Omega \cos\tau \bar{a}'_y + \sin\tau \bar{a}'_z. \quad (14)$$

For convenience \bar{a}_x and \bar{a}_z , the unit vectors associated with the cell, can be chosen such that the plane of incidence in the x, y, z coordinate system is normal to the vector \bar{a}_z . Thus

$$\bar{a}_z = (\bar{n}^i \times \bar{a}_y) / |\bar{n}^i \times \bar{a}_y|, \quad \bar{a}_x = \bar{a}_y \times \bar{a}_z \quad (15)$$

and the expression for \bar{n}^i in the x, y, z coordinate system is

$$\begin{aligned} \bar{n}^i &= (\bar{n}^i \cdot \bar{a}_x) \bar{a}_x + (\bar{n}^i \cdot \bar{a}_y) \bar{a}_y \\ &= \sin\theta_0 \bar{a}_x - \cos\theta_0 \bar{a}_y \end{aligned} \quad (16a)$$

where

$$\cos\theta_0 = \cos(\theta'_0 + \Omega) \cos\tau. \quad (16b)$$

The angle ψ_F^i between the plane of incidence in the fixed coordinate system (x', y', z') and the plane of incidence in the coordinate system (x, y, z) associated with the cell is given by

$$\cos\psi_F^i = \frac{\cos\tau \sin(\theta'_0 + \Omega)}{\sin\theta_0} \quad (17a)$$

and

$$\sin\psi_F^i = \frac{\sin\tau}{\sin\theta_0}. \quad (17b)$$

For backscatter $\bar{n}^f = -\bar{n}^i$. Thus the angle ψ_F^f between the plane of scatter in the fixed coordinate system (x', y', z') and the plane of scatter in the coordinate system associated with the cell is

$$\psi_F^f = -\psi_F^i. \quad (18)$$

The matrix that transforms the incident vertically and horizontally polarized waves in the fixed coordinate system to vertically and horizontally polarized waves in the cell coordinate system is therefore (Bahar, 1981a,b)

$$T_F^i = \begin{bmatrix} \cos \psi_F^i & \sin \psi_F^i \\ -\sin \psi_F^i & \cos \psi_F^i \end{bmatrix} \quad (19)$$

Similarly, the matrix that transforms the scattered vertically and horizontally polarized waves in the cell coordinate system back into the vertically and horizontally polarized waves in the fixed coordinate system is

$$T_F^f = \begin{bmatrix} \cos \psi_F^f & -\sin \psi_F^f \\ \sin \psi_F^f & \cos \psi_F^f \end{bmatrix} \quad (20)$$

Thus in view of (18), $T_F^f = T_F^i$. The coefficients D^{PQ} in (8) are elements of a 2×2 matrix D given by

$$D = C_o^{in} T^f F T^i \quad (21)$$

in which C_o^{in} is the cosine of the angle between the incident wave normal \bar{n}^i and the unit vector \bar{n} normal to the rough surface of the cell $h_F(x, z)$. Thus

$$C_o^{in} = -\bar{n}^i \cdot \bar{n} = \cos \theta_o^{in} \quad (22)$$

where \bar{n}^i is given by (16) and \bar{n} is given by (7a) with $f_F(x, y) = y - h_F(x, y)$. The elements of the scattering matrix F in (21) are functions of the unit vectors \bar{n}^i, \bar{n}^f and \bar{n} as well as the media of propagation above and below the rough surface S (Bahar, 1981a). The matrix T^i transforms the vertically and horizontally polarized waves in the cell coordinate system $(\bar{a}_x, \bar{a}_y, \bar{a}_z)$ to vertically and horizontally polarized waves in the local coordinate system that conforms with the rough surface, $\bar{n}_1, \bar{n}_2, \bar{n}_3$ (12). Similarly, the matrix T^f transforms the vertically and horizontally polarized waves in the local coordinate system back into vertically and horizontally polarized waves in the cell coordinate system (Bahar, 1981a).

To account for the arbitrary orientation of the cell, the matrix D in (21) must be post-multiplied by T_F^i and pre-multiplied by T_F^f . Thus the elements of the matrix D in (8) must be replaced by the elements of the matrix D_F where

$$D_F = T_F^f D T_F^i \quad (23)$$

Furthermore, in view of the effective filtering by the SAR of the very large scale spectral components of the rough surface $f(x', z') = 0$, the spectral density function for the rough surface $f_F(x, y) = 0$ associated with the resolution cell F is given by

$$W_F(v_{\bar{x}}, v_{\bar{z}}) = \begin{cases} W(v_{\bar{x}}, v_{\bar{z}}) & , k \geq k_s \\ 0 & , k < k_s \end{cases} \quad (24)$$

where $W(v_{\bar{x}}, v_{\bar{z}})$ is the spectral density function for the surface S , $f(x', z') = 0$. The wavenumber k_s is

$$k_s = 2\pi/L_s < k_d \quad (25)$$

where L_s is the width of the area of the cell illuminated by the SAR. The very large scale surface consisting of the spectral components $0 < k < k_s$ are responsible for tilting the resolution cell with respect to the mean sea surface.

Thus on replacing the spectral density function W (2a) for the surface S by the spectral density function W_F for the cell F (24) and on replacing the elements D^{PQ} of the matrix D by the elements D_F^{PQ} of the matrix D_F (23) the expression (3) can be used to determine the normalized backscatter cross section for an arbitrarily oriented cell F . In view of (19) and (20) the expressions for these backscatter cross sections are explicit functions of the tilt angles Ω and τ . For the special

case $\tau = 0$ (tilt is in the plane of incidence) the matrices T_F^i and T_F^f reduce to identity matrices and

$$\cos \theta_0 = \cos(\theta'_0 + \Omega) . \quad (26)$$

Thus for $\tau = 0$

$$\left. \frac{\partial \theta_0}{\partial \Omega} \right|_{\theta'_0 = \text{const}} = \left. \frac{\partial \theta_0}{\partial \theta'_0} \right|_{\Omega = \text{const}} \quad (27)$$

and

$$(\partial \langle \sigma^{PQ} \rangle / \partial \Omega)_{\theta'_0 = \text{const}} = (\partial \langle \sigma^{PQ} \rangle / \partial \theta'_0)_{\Omega = \text{const}} . \quad (28)$$

Therefore to obtain $\partial \langle \sigma^{PQ} \rangle / \partial \Omega$ for $\Omega = 0$ and $\tau = 0$ it is sufficient to evaluate $\langle \sigma^{PQ} \rangle$ as a function of θ'_0 with both Ω and τ set equal to zero. The value for $\partial \langle \sigma^{PQ} \rangle / \partial \tau$ can either be evaluated analytically since D_F^{PQ} (23) is an analytic function of τ , or the derivative could be evaluated numerically.

4. ILLUSTRATIVE EXAMPLES

For the illustrative examples presented in this section, the following specific form of the surface height spectral density function is selected (Brown, 1978)

$$W(v_{\bar{x}}, v_{\bar{z}}) = \frac{2}{\pi} S(v_{\bar{x}}, v_{\bar{z}}) = \begin{cases} \left(\frac{2}{\pi}\right) B k^4 / (\kappa^2 + k^2)^4 & k \leq k_c \\ 0 & k > k_c \end{cases} \quad (29)$$

where W is the notation used by Rice (1951) and S is the notation used by Brown (1978). For the assumed isotropic model of the sea surface

$$\begin{aligned} B &= 0.0046 \\ \left. \begin{aligned} k^2 &= v_{\bar{x}}^2 + v_{\bar{z}}^2 \text{ (cm)}^{-2} \\ \kappa &= (335.2 V^4)^{-1/2} \text{ (cm)}^{-1} \end{aligned} \right\} , \quad \left. \begin{aligned} k_c &= 12 \text{ (cm)}^{-1} \\ V &= 4.3 \text{ (m/s)} \end{aligned} \right\} \quad (30) \end{aligned}$$

i. which k_c is the spectral cutoff wavenumber (Brown 1978) and V is the surface wind speed. The wavelength for the electromagnetic wave is

$$\lambda_0 = 3.0 \text{ cm } (k_0 = 2\pi / \lambda_0 \text{ (cm)}^{-1}) . \quad (31)$$

The relative complex dielectric coefficient for the sea is

$$\epsilon_r = 48 - i35 \quad (32)$$

and the permeability for the sea is the same as for free space ($\mu_r = 1$).

The mean square height for the small scale surface h_s is given by

$$\langle h_s^2 \rangle = \int_0^{2\pi} \int_{k_d}^{k_c} \frac{W(k)}{4} k dk d\phi = \frac{B}{2} \left[\frac{1}{k_d^2} - \frac{1}{k_c^2} \right] . \quad (33)$$

The mean square slope for the large scale surface h_l within the resolution cell, is

$$\sigma_{ls}^2 = \langle h_{ls}^2 \rangle = \int_0^{2\pi} \int_{k_s}^{k_d} \frac{W(k)}{4} k^3 dk d\phi \quad (34)$$

in which k_s is given by (25). The mean square height for the large scale surface h_l is

$$\langle h_{\ell}^2 \rangle = \int_0^{2\pi} \int_0^{k_d} \frac{W(k)}{4} k dk d\phi \quad (35)$$

For $\beta = 4k_o^2 \langle h_{\ell}^2 \rangle = 1.0$, $k_d = 0.201$. For $L_s = 300, 1000$ and 2500 cm (25)

$\sigma_{\ell s}^2 = 0.0102, 0.0143$ and 0.0152 respectively

and

$k_o^2 \langle h_{\ell}^2 \rangle = 21.9, 173$ and 357 respectively. The slope probability density function within a resolution cell is assumed to be Gaussian; thus

$$p(h_x, h_z) = \frac{1}{\pi \sigma_{\ell s}^2} \exp \left[-\frac{h_x^2 + h_z^2}{\sigma_{\ell s}^2} \right] \quad (36)$$

and the physical optics (specular point) backscatter cross section is (8) (Bahar, 1981a)

$$\langle \sigma_{\infty}^{PQ} \rangle_B = \delta_{PQ} \frac{\sec^4 \theta_o}{\sigma_{\ell s}^2} \exp \left[-\frac{\tan^2 \theta_o}{\sigma_{\ell s}^2} \right] |R_p|^2 \quad (37)$$

in which δ_{PQ} is the Kronecker delta and $R_p(P=V,H)$ is the Fresnel reflection coefficient for the vertically or horizontally polarized waves (Bahar, 1981a,b).

In Fig. 1a, and b $\langle \sigma^{VV} \rangle$, and $-(d\langle \sigma^{VV} \rangle / d\Omega) / \langle \sigma^{VV} \rangle$ are plotted for $\Omega = 0$ and $\tau = 0$ as functions of θ_o' the angle of incidence with respect to the fixed reference system (x', y', z') . In these figures $L_s = 300, 1000$ and 2500 cm.

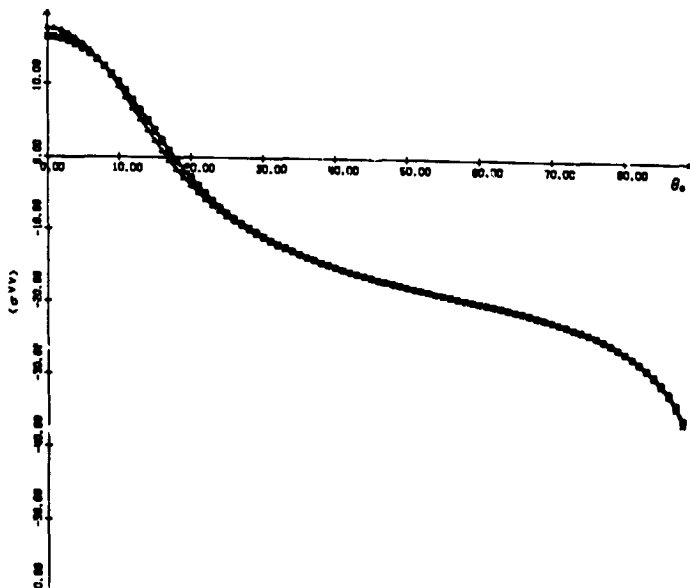


Figure 1a. $\langle \sigma^{VV} \rangle$, for $\Omega = 0$ and $\tau = 0$ as a function of θ_o' .
(Δ) $L_s = 300$ cm, (\circ) $L_s = 1000$ cm,
(\square) $L_s = 2500$ cm.

ORIGINAL PAGE IS
OF POOR QUALITY

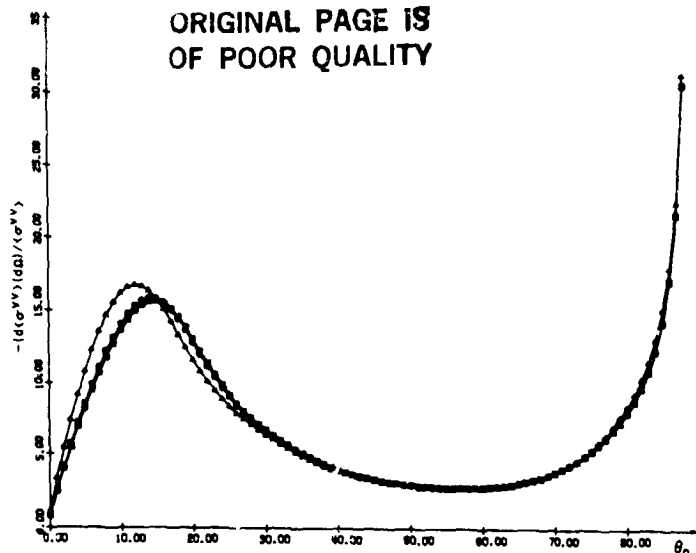


Figure 1b. $-(d\langle\sigma^{VV}\rangle/d\Omega)/\langle\sigma^{VV}\rangle$ for
 $\Omega = 0$ and $\tau = 0$ as a function of
 θ_0' . (Δ) $L_s = 300$ cm,
(\circ) $L_s = 1000$ cm,
(\square) $L_s = 2500$ cm.

In Fig. 2a, and b these results are repeated for $\langle\sigma^{HH}\rangle$. It is interesting to note that the effective filtering of the very large scale spectral components of the rough surface ($0 < k < k_s$) by the SAR does not significantly change the value of σ^{PQ} unless $L_s < 300$ cm. As one may expect, the modulation of the scattering cross sections in the plane of incidence $|d\langle\sigma^{VV}\rangle/d\Omega|$ is strongest for the SAR corresponding to the narrowest effective beam width $L_s = 300$ cm. Except for near-normal incidence the relative modulation $|d\langle\sigma^{PQ}\rangle/d\Omega|/\langle\sigma^{PQ}\rangle$ is larger for the horizontally polarized waves than for the vertically polarized waves. The largest relative modulation of the like polarized cross sections occurs in the transition region where the contribution to the cross section due to Bragg scatter becomes larger than the contribution due to specular point scatter namely at about 10° - 15° (see Figs. 1b and 2b).

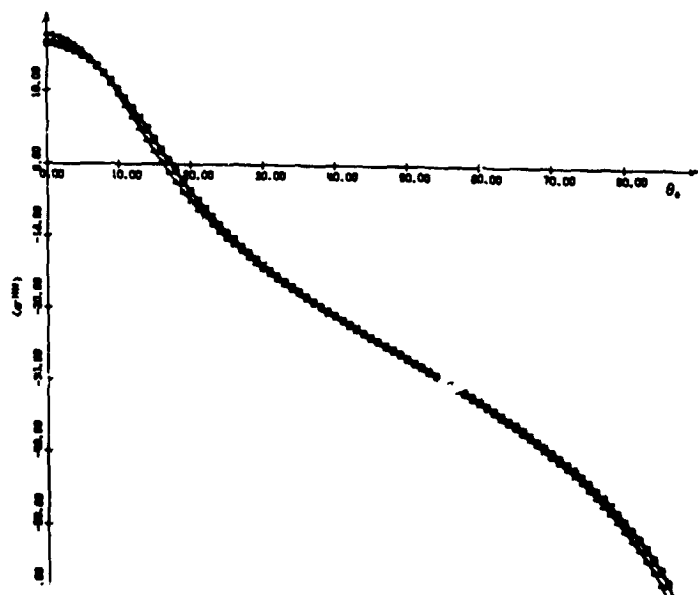


Figure 2a. $\langle\sigma^{HH}\rangle$, for $\Omega = 0$ and
 $\tau = 0$ as a function of θ_0' .
(Δ) $L_s = 300$ cm, (\circ) $L_s = 1000$ cm,
(\square) $L_s = 2500$ cm.

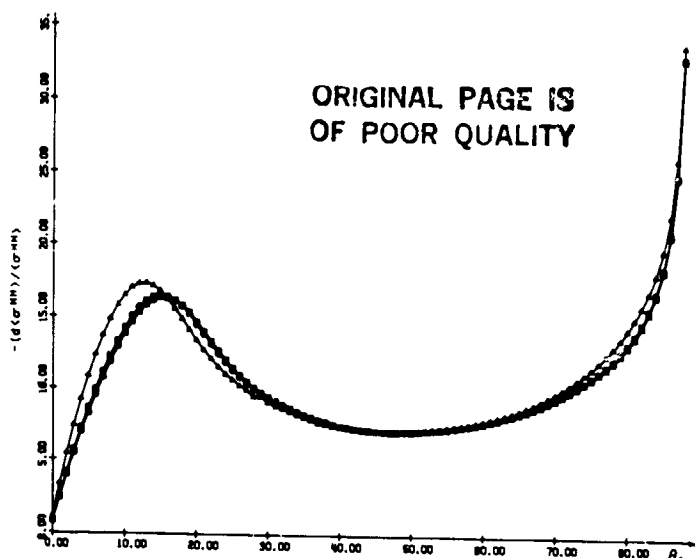


Figure 2b. $-(\langle \sigma^{HH} \rangle / d\Omega) / \langle \sigma^{HH} \rangle$ for $\Omega = 0$ and $\tau = 0$ as a function of θ_o^i . (Δ) $L_s = 300$ cm, (\circ) $L_s = 1000$ cm, (\square) $L_s = 2500$ cm.

5. CONCLUDING REMARKS

The full wave approach is used to determine the scattering cross sections for arbitrarily oriented resolution cells on random rough surfaces illuminated by synthetic aperture radars. The purpose of this analysis is to determine the modulation of the like polarized scattering cross sections as the normal to the cells tilt in and perpendicular to the plane of incidence. The full wave approach accounts for shadowing and both specular point scattering as well as Bragg scattering in a self-consistent manner. Thus, the scattering cross sections are expressed as weighted sums of two cross sections. The first cross section is associated with the filtered surface consisting of the large-scale spectral components of the rough surface. The second cross section is associated with the surface consisting of the small-scale spectral components. It can be shown that if the large-scale spectral components of the surface of the cell are neglected, the second cross section accounts for first order Bragg scattering and the results are in agreement with earlier published results (Alpers et al., 1981). However, for typical terrain or sea surfaces, the large-scale spectral components are not negligible.

By using the full wave analysis, the modulation of the like and cross polarized cross sections can be determined for all angles of incidence and tilt angles. On the other hand, first order Bragg scatter theory does not account for backscattering near normal to the surface of the cell (Alpers et al., 1981). The results based on the two-scale model indicate that the relative modulation of the like polarized backscatter cross section is maximum for angles of incidence between 10° and 15° (depending on polarization and effective width of the resolution cell, L_s). The analyses based on first order Bragg scatter do not provide these results. It is also shown that as the angle of incidence approaches zero, the modulation of the scattering cross sections in and perpendicular to the plane of incidence becomes comparable.

When the normal to the cell is tilted in the direction normal to the plane of incidence ($\tau \neq 0$), the full wave analysis not only accounts for the change in the local angle of incidence θ_o^i but also takes into account the fact that the local planes of incidence (or scatter) are not parallel to the reference planes of incidence for scatter), namely $\psi_F^i = -\psi_F^f \neq 0$.

Since Alpers et al. (1981) do not account for the effects of the large scale spectral components of the surface within the resolution cell the results presented here for the modulation of the like polarized scattering cross sections near normal incidence are significantly different from those given by Alpers et al.

6. REFERENCES

- Alpers, W. R., D. B. Ross and C. L. Rugenach (1981): On the detectability of ocean surface waves by real and synthetic aperture radar, J. Geophys. Res., 86(C7), 6481-6498.
- Bahar, E. (1981a): Scattering cross sections from rough surfaces--full wave analysis, Radio Sci., 16(3), 331-341.
- Bahar, E. (1981b): Scattering cross sections for composite random surfaces--full wave analysis, Radio Sci., 16(6), 1327-1335.
- Bahar, E., D. E. Barrick and M. A. Fitzwater (1983): Computations of scattering cross sections for composite surfaces and the specification of the wavenumber where spectral splitting occurs, IEEE Transactions on Antennas and Propagation, to be published.
- Barrick, D. E. (1970): Rough surfaces, in Radar Cross Section Handbook, Chapter 9, Plenum Press, New York.
- Brown, G. S. (1978): Backscattering from a Gaussian-distributed perfectly conducting rough surface, IEEE Transactions on Antennas and Propagation, AP-26(3), 472-482.
- Rice, S. O. (1951): Reflection of electromagnetic waves from a slightly rough surface, Communication of Pure and Applied Math., 4, 351-378.
- Sancer, M. I. (1969): Shadow-corrected electromagnetic scattering from a randomly rough surface, IEEE Transactions on Antennas and Propagation, AP-17(5), 577-585.
- Smith, B. G. (1967): Geometrical shadowing of a randomly rough surface, IEEE Transactions on Antennas and Propagation, AP-15(5), 668-671.
- Valenzuela, G. R. (1968): Scattering of electromagnetic waves from a tilted slightly rough surface, Radio Sci., 3, 1051-1066.
- Valenzuela, G. R., M. B. Laing and J. C. Daley (1971): Ocean sea spectra for the high frequency waves as determined from airborne radar measurements, J. Marine Res., 29, 69-84.

This paper was sponsored by the U. S. Army Research Office, Contract No. DAAG-29-82-K-0123 and the Wave Propagation Laboratory, NOAA. The text of the full paper will be published in Radio Science.

TRACKING OCEAN WAVE SPECTRUM FROM SAR IMAGES

A. D. Goldfinger, R. C. Beal, F. M. Monaldo, D. G. Tilley
The Johns Hopkins University/Applied Physics Laboratory
Johns Hopkins Road, Laurel, Maryland 20707, USA

ABSTRACT

For several years we have been working on an end-to-end algorithm for recovery of ocean wave spectral peaks from SAR images. We report on the progress that has been made, and show that current approaches are allowing precisions of 1 percent in wave number, and 0.6 deg in direction.

1. INTRODUCTION

A SAR image spectrum is a complex product of the actual ocean wave spectrum, the physics of the scattering process, the SAR instrument, the processing algorithms, and many other effects and parameters. From one or more of these spectra, we seek to either recover the actual ocean wave energy spectrum or to estimate other derived parameters of interest, such as the locations of storm sources.

An overall mode_ is shown in Fig. 1. The left side shows the effects that occur in the production of a SAR spectrum. The right side shows the steps we are undertaking in recovery of information from such a spectrum.

Starting from the actual ocean surface, the physics of the microwave scattering process determines a distribution of scattering cross-section on the sea surface, the so-called " σ_0 map". The physics of this process was the subject of a workshop held at APL in October 1982. We will not discuss this further here but instead refer the interested reader to Beal (1982).

The σ_0 map is viewed by the SAR instrument and three types of corruption occur:

1. Dynamic effects: due to motion of the sea surface, scattered energy is defocused and/or displaced in the SAR image. Both effects serve to decrease azimuth (along-track) resolution, creating a roll-off in the system transfer function for energy with high azimuth wave number. This is described by Monaldo (1983) and Beal, et al. (1983).
2. SAR instrument: the impulse response of the SAR instrument determines a modulation transfer function (MTF), which may vary with time, and certainly is a function of the SAR processor employed.

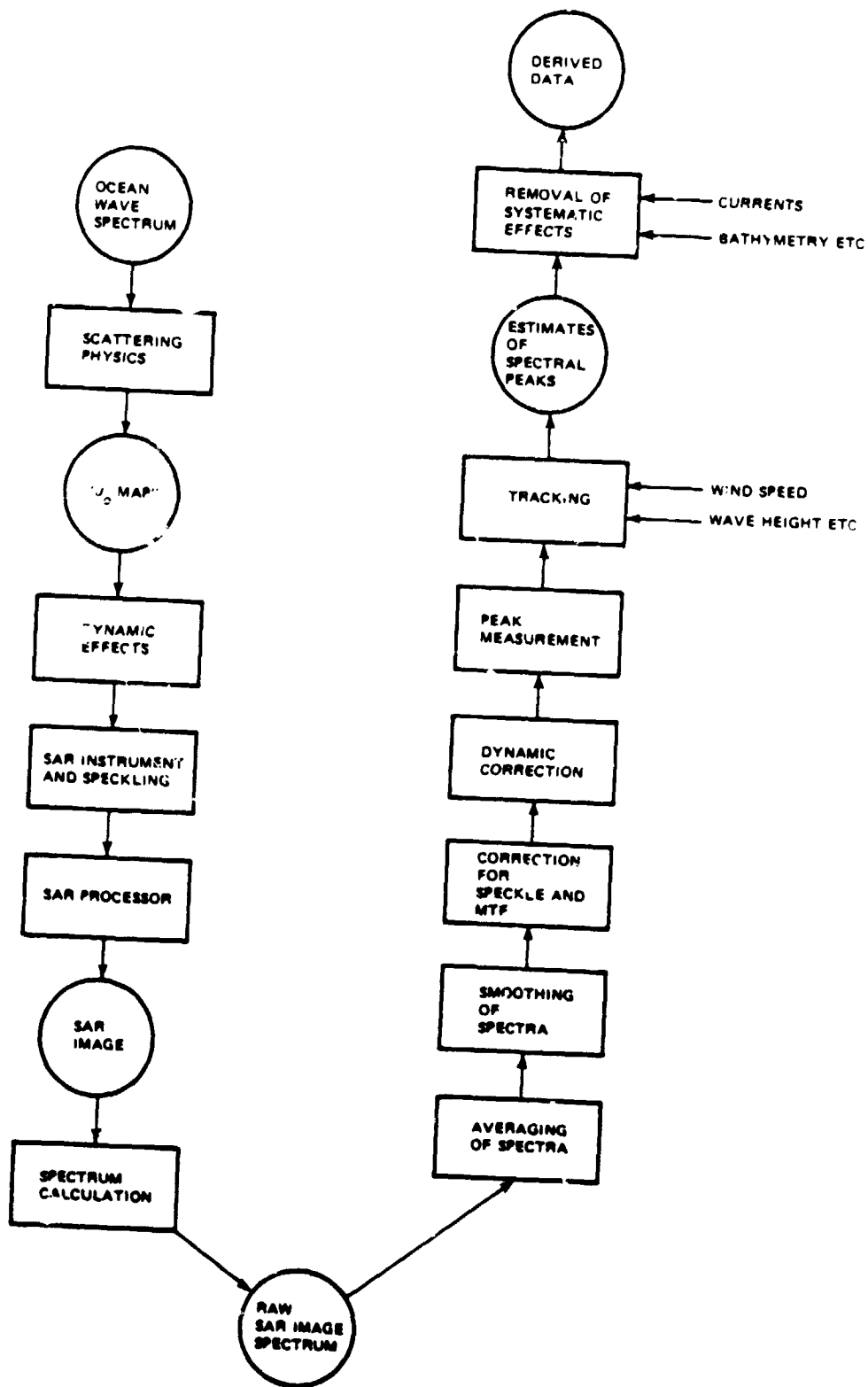


Fig. 1 End-to-end model.

3. Speckle: the coherence of the scattering process results in constructive or destructive interference of the energy returned from each resolution cell. This causes the image to appear speckled. Viewed as an independent process, the effect on image spectra is discussed by Goldfinger (1982). Below, we show what happens when speckling and MTF are considered together.

The final two steps in the production of a SAR spectrum are the computations involved in SAR processing and calculation of the image spectrum. That SAR processor effects are important is demonstrated by Goldfinger (1980).

Armed with the "raw" image spectrum, we go through the series of steps shown on the right side to produce the final estimate of the ocean wave energy spectrum or derived parameters. Since the raw spectra are noisy, it is desirable to average sequential spectra and smooth individual spectra. Following this, the system MTF, which has been estimated by calibration procedures outlined by Beal, et al. (1981), is used to correct for the MTF-speckle effects by an algorithm we describe below. Next, a correction for the dynamic azimuth roll-off is applied, as discussed by Monaldo (1983); and further averaging and smoothing are performed, if needed.

Finally, the spectral peaks are located, measured, and tracked along the pass. The tracking filter to be used can incorporate independent parameters such as wave height or wind velocity in determination of the appropriate filter gains. More will be said of this below.

If derived data, such as storm source position, are desired, it may be necessary to further correct the spectral peak positions for systematic effects such as bathymetry or currents before performing whatever computations are necessary, such as backward and forward extrapolation of wave vectors.

In presenting the above model, we have made the cavalier assumption that the various effects can be separated. For example, we have assumed that the dynamic motion effects can be separated from the SAR instrument and speckling effects. Such assumptions should be regarded as provisional rather than dogmatic. We expect to test each such assumption in turn, and to combine effects when we find they cannot be separated.

For example, in our early work, we assumed that the effects of MTF and speckle could be treated independently. However, a theoretical analysis has shown that this is not true, and hence the two effects are now combined in the model.

2. PROGRESS ON THE PROBLEM

For several years, we have been attempting to understand the above end-to-end process. Our understanding is still incomplete, but partial progress has already been reported in the references. Below, we report on the current status of several items.

2.1 Scattering Physics

Although the "transfer function" due to this process is the subject of current controversy (Beal, 1982), we have found it useful to assume that the relationship between ocean surface slope and radar cross-section is linear. We do so for two reasons:

- a. If the transformation between slope and cross-section were strongly nonlinear, then the appearance of higher-order harmonics and intermodulation products of the fundamental ocean frequencies could be expected. Such artifacts have not been observed in SAR image spectra gathered in regions of open water
- b. The primary nonlinear aspect of SAR ocean imagery does not appear to reside in the slope to radar cross-section transformation but rather in the distortion of the SAR image introduced by the presence of ocean surface movement. This nonlinearity, we have shown, can be modeled as a simple resolution loss in a linear system.

Thus, at present, a linear model is still proving useful for the ocean surface slope-radar cross-section relationship.

2.2 Dynamic Effects

It is now well established that wave motion at high sea states causes an azimuth wave number fall-off that tends to rotate the apparent direction of the spectral peaks toward the range (cross-track) direction (Monaldo, 1983). Below, we report the progress we have made in correcting for this effect.

2.3 SAR Instrument and Speckle

The effect of coherent speckle on image spectra in a system with unity transfer function has been treated (Goldfinger, 1982). If $S_0(\underline{k})$ is the spectrum of the σ_0 map, the mean SAR image spectrum will be:

$$S'(\underline{k}) = S_0(\underline{k}) + \frac{1}{N} \int d\underline{k} S_0(\underline{k}) \quad (1)$$

where N is the number of looks. That is, the mean image spectrum has a bias added that is proportional to the integrated spectral power. The situation becomes more complex when the system modulation transfer function (MTF) is added. The speckle and MTF effects cannot be separated. We have shown that for Gaussian systems:

$$S'(\underline{k}) = M(\underline{k}) \left[S_0(\underline{k}) + \frac{C}{N} \int d\underline{k} M(\underline{k}) S_0(\underline{k}) \right] \quad (2)$$

where M is the MTF and C is a constant. Thus, the spectrum is now weighted by the MTF, as is the power integral taken in the bias term.

For non-Gaussian systems, the result is more complex; but analysis of the SEASAT MTF has shown that it is well approximated by a Gaussian, so eq. (2) can be used. Analysis of the statistics of the individual spectra shows that the assumptions used in deriving eqs. (1) and (2) are valid (Monaldo, 1983).

2.4 SAR Processing Effects

In Goldfinger (1982) and (1980) we have investigated the effects of processor signature in determining system MTF, and shown how to calibrate this aspect of the end-to-end system (Tilley, 1983). We have shown that the total SAR system must be separately calibrated for each SAR processor that is used. This area is now well enough understood that no further work appears necessary.

2.5 Smoothing and Averaging of Spectra

In the averaging of spectra, we encounter a trade-off between averaging more spectra to increase statistical reliability and averaging fewer spectra to examine changes in the ocean spectrum that occur on small spatial scales. Based upon our observation and analysis of data from pass 1339, which covered a 900×100 km region off the eastern coast of the United States on September 28, 1978, it was found that spectral variations on the scale of 30 to 40 km tended to be random rather than systematic. Evidence based upon measurement of the correlation distance of the spectrum tended to confirm that these small-scale variations were more characteristic of the instrument and scattering processes than of actual variations of the sea surface. Accordingly, we chose to smooth spectra with a Gaussian kernel extending over about 40 km (i.e., for spectra spaced 6.25 km apart, 15 spectra were averaged along-track with a Gaussian weighting kernel of half width 40 km). This smoothing appeared to be fairly optimal for pass 1339, in that it revealed the local variability caused by the Gulf Stream as well as shallow water bottom features. Whether this will be generally true for other passes remains to be seen.

In addition to along-track averaging, we have usually applied k-space smoothing to individual spectra. A typical Gaussian smoothing distance was seven wave number intervals. Again a trade-off between resolution and statistical reliability occurs.

2.6 Correction for Speckle and MTF

Based upon eq. (2), we have determined the following algorithm for recovering spectra from a SAR image:

- a. Estimate MTF by taking the spectrum of a SAR image of a uniform scene (e.g., a field).
- b. Correct the specimen SAR spectra by dividing by MTF and then subtracting a bias.

The efficacy of this algorithm in regions of low to moderate sea state has been reported by Beal and Tilley (1980). The spectral peak

positions so obtained have been shown to be highly consistent with known storm sources (Monaldo, 1983). The algorithm is thus well established, except that in cases of high sea state it must be combined with the procedure for azimuth fall-off correction. In general, the correction can be applied only out to azimuth wave numbers well above the noise. The azimuth fall-off problem apparently can be eliminated only by orbiting very low altitude (~ 250 km) SAR systems.

2.7 Dynamic Correction

We have attempted to correct the azimuth fall-off by using a linear semi-empirical model. A Gaussian function in azimuth wave number is fit to a region of the spectrum assumed not to contain any actual spectral power (i.e., the region of very high wave range number). The entire spectrum is then divided by this correction factor.

When this is done, the position of the observed spectral peaks are seen to increase their consistency with known storm sources. Thus, empirical evidence exists which confirms the value of this approach. However, at this time, the procedure and its limitations are still not adequately understood theoretically, a situation we hope to improve in the future.

2.8 Peak Measurement

So far, three algorithms have been used to determine peak position:

1. Manual: the spectrum is displayed to an operator who uses cross hairs and a joystick to subjectively locate the peak.
2. Automatic/Peak: the peak value of the spectrum is selected automatically.
3. Automated/Center of Gravity: the center of gravity of all pixels exceeding some fraction of the peak is calculated.

Ideally, when presenting spectra to an operator for manual measurement, they should be arranged in random sequence. In our initial study, however, this was not done, and the spectra were presented sequentially. As a result, some "subjective tracking" was performed in obtaining the manual measurements.

At the moment, method 3 appears to be easily feasible, and is at least as accurate as method 1. Method 2 is most noisy.

2.9 Tracking

Most satellite SAR data sets consist of a series of images taken at roughly the same time along an extended swath of ocean coverage. If the scale of ocean variability is large compared to the separation of adjacent images, spectral features can be tracked from one frame to the next with improved accuracy of location.

To date, we have applied simple smoothing filters and experimented with more complex Kalman filters. To construct the latter, we have represented the system state vector as the following superposition:

$$\underline{k}(t) = \underline{k}_0(t) + \delta \underline{k}_s(t) + \delta \underline{k}_c(t) \quad (3)$$

in which \underline{k} is the system state, composed of \underline{k}_0 , the actual wave number, $\delta \underline{k}_s$, small-scale variations, $\delta \underline{k}_c(t)$, the occasional jumps due to current boundaries. Statistically, we model \underline{k}_0 as a random walk, $\delta \underline{k}_s$ as a Gaussian process with exponential autocorrelation, and $\delta \underline{k}_c$ as a Poisson process.

In choosing filter parameters, we have used the following recently-derived information:

- a. On a scale of 10 to 20 km, the variability observed in ocean spectra is due to instrumental or noise effects rather than systematic variation of the ocean waves. Therefore, tracking filters that smooth over such distances will not destroy useful information.
- b. The rms errors in spectral peak measurement are dependent upon mean wind speed. A simple linear model ($\sigma^2 = A + BU$, where σ^2 is the error in spectral peak measurement and U is wind speed) has been fit to the data. Therefore, a filter whose gains are dependent on wind speed or other environmental parameters would be of value.

3. RESULTS SO FAR

Figures 2 and 3 show the results of a typical application of our end-to-end estimation procedure to the primary spectral peak of pass 1339.

A preliminary analysis of the residuals along the pass shows that spectral peaks can be measured with a wave number precision of .0003 to .0004 rads/m (i.e., ~ 1 percent of mean wave number) and an angular precision of 0.6 deg. We emphasize that this is the result of detailed analysis of a particular wave system over a single pass, and hence, should not yet be generalized to other passes or circumstances.

4. REFERENCES

- Beal, R. C. and D. G. Tilley, 1980: Optimal spatial filtering and transfer function for SAR ocean wave spectra. Proceedings of Workshop on SAR Image Quality, ESA Report SP-172, Frascati, Italy.
- Beal, R. C., A. D. Goldfinger, D. G. Tilley and W. J. Geckle, 1981: Calibration strategies for spaceborne synthetic aperture radar. JHU/APL Report CP-084.
- Beal, R. C., 1982: SEASAT SAR workshop on ocean wave spectra. JHU/APL Internal Report SLR-83U-019.

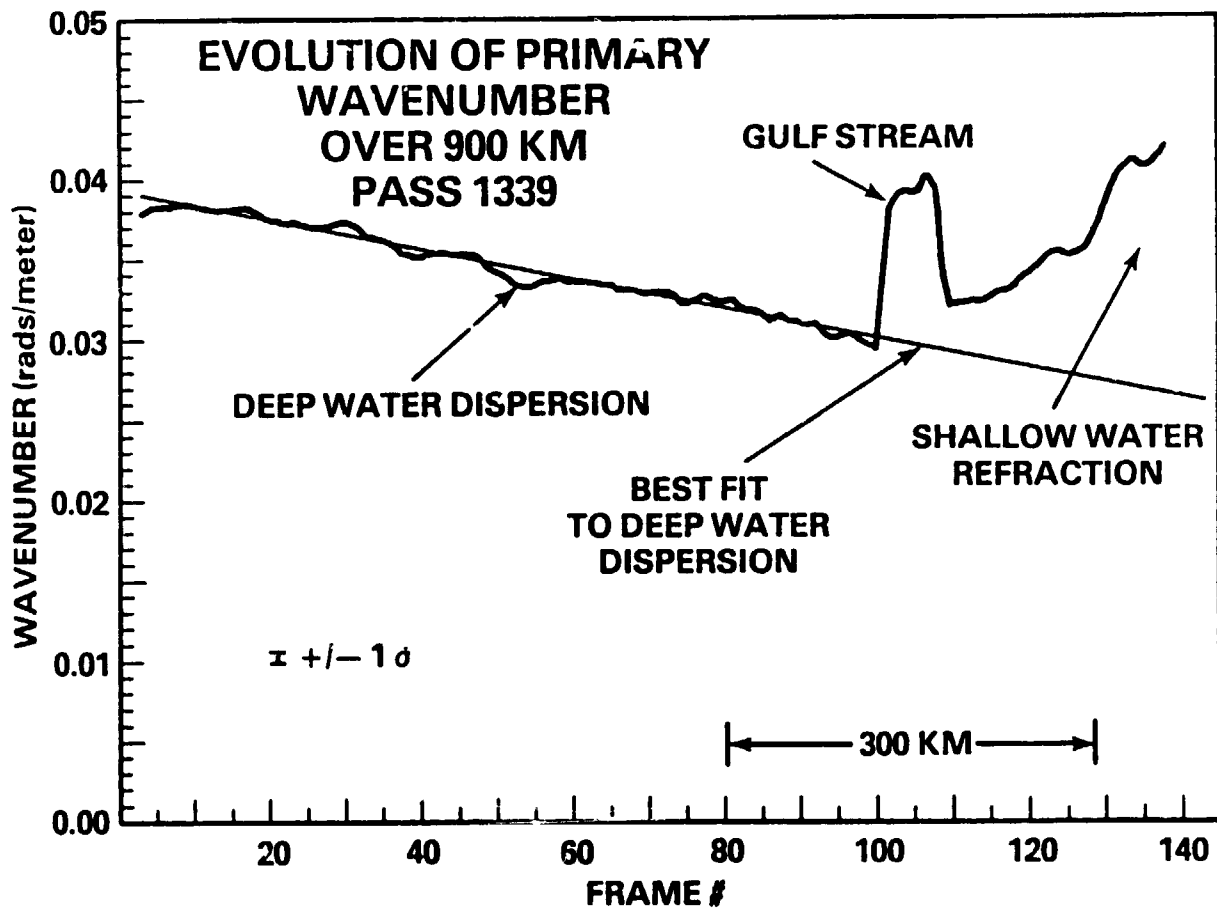


Fig. 2 Wavenumber variation.

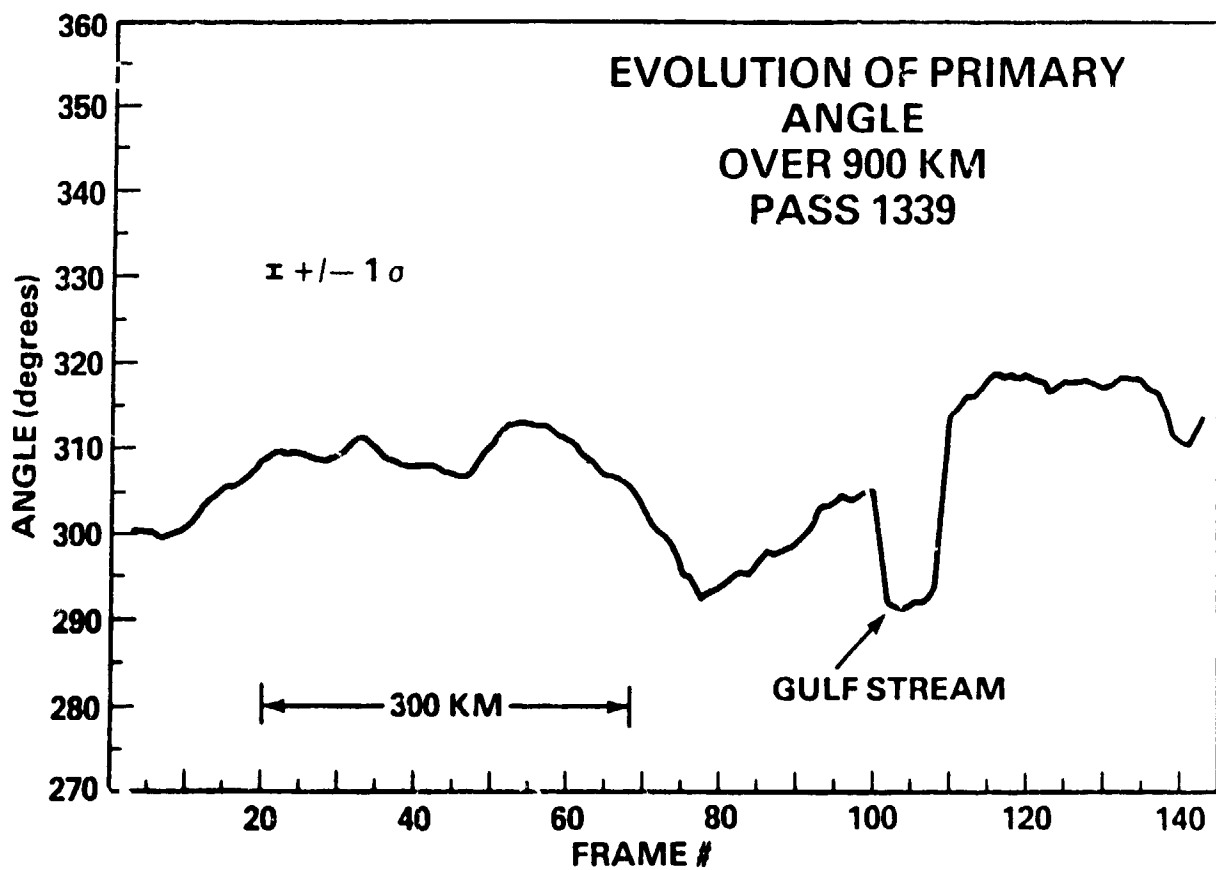


Fig. 3 Angle variation.

- Beal, R. C., D. G. Tilley and F. M. Monaldo, 1983: Large and small-scale spatial evolution of digitally processed ocean wave spectra from SEASAT synthetic aperture radar. J. Geophys. Res., 88, (C3), 1761-1778.
- Goldfinger, A. D., 1980: SEASAT SAR processor signatures: Point targets. JHU/APL Report CP-078.
- Goldfinger, A. D., 1982: Estimation of spectra from speckled images. IEEE Trans. on Aerospace and Electronic Systems, Vol. AES-18, 675-681.
- Monaldo, F. M., 1983: Tracking ocean surface waves using spaceborne SAR image spectra corrected for ocean surface movement. Proc. 1983 IGARS Symposium.
- Tilley, D. G., 1983: Fourier analysis of SAR speckle for polynomial synthesis of spectral corrections applied to SEASAT oceanic data. Proc. 1983 IGARS Symposium.

SAR IMAGERY OF OCEAN-WAVE SWELL TRAVELING IN AN ARBITRARY DIRECTION

Clifford L. Rufenach
NOAA/ERL/Wave Propagation Laboratory
Boulder, Colorado 80303

Robert A. Shuchman and David R. Lyzenga
Radar Science Laboratory
Environmental Research Institute of Michigan
Ann Arbor, Michigan 48107

ABSTRACT

The intensity wave-like patterns observed in Synthetic Aperture Radar (SAR) are known to be caused by two mechanisms: the microwave radar cross-sectional amplitude modulation due to tilt and hydrodynamic interaction of the long ocean waves, and intensity modulation due to the motion of the long ocean waves. Two-dimensional closed form expressions of intensity wave patterns based on ocean wave swell are developed. They illustrate the relative importance of the amplitude and motion modulations; furthermore, they show that velocity bunching and a distortion due to the phase velocity of the ocean wave field are independent of the focus adjustment, provided that the second-order temporal effects are neglected. Second-order effects are small only over a limited range of ocean/radar parameters. Future modeling work should concentrate on two-dimensional expressions and numerical methods, including the anisotropy of the amplitude modulation, that will allow quantitatively compared with measurements.

1. INTRODUCTION

The interpretation of ocean wave imagery is an area of active research in microwave remote sensing of the ocean surface. The principles of Synthetic Aperture Radar (SAR) are well understood for point targets; see, for example, Raney (1971). However, SAR signatures caused by random and systematic motion of an extended surface such as the ocean are not as well understood but are of considerable interest.

To construct a SAR image, the radar utilizes the Doppler shift or equivalently its phase history, produced by the uniform platform velocity, to locate targets in the flight direction. If the targets move during the time interval required to form the phase history, then the history is modified and target locations differ from the ones expected for stationary targets. Suppose that an ensemble of targets are moving uniformly in the flight direction; then there is no relative position error between the targets. However, suppose that targets exist that are spatially separated in the flight direction with different radial velocity components. The radar then senses the displaced Doppler histories in the flight direction, by a process called "velocity bunching." This bunching, which is unique to the SAR, can allow the detection of ocean waves and ocean-current boundaries even when the radar cross section is uniform. However, second-order temporal (quadratic phase) effects that include the random nature of the surface also called scene coherence and the

orbital acceleration of the long waves can degrade the wave imaging process caused by velocity bunching.

The previous interpretation of ocean wave imagery has usually emphasized the image formation process along the flight direction, while others have considered the two orthogonal directions, along the flight and cross-flight slant range directions (see, e.g., Alpers and Rufenach (1979); Jain (1981); Valenzuela (1980); Harger (1980); Alpers et al. (1981)). The purpose of the present work is to extend earlier results to ocean waves traveling in an arbitrary direction and include the motion of temporal amplitude modulation. To accomplish this generalization, it is necessary to develop a two-dimensional, analytical expression based on the two mechanisms responsible for wave-like patterns in the imagery: (1) the cross-sectional modulation due to tilt and hydrodynamic effects, also called amplitude modulation or the modulation transfer function, and (2) the intensity modulation due to ocean wave motions. The relative importance of amplitude and artificial modulation based on an arbitrary long ocean wave orientation must be included for quantitative modeling. Furthermore, for typical ocean/radar parameters, the image formation process is non-linear except for limited ocean-wave parameters. Therefore, a closed form expression for this mapping is not usually available except for the case when the mapping is linear. However, a two-dimensional description is useful because it gives physical insight even under the above restrictions.

Jain (1981), and Shuchman and Zelenka (1978) have made specialized measurements where the maximum image contrast occurs at a focus adjustment different than expected for a stationary surface. SAR images are brought into focus at the focal (reference) plane by adjusting the matched filter chirp rates such that $\Delta b_x = \Delta b_r = 0$ in Eq. (6). Jain (1981) has suggested that this defocus is equal to the azimuthal component of the long wave phase velocity; whereas Alpers et al. (1981) has suggested that it is the radial component of the orbital acceleration of long ocean waves that causes this defocus. The expressions developed in the present work may help resolve the focus adjustment discrepancy. Also, we show that the amplitude modulation, which is not a focusing phenomenon, can also cause distortions in the inferred ocean wave field which may be important for slow flying aircraft measurements. Furthermore, the two-dimensional encountered wave-like patterns are given in terms of the apparent ocean wavelength and direction caused by the phase velocity of ocean wave swell which is relevant for both synthetic and real aperture radars.

2. SYSTEM MODEL

Suppose that a radar platform is moving with velocity V along the x direction. Furthermore, assume that a point radar scatterer is located at a range r on the surface at x , y , and at a range R at midbeam, $x = Vt$, as illustrated in Fig. 1. The surface elevation associated with the wave field is

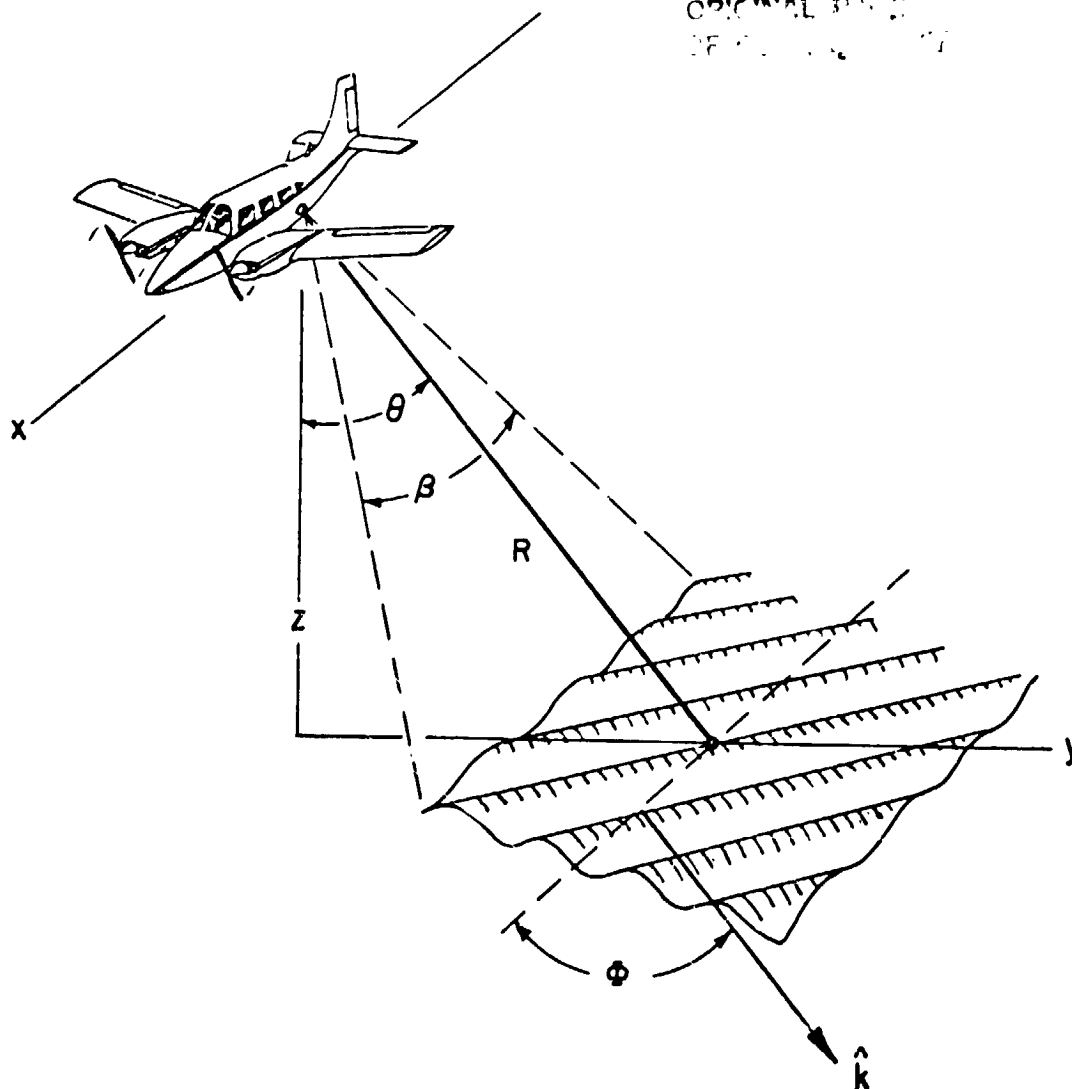


Figure 1. Artist's concept of radar/ocean geometry; θ is the angle of incidence, ϕ is the azimuth angle between \hat{k} the long ocean wave number and the flight direction and β is antenna beamwidth. A component of the long waves is traveling in the same direction as the flight direction; i.e., $\phi \neq 90^\circ$.

$$\zeta(x,y,t) = \sum_{n=1}^{\infty} \zeta_n \cos(k_{xn}x + k_{yn}y - \omega_n t) \quad (1)$$

where the ocean wavenumbers k_{xn} , k_{yn} are the components along the x- and y-directions, respectively, $k_{xn} = k_n \cos \phi_n$, $k_{yn} = k_n \sin \phi_n$, and $k_n = \sqrt{k_{xn}^2 + k_{yn}^2}$.

The complex amplitude signal backscattered from the ocean surface depends on the reflectivity properties of the surface including the time dependence of

the amplitude modulation due to the long ocean waves. The complex amplitude received at the platform based on a point scatterer, following Hasselmann (1980), is

$$dA(t, \tau) = G(x - Vt, y) E(\tau - \tau') e^{-i(b_y t^2 + b_r \tau^2)} a(x, y, t) dx dy \quad (2)$$

where G is a factor that includes the antenna-weighting function $E(\tau)$ is the pulse-weighting function, b_y is the azimuth chirp rate, b_r is the range chirp rate, and $a(x, y, t)$ is the complex amplitude reflectivity. The dependence of $A(t, \tau)$ on τ (fast time) is used in processing to determine the slant range-positions of the scattering element; the Doppler signature is related to the platform velocity and slow variability of the reflective surface through t (slow time) to infer the azimuthal x -position of the scattering element.

The received signal is compared with a reference signal in the processor which is also called a matched filter represented here by $h(t, \tau)$. The two-dimensional convolution whose output is the image complex amplitude for a point scatterer is

$$A(t-t', \tau-\tau') = \iint A(t_1-t, \tau_1-\tau) h(t'-t_1, \tau'-\tau_1) dt_1 d\tau_1 \quad (3)$$

Backscattered microwave signals from the rough sea surface are described by a two-scale Bragg scattering model first introduced by Wright (1968) and Bass et al. (1968). This model is consistent with wavelike amplitude patterns observed in imaging radar, provided that the radar resolution is smaller than the long ocean wavelength. Initially, this amplitude modulation was explained by the geometric tilting of the long ocean waves in a local reference plane. Some years later, after more complete analysis, it was shown that the straining of the short (say 1-100 cm) waves by the long waves also influenced the modulation. This straining, also called hydrodynamic interaction, causes an asymmetrical distribution of the short waves with respect to the long waves (Keller and Wright, 1975).

An extension of the previous SAR results, which shows that the amplitude modulation is dependent on the match filtering, is more easily accomplished by restricting the model to ocean wave swell, which to a first approximation can be represented by a sinusoidal long ocean wave. This simplifies Eq. (1) to one Fourier component, $\zeta(x, y, t) = \zeta_0 \cos(\hat{k}_x x + \hat{k}_y y - \hat{\omega} t)$. Therefore the complex amplitude reflectivity can be approximated by

$$a(x, y, t) \approx \left[1 + \frac{\hat{a}}{2} \cos(\hat{k}_x x + \hat{k}_y y - \hat{\omega} t) \right] e^{-i\hat{\phi}(x, y, t)} \quad (4)$$

where \hat{a} is the complex amplitude modulation index caused by the long ocean waves, $\hat{\phi}$ is the phase perturbations caused by the orbital motion, and the hat "-" indicates long ocean wave parameter. For the present model the scene coherence is neglected. The reader interested in this coherence is referred to Raney (1980), Rufenach and Alpers (1981), and Lyzenga and Shuchman (1983). The phase perturbation can usually be approximated by

$$\hat{\phi} \equiv 2k_0(\hat{u}_r t + \hat{a}_r/2 t^2), \quad (5)$$

where k is the radar wavenumber, and \hat{u}_r and \hat{a}_r are radial components of the orbital velocity and acceleration of the long waves, respectively. The amplitude modulation index can be approximated by $\dot{m} = \dot{m}_0 \sqrt{k_x^2 + k_y^2}$ based on ocean wave swell where \dot{m}_0 is the modulation transfer function given by others (see, e.g., Keller and Wright, 1975); and dependent on ocean/radar parameters. For example, suppose the long ocean waves are traveling along the radar look direction (range traveling waves) and the receiving and transmitting antennas are horizontally polarized then $m_0 = 4(\tan\theta + \cot\theta)$ or vertically polarized $m_0 = -2 \sin 2\theta/(1 + \sin^2\theta) + 4 \cot\theta$ (Rufenach et al., 1983).

The image is brought into focus in a reference plane by adjusting the quadratic phase of the matched filter. In practice, this focus adjustment is usually achieved on an optical processor by adjustments of the focal length between the platform and a stationary reference surface. Therefore the matched filter is given by

$$h(t, \tau) = e^{-i(b'_x t^2 + b'_r \tau^2)}, \quad (6)$$

where the reference chirp rates b'_x and b'_r may differ from the received chirp rates $b_x = k_0 V^2/R$ and $b_r = 2B_r/T_r$ by the differential rate $\Delta b_x = b'_x - b_x$ and $\Delta b_r = b'_r - b_r$. The received envelope of the chirp signal is related to the azimuthal bandwidth $B_x = b_x T_x/2$ and range bandwidth $B_r = b_r T_r/2$ where T_x and T_r are the azimuth integration time and the rf pulse duration, respectively.

The intensity modulation based on a point scatterer riding an ocean swell and assuming a Gaussian antenna weighting

$$G(t, \tau) = \exp\left[-\frac{2}{T_x^2} (t' - t)^2 - \frac{2}{T_r^2} (\tau' - \tau)^2\right] \quad (7)$$

is obtained by substituting Eqs. (2), (4), and (6) into Eq. (3) based on the high radar wavenumber limit ($k_0 \rightarrow \infty$), and assuming $m \ll 1$. Following Rufenach and Alpers (1981), and Hasselmann (1980) for temporal-to-spatial coordinate transformation and using straightforward but tedious mathematics,

$$|\Delta|^2 = \frac{\pi}{2} \left(1 + \frac{\Delta b_x}{b_x}\right) \left(1 + \frac{\Delta b_r}{b_r}\right) T_x^2 T_r^2 [1 + \cos(\hat{k}_x' x + \hat{k}_r' r)]$$

$$\exp\left[-\left(\frac{\pi}{\rho_x}\right)^2 \left(1 + \frac{\Delta b_x}{b_x}\right)^2 (x' - x + \frac{R}{V} \hat{u}_r')^2 - \left(\frac{\pi}{\rho_r}\right)^2 \left(1 + \frac{\Delta b_r}{b_r}\right) (r' - r)^2\right] \quad (8)$$

where $\hat{k}_x' = \hat{k}_x \left(1 - \frac{\hat{\omega}/k_x}{V}\right)$ is the apparent long ocean wavenumber,

c is the velocity of light

and $\rho_x = \frac{\pi}{2} \frac{V}{B_x}$,

$$\rho_r = \pi \frac{c}{B_r},$$

and $\hat{u}_r' = \frac{\hat{u}_r}{1 + \frac{\Delta b_x}{b_x}}$.

The high wavenumber limit is taken with the azimuth antenna diameter constant which means that the integration time is sufficiently small that all quadratic phase effects such as orbital acceleration can be neglected. The above expressions apply for an image whose azimuth scale is equal to the radar antenna beamwidth. Equation (8) illustrates that the amplitude modulation field as measured in radar images can be distorted from the actual wave field on the ocean surface. This distortion occurs only along the flight direction. Furthermore, this distortion is not caused by a quadratic phase effect. Indeed, the type of distortion in Eq. (8) is most important for slow flying aircraft when the long ocean waves are traveling along the flight direction, relevant for both synthetic aperture and real aperture radars. Equation (8) shows the dependence of amplitude modulation on image formation based on a point scatterer riding on a monochromatic ocean wave swell.

The image response based on a distributed surface such as the ocean is obtained by summing all the elementary point scatterer contributions:

$$I(x', r') = \iint |\Delta|^2 dx dr. \quad (9)$$

Using the assumptions of Alpers and Rufenach (1979) namely

ORIGINAL PAGE IS
OF POOR QUALITY

$$\dot{m}, \hat{u}_r \text{ and } \left| 1 + \frac{R}{V} \frac{d\hat{u}_r}{dx} \right|,$$

not varying much within a resolution cell we obtain

$$I(x', r') = \frac{\pi/4 T_x^2 T_r^2}{\left| 1 + \frac{R}{V} \frac{d\hat{u}_r}{dx} \right|} \left(1 + \frac{\Delta b_x}{b_x} \right) \left(1 + \frac{\Delta b_r}{b_r} \right) [1 + \dot{m}_{sar} \cos(\hat{k}'_x x' + \hat{k}'_r r')] \quad (10)$$

$$\text{where } \dot{m}_{sar} = \dot{m} \exp \left[-\frac{1}{4\pi^2} \left(\hat{k}'_x^2 \frac{\rho_x^2}{\left(1 + \frac{\Delta b_x}{b_x} \right)^2} + \hat{k}'_r^2 \frac{\rho_r^2}{\left(1 + \frac{\Delta b_r}{b_r} \right)^2} \right) \right].$$

Furthermore, if $\frac{R}{V} \frac{d\hat{u}_r}{dx} \ll 1$ then Eq. (10) simplifies to

$$I(x', r') \approx K \left(1 - \frac{R}{V} \frac{d\hat{u}_r}{dx} \right) [1 + \dot{m}_{sar} \cos(\hat{k}'_x x' + \hat{k}'_r r')] \quad (11)$$

where $K = \pi/4 T_x^2 T_r^2 \left(1 + \frac{\Delta b_x}{b_x} \right) \left(1 + \frac{\Delta b_r}{b_r} \right)$ or in terms of ocean wave swell parameters

$$I(x', r') \approx K [1 + \eta_0 \cos(k'_x x' + k'_r r') + |\dot{m}_{sar}| \cos(k'_x x' + k'_r r' + \delta)] \quad (12)$$

where $\eta_0 = R/V \zeta_0 \hat{\omega} \hat{k}_x \sqrt{\sin^2 \theta \sin^2 \phi + \cos^2 \theta}$ is the amplitude of the velocity bunching, $|\dot{m}_{sar}| \approx m_0 \zeta_0 \sqrt{\hat{k}_x^2 + \hat{k}_y^2}$ provided the radar resolution filtering of the long waves is neglected, and δ is the phase angle of the amplitude modulation. For tilt modulation $\phi = \pi/2$, which means that the surface elevation is 90° out of phase with the amplitude modulation. Equations (10) and (11) show that wave-like patterns in the image caused by ocean wave swell are due to two mechanisms: velocity bunching and amplitude modulation. These equations hold only over a narrow range of ocean/radar parameters since quadratic effects such as orbital acceleration have been neglected. However, they do illustrate the relative importance of the real and artificial modulations. The amplitude modulation is the factor within the square brackets in Eqs. (10) and (11). Equation (11) and (12) are linear expressions relating the wave field to the image intensity modulation.

The Synthetic Aperture Radar is generally considered to be a sensor that can measure the dominant ocean wavelength and direction. Under certain limited conditions, significant distortions can occur in both the observed wavelength and direction. Using Eq. (10) or (11) gives

$$\hat{k}'_x = \hat{k}_x - \hat{\omega}/V \quad (12)$$

$$\hat{k}'_y = \hat{k}_y \quad (13)$$

where primed parameters indicate apparent parameters, whereas the unprimed parameters refer to the actual wavefield. Therefore, the apparent wavelength is

$$\hat{\lambda}' = \hat{\lambda} \left| 1 - \frac{\hat{\omega}/\hat{k}_x}{V} \right| \quad (14)$$

where $\hat{\lambda}' = 2\pi/\hat{k}'$ and $\hat{k} = \frac{\hat{k}_x}{\cos \hat{\phi}}$,

and the apparent direction is

$$\hat{\phi}' = \tan^{-1} \left[\frac{\sin \hat{\phi}}{\cos \hat{\phi} + \frac{\hat{\omega}/\hat{k}}{V}} \right] \quad (15)$$

As an example consider two cases in which deep water swell with $\hat{\lambda} = 250$ m is traveling along and opposite to the sensor flight direction. Suppose further that the sensor is a slow-flying aircraft with $V = 100$ m/s. The phase velocity is $\hat{\omega}/\hat{k}_x = 20$ m/s which gives $\hat{\lambda}' \approx 250 (1 \pm 0.2) = 200, 300$ m. This illustrates that significant distortion can be due to other than non-linear effects under certain conditions. However, it should be noted that non-linearities, caused by orbital acceleration are likely to dominate on most occasions.

3. DISCUSSION AND SUMMARY

The wave-like patterns observed in SAR imagery are caused by two mechanisms: (1) the radar cross-sectional (amplitude) modulation due to tilt and hydrodynamic modulation by the long ocean waves and (2) intensity modulation due to the motion of the ocean surface which is unique to SAR. The motion-induced modulation can be separated into modulation enhancement and degradation due to the systematic orbital acceleration of the long waves and the degradation of the modulation due to the stochastic character of the wind waves. The radar amplitude modulation is dominant for ocean waves traveling perpendicular to the flight direction whereas the motion-induced modulation may dominate when ocean waves are traveling along the flight direction.

Determination of the relative importance of these underlying mechanisms is essential to a complete understanding of the radar interaction with the ocean waves and the modeling of SAR wavelike patterns; for example, see, Lyzenga et al., 1984. Interest in the different mechanisms has increased in recent years since it is difficult to separate them except for the special case when the waves are traveling exactly perpendicular to the flight direction (range

waves). For this case, motions on the surface are negligible. Most of the theoretical work has emphasized the modulation due to ocean wave motion and its associated non-linearities. A two-dimensional closed form expression is not available except over a limited range of ocean/radar parameters. This has led some workers to consider Monte Carlo numerical methods to model the image-formation process (Alpers, 1983). Two-dimensional expressions have been developed which are valid over a limited range of ocean/radar parameters. Indeed in this limited range, the Monte Carlo results that required numerical computation could be compared with closed form results such as Eqs. (10) and (11).

Equations (10) and (11) include the effects of both radar amplitude and velocity bunching modulation. These equations show the following salient features: (1) Velocity bunching is independent of focus adjustment, provided that the quadratic phase is negligibly small which normally means short integration times; however, focus adjustment will degrade the image in the same manner as in a stationary scene, and (2) Ocean wave field distortion caused by the motion of the wave field (phase velocity of the long waves) relative to the platform velocity is independent of focus adjustment, again provided that the quadratic phase is negligibly small. These conclusions are in disagreement with Jain (1981), who claims that the focus adjustment is equal to the azimuth component of the long wave phase velocity. Furthermore, the dependence of the focus adjustment on orbital acceleration as suggested by Alpers et al. (1981), is not relevant since these expressions are not valid when the orbital acceleration is important.

It is recommended that future work continue to emphasize development of quantitative two-dimensional models which give the relative importance of amplitude and motion modulation for any arbitrary orientation of the ocean wave field. Furthermore, the anisotropy of the amplitude modulation must be included in order to quantify this modulation.

ACKNOWLEDGMENTS

The NOAA portion of this work was partially supported by NASA Headquarters (Ocean Processes Branch) under work order number W-15,084. The ERIM portion of this work was supported by NASA Headquarters (Ocean Processes Branch) and ONR under contract No. N00014-81-C0692. The NASA technical monitors are Dr. Lawrence, F. McGoldrick and Dr. William Patzert and the ONR technical monitor is Mr. Hans Dolezalek.

REFERENCES

- Alpers, W. R., 1983: Monte Carlo simulations for studying the relationship between ocean wave and synthetic aperture radar image spectra. *J. Geophys. Res.*, 88(C3), 1745-1759.
- Alpers, W. R., and C. L. Rufenach, 1979: The effect of orbital motions on synthetic aperture radar imagery of ocean waves. *IEEE Trans. Antennas Propagat.* AP-27, 685-690, September.
- Alpers, W. R., R. B. Ross, and C. L. Rufenach, 1981: On the detectability of ocean surface waves by real and synthetic aperture radar. *J. Geophys.*

Res., 86(C7), 6481-6498.

Bass, F. G., I. M. Fuks, A. I. Kalmykov, I. E. Ostrovsky and A. D. Rosenberg, 1968: Very high frequency radiowave scattering by a disturbed sea surface. IEEE Trans. Antennas and Propagat., AP-16, 554-568.

Harger, R. O., 1980: The side-looking image of time variant scenes. Radio Sci. 15(4), 749-756.

Hasselmann, K., 1980: A simple algorithm for the direct extraction of the two-dimensional surface image spectrum from the return signal of a synthetic aperture radar. Int. J. Remote Sensing, 1(3), 219-240.

Jain, A., 1981: SAR imaging of ocean waves: Theory. IEEE J. Oceanic Eng. OE-6(4), 130-139.

Keller, W. C., and J. W. Wright, 1975: Microwave scattering and straining of wind generated waves. Radio Sci., 10, 139-147.

Lyzenga, D. R., and R. A. Shuchman, 1983: Analysis of scatter motion effects in Marsen X band SAR imagery. J. Geophys. Res. 88(C14), 9769-9775.

Lyzenga, D. R., R. A. Shuchman, J. D. Lyden and C. L. Rufenach, 1984: SAR imaging of waves in water and ice: Evidence for velocity bunching. J. Geophys. Res. accepted for publication.

Raney, R. K., 1971: Synthetic aperture imaging radar and moving targets. IEEE Trans. Aerosp. Electron. Syst., AES-7, 499-505.

Raney, R. K., 1980: SAR processing of partially coherent phenomena. IEEE Trans. Antennas Propagat. AP-28, 777-787.

Rufenach, C. L., and W. R. Alpers, 1981: Imaging ocean waves by synthetic aperture radars with long integration times. IEEE Trans. Antennas Propagat. AP-29(3), 422-428.

Rufenach, C. L., J. R. Apel, L. S. Fedor and F. I. Gonzalez, 1983: Surface and internal ocean wave observations. Advances in Geophysics, ed. Barry Saltzman, in press.

Shuchman, R. A., and J. S. Zelenka, 1978: Boundary Layer Meteorol., 13, 181-192.

Valenzuela, G. R., 1980: An asymptotic formulation for SAR images of the dynamical ocean surface. Radio Sci., 15, 105-114.

Wright, J. W., 1968: A new model for sea clutter. IEEE Trans. Antennas and Propagat., 16, 217-223.

OCEAN WAVES AND TURBULENCE AS OBSERVED WITH AN ADAPTIVE COHERENT
MULTIFREQUENCY RADAR

L N84 27279

Dag T Gjessing and Jens Hjeltnad
Royal Norwegian Council for Scientific and Industrial Research,
Environmental Surveillance Technology Programme
P.O. Box 25, N-2007 Kjeller, Norway

ABSTRACT

An adaptive coherent multifrequency radar system has been developed for several applications. By means of this, the velocity distribution (Doppler spectrum) and spectral intensity of 15 different irregularity scales (waves and turbulence) can be measured simultaneously. Changing the azimuth angle of the antennas at regular intervals, the directivity of the wave/turbulence pattern on the sea surface can also be studied.

Using this radar system, series of measurements for different air/sea conditions have been carried out from a coast-based platform in Southern Norway. Experiments in the Atlantic were also performed with the same equipment making use of the NASA Electra aircraft.

There are many air/sea phenomena which play a role in relation to backscattering of radio waves in the microwave region: gravity waves "modulate" the capillary wave structure, overturning wave crests produce focussing effects and also periodic regions of strong turbulence, the boundary layer wind field with strong turbulence amplified by the ocean waves will conceivably leave a patchy and even periodic footprint on the sea surface.

By virtue of the fact that our multifrequency radar allows us to measure the velocity distribution ("coherent and incoherent component") associated with 15 different ocean irregularity scales simultaneously in a directional manner, it is possible to study the different air/sea mechanisms in some degree of detail.

1 INTRODUCTION

Radio methods have a substantial potential in the study of the irregularity structure of the sea surface for several reasons:

- They provide a rather unique possibility to measure the directional wave spectra with good directional resolution
- By means of a multifrequency radio method wavelength and wave velocity can be measured independently
- It is also possible to distinguish between coherent wave motion and incoherent motion (turbulence)

We shall present a detailed theoretical and experimental study of the sea surface. We shall in particular demonstrate that a microwave illuminator can be tailored so as to optimize the coupling between electromagnetic waves and ocean waves.

There are three different problem areas:

- A. One must obtain an understanding in regard to the coupling mechanisms between the electromagnetic waves on the one hand, and the sea surface on the other.

- B. Having established information about the sea surface as a scattering surface for radio waves (the delay function $f(\vec{r}, t)$ or the spectrum $E(\vec{K}, \omega)$), it remains to establish the relationship between this "description domain of the radio scientist" and that of the ocean scientist, who want information about most significant wave-height, wave-height spectra etc.

To convert from scattering cross-section to wave-height one needs information about how gravity waves and other large scale phenomena affect the small scale phenomena (capillary waves) which are comparable with the wavelength of the radio field and which are responsible for the scattering.

- C. One needs an understanding of the fundamental hydrodynamic mechanisms.

In the current contribution we shall confine ourselves to problem area A. the interaction between electromagnetic waves and an irregular ocean surface. (See also Gjessing, Hjelmstad, Lund (1984)).

2 SCATTERING FROM A ROUGH SURFACE

2.1 A summary of basic theory

In recent contributions (Gjessing, 1981 a and b), a somewhat detailed discussion was presented of the properties of the electromagnetic field scattered from a rough surface.

The basic scattering equation can be expressed as

$$E_s(\vec{K}, t) = \int_{-\infty}^{\infty} f(\vec{r}, t) e^{-j\vec{K} \cdot \vec{r}} d^3\vec{r} \quad (2.1)$$

$$\vec{K} = \vec{k}_j - \vec{k}_s \quad \text{and} \quad |\vec{K}| = \frac{4\pi}{\lambda} \sin \theta/2$$

λ is wavelength and θ scattering angle.

In order to obtain backscatter from a scattering surface, the surface must have a structure, regular or irregular, containing scale sizes $L = \frac{2\pi}{K} = \lambda/2$.

Referring again to equation (2.1), \vec{r} is a position vector, t is time and $f(\vec{r})$ is the delay function characterizing the surface. This complex function tells us how the scattering elements contributing to the "bulk scattering cross-section σ " are distributed spatially.

Resolving \vec{r} and \vec{K} into orthogonal coordinates in the horizontal plane

$$E(\vec{K}) = \left\{ \int_{-\infty}^{\infty} f(z) e^{-jK_z z} dz \right\} \delta(K_x x) \quad (2.2)$$

where δ denotes a Dirac delta function.

The scattered field $E(K)$ vanishes unless K_x is zero. Hence, $E(\vec{K}) = 0$ unless \vec{K} is normal to the wave crest.

Let us assume that we illuminate the sea surface with a beam whose width is limited so as to cut out a section D of the ocean wave front (see figure 1).

ORIGINAL PAGE IS
OF POOR QUALITY

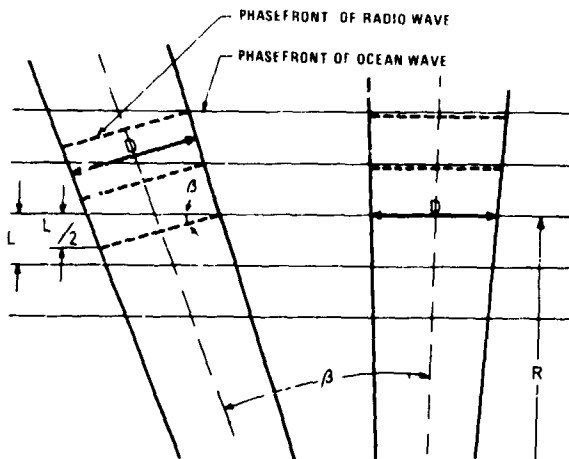


Figure 1 The geometry of the truncation (convolution) process

$$\beta = \tan^{-1} \left(\frac{L}{2D} \right)$$

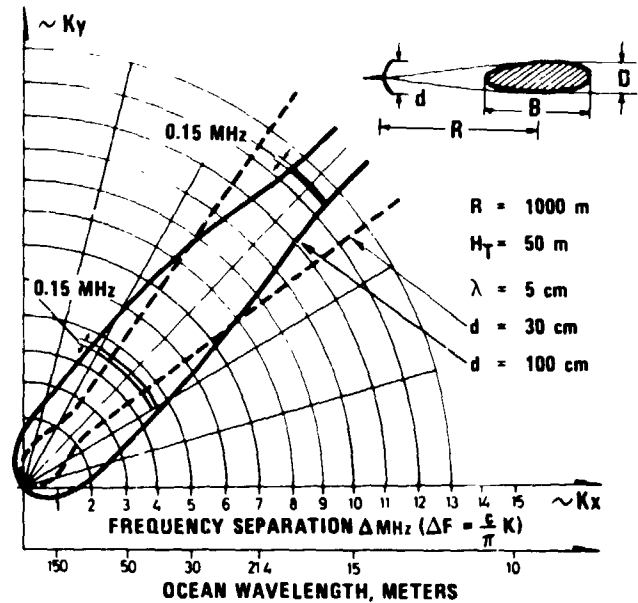


Figure 2 The angular resolution of our radar varies with ocean wavelength. As the ocean wavelength decreases, the resolution approaches that of the antenna beamwidth.

In this case $E(K_x)$ will be of a sine form instead of the Dirac delta function when approximating the antenna beam function to a rectangular distribution.

Thus, if D be the width of the truncation influencing $f(x)$, and $K = \frac{2\pi}{L}$ be the wavenumber of the one-dimensional delay function $f(z)$, (L is the ocean wavelength) then the angular width (angle between nulls) 2α of the $E(K_x)$ function is

$$2\alpha = \frac{L}{D} \quad (2.3)$$

This is a relationship well known from antenna theory. The beamwidth 2α (azimuth resolution) is determined by the antenna aperture D expressed in wavelengths L . (See figure 1).

This is illustrated in figure 2 and verified experimentally in figure 13.

The radar antenna is illuminating a range interval B measured along the direction of wave propagation. This leads to a truncation of the delay function $f(r)$. Then $\delta F_r = 0.16 \frac{C}{B}$ for an exponential function (Gjessing 1931b).

We shall now suggest a simple mathematical model based on basic and rather intuitive physical arguments to provide a simple way of assessing the experimental findings. We assume that long ocean waves (wavenumber approaching cut-off K_0) are unidirectional. The higher the wavenumber, the larger is the angular spread. For waves in the wavenumber region above K_0 , the irregularity structure is isotropic. We therefore write the complex irregularity spectrum simply as

$$E(\vec{K}) = E(|\vec{K}|, \theta) \\ = K^{-n} (\cos \theta)^s$$

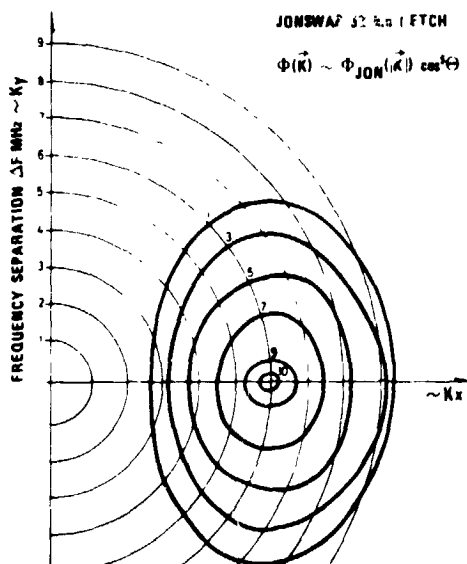


Figure 3 Complex wave spectrum calculated from the simple model presented

$$K_0 = 0, \quad K_s = \frac{2\pi}{5} \text{ m}^{-1}$$

ORIGINAL PAGE IS
OF POOR QUALITY

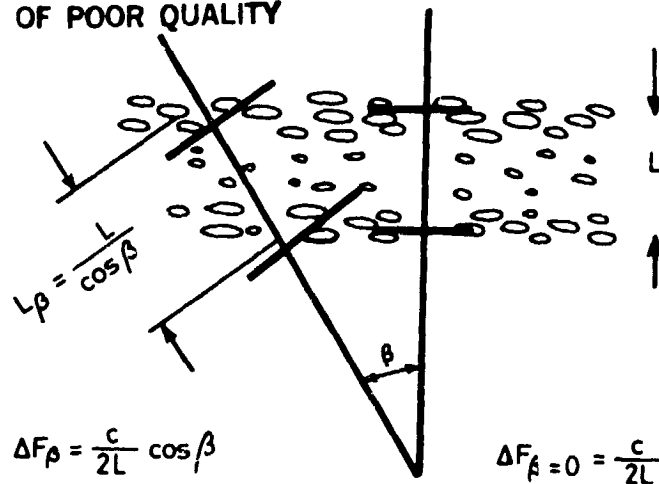


Figure 4 Scattering from turbulent irregularities caused by the "footprint" of a local wind field interacting with the wave structure of the sea

where s , the planeness parameter, is expressed as

$$s = \frac{K_s - K}{K - K_0}$$

where K_0 is the wavenumber corresponding to the short wavenumber cut-off, and K_s is the wavenumber at which the ocean surface structure becomes "random" and isotropic with no prevailing wave direction.

A local wind field may through shear mechanisms break up the coherency of the ocean wave ridge. The effect of this is to widen the angular distribution of the back-scattered radar wave considerably, as illustrated in figure 4.

Here we have obtained that the wave crests and troughs are broken up by turbulence and wave backing phenomena such that there is no "phase matching" between radio wave and ocean wave over the illuminated area contrary to the coherent case depicted in figure 1.

Thus, when turning the antennas on azimuth angle β , the radio wave sees a dominating ocean irregularity scale which is increased from L when $\beta=0$ to

$$L_\beta = \frac{L}{\cos \beta}$$

This is illustrated in figure 4. Note that for certain values of K (and the corresponding ΔF) the back-scattered radio signal will increase with increasing azimuth angle symmetrically on either side of the $\beta=0$ direction. For experimental verification, the reader is referred to figures 11 and 13.

It is well known from turbulence theory that the nearness of a rough boundary such as the sea surface results in a low wavenumber suppression of the turbulence field

and also to anisotropy (see e.g. H Panovsky 1960). (Modulation of the sea surface by the wind turbulence, anisotropic irregularity structure on the sea surface with an axis of symmetry determined by the direction of the local mean wind (Gjessing 1962).)

2.2 The multifrequency radar principle, frequency difference matching

Up to this point we have been dealing with electromagnetic waves having wavelengths which are comparable with the irregularity scale of the scattering surface.

We shall now investigate what information we can derive by matching some beat patterns (difference frequency) to the irregularity scales of the sea surface. Figure 5 illustrates the physics of the problem.

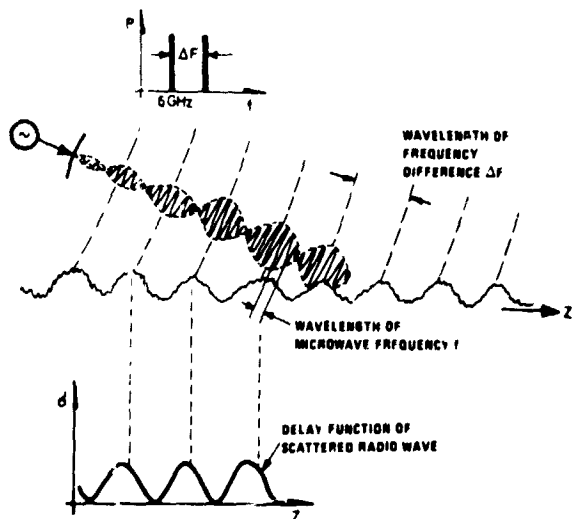


Figure 5. The interaction of electromagnetic waves with the sea surface

For this ΔK matching scheme to work (see e.g. Plant 1977), the scattering surface obviously must have irregularities which contribute to the delay function $f(z)$ for scales corresponding to the difference wavenumber ΔK . If the gravity wave structure shows up in the delay function $f(z)$, i.e. if the spectrum of $f(z)$ has Fourier components matching the wavenumber ΔK , we would experience a radar return at the beat frequency $\Delta\omega = c\Delta K$.

There are many ostensible explanations for this "modulation" of the small scale structure (to which the wavenumber \vec{K} is matched) by the long wave phenomena (to which ΔK is matched). (See e.g. Plant 1977, Plant and Schuler 1980).

It is well known that the scattering cross-section of a surface increases with incidence angle. From a sinusoidal gravity wave we shall get maximum low angle return at the point of maximum slope. The turbulent

intensity is governed by damping factors such as shear forces (Lumley 1969). Orbital motion within the wave structure changes the velocity shear periodically in phase with the gravity wave. Shadowing effects may enhance the patchiness of the radar illumination. Breaking waves and white capping resulting from the local wind field etc complicates the issue still further.

Having presented intuitive arguments based on physical interpretations, now let us describe the principle of the multifrequency radar mathematically.

We start with the simple and general expression given earlier

$$V(\frac{\omega}{c}) = E(\vec{K}) = \int_V f(\vec{z}) e^{-j\vec{K} \cdot \vec{z}} d^3z \quad (2.4)$$

and we compute the covariance $E(\vec{K}) E^*(\vec{K} + \Delta\vec{K})$ obtaining

$$E^*(\vec{K}) E(\vec{K} + \Delta\vec{K}) = e^{-j\Delta\vec{K} \cdot \vec{z}} \cdot \int R(\vec{r}) e^{-j\vec{K}\vec{r}} \cdot e^{-j\Delta\vec{K}\vec{r}} d^3r \quad (2.5)$$

$R(\vec{r})$ is the complex autocorrelation of the delay function $f(z)$. The phase factor

of the autocorrelation function (the term $e^{-j\Delta\vec{K}\cdot\vec{z}}$) is rapidly oscillating with $\Delta\vec{K}$ since the space coordinate \vec{z} is large.

The factor $e^{-j\vec{K}\cdot\vec{r}}$ represents the modulation of the spatial autocorrelation function by the radar carrier. But as the radar wavelength (5 cm) is orders of magnitude smaller than the scales of interest on the sea surface, this factor will not affect the measured sea-surface signature because the individual scatterers move independently such that the effect of the rapidly rotating phase factor will be averaged out.

This can also be argued for mathematically by noting that the integral is of the form of a Fourier integral which is symmetrical with respect to \vec{K} and $\Delta\vec{K}$. Taking \vec{K} and \vec{r} as the Fourier pair of variables, and making use of the fact that the Fourier transform of a product is equal to the convolution of the Fourier transform of each factor, the integral converges to

$$\int_{\vec{r}} R(\vec{r}) e^{-j\Delta\vec{K}\cdot\vec{r}} e^{-j\vec{K}\cdot\vec{r}} d^3\vec{r} = \delta(\vec{K}) * \phi(\vec{K}-\Delta\vec{K}) \\ = \phi(\Delta\vec{K}) \quad (2.6)$$

where $*$ denotes convolution and δ is Dirac's delta function. $\phi(\Delta\vec{K})$ is the wave-number spectrum which again is the Fourier transform of the spatial autocorrelation function $R(\vec{r})$.

As $\vec{K} \gg \Delta\vec{K}$, the term $\phi(\vec{K})$ will vanish because \vec{K} assumptionally is greater than the scattering medium cut-off wavenumber. As an example, note that if $\frac{K}{\Delta K} = 1000$, $\phi(K)/\phi(\Delta K) = 10^6$ for a rectangular distribution of scattering elements.

Normalizing this expression, we get the following familiar expression for a given fixed monostatic transmitter/receiver position

$$\frac{E^* \left(\frac{\omega}{c} \right) E \left(\frac{\omega+\Delta\omega}{c} \right)}{|E \left(\frac{\omega}{c} \right)|^2} = \frac{e^{-j\frac{\Delta\omega}{c}z} \int R(\vec{r}) e^{-j\frac{\Delta\omega}{c}\cdot\vec{r}} d^3\vec{r}}{A} \quad (2.7)$$

where A is a normalizing factor of the form $\int R(\vec{r}) d\vec{r}$.

Equation (2.7) states that the envelope of the complex correlation in the frequency domain of waves scattered back from a surface is given by the autocorrelation function $R(\vec{r})$ characterizing the surface.

2.3 The motion pattern of the sea surface

In the section above, we have shown that frequency components with mutual frequency spacing F couple to irregularity scale sizes $\Delta L = \frac{c}{2\Delta F}$.

We have already observed that the irregularity structure (the delay function) of the sea surface is determined by several mechanisms. Gravity waves are well behaved, and propagate at a velocity

$$v = \sqrt{\frac{g}{K}} = \sqrt{\frac{gL}{2\pi}} \quad (2.8)$$

where L is the wavelength.

Since the Doppler shift produced by a scatterer at velocity \vec{v} is given by $f = \frac{1}{2\pi} \vec{K} \cdot \vec{v}$

$$f = \frac{2\Delta F}{c} \sqrt{\frac{gL}{2\pi}} \quad (2.9)$$

giving

$$f = \sqrt{\frac{g\Delta F}{\pi c}} \quad (2.10)$$

We select a given ΔF_1 (which is the same as selecting a given irregularity scale L_1), and we measure how the frequency covariance function

$$R(\Delta F_1, t) = V(F, t) V^*(F + \Delta F_1, t)$$

is varying with time t . We then compute the power spectrum of the frequency covariance function $R(\Delta F_1, t)$.

If then the ordered gravity waves dominate over the incoherent velocity components which ride on the gravity waves, we would expect the Doppler spectrum to have a maximum at the frequency corresponding to the dispersion relation of gravity waves (eq (2.10) above), and we would expect a Doppler broadening determined by the velocity spread δV .

3 EXPERIMENTAL RESULTS

The adaptive multifrequency radar system developed by the authors' organization has been used for several applications: ship and aircraft identification, measurement of sea surface from a ground-based station and from an aircraft. A brief highlighting of results related to the sea surface will now be given.

3.1 Directional ocean wave spectra observed from the NASA Electra aircraft

Illuminating the sea surface by a fixed 14° beamwidth side-looking antenna pointing 10° downwards relative to the horizontal plane, the ocean wave spectra were determined for various azimuth directions and for 15 different ocean wavelengths in the interval from some 16 m (corresponds to $\Delta F = 8$ MHz) to 300 m (corresponding to $\Delta F = 1/2$ MHz). For each frequency separation ΔF the frequency covariance function $V(F, t) V^*(F + \Delta F, t)$ was computed.

The NASA Electra operated north-east of Wallops Flight Facility (38.49.2 N - 74.24 W) at an altitude of 12 000 ft, January 20, 1983, time 2203Z.

Banking the aircraft 10° so that the antennas were pointing at a depression angle of 20° , the aircraft completed a 360° circle. In this way the antenna was illuminating essentially the same area on the sea surface at all azimuth directions. The longitudinal dimension of the footprint is approximately 5600 m, whereas the transverse dimension is approximately 2000 m.

Flying in a closed circle, the frequency covariance function $V(F) V^*(F + \Delta F)$ was computed for 15 different values of ΔF for all azimuth angles. The results are shown in figure 6. Note that the Bragg angle is clearly visible for the longer wavelengths (215 - 88 m).

In terms of aircraft altitude H , depression angle α and antenna beamwidth $\Delta\theta$ we get the following expression for the Bragg angle

$$\theta = \frac{L}{2H} \frac{\sin \alpha}{\sin(\frac{\Delta\theta}{2})}$$

This is presented in figure 7. Note the good agreement between theory and experimental results.

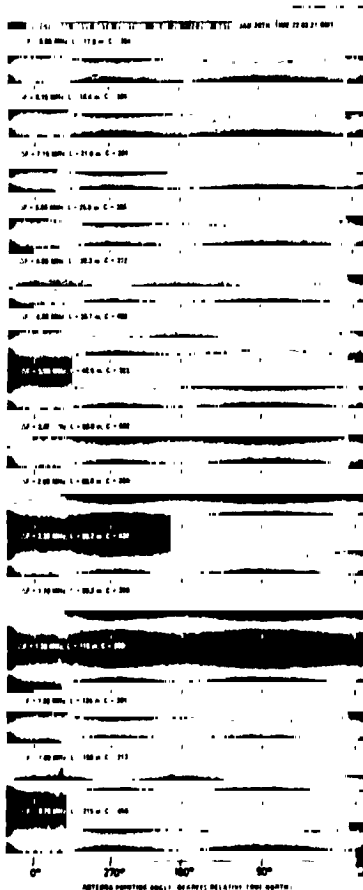


Figure 6

The aircraft flew in a closed circle pointing the antennas 30° down from 12 000 ft. The covariance function $V(F)V(F+\Delta F)$ is shown for 15 different values of ΔF .

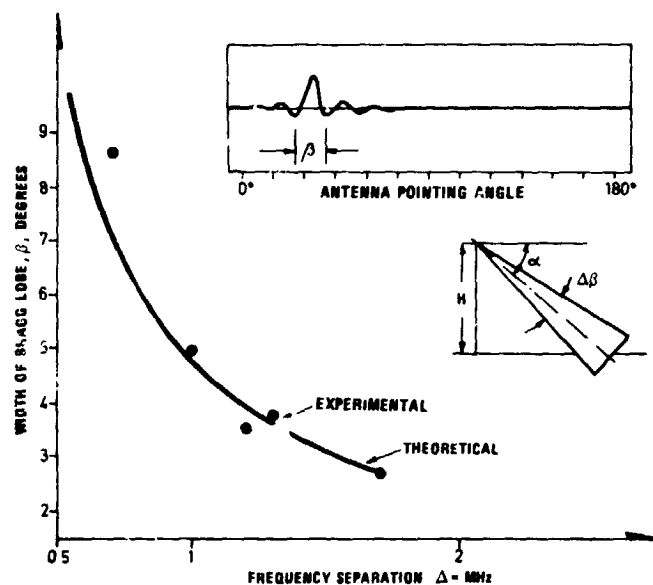


Figure 7 The measurement of Bragg angle is compared with theory. Note that the aircraft altitude is 12 000 ft, depression angle 30° and beamwidth 14° .

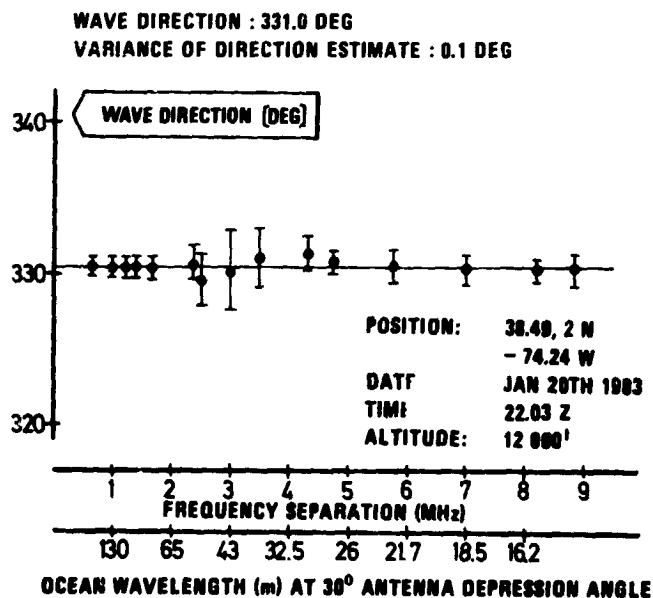


Figure 8 Wave direction plotted as a function of wavelength

ORIGINAL PAGE 19
OF POOR QUALITY

Noting the two azimuth angles corresponding to destructive interference on either side of the wave direction, this can be determined with great precision as shown in figure 8.

Finally, for an azimuth direction corresponding to that of the propagation direction of the ocean waves, the distribution with wavelength of the scattering cross-section is computed. This is shown in figure 9. Note that two wavelengths dominate, 130 m and 18 m.

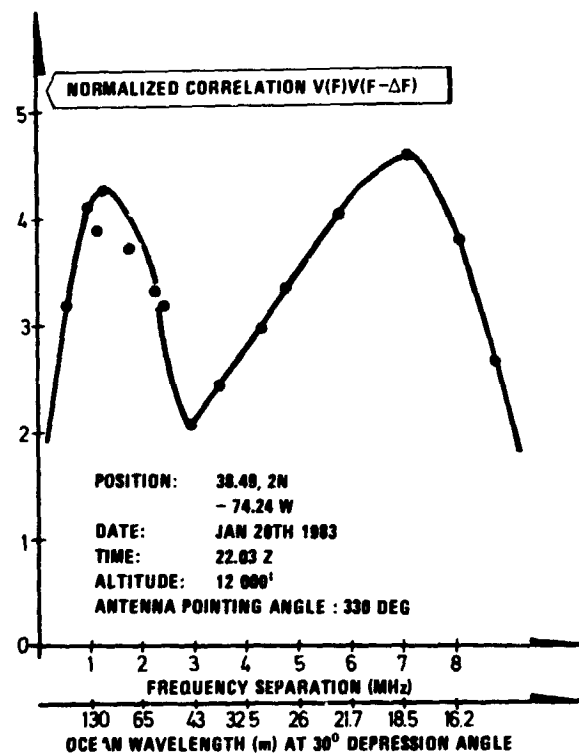


Figure 9 There are two dominating wavelengths, 130 m and 18 m.

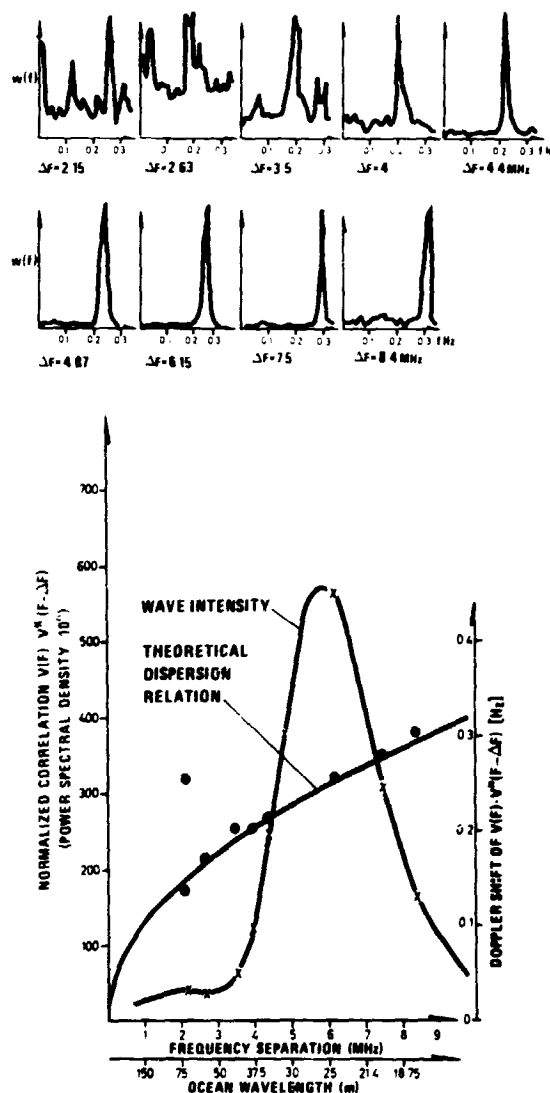


Figure 10 Spectra of wavelength and wave velocity. Note that wavelengths shorter than that corresponding to the spectral peak move at constant velocity. This is not the case for longer scales. The results are from Langesund 12 March 81 at 1030 local time, the azimuth direction being 137° .

3.2 Directional spectra obtained from ground-based station on a cliff

The complex field strength was recorded over a period of some 12 minutes before the azimuth angle was changed, thus obtaining a plot of power spectral density and Doppler spectrum as a function of frequency separation (ocean wavelength). A typical result is shown in figure 10.

ORIGINAL PAGE IS
OF POOR QUALITY

First, consider the results obtained on March 12, 1981 (1010 - 1235 local time).
The weather and sea state can be characterized as follows:

- Wind direction 90° (East)
- Wind speed approximately 8 m/s
- Wave height 1.4 m peak to peak
- Waverider gives maximum wave height for $f = 0.225$ Hz
- Wind decreasing at noon, turning northerly. Wave height reduces to 1 m peak to peak, choppy sea

Figure 12 shows the wave intensity for a particular azimuth direction and also the Doppler spectra associated with various scale sizes. Note the very well defined spectral peak in the intensity versus wavelength distribution. Note also that the Doppler frequency is in very good agreement with the theoretical dispersion relation. There seems to be a slight, but consistent, displacement to higher Doppler frequency. This is a result of an inward current.

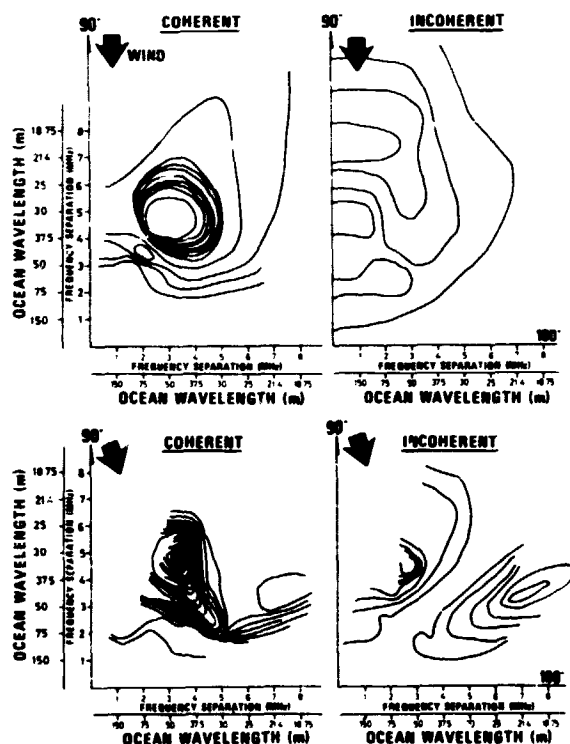


Figure 11 Isolines of spectral intensity $\Phi(\Delta\vec{K})$ in the K_x - K_y plane. Note the effect of changes in wind direction on the coherent irregularity spectrum. Note that the upper set of maps was obtained on 12 March 1981, 1010 to 1135 local time, whereas the lower set refers to the situation during the time interval 1135 to 1235.

Finally, in figure 11, we present the two-dimensional irregularity spectrum summing up the description of the sea-surface structure. Here we have plotted the isolines of spectral intensity, or more specifically the quantity $V(F) V^*(F+\Delta F)/V(F)^2$, in the K_x - K_y plane. This presentation should be compared with those of figures 2, 3 and 4. Note also that the isolines of spectral intensity $\Phi(\Delta\vec{K})$ are obtained directly from a set of one-dimensional spectra such as those shown in figure 10.

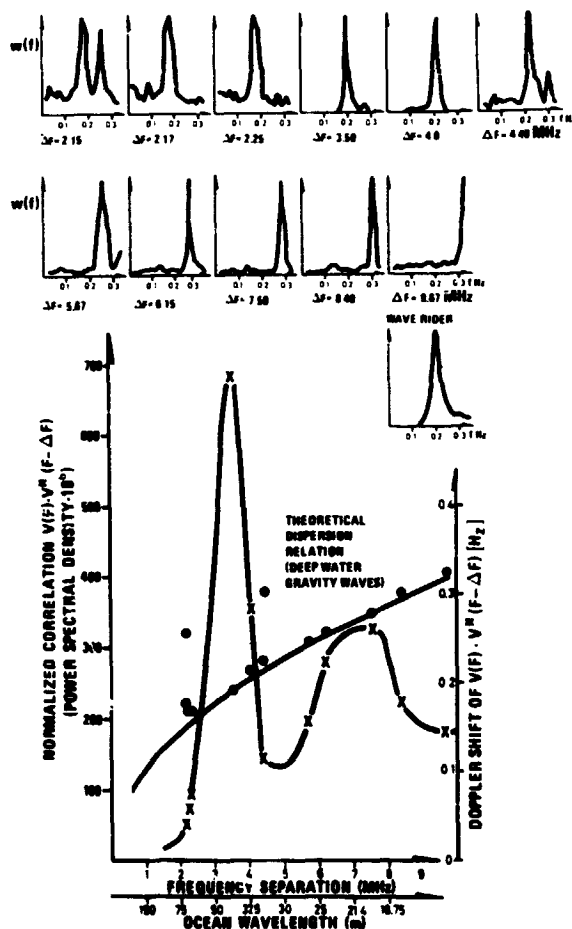
As will be seen, we distinguish between coherent and incoherent components. With "coherent component" we refer to the dominant Doppler spectral line caused by the "coherent" gravity wave ($f = \sqrt{\frac{g\Delta F}{\pi C}}$).

The incoherent component is the "residue intensity" of the Doppler spectrum (the contribution from the skirts) obtained when the coherent contribution wave is subtracted. It can be visualized as all the random turbulent velocity contributions outside the short velocity interval dominated by the gravity wave. Note, however, that although the velocity of the scatterers vary widely as seen e.g. from figure 10, the difference frequency ΔF selects a narrower range of irregularity scales centered round the scale size L given by

$$L = \frac{c}{2\Delta F}$$

If these weak incoherent irregularities were entirely due to the local wind field, one would expect the local wind direction to provide an axis of symmetry. Unfortunately, the antenna systems were not flexible enough to be turned beyond the east direction ($\theta = 90^\circ$). It is therefore difficult to establish such a symmetry. The coherent contribution, however, has a pronounced axis of symmetry determined by the direction of the most energetic ocean wave. We see that the angular distribution is far from $\cos^2\theta$ distributed, long waves are more plane than the shorter ones, as suggested in figure 3.

The lower set of directional spectra in figure 11 gives the situation one hour later when the wind has turned from east towards north. We see that the most energetic waves (the "eye" of the isoplot chart) have not changed direction, whereas the shorter scales and weaker disturbances are reoriented slightly. The distribution of the incoherent (turbulent) irregularities is drastically altered.



On 18 March 1981 there is no wind before noon. At 1330 the wind speed is 10 m/s from south, bringing the water height up to 2.5 m. The complex K plot shows a unidirectional spectrum.

Two hours later, when the wave height has increased to 2.5 m peak to peak, and wind has turned easterly, the irregularity structure is very much altered. This most striking feature has (as indicated in figure 12 and also summarized in figure 13) the very pronounced appearance of a second peak at a wavelength of 25 m whereas the dominating spectral peak is still 50 m. Note that this two-peak spatial spectrum for a particular azimuth direction is not very pronounced in the wave-rider spectrum. This, presumably is a result of the omnidirectional response pattern of the wave-rider. Note also that figure 12 shows a very pronounced two-peak structure in the Doppler spectrum for an ocean wavelength of some 70 m. Finally, figure 13 sums up the results of the afternoon run in the form of $\Phi(\Delta K)$ isolines for the coherent as well as for the incoherent components. Note that the wavelength corresponding to peak spectral intensity varies with azimuth angle.

Figure 12 Spatial and temporal wave spectra for an azimuth direction of 140° . Location is Langesundsfjorden, time is 18 March 81, 1525 local time

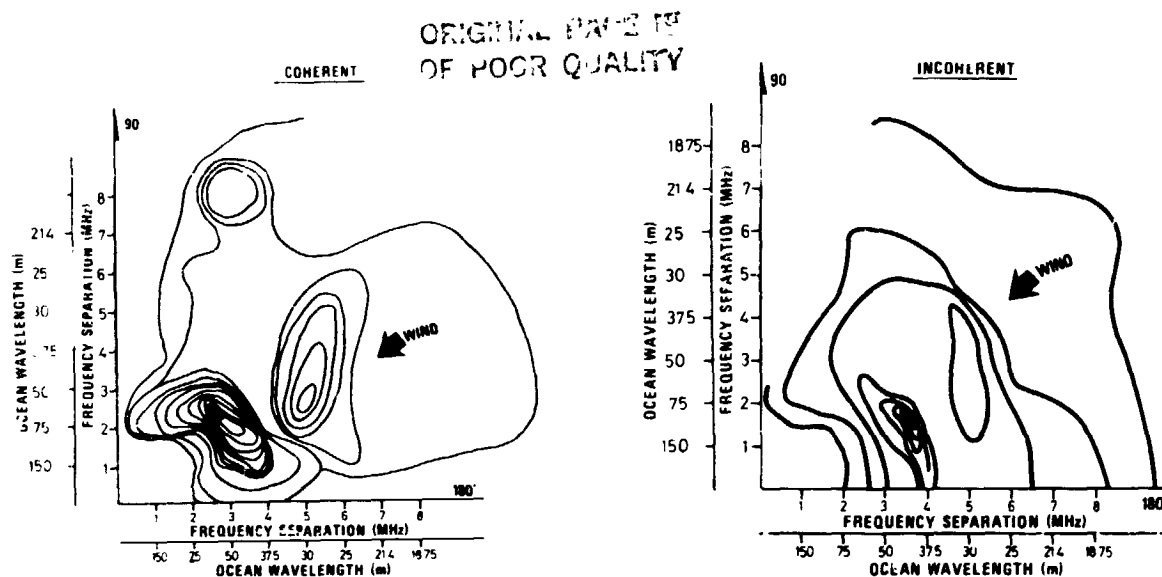


Figure 13 The two-dimensional ocean irregularity spectrum (isolines of $\phi(\Delta K)$) when the wave height has increased to 2.5 m peak to peak and the wind has turned towards east

Acknowledgements

The authors would like to acknowledge the very valuable services rendered by Dr Dagfin Brodtkorb and Jan Wøien of A/S Informasjonskontroll who laboriously and conscientiously did all the data recording and computer data reduction. They also developed most of the computer software and played a very active role in the planning of the data analysis.

The authors would also like to acknowledge the contribution by Dr Anton Kjelaas who developed much of the basic software and took part in the preliminary campaigns.

The multifrequency radar is based on a 960 channel radio relay link generously provided by Mr Bjarne Standahl of Elektrisk Bureau, Division NERA, and the waverider and wind measuring equipment was generously provided by Dr Torkild Carstens of the Norwegian Hydrodynamic Laboratories.

The sea surface measurements performed from the NASA Electra aircraft were made possible by the kind invitation of Dr David Atlas of NASA for which the authors are much indebted.

REFERENCES

- Alpers, W.R. and K. Hasselmann, 1978: The two-frequency microwave technique for measuring ocean wave spectra from an airplane or satellite. *Boundary Layer Meteorol*, 13, 215-230.
- Barrick, D.E., 1972: First order theory and analysis of MF/HF/VHF scatter from the sea. *IEEE Trans AP-20*.
- Bass, F.G. and I.M. Fuks, 1979: Wave scattering from statistically rough surfaces. Pergamon Press.
- Bretherton, E.P., 1969: Waves and turbulence in stratified fluids. *Radio Sci*, 4, 1279-1287.
- Clifford, S.F. and D.E. Barrick, 1978: Remote sensing of sea state by analysis of backscattered microwave phase fluctuations. *IEEE Trans AP-26*, 699-705.

- Gjessing, Dag T., 1962: On the scattering of electromagnetic waves by non-isotropic inhomogeneities in the atmosphere. *J Geophys Res*, 67, 3.
- Gjessing, Dag T., 1964: Determination of isotropy properties of the tropospheric permittivity and wind velocity fields by radio-propagation methods. *J Geophys Res* 69, 4.
- Gjessing, Dag T. and F. Irgens. 1964a: On the scattering of electromagnetic waves by a moving tropospheric layer having sinusoidal boundaries. *IEEE Trans AP-12.1*.
- Gjessing, Dag T. and F. Irgens, 1964b: Scattering of radio waves by moving atmospheric rippled layers: A simple model experiment. *IEEE Trans AP-12.6*.
- Gjessing, Dag T., 1981a: Adaptive techniques for radar detection and identification of objects in an ocean environment. *IEEE J Ocean Engineer*, OE-6.1
- Gjessing, Dag T., 1981b: Adaptive radar in remote sensing. Ann Arbor Science Publisher Inc.
- Gjessing, Dag T., J. Hjelmstad and T. Lund, 1982: A multifrequency adaptive radar for detection and identification of objects. Results of preliminary experiments on aircraft against a sea-clutter background. *IEEE Trans AP-30*, 3, 351-365.
- Gjessing, Dag T., J. Hjelmstad and T. Lund, 1984: Directional ocean wave spectra as observed with multifrequency continuous wave radar. Review paper in *International Journal of Remote Sensing*, January 1984.
- Hasselmann, K. et al., 1973: Measurements of wind-wave growth and swell decay during the Joint North Sea Wave Project (JONSWAP). *Ergänzungsheft zur Deutschen Hydrographischen Zeitschrift*. Reihe A/80, 12.
- Jones, L. and D.E. Weissman, 1981: The two frequency microwave scatterometer measurements of ocean wave spectra from an aircraft. *Oceanography from Space*. Proc. COSPAR/SCOR/IUCRM Symposium, ed. J.F.R. Gower. Plenum Press, N.Y.
- Lumley, J.L., 1967: Theoretical aspects of research on turbulence in stratified flows. *Atmospheric turbulence and radio wave propagation*, ed. A.M. Yaglom and V.I. Tatarsky. Publishing House NAUKA, Moscow, pp 105-112.
- Panowsky, H.A. and R.A. McCormick, 1960: The spectrum of vertical velocity near the surface. *Quart J Ray Met Soc*.
- Phillips, O.M., 1969: The dynamics of the upper ocean. Cambridge Univ. Press, p 159-.
- Plant, W.J., 1977: Studies of backscattered sea return with a CW dual-frequency X-band radar. *IEEE Trans AP-25*, 1.
- Plant, W.J. and D.L. Schuler, 1980: Remote sensing of the sea surface using one and two frequency microwave. *Radio Sci*, 15, 3, 605-615.
- Schuler, D.L., 1978: Remote sensing of directional gravity wave spectra and surface currents using a microwave dual-frequency radar. *Radio Sci*, 13, 2.
- Tatarsky, V.E., 1961: Wave propagation in a turbulent medium, translated by R.A. Silverman. McGraw-Hill, New York.
- Tomiyasu, K., 1971: Short pulse wide-band scatterometer ocean surface signature. *IEEE Trans GE-9*, 175-177.
- Valenzuela, G.R., 1978: Scattering of electromagnetic waves from the ocean. Surveillance of environmental pollution and resources by electromagnetic waves. Proc. NATO Advanced Study Institute, Spåind, Norway 9-19 April 1978. ed. T.Lund.
- Waterman, A.T., D.T. Gjessing and C.L. Liston, 1961. Statistical analysis of transmission data from a simultaneous frequency- and angle scan experiment. Contribution to the URSI Spring Meeting, Washington DC., 1961.
- Weissman, D.E. and J.W. Johnson, 1977: Dual frequency correlation radar measurements of the height statistics of ocean waves. *IEEE J Ocean Engineer*, OE-2. 74-83.
- Weissman, D.E., J.W. Johnson and J.T. Ramsey, 1982: The delta-K ocean wave spectrometer: Aircraft measurements and theoretical system analysis. Proc. IGARSS -82.
- Woods, J.D., 1969a: On Richardson's number as a criterion for laminar-turbulent-laminar transition in the ocean and atmosphere. *Radio Sci*, 4, 12, 1289-1298.
- Wright, J.W., 1968: A new model for sea clutter. *IEEE Trans AP-16*. 217-223.
- Wright, J.W., W.J. Plant, W.C. Keller and L. Jones, 1980: Ocean wave-radar modulation transfer functions from the West Coast Experiment. *J Geophys Res*. 85, C9, 4657-4966.

THE DUAL-FREQUENCY SCATTEROMETER RE-EXAMINED

W. J. Plant and A. B. Reeves

U. S. Naval Research Laboratory
Washington, D. C. 20375

ABSTRACT

We demonstrate here that the utility of dual-frequency scatterometers in measuring ocean wave directional spectra can be increased by adding a third frequency to the system. We show that the background which effectively limits signal detectability in dual-frequency operation can be made a part of the signal through the addition of this third frequency. Thus signal detectability is limited only by system thermal noise and space-based operation becomes more feasible.

1. INTRODUCTION

The operation of the dual-frequency scatterometer when receiving backscatter from the ocean surface is now well understood. It has been shown, both experimentally and theoretically, that the power spectrum of the received signal consists of a sharp line which obeys an ocean gravity wave dispersion relation superimposed on a broad background spectrum resulting from the convolution of the doppler spectra from the two transmitted frequencies (Plant 1977). This is illustrated in Figure 1.

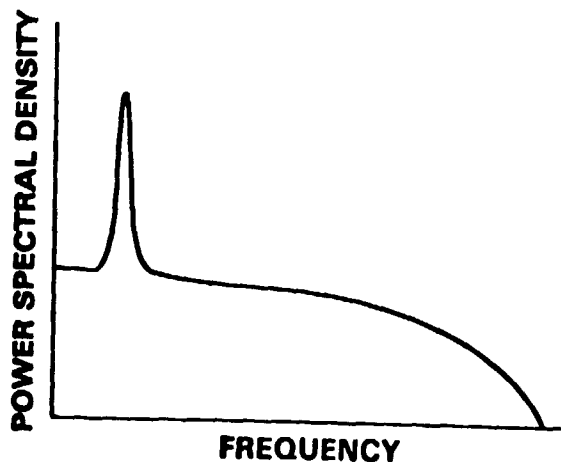


Figure 1 Power spectrum of the output of a dual-frequency scatterometer.

The intensity of the sharp line is a measure of the amplitude of the ocean wave whose frequency corresponds to that of the line. The background spectrum, however, is essentially independent of this wave amplitude. Thus the proper measure of the detectability of ocean waves by the dual-frequency scatterometer is the ratio of the integral of the sharp line to the integral of the background spectrum. This ratio χ is well described in deep water by the following equation:

$$\chi = \frac{2\pi^2 |m|^2 S}{A} \quad (1)$$

where m is the modulation transfer function, S is the wave slope spectral density evaluated at constant wavenumber and A is the illuminated area (Plant and Schuler, 1980). Alpers and Hasselmann (1978) have shown that even if the background spectrum is low-pass filtered to increase χ by the ratio of the natural bandwidth to the filtered bandwidth, a typical value for χ from satellite altitudes would be 1.8. Thus the detectability of the wave is quite low under these conditions.

In this paper we will show that if the number of transmitted frequencies is increased to three and if proper processing of the received signal is performed then this constraint on wave detectability can be removed. We will show that if the three transmitted frequencies are equally spaced, then the background signal is also proportional to the amplitude of the detected ocean wave. Under these conditions the proper measure of wave detectability is the ratio of the intensity of the sharp line plus the background intensity to the system thermal noise. Thus ocean waves may be much more easily measured using such a three-frequency system.

2. THEORY

The concept is most easily approached by considering four transmitted frequencies as shown in Figure 2.

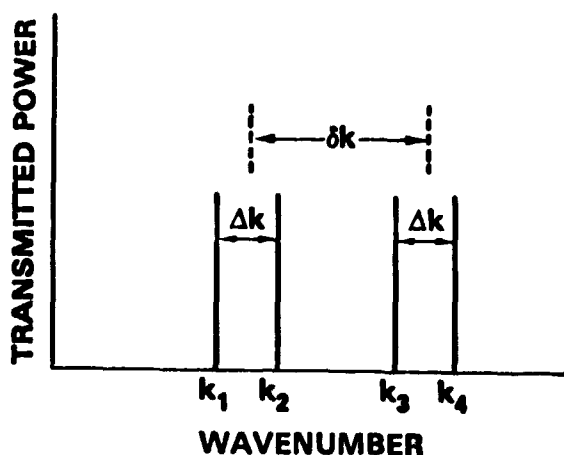


Figure 2 Transmitted signals used to generalize dual-frequency operation.

Transmitted wave numbers will be k_1 , $k_2 = k_1 + \Delta k$, $k_3 = k_1 + \delta k$, $k_4 = k_2 + \delta k$. Back-scatter from the ocean may be most conveniently described in terms of a two-scale model and a complex reflectivity. Thus the field E_1 received due to any one of our transmitted frequencies (whose wavenumber is k_1 and whose Poynting vector is unity at the surface) may be represented by,

$$E_1(t) = \int r(\underline{x}, t) e^{i 2 \underline{k}_1 \cdot \underline{x}} d\underline{x} \quad (2)$$

where \underline{x} is a horizontal position vector, t is time, and $r(\underline{x}, t)$ is the complex reflectivity. The standard assumption, which is supported experimentally, is that the covariance function of this complex reflectivity may be represented by

$$\begin{aligned} \langle r(\underline{x}, t) r^*(\underline{x} + \underline{\zeta}, t + \tau) \rangle &= \sigma_0(\underline{x}, t) R(\underline{x}, t, \tau) \delta(\underline{\zeta}) \\ \langle r(\underline{x}, t) r(\underline{x} + \underline{\zeta}, t + \tau) \rangle &= 0 \end{aligned} \quad (3)$$

where σ_0 is the normalized radar cross section, R is the autocorrelation function so that $R(\underline{x}, t, 0) = 1$, $\delta(\underline{\zeta})$ is the δ -function and $\langle \rangle$ represents an ensemble average. Using (2) and (3), we have,

$$\langle E_1(t) E_j^*(t + \tau) \rangle = \int \sigma_0(\underline{x}, t) R(\underline{x}, t, \tau) e^{i 2(\underline{k}_1 - \underline{k}_j) \cdot \underline{x}} d\underline{x}. \quad (4)$$

Experiment shows that R falls to zero rapidly with τ . Since $R=1$ at $\tau=0$, a good first order approximation for our purpose here is to ignore the dependence of R on x and t . Then (4) may be written

$$\langle E_1(t) E_j^*(t + \tau) \rangle = R(\tau) \sigma_0(\underline{K}, t) \quad (5)$$

where $\underline{K} = (2(k_1 - k_j) \cos \theta, 0)$ and θ is the grazing angle. If $\tau=0$ and $i=j$, Equation (4) is simply a definition of the radar cross-section.

In processing dual-frequency scatterometer return, the two received signals are multiplied together and a power spectrum of the product is computed. Formally, the power spectrum is obtained by multiplying the product by a time-delayed version of itself, averaging over time and transforming with respect to the lag variable. Here we generalize by letting the time-lagged signal be the product of the third and fourth transmitted signals. That is we cross-correlate the products $E_1 E_2^*$ and $E_3 E_4^*$ rather than autocorrelate $E_1 E_2^*$. Gaussian statistics hold adequately for short time intervals so we may write,

$$\begin{aligned} \langle E_1 E_2^*(t) E_3^* E_4(t+r) \rangle &= \langle E_1 E_2^* \rangle \langle E_3^* E_4 \rangle + \langle E_1 E_3^* \rangle \langle E_2^* E_4 \rangle \\ &+ \langle E_1 E_4 \rangle \langle E_2^* E_3^* \rangle. \end{aligned} \quad (6)$$

The last term is zero by virtue of (3) while the other terms yield,

$$\langle E_1 E_2^*(t) E_3^* E_4(t+r) \rangle = \tilde{\sigma}_0(\Delta \underline{k}, t) \tilde{\sigma}_0(\Delta \underline{k}, t+r) + R^2(r) \tilde{\sigma}_0^2(\delta \underline{k}, t) \quad (7)$$

Here $\Delta \underline{k} = (2\Delta k \cos \theta, 0)$, $\delta \underline{k} = (2\delta k \cos \theta, 0)$.

Averaging over t and transforming with respect to r yields the cross-power spectrum,

$$P(f) = \overline{\tilde{\sigma}_0(\Delta \underline{k}, t) \tilde{\sigma}_0(\Delta \underline{k}, t+r)} e^{12\pi f r} dr + \tilde{R}^2(f) \overline{\tilde{\sigma}_0^2(\delta \underline{k}, t)} \quad (8)$$

where overbars are time averages, and $\tilde{R}^2(f)$ indicates the Fourier Transform of $R^2(r)$. Since the pattern of σ_0 moves along with the surface wave, the first term yields the same sharp line as the standard dual-frequency method. Similarly, the second term yields the broad background term; if $\delta k=0$, it is identical to the standard term. In general, however, $\delta k \neq 0$ and the second term is not proportional to the mean square value of $\sigma_0(t)$ but to the power spectral density of $\sigma_0(\underline{x}, t)$ evaluated at $\delta \underline{k}$. Figure 3 illustrates this difference.

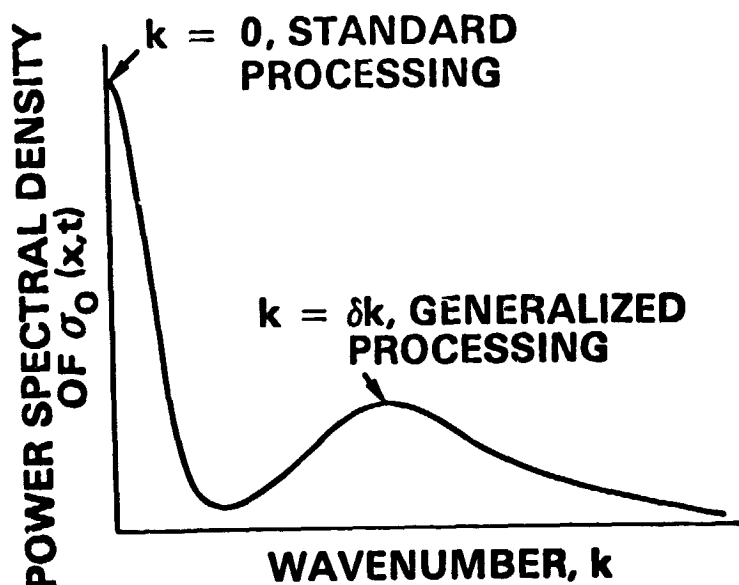


Figure 3 Wavenumber spectrum of $\sigma_0(\underline{x}, t)$ showing wavenumbers at which the background signal is evaluated using standard processing and generalized processing.

If we integrate Equation (8) over frequency, we get,

$$P = \overline{\sigma_o^2(\Delta k, t)} + \overline{\sigma_o^2(\delta k, t)} \quad (9)$$

In particular, if $\Delta k = \delta k$ so that three equally-spaced signals are transmitted, then

$$P = 2 \overline{\sigma_o^2(\Delta k, t)}. \quad (10)$$

Since this spectral density of σ_o evaluated at Δk is proportional to the wave slope spectral density through the transfer function m , the entire received signal is proportional to the intensity of the ocean wave of wave number Δk and the background signal has become part of the desired signal.

3. EXPERIMENT

We have experimentally evaluated the ratio $x_a^{-1} = \overline{\sigma_o^2(\delta k, t)} / \overline{\sigma_o^2(\Delta k, t)}$ for a fixed Δk using measurements taken on the Chesapeake Bay. The results of this study are presented in Figure 4 along with the standard dual-frequency

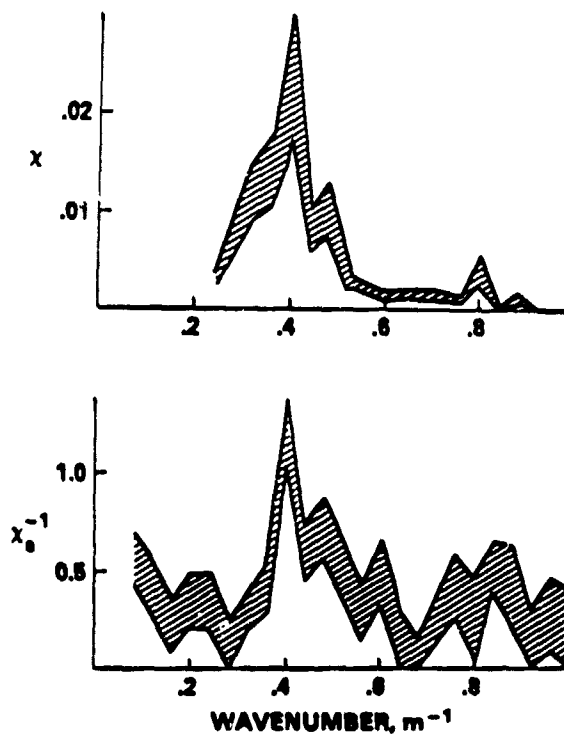


Figure 4 Normalized wavenumber spectrum of $\sigma_o(x, t)$ obtained on April 15, 1981 on the Chesapeake Bay. The top graph was obtained from the intensity of the standard dual-frequency resonance line. The lower graph was produced by integrating the background obtained with the generalized processing scheme. x and x_a^{-1} are defined in the text.

output $x = \frac{\sigma_0^2(\Delta k, t)}{\sigma_0^2(0, t)}$ as a function of Δk . Both the integrated background signal in the generalized method (x_{-1}) and the integral of the sharp peak in the standard method (x) indicate^a that a 15 meter dominant wave was present on the surface. This result shows that the background in the generalized method is proportional to surface wave amplitude, in agreement with the above analysis. A paper describing these measurements in detail is currently in preparation.

4. CONCLUSION

The three-frequency scatterometer described here is perhaps the most promising technique for the measurement of ocean wave directional spectra from space. Unlike dual-frequency or short-pulse spectrometers, signal detectability is limited only by thermal noise. Unlike synthetic aperture techniques, the ocean wave spectrum can be obtained from the system output through a linear transfer function. We suggest that a program to check system performance by operating a three-frequency scatterometer from an aircraft should be undertaken as soon as possible.

5. REFERENCES

- Alpers, W. and K. Hasselmann (1978), The Two Frequency Microwave Technique for Measuring Ocean-Wave Spectra from an Airplane or Satellite, *Boundary Layer Meteorol.*, 13, 215-230.
- Plant, W. J. (1977), Studies of Backscattered Sea Return with a CW, Dual-Frequency, λ -Band Radar, *IEEE Trans. Antennas Propagat.*, AP-25, 28-36.
- Plant, W. J. and D. L. Schuler (1980), Remote Sensing of the Sea Surface Using One- and Two-Frequency Microwave Techniques, *Radio Science*, 15, No. 3, 605-615.

AN IMPROVED DUAL-FREQUENCY TECHNIQUE FOR THE
REMOTE SENSING OF OCEAN CURRENTS AND WAVE SPECTRA

Dale L. Schuler
Wah P. Eng

U. S. Naval Research Laboratory
Washington, D. C. 20375, USA

ABSTRACT

Investigators in several countries have been studying a two-frequency microwave radar technique for the remote-sensing of directional ocean wave spectra and surface currents. This technique is conceptually attractive because its operational physical principle involves a spacial electromagnetic scattering resonance with a single, but selectable, long gravity wave. Multiplexing of signals having different spacing of the two transmitted frequencies allows measurements of the entire long wave ocean spectrum to be carried out. The two-frequency scatterometer signal/background ratio is, using conventional processing, only adequate for measurements made at or relatively near the dominant wave wavenumber when sufficient temporal averaging of spectra is employed.

A new scatterometer has been developed and experimentally tested which is capable of making measurements having much larger signal/background values than were previously possible. This new instrument couples in a hybrid fashion the resonance technique with coherent, frequency-agility radar capabilities. This scatterometer is presently configured for supporting a program of surface-current measurements. Straightforward system modifications will allow directional measurements of ocean wave slope spectra to be carried out as well as current measurements.

1. INTRODUCTION

The operation of dual-frequency scatterometers in detecting microwave backscatter from the ocean surface is now well understood. Such scatterometers transmit two microwave signals separated in frequency by some Δf which is in the Megahertz range. Return signals due to each of the transmitted signals are separately received and then multiplied together. The power spectrum of the resultant output appears as shown schematically in Fig. 1. It consists of the sum of a broad background spectrum and a sharp " Δk -line". The background spectrum is the result of a convolution of the Doppler spectra of the two received microwave signals and consequently has a width of a few tens to a few hundred Hertz. The Δk -line, on the other hand, is the result of a resonance between the beat pattern of the two electromagnetic signals and the modulation pattern of the short ocean surface waves (centimetric "Bragg waves") responsible

for the backscatter. It has a width of a few tenths to a few Hertz depending on the relative speed of the microwave antenna and the ocean surface. (Plant, 1977; Alpers and Hasselman, 1978; Jackson, 1981).

The frequency of the center of the k -line is exactly equal to the frequency of the ocean surface wave which travels along the horizontal radar look direction and whose wavenumber, K_w , is $2k \cos \theta$ where k is the wavenumber separation of the transmitted microwave signals and θ is the grazing angle (Plant, 1977). If a current exists on the surface, the wave of wavenumber K_w will be advected by the current and its frequency in the antenna's frame of reference will change. By this means surface currents along the horizontal radar look direction can be measured using dual-frequency scatterometers (Schuler, 1978; Alpers et al., 1980). By varying k , vertical profiles of horizontal currents along the radar look direction can also be determined (Schuler, et al., 1981). One requirement for such measurements is, of course, that the k -line can be easily distinguished from random variance in the background level. This requirement is frequently not well satisfied and therefore severely limits applicability as well as the accuracy of the technique (Schuler, 1978).

The ratio of intensities of k -line and background spectrum, χ , has been shown to be related to the surface wave slope spectral density $S(\vec{K}_w)$ by the equation

$$\chi = \frac{2\pi^2 |m|^2 S(\vec{K}_w) \coth^2(K_w d)}{A} \quad (1)$$

where d is water depth, A is illuminated area, and m is the modulation transfer function relating Bragg wave modulation to the slope of the long surface wave. (Alpers and Hasselmann, 1978; Plant and Schuler, 1980). The inverse dependence of χ on A has been observed experimentally (Plant and Schuler, 1980; Johnson et al., 1982) and the equation has been shown to account well for observed values of χ (Schuler, et al., 1982; Johnson and Weissman, 1983). Alpers and Hasselman (1978) pointed out that this signal to background ratio can be increased by low pass filtering but their best estimate of such a ratio was only 1.8 for measurements from satellite altitudes. Thus, once again, the background clutter spectrum was the predominant factor limiting system performance.

In this study we have attempted to apply frequency agility techniques to dual-frequency scatterometer measurements of the ocean. In this case it is necessary to discuss two distinct types of frequency separations. In addition to the Δf separation between transmitted pairs of signals, the carrier, or center, frequency of successive pairs of signals will be offset from one another by some δf . The sensor still remains a "dual-frequency" system in the sense that the first step in processing is to multiply returns corresponding to transmitted frequencies separated by Δf .

2. EXPERIMENTAL INSTRUMENTATION AND CONDITIONS

The experimental results presented in this paper were obtained at a Naval Research Laboratory field-site located on 36.6 m cliffs overlooking the Chesapeake Bay. The dual-channel, coherent radar was built at the Naval Research Laboratory and was operated at a frequency of 1.28 GHz. The basic operating parameters for this scatterometer system are given in Table 1. Both channels of the radar system are fully coherent, i.e., signal phase information is preserved. The signal coherency is retained by beating the return signal down first to IF, and then to a variable audio offset frequency (25 Hz for these experiments) which is set sufficiently high to avoid fold-over of any of the spectral components of the backscatter Doppler spectrum. This frequency-agile, dual-transmission channel radar system derives its operational flexibility from the use of an EPROM (Erasable Programmable Read-Only Memory) controlled fast-switching (20 μ s/step) frequency synthesizer. The EPROM contains instructions to program the synthesizer to create a set of output carrier frequencies $[f_i]$ where, $i = 1, \dots, N_c$ ($1 \leq N_c \leq 98$). External counting circuits, controlled by the system PRF pulses, are used to step through the EPROM stored instructions and to continually repeat the cycle. The value of N_c may be manually set to any integer value within its range. The individual output frequencies f_i are held constant for 100 μ s, and then are reprogrammed to a new value. A diagram showing the time dependence of transmitted frequencies corresponding to the two received channels is given in Figure 2. These diagrams resemble two "staircases" with one offset in time relative to the other by an interpulse period. Backscattered returns due to transmissions when the channel separation was $\Delta f'$ were utilized in the computer processing of the data while those due to Δf were suppressed. A synchronization signal was derived by using digital counting circuits and a D/A converter. For the measurements reported here the difference frequency Δf between the two L-Band channels ($f_i, f_i + \Delta f$) was held constant at a value of 10 MHz. This separation allowed us to resonate spatially with water waves of 15 m wavelength. This value was chosen because waves of this wavelength often are the dominant wave at the Chesapeake Bay site. The values of f_i were stepped from 1.230 GHz to 1.328 GHz in 1 MHz steps. The 1 MHz spacing was selected a priori using the initial assumption (Pidgeon, 1967) that frequency changes equal to or greater than $(T)^{-1}$ (where T = the transmitted pulsewidth) would be adequate to decorrelate the backscattered returns. The work of Voles (1966) indicates that larger separations may be necessary in the presence of long waves but no experimental evidence was to substantiate that conclusion.

The processing of the fully coherent output signal $S_o(t)$ from the radar consists of three steps (1) range gating of the returns, (2) separation of the two interleaved frequency channels, and finally (3) processing of the N frequency-agile signals which occur during the transmission time of the synchronization staircase.

For the present studies, samples of the backscattered return were taken at a two-way delay of 5 μ s (0.75 km) from the radar site at a grazing angle of 3° . The scattering cell dimensions were determined, at this low grazing

angle, by the pulse width (1 μ s) and the azimuthal beamwidth of the antenna pattern (6° at the two-way 3 dB power point). These parameters indicate that the scattering cell was 150 m radially by 79 m azimuthally. The data reported here were taken during an eight hour period on 15 April 1982.

Wind-generated waves traveled towards shore in water which was 25 m in depth; our work indicates a dominant wavelength of 15m. The wind during the tests was from the NNE at 15-20 kts as measured by an anemometer at a height of 43 m above the sea surface. The antennas were pointed into the dominant wave direction which was observed to be from the NE. Scattered whitecaps were present. The outputs of the two radar channels as well as the synchronization signal were recorded on an analog, four-channel tape recorder operating at 30 ips. Subsequent experiments (November, 1983) conducted from the CERC Pier Duck, NC have yielded results in agreement with the measurements reported on in this paper.

3. DUAL FREQUENCY DOPPLER SPECTRA USING FREQUENCY-AGILE SIGNALS

The output data that were recorded consisted of a burst of up to forty-nine multiplexed, frequency-agile samples of coherent sea backscatter for both radar channels, and a synchronization signal. Our initial processing of this multiplexed time signal was both direct and simple. The output data from the two different frequency channels were passed through a laboratory multiplier and then through a low-pass filter. The time-constant of the filter was set so as to sum the N sequential frequency-agile samples together coherently. This smoothed signal was then Fourier transformed by a laboratory analyzer (Nicolet Model 444) and a power spectrum was formed. A number, generally 32, of these power spectra were then averaged together. This mode of processing is fast and effective (i.e., Δk -line detectability is greatly improved). Figure 3 illustrates the improvements in the ratio of Δk -line to background spectral intensity that can be obtained with twenty minutes of sequentially recorded data which had N = 1, 24 and 49 frequency-agile transmitted signals. It is apparent that the Δk -line processed in the conventional way (i.e., with N = 1) is almost unusably weak, whereas, the one obtained with N = 49 has been improved by almost 6.5 dB above the background intensity level. This laboratory or "immediate" mode of processing, therefore, produces a significant improvement in signal detectability.

A study was conducted to determine if the dual-frequency resonance line detectability improvements derived from the use of frequency-agility would be sufficient to obviate the need for additional temporal averaging of spectra. If such averaging could be eliminated, then a real-time sensor could be developed which would monitor Δk -line strength and line position in real-time. Real-time processing would allow ocean surface currents to be monitored continuously. The frequency-agile (N = 49) data were played through the Nicolet 444 analyzer. This analyzer has the capability of allowing selection of any of its 400 frequency bins (via placement of a cursor) for study. The output of the selected bin was available at an output port of the analyzer and was recorded on an y-t recorder. Arbitrarily selecting a detection threshold of 6 dB (line strength above the

adjacent background) the data tapes were examined to determine what fraction of the time this threshold was exceeded. The time histories of the magnitude of the peak and the background are shown in Figures 4(a) and (b).

The resonance peak exceeded this threshold 16.5% of the time when the signal was not frequency-agile ($N = 1$) and the signal variance was approximately equal to the mean. When the "immediate" laboratory processing was applied to the same data using $N = 49$ frequency-agile carrier frequencies, the short-term (<10 sec) signal variance was reduced significantly and the detection criterion was exceeded during 95% of the length of the time record.

It is useful to represent this laboratory processing mode mathematically so that it can be compared later with the processing algorithm used on the computer. The signals coming from the two system output channels (which are proportional to the coherently detected backscattered fields) may be represented as $E(t, f_n)$ and $E(t, f_n + \Delta f)$ where f_n is the n^{th} transmitted carrier frequency of the frequency-agile signal set. The low-frequency output of the laboratory multiplier may then be represented as

$$P_n(t) = E(t, f_n) \cdot E^*(t, f_n + \Delta f) \quad (2)$$

where, $f_n = f_0 + \delta f$, $f_0 = 1.23$ GHz, and δf is stepped from 0 to N MHz in 1 MHz steps, $\Delta f = 10$ MHz.

The effect of the low-pass filter which follows the multiplier is to convolve $P_n(t)$ with a filter weighting function $W(t)$, which is the Fourier-transform of the pass-band characteristic of the filter, to form a signal $V(t)$ given by

$$V(t) = \int_{-\infty}^{\infty} P_n(\tau) W(t - \tau) d\tau$$

or, approximately

$$V(t) = \int_{T/2}^{T/2} P_n(\tau) W(t - \tau) d\tau \approx \sum_{n=0}^N P_n(t) \quad (3)$$

where,

$$T = [2\Delta f_f]^{-1}, \Delta f_f = \text{the filter 10dB cut-off width.}$$

The signal $V(t)$ is then processed in a laboratory Fourier analyzer (Nicolet Model 444). The output of this analyzer is a result of Fourier-transforming the input signal $V(t)$, squaring it, and ensemble averaging over a number of data records to form

$$\begin{aligned} \overline{|V(\omega)|^2} &= \overline{\left| \sum_{n=0}^N \tilde{P}_n(\omega) \right|^2} \\ &= \overline{\sum_{n=0}^N |\tilde{P}_n(\omega)|^2} \\ &\quad + \sum_{n=0}^N \sum_{\substack{l=0 \\ l \neq n}}^N \overline{\tilde{P}_n(\omega) \tilde{P}_l(\omega)} \end{aligned} \quad (4)$$

where, $\tilde{}$ represents a Fourier transformed quantity and ω is radian frequency. The notations $P_n(\omega)$ means the Fourier transform of the return signal pair whose carrier frequency was N MHz above a base frequency of 1230 MHz.

It should be noted that the smoothing time T of the filter need not be exactly equal to the repetition period T_R of the frequency-agile signal set. If it is made longer then T_R no new terms appear in Eq. (4) until the extension exceeds the temporal decorrelation time (at 1.23 GHz) of the sea itself.

Eq. (4) shows that the simple processing scheme results in an average spectrum which may be represented as a sum of auto- and cross-spectra between dual-frequency pairs having carrier frequency offsets Δf ranging from 0 to N MHz. We expect that returns due to transmitted frequencies separated by more than an inverse pulse width (in this case by more than 1 MHz) will be highly decorrelated. Thus we would expect lower background signals for cross- than auto-spectra in our sum. Since conventional processing consists of summing only auto-spectra, a net background reduction is to be expected for $|V(\omega)|^2$.

5. PROPERTIES OF CROSS SPECTRA OF FREQUENCY-AGILE RETURNS

In order to investigate the validity of the results of the previous section in detail, we computed cross-spectra of P_n and P_l and compared them with the power spectrum of P_n itself. To accomplish this, the data described earlier were processed using a MINC/LSI-11 computer. The procedure consisted of (1) multiplying the multiplexed signals together and, (2) demultiplexing the N product signals (Figure 5). The result of this operation was a set of individual time-series of samples of the multiplied fields $P(t)$ for all possible values of carrier frequency offset over the range $0 \leq n \leq N$. These time-series were then (redundantly) re-sampled and stored as disc files by the computer. It should be emphasized that these files contained return signals $P(t)$ which were due to transmissions whose frequency separation was constant (10 MHz) but whose carrier frequency offsets varied in 1 MHz steps. Mean square

voltage levels of these digitized signals were constant to within 10% up to 35 MHz separation. Cross- and auto-spectra were then computed using the digitized data.

In most cases, twenty-five seconds of each of two records corresponding to different carrier frequencies were transformed using a uniform time window. The product of the two transforms was computed and stored. A total of N time records were stored on disc, where $N = 24$ for the first data set and $N=36$ for the second. Therefore the number of cross-spectra between records whose carrier frequencies were separated by δf which could be averaged together was $N-\delta f$ if δf is in MHz. This process was repeated four times so that the total number of cross-spectra we were able to average together was $4(N-\delta f)$. For instance, the second data set yielded 144 auto-spectra which were then averaged. In one instance, discussed below, we transformed the entire 100 second data record and summed various combinations of auto- and cross-spectra. In this single case, the second data set was augmented to yield a maximum δf of 47.

Figure 6 gives examples of spectra computed using 25 second records. Figure 6(a) is the auto-spectrum computed for the first data set with 48 degrees of freedom. Figures 6(b) and (c) show the magnitude and phase of the cross-spectrum between digital files corresponding to $\delta f = 10$ MHz. These were computed with 28 degrees of freedom. Apparent in this figure is the decrease in background level relative to K -line intensity which led to the results of Section 3 (note the scale change from (a) to (b)). The phase of the cross-spectrum is quite erratic due to low number of degrees of freedom used in the computation. Note, however, that it is near zero in the frequency range of the spectral peak where the coherence between the input signals is relatively high.

Figure 7 shows the result of simulating on the computer the frequency-agile processing technique described in Section 3. The resolution is higher in this figure than the last since the whole 100 second record was transformed. In the figure, N_s represents the total number of spectra averaged. Note that twice this number is not the total degrees of freedom since many records were used redundantly. Rather the number of degrees of freedom is constant at 96. The average of auto-spectra shown in Figure 7(a) correspond to the first term on the right of Eq. (4), that is to conventional dual-frequency processing. The spectrum obtained by averaging all auto- and cross-spectra from the second data set is shown in Figure 7(b). This spectrum corresponds to the frequency-agile technique output described by Eq. (4). The improvement in signal-to-background ratio for this spectrum compared to that of Figure 7(a) is 10.2 dB. This is larger than that reported in Section 2 becomes only part of the 20 minute record used in Section 2 was used here. Finally, an additional improvement in signal-to-background ratio of 2.8 dB is obtained by summing only cross-spectra as shown in Figure 7(c) and (d). Thus this method of processing results in a total improvement over conventional processing of 13 dB, again confirming that signal detectability is better for cross-spectra than auto-spectra.

5. CONCLUSIONS

We have demonstrated that processing dual-frequency data in a frequency-agile mode can provide significant reduction or, in some cases,

complete removal of the clutter background limitations on dual-frequency operation. The method consists of forming standard, dual-frequency products of signal pairs but then performing the final multiplication or spectral density calculation using products formed at different carrier frequencies.

When Doppler spectra for current measurements are the desired product, we have demonstrated that a simple frequency-agile processing scheme (the "immediate" laboratory mode) can produce significant improvement in signal-to-background ratio of up to 10 dB.

6. REFERENCES

- Alpers, W. and Hasselmann, K., 1978: The Two Frequency Microwave Technique for Measuring Ocean-Wave Spectra from an Airplane or Satellite. *Boundary-Layer Met.* 13, 215.
- Alpers, W., Schroter, J., Schlude, F., Muller, T. H. J., and Koltermann, K. P., 1980: Ocean Surface Current Measurements by an L-Band Two-Frequency Microwave Scatterometer. *Radio Sci.*, 16, 93.
- Jackson, F. C., 1981: An Analysis of Short Pulse and Dual Frequency Radar Techniques for Measuring Ocean Wave Spectra from Satellites. *Radio Sci.*, 16, 1385.
- Johnson, J. W., Weissman, D. E., and Jones, W. L., 1982: Measurement of Ocean Gravity Wave Spectrum from an Aircraft Using the Two-Frequency Microwave Resonance Technique. *Int. J. Remote Sensing*, 3, 383.
- Johnson, J. W., and Weissman, D. E., 1983: Validation of the Two-Frequency Microwave Resonance Technique from an Aircraft: A Quantitative Estimate of the Directional Ocean Surface Spectrum. Submitted to *Radio Science*.
- Pidgeon, V. W., 1967: Time, Frequency, and Spatial Decorrelation of Radar Sea Return. Johns Hopkins University Applied Physics Laboratory Memo No. BPD-670-7.
- Plant, W. J., 1977: Studies of Backscattered Sea Return with a CW, Dual-Frequency X-Band Radar. *IEEE Trans, Antennas Propagat.*, AP-25, 28.
- Plant, W. J. and Schuler, D. L., 1980: Remote Sensing of the Sea Surface Using One- and Two-Frequency Microwave Techniques. *Radio Science*, 15, 605.
- Schuler, D. L., 1978: Remote Sensing of Directional Gravity Wave Spectra and Surface Currents Using a Microwave Dual-Frequency Radar. *Radio Science*, 13, 321.
- Schuler, D. L., Plant, W. J., and Eng, W. P., 1981: Remote Sensing of the Sea Using One- and Two-Frequency Microwave Techniques. *Oceanography from Space*, Ed. by J. F. R. Gower, Plenum Press, New York.
- Schuler, D. L., Plant, W. J., Eng, W. P., Alpers, W., and Schlude, F., 1982: Dual-Frequency Microwave Backscatter from the Ocean at Low Grazing Angles: Comparison with Theory. *Int. J. Remote Sensing*, 3, 363.
- Voles, R., 1966: Frequency Correlation of Clutter. *Proc. IEEE (Letters)*, 54, 81.

DUAL-FREQUENCY DOPPLER SEA SPECTRA

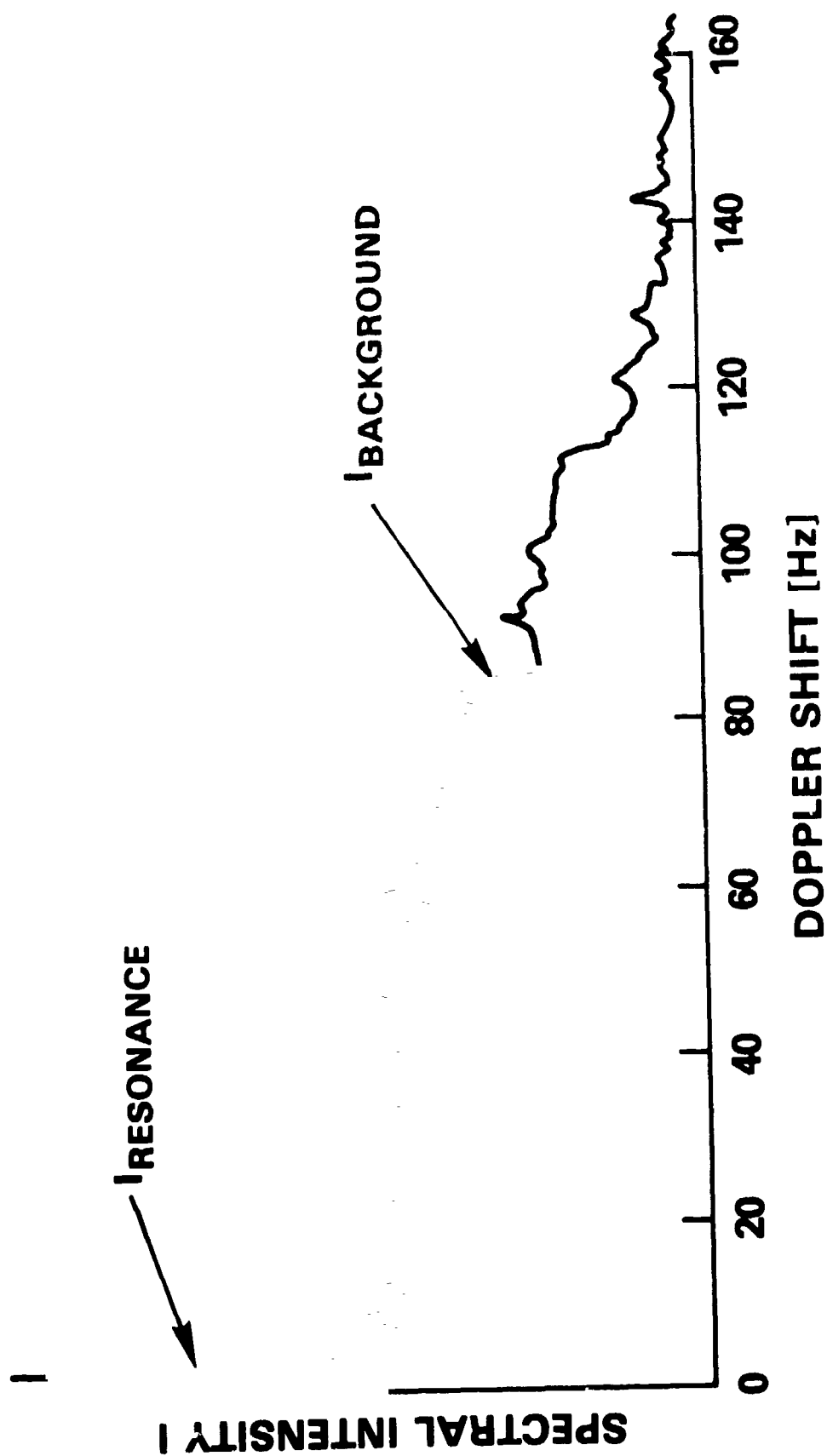


Figure 1 Power spectrum of the output of dual-frequency scatterometer.

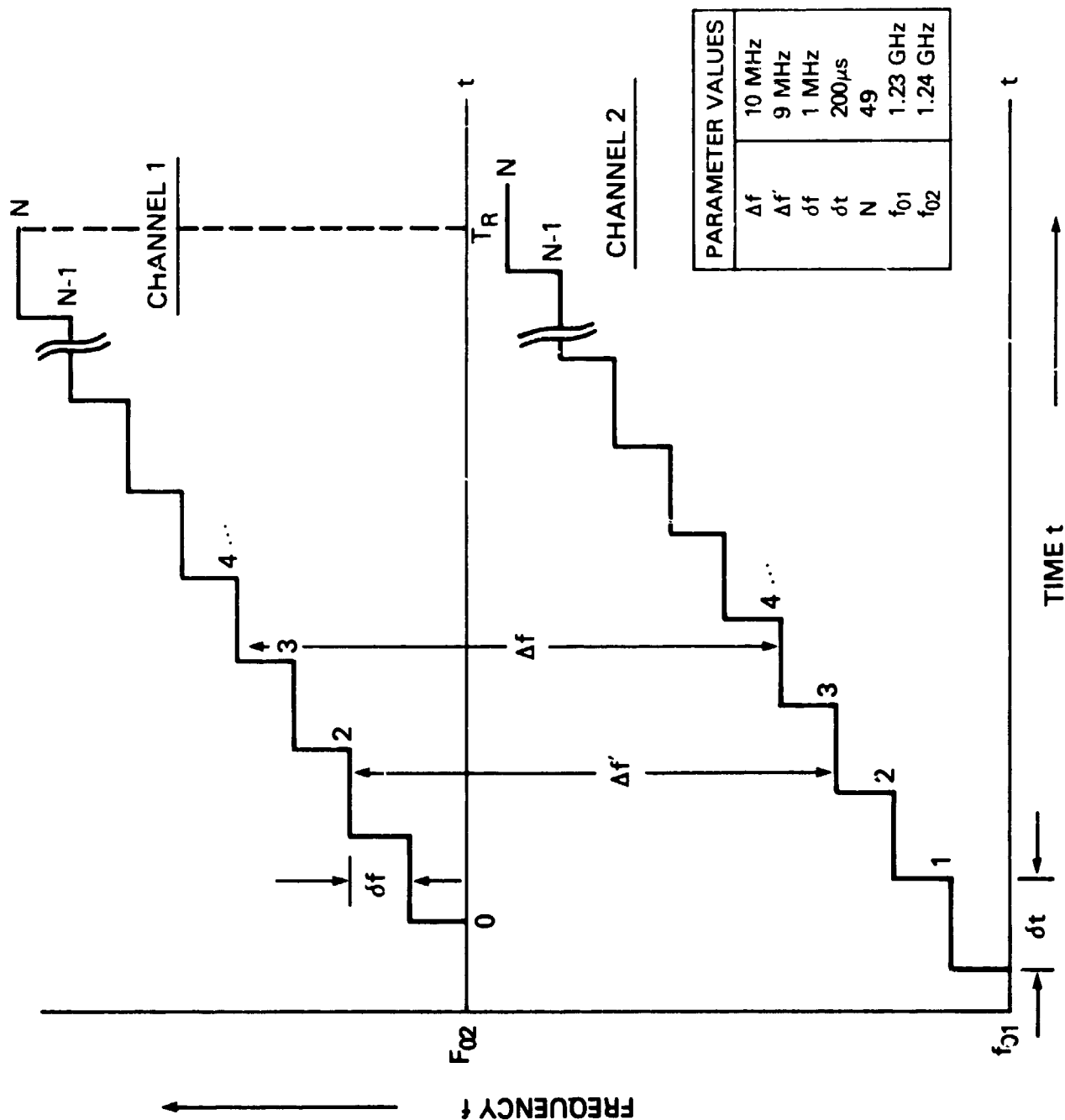


Figure 2 Received signal timing diagram for two channels of the frequency-agile, dual-frequency scatterometer used in this study.

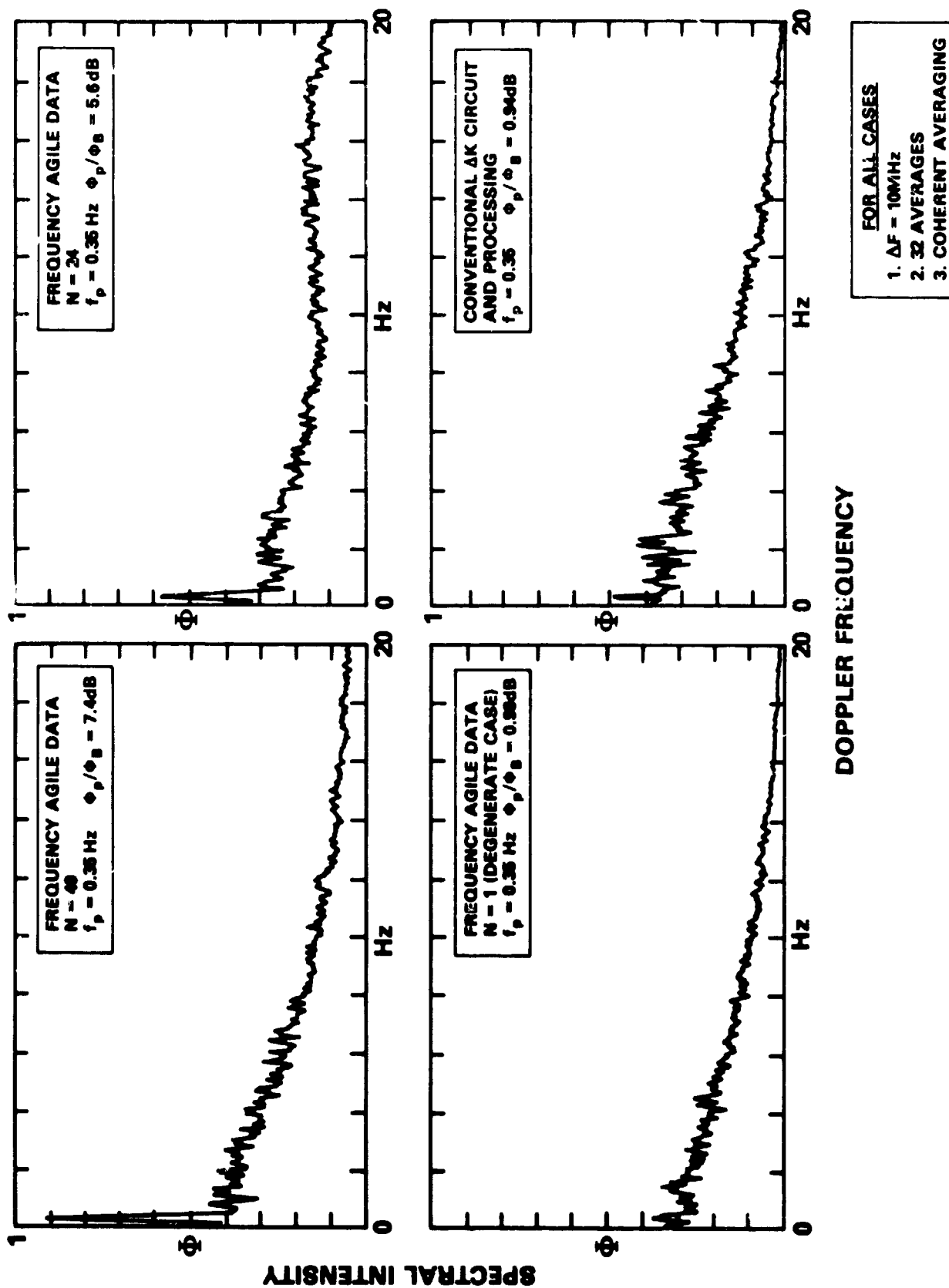


Figure 3 Output spectra of the frequency-agile, dual-frequency scatterometer using laboratory processing ("immediate" mode). (a) One carrier frequency (standard dual-frequency mode), (b) Twenty-four carrier frequencies, and (c) Forty-eight carrier frequencies.

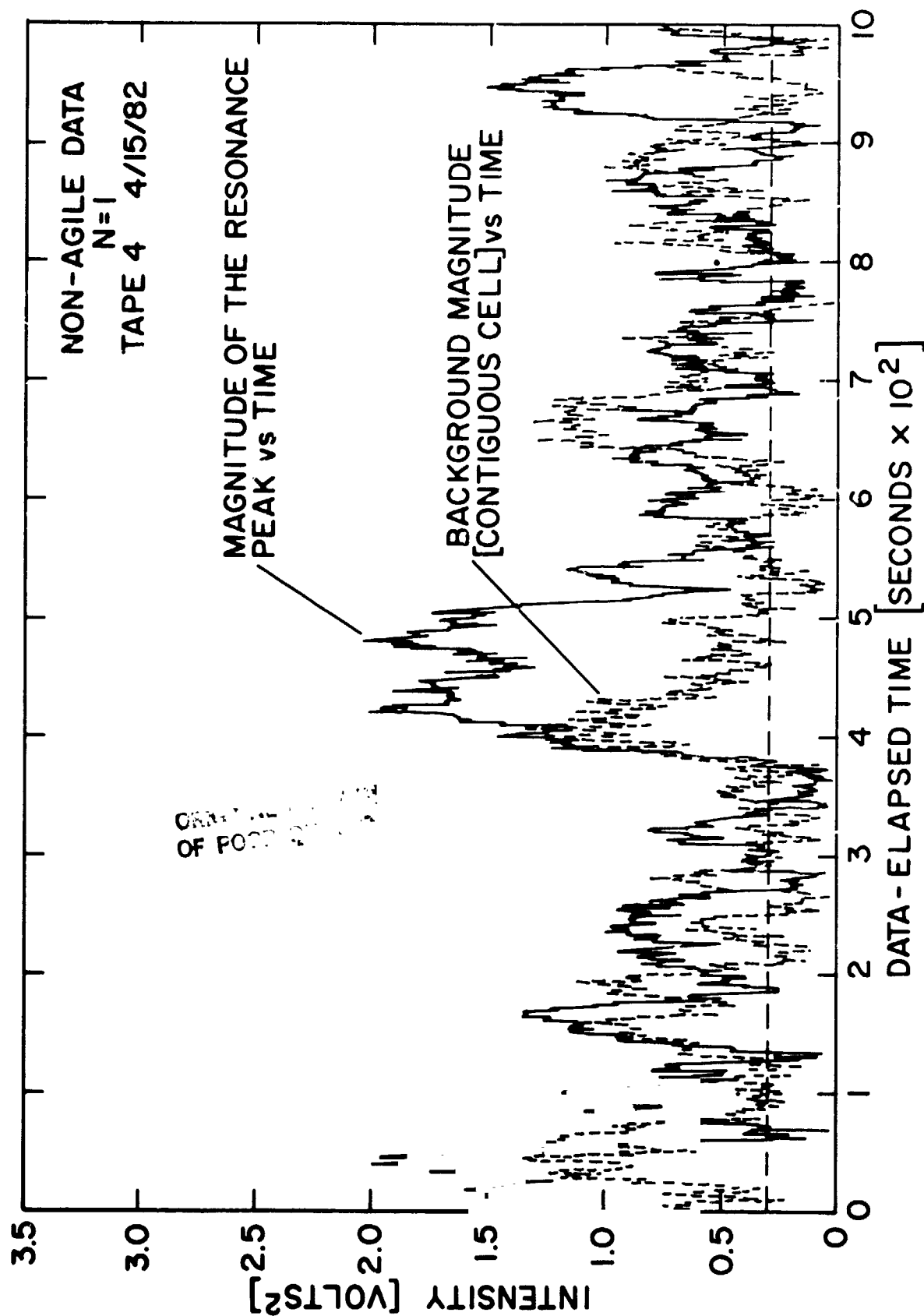


Figure 4 Time dependence of Δk -line and background spectral densities.
(a) Standard dual frequency processing.

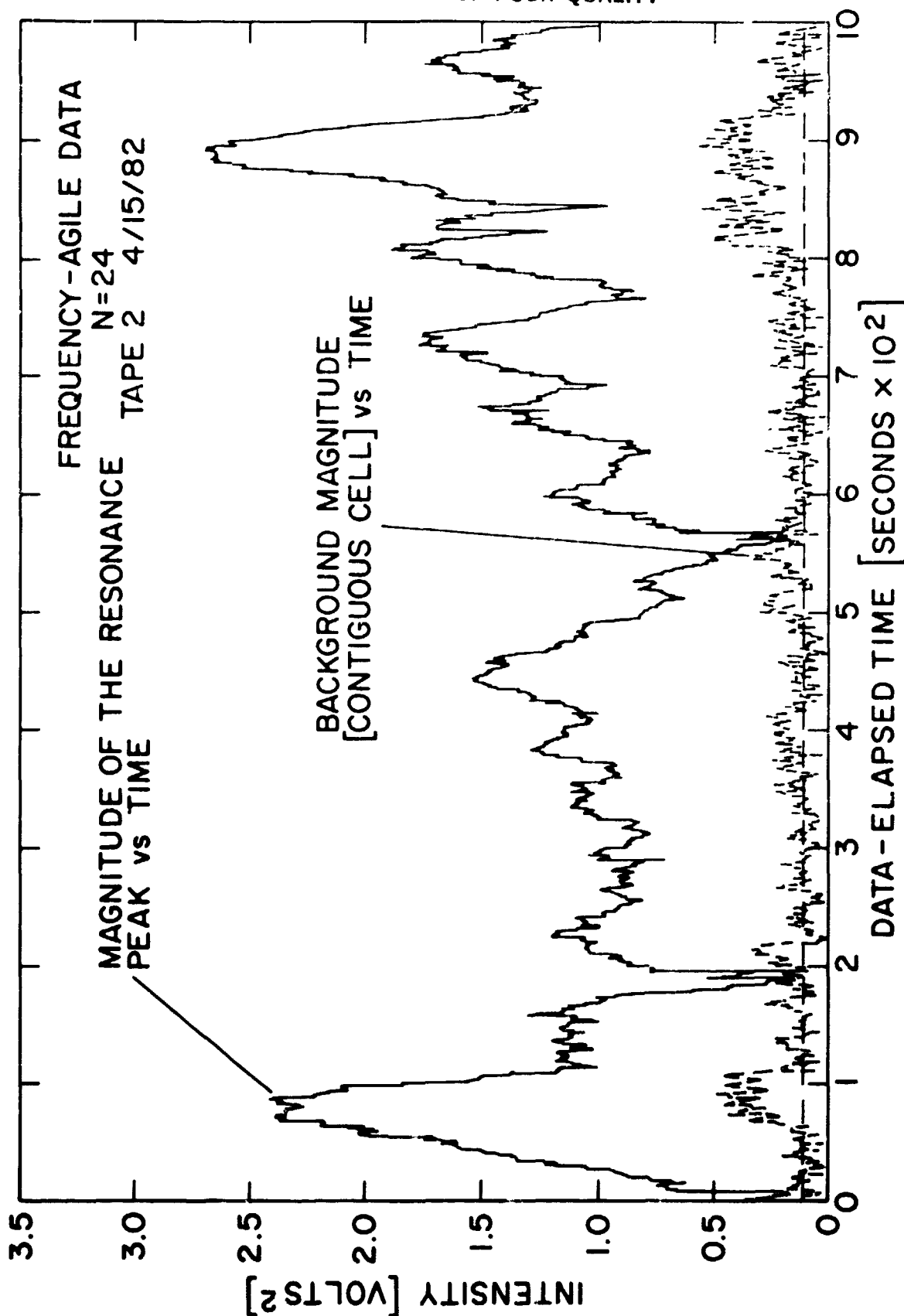


Figure 4 Time dependence of λ_k -line and background spectral densities.
(b) Laboratory processing of the frequency-agile, dual-frequency scatterometer data.

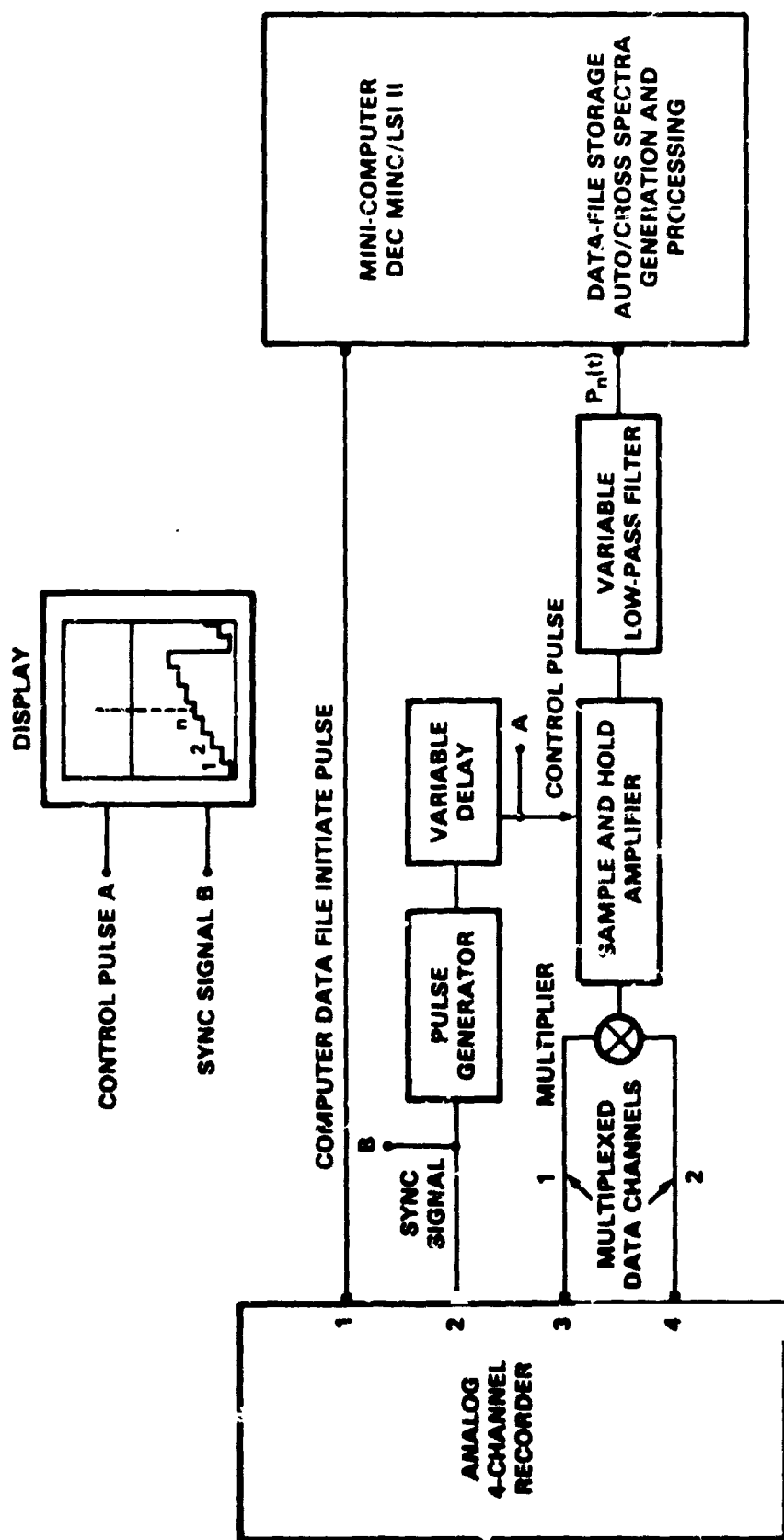


Figure 5 Schematic of signal processing for computer analysis.

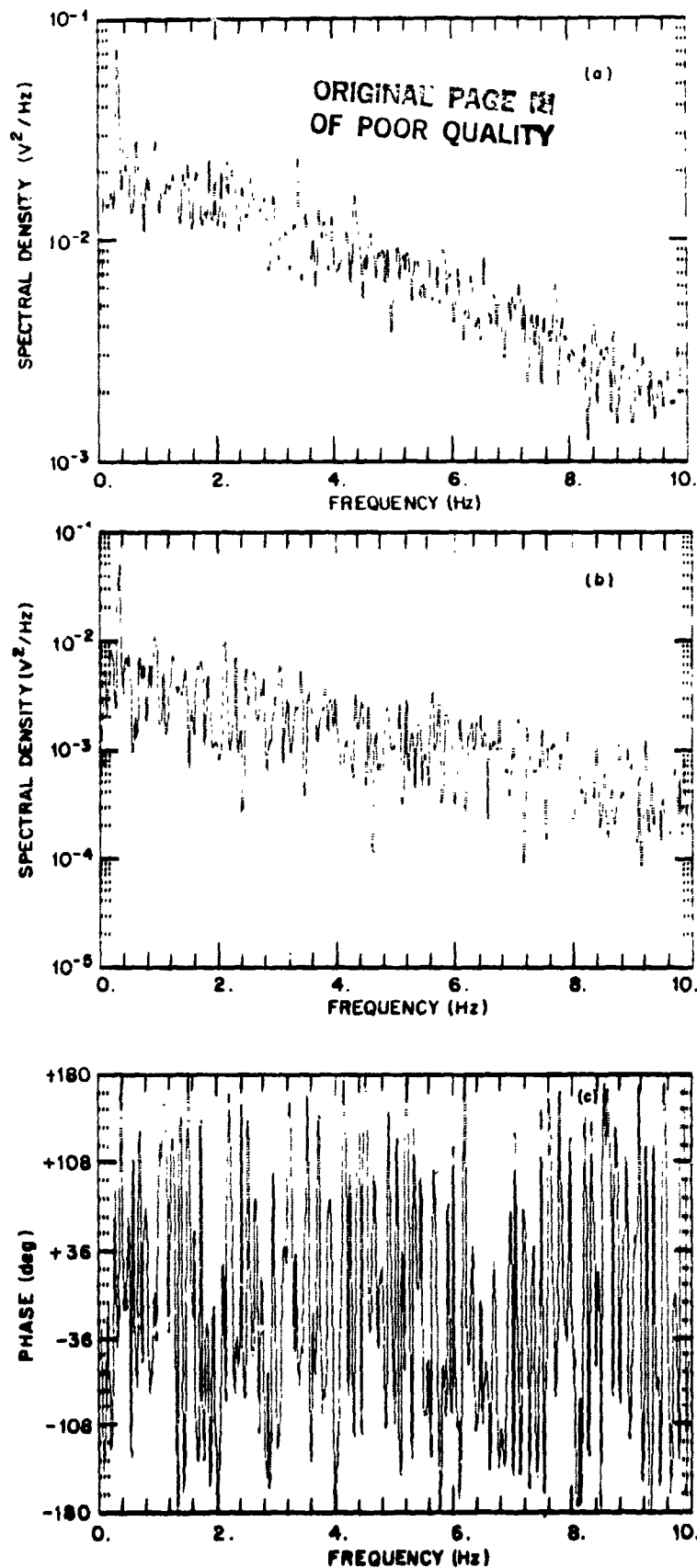


Figure 6 Auto- and cross-spectra of frequency-agile, dual-frequency scatterometer output. (a) Auto-spectrum calculated with 48 degrees of freedom. (b) Magnitude of the cross-spectrum with $\Delta f = 10$ MHz calculated with 28 degrees of freedom. (c) Phase of the same cross-spectrum.

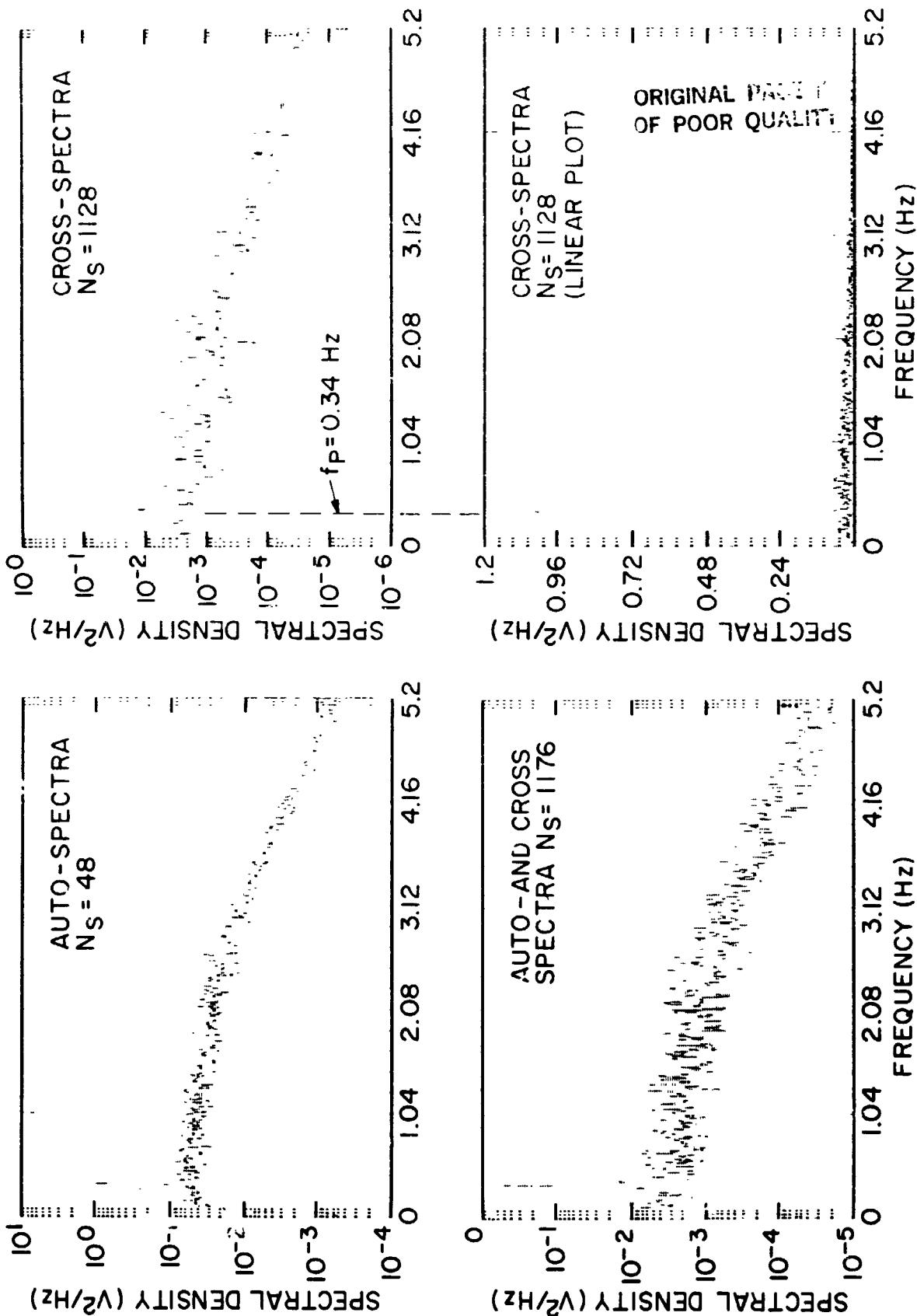


Figure 7 Computer processing of frequency-agile data. (a) Auto-spectra (standard mode), (b) spectrum resulting from summing auto- and cross-spectra for all possible carrier frequencies, (c) spectrum resulting from summing cross-spectra for all carrier frequencies greater than zero, and (d) spectrum of (c) on a linear scale.

MEASUREMENTS OF OCEAN WAVE SPECTRA AND MODULATION TRANSFER FUNCTION
WITH THE AIRBORNE TWO FREQUENCY SCATTEROMETER

David E. Weissman
Hofstra University
Hempstead, New York 11550

James W. Johnson
NASA Langley Research Center
Hampton, Virginia 23665

ABSTRACT

The results of this research show that the directional spectrum and the microwave modulation transfer function of ocean waves can be measured with the airborne two frequency scatterometer-microwave resonance technique. The results here are favorable to the future application of this or similar techniques from airborne or spaceborne platforms. Similar to tower based observations, the aircraft measurements of the modulation transfer function show that it is strongly affected by both wind speed and sea state. Also detected were small differences in the magnitudes of the MTF between downwind and upwind radar look directions, and variations with ocean wavenumber. Unexpected results were obtained that indicate the MTF inferred from the two frequency radar is larger than that measured using single frequency, wave orbital velocity techniques such as tower based radars or "ROWS" measurements from low altitude aircraft. Possible reasons for this are discussed. The ability to measure the ocean directional spectrum with the two frequency scatterometer, with supporting MTF data, is demonstrated.

1. INTRODUCTION

This study is advancing the ability of active microwave radar to measure ocean wave spectra from high altitude aircraft. The experimental data analyzed here was acquired during the Atlantic Remote Sensing Land Ocean Experiment (ARSLOE) during November 1980. The NASA Langley two frequency scatterometer participated onboard the P-3 aircraft, and was able to receive supporting ocean data from the surface contour radar (operated by the NASA Wallops Flight Center), almost simultaneously. Directional spectra and non-directional spectra were available from the XERB buoy. The spectrum of the sea surface reflectivity can be measured directly from the backscattered signals at the two closely spaced microwave frequencies. The cross product of these signals displays a resonance whose intensity is analyzed using theoretical relationships and models that have been developed independently by three groups of researchers, (Alpers and Hasselmann, 1978; Plant and Schuler, 1980; and Johnson and Weissman, 1984). The validity of this equation was established in an earlier phase of this experimental data analysis.

The microwave radar frequency is K_u-band (14.6 GHz), and operates with two "simultaneous" (interrupted CW using time multiplexed long pulses) frequencies, that can be separated by a variable amount from 1 to 20 MHz. Data was collected during many high altitude flight lines between altitudes of 2800 to 7000 feet. Complete details of the

aircraft radar, its flight patterns, data collection and processing, and the supporting surface contour radar results can be found in the recent paper by Johnson and Weissman (1984).

The two frequency resonance technique samples one ocean wavelength with each Δf , which is then varied to allow a sweep (or tuning) through the ocean spectrum. At each Δf , the intensity of the cross spectrum between the backscattered microwave signals depends on the wave height or energy at that corresponding ocean wavenumber, and on the modulation transfer function, for that component. The MTF determines the strength of radar visibility for each ocean wave; it is produced by the local variations of roughness of the centimeter waves that contribute most to the microwave backscatter. One of the sources of these roughness variations is known to be the orbital velocity of the individual large gravity wave, as explained and demonstrated by Wright and his colleagues (Wright, 1978; Keller and Wright, 1975; Wright et. al., 1980). The results presented in this paper indicate that additional sources of modulation exist. Previous identification and discussions of this "non-wave induced modulation" have been given by Wright, et. al. (1980) and Plant, et. al. (1983).

Another feature of this experiment was the directional discrimination capability of the radar, as a result of its large illuminated surface area, relative to the dimensions of the long gravity waves. In effect, all MTF results presented in this study are directional because of this spatial filtering effect. The data taken on Nov. 13 observed the wave spectrum from 4 different directions. On this day, the surface spectrum was a combination of swell and a wind driven sea, differing in direction by 45° . The flight directions "A" and "B" in Fig. 1 show two of the directions in which the two frequency scatterometer made measurements. The directional spectra measured by the buoy in these flight directions is shown in Fig. 2. and the two frequency resonance results in Fig. 3 show a discrimination between these two different spectra. The analysis of this data shows differences in the magnitude of the directional MTF for these two directions.

2. EXPERIMENT DESCRIPTION AND DATA ANALYSIS

2.1 Aircraft Radar Operation

The data analyzed in this study was acquired from about 20 to 70 km offshore, near Duck, N.C. The flight operations and details of the illumination geometry are presented in the paper by Johnson and Weissman (1984). Of strong interest in this experiment was the behavior of the modulation transfer function as a function of illuminated area and the incidence angle of the radar wave. The illuminated area and the dimensions relative to the ocean wavelength were varied over a substantial range as the aircraft altitude varied from 2800 to 7000 ft, and as the incidence angle ranged from 16° to 50° . These conditions were met with the Nov. 12 data, which also included upwave and downwave flight directions. The smallest illuminated area was 4.8 km^2 and the largest, 46 km^2 . The shapes of these areas could be approximated by an ellipse, with an axial ratio of 2 or less. The four different flight directions employed on Nov. 13 were at a fixed altitude and incidence angle; 4500 feet and 25° from nadir. Support to the Nov. 12 radar data was given by the surface contour radar and the single frequency wave spectrometer referred to as the "ROWS" technique. The details of converting the backscattered two frequency signals into resonance intensity, $X(k)$, is discussed in the above reference. The results are shown in Fig. 3 and 4.

2.2 Buoy Data

The only surface measurement useful on Nov. 13 was that from the XERB buoy located 40 km offshore. This instrument is operated and supported by the NOAA Data Buoy Center. It is a pitch/roll/heave sensor, located where the water depth was 30 meters (Progress Report for NDBO Wave Measurement Systems, 1982). The products available for the estimation of wave spectra are five Fourier coefficients, evaluated at discrete frequencies spanning the practical range of interest. These Fourier coefficients are computed from the motions of the buoy as determined by the elevation and slope sensors. Usually these spectral values (cospectra and quadspectra) are telemetered to shore where they are converted to Fourier coefficients and then directional spectra. Unfortunately, one channel malfunctioned and destroyed the C_{33r} information that is used to compute the A_2 coefficient. The other term, C_{22r} , was intact. In order to fill this gap in the needed wave information, a study was made of the fundamental spectral relations (Kinsman, 1965). This revealed an auxiliary method for recovering C_{33} , from the other measurements. This idea has been used here (with complete updated listings of the other quantities provided by Mr. K. Steele of the NDBO center) to generate directional spectra that appear to be valid (see Appendix). The directional wave height spectrum is estimated for Flight line A & B on Nov. 13, as shown in Fig. 2. These results are then used to infer the modulation transfer function from the aircraft two-frequency data.

3. SYSTEM EQUATION AND MODULATION TRANSFER FUNCTION

The equation that relates the surface elevation spectrum to the two-frequency resonance response is:

$$\chi(k) = \frac{2\pi^2 |m(k)|^2 k^2 E(k, 0)}{A} \quad (1)$$

where k = wavenumber of ocean wave that is in resonance with two-frequency EM wave

$\chi(k)$ = ratio of resonance intensity to background spectrum energy (modulation strength)

$E(k, 0)$ = directional wave spectrum in "0" direction

$m(k)$ = modulation transfer function for ocean wave of wavenumber, k .

A critical assumption in this model is that the reflectivity variation sensed by the radar at each wavenumber is moderately coherent with that part of the height and slope spectrum. A more general relation, on which the above equation is based, is:

$$\chi(k) = \frac{2\pi^2 \bar{\Phi}_R(k, 0)}{A} \quad (2)$$

where $\bar{\Phi}_R(k, 0)$ is the instantaneous two-dimensional reflectivity spectrum. The concept of modulation transfer function is then based on an input-output relation point of view, in which the surface slope spectrum, $k^2 E(k, 0)$ is the input and $\bar{\Phi}_R(k, 0)$ is the output. Then:

$$|m(k)|^2 = \frac{\bar{\Phi}_R(k, 0)}{k^2 E(k, 0)} \quad (3)$$

Detailed studies of this relation and the modulation function can be found in the recent paper by Plant, Keller and Cross (1983).

The key contribution of these ARSLOE results is to use Equation (1) to either:

- A. determine the MTF across a range of conditions of radar parameters (incidence angle, flight direction, altitude and wavenumber) and with different types of surface conditions, using $X(k)$ obtained from the two-frequency resonances.
- B. determine the directional surface spectrum using estimates of the MTF from non-directional spectrum measurements and the values of $X(k)$ mentioned above.

As discussed in the paper by Johnson and Weissman (1984), supporting measurements of the MTF, its spectral variation and its coherence properties, were made with a single frequency radar that receives and correlates the backscattered power and Doppler variations (related to the surface orbital velocity) to achieve an independent measurement of this quantity.

One important assumption in the use of Eq. (1) to (3) is that the aircraft velocity is much larger than the phase velocity of the ocean wave that is in resonance with each " Δk ". Then the resonance observed from the aircraft is not sensitive to whether or not these periodic reflectivity patterns are coherent with the orbital velocity of the surface waves. Then the MTF measured with single frequency radars are not equivalent to those measured with the two frequency radar, but they are believed to be closely related to each other. This topic needs further study.

4. MEASURED MTF RESULTS

The MTF results to be presented first are those derived from Eq. (1) for the various flight parameters of Nov. 12. A value of the MTF can be calculated at each Δk (or difference electromagnetic wavenumber) so that each flight line yields the functional dependence of the MTF vs. the matching ocean wavenumber, at a fixed altitude and angle, and direction relative to the wind. Twelve of these functions have been computed for the Nov. 12 data (and supported by the SCR derived wave spectra) and two from the "A" and "B" lines of Nov. 13 (based on buoy derived spectra). The functions obtained from the Nov. 12 data have been plotted individually for each upwave and downwave path in Fig. 5 to 7, those for the Nov. 13 data are in Fig. 8. An additional MTF was computed, based on the non-directional spectrum measured by the buoy on Nov. 13. This calculation is performed by integrating the resonance response ($X(k, \theta)$ in Eq. 1) over 360° in θ , at each value of k . The right half of Eq. 1 then contains the non-directional spectrum term.

Analysis of these results was done from several points of view. Almost all share the following characteristics: the magnitudes start high at the lowest wavenumbers, then decrease to a definite minimum about $k=.06$ to $.08$, then usually rise by at least 25% or up to 100% above this minimum. This is often followed by a gradual change at the higher k values, either an increase or decrease. Another definitive and general result is that the magnitudes differed strongly on these two days, in accordance with the environmental conditions. On Nov. 12, the winds were high, about 12 m/s, with accompanying high waves. The MTF values averaged in the range from 8 to 16. In contrast, on Nov. 13 the values were usually between 20 and 40. The factor of two increase shows a good correlation with the inverse of the wind which, on this day was below 6 m/s when the flights were made. This is in good agreement with measure-

ments of the MTF conducted from towers (Plant. et. al. 1983; Weissman, 1983) where the magnitude was observed to depend inversely on the local wind, and on other environmental parameters.

Special attention was also given to other characteristics of the MTF, such as its dependence on incidence angle, upwind vs. downwind look directions, and any variations caused by changes of the flight path relative to the wind direction. Across the spectrum of wavenumbers from $k = .05$ to $.14$, ratios of the MTF looking downwave vs. upwave have been computed to test for significant differences. These results are in Fig. 9 and 10. The data for incidence of 16° to 25° in Fig. 9 display no bias one way or the other. These ratios average to about unity, across the whole spectrum. The effect of incidence angle becomes important at values at 40° to 50° , where this ratio takes on a definite wavenumber dependence. The down-wave to upwave ratio is usually greater than 1, and is often well above this value. The interesting property of all three data sets is that this function increases strongly with k , above $k = .10$, resulting in ratios of 1.5 to 2.7. The interpretation of these results should be done in a more general context, because previous studies of this ratio were conducted and discussed by Wright (1978), who found a strong wind influence on these characteristics in addition to variations of this ratio from unity.

The other important dependence of the MTF studied is that due to incidence angle. Flight operations on Nov. 12 encompassed a range from 16° to 50° , substantial enough to test conditions of interest for the remote sensing of ocean waves. Considering the large assortment of wavenumber values in the data set, a simplification was performed to work with the average of a subset of values of the MTF measured along each flight line. The data from each of the Figures from 5 to 7 was averaged, but only values of MTF whose wavenumbers are in the range $.05 \leq k \leq .09$ were included in the average. These twelve average values are plotted in Fig. 11. The upwind/downwind condition creates a small "random" fluctuation, but they still show a definite trend, downward with increasing incidence angles. For the 16° case, the MTF ranges from 9.7 to 13.2, while at 40° its from 8.3 to 10.4, and the 50° value is 9.2. Numerically, this is not a large effect, but detecting its presence will be helpful in sorting out other dependencies in future applications.

5. CONCLUSIONS

Our major findings are the functional dependencies of the MTF on ocean surface wavenumber, flight direction and incidence angle. The large data set allows the quantitative description of these dependencies, as seen in Fig. 5 to 11. Small incidence angle dependence means that future remote sensing systems need not be limited in the choice of incidence angle of the radar beam. A difference in magnitude between the aircraft and tower results was also detected and found to be plausible, on physical grounds. In addition, the effects of environmental conditions have also been seen and analyzed: increases in wind speed and sea state cause strong decreases in the MTF. With this new knowledge, the two frequency scatterometer can now be considered a useful instrument for the measurement of ocean surface spectrum by aircraft. For the MTF, no theoretical explanation of these scattering effects based on electromagnetic scattering theory and air-flow over ocean waves (including all short capillary generation mechanisms) has yet been achieved.

Much progress has been made on accumulating tower based radar results and wave follower measurements under a variety of air-sea conditions (Plant, et. al., 1983; Hsiao and Shemdin, 1983), but more is necessary in order to explain the aircraft results. Such questions as: "what are the physical sources that generate the short capillary waves which are modulated by the long waves" and "why should the MTF observed from an aircraft be different from what is measured on an ocean platform", need to be

addressed.

It is recommended that two topics be focussed on to advance this technique:

- (1) Learning more about the mechanism for the modulation of ocean waves (their origin, linearity, and coherence with the orbital velocity) that is detected by remote sensing radars.
- (2) Combined (dual) sensor capabilities to improve the measurement accuracies of each separate instrument. Simultaneous two frequency scatterometry and conventional scatterometry would measure wave spectra plus wind speed. Since both quantities affect each sensor, the accuracy of each sensor could be improved.

6. APPENDIX

Calculation of $A_2(f)$, the Wave Spectrum Angular Coefficient by Substitution for the Missing Spectrum, $C_{33}(f)$

Our application of the XERB buoy data to compute the surface directional spectrum involves using the well known Fourier Series approximation (in the notation and format of the NOAA Data Buoy Office), with the smoothing coefficients developed by Longuet-Higgins:

$$S(f, \theta) = \frac{1}{2} A_0 + A_1 \left(\frac{2}{3} \right) \cos(\theta) + B_1 \left(\frac{2}{3} \right) \sin(\theta) + A_2 \left(\frac{1}{6} \right) \cos(2\theta) + B_2 \left(\frac{1}{6} \right) \sin(2\theta)$$

These coefficients are computed from the several spectral functions measured directly by the buoy. Among these are: C_{11} , the auto-spectrum of the surface elevation, with C_{22} and C_{33} , the auto-spectra of the two orthogonal components of slope. The difficulty encountered was for $A_2(f)$ only, which depends on $C_{22}(f) - C_{33}(f)$. For the duration of the experiment, $C_{33}(f)$ was not available because of a malfunction, and only C_{22} and C_{11} and the other terms were being returned to shore for data processing.

It was observed, in the course of this study, that a fundamental relation exists among C_{11} , C_{22} and C_{33} . From Longuet-Higgins, et. al. (1963) it is easily proved that:

$$k^2 C_{11} = C_{22} + C_{33}$$

Therefore $A_2(f)$ can be computed from:

$$C_{22} - C_{33} = 2 C_{22} - k^2 C_{11}$$

This substitution, and the available data listing for the other coefficients made it possible to derive valid estimates of the wave directional spectrum for Nov. 13, for application to the two frequency scatterometer analysis.

7. ACKNOWLEDGEMENTS

The results obtained in this study were made possible by the supporting ocean spectrum data from the Surface Contour Radar provided by Dr. Edward J. Walsh of the NASA Wallops Flight Center. His interest and cooperation in this study is greatly appreciated. We also appreciate the advice of Mr. Kenneth Steele of the NOAA Data Buoy Office, who provided us with the best available data set for Nov. 13. We thank Dr. William J. Plant of the Naval Research Laboratory for enlightening and stimulating discussions in the course of this study.

Support for this study, which was provided by the NASA Oceanic Processes Program, Dr. W. Stanley Wilson, Chief, through Grant NAGW-468, is gratefully acknowledged.

8. REFERENCES

- Alpers, W. and K. Hasselmann, 1978: The two frequency microwave technique for measuring ocean surface wave spectra from an airplane or satellite. *Boundary Layer Meteor.*, 13, 215-230
- Hsiao, S.V. and O.H. Shemdin, 1983: Measurements of wind velocity and pressure with a wave follower during MARSEN. *J. Geophys. Res.*, 88, C14, 9841-9850
- Johnson, J.W. and D.E. Weissman, 1984: The two-frequency microwave resonance technique from an aircraft: a quantitative estimate of the directional ocean surface spectrum. *Radio Sci.* (in press)
- Keller, W.C. and J.W. Wright, 1975: Microwave scattering and the straining of wind-generated waves. *Radio Sci.*, 10, 139-147
- Longuet-Higgins, M.S., D.E. Cartwright, and N.D. Smith, 1963: Observations of the directional spectrum of sea waves using the motions of a floating buoy. *Ocean Wave Spectra*, Prentice-Hall, Inc., Englewood Cliffs, N.J., 111-136
- Plant, W.J. and D. Schuler, 1980: Remote sensing of the sea surface using one and two frequency microwave techniques. *Radio Sci.*, 15, 605-615
- Plant, W.J., W.C. Keller and A. Cross, 1983: Parametric dependence of ocean wave-radar modulation transfer function. *J. Geophys. Res.*, 88, C14, 9747-9756
- Progress Report for NDBO Wave Measurement Systems Development and Field Testing (1980-1982), Sept. 1982, Publ. #F-344-3, U.S. Dept. of Commerce, NOAA Office of Ocean Technology and Engineering Services, NOAA Data Buoy Office NSTL Station, MS 39529
- Weissman, D.E., 1983: The dependence of the radar modulation transfer function on environmental conditions and wave parameters, Final Report, ONR Contract N00014-83-M-0081, August 1983
- Wright, J.W., 1978: Detection of ocean waves by microwave radar: the modulation of short gravity-capillary waves. *Boundary Layer Met.* 13, 87-105
- Wright, J.W., W.J. Plant, W.C. Keller and W.L. Jones, 1980: Ocean wave radar-modulation transfer functions from the West Coast Experiment, *J. Geophys. Res.* 85, 4957-66

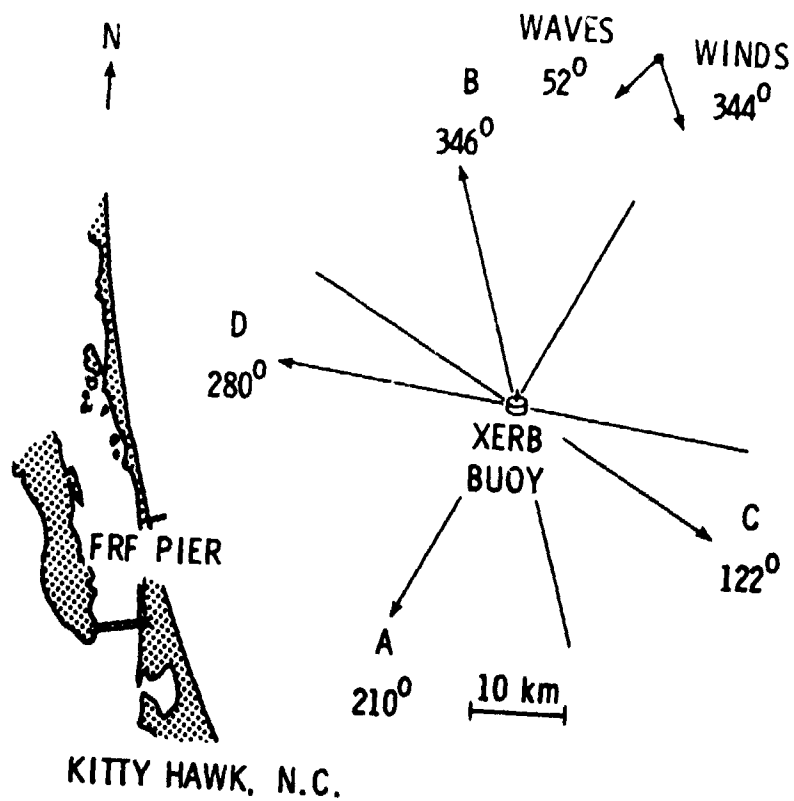
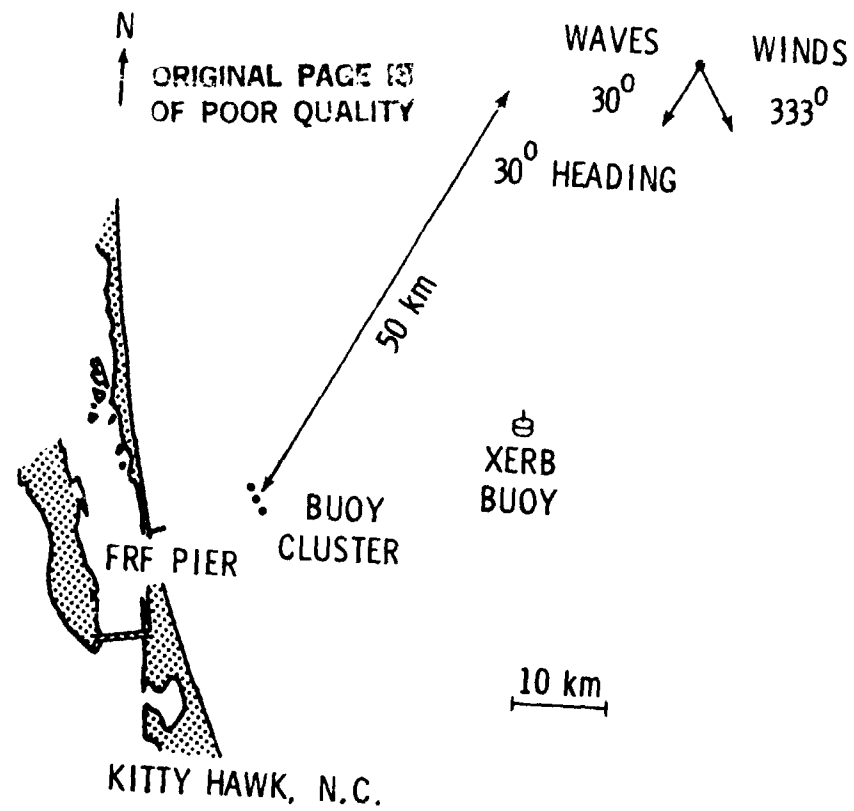


Fig. 1 ARSLOE Experiment Site, top: Nov. 12 flight paths;
bottom: Nov. 13 flight paths

DIRECTIONAL WAVE SPECTRA FROM BUOY
DATA AND THE TWO FREQUENCY RADAR
RESONANCE - NOV. 13

SOLID CURVE - BUOY DATA
O - OPEN CIRCLES - AIRCRAFT RADAR

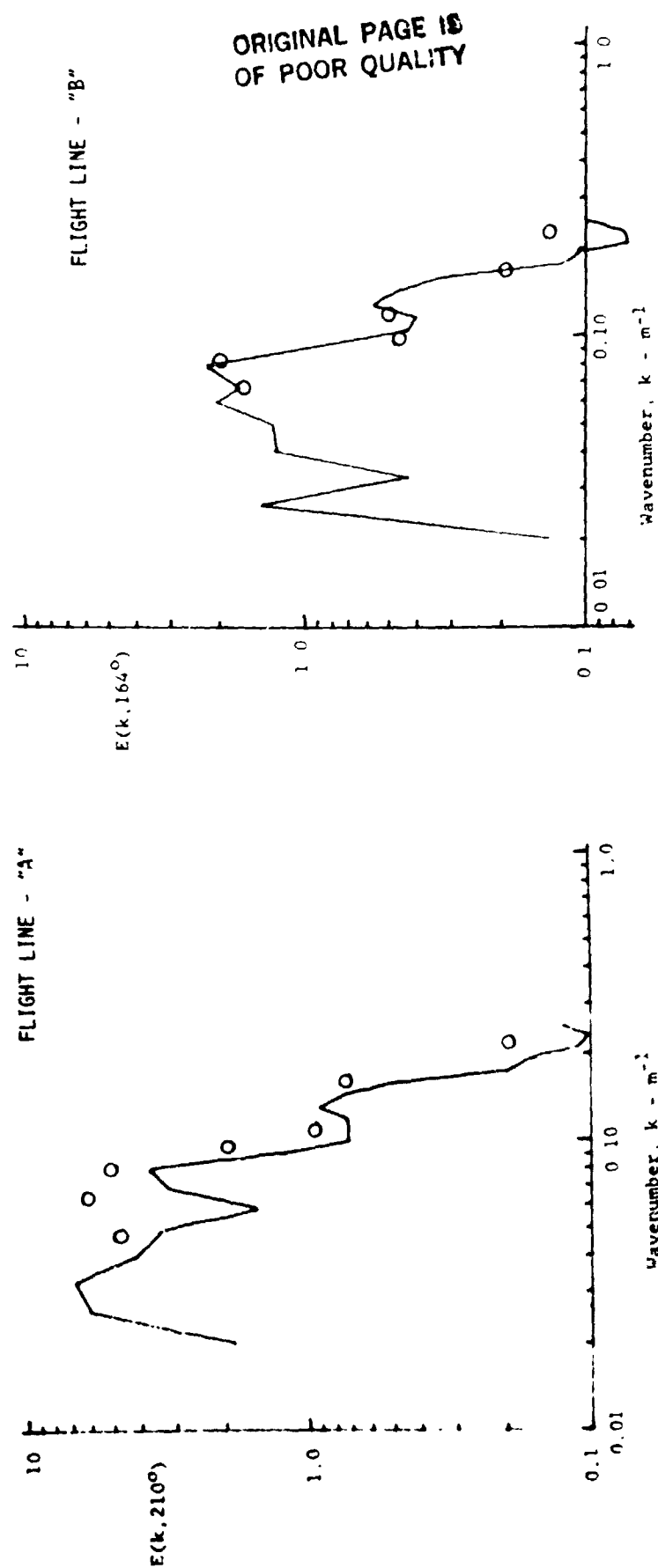


Fig. 2

ARSLOE, 11/13/80

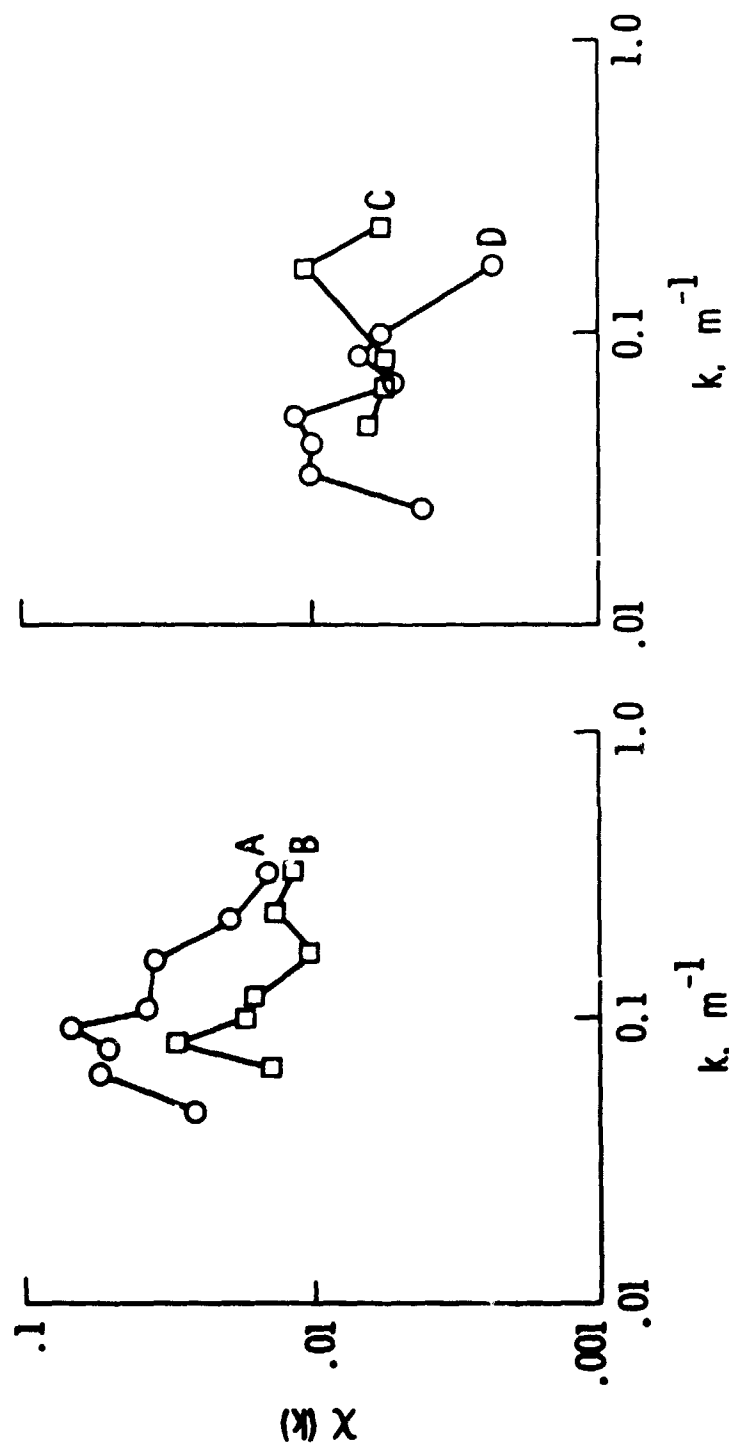
 $\theta = 25^\circ$ $H = 1370 \text{ m}$ 

Fig. 3 Radar modulation spectra demonstrating the dependence upon radar viewing direction: lines A - radar aligned with dominant wave direction, B - radar aligned with wind direction, C & D - radar aligned with neither

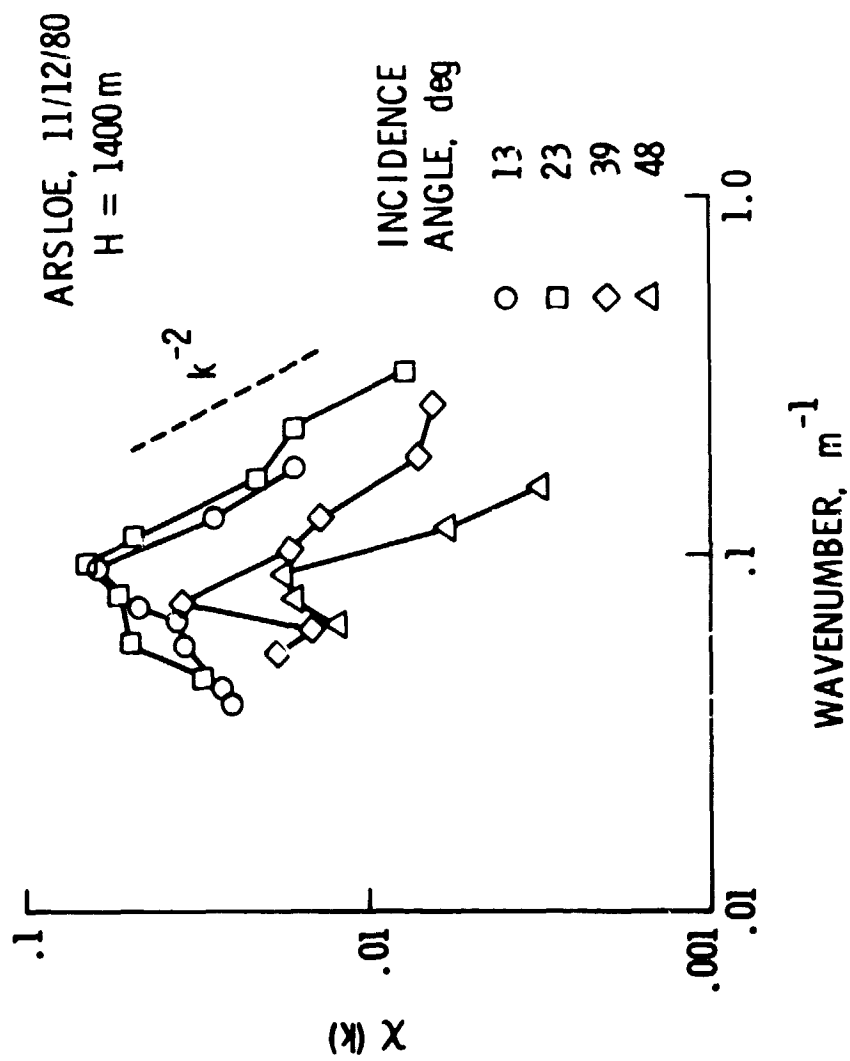


Fig. 4 Radar modulation spectra measured during ARSLOE at a variety of incidence angles

MODULATION TRANSFER FUNCTION VS.
OCEAN WAVENUMBER

NOV. 12 DATA

SOLID CURVES - UPWAVE

DOTTED CURVES - DOWNWAVE

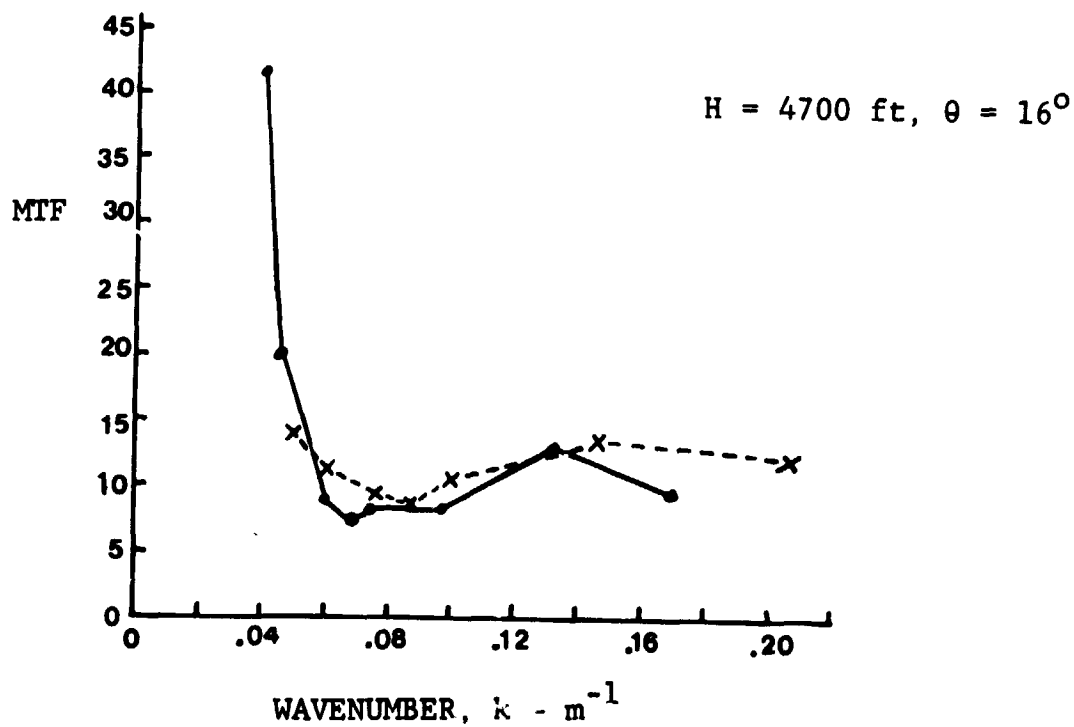
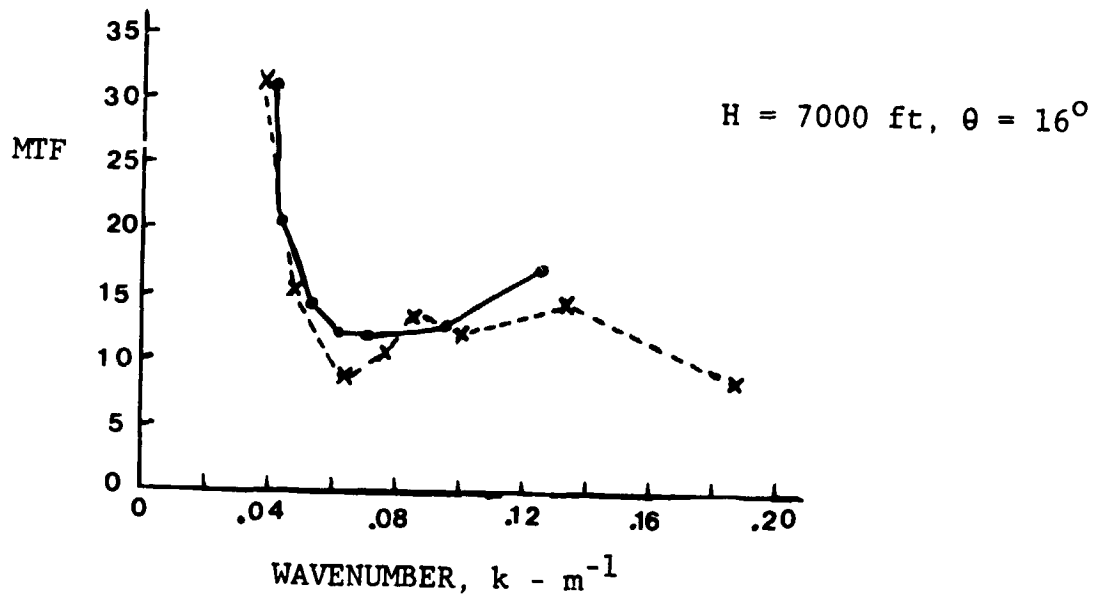


Fig. 5 Two Frequency Scatterometer inferred modulation transfer function versus ocean wavenumber

MODULATION TRANSFER FUNCTION VS.
OCEAN WAVENUMBER

NOV. 12

SOLID CURVE - UPWAVE
DOTTED CURVE - DOWNWAVE

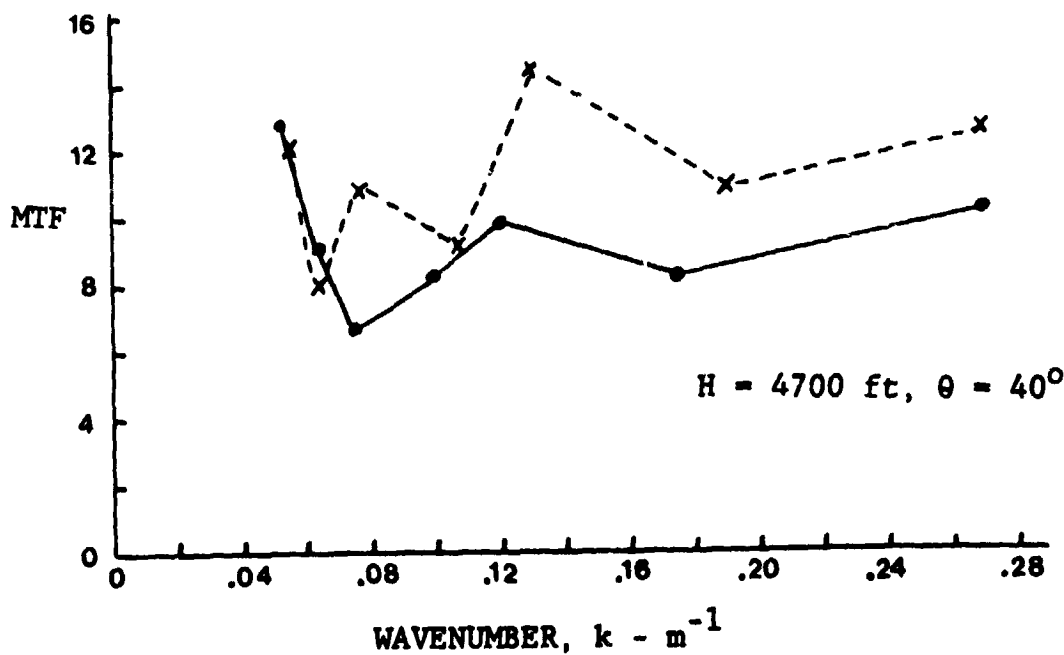
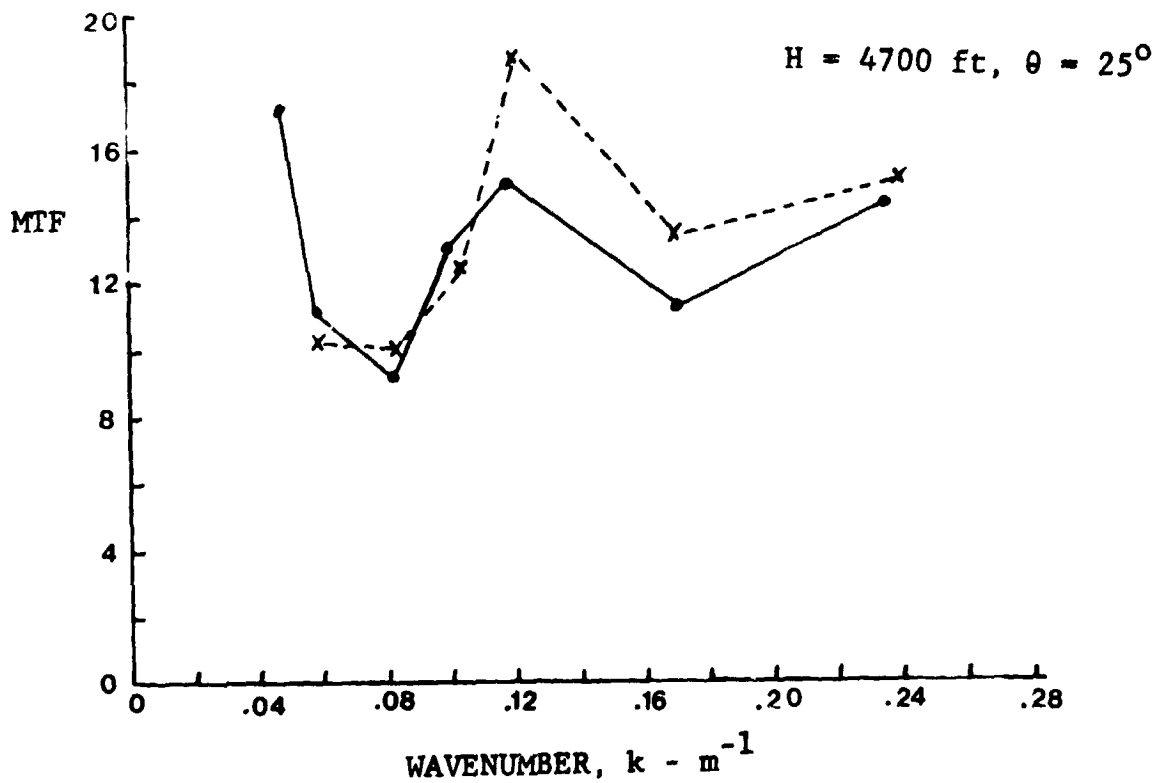


Fig. 6 Two Frequency Scatterometer inferred modulation transfer function versus ocean wavenumber

MODULATION TRANSFER FUNCTION VS.
OCEAN WAVENUMBER

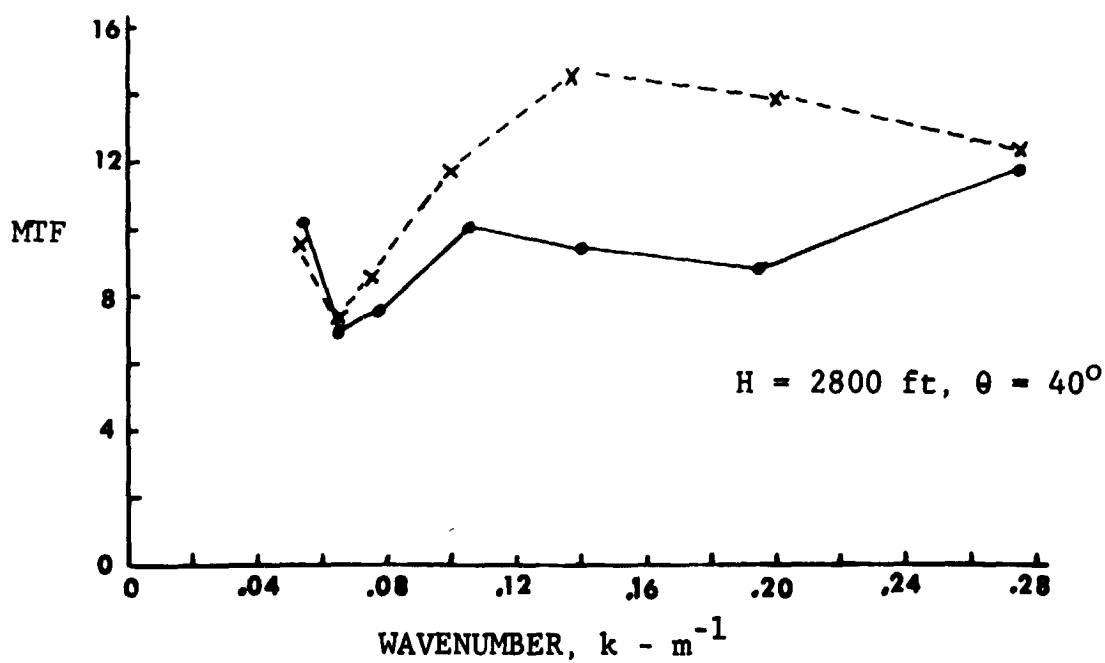
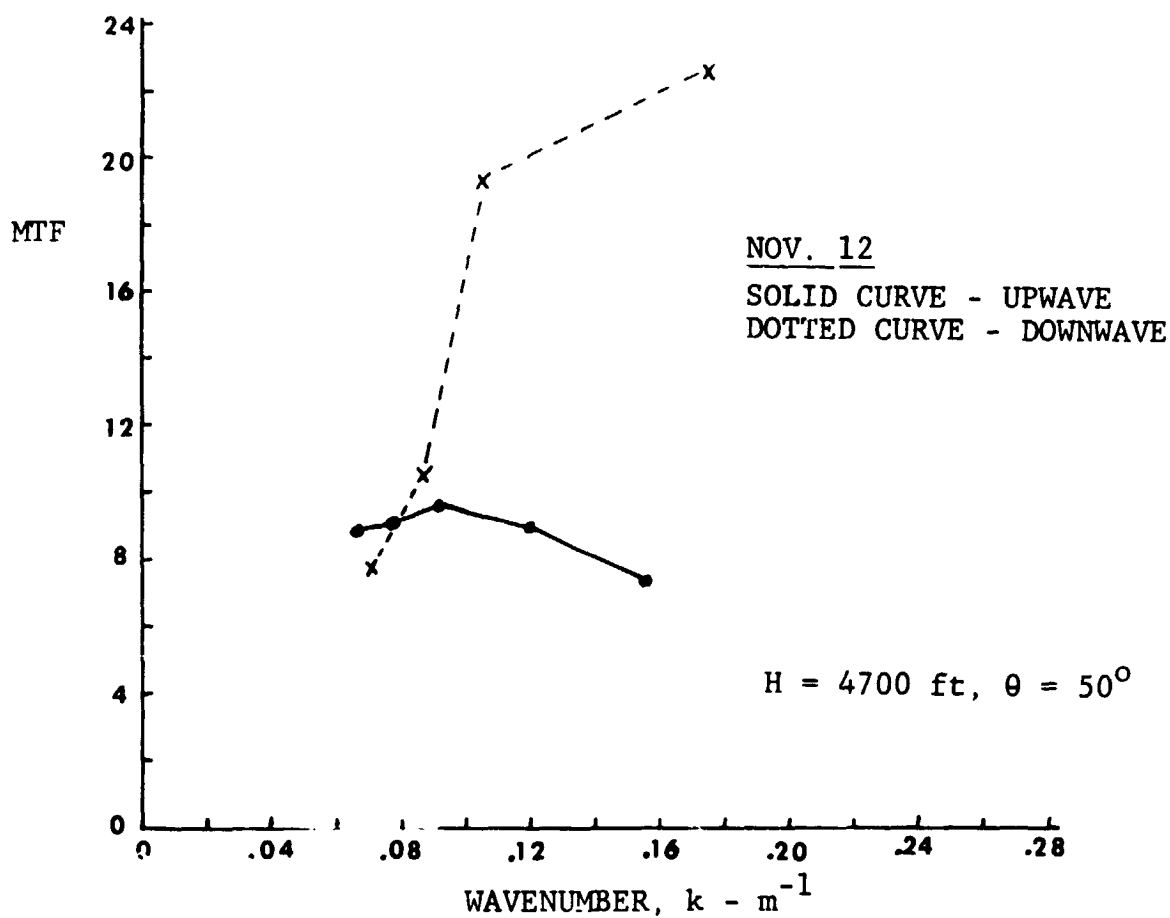


Fig. 7 Two Frequency Scatterometer inferred modulation transfer function versus ocean wavenumber

MODULATION TRANSFER FUNCTION VS.
OCEAN WAVENUMBER

NOV. 13

H = 4500 ft

$\theta = 25^\circ$

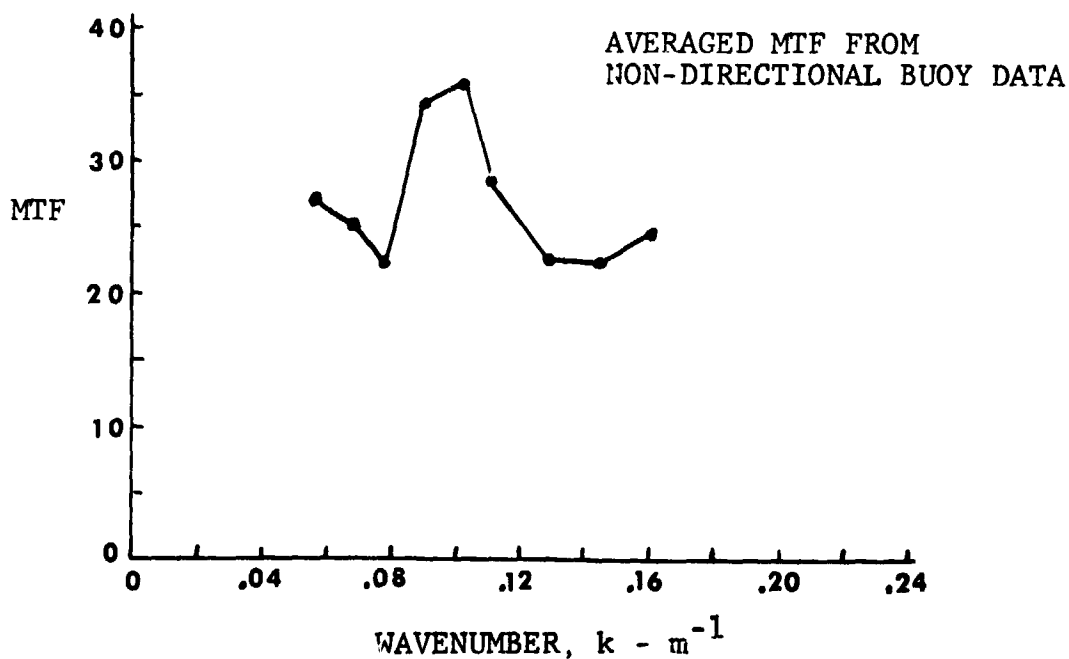
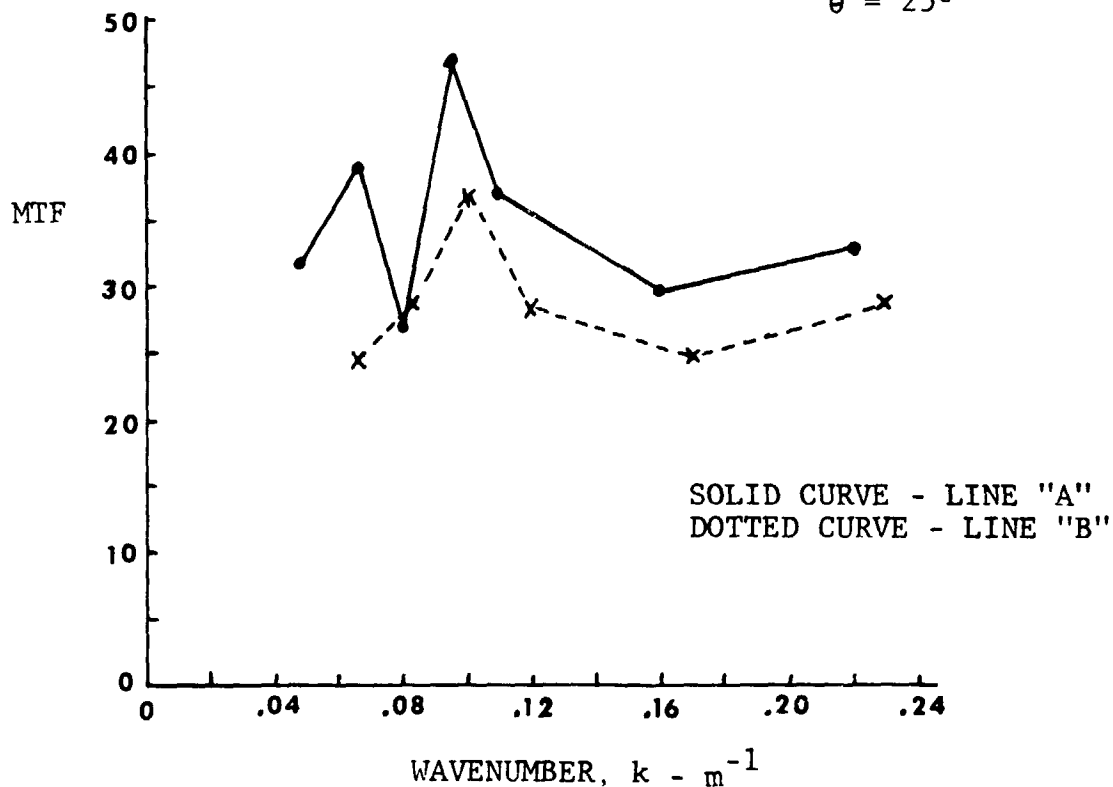


Fig. 8 Two Frequency Scatterometer inferred modulation transfer function versus ocean wavenumber, Nov. 13; top: values obtained from flight lines "A" & "B" using buoy directional data with radar data; bottom: results obtained by averaging radar and buoy measurements over 360° , using 4 flight directions.

RATIO OF DOWNWAVE MTF TO UPWAVE MTF

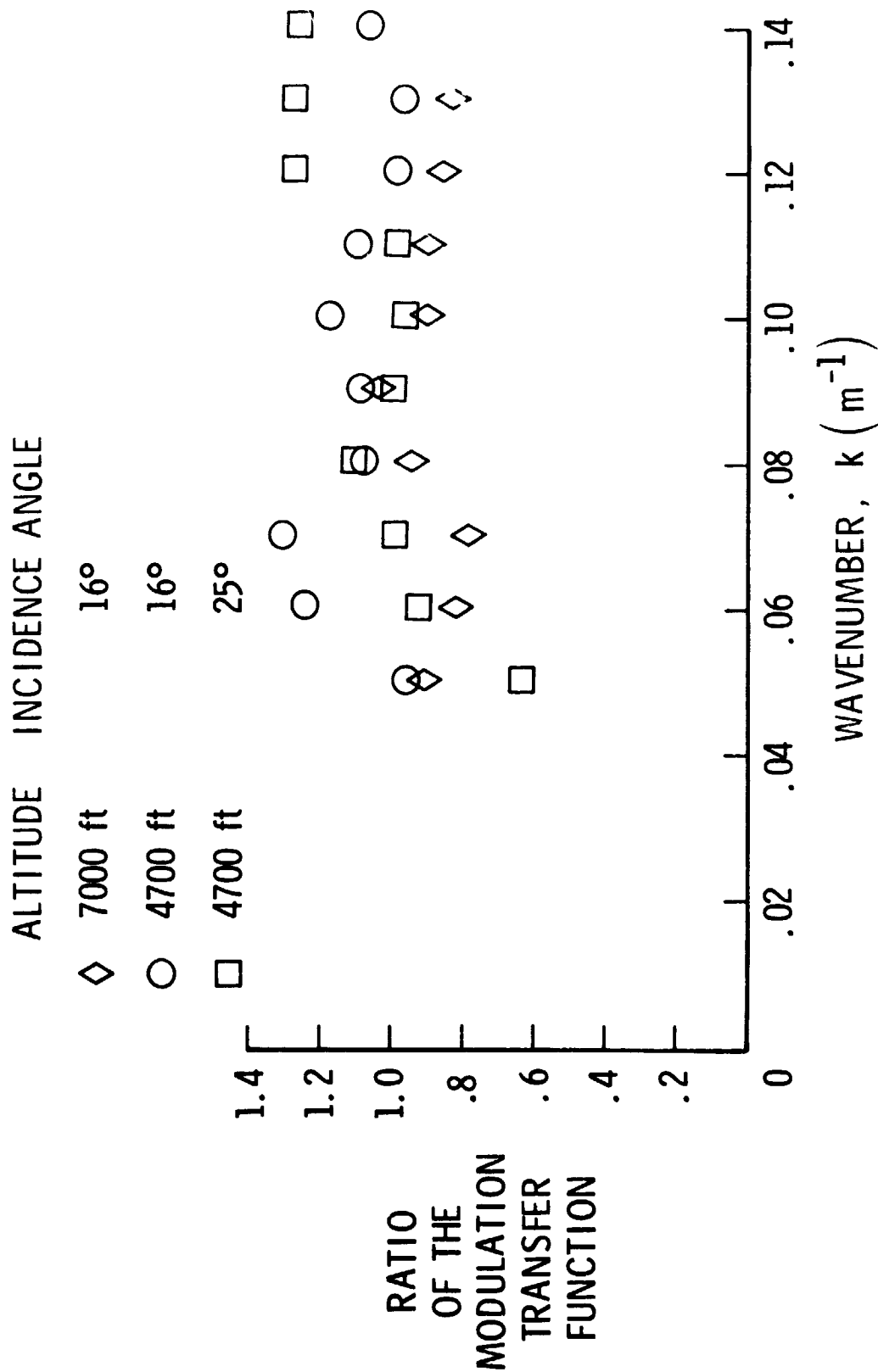
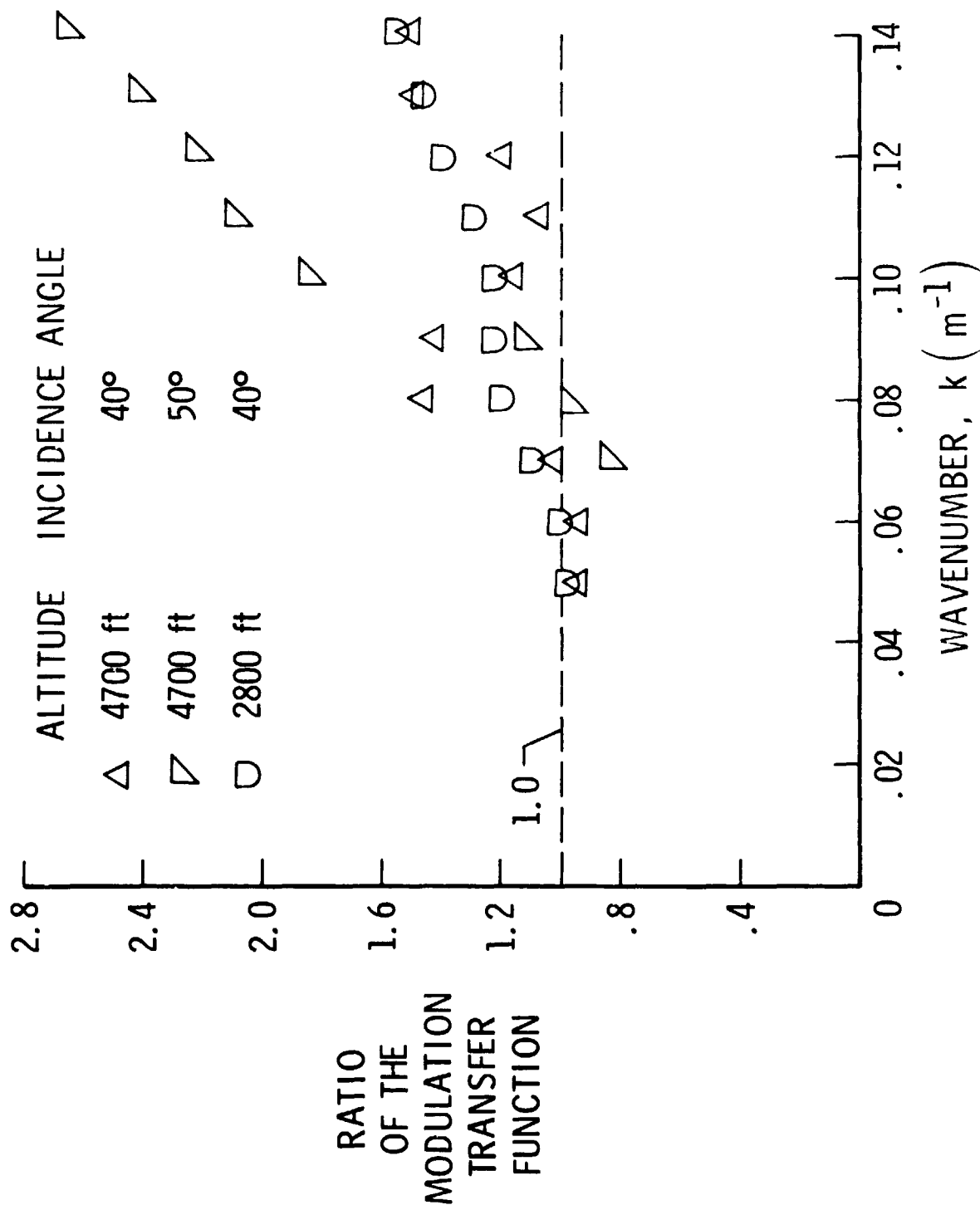


Fig. 9

RATIO OF DOWNWAVE MTF TO UPWAVE MTF



MTF AVERAGED OVER $.05 \leq k \leq .09$

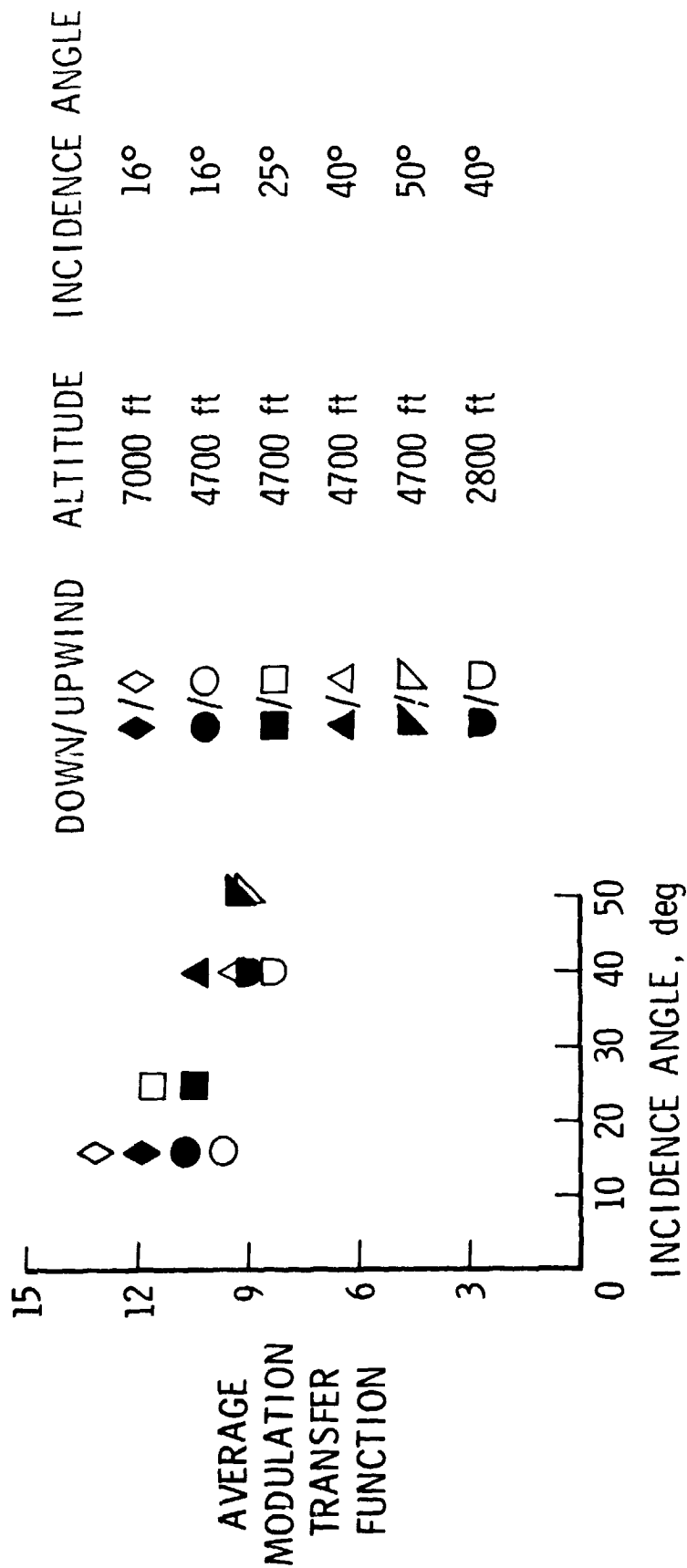


Fig. 11

SOME CASE STUDIES OF OCEAN WAVE PHYSICAL PROCESSES UTILIZING THE
GSFC AIRBORNE RADAR OCEAN WAVE SPECTROMETER

F. C. Jackson
NASA Goddard Space Flight Center
Laboratory for Atmospheric Sciences
Greenbelt, Maryland, USA

ABSTRACT

The NASA K_u -band Radar Ocean Wave Spectrometer (ROWS) is an experimental prototype of a possible future satellite instrument for low data rate global waves measurements. The ROWS technique, which utilizes short-pulse radar altimeters in a conical scan mode near vertical incidence to map the directional slope spectrum in wave number and azimuth, is briefly described. The potential of the technique is illustrated by some specific case studies of wave physical processes utilizing the aircraft ROWS data. These include i) an evaluation of numerical hindcast model performance in storm sea conditions, ii) a study of fetch-limited wave growth, and iii) a study of the fully-developed sea state. Results of these studies, which are briefly summarized, show how directional wave spectral observations from a mobile platform can contribute enormously to our understanding of wave physical processes.

1. INTRODUCTION

A simple method for measuring the vector wave number spectrum of ocean surface gravity waves from aircraft and satellite platforms using modified radar altimeters has been described and investigated theoretically by Jackson (1981) and demonstrated experimentally by Jackson *et al.* (1984a). In this paper, rather than dwell on the details of the technique, we will present some specific aircraft results that will serve to illustrate the enormous potential of this measurement technique for furthering our understanding of wave physical processes.

The GSFC K_u -band Radar Ocean Wave Spectrometer (ROWS) is a noncoherent, short pulse radar that uses a near-nadir directed conically scanning antenna to map wave directionality. Table 1 gives the pertinent instrument characteristics. Figure 1 depicts the aircraft measurement geometry. A small rotary antenna bore-sighted to 16° incidence produces a footprint at the nominal 10 km aircraft altitude measuring approximately 1500 m in the range (x) dimension and 700 m in the orthogonal azimuthal (y) dimension. The surface is probed in the range dimension using 12.5 ns compressed pulses. At the nominal incidence angle for peak power return, $\theta = 13^\circ$, the surface range resolution is 8 m. The directional resolution of the ROWS is obtained by a simple phase front matching condition between electromagnetic and ocean wave Fourier contrast wave components across the relatively broad azimuth beamwidth. That is, the broad beamwidth functions to isolate, or resolve, ocean Fourier components whose wave vectors $k = (k, \phi)$ are aligned with the radar azimuth ϕ . In this respect, the ROWS technique is similar to the dual frequency technique investigated by Alpers and Hasselmann (1978). Let the fractional cross section variation for any pixel (x, y) be denoted $\delta\sigma/\sigma$. The fractional reflectivity modulation m seen by the radar is given by $\delta\sigma/\sigma$ averaged laterally across the beam. If $G(y)$ denotes the lateral gain pattern, then

RADAR OCEAN WAVE SPECTROMETER

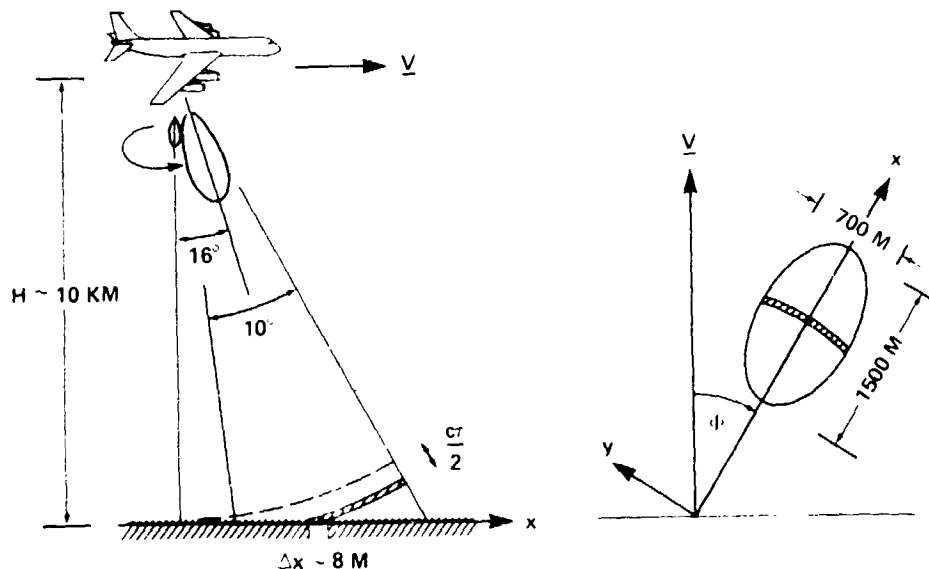


Figure 1. ROWS Measurement Geometry.

TABLE 1. ROWS INSTRUMENT CHARACTERISTICS

Frequency:	13.9 GHz
Pulse type:	Linear FM, 100 MHz, 1.2 μ s chirp
Pulse length:	12.5 ns compressed
Peak power:	2 kW
PRF:	100 Hz max
Detection:	Noncoherent, square law
Antenna:	10° elevation X 4° azimuth printed circuit, 16° incidence boresight, 6 rpm rotation rate
Data:	Digital, max 1024 six bit word frame size, sample gate width selectable 2, 5, ... ns; recording at full PRF

$$m(x, \phi) = \delta W/W = \frac{\int G^2(y) (\delta\sigma/\sigma) dy}{\int G^2(y) dy} \quad (1)$$

where $\delta W/W$ is the fractional modulation in received power (averaged over the clutter fluctuations).

In the near-vertical specular backscatter regime in which the ROWS operates, the cross-section variation is primarily a geometrical tilting effect, hydrodynamic modulation effects being of second order. Provided the large-wave steepness is small compared to the total surface roughness as measured by the total (diffraction-effective) mean square slope β^2 , then the cross section variation will be proportional to the large-wave slope component in the plane of incidence $\partial\zeta/\partial x$ as

$$\frac{\delta\sigma}{\sigma} = \left(\cot \theta - \frac{1}{\sigma} \frac{\partial\sigma}{\partial\theta} \right) \frac{\partial\zeta}{\partial x} \quad (2)$$

where θ is the angle of incidence and σ^0 is the average cross section of the surface. In (2) the first term represents a linearized area tilt term while the second term represents the rigid rotation of the small-scale scattered power pattern by the large wave slopes. The average cross section is proportional to the probability density function of surface wave slopes evaluated at the specular condition for backscatter (namely, slope = $\tan \theta$). Assuming a Gaussian isotropic distribution of slopes, the cross-section roll-off is given approximately by

$$\frac{1}{\sigma^0} \frac{\partial \sigma^0}{\partial \theta} = - \frac{2 \tan \theta}{\beta^2} \quad (3)$$

where again β^2 is the total mean square slope.

Assuming that the water wavelength $2\pi/k$ is small compared to the azimuth beamwidth L_y , $kL_y \gg 1$, it follows that the spectrum of $m(x, \phi)$ is proportional to the directional wave slope spectrum. If the gain pattern is assumed to be Gaussian, $G(y) = \exp(-y^2/2L_y^2)$, one finds that in the limit of large kL_y the directional modulation spectrum is given by

$$P_m(k, \phi) = \frac{\sqrt{2\pi}}{L_y} \left[\cot \theta - \frac{2 \tan \theta}{\beta^2} \right]^2 k^2 F(k, \phi) \quad (4)$$

where F is the polar-symmetric directional height spectrum, defined such that the height variance,

$$\langle \epsilon^2 \rangle = \int_0^\infty \int_0^\pi F(k, \phi) k dk d\phi \quad (5)$$

We note that in (1) the azimuth coordinate y was treated as rectilinear; this is permissible for directionally spread seas. The wave front curvature enters, along with the finite footprint size and antenna rotation, in determining the directional resolution. In the satellite case the resolution is typically 7° (200 m water wave), while in the aircraft case the resolution is typically 20° .

The ROWS data processing, described in detail in Jackson *et al.* (1984a), consists of first correcting for the wave front sphericity on a pulse by pulse basis on going from the signal delay time to the surface range coordinate x , and then integrating the pulse returns in surface-fixed range bins over a time corresponding to 15° of antenna rotation ($N = 42$ pulses). The surface tracking is accomplished using an input aircraft speed. The modulation $m(x, \phi)$ is then computed by normalizing by an estimate of the average power envelope $\langle W(x, \phi) \rangle$ obtained by averaging over several antenna rotations. Unity is then subtracted and the data are rewindowed and the spectrum $P_m(k, \phi)$ computed by fast Fourier transform. The final estimates of P_m are obtained by averaging the spectra over several antenna rotations, subtracting a computed residual fading spectrum, and correcting for the finite pulse response (20% spectral roll-off at 40 m wavelength).

We note that the tilt model solution (4) has been shown by Jackson (1981) to correspond to the first term in a series expansion of the geometrical optics solution for P_m , where the ordering parameter is the large-wave steepness. Non-linear terms, both electromagnetic and hydrodynamic, were found to be small provided that i) F^2 is sufficiently large (wind speeds greater than ca. 5 ms^{-1}), ii) the incidence angle lies in the range of 8° - 16° , and iii) the large-wave slope is not too large (steepness < 0.10). The ROWS technique in general, and the tilt model result in particular, have been extensively validated by Jackson *et al.* (1984a). In the following, we will illustrate the power of the ROWS technique

by presenting several case studies of ocean wave physical processes utilizing the ROWS data. The data to be shown have been transformed from slope spectra to height spectra in the frequency domain assuming the linear deep-water dispersion relationship. Also, we have symmetrized the observed 260° modulation spectrum so that it is strictly polar-symmetric (this has the effect of doubling the degrees of freedom and eliminating any upwave/downwave asymmetry that may result from second order effects). The height spectra are computed from the symmetrized modulation spectra according to

$$S(f, \alpha) = (2/\alpha f) P_m(k, \alpha) \quad (5)$$

where α is the sensitivity coefficient, the factor of $k^2 F$ in (4), f is the frequency in Hz, and where S is defined so that the variance $\langle \eta^2 \rangle = \int \int S(f, \alpha) df d\alpha$. The final spectra shown here were obtained from nine or more independent rotations, and so the degrees of freedom of the directional spectra shown here number no less than $2 \times 9 \times \pi \times 26 = 26$. The degrees of freedom for the nondirectional spectra number several hundred (this confidence limit is not shown).

2. EVALUATION OF HINDCAST MODEL PERFORMANCE IN STORM CONDITIONS

Our present understanding of the basic physics of ocean waves is to a large extent embodied in numerical wave forecast/hindcast models, specifically, in the right hand side of the spectral energy transport equation. Considerable uncertainty exists in the parameterization of wave spectral growth (and decay) under the action of variable winds, particularly in the specification of directional distributions and the redistribution of wave energy over direction in turning wind fields. This is abundantly clear from Hasselmann's (1984) model intercomparison report. We have undertaken a study with V. Cardone (Oceanweather, Inc.) comparing ROWS data taken in the Norwegian Sea during an intense storm to special hindcast runs with well-specified wind fields (or as well-specified as possible). The comparison is particularly interesting because the storm not only produced very high seas (ca. 10 m), but created a complex, rapidly evolving wave field. The comparison thus provides a strong test of model performance. Initial model runs have been made with a fine-mesh (100 km/3 hr) version of Cardone et al.'s (1976) ODGP discrete spectral model (a variant of the U. S. Navy's operational SOWM model) and with a coupled discrete model, the SAIL model (cf. Hasselmann, 1984). The hindcasts used all available ship wind reports on record and aircraft winds obtained during a low-level flight leg. The modeled area was the N. E. Atlantic, and the spin up time (before the flight of interest) was two weeks.

The NASA Ames' CV-990 flight track and ROWS data takes between ca. 0800 Z and 1000 Z on Nov. 3, 1978 are shown in Figure 2 along with the nearby ODGP model grid points. The flight track constitutes a box pattern measuring ca. 150 km (N-S dimension) by 700 km (SW-NE direction). The aircraft altitude was ca. 10 km. Ten ROWS files were obtained in the flight box; these are indicated by the letters A-J in Figure 2. At the northern end of the box, close to file A, is the weather station Tromsøflaket (TROMSO) which provided 3-hourly wind reports and Waverider wave spectra observations. The synoptic situation at 1800 Z on Nov. 2 at about the peak of the storm is shown in Figure 3. By flight time, the low had moved to the north of the box, and the winds had shifted to westerly over the northern end of the box. The high pressure ridge also moved northward, its axis transecting the midsection of the box at the time of the flight. Figure 4 is a presentation of the ten files of ROWS data in the form of polar contour plots of directional height spectra laid out on a map of the Norwegian Sea. The spectra, contoured at equal intervals, are scaled to the peak values; absolute

ORIGINAL PAGE IS
OF POOR QUALITY

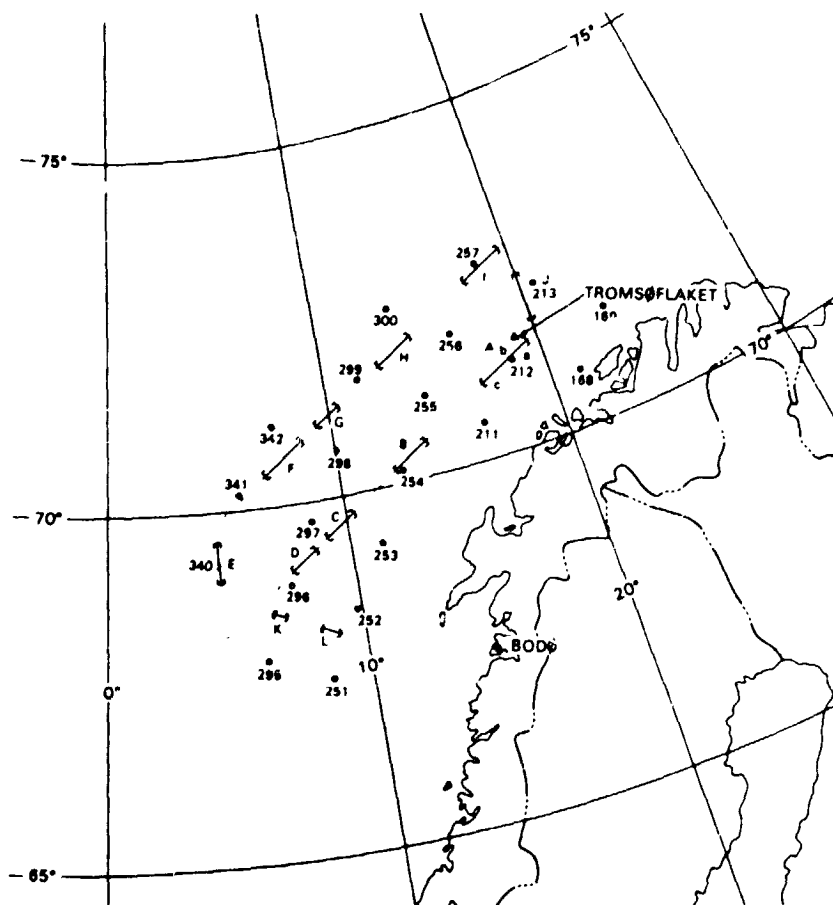


Figure 2. CV-990 Flight Track and ROWS Data Takes on Nov. 3, 1978, 0800-1000 Z.

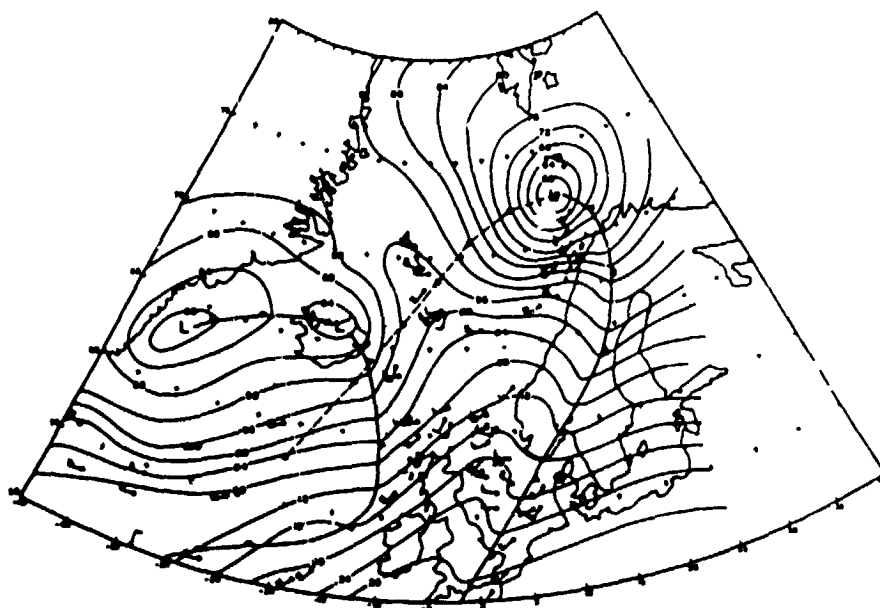


Figure 3. Nov. 2 1800 Z Synoptic Chart Showing Norwegian Sea Storm.

energy levels are indicated by the estimated significant wave heights given numerically in meters beside each spectrum. The spectra shown are one-sided. The 180° ambiguity in the ROWS spectra was resolved and the true direction of wave travel determined on the basis of the synoptic situation. The synoptic view of the wave field in Figure 4 shows two major wave trains traveling at nearly right angles to each other. The NE travelling component appears to enter the box at the southern end more or less as swell, decay slightly, and then grow rapidly in the stronger winds in the northern end of the box, where the winds are westerly at ca. 20 ms^{-1} . The NE direction of this wave train is maintained over the entire 700 km distance of the flight legs. Only at the northernmost location does one see energy appearing in the local wind direction (this is evident in the comma shape of file A). The SE traveling component is evidently a pulse of wave energy generated in the western sector of the rapidly moving cyclone at about the 1800 Z map time (Figure 3).



Figure 1. ROWS Directional Height Spectra in Norwegian Sea Storm. Tick marks are 0.05 Hz. Spectra are scaled to peak values. The numbers indicate wave heights in meters.

An indication of the quality of the ROWS data is given by Figure 5, which compares the nondirectional spectrum of file A/subfile a with the TROMSO Wave-rider spectrum. The agreement is seen to be excellent.

The results of the first ODGP model run showed basically good agreement with the ROWS and TROMSO significant wave heights and nondirectional spectra. However, comparison of directional spectra showed immediately that the model had failed to produce the SE travelling component in the strength observed. This was seen to be due a poor kinematic analysis for the data-sparse western sector of the cyclone. Figure 6 compares the ROWS spectrum for file B with the ODGP hind-cast spectrum for grid point 254 (0900 Z) in FNOC/SOWM/ODGP variance format. Only a trace of the SE travelling component is seen at higher frequency. We see further in Figure 6 that the hindcast is also severely underestimating the strength of the NE travelling component, which is only weakly represented in the hindcast as an islet of energy near 0.065 Hz. The hindcast is evidently putting the energy of the NE component (to 45°) into the local wind direction (to 90°). While the model errors here are obvious, it is important to note that they are often masked in the nondirectional spectrum: Thus, the nondirectional spectra corresponding to Figure 6 shown in Figure 7 are quite close and give no clue as to the seriousness of the actual hindcast error. That the model should perform better for the integrated properties should not be surprising since the greatest uncertainty in wave models today lies in the modelling of the directional response to varying winds (the directional relaxation problem).

A second ODGP model run with a new kinematic analysis of the western sector of the cyclone essentially correctly reproduced the observed SE directed components. However, the model still tended to place more energy in the local wind direction than actually observed. A first run of the SAIL model exaggerated this tendency in the ODGP. Additional runs with the SAIL model will be made with slower directional relaxation rates; also the the nondirectional growth rates will be tuned to maximize the agreement with the ROWS (and TROMSO) wave observations. In summary, this hindcast comparison shows i) how the ROWS observations pointed immediately to wind field specification errors, and ii) that the directional relaxation rates, especially of the newer-generation coupled models (cf., Hasselmann, 1984) are too fast. This latter observation is supported by the results of the next case study.

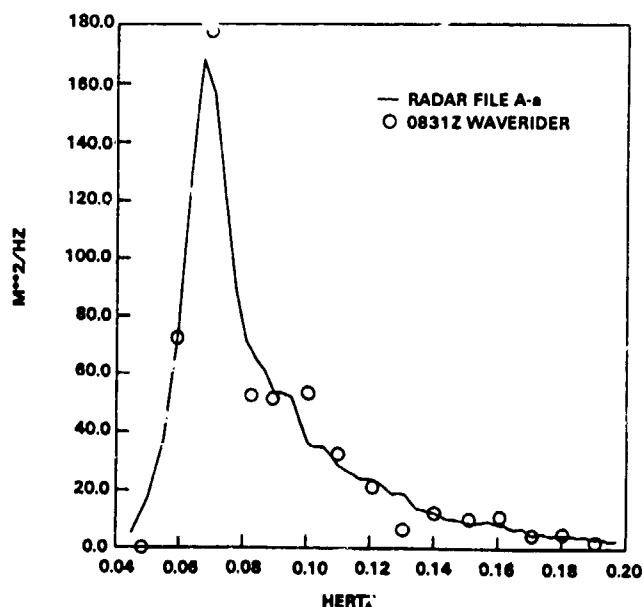


Figure 5. Comparison of ROWS Nondirectional Spectrum with TROMSO Waverider.

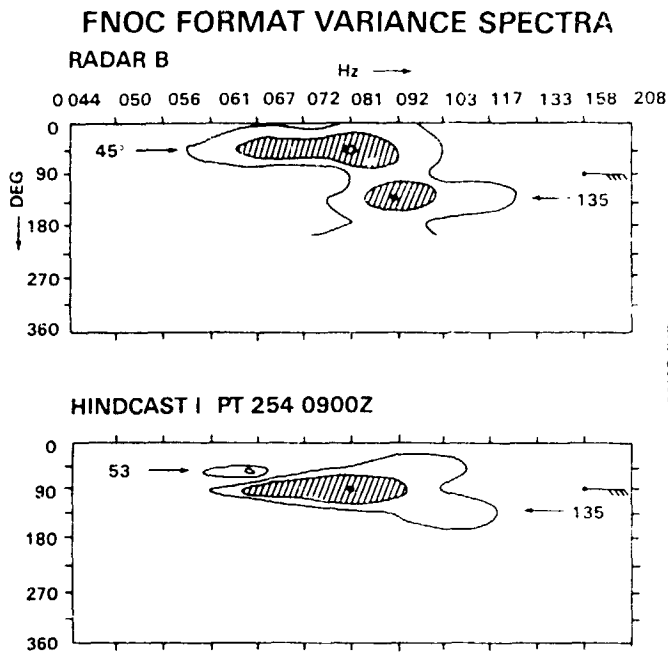


Figure 6.

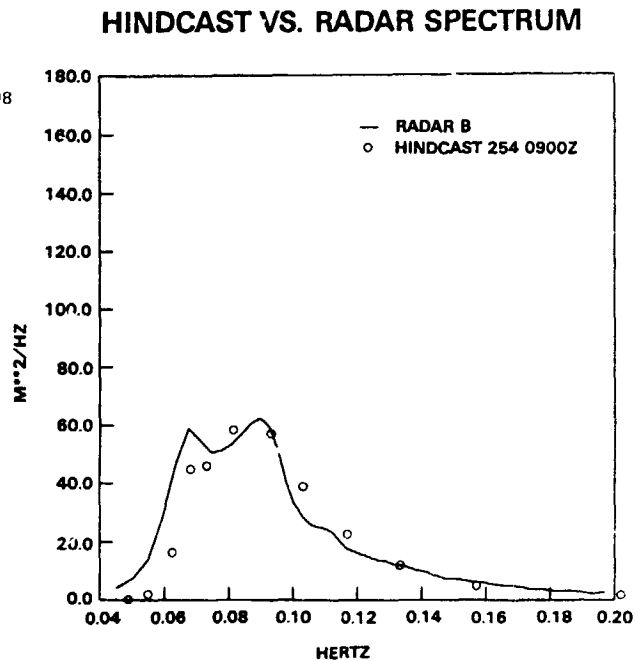


Figure 7.

3. FETCH LIMITED WAVE GROWTH OBSERVED DURING MASEX

The GSFC radar was installed on the NASA Wallops' P-3 aircraft in 1982 with an improved antenna system installation (which eliminated diffraction problems experienced in the Fall '78 Mission data). The main reason for the switch of platforms for the ROWS was to be able to fly in concert with E. Walsh's Surface Contour Radar (SCR), a 36 GHz, direct topographic mapping radar, in order to obtain high resolution directional spectra for intercomparison/validation purposes. The ROWS participated in three joint flights with the SCR during the MASEX (Meso-scale Air-Sea Exchange) experiment in January 1983. Besides systems intercomparison, the flight objective was to obtain data on the evolution of the directional spectrum with fetch during strong cold air outbreaks off the east coast of the U. S. Figure 8 shows the ROWS flight track (7 km altitude) for the 1/16 MASEX flight, the tape/file numbers being indicated by numbers and letters. The wind was approximately 12 ms^{-1} blowing offshore normal to the coast and to within a few degrees of the flight track. Figure 9 is a selection of the ROWS directional height spectra from the 1/16 flight. Figure 10 shows the entire sequence of ROWS-inferred nondirectional spectra for the flight leg extending out to ca. 300 km. The ROWS directional spectra of Figure 9 show two nearly equally energetic wave components, one travelling downwind, the other travelling in directions nearly opposite to the line-of-sight directions to the mouth of the Delaware Bay. The angles of the 'Delaware Bay' component are seen to be steeper than the line-of-sight angles to the mouth of the bay; this is apparently due to refraction near the mouth of the Bay. The existence of this strong off-wind component was first discovered by Walsh et. al. (1982). It is evidently due to fact that the waves outside the mouth of the bay have a 'leg up' over the waves further south along the coast. These waves may then enter a more rapid growth stage (Miles' growth) earlier than the downwind waves along the track. There is also the possibility that these waves are preferentially grown (in file 4-c these waves are

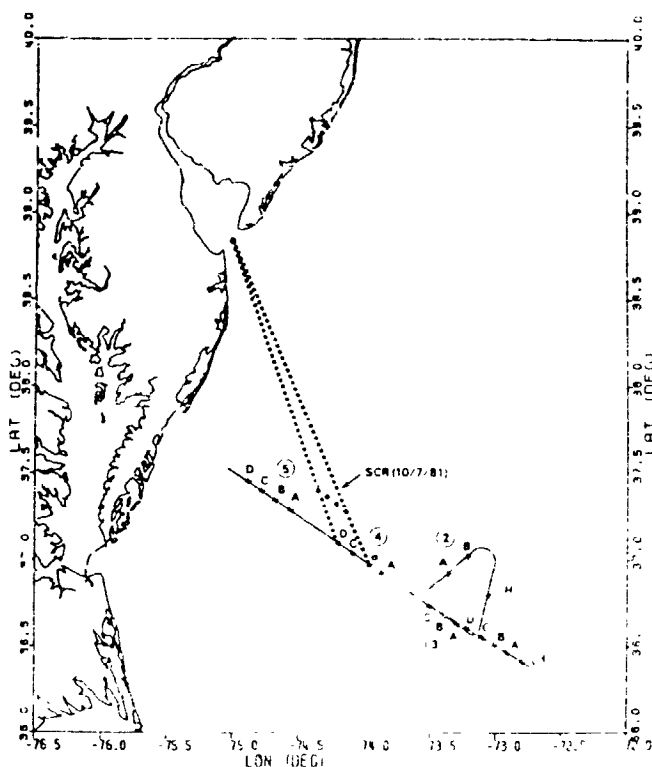


Figure 8. Flight Track and ROWS Data Takes for MASEX 1/16/83 Flight. Wind is normal to coast and parallel to flight track.

seen to exceed the downwind component) because they are very close to the Phillips' resonance curve (shown as the horizontal line in Figure 9). Most important, we observe in these spectra that over the entire fetch the off-wind component does not turn into the wind direction: It is not 'absorbed' by the 'local wind sea' (downwind component) until its mean direction lies well within the directional spread of the downwind component. This observation runs counter to current theory (Hasselmann, 1984) which would ascribe a strong directional coupling to the two components. On the contrary, the two components appear to be uncoupled, or at the most only weakly coupled. This behavior is consistent with what we have observed in the Norwegian Sea hindcast study. Preexisting components are not easily turned into the wind direction, nor do they tend to be absorbed by the local wind sea. This conclusion was reached also by Holthuijsen (1983) who found strong off-wind components in fetch-limited spectra in the North Sea, also due to coastline irregularities. The ROWS (and SCR) spectra from the two other MASEX flights similarly show strong off-wind components that point clearly to major embayments in the Middle Atlantic Bight. Similarly, also, these components appear to be decoupled from the downwind component. Figure 11 is a ROWS height spectrum from a flight down-fetch of Long Island which shows dominant wave energy not in the wind direction (to 160°), but at an angle pointing to the center of the Block Island/Rhode Island Sound complex.

The ROWS data of Figure 11 can be compared to nearly colocated SCR data in Figure 12. The overall agreement is seen to be excellent. Slight discrepancies are most likely due to collocation discrepancies, both spatial and temporal. It is worth noting here that apart from stereo photography, only the SCR could have provided this kind of high resolution intercomparison data.

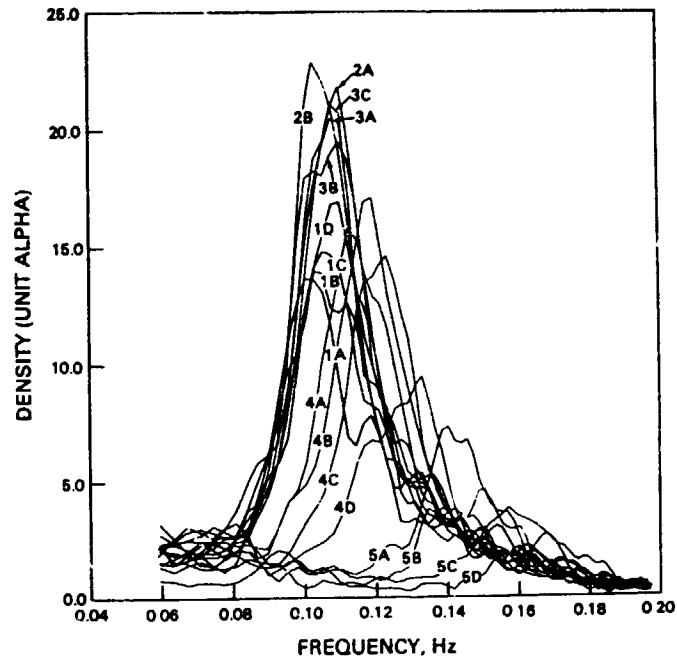
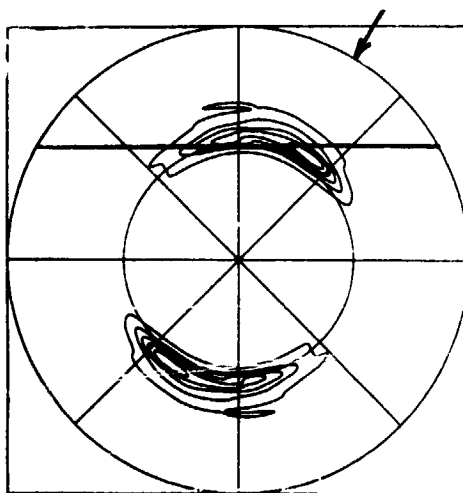
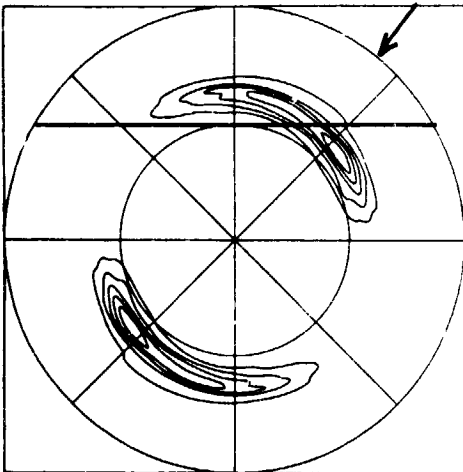
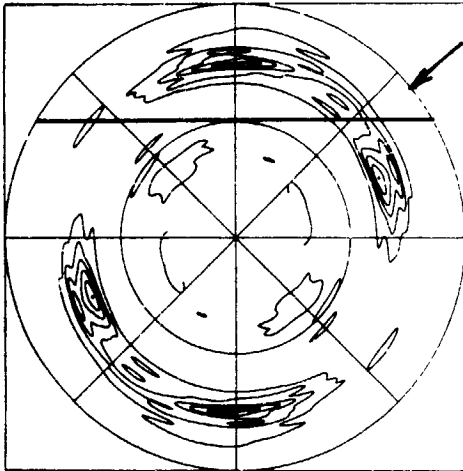


Figure 10. ROWS Nondirectional Spectra from 1/16 MASEX Flight for Unit Sensitivity Coefficient.

Figure 9. Examples of ROWS Directional Height Spectra from 1/13 MASEX Flight. From top to bottom the files shown are (cf. Figure 8, 5B, 4C, and 3C). The aircraft heading, equals the (anti) wind direction, is to the top of the page. The arrows indicate the line-of-sight angles to the mouth of the Delaware Bay. The horizontal lines are the Phillips' resonance curve. The spectra are contoured with six equally spaced contour intervals scaled to the peak values. Frequency rings are 0.10 Hz and 0.20 Hz.

ORIGINAL PAGE IS
OF POOR QUALITY

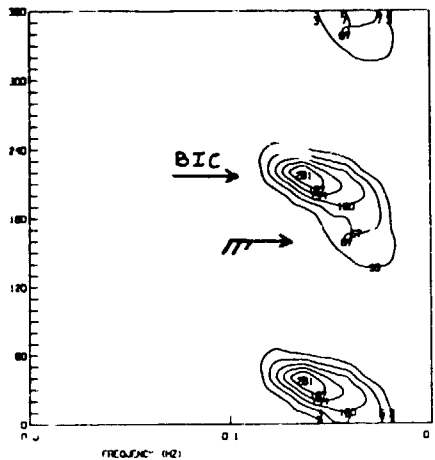


Figure 11. ROWS Height Spectrum from 1/20 MASEX Flight. BIC is Block Island Component.

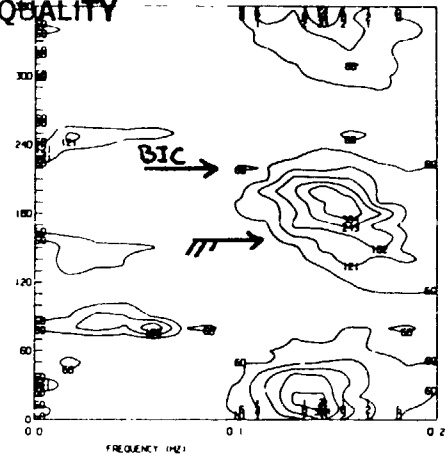


Figure 12. SCR Height Spectrum for Comparison to Figure 11. Colocation is not exact.

A thorough analysis of the MASEX data set should go a long way to resolving some fundamental issues in the physics of wind-generated ocean waves, at least in the macroscopic, or practical modelling sense.

4. 'THE SON OF SWOP'-- AN OBSERVATION OF A FULLY DEVELOPED SEA

A detailed analysis of a Fall '78 Mission ROWS observation of a fully developed sea in the N. E. Pacific and intercomparison with a pitch-roll buoy is given by Jackson (1984b). The ROWS-observed directional spectrum of the 3.3 m significant wave height sea is given in Figure 13, and the nondirectional comparison with the buoy is given in Figure 14. The directional comparison (not shown here) gave excellent agreement in terms of the mean wave directions and directional spreads as functions of frequency.

The observed spectrum in Figure 13 bears such a remarkable resemblance to the classical SWOP (Stereo Wave Observation Project) spectrum (Pierson, 1960) that we have dubbed this ROWS spectrum 'The Son of SWOP'. The two spectra have nearly identical half power widths (80° at peak to 120° at high frequency), and both spectra exhibit nearly identical bimodal structures which accord with the Phillips' resonance condition. The Phillips' resonance angles γ , determined according to the resonance condition,

$$U_c \cos \gamma = c(f) = g/2\pi f \quad (6)$$

where U_c is the windspeed, or convection velocity, and c is the water wave phase speed, are indicated by the arrows in Figure 15, where $U_c = 14.2 \text{ ms}^{-1}$ is chosen to give $\gamma = 0$ at $f = 0.11 \text{ Hz}$. The agreement with the observed modal angles is seen to be very good. This observation is seen to confirm Phillips' original contention (Phillips, 1958) that the SWOP spectrum bimodality was a real manifestation of the resonance mechanism and not a statistical fluke.

ORIGINAL PAGE IS
OF POOR QUALITY

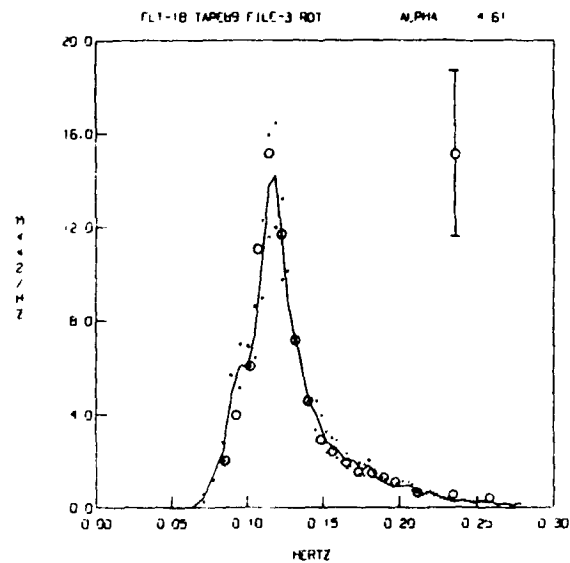
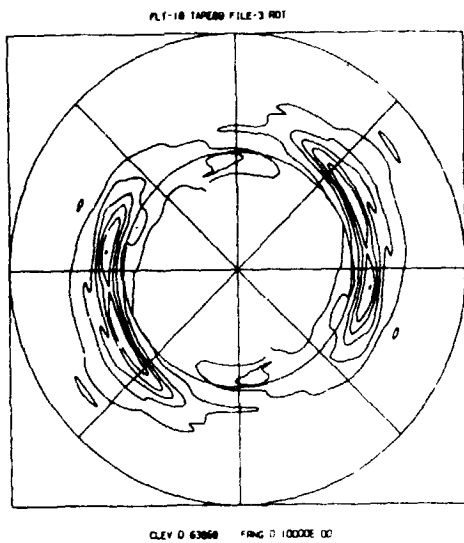


Figure 13. 'Son of SWOP' Height Spectrum. Figure 14. Nondirectional Height Spectrum Corresponding to Figure 13. Solid line is radar, circles buoy. Dots are radar confidence intervals.

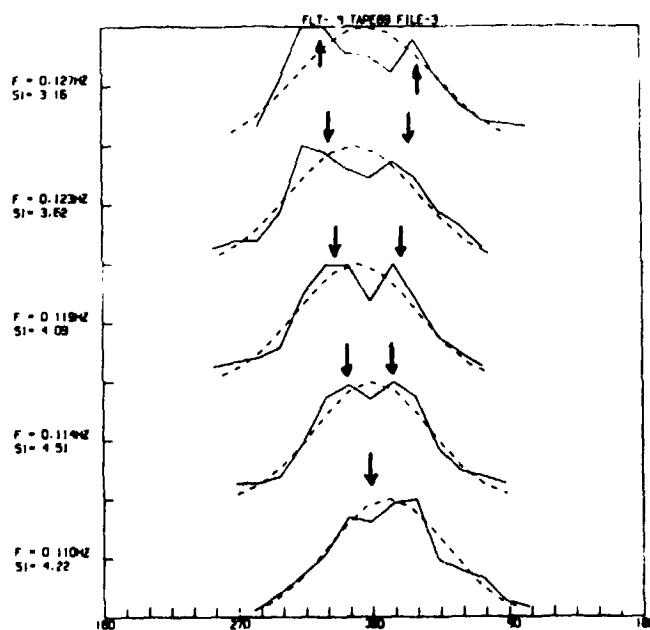


Figure 15. 'Son of SWOP' Directional Cuts (Normalized to Peak) with Phillips' Resonance angles indicated by arrows.

5. CONCLUSION

This paper has emphasized the use of the ROWS in case studies of wave physical processes. The results, while preliminary, give an idea of the enormous potential of this remote sensing technique. Further study of the Norwegian Sea case and the MASEX data should permit more concrete, quantitative statements regarding wave growth and directional relaxation. The 'Son of SWOP' observation fairly conclusively demonstrates that the Philips' resonance mechanism is indeed operative in the the fully developed sea state and is a major factor in determining the directional structure.

We have not dwelt on the details of the ROWS technique here, its accuracy, or its ultimate space application. These aspects have been extensively dealt with in Jackson (1981) and Jackson et al. (1984a). However, the reader may appreciate the remarkable accuracy of the indirect ROWS measurements by again examining the Waverider buoy, SCR, and pitch-roll buoy comparisons given respectively in Figures 5, 12, and 14: The technique appears to be very accurate, at least for sea states above 1 m, and providing the windspeed is greater than ca. 5 ms^{-1} . Similar accuracy is possible with a spacecraft system employing present generation short pulse radar altimeters.

6. REFERENCES

- Alpers, W. and K. Hasselmann, 1978: The two-frequency microwave technique for measuring ocean wave spectra from an airplane or satellite. *Boundary-Layer Meteorol.*, 13, 215-230.
- Cardone, V., W. J. Pierson, and E. G. Ward, 1976: Hindcasting the directional directional spectrum of hurricane-generated waves. *J. Petrol. Technol.*, 385-394.
- Hasselmann, K. (Ed.), 1984: Sea Wave Modeling Project. *Proc. Symp. Wave Dynamics and Radio Probing of the Ocean Surface*, Plenum Press (in press).
- Holthuijsen, L. H., 1983: Observations of the directional distribution of ocean wave energy in fetch-limited conditions. *J. Phys. Oceanog.*, 13, 191-207.
- Jackson, F. C., 1981: A synthesis of short pulse and dual frequency radar techniques for measuring ocean wave spectra from satellites. *Radio Sci.*, 16, 1385-1400.
- Jackson, F. C., W. T. Walton, and P. L. Baker, 1984a: Aircraft and satellite measurement of ocean wave directional spectra using scanning-beam microwave radars. *Proc. Symp. Wave Dynamics and Radio Probing of the Ocean Surface*, Plenum Press (in press).
- Jackson, F. C., W. T. Walton, and C. Y. Peng, 1984b: A comparison of in-situ and airborne radar observations of ocean wave directionality. *J. Geophys. Res.* (in press).
- Phillips, O. M., 1958: On some properties of the spectrum of wind-generated ocean waves. *J. Marine Res.*, 16, 231-240.
- Pierson, W. J. (Ed.), 1960: The directional spectrum of a wind-generated sea as determined from data obtained by the Stereo Wave Observation Project. *Meteorol. Papers*, 2, (6), New York Univ., New York.
- Walsh, E. J., D. W. Hancock, III, D. E. Hines, and J. E. Kenney, 1982: Development of the fetch-limited directional wave spectrum. *Oceans '82 Conference Record*, Marine Tech. Soc., Wash., D. C., 820-825.

NON-GAUSSIAN STATISTICAL MODELS OF SURFACE WAVE FIELDS
FOR REMOTE SENSING APPLICATIONS

Norden E. Huang
NASA, Goddard Space Flight Center
Greenbelt, MD 20771

Based on the complete Stokes wave model with the bias term and using a simple mapping approach and an iteration solution method, we established a formula for the joint probability density function of the surface slope-elevation of a nonlinear random wave field. The formula requires three parameters to define the whole density function: the rms surface elevation and slope values and the significant slope. This model represents the dynamics of the wave in a more direct way than the Gram-Charlier approximation. Based on this new statistical model and laboratory experiments, formula and numerical values of EM bias and dynamics bias are derived. The results indicate that various biases should be considered seriously if accuracy of the altimeter measurement is required in centimeter range.

1. INTRODUCTION

Wind waves are always random. The randomness is the result of the generating forces as well as the consequence of the dynamic processes in wave evolution which induce different kinds of instabilities. Consequently, the only meaningful descriptions of the wind wave fields are the various statistical measures; among them the probability density functions of the surface elevation and slope are the most basic ones. With the recent development of active microwave remote sensing techniques, the need for the statistical description of the ocean becomes more urgent, for the return signals of the radars are various convolution of radar signals and the ocean surface and these return signals are our only information sources. Successful extraction of the geophysical parameter, therefore, depends critically on our knowledge of the ocean surface statistical properties. For the remote sensing applications, the most important statistical measure is the joint probability density function of the slope and elevation of the ocean surface.

This specific probability density function is necessary for evaluating the back-scattering equation for a near nadir-looking radar as stated by Barrick (1972), Brown (1978), Valenzuela (1978), and Jackson (1979). Unfortunately, due to the nonlinear nature of the ocean waves, a realistic functional form has been elusive. Faced with this difficulty, past investigators have adopted a simple model that assumes all the statistical processes to be Gaussian and joint Gaussian. With this assumption, the statistical properties of the ocean surface become totally independent of the controlling dynamic processes. Consequently, the treatment of the ocean surface statistics is no different from any other random Gaussian process such as the noise of electronic circuitry. Indeed, most of the present statistical results used in describing the ocean surface can be traced to the classical set of papers by S. O. Rice (1944, 1945 and 1948), with certain extensions into two dimensions by Longuet-Higgins (1957, 1963, for example). Because the randomness of the ocean surface wave is the consequence of the generating forces as well as the controlling nonlinear dynamic processes which include various types of instabilities (see, for example, Phillips, 1977 and Yuen and Lake, 1982), the resulting surface geometry can not be adequately described by a linear superposition of statistically independent events. Thus the statistical process can not be Gaussian. Therefore, any results based on a Gaussian assumption,

though perhaps useful for some qualitative purposes, do not satisfy the need of our present and future engineering and remote sensing requirements.

The nonlinear effect of gravity waves on statistical properties of the wave field has been investigated first by Longuet-Higgins (1963), who treated the surface statistics as nearly Gaussian and represented it by a Gram-Charlier series in which the skewness of the surface elevation was determined through rigorous dynamic equations. This analysis was later extended by Jackson (1979) to the joint probability density distribution of slope and elevation. These results represented a major breakthrough in the non-Gaussian statistical description of the ocean surface. Successful as they were, there are certain shortcomings: the approximation gives negative density values and it requires higher moments to implement. These shortcomings put a limitation the applications of the results.

Recently we established a mapping technique to model the non-Gaussian process of the ocean surface. This technique was first used by Tayfun (1980), and was later successfully modified and applied to the non-Gaussian processes described by the nonlinear surface wave elevation density function (Huang et al, 1983) and joint slope and elevation density function (Huang et al, 1984). In this paper we will summarize the technique used in constructing the non-Gaussian density functions and discuss the specific applications to the remote sensing techniques.

2. THE NEW STATISTICAL MODEL

The new statistical model for a nonlinear deep water wave field is based on the Stokes expansion, i.e.

$$\zeta = \frac{1}{2} a^2 k + a \cos \chi + \frac{a^2 k}{2} \cos 2\chi + \frac{3a^3 k^2}{8} \cos 3\chi + \dots \quad (2.1)$$

Let us start by considering the linear Gaussian case for which the sea surface can be represented by

$$\zeta_1 = a \cos \chi, \quad (2.2)$$

with χ as the phase function

$$\chi = kx - nt + \phi,$$

where k is the wave number, n is the frequency and ϕ is an arbitrary phase shift uniformly distributed. It is well known that if a is Rayleigh, the ζ_1 is zero-mean Gaussian (see, for example, Papoulis, 1965). For the same amplitude and phase function,

$$\zeta_2 = a \sin \chi, \quad (2.3)$$

is also Gaussian. Furthermore, ζ_1 and ζ_2 are statistically orthogonal to each other.

Based on ζ_1 and ζ_2 , we can define the normalized random variables

$$Z_1 = a \cos \chi / (\bar{a}^2/2)^{1/2}; \quad Z_2 = a \sin \chi / (\bar{a}^2/2)^{1/2}, \quad (2.4)$$

with the overbar indicating mean quantity, and the joint probability of Z_1 and Z_2 is simply

$$p(Z_1, Z_2) = \frac{1}{2\pi} \exp \left\{ -\frac{1}{2} (Z_1^2 + Z_2^2) \right\}. \quad (2.5)$$

If the surface wave profile is represented by the Stokes wave, a normalized zero-mean random variable can be defined as

$$\eta = \frac{\zeta - \bar{\zeta}}{(\overline{\zeta^2} - \bar{\zeta}^2)^{1/2}} = \frac{\zeta - \bar{\zeta}}{\sigma}, \quad (2.6)$$

where σ is the standard deviation of the surface elevation. From (2.1) we can also get the surface slope

$$\zeta_x = -ak \sin \chi - a^2 k^2 \sin 2\chi - \frac{9}{8} a^3 k^3 \sin 3\chi - \dots \quad (2.7)$$

Again, we can define another normalized zero-mean random variable from (2.7) as

$$\xi = \zeta_x / (\overline{\zeta_x^2})^{1/2}. \quad (2.8)$$

In terms of Z_1 and Z_2 , η and ξ become

$$\eta = \frac{Z_1}{N} + \frac{Z_1^2}{N^2} \sigma k + \frac{3}{8} \frac{Z_1^3 - 3Z_1 Z_2^2}{N^3} \sigma^2 k^2 - \sigma k; \quad \xi = -\frac{Z_2}{M} - \frac{2Z_1 Z_2}{MN} \sigma k - \frac{9}{8} \frac{3Z_1^2 Z_2 - Z_2^3}{MN^2} \sigma^2 k^2, \quad (2.9)$$

in which

$$N = (1 + 8\pi^2 \xi^2)^{1/2},$$

$$M = (1 + 16\pi^2 \xi^2)^{1/2},$$

and ξ is the significant slope of the wave field defined as

$$\xi = (\overline{\zeta^2})^{1/2} / \lambda,$$

with $\lambda = 2\pi/k$.

Since we know the joint density function of Z_1 and Z_2 , it is easy to write the joint density function of any two functions of Z_1 and Z_2 through a mapping technique known as the fundamental theorem of probability (Papoulis, 1965), i.e.

$$p(z_1, z_2) dz_1 dz_2 = p\{z_1(\eta, \xi), z_2(\eta, \xi)\} J\left(\frac{z_1, z_2}{\eta, \xi}\right) d\eta d\xi, \quad (2.10)$$

in which $J()$ is the Jacobian of the transformation.

Following this method, Huang et al. (1984) obtained the joint slope-elevation density function as:

$$p(\eta, \xi) = \frac{NM}{2\pi} \left\{ 1 - 4\eta\sigma k + \left[(23\eta^2/2 - 4) + 9M^2\xi^2/2N^2 \right] \sigma^2 k^2 \right\} \cdot \exp \left\{ -\frac{1}{2} \left[\frac{N^2\eta^2 + M^2\xi^2 - [2\eta(\eta^2 - 1)N^2 + 4\eta\xi^2 M^2] \sigma k}{(17\eta^4/4 - 6\eta^2 + 1 + 9M^2\eta^2\xi^2/4N^2) N^2} + \frac{[37\eta^2\xi^2/4 - 4\xi^2 + 9M^2\xi^4/4N^2] M^2}{(17\eta^4/4 - 6\eta^2 + 1 + 9M^2\eta^2\xi^2/4N^2) N^2} \right] \sigma^2 k^2 \right\}. \quad (2.11)$$

Statistically, the joint specular point and elevation distribution is the conditional distribution of

$$p(\xi | \sigma\xi = 0). \quad (2.12)$$

For a long crested wave field or a narrow band of energy spread case,

$$p(\zeta | \nabla \zeta = 0) \simeq p(\zeta | \zeta_x = 0). \quad (2.13)$$

Thus a good approximation of the specular point distribution can be obtained by simply setting $F = 0$ in (2.11). Hence, in terms of the normalized variable,

$$p(\eta | \zeta = 0) = \frac{MN}{2\pi\hat{a}} \left[1 - 4\eta\sigma k + \left(\frac{23}{2}\eta^2 - 4 \right) \sigma^2 k^2 \right] \cdot \exp \left\{ -\frac{1}{2} \left[\frac{N^2\eta^2 - 2\eta(\eta^2 - 1)N^2\sigma k}{+ \left(\frac{17}{4}\eta^4 - 6\eta^2 + 1 \right) N^2\sigma^2 k^2} \right] \right\} \quad (2.14)$$

where \hat{a} is the normalized factor to guarantee

$$\int_{-\infty}^{\infty} p(\eta | \zeta = 0) d\eta = 1.$$

From equation (2.11) and 2.14) we can see that the density functions are obviously skewed with respect to η . This skewness is caused by the harmonic distortion of the wave profile described by Stokes expansion. Comparison between the theoretical and experimental results have been presented by Huang *et al.* (1983, 1984). The agreements are all good.

3. REMOTE SENSING APPLICATIONS

A particularly interesting aspect of the specular point density functions is the location of the mean. More specifically, the difference between the mean of the specular point density and the mean of the surface elevation density functions. This difference is the critical electromagnetic bias (Jackson, 1979; Walsh *et al.*, 1983), for the mean sea surface measured by any nadir looking electromagnetic device is not the true mean but the mean of the reflecting facets or the specular points. Based on our observational data, the mean is determined and plotted as a function of the significant slope in Figure 3.1. The data show an almost linear increasing of the bias. The mean value of the theoretical model can be calculated by the ratio of the first moment to the zeroth moment of the density function. The value of the bias is the difference between the corresponding values of the mean in specular point density and elevation density functions. The numerical value calculated based on (2.14) is also given in figure 3.1. Although they do not exactly coincide, the trend is unmistakable. Better model with more realistic wave profile in two-dimension may be needed.

Another aspect of the nonlinear effects in the wave profile is the non-zero mean - the deviation of the local mean surface under waves from the undisturbed calm surface. The existence of this non-zero mean in a nonlinear wave train has been shown by Stokes (1880), Rayleigh (1917), De (1955) and, more recently, Schwartz (1974) and Longuet-Higgins (1975). In the past, the term $a^2k/2$ in equation (2.1) has been treated as a negligible constant in all wave studies. It is discarded by simply shifting the coordinate system up by the exact amount of $a^2k/2$. This is permissible as long as our interest in the oscillatory part of the motion. But the coordinate shifting is no longer permissible for our present interest because the amount shifted is precisely the dynamic sea state bias which could have far reaching consequence in the accurate determination of the mean sea surface using an altimeter.

The existence of this non-zero mean in a nonlinear wave train can be explained by mass balance in the wave motion. It has been shown by Stokes that a non-zero mean mass transport always accompanies the wave motion. For deep water waves, this

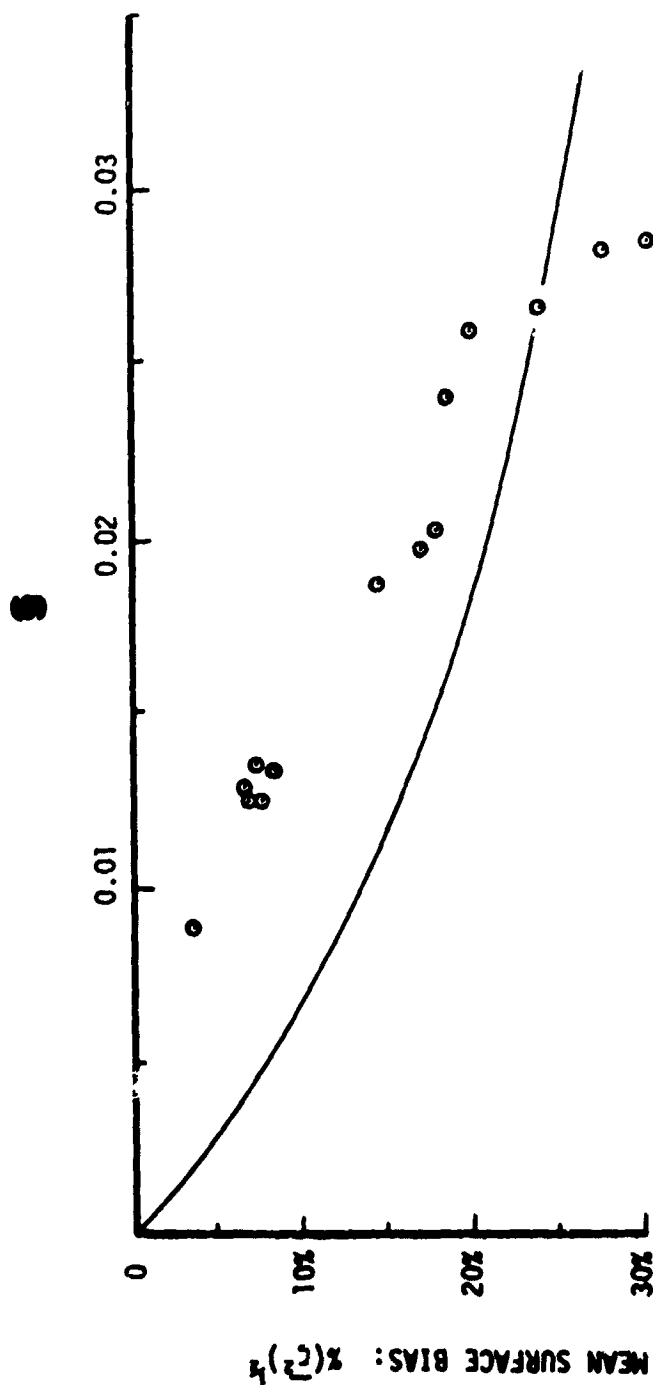


FIGURE 3.1 EM Bias as function of significant slope.
 — numerical value according to the new statistical model
 ○ Laboratory simulated data.

velocity is

$$u_z = a^2 n k e^{2kz} \quad (3.1)$$

where Z is the vertical position of a particle. The rate of total mass transport through any vertical section is given by

$$Q = \int_{-\infty}^0 a^2 n k e^{2kz} dz = a^2 n / 2 \quad (3.2)$$

The surface elevation change caused by this mass transport can be calculated as

$$\Delta h_v = QT / \lambda, \quad (3.3)$$

in which T and λ are the wave period and wave length respectively. Using the definition of wave number and frequency, one can easily show the equivalence between (3.3) and the constant term in (2.1).

For a random wave field, the Stokes drift is given by Huang (1971) as

$$u_z = \iint_{\underline{k}, n} 2nk X(\underline{k}, n) e^{2|\underline{k}|z} d\underline{k} dn \quad (3.4)$$

Therefore, the rate of the total mass transport is

$$Q = \int_{-\infty}^0 u_z dz \quad (3.5)$$

and the bias is

$$\begin{aligned} \Delta h_w &= \int_{-\infty}^0 \iint_{\underline{k}, n} \frac{|\underline{k}|}{n} 2nk X(\underline{k}, n) e^{2|\underline{k}|z} d\underline{k} dn dz, \\ &= \iint_{\underline{k}, n} \underline{k} X(\underline{k}, n) d\underline{k} dn, \end{aligned} \quad (3.6)$$

in which $X(\underline{k}, n)$ is the directional wave number frequency spectrum. In order to evaluate (3.6), a specific spectrum form has to be adopted. Since the quantity sought here is a scalar, Δh , we can reduce (3.6) by using the dispersion relationship to eliminate k and reduce $X(\underline{k}, n)$ to a simple frequency spectrum. Then adopting the simplified Wallops spectrum model (Huang et al., 1981), we obtain

$$\Delta h_w = 2\pi (\bar{\gamma}^2)^{1/2} \xi (m-1)/(m-3), \quad (3.7)$$

where m is a simple function of the significant slope, ξ , defined by

$$m = \left\lceil \log (\sqrt{2} \pi \xi)^2 / \log 2 \right\rceil,$$

and

$$\xi = (\bar{\gamma}^2)^{1/2} / \lambda_0,$$

with λ_0 as the wave length of the wave having a frequency at the peak of the spectrum, η_0 .

If the significant wave height, $H_1/3$, is used as in most practical applications, (3.7) can be written as

$$\Delta h_w = \frac{\pi}{2} \xi H_1/3 (m-1)/(m-3) \quad (3.8)$$

The typical value of ξ in the open ocean is around 0.01, which gives the value of m around 10; the dynamic sea state bias, Δh , would be around 1.5% of the significant wave height. During a storm, the ξ value could reach 0.02 as an upper bound, and then Δh would be as high as 3% of $H_{1/3}$. For the sea state dominated by swell, however, the dynamic bias can almost be neglected because ξ would be of the order of 0.001 or less.

As an estimate of the magnitude of this bias, we use the empirical formula given by Neumann and Pierson (1965), then

$$H_{1/3} = 2.12 \times 10^{-2} W^2 \quad (3.9)$$

for a fully developed sea. Under such conditions the phase velocity of the energy containing waves equals the wind speed. Thus the sea state bias can be written as

$$\Delta h_w = 2.75 \times 10^{-4} W^2 (m-1)/(m-3). \quad (3.10)$$

This value is plotted in Figure 3.2. For all wind speed, the high sea state this bias is not negligible.

4. CONCLUSION

In this study, we summarized the non-Gaussian statistical models based on Stokes Wave expansion. The new statistical model indicates the existence of skewness which is the cause of the EM bias in the remote sensing application. Furthermore, the existence of the non-zero mean in Stokes expansion which contributed to the Skewness can also cause a dynamic bias. The magnitudes of both bias terms are estimated. For future altimeter applications, we should seriously consider the correction of these biases.

5. REFERENCES

- Barrick, D. E., 1972. "Remote Sensing of Sea State by Radar," Remote Sensing of the Troposphere, V. E. Derr, ed., U.S. Government Printing Office, Washington, D.C.
- Brown, G. S., 1978. "Backscattering from a Gaussian Distributed Perfectly Conducting Rough Surface," IEEE Trans., AP-26, 472-482.
- De, S. C., 1955. "Contributions to the Theory of Stokes Waves." Proc. Camb. Phil. Soc., 51, 713-736.
- Huang, N. E., 1971. "Derivation of Stokes Drift for a Deep-Water Random Gravity Wave Field," Deep-Sea Res., 18, 255-259.
- Huang, N. E., S. R. Long, C. C. Tung, Y. Yuen, and L. F. Bliven, 1981. "A Unified Two-Parameter Wave Spectral Model for a General Sea State," J. Fluid Mech., 112, 203-224.
- Huang, N. E., S. R. Long, C. C. Tung, Y. Yuan, and L. F. Bliven, 1983. "A Non-Gaussian Statistical Model for Surface Elevation on Nonlinear Random Wave Fields," J. Geophys. Res., 88, 7597-7606.

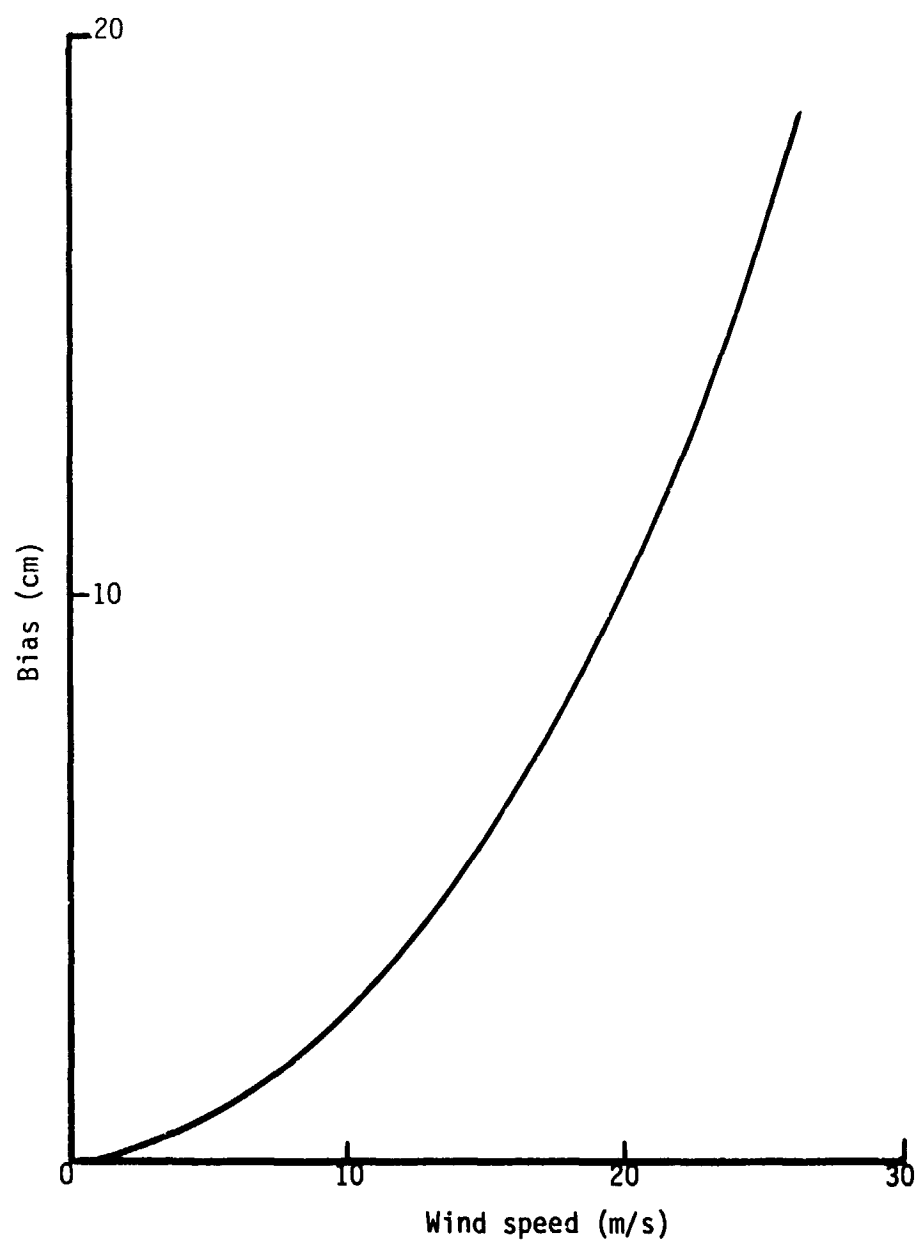


FIGURE 3.2 The Dynamic Bias as function of wind speed.

- Huang, N. E., S. R. Long, L. F. Bliven and C. C. Tung, 1984. "The Non-Gaussian Joint Probability Density Function of Slope and Elevation for a Nonlinear Gravity Wave Field," J. Geophys. Res., (In Press).
- Jackson, F. C., 1979. "The Reflection of Impulses from a Nonlinear Random Sea," J. Geophys. Res., 84, 4939-4943.
- Longuet-Higgins, M. S., 1957. "The Statistical Analysis of a Random Moving Surface," Phil. Trans., 249, 321-387.
- Longuet-Higgins, M. S., 1975. "Integral Properties of Periodic Gravity Waves of Finite Amplitude," Proc. R. Soc. Lond., A 342, 157-174.
- Longuet-Higgins, M. S., 1963. "The Effect of Nonlinearities on Statistical Distributions in the Theory of Sea Waves," J. Fluid Mech., 17, 459-480.
- Neumann, G. and W. J. Pierson, 1966. "Principles of Physical Oceanography," Prentice-Hall, Inc., Englewood, NJ.
- Papoulis, A., 1965. "Probability, Random Variables and Stochastic Processes, McGraw Hill, New York, 583 pp.
- Phillips, O.M., 1977. "The Dynamics of the Upper Ocean, 2nd ed., Cambridge U. Press, Cambridge.
- Rayleigh, Lord, 1917. "On Periodic Irrotational Waves at the Surface of Deep Water," Phil. Mag., 33, 381-389.
- Rice, S. O., 1944. "Mathematical Analysis of Random Noise," Bell System Tech. J., 23, 282-332.
- Rice, S. O., 1945. "Mathematical Analysis of Random Noise," Bell System Tech. J., 24, 46-107.
- Rice, S. O., 1948. "Statistical Properties of a Sine Plus Random Noise," Bell System Tech. J., 27, 109-157.
- Schwartz, L. W., 1974. "Computer Extension and Analytic Continuation of Stokes' Expansion for Gravity Waves," J. Fluid Mech., 62, 553-578.
- Stokes, G. G., 1980. "Supplement to a paper on the Theory of Oscillatory Waves, Math and Phys. Papers, 1, 314-326, Cambridge U. Press.
- Tayfun, M. A., 1980. "Narrow-band Nonlinear Sea Waves," J. Geophys. Res., 85, 1548-1552.
- Valenzuela, G. S., 1978. "Theories for the Interaction of Electromagnetic and Oceanic Waves - A Review," Boundary-Layer Meteorol., 13, 61-85.
- Walsh, E. J., D. W. Hancock, D. E. Hines, and J. E. Kenney, 1983. "Electromagnetic Bias of the 36 GHz Radar Altimeter Measurements of MSL," Marine Geoid (in press).
- Yuen, H. C., and B. M. Lake, 1982. "Nonlinear Dynamics of Deep-Water Gravity Waves," Adv. Appl. Mech., 22, 67-229.

A TENTATIVE UNIFIED SEA MODEL FOR SCATTERING AND EMISSION

A. Guissard and P. Sobieski
Faculte Des Sciences Appliquees
Laboratoire De Telecommunications Et D'Hyperfrequences
Batiment Maxwell - Place Du Levant 3
B-1348 Louvain-La-Neuve, Belgium

ABSTRACT

There presently exists a growing interest in the remote sensing of the large ocean areas, in an attempt to gain a better knowledge and understanding in several scientific fields, including oceanography and meteorology. Space-borne microwave instruments have been proved very useful to reach that objective; they are of both the active and passive nature. Radars response is determined by the backscattering properties of the sea surface, implying for its interpretation the knowledge of the scattering cross section in one direction only, while radiometers response is determined by the emissivity of the sea which is related to an integral of the bistatic scattering cross section over all possible directions in a complete hemisphere. If we do not remain at the level of purely empirical results, but try to rely on a rigorous theoretical formulation, the relationships between radiometric and radar measurements is far from being evident, and few people have investigated this aspect of the problem.

Also when the results of the observations are related to the physical parameters of the observed scene, as the sea surface temperature and the wind speed, difficulties appear, because there is not necessarily a unique solution for the values of the physical parameters, given a set of measurements. Considering more particularly the measurement of the wind speed and of related parameters such as the significant wave height, there is not a unique relationship between wind speed and sea roughness, because a given sea surface may be the result of various wind conditions.

Our work is an attempt to relate active and passive observations of the sea surface to each other, considering that more information can be obtained from a set of instruments when they are not just considered as a juxtaposition of separate and independent boxes, but as a single complex instrument. A careful review of several approaches to the solution of the scattering problem for a random rough surface has been performed. Inherent simplifications, and inconsistencies, are pointed out. To reduce the computation time to reasonable values, an approximate model is selected and some numerical results will be presented in order to illustrate the benefit that can be gained by a unified approach.

N84 27286

APPLICATIONS OF AIRBORNE REMOTE SENSING IN ATMOSPHERIC SCIENCES RESEARCH

Robert J. Serafin
National Center for Atmospheric Research*
P.O. Box 3000, Boulder, Colorado 80307, USA

Gerard Szejwach
Laboratoire de Meteorologie Dynamique
Palaiseau Cedex, France

Byron B. Phillips
National Center for Atmospheric Research*
P.O. Box 3000, Boulder, Colorado 80307, USA

ABSTRACT

This paper explores the potential for airborne remote sensing for atmospheric sciences research. Passive and active techniques from the microwave to visible bands are discussed. It is concluded that technology has progressed sufficiently in several areas that the time is right to develop and operate new remote sensing instruments for use by the community of atmospheric scientists as general purpose tools. Promising candidates include Doppler radar and lidar, infrared short range radiometry, and microwave radiometry.

1. INTRODUCTION

Aircraft have been used profitably in atmospheric sciences research for several decades. The principal advantage of an airborne platform is clearly its mobility, which allows it to sample the atmosphere in regions in and near the weather and in geographical regions around the globe. It has been traditional for researchers to use aircraft to make very high resolution, in situ measurements of air motion, temperature, moisture, cloud particle size distribution, liquid water, hydrometeor phase, trace gases, and aerosols. In situ measurements, while very precise, suffer from at least two significant problems. First, is the fact that measurements made along a given aircraft flight track sample a very small volume of the atmosphere. For example, a particle spectrometer, flown through a cloud, will have a total sampling volume of less than a cubic meter per kilometer of path length. There are therefore significant concerns as to how representative such measurements are of precipitation processes in other regions of a cloud. Even small cumulus congestus encompass a total volume well in excess of 10^6 m³. Secondly, in situ probes are adversely affected by icing and liquid water in clouds and may in certain circumstances become inoperative.

The first of these problems has tended to be mitigated in part by the extensive use of ground-based and satellite remote sensing techniques, which have provided information on the larger scale structures of clouds and precipitation, while the aircraft have concentrated on the microphysical and smaller scale measurements. Contamination of in situ probes by the cloud environment remains a problem.

*The National Center for Atmospheric Research is sponsored by the National Science Foundation.

There exist several important reasons for incorporating remote sensing techniques to a greater degree on research aircraft. First, is the great emphasis now being placed on mesoscale meteorology as articulated in the documents prepared for a national Stormscale Operational and Research Meteorology (STORM) program in the United States. In order to conduct a true multi-scale investigation, that is, to examine in a definitive way the scale interactions from the meso-alpha to meso-gamma scales, it is essential that instrumental coverage be extended to areas of the size of one-third of the United States. The limited number of research, land-based remote sensors will dictate strongly that more remote sensing be added to research aircraft for adequate three-dimensional observations of the meso-beta and meso-gamma scales. In addition, the mesoscale programs of the future will place greater emphasis on coastal regions, requiring extensive measurement capabilities over the oceans where surface arrays of remote sensors are exceedingly difficult, if not impossible, to deploy.

In a similar vein, it is expected that there will be new thrusts in global and regional atmospheric chemistry and that combining chemistry with meteorological measurements will take on a greater importance than in the past. Global chemistry measurement programs will require long-range flights over the open oceans. In these flights it will be essential to define better the kinematic and thermodynamic properties of the atmosphere through the use of remote sensing. In regional studies related to acid rain, in situ microphysical and aqueous chemical measurements must be augmented by information on the structure and phase of precipitation as well as on the kinematic properties of clouds.

These scientific thrusts clearly point out the need for expanded use of remote sensors on research aircraft. If the potential of airborne remote sensing can be realized, it is possible to conceive of arrays of research aircraft used as highly mobile beta and gamma scale networks, approximating closely the capabilities of the more traditional, but fixed, surface research arrays.

2. STATUS

Appendix A provides a bibliography of papers describing remote sensing techniques that could be deployed from aircraft platforms. Appendix B is a list of remote sensing instruments, available within NASA, which have been constructed and tested to varying degrees. Neither appendix is exhaustive of the state of the art, rather each is illustrative of how much work has been accomplished in the field.

In light of the considerable history of ground-based remote sensing and of the considerable research and development that has been conducted, one can legitimately ask why remote sensing has been so sparsely used in research aircraft to date. The reasons for this are many. Perhaps most significant is the fact that at the present time airborne remote sensing remains in the developmental stage. Consequently, remote sensing tools tend to exist within the domain of specialists (scientists and engineers) whose interests lie primarily with the development and/or demonstration of observational techniques rather than with the interpretation of the data for atmospheric research. This situation is similar to that which existed 15 years ago in the field of Doppler radar meteorology. Doppler radar has now become a widespread research and operational tool for meteorology partly because of major technological advances which took place in the late 1960's and early 1970's. More important, however, was the technology transfer that took place between the radar meteorologists of the late 1960's and the broader community of users. This technology transfer has resulted in widespread acceptance of Doppler radar as a tool for meteorologists who know little or nothing about radar. A similar technology transfer must take place if other remote sensing techniques are to be effectively utilized.

A second reason for the sparse use of remote sensing techniques is the simple fact that most remote sensors have not delivered all of the potential that has been promised. The spatial resolution of passive techniques has been limited. For

example, microwave radiometric techniques provide generally unacceptable resolution in the vertical for profiling of temperature and humidity. Aerosol backscattering cross sections have not always been adequate for reliable coherent lidar measurements at all altitudes in the troposphere. Doppler radar use on aircraft has been slow to develop because of uncertainties related to ground clutter contamination through antenna side lobes. The need for compensation for aircraft yaw, pitch, and roll adds complexity and attendant cost to coherent radar or lidar measurements from the airborne platform.

It is also true that many of the developmental remote sensing instruments have not been packaged well for airborne use in that they are heavier, larger, and consume more power than is desirable for many applications. Indeed, it is clear that smaller aircraft, of the class of the NCAR King Air, will be limited in their ability to accommodate many remote sensing instruments. Because of this, larger aircraft such as NASA's Convair 990, NOAA's P-3's, and high altitude aircraft such as the NASA U-2 have been the platforms of choice. The high costs of operating these aircraft have served as impediments to many who would wish to use advanced remote sensing systems for their airborne research. Aircraft have been used for testing these sensors but often times their general purpose use on aircraft platforms has been overlooked. In addition, much remote sensing development has been undertaken for eventual use from satellites.

Despite these impediments, however, the future now is bright for airborne remote sensing. There are many remote sensing techniques, both active and passive, which can contribute substantially to the scientific challenges of the future. Short range, rapid response measurements of temperature, water vapor, liquid water, winds and turbulence are all possible using infrared radiometry, microwave refractometry, and continuous wave Doppler lidar velocimetry. Pulsed Doppler radar systems will make measurements of hydrometeor and wind structure in precipitation. Polarimetric radar techniques will help to determine the three-dimensional structure of precipitation phase and its evolution. Pulsed Doppler lidar methods are needed for measurement of winds and turbulence in regions free of cloud and precipitation. For measurements of liquid water, research is now under way on microwave radiometric techniques for measurement of the three-dimensional structure of the liquid water fields in clouds.

3. SOME PROMISING CANDIDATES

3.1 Microwave Doppler Radar

It is our view that the earliest significant scientific payoff will come from airborne Doppler radar. Mueller and Hildebrand (1983) describe the capabilities of airborne Doppler radar for two- and three-dimensional measurements of air motion in precipitation. This work, a cooperative effort between NOAA and NCAR, has illustrated that properly processed airborne Doppler radar measurements differ only in small detail from those made by ground-based systems and moreover are as physically plausible as are those obtained from the surface radars. Before the end of this decade, we should see improved Doppler radars on both of the NOAA P-3 aircraft, on the NCAR Electra, and on the NCAR King Air. These radars should be designed with adaptability to other aircraft in mind. In particular, there is a great need for down-looking Doppler measurements from high altitude aircraft flying over convective storms. These vertically pointing measurements, when combined with horizontally scanned data from lower altitude aircraft, will permit accurate estimates of the vertical fluxes of mass and moisture in mesoscale convective systems and in tropical cyclones.

Aircraft platforms will dictate that some compromises in system performance be made. Wavelengths at X or K band will probably be used which will provide acceptable spatial resolution but which will prohibit quantitative precipitation measurement in heavy rain. Such effects are however mitigated in part by the mobility of the platform. The initial implementation on research aircraft will be single wavelength

systems. More sophisticated systems are likely to follow which will provide wavelength and polarization diversity capabilities for more quantitative determination of precipitation phase and evolution.

3.2 Doppler Lidar

Doppler lidar is also ready for deployment from aircraft. While pulsed systems still require development, CW Doppler lidar can be effectively utilized now. Cannel et al. (1983) describe a CW system which has been installed on the Royal Aircraft Establishment (RAE) HS-125 for studies of wind shear. The system has proven to be reliable, accurate, and easy to maintain. Keeler and Serafin (1983) have suggested that a scanning CW system, focused a few meters ahead of an aircraft can be used as a substitute for mechanical three-dimensional gust probes such as that described by Lenschow (1978). The feasibility of the lidar gust probe system is expected to be demonstrated further through test flights in the spring of 1984 in a collaborative effort between the British Royal Signals and Radar Establishment, the RAE, and NCAR. Successful tests will lead to the design and development of a scanning research system for the NCAR aircraft.

The great interest in wind measurements from space as described by Huffaker (1983) is resulting in substantial new development in pulsed CO₂ systems for air motion measurements. Bluestein et al. (1983) have reported on comparisons between wind field measurements obtained by airborne pulsed Doppler lidar and ground-based pulsed Doppler radar. Their results show good agreement between the radial velocity fields but poor correlation in the derived eddy fields. Considerably more research and development is necessary in order to make pulsed systems practical for general purpose use. However, the potential for vector wind field determination in the clear troposphere is so important scientifically that this work is certain to continue to its successful fruition.

3.3 Infrared Radiometric Measurement of In-cloud Temperature

Great difficulties are encountered with present in situ probes for accurate temperature measurements within clouds because of dynamic heating and wetting effects. Reverse flow housings have been designed to inertially separate air and cloud particles; however, these are as yet questionably effective and generate additional problems because of flow turbulence around the sensor element. With proper design, remote radiometric measurements can be obtained in the near-field of the aircraft without suffering these deleterious effects.

Radiometric measurements of temperature in and out of clouds have been made previously in the 15 μm infrared carbon-dioxide rotational band. Recently, Albrecht et al. (1979) have reported on a series of measurements using a moderately narrow band thermistor bolometer detector centered at 14.8 μm . The effective free-air sample path length was of the order of 100-200 meters at lower flight altitudes. Larger sized hydrometeors at nonequilibrium temperatures within the sample volume caused the measured temperature to be weighted in an unknown fashion by precipitation, while cloud particles caused significant sample volume variations for measurements made in clouds. Other errors originate because of temperature variations within the radiometer itself as a result of its exposure to the variable temperature environment of the aircraft at flight altitudes.

These problems at 15 μm wavelengths appear to be eliminated as a result of a 4.3 μm radiometer by Ophir Corporation, Denver, Colorado, being developed under NCAR contract. At 4.3 μm , sapphire optics can be used with negligible emission temperature error at all flight altitudes. A fast response sensitive lead selenide (PbSe) detector can be used, which more than compensates for the lower radiance at 4.3 μm as compared to 15 μm . The sample path length is such that two-thirds of the received energy originates within the first two meters and almost all the energy received is from the first ten meters of sample path. Because few hydrometeors or precipitation

size will be present in this restricted sample volume, errors originating from precipitation are negligible. A prototype $4.3 \mu\text{m}$ radiometer has been flight tested from NCAR's Queen Air research aircraft. The results confirmed that the remote radiometric-measured air temperature is independent of speed (dynamic heating effects) and the presence of cloud (wetting). Construction of the first radiometer for airborne use is planned to occur early in 1984 with flight testing scheduled during September/October of that year. Design accuracies of 0.2°C and a frequency response of at least 10 Hz are expected to be achieved. The successful development of this device will pave the way for a differential absorption technique, in the same wavelength regime, for high frequency humidity measurements.

Two additional variations are worthy of note. First, through selection of different optical narrow-band filters, the radiometer can be shifted to nearby wavelengths which are either out-of-band or on the edge of the band. This provides a means for sensing other parameters. For example, a radiometer operated with a narrow band filter centered on $3.7 \mu\text{m}$ will operate in an "atmospheric window" and can be used for remote surface temperature measurements (of sea surface, clouds, land surfaces, etc.). This variation is planned for development concurrently with the in-cloud temperature radiometer. Similarly, for either lead selenide or thermistor bolometer detectors, it is possible to "de-tune" the radiometer center wavelength to the edge of the absorption band such that sample path lengths are greatly increased. This allows remote temperature measurements which can be weighted with respect to range. With appropriate scanning in elevation or wavelength, radiometers can therefore be used to obtain temperature profiles above and below the aircraft flight altitude. Such airborne application would be useful for boundary layer and inversion studies. Also, because the sampling range increases with decreasing air density, this application would be useful for studies of tropopause folding at higher flight altitudes. This concept has been used on NASA aircraft.

3.4 Tomographic Radiometric Measurement of Liquid Water in Clouds

A measurement of the emission from a spatial atmospheric distribution of particulates can be particularly useful for the detection and monitoring of parameters such as pollutants or naturally occurring atmospheric distributions, e.g., liquid water content in clouds. If a large number of such measurements along a series of intersecting rays can be utilized, then it is possible to compute the distribution through the use of tomographic mathematical inversion procedures. Such procedures have been in use in geophysical exploration, in radio astronomy, and especially in medicine for over a decade. The technique is applicable for optical or microwave frequencies. Warner et al. (1984) describe a ground-based system.

Jack Warner (NCAR, Boulder, Colorado, USA) and Sean Twomey (University of Arizona, Tucson, Arizona, USA) are collaborating on the development of the tomographic technique using scanning microwave radiometers from aircraft for the remote sensing of liquid water content in clouds. The aircraft radiometers would be mounted to subtend a fixed fore-aft angle such that multiple rays would be provided as the aircraft flies beneath isolated, developing cumulus clouds. Simulations and a field test of ground-based scanning radiometers operating at a wavelength of near 1 cm (K-band) have been carried out, with the result that it appears possible using the tomographic inversion technique to measure the two-dimensional distribution of liquid water content in an isolated cloud to an accuracy of 0.1 g m^{-3} with a spatial resolution of a few hundred meters. In principle, similar results should be obtainable from the aircraft configuration. It should be noted that at the K-band wavelength, the presence of ice particles is nearly invisible because of a greatly reduced emissivity of ice as compared to liquid water. It is also important to note that the method is accurate for drop distributions without appreciable water content in drops greater than 1 μm diameter. Field flight tests are planned for 1985.

3.5 Temperature and Humidity Profiling

While coherent lidar and radar will provide accurate measurements of air motion in the clear air and in precipitation respectively, accurate and high resolution measurements of temperature and moisture remain difficult problems. Radiometric measurements in the oxygen and water vapor bands such as described by Hogg et al. (1983) provide estimates of the profiles of moisture and temperature but with poor resolution in the vertical. However, these techniques may be more useful from aircraft than from fixed surface locations because, although vertical resolution will not be improved, the mobile aircraft platform will permit measurements of the meso-scale variability of temperature and moisture in the horizontal with substantially higher resolution in the horizontal than is available from satellites. The result will be a set of measurements from satellite and aircraft that complement one another by providing both large aerial coverage and high horizontal resolution.

3.6 Incoherent Lidar

Pulsed incoherent lidar is also now suitable for aircraft use. Single wavelength systems can be inexpensive but tend not to be quantitative with respect to detailed properties of the aerosol or molecular backscattering medium. They do however provide important information on boundaries and structure. Single wavelength lidar will therefore be very useful for examining boundary layer height, structure, and evolution, and because of the airborne platform, the mesoscale variability of these properties can also be observed. In a similar vein, single wavelength lidar is suitable for making highly accurate measurements of cloud tops and cloud structure. Differential absorption lidar is more costly but offers more information. Profiles of gaseous constituents including water vapor should be possible in the troposphere.

4. THE NEXT STEPS

There is little doubt that the atmospheric sciences community can use airborne remote sensing very profitably. Indeed, scientific headway in studies of mesoscale systems and atmospheric chemistry will be hampered significantly unless aircraft are suitably equipped to duplicate, in part, the measurement capabilities of surface-based networks. This paper, like many others on this subject, has addressed the issue of potential, but promising candidates for airborne remote sensing have been discussed for two decades. The challenge facing the atmospheric sciences community now is to put these techniques to use effectively. There is no universal formula for success, but the following ingredients are considered by the authors to be important.

- First, there must be an established scientific need and that need should come from the community of users, rather than from the instrument system developer.
- Second, users must be committed to the development process, working cooperatively with the instrument developer. In this way it is assured that what is developed will be useful to the nonspecialist.
- Third, the instrument must be well engineered, that is, acceptably easy to use. Considerable attention must therefore be paid to reliability, calibration, display, data recording, and data analysis.
- Fourth, if airborne remote sensing is to advance to its potential, the larger aircraft platforms available in various agencies must be made available for the community at large to use with as few strings attached as possible.
- Fifth, there must be a commitment by the agency or group, into whose custody these instruments are placed, to provide adequate funding for maintenance of the hardware and for guaranteeing operational readiness.

- Finally, adequate feedback between scientific users and operators must take place. This can be accomplished most effectively by establishing scientific competence within the framework of the operational team.

Within our community, we expect to see widespread use of airborne Doppler radar in three to five years. Coherent CW lidar may also be available in this time frame. Short range rapid response temperature measurement may achieve operational status in two to three years. Airborne pulsed lidar and microwave radiometric techniques are also critically needed and should be developed as research tools within five years.

5. ACKNOWLEDGMENTS

The authors would like to acknowledge the helpful comments that they received from Jack Warner and the information transmitted to them by Dave Atlas. Special thanks are also given to Carol Nicolaidis, Regina Gregory and Diane Wilson who helped to prepare the manuscript.

6. REFERENCES

- Albrecht, B.A., S.K. Cox and W.H. Schubert, 1979: Radiometric measurements of in-cloud temperature fluctuations. J. Appl. Meteor., 18, 1066-1071.
- Bluestein, H.B., E.W. McCaul, Jr. and D.E. Fitzgerald, 1983: Airborne Doppler lidar and ground-based Doppler radar observations of a thunderstorm in Oklahoma. In Preprint Vol., 21st Conference on Radar Meteorology, Edmonton, Canada, September. Amer. Meteor. Soc., Boston, Mass., 85-90.
- Cannell, R. Foord, J.M. Vaughan and A. Woodfield, 1983: The RSRE/RAE laser true airspeed system (LATSAS). In Preprint Vol., 2nd Topical Meeting on Coherent Laser Radar: Technology and Applications, Aspen, Colorado, 1-4 August. Opt. Soc. Am., Washington, D.C., WA4.
- Hogg, D.C., F.O. Guiraud, J.B. Snider, M.T. Decker and E.R. Westwater, 1983: A steerable, dual-channel microwave radiometer for measurement of water vapor and liquid in the troposphere. J. Climate Appl. Meteor., 22(5), 789-806.
- Huffaker, R.M., 1983: Global wind measuring satellite system (WINDSAT) feasibility studies. In Preprint Vol., 2nd Topical Meeting on Coherent Laser Radar: Technology and Applications, Aspen, Colorado, 1-4 August. Opt. Soc. Am., Washington, D.C., TuC1.
- Keeler, R.J., and R.J. Serafin, 1983: An airborne coherent lidar for turbulence measurement. In Preprint Vol., 2nd Topical Meeting on Coherent Laser Radar: Technology and Applications, Aspen, Colorado, 1-4 August. Opt. Soc. Am., Washington, D.C. MC6.
- Lenschow, D.H., C.A. Cullian, R.B. Friesen and E.N. Brown, 1978: The status of air motion measurements on NCAR aircraft. In Preprint Vol., Fourth Symposium on Meteorological Observations and Instrumentation, Denver, Colorado, April 10-14. Amer. Meteor. Soc., Boston, Mass. 433-438.
- Mueller, C.K., and P.H. Hildebrand, 1983: The structure of a microburst: As observed by ground-based and airborne Doppler radar. In Preprint Vol., 21st Conference on Radar Meteorology, Edmonton, Canada, September. Amer. Meteor. Soc., Boston, Mass., 602-608.
- Warner, J., J.F. Drake and P.R. Krehbiel, 1984: Microwave tomography as a means of determining liquid water profiles in cloud. (To be presented) Ninth Int. Conference on Cloud Physics, August 21-23, Tallin, Estonia, USSR. International Association of Meteorology and Atmospheric Physics (IAMAP), Geneva, Switzerland.

APPENDIX A

Bibliography

- Abshire, J.B., and J.E. Kalshoven, Jr., 1983: Multicolor laser altimeter for barometric measurements over the ocean. Experimental. Appl. Opt., 22(17), 2578-2585.
- Astheimer, R.W., 1962: An infrared radiation air thermometer. Proc. 2nd Symposium on Remote Sensing of Environment, October 15-17. Infrared Laboratory, Institute of Science and Technology, University of Michigan, Ann Arbor, Michigan, 375-391.
- Benedetti-Michelangeli, G., F. Congeduti and G. Fiocco, 1972: Measurement of aerosol motion and wind velocity in the lower troposphere by Doppler optical radar. J. Atmos. Sci., 29(5), 906-910.
- Bilbro, J.W., and W.W. Vaughan, 1978: Wind field measurement in the nonprecipitous regions surrounding severe storms by an airborne pulsed Doppler lidar system. Bull. Amer. Meteor. Soc., 59(9), 1095-1100.
- Browell, E.V., A.F. Carter, S.T. Shipley, R.J. Allen, C.F. Butler, M.N. Mayo, J.H. Siviter, Jr. and W.M. Hall, 1983: NASA multipurpose airborne DIAL system and measurements of ozone and aerosol profiles. Appl. Opt., 22(4), 532-534.
- Chang, A.T.C., and T.T. Wilheit, 1979: Remote sensing of atmospheric water vapor, liquid water, and wind speed at the ocean surface by passive microwave techniques from the Nimbus 5 satellite. Radio Sci., 14(5), 793-802.
- Coffeen, D.L., and J.E. Hansen, 1972: Airborne infrared polarimetry. Eighth Int. Symp. on Remote Sensing of Environment, October 2-6, Ann Arbor, Mich. Environmental Research Institute of Michigan, Ann Arbor, Mich., 515-522.
- Collis, R.T.H., 1970: Lidar. Appl. Opt., 9(8), 1782-1788.
- Curran, R.J., H.L. Kyle, L.R. Blaine, J. Smith and T.D. Chen, 1981: Multichannel scanning radiometer for remote sensing cloud physical parameters. Rev. Sci. Instrum., 52(10), 1546-1555.
- Davis, P.A., 1971: Applications of an airborne ruby lidar during a BOMEX program of cirrus observations. J. Appl. Meteor., 10, 1314-1323.
- Griggs, M., and W.A. Marggraf, 1967: Measurement of cloud reflectance properties and the atmospheric attenuation of solar and infrared energy. U.S. Air Force Cambridge Research Laboratories, #AFCRL-68-0003, Cambridge, Mass.
- Jones, W.L., P.G. Black, V.E. Delmore and C.T. Swift, 1981: Airborne microwave remote-sensing measurements of hurricane Allen. Science, 214, 274-280.
- Johnson, J.W., D.E. Weissman and W.L. Jones, 1982: Measurements of ocean surface spectrum from an aircraft using the two-frequency microwave resonance technique. Int. J. Remote Sensing, 3(4), 383-407.
- Kaplan, L.A., 1959: Inference of atmospheric structure from remote radiation measurements. J. Optical Sci. of America, 49(10), 1004-1007.
- Kaufman, Y.J., T.W. Brakke and E. Eloranta, 1983: Field experiment to measure the radiative characteristics of a hazy atmosphere. Fifth Conference on Atmospheric Radiation, October 31 - 4 November, Baltimore, Maryland. AMS, Boston, Mass., 224-227.

- Knollenberg, R.G.. 1981: Clouds, Their Formation, Optical Properties, and Effects. Peter V. Hobbs and Adarsh Deepak, (Eds.), Academic Press, 497 pp.
- Kuhn, P., F. Caracena and C.M. Gillespie, Jr., 1977: Clear air turbulence: Detection by infrared observations of water vapor. Science, 196, 1099-1100.
- Kuhn, P.M., and H.K. Weickmann, 1969: High altitude radiometric measurements of cirrus. J. Appl. Meteor., 8, 147-154.
- Lipes, R.G., R.L. Bernstein, V.J. Cardone, K.B. Katsaros, E.G. Njoku, A.L. Riley, D.B. Ross, C.T. Swift and F.J. Wentz, 1979: Seasat scanning multichannel microwave radiometer: Results of the Gulf of Alaska workshop. Science, 204, 1415-1417.
- Liu, K-N, 1977: Remote sensing of the thickness and composition of cirrus clouds from satellites. J. Appl. Meteor., 16, 91-99.
- McIlrath, T.J., 1980: Fluorescence lidar. Optical Eng., 19(4), 494-502.
- McMillin, L.M., 1975: Estimation of sea surface temperatures from two infrared window measurements with different absorption. J. Geophys. Res., 80(36) 5113-5117.
- Okamoto, K., S. Yoshikado, H. Masuko, T. Ojima, N. Fugono, K. Nakamura, J. Awaka and H. Inomata, 1982: Airborne microwave rain-scatterometer/radiometer. Int. J. Remote Sensing, 3(3), 277-294.
- Ryan, R.T., H.H. Blau, Jr., P.C. von Thuna, M.L. Cohen and G.D. Roberts, 1972: Cloud microstructure as determined by an optical cloud particle spectrometer. J. Appl. Meteor., 11, 149-156.
- Saunders, P.M., 1967: Aerial measurement of sea surface temperature in the infrared. J. Geophys. Res., 72(16), 4109-4117.
- _____, 1970: Corrections for airborne radiation thermometry. J. Geophys. Res., 75(36), 7596-7601.
- Smith, W.L., H.B. Howell and H.M. Woolf, 1979: The use of interferometric radiance measurements for sounding the atmosphere. J. Atmos. Sci., 36(4), 566-575.
- Spinhirne, J.D., M.Z. Hansen and J. Simpson, 1983: The structure and phase of cloud tops as observed by polarization lidar. J. Climate Appl. Meteor., 22(8), 1319-1331.
- Swift, C.T., W.L. Jones, Jr. and W.L. Grantham, 1980: Microwave remote sensing. IEEE Anten. Prop. Soc. Newsletter, 22(5), 5-8.
- Szejwach, G., 1982: Determination of semi-transparent cirrus cloud temperature from infrared radiances: Application to METEOSAT. J. Appl. Meteor., 21(3), 384-393.
- _____, T.T. Wilheit, R.A. Nieman and I. Jobard, 1983: Microwave radiometry as a probe of precipitation physics. Fifth Conference on Atmospheric Radiation, October 31 - 4 November, Baltimore, Maryland. AMS, Boston, Mass., 65-67.
- Valovic, F.R., 1968: Infrared measurements of jet-stream cirrus. J. Appl. Meteor., 7, 817-826.

C-4

- Wang, J.R., J.L. King, T.T. Wilheit, G. Szejwach, L.H. Gesell, R.A. Nieman, D.S. Niver, B.M. Krupp and J.A. Gagliano, 1983: Profiling atmospheric water vapor by microwave radiometry. J. Climate Appl. Meteor., 22(5), 779-788.
- Wilheit, T.T., A.T.C. Chang, J.L. King and E.B. Rodgers, 1982: Microwave radiometric observations near 19.35, 92 and 183 GHz of precipitation in tropical storm Cora. J. Appl. Meteor., 21(8), 1137-1145.
- Wilheit, T.T., Jr., and M.G. Fowler, 1977: Microwave radiometric determination of wind speed at the surface of the ocean during BESEX. IEEE Trans. Anten. and Prop., Vol. AP-25, 111-120.
- Wu, M.-L.C., and R.J. Curran, 1983: Remote sensing of cloud radiation and micro-physical parameters. Fifth Conference on Atmospheric Radiation, October 31 - 4 November, Baltimore, Maryland. AMS, Boston, Mass., 72-75.
- Zuev, V.E., 1982: Laser Beams in the Atmosphere. James S. Wood (Translator), Consultants Bureau, 504 pp.

APPENDIX B

NASA/Goddard Space Flight Center

Remote Sensing Instrument Inventory

This Appendix list a number of the remote sensing instruments that may be available from the Goddard Space Flight Center. The information was provided to the authors through the courtesy of David Atlas, Chief of Goddard's Laboratory for Atmospheric Sciences. Details about these instruments can be obtained from Joseph McGoogan at the Wallops Island Flight Facility.

INDEX/GLOSSARY

<u>Catalog Number</u>	<u>Acronym</u>	<u>Instrument Name</u>
1	MCR	Multispectral Cloud Radiometer
2	CTS	Cloud Top Scanner
3	CLS	Cloud Lidar System
4	AMMS	Advanced Microwave Moisture Sounder
5	BRFI	Bidirectional Reflectance Field Instrument
6	LAPR II	Linear Array Pushbroom Radiometer
7		Biometer
8	OSC-I	Ocean Color Scanner-I
9	HCM	Heat Capacity Mapper
10	MLA(Sim)	Multispectral Linear Array Simulator
11	RMR	Rain Mapping Radiometer
12	CZCS	Coastal Zone Color Scanner
13	ALRS	Airborne Laser Ranging System
14	AMMR	Aircraft Multichannel Microwave Radiometer
15	LBMR	L-Band Microwave Radiometer
16	SWIR	Short Wave Infrared Radiometer
17	MLA	Multispectral Linear Array
18	RLS	Raman LIDAR System
19	OCE	Ocean Color Experiment
20	M'S	Bendix Modular Multiband Scanner
21	NS001	Thematic Mapper Multispectral Scanner
22	U-2 TMS	U-2 Thematic Mapper Simulator
23	U-2 LAS	U-2 Linear Array Scanner
24		Hygrometer
25	AOL	Airborne Oceanographic LIDAR
26	AAFE ALT	AAFE Radar Altimeter
27	SCR	Surface Contour Radar
28	ROWS	Radar Ocean Wave Spectrometer
29	ASAS	Advanced Solid State Array Spectrometer
30	PRT	Precision Radiation Thermometer

EVALUATION OF METEOROLOGICAL AIRBORNE DOPPLER RADAR

Peter H. Hildebrand and Cynthia K. Mueller
National Center for Atmospheric Research*
P.O.Box 3000, Boulder, Colorado 80307, USA

ABSTRACT

This paper will discuss the capabilities of airborne Doppler radar for atmospheric sciences research. The evaluation is based on airborne and ground-based Doppler radar observations of convective storms. The capability of airborne Doppler radar to measure horizontal and vertical air motions is evaluated. Airborne Doppler radar is shown to be a viable tool for atmospheric sciences research.

1. INTRODUCTION

Ground-based Doppler radars have been used since the 1960's to measure air and cloud particle motions in a wide variety of situations. Excellent reviews are given by Atlas (1964), Lhermitte (1966), Doviak et al (1979) and Carbone et al (1980). Multiple Doppler radar techniques have been extensively used to study atmospheric phenomena including convective clouds (e.g. Lhermitte, 1975; Heymsfield et al, 1980; Ray et al, 1981) stratiform clouds (e.g. Heymsfield, 1979) and boundary layer structure (e.g. Kropfli and Hildebrand, 1980). These and other studies have shown ground-based Doppler radars to be valuable instruments for atmospheric sciences research, which enable the measurement of air motions over large volumes in short lengths of time. Ground-based Doppler radar studies are limited to the observation of phenomena which develop within or traverse the area covered by the radars. Many meteorological phenomena cannot be observed adequately by ground-based Doppler radars because of their size or their distance from the radars.

The recent interest in airborne Doppler radar has resulted from the anticipated ability of the airborne Doppler radar to transcend some of the problems inherent with ground-based radars. Early tests of the airborne Doppler radar aboard the NOAA P-3 aircraft (Trotter et al, 1980, 1981) investigated the capabilities of the airborne Doppler system to function in the aircraft environment. These tests indicated that cloud particle velocities measured by the airborne Doppler radar were generally within about 1 m/s of comparable velocities measured simultaneously by a ground-based Doppler radar.

More extensive tests of airborne Doppler radar capabilities have been presented by Jorgensen et al (1983a), Hildebrand et al (1983a) and Mueller and Hildebrand (1983). Jorgensen et al (1983a) presented comparisons of airborne and ground-based Doppler radar measurements of horizontally homogeneous stratiform precipitation. They compared dual Doppler-derived horizontal wind fields from airborne and ground-based Doppler radar systems. Their measurements showed agreement between the airborne and ground-based horizontal vector fields, but a lack of agreement between the vector eddy fields measured by the two systems. This lack of agreement between the airborne and ground-based systems was attributed to the long data collection period, the non-stationarity of the wind field over this period, and to differences in the sampling characteristics of the two systems.

*The National Center for Atmospheric Research is sponsored by the National Science Foundation.

They also presented a direct comparison of precipitation fall speeds as observed by airborne and ground-based Doppler radars. These measurements indicated that the airborne and ground-based mean Doppler velocity measurements agreed to $\ll 1$ m/s, but that the variance of the airborne mean fall speed measurements was considerably larger than that measured by the ground-based system (about 1.4 vs $0.25 \text{ m}^2/\text{s}^2$ for the airborne vs ground Dopplers). The increased variance noted in the airborne data was attributed to variabilities and uncertainties of the order of 0.3 degrees in the airborne Doppler antenna position. Jorgensen et al (1983b) and Marks and Houze (1983) presented analyses of convective storm and hurricane structures using the P-3 airborne Doppler data.

Mueller and Hildebrand (1983) and Hildebrand et al (1983a) presented analyses of airborne and ground-based Doppler radar data collected under more optimal conditions.

These analyses are extended in the present paper to include more careful comparisons of vertical and horizontal air motions within convective storms as measured by airborne and ground-based Doppler radars. The strengths and weaknesses of both systems are noted and some comments are made concerning the utility of airborne Doppler radar in measuring atmospheric air motions. Hildebrand et al (1983b) discuss characteristics of airborne Doppler radars, and recommend some conventions which will ease the incorporation of the airborne radar data into multiple Doppler analyses. They also discuss some strategies of operation for airborne Doppler radar.

2. DATA COLLECTION

The data used in this paper were collected during the Joint Airport Weather Study (JAWS) experiment during June 1982. During JAWS the NCAR Doppler radars, CP2 and CP4, were located within <30 km of each other near Denver, Colorado as shown in Fig. 1. These radars have about 1 degree beams, and contiguous 150 m range bins. During JAWS these radars generally scanned in a series of sector scans, with beams separated by less than 1 deg in azimuth and elevation. The volume scan time was generally < 3 minutes. The CP2 radar is a dual wavelength X and S-band radar, with the S-band being Doppler. The CP4 is a C-band Doppler radar.

The NOAA P-3 airborne Doppler radar is summarized in Jorgensen et al (1983a) and Hildebrand et al (1983b). The radar is located in the tail of the P-3 aircraft and scans in a vertical plane normal to the ground track. The antenna scans are corrected for the drift and pitch of the aircraft so that the airborne Doppler-measured radial velocities are measured relative to the ground. The aircraft's forward motion translates the beam through space in such a fashion as to produce a helical scan surface with the aircraft track at the center. The aircraft flies about 1 km in the time it takes to complete one scan. This X-band radar has a beamwidth of 1.9 degree in the cross-track direction and 1.35 degree in the along track direction. The scan and sampling rates for the radar are such that one beam of data is collected every degree in the vertical direction. The airborne Doppler radar collects 256 bins of data per beam, with 75 m deep bins spaced at 150 or 300 m intervals. The data used in this paper are at 150 m spacing.

3. MEASUREMENT OF HORIZONTAL VELOCITIES

On 25 June 1982, the airborne and ground-based Doppler radars observed a thunderstorm which was located about 40 km southwest of the ground-based radars. The analysis location and the P-3 flight track are indicated in Fig. 1.

The storm had a maximum reflectivity of about 55 dBZ and was moving towards the northeast at about 10 m/s. These data are well suited for evaluating the capabilities of the airborne Doppler radar to measure horizontal velocities within storms.

The ground radars scanned the storm several times at 2-3 minute intervals. At the same time, the airborne Doppler collected data while flying at a distance of 15-25 km from the storm. The P-3 data were collected over a 7 minute period which was centered upon the time when the ground-based radars were collecting data. In order to correct for errors in the P-3 position, the aircraft position was adjusted such that the interpolated radar reflectivity fields from the aircraft and ground radars matched in location. This involved adjustments to the P-3 position of 1-2 km in the south and west directions. (Subsequent to the preliminary results presented herein, an improved adjustment has been developed. This new adjustment differs from the one used in the data presented here by about 1 km.).

The data from the two airborne Doppler flight tracks and from the ground-based Doppler radars were interpolated to a common cartesian grid having dimensions 1 x 1 x 0.6 km in the X, Y, and Z directions. The inverse square interpolation filter had the same scale. During the interpolation, each beam was advected according to the assumed advection velocity of the storm, and the time of data collection of that beam of radar data.

With four radars available for a multiple analysis (CP2, CP4 and the P-3 from two vantage points), several different analyses were generated. Only three will be presented here. These three, shown in Fig. 2, include the airborne only analysis (upper right), the ground based only analysis (lower left)

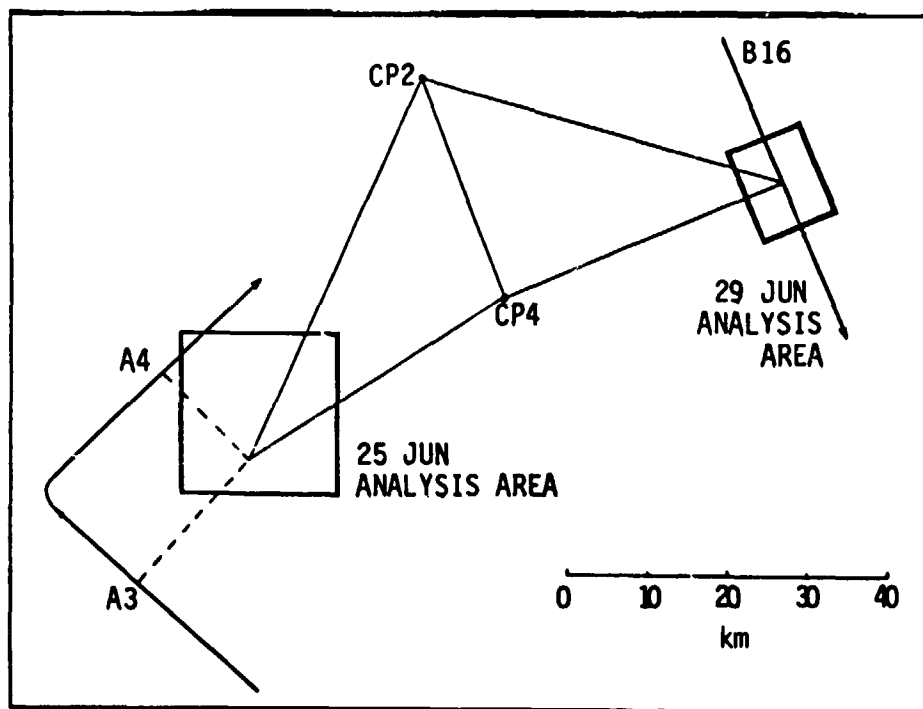
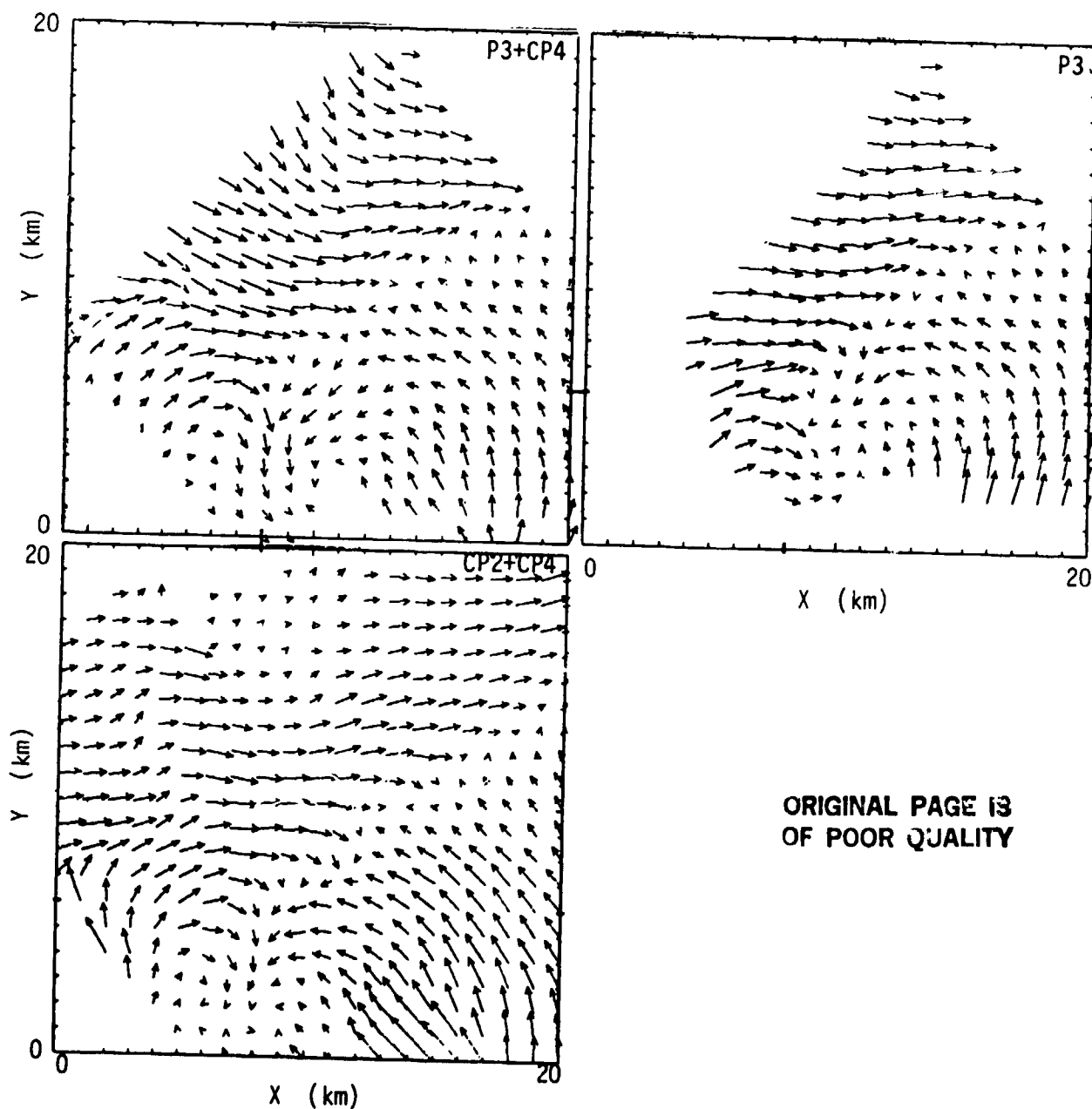


Figure 1. Map showing the location of the ground-based Doppler radars during the JAWS experiment. Also shown are the multiple Doppler radar analysis areas on the two days of the experiment, 25 and 29 June 1982. The flight tracks from 25 June (A3 and A4) and from 29 June (B16) are also shown.

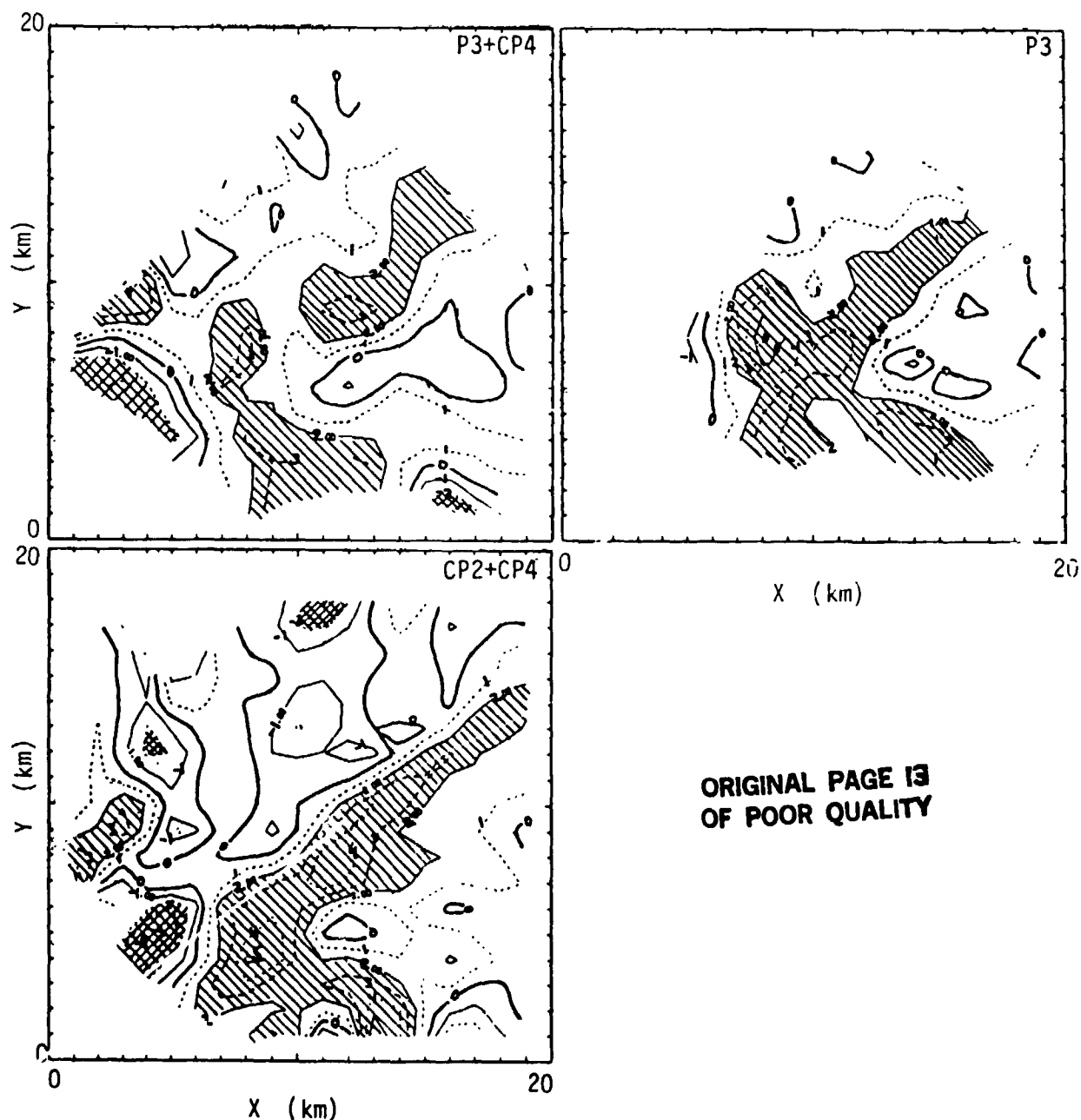
and a combined analysis (upper left) which made use of the second P-3 flight track (A4) and the CP4 radar. Additional analyses which made use of the P-3 + CP2 or the P-3 + CP2 + CP4 were little different from the P-3 + CP4 analysis (upper left). Inspection of the three vector fields in Fig. 2 indicates striking similarities. All three horizontal vector fields (taken from 4.0 km msl or 2.4 km agl) show a convergence line running diagonally up to the right through the data, and the southward outflow on the south side of the storm. The results shown here are indicative of those observed at other levels in the storm.



ORIGINAL PAGE IS
OF POOR QUALITY

Figure 2. Horizontal wind vector fields at the 2.4 km agl level for three different multiple Doppler analyses. The upper left analysis uses airborne Doppler data from flight track A4 plus the CP4 ground based radar. The upper right analysis uses airborne Doppler from flight tracks A3 and A4. The lower left analysis uses data from ground-based CP2 and CP4 radars. A 10 m/s wind vector is 1 km long.

A more stringent test of the analyses lies in comparison of the convergence fields. Fig. 3 shows three convergence fields which correspond to the vector fields of Fig. 2. Areas of convergence of greater than $2 \times 10^{-3} \text{ s}^{-1}$ are hatched; areas of less than $-2 \times 10^{-3} \text{ s}^{-1}$ are cross-hatched. These analyses indicate that while the different analyses depicted similar convergence fields, some differences are also noted. All three analyses note the area of convergence noted in Fig. 2. The airborne-only and the ground based-only analyses (upper right and lower left) also indicate similar convergence maxima of $5 - 6 \times 10^{-3} \text{ s}^{-1}$; however, the position they indicate for the maximum is somewhat different. This difference is, in part, due to the error in aircraft location.



ORIGINAL PAGE 13
OF POOR QUALITY

Figure 3. Horizontal convergence fields corresponding to the vector fields of Fig. 2. The contours are in units of 10^{-3} s^{-1} . Areas with convergence greater than $2 \times 10^{-3} \text{ s}^{-1}$ are hatched; areas less than $-2 \times 10^{-3} \text{ s}^{-1}$ are cross-hatched.

An additional means of comparing the quality of the analyses lies in resampling the three-dimensional wind fields. For each analysis in Fig. 2 a radial velocity field was generated which corresponded to what the CP2 radar would see if it looked at this analysis. This "resampled" radial velocity was then subtracted from what the CP2 radar actually saw. This difference is displayed in Fig. 4. On the left side of the figure is the CP2 radial velocity difference for the P-3 + CP4 analysis. On the right side of the figure is the CP2 radial velocity difference for the airborne-only analysis (P-3 tracks A3 and A4). In both cases, differences greater than $+2$ m/s are shaded. The airborne-only analysis agrees to better than 2 m/s except in the core of the storm near the updraft. Two possible causes of error include the approximately 1 km error in aircraft location and the relatively long time required to collect the airborne Doppler data (about 7 minutes). Both effects could degrade the wind measurements, particularly in areas of high temporal and spatial gradients such as near the edge of an updraft or downdraft.

The areas of large error for the P-3 + CP4 analysis (left portion of Fig. 4) tend to be concentrated to the sides, away from the convergence area. The reason for this error pattern is not clear. Based on the radar locations (Fig. 1.), it appears the poorest geometry should occur toward the north edge of the analysis area. While the effects of the 1 km aircraft location error certainly enter this comparison, these explanations shed little light on the results shown in Fig. 4. Similar figures which contain data from CP2 are not shown for, as expected, they contain only numbers smaller than about 1 m/s.

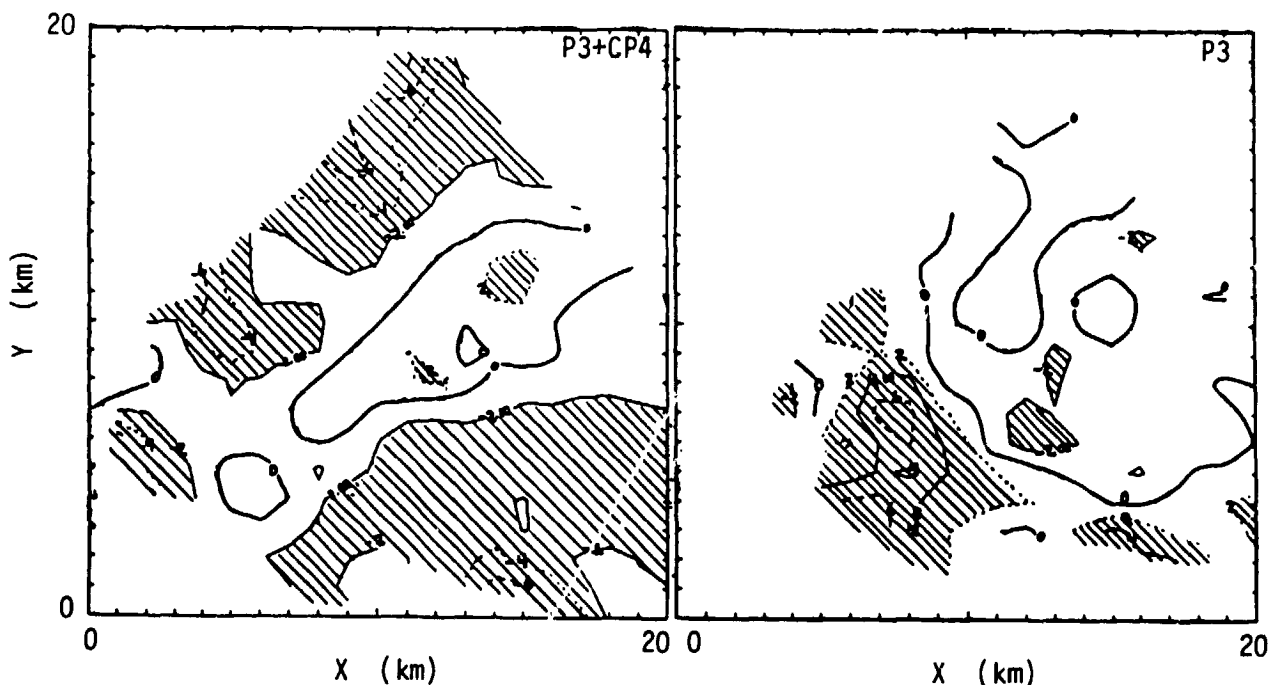


Figure 4. The difference between the observed CP2 radial velocities and resampled radial velocities taken from the top two analyses of Fig. 2. The resampled radial velocities are what the CP2 radar would see were it to observe the wind fields depicted in the upper portion of Fig. 2. The contours are in units of 1 m/s. Areas of > 2 m/s or < -2 m/s are hatched.

4. MEASUREMENT OF VERTICAL VELOCITIES

On 29 June 1982 the P-3 aircraft flew directly through a microburst-producing thunderstorm at an altitude of 4.5 km agl. The aircraft made repeated passes through the storm until the severity of the storm became too great for further penetration. During this time the storm was observed by the ground-based CP2 and CP4 radars. Due to the location of the airborne Doppler immediately above the microbursts, this case provides a good evaluation of the airborne Doppler radar's ability to measure vertical storm velocities, while operating in conjunction with ground-based Doppler radars. This test is one of the primary areas of interest expressed in the 1979 Multiple Doppler Radar Workshop (Carbone et al, 1980).

In this case the airborne Doppler was operated as described above. The ground-based Doppler radars scanned with a volume scan time of about 2.5 minutes. At the center of the analysis volume (Fig. 1) the horizontal data density was 0.3 km and the vertical data density was 0.25 km. The data from the airborne and ground-based radars were interpolated to a cartesian grid which was rotated such that the Y axis was parallel to the aircraft flight track. For the airborne Doppler radar data the grid resolution and interpolation filter length was $0.35 \times 1.05 \times 0.25$ km in the X, Y and Z directions. The ground-based Doppler data were interpolated on a similar grid which had a 0.35 grid spacing and filter length in the Y direction. Otherwise the analyses were identical. The difference in the airborne and ground-based analyses was selected because of the ~ 1 km data spacing of the airborne Doppler data in the Y direction. Due to this wide data spacing and the strong distance weighting, the interpolated airborne data are not well smoothed in the Y direction. This problem was exacerbated by having the grid nearly coincide with the airborne Doppler data collection locations in the Y direction. The ground-based Doppler data, on the other hand, are much denser in the Y direction. When interpolated using an identical filter and grid, the ground-based data are smoother than the airborne Doppler data. Due to the small scale of the observed microburst a higher resolution ground-based Doppler analysis was necessary in order that the results be as closely comparable as possible.

Some sample data are presented in Fig. 5. The horizontal wind vector field at the top of the figure is ground radar data from 0.1 km agl. Vertical cross-sections at the bottom of Fig. 5 show the X-Z wind vectors in the Y=3.5 km and Y=11 km planes. For each plane, two analyses are shown. The top analysis is a ground-based (CP2 + CP4) analysis in which the vertical velocity vectors were derived using continuity and the assumption of zero vertical velocity at the ground. The lower analysis is derived using the airborne Doppler data for derivation of the vertical velocity. The airborne radial velocity values are corrected for the horizontal velocities observed by the ground-based radars and for a hydrometeor fall speed which was based on the observed radar reflectivity value. The residual radial component was attributed to the vertical velocity. Both vertical velocity contours and X-Z wind vectors are presented. The radar reflectivity fields are shown as the background contours, behind the U-W wind vectors in the lower section of the figure.

In the left hand column (Y=3.5 km) the different vertical velocities agree well in the center of the figure, where both analyses show a downdraft peak of >12 m/s. To the left of that downdraft, both analyses show a second downdraft; however, the two analyses are somewhat different. The ground-based analysis shows an updraft at about X=2.5 km then another downdraft area between X=0.5 and X=1.5 km. In contrast, the airborne Doppler shows a uniform area of downdraft on the left side of the figure. The airborne Doppler evaluation of

ORIGINAL PAGE 13
OF POOR QUALITY

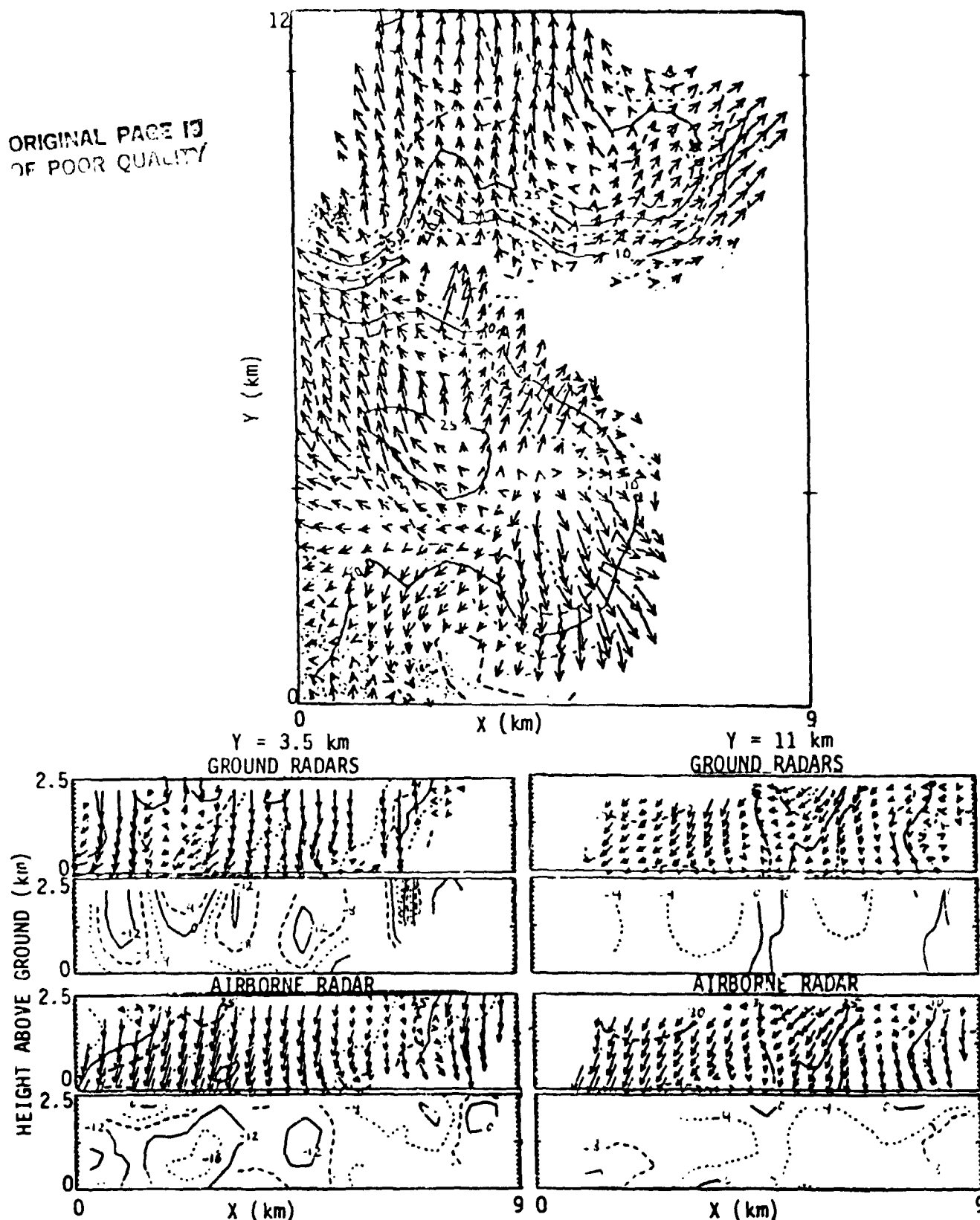


Figure 5. Vertical velocity analyses based on airborne and ground-based Doppler radars. The upper portion of the figure is a horizontal wind vector field at the 0.1 km agl level, based on the ground radars. The lower left portion shows vertical cross-sections located at $Y=3.5$ km for the airborne and ground-based analyses. Both the U-W vector fields and the W contours are shown. The lower right portion is a similar vertical cross-section located at $Y=11$ km. The reflectivity is shown as background to the airborne Doppler D-W wind fields.

the vertical velocities seems in better agreement with the reflectivity profile which is shown in the next to bottom frame of the figure. The analysis in the upper frame shows fairly strong dV/dY in that area which could be mis-estimated due to the poor geometry of the ground Doppler radars for making velocity measurements in the Y direction.

Agreement is also seen in the $Y=11$ km vertical planes in the lower right of Fig. 5. There, both analyses present a minimum in vertical velocity at about $X=4.5$ km, and both analyses show downdrafts of about 4 m/s through much of the rest of the $Y=11$ plane. The major difference between these two analyses lies at the edges of the plane near $X=1$ and $X=8$, where the airborne analysis (lower) shows intensified downdrafts and the ground based analysis (upper) shows weakened downdrafts. There appears as much reason to question the ground based horizontal divergence fields as there is to question the airborne radial velocity fields.

5. DISCUSSION

These comparisons of airborne and ground-based Doppler radar data are encouraging. Although the results must be regarded as preliminary at this point, they indicate that the airborne Doppler data generally are in qualitative agreement with the ground-based Doppler data. Examples have been presented which use the airborne Doppler primarily to measure horizontal velocities. This mode of use of airborne Doppler radar was recognized in the Multiple Doppler workshop and is of interest for the GALE and STORM experiments. Our analyses indicate areas in which the airborne Doppler is measuring the same things as the ground-based Dopplers, and areas where differences are observed. Generally these differences are small with respect to the total natural velocity differences; however, they are not negligible. The comparison of vertical velocities from the airborne and ground-based Doppler radars produced similar results. Again, there was general qualitative agreement between the two analyses and areas of good and poor agreement in different locations in the analysis. Current extensions of the preliminary results presented here suggest that several effects may be contributing to the observed differences. These effects include the temporal evolution and the advection problems mentioned above, as well as ground clutter and side lobe effects which can be inferred to exist in the data. In addition, there are indications that analysis decisions such as grid spacing and filter shape, as well as radar location, may have significant effects on the analysis. These effects are currently being investigated.

These analyses are currently being extended to include additional cases which include different geometries and an additional radar. Planned extensions of the work include evaluation of multiple Doppler radar analysis decisions on the analysis results as applied to this problem. If available, corroborating aircraft and surface mesonet information will be used for independent verification of analysis results. The implications of the present finding for the design of field projects using airborne Doppler radar is being considered.

6. ACKNOWLEDGEMENTS

We would like to express our gratitude to the many people who ably assisted in collecting and analyzing these data. The analyses presented herein are a part of a joint NCAR/NOAA airborne Doppler radar development effort. The major collaborators in this effort include Dr. David Jorgensen and his colleagues at the Hurricane Research Laboratory. Their pioneering use of airborne Doppler in hurricane research provides a major stimulus for this development.

The assistance of Dr. Gus Emmanuel and the NOAA/OAO aircraft crew is gratefully acknowledged. From NCAR, the assistance of Charles Frush, Marina Skumanich, Dick Oye, Debby Lawrence and Peggy Taylor is gratefully acknowledged. Dr. John McCarthy and the JAWS project staff provided the ground-based Doppler radar data and helpful assistance. JAWS was funded by the NSF through NCAR, by the FAA through DTFA01-82-Y-10513, by NASA through H-59314P, and by NOAA through a cooperative agreement with PROFS.

7. REFERENCES

- Atlas, D., 1964: Advances in radar meteorology. Advances in Geophysics, Vol. 10, Academic Press, 318-478.
- Carbone, R.L., F.I. Harris, P.H. Hildebrand, R.A. Kropfli, L.J. Miller, W. Moninger, R.G. Strauch, R.J. Doviak, K.W. Johnson, S.P. Nelson, P.S. Ray and M. Gilet, 1980: The Multiple Doppler Radar Workshop, Bull. Amer. Meteor. Soc., 61, 1169-1203.
- Doviak, R.J., R.S. Zrnic, and D.S. Sirmans, 1979: Doppler weather radar. Proc. of the IEEE, 67, 1522-1553.
- Heymsfield, G.M., 1979: Doppler radar study of a warm frontal region. J. Atmos. Sci., 36, 2093-2107.
- Heymsfield, A.J., A.R. Jameson and H.W. Frank, 1980: Hail growth mechanisms in a Colorado storm: Part II: Hail formation processes. J. Atmos. Sci., 37, 1779-1807.
- Hildebrand, P.H., C.L. Frush, C. K. Mueller, D.P. Jorgensen, and T. Schricker, 1983a: Test of an airborne pulse-Doppler meteorological radar. Preprints 21st Conf. on Radar Meteor., Edmonton, Canada. Amer. Meteor. Soc., 437-444.
- _____, C. Walther, C.L. Frush, and C. K. Mueller, 1983b: Airborne weather radar: evaluation and discussion of applications. Preprints, 21st Conf. on Radar Meteor., Edmonton, Canada. Amer. Meteor. Soc., 270-277.
- Jorgensen, D.P., P.H. Hildebrand, C.L. Frush, 1983a: Feasibility test of an airborne pulse Doppler meteorological radar. J. Climate Appl. Meteor., 22, 744-757.
- _____, R.W. Burpee and K. C. Belle, 1983b: Airborne Doppler radar estimates of the air motions associated with a sea breeze induced precipitation line. Preprints 21st Conf. on Radar Meteor., Edmonton, Canada, Amer. Meteor. Soc., 670-674.
- Kropfli, R.A., and P.H. Hildebrand, 1980: 3-D wind measurement in the optically clear planetary boundary with dual-Doppler radar. Radio Science, 15, 283-296.
- Lhermitte, R.M., 1966: Application of the pulse-Doppler radar technique to meteorology. Bull. Amer. Meteor. Soc., 47, 703-711.
- _____, 1975: Dual-Doppler radar observations and study of seabreeze convective storm development. J. Appl. Meteor., 14, 1346-1361.
- Marks, F.D. and R.A. Houze, Jr., 1983: Three dimensional wind field in the developing inner core of hurricane Debby. Preprints 21st Conf. on Radar Meteor., Edmonton, Canada, Amer. Meteor. Soc., 298-304.
- Mueller, C.K., and P.H. Hildebrand, 1983: The structure of a microburst as observed by ground-based and airborne Doppler radar. Preprints 21st Conf. on Radar Meteor., Edmonton, Canada, Amer. Meteor. Soc., 602-608.
- Ray, P.S., B.C. Johnson, K.W. Johnson, J.S. Bradberry, J.J. Stephens, K.K. Wagner, R.B. Wilhelmson and J.B. Klemp, 1981: The morphology of several tornadic storms on 20 May 1977. J. Atmos. Sci., 38, 1643-1663.
- Trotter, B.L., C.L. Frush and R.G. Strauch, 1980: An airborne pulse-Doppler radar for meteorological research. Preprints 19th Conf. Radar Meteorology, Miami Beach. Amer. Meteor. Soc., 110-114.
- _____, R.G. Strauch and C.L. Frush, 1981: Evaluation of a meteorological airborne pulse-Doppler radar. NOAA Tech. Memo. ERL WMP0-45, Boulder, 55 pp.

LN84 27288

MICROWAVE REMOTE SENSING OF OCEAN SURFACE
WIND SPEED AND RAIN RATES OVER
TROPICAL STORMS

C. T. Swift and D. C. DeHORITY
University of Massachusetts
Department of Electrical and Computer Engineering
Amherst, Massachusetts 01003 USA

Peter G. Black
National Oceanic and Atmospheric Administration
Atlantic Oceanographic and Meteorological Laboratory
4301 Rickenbacker Causeway, Miami, Florida 33149 USA

Jian-Zhong Chien
Tsinghua University/Department of Radio Electronics
Peking, People's Republic of China

ABSTRACT

The value of using narrowly spaced frequencies within a microwave band to measure wind speeds and rain rates over tropical storms with radiometers is reviewed. The technique focusses on results obtained in the overflights of Hurricane Allen during 5 and 8 of August, 1980.

Introduction

On 5 and 8 August, 1980, a C-Band Stepped Frequency Microwave Radiometer (SFMR) overflew Hurricane Allen for the purpose of measuring rain rate and ocean surface wind speed. The SFMR was placed in a mode whereby it could sequentially step between frequencies of 4.5, 5.0, 5.6, and 6.6 GHz. The strategy of the experiment was to recognize that the rain column is only weakly attenuating at C-Band, thus providing continuous observations of the wind-driven ocean surface, even for heavy rain rates. The frequency stepping technique was devised as a means to separate dispersive atmospheric emission from the nondispersive ocean surface emission. The envelope of four-frequency brightness temperatures will increase and decrease in proportion to the percentage of surface foam, and is therefore a measure of the surface wind speed. The relative differences in brightness temperature is a measure of the rain opacity, which is at least proportional to the square of the electromagnetic wavelength.

The preliminary results were reported in a brief paper⁽¹⁾. Because of space limitations, the retrieval scheme was presented without derivation. A more detailed derivation will be given here, including a brief discussion of the results that have already been reported.

In the time period since the original results were reported, the activity has concentrated on upgrading the algorithm, and resolving calibration issues that surfaced in the detailed analysis of the data. Deadline pressures for the publication of this paper have precluded presentation of graphics; however, the results will be presented during the oral delivery of the paper.

Derivation of the Algorithm

As usual, all first principle algorithms used for the analysis of microwave radiometer data begin with the radiative transfer equation, which is given by:

$$T_B = (1-\epsilon) T_C e^{-2\tau_\infty} + T_{AIR} + (1-\epsilon) T_{AIR} e^{-\tau_\infty} + \epsilon T_S e^{-\tau_\infty} \quad (1)$$

where:

T_B = brightness temperature

ϵ = surface emissivity

τ_∞ = atmospheric opacity

T_S = ocean surface temperature

T_C = residual 2.7K cosmic background

The quantity T_{AIR} is the equivalent brightness temperature of the atmospheric column which, in the absence of scattering, is given by

$$T_{AIR} = \int_{\tau(0)}^{\tau(h)} T(z) e^{-\tau(z)} d\tau(z)$$

Where z is a distance above the surface, h is the height at which observations are conducted, $T(z)$ is the true air temperature at height z , and $\tau(z)$ is the opacity at z .

If we conduct measurements at high altitudes so that $\tau(h) \approx \tau_\infty$, and replace $T(z)$ by some average temperature $\langle T \rangle$, then it easily follows that

$$T_{AIR} = \langle T \rangle [1 - e^{-\tau_\infty}] \quad (2)$$

We now rearrange (1) to express T_B in the following form:

$$T_B = T_C e^{-2\tau_\infty} + T_{AIR} [1 + e^{-\tau_\infty}] + \epsilon [T_S e^{-\tau_\infty} - T_C e^{-2\tau_\infty} - T_{AIR} e^{-\tau_\infty}] \quad (3)$$

Substituting (2) into (3) gives

$$T_B = T_C e^{-2\tau_\infty} + \langle T \rangle [1 - e^{-2\tau_\infty}] + \epsilon [(T_S - \langle T \rangle) + (\langle T \rangle - T_C) e^{-\tau_\infty}] e^{-\tau_\infty} \quad (4)$$

As a first iteration, we assume that $T_S \approx \langle T \rangle$, in which case, the surface emissivity becomes

ORIGINAL PAGE IS
OF POOR QUALITY

$$\epsilon \cong \frac{\left[\frac{\langle T \rangle - T_C}{\langle T \rangle} \right] - \left[\frac{\langle T \rangle - T_B}{\langle T \rangle} \right] e^{2\tau_\infty}}{\frac{\langle T \rangle - T_C}{\langle T \rangle}} \quad (5)$$

We now assume that the opacity due to rain varies with electromagnetic frequency to some power k , and that the emissivity is constant over the bandwidth of the measurements. Thus, if f_1 is the lower frequency, and f_2 is the upper frequency, (5) can be expressed as two simultaneous equations to eliminate ϵ and solve for τ_R , the opacity due to rain at frequency f_1 . The result is:

$$e^{-\tau_R} = \left[\frac{\langle T \rangle - T_B(f_2)}{\langle T \rangle - T_B(f_1)} \right] \frac{1}{2 \left[(f_2/f_1)^k - 1 \right]} \quad (6)$$

Where $T_B(f_2)$ is the measured brightness temperature at the upper frequency and $T_B(f_1)$ is that at the lower frequency. In the original paper, the exponential k was empirically determined through a best fit to the surface truth. This ad hoc procedure is not necessary if a third frequency is utilized. The surface emissivity is determined by solving for the opacity using (6), and substituting the result into (5). Wind speed and rain rate are then empirically derived from the retrieved values of ϵ and τ_R . With ϵ_0 as the emissivity of smooth water, the following linear relationship between increased brightness temperature ΔT_B and wind speed W was assumed:

$$\Delta T_B = (\epsilon - \epsilon_0) T_S = K_1 W \quad (7)$$

where K_1 was assumed to be $0.7 \text{ KM} \cdot \text{sec}^{-1}$. The rain rate R was assumed to be a linear function of τ_R , such that

$$R = K_2 \tau_R \quad (8)$$

A value of $K_2 = 320 \text{ mm} \cdot \text{hr}^{-1}$ was assumed for the retrievals, which was later found to be high by approximately a factor of 2.

Summary of Initial Results

The first of many passes through Hurricane Allen was north to south. The radiometric brightness temperatures for 4.5, 5.0, 5.6, and 6.6 GHz are shown in figure 1. Heavy rain rates in the northern eye wall (point A) result in a large

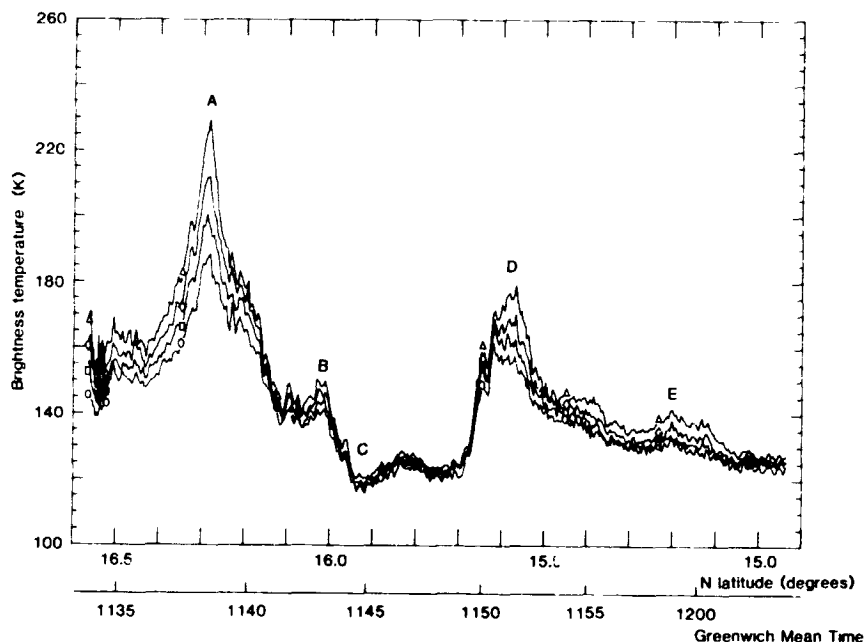


Fig. 1. Radiometer brightness temperature at four frequencies between 4.5 and 6.6 GHz. Higher brightness temperatures are associated with higher frequencies.

separation between the curves for 4.5 and 6.6 GHz. Point B locates the presence of an inner eye wall, and point C is the center of the eye where data from all frequencies merge, indicating no rain. Some rain is indicated in the southern eye wall, (point D). The variation of the envelope is indicative of the variation in ocean surface wind speed at points along the pass. Retrievals of wind speed and rain rate are shown in figures 2 and 3, respectively. The discrete points represent in situ measurements which were used to determine the exponent k that describes the wavelength dependency of the opacity.

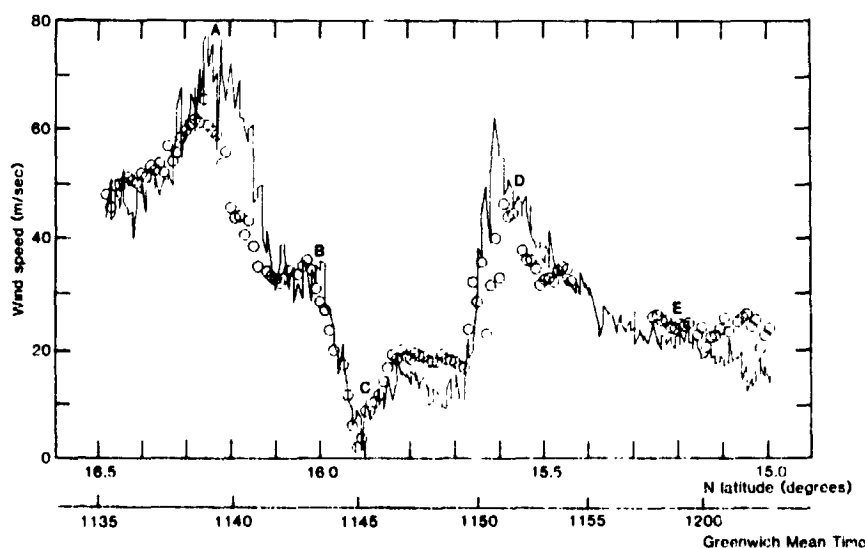


Fig. 2. Surface wind speed derived from magnitude of radiometer brightness temperature (continuous line) and from the P-3 flight-level inertial navigation system (cycles).

ORIGINAL PAGE IS
OF POOR QUALITY

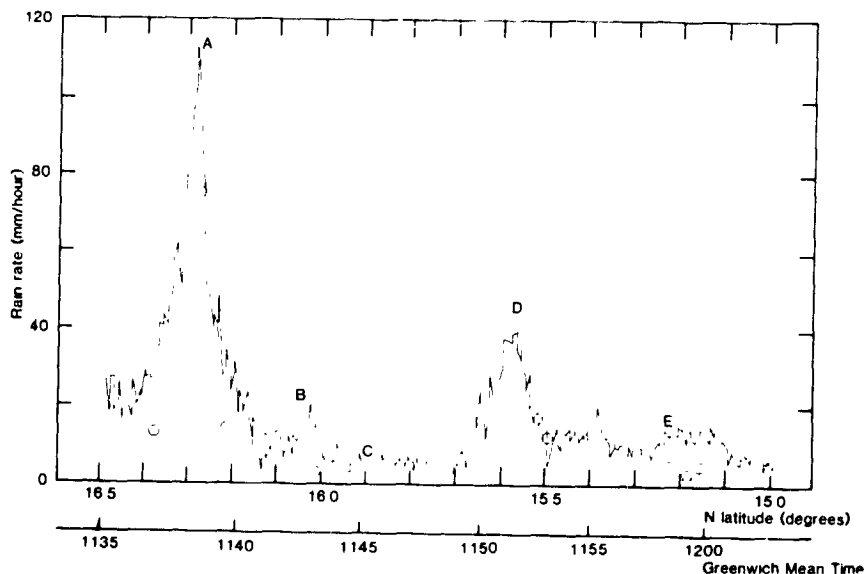


Fig. 3. Rain rate derived from magnitude of radiometer brightness temperature (continuous line) and from the radar composite obtained from the P-3 (circles).

The major conclusion to be drawn from these results is that the SFMR can measure wind speeds exceeding 70 m sec^{-1} , and rain rates exceeding $50 \text{ mm} \cdot \text{hr}^{-1}$. A potential technique of observing hurricanes from safe altitudes was therefore demonstrated.

Present Status of Data Analysis

Over a score of passes through Hurricane Allen have been analyzed by the NASA Langley Research Center using a two frequency algorithm. The activity at the University of Massachusetts has focussed on advancing the algorithm and resolving calibration issues that were discovered in the detailed analysis of the data. The algorithm has been modified to include more detail, such as atmospheric lapse rate, and a variable wavelength dependency of rain attenuation based on published data. Work is well underway to develop a three-frequency algorithm to retrieve not only rain rate, and ocean surface wind speed, but also the wavelength dependency factor, k . This is done by introducing a third frequency f_3 , and interacting equation (6) to retrieve k .

The calibration issue has been resolved, and self-consistent retrievals of rain rate and wind speed are achieved by using various combination of frequency pairs.

Concluding Remarks and Generic Issues

The major impact of this research is that a means is now available to probe hurricanes at safe altitudes above the storm, rather than routinely sending aircraft into the turbulent and dangerous boundary layer. In addition, the retrieval algorithm is so simple that real time processing is possible to relay first order

estimates of rain rate and ocean surface wind speed to a central weather facility. Thus, meteorologists can quickly assess the status of the storm and perhaps predict its path. More research flights are needed to better refine the algorithm. For example, research is needed to relate rain opacity to rain rate; and it is not clear at this time that there is a simple linear relationship between wind speed and increased brightness temperature. There is also a fundamental need to relate the remote sensing measurement to ocean surface wind stress. Finally, there is a need to determine whether or not the stepped frequency technique can be used to infer rainfall over land. There is a potential of doing this by observing relative differences in brightness temperature between frequencies, and ignoring the envelope, which is presumably the spatial variation in the emissivity of land.

At the present time, more aircraft flights are needed in connection with high quality surface truth.

References

Jones, W. L., P. G. Black, V. E. Delnore, and C. T. Swift, 1981: Airborne microwave remote sensing measurements of Hurricane Allen. *Science*, 214, 274-280.

ALTIMETER HEIGHT MEASUREMENT ERRORS INTRODUCED BY THE
PRESENCE OF VARIABLE CLOUD AND RAIN ATTENUATION

Francis M. Monaldo and Julius Goldhirsh
The Johns Hopkins University/Applied Physics Laboratory
Johns Hopkins Road, Laurel, Maryland 20707

Edward J. Walsh
NASA/Goddard Space Flight Center
Wallops Flight Facility
Wallops Island, Virginia 23337

ABSTRACT

It has recently been recognized that spatially inhomogeneous clouds and rain can substantially affect the height precision obtainable from a spaceborne radar altimeter system (Walsh, et al., 1983). Through computer simulation, it has been found that typical levels of cloud and rain intensities and associated spatial variabilities may degrade altimeter precision at 13.5 GHz and, in particular, cause severe degradation at 35 GHz. This degradation in precision is a result of radar signature distortion caused by variable attenuation over the beam limited altimeter footprint. Because attenuation effects increase with frequency, imprecision caused by them will significantly impact on the frequency selection of future altimeters.

In this paper we examine the degradation of altimeter precision introduced by idealized cloud and rain configurations as well as for a realistic rain configuration as measured with a ground based radar.

1. INTRODUCTION

As the requirements for precision in geodetic surveys grow more stringent and as physical oceanographers begin to exploit altimeter data to study ocean-wide circulation dynamics, the precision demands on height measurements by future radar altimeters become more severe. Hence, error sources that could previously be legitimately ignored must now be considered. The precision degradation caused by spatially variable cloud and rain attenuation patterns is one such error source.

When the narrow radar pulse transmitted from the altimeter reflects from the ocean surface it is significantly spread by the ocean surface roughness. This pulse broadening, while valuable in that it provides an estimate of ocean surface wave height, degrades the ability of the altimeter to measure the range between the satellite and the surface. To reconstruct the position of the leading edge of the pulse, the entire pulse waveform shape is processed in a tracking algorithm. Distortion of this waveform shape will necessarily degrade the precision with which the track point can be determined.

The beam-limited surface footprints of spaceborne radar altim-

eters of the Seasat class are on the order of 20 km. If the rain and cloud attenuation is uniform over an altimeter footprint, the total return signal power is reduced, the waveform shape remains unchanged and the altimeter tracking algorithm height estimate is unaffected. In this paper we focus on the situation where altimeter precision is degraded because attenuation levels within the footprint are laterally inhomogeneous, distorting the return waveform shape.

2. RAIN CELL AND CLOUD ATTENUATION LEVELS AND SCALE SIZES

Cloud liquid water content and rain intensity vary considerably both spatially and temporally. As such, these quantities should be dealt with statistically. This section is designed to give the reader a general appreciation of these quantities. Later we will consider the computer simulation of the passage of an altimeter over various plausible, idealized cloud and rain attenuation patterns as well as the passage of such an altimeter over actual, measured rain cells to determine the effect of these on altimeter measurement of range to the sea surface.

2.1 Clouds

Cloud liquid water content, upon which attenuation depends, is highly variable. Liquid water content may fluctuate between a small fraction to several gm/m^3 over a cloud width of 1 to 2 km (Ackerman, 1959). Ackerman (1967) has also measured liquid water contents ranging from 0.5 to 2.5 gm/m^3 over distances exceeding 9 km. To the authors' knowledge there are no statistics available relating cloud size directly to liquid water content levels. However, Lopez (1977) and Kuettner (1971) have determined typical scale dimensions for the cumulus clouds and cloud streets based on either optical or refractive measurements to be on the order of several kilometers.

Interpolating the results of Gunn and East (1954), the attenuation coefficient, normalized to cloud liquid water content, is approximately 0.17 (dB/km)/(gm/m^3) at 13.5 GHz and 1.1 (dB/km)/(gm/m^3) at 35 GHz. Cole (1961) has provided average liquid water contents for various common cloud types.

Table 1 summarizes and combines these results by estimating the average two-way attenuation through a 1 km thick cloud for four common cloud types at both 13.5 and 35 GHz. Note that the total attenuation may vary between 0.034 and .85 dB at 13.5 GHz and 0.22 and 5.5 dB at 35 GHz.

2.2 Rain

Assuming a Marshall-Palmer (1948) drop size distribution, the attenuation coefficient at 13.5 GHz is 0.06 dB/km at the small rain rate of 2 mm/hr, 0.4 dB/km at the moderate rain rate of 10 mm/hr, and 0.9 dB/km at the large rain rate of 20 mm/hr. At 35 GHz, the attenuation coefficients are 0.5, 2.4, and 5.0 dB/km for the rain rates, 2, 10, and 20 mm/hr, respectively (Goldhirsh and Rowland, 1982). Table 2 summarizes the results by providing the two-way attenuation at 13.5 and 35 GHz, at various rain rates for both a

Table 1 Cloud Attenuation Levels

Frequency (GHz)	Normalized Attenuation Coefficient (dB/km) / (gm/m ³)	Cloud Type	Liquid Water Content (gm/m ³)	Total, Two-Way Attenuation Thru a 1 km Thick (dB)
13.5	0.17	Stratiform	0.1-0.2	0.034-0.068
		Cumulus Humilis	1.0	0.34
		Cumulus Congestus	2.0	0.68
		Cumulonimbus	2.5	0.85
35	1.1	Stratiform	0.1-0.2	0.22-0.44
		Cumulus Humilis	1.0	2.2
		Cumulus Congestus	2.0	4.4
		Cumulonimbus	2.5	5.5

Table 2 Rain Attenuation Levels

Frequency (GHz)	Rain Rate (mm/hr)	Attenuation Coefficient (dB/km)	Total, Two-Way Attenuation (dB)	
			1 km Rain Cell Height	5 km Rain Cell Height
13.5	2	0.06	0.12	0.6
	10	0.4	0.8	4.0
	20	0.9	1.8	9.0
35	2	0.5	1.0	5.0
	10	2.4	4.8	24.0
	20	5	10.	50.0

Table 3 Track Point Error for Single Cloud Case (Cloud thickness = 1 km; Liquid water content = 1 gm/m³)

Frequency (GHz)	SWH (m)	Track Point Shift (cm)		
		Maximum Instantaneous	1 Second Average	3 Second Average
13.5	2	3.9	2.2	0.6
13.5	4	8.0	4.0	1.2
35	2	17.6	6.3	2.9
35	4	41.5	20.4	7.2

1 km and 5 km rain cell height. Note that at 13.5 GHz and a 5 km rain cell height, the total attenuation varies between 0.6 and 9 dB and at 35 GHz, it varies between 5 and 50 dB over the rain rate range 2-20 mm/hr.

3. ALTIMETER PRECISION DEGRADATION

The effect of clouds and rain on altimeter performance is dependent upon two parameters: the spatial scales of attenuation variability relative to the altimeter beam-limited footprint and the magnitude of the attenuation.

In this section we will model the effect on the altimeter estimate of the range to mean sea level as it passes over (1) plausible, idealized cloud and rain attenuation patterns and (2) actually measured rain cell attenuation patterns.

3.1 Simulation of Altimeter Return Waveform Distortion

Figure 1 provides a schematic representation of the geometry of the simulations employed to estimate waveform shape distortions caused by various attenuation patterns. Each annular region in the altimeter footprint corresponds to a constant ocean surface area responsible for backscatter into a single range bin. An idealized, cylindrical attenuation cell is shown to intersect the footprint. This cell may represent either a cloud or a rain cell. It is clear that different fractions of each annular region intersect with the given cell. Hence, a different attenuation level may be associated with each range bin. Construction of the return pulse shape was performed for one annular region at a time. Each annular region was subdivided into 16 angular sections. For each one of these sections the power return to the radar was calculated assuming no fading noise present. The calculation included any attenuation. The angular sections were integrated to obtain the power from an entire annular region. This power was in turn weighted by the antenna pattern to estimate the power return in the appropriate range bin. In this way, the entire waveform shape was constructed, range-bin-by-range-bin.

The estimate of the position of the leading edge of the return pulse is dependent upon the particular tracking algorithm used. The tracking algorithm used on Seasat was chosen because its track point bias at high sea states is much lower than that of a threshold level tracking algorithm (MacArthur, 1978). The Seasat algorithm used the entire waveform shape to fashion its track point estimate. The simulations undertaken employed the Seasat tracking algorithm to determine track point position.

In these simulations we examined altimeter operating at 13.5 and 35 GHz, with a 1 m dish at an altitude of 800 km with a ground track velocity of 7 km/s.

3.2 Idealized Cloud and Rain Cell Attenuation Patterns

Three idealized rain/cloud models were chosen to demonstrate the effect of rain and cloud attenuation on the altimeter measurement of the range to mean sea level. Although these models are idealized,

ORIGINAL PAGE IS
OF POOR QUALITY

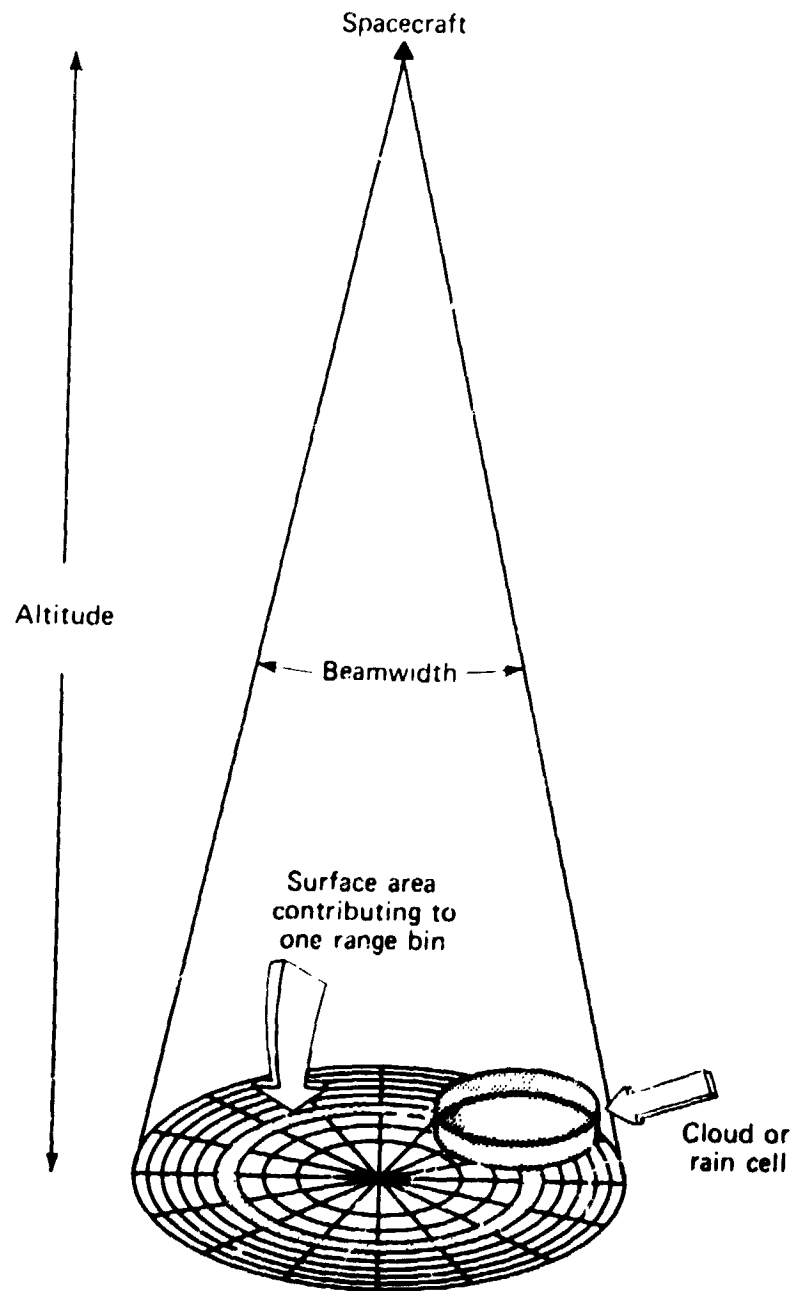


Figure 1 Altimeter-Attenuation Cell Configuration

they were chosen to represent plausible rain and cloud attenuation levels and scale sizes consistent with those discussed in Section 2.

The following rain/cloud models were considered in this analysis: (1) A cylindrical cloud of 5 km diameter and 1 km thickness with a liquid water content, M , of 1 gm/m^3 . (2) A cylindrical rain cell of 5 km diameter and 5 km thickness with a rain rate of 10 mm/hr. (3) A sinusoidally attenuating cloud medium with spatial wavelengths of 5, 2.5, and 1.0 km. The maximum two-way attenuation being 0.34 dB at 13.5 GHz and 2.2 dB at 35 GHz ($M=1 \text{ gm/m}^3$). This type of cloud variation is representative of the periodic attenuation associated with "cloud streets". For models 1 and 2 the altimeter is assumed to pass directly over the cloud or rain cell center. In model 3, the altimeter ground track is assumed perpendicular to the cloud street crests.

For the single cloud condition described above, the instantaneous track point shift can be quite significant, but when averaged over a 1 or 3 s interval, the mean track point shift reduces substantially (Table 3). For the 35 GHz case, the mean track point error is still large compared to the TOPEX requirement of a few centimeter precision (TOPEX Science Working Group Report, 1981).

Table 4 presents the track point shift associated with cloud streets. Note that as the wavelength of the cloud streets decreases, the track point shift gets smaller. This is because the attenuation variations begin to occur at small enough scales that they are partially averaged over within each pulse. The table also indicates that the maximum track point shift is much higher for 35 GHz than for 13.5 GHz.

It is also important to note that track point errors generally increase with significant wave height (SWH). At larger ocean wave heights, the return pulse is spread out smearing the leading edge of the pulse. This is further compounded by the introduction of a spatially variable attenuation described here.

Consider now track point shifts for the case of the single cylindrical rain cell of 5 km height and 10 mm/hr rain rate. It is clear from Table 5 that the larger attenuation values associated with rain introduce substantially greater track point shifts. Even after 1 and 3 s averages, the track point shifts at 13.5 GHz are well outside the precision requirements of Seasat, GEOSAT and TOPEX. At 35 GHz the situation is worse.

3.3 Effects Due to Measured Rain Cell Attenuation

To augment the results obtained for idealized rain patterns we considered a sample of rain attenuation profiles obtained by a ground based radar situated at Wallops Island, Virginia. The attenuation profile was constructed from a corresponding radar reflectivity profile employing a low elevation radar scan (Goldhirsh, 1979). The radar reflectivity corresponding to each adjacent pulse volume of resolution 150 m was converted to an equivalent attenuation coefficient employing an empirical relation derived from measured rain drop size distribution data (Goldhirsh, 1979). The integrated

Table 4 Maximum Instantaneous Track Point Shifts for the Cloud Street Case (Maximum Liquid Water Content = 1 gm/m^3)

Frequency (GHz)	SWH (m)	Track Point Shift at Various Cloud Street Wavelengths (cm)		
		1.0 km	2.5 km	5.0 km
13.5	2	0.7	0.9	2.6
35	2	6.4	8.3	13.3

Table 5 Track Point Error for Rain Cell Case (Rain Height = 5 km; Rain Rate = 10 mm/hr)

Frequency (GHz)	SWH (m)	Track Point Shift (cm)		
		Maximum Instantaneous	1 Second Average	3 Second Average
13.5	2	97.1	45.7	14.9
13.5	4	93.2	50.5	15.6
35	2	119.7	64.6	21.7
35	4	150.6	86.6	30.6

Table 6 Track Point Shifts for a Measured Rain Attenuation Case. Assumes 2 m SWH.

Frequency (GHz)	Maximum Attenuation (dB)	Track Point Shifts (cm)		
		Maximum Instant.	RMS of 1 Second Averages	RMS of 3 Second Averages
13.5	9.7	25.3	3.5	1.1
35	47.4	124.7	14.7	10.2

(+)

attenuation with height was constructed assuming the rain to be uniform with altitude over a 4 km cell height. Figure 2a shows the resulting attenuation profile associated with an estimated maximum rain rate of about 25 mm/hr. The actual attenuation at 13.5 GHz varies from 0 to 9 dB. In Figure 2b track point errors induced by this attenuation are plotted for a SWH of 2 m. A similar simulation was derived at 35 GHz (not shown).

Results of these simulations are given in Table 6. Instantaneous track point errors are many centimeters at both frequencies. By averaging over 1 to 3 seconds the track point errors at 13.5 GHz are reduced to 3.5 and 1.1 cm, respectively. At 35 GHz the instantaneous error can be many tens of centimeters and the averaged errors still exceed 10 cm. Much larger track point errors at 35 GHz as opposed 13.5 GHz are caused by both the larger attenuations at 35 GHz and the smaller footprint of the beam.

Two additional points are worthwhile noting. First, the track point shift in Figure 2b shows no mean trend as the mean absorption of Figure 2a increases. This emphasizes our earlier statement that only inhomogeneities of absorption cause track point shifts. Second, the results of Table 6 for 35 GHz are somewhat academic because no actual radar would have sufficient signal-to-noise margin to be able to tolerate a 47 dB attenuation and maintain track.

4. CONCLUSIONS

We have demonstrated for both idealized rain and cloud configurations as well as measured rain rate variabilities, significant altimeter degradation may occur at 13.5 and 35 GHz. Although averaging track points over several seconds may mitigate these errors, they may still be unacceptably high.

At 13.5 GHz, the effect of clouds on the average track point shift is generally small (approximately 1 cm for cylindrical model and less than 3 cm for the cloud street model). On the other hand, rain rates as high as 10 mm/hr may produce unacceptably high range uncertainties (e.g., isolated rain cell case).

At 35 GHz, both the effects of clouds and rain may, in general, seriously degrade the track point errors. Errors as high as 7 cm for isolated clouds and 13 cm for cloud streets may occur. For rain rates of 10 mm/hr, absorptions as high as 47 dB and track point errors as high as 31 cm may be produced. The employment of future conventional type altimeter systems operating at 35 GHz and higher is not recommended.

Since track point errors at 13.5 GHz may seriously be degraded by rain, it is recommended that future altimeters operating at this frequency employ rain detecting capabilities to flag rain corrupted data.

ORIGINAL PAGE IS
OF POOR QUALITY

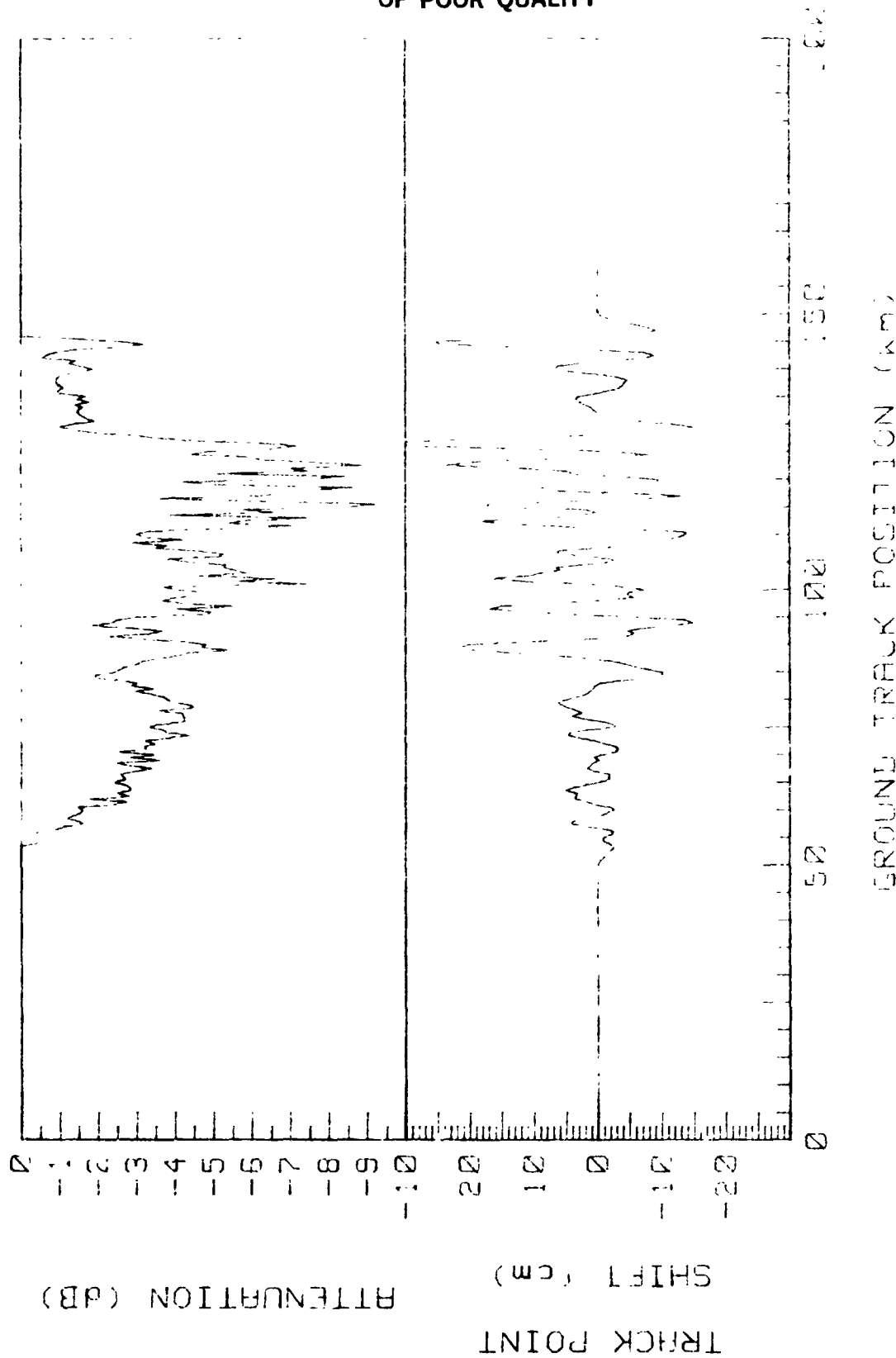


Figure 2 Track Point Shift and Measured Attenuation at
13.5 GHz as a Function of Ground Track Position

5. REFERENCES

- Ackerman, B., 1959, "The Variability of the Water Contents of Tropical Cumuli", J. of Appl. Meteorology, Vol. 16, April, pp. 191-198.
- Ackerman, B., 1967, "The Nature of Meteorological Fluctuations in Clouds", J. of Appl. Meteorology, Vol. 6, February, pp. 61-71.
- Cole, A.E., 1961, "Handbook of Geophysics", (Chapter 7, Clouds), The Macmillan Company, New York, p. 88.
- Goldhirsh, J., 1979, "A Review on the Application of Non-attenuating Frequency Radars for Estimating Rain Attenuation and Space Diversity Performance", IEEE Transactions on Geoscience Electronics, Vol. GE-17, No. 4, October, pp. 218-239.
- Goldhirsh, J. and J.R. Rowland, 1982, "A Tutorial Assessment of Atmospheric Height Uncertainties for High Precision Satellite Altimeter Missions to Monitor Ocean Currents", IEEE Trans. on Geosci. and Remote Sensing, Vol. GE-20, No. 4, October, pp. 418-434.
- Gunn, K.L.S. and T.W.R. East, 1954, "The Microwave Properties of Precipitation Particles", Q. J. of the Royal Meteor. Soc., Vol. 80, pp. 522-545.
- Kuettner, J.P., 1971, "Cloud Bands in the Earth's Atmosphere - Observation and Theory", Tellus, Vol. 23, pp. 404-425.
- Lopez, R.F., 1977, "The Lognormal Distribution and Cumulus Cloud Populations", Monthly Weather Review, Vol. 105, July, pp. 865-872.
- MacArthur, J.L., 1978, "Seasat-A Radar Altimeter Design Description", JHU/APL Technical Report SDO-5232, November.
- Marshall, J.S. and W. McK. Palmer, 1948, "The Distribution of Rain Drops with Size", J. Meteorology, Vol. 5, pp. 165-166.
- TOPEX Science Working Group Report, 1981, "Satellite Altimetric Measurement of the Ocean", Jet Propulsion Laboratory, Pasadena, CA., Tech. Rep. Document No. 400-111, March.
- Walsh, E., F.M. Monaldo and J. Goldhirsh, "Rain and Cloud Effects on a Satellite Dual Frequency Radar Altimeter Operating at 13.5 and 35 GHz", IEEE Trans. on Geosci. and Remote Sensing, in press.

IMPROVED RESOLUTION RAIN MEASUREMENTS
FROM SPACEBORNE RADAR ALTIMETERS

Julius Goldhirsh and Frank Monaldo
The Johns Hopkins University
Applied Physics Laboratory
Johns Hopkins Road
Laurel, Maryland 20707

ABSTRACT

It is demonstrated that improved resolution measurements of precipitation may be obtained from satellite borne radars with antenna beams having relatively large surface footprints. The method employs deconvolution and Fourier transform procedures, and assumes a knowledge of the antenna beam pattern. As an example, the technique is specifically directed towards the application of future spaceborne radar altimeters which may contain additional range gates to enable the measurement of rain at altitude. It is demonstrated that because of the natural variability of rain in the lateral extent, the standard beam averaging over the footprint could easily produce erroneous interpretations of the intensity of rain and its extent. On the other hand, many of these ambiguities may be removed employing the deconvolution techniques described.

Rain measurement of the type described here are considered vital from the standpoint of representing a flag for altimeter data that may be corrupted by rain. It also provides sorely needed rain data over the oceans where little or no such data is available.

1. INTRODUCTION

It has been pointed out that rain may distort and/or attenuate the sea surface echo returns of signals originating from spaceborne radar altimeters, resulting in gross errors of the mean sea height (Walsh, et al., 1983). The employment of a "piggyback" modification to future spaceborne altimeter systems has been suggested for measuring or monitoring the presence of rain at altitude (Goldhirsh and Walsh, 1982). The experimenter may employ this rain information as a flag for culling out the concomitant ocean surface measurements, as well as to provide additional meteorological information regarding the characteristics of precipitation.

A difficulty that is encountered in the measurement of precipitation with satellite borne, range gated radars deals with the poor resolution encountered because of the large beamwidth associated with the radar antenna located at relatively large distances from the earth. For example, the 3 dB down points for the one way antenna gain function corresponding to the Seasat altimeter antenna (1.6 degree beamwidth) located at an altitude of 800 km, gave rise to a 22.3 km diameter footprint at the earth's surface. Rain is, in general, highly variable along the horizontal extent, especially for convective types of precipitation (e.g., thunderstorms). Even

for stratiform rains (e.g., widespread precipitation), it is common for imbedded or convective cells of more intense rain rates to exist (Goldhirsh, 1983). As the return echo signal from a precipitating medium represents the convolution of the square of the gain and the true rain reflectivity profile (as will be demonstrated in Section 2), the rain reflectivity deduced from the beam averaged echo signal may be significantly smaller than the true reflectivity level. Furthermore, as the antenna sweeps by the rain structure on the ground, the inevitable beam averaging may smooth out the highly variable rain structure such as to give a distorted picture of the ground rain intensity profile.

2. FORMULATION OF THE PROBLEM

Consider the configuration depicting a satellite at an altitude, R_0 , above the mean sea surface. The satellite is assumed to have a pulsed radar having a downward pointing antenna with a beamwidth, θ_0 . We shall examine here the backscatter from the precipitation contained within a pulse volume centered at a range R .

The echo power is primarily due to backscatter from an array of raindrops within a pulse volume defined by the beamwidth and the range resolution of the pulse.

This echo power may be shown to be given by (Goldhirsh and Monaldo, 1983),

$$P_r = C_o \cdot Z_c \quad (1)$$

where

$$Z_c(x_o) = \left(\frac{8 \ln 2}{\pi x_1 y_1} \right) \iint Z_{eq}(x, y) \exp \left\{ - (8 \ln 2) \left[\left(\frac{x - x_o(t)}{x_1} \right)^2 + \left(\frac{y}{y_1} \right)^2 \right] \right\} dx dy \quad (2)$$

$$\text{where,} \quad C_o = \left[\left(\frac{c \pi^3 |K_o|^2}{1024 \ln 2} \right) T G_o^2 \theta_1 \phi_1 F(B) L_T L_R \frac{P_T}{R^2 \lambda^2} \right] \quad (3)$$

where $|K_o|^2 = |(m^2 - 1)/(m^2 + 2)|$ and where the quantity $Z_c(x_o)$ is referred to as the effective beam averaged radar reflectivity factor where C_o is an effective constant. Also, m is the complex reflective index of water drops, c is the velocity of light (m/sec), T is the pulse width (sec), P_T is the transmitted power (watts), λ is the wavelength (meters), L_T, L_R is the transmitter and receiver losses, respectively (≤ 1), R is the range from the radar to the center of the pulse volume, x_1, y_1 are the footprint lengths along the principal planes of the gain function, x_o is the displacement of the beam nadir along the x direction in units of meters from a fixed origin at the ground and x, y is the planar dimensions relative to a fixed origin.

In the derivation of (2) we have integrated over the range resolution in the range direction given by $\delta = (cT/2) \cdot F(B)$, where $F(B)$ is an effective loss factor due to an assumed Gaussian filter response at the receiver (Doviak and Zrnica, 1979). For a matched filter linear receiver, $F(B) = -2.3$ dB. As a representative beam structure, we have assumed in the derivation of (2) the Probert-Jones

(1962) form of the one way gain function; namely a Gaussian structure.

$Z_{eq}(x,y)$ is the effective radar reflectivity factor for rain defined by,

$$Z_{eq} = \left(\frac{\lambda^4}{\pi^5 |K_o|^2} \right) \int_D \sigma(D) N(D) dD \quad (m^3) \quad (4)$$

where, $\sigma(D)$ is the backscatter cross section for a drop of diameter, D and $N(D)dD$ is the number of drops between the sizes of D and $D+dD$ per unit volume.

It is also tacitly assumed that the attenuating effects due to precipitation may be ignored. This assumption becomes tenable if the pulse volume near the top of the rain region is sampled. This may create the condition such that there is a negligible path length over which the signal propagates within the sampled volume.

3. BEAM AVERAGED RADAR REFLECTIVITY FACTOR EXPRESSED AS A CONVOLUTION INTEGRAL

Assume the equivalent reflectivity factor within the integrand of (2) may be expressed by the product relationship

$$Z_{eq} = Z_1(x) Z_2(y) \quad (5)$$

Substituting (5) into (2)

$$Z_c = \left(\frac{8 \ln 2}{x_1 y_1} \right) I_y I(x_o) \quad (6)$$

where

$$I_y = \int_{-\infty}^{\infty} Z_2(y) g(y) dy \quad (7)$$

$$I(x_o) = \int_{-\infty}^{\infty} Z_1(x) g(x-x_o) dx \quad (8)$$

where

$$g(y) = \exp \left[- (8 \ln 2) \left(\frac{y}{y_1} \right)^2 \right] \quad (9)$$

$$g(x) = \exp \left[- (8 \ln 2) \left(\frac{x}{x_1} \right)^2 \right] \quad (10)$$

It is interesting to note that $I(x_o)$ as given by (8) may alternately be expressed as the convolution of the gain square function, $g(x)$, and the reflectivity factor, $Z_1(x)$, where both are taken in the x direction. Hence,

$$I(x_o) = Z_1(x) * g(x) \quad (11)$$

where the * denotes the convolution.

4. EXTRACTING THE RADAR REFLECTIVITY FACTOR PROFILE FROM THE CONVOLUTION INTEGRAL

By taking the Fourier transform of both sides of (11), and employing a fundamental property of the convolution integral, we obtain

$$I(\omega) = Z_1(\omega) G(\omega) \quad (12)$$

where

$$I(\omega) = \int_{-\infty}^{\infty} I(x_0) \exp(-j\omega x_0) dx_0 \quad (13)$$

$$Z_1(\omega) = \int_{-\infty}^{\infty} Z_1(x) \exp(-j\omega x) dx \quad (14)$$

$$G(\omega) = \int_{-\infty}^{\infty} g(x) \exp(-j\omega x) dx \quad (15)$$

where $I(\omega)$, $Z_1(\omega)$, and $G(\omega)$ are respectively the Fourier transforms of $I(x_0)$, $Z_1(x)$ and $g(x)$ are given by (13) through (15). It is apparent that by solving for $Z_1(\omega)$ in (12) and applying the inverse transform to both sides (i.e., $FT^{-1}\{\}$), the profile $Z_1(x_0)$ may be established. That is,

$$Z_1(x_0) = FT^{-1} \left\{ \frac{I(\omega)}{G(\omega)} \right\} = \frac{1}{2\pi} \int_{-\infty}^{\infty} \frac{I(\omega)}{G(\omega)} \exp[+j\omega x_0] d\omega \quad (16)$$

Equation (16) represents the general formula for extracting the reflectivity profile in the x direction, given a knowledge of the measured echo power, $P_r(x_0)$, obtained as the beam sweeps the rain profile as a function of x_0 .

Substituting (10) into (15), the Fourier transform of the gain function is given by,

$$G(\omega) = \frac{1}{2} \left[\frac{\pi x_1^2}{2 \ln 2} \right]^{1/2} \cdot \exp \left[- \frac{\omega^2 x_1^2}{32 \ln 2} \right] \quad (17)$$

Substituting (17) into (16), we obtain,

$$Z_1(x_0) = \left(\frac{2 \ln 2}{\pi^3 x_1^2} \right)^{1/2} \int_{-\infty}^{\infty} I(\omega) \exp \left[+ \frac{\omega^2 x_1^2}{32 \ln 2} + j\omega x_0 \right] d\omega \quad (18)$$

Equation (18) represents the resulting expression for the reflectivity profile, where $I(\omega)$ is the Fourier transform of $I(x_0)$ obtained through the beam averaged power measurement.

5. EXPECTED POWER LEVELS FOR A REPRESENTATIVE SATELLITE BORNE RADAR

General Case

In this Section we estimate the minimum detectable beam averaged reflectivity factor and the corresponding rain rate. As an example, we shall assume similar radar parameters as those for the Seasat radar altimeter (MacArthur, 1978). These are given as follows: $\lambda = 2.22 \times 10^{-2}$ m; $P_t = 2 \times 10^3$ watts; $T = 3.2 \times 10^{-6}$ sec; $R = 8 \times 10^5$ m; $\theta_1 = \phi_1 = 1.6^\circ$ (2.792×10^{-2} radians); $G = 40.6$ dB (1.148×10^4); $L_T = -0.9$ dB (0.813); $L_R = -1.2$ dB (0.758); $|K_O|^2 = 0.9$; $F(B) = -2.3$ dB (0.59). Substituting these parameter values into (3), the power reduces to

$$P_r \text{ (dBm)} = -140.5 + \text{dBZ} \quad (19)$$

where the reflectivity factor, Z_c is in mm^6/m^3 , P_r is in dBm, and $C_0 = 8.9 \times 10^{-15}$. Also dBZ is defined by,

$$\text{dBZ} = 10 \log_{10} Z_c \quad (20)$$

Assuming a unity signal to noise ratio of -115 dBm (5 dB smaller than the Seasat case), and solving for dBZ, we obtain $(\text{dBZ})_{\min} = -115 + 140.5 = 25.5$. Hence, the radar is capable of detecting beam averaged reflectivity factors of 25.5 dB and larger with a signal to noise ratio of 1 or larger.

To further amplify the above example, we assume the following empirical relation relating the rain rate R_r , expressed in mm/hr, to the reflectivity factor, expressed in mm^6/m^3 ,

$$R_r = (Z_c/200)^{0.625} \quad (21)$$

This relationship is consistent with the assumption of a Marshall-Palmer drop size distribution (1948). Relating (21) and (20)

$$R_r = (3.65 \times 10^{-2}) 10^{(.0625 \cdot \text{dBZ})} \quad (22)$$

Substituting a dBZ of 25.5 into (22) results in $(R_r)_{\min} = 1.4$ mm/hr.

In summary, assuming radar parameters which are the same as the Seasat altimeter, a unity signal to noise ratio of -115 dBm results in a 25.5 beam averaged reflectivity factor which is equivalent to an estimated 1.4 mm/hr rain rate.

6. DECONVOLUTION ON AN ARBITRARY REFLECTIVITY PROFILE

In this Section we demonstrate the power of the deconvolution technique in recovering high resolution reflectivity profiles. We implement this technique employing deconvolution methods as described in Section 3 and radar data of a rain reflectivity profile acquired employing a ground based radar at Wallops Island, Virginia.

In Figure 1a (solid curve) we show, as an example, a typical measured reflectivity profile over a distance interval of 90 km. This profile was obtained with a radar operating at S band (2.8

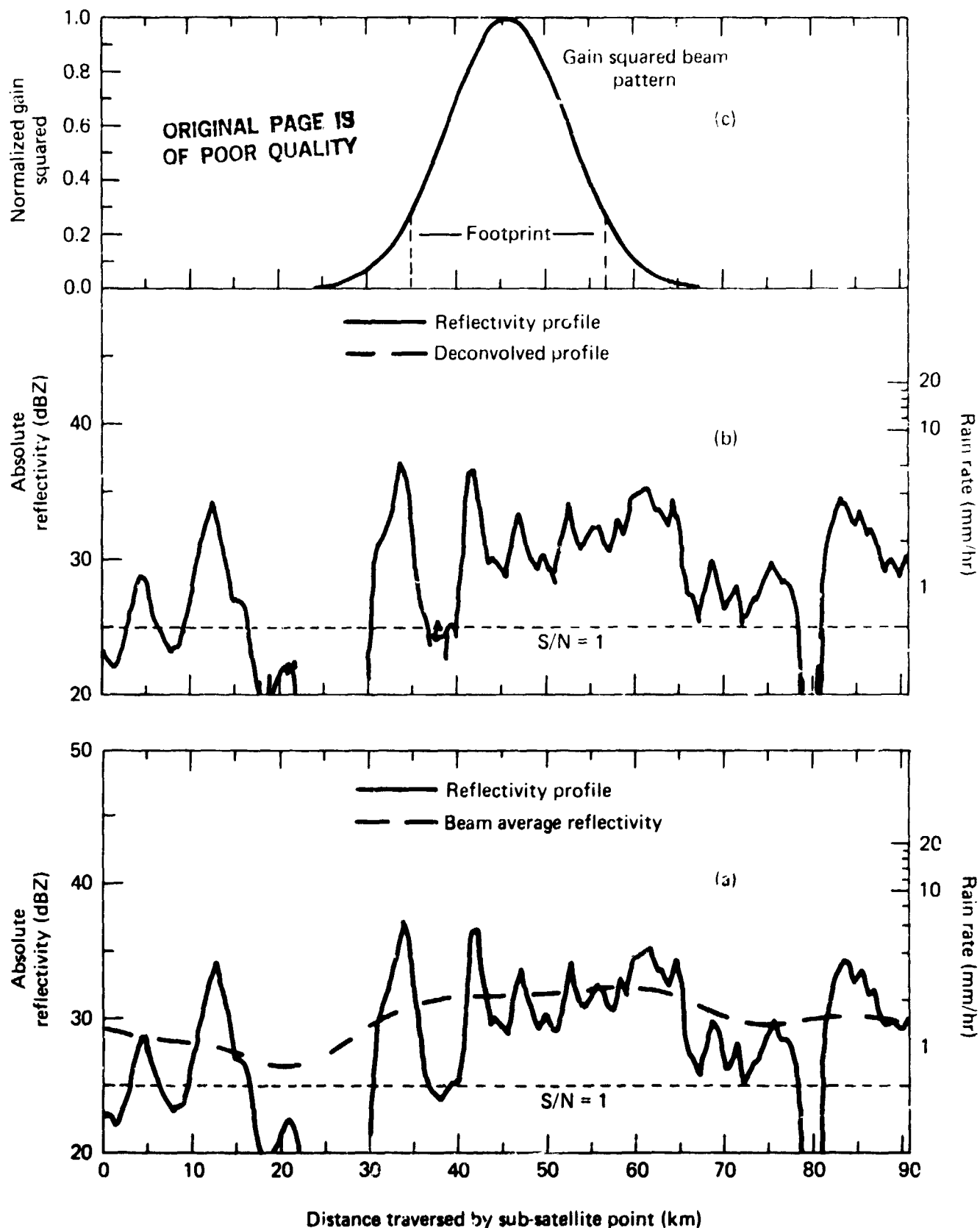


Figure 1 (a) Measured reflectivity factor profile (solid curve) and beam averaged levels (dashed curve). (b) Measured reflectivity factor profiles (solid line) and deconvolved profile (solid and dashed). (c) Gain squared beam pattern.

CHZ), a low elevation angle pointing (0.5° relative to the local horizon), and a 150 m range resolution (pulsewidth = 0.5 μ sec) (Goldhirsh, 1979). The profile corresponds to the rain day January 2, 1979 and was obtained at 9:34 a.m. local time.

Shown in Figure 1-(a) is a dashed curve which represents the beam averaged reflectivity factor with values sampled every 0.7 km. This is the reflectivity that would be measured assuming the footprint of the satellite borne radar (whose parameters are given in Section 4) sweeps by the reflectivity profile. This curve was calculated by injecting the true reflectivity profile into the integral (2), where a uniform reflectivity is assumed in the cross track direction. The profile was assumed periodic in the calculation of the beam averaged values in the vicinity of the 0 and 90 km distance intervals. We note that beam averaging considerably smooths the variations of the true profile. In fact, the smoothing appears so extreme that it is difficult to visually correlate the beam averaged reflectivity with the actual profile. Also shown by the short dashed horizontal line, is the level of absolute reflectivity which would result in a unity signal to noise ratio. This corresponds to a beam averaged reflectivity factor level of approximately 25 dBZ. We note the simulated measured beam average values exceed this lower threshold level.

The right hand scale denotes the corresponding rain rate levels in mm/hr employing the empirical relationship given by,

$$R_r = 4.0 \times 10^{-3} 10^{(.086 \text{ dBZ})} \quad (23)$$

This result was calculated from drop size distribution measurements made at Wallops Island for the same rain event. We note that over the reflectivity interval, the rain rate levels are between .4 and 7 mm/hr.

In Figure 1-(c) (upper figure) is depicted the gain squared variation taken over the same abscissa scale as the actual reflectivity. It is interesting to note that considerable variation in the reflectivity profile exists over the 22.3 km footprint corresponding to the 6 dB down gain squared points.

To implement the computer simulation, the Fourier and inverse transforms were replaced by their series approximations. Specifically, the Fourier series of the gain-squared antenna pattern and the beam averaged reflectivity were computed; otherwise, the technique employed is the same as described in Section 4.

In Figure 1-(b) the dashed line represents the high resolution reflectivity data that was recovered from the beam averaged reflectivity employing the deconvolution technique. Where no dashed line is observed, the recovered level coincides with the actual reflectivity values (solid line). We note that differences are evident mostly at the very low reflectivities, equivalent to negligible rain rates, and are due to computational imprecision. This computer simulation confirms the thesis that the high resolution data can, in principle, be recovered from the beam averaged data. The above simulation was performed without injecting any contributions due to noise. The effects of noise on the resultant reflectivity profile are

examined in Section 7.

It is interesting to note that the technique is able to recover reflectivity factors at levels below the threshold noise level for the beam averaged case (i.e., below 25 dBZ). This may be attributed to the fact that the beam averaged measurement is a single measurement made by the receiver at a fixed point in space. On the other hand, the deconvolved measurement is one which employs a series of beam averaged measurements over ranges (in the example), exceeding 100 km. The effective bandwidth of the system is considerably reduced since the effective integration time is substantially increased.

7. EFFECT OF NOISE ON THE DECONVOLUTED SIGNAL

In Figure 2 we demonstrate the effect of intrinsic noise on the deconvolved signal. In Figure 2-(a) is depicted the true reflectivity profile given by the solid line and the beam averaged echo (dashed line). Superimposed on the beam averaged echo is the Rayleigh fading noise introduced by the rain itself. As an example, we assume the capability of measuring 400 independent samples. The estimate of the average power for such a case follows a Gaussian probability density distribution (Goldhirsh, 1979). A sample size of 400 hence produces a standard error of $.05\%$ (reciprocal of the square root of the sample size) or approximately 0.2 dB rms statistical uncertainty.

In Figure 2-(b) are shown deconvolved signals for two cases. The solid curve represents the deconvolved result derived from a beam averaged estimate corresponding to 400 independent samples as described in the above paragraph. As a basis of comparison, we show also the deconvolved result derived from the beam averaged estimate employing an extreme sample size of 10^4 independent samples.

8. CONCLUSIONS

We note that introducing noise to the technique seriously degrades the deconvolved result. However, in spite of this degradation, considerably more information is obtained regarding the magnitude and scale dimensions of the rain employing the convolution method than is obtained by the beam averaged case.

Although this method has been tailored for the measurement of rain employing a radar, its application to other types of satellite remote sensors should be explored.

9. ACKNOWLEDGEMENTS

This work was supported by NASA Goddard, NASA Wallops Flight Center, Wallops Island, Virginia 23337. Many thanks to Karen E. Melvin for typing this manuscript.

ORIGINAL PAGE 13
OF POOR QUALITY

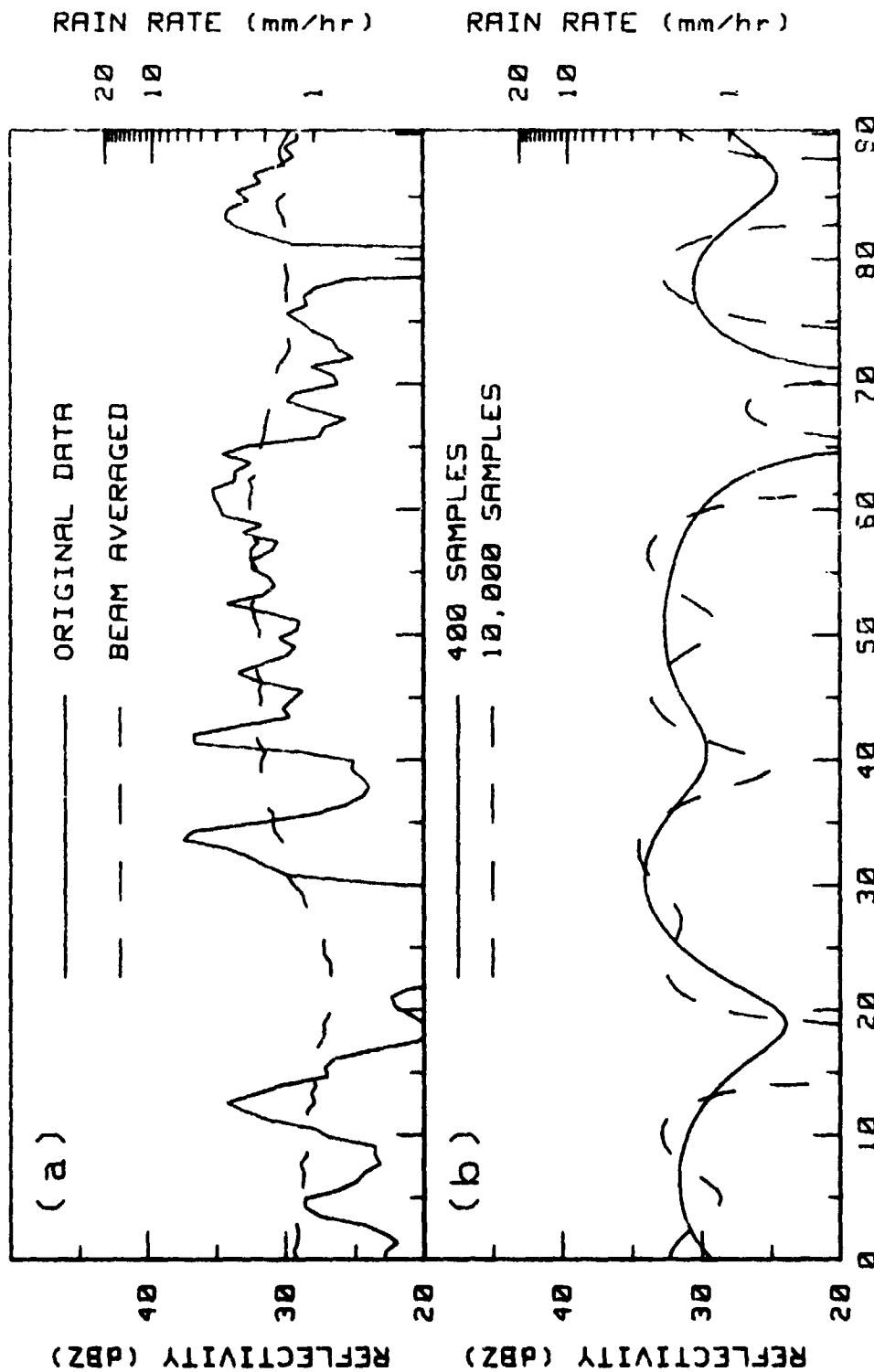


Figure 2 (a) True reflectivity factor profile (solid curve) and the corresponding beam averaged reflectivity factor with superimposed Gaussian statistical noise distribution corresponding to a sample size of 400 (dashed curve). (b) Deconvolved reflectivity factor profiles for sample sizes of 400 (solid curve) and 10,000 (dashed curve).

10. REFERENCES

- Doviak, R.J. and D. Zrnic, 1979, "Receiver Bandwidth Effects on Reflectivity and Doppler Velocity Estimates", J. of Applied Meteorology, Vol. 18, No. 1, January, pp. 70-76.
- Goldhirsh, J., 1979, "A Review on the Application of Non-attenuating Frequency Radars for Estimating Rain Attenuation and Space Diversity Performance", IEEE Transactions on Geoscience Electronics, Vol. GE-17, No. 4, October, pp. 218-239.
- Goldhirsh, J. and W.J. Walsh, 1982, "Rain Measurements from Space Using a Modified Seasat-Type Radar Altimeter", IEEE Transactions on Antennas and Propagation, Vol. AP-30, No. 4, July, pp. 726-733.
- Goldhirsh, J., 1983, "Rain Cell Size Statistics as a Function of Rain Rate for Attenuation Modeling", IEEE Transactions on Antennas and Propagation, September, Vol. AP-31, No. 5, pp. 799-801.
- Goldhirsh, J. and F. Monaldo, 1983, "Improved Resolution Rain Measurements from Spaceborne Radar Altimeters Employing Deconvolution Methods", Technical Report SLR83U-038, Applied Physics Laboratory, Johns Hopkins Road, Laurel, Maryland 20707.
- MacArthur, J.L., 1978, "Seasat-A Radar Altimeter Design Description", JHU/APL Report #SDO-5232, November.
- Marshall, J.S. and W. McK. Palmer, 1948, "The Distribution of Raindrops with Size", J. Meteor., Vol. 5, pp. 165-166.
- Probert-Jones, J.R., 1962, "The Radar Equation in Meteorology", Quarterly Journal of Royal Meteorological Society, Vol. 88, pp. 485-495.
- Walsh, E.J., F.M. Monaldo and J. Goldhirsh, 1983, "The Influence of Rain and Clouds on a Satellite Dual Frequency Altimeter System Operating at 13 and 35 GHz", Proceedings of the 1983 International Geoscience and Remote Sensing Symposium (IGARSS'83), August 31-September 2, 1983, San Francisco, California, pp. TA 5.1 - 5.10.

OBSERVING ATMOSPHERIC WATER IN STORMS
WITH THE NIMBUS 7 SCANNING MULTICHANNEL
MICROWAVE RADIOMETER

Kristina B. Katsaros

Robert M. Lewis

Department of Atmospheric Sciences
University of Washington
Seattle, Washington 98195
U.S.A.

ABSTRACT

Employing data on integrated atmospheric water vapor, total cloud liquid water and rain rate obtainable from the Nimbus 7 Scanning Multichannel Microwave Radiometer (SMMR), we study the frontal structure of several mid-latitude cyclones over the North Pacific Ocean as they approach the West Coast of North America in the winter of 1979. The fronts, analyzed with all available independent data, are consistently located at the leading edge of the strongest gradient in integrated water vapor. The cloud liquid water content, which unfortunately has received very little in situ verification, has patterns which are consistent with the structure seen in visible and infrared imagery. The rain distribution is also a good indicator of frontal location and rain amounts are generally within a factor of two of what is observed with rain gauges on the coast. Furthermore, the onset of rain on the coast can often be accurately forecast by simple advection of the SMMR observed rain areas.

1. INTRODUCTION

The Scanning Multichannel Microwave Radiometer, SMMR, on Nimbus 7 has been observing brightness temperatures of the Earth and its atmosphere since October 1979, and is still functioning at the time of writing of this report, early 1984. This is quite an engineering accomplishment. A long time series like this is always valuable in geophysical work. Degradation of sensors with time makes interpretation in terms of absolute values difficult, however, and it is wise not to overinterpret. Even though there have been many passive microwave sensors launched over the last decade (Njoku 1982), the SMMR instrument was experimental and there has been considerable difficulty with calibration and correction for the antenna pattern. Gloersen et al. (1984) describe the NASA appointed experiment team's efforts at sorting out these problems, and the work continues. Involved with the engineering type difficulties are the limitations in our ability to assess the accuracy of the geophysical interpretation, because our algorithms are based on very incomplete understanding of the geophysical phenomena per se as well as incomplete understanding of the interaction of microwave radiation with them. These limitations of the present state-of-the-art are the challenge which we must meet vigorously, because as we hope to illustrate with the case studies below, the information obtainable from SMMR - in our case atmospheric water parameters - is tantalizing. It is far more detailed than one might have expected, and provides entirely new kinds of geophysical measurements. History teaches us that the availability of new types of data usually leads to new depths of understanding. Besides the uses one can foresee in research, the SMMR-derived measurements of

atmospheric water parameters also has potential for improving short-range weather forecasting over the sea and in coastal regions.

This study is part of the Nimbus 7 Experiment Team's effort to verify the geophysical parameters produced by the algorithms. In this report we only present data from the first year's record of brightness temperatures which have now been archived. The choice of study area and time frame is based on the availability of high quality in situ data from the CYCLonic Extratropical Storms (CYCLES) Project carried out by the University of Washington Cloud Physics Group under Professor Peter V. Hobbs.

2. BACKGROUND ON THE SCANNING MULTICHANNEL MICROWAVE RADIOMETER DATA

For the two case studies reported here we use SMMR data on integrated water vapor, integrated liquid water and rainfall rate. The water vapor emission is measured at 21 GHz near the maximum of the 22 GHz water vapor band, and the Rayleigh and Mie type scattering by cloud and rain drops is observed at 18 and 37 GHz. These emissions can only be discerned against the background of the oceans, which has low brightness temperature due to its low emissivity. Land surfaces emit strongly obscuring cloud and water vapor emissions. Thus, passive microwave sensing of atmospheric water can only be used over the oceans at these frequencies.

2.1 Brief Description of the SMMR Instrument

The Scanning Multichannel Microwave Radiometer consists of five concentric antennae, which measure radiances at 6.6, 10.4, 18, 21, and 37 GHz in two polarizations. The Nimbus 7 SMMR scanned 25° to each side of nadir from an altitude of 800 km resulting in ground resolution of 60 km for the 18 and 21 GHz channels and a possible maximum resolution of 30 for the 37 GHz channel. Verification of the interpretation of SMMR-derived atmospheric water parameters has been done to a greater extent for the sister instrument on the Seasat Satellite which operated for three months in 1978 (e.g., Katsaros et al., 1981; Taylor et al., 1983; Alishouse, 1983; McMurdie, 1983). The integrated water vapor has consistently been found to agree both in mean and standard deviation with values obtained by integrating the vapor content measured by radiosonde ascents. The calculated liquid water contents show patterns which agree qualitatively with the cloud distribution on visible or infrared satellite images and the rain rates produced by SMMR algorithms typically agree in a qualitative sense with the subjective coding of rainfall in the synoptic ship reports.

2.2 Algorithms

The results presented here are based on the integrated water vapor data archived in the geophysical data record, which has been calculated with an algorithm according to Wilheit and Chang (1980). However, bias corrections to the brightness temperatures and other corrections have also been applied (see Nimbus 7 SMMR User's Guide, 1984). The cloud liquid water and rainfall rate were calculated with special so-called "team" algorithms from the 18 GHz and 37 GHz horizontal polarization brightness temperatures. Cloud liquid water and rainfall rate are not archived due to the very limited verification and the much greater uncertainty in the underlying physics for these parameters. Emissions at 37 GHz by raindrops are known to depend on the freezing level in the cloud and the drop size distribution, but variations in these quantities are not at present included in any way in the algorithms.

The liquid water algorithm gives "funny numbers," i.e., there are even negative numbers at present, but this is probably only a bias effect, and the

ORIGINAL PAGE IS
OF POOR QUALITY

patterns obtained by contouring appear reasonable. The rainfall rate algorithm used was the following:

$$RR = (TB_{37H} - 190)/10.0 \quad (1)$$

where RR is the rain rate with units of mm/hr, TB_{37H} is the brightness temperature in the 37 GHz horizontal polarization channel.

3. CASE STUDIES

It is fortunate that early in the Nimbus 7 mission the CYCLES project was operating radars and rain gauges on the west coast of the State of Washington. Information on the rain distribution and amounts from these two sources will be brought to bear on the SMMR observations in case study A below. Because of the fine resolution of the 5.45 cm wavelength radar from the National Center for Atmospheric Research (1° beamwidth, 280 m range gate spacing) and the fine resolution of the tipping bucket rain gauges (typically 0.05 mm), we have the opportunity to look at whether the known mismatch between the resolution of SMMR (at best 30 km) and typical spatial scales of precipitating areas is a serious problem. The rain areas are often oblong, typically 3 to 5 km wide and 18 to 41 km long in these storms (e.g. Persson, 1980).

3.1 Case Study A: Portion of Orbit 1743 Off the Coast of the Pacific Northwest, Centered at 0104 PST, 27 February 1979

The SMMR swath for this study intersected a well defined cold front as it was crossing the coastline of the State of Washington. It is seen in the surface weather map for 0100 PST (Fig. 1) and the GOES-West IR imagery at 0045 PST (Fig. 2). The SMMR map of integrated water vapor is found in Fig. 3. The frontal location shown has been found independently of the SMMR data by careful examination of the CYCLES data and standard synoptic information, including buoy reports, and the GOES-West imagery. Notice how the front lies along the leading edge of the water vapor gradient, which is in good agreement with the findings from Seasat SMMR data by Katsaros and McMurdie (1983); notice how the integrated water vapor appears to define the frontal location more precisely than other available information. The integrated liquid water patterns (Fig. 4), in spite of the odd looking negative numbers, show contours nicely aligned with the edge of both the cloud band and the front.

Figure 5 is a plot of the SMMR rain rates (30 km resolution). The undulated 1 mm/hr rain rate contour duplicates almost exactly the detailed frontal analysis (see insert) of Hobbs and Persson (1982) based on doppler radar data and valid at 0100 PST. Evidently SMMR reveals the same meso-scale features occurring along the cold front as seen by the sophisticated radar.

We find, however, that the SMMR rain rates are generally lower than rain gauge values by a factor of 3 to 4, if we advect raining air parcels unchanged towards the coast with velocities estimated from synoptic wind fields and the frontal motion (cf. table in Gloersen *et al.*, 1984). Although most of the precipitation occurs as widespread rain in these midlatitude cyclones, some of the discrepancy may be due to insufficient resolution of SMMR. However, possible effects of the topography on the rain gauge values make it difficult to draw definite conclusions about the seriousness of this limitation (for further discussion see Katsaros and Lewis, 1984). The time of the onset of coastal precipitation appears to be predictable 12 to 24 hours in advance with good accuracy (within two to three hours) by this advection technique found from this and several other case studies. In other case studies we have examined (all during February and March, 1979), SMMR

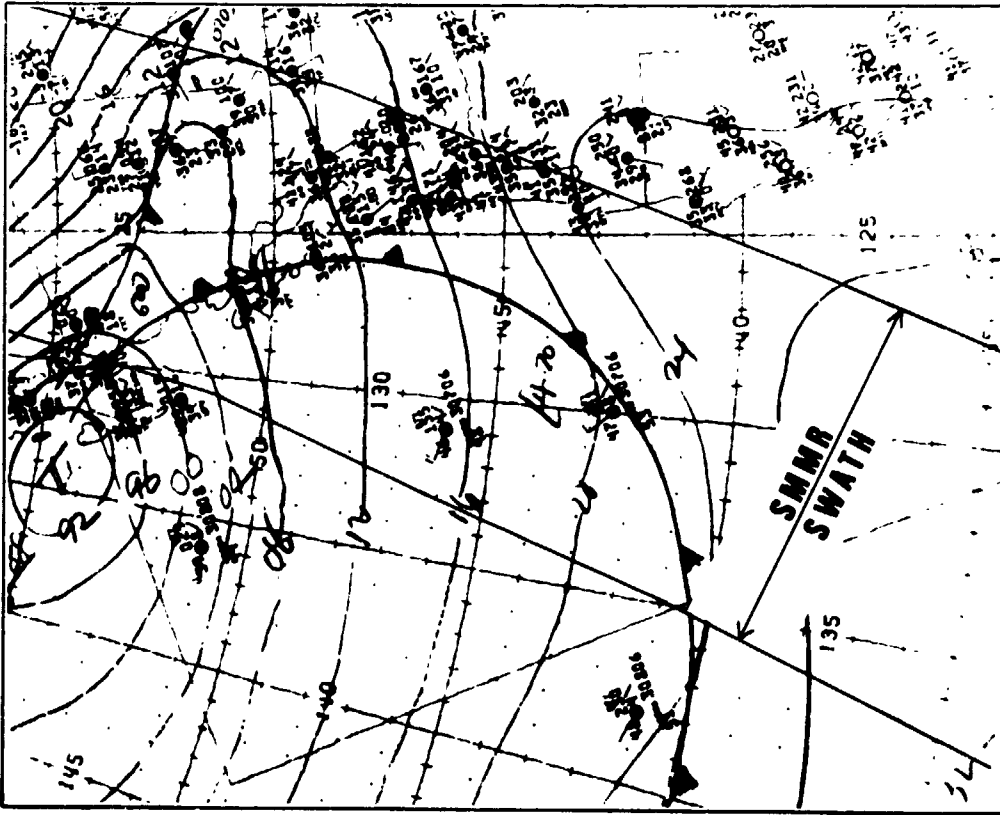


Fig. 1. The National Weather Service surface weather map analysis valid at 0100 Pacific Standard Time (PST) 27 February, 1979. The boundary of the SMMR swath is superimposed.



Fig. 2. Infra-red imagery from the GOES-West satellite valid at 0045 PST 27 February, 1979. The dark solid line depicts the position of the cold front at 0100 PST as determined from buoy data, results from Hobbs and Persson (1982), and from the IR imagery itself.

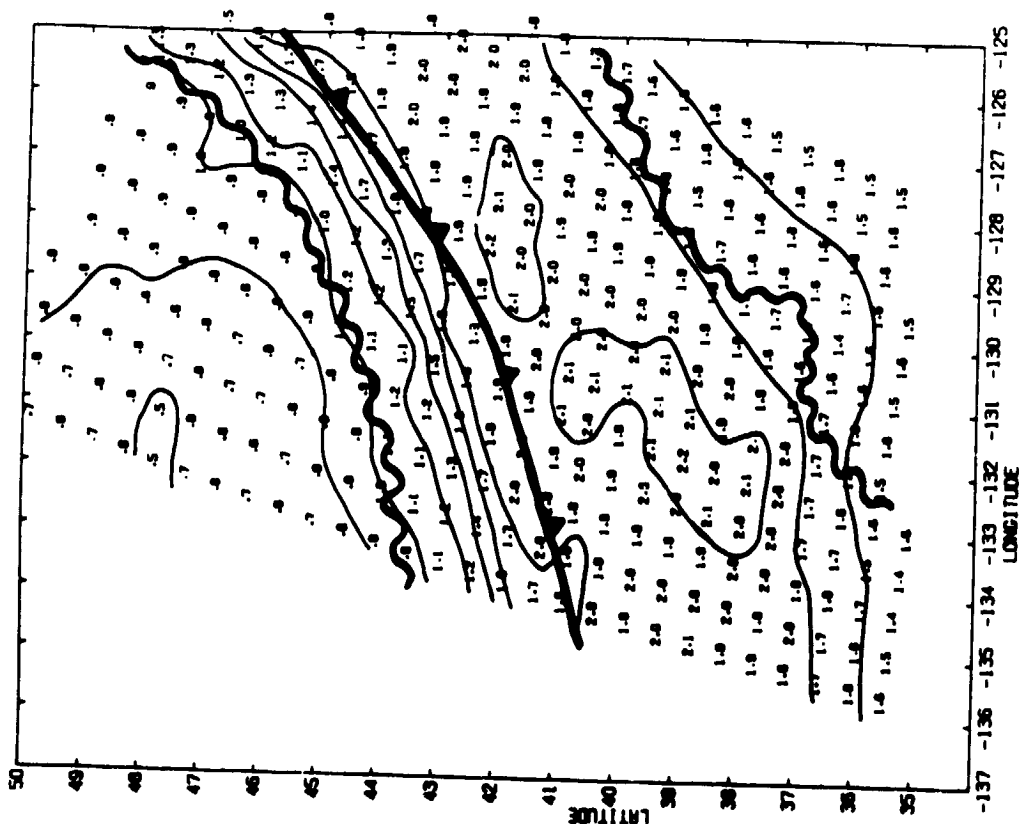


Fig. 3. SMR values of integrated water vapor (gm/cm^2). The thin lines are contours at intervals of 0.2. The thick wavy lines depict the frontal cloud band and southern boundaries of the frontal cloud band revealed by IR imagery (Fig. 1). Also shown is the location of the cold front as determined from independent data.

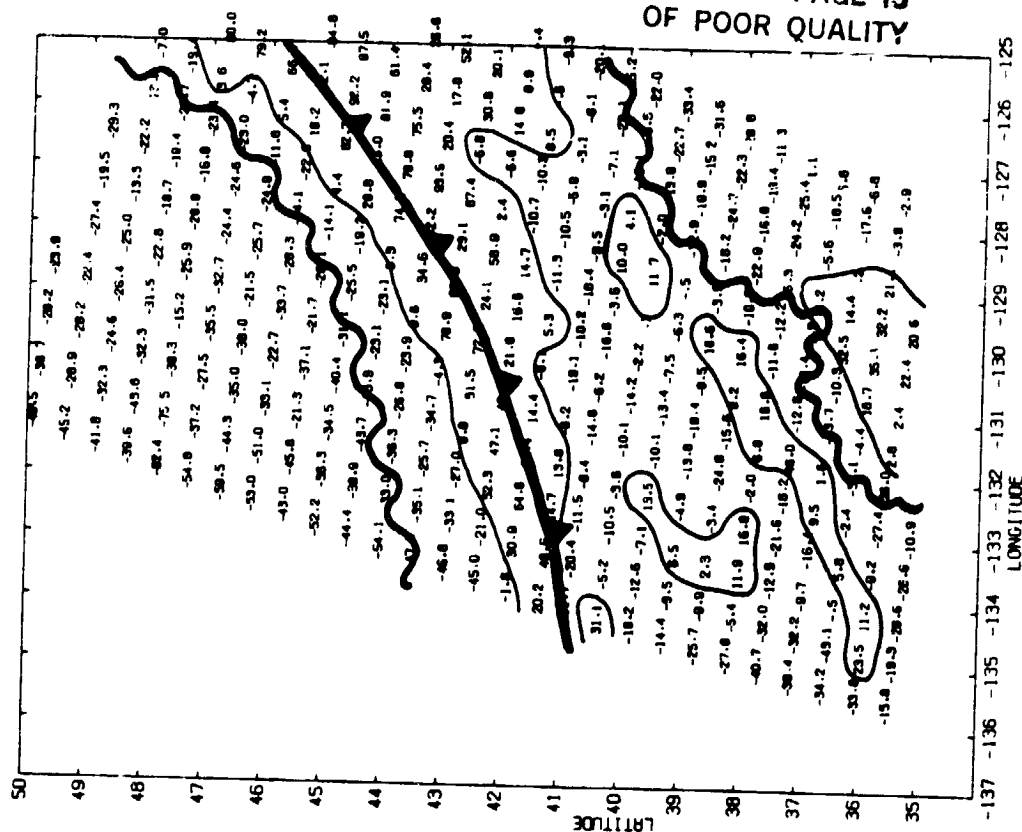


Fig. 4. SMR pattern of total cloud liquid water content. Units are $10^{-4} \text{ gm}/\text{cm}^2$ but an unknown problem which is thought to cause a constant bias effect has resulted in some negative numbers. The thin solid lines denote the zero contour. All else as in Fig. 3.

ORIGINAL PAGE 19
OF POOR QUALITY

rain rates are found to be in much better agreement with observed coastal rainrates, being of the same general magnitude (cf. Katsaros and Lewis, 1984).

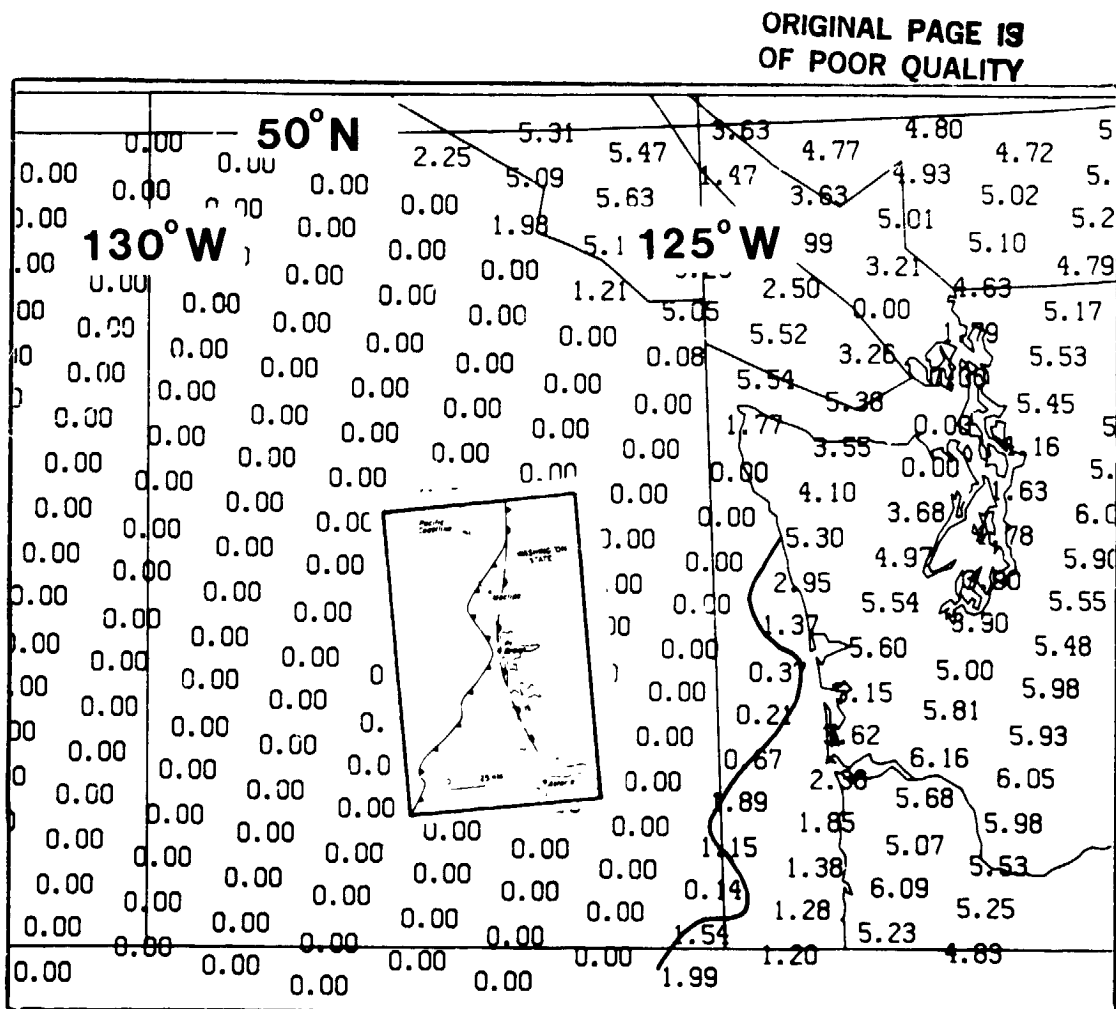


Fig. 5. SMMR rainrates from part of orbit 1743 (mm/h). Half of the data is plotted (only half of the columns but all of the rows). The 1 mm/h contour has been drawn using all of the data. And shown both oriented and to scale is a reproduction of Fig. 9 of Hobbs and Persson (1982) depicting their analysis of the surface frontal location near the coast.

3.2 Case Study B: Portion of Orbit 1992 Off the Coast of the Pacific Northwest, Centered at 0119 PST, 17 March, 1979

This swath of Nimbus 7 SMMR data crossed a weak occluded frontal system on a southbound pass. The frontal location, determined without the use of SMMR

information, coincides closely with the back edge of the cloud band on the GOES-West image (Fig. 6) and has been superimposed on the SMMR integrated water vapor map (Fig. 7).

Again we see that the cold front coincides with the leading edge of the strong gradient in integrated water vapor. In addition, notice the interesting structure observed by SMMR ahead of the front. For example, the tongue of dry air diagnosed immediately east of the front appears to correspond to a break in the cloud band which exposed the ocean surface to the "view" of the GOES-West satellite (the 1.8 gm/cm^2 contour has been superimposed on the infrared image in Fig. 6).

The liquid water content pattern (not shown) places highest values along and just ahead of the cold front. SMMR diagnoses a double band of high liquid water content showing some similarity to the double-banded nature of the clouds south of 42°N (see Fig. 6).

The SMMR rainfall pattern (also not shown) diagnoses a region of rain occurring north of 44°N , with its eastern edge located coincidentally with the surface front and extending eastward by as much as 200 km.

4. CONCLUDING REMARKS

The new type of data provided by passive microwave sensing of the atmosphere over the sea provides us with the challenge of fully learning to understand what these signals mean and with the opportunity to put the data in the contexts of both operational and research work.

4.1 Summary of Findings

In spite of the limited background knowledge for development of the SMMR algorithms for atmospheric integrated water vapor, liquid water and rain rate, for the "old" mid-latitude cyclones we have studied, these parameters look very convincing. Even if we must think of some of this information as qualitative at this stage, it is at least as useful as the familiar satellite imagery in locating surface fronts over the sea. We can identify liquid water regions within cloud systems, and they are in expected regions when compared to cloud imagery and location of fronts. The rainfall data can also identify frontal locations. They show meso-scale features of rainfall distribution in agreement with present knowledge about such structures, and the amounts given by the very simple algorithms are of the same magnitude as the areal rainfall average for most of our case studies.

4.2 Gaps in Our Knowledge or Understanding

We have several kinds of gaps in our knowledge related to SMMR measurements and the water in the atmosphere as vapor, cloud droplets or raindrops:

First, we have incomplete information about how these parameters vary on the meso-scale, and, in particular, how they vary in storms at different stages of their development and in different regions of the ocean. This information is potentially obtainable from passive microwave measurements, but without some knowledge of the variability from other work, we cannot estimate what errors we might incur with limited spatial resolution.

Second, we don't know how accurately passive microwave instruments can determine liquid water content and rainfall rate, since we have not yet verified

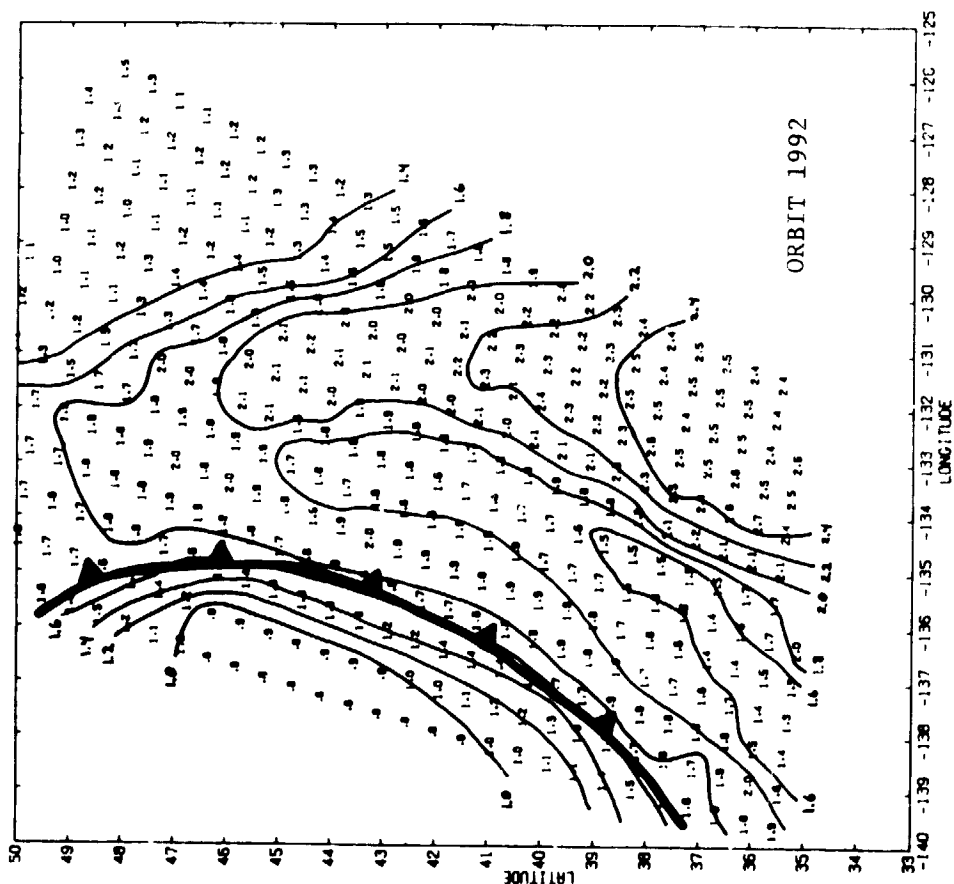


Fig. 7. SMR values of integrated water vapor (gm/cm^2) obtained at 0116 PST 17 March, 1979. Contours are drawn at $0.2 \text{ gm}/\text{cm}^2$ intervals. The independently determined cold frontal location is superimposed.

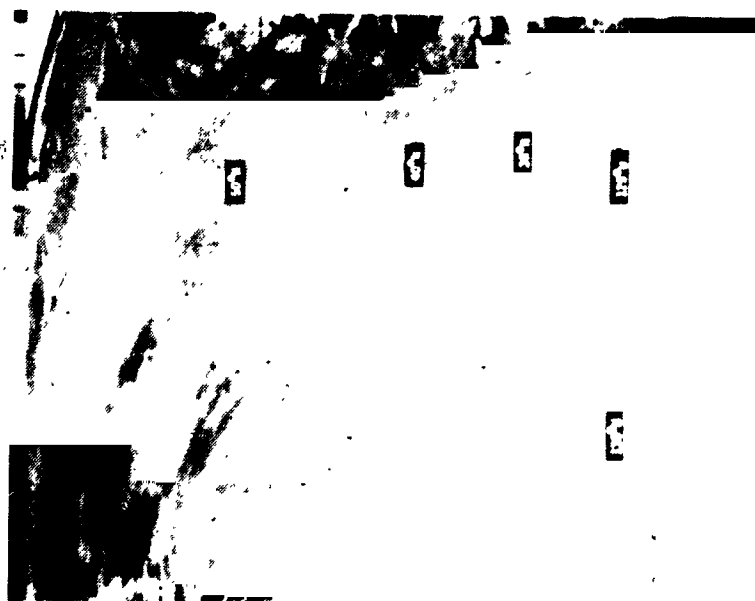


Fig. 6. GOES-West enhanced IR imagery valid at 0215 PST 17 March, 1979. The equivalent blackbody temperature scale is defined at the top in intervals of 10°C . Superimposed is the $1.8 \text{ gm}/\text{cm}^2$ water vapor contour (from Fig. 7).

the algorithms on the relevant spatial scales. Theoretical studies by Wilhelm et al. (1977) show dependencies on assumed dropsize distribution and freezing level. How variable are these parameters? Can they be accounted for by adding another measurable quantity to the algorithms?

Third, we don't know how to use some of this new information. If real time integrated water vapor maps consistently tell us where the fronts are, an operational meteorologist would certainly know how to use that information, but how do we use integrated cloud liquid water and rainfall data? Can we relate these measures to the energetics or development of a storm (particularly its future)? If we only have occasional sampling from polar orbiting satellites, how do we make use of the information operationally or statistically for climatology?

It is known that total cloud liquid water content can be used to parameterize the absorption of visible light by the cloud and it is also a measure of emissivity of infrared radiation (e.g. DeVault and Katsaros, 1982). Could we use these relationships to calculate the radiative heat budget at the sea surface?

Other possible uses for this type of data is in estimating the role of water phase chemistry in the atmosphere and to estimate precipitation efficiency from the relative values for cloud liquid water and rainfall rate (Dean Hegg, 1984, personal communication). Can microwave data be obtained accurately enough for such interpretations?

Integrated water vapor in conjunction with sea surface temperature and winds have been used to estimate the evaporation rate from the sea (W. T. Liu, personal communication). What is the ultimate accuracy of such parameterizations?

4.3 Recommendations for Further Work and Experiments

We need direct comparisons between passive microwave observations of storm systems and in situ areally averaged measurements of the relevant parameters. This would require dedicated experiments designed specifically for this purpose (at least some dedicated resources) using two or more instrumented aircraft and perhaps upward looking radiometers on small islands or ships.

We also need to pursue theoretical and experimental work on finding the optimum microwave frequencies or combination of frequencies for measuring the various atmospheric water parameters.

And, now that these new measures are within reach, we need simulation type experiments to find imaginative ways to include them in the diagnosis and prognosis of atmospheric storms.

5. REFERENCES

Alishouse, J. C., 1983: Total precipitable water and rainfall determinations from the Seasat Scanning Multichannel Microwave Radiometer (SMMR). J. Geophys. Res., 88, 1929-1935.

DeVault, J. E. and K. B. Katsaros, 1982: Remote Determination of Cloud Liquid Water Path from Bandwidth-Limited Shortwave Measurements. Contribution No. 646, Dept. of Atmospheric Sciences, University of Washington, Seattle, WA.

- Gloersen, P., D. J. Cavalieri, A. T. C. Chang, T. T. Wilheit, W. J. Campbell, O. M. Johannessen, K. F. Kunzi, D. B. Ross, D. Staelin, E. P. L. Windsor, F. T. Barath, P. Gudmandsen, E. Langham, R. O. Ramseier and K. B. Katsaros, 1983: A summary of results from the first Nimbus 7 SMMR observations. *J. Geophys. Res.* (submitted).
- Hobbs, P. V. and P. O. G. Persson, 1982: The mesoscale and microscale structure and organization of clouds and precipitation in midlatitude cyclones. Part V: The substructure of narrow cold-frontal rainbands. *J. Atmos. Sci.*, 39, 280-295.
- Katsaros, K. B. and K. M. Lewis, 1984: Studies of Atmospheric Water Parameters in North Pacific Cyclones with the Nimbus 7 Scanning Multichannel Microwave Radiometer. Technical Report, Contracts NAS 5-26262, NAG 5-354. Dept. of Atmospheric Sciences, University of Washington, Seattle, WA (in preparation).
- Katsaros, K. B. and L. A. McMurdie, 1983: Atmospheric water distribution in cyclones as seen with Scanning Multichannel Microwave Radiometers (SMMR). Presentation made at IGARSS'83, San Francisco, CA, 31 August-2 September, 1983.
- Katsaros, K. B., P. K. Taylor, J. C. Alshouse and R. J. Lipes, 1981: Quality of Seasat SMMR (Scanning Multichannel Microwave Radiometer) atmospheric water determinations. *Oceanography from Space*, 691-706, Plenum Publishing Corp., New York.
- McMurdie, L. A., 1983: Seasat Passive Microwave Observations of North Pacific Cyclones. M.S. Thesis, Dept. of Atmospheric Sciences, University of Washington, Seattle, WA.
- Nimbus 7 Scanning Multichannel Microwave Radiometer, User's Guide, 1984 (in preparation).
- Njoku, E. G., E. J. Christensen and R. E. Cofield, 1980: The Seasat Scanning Multichannel Microwave Radiometer (SMMR) antenna pattern correction development and implementation. *IEEE J. Oceanic Eng.*, OE-5, No. 2, 125-137.
- Persson, P. O. G., 1980: The Small Mesoscale Structure and Microphysics of a Narrow Cold-Frontal Rain Band. M.S. Thesis, Dept. of Atmospheric Sciences, University of Washington, Seattle, WA.
- Taylor, P. K., T. H. Guymer, K. B. Katsaros and R. G. Lipes, 1983: Atmospheric water distributions determined by the Seasat Multichannel Microwave Radiometer. Variations in the Global Water Budget, 93-106, A. Street-Perrott et al., eds. D. Reidel Publishing Company, Dordrecht, Holland.
- Wilheit, T. T. and A. T. C. Chang, 1980: An algorithm for retrieval of ocean surface and atmospheric parameters from the observations of the Scanning Multichannel Microwave Radiometer (SMMR). *Radio Science*, 15, 525-544.
- Wilheit, T. T., A. T. C. Chang, M. S. V. Rao, E. B. Rodgers and J. S. Theon, 1977: A satellite technique for quantitative mapping rainfall rates over the ocean. *J. Appl. Meteor.*, 16, 551-560.

6. ACKNOWLEDGEMENTS

This work was performed under NASA Grant NAG 5-354. We appreciate the valuable advice from Prof. Richard J. Reed on the frontal analysis and the assistance rendered with the typing of this manuscript by Ms. Sylvia Lavin. Contribution No. 696, Department of Atmospheric Sciences, University of Washington Seattle, WA, U.S.A.

TEMPERATURE AND HUMIDITY PROFILES IN THE ATMOSPHERE FROM SPACE BORNE LASERS
(a feasibility study)

Hartmut Grassl and Peter Schlüssel
Institut für Meereskunde
Düsternbrooker Weg 20
D - 2300 Kiel 1 , FRG

ABSTRACT

Computer simulations of the differential absorption lidar technique in a space craft for the purpose of temperature and humidity profiling indicate:

- 1) Current technology applied to O₂ and H₂O lines in the .7 to .8 μ m wavelength band gives sufficiently high signal-to-noise ratios (up to 50 for a single pulse pair) if backscattering by aerosol particles is high, i.e. profiling accurate to 2 K for temperature and 10 % for humidity should be feasible within the turbid lower troposphere in 1 km layers and with an averaging over approximately 100 pulses.
- 2) The impact of short term fluctuations in aerosol particle concentration is too big for a one laser system. Only a two laser system firing at a time lag of about 1 millisecond can surmount these difficulties.
- 3) The finite width of the laser line and the quasi-random shift of this line introduce tolerable, partly systematic errors.

1. INTRODUCTION

The retrieval of temperature and humidity profiles from radiances measured with current space borne passive radiometers mainly suffers from a poor height resolution. Therefore any system increasing the number of independent informations - equivalent to enhanced height resolution - at the same or even slightly reduced accuracy level is highly desirable. The present study simulates the backscattering of laser light by the atmosphere to a space craft flying at 250 or 800 km above the earth surface. The main goals of this study, temperature and humidity profiles, need at least two wavelengths, while the aerosol backscattering profiles in clear atmospheres and above clouds as well as cloud top detection can be determined from a single wavelength lidar.

We report on temperature and humidity profiles from a two wavelength differential absorption lidar (DIAL). Quite a number of parameters, which all influence the backscattering of laser light and the accuracy of its detection have been set to realistic values or varied within realistic ranges in order to assess their impact on the signal-to-noise ratio (SNR):

- tropospheric and stratospheric aerosol particles
- absorber amount (for humidity profiles only)
- laser power (remaining within technologically feasible ranges)
- instability of the laser wavelength
- width of the laser line
- shift of the O₂ or H₂O line center with atmospheric pressure
- time integration (equivalent to layer thickness desired)
- line shape of the atmospheric absorption line
- space averaging (necessary to increase SNR)

2. BASIC EQUATIONS

We start with the lidar equation describing the power received at the detector $P(r)$ after backscattering of laser power P_0 by a substance at distance r .

$$P(r) = P_0 \eta_0 \eta_1 A^* \frac{\tau c}{2} \cdot \frac{1}{r^2} \beta(r) \exp \left(-2 \int_0^r e(r') dr' \right) \quad (1)$$

with P_0 = emitted laser power accounting for losses within the laser optics

η_0 = correction for beam overlapping

η_1 = optical efficiency of the receiving system

A^* = effective receiver area

τ = pulse length

c = velocity of light

$\beta(r)$ = backscattering coefficient at distance r

$e(r)$ = extinction coefficient at distance $r' = r$

Discretization of the integral in (1) into m finite layers with thickness Δr and formulation for two wavelengths λ_1 and λ_2 leads to the ratio of signals

$$\frac{P(r, \lambda_1)}{P(r, \lambda_2)} = \frac{\beta(r, \lambda_1)}{\beta(r, \lambda_2)} \cdot \frac{\prod_{i=1}^{m=r/\Delta r} \exp(-2e(r'_i, \lambda_1)\Delta r)}{\prod_{i=1}^m \exp(-2e(r'_i, \lambda_2)\Delta r)} \quad (2)$$

where $r' = r - \Delta r/2$ has been introduced. Writing (2) in terms of the layer $i-1$ leads to a recursion formula, which - after the neglect of the wavelength dependence of β (certainly valid for $\Delta\lambda \leq 2\text{nm}$) - is reduced to

$$\frac{P(r, \lambda_1)}{P(r, \lambda_2)} = \frac{P(r-\Delta r, \lambda_1)}{P(r-\Delta r, \lambda_2)} \cdot \frac{\exp(-2k(r', \lambda_1)\Delta r)}{\exp(-2k(r', \lambda_2)\Delta r)}$$

Resolved for the differential absorption coefficient $\Delta k(r') = k(r', \lambda_1) - k(r', \lambda_2)$ we get

$$\Delta k(r') = -\frac{1}{2\Delta r} \cdot \ln \left(\frac{P(r, \lambda_1) \cdot P(r-\Delta r, \lambda_2)}{P(r, \lambda_2) \cdot P(r-\Delta r, \lambda_1)} \right) \quad (3)$$

If one laser wavelength, λ_2 , is in a window between absorption lines, the differential absorption coefficient $\Delta k(r') = k(r', \lambda_1)$. Now adopting the Lorentz line shape the absorption coefficient at wavenumber ν reads

$$k_\nu(r') = \frac{S(r')}{\pi} \cdot \frac{\alpha(r')}{(\nu - (\nu_0 - \delta(r')))^2 + \alpha(r')^2} \quad (4)$$

where S = line intensity depending on temperature T

ν_0 = central wavenumber at standard conditions

α = line halfwidth depending on T and pressure p

δ = line shift depending on T and p

we introduce one of the desired parameters: temperature T .

Accounting for the temperature and pressure dependence of S and

$$S(r') = S_0 n(r') \left(\frac{T_0}{T(r')} \right)^\delta \exp \left(- \frac{E_0}{k_0} \left(\frac{1}{T(r')} - \frac{1}{T_0} \right) \right) \quad (5)$$

$$\alpha(r') = \alpha_0 \cdot \frac{p(r')}{p_0} \cdot \left(\frac{T_0}{T(r')} \right)^{1/2}$$

we have to handle some more parameters,

S_0 = line strength at reference temperature T_0
 E_0 = energy of the lower state
 k_0 = Boltzmann's constant
 δ = molecular constant depending on degrees of freedom for rotation
 ($\delta = 1$ for linear molecules, $\delta = 1.5$ for H_2O)
 α_0 = halfwidth at T_0, p_0
 p_0 = 1 atm pressure

but we also find the second desired parameter: the number density $n(r')$ of the molecule having a line at ν_0 . Insertion of (4) for $\nu = \nu_0$ and of (5) into (3) gives the basic equation for temperature determination as long as n/p is known.

$$k_\nu = \frac{S_0 p_0}{1.132 \pi \alpha_0} \cdot \frac{n}{p} \left(\frac{T_0}{T} \right)^{\delta-1/2} \exp \left(- \frac{E_0}{k_0} \left(\frac{1}{T} - \frac{1}{T_0} \right) \right) \quad (6)$$

For given T and p this expression can be reformulated to allow for instance water vapor determination.

$$n_{H_2O} = \frac{k_\nu \cdot 1.132 \pi \alpha_0 p}{S_0 p_0} \cdot \left(\frac{T}{T_0} \right)^{\delta-1/2} \exp \left(- \frac{E_0}{k_0} \left(\frac{1}{T} - \frac{1}{T_0} \right) \right) \quad (7)$$

A more thorough treatment of the DIAL technique should account for the Doppler and Voigt line shape too. However, since the subsequent error equations are also valid for the Doppler line shape and deviations from the Lorentz line shape in the troposphere are well within the errors of laser line shape knowledge, we omit in accordance with a statement by Megie et al (1983) a thorough treatment of Voigt line profiles.

3. ERROR ASSESSMENT

We define the error of a function $f(x_i; i=1, \dots, m)$ by

$$\Delta f(x_i; i=1, \dots, m) = \sum_{i=1}^m \left| \frac{\partial f_i}{\partial x_i} \right| \Delta x_i \quad (8)$$

which resolved for Δx_j reads

$$\Delta x_j = (\Delta f - \sum_{i=1}^m \left| \frac{\partial f_i}{\partial x_i} \right| \Delta x_i) / \left| \frac{\partial f_i}{\partial x_j} \right| \quad (9)$$

ORIGINAL PAGE IS
OF POOR QUALITY

Applying (9) to (3) we get for the absorption coefficient

$$\begin{aligned} \Delta k(r') &= \frac{1}{2(\Delta r)^2} \ln \left(\frac{P(r, \lambda_1) P(r - \Delta r, \lambda_2)}{P(r, \lambda_2) P(r - \Delta r, \lambda_1)} \right) \Delta r + 2 \left| \frac{1}{2\Delta r} \frac{1}{P(r', \lambda_1)} \right| \Delta P(r', \lambda_1) \\ &+ 2 \left| \frac{1}{2\Delta r} \frac{1}{P(r, \lambda_2)} \right| \Delta P(r, \lambda_2) \\ &\approx \frac{1}{\Delta r \cdot \text{SNR}_1} + \frac{1}{\Delta r \cdot \text{SNR}_2} \end{aligned} \quad (10)$$

The approximation uses $P/\Delta P = \text{SNR}$ and neglects the first term in (10), which is of the order of 10^{-6} to 10^{-8} for an error of 10 m in the determination of $\Delta r = 1$ km and for an optical depth $\tau^* = k(r) \Delta r$ between 10^{-3} and 10^{-1} , while the second and the third vary from 10^{-1} to 10^{-3} for SNR between 1 and 100. Calculating $\Delta T/T$ according to (9) using (6) yields

$$\frac{\Delta T}{T} = \frac{1}{\left| \frac{E_0}{k_0} \frac{1}{T} - \frac{1}{2} + \delta \right|} \left(\frac{\Delta P}{P} + \frac{\Delta n}{n} + \frac{1}{k_v} \cdot \left(\frac{1}{\Delta r \cdot \text{SNR}_1} + \frac{1}{\Delta r \cdot \text{SNR}_2} \right) \right) \quad (11)$$

The application of (9) to (7) finally gives the relative error $n_{\text{H}_2\text{O}}/n_{\text{H}_2\text{O}}$ for water vapor profiling.

$$\frac{\Delta n}{n} = \frac{\Delta P}{P} + \left| \frac{E_0}{k_0} \frac{1}{T} + \frac{1}{2} - \delta \right| \frac{\Delta T}{T} + \frac{2}{\Delta r k_v \text{SNR}} \quad (12)$$

4. THE SIGNAL-TO-NOISE RATIO

The error equations (10) - (12) mainly depend on SNR at the detector. The most important noise sources for this study (fixed to the $.75 \mu\text{m}$ wavelength region) are:

- 1) shot noise caused by statistical fluctuations of photons constituting the signal current
- 2) background noise due to backscattered or reflected sun light

All other noise sources have been shown to be negligible (Endemann, 1983). For the above noise sources Megie and Menzies (1980) propose

$$\text{SNR} = \frac{N_k}{(N_k + N_B)^{1/2}} \quad (13)$$

with the number of backscattered photons received per unit time from layer k

$$N_k = \frac{P_k}{hf} \eta^* \frac{2\Delta r}{c} \quad (14)$$

and the number of background photons per unit time

$$N_B = \frac{I_B A^* \Omega^2 \pi B}{hf} \eta_1^* \eta_2^* \frac{2\Delta r}{c} \quad (15)$$

P_k = signal power from layer k after passage through the front filter in front of the detector

η_1^* = filter transmission

η_2^* = quantum efficiency of the detector

f = frequency ($f = c/\lambda$)

I_B = background radiance

Ω = field of view of the receiver optics

B = filter bandwidth

h = Planck's constant

5. RESULTS

5.1 Impact of Variations in Aerosol Particle Concentration

Before we discuss the signal-to-noise ratio of the proposed system the errors due to random fluctuations of aerosol particle concentration in both the horizontal and vertical direction between two pulses of a multi-wavelength lidar are presented. Table 1 clearly demonstrates, that there is no way to get accurate profiles with only one laser shifting wavelength within 0.1 second. If particle concentration varies by only 0.1 percent - still unrealistically low - between two pulses, the relative error calculated from 100 trials with a random number generator reaches at the maximum 0.7, 0.4, and 2.1 percent for temperature T , pressure p and number density n_{H_2O} in the troposphere

Table 1: Maximum error in percent caused by variations in aerosol particle concentration between two pulses.

Variation	$\Delta T/T$	$\Delta p/p$	$\Delta n/n (H_2O)$	level
1 %	20.0	8.0	37.0	troposphere
0.1%	1.6	2.3	11.0	stratosphere
	0.7	0.4	2.1	troposphere

5.2 Signal-to-Noise Ratio (SNR)

This section sticks to a two laser system, as shown to be necessary within the previous section. The separation of pulses has to be below a millisecond in order to neglect particle concentration changes. The SNR calculations include the major noise sources: shot noise and background noise of the sunlit atmosphere as expressed in (13) - (15). Other noise sources have been handled by Endemann (1983) and shown to be negligible for the proposed system whose performance will be tested under laboratory conditions.

SNR depends on such a variety of parameters that part of them has been fixed in order to assess the influence of some specifically. In accordance with the envisaged hardware development we have set: $\eta_1^* = 0.45$, $\eta_2^* = 0.18$ (Endemann, 1983a), $A^* = 0.25 \text{ m}^2$, $\Omega = 0.5 \text{ mrad}$, $B = 1 \text{ nm}$, $\Delta r = 1 \text{ km}$; I_B varies from 0 (night) to 5 (standard illumination) and $200 \text{ W m}^{-2} \text{ sr}^{-1} \text{ m}^{-1}$ (strong sun glint or thick clouds). The central wavenumber $\nu = 12975 \text{ cm}^{-1}$, $P_0 = 25 \text{ MW}$, and the height of the space craft varies from 250 to 800 km. The line parameters used are summarized in table 2. The first atmosphere adopted is a standard atmosphere for 60°N, July,

ORIGINAL PAGE 13
OF POOR QUALITY

with 23 km horizontal visibility at the ground and an aerosol scale height of 1.25 km. The SNR values displayed in figures 1 and 2 for 250 and 800 km clearly demonstrate:

$SNR \approx 10$ for a single shot is only achievable within the troposphere. SNR for the on-line shot is drastically reduced for the stronger O_2 line. However, this does not mean enhanced temperature error, because the concomitant increase in optical depth $\tau = \Delta r \cdot k(r')$ more than compensates this reduction. An additional constraint is: measurements must be taken outside sun glint areas. Within these first figures we did not tune aerosol backscattering in order to reach higher SNR.

Table 2: Lines and windows chosen

wavelength λ	wavenumber ν	absorber and use	line strength S_0	halfwidth α_0	lower state energy E_0
μm	cm^{-1}		cm	cm^{-1}	cm^{-1}
0.7707129	12975.000	window; T			
0.7711989	12966.823	O_2 ; T	$0.734 \cdot 10^{-26}$	0.042	1803.18
0.7698983	12988.728	O_2 ; T	$0.431 \cdot 10^{-25}$	0.042	1422.502
0.7866600	12711.972	H_2O ; n	$0.362 \cdot 10^{-24}$	0.0655	704.214
0.7867201	12711.000	window; n			

⁺ at 296 K and 1013.25 hPa

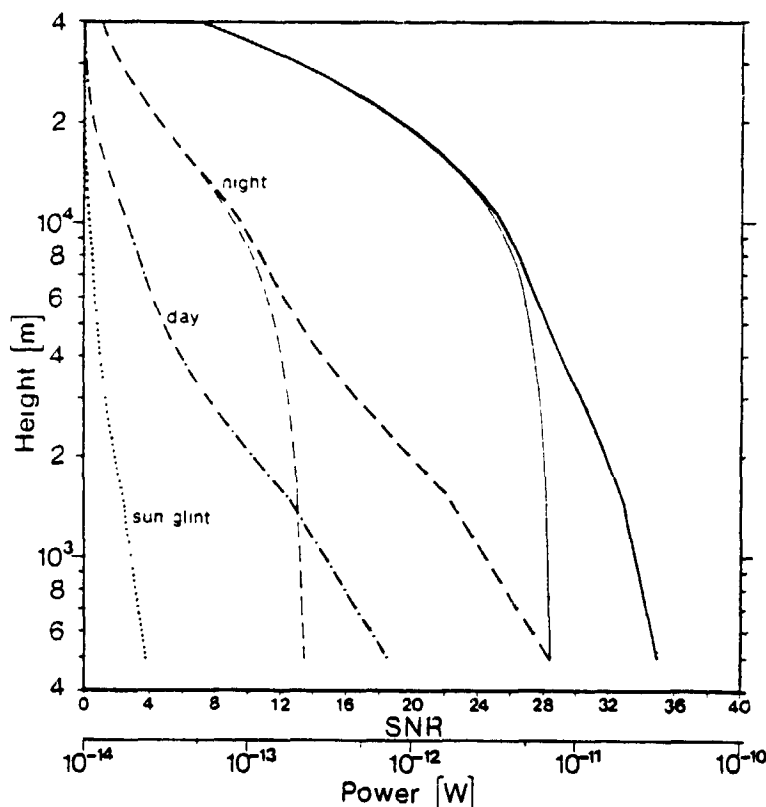


Figure 1: Vertical profiles of backscattered power (—) and SNR for a standard atmosphere at 60°N, July, with 23 km horizontal visibility, aerosol scale height 1.25 km, space craft at 250 km. The thicker curves stand for the weak O_2 line, thinner ones for the stronger line. Pulse energy for all the simulations is kept at 0.5 J.

ORIGINAL PAGE IS
OF POOR QUALITY

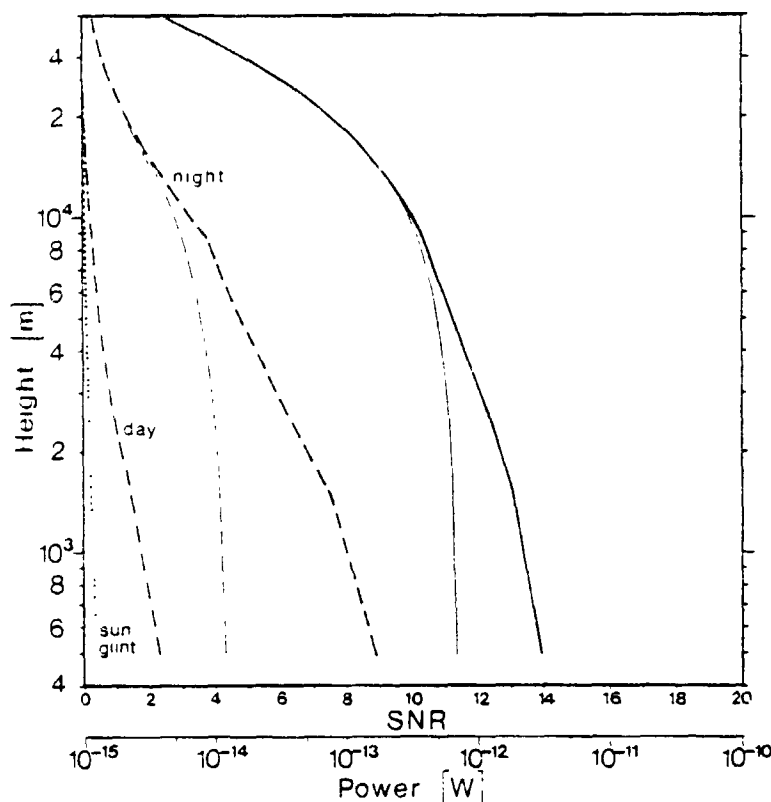


Figure 2: As fig.1, however space craft at 800 km

Since figures 1 and 2 show SNR for one pulse pair, an averaging over 100 pulse pairs, which will be tolerable from the point of view of horizontal resolution, gives $SNR > 100$ in large parts of the troposphere for a space craft at 250 km. Using a standard aerosol model (Lenoble and Brogniez, 1983) for continental areas in the troposphere and a young (1 month) stratospheric aerosol layer of volcanic origin SNR is enhanced compared to the atmospheric model in figures 1 and 2, now surmounting the value 10 even for a space craft at 800 km under night conditions. All the other aerosol models proposed, which were input to our programme but are not shown, do not give strongly different results. They all point to the drastic dependence on aerosol particle concentration. Rayleigh scattering can not give high enough SNR.

5.3 Relative Temperature and Humidity Error

The error equations (11) and (12) were explored under a variety of situations. However, the only figure displayed already contains the main result. The temperature error $\Delta T/T$ in the lowest troposphere (figure 4) for $\Delta r = 2$ km is below 2 K only for SNR_2 (window wavelength) ≥ 200 and rather low total optical depth τ^* of the line. For water vapor profiling very similar results exist. However, the relative error $\Delta n/n$ at $SNR_2 \geq 200$ is only below 0.1 at a $E_0 = 900 \text{ cm}^{-1}$. The dependence on τ^* is unchanged.

ORIGINAL FILED IN
OF POOR QUALITY

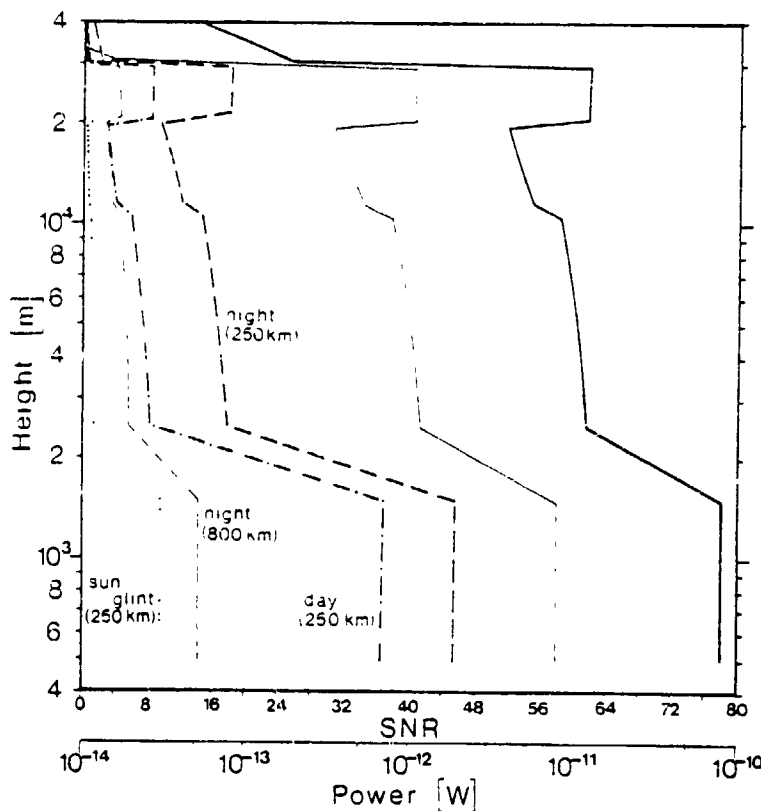


Figure 3: Vertical profiles of backscattered power (—) and SNR for a standard atmosphere at 60°N , July, with continental aerosol in the troposphere and volcanic aerosol in the stratosphere, one month after eruption. Thick lines for a space craft at 250 km, thin lines for a space craft at 800 km.

6. ERRORS CAUSED BY THE FINITE WIDTH OF THE LASER LINE

Most simulations hitherto reported neglect the laser line width. According to Browell et al (1983) present lasers have a line width of 3 pm, corresponding to 0.05 cm^{-1} at $0.7\text{ }\mu\text{m}$. Korb and Weng (1982) assume 0.02 cm^{-1} . Thus the laser line width is comparable to the halfwidth of the O_2 and H_2O lines chosen. Since the above simulations assume the laser line to be monochromatic and to meet the absorption line center we have to assess the errors thus introduced. The optimal approach would be: revised analytic solutions. Here we adopt an inferior approach. We average transmissions due to gaseous absorption within one layer spectrally, symmetric to the line center. The differential absorption coefficients thus obtained are handled as before with the monochromatic approach. The result is a systematic error. Assuming a rectangular laser line of width 0.05 cm^{-1} the relative temperature error varies from +1.1 percent in the upper atmosphere to -0.53 percent in the lower troposphere. Assuming a triangular distribution, where the laser line intensity has dropped to 1/8 at 0.025 cm^{-1} distance from the center, $\Delta T/T$ lies between -0.01 and +0.12 percent. The relative humidity error $\Delta n/n$ then varies between +2.0 and -0.95 percent.

ORIGINAL PAGE IS
OF POOR QUALITY

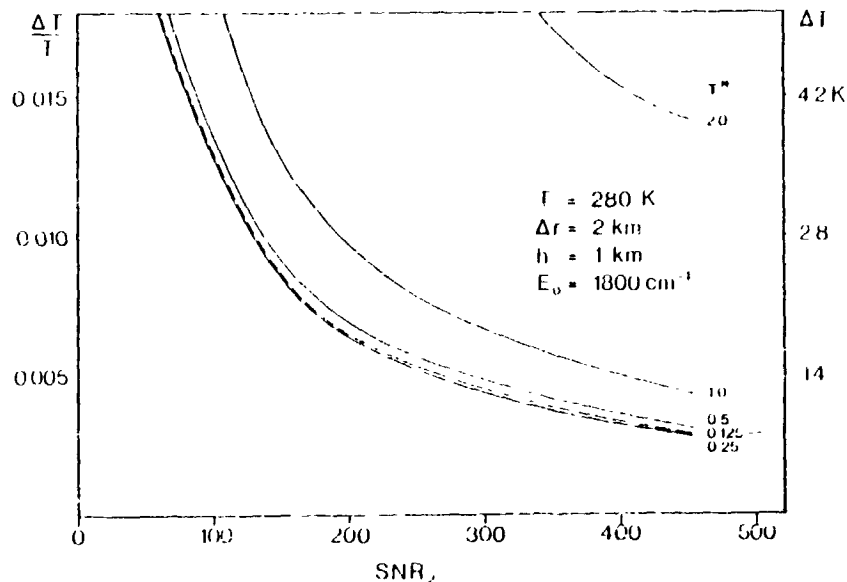


Figure 4: Relative temperature error $\Delta T/T$ as a function of the signal-to-noise ratio for the window position, SNR_2 , for different total optical depth τ^* as indicated.

7. FLUCTUATIONS OF LASER FREQUENCY

The instability of the laser frequency also causes errors, which in this case will not be systematic. After Browell et al (1983) contemporary lasers show fluctuations of ± 0.3 pm, approximately a tenth of the halfwidth of the absorption lines. We simulated these fluctuations by shifting the laser line in two different ways:

- 1) random shift with equal probability for all deviations within ± 0.3 pm;
- 2) random shift with a Gaussian distribution and a standard deviation $\sigma = 0.3$ pm and accounting for a finite triangular laser line width of 3 pm (10% level).

$\Delta T/T$ varies from nearly 0 percent to 0.1 percent for both cases depending on height level. The values $\Delta n/n$ reach 1.5 percent. This, however has to be compared to the $\Delta n/n$ from (12) and thus is not intolerably high. All numbers reported are valid for the troposphere only and after an averaging over 100 realisations.

8. INFLUENCE OF A POSSIBLE ABSORPTION LINE SHIFT WITH PRESSURE

The absorption lines of atmospheric gases are not fixed to a distinct wavelength. Their shift is negligibly small for many applications. The shift $\delta = \alpha/2.75 \text{ p/p}_0(T_0/T)$ is comparable to the laser line shift. δ ranges from 0.002 cm^{-1} at 50 hPa and 220 K to 0.018 cm^{-1} at the ground at 290 K. A laser signal thus centered at the absorption line at the tropopause is off the center to the shortwave wing of the line in the lower troposphere. The systematic error reaches -0.8 percent for $\Delta T/T$ in the lower troposphere, while for the values $\Delta n/n$ we have to expect up to -12 percent. There should again be pointed out, that the δ chosen is a theoretical estimate which needs verification.

9. CONCLUSIONS

The major result of this study is:

Tropospheric temperature and humidity profiles in 1 to 2 km layers may be determined by a space borne DIAL using present technology to an accuracy of better than 2 K or 10 percent respectively under the following conditions:

- 1) Two laser system firing with a time lag below 1 millisecond.
- 2) Averaging over at least 100 pulses for a space craft at 250 km height.
- 3) Averaging over some hundred pulses for a space craft at 800 km.
- 4) Highest accuracy is found for both temperature and humidity with O_2 and H_2O lines respectively at total optical depth at the line center within the 0.1 to 0.5 range.
- 5) The optical depth of the pure Rayleigh scattering atmosphere in window areas has to be strongly enlarged by aerosol particles, i.e. only turbid atmospheres give reliable results.

Major gaps found:

- 1) The impact of laser line width and laser line position fluctuations or accuracy has to be investigated in more detail.
- 2) The poor knowledge of absorption line shift with atmospheric pressure hampers an assessment of its importance for DIAL from space.

10. ACKNOWLEDGEMENT

The main part of this study has been funded by Battelle Institut, Frankfurt, FRG via a subcontract within a technology study of the European Space Agency.

11. REFERENCES

- Browell, E.V., Carter, A.F., Shipley, S.T., Allen, J.R., Butler, C.F., Mago, M.N., Siviter Jr, J.H., Hall, W.M. 1983: NASA Multipurpose Airborne DIAL System and Measurements of Ozone and Aerosol Profiles. Appl. Opt. 22, 522-534
- Endemann, M. 1983: Applications of Laser for Climatology and Atmospheric Research. Battelle Report for Contract No. 4868/81/NL/HP (SP)
- Endemann, M. 1983a: Private communication
- Korb, C.L. and Weng, C.Y. 1982: A Theoretical Study of a Two-Wavelength Lidar Technique for the Measurement of Atmospheric temperature Profiles. J. Appl. Met. 21, 1346-1355
- Lenoble, J. and Brogniez, C. 1983: A Comparative Review of Radiation Aerosol Models. Contr. Atm. Phys., in press
- Megie, G. and Menzies, R.T. 1980: Complementary of UV and IR Differential Absorption Lidar for Global Measurements of Atmospheric species. Appl. Opt. 19, 1173-1183
- Megie, G., Cahen, C. and Flamant, P. 1983: Comments on 'A Theoretical Study of a Two Wavelength Lidar Technique for the Measurement of Atmospheric Temperature Profiles. J. Climate a. Appl. Met. 22, 1136

(+)

EN84 27203

A NEW TECHNIQUE FOR MONITORING THE
WATER VAPOR IN THE ATMOSPHERE

Harold D. Black and Arie Eisner
The Johns Hopkins University
Applied Physics Laboratory
Johns Hopkins Road
Laurel, MD 20707
(USA)

ABSTRACT

In correcting satellite doppler data for tropospheric effects, we have found that we can infer the precipitable water vapor (PWV) at the tracking site. The determination proceeds via a least-squares fit of a refraction parameter to each fifteen-minute pass of data.

For its success, the technique depends on having: 1) an ephemeris for the satellite, 2) an analytic model for the refraction range effect that is good to a few centimeters, 3) doppler (range difference or cycle count) data with noise level below 10 centimeters, and 4) a surface pressure/temperature measurement at the tracking site.

The PWV is a by-product of the computation necessary to correct the doppler data for tropospheric effects. We have tried for a number of years to reliably isolate the tropospheric refractive effect in the doppler shift measurement. It is only recently that we have succeeded in doing this. Our recent success was due to a formulation of the refraction integral which minimized the necessity for explicit water vapor, temperature and pressure profiles.

1. THE DOPPLER SHIFT AND THE REFRACTIVE EFFECT

A common and convenient model of the doppler shift measurement contains the range to the satellite at two contiguous times. These ranges are corrupted by tropospheric effects which can be written:

$$\Delta s = 10^{-6} \int (N_d + N_w) d\rho \quad (1)$$

wherein

N_d is the "dry" refractivity

N_w is the "wet" refractivity

The Smith-Weintraub expressions for these are:

$$N_d = 77.6 P/T$$

$$N_w = (3.73 \times 10^5 \text{ } ^\circ\text{K}^2/\text{mbar}) e/T^2$$

wherein

(e,T,P) are the (water vapor pressure, temperature total atmospheric pressure) at a point within the troposphere.
Units consistency requires e and P in millibars and T in $^\circ\text{K}$

Physical rigor (Fermat's principle) insists that the integration path be an extremum. Except at low elevation angles, this requirement is not important as ray-tracing studies show; we can use the instantaneous straight line connecting the satellite and observer for the integration path. If we then change variables from ρ to h (see Fig. 1), we obtain

$$\Delta s = 10^{-6} \int_0^{h_d} (N_d + N_w) \left[1 - \left(\frac{\cos E}{1 + h/\text{Re}} \right)^2 \right]^{1/2} dh \quad (2)$$

Since both the wet and dry troposphere extend to heights that are small compared to the radius of the earth, $h/\text{Re} < h_d/\text{Re} \approx 0.007$, we replace eq. (2) with

$$\Delta s = 10^{-6} \cdot I_{dw} \cdot \int_0^{h_d} (N_d + N_w) dh \quad (3)$$

wherein

$$I_{dw} \triangleq \left[1 - \left(\frac{\cos E}{1 + \chi_{dw} h_d/\text{Re}} \right)^2 \right]^{-1/2} \quad (4)$$

and

$$0 < \left| \chi_{dw} = \chi_{dw}(e,T) \right| < 1$$

ORIGINAL PAGE IS
OF POOR QUALITY

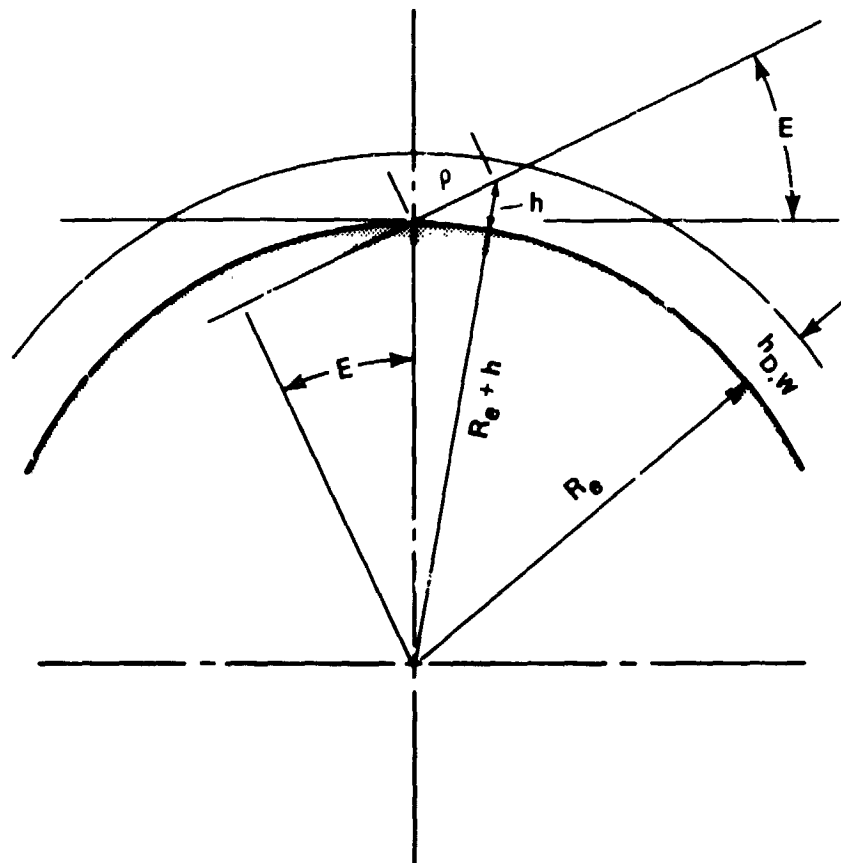


Fig. 1 Tropospheric geometry.

Using explicit models of N_d and N_w which, in turn, require models for the atmospheric state, we were able to show that eq. (3) and (4) could be written

$$\Delta s = \left[10^{-6} \int (N_d + N_w) dh \right] \cdot \left[1 - \left(\frac{\cos E}{1 + 0.001} \right)^2 \right]^{-1/2} \quad (5)$$

with an error which did not exceed a few centimeters if we do not use elevation angles less than 7.5° . Above 20° the form is practically exact, i.e., the error is, at most, a few millimeters.

Equation (5) is a convenient separation (amplitude . geometry), moreover, in the amplitude

$$\Delta s_h = 10^{-6} \int_0^{h_d} (N_d + N_w) dh \quad (6)$$

We have absorbed, "buried", the difficult problems of modeling the atmospheric state as a function of the surface conditions. We say 'difficult'; the water vapor is not uniformly distributed in the half space above the observing site, and modeling has fundamental limitations.

We used eq. (5) as a model of the tropospheric range effect and associated an amplitude, eq. (6), with each fifteen-minute pass of data. We fitted the amplitude without any a priori constraints on the value of Δs_h ; although we have, with a surface pressure measurement, a lower bound

(the dry effect = $10^{-6} \int_0^{h_d} N_d dh$) which is 85-90 percent of the

combined wet-dry integral. This dry integral is very closely 2.305 (meters) times the surface pressure in atmospheres. To isolate the tropospheric amplitude, we performed a four-parameter fit; the three additional parameters absorbed orbit, position and frequency biases.

2. RESULTS

We have used doppler data characterized as follows:

1. Obtained at a globally-distributed set of tracking sites from two of the Transit satellites, 30140 and 30180.

2. One two-day data span was obtained during February 1980 (days 48-49) and another during July 1982 (days 197-198). Each span contained approximately eighty passes.

Results of the amplitude fitting for days 197-198 are shown in Fig. 2. The lower bound, the straight line, is a consequence of the Hopfield theory (see Refs. 2 and 4). Data points falling below this straight line are "wild" (invalid). There are four of these. The distance from each of the valid data points to the straight line is the wet term

$$10^{-6} \int N_w dh$$

We then computed the mean value (for the valid data) at each of the sites; mean over two days for each of the two data sets. Four stations were represented in both data sets: Johannesburg, South Africa; Las Cruces, New Mexico; San Jose Dos Campos, Brazil; and Herndon, Virginia. The data at these four sites agree with the (usually true) finding that the atmosphere contains more water vapor in the summer than it does in the winter, Fig. 3. A tabulation of the results shown in Fig. 3 is given in Table 1. From Fig. 3 we see that synoptically the wet term is about 10 percent of the dry.

3. PRECIPITABLE WATER VAPOR

The 'wet' range integral for a vertical path can be written, using the Smith-Weintraub expression for the refractivity:

$$\Delta s_w = 0.373 \int_0^{h_d} \frac{e}{T^2} dh \quad (7)$$

and assuming the water vapor obeys the perfect gas law:

$$e = \rho_e RT \quad (8)$$

we have

$$\Delta s_w = 0.373 R \int \frac{\rho_e}{T} dh \quad (9)$$

and, in turn, a linear decrease of temperature with height facilitates an expansion in terms of the moments of the water vapor distribution.

$$\Delta s_w = \frac{0.373}{T_0} R \rho_w \left\{ \frac{1}{\rho_w} \int \rho_e dh + \frac{L}{T_0 \rho_w} \int h \rho_e dh + \dots \right\} \quad (10)$$

alternately,

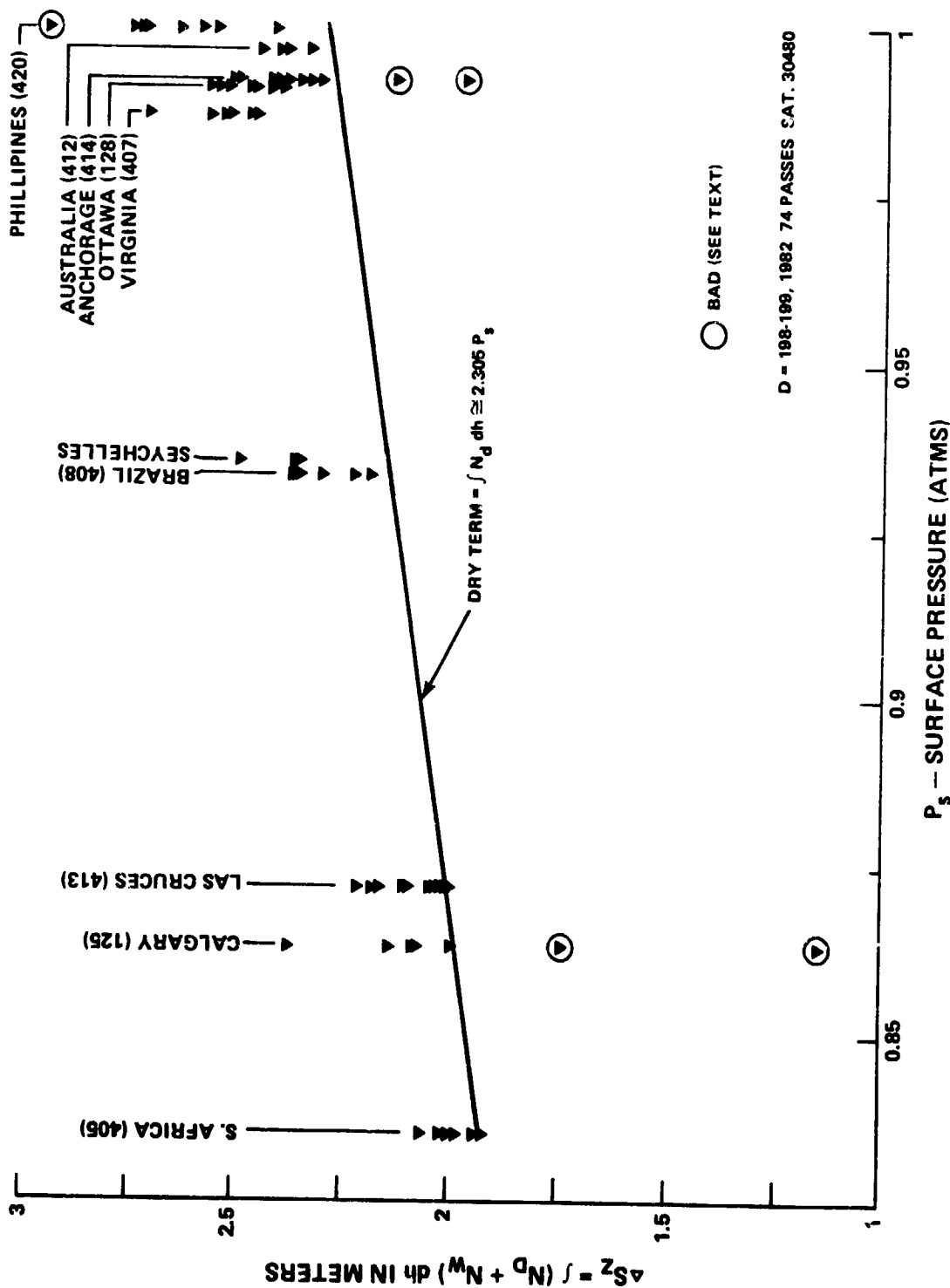


Fig. 2 Fitted tropospheric.

ORIGINAL PAGE 19
OF POOR QUALITY

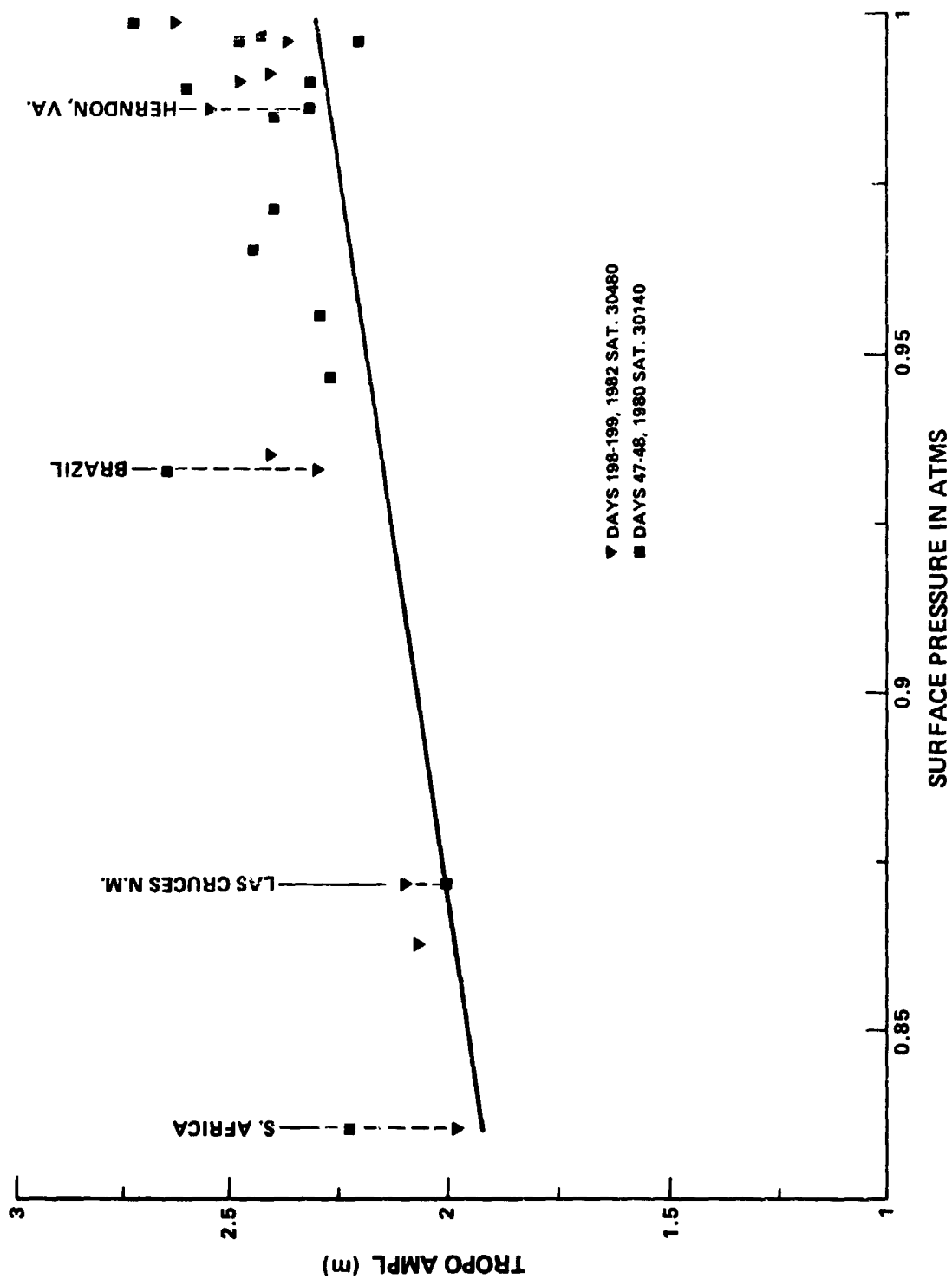


Fig. 3

Table 1
Troposphere Fitting Results

STATION	LATITUDE (DEGREES)	ALTITUDE (METERS)	SAT 30140		SAT 30480	
			FITTED TROPO D = 47.48 1980 METERS	No. OF PASSES	FITTED TROPO D = 198.199 1982 METERS	No. OF PASSES
414	ANCHORAGE, AL.	+61°			2.34 ± 0.16	11
125	CALGARY, CANADA	+51°			1.95 ± 0.37	8
021	BRUSSELS, BELGIUM	+51°		7		
128	OTTAWA, CANADA	+45°			2.47 ± 0.06	9
300	MINNESOTA, USA	+45°	2.40 ± 0.40	5		
641	FLORENCE, ITALY	+44°	2.45 ± 0.15	6		
313	MAINE, USA	+44°	2.60 ± 0.33	6		
407	HERNDON, VA	+39°	2.43 ± 0.12	6		
027	JAPAN	+39°	2.32 ± 0.12	8	2.54 ± 0.09	6
330	CALIFORNIA	+34°	2.32 ± 0.33	7		
113	N. MEXICO	+32°	2.27 ± 0.18	5		
413	N. MEXICO	+32°	2.00 ± 0.22	5		
192	AUSTIN, TEXAS	+30°	2.40 ± 0.30	6	2.10 ± 0.08	8
341	HAWAII	+21°	2.29 ± 0.24	4		
422	SAN MIGUEL, P.I.	+15°			2.67 ± 0.16	8
023	GUAM	+13°	2.48 ± 0.07	5		
420	SEYCHELLES, ISLAND	- 4°			2.55 ± 0.29	4
424	AMERICAN SAMOA	-14°	2.73 ± 0.17	4		
008	BRAZIL	-23°	2.65 ± 0.23	3		
408	BRAZIL	-23°			2.30 ± 0.08	6
105	S. AFRICA	-26°	2.23 ± 0.21	7		
405	S. AFRICA	-26°			1.98 ± 0.05	7
412	SMITHFIELD, AUSTRALIA	-34°			2.37 ± 0.05	8
019	ANTARCTICA	-78°	2.21 ± 0.31	6		
			2.39 ± 0.23	84	2.33 ± 0.23	75

☐ SUMMER
 ☐ WINTER

$$\Delta s_w = \frac{1.722 \times 10^3}{T_0} \left[\frac{1}{\rho_w} \int \rho_e dh \right] \left[1 + \frac{L h_{wv}}{T_0} \right]$$

ρ_w is the density of (liquid) water. T_0 is the surface temperature ($^{\circ}\text{K}$) and L is the (absolute value of the) temperature lapse rate ($\approx 6.5^{\circ}/\text{km}$), h_{wv} is the scale height of the water vapor in the atmosphere ($\approx 2.2 \text{ km}$). Each of the terms in the expansion, eq. (10), has units of height. The first term, the dominant one, is the "precipitable water vapor". The dimensionless term in front is about 6.0. It is precisely 6.0 for $T_0 = 287^{\circ}\text{K}$. The second term (the first moment in the expansion) is approximately 5 percent of the precipitable water vapor (Ref. 3). The second moment is a factor of ten less than the first. Consequently, we can, with surface temperature and pressure measurements, interpret our results for the (wet) range effect in terms of precipitable water vapor.

4. CONCLUDING REMARKS

In keeping with the spirit of this meeting, the significant findings from this study are:

1. It is possible to determine the total atmospheric water vapor using microwave doppler measurements. This measurement differs from the water vapor measurements made with radiosondes or with microwave radiometers. The latter two produce water vapor estimates along a profile through the atmosphere. The doppler technique produces a different sort of estimate; it is a 'bulk' estimate over that fraction of the troposphere swept out by the satellite-observer vector. Typically a region extending out to 150 km, on the satellite side of the observing site, will be sampled (see Ref. 1). Each of these kinds of measurements have their uses.

It would be interesting and useful to study the correlation between the different kinds of measurements. The data currently exists to do this.

2. It is possible to derive a model of the tropospheric range effect which is accurate to a few centimeters. The 'thinness' of the troposphere (compared with the radius of the earth) is an essential fact in developing the model. By model we mean one in which there is a clear separation of geometry on the one hand and an atmospheric-state-dependent amplitude on the other.

3. The tropospheric range amplitude is (demonstrably) separable from the other errors affecting the doppler shift. The accuracy with which the tropospheric range effect is isolated depends on the accuracy of the modeling and the noise level of the data. The existing data noise is about 10 cm (in range difference), and we are currently unable to fully exploit the accuracy implicit in the theory.

It is easily within the current state-of-the-art to build satellites and ground equipment which will reduce the noise level of the data. Equally important for these purposes would be raising the frequency pair from 150/400 MHz to (say) 400/1200 MHz to reduce the higher order ionospheric effects in the data.

5. REFERENCES

Black, H.D., 1978: An easily implemented algorithm for the tropospheric range correction. J. Geophys. Res., Vol. 83 (E4).

Goldfinger, A.D., 1980: Refraction of microwave signals by water vapor. J. Geophys. Res., Vol. 85 (C9).

Hopfield, H.S., 1971: Tropospheric effect on electromagnetically measured range: Prediction from surface weather data. Radio Science, Vol. 6, No. 3, pp. 357-367.

This paper is a synopsis of: Black, H.D., and Eisner, A., 1983: Correcting satellite doppler data for tropospheric effects. APL/JHU Report SDO-6777. Also in press in the J. Geophys. Res.

CASE STUDIES OF NOAA 6/TIROS N DATA IMPACT ON NUMERICAL WEATHER FORECASTS

Leonard M Druyan
Dept. of Geography, Bar Ilan University
Ramat Gan, Israel

Zvi Alperon and Tamar Ben-Amram
Israel Meteorological Service, Bet-Degan, Israel

1. INTRODUCTION

The impact of satellite temperature soundings on numerical forecasts was reviewed by Ohring(1979) who summarizes that "The small average impact obtained is the result of a combination of positively influenced and negatively influenced forecasts and not the result of a consistent impact on each forecast." Moreover, "The small effect of the satellite data is also evidenced by almost all qualitative and synoptic evaluations of their impact." This appraisal has been sustained by Atlas et al.(1982) who determined by subjective evaluation of numerical prognostic maps that a significant improvement due to the assimilation of satellite data into the initial specification resulted in only a very small proportion of their case studies.

The above refers to the impact of satellite temperatures from systems which pre-date the launching of the third generation of vertical sounding instruments aboard TIROS N (13 Oct 1978) and NOAA 6 (27 June 1979). The first evaluation of soundings from TIROS N was reported by Phillips, et al.(1979) who found that oceanic, cloudy retrievals over NH mid-latitudes show a cold bias in winter. Gruber and Watkins(1982) confirmed this for both satellite systems using a larger data base. They also showed that RMS differences between retrievals and co-located radiosonde observations within the swath 30-60N during the 1979-80 winter were generally 2-3K in clear air and higher for cloudy columns. This implies approximately the same error level as that summarized by Ohring(1979) for previous sensors.

Broderick(1980,1981) has reported two case studies which show a positive impact of TIROS N temperatures on the analysis of synoptic weather systems. In both cases analyses prepared from only satellite temperatures seemed to give a better definition to weather systems' thermal structure than that provided by corresponding NMC analyses without satellite data.

Thomasell, et al.(1983) summarized the results of a set of 14 numerical forecast experiments performed with the PE model of the Israel Meteorological Service (IMS); these were designed to test the impact of TIROS N and NOAA 6 temperatures within the IMS analysis and forecast cycle. Their study discusses the satellite data coverage over the NH, the mean area/period SI and RMS verification scores and the spatial distribution of SAT versus NO SAT forecast differences. They find mixed results regarding the benefit derived from the satellite data although they conclude that positive forecast impact does occur over ocean areas where the extra data presumably improves the specification which is otherwise available from conventional observations.

Broderick(1983a,b,c) examined the forecast impact for three cases from the same set of experiments (1-14 Jan 1980). In one he found that satellite temperatures, some of dubious quality, observed over the Atlantic Ocean contributed to better forecasts over Iceland and central Europe although a worse result was verified over Spain. The second study showed that the better scores of a forecast based also on satellite data and verified over North America actually represented a mixed impact on the forecast synoptic patterns. His third case shows a superior 48hr 500 mb forecast over the western US due to the better initial specification afforded by satellite-observed temperatures over the north Pacific Ocean.

2. EXPERIMENTAL DESIGN

This report describes three case studies of satellite temperature impact (from NOAA 6 and TIROS N) on analyses and forecasts made by the IMS. The first of these is from the same group of experiments described above, the second is from another series (6-30 Jan 1979) which is during the special FGGE observing period and the third is from the series made for the period 20-27 Dec 1979. The experiments were made as part of a cooperative study in which NESDIS provided temperature retrieval data to the IMS; results are being analyzed both in Israel and at NESDIS. Satellite data observed over water and over north Africa were assimilated into the IMS objective analysis routine to create the initial conditions for 48hr numerical SAT forecasts by the IMS model. Analyses were made in parallel from non-satellite data sources and these initialized the NO SAT forecasts with which the first kind were eventually compared. The IMS model simulates atmospheric circulation by solving the primitive equations at five vertical levels on a cartesian grid (380km interval) which covers most of the NH. The model does not simulate the hydrological cycle nor does it account for diabatic heating.

3. CASE 1, INITIAL CONDITIONS 12GMT 13 JAN 1979

Figure 1 shows the significant differences in the initial conditions of the SAT and NO SAT analyses. The initial 1000-500mb thicknesses show that the satellite temperatures (observed within a time window of +3hr) have introduced a rather cold tongue over the central Atlantic Ocean which lowers thicknesses there by 60-90m as compared with NO SAT. This area is southeast of a 500mb vorticity maximum evident on both analyses (figures 2A, 2B) and it creates a sharper trough oriented northwest-southeast near 40W in the SAT specification. This also creates a broader area of positive vorticity advection (PVA) south of about 47N for the SAT atmospheric state at the hour of these initial conditions.

South of Newfoundland (30-40N, 55W) satellite temperatures have defined warmer thicknesses (figure 1) which are as much as 120m greater than those in the counterpart analysis. As a result, NO SAT puts a 500mb trough at 51W while SAT shows a shallower wave further east (figures 2A, 2B).

Large differences in the 48hr 500mb forecasts are outstanding over the eastern Atlantic Ocean. Additional penetration of the SAT cold tongue has brought a sharp 500mb trough to 20-25W while NO SAT predicts a shallow wavesome 10° longitude further east (figures 3A, 3B). The SAT forecast heights along the trough axis (between 39-49N) are more than 180m lower than those predicted by NO SAT. The verification analysis (figure 3C) shows that the deepening of the trough by SAT north of about 40N is exaggerated giving heights 150m too low. NO SAT forecasts more reasonable heights but shows no indication of the troughing observed

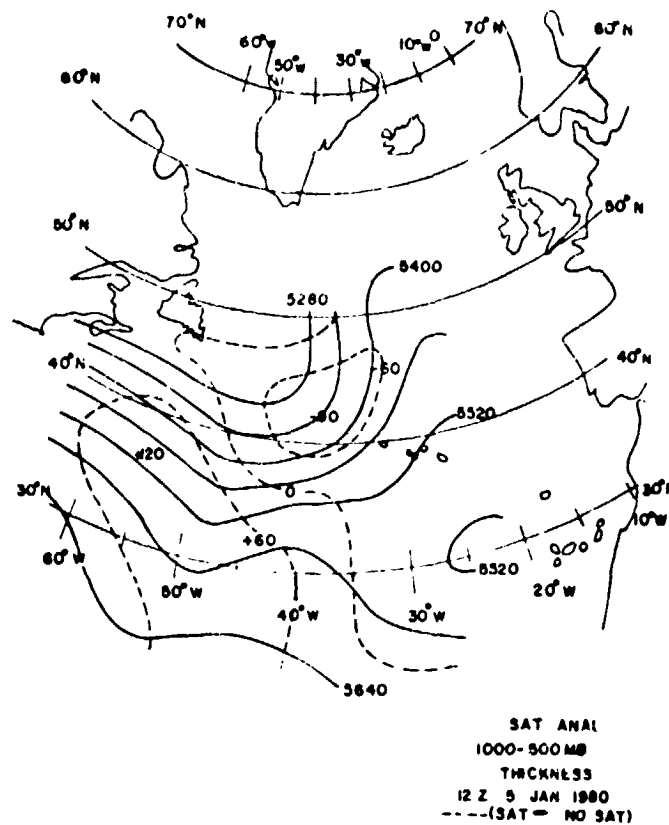


Fig. 1. Initial 1000-500 mb thickness and differences from NO SAT.

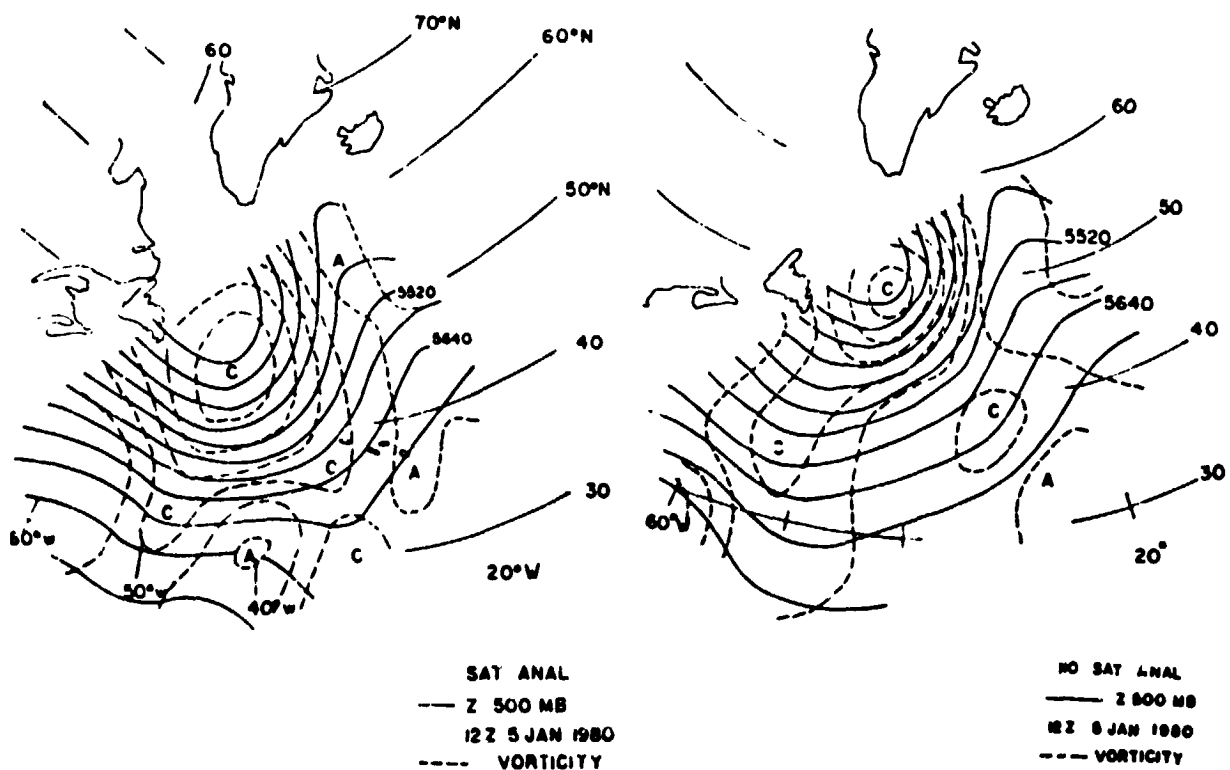


Fig. 2A. Initial 500 mb heights and vorticity for SAT.

Fig. 2B. Initial 500 mb heights and vorticity for NO SAT.

ORIGINAL PAGE 19
OF POOR QUALITY

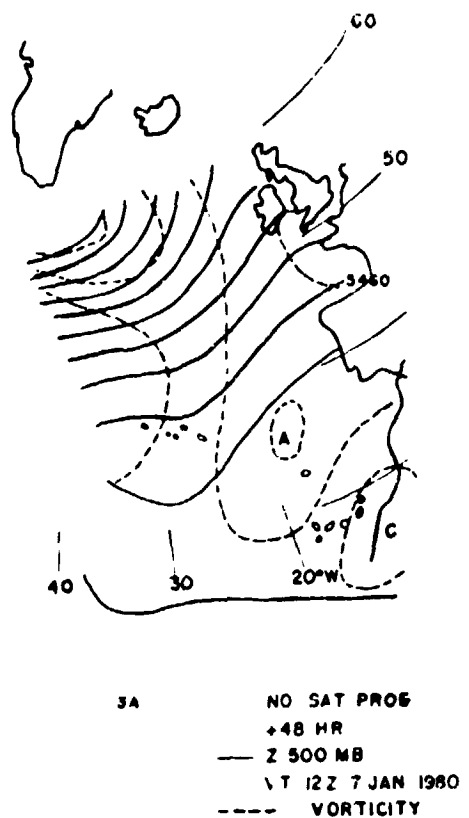


Fig. 3A. 48 hr 500 mb height and vorticity forecast for NO SAT.

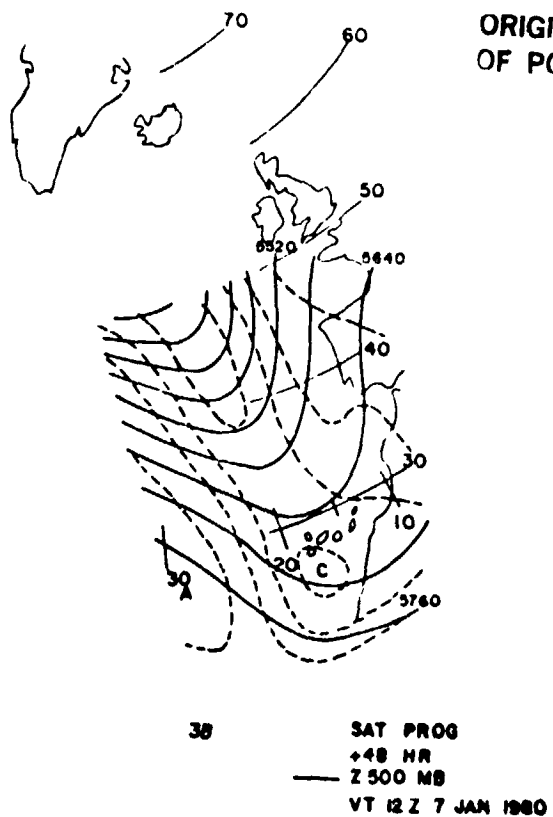


Fig. 3B. 48 hr 500 mb height and vorticity forecast for SAT.

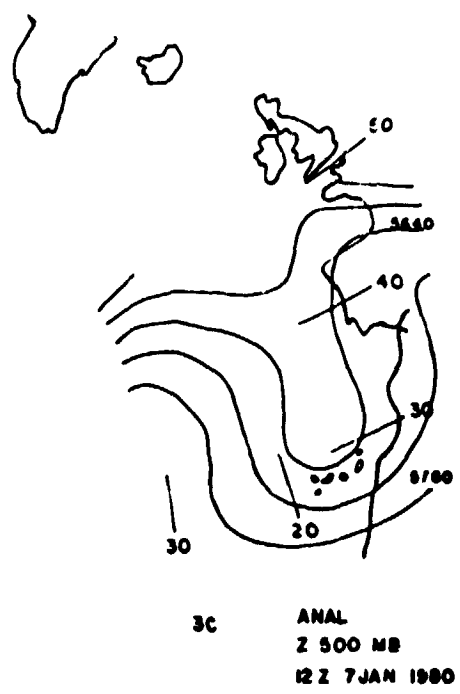


Fig. 3C. Verification 500 mb analysis for 48 hr forecasts.

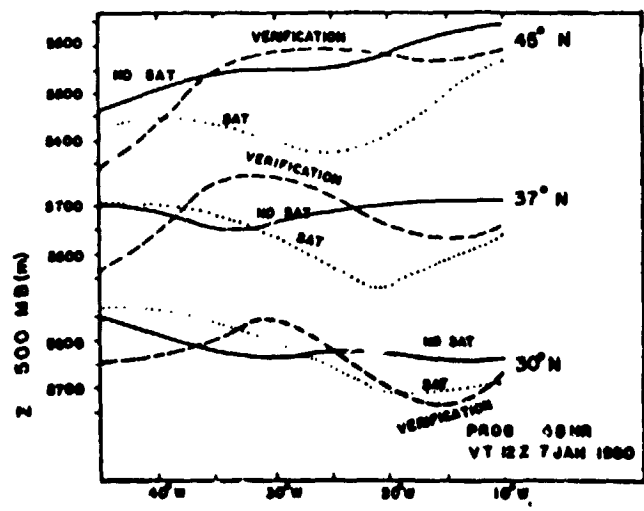


Fig. 4. Longitudinal cross-sections of NO SAT and SAT 48 hr forecasts of 500 mb height versus verification values at selected latitudes.



at 15W. Further south, however, the SAT 500mb prog is clearly superior. It forecasts the trough quite close to its analyzed longitude and correctly places its apex in the vicinity of the Canary Islands where it forecasts a vorticity maximum in contrast to the NO SAT forecast of negative vorticity advection there and a vorticity minimum where the trough ought to be, north of the islands. The NO SAT trough instead lags to the west by some 13° longitude. Over the coastal waters of northwest Africa the SAT prog is within 30m of the verification while the NO SAT is more than 110m too high. Figure 4 shows height-longitude cross-sections of the 48hr forecast and analyzed 500mb pressure surface for three representative latitudes. This depiction emphasizes the spurious deepening of the SAT forecast in the northeast alongside the positive impact over the southeast. The positive impact can be related to the initially greater PVA at low latitudes ahead of the short wave (figure 2A, 48h) due to the inclusion of satellite temperatures in the initial specification. It is interesting to note that surface observations report some shower activity and Cb clouds at the southern end of the trough, weather more consistent with the SAT prog.

4. CASE 2, INITIAL CONDITIONS 12CMT 13 JAN 1979

In the series of experiments from which this case was taken, satellite temperatures observed from 3hr before to 6hr after synoptic time were assimilated to create SAT initial conditions. The wider window was necessary to assure adequate satellite coverage over the Atlantic Ocean. In the case at hand, dense coverage was obtained west of 50W with the result of changing the position and structure of a cold tongue southeast of Newfoundland. Colder satellite temperatures downstream (up to 100m in thickness colder) defined a new axis position which is northeast of the NO SAT position. Moreover, satellite thicknesses are up to 120m warmer to the rear of the trough making the SAT version sharper. The SAT initialization therefore changes the trough position and also decreases its wave length giving it a higher vorticity maximum.

After 48hr the Atlantic trough is oriented north-south along about 27.5W. Positive vorticity advection has moved eastward to the south of Iceland and the downstream ridge is at 0° longitude over the North Sea, slanting SSE across the British Isles to Spain. At sea-level the coastal ridge reaches from Scandinavia to central Europe. The cyclonic vorticity over the northern part of the ocean tilts to the northeast down to an open sea-level pressure trough from Iceland to Scotland.

The NO SAT 48hr 500mb forecast erroneously predicts a strong ridge from Greenland to Iceland to the southeast Atlantic. This happens to be the verified position of the trough! The northern British Isles, which should be downstream or an approaching trough are instead kept under the fair-weather downstream side of the upper ridge and directly under the sea-level ridge. Here the Atlantic trough is forecast along about 40W aloft and about 25W at sea-level.

The SAT prog is better in several important respects. Although here too the northern part of the forecast ridge lags too far west, its predicted position over the British Isles is fairly accurate and its sea-level ridge is correctly moved eastward so that the area of the British Isles verges on approaching cyclonic flow. The difference in the forecasts is a consequence of the accelera-

tion eastward of the SAT trough and ridge system during the first 24hr of the forecast. The phase difference between the two forecast modes explains why ridging was replaced by troughing west of the British Isles in the SAT prog and not in its counterpart.

The different circulation forecasts imply different weather forecasts for the British Isles. The weather over the British Isles at the time of the initial conditions was fair due to a sea-level high pressure system which was under an area of likely subsidence east of the upper ridge axis. As the anticyclonic system drifted eastward, southwest England and Ireland came under the influence of over-running from an approaching warm front advected by the southwest flow west of the upper ridge line. Rain was already observed ahead of the front by 06GMT 14 Jan and it spread to northern England and Scotland within the next 24hr. The analyses show that the warm front moved northeastward ahead of the strong southwesterlies aloft and was positioned under the 500mb ridge axis which also marked the western boundary of a large 500mb temperature gradient. The advantage offered by the SAT prog which correctly brings the ridge line to the British Isles by 14 Jan, while the NO SAT fails to do this even by 15 Jan, is that it provides the guidance for a superior weather forecast. The correct association of the warm front and its precipitation pattern with the upper ridge axis in the initial conditions could have led to a correct forecast of rain onset on 14 Jan based on the SAT prog but not the NO SAT.

In this case the satellite data responsible for the positive forecast impact were observed over the Atlantic Ocean 5½hr after the synoptic time. Since the cold tongue was moving eastward quality temperature observations from more than 5hr after the designated time of initialization should have "seen" the trough further downstream than the analysis constructed from the first guess field plus a sparse coverage of radiosonde observations. It is therefore difficult to separate the impact from satellite data per se from any advantage realized by blending late data into the analysis in a synoptically sensitive region. Either way the satellite's advantage as a source of time-continuous data is demonstrated.

5. CASE 3, INITIAL CONDITIONS 12G 21 1979

Comparison of the 1000-500mb thickness patterns of the initial conditions shows that the satellite data defined warmer conditions in the lower troposphere over much of the Atlantic Ocean. A swath of satellite observed temperatures taken very close to the synoptic time initialized the thicknesses some 60-100m higher than in the NO SAT analysis over a large area southeast of Newfoundland and some 60-90m higher near southern Greenland. These differences between the SAT and NO SAT initial conditions occur on the eastern flank of a cold trough which extends from northeast Canada southward to the western Atlantic. The higher thicknesses east of the trough in the SAT version make the cold tongue sharper and move it slightly west of the NO SAT position, especially southwest of Greenland. The cyclonic curvature is somewhat flattened in the NO SAT representation near southern Greenland.

The verification after 48hr shows development of the trough into a deep baroclinic system near southeast Greenland. A sea-level low is analyzed just west of Iceland and is reflected aloft by the sharp 500mb trough slightly further west and oriented north-south along 35°. East of this trough strong southwesterly flow overlies surface northwesterlies indicating strong cold advection from 35W to 20W. Still further to the east, northwest of the British Isles, the pattern

changes to one of weak warm advection.

Neither system predicts the sea-level cyclone near Iceland and this undoubtedly reflects an inadequacy of the numerical model. Similarly, the model does not predict a very sharp trough at 500mb. However, the SAT prog does show a somewhat broader trough slightly downstream of the analyzed position. The NO SAT prog, on the other hand, predicts an even less sharp trough which is much too far east. Its heights are up to 350m too low in this region while the SAT errors do not exceed 200m.

The NO SAT 48hr sea-level prog shows a sharp trough east of its upper-air position; it is predicted to have traversed Scotland leading a wedge of cold air advection which is therefore forecast over the northern British Isles. Observations show that this area is far ahead of the cold air at the verification time and the cold front actually reaches the British Isles only a day later. The more upstream position of the SAT forecast upper trough finds similar expression in its 48hr sea-level prog. Here, the cold air advection zone, while some 10° longitude too far east, nevertheless reaches only to about 8W; this predicted cold front bisects Ireland but the prog keeps the cold air west of Scotland. One practical impact of the satellite data is therefore the delay in the forecast incursion of cold air over the northern British Isles.

In summary, satellite observed temperatures apparently corrected the too cold initial NO SAT specification east of a major trough system over the Atlantic. The poorer specification combined with model inadequacies caused a more rapid propagation of vorticity than observed. Moreover, the larger zonal component of the upper flow produced a more tilted and faster moving wedge of cold air whose predicted arrival over the British Isles was about 24hr too early. Although the SAT forecast showed the symptoms of the model error, its better initial specification mitigated the timing error leading to a superior 48hr forecast.

6. CONCLUSIONS

The study has shown several examples of the impact of NOAA 6 and TIROS N temperature observations on IMS numerical circulation forecasts. Impacts were traced to the differences that the satellite data made in the initial specification of the atmospheric state. The differences in the progs were shown to be an improvement over several geographic areas and to constitute a degradation over at least one area. These case studies support the previous finding that the ocean areas offer the greatest potential for positive impact and we would add the requirement that the enhanced specification be made over synoptically sensitive areas. Impacts in the circulation progs was shown to constitute significantly different weather forecast guidance. The potential for satellite temperatures in numerical forecasting should be studied via their impact when and wherever their error statistics can be documented.

7. ACKNOWLEDGEMENTS

The research was supported by the Office of Climate and Atmospheric Research, NOAA. The research contract was administered in Israel by Tel-Aviv University.

ORIGINAL PAGE 13
OF POOR QUALITY

8. REFERENCES

- Atlas, R., M. Chil and M. Halem, 1982: The effect of model resolution and satellite sounding data on GLAS model forecasts. Mon. Wea. Rev. 110, 662.
- Broderick, H., 1980: Structure of a baroclinic zone using TIROS-N retrievals. Preprint Volume, 8th Conf. on Weather Forecasting & Analysis(AMS).
- _____, 1981: The impact of TIROS-N soundings on the analysis of a cyclone. Preprint Volume: 5th Conf. on Numerical Weather Prediction(AMS).
- _____, 1983a: A case study of the impact of satellite temperature soundings on an analysis/forecast system. NESDIS, unpublished.
- _____, 1983b: Case of 12GMT Jan 8, 1980- Europe impact. NESDIS, unpublished.
- _____, 1983c: Case of 12GMT Jan 11, 1980- North America Impact. NESDIS, unpublished.
- Gruber, A. and C. Watkins, 1982: Statistical assessment of the quality of TIROS-N and NOAA-6 satellite soundings. Mon. Wea. Rev. 110, 867.
- Ohring, G., 1979: Impact of satellite temperature sounding data on weather forecasting. Bull. Amer. Meteor. Soc. 60, 1142.
- Phillips, N., L. McMillin, A. Gruber and D. Wark, 1979: An evaluation of early operational temperature soundings from TIROS-N. Bull. Amer. Meteor. Soc. 60, 1188.
- Thomasell, Chang, Wolfson, Gruber and Ohring, 1983: The impact of satellite soundings and their distribution on forecast accuracy. NESDIS, unpublished.

THE IMPACT OF SATELLITE TEMPERATURE SOUNDINGS
ON THE FORECASTS OF A SMALL NATIONAL METEOROLOGICAL SERVICE

Noah Wolfson¹, Albert Thomasell, Zvi Alperson², Harold Brodrick,
Jy-Tai Chang³, Arnold Gruber, and George Ohring
National Environmental Satellite, Data and Information
Service, NOAA
Washington, D.C. 20233

ABSTRACT

The impact of introducing satellite temperature sounding data on a numerical weather prediction model of a small national weather service is evaluated. The Israel Meteorological Service model, a dry, 5-level, primitive equation model covering most of the Northern Hemisphere, is used for these experiments. Series of parallel forecast runs out to 48 hours are made with three different sets of initial conditions: 1) NOSAT runs, in which only conventional surface and upper air observations are used, 2) SAT runs, in which satellite soundings are added to the conventional data over oceanic regions and North Africa, and 3) ALLSAT runs, in which the conventional upper air observations are replaced by satellite soundings over the entire model domain. The impact on the forecasts is evaluated using three verification methods: 1) RMS errors in sea level pressure forecasts, 2) systematic errors in sea level pressure forecasts, and 3) errors in subjective forecasts of significant weather elements for a selected portion of the model domain. For the relatively short range (<48 hours) of the present forecasts, the major beneficial impacts on the sea level pressure forecasts are found precisely in those areas where the satellite sounding are inserted and where conventional upper air observations are sparse - i.e., the oceanic areas. Both the RMS and systematic errors are reduced in these regions. The subjective forecasts of significant weather elements are also improved with the use of the satellite data. Of special interest is the result that the ALLSAT forecasts are of a quality comparable to the SAR forecasts.

¹National Research Council Research Associate

²Israel Meteorological Service, Bet-Dagan Israel

³Systems and Applied Sciences Corporation

ABSTRACT

The impact of introducing satellite temperature sounding data on a numerical weather prediction model of a small national weather service is evaluated. The Israel Meteorological Service model, a dry, 5-level, primitive equation model covering most of the Northern Hemisphere, is used for these experiments. Series of parallel forecast runs out to 48 hours are made with three different sets of initial conditions: 1) NOSAT runs, in which only conventional surface and upper air observations are used, 2) SAT runs, in which satellite soundings are added to the conventional data over oceanic regions and North Africa, and 3) ALLSAT runs, in which the conventional upper air observations are replaced by satellite soundings over the entire model domain. The impact on the forecasts is evaluated using three verification methods: 1) RMS errors in sea level pressure forecasts, 2) systematic errors in sea level pressure forecasts, and 3) errors in subjective forecasts of significant weather elements for a selected portion of the model domain. For the relatively short range (≤ 48 hrs) of the present forecasts, the major beneficial impacts on the sea level pressure forecasts are found precisely in those areas where the satellite soundings are inserted and where conventional upper air observations are sparse - i.e., the oceanic areas. Both the RMS and systematic errors are reduced in these regions. The subjective forecasts of significant weather elements are also improved with the use of the satellite data. Of special interest is the result that the ALLSAT forecasts are of a quality comparable to the SAT forecasts.

1. INTRODUCTION

The concept of radiometric sounding of atmospheric temperature profiles was first demonstrated with data gathered by infrared spectrometers on the Nimbus-3 satellite in 1969. Operational satellite soundings over oceanic areas were introduced by the VTPR (Vertical Temperature Profile Radiometer) instrument on the NOAA-2 satellite in 1972. Since 1979 (Smith et al 1979) the operational sounding system has been the TOVS (TIROS Operational Vertical Sounder) on the polar orbiting TIROS-N series of satellites. Early evaluations of the impact of satellite temperature soundings on numerical weather predictions showed only marginal improvements, except for the Southern Hemisphere, where, because of the sparsity of conventional observations, significant improvements were noted. More recent studies are somewhat more encouraging, Bengtsson et al., (1983) Halem et al., (1983).

Most previous evaluations of the impact of satellite soundings on weather forecasts have been based upon forecast models used by the larger meteorological services of the world. In the present study we examine the impact of satellite temperature soundings on the numerical predictions of a rather small national weather service - the Israel Meteorological Service (IMS). In addition to an evaluation of the impact on the forecast atmospheric flow field, we also evaluate the impact on subjective forecasts of actual surface weather elements. Preliminary results were reported by Thomasell et al., (1983) and Wolfson et al., (1983).

2. ANALYSIS PROCEDURE

2.1 Experimental Design

The experiment was performed with the Israel Meteorological Service numerical weather prediction model, which is a dry, 5-level, primitive equation model. It operates at 5 sigma levels defined on an octagonal polar stereographic grid of 1844 points covering a large part of the northern hemisphere. The grid is aligned with 5°W longitude, is offset from the North Pole toward the Mediterranean Sea, and has a grid mesh of 360 km, true at 60°N. The integration domain is shown in figure 1. The model uses a 10-minute time step. The forecast variables are wind, absolute temperature and surface pressure. Geopotential is computed through temperature. Initial conditions, produced by a Cressman-type analysis (1959) scheme, comprise height and temperature at ten mandatory pressure levels from 1000 mb to 100 mb, plus surface pressure. Balanced winds are computed from the heights. For input to the model, the analyses are interpolated to the 5 sigma surfaces, and for display, the information is interpolated back to pressure coordinates. In these experiments, the analysis procedure used a 12-hour old analysis for a first guess. Conventional data for this model comprise radiosonde observations and standard surface and ship observations. Parallel forecast runs were made with the model with three different sets of upper air data providing initial conditions. For the NOSAT experiment the upper air data comprise conventional rawinsonde data, for the SAT experiment satellite sounding data are added, and for the ALLSAT experiment the conventional rawinsonde data are excluded.

For the SAT experiment satellite sounding data were introduced over the oceanic areas and over the North-African continent, where they supplemented sparse conventional data. For the ALLSAT experiment, satellite data were used over all of the area covered by the IMS model. All runs included sea level pressure as observed by the synoptic stations and ships. No aircraft or satellite-derived winds were used. As a result of this configuration of the operational system, the initial sea level pressure maps are identical for all experiments.

The model was run in the form indicated in Table 1 for up to 48 hours. The forecast fields were available for 12, 24, 36, and 48-hour projections. Data sets were available for three different time periods and the details for each experiment are given in Table 1. In each experiment the NOSAT forecast errors provided the reference against which SAT or ALLSAT forecast errors were compared.

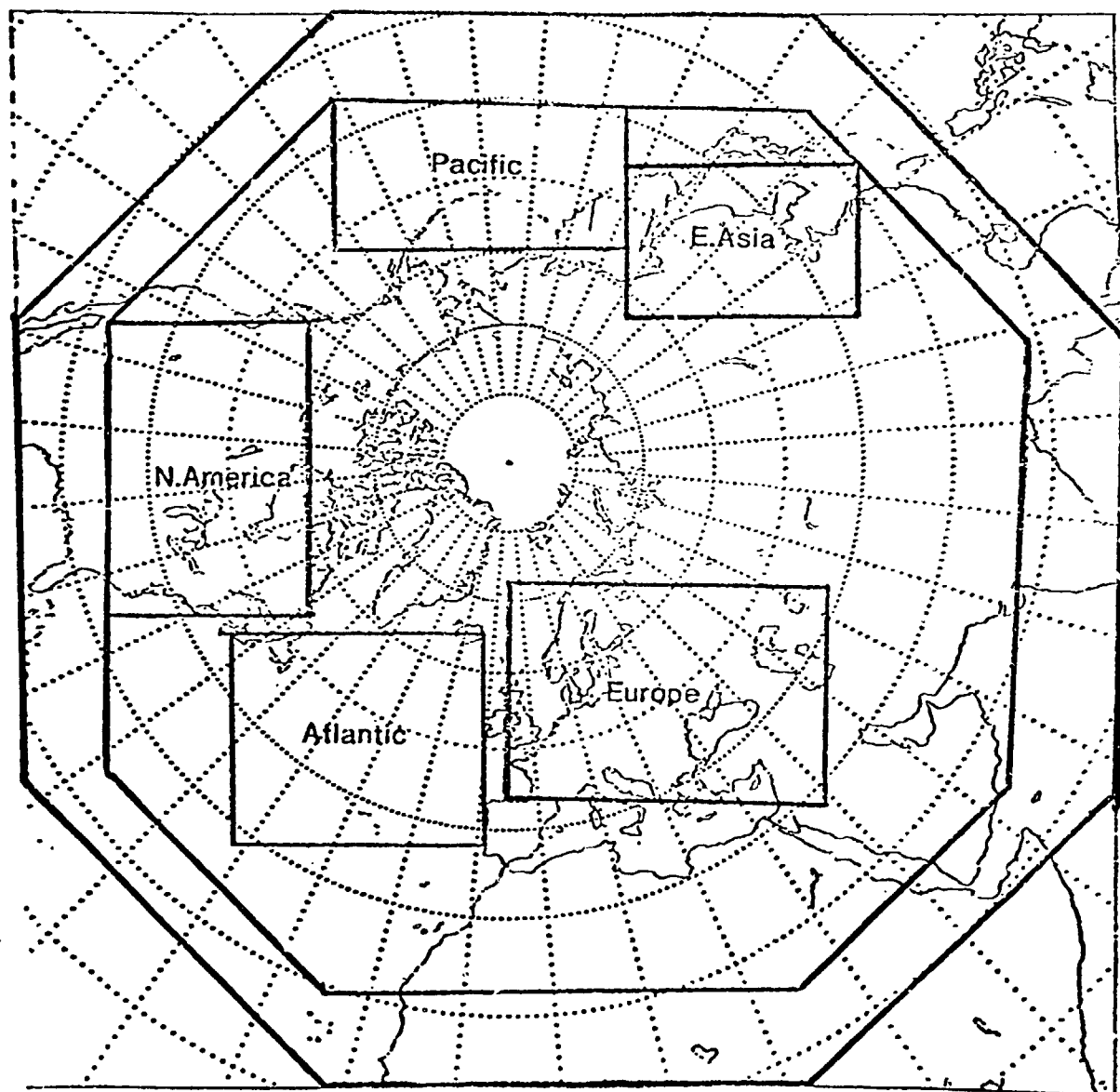


Fig. 1.

Areas covered by Israel Meteorological Service numerical weather prediction model (outer octagon) and areas (rectangles) used for verification.

Table 1: Characteristics of the different experiments

Experiment No.	Period	Number of Satellites	Time Window for Satellite Data Insertion (HR)	Forecast Initial Time(GMT)	Experiment Type
1	1-12 Jan 1980	2	± 3	00, 12	SAT
2	15-23 Jan 1979	1	-3, + 6	12	SAT
3	20-25 Dec 1979	2	± 3	12	SAT
4	1-12 Jan 1980	2	± 4.5	12	ALLSAT
5	20-25 Dec 1979	2	± 4.5	12	ALLSAT

The time window (around analysis time) for the introduction of satellite data in the January 1980 and December 1979 data sets, when two operational satellites were available, was set to ± 3 hours. This time range was considered to be a practical one for an operational system. It resulted in good data coverage for the western Atlantic for all the runs; however, the eastern Atlantic was only partially covered by satellite data at 12 GMT, and was not covered at all at 00GMT. Since, in regions of no observations the 12-hour old analysis defines the current analysis, a 12 hr discontinuity in the data was created along a line roughly north-south in the middle Atlantic. The time window for including satellite data in the January 1979 (experiment 2) data set, -3 to + 6 hours, was chosen to get enough data from the one available satellite to provide adequate coverage for the eastern Atlantic ocean. The time window for the ALLSAT runs (experiments 4 and 5) was set to ± 4.5 hours. This resulted in nearly complete coverage of the model domain by the two-satellite system.

This paper will present and discuss results only of the impact on the sea level pressure forecasts. It is felt that, because of sparse radiosonde coverage over the oceans and the short range of the forecast, most of the impact should be found over the oceanic areas. At sea level, pressure is fairly well observed over the oceans; this allows the forecast fields to be verified with confidence there.

3. RESULTS

3.1 RMS analysis

The forecast sea level pressure fields were compared with their correspond-

ing verifying analysis fields and RMS differences were calculated for each of the five verification regions for each of the five experiments, for forecast periods of 24 and 48 hours. These areas are presented in figure 1. The RMS differences for 48 hr are presented in Table 2, where a negative sign means that satellite data result in a beneficial impact. To help determine which numbers are significant, Student's t test was applied. We have adjusted the numbers of degrees of freedom to account for the statistical dependence of consecutive days.

Table 2: Average difference (SAT or ALLSAT -Minus NOSAT) RMS errors of 48 hour sea level pressure forecasts. Negative values indicate beneficial impact of satellite data. Statistically significant values at the 95% confidence level are underlined.

Exp.	Exp. period	Exp. type	E. Asia	Europe	N. America	Pacific O.	Atlantic O.
1	1-12 Jan 1980	SAT	<u>-0.5</u>	-0.1	0.1	<u>-1.7</u>	<u>-1.1</u>
2	15-23 Jan 1979	SAT	<u>-1.4</u>	<u>-1.0</u>	0.1	<u>-2.7</u>	<u>-0.8</u>
3	20-25 Dec 1979	SAT	-0.1	<u>-0.6</u>	-0.2	<u>-1.9</u>	<u>-1.1</u>
4	1-12 Jan 1980	ALLSAT	0.2	0.3	<u>0.8</u>	-1.2	-1.0
5	20-25 Dec 1979	ALLSAT	<u>-2.5</u>	-0.5	-0.2	<u>-5.7</u>	<u>-1.0</u>

3.1.1 Experiments 1, 2, and 3, -SAT experiments

Table 2 clearly shows that consistently beneficial impacts are found over the oceanic regions. For the Pacific Ocean the average reduction in RMS error is about 2 mb; for the Atlantic region the reduction is about 1 mb. The impacts over the continental verification areas are smaller but still beneficial, except for North America where there is no significant impact. Western North America is very close to the model boundary and accurate representation of synoptic systems and especially jet-streams from westerly and southerly directions is difficult. Of the first three experiments, only experiment 2 had satellite data in the eastern Atlantic; note the improved impact over Europe in this experiment. The results indicate that for these relatively short forecasts the largest impact is located over the oceanic regions, where the satellite data are inserted and where conventional observations are scarce.

3.1.2 Experiments 4 and 5 - ALLSAT experiments

Experiments 4 and 5 are all satellite data experiments. They examine the possibility of utilizing only satellite soundings for upper air observations, i.e. no radiosonde observations are used; however surface data are required to provide a reference level for the satellite soundings. The results are presented in Table 2.

Table 2 shows that over the oceanic areas the ALLSAT shows lower RMS errors than NOSAT. The improvement is more apparent over the Pacific Ocean than over the Atlantic Ocean. The results over the continental areas are mixed. For January 1980 they show up to a 1 mb increase in the RMS versus NOSAT and SAT, but for December 1979 an improvement is observed over East-Asia Europe and North America.

3.2 Systematic errors

This section deals with the geographic distribution of the systematic error of the numerical forecast model used in these experiments, and the impact of satellite data on the systematic error. The mean or systematic forecast error at a gridpoint p is given by

$$\bar{E}_x(p) = \frac{1}{N} \sum_{n=1}^N (\bar{X}_f(p, n) - \bar{X}_a(p, n)) \quad (1)$$

where \bar{X}_f and \bar{X}_a are the forecast and the verifying analyzed values, respectively, and N is the sample size or number of maps over which the average is calculated. It is easily seen that

$$E_x(p) = \bar{X}_f(p) - \bar{X}_a(p), \quad (2)$$

and that a field of systematic errors may be computed as the difference between the average forecast field and the average verification analysis. The importance of analyzing systematic errors lies in the fact that the sources for this error can usually be identified and even treated.

The systematic errors and their differences were calculated for all five experiments. The Student t test at the 95% confidence level was used to determine significance. From an examination of the results from all our experiments (not shown), the following can be stated:

- (a) Most of the impact is positive (i.e., beneficial)
- (b) Impact was found in or very close to those areas where satellite data had been inserted.
- (c) Most of the statistically significant impact areas are associated with the presence of well developed lows e.g., the Icelandic or Aleutian lows. The impact is usually found to the southeast of the centers of those average systems.
- (d) The magnitude of the impact over the Atlantic Ocean is smaller than that over the Pacific.

The above results suggest that the statistically significant (95% confidence level) contribution of the satellite data in reducing the systematic error is realized in the area of active weather systems. This is physically reasonable, since we expect that the satellite data, although noisier than conventional rawinsonde observations (Gruber and Watkins, 1982) do have the capability of delineating the large horizontal temperature structure typically associated with active weather systems. Thus the signal to noise ratio is large enough to result in significant reduction of the systematic error.

It was also found that negative impact occurs in areas of time discontinuity in the data.

Such discontinuities can occur on the border lines:

- 1) between those areas where satellite data are inserted and those areas which are not updated by either satellite or conventional observations,
- 2) between neighboring swaths of observations taken by different satellites at different times.

4. SUBJECTIVE WEATHER FORECASTING

One disadvantage of the RMS measure of accuracy is that there is not a direct correspondence between reduction in RMS height or pressure errors and the quality of actual weather forecasts, which affect our everyday life. A more direct way to gauge the impact of the satellite data would be through the vehicle of subjective weather forecasts.

4.1 Subjective weather forecasting

To evaluate the impact of the satellite sounding data on the routine weather forecasts, subjective weather forecasts were issued for a network of stations presented in figure 2. The stations are located about 500 km apart from each other so that synoptic scale effects could be detected. The forecasted elements were: wind speed and direction, cloud amount and type, and precipitation. Each element was forecasted independently. The forecasts were given in categories which are presented in Table 1 and were issued for 12, 24, and 48 hours.

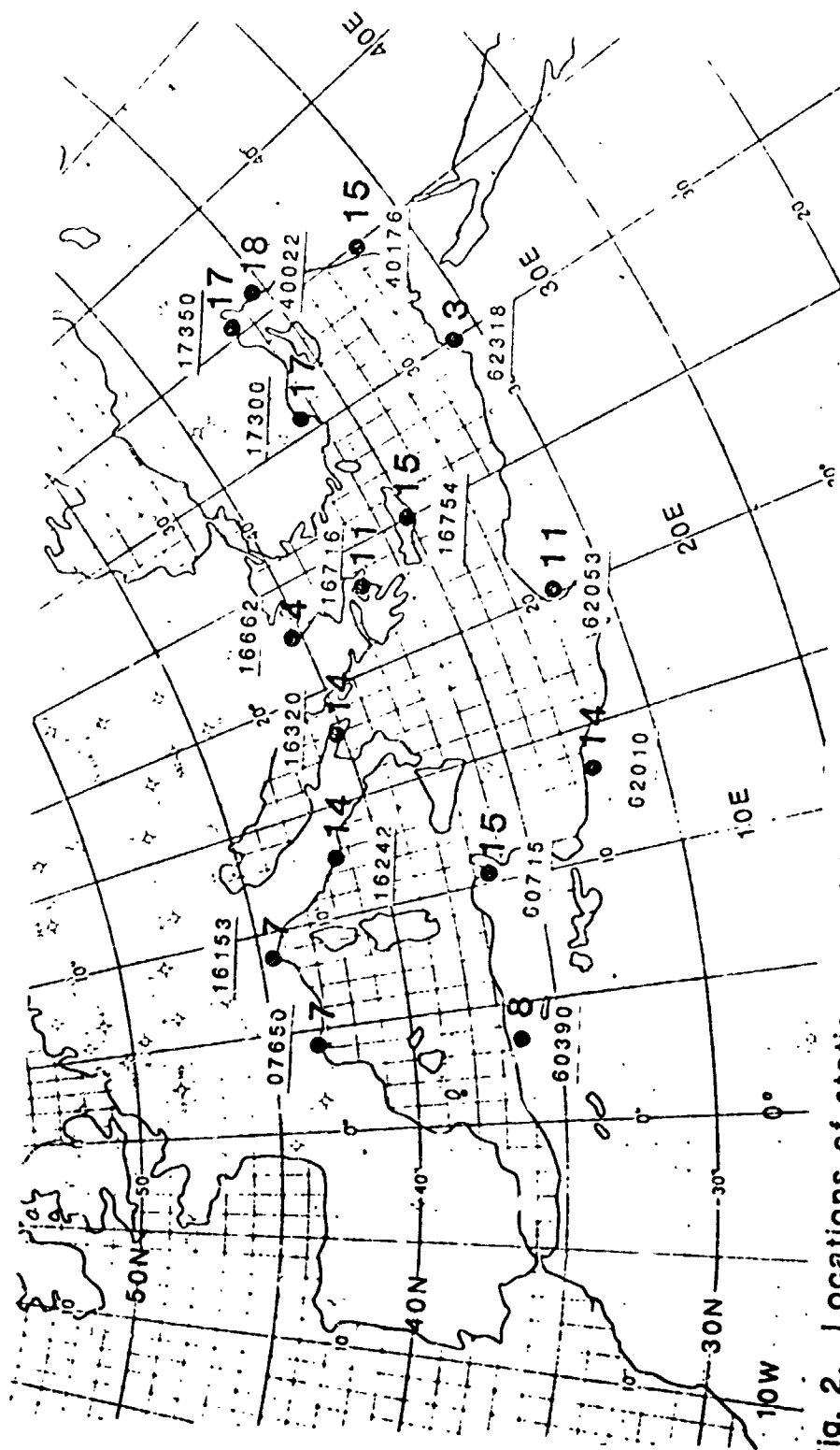
Table 1: Forecast categories for weather elements.

Elements	category 1	category 2	category 3	category 4
wind speed (ff)	ff < 15 kt	ff ≥ 15 kt		
wind direction (dd)	0° < dd ≤ 90°	90° < dd ≤ 180°	180° < dd ≤ 270°	270° < dd ≤ 360°
cloud type	clear	low	middle	high
cloud amount (N, octas)	0 ≤ N ≤ 2	3 ≤ N ≤ 4	5 ≤ N ≤ 6	7 ≤ N ≤ 8
precipitation	yes	no		

4.2 Forecast procedure and verification

The procedure for issuing the subjective weather forecast was as follows. First the forecaster was presented with two sets of forecast maps as produced by the numerical prediction model with (SAT) and without (NOSAT) satellite data, but was not told which was which. He then issued two weather forecasts for each station using the two sets of numerical forecast maps. The number of maps available was limited because of practical reasons. The following maps have been used:

- (1) Current operational sea level pressure as analyzed at the IMS.
- (2) Forecasted sea level pressure and the 500-1000mb thickness.
- (3) Current and forecasted 500mb height and vorticity.



The Hansen-Kuipers (HK) Score which is the hit rate minus the false alarm rate (Mason 1982) was used for verification purposes. This score has two advantages:

- (1) It discourages persistence or climatologically based forecasts by resulting in very low scores for this type of technique.
- (2) The score is independent of the frequency of the forecasted events.

4.3 Results

Satellite impact on the subjective weather forecasts may be evaluated by addressing the following problems:

- (1) What is the geographical distribution of the impact?
- (2) At what forecast time was the impact realized?
- (3) How was the quality of the forecasts changed?

4.3.1 Spatial distribution of the impact

The cumulative combined 12, 24, and 48 hours spatial distribution of the percentage of different station precipitation forecasts is presented in figure 2. One may observe that there are preferred areas where the number of different forecasts maximizes. The maximum difference area stretches from the Iiranean Sea through Crete to the northeastern corner of the Mediterranean Sea. This area coincides roughly with one of the frequent cyclonic tracks in the Mediterranean Sea.

4.3.2 Forecast Quality

The impact of the satellite sounding data expressed in HK units, in which a higher score means a better forecast, was calculated using the impact for each station as an observation point. The Student t test was used to assess the statistical significance. The results are shown in Table 4.

Table 4: Average HK scores for precipitation forecasts with and without satellite data.

(significant results at the 95% confidence level are underlined)

	January 1980			January 1979		
Time (hrs)	12	24	48	12	24	48
HK with satellite	.55	.43	.28	.35	.44	.27
HK without satellite	.49	.35	.29	.31	.35	.30
Impact	.06	<u>.08</u>	-.01	.04	<u>.09</u>	-.03

Most of the impact is positive but not always statistically significant.

5. CONCLUSIONS

Our results indicate that a small national weather service using a modest numerical weather prediction model can improve its numerical predictions of sea level pressure and, through subjective interpretation of the numerical predictions, its forecasts of significant weather elements by including satellite temperature soundings in the initial conditions for the model. However, we believe that the degree of improvement to be expected will depend on the details of the model's analysis and forecast system. For example, the Israeli forecast model uses a 12-hour old analysis as the first guess field for the current analysis. In sparse data regions, satellite soundings, despite their inherent errors, improve the analysis over that based upon the 12-hour old analysis and a few current radiosondes. Models using a 12-hour forecast for a first guess field may show different impacts.

Our results indicate that forecasts based upon an observing system consisting of surface observations and satellite soundings may be better than forecasts based on the conventional surface and upper air observing network, and are comparable to forecasts based on a hybrid satellite sounding and conventional data system. This result has important implications for the planning of future observing systems and should be verified in experiments with more sophisticated numerical forecast models.

ACKNOWLEDGEMENT

This research was supported by the Office of Climate and Atmospheric Research, NOAA. The authors also thank Ms. R. Woodard for typing the manuscript, and Mr. R. Ryan for preparing the figures.

REFERENCES

- Bengtsson, L.M., Kanemitsu, P. Kallberg and S. Uppala, 1982: FGGE research activities at ECMWF. Bulletin American Meteorological Society, Vol. 63, pp. 227-303.
- Cressman, G.P., 1959: An operational objective analysis system. Monthly Weather Review, 87, pp. 367-374.
- Gruber, A., and C.D. Waters, 1982: Statistical Assessment of the Quality of TIROS-N and NOAA-C Satellite Soundings. Monthly Weather Review, 110, 867-876.
- Halen, M., E. Kalnay, W.E. Baker and R. Atlas, 1982: An assessment of the FGGE satellite observing system during SOP1. Bulletin American Meteorological Society, 63, pp. 407-426.
- Mason, I., 1982: On scores for yes/no forecasts. Preprints Ninth Conference Weather Forecasting and Analysis. June 28-July 1, 1982. Seattle, Washington, 483 pp.
- Smith, W.L., H.M. Woolf, C.M. Hayden, D.Q. Wark, and L.M. McMillin, 1979: The TIROS-N Operational Vertical Sounder. Bulletin of the American Meteorological Society, 60, pp 1177-1187.
- Thomasell, A., Jy. T. Chang, N. Wolfson, A. Gruber and G. Ohring, 1983: The impact of satellite soundings and their distribution on forecast accuracy. Preprints Sixth Conference on Numerical Weather Prediction. 6-9 June 1983, Omaha, Nebraska, 421 pp.
- Wolfson, N., A. Thomasell, G. Ohring, A. Gruber, H. Brodrick and Jy. T Chang, 1983: The impact of satellite sounding data on the systematic error of a NWP. Preprints Sixth Conference on Numerical Weather Prediction. 6-9 June 1983, Omaha, Nebraska, 421 pp.

LN84 27296

THE VARIABILITY OF THE SURFACE WIND FIELD
IN THE EQUATORIAL PACIFIC OCEAN: CRITERIA FOR SATELLITE MEASUREMENTS

David Halpern
NOAA Pacific Marine Environmental Laboratory
7600 Sand Point Way NE
Seattle, WA 98115, U.S.A.

ABSTRACT

The natural variability of the equatorial Pacific surface wind field is described from long-period (1.0-2.5 years) surface wind measurements made at three sites along the equator (95°W, 109°30'W, 152°30'W). These data, which were obtained from surface buoys moored in the deep ocean far from islands or land, provide adequate criteria to adequately sample the tropical Pacific winds from satellites.

1. INTRODUCTION

Variations in the surface wind field in the equatorial Pacific yield rich responses in the upper ocean circulation and thermal fields; the generation of Kelvin waves (Knox and Halpern, 1982) and of the spectacular 1982-83 equatorial Pacific warm event (Halpern et al., 1983) are two examples. While knowledge of the large-scale spatial and temporal structures of the tropical wind field is essential to our understanding of global ocean-atmosphere climate variability, our techniques to describe the fluctuations of the surface wind field are poor and require much improvement. Because the wind and mass fields are not strongly coupled in low latitudes, quasi-geostrophic models are inadequate, and wind observations are more important than atmospheric pressure measurements. Wind observations from ships, cloud-tracking via satellite measurements, and satellite microwave measurements are three techniques that provide wind coverage over large areas in low latitudes. Sampling of winds by ships is too sporadic in time and space, especially for scales smaller than about one month and 1000 km, e.g., within 10° of the Pacific equator. The data base for the 1947-72 wind climatology produced by Wyrski and Meyers (1976) consisted of approximately 3 observations per day per 10° square. Winds determined from cloud drift observations are considered an interim solution until such time (perhaps as early as 1989) as continuous measurements (e.g., microwave radiometer, radar altimeter, multi-directional scatterometer) are made from satellites. In the design of a satellite wind measuring system, the orbit configuration, mission duration, geographical coverage, footprint dimensions, accuracy and resolution of measurements, time interval between repeated orbits, and verification and ground truth studies must all be considered in the context of the natural variability of the surface wind field. This paper describes the variability of surface winds measured continuously at a few locations in the tropical Pacific remote from islands and land. Possible errors in the satellite measured wind field will be discussed.

2. DATA AND INSTRUMENTATION

Moored wind measurements were made at 3.5-3.8 m height with a vector-averaging wind recorder (VAWR) mounted on a 2.44 m diameter toroidal surface float supporting

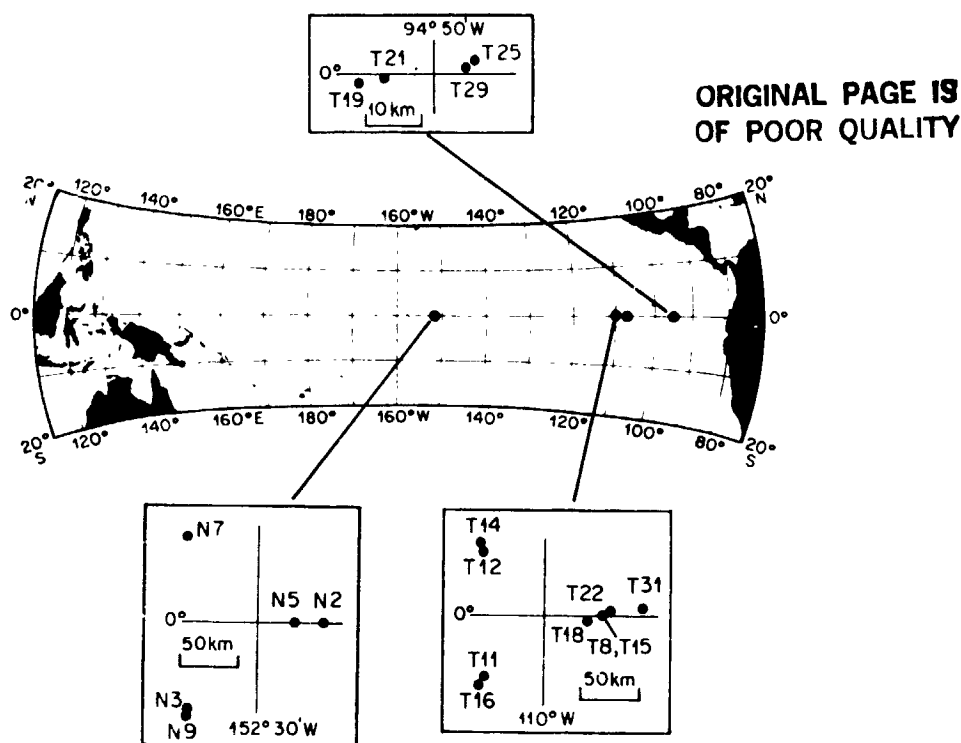


Figure 1. Locations of equatorial moored wind measurements described in this paper. Water depths at the mooring sites varied from about 3400 to 5100 m. The closest equatorial islands are the Galápagos Islands ($\sim 0^\circ$, 91°W) to the east and Jarvis Island ($\sim 0^\circ$, 160°W) to the west. Deployment intervals were about four to six months. At 0° , 95°W the mooring intervals were: T19, 4 July - 25 October 1981; T21, 7 November 1981 - 2 April 1982; T25, 4 April - 4 November 1982; and T29, 5 November 1982 - 18 April 1983. The 0° , 108°W site (mooring T27; $00^\circ 01.0'\text{S}$, $108^\circ 00.2'\text{W}$) began in April 1982. The mooring durations at 0° , $109^\circ 30'\text{W}$ were: T8, 10 August 1980 - 5 February 1981; T15, 7 February - 9 July 1981; T18, 11 July - 28 October 1981; T22, 31 October 1981 - 15 April 1982; T31, 27 October 1982 - 23 April 1983; T12, 11 August 1980 - 31 January 1981; T14, 2 February - 7 July 1981; T11, 13 August 1980 - 3 February 1981; and T16, 4 February - 11 July 1981. Near 0° , $152^\circ 30'\text{W}$ the mooring intervals were: N2, 24 April - 9 October 1979; N3, 30 April - 9 October 1979; N5, 13 October 1979 - 9 February 1980; N7, 16 February - 2 June 1980; and N9, 16 February - 2 June 1980.

a 3 m high aluminum tower with a platform on top. Figure 1 summarizes the locations and record-lengths of the equatorial Pacific wind measurements used in this paper. The VAW^o was mounted through a hole in the platform, with the heights of the 9 cm x 17 cm balanced wind vane and Climet model 011-2B 3-cup anemometer were about 0.5 m above the platform. The VAWR operated continuously and recorded integrated values of east-west (u ; positive eastward) and north-south (v ; positive northward) speeds at 15 min intervals. The anemometer was calibrated at eight speeds over the range $1.5\text{--}24.5\text{ m s}^{-1}$ in the wind tunnel of the Atmospheric Sciences Department, University of Washington, before and after the observation periods. The after- and before-calibration curves differed by less than 0.1 m s^{-1} at speeds below 10 m s^{-1} and about 0.2 m s^{-1} at 15 m s^{-1} .

Mooring motion is known to contaminate wind measurements made from surface-following buoys which move horizontally and vertically to follow the contour of the sea surface. Visual observations indicate that the rotational motion about the buoy's vertical axis (i.e., yawing) is negligible. However, the pitch and roll motion of the buoy can increase the apparent scalar averaged wind speed, cause

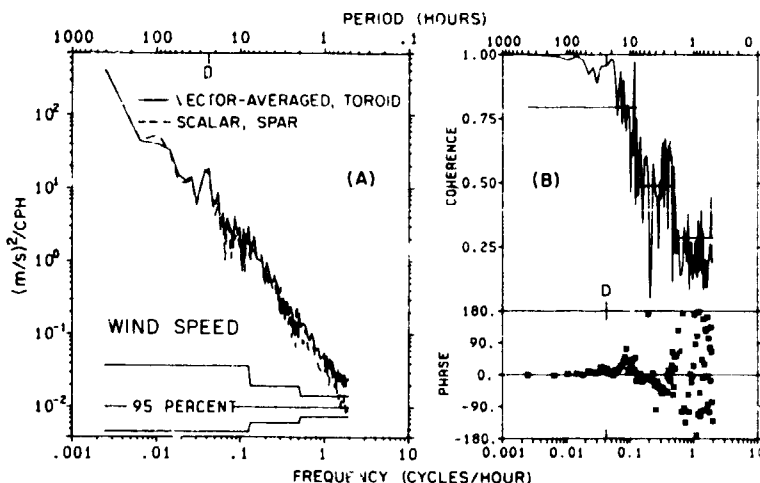


Figure 2. (A) Spectral estimates of wind speed fluctuations. (B) Coherence and phase difference between spar buoy scalar speeds and toroidal buoy vector-averaged speeds. The "95 percent" represents the 95% confidence levels determined from the chi-square distribution and applicable to each curve. The three short horizontal lines drawn on the plot of the magnitude of the coherence represent the 95% confidence limits. In (A) and (B), D indicates the diurnal frequency.

overspeeding of the 3-cup anemometer, and cause the anemometer to measure over a range of heights. It was found (Figure 2) that for frequencies below 0.5 cycle per hour (cph), VAWR wind speed measurements recorded from a vertically stable spar buoy and our surface-following buoy were nearly identical and highly correlated, indicating a negligible influence of mooring motion. In the intercomparison test the surface-following buoy and spar buoy were separated by 10 km; had they been closer together, the frequency corresponding to 0.5 cph probably would have been higher. There was no evidence of a distinct spectral flattening (*i.e.*, a less rapid decrease of spectral estimates with increasing frequency) at frequencies >1 cph, which *a priori* was expected if mooring motion and sensor noise contributed spurious motions to the measurements. Since the 15-min vector-averaged wind speeds were rarely greater than 10 m s^{-1} , a speed equivalent to surface wave amplitudes $\geq 1 \text{ m}$, the wind sensors were practically never in the shadow of a wave crest unless the swell was unusually large.

Record gaps occurred because instrumentation did not always operate properly, buoys broke loose from their mooring line, and buoy recovery operations usually preceded deployments. The 1-2 day record gap resulting from mooring recovery and deployment operations at four to six month intervals was filled by linear interpolation. The 13-month record at 0° , $152^\circ 30' \text{W}$ was formed by combining the 24 April 1979 - 9 February 1980 data at 0° , 152°W with the 16 February - 2 June 1980 measurements at $0^\circ 37' \text{N}$, $153^\circ 04' \text{W}$. In the 29-month record at 0° , $109^\circ 30' \text{W}$ a six month (April - October 1982) segment was measured at 0° , 108°W . On different occasions moored wind observations were also recorded at sites approximately 75 km north and south of the equator near 153°W and 110°W . As will be shown (Figure 5), for frequencies below about 2-3 cycle per day (cpd) the surface wind vectors were coherent at the 95% confidence level with zero phase difference, indicating that time variations of the low-frequency wind vectors occurred simultaneously over distances up to 150 km. The 50% noise level occurred at about 1 cpd.

3. OBSERVATIONS

At 95°W , $109^\circ 30' \text{W}$ and $152^\circ 30' \text{W}$ the vector-mean wind directions were representative of southerly, southeasterly and easterly trade winds, respectively,

Table 1. Statistics of 2-hour vector-averaged east-west (u; positive eastward) and north-south (v; positive northward) wind components. Wind direction is defined as the direction (clockwise from true north) in which the wind is blowing. See text for definition of steadiness.

	0°, 152°30'W 24 Apr 79-2 Jun 80	0°, 109°30'W 10 Aug 80-20 Dec 82	0°, 95°W 4 Jul 81-19 Apr 83
Mean u (m s^{-1})	-5.2	-3.6	-1.5
Mean v (m s^{-1})	0.6	3.1	3.9
Standard deviation u (m s^{-1})	2.0	1.7	2.0
Standard deviation v (m s^{-1})	1.6	1.7	2.1
Vector-mean speed (m s^{-1})	5.6	5.1	4.8
Vector-mean direction (°T)	277	311	338
Mean steadiness (percent)	94	95	90

i.e., the surface wind vector from 95 to 152°W rotated counterclockwise (Table 1). (Wind direction is defined as the direction in which the wind is blowing.) This pattern is similar to the 1947-72 climatological-mean wind distribution computed by Wyrski and Meyers (1976). The vector-mean wind speed, which was not large ($\sim 5 \text{ m s}^{-1}$), and the mean zonal wind speed increased toward the west; in contrast, the mean meridional wind component increased dramatically eastward (Table 1). The magnitude of the variability of the 2-hour wind data, as measured by the standard deviation, was generally equivalent to about 50% of the mean speed; on occasions the standard deviation was greater than the mean speed (Table 1).

The steadiness of the monthly wind is defined as the ratio of the magnitude of the monthly mean wind vector, $(\bar{u}^2 + \bar{v}^2)^{1/2}$, to the monthly mean magnitude, $(u^2 + v^2)^{1/2}$, expressed in percent. The u and v values are the 2-hour averaged data and an overbar represents a calendar-month time average. The steadiness is primarily a measure of directional variability; steadiness equals zero for winds which shift randomly and have a zero resultant speed, and equals one for winds which always blow in the same direction. A feature of the trade wind is its relatively high steadiness (Table 1). At each site the lowest monthly steadiness value (39% at 95°W; 76% at 109°30'W; 86% at 152°30'W) was associated with the smallest vector-averaged monthly wind speed (1.1 m s^{-1} at 95°W; 2.6 m s^{-1} at 109°30'W; 3.4 m s^{-1} at 152°30'W). The anomalously low monthly wind speed at 95°W happened in February 1983 when the normally occurring easterlies collapsed and became westerlies because of the spectacular 1982-83 El Niño Southern Oscillation (ENSO) episode. The arrival of ENSO winds at 95°W in February 1983 and their persistence through the end of our observations in April (Figure 3C) caused the relatively low value of the record-length mean steadiness, e.g., prior to the January 1983 arrival of the ENSO winds at 95°W the July 1981-December 1982 steadiness was 96%, which is similar to the values obtained at 109°30'W and 152°W.

Although the wind data were relatively steady in direction, the u and v series often contained quite intense mesoscale activity with time scales from a few days to a few weeks (Figures 3A and 3B). While the 15-min vector-averaged recorded data were very seldom in excess of 10 m s^{-1} , the trade wind was interrupted by relatively calm conditions (March 1981 at 109°30'W (Figure 3B)) and by an ENSO related prolonged reversal in direction (March-April 1983 at 95°W (Figure 3C)). The 1982-83 ENSO westerly wind originated in the western Pacific and propagated across the Pacific at about 1 m s^{-1} ; however, it is not usual for the trade wind in the eastern Pacific to reverse direction even during an El Niño. Monthly mean surface wind speeds ranged from about 3 to 7 m s^{-1} with seasonal wind speed changes typically $2\text{-}3 \text{ m s}^{-1}$ and interannual variations of $1\text{-}2 \text{ m s}^{-1}$ in the central Pacific (Figure 3C).

Spectral estimates of the u and v time series with zero mean value and zero least-square linear trend were computed from Cooley-Tukey Fourier transforms using the perfect Daniell frequency window of variable width (Figure 4). For each spectrum the sum over positive frequencies was equal to the total variance. For

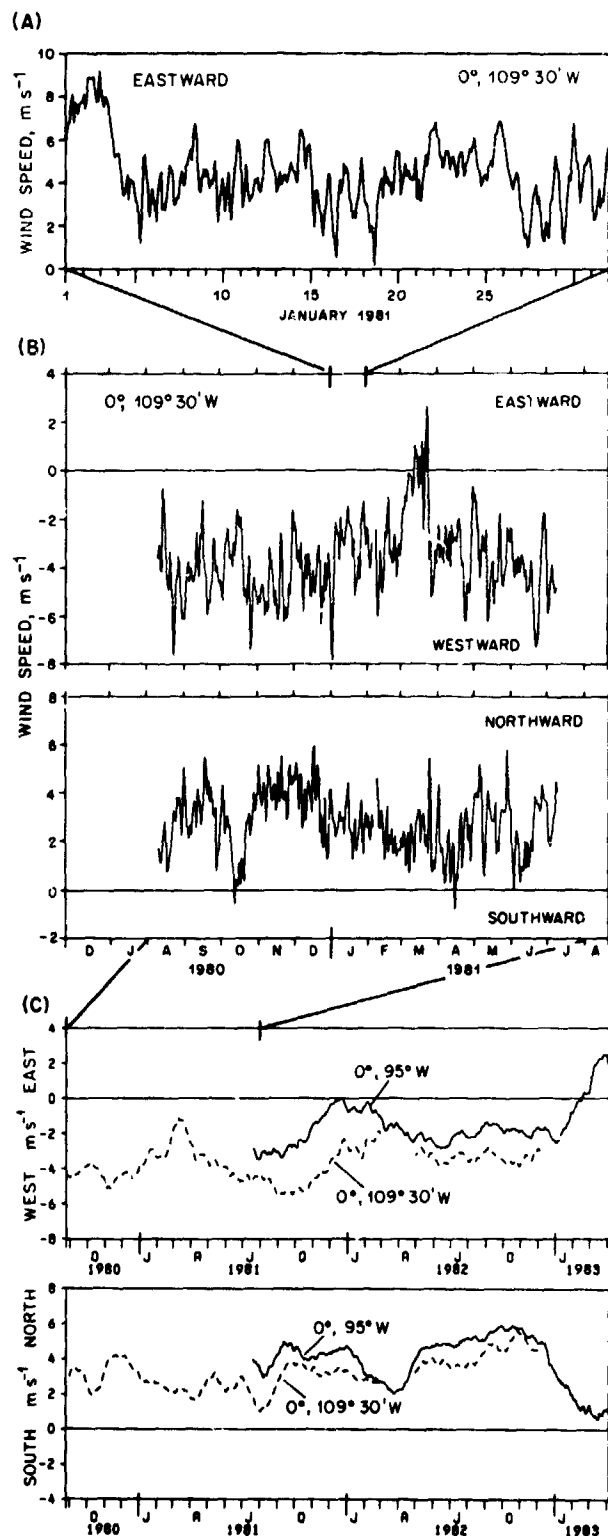
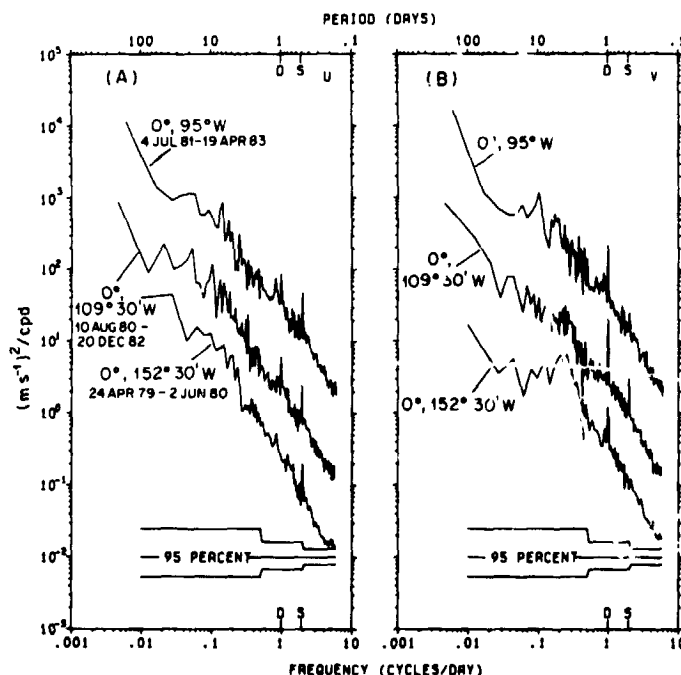


Figure 3. Time series of moored wind measurements. (A) Two-hour vector-averaged values of zonal wind at $0^\circ, 109^\circ 30' W$ during January 1981. (B) Daily vector-averaged values of zonal and meridional wind at $0^\circ, 109^\circ 30' W$ from August 1980 to July 1981. (C) Low-pass (31-day running mean) filtered zonal and meridional wind data at $0^\circ, 109^\circ 30' W$ (dashed line) and $0^\circ, 95^\circ W$ (solid line).

the u component (Figure 4A) there was a 1:1 correspondence between the shapes of the 95°W, 109°30'W and 152°30'W spectra for frequencies greater than 1 cpd; the 152°W u spectra did not show evidence of a diurnal peak rising above the background. At 95°W and 109°30'W the u spectra were similar for all frequencies. For the v component (Figure 4B) the spectral shapes had a 1:1 correspondence above 0.25 cpd. A distinct 0.03-0.3 cpd spectral flattening occurred in the v spectrum at 152°30'W. At 95°W the spectral levels of u and v were fairly similar throughout the frequency range, except at the tidal frequencies; at 110°W the u component spectral levels were greater than the v series from about 0.02 to 0.2 cpd, and at 152°W the u and v spectral shapes and levels were dramatically different for frequencies below 0.2 cpd, with u values being significantly greater. At frequencies above ~ 0.25 cpd the spectral levels decreased uniformly with increasing frequency (except at tidal frequencies), with a slope of about -1.25 for each of the u components, -1.3 for the v component at 95°W and 109°30'W, and -1.5 for the v component at 152°30'W. At the diurnal period the amplitude of v was greater than u at each of the equatorial sites; the diurnal period rms amplitude was much smaller at 152°W (Table 2). The maximum spectral peak within the 3-7 day band occurred in v at 152°W; at 95 and 110°W it is unclear whether wind energy in this frequency range was greater than the background level.

Figure 5 shows the magnitudes of the coherences and phase differences between simultaneous wind measurements made in two small-scale regions near the equator, one at 109°30'W (Figure 5A) and the other at 152°W (Figure 5B), and along the equator between 109°30'W and 95°W (Figure 5C). For frequencies below about 2-3 cpd the wind vectors near 0°, 109°30'W were generally coherent at the 95% confidence level, with zero phase difference over the small-scale buoy array (Figure 5A); a similar result was found at 152°W (Figure 5B). Thus, for distances up to at least 150 km the time variations of the low-frequency wind vectors occurred



ORIGINAL PAGE IS
OF POOR QUALITY

Figure 4. Spectral estimates of (A) zonal and (B) meridional wind components at the three equatorial sites. The 109°30'W and 95°W spectral levels are plotted, respectively, one and two decades higher than measured. The "95 percent" represents the 95% confidence levels determined from the chi-square distribution and applicable to each curve. D and S indicate the diurnal and semidiurnal frequencies.

Table 2. Root-mean-square amplitudes of wind measurements for different frequency intervals. Units = m s^{-1} . For analysis of diurnal and semidiurnal motions, a 405.3 day record-length was used at each site; at 95°W and 109°30'W simultaneous observations during 4 July 1981 to 14 August 1982 were used. At lower frequencies the rms amplitudes were computed over the maximum record-length: 24 April 1979 - 2 June 1980 at 152°30'W; 10 August 1980 - 20 December 1982 at 109°30'W; 4 July 1981 - 19 April 1983 at 95°W.

	0°, 152°30'W	0°, 109°30'W	0°, 95°W
Semidiurnal u	0.10	0.07	0.11
Semidiurnal v	0.06	0.10	0.10
Diurnal u	0.11	0.14	0.19
Diurnal v	0.25	0.26	0.30
0.143-0.333 cpd v	0.93	0.61	0.75
0.033-0.1 cpd u	0.56	0.57	0.64
0.033-0.1 cpd v	1.23	0.79	0.75
0.1-6.0 cpd u	1.27	1.13	1.21
0.1-6.0 cpd v	1.39	1.10	1.36

simultaneously. If the velocity fluctuations are linearly related, then 100 times the square of the coherence (i.e., 100 Coh^2) represents the percentage of the total variance which can be explained by a linear relationship existing between two wind records, and the quantity $(1-\text{Coh}^2)$ represents the noise and/or nonlinear relationship. The 50% noise level occurred at about 0.3-0.5 cpd at 109°30'W and 0.5-1.0 cpd at 152°W. For longer separation distances such as the 1600 km between the measurements at 95°W and 109°30'W, the wind vectors were coherent with 95% statistical significance within selected time scales: in u and v, the seasonal time scale of 100 days or more; in v, the 3-5 day and diurnal periods; and in u and v, the semidiurnal period (Figure 5C). Only at the seasonal time scale was the magnitude of the large-scale coherence greater than the 50% noise level.

4. RESULTS

Along the equator at 95°W, 109°30'W and 152°30'W the u and v spectral levels decreased with increasing frequency, falling off roughly as $f^{-1.25}$ to $f^{-1.5}$ (f = frequency). Similar spectral slopes have been observed in the Intertropical Convergence Zone (ITCZ) region in the Pacific near 6-8°N, 150°W (Halpern, 1979) and in the eastern Atlantic (Halpern, 1980). Comparing the 0°, 152°30'W wind observations with similar measurements made at 7°N, 150°W during 7 November 1977 to 22 March 1978 (see Halpern (1979) for wind characteristics at 7°N, 150°W), which at that time was located under the ITCZ, shows (Figure 6) that the 7°N u and v spectral estimates were consistently higher than the 0° estimates, especially above 1 cpd for the u and v values and below 0.2 cpd for the v component. The greater variability at higher frequencies at 7°N was probably due to cloud cluster motions associated with convergence along the ITCZ. The dramatic difference of the v spectral estimates below 0.15 cpd suggests a latitudinal attenuation of large-scale meridional motions (perhaps associated with easterly waves primarily confined to the equatorial trough).

Of the wind measurements recorded at 95°W, 109°30'W and 152°30'W, only the v spectrum at 152°30'W contained indications of a 3-7 day spectral peak (Figure 4) with rms amplitude of nearly 1 m s^{-1} (Table 2). It is tempting to speculate that the amplitude of the statistically (at the 95% confidence level) significant meridional (but not zonal) wind energy at 4-5 days at Canton Island (2°46'S, 171°43'W) (Wunsch and Gill, 1976) diminishes eastward. The origin of the 4-day meridional wind oscillation is unclear. The u and v spectral shapes of the Canton Island and 152°30'W wind data were very similar.

At frequencies below 2-3 cpd and over north-south or east-west distances of 150 km the wind fluctuations near 0°, 109°30'W and 0°, 152°30'W were coherent (at

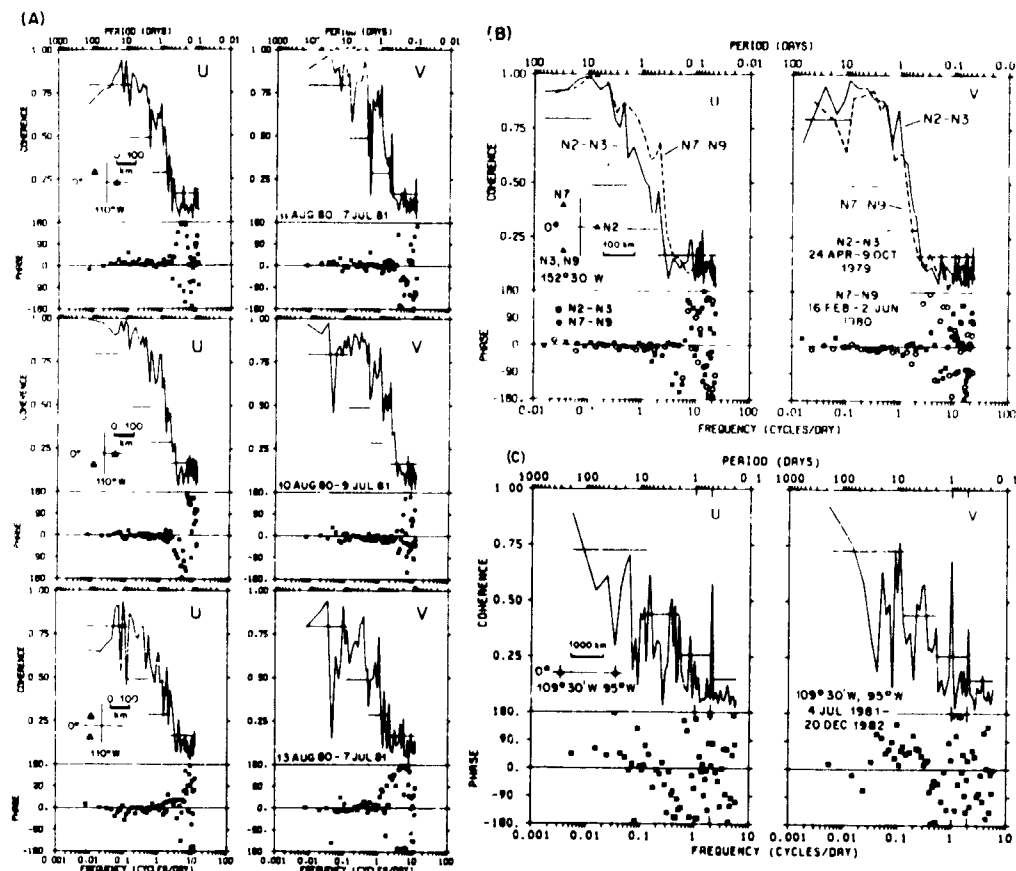


Figure 5. Magnitude and phase difference of the coherence between simultaneous wind measurements from small-scale buoy arrays near (A) 0° , 110°W and (B) 0° , $152^\circ30'\text{W}$, and (C) between 95°W and $109^\circ30'\text{W}$. Locations of wind data and durations of measurements are shown within the u and v (respectively) coherence magnitude diagrams. The four short horizontal lines in the magnitude portion of the diagram represent the 95% confidence limit of the coherence estimate. In (C) a positive phase difference corresponds to the wind variation occurring earlier at 95°W than at $109^\circ30'\text{W}$.

the 95% confidence level), with little phase difference. This maximum-coherent-frequency (mcf) was nearly 10 times greater than the mcf observed over similar distances along 150°W near the ITCZ (Halpern, 1979), presumably because of the considerable amount of small-scale atmospheric motions, such as C-scale convection, occurring near the ITCZ. The ~ 0.5 cpd frequency of the 50% noise level associated with the ~ 150 km scale arrays near $1^\circ30'\text{W}$ and $152^\circ30'\text{W}$ was about 3 times greater than Halpern (1979) found at 150°W under the ITCZ. While there was little evidence of a 0.2-0.35 cpd spectral peak at 95°W and $109^\circ30'\text{W}$ (Figure 4), apparently these fluctuations were coherent (at the 95% confidence level), with about a 45° phase difference, which corresponds to a 0.5 day time delay for a 4-day easterly wave; the coherence magnitudes were less than the 50% noise level (Figure 5).

If the observed time/space scales (100 day/1600 km and 0.5 day/150 km) are joined by a line, then by interpolation the horizontal distance associated with coherent wind fluctuation for one month time scale would be ~ 1250 km. That this value is greater than the one determined by extrapolation from the small-scale array near 7°N , 150°W (Halpern, 1979) is consistent with the higher frequency-wavenumber variability occurring near the ITCZ.

The v component spectrum (Figure 4B) at each of the 3 equatorial sites contained statistically significant (at the 95% confidence level) diurnal-period

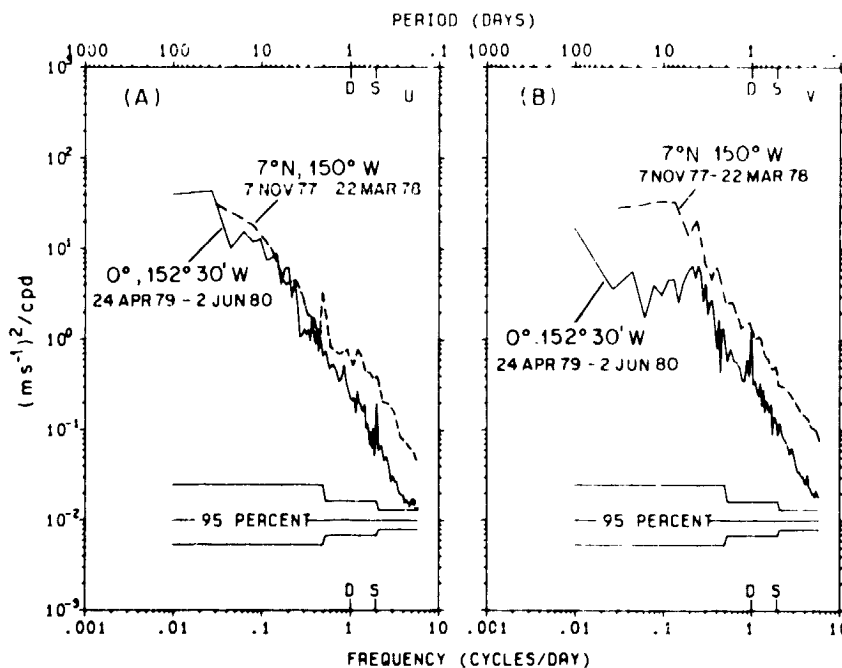


Figure 6. Spectral estimates of (A) zonal and (B) meridional wind components at an equatorial and off-equatorial site near 150°W. The "95 percent" represents the 95% confidence level determined from the chi-square distribution and applicable to each curve.

fluctuations with a zonally-averaged rms amplitude of 0.27 m s^{-1} (Table 2). At 95°W and 109°30'W the average rms amplitude of the u component diurnal-period oscillation was 0.15 m s^{-1} . Interestingly, the wind spectra at 7°N, 150°W (Figure 6) and in the eastern Atlantic near 9°N, 23°W (Halpern, 1980) did not contain statistically significant diurnal-period spectral peaks, presumably because the background level of variability was considerably higher due to the nearness of the ITCZ. At 1 cpd the wind fluctuations over ~150 km distances near 152°30'W and 109°30'W and over 1600 km between 95°W and 109°30'W were coherent at the 95% confidence level, with magnitudes equal to or greater than the 50% noise level (Figure 5).

5. DISCUSSION

Schemes to adequately measure the temporal and spatial variability of the surface wind field over the equatorial ocean involve the consideration of many factors, for it is not possible for a single satellite to cover completely the full spectrum of variability everywhere. For example, to sample the diurnal-period wind oscillation would require a ground track which repeated every 0.5 days or sooner; however, the equatorial distance between adjacent orbits of a single spacecraft would be nearly 5000 km (Allan, 1983), reducing the geographical coverage quite significantly. Thus, temporal repeatability, geographical coverage and the natural variability of the winds must be considered together. One compromise is a 2-day repeat cycle. This provides a Nyquist frequency of 0.25 cpd, which is the observed average frequency where the spectral slope changes to -1.25 or steeper. Except for the diurnal-period oscillations, the aliased energy folded into lower frequencies will be a small fraction of the low-frequency motions. For a 2-day repeat cycle the 1500 km nodal distance at the equator is about equal to the distance over which the diurnal-period wind oscillation was correlated, so that data from adjacent ground tracks can be used in the study of atmospheric tides. The degree to which

the aliasing of the diurnal tidal wind fluctuation, which has an rms vector-mean speed amplitude of 0.3 m s^{-1} (or 6% of the vector-mean speed), can be reduced needs further study.

Considerable mesoscale (say, 3-30 days) variability occurs in the equatorial wind field, e.g., the zonally-averaged rms amplitude of the 0.033-1.0 cpd fluctuations was 1.1 m s^{-1} . While this is nearly 30-50% of seasonal changes in the annual cycle of the wind field, it is only about 50-60% of the $\pm 2 \text{ m s}^{-1}$ instrumentation error expected of the satellite wind measuring systems, assuming no major improvements in sensor accuracy from the systems used on SEASAT. Thus, a new generation of satellite wind measuring sensors needs to be developed.

The distance between the satellite's ground track at the equator should be no larger than about 750 km, which is the computed (albeit from our limited data set) coherent spatial scale corresponding to our hypothetical satellite's Nyquist period for a 2-day repeat cycle.

Over the oceans the frequency-wavenumber spectrum of the surface wind field is poorly known because of the difficulty of making continuous measurements for long periods. Only accurate spacecraft sensors adequately deployed can provide the needed data. An effective design of a satellite wind measuring system must consider the observed scales of surface wind variability in the equatorial Pacific Ocean, a vast region important to global climate.

6. ACKNOWLEDGEMENTS

I am extremely grateful to A. Shepherd and S. Newell for calibrating and maintaining the moored wind recorders, E. Duley and D. Fenton for assembling and preparing the moorings, and P. Freitag for processing the wind data and preparing the computer-generated diagrams used in this report. The measurements near 0° , 152°W were obtained with partial support from NSF's International Decade of Ocean Exploration Office (NORPAX/OCE79 22866). My equatorial ocean-atmosphere interaction studies are supported by NOAA's Equatorial Pacific Ocean Climate Studies program (EPOCS/ERL Project No. 8K2A2002); this support is gratefully acknowledged. Contribution No. 694 from the NOAA/ERL Pacific Marine Environmental Laboratory.

9. REFERENCES

- Allan, T. D. (1983) A review of SEASAT. In: *Satellite Microwave Remote Sensing*, T. D. Allan, editor, Halstead Press, New York, 15-44.
- Halpern, D. (1979) Surface wind measurements and low-level cloud motion vectors near the Intertropical Convergence Zone in the central Pacific Ocean during November 1979 to March 1978. *Mon. Wea. Rev.*, 107, 1525-1534.
- Halpern, D. (1980) Variability of near-surface currents in the Atlantic North Equatorial Countercurrent during GATE. *J. of Phys. Oceanogr.*, 10, 1213-1220.
- Halpern, D., S. P. Hayes, A. Leetmaa, D. V. Hansen and S. G. H. Philander (1983) Oceanographic observations of the 1982 warming of the tropical eastern Pacific. *Science*, 221, 1173-1175.
- Knox, R. A. and D. Halpern (1982) Variations in transport of equatorial currents in the central and eastern Pacific Ocean. *J. Mar. Res.*, 40 Supplement, 329-339.
- Wunsch, C. and A. E. Gill (1976) Observations of the equatorially trapped waves in Pacific sea level variations. *Deep-Sea Res.*, 23, 371-390.

E. Paul McClain
National Environmental Satellite, Data, and Information Service, NOAA
Federal Building 4, Washington, DC 20233, USA

ABSTRACT

Visual and infrared measurements from the five-channel AVHRR on the NOAA-7 satellite are used operationally to derive sea surface temperatures. The multi-channel data are used to perform daytime and nighttime cloud-detection tests, and the several atmospheric-window channels in the thermal infrared are used to correct for atmospheric attenuation. Monitoring of the sea surface temperature product with buoy data indicates stability in mean bias ($\leq +0.1^{\circ}\text{C}$) and rms difference ($0.6\text{--}0.8^{\circ}\text{C}$.) with little variation by season or geographic area. Global mapping enables the derivation of monthly mean isotherms, monthly and annual changes, and anomaly patterns relative to climatology. Problems have been associated with noise in the $3.7\mu\text{m}$ window channel, and with the injection of substantial volcanic aerosol into the stratosphere by the El Chichón eruption. Multi-channel sea surface temperature charts are used in studies of such phenomena as equatorial long waves and the recent El Niño episode.

1. INTRODUCTION

Sea surface temperature fields on several spatial and temporal scales are of considerable interest to oceanographers, meteorologists, and climatologists. The irregular distribution and often variable quality of conventional intake temperatures from commercial ships, and the paucity of higher quality XBT and buoy observations, has stimulated interest in the repetitive and comprehensive coverage afforded by Earth-orbiting spacecraft.

Routine processing of infrared (IR) data from the NOAA series polar orbiting environmental satellites for global distributions of sea surface temperature (SST) began late in 1972 (Brower et al., 1976). Although the radiometers at that time performed their primary task of nighttime cloud imaging satisfactorily, the IR measurements were rather noisy and thus cloud-filtering was cumbersome and not as effective as required for extraction of SSTs. Furthermore, the single atmospheric "window" channel in the thermal-IR part of the spectrum did not permit adequate correction for atmospheric attenuation, chiefly by water vapor, which is very appreciable in tropical regions. Subsequent attempts to improve upon both cloud detection and atmospheric corrections by incorporating data from atmospheric sounders aboard the spacecraft were only partially successful (Walton et al., 1976). Although still based on IR measurements from a single window channel, higher-resolution, lower noise-level radiometric data from the Advanced Very High Resolution Radiometer (AVHRR) on the TIROS-N generation of NOAA operational satellites (Schwalb, 1978), together with better sounder measurements, enabled further improvements in SSTs (Walton, 1980).

Electrical interference in the $3.7\mu\text{m}$ window channel of the first AVHRR (on TIROS-N) hindered early development and implementation of multiple-window techniques, but simulations and preliminary testing with measurements from the second AVHRR (on NOAA-6) were quite encouraging (McClain, 1980). The third AVHRR (on NOAA-7) has

three IR window channels, and operational processing of multi-channel SST (MCSST) commenced in November of 1981 (McClain et al., 1983).

This paper will give brief discussions of NOAA's MCSST processing, validation of MCSSTs, some global and regional products, and recent improvement activities. Use of MCSST analyses in atmospheric/oceanographic research, and some gaps in our knowledge or understanding, will be addressed.

2. DESCRIPTION OF MULTICHANNEL SST (MCSST) METHOD

Spatial resolution of the AVHRR at nadir is 1.1 km locally and nominally 4 km regionally and globally. Measurements are made in the visual (0.58-0.68 μm), reflected IR (0.725-1.1 μm), and in three emitted-IR windows (3.55-3.93, 10.3-11.3, and 11.5-12.5 μm). Each orbital swath is about 2500 km wide on the Earth and each geographic area is viewed near 0300 and 1500 local time. Only the IR channels have provision for onboard calibration.

2.1 Cloud Detection Tests

Bi-directional reflectance measurements from the visual or reflected-IR channels are primary in the daytime cloud tests. Visible cloud threshold tests take advantage of the ocean/atmosphere reflectance being very low in the absence of clouds or glitter (specular reflectance). These thresholds have been determined as a function of solar zenith angle, satellite zenith angle, and azimuth of the viewed spot. When clouds partially fill a scanspot of the radiometer, reflectances from neighboring scanspots will generally differ by more than the low noise level of the measurements. This provides the basis for an additional test, essentially requiring spatial uniformity. Because both visible threshold and visible uniformity tests can erroneously fail in glitter-contaminated areas, the option exists to use the nighttime IR-uniformity test in the daytime as well.

Nighttime cloud tests, of necessity, are based on data from the thermal-IR channels of the AVHRR. Threshold tests utilize the highest and lowest historically observed ocean surface temperatures; and a spatial uniformity test takes advantage of the high spatial resolution and low noise levels of the IR data taken in conjunction with the expectation of low horizontal gradients in both the SST and atmospheric attenuation. These assumptions are satisfied in most ocean areas and meteorological situations, but can fail at times, usually in coastal areas. Although these are the primary tests, a special test is used to detect low-altitude stratus clouds with uniform cloud top temperatures and that fill the radiometer's field of view. The reflectivity of optically-thick water droplet clouds is significantly greater at 3.7 than at 11 μm , and this has the effect of making the $T_{3.7}-T_{11}$ difference much more negative than under any cloud-free conditions (McClain et al., 1983). Two other final filters can be used at night to remove a small residue of cloud-contaminated cases. The first such test intercompares the MCSST values obtained from the dual-window, split-window, and triple-window equations (see next section), which have differing sensitivities to the presence of sub-resolution cloud contamination, and requires that they agree to within some limit, generally 0.5-1.0C. The second test requires that the triple-window MCSST not deviate markedly from the climatological SST (by more than 4-7°C, dependent on the climatological SST gradient).

2.2 Correction for Atmospheric Attenuation

Although the idea of using the different atmospheric transmittance characteristics of the several window regions in the infrared to devise an atmospheric attenuation correction scheme for satellite-derived SST goes back to at least Anding and Kauth (1970), the theoretical basis was explicated by Prabhakara et al. (1974)

and McMillin (1975), with the former being the first to verify the approach with radiometric measurements from space. A number of AVHRR simulations using model atmospheres and atmospheric transmittance models have been performed, among them Deschamps and Phulpin (1980), McClain (1981), and Barton (1983), and all found highly linear relations between the atmospheric correction and various combinations of channel brightness temperatures or brightness temperature differences, with standard errors of estimation generally falling in the 0.1-0.3°C range.

NOAA's operational MCSST equations from NOAA-7 were derived from the following simulation equations (°K in, °C out), which are based on a seasonally and geographically diverse set of 64 atmospheric soundings from marine areas of the world and atmospheric transmittance models (Weinreb & Hill, 1980):

$$T_{3/4} = T_{11} + 1.4887(T_{3.7} - T_{11}) - 271.85 \quad (\text{dual-window}) \quad (1)$$

$$T_{4/5} = T_{11} + 2.4917(T_{11} - T_{12}) - 273.48 \quad (\text{split-window}) \quad (2)$$

$$T_{3/4/5} = T_{11} + 0.95321(T_{3.7} - T_{12}) - 272.54 \quad (\text{triple-window}) \quad (3)$$

No explicit allowance for aerosol is incorporated in this set of equations, and the IR reflectance, the satellite zenith angle, and the sea-air temperature difference are all assumed to be zero.

3. VALIDATION OF MCSST RETRIEVALS

Initial testing of Eqn. (1) with NOAA-6 data (McClain, 1981) revealed temperature-dependent biases of up to 2°C and a root mean square (rms) difference of 1.1°C. A relatively small set of expendable bathythermograph (XBT) and moored buoy measurements was employed to define temperature-dependent bias corrections for initial incorporation in the several MCSST operational algorithms (McClain et al., 1983). More extensive sets of drifting buoy observations have been collected and matched to satellite measurements over diverse geographic areas and all seasons to determine the coefficients for the current operational equations (Strong and McClain, 1984), given below:

$$T_{4/5D} = 1.0346T_{11} + 2.58(T_{11} - T_{12}) - 283.21 \quad (\text{day}) \quad (4)$$

$$T_{3/4} = 1.0008T_{11} + 1.50(T_{3.7} - T_{11}) - 273.34 \quad (5)$$

$$T_{4/5N} = 1.0350T_{11} + 2.58(T_{11} - T_{12}) - 283.18 \quad (\text{night}) \quad (6)$$

$$T_{3/4/5} = 1.0170T_{11} + 0.97(T_{3.7} - T_{12}) - 276.58 \quad (7)$$

Validation of these equations with respect to independent satellite measurements and data from a totally different set of drifting buoys is given by the statistics in Table 1. It should be noted that although MCSST equations involving measurements from the 3.7µm channel can be used in the daytime, care must be taken to avoid sun glitter areas. Reflected solar radiation there elevates the brightness temperature above the value corresponding to emission alone.

Table 1. Validation of MCSSTs with respect to drifting buoy data

Equation	Split-window		Triple-window	Dual-window
	day	night	night	night
N	68	84	84	84
bias	-0.02	-0.08	-0.01	+0.02
rmsd	0.49	0.62	0.57	0.79

4. GLOBAL MAPPING OF MCSST

Using satellite zenith angles of up to 45°, 12 hourly global coverage of 4-km AVHRR scanspot data is used to process hundreds of thousands of 11x11 scanspot arrays, called targets, over the oceans daily. Cloud tests and atmospheric corrections are applied to 2x2 unit arrays (8x8 km) within the targets, targets being centered about every 25 km. Using the most centrally located (day) or the warmest (night) of the cloudfree unit arrays within the target, 15,000-20,000 daytime and about 20,000 nighttime MCSST retrievals are made each day over the globe. The less constrained daytime cloud tests allow observational densities of up to 25 retrievals per target as an option.

A variety of contoured MCSST fields is generated from the 8-km resolution retrievals, which are nominally spaced every 25 km or less depending on cloud distribution and daytime observational density mode. All the daily (daytime and nighttime) MCSST retrievals are composited onto weekly 100-km (global) and 50-km (regional) grids, and a 14-km grid for coastal areas is under testing. The search distance for each grid point is an inverse function of the SST gradient, being a maximum of 200 km for the 100-km grid. Each MCSST retrieval within the search area is weighted, the maximum weight being applied to those within 1/3 of a grid interval, and the weight decreasing with the square of the distance from there. The distance-weighted average retrievals for each grid point each day are composited into a weighted average for the week by further weighting each retrieval as an inverse function of its age.

The final weekly fields are contoured at 1°C intervals with the isotherms being dashed in areas where the grid-point MCSSTs have not been updated within the past seven days. Figure 1 is an example of a 50-km regional chart in the eastern equatorial area of the Pacific.

All MCSST retrievals for the month are collected and averaged in 2.5° latitude/longitude bins for purposes of generating fields of monthly means, departures from historical means, (i.e., anomalies), month-to-month and year-to-year changes, etc. Figure 2 is a portion of the monthly anomaly chart for September 1982 during the early stages of a recent El Niño episode.

5. MCSST IMPROVEMENTS

Although the basic bias-corrected MCSST algorithms have been performing adequately under most conditions, certain situations are in need of further study. Among these are corrections for very large satellite zenith angles, for very large sea/air temperature differences, and for severe aerosol conditions.

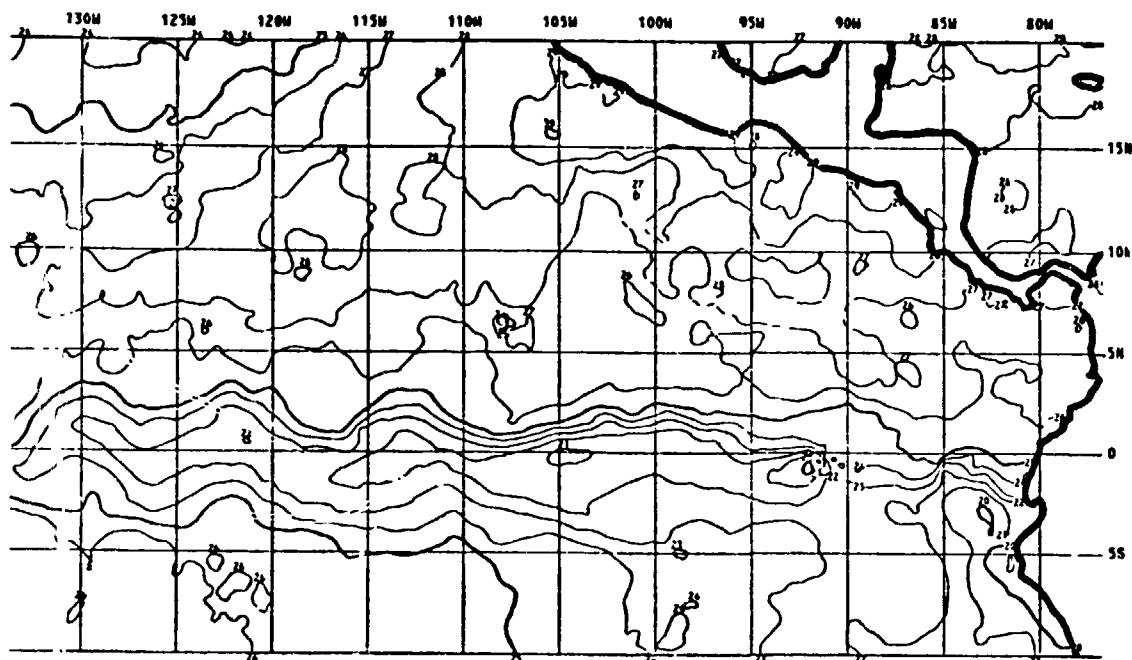


Figure 1. 50-km MCSST analysis, week ending Nov. 8, 1983, in eastern equatorial Pacific

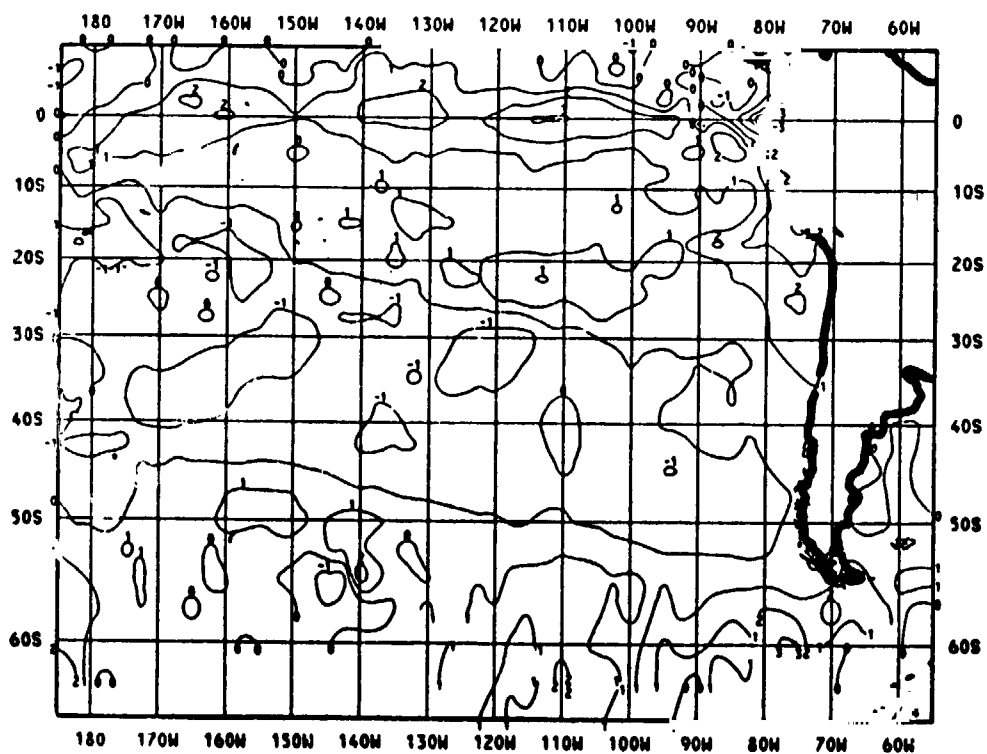


Figure 2. Portion of global MCSST monthly mean anomaly for September 1982

5.1 Large Satellite Zenith Angles

ORIGINAL PAGE IS
OF POOR QUALITY

Although the longer path length through water vapor at higher satellite zenith angles (sza) results in larger brightness temperature differences, and thus larger atmospheric corrections, it can be shown by simulation that this implicit compensation is inadequate when $\text{sza} > \sim 45^\circ$, particularly in the moistest atmospheres. Adding a term of the form $K(T_i - T_j)(\sec \theta - 1)$ where T_i and T_j are brightness temperatures in two of the window channels, θ is the sza, and K is a constant, enables improved corrections at sza values of $45\text{--}60^\circ$. Table 2 below compares the satellite minus buoy/XBT statistics for 22 daytime (eastern North Atlantic) and eight night-time (Mediterranean) matchups in March 1982 using Eqn. (2) and the following NOAA/NESDIS split-window simulation equation (Llewellyn-Jones, 1983):

$$T_{4/5\text{sza}} = T_{11} + 2.346(T_{11} - T_{12}) + 0.655(T_{11} - T_{12})(\sec \theta - 1) - 273.30 \quad (8)$$

Table 2. Split-window MCSSTs with and without sza correction terms (Llewellyn-Jones, 1983)

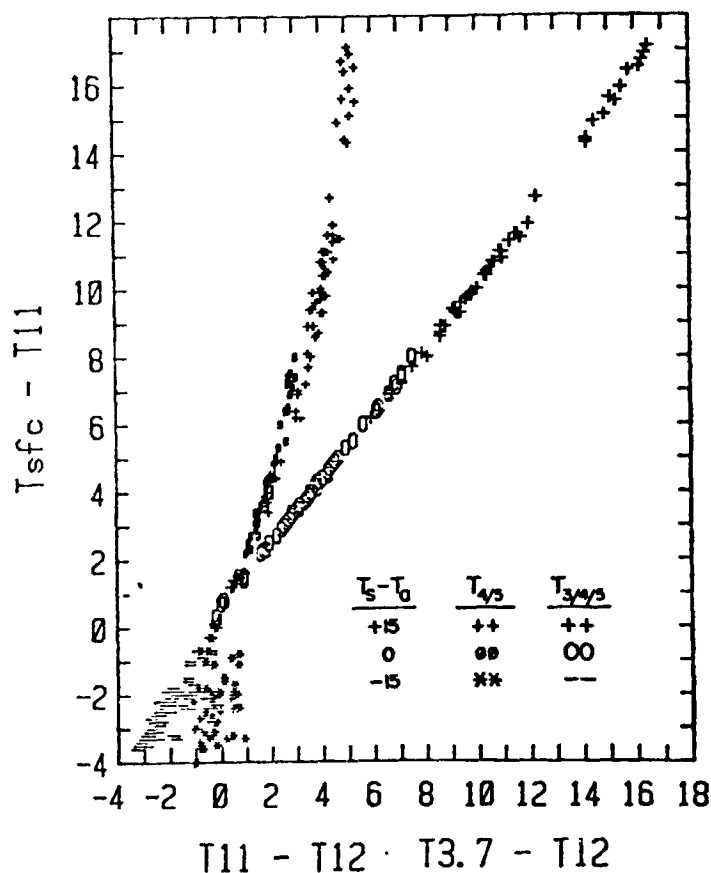
Equation	N	bias	rmsd
(2)	28	-0.44	0.67
(8)	28	-0.15	0.44

5.2 Large Sea/Air Temperature Differences

It can be demonstrated by simulation that sea/air temperature differences (sa Δ T) of to $5\text{--}10^\circ\text{C}$, particularly if positive (sea warmer), result in very little error in retrieved MCSST when the algorithms based on sa Δ T=0 are used. The very large negative sa Δ T values, however, that are common in some areas (e.g., the Great Lakes and just off the NE coast of the USA in late spring and early summer) are associated with significant errors when certain of the MCSST equations are used. It is clear from the split-window and triple-window simulations in Fig. 3 that the latter equation is the preferred one in such situations, although the usual care to avoid specular reflection (glitter) areas must be taken in the daytime. Table 3 gives the bias and rms differences when the surface temperature is predicted by Eqn. (3) or Eqn. (4) using simulation data sets corresponding to $T_s - T_a = -15$, 0, and $+15^\circ\text{C}$.

Table 3. Simulations with MCSST equations assuming $T_s - T_a = 0$

$T_s - T_a$	Split-window equation			Triple-window equation		
	N	bias	rmsd	N	bias	rmsd
-15	67	+1.30	1.86	67	+1.04	1.10
0	67	+0.00	0.38	67	-0.01	0.07
+15	67	-0.63	1.76	67	-0.05	0.37



ORIGINAL PAGE IS
OF POOR QUALITY

Figure 3. Split-window ($T_{4/5}$) and triple-window ($T_{3/4/5}$) atmospheric corrections for simulated extreme sea-air temperature differences

5.3 Severe Aerosol Situations

The dust veil from the eruption of El Chichón in April 1982 had a severe impact on MCSST processing for over a year, especially in the band from about 0-30°N latitude (Strong et al., 1983). Not only were daytime MCSST cloud tests failed because of reflected radiation from the volcano cloud, but nighttime retrievals were characterized by substantial negative biases from increased attenuation by minute sulfuric acid droplets at very low temperatures. The Weinreb & Hill (1980) atmospheric transmittance models were used with a diverse set of 56 atmospheric soundings, with and without hypothesized El Chichon type aerosols, to determine simulated brightness temperatures for the AVHRR window channels. The left two graphs of Fig. 4 show the simulated triple-window relation between the attenuation temperature depression in T_{11} and the temperature difference ($T_{3.7} - T_{12}$). The aerosol-free data show the unique linear relation with extremely small scatter that is the basis of Eqn. (3) discussed in Sec. 2.2. The lower-left graph shows the same relation when two other aerosol concentrations are included, the 56 soundings being evenly divided into three aerosol classes. Each class exhibits a different relationship; i.e., no unique solution for SST appears. The graph at the right shows an alternative triple-window relationship, the temperature depression in T_{12} vs. $T_{3.7} - T_{11}$, but with the same aerosol classes as at lower left. Although the scatter is greater than in the aerosol-free case, there appears a unique relationship that is not sensitive to aerosol concentration. Preliminary testing of a volcano MCSST algorithm based on this result was encouraging, but extensive testing was precluded by a severe noise problems in the 3.7 μm channel (see Sec. 7).

In addition, efforts are underway to extend the work of Griggs (1981) to severe aerosol conditions, and then to develop corrections to MCSSTs based on dynamic estimates of aerosol optical thickness from concurrent visual channel AVHRR data (Schwedfeger et al., 1983). Other extreme aerosol situations, such as Saharan dust outbreaks over the eastern subtropical Atlantic, also are known to affect certain MCSST retrievals, but investigations of these are just getting underway.

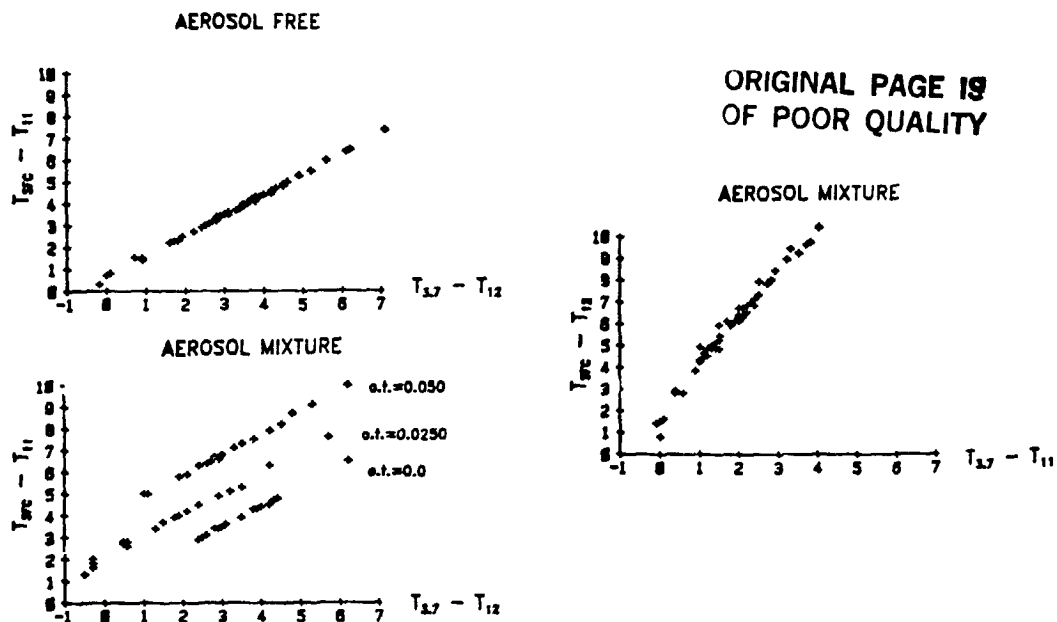


Figure 4. Multi-window atmospheric corrections for simulated volcanic aerosols

6. USE OF MCSSTs IN ATMOSPHERIC/OCEANIC RESEARCH

Although available operationally for just two years, and plagued during much of that time with El Chichon effects and noise problems in the 3.7 m data, MCSSTs are seeing increased use both operationally and in research. Legeckis' investigation of equatorial long waves in the eastern equatorial Pacific continues to be greatly aided by the regional 50-km charts (Legeckis et al., 1983). Some of these westward-moving waves are readily apparent in the isotherms in Fig. 1. The El Nino episode of 1982-83 was unusual in many respects (Rasmusson and Wallace, 1983), but among them was the intense positive SST anomaly that first began to develop along the equator between the Galapagos and the date line during the late summer of 1982. Few ships or other *in situ* observations were available in this area, especially during the early stages, and the MCSST analyses were the first operational charts to clearly depict the extent and amplitude of the anomalously warm water in that region (Strong, 1983). The anomaly as it was in September 1982 is seen in Fig. 2. MCSST techniques also were employed extensively by researchers involved in the Gulf Stream Rings Project (Brown, 1983).

7. CONCLUDING REMARKS

Although some of the physical processes are not really accounted for in the fairly simple theoretical models employed to date, especially those associated with high concentrations of aerosols, the effects of most are sufficiently small and/or compensating that their net effect on the MCSST is also rather small, thus accounting for the stability of the good area-wide and season-wide accuracies measured relative to drifting buoys. Similar matchup statistics have been obtained daily on a global basis as part of the MCSST operational processing with respect to intake temperatures from so-called ships of opportunity. The statistics against ships tend to be poorer and more variable than those against drifting huoyos (Strong and McClain, 1984), but this follows from the fact that ship SSTs matched with other ship SSTs (within 24 hours and 100 km) consistently have been found to have differences with a standard deviation of 1.5-2.0°C. There is the

possibility of increasing the accuracy of multi-window SSTs yet further by adding further by adding multiple viewing-angle capability. The results of simulations at the Rutherford Appleton Laboratory in England have been encouraging (Llewellyn-Jones, 1983), and this approach is incorporated in the design of the Along Track Scanning Radiometer proposed for the ERS-1 satellite.

A often asked question is the difference to be expected between the "skin temperature" sensed by a radiometer in space and a "bulk temperature" measured by an in situ sensor on a buoy (depth of 1 meter) or in a ship's water-intake manifold (depth of perhaps 10 meters). This skin minus bulk temperature difference should be 0.2°C or less with well-mixed upper layers; but in the daytime under a high sun and very light winds, the skin temperature can easily be elevated several degrees above that at depth.

A recurring engineering problem has been electrical interference in the 3.7 μ m channel, the noise level increasing with time following launch of the spacecraft. The less severe noise levels can be compensated for in the MCSST processing (e.g., using larger unit arrays) at the consequent expense of lower observational densities and somewhat degraded accuracies from poorer cloud filtering. NOAA-7 noise levels had increased so much by June 1981 that it necessitated abandonment of this channel because of serious nighttime SST product degradation. Outgassing procedures were carried out on NOAA-7 for a week in September 1983, and this reduced the noise to very low levels again. Monitoring is being maintained to ascertain whether the noise returns and at what rate of increase.

Although serious attempts to map sea surface temperature globally from space have been underway since early in the 1970's, only since late in 1981 when multi-channel sea surface temperatures began to be processed operationally from AVHRR measurements, have the coverage and accuracy achieved levels where oceanographers and meteorologists alike are beginning to use satellite-derived SSTs in their activities. With good coverage provided by satellite-based sea surface temperatures in the Southern Hemisphere oceans and other data-sparse areas, a truly global time series becomes feasible.

8. ACKNOWLEDGEMENTS

The author acknowledges the important contribution of C. C. Walton to the subsection on severe aerosol situations, the assistance of A. E. Strong to the subsection on large sea/air temperature differences, and the help of O. L. Smith by typing of the manuscript.

9. REFERENCES

- Anding, D. and R. Kauth, 1970: Estimation of sea surface temperature from space. *Remote Sensing of Environ.*, 1, 217-220.
- Barton, I. J., 1983: Dual channel satellite measurements of sea surface temperature. *Quart. Jour. Roy. Met. Soc.*, 109, 365-378.
- Brower, R. L., H. D. Gohrband, W. G. Pichel, T. L. Signore, and C. C. Walton, 1976: Satellite derived sea surface temperatures from NOAA spacecraft. NOAA Tech. Memo. NESS 78, U.S. Dept. of Commerce, Wash., DC, 74 pp.
- Brown, O. B., 1983: personal communication. Rosenstiel School of Marine and Atmospheric Science, Univ. of Miami, Coral Gables, FL 33124.
- Deschamps, P. Y. and T. Phulpin, 1980: Atmospheric correction of infrared measurements of sea surface temperature using channels 3.7, 11, and 12 μ m. Boundary

- Griggs, M., 1981: AVHRR measurements of atmospheric aerosol over oceans. Report, NOAA Contr. #MO-A01-78-0J-4092, Sci. Applic., Inc., LaJolla, CA., 50 pp.
- Legeckis, R., W. Pichel, and G. Nesterczuk, 1983: Equatorial long waves in geostationary satellite observations and in a multi-channel sea surface temperature analysis. *Bull. Am. Meteor. Soc.*, 64, 133-139.
- Llewellyn-Jones, D. T., 1983: in *Satellite-Derived Surface Temperature: Workshop II*. NASA/JPL, Pasadena, CA (in press).
- McClain, E. P., 1981: Multiple atmospheric-window techniques for satellite-derived sea surface temperatures. *Oceanography From Space* (J.F.R. Gower, Ed.). Plenum Press, New York, NY, 73-85.
- McClain, E. P., W. G. Pichel, C. C. Walton, Z. Ahmad, and J. Sutton, 1983: Multi-channel improvements of satellite-derived global sea surface temperatures. *Adv. Space Res.*, 2, 43-47.
- McMillin, L. M., 1975: Estimation of sea surface temperatures from two infrared window measurements with different absorption. *Jour. of Geophys. Res.*, 80, 5113-5117.
- NASA/JPL, 1983: *Satellite-Derived Surface Temperature: Workshop I*. JPL Publ. 83-34, Pasadena, CA, 147 pp.
- Prabhakara, C., G. Dalu, and V. G. Kunde, 1974: Estimation of sea surface temperature from remote sensing in the 11 to 13 μ m window region. *Jour. of Geophys. Res.*, 79, 5039-5044.
- Rasmusson, E. M. and J. M. Wallace, 1983: Meteorological aspects of the El Nino/Southern Oscillation. *Science*, 222, 1195-1202.
- Schwalb, A., 1978: The TIROS N/NOAA A-G satellite series. NOAA Tech. Memo. NESS 95, U.S. Dept. of Commerce, Wash., DC, 75 pp.
- Schwedfeger, A., L. L. Stowe, and A. Gruber, 1983: Sensitivity of Earth radiation budget parameters for El Chichon volcanic aerosol as estimated from NOAA-7 AVHRR data. Preprint 5th Conf. Atmos. Rad., Baltimore, MD. 3pp.
- Strong, A. E., 1983: El Nino observations by remote sensing. *Proceed. 17th Internat. Symp. on Remote Sens. Environ.*, Ann Arbor, MI, 177-184.
- Strong, A. E. and E. P. McClain, 1984: Improved ocean surface temperatures from space--comparisons with drifting buoys. *Bull. Am. Meteor. Soc.* (in press).
- Walton, C. C., R. L. Brower, and T. L. Sigmere, 1976: Satellite-derived sea surface temperatures by multi-channel regression. *Proceed. COSPAR Symp. on Meteor. Obs. from Space*, COSPAR XIX, Philadelphia, Pa., 8-10 June 1976, 155-159.
- Walton, C. C., 1980: *Deriving sea surface temperatures from TIROS-N data. Remote Sensing of Atmospheres and Oceans*, Academic Press, 547-579.
- Weinreb, M. P. and M. L. Hill, 1980: Calculations of atmospheric radiances and brightness temperatures in infrared window channels of satellite radiometers. NOAA Tech. Memo. NESS 80. U. S. Dept. of Commerce, Wash., DC, 40 pp.

N84 27208

SATELLITE TECHNIQUES FOR DETERMINING THE GEOPOTENTIAL FOR SEA-SURFACE ELEVATIONS

Vincent L. Pisacane
The Johns Hopkins University/Applied Physics Laboratory
Johns Hopkins Road, Laurel, Maryland 20707, USA

ABSTRACT

Spaceborne altimetry with measurement accuracies of a few centimeters has the potential for determining sea-surface elevations necessary to compute accurate three-dimensional geostrophic currents from traditional hydrographic observations. The limitation in this approach is the uncertainties in our knowledge of the global and ocean geopotentials which produce satellite and geoid height uncertainties about an order of magnitude larger than the goal of about 10 cm. This paper begins with a description of the quantitative effects of geopotential uncertainties on processing altimetry data. This is followed by a review of existing models which are shown to be inadequate. Potential near-term improvements, not requiring additional spacecraft, are discussed. However, even though there would be substantial improvements at the longer wavelengths, the oceanographic goal would not be achieved. The potential NASA Geopotential Research Mission (GRM) is described. This mission should produce geopotential models that are capable of defining the ocean geoid to 10 cm and near-earth satellite positions significantly better. For completeness, the state-of-the-art and the potential of spaceborne gravity gravimetry is described as an alternative approach to improve our knowledge of the geopotential.

1. INTRODUCTION

This paper addresses the importance of an accurate representation of the geopotential in physical oceanography, its current state of knowledge and possible near-term and long-term improvements.

If the oceans were static and subject only to gravitational and centrifugal forces, they would conform to a conceptual surface called the geoid on which the gravity potential function (or geopotential) is a constant. The oceans are not static, and transport of heat, salt, and momentum have a profound effect on climate. As a result, study of the temporal and steady-state circulation of the oceans is important. These motions are governed by the equations of fluid dynamics and solution is dependent on conditions at the boundaries and throughout the medium. Velocities at the ocean surface are primarily induced by wind stress and differences in pressure. On the rotating earth, ocean pressure differences give rise to geostrophic velocities resulting from a balance between pressure and coriolis forces such that the velocity is normal to the pressure gradient. Surface pressure differences are caused by departures of the ocean surface from the ocean geoid. These departures, called sea-surface elevations, can be as large as 1 to 2 meters in the broad ocean areas and significantly larger at the land-sea interfaces.

The relation between the surface geostrophic velocity and change in sea-surface elevation is given by

$$v = (g/f)(\partial H/\partial x)$$

where g is the local acceleration of gravity ($\approx 9.8 \text{ m.s}^{-2}$), $f = 2\Omega \sin(\text{latitude})$ where Ω is the angular velocity of the earth ($7.27 \times 10^{-5} \text{ s}^{-1}$), and $\partial H/\partial x$ is the horizontal slope of the sea-surface elevation. An uncertainty in sea-surface elevation of 10 cm

over a distance of 1000 km would result in a velocity uncertainty of $1 \text{ cm} \cdot \text{s}^{-1}$ at a latitude of 45 degrees. This would be sufficient for a better understanding of current velocities.

A gross quantitative understanding of large-scale ocean circulation has resulted from shipboard measurements. Velocities based on density distributions inferred from in situ measurements can be determined to within a local constant if the sea-surface elevations are unknown. Determination of this constant is possible by in situ measurement of velocity. However, in practice this is not usually feasible as it would take months to average the small-scale velocity variations. Alternatively, the constant can be determined from the suspect assumption that the velocity vanishes at some level in the ocean called the level-of-no-motion. The inability to accurately determine this constant has been a limitation to the quantitative description of the geostrophic current systems.

With the advent of spaceborne microwave altimetry a solution is possible. With its inherent global coverage and measurement accuracy, altimetry has the potential for determining sea-surface elevations to a few centimeters. This, together with traditional hydrographic observations, would make possible determination of the three-dimensional geostrophic currents unencumbered by the assumption of a level-of-no-motion. However, the effectiveness of this approach is limited by uncertainties in our knowledge of the global geopotential and the ocean geoid.

2. SATELLITE ALTIMETRY

Spaceborne nadir pointing high resolution microwave radar altimetry has been an exciting source of data for ocean topography (Chovitz, 1983; and Marsh, 1983). Instrument range measurement precision has improved steadily from the 1 to 2 m for Skylab and the 30 to 40 cm for GEOS-3 to the 5 to 7 cm for SEASAT. Two new spaceborne altimeter missions are planned. The U.S. Navy program, GEOSAT, is undergoing fabrication at The Johns Hopkins University Applied Physics Laboratory with launch scheduled in the fall of 1984 (Pisacane and DeBra, 1983). Primary purpose of the mission is to better determine the ocean geoid by essentially completing the SEASAT mission. By collecting data at widely spaced intervals of time errors caused by time dependent sea-surface elevations, can be minimized. Instrument accuracy should be the same as SEASAT because it is essentially of the same design with improvements of an engineering nature. The second program is TOPEX which is a NASA venture now in the planning and instrument development stage. The primary purpose of TOPEX is to determine sea-surface elevations. An official new start is projected for 1985 with launch expected in 1988 or 1989.

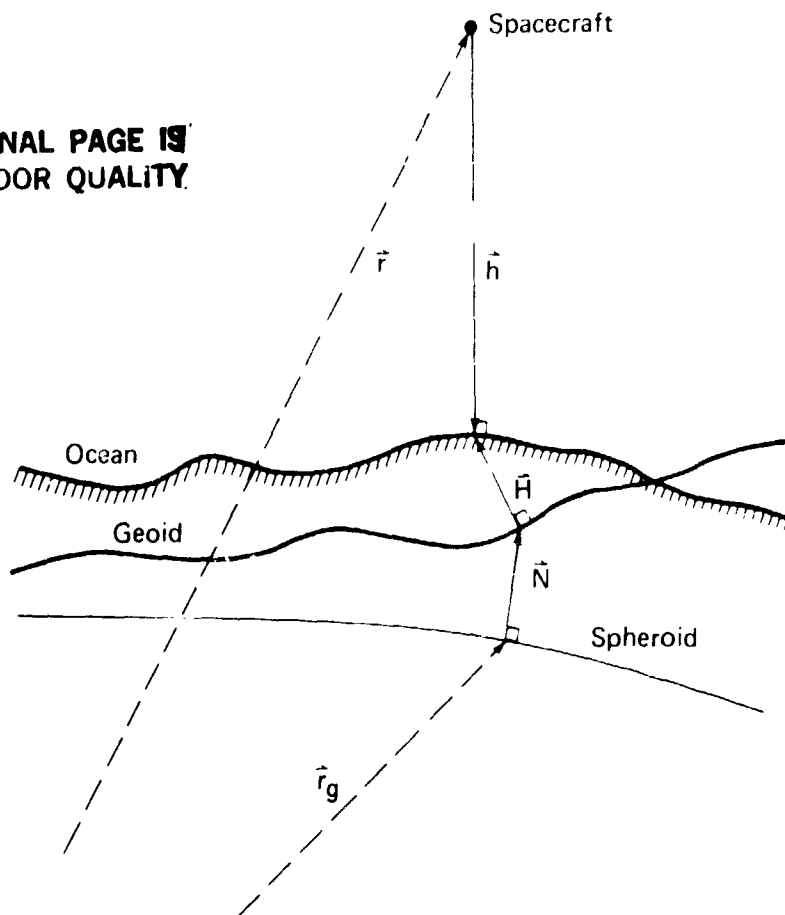
Figure 1 shows the geometrical configuration of satellite altimetry. From the altimetry data, h can be inferred where \vec{h} is the distance from the center of mass of the spacecraft to that point on the ocean nearest to it. Sea-surface elevation H is given in terms of \vec{h} by

$$\vec{H} = \vec{r} - \vec{h} - \vec{N} - \vec{r}_g$$

where \vec{N} is geoid height vector and \vec{r} and \vec{r}_g are the position vectors to the center of mass of the spacecraft and to the subsatellite point on the reference surface respectively. Errors in δH are

$$\delta H = \frac{\vec{H}}{H} (\delta \vec{r} - \delta \vec{h} - \delta \vec{N})$$

ORIGINAL PAGE IS
OF POOR QUALITY



Position vectors from center of mass reference frame:

\vec{r} = satellite

\vec{r}_g = reference spheroid

Height vectors:

\vec{h} = altimeter measurement

\vec{H} = sea surface elevation

\vec{N} = geoidal height

Fig. 1 Satellite altimetry geometry.

Because the vectors are near parallel,

$$\delta H \approx \delta r - \delta h - \delta N$$

so that errors in the satellite altitude, the measurements, and the geoid height have the same sensitivity. Because of the large footprint of the altimeter, i.e., ~ 1 km, errors in spacecraft position orthogonal to \vec{h} are of second order. Consequently, r , h , and N all need be determined to the same degree of accuracy.

Contributions to δh are uncertainties in instrumentation delays, distance from the center of mass to the electrical center of the antenna, spacecraft attitude, propagation velocity, the effect of ocean surface characteristics, and random noise. These are discussed in depth by Marsh (1983) and Tapley et al (1982) and will not be considered here as other errors dominate. Errors that contribute to δr , i.e., satellite altitude, are of two types: those from the spacecraft tracking system (e.g., station location, propagation velocity, and instrumentation errors) and modeling of the forces that act on the spacecraft, (e.g., gravity, radiation pressure, and drag) that are necessary to correlate tracking data taken at different times. Today, the dominant error in determining satellite ephemerides from tracking systems such as laser and radiofrequency doppler is the uncertainty in the global geopotential. This uncertainty manifests itself in tracking station position errors and errors in the gravity forces. Errors in the geoidal height, δN , follow directly from both errors in and truncation of models of the geopotential. Because of density inhomogeneities, primarily in the earth's crust, the geoid is not a smooth surface and can depart from the reference oblate spheroid surface by as much as 100 m.

The total gravitational potential, V^* , can be represented in terms of spherical harmonics by

$$V^*(r, \lambda, \phi) = V_0 + V,$$

where

$$V_0 = \frac{GM}{r}, \text{ the Newtonian potential;} \quad (1)$$

$$V = \sum_{\ell=2}^{\infty} \sum_{m=0}^{\ell} V_{\ell m}$$

$$V_{\ell m} = \frac{GM}{R} \left(\frac{R}{r}\right)^{\ell+1} (C_{\ell m} \cos m\lambda + S_{\ell m} \sin m\lambda) P_{\ell m}(\cos \phi) \quad (2)$$

G = universal gravitational constant

M = mass of earth

R = normalizing radius, generally the mean equatorial radius

r, λ, ϕ = radius, longitude and colatitude

$P_{\ell m} = (1 - t^2)^{m/2} \frac{d^m}{dt^m} P_{\ell}(t)$, associated Legendre function of the first kind

$P_{\ell}(t) = \frac{1}{2^{\ell} \ell!} \frac{d^{\ell}}{dt^{\ell}} (t^2 - 1)^{\ell}$, Legendre polynomials

$C_{\ell 0} = \frac{1}{M} \int \left(\frac{r'}{R}\right)^{\ell} P_{\ell}(\cos \phi') dM$

$$\begin{pmatrix} C_{\ell m} \\ S_{\ell m} \end{pmatrix} = \frac{2(\ell-m)!}{M(\ell+m)!} \int \left(\frac{r'}{R}\right)^\ell P_{\ell m}(\cos \phi') \begin{pmatrix} \cos m\lambda' \\ \sin m\lambda' \end{pmatrix} dM \quad m \neq 0$$

ORIGINAL PAGE IS
OF POOR QUALITY

r', λ', ϕ' = integration parameters over the mass of the earth

$C_{\ell m}, S_{\ell m}$ are the harmonic coefficients which are unknown integrals of the mass distribution of the earth. Following Dunnell et al (1977), the spherical harmonic $V_{\ell m}$ can be represented in Kepler elements ($a, e, i, \Omega, \omega, M$) for near zero eccentricity by

$$V_{\ell m} = \frac{GM}{R} \left(\frac{R}{a}\right)^{\ell+1} \sum_{p=0}^{\ell} I_{\ell mp} S_{\ell mp} \quad (3)$$

Where

$$S_{\ell mp} = \begin{bmatrix} C_{\ell m} \\ -S_{\ell m} \end{bmatrix} \begin{matrix} (\ell-m)\text{even} \\ (\ell-m)\text{odd} \end{matrix} \cos \phi_{\ell mp} + \begin{bmatrix} S_{\ell m} \\ C_{\ell m} \end{bmatrix} \begin{matrix} (\ell-m)\text{even} \\ (\ell-m)\text{odd} \end{matrix} \sin \phi_{\ell mp} \quad (4)$$

$$\phi_{\ell mp} = (\ell-2p)\beta + m(\Omega - \theta). \quad (5)$$

a is the semimajor axes, $I_{\ell mp}$ is a function of the inclination, $\beta = M + \omega$ is the argument of latitude, Ω is the longitude of the ascending node, and θ is the right ascension of Greenwich relative to Aries. This provides a convenient representation of the geopotential for deriving both the geoid height and the effect of the harmonic coefficients on satellite motion. Geoid undulations can be determined from the Bruns theorem as

$$N = \frac{V-U}{g} = \sum_{\ell=2}^{\infty} \frac{V_{\ell} - U}{g} \quad (6)$$

where $g = GM/R^2$ is the local acceleration of gravity and U is the difference of the potential of the ellipsoidal reference surface with the Newtonian potential for which all terms for $\ell > 2$ can be neglected. Substituting for V and approximating a by R gives

$$N_{\ell} = \frac{V_{\ell} - U}{g} \sim \sum_{m=0}^{\ell} \sum_{p=0}^{\ell} R I_{\ell mp} S_{\ell mp} \quad \ell > 2 \quad (7)$$

Perturbations in the radial direction of a satellite in a near-circular orbit, following Dunnell et al (1977), are

$$\delta r = \sum_{\ell=2}^{\infty} \delta r_{\ell}$$

where

$$\delta r_{\ell} = - \frac{GM}{R^2} \left(\frac{R}{a}\right)^{\ell+2} \sum_{m=0}^{\ell} \sum_{p=0}^{\ell} \left[\ell + 1 - \frac{2n(\ell-2p)}{\dot{\phi}_{\ell mp}} \right] \frac{I_{\ell mp} S_{\ell mp}}{(n^2 - \dot{\phi}_{\ell mp}^2)} \quad (8)$$

Because of the linear nature of the expressions for N_{ℓ} and δr_{ℓ} in terms of the harmonic coefficients $C_{\ell m}$ and $S_{\ell m}$, equations (7) and (8) can also be interpreted as determining the effect of uncertainties in the harmonic coefficients.

Estimates of the relative values of δr_{ℓ} and N_{ℓ} can be determined as follows. If the earth were essentially nonrotating such that $\Omega - \theta$ is a constant then

$$\dot{\phi}_{\ell mp} = (\ell - 2p)n$$

and using $n^2 = GM/a^3$, equation (8) can be written as

$$\delta r_{\ell} = R \sum_{\ell=2}^{\infty} \left(\frac{R}{a}\right)^{\ell-1} \sum_{m=0}^{\ell} \sum_{p=0}^{\ell} \frac{(\ell-1)}{(\ell-2p)^2-1} I_{\ell mp} S_{\ell mp} \quad (9)$$

The maximum contribution to the perturbation from the harmonic coefficients at a given frequency $\pm (\ell-2p)n$ occurs when ℓ is a minimum for which p must be either 0 or ℓ . For the highest frequency in δr_{ℓ} , denoted by $\delta r_{\ell}|_{\phi=\pm \ell n}$, the perturbation is

$$\delta r_{\ell}|_{\phi=\pm \ell n} = R \left(\frac{R}{a}\right)^{\ell-1} \sum_{m=0}^{\ell} \frac{1}{\ell+1} [I_{\ell m 0} S_{\ell m 0} + I_{\ell m \ell} S_{\ell m \ell}] \quad (10)$$

Similarly, for N_{ℓ}

$$N_{\ell}|_{\phi=\pm \ell n} = R \sum_{m=0}^{\ell} [I_{\ell m 0} S_{\ell m 0} + I_{\ell m \ell} S_{\ell m \ell}] \quad (11)$$

Then the amplitude or the uncertainty of the ratio of the perturbation in satellite height to the geoid undulation at a frequency ℓn is

$$\left. \frac{\delta r_{\ell}}{N_{\ell}} \right|_{\phi=\pm \ell n} = \left(\frac{R}{a}\right)^{\ell-1} (\ell+1)^{-1} \quad (12)$$

This ratio as a function of harmonic degree for two satellite altitudes is given in Figure 2. Attenuation of the ratio as ℓ increases demonstrates the difficulty in determining small-scale variations in the geopotential by measurement of orbit perturbations. This also demonstrates that the orbit is less effected by contributions of the harmonic coefficients at higher degree ℓ . Rotation of the earth introduces frequencies that are smaller than orbital, $\dot{\phi}_{\ell mp} < n$, such that the magnitude of the orbital perturbations are enhanced by the factor $\dot{\phi}_{\ell mp}^{-1}$. Consequently, the more significant perturbations occur at the longer wavelengths and small-scale

altimeter variations are primarily a result of the topography of the ocean surface. Equations (10) and (11) demonstrate that small variations in the mean Kepler elements produce second-order effects in both the satellite altitude perturbation and the ocean geoid. This is the mathematical justification of using an orbit with a repeating ground track so that the geopotential uncertainties result in highly correlated errors. Variations in the altimeter measurements can then be interpreted as time dependent components of sea-surface elevations.

To determine the absolute sea surface elevation requires a global geopotential model to determine the satellite altitude which is far less detailed than the model required to define the ocean geoid.

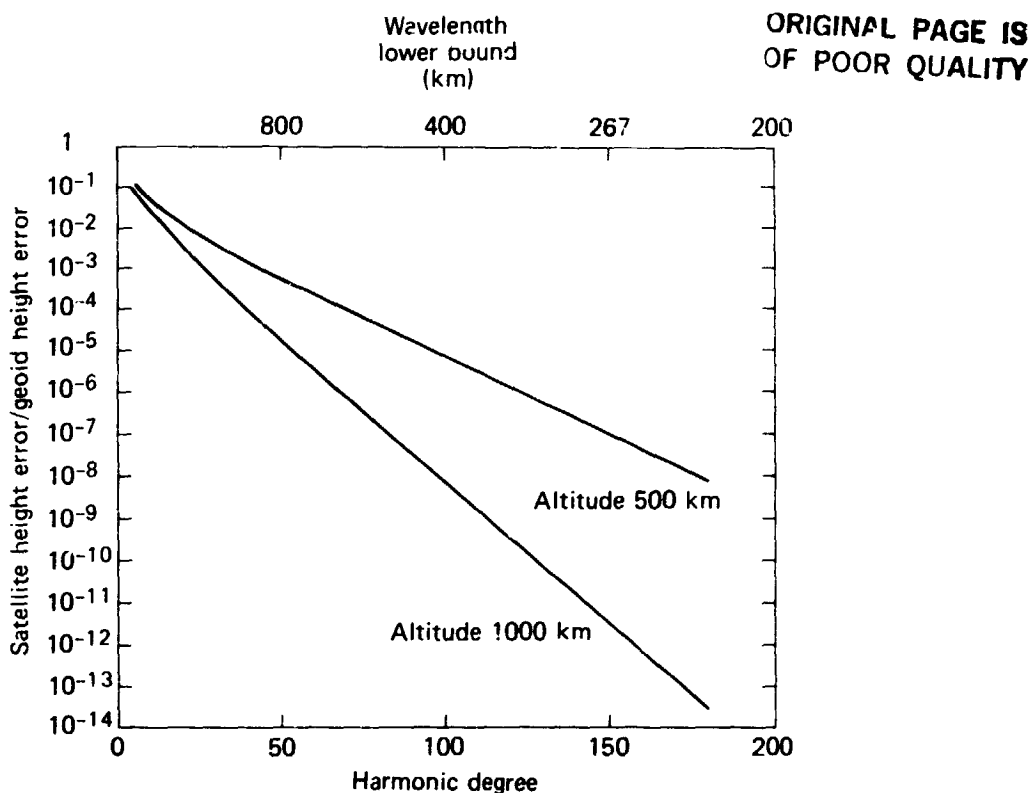


Fig. 2 Ratio of satellite height error to geoid height error versus harmonic degree.

3. GEOPOTENTIAL MODELING STATUS

A review of the current status of modeling the geopotential is available (Lerch 1983). These models use various sources of data: orbit perturbations through laser and radio frequency doppler observations, satellite altimetry, and measurements of terrestrial gravity anomalies. Resolutions are as small as a half-wavelength of one degree.

Over the years, NASA has generated the Goddard Earth Model (GEM) series which has been the accepted standard. The latest in the series are GEM-9 and 10 (Lerch et al, 1979), GEM-10B and 10C (Lerch et al, 1981), and GEM-L2 (Lerch et al, 1983). Characteristics of these models are given in Table 1. GEM-9 and GEM-L2 are based solely on satellite tracking data, GEM-10 is based on the data used in GEM-9 but augmented by terrestrial gravity anomaly measurements, and GEM-10B and 10C use satellite tracking, surface gravimetry and GEOS-3 altimetry. Various measures of accuracy for GEM-9, 10, 10B and 10C are given in Table 2.

For orbit determination GEM-9, 10, 10B and 10C are comparable with a radial accuracy of about 1 to 2 meters. This compares favorably to the 1 to 2 meters estimated for the satellites of the Navy Navigation Satellite System at about 1000 km. The GEM-L2 model is reported to be superior to the earlier models by more accurate determination of the harmonic coefficients up to degree and order 4. The orbit errors for the LAGEOS spacecraft at an altitude of almost 5900 km were reduced from 2m with GEM-9 to 0.30 cm for GEM-L2. There has not yet been evaluation of this model for low altitude satellites.

The measures of accuracy given in Table 2 indicate that the GEM-10C model has an edge in reproducing the ocean geoid. An accuracy of 1 to 2 meters in geoid height is suggested, and an anomaly accuracy of 4 to 7 mgal for 1 degree regions has been reported (Lerch et al, 1983).

Table 1

Goddard Earth Models (Lerch et al 1981 1983)

Name	Year	Degree complete	No. of Coef's	Minimum wavelength		Data		
				km	deg	Satellite tracking	Surface grav.metry	GEOS-3 altimetry
GEM - 9	1979	20	566	2000	9	✓		
GEM-10	1979	22	594	1820	8.2	✓	✓	
GEM-10B	1981	36	1296	1110	5	✓	✓	✓
GEM-10C	1981	180	32,400	222	1	✓	✓	✓
GEM-L2	1983	20	566	2000	9	✓		

Table 2

Accuracy assessment of ocean geoid (Lerch et al 1981)

Comparisons	Models			
	GEM-9	GEM-10	GEM-10B	GEM-10C
Geoid heights (m)				
GEOS-3 altimetry - trench areas*	2.90	2.87	2.47	1.22
GEOS-3 altimetry - nontrench areas*	1.92	1.80	0.94	0.75
Skylab altimetry	3.2	3.0	2.3	
Seasat altimetry			1.0	
GEOS-3 radial position from crossing analysis	~1	1.34	1.00	
Anomalies (mGal)				
GEOS-3 altimeter, 5° blocks	4.7			
Terrestrial, 5° blocks	0.4			

*After bias and tilt have been fit to remove orbit errors.

4. NEAR TERM IMPROVEMENTS

A workshop was held in February 1982 to address future directions for developing improved models of the geopotential (NASA, 1982). One recommendation was to develop improved models that did not require additional spacecraft to be launched. The consensus was that perhaps up to a 50 percent reduction in errors up to degree 10, i.e., half-wavelengths of 2000 km, with lesser improvements at higher degree could be achieved. These improvements would be realized through two activities. This first would be to develop improved modeling tools, i.e., software incorporating improved physical, mathematical and statistical models taking advantage of the enormous computational speeds and storage now available. The second is to improve the quality and quantity of the existing data by reprocessing, to add additional data from satellites not previously used, to incorporate the SEASAT altimetry data, and to collect additional laser and radio frequency doppler observations in new campaigns.

This effort has not yet been formally undertaken. However, even if all expectations were realized, it would not satisfy the requirements for either orbit determination or the ocean geoid to use altimetry data for the time-invariant surface geostrophic currents.

5. GEOPOTENTIAL RESEARCH MISSION (GRM)

Significant improvements in the global geopotential will be possible as a result of the GRM, formerly GRAVSAT, which is under study by NASA (Pisacane et al, 1982; and Keating, 1983). Accuracy of the global geopotential should be adequate for determining the sea-surface elevations to 10 cm from altimetry data. This program is still in the study phase with the possibility of a new start in 1988 or later and launch in 1992 or later.

Terrestrial tracking of near-earth spacecraft to refine the geopotential is limited. Uncertainties in the propagation velocity, in the ionosphere and especially the atmosphere, can induce data reduction errors larger than the orbital perturbations of interest. To increase the magnitude of the orbital perturbation it is necessary to decrease the altitude as low as possible. At the 160 km altitude of the GRM spacecraft, it would require about 276 stations uniformly distributed to provide global coverage. At this low altitude, the drag force uncertainty is about three orders of magnitude larger than the gravity forces of interest. These limitations are overcome in the GRM by satellite-to-satellite tracking between two satellites in near circular polar orbits separated by distances of 100 to 300 km. The disturbing effects of drag and radiation pressure and in addition, orbit altitude maintenance can be accomplished by the Disturbance Compensation System (DISCOS). This device which was successfully demonstrated on an advanced navigation satellite in 1972, TRIAD, uses a mass expulsion system to force the spacecraft to follow the motion of a free proof mass in a cavity which is shielded from the atmosphere and solar radiation.

Studies have defined the system characteristics given in Table 3. A mission of about 7 months, 6 of which will be operational, will require about 1400 kg of hydrazine fuel for each spacecraft, just under half the total mass. An artist's conception is shown in Figure 3. The two spacecraft will be launched by a single shuttle mission from the Western Launch Facility. Range-rate measurements between the two proof masses will be made to $1 \mu\text{m}\cdot\text{s}^{-1}$ at 4 s intervals. This will be accomplished in part by a radio frequency satellite-to-satellite doppler system. A laboratory instrument has been developed and tested. Differences with measurements from a laser interferometer were significantly less than the goal, i.e., about $0.03 \mu\text{m}\cdot\text{s}^{-1}$ rms. With a measurement precision of $1 \mu\text{m}\cdot\text{s}^{-1}$ at 160 kms altitude, the global geoid as a function of degree should be recovered to the accuracy depicted in Figure 4.

Table 3

GRM spacecraft characteristics

Orbit	
Altitude	≈ 160 km
Inclination	90 ± 1 deg
Lifetime	1/2 year (operational)
Launch	Shuttle
Separation	Variable 100 to 300 km
Physical characteristics	
Length	4.8 m
Body diameter	0.9 m
Solar panels (2)	1.5 m x 3.5 m
Mass	2900 kg (1400 kg hydrazine)
Power	
Solar panels (2) and body mounted cells	400 W (average)
Tracking systems	
Proof mass to proof mass	$1 \mu\text{m} \cdot \text{s}^{-1}$
Ground based	100 m

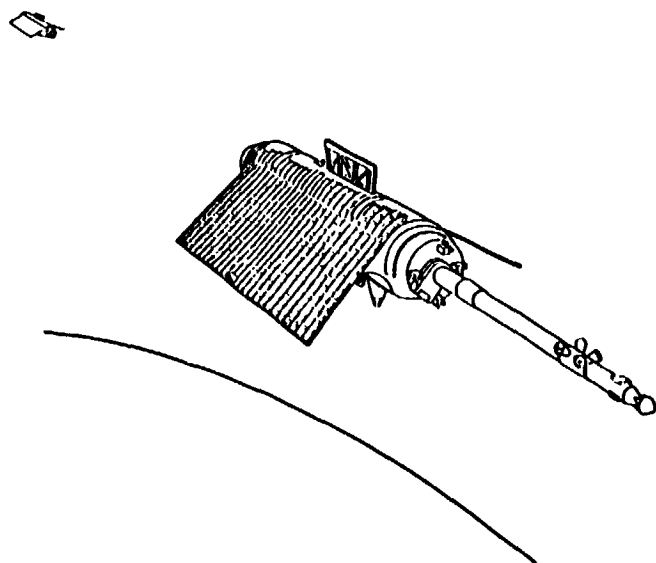


Fig. 3 Artist concept of the Geopotential Research Mission.

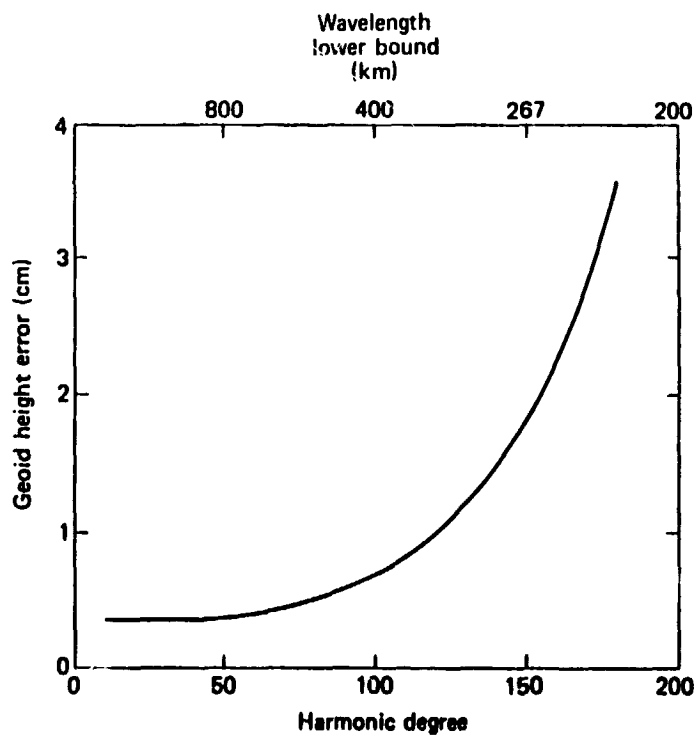


Fig. 4 Geopotential Research Mission (GRM) geoid height uncertainty.

Total geoid height error should be less than 10 cm and satellite altitude error at 850 km should be about one order of magnitude less.

The GRM should be able to provide a global geopotential with sufficient accuracy to limit the geopotential modeling error of the geoid to less than 10 cm.

6. SATELLITE GRADIOMETERS

Satellite-borne gravity gradiometers have been proposed to effect further improvements in determining the geopotential. This approach is currently envisaged as a follow-on to the GRM. To satisfy the objectives of the GRM, measurement precision of about $5 \times 10^{-3}E$ ($1E = 10^{-9}s^{-2}$) is necessary at the same spacecraft altitude, 160 km. As a result, a measurement accuracy of $10^{-4}E$ over a 4 to 8 s interval is necessary to provide an improvement. Reviews of the current state-of-the-art of gravity gradiometry are given by Wilcox and Scheibe (1983) and Pisacane (1983).

Current mobile gravity gradiometers can measure to about $1E$. Fundamental limitations are the instability of the materials, thermal distortion, stability of the scale factor and Brownian noise. To achieve the required accuracy it will be necessary to take advantage of cryogenic technology which should reduce each of the errors described above and most significantly the Brownian contribution. An instrument under development at the University of Maryland uses two opposed superconducting proof masses on a soft suspension and two superconducting sensing coils in a pancake shape (Paik, 1981). Two SQUID amplifiers are used to detect the motion from which the gravity gradient is determined. A single-axis instrument has been tested and a three-axis vector gradiometer should be completed in the near term. A design using a superconducting cavity oscillator accelerometer also appears to have promise (Reinhardt et al, 1982). Other instruments have been proposed as an interim step to achieve $10^{-2}E$. These are the Bell Aerospace Miniature Electrically Suspended Accelerometer (MESA) and the ONERA proposed CACTUS instrument.

A spaceborne gravity gradiometer mission in the late 1990's is a possibility. The specific improvement in the geopotential will depend on the extent of the reduction of errors below $5 \times 10^{-3}E$.

7. CONCLUSION

Spaceborne microwave altimetry has the potential for measuring sea surface elevations to a few centimeters. To properly interpret these data for surface geostrophic currents, it is necessary to make significant advances in modeling the geopotential. The NASA GRM has the potential for meeting the 10 cm accuracy requirement for the global geoid. The success of this mission will be a significant achievement in the three-dimensional determination of the geostrophic currents.

8. ACKNOWLEDGMENT

The author wishes to acknowledge that part of the efforts reported on here were funded through the National Aeronautics and Space Administration Geodynamics Program, Geodynamics Program Office, Office of Space Science and Applications.

9. REFERENCES

Chovitz, B.H., 1983: Geodetic results from SEASAT. Marine Geodesy, 7, 1-4, 315-331.

- Dunnell, C.A., P. Ferriter, G. Gebel, H.S. Hopfield, M.M. Schaefer, and S.M. Yionoulis, 1977: Applied Physics Laboratory, National Geodetic Satellite Program, National Aeronautics and Space Administration Report SP-365, 87-138.
- Keating, T., 1983: Geopotential Research Mission, AAS/AIAA Astrodynamics Spacecraft Conference, Lake Placid, New York.
- Lerch, F.J., 1983: Status of the geopotential, Reviews of Geophysics and Space Physics, U.S. National Report to International Union of Geodesy and Geophysics 1979-1982, 21, 3, 560-565.
- Lerch, F.J., S.M. Klosko, R.E. Laubscher, and C.A. Wagner, 1979: Gravity model improvement using GEOS-3 (GEM-9 and 10), J. Geophys. Res., 84, B8, 3897-3916.
- Lerch, F.J., B.H. Putney, C.A. Wagner, and S.M. Klosko, 1981: Goddard earth models for oceanographic applications (GEM 10B and 10C), Marine Geodesy, 5, 2, 145-187.
- Lerch, F.J., S.M. Klosko, and G.B. Patel, 1983: A refined gravity model from LAGEOS (GEM-L2), NASA Technical Memorandum 84986, GSFC, Greenbelt, Md. 20771.
- Marsh, J.G. 1983: Satellite altimetry, Reviews of Geophysics and Space Physics, U.S. National Report to International Union of Geodesy and Geophysics 1979-1982, 21, 3, 574-580.
- NASA (National Aeronautics and Space Administration), 1982: The report of the gravity field workshop held at NASA Goddard Space Flight Center February 24-26, 1982, Greenbelt, Maryland, NASA Technical Memorandum 84003, GSFC, Greenbelt, MD 20771.
- Paik, H.J., 1981: Superconducting tensor gravity gradiometer. Proceedings of the Second International Symposium on Inertial Technology for Surveying and Geodesy, Banff, Canada, 555-568.
- Pisacane, V.L., 1983: New Techniques, Reviews of Geophysics and Space Physics, 21, 3, U.S. National Report to International Union of Geodesy and Geophysics, 1979-1982, 585-592.
- Pisacane, V.L., J.C. Ray, J.L. MacArthur, and S.E. Bergeson-Willis, 1982: Description of the dedicated gravitational satellite mission (GRAVSAT), IEEE Trans. Geoscience and Remote Sensing, GE-20, 3, 315-321.
- Pisacane, V.L. and D.B. DeBra, 1983: Satellite Technology Developments in Gravity Research, 34th Congress of the IAF, Budapest, Hungary (in press).
- Reinhardt, V.S., F.O. Von Bun, and J.P. Turneure, 1982: A superconducting accelerometer for spacecraft gradiometry, IEEE Position Location and Navigation Symposium, Atlantic City, NJ.
- Tapley, B.D., G.H. Born, and H.E. Parke, 1982: The SEASAT altimetry data and its accuracy assessment, J. Geophys. Res., 87, C5, 3179-3188.
- Wilcox, L.E. and D.M. Scheibe, 1983: Gravimetry, Review of Geophysics and Space Physics, 21, 3, U.S. National Report to International Union of Geodesy and Geophysics, 1979-1982, 537-543.

THE SATELLITE ALTIMETER AS A PLATFORM FOR OBSERVATION OF THE OCEANIC MESOSCALE

Paper Synopsis

Jim L. Mitchell
Remote Sensing Branch
Naval Ocean Research and Development Activity
NSTL, MS 39529

Attempts to use the satellite radar altimeter as a platform to provide synoptic monitoring of the oceanic mesoscale are faced with two critical issues: removal of geoid error or "contamination" and selection of optimum space/time sampling strategies. Long wavelength (10^4 km) orbit determination errors, on the other hand, are not so critical a problem as for altimeter measurements of the basin scale circulation. Both issues must be addressed within the constraints provided by simple orbital mechanics which dictates the laydown pattern of the satellite's groundtracks in space/time. Other issues arise and must be assessed. These are: adequate mission duration scales and the problems of geophysical noise sources and instrumental noise which degrade the effective alongtrack spatial resolution of the altimeter.

The major obstacle facing the use of the altimeter for mesoscale observation is the generally unknown nature of the marine geoid with the precisions necessary for its removal on spatial scales of order 10^2 km. We briefly examine this problem by using both GEOS-3 and SEASAT altimetry of the NW Atlantic during the period July 27, 1978 to August 26, 1978 in an attempt to spatial map mesoscale topography in the region from 25°N to 42°N latitude and from 60°W to 75°W longitude. Orbit error correction is provided by removal of an independent linear tilt and bias for each track through this region. This simple detrending is adequate for removal of residual orbit error to an acceptable level of precision for both GEOS-3 and SEASAT. Comparisons are made between such simple detrending and a regional minimization of crossover point differences. While the latter procedure is invaluable as a tool for modelling large-scale orbit determination error, the procedure's tendency to minimize topography associated with temporal fluctuations make its regional application a less desirable approach for mapping the quasi-geostrophic mesoscale.

Gridded differences of the detrended topography with the Marsh-Chang gravimetric geoid of the region result in a topographic residual field of approximately 35 km spatial resolution. Favorable comparisons are made between the objectively mapped field and that deduced from concurrent in situ observation. Notable problems are introduced by the presence of non-isostatic seamounts, notably the Muir and Kelvin seamounts. Comparisons are made with existing gridded bathymetry of the region. As well, the level of geoid contamination associated with cross-track separation distances is assessed using data from the 3-day repeat cycles of SEASAT. The utility of repeat tracks ("collinear") data is emphasized.

Apparent "smearing" of a number of cold core rings raises the issue of optimum tradeoffs to be made between cross-track separation distance and the period of repeat track closure. The problems of synopticity as well as definition of a stationary ensemble mean topography with collinear tracks, are examined and a resulting optimum strategy for synoptic observation of the quasi-geostrophic mesoscale is presented.

N84 27300

THE EVOLUTIONARY TREND IN AIRBORNE AND SATELLITE RADAR ALTIMETERS

Leonard S. Fedor
NOAA/Wave Propagation Laboratory
325 Broadway
Boulder, CO 80303

Edward J. Waish
NASA Goddard Space Flight Center
Wallops Flight Facility
Wallops Island, VA 23337

ABSTRACT

This paper looks at the manner in which airborne and satellite radar altimeters have developed and where the trend is leading. The airborne altimeters have progressed from a broad-beamed, narrow pulsed, nadir looking instrument, to a pulse-compressed system that is computer controlled, to a scanning pencil-beamed system that can produce a topographic map of the surface beneath the aircraft in real time. The future of the airborne systems seems to lie in the use of multiple frequencies. The satellite altimeters have evolved towards multi-frequency systems with narrower effective pulses and higher pulse compression ratios to reduce peak transmitted power while improving resolution. Future applications seem to indicate wide swath systems using interferometric techniques or beam-limited systems using 100 m diameter antennas.

1. INTRODUCTION

In this paper we will take the term "radar altimeter" to mean a radar system whose data product is primarily a direct range measurement of the sea surface elevation. This eliminates from consideration synthetic aperture radars, side-looking radars, and wave spectrometers since they use range measurements to identify a region on the sea surface from which they measure the backscattered power, not the elevation. We will discuss the airborne systems first since their development has anticipated the satellite systems.

2. AIRBORNE RADAR ALTIMETERS

Table 1 compares the features of three airborne radar altimeter systems of increasing sophistication. The first system was developed in a cooperative effort between the Naval Research Laboratory (NRL) and NASA/GSFC Wallops Flight Facility (WFF) to investigate sea surface scattering experimentally. NRL designed and built two X-band radars capable of transmitted pulse durations down to 1 nsec. The initial radar (Yaplee et al., 1971) investigated near surface scattering from the Chesapeake Light Tower located in the Atlantic Ocean fifteen miles east of Norfolk, Virginia. The second system (Yaplee et al., 1972) was flown in a WFF C-54 aircraft.

The transmitter and receiver horns (5° two-way beamwidth) were mounted side by side and looked at nadir through a port cut in the bottom of the fuselage of the aircraft. The received signal was amplified at RF and fed directly into a diode detector with a very fast response time. The detector output was displayed on the sampling scope whose storage also permitted A/D conversion for recording on magnetic tape.

ORIGINAL PAGE 19
OF POOR QUALITY

The transmitter operated at 9.75 GHz with a pulse-repetition frequency of 90 kHz. Although a narrower pulse was transmitted and individual pulses recorded the "individual" pulses did not correspond to a single transmitted pulse. The sampling scope technique sequentially looked at different ranges for the returned pulses corresponding to a series of transmitted pulses. The range changed by one quantization for every six pulses but because they were so highly correlated there was no reduction of the Rayleigh fading of the signal. The output display rate was 90 Hz. At the beginning of each sweep, seven external channels were sampled followed by 160 data points from the sampling scope. In a typical display the 160 sample points would cover a 100-nsec time interval for a radar range window of 15 m and a range quantization of 0.625 nsec.

In 1973 this pulse-limited system acquired data at 3 km altitude under various wind and sea conditions during the Joint North Sea Wave Project (JONSWAP-2) off the coastal island of Sylt in Germany. The ability of such systems to measure significant wave height (SWH) was well demonstrated by inter-comparison with waverider and pitch-roll buoys, a shipborne wave recorder, and a laser profilometer (Walsh et al., 1978).

It was recognized that to achieve high resolution at manageable peak power from space would require leaving the narrow pulses generated by the NRL radar and going to pulse-compression techniques. Also, the data volume which would be associated with increasing the PRF to decrease the noise in the range measurement needed to be reduced. To verify the viability of this approach, Hughes Aircraft, working with WFF under the NASA Advanced Applications Flight Experiments (AAFE) program, developed an airborne pulse compression radar altimeter operating at 13.9 GHz. The AAFE Altimeter was first flown in 1975 and achieved its 3 ns resolution using a wide bandwidth linear FM transmit waveform and a deramp stretch pulse compression processor. The wideband signal is generated by an acoustic Reflective Array Compressor (RAC) device which expanded a narrow pulse into an FM-modulated 3 μ s pulse. The deramp processor is essentially a correlation mixer which mixed the returned signal with a chirped local oscillator (LO) signal. The LO is a replica of the transmit waveform which is accurately controlled by the altitude tracker to be nearly time coincident with the return pulse. The output of the signal processor is taken from a bank of filters which corresponds to 24 sampling range cells over a 10 m range window.

In addition to testing the 1000 to 1 pulse compression application, this system had greatly increased sophistication. It is computer controlled and has selectable PRF, pulse width, and range tracker parameters. It preaverages return pulses over 0.1 second intervals to reduce the data volume, and computes and displays SWH in real time, in addition to range and AGC. Its tracking accuracy is better than 10 cm.

Up to this point, a pulse-limited radar altimeter's capabilities were limited to measuring the range to the sea surface, the backscattered power, and the SWH of the height distribution. It was decided to build a computer controlled, scanning narrow-beamed, radar system at 36 GHz which could generate a false-color coded elevation map of the sea surface below the aircraft in real time and routinely produce ocean directional wave spectra with off-line data processing. The Surface Contour Radar (SCR), developed jointly by NRL and WFF under the AAFE program, became operational in 1978. The system (Kenney et al., 1979) has an oscillating mirror which scans a $0.85^\circ \times 1.2^\circ$ pencil-beam laterally at 10 Hz to measure the elevations at 51 evenly spaced points on the surface below the aircraft (Figure 1). At each of the points the SCR measures the slant range to the surface and corrects in real time for the off-nadir angle of the beam to produce the elevation of the point in question with respect to the horizontal reference. The elevations are false-color coded and

ORIGINAL PAGE IS
OF POOR QUALITY

displayed on the SCR color TV monitor so that real time estimates of SWH, dominant wavelength, and direction of propagation can be made. The real time display allows the aircraft altitude and flight lines to be optimized during a flight over a visibility obscured sea without prior knowledge of the wave conditions.

The limited peak power available at 36 GHz precludes the transmission of a 1 ns pulse, but the SCR employs a different modulation technique than the AAFE Altimeter. The continuous wave (CW) transmitter is biphase modulated by a digitally generated maximal length code sequence. The return signal is autocorrelated by a like sequence with a variable time delay inserted. The code length and clock rate can be varied, providing selectable range resolutions of 0.15, 0.30, 0.61, and 1.52 m. For the 0.15 m resolution there is an effective 2048 to 1 compression ratio. At the maximum beam scan rate of 10 Hz the range window is 4 m for the 0.15 m resolution.

Transformation by a two-dimensional FFT of the elevation map generated by the SCR produces the sea surface directional wave spectrum (DWS). Comparison of the SCR DWS with in-situ sensors was made during the Atlantic Remote Sensing Land Ocean Experiment (ARSLOE), a multiorganization experiment held October 6-November 30, 1980, near Duck, North Carolina. When the SCR DWS was compared with waveriders and the XERB and ENDECO pitch-and-roll buoys, there was excellent agreement between the non-dimensional spectrum and the angles associated with the A_1 , B_1 , and A_2 , B_2 Fourier coefficients. There were indications that the in-situ sensors had calibration problems with the magnitudes of the higher Fourier coefficients, and that the radar system may be able to measure up to 13 Fourier coefficients compared to the five of the pitch-and-roll buoys. The high spatial resolution and rapid mapping capability over extensive areas make the SCR ideal for the study of fetch-limited wave spectra, diffraction and refraction of waves in coastal areas, and hurricanes and other highly mobile wave phenomena.

The future of airborne altimetry lies in using multifrequency systems to refine our knowledge of the effects of frequency dependent surface scattering as well as the perturbing effects of rain and clouds. Preliminary work has already begun in this area using the combination of the AAFE Altimeter and the SCR which are both presently located on the WFF P-3 aircraft.

Since the SCR measures both returned power and elevation to high spatial resolution, it can determine for various sea states how the backscattered power per unit area varies as a function of the displacement from MSL (Walsh et al., 1984). The SCR uses its pencil beam to determine the spot on the surface to be interrogated. This allows independent histograms of the sea surface height distribution and the return power distribution to be developed from SCR data. The return power distribution (which is what an orbiting altimeter would measure) is shifted towards the troughs relative to the surface height distribution. The measurements indicate that the range measured by a 36 GHz pulse-limited altimeter in space would be biased approximately 1.1% of the value of SWH towards the troughs. However, the EM bias of an altimeter operating at 13 GHz is of more immediate interest because of the TOPEX mission. Since the AAFE Altimeter does not have the spatial resolution to measure EM bias by itself, the SCR will take simultaneous data at 850 m altitude with the AAFE Altimeter (13 GHz) to provide a direct measure of EM bias at 13 GHz.

The indications are that satellite altimeters operating at 13 GHz should be subject to an EM bias equal to 3% of the significant wave height (SWH) but this has not been directly verified. Because of the high spatial resolution of the pencil beam of the SCR, its range measurements are not subject to the EM bias effect and it can determine the actual aircraft altitude. The SCR and AAFE Altimeter will take data simulta-

neously during the NOAA Arctic Cyclone Experiment in January, 1984, while the aircraft proceeds offshore of Greenland under fetch-limited conditions and returns. The antennas of the two systems have been colocated. The ranges determined from the systems will be subtracted and any bias removed to make the difference zero at the start of the flight where the wave height was low. The range difference between the two instruments should increase to 30 cm as the wave height increases to 10 m and then decrease back to zero as the aircraft returns to shore. Figure 2 shows some preliminary data acquired at 1350 m altitude with the SCR-AAFE Altimeter combination. The top of the figure shows the variation in the raw altitude measurements of the two systems. The bottom of the figure shows the range difference between the two systems after some minor corrections to the SCR data. The high frequency noise in the range difference is not a problem since SWH has a slow, trending variation and the data could be averaged over several minutes. A potential problem is the slow oscillation in the mean value which was probably induced by aircraft pitch and roll effects on the AAFE Altimeter. The altimeter beamwidth has been broadened from 15° to 45° to eliminate the attitude sensitivity and a delay line has been added to allow it to operate at 850 m altitude where the signal level and spatial resolution on the SCR is better.

3. SATELLITE RADAR ALTIMETERS.

Table 2 compares the features of four satellite radar altimeters. Three of these radars have been placed in orbit. The first was aboard Skylab, which was launched in May, 1973. The second was on GEOS 3, launched in March, 1975, and the third was aboard Seasat-1, launched in June, 1978. The AAFE Altimeter was the prototype of the Seasat altimeter which used a similar pulse compression technique and effective pulse and also preaveraged returned pulses over 0.1 sec. These altimeters contributed to geodesy and earth physics and measured ocean mesoscale features, wave height, wind speed and ice boundaries.

The Geosat altimeter is scheduled for launch in the fall of 1984 and the ERS-1 altimeter is projected for 1988. Geosat and ERS-1 are essentially Seasat class altimeters. The TOPEX altimeter is under development. Table 2 shows that the trend has been towards more narrow effective pulses and higher PRF. There has not been much motivation for narrowing the effective pulse width beyond the 3 ns width achieved on Seasat. However, the pulse compression ratio has increased so that a longer transmitted pulse with lower peak power could be utilized.

To date, the satellite altimeter has been a narrow swath instrument, but studies have been carried out which indicate the possibility that a multibeam altimeter with additional beams displaced 25 to 50 km on either side of the nadir beam could greatly improve the ocean mesoscale feature mapping capability. One suggestion for the multibeam altimeter (Bush et al., 1984) is to use a TOPEX class altimeter and augment the nadir tracking pulse-limited altimeter with an additional antenna deployed cross-track (Figure 3). Each of the antennas would have multiple feeds to permit the illumination of patches both left and right of nadir. The antenna pair would be connected by a T and driven by a single transmitter-receiver so that interference lobes would be produced. Each interferometer lobe would produce a return similar to that which would be obtained from a large antenna, allowing the radar to obtain precision off-nadir altimetry by centroid tracking the central interferometer lobe. A single antenna would be used to track the nadir.

Satellite roll constitutes a problem when trying to accurately measure range to a point off-nadir. In an 800 km orbit, a multibeam altimeter looking 50 km cross track would experience a 1 cm range change if the satellite roll angle changed by only 200

nanoradians. How would one tell the difference between a roll angle change and a meso-scale surface feature? The solution is to measure the roll independently. Measurements (Green et al., 1979) on a modified breadboard Dry Rotor Inertial Reference Unit-II (DRIRU-II is the NASA standard dual redundant attitude reference for spacecraft) have demonstrated its ability to measure angles to a precision of better than 100 nanoradians over a period of one hour. Achieving this angular noise performance assumes a system operating in conjunction with other sensors and algorithms which can estimate changes in the fixed drift of the gyro. Since mesoscale features would be high frequency occurrences with encounter times on the order of ten seconds compared to the slow, trending variation of roll whose dominant period would be on the order of an orbit for a free flying satellite, low-pass filtering of the range data could supply the information needed by the attitude system. The effect of the roll variation could then be subtracted from the range data for studying mesoscale features.

The advent of the space shuttle has made feasible the deployment of large antennas in space. A large antenna would allow a down-looking real aperture imaging system that has several advantages over the SAR. It could image the reflectivity of the surface while it simultaneously measured the altitude, viewing the surface at near normal incidence. The near nadir imaging capability would provide a viewing angle that could easily be matched with other imagery such as from cameras and IR scanners. Studies have shown that near nadir radar is particularly sensitive to the ripening of crops and soil moisture. The image production is a very simple low data rate assignment of reflectivity to a ground position not requiring the motion compensation, Fourier transformations, or high data rates normally associated with SAR systems. The additional height information provided for each resolution area would contribute to understanding terrain contributions to plant conditions, measurement of plant heights or growth rates, determination of snowdepths, resolving atmospheric conditions such as rain, and surveillance of ships and/or aircraft and other applications.

Large antenna studies such as recently conducted at the NASA Marshall Space Flight Center (MSFC) and presently being conducted at the NASA Langley Research Center (LaRC) are directly leading to the feasibility of a pushbroom image and contouring (PIC) radar for future earth observations. The Harris Corporation (Marvin Sullivan, private communication) is under contract to LaRC to fabricate a 15 m diameter hoop-column space antenna which is a one-seventh scale engineering model for an eventual flight application of a 100 m diameter antenna. The 15 m diameter antenna is presently being assembled and is scheduled for RF testing in late 1984. It is projected to be flight tested on the space shuttle in the 1986-87 time frame. In its initial configuration the collapsible antenna will be roughness limited to a maximum operating frequency of 6 to 8 GHz. However, the addition of more contouring cabling could increase its frequency response up to 13 GHz.

Recent algorithm development for satellite radar altimeters has focused on instruments of the Seasat class. Since that instrument has the demonstrated capability of measuring surface height variations to less than 10 cm, significant wave height to within 10 cm of data buoys, and surface wind speeds to within 1.4 m/s of the data buoys, the need for a new generation instrument might be questioned. But bear in mind that the maximum wave height in the buoy comparisons was approximately 5.5 m and the bulk of the wind speed values were less than 15 m/s (Fedor and Brown, 1982). Although the Seasat altimeter worked very well, none of the above measurements have been verified within severe storm regions; not necessarily because of the high wind speeds and wave heights associated with storms, but due to the presence of rain which attenuates and distorts the transmitted pulse. The ideal instrument to use to correct for the effects of precipitation is the radar altimeter itself, since the data

ORIGINAL PAGE 19
OF POOR QUALITY

corrections will be co-located in space and time with the data to be corrected. When the proper techniques and algorithms exist, the instrument could provide its own measurement of rain rate. The advantage of aircraft borne instruments for this development is that it is economically reasonable to design experiments in an iterative fashion, to test techniques and theories, and to compare the results with the data from other instruments.

The Seasat class radar altimeters were specifically designed for ocean returned pulses which assumed a distribution of specular points. When the pulse is reflected from a few smooth surfaces, the signal can be highly peaked and variable, making it difficult to track and estimate returned power with the existing algorithms. It is necessary to develop models for surfaces that are encountered over land, sea ice, and sheet ice. It would be beneficial to develop a new generation aircraft borne radar altimeter as a mobile laboratory to expand the capabilities of future satellite radar altimeters. In addition, it could be used as an AIR/SEA interaction instrument in concert with other remote sensing instruments both meteorological and oceanographic, in a variety of experiments. These experiments would be concerned with hostile environments (such as provided by tropical and extra-tropical cyclones and the marginal ice zone), oceanographic features provided by current systems, and the passage of meteorological fronts.

In order to be able to provide the research capabilities for problems such as described above, the Advanced Technology Airborne Radar Altimeter (ATARA) would have to have several distinct characteristics. First, it would need to have at least 100 dB of dynamic range in order to sample the large specular returns encountered from new sea ice without saturating and also weak returns from rain and liquid water above the surface. Within existing technology, it is possible to provide intensive sampling of the returned pulse both from and above the surface. It is possible to sample the whole returned pulse using several thousand sampling gates. Having the capability of recording every pulse return would aid in the development of scattering models over land and ice, improved tracking algorithms that would automatically respond to the type of surface being interrogated, and precipitation models that would extend the physical parameters that can be measured by a radar altimeter. ATARA would have on board data processing capabilities that could be refined for eventual satellite applications. It would be used as a validation instrument for future satellite radar altimeters.

The development of airborne and satellite radar altimeters has been closely intertwined. Although ATARA could provide the research tool to understand some of the more complex returns encountered by the satellite instruments, each has unique operational capabilities. The airborne altimeter could be used in specific experiments to understand physical processes, while the satellite altimeter could provide high resolution global measurement of the same processes.

4. ACKNOWLEDGEMENTS

The author acknowledges stimulating conversations with J. T. McGoogan of NASA/GSFC and J. L. MacArthur of the John Hopkins University/Applied Physics Laboratory concerning the advanced systems discussed in this paper.

5. REFERENCES

Bush, G. B., E. B. Dobson, R. Matyskiela, C. C. Kilgus, and E. J. Walsh (1984), "An analysis of a satellite multibeam altimeter," Marine Geodesy, Vol. 8, No. 1,2,3,4, in press.

Fedor, L. S., and G. S. Brown (1982), "Waveheight and wind speed measurement from the SEASAT radar altimeter," Journal of Geo. Res., Vol. 87, No. C5, April, pp.3254-3260.

Green, K. E. Oshika, R. Van Alstine (1979), "Spectral noise performance of a high accuracy dry tuned gyroscope and the NASA Standard Redundant Dry Rotor Inertial Reference Unit (DRIRU II), presented at the Ninth Biennial Guidance Test Symposium, Holloman AFB CIGTF, ADTC-TR-79-11 (Volume 1), October.

Kenney, J. E., E. A. Uliana, and E. J. Walsh (1979), "The surface contour radar, a unique remote sensing instrument," IEEE Trans. on Microwave Theory and Tech., Vol. MTT-27, No. 12, December, pp. 1080-1092.

Walsh, E. J., E. A. Uliana, and B. S. Yapplee (1978), "Ocean wave heights measured by a high-resolution pulse-limited radar altimeter," Boundary Layer Meteor., Vol. 13, pp. 263-276.

Walsh, E. J., D. W. Hancock, III, D. E. Hines, and J. E. Kenney (1984), "Electromagnetic bias of 36 GHz radar altimeter measurements of MSL," Marine Geodesy, Vol. 8, No. 1,2,3,4, in press.

Yapplee, B. S., A. Shapiro, D. L. Hammond, B. B. Au, and E. A. Uliana (1971), "Nanosecond radar observation of the ocean surface from a stable platform," IEEE Trans. Geosci. Electron., GE-9, 170-174.

Yapplee, B. S., A. Shapiro, E. A. Uliana, D. L. Hammond, and K. J. Craig (1972), "Experiment verification of proposed Skylab altimeter measurement," paper presented at the 15th Plenary Meeting of COSPAR, Madrid, Spain, May 1972.

Table 1. A COMPARISON OF AIRBORNE ALTIMETER PARAMETERS

	1971 NRL NANOSECOND RADAR	1975 AAFE ALTIMETER	1978 SURFACE CONTOUR RADAR
ALTITUDE INTERVAL (m)	surface to 4000	850 to 4000	surface to 1500
ANTENNA BREADTH	7.0°	15° or 45°	1.2° X 0.85° (2-way)
FREQUENCY (GHz)	9.75	13.9	36
PEAK RF POWER (W)	10	20	10
AVERAGE RF POWER (W)	0.0009	0.05	10
PULSEWIDTH (UNCOMPRESSED)	1 ns	3 μ s	CW
PULSEWIDTH (ns) (COMPRESSED)	---	3	1, 2, 4, 10
TRANSMITTER PRF (KHz)	90	0.85	90
OUTPUT WAVEFORM FREQUENCY (Hz)	90	10	20 raster lines
RANGE WINDOW (m)	15	10	4 at 1 ns resolution 8 at 2 ns resolution
FOOTPRINT DIAMETER (m)	12 at 150 m alt. 60 at 3 km alt.	104 at 3 km alt.	6 X 8 at 400 m altitude 11 X 16 at 800 m altitude
ALTITUDE PRECISION (rms)	< 10 cm	< 10 cm	< 10 cm

Table 2. A COMPARISON OF SATELLITE ALTIMETER PARAMETERS

	1973 SKYLAB	1975 GEOS-3 (Intensive)	1978 SEASAT-1	TOPEX
MEAN ALTITUDE (km)	435	840	800	1334
ANTENNA BEAMWIDTH (°)	1.5	2.6	1.6	1.04 at K_u band 2.6 at C band
FREQUENCY (GHz)	13.9	13.9	13.5	13.7 (K_u) 5.3 (C)
PEAK RF POWER (kW)	2	2	2	0.020 (K_u) 0.020 (C)
AVERAGE RF POWER (W)	0.05	0.24	6.5	8 (K_u) 2 (C)
PULSEWIDTH (UNCOMPRESSED)	100 ns	1 μ s	3.2 μ s	102 μ s
PULSEWIDTH (ns) (COMPRESSED)	---	12.5	3.125	3.125
REPETITION FREQUENCY (Hz)	250	100	1020	4000 (K_u) 1000 (C)
RANGE WINDOW (m)	60	15	29	62
FOOTPRINT DIAMETER (km)	8	3.6	1.7	2.2
ALTITUDE PRECISION (rms)	< 1 m	< 50 cm	< 10 cm	2.4 cm at 2 m SWH 2.7 cm at 4 m SWH 3.2 cm at 8 m SWH

ORIGINAL PAGE 19
OF POOR QUALITY

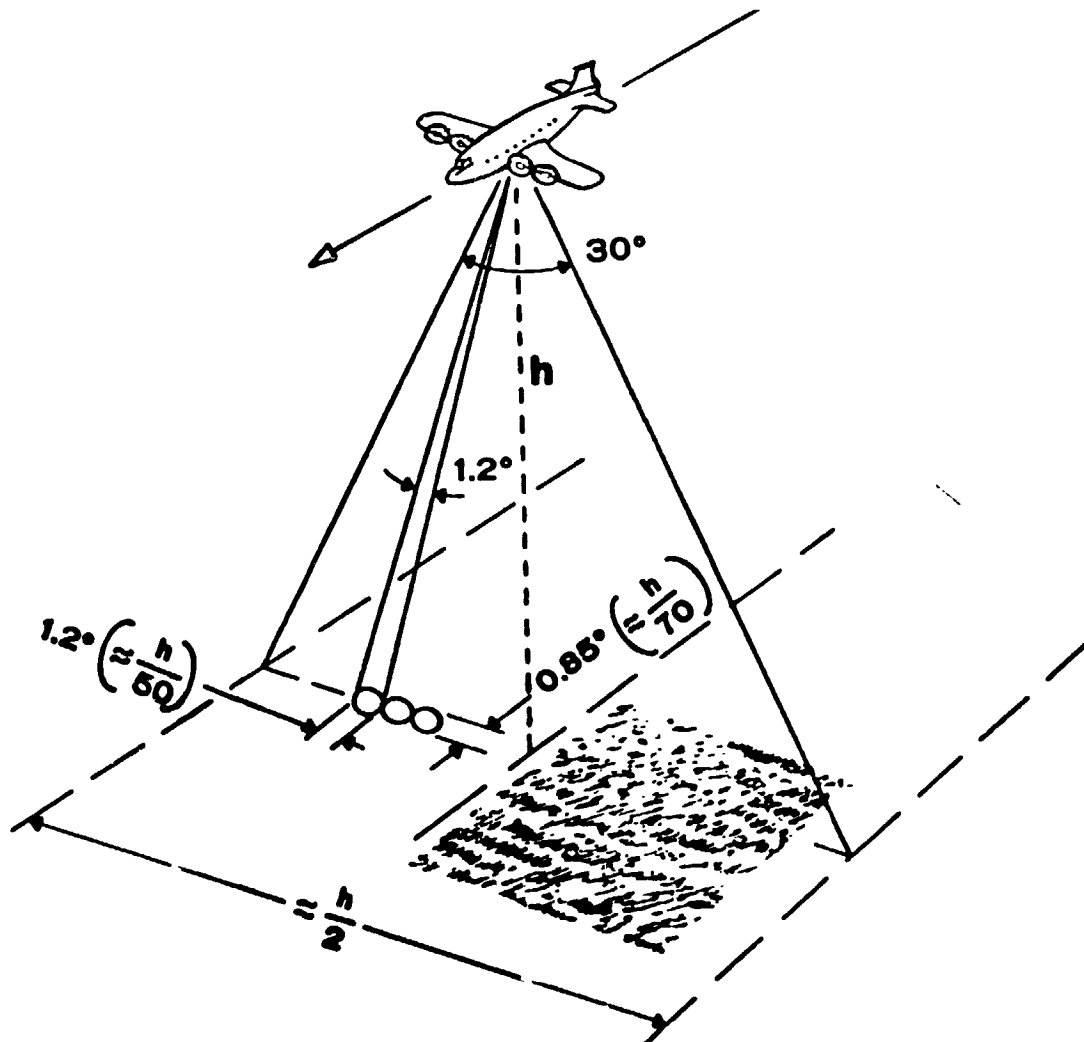


Figure 1. The basic measurement geometry of the Surface Contour Radar.

ORIGINAL PAGE IS
OF POOR QUALITY

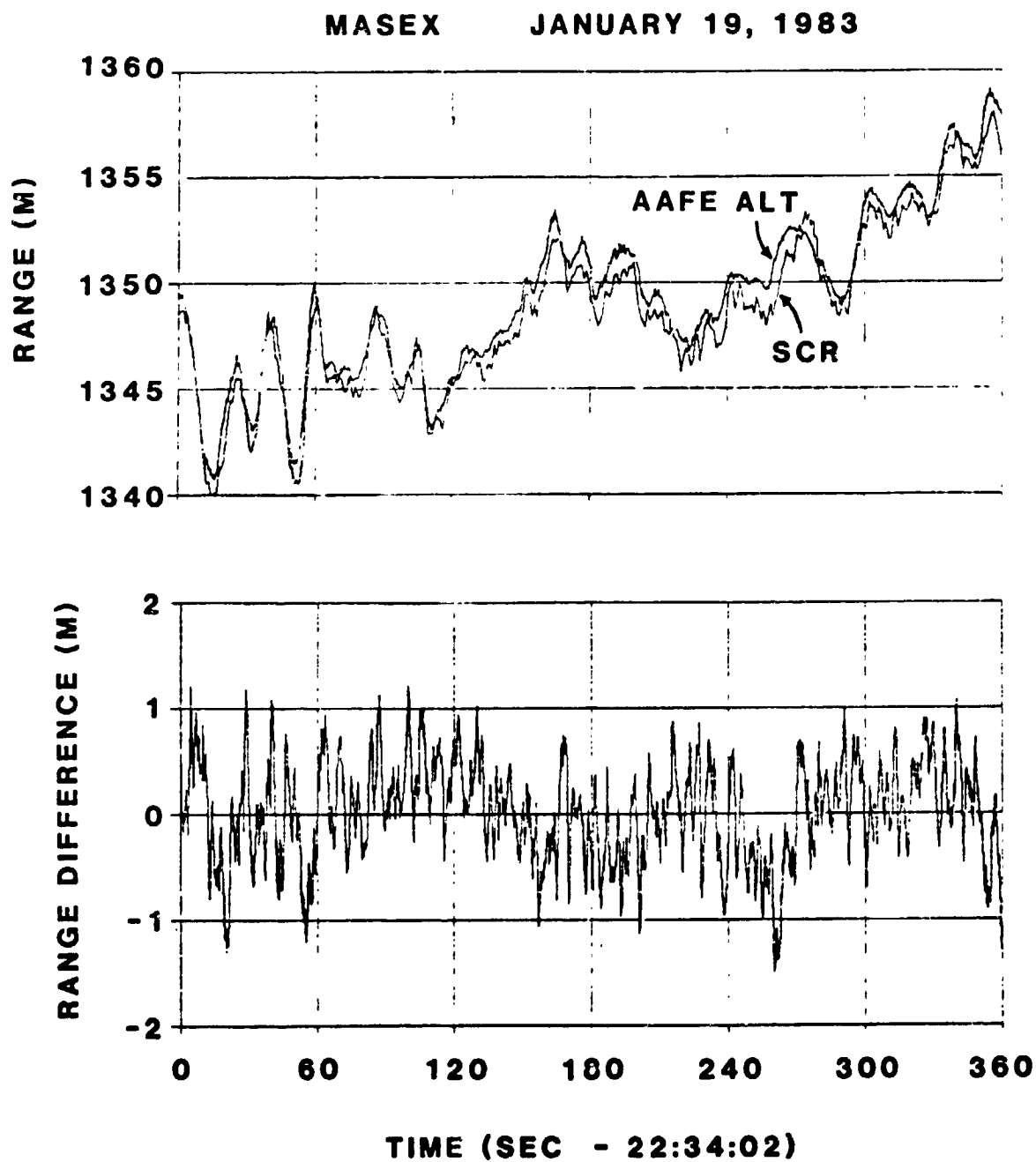


Figure 2. Preliminary range difference measurements for the AAFE Altimeter and the Surface Contour Radar.

ORIGINAL PAGE 19
OF POOR QUALITY

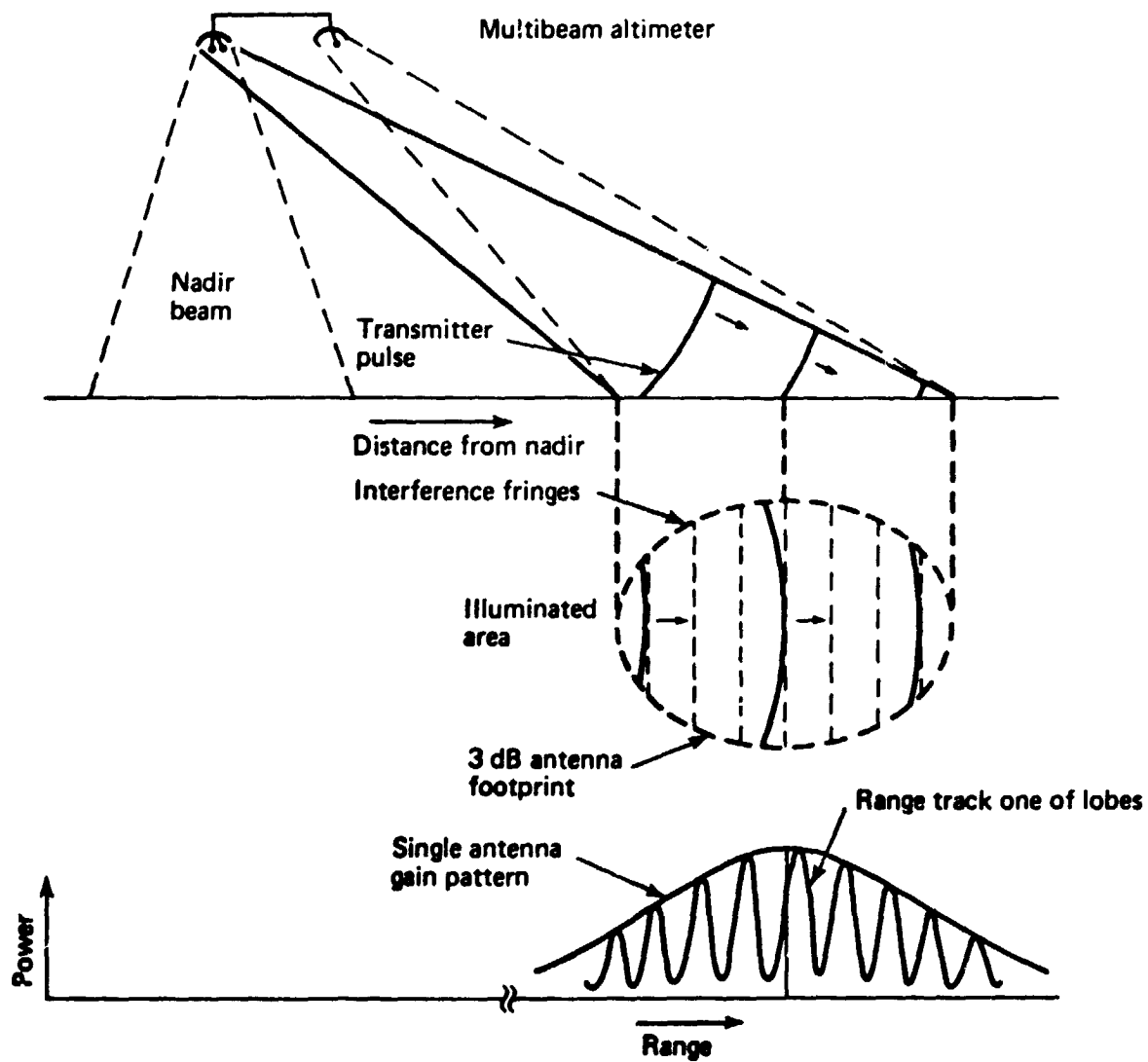


Figure 3. The basic measurement geometry of the interferometric multibeam altimeter.

ON THE DETECTION OF UNDERWATER BOTTOM TOPOGRAPHY
BY IMAGING RADARS

Werner Alpers

Institut für Meereskunde, Universität Hamburg,
and Max-Planck Institut für Meteorologie,
Bundesstr. 55, 2 Hamburg 13, F. R. Germany

ABSTRACT

A simple theoretical model explaining basic properties of radar imaging of underwater bottom topography in tidal channels is presented. The surface roughness modulation is described by weak hydrodynamic interaction theory in the relaxation time approximation. In contrast to previous theories on short wave modulation by long ocean waves, a different approximation has to be used when describing short wave modulation by tidal flow over underwater bottom topography. The modulation depth is in this case proportional to the relaxation time of the Bragg waves. The large modulation of radar reflectivity observed in SEASAT-SAR imagery of sand banks in the Southern Bight of the North Sea can be explained by assuming that the relaxation time of 34 cm Bragg waves is of the order of 30-40 seconds.

1. INTRODUCTION

It has been known for more than 10 years that real aperture radar (RAR) imagery taken over sea areas with strong tidal currents (tidal channels) sometimes shows features that seem to be related to underwater bottom topography (de Loor and van Hulten, 1978; de Loor, 1981; Mcleish et. al., 1981). The same phenomenon has also been observed in synthetic aperture radar (SAR) imagery obtained by the SEASAT satellite (Fu and Holt, 1982; Lodge, 1983; Kenyon, 1983; Lyzenga et. al., 1983). The sea-floor topography (bathymetry) causing these radar signatures sometimes lies tens of meters below the sea surface. An example of such imagery is the SEASAT-SAR image shown in Fig. 1.

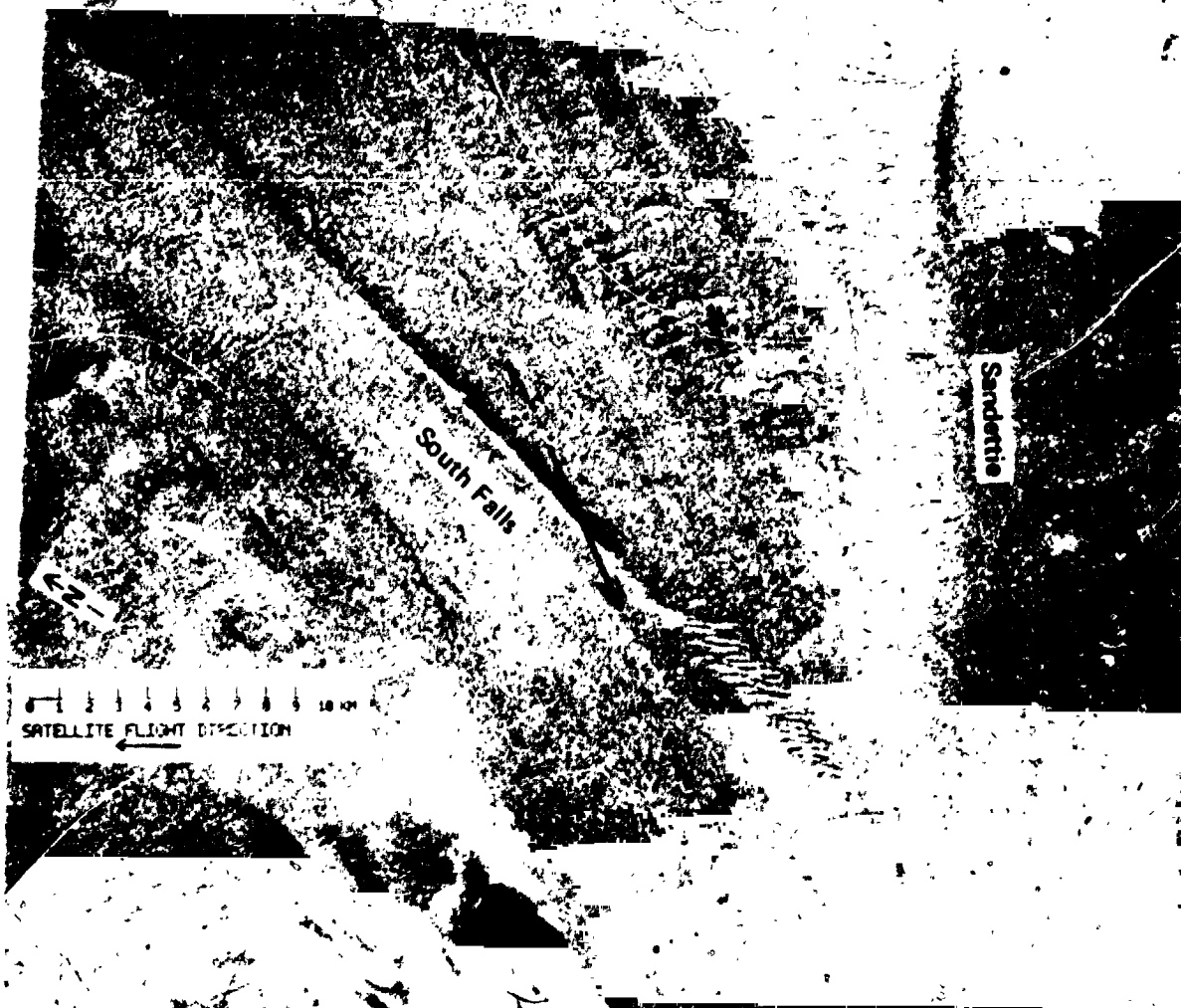


FIG.1: Digitally processed SEASAT-SAR image of the Southern Bight of the North Sea from orbit 762 (Aug. 19, 1978, 6:46 UT) with frame center at $51^{\circ}19'N$, $1^{\circ}52'E$. The land area in lower left hand corner is the English coast near Ramsgate. The V-shaped feature in the center are the sand banks South Falls and Sandettie. South Falls is about 30 km long, 600-800 m broad and rises from the sea floor of a depth of about 30-40 m to within 7 m of the sea surface.

The imaging of underwater bottom topography by real or synthetic aperture radar seems not to be understandable at first sight, because the penetration depth of the electromagnetic waves emitted by the radar into sea water is only of the order of millimeters to centimeters. Therefore, surface effects related to the sea-floor topography must be responsible for the radar imaging.

Since radar signatures of bathymetry are only observed when strong (tidal) currents are present, we are led to the hypothesis that these radar signatures are caused by surface current variations associated with underwater bottom topography. Variable surface currents modify the short-scale surface roughness, and this roughness variation is sensed by the radar. Since most imaging radars operate at incidence angles between 20 and 70 degrees the radar backscattering is dominated by Bragg scattering (Valenzuela, 1978). Consequently, cross-section modulation results from the modulation of the spectral energy of the Bragg waves.

Cross section modulation determines the image intensity or grey tone level variations in real aperture radar imagery. However, in case of synthetic aperture radar, in addition to this amplitude modulation, also phase modulation or velocity bunching contributes to the imaging (Larson et.al. 1976; Alpers and Rufenach, 1979; Alpers et.al. 1981). In most cases of SAR imaging of bathymetry, however, the contribution of velocity bunching to the imaging mechanism is small (Alpers and Hennings, 1984). Therefore we will discuss in this paper only amplitude or cross section modulation.

2. BATHYMETRY - CURRENT INTERACTION

The interaction of a 3-dimensional time-variable current field with 3-dimensional underwater bottom topography (bathymetry) can sometimes be a very complex process which does not allow a simple mathematical description. Nevertheless, in this paper we make the simplest possible assumption that the current flow over the bathymetry is laminar, free of any vertical current shear and only weakly time dependent. Furthermore, we assume that the tidal velocity component U_{\perp} normal to the direction of the underwater bank obeys the continuity equation

$$U_{\perp}(x_{\perp})d(x_{\perp}) = \text{const}$$

ORIGINAL PAGE IS
OF POOR QUALITY (1a)

and that the parallel component U_{\parallel} remains constant,

$$U_{\parallel} = \text{const.} \quad (1b)$$

Here $d(x_{\perp})$ denotes a depth profile along a line perpendicular to the ridge direction (x_{\perp}).

Current measurements on and off the sand bank South Falls by Venn and Olier (1983) in the Southern Bight of the North Sea (north-eastern approach to the English Channel), where the tidal current flows across the bank at an oblique angle, have confirmed that equations (1a) and (1b) are acceptable first order approximations. (However, deviations from these simple relations are observed, and a more refined theory should account for them).

3. CURRENT - BRAGG WAVE INTERACTION

Since the variation of the surface current due to interaction with bathymetry has space and time scales that, in general, are small compared with the space and time scales of the Bragg waves, the current -Bragg wave interaction can be described by a WKB (Wentzel - Kramers - Brillouin)-type interaction theory. In this theory the transport equation, which describes the variation of the spectral energy density of short waves in a slowly varying current field, is the action balance or radiation balance equation (Hasselmann et al., 1973; Keller and Wright, 1975; Alpers and Hasselmann, 1978; Wright, 1978). This equation reads

$$\frac{dN}{dt} = \mathcal{L}[N] = \left[\frac{\partial}{\partial t} + \underline{x} \frac{\partial}{\partial \underline{x}} + \underline{k} \frac{\partial}{\partial \underline{k}} \right] N = S(\underline{x}, \underline{k}, t) \quad (2)$$

where

$$N(\underline{x}, \underline{k}, t) = E(\underline{x}, \underline{k}, t) / \omega' \quad (3)$$

is the action spectrum, $E(\underline{x}, \underline{k}, t)$ the wave spectrum, ω' the intrinsic frequency of the wave in a reference system which is locally at rest, \underline{x} the space variable, \underline{k} the wavenumber and $S(\underline{x}, \underline{k}, t)$ a source function. The waves propagate along trajectories in 4-dimensional phase space which are given by the ray equations

$$\dot{\underline{x}} = \frac{\partial \omega}{\partial \underline{k}}, \quad \dot{\underline{k}} = - \frac{\partial \omega}{\partial \underline{x}}$$

where

$$\omega(\underline{x}, \underline{k}, t) = \omega'(\underline{k}) + \underline{k} \cdot \underline{U}(\underline{x}, t) \quad (5)$$

denotes the wave frequency in the moving medium with variable velocity $\underline{U}(\underline{x}, t)$.

We assume that the variable surface current only leads to small deviations of the action density from equilibrium. Therefore, we write the action density N and the surface current \underline{U} as sums of a constant equilibrium term and a time dependent perturbation term

$$N(\underline{x}, \underline{k}, t) = N_0(\underline{k}) + \delta N(\underline{x}, \underline{k}, t) \quad (6)$$

$$\underline{U}(\underline{x}, t) = \underline{U}_0 + \delta \underline{U}(\underline{x}, t) \quad (7)$$

Furthermore, we approximate the source term S by a diagonal operator

$$S(\underline{x}, \underline{k}, t) = \mu \delta N(\underline{x}, \underline{k}, t) \quad (8)$$

where μ is a parameter with dimension $(\text{time})^{-1}$. μ is called relaxation rate and $\tau_r = \mu^{-1}$ the relaxation time. Physically, τ_r is a system constant describing the response of the wave system to small deviations from equilibrium caused by surface current variations. It is determined by the combined effect of wind excitation, energy transfer to other waves due to conservative resonant wave-wave interaction, and energy loss due to dissipative processes like wave breaking. No measurements of the relaxation time in the open ocean exist. However, from theory we expect that τ_r is of the order of 10 to 100 wave periods. Applied to SEASAT-SAR Bragg waves, which have a wavelength of 34 cm and a wave period of 0.47 s, this means that τ_r should lie in the range between 4.7 and 47 seconds. In this paper we consider τ_r (or μ) as a free parameter. Inserting eqns. (6), (7) and (8) into eqn. (2) and only keeping first order terms yields

$$\left[\frac{\partial}{\partial t} + (\underline{c}_g + \underline{U}_0) \cdot \frac{\partial}{\partial \underline{x}} + \mu \right] \delta N = \underline{k} \cdot \frac{\partial \underline{U}}{\partial \underline{x}} \cdot \frac{\partial N_0}{\partial \underline{k}} \quad (9)$$

The time scales of the three terms on the left hand side are given by the local time T , the advection time τ_a , and the relaxation time τ_r . The local time is of the order of the period of the semi-diurnal tide divided by 2π , which is $12.5/2\pi \text{ h} \approx 2\text{h}$, and the advection time is given by

$$\tau_a = \left| (\underline{c}_g + \underline{u}_0) \cdot \underline{K} \right|^{-1} \quad \text{ORIGINAL PAGE IS OF POOR QUALITY} \quad (10)$$

where \underline{K} is the wavenumber of the bottom topography.

For tidal flow over large-scale underwater bottom topography, such as sand banks, both, the local time T and the advection time τ_a , are usually much large than the relaxation time τ_r . Therefore the first two terms on the left hand side of eqn. (9) can be neglected in comparison with the third term.

This approximation is applicable for describing short surface wave modulation by tidal flow over bathymetry, but it is completely different from the approximation applicable for describing short wave modulation by long surface waves. In this case, the local time is given by Ω^{-1} , where Ω is the radian frequency of the long surface wave. Ω^{-1} is typically of the order of 1 or 2 seconds, which is small compared to the relaxation time τ_r . Therefore, the first term in eqn. (9) is dominant in this case.

We now insert eqn. (4) and the dispersion relation for short surface waves into eqn. (9) and consider only those waves which travel towards or away from the antenna look direction (Bragg waves). If we define the projection of the antenna axis onto the horizontal plane as x-direction, then in case of tidal flow over large-scale bottom topography, we obtain the result

$$\frac{\delta E}{E_0} = - \frac{4 + \gamma}{\mu} \frac{\partial U_x(x)}{\partial x} \quad (11)$$

and in case of long surface waves

$$\frac{\delta E}{E_0} = - \frac{4 + \gamma}{\Omega} \frac{\partial U_x(x)}{\partial x} \quad (12)$$

Here γ denotes the ratio between the group and phase velocity of the short waves. For gravity waves we obtain $\gamma = 0.5$, and for capillary waves $\gamma = 1.5$. In deriving eqns. (11) and (12) we have assumed that the spectral energy of the short waves

is proportional to $|u|^{-4}$.

ORIGINAL PAGE IS
OF POOR QUALITY

Note, that according to Bragg scattering theory,

$$\frac{\delta\sigma}{\sigma_0} = \frac{\delta E}{E_0} \quad (13)$$

where $\frac{\delta\sigma}{\sigma_0}$ denotes the relative cross section modulation.

Comparison of eqns. (11) and (12) shows that in the first case the modulation is proportional to $\mu^{-1} = \tau_r$ and in the second case proportional to $\Omega^{-1} = (2\pi)^{-1} T_w$, where T_w is the period of the long surface wave. We will show below that for the SEASAT-SAR Bragg waves τ_r is of the order of 30 to 40 seconds. This means that for the same current gradient, the modulation by tidal flow over bathymetry is a factor 15-40 larger. On the other hand, the surface current gradient generated by tidal flow over bathymetry is usually much smaller than the surface current gradient generated by the orbital motion of long surface wave (typically one order of magnitude smaller). Therefore we obtain the net result, that the cross section modulation ("modulation depth") associated with tidal flow over sand banks is of the same order of magnitude, or even larger than the modulation associated with long surface waves.

Physically, this result is a consequence of the fact that in the case of tidal flow over bathymetry the weak interaction can act sufficiently long on the short wave system. The limit is given by the relaxation time. In case of short wave modulation by long surface waves, the short waves have not sufficient time to build up a strong modulation because their dwell-time in flow regions with positive or negative velocity gradients is determined by the period of the long surface waves.

If the partial time derivative and advection terms in eqn. (9) are neglected, then eqn. (9) states, that the relaxation of the action density perturbation is balanced by "straining" exerted on the wave system by the spatially varying current \underline{U} . The right hand side of eqn. (9) represents a refraction term. It originates from the fact that the spatially variable current \underline{U} refracts the short waves, i.e., changes their wavenumber. A wavenumber change causes a local perturbation of the equilibrium action (or energy) density spectrum of the short

waves, because the short wave spectrum varies as a function of wavenumber. Thus, the steeper N is, as a function of wavenumber, the larger is the modulation. Note also that the modulation is proportional to the current gradient.

In those cases where the advection time τ_a is not small compared to the relaxation time τ_r , the second term on the left hand side of eqn. (9) has to be retained. The inclusion of this term results in the addition of a low-pass filter to the imaging process. This is discussed in detail in Alpers and Hennings (1984).

4. RELATIONSHIP BETWEEN BATHYMETRY AND CROSS SECTION MODULATION

By combining the results of sections 2 and 3 we can derive an expression relating the cross section modulation to the large scale bottom topography and the tidal current field. Inserting eqns. (1a), (1b) and (11) into eqn. (11) yields

$$\frac{\delta\sigma}{\sigma_0} = \frac{4+\gamma}{\mu} |U_0| d_0 \cos\gamma \cos^2\phi \frac{\text{grad}_\perp d}{d^2} \quad (14)$$

Here ϕ denotes the angle between the flight and the sand bank direction, γ the angle between the $x_{||}$ - and the (undisturbed) flow direction, $\text{grad}_\perp d$ the gradient of the depth profile in direction perpendicular to the bank crest, d_0 the water depth outside the bank area, and $|U_0|$ the modulus of the undisturbed current velocity.

Inspection of eqn. (14) shows that radar signatures of sand banks always have double sign, which means that the radar image is composed of image elements having both enhanced and reduced grey levels relative to the local mean. The sign of the modulation is such that increased radar reflectivity occurs always on the downstream side, and reduced radar reflecting on the upstream side of the sand bank.

Furthermore, eqn. (14) shows that the modulation depth increases with tidal velocity and decreases with water depth. The modulation pattern is not correlated with the depth profile d , but with $d^{-2} \text{grad}_\perp d$.

In particular, eqn. (14) predicts that the cross section modulation vanishes when - the tidal velocity is zero ($|U_0| = 0$)

- the bank crest is aligned parallel to the current direction ($\psi = 90^\circ$)
 - the bank crest is aligned parallel to the radar look direction ($\phi = 90^\circ$)
- (However, we do not expect that the last statement fully holds, because it is a consequence of the fact that our hydrodynamic interaction model does not include the interaction between short surface waves travelling in different directions)

According to eqn. (14) the modulation depth depends on the relaxation time $\tau_r = \mu^{-1}$. We expect that, to first order, τ_r is independent of wind direction. However, it is likely that τ_r decreases with wind speed.

In order to obtain an estimate of the relaxation time we analyzed digitally processed SEASAT-SAR imagery and made several image intensity scans across sand banks in the Southern Bight of the North Sea (north eastern approach to the English Channel) and compared them with bathymetry. One scan was made across South Falls along the line shown in Fig.1. The arrow indicates the direction of the tidal flow at the time of the overflight. The tidal current velocity was 0.60 m/s and the wind was blowing from 135° N at 4 m/s. This image was processed on the MDA (McDonald Dettweiler and Associates) digital SEASAT processor by the Deutsche Forschungs- und Versuchsanstalt für Luft- und Raumfahrt at Oberpfaffenhofen, FRG. The resolution is 25m * 25m (4 looks).

Our analysis shows that we can explain the measured modulation depth if we assume a relaxation time of the order of 30-40 seconds for the SEASAT-SAR Bragg waves (for a wind speed of 4 m/s). This value corresponds to 60-80 wave periods of 34 cm waves.

5. CONCLUSIONS

We have confronted the predictions of our imaging theory with existing experimental data. It seems that the predictions are largely confirmed. However, it should be stressed that we consider this theory only to be a first-order theory.

Finally, we want to suggest the use of radar imagery of bathymetry in tidal channels as a practical means for measuring the relaxation time of short surface

waves in the open ocean.

ACKNOWLEDGEMENT

This research was supported by the Deutsche Forschungsgemeinschaft (SFB 94, Meeresforschung Hamburg).

REFERENCES

- Alpers, W., and K. Hasselmann, 1978: The two-frequency microwave technique for measuring ocean wave spectra from an airplane or satellite, Appendix B, Boundary-Layer Meteorol., vol. 13, 215-230.
- Alpers, W. R., and C. L. Rufenach, 1979: The effect of orbital motions on synthetic aperture radar imagery of ocean waves, IEEE Trans. Antennas Propagat., AP-27 (5), 685-690.
- Alpers, W. R., D. B. Ross, and C. L. Rufenach, 1981: On the detectability of ocean surface waves by real and synthetic aperture radar, J. Geophys. Res. 86, 6481-6498.
- Alpers, W., and I. Hennings, 1984: A theory of the imaging mechanism of underwater bottom topography by real and synthetic aperture radar, submitted to J. Geophys. Res..
- de Loor, G. P., 1981: The observation of tidal patterns, currents and bathymetry with SLAR imagery of the sea, IEEE, Geoscience and Electronics, (USA), OE-6, 124-129.
- de Loor, G. P. and H. W. Brunsveld van Hulten, 1978: Microwave measurements over the North Sea, Boundary-Layer Meteorology, 13, 113-131.
- Fu, L.-L., and B. Holt, 1982: SEASAT views oceans and sea ice with synthetic-aperture radar, JPL publication 81-120, Pasadena, California.
- Hasselmann, K, et.al., 1973: Measurements of wind-wave growth and swell decay during the joint North sea wave Project (JONSWAP), Deut. Hydrogr. Z., 8 (suppl. A.).

Keller, W. C. and J. W. Wright, 1975: Microwave scattering and straining of wind generated waves, Radio Sci., vol. 10, 139-147.

Kenyon, N. H., 1983: Tidal current bedform investigated by SEASAT, in T. D. Allen, Ed., Satellite Microwave Remote Sensing, Ellis Horwood, Series in Marine Science, Chichester, England, Chapter 16.

Larsen, T. R., L. I. Moskowitz, and J. W. Wright, 1976: A note on SAR imagery of the ocean, IEEE Trans. Antennas Propagat. vol. AP-24, 393-394.

Lodge, D. W. S., 1983: Surface expressions of bathymetry on SEASAT synthetic aperture radar images, Int. J. Remote Sensing, Vol. 4, 629-653.

Lyzenga, D. R., R. A. Shuchman, E. S. Kasischke and G. A. Meadows, 1983: Modeling of bottom-related surface patterns imaged by synthetic aperture radar, 1983 International Geoscience and Remote Sensing Symposium (IGARSS 83), San Francisco, Aug. 31 - Sept. 2, 1983, Digest, Vol. 2, 7.1 - 7.10.

McLeish, W., D. J. P. Swift, R. B. Long, and D. Ross, 1981: Ocean surface patterns above sea-floor bedforms as recorded by radar, Southern Bight of North Sea, Marine Geology, 43, M1-M8.

Valenzuela, C. R., 1978: Theories for the interaction of electromagnetic and ocean waves - a review, Boundary-Layer Meteorol., 13, 61-85.

Wright, J. W., 1978: Detection of ocean waves by microwave radar; the short gravity-capillary waves, Boundary-Layer Met., 13, 101-102.

N84 27302

40

MODELING OF SAR SIGNATURES OF SHALLOW WATER OCEAN TOPOGRAPHY

R.A. Shuchman, A. Kozma, E.S. Kasischke, and D.R. Lyzenga
Radar Division
Environmental Research Institute of Michigan
P.O. Box 8618
Ann Arbor, Michigan 48130

ABSTRACT

A hydrodynamic/electromagnetic model has been developed for the purpose of explaining and quantifying the relationship between the Seasat synthetic aperture radar (SAR) observed signatures and the bottom topography of the ocean in the English Channel region of the North Sea. The model uses environmental data (wind, current and water depth changes), and radar system parameters (frequency, polarization, incidence angle and resolution cell size) as inputs and predicts SAR-observed backscatter changes over topographic changes in the ocean floor. The model results compare quite favorably with the actual Seasat SAR-observed backscatter values. The comparisons between the model and the actual data are all within 1.5 dB. The developed model is valid for only relatively shallow water areas (i.e., less than 50 meters in depth) and suggests that for bottom features to be visible on SAR imagery, a moderate to high velocity current (0.40 m/s or greater) and a moderate wind (between 1 and 7.5 m/sec) must be present.

1. INTRODUCTION

The Seasat synthetic aperture radar (SAR) launched in 1978 by NASA, collected ocean imagery during approximately 200 of the 1500 orbits it was in operation. Although this SAR system operated at L-band (23.5 cm), a wavelength which does not penetrate an appreciable distance into the water, the data from Seasat revealed many patterns that are apparently related to subsurface or bottom features. An extensive study reported by Kasischke, et al. (1983 and 1983a) examined all passes of Seasat SAR imagery collected over non-frozen ocean regions for evidence of bottom-related surface signatures. In this study, the positions of the unidentified patterns which were suspected to be bottom-induced were determined by identifying known land areas or through the use of satellite ephemeris records. Hydrographic charts from these areas were examined to determine whether or not the patterns occurred over a distinct bottom feature.

Of the some 200 orbits of Seasat-SAR imagery examined, approximately 80 percent were found to contain patterns on the imagery which could be correlated to a distinct bottom feature. Kasischke, et al. (1983) reports on 35 test cases which were rigorously examined and the surface patterns on the imagery compared with hydrographic charts and ancillary data (environmental conditions coincident with the satellite overpass). These test cases are presented in Table 1.

The probable cause for observation of many of these features is that they induce local changes in the ocean surface currents which in turn cause changes in the small scale wave structure on the ocean surface. The observed SAR backscatter is a function of this small scale, or Bragg roughness (Wright, 1966 and Vesecky and Stewart, 1982). Many of the subsurface features observed by Seasat have been explained through the use of hydrodynamic/electromagnetic numerical modeling efforts.

ORIGINAL PAGE 19
OF POOR QUALITY

TABLE 1
SUMMARY OF SEASAT SAR IMAGERY EXAMINED FROM BATHYMETRIC FEATURES
(modified from Kasischke, et al., 1983)

Study Site (Location)	Seasat Revolution	Date	Time (GMT)	Bottom Feature(s) *
Little Bahama Bank --				
Grand Bahama Island	407	25 July 1978	12:46	EB
	651	11 August 1978	12:26	EB
Great Bahama Bank -- Bimini	407	25 July 1978	12:46	EB
	651	11 August 1978	12:26	EB
Great Bahama Bank --	407	25 July 1978	12:46	EB
Southern Edge	651	11 August 1978	12:26	EB
Tongue of the Ocean	450	28 July 1978	06:23	EB, SWS
	529	02 August 1978	18:37	EB, SWS
	694	14 August 1978	07:37	EB, SWS
	1024	06 September 1978	09:18	EB, SWS
	1110	12 September 1978	09:43	EB, SWS
	1153	15 September 1978	09:56	EB, SWS
	1196	18 September 1978	10:09	EB, SWS
	1239	21 September 1978	10:21	EB, SWS
	1282	24 September 1978	10:34	EB, SWS
	1325	27 September 1978	10:47	EB, SWS
	1368	30 September 1978	11:00	EB, SWS
	1411	03 October 1978	11:12	EB, SWS
Haiti -- Rochelois Bank	432	31 July 1978	11:28	SI
Bermuda	1267	23 September 1978	14:20	SI
Nantucket Shoals	880	27 August 1978	12:25	SWS
Cook Inlet, Alaska	289	17 July 1978	11:50	SWS, MB
North Rona Rock	762	19 August 1978	06:41	SI
Sula Sgier	762	19 August 1978	06:41	SI
English Channel	762	19 August 1978	06:41	SWS, MB
	957	01 September 1978	21:40	SWS
	1430	04 October 1978	20:42	SWS
	1473	08 October 1978	00:15	SWS
Northeast Atlantic	547	04 August 1978	06:15	DWB, DWR, DWS, DWSM
	556	04 August 1978	21:35	DWB, DWR, DWS, DWSM
	599	07 August 1978	21:43	DWB, DWR, DWS, DWSM
	633	10 August 1978	06:29	DWB, DWR, DWS
	642	10 August 1978	21:50	DWR, DWS, DWSM
	719	16 August 1978	06:43	DWB, DWR, DWS
	757	18 August 1978	22:40	DWB, DWR, DWS
	762	19 August 1978	06:41	DWB, DWR, DWS
	791	21 August 1978	07:24	DWB, DWR, DWS, DWSM
	834	24 August 1978	07:30	DWB, DWR, DWS
	958	01 September 1978	23:54	DWB, DWR
	1006	05 September 1978	08:15	DWB, DWR, DWS
	1044	08 September 1978	00:18	DWB, DWR
	1049	08 September 1978	08:27	DWB, DWR, DWS
	1087	11 September 1978	00:30	DWB, DWR

*Bottom Feature Key:

DWB Deep Water Bank
DWR Deep Water Ridge
DWS Deep Water Shelf
DWSM Deep Water Seamount
EB Edge of Bank in the Caribbean
MB Mud Bank
SL Shoal area surrounding an island
SWS Shallow Water Sand Bank

One of the most dramatic and least expected results obtained from Seasat was the observation of very distinct patterns related to transverse sand waves and longitudinal sand bars. These features are summarized by the SWS symbol on Table 1. These SAR-observed features correspond very well to the local bottom bathymetric features and have been noted on SAR data of ocean regions of up to 50 meters in depth. Examination of environmental data (winds, gravity waves, air/sea temperature, density stratification and currents) indicates the SAR observed features are only present when a tidal current (0.4 m/s or greater) is flowing over the bottom and a minimum wind (~1 m/s) with a favorable direction is present. This minimum wind is necessary to generate ocean Bragg waves which reflect the radar's incident electromagnetic waves. It is hypothesized that the refraction, straining, and in some cases, blocking of these Bragg waves by the currents is responsible for the observed bottom features.

One of the most vivid of these shallow water sand banks (SWS) expressions examined in the Seasat study are those associated with shoal regions of the Southern Bight of the North Sea (English Channel). This region is characterized by shallow (less than 50 meter water depth), subaqueous banks and sand waves, and it is this test site that was utilized in this study.

This paper first presents a theory for SAR detection of ocean surface patterns. This SAR imaging mechanism is then utilized along with a hydrodynamic theory to describe the observation of subsurface features on the Seasat SAR English Channel data set. The hydrodynamic/electromagnetic theory is then combined into a numerical model whose results are compared to the actual Seasat SAR data.

2. SAR IMAGING MECHANISMS

The patterns observed on SAR images of the ocean surface are the result of a complex set of imaging mechanisms including real modulations and effects due to the motion of the surface. In addition, the detectability of any given surface pattern is influenced by the variability of the background signal, which is due to speckle as well as random surface fluctuations.

Real modulations consist of variations in the small-scale and large scale roughness, where the length scale depends on the radar wavelength. Small-scale roughness influences the radar return through the Bragg scattering mechanism, and possibly also through "wedge scattering" from cusped waves (Lyzena, et al., 1983). There is a general consensus within the radio-oceanography community that a Bragg-Rice scattering theory can explain to a large degree the SAR-observed backscatter values obtained from the ocean surface at intermediate incidence angles (20-60°). That is, the transmitted radar energy with wave number k_0 interacts in a resonant or interference fashion with ocean surface waves with wave number k_w such that

$$k_w = 2k_0 \sin \theta, \quad (1)$$

where $k_w = 2\pi/L$ and $k_0 = 2\pi/\lambda$, L and λ are the wavelengths of the surface waves and the radar respectively, and θ is the incidence angle. Large-scale roughness perturbations cause a change in the Bragg scattering due to a local tilting of the surface as well as changes in the amount of specular reflection. For the case of internal waves and bottom topographic features, the real modulations are result

ORIGINAL PAGE IS
OF POOR QUALITY

of interactions between wind-generated surface waves and the surface currents induced by the subsurface phenomena of interest. This real modulation represents what a "real aperture" imaging radar or scatterometer would observe.

Motion effects are also a primary contributor to SAR images of the ocean surface. Recall SAR, to achieve its high resolution, observes the ocean for a period of time (the integration time) to generate the synthetic antenna. A moving ocean surface results in a perturbation of the phase of the scatterers during this time interval and this results in an altered image (Jain, 1978; Alpers and Rufenach, 1979; and Shuchman, et al., 1981). Ordered motions of the sea surface, such as orbital velocities and accelerations due to gravity and internal waves, can cause velocity bunching (i.e., periodic regions of increased and decreased image intensity) in the images (Alpers, et al., 1981). Scatterer accelerations degrade the resolution of the images in a predictable way (Lyzenga and Shuchman, 1983). A second category of motions which are random in nature also contribute to the SAR signatures of the ocean. Random motions cause azimuth smearing or streaking of the images. Random motions on a scale smaller than the SAR resolution may be described in terms of the coherence time or lifetime of the ocean scatterers.

The third factor which contributes to the detectability of SAR-observed signatures is the background signal variability. This variability is due to both speckle and large-scale surface variations which are unrelated to the phenomenon of interest. Speckle is a result of the coherent nature of the SAR system (Harger, 1970). Scatterers which are randomly distributed within each pixel interfere either constructively or destructively to create the "salt and pepper" images characteristic of a SAR. The speckle size is a function of the spatial resolution. The speckle intensity can be reduced by utilizing multi-look processing (or noncoherent addition) techniques during processing of the SAR signals.

Random surface variations also contribute to the background variability in SAR ocean surface images. These large-scale variations can be a result of a number of oceanographic phenomena including gravity waves, either well organized or random in nature, variable wind creating patchiness on the ocean surface, rain squalls, and mesoscale features such as ocean fronts (Shuchman, 1982).

3. DATA DESCRIPTION

Four Seasat revolutions provide SAR coverage of the Southern Bight region of the North Sea and English Channel. The SAR swaths (100 km wide) are indicated as rectangles on Figure 1. The SAR passes used in the study are Revolutions 762, 957, 1430, and 1473. As indicated on Table 2 (a summary of SAR data collected over the test site), the satellite overpasses span the time from August 19 to October 8, 1978, representing late summer conditions in the Channel. Note from Table 2 and Figure 1 that Revolutions 957, 1430, and 1473 have generally the same orientation (i.e., radar look direction with respect to the Channel), while Revolution 762 represents the nearly orthogonal look direction. The English Channel test site is characterized by a series of longitudinal and transverse sand waves which are situated in water depth varying from approximately 50 to 3 meters (Kenyon, et al., 1979). Table 3 summarizes the environmental conditions present in the English Channel at the time of the four Seasat passes.

Figure 2 is a detailed comparison of the radar image and the bathymetric chart of the bottom in the test area for Revolution 762. From Figure 2, it can be noted

ORIGINAL PAGE 19
OF POOR QUALITY

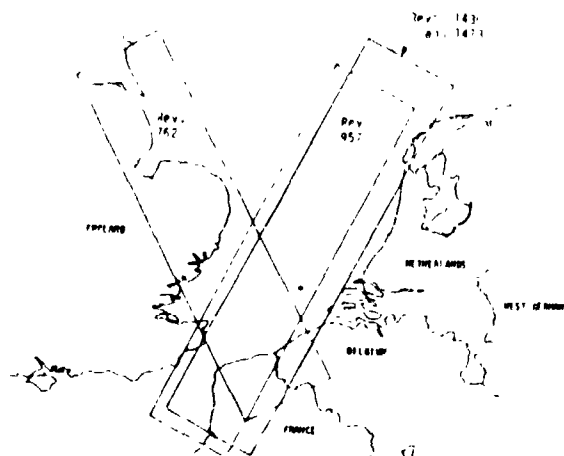


FIGURE 1. GROUND COVERAGE OF SEASAT REVOLUTIONS USED FOR ENGLISH CHANNEL ANALYSIS

TABLE 2
SAR SYSTEM AND SATELLITE PARAMETERS FOR STUDY SITES

Revolution	Date	Node	Time Over Target Channel (GMT)	Satellite Heading (T°)	SAR Look Direction (T°)	Incident Angle (Degrees) Near-Far
762	8-19-78	25.02	06:30	333°	63°	20°-25.2°
957	9-1-78	172.05	21:40	223°	313°	19.6°-24.9°
1430	10-4-78	172.76	00:40	223°	313°	19.6°-24.9°
1473	10-9-78	172.26	00:15	223°	313°	19.6°-24.9°

TABLE 3
ENVIRONMENT DATA RECORDED AT THE TIME OF SATELLITE OVERPASS

Revolution	Visibility of Subsurface Features	Wind Speed Direction	Water Temp.	Air Temp.	Wave H.	Period of Swells	Current ² Speed and Direction	Current ³ 30°-60° and Direction	A Typical Water Depth at Feature	Refr. no. Number ⁴ $n = c/v$	Reynolds ⁵ $Re = \rho u \lambda / \mu$
762	Very Visible	4.0 kn 106°(T)	16.6°(C)	17°(C)	0.5 m	1 s	1.4 kn 210°(T)	1.0 kn 226°(T)	7.5 m	0.00	3.0×10^5
957	Very Faint	10.0 kn 120°(T)	16.8°(C)	15°(C)	1.0 m	4 s	0.2 kn 210°(T)	0.2 kn 170°(T)	12.1 m	0.01	0.77×10^5
1430	Very Faint	21.0 kn 315°(T)	16.8°(C)	11°(C)	1.0 m	6 s	1.3 kn 30°(T)	1.5 kn 09°(T)	13.1 m	0.00	6.17×10^5
1473	Moderately Visible	11.0 kn 15°(T)	15.2°(C)	15°(C)	0.5 m	3 s	1.2 kn 210°(T)	0.7 kn 210°(T)	10.0 m	0.00	6.70×10^5
		200°(T)						200°(T)			

1 kn = 0.51 m/s

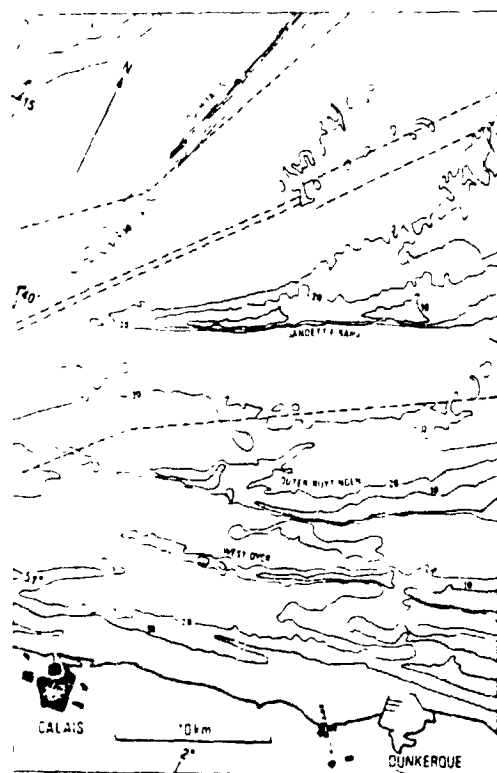
¹Standard meteorological convention (i.e., direction from).

²Direction current is flowing towards (value is near beach falls and bank).

³Average current value for test area.

⁴Values repeated from Table 1 for completeness.

⁵NOTE: In all cases, the water column was unstratified, and no pycnocline or ocean null was present.



(The dashed lines in the figure
are recommended ship routes)

FIGURE 2. COMPARISON OF SAR IMAGE AND CHART OF THE SEA BED
EAST OF DOVER STRAITS

that the sand waves are visible with stronger radar returns resulting on the down current side of their crest lines. The transverse sand waves are predominantly on the gentler slope of the asymmetrical longitudinal sand waves (or banks) and their crest lines bend around to trend increasingly more parallel to the longitudinal sand wave axis. Kenyon (1981) reports at the time of this image collection a current of 1-2 m/s was flowing 20° obliquely to the longitudinal sand waves and parallel to the orthogonal of the transverse waves. It is further noted that analysis of sidescan sonar records from near South Falls has revealed additional transverse sand waves which are not seen on the image (Kenyon, 1981 and Caston 1979).

4. MODELING OF BOTTOM DEPTH-RELATED PATTERNS ON SAR IMAGERY

In order to better quantify the relationship between SAR-observed sand ridges and environmental (wind, water depth, current speed, water temperature, etc.) and the SAR system (frequency, polarization, resolution, incident angle, look direction, etc.) parameters necessary to image these features, a hydrodynamic/electromagnetic modeling effort was undertaken.

A flow chart for the hydrodynamic/ electromagnetic model is presented in Figure 3. The model utilizes both environmental and SAR system parameters as inputs. The environmental inputs include: wind speed (m/s) and direction (degrees); initial current velocity (m/s) and direction (degrees); and water depth (m) on a grid basis. The SAR system parameters include: wavelength (cm); polarization (either vertical or horizontal); incidence angle (degrees), radar look angle (degrees), and resolution (m). The model first calculates the Bragg ocean wavelength using a two-scale scattering model where the long waves or slopes are neglected. A current profile is then computed as a function of the irregular topography (changing depth).

ORIGINAL PAGE IS
OF POOR QUALITY

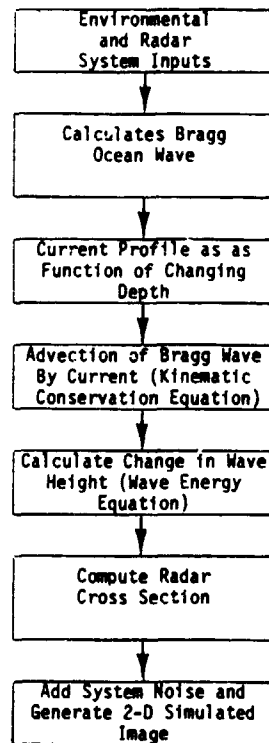


FIGURE 3. FLOW CHART FOR HYDRODYNAMIC/ELECTROMAGNETIC MODEL

The interaction of a tidal current with the bottom is presently described in terms of a simple quasi-one-dimensional model. The model considers a linear ridge of effectively "infinite" length with a parabolic cross section. This is equivalent to assuming that the component of the current parallel to the ridge is constant, i.e., that none of the water is allowed to flow around the shallow feature. Thus, only the perpendicular component varies, and this component can be calculated simply by conservation of mass. Assuming that the vertical current profile is constant, the surface velocity is then given by

$$V_x(X) = V_x(X_0) \frac{Z_0}{Z} \quad (2)$$

$$V_y(X) = V_y(X_0) \quad (3)$$

where $V_x(x_0)$ and $V_y(x_0)$ are the perpendicular and parallel components of the current outside of the ridge respectively, Z_0 is the depth at the location (x_0) , and Z is the depth at the location (x) under consideration.

The interaction of surface gravity waves with a variable current has been described by Hughes (1978) and Phillips (1977, 1981), among others. This interaction is described by two equations, the kinematic (or wave) conservation equation, and the wave action (or energy) equation. The former equation may be written as

$$\frac{\partial \vec{k}}{\partial t} + \vec{\nabla}(\omega + \vec{k} \cdot \vec{V}) = 0 \quad (4)$$

where k is the wave number, $\omega = \sqrt{gk}$ is the radian frequency of the wave, and V is the current velocity. In the steady-state case, the first term (i.e., the time derivative) may be ignored. For the one-dimensional case considered in the simple current interaction model, the solution of this equation may be written as

$$\omega + k_x V_x = \omega_0 + k_{x0} V_{x0} \quad (5)$$

$$k_y = k_{y0} \quad (6)$$

where k_x and k_y are the wave number components perpendicular and parallel to the ridge, respectively, and k_{x0} , k_{y0} are their values in the constant-current region away from the ridge. These equations express the changes in the wavelength and direction of a wave entering a variable current.

The changes in wave amplitude are described by the wave action equation, which may be written as

$$\frac{\partial \phi}{\partial t} + \left(\vec{V} + \frac{\partial \omega}{\partial \vec{k}} \right) \cdot \vec{\nabla} \phi = \beta \phi \left(1 - \frac{\phi}{\phi_\infty} \right) \quad (7)$$

where $\phi = \psi/\omega$ is the action spectrum, ($\psi(k)$ is the wave height spectrum), β is a wave growth parameter related to the wind speed and direction (Hughes, 1978), and ϕ_∞ is the equilibrium spectrum for the given wind conditions. The solution of this equation for the steady-state one-dimensional problem under consideration may be written in terms of the wave height spectrum as

$$\frac{1}{\psi(k)} = \frac{1}{\psi_\infty(k)} + \frac{1}{\psi_0(k_0)} - \frac{1}{\psi_\infty(k)} e^{-\beta(x-x_0) \left(u_x + \frac{\partial \omega}{\partial k_x} \right)^{-1}} \quad (8)$$

where the wave number k is related to the initial wave number k_0 (at a location away from the ridge).

As an example, consider the case of a wave field being carried by a current over a ridge in the bottom. As the wave propagates into a region of increasing current (i.e., as it approaches the ridge), it is elongated and the amplitude is decreased. If there is a wind in the same direction ($\beta > 0$), the amplitude

gradually builds back up toward its equilibrium value. After the wave passes the shallowest point, the current then decreases and the waves become shorter and of higher amplitude. Under zero-wind conditions, the amplitude would return to the original value resulting in only a dark band over the ridge. For a wind in the same direction as the current, the wave amplitude would increase beyond the initial value, resulting in regions of both lesser and greater wave height or surface roughness than the "background" value.

The wave height spectra obtained from this model were used to compute changes in the radar cross section of the surface, using a composite scattering model. Noise is then added to the modeled output to simulate speckle in the Seasat data and a two-dimensional image is generated.

Quantitative results from this model were compared with a series of relative radar backscatter measurements made from digital and optical data from the four Seasat SAR English Channel revolutions. The backscatter measurements were made at the output plane of the ERIM optical SAR processor using an optical probe; thus, the effects of recording the radar data on film could be neglected.

In addition to the optical measurement, the digital data for Revolution 762 was also analyzed. The digital data was averaged to obtain backscatter values representing the same area as the optical probe.

Three locations within the English Channel were selected for detailed study (i.e., the generation of modeled results). The English Channel test sites included South Falls and Sandettie Sand Banks (see Figure 2 for location) and a series of transverse sand waves resting in approximately 32 meters of water, the wave crests of which are aligned perpendicularly to Sandettie Bank. The transverse sand waves have a wavelength of approximately 400 meters and amplitude of 6.5 meters with the crests of the sand waves approximately 25 m below the water surface.

Figure 4 shows the optically generated 25 km quarter swath images for the four revolutions of the English Channel and also indicates the location of an optical scan made over the vicinity of South Falls (1A). Note the optical images confirm that the sand features are very visible on Revolution 762 imagery, moderately visible on Revolution 1473 imagery, and not visible (or very faintly visible) on imagery from Revolutions 1430 and 957. Also shown on the figure are the locations of optical scans (2A) made over the Sandettie Bank. The location of the transverse sand wave measurement is indicated as the letter 3A. Recall the SAR system and environment parameters for these four revolutions are summarized in Tables 2 and 3, respectively.

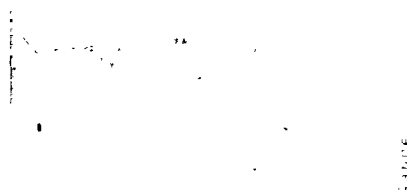
A model-generated reflectivity map of South Falls Revolution 762 is presented in Figure 5. In this figure, the computer-generated gray map represents an area of 2.5 x 2.5 km where each value (pixel) represents 20 x 20 m. As presented on the legend of the figure, each symbol on the gray map represents a 0.5 dB level. Figure 6 represents the idealized cross section of South Falls at the time of satellite overpass which was modeled. The reflectivity map presented in Figure 5 demonstrates the capability of the model to provide a two-dimensional output (i.e., a simulated SAR image).

Table 4 summarizes the modeled versus actual SAR backscatter values. For the modeled and actual SAR backscatter values, the change in the σ_0 value across the bottom feature is given. Both the optically- and digitally-extracted backscatter values are presented in Table 4. These optical and digital values differed by

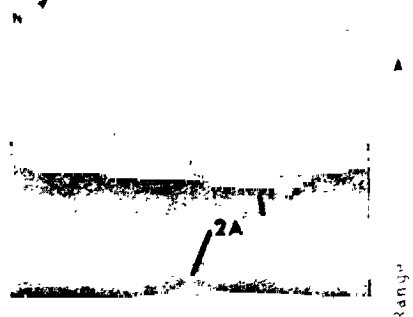
ORIGINAL PAGE IS
OF POOR QUALITY



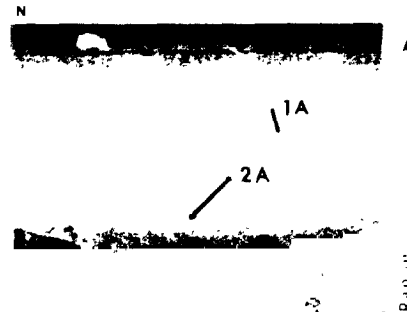
REV. 762



REV. 762



REV. 1439



REV. 1439

FIGURE 4. SAR IMAGERY OF THE ENGLISH CHANNEL SHOWING THE LOCATIONS OF BACKSCATTER MEASUREMENTS MADE OVER SOUTH FALLS AND SANDETTIE BANKS (Azimuth is Horizontal)

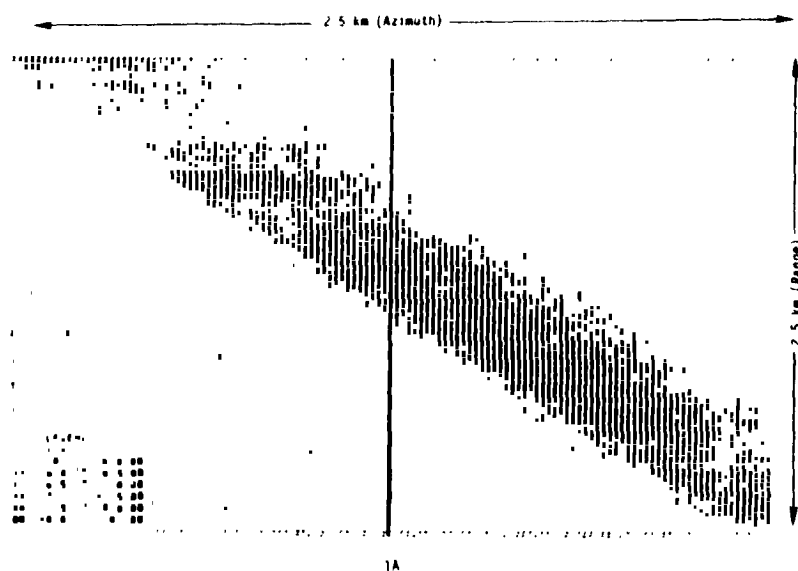


FIGURE 5. MODELLED BACKSCATTER MAP FOR REV. 762 SHOWING GOOD VISIBILITY OF SOUTH FALLS

ORIGINAL PAGE IS
OF POOR QUALITY

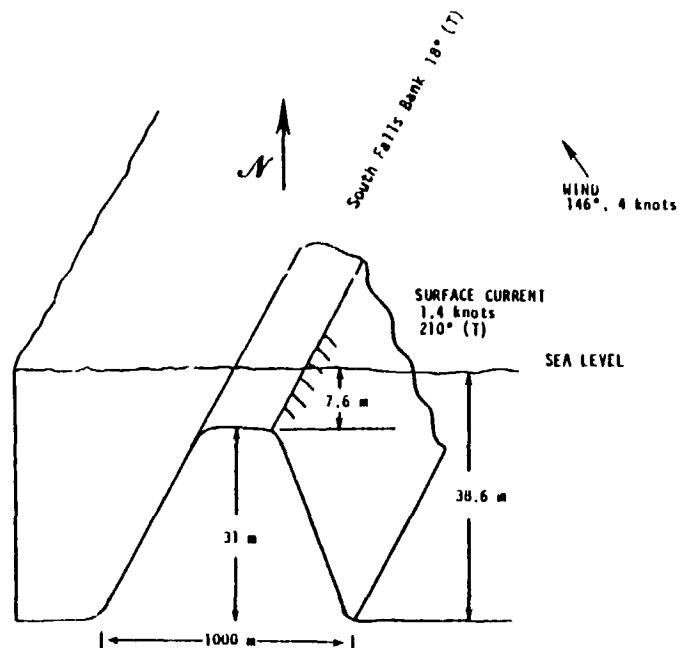


FIGURE 6. IDEALIZED CROSS SECTION OF SOUTH FALLS,
SEASAT REVOLUTION 762

TABLE 4
COMPARISON BETWEEN MODELED AND ACTUAL SAR BACKSCATTER VALUES

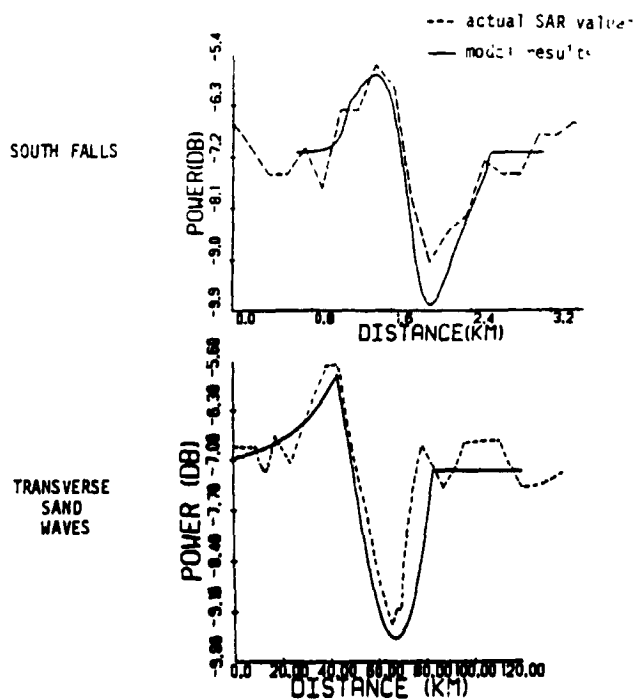
Revolution	Subsurface Feature	EM Model Results (dB)			Actual Seasat SAR Backscatter Values (dB)		
		Min. σ_0	Max. σ_0	σ_0	Min. σ_0	Max. σ_0	σ_0
762	South Falls	-2.7	1.3	4.0	-2.4	1.4	3.8 (D)
					-2.2	1.1	3.3
957	South Falls	-0.2	0.1	0.3	0.0	0.0	0.0
1430	South Falls	-0.4	0.3	0.7	0.0	0.0	0.0
1473	South Falls	-0.6	0.5	1.1	-1.7	0.9	2.6
762	Transverse Sand Waves	-2.4	1.3	3.7	-2.3	1.6	3.9 (D)
762	Sandette Sand Bank	0.0	0.0	0.0	-3.1	2.0	5.1 (D)
957	Sandette Sand Bank	0.0	0.1	0.1	-0.2	0.1	0.3
1430	Sandette Sand Bank	0.0	0.0	0.0	-0.3	0.3	0.6
1473	Sandette Sand Bank	-0.5	0.4	0.9	-0.8	1.1	1.9

(D) indicates Seasat SAR backscatter value was obtained from digital data.
Note actual measurements are relative backscatter, they have been normalized to average model value.

less than 0.5 dB. Note that the table gives relative backscatter values, and thus the problem of absolute calibration is avoided. Examination of the South Falls case reveals a model prediction of backscatter variations of 0.3 and 0.7 dB for Revolutions 957 and 1430, respectively. The Seasat images for these revolutions showed very faint or invisible features near South Falls, and the optical measurements yielded no measurable change in radar cross section over the ridge.

For Revolution 1473, the model predicted a backscatter variation of 1.1 dB over South Falls and the empirical measurements showed a variation of about 2.5 dB across the ridge. The image for this revolution shows a clearly identifiable feature corresponding to South Falls, although the feature is less distinct than in Revolution 762. The fact that the measured decrease in the radar return is larger in magnitude than the model result, while the measured increase is about the same, appears to indicate that the actual wind regeneration effect was smaller than that incorporated in the model. It should be noted that there is a fairly wide disparity in measurements of the wind growth rate, and this parameter is not completely understood at the present time (Hughes, 1978).

To further validate the model, the digital SAR data from Revolution 762 was compared in detail with the model results. Figure 7 represents a one-dimensional slice of model results compared with the actual SAR digital backscatter values of the same area. On the figures, the solid lines indicate the radar cross section calculated from the model, while the dotted line is the relative radar cross section obtained from the digitally processed Seasat SAR data. Presented on the figure are comparisons between model and actual values for the South Fall Bank and transverse waves corresponding to Revolution 762 environmental conditions. The comparison between model and actual data is quite good for both South Falls and the transverse waves case. The model and actual SAR backscatter are within 1.0 dB of each other everywhere on the two graphs. The sharp peak in the transverse sand wave case is predicted by the model, and is a result of wind direction with respect to the ridge and the current.



ORIGINAL PAGE IS
OF POOR QUALITY

FIGURE 7. MODEL VS. ACUAL BACKSCATTER
CROSS SECTION FOR REVOLU-
TION 762 SOUTH FALLS AND
TRANSVERSE SAND WAVES CASE

The hydrodynamic model predicted no change in radar cross section over the Sandettie Sand Bank for the Revolution 762 case, where the bank is aligned in the cross-track direction. The fact that this feature was observed, with approximately a 5 dB change in backscatter, appears to indicate an additional mechanism not incorporated in the model. This additional mechanism will be discussed in the next section. Modeled results over the Sandettie test site for Revolutions 957 and 1473 were in better agreement with actual SAR values (to within 1.0 dB).

In summary, it appears that when the calculated variation in the radar cross section is greater than 1 dB, the feature is visible in the Seasat SAR image. When the calculated variation is less than 1 dB, the feature is very faint or not visible in the image.

5. DISCUSSION OF MODEL RESULTS

The hydrodynamic/electromagnetic model was run for three locations within the English Channel test site. Table 4 summarized the comparison between the modeled and actual backscatter values. As presented earlier, the modeled results compare quite favorably (within 1.5 dB) to the actual Seasat SAR values.

The notable exception to the favorable comparison was the Sandettie Sand Bank test site for Revolution 762. Recall from Figures 1 and 2 that Sandettie Bank, as imaged during Orbit 762, is aligned along the radar line of sight.

The alignment of Sandettie Bank on Revolution 762 is such that the bank's long axis is within a few degrees of the across-track direction of the SAR coordinate system. Using the simplified current model described earlier (Eqs. 2 and 3), the current component (V_y) in the across-track direction is constant for this case. Therefore, the Bragg waves are not influenced by this current, as indicated by Eq. (6), and the model does not predict any change in radar cross section across Sandettie Bank. This is in apparent contradiction to the SAR image, which shows a distinct variation in this region.

The apparent failure of the model for this feature may be due to several reasons, including the following: (1) the simple current model may not be adequate for this case, and there may actually be changes in V_y along the ridge, (2) the fact that the ridge is not smooth, i.e., there are numerous transverse sand waves along the ridge which are actually responsible for the observed image variations, and (3) the radar return is influenced by changes in other surface waves.

The latter possibility is suggested by the fact that there are likely to be large perturbations of waves traveling in a direction other than the across-track direction. The response of the radar to those waves could be due to non-Bragg scattering mechanisms or to non-linear wave-wave interactions which influence the Bragg waves. One possible reason for these non-linear interactions could be the existence of large wave amplitudes occurring due to wave blocking.

Each individual component of the small-scale ocean surface wave structure will be blocked when it encounters an adverse current velocity of magnitude level equal to one-half its phase speed (or equal to the group speed for this wave component). As an example, the Bragg waves for an L-band radar system with Seasat radar geometry will be blocked by a change in the adverse flow rate of 0.36 m/s from the ambient level. For conditions of Sandettie Bank, a change in local water depth of 1.9 m along the crest of the ridge is sufficient to induce blocking of the Bragg wave. This range of depth change is certainly within the realm of possibility for this region of the English Channel. Should the depth undulate along the crest

of the ridge, periodic blocked wave structures should exist in the received radar backscatter signal.

6. SUMMARY AND RECOMMENDATIONS

A hydrodynamic and electromagnetic modeling effort has been undertaken for the purpose of explaining and quantifying Seasat synthetic aperture radar (SAR) backscatter signatures that relate to the bottom topography of the oceans. Large quantities of Seasat SAR imagery have been reviewed revealing the existence of surface expressions of sub-surface features on many passes of imagery. The most vivid of these cases are those surface expressions associated with shoal regions (50 meters and less water depth) east of Nantucket Island and the Southern Bight of the North Sea (English Channel). The English Channel, characterized by shallow, sub-aqueous banks and sand waves, was studied as part of this modeling effort.

The hydrodynamic model developed and utilized within this study embodies the interaction of a tidal current with the bottom features and the interaction of the surface Bragg waves with the current variations. The hydrodynamic model utilizes as inputs environmental data (wind, waves, currents, depth, tides and density stratification) coincident with the SAR data collection and predicts as output the change in the small scale roughness (i.e., Bragg wave amplitude) of the ocean surface.

A SAR reflectivity model for the ocean was also developed as part of this study. A specialized form of the developed SAR electromagnetic model utilized the small scale roughness as produced by the hydrodynamic model along with the Seasat SAR system parameters (frequency, polarization, incident angle and resolution) to generate SAR reflectivity gray maps of images showing varying degrees of bottom features. This specialized SAR model neglected scatterer motion effects and large slope change. It should be noted that neglecting these two factors did not diminish the prediction capability of the model, except possibly in one case in which the bottom feature (ridge) was aligned in the across-track direction.

Four Seasat passes showing various degrees of bottom feature visibility were selected for use in the model verification. The surface expressions were first correlated with depth changes. The modeled results predicted SAR features associated with bottom topography which agreed, at least to a first order, with actual SAR observations. The predictions agreed qualitatively with the observations in the sense that bright and dark bands are observed in the SAR images in the locations predicted by the model. The predictions also agree quantitatively with measurements of the radar cross section to within 1.5 dB, except in the case of a bottom feature (ridge) aligned in the across-track direction. Based on these cases, features appear to be visible in the Seasat SAR imagery if the backscatter variations predicted by the model are larger than 1 dB.

Based upon the results of this investigation, the following conclusions can be made regarding the environmental conditions required for visibility of bottom topographic features in SAR imagery. These conditions may be stated as follows:

1. A tidal current of at least 0.40 m/sec (0.80 Kts) must be present.
2. A wind of at least 1 m/s (2 Kts), but not greater than 7.5 m/s (15 Kts) must be present, with at least some component in the radar range direction.

These conclusions have been reached on the basis of the model as presently developed and as applied to relatively distinctive shallow bottom features in the English Channel. The actual limits on the current and wind may be different for other geographical locations, and could be further refined by more extensive model development and verification.

The problems associated with further development and testing of this model include obtaining adequate sea truth collected concurrently with SAR data. Specifically, actual depth values registered to the SAR images need to be obtained along with the two-dimensional current profile that was present at the time of SAR overflight. Further aircraft and spaceborne SAR programs (i.e., SIR-B and ERS-1) could certainly address this deficiency. From a theoretical standpoint, certain aspects of the model need to be improved to properly simulate all geometries. In particular, wave blocking and perhaps non-linear long-wave/short-wave interaction must be taken into account.

7. ACKNOWLEDGEMENTS

The work reported in this paper was performed at the Environmental Research Institute of Michigan (ERIM) under contract in part to four government agencies. The agencies and the technical monitors include: Office of Naval Research (Mr. Hans Dolezalek), Defense Mapping Agency/Naval Research Laboratory (Dr. James Hammack, and Mr. Peter Mitchell), National Oceanic and Atmospheric Administration (Mr. John W. Sherman, III), and the National Aeronautics and Space Administration (Drs. Lawrence McGoldrick and William Patzert). The contract numbers for these funded research activities are: ONR Contract N00014-81-C-2254, DMA Contract 800-78-C-0060, NRL Contracts N00014-81-C-2254 and N00014-82-C-2308, ONR (NASA) Contract N00014-81-C-0692; and NOAA/NASA Seasat Announcement of Opportunity Contract MO-A01-78-00-4339.

8. REFERENCES

- Alpers, W.R. and C.L. Rufenach, The Effect of Orbit Motions on Synthetic Aperture Radar Imagery of Ocean Waves, IEEE Trans. Antennas Propagat., Vol. AP-27, pp. 635-690, 1979.
- Alpers, N.R., D.B. Ross, and C.L. Rufenach, On the Detectability of Ocean Surface Waves by Real and Synthetic Aperture Radar, J. Geophys. Res., 86, 6481, 1981.
- Caston, G.F., Wreck Marks: Indicators of Net Sand Transport, Marine Geology, Vol. 33, pp. 193-204, 1979.
- Harger, R.O., Synthetic Aperture Radar Systems, Academic Press, New York, NY, 240 pp., 1970.
- Hughes, B.A., The Effect of Internal Waves on Surface Wind Waves: Part 2, Theoretical Analysis, J. Geophys. Res., 83, pp. 455-465, 1978.
- Jain, A., Focusing Effects in Synthetic Aperture Radar Imaging of Ocean Waves, J. Appl. Phys., Vol. 15, pp. 323-333, 1978.
- Kasischke, E.S., R.A. Shuchman, D.R. Lyzenga, and G.A. Meadows, Detection of Bottom Features on Seasat Synthetic Aperture Radar Imagery, Photogrammetric Engineering and Remote Sensing, Vol. 49, No. 9, pp. 1341-1353, 1983.

Kasischke, E.S., R.A. Shuchman, J.D. Lyden, G.A. Meadows, D.R. Lyzenga, and E.M. Jurecki, The Use of Satellite and Aircraft SAR to Detect and Chart Hazards to Navigation, ERIM Final Report No. 163000-1-F, Ann Arbor, MI (in press), 1983a.

Kenyon, N.H., Bedforms of Shelf Seas Viewed with Seasat Synthetic Aperture Radar, in Advances in Holographic Surveying, ed. by M.J. Wright, Society for Underwater Technology, London, pp. 69-73, 1981.

Kenyon, N.H., R.H. Belderson, A.H. Stride, and M.A. Johnson, Offshore Tidal Sand Boules as Indicators of Net Sand Transport and as Potential Deposits, in Holocene Marine Sedimentation in the North Sea Basin, Selected Papers from the IAS Meeting, Texel, Netherlands, ed. by S.D. Nio, R.T.E. Schuttenhelm and T.C.E. Van Weering, IAS Spec. Pub. 5., 1979.

Lyzenga, D.R. and R.A. Shuchman, Analysis of Scatterer Motion Effects in MARSEN X-Band SAR Imagery, J. of Geophys. Res., Vol. 88, No. C11, 1983.

Lyzenga, D.R., A.L. Maffett, and R.A. Shuchman, The Contribution of Wedge Scattering to the Radar Cross Section of the Ocean Surface, IEEE Trans. on Geoscience and Remote Sensing, Vol. GE-21, No. 4, pp. 502-204, 1983.

Phillips, O.M., The Dynamics of the Upper Ocean, Second Ed., Cambridge Univ. Press, 1977.

Phillips, O.M., The Structure of Short Gravity Waves on the Ocean Surface, in Spaceborne Synthetic Aperture Radar for Oceanography, ed. by R.C. Beal, P.S. DeLeonibus, and I. Katz, Johns Hopkins Univ. Press, Baltimore, MD, pp. 24-31, 1981.

Shuchman, R.A., A.L. Maffett, and A. Klooster, Static and Dynamic Modeling of a SAR Imaged Ocean Scene, IEEE J. Oceanic Eng., Vol. OE-6, 1981.

Shuchman, R.A., Quantification of SAR Signature of Shallow Water Ocean Topography, University of Michigan PhD Dissertation, Ann Arbor, Michigan, 130 pp., 1982.

Vesecky, J.F. and R.H. Stewart, The Observation of Ocean Surface Phenomenon Using Imagery from the Seasat Synthetic Aperture Radar - An Assessment, J. Geophys. Res., 87, pp. 3397-3430, 1982.

Wright, J.W. Backscattering from Capillary Waves with Application to Sea Clutter, IEEE Trans. Antenna Propagat., Vol. AP-14, pp. 749-754, 1966.

N84 27303

COASTAL BATHYMETRY AND CURRENTS FROM LANDSAT DATA

Norman Rosenberg
Faculty of Engineering
Tel Aviv University
Ramat Aviv, Israel

ABSTRACT

Landsat scenes of coastal areas should be useful for bathymetry and for mapping sediment flow if scatter from bottom and suspended matter can be separated by multi-date analysis. Several filter algorithms have been developed to reduce both artifacts and random noise while retaining meaningful structures such as breakwaters and underwater reefs.

Results of application of these filters to Landsat scenes of the Israeli coast will be presented.

N84 27304

ON THE RESPONSE TO OCEAN SURFACE CURRENTS IN SYNTHETIC APERTURE RADAR IMAGERY

by

O.M. Phillips
Department of Earth & Planetary Sciences
The Johns Hopkins University
Baltimore, Md. 21218

ABSTRACT

The balance of wave action spectral density for a fixed wave-number is expressed in terms of a new dimensionless function, the degree of saturation, b , and is applied to an analysis of the variations of this quantity (and local spectral level) at wave-numbers large compared to that of the spectral peak, that are produced by variations in the ocean surface currents in the presence of wind input and wave breaking. Particular care is taken to provide physically based representations of wind input and loss by wave breaking and a relatively convenient equation (4.2) is derived that specifies the distribution of the degree of saturation in a current field, relative to its ambient (undisturbed) background in the absence of currents. The magnitude of the variations in b depends on two parameters, U_0/c , where U_0 is the velocity scale of the current and c the phase speed of the surface waves at the (fixed) wave-number considered or sampled by SAR, and $S = (L/\lambda) (u_*/c)^2$, where L is the length scale of the current distribution, λ the wavelength of the surface waves and u_* the friction velocity of the wind. When S is large (of order 10 or more) the distribution of b is insensitive to currents for which $U_0/c \sim 1$, but when S is of order unity or less, significant variations in b are produced. A convergence zone is associated with a maximum in b relative to its ambient levels of

$$b_{max} = \left\{ 1 + \frac{q}{4\pi m} \frac{U_0}{c^3} \right\}^{1/(n-1)}$$

where $m \sim 0.04$ and $n \sim 3$. This would appear as a bright line in the SAR imagery. In general, local maxima in b (and the return SAR signal) should be observed if the local current strain rate scale

$$U_0/L \geq 0.12 g^{-1/2} \lambda^{-3/2} u_*^2.$$

A local divergence or upwelling reduces the relative degree of saturation; when S is small the reduction is by the factor $(1 + 2U_0/c)^{-9/2}$ and continues until the waves grow back to the equilibrium level under the influence of the wind. A divergence line could be imaged as a line across which the return decreases from

the ambient level upwind, to a low level downwind, gradually recovering to the ambient.

1. Introduction

The variety of instruments now available for active radio probing of the ocean surface makes possible the observation over a wide area of oceanic features ranging from capillary and microscale breaking waves to long ocean swells. Variations in the return signal with position on the ocean surface gives indications of even large scale features such as mesoscale ocean eddies and the distribution of surface wind stress. The scales of the surface features responsible for the return signal depends upon the wavelength of the incident radiation. When the angle of incidence on the water surface is not close to normal, and the wavelength of the radiation is large compared with the scales of occasional local occurrences such as breaking waves, the return signal seems, as a result of careful measurements such as those of Keller and Wright (1975) to be predominantly the result of first order Bragg scattering from freely travelling surface waves. The wave-number k of the surface wave sensed is

$$k = 2k_i \sin \theta \quad 1.1$$

where k_i is the wave-number of the incident radiation and θ the angle of incidence; the depression angle is $\frac{1}{2}\pi - \theta$. A real or synthetic aperture radar (SAR) at a frequency of 1.5 GHz responds to a surface wavelength of the order of 10cm at a depression angle of 30° or so, and a high resolution image such as that from SAR gives, in the pattern of intensity variations in the return signal, the pattern of local energy density of surface disturbances at this scale.

Some of these patterns are extremely intriguing. Beal et al. (1981) show a number of examples obtained from SEASAT, one noteworthy one giving surface expressions at this scale of tidal flow over the Davis Shoals, south and east of Nantucket Island. Another, off the mouth of the Chesapeake Bay suggests a complex pattern of eddies (or perhaps water masses); at high resolution the individual swell crests can be discerned. Fascinating as these images are, it is far from clear how they should be properly interpreted or what quantitative information they may contain. If we accept the premise that the images are derived primarily from freely travelling short gravity waves, modified by longer waves and currents, then it should be possible to infer at least some properties of the current field, in particular, from the imagery. The short gravity waves sensed by the SEASAT SAR do have a significant 'lifetime' of propagation, unlike capillary waves which are transient and fugitive, and their interaction with longer waves and currents may significantly modify their distribution over the ocean surface. The object of this paper is to determine the extent to which this can occur and to seek relations by which quantitative information might be obtained from this imagery.

ORIGINAL PAGE IS
OF POOR QUALITY

2. Action input and dissipation processes at short gravity wave scales.

Since we will be concerned with interactions between the short gravity waves and surface currents, the wave dynamics are specified most conveniently by the balance of action spectral density $N(\underline{k})$, which is related to the spectrum of surface displacement $\Psi(\underline{k})$ by

$$N(\underline{k}) = (g/\sigma) \Psi(\underline{k}) = (g/k)^{1/2} \Psi(\underline{k}), \quad (2.1)$$

where σ is the intrinsic frequency and $\Psi(\underline{k})$ is normalized such that

$$\int \Psi(\underline{k}) d\underline{k} = \bar{\xi}^2,$$

the mean square surface displacement. The spectral energy density of the wave field is $\rho g \Psi(\underline{k})$, where ρ is the water density.

Following energy paths, the balance of wave action spectral density is given by

$$\frac{d}{dt} N(\underline{k}) = \frac{\partial N}{\partial t} + (\underline{C} + \underline{U}) \cdot \nabla N = - \nabla_{\underline{k}} \cdot \underline{I}(\underline{k}) + S_w - D, \quad (2.2)$$

(see, for example, Phillips, 1980) where $\underline{C} = \nabla_{\underline{k}} \sigma$ represents the group velocity and \underline{U} the velocity of the surface current. The exchanges of action density among different wave components by wave-wave interactions are specified by the first term on the right, in which $\underline{I}(\underline{k})$ is the flux of action spectral density in the wave-number plane. These interactions, in a gravity wave system, are conservative so that the interval over all \underline{k} vanishes. The two remaining terms specify the spectral distribution of action input from the wind and the loss of action density (which at these scales is predominantly the result of sporadic wave breaking or possibly the formation of parasitic capillaries). Our present degree of understanding of the three processes represented on the right hand side of (2.2) decreases monotonically in the order in which they are written though, as we shall see, some useful progress can be made.

The specification of the wave field is completed by use of the kinematical conservation equation

$$\frac{\partial \underline{k}}{\partial t} + \nabla(\sigma + \underline{k} \cdot \underline{U}) = 0 \quad (2.3)$$

together with the condition that $\nabla \times \underline{k} = 0$ and the dispersion relation giving the intrinsic frequency in terms of the wave-number magnitude:

$$\sigma = (gk)^{1/2} \quad (2.4)$$

If the underlying current is non-uniform, the wave-number \underline{k} of an energy packet varies as it propagates across the surface - $\underline{k} = \underline{k}(x, t)$. On the other hand, in remote sensing by radar (such as the L-band SAR), the Bragg scattering condition selects an almost fixed surface wave-number \underline{k} in (1.1), so that it is convenient in this context to re-write (2.2) to refer to a fixed, rather than a variable wave-number. From (2.3),

$$\begin{aligned} \frac{\partial k_i}{\partial t} &= - \frac{\partial}{\partial x_i} (\sigma + k_j U_j) \\ &= - \left(\frac{\partial \sigma}{\partial k_j} \frac{\partial k_j}{\partial x_i} + U_j \frac{\partial k_j}{\partial x_i} + k_j \frac{\partial U_j}{\partial x_i} \right). \end{aligned}$$

But since $\nabla \times \underline{k} = 0$ and $C_j = \partial \sigma / \partial k_j$,

$$\frac{\partial k_i}{\partial t} = \frac{\partial k_i}{\partial t} + (C_j + U_j) \frac{\partial k_i}{\partial x_j} = - k_j \frac{\partial U_j}{\partial x_i}, \quad (2.5)$$

and since $N = N(\underline{k}, \underline{x}, t)$,

$$\frac{\partial N}{\partial t} = \frac{\partial N}{\partial t} + (C_j + U_j) \frac{\partial N}{\partial x_j} - k_j \frac{\partial U_j}{\partial x_i} \frac{\partial N}{\partial k_i} = - \frac{\partial \tau_i}{\partial x_i} + S_w - D, \quad (2.6)$$

now for a fixed wave-number \underline{k} .

To progress beyond this point, we need some assessment of the magnitude and nature of the terms represented schematically on the right of (2.2) or (2.5). The spectral energy and action transfers have been investigated extensively by Hasselmann and his co-workers, by West (1984) and by Fox (1976). There is little doubt that resonant spectral energy transfers influence significantly the components near the spectral peak and, as suggested by Kitaigorodskii (1984) over a range of higher frequencies up to those for which $c/u_* \sim 5$ at most. Just above the frequency of the spectral peak, the fractional rate at which action is acquired or lost by wave interactions per wave period in an active wave field is of the order 10^{-4} (Phillips, 1980) and this can be taken as an upper limit to the rate appropriate to smaller scales (0.1 to 1m) of interest here. Even so, it is, as we shall see, generally less by at least an order of

magnitude than the rate at which action is acquired by short gravity waves from the wind, provided the wind is sufficient to produce any such components at all.

The energy transfer from wind to waves has been the subject of many theoretical and experimental enquiries during the past twenty-five years which have, if nothing else, demonstrated the complexity and variety of processes involved. At these small scales with wind blowing, the wave components are certainly of finite amplitude, with intermittently high curvature at their crests producing bursts of parasitic capillaries and occasional breaking. Air flow separation accompanies breaking as Banner and Melville (1976) have shown and Banner (1984) demonstrates that an enhanced local energy and momentum flux to the waves occurs as a result. Both the short waves and the wind are modulated and deflected by the longer waves and swell so that for the purposes of providing a more concrete expression for S_w in (2.2), the best guide is given by the results of careful measurements interpreted in the light of only very general theoretical considerations. Plant (1982), suggests from an examination of such measurements that

$$\begin{aligned} S_w(k) &= 0.04 \sigma (u_*/c)^2 \cos \theta \cdot N(k) \\ &= m \sigma (u_*/c)^2 N(k), \text{ say,} \end{aligned} \quad (2.7)$$

where u_* is the friction velocity, $c = (g/k)^{1/2}$, the phase speed of the component and the angle between k and the wind. Plant believes the numerical coefficient to be accurate to within about fifty per cent. Mitsuyasu and Honda (1984) give a similar expression derived from their experiments, with a numerical coefficient of 0.07 but with no directional factor included. Phillips (1980) estimated a coefficient of 0.05 and Gent and Taylor's (1976) numerical calculations give approximately 0.07 -- the relatively small scatter of values obtained from independent calculations or sets of measurements gives some confidence that this is a reasonably accurate representation over the range $1 > u_*/c > 0.1$ that includes most short wave cases of interest. The specific directional factor ($\cos \theta$) suggested by Plant is less certain. Nevertheless, the base of data he used is both extensive and carefully evaluated, so that (2.7) can be adopted with reasonable confidence as a useful semi-empirical representation. Since we are principally concerned with short wave components with wavelengths of 10cm or more and with wind speeds of order 10 m/s or less, the pertinent values of u_*/c do occupy the range specified above and the fractional rate at which action is acquired from the wind per wave period,

$$\frac{2\pi S_w(k)}{\sigma N(k)} \sim 0.3 (u_*/c)^2 \cos \theta$$

ranges from 0.3 to 3×10^{-3} and is at least an order of magnitude larger than the net rate associated with wave-wave interactions.

If the short wave components of the field have reached a state of statistical equilibrium in a region undisturbed by currents, then $dN(k)/dt = 0$ and since for these components $\nabla_k \cdot T$ is negligible, the densities of short wave breaking or parasitic capillaries must adjust themselves so that the dissipation D balances the wind input rate. Most previous observational studies on wave breaking such as those of and Toba and Kunishi (1970) have sought direct relationships between the density of whitecap coverage and wind stress. These implicitly assume such a statistical balance; our primary concern here is the response of the short wave structure when the balance is disturbed. Whether or not a particular wave crest breaks depends, in fact, on its configuration and time development and not directly on the wind speed, since (for example) breaking can be induced by a local adverse current, independent of the wind speed, and suppressed when the waves overtake a locally favourable current. Accordingly, D must be regarded intrinsically as a functional of the local spectral density, not the wind speed; its dependence on wind speed arises only insofar as this influences the spectral level or possibly, in the case of very short waves, as it influences the microscale breaking criterion through the surface drift (Phillips and Banner, 1974).

The spectral level is conveniently specified by the dimensionless function

$$B = g^{-1/2} k^{3/2} N(k) = k^4 \psi(k), \quad (2.8)$$

which, in any particular spectrum, can be regarded as a function of k/k_0 , where k_0 is the wave-number of the spectral peak. This function can be called 'the degree of saturation'. The simple idea of a saturation range at high wave-numbers of the gravity wave (Phillips, 1958) assumed a hard upper limit B_s , independent of k/k_0 , for B (the saturation range 'constant'), any further increase in the spectral level being prohibited by immediate wave breaking. Within the present conceptual framework, this corresponds to a dissipation function D that is negligibly small when $B < B_s$ but discontinuous (and in fact undefined) as $B \rightarrow B_s$. It is more realistic to assume that the action dissipation rate D is a continuous function of the degree of saturation B that is zero when $B = 0$, remains very small while B is significantly less than the old saturation range 'constant' when breaking is rare, and then increases rapidly when B approaches B_s and short wave breaking becomes denser in space and more frequent in time. Its form is then as indicated schematically in figure 1.

Also shown in figure 1 is the wind source term (2.7) which can now be written as

$$S_w(k) = 0.04 \cos \theta (u_* / c)^2 g k^{-4} B(k/k_0) \quad (2.9)$$

from (2.8). For a particular wave-number this is linear in B to the accuracy of the expression (2.7) and the slope increases quadratically with u_* . The short waves are in statistical equilibrium at the degree of saturation B defined by the intersection of these two curves. Note that, according to this description, the degree of saturation under equilibrium conditions may increase somewhat with wind speed, but the generally good observational support for the original idea of a 'hard' saturation range indicates that the variation with wind speed must be weak and the curve of D as a function of B must increase very rapidly indeed.

Before our specification can be completed for the spectral density of action dissipation, there is one further conceptual difficulty that must be faced. Does the function D for a particular wave-number depend on the degree of saturation at that wave-number only or on its value over a range of surrounding (or perhaps distant) wave-numbers? An individual breaking event is localized in space within a distance probably of order k^{-1} ; in Fourier space its influence is distributed over a range of wave-numbers of order k . Also, the statistics of wave breaking at a certain scale (defined by the phase speed of the breaking crest) cannot be expected in general to depend on the spectral density or the degree of saturation at that scale alone, but over a range of scales. Consequently the statistical characteristics of wave breaking and the dynamical consequences of breaking on the wave field both involve a possibly wide spectral range. If, however, the degree of saturation B is almost constant over this range, a condition that might be anticipated under steady wind conditions, then on similarity grounds one might assert that

$$D = gk^{-4} f(B) \quad (2.10)$$

In situations in which a much longer swell is present, the degree of saturation of the short waves will vary with respect to phase of the swell, being greater near the crests (with local breaking) and much smaller in the troughs. Although an expression such as (2.10) may hold locally, the overall mean rate of action dissipation will depend not only on the mean degree of saturation but also on the swell slope, and this further parameter should be included in (2.10).

The function $f(B)$ is illustrated only schematically in figure 1. Although its detailed form is not known at this stage, it may be possible to determine some of its characteristics more explicitly from laboratory or field observations. If the short waves are in a statistical balance between wind and dissipation, in the absence of much longer waves or swell, the degree of saturation attained is defined by the balance of (2.9) and (2.10):

$$0.04 \omega^2 \theta (u_*/c)^2 B = f(B). \quad (2.11)$$

ORIGINAL PAGE IS
OF POOR QUALITY

The variation of the degree of saturation with wind stress (normalized by phase velocity) is then

$$\frac{\partial B}{\partial (u_* / c)^2} = 0.04 \cos \theta \left[\frac{\partial}{\partial B} \left(\frac{f(B)}{B} \right) \right]^{-1} \quad (2.12)$$

According to the simplest ideas of a saturation spectrum independent of wind speed, the right hand side of (2.11) would be zero since the slope of $f(B)$ is infinite at saturation. On the other hand, if a variation with wind speed of B as specified by (2.12) could be established reliably, then this would define the slope of the curve $f(B)$ near equilibrium.

Another constraint is provided by the observation that the local action density of these short waves on the ocean is stable to perturbations on a scale large compared with the wavelength, in the sense that if locally the action density is high, the increased spectral density of breaking reduces it, and if it is low, the decreased spectral density of breaking allows the wind input to restore the equilibrium. The larger, dominant wave components at large fetch and duration may show a 'groupiness' as a result of the instabilities associated with non-linear wave interactions, but as we have seen, the time scales of these instabilities at higher wave-numbers are negligibly slow compared with those of the wind input and wave breaking. If under a constant wind field, the degree of saturation B is perturbed by an amount B' , then with the neglect of the resonant interactions, we have for the rate of change of the perturbation in action spectral density N' ,

$$\frac{\partial N'}{\partial t} = S_w(B + B') - D(B + B')$$

Since $N' = gk^{-4} \sigma^{-1} B'$ and in the equilibrium state $S_w(B) = D(B)$, this can be expressed, using (2.9) and (2.10) as

$$\frac{1}{\sigma} \frac{\partial B'}{\partial t} = m (u_* / c)^2 B' + [f(B) - f(B + B')], \quad (2.13)$$

where $m = 0.04 \cos \theta$. For small perturbations B'

$$\frac{1}{\sigma} \frac{\partial B'}{\partial t} = \left\{ m \left(\frac{u_*}{c} \right)^2 - \frac{\partial f}{\partial B} \right\} B',$$

ORIGINAL PAGE IS
OF POOR QUALITY

and the condition for statistical stability is

$$\frac{\partial f}{\partial B} > m \left(\frac{u_*}{c} \right)^2, \quad (2.14)$$

which, in terms of figure 1, implies that the slope of the curve D as a function of B must be greater than that of S_w at the point of intersection (as, indeed, we had anticipated). As u_*/c increases, the equilibrium point rises and the slope df/dB at the equilibrium point increases even more rapidly. If the curve $f(B)$ can be expressed reasonably accurately as a power law, the relaxation rate

$$\gamma = \left\{ \frac{\partial f}{\partial B} - m \left(\frac{u_*}{c} \right)^2 \right\} \sigma \quad (2.15)$$

can be expressed simply and explicitly in terms of u_*/c . For, suppose that

$$f(B) = aB^n \quad (2.16)$$

where n is certainly greater than one, then at equilibrium

$$m(u_*/c)^2 B = aB^n$$

so that

$$f'(B) = n a B^{n-1} = n m (u_*/c)^2$$

and

$$\gamma = m(n-1) (u_*/c)^2 \sigma \quad (2.17)$$

Even though the numerical value of n is not known (one might guess something in the range 3 to 5) this is a useful result. It can be written alternatively as

$$\gamma = m(n-1) u_*^2 g^{-2} \sigma^3 \quad (2.18)$$

showing that, for a given wind stress, the relaxation rate towards equilibrium increases as the cube of the frequency for these short wave components.

ORIGINAL PAGE IS
OF POOR QUALITY

If, however, the perturbation in B is not small, the expected strong non-linearity in $f(B)$ when B is small indicates that the recovery will be different for a local increase in degree of saturation than it will be for a decrease. If the decrease in B is such that $f(B)$ is then negligible and breaking virtually ceases, the recovery will be initially at the undamped growth rate, (proportional to the slope of the line in figure 1 marked S_w) which may be much slower than r (proportional to the difference in the two slopes at the intersection.) A large local increase in B is then expected to disappear more rapidly by much enhanced breaking than a large local decrease in which breaking ceases. If, at equilibrium between breaking and wind input so that $S_w = D$, the degree of saturation is B_0 , then from (2.9) and (2.10)

$$m(u_*/c)^2 gk^{-4} B_0 = gk^{-4} aB_0^n$$

when the representation (2.16) is used. Consequently

$$a = m(u_*/c)^2 B_0^{1-n}$$

and the balance of the last two terms on the right hand side of (2.16) can be written in terms of this equilibrium level as

$$gk^{-4} \cdot m(u_*/c)^2 (1 - (B/B_0)^{n-1})B \quad (2.19)$$

3. The influence of a background sea state on mean short wave properties at given k .

The short ocean wave components that are generally responsible for radar back-scattering do not, of course, exist in isolation. Longer waves or swell produce modulations in the intensity of the back-scattered return, measured by Wright et al (1980) with a spatial scale of variation that images the long wave field. Bell (1981) has made use of these modulations to study the evolution and propagation of swell across the Atlantic continental shelf of the United States. Frequently, the orbital velocities associated with these longer waves are larger than the propagation speeds of the short components sensed and one's intuitive feeling might be that an irregular or random field of longer waves would so scramble the propagation characteristics of the shorter waves as to obscure any likelihood interpreting the large scale patterns in their intensity in terms of currents. However, this particular concern does not seem to be justified.

Consider a surface current field $U(x,t)$ whose scales of spatial and temporal variations L and T are large compared with the wavelength and period of long waves or swell, the scales over which the tangential components of their orbital velocity u

ORIGINAL PAGE IS
OF POOR QUALITY

varies. Local mean values of the wave field, indicated by an overbar, are defined over scales that are small compared with those of the current field but large compared with those of the swell. Fluctuations or modulations produced by the swell are represented by the difference between the actual values and the mean values defined in this way. Thus, the action density is represented as $N(x,t) + N'$, the short wave group velocity a constant k (which varies because of the variations in the local g at the surface as the short waves ride over the swell) by $\bar{C} + C'$, and so forth. If the short waves are everywhere close to saturation under the balance of wind input and wave breaking then (2.5) can be written as

$$\frac{\partial N}{\partial t} + (\bar{C}_j + U_j + u_j) \frac{\partial N}{\partial x_j} - k_j \frac{\partial}{\partial x_i} (U_j + u_j) \frac{\partial N}{\partial k_i} = -\gamma(N - N_0) \quad (3.1)$$

where resonant wave-wave interactions are neglected, N_0 is the equilibrium value of N in the absence of long waves or currents and γ the relaxation rate of the previous section. Substitution of local mean and fluctuating quantities into (3.1) and averaging gives

$$\begin{aligned} \frac{\partial \bar{N}}{\partial t} + (\bar{C}_j + U_j) \frac{\partial \bar{N}}{\partial x_j} - k_j \frac{\partial U_j}{\partial x_i} \frac{\partial \bar{N}}{\partial k_i} \\ = - \overline{(\bar{C}_j' + u_j)} \frac{\partial \bar{N}}{\partial x_j} + k_j \overline{\frac{\partial u_j}{\partial x_i} \frac{\partial N'}{\partial k_i}} - \gamma(\bar{N} - N_0). \end{aligned} \quad (3.2)$$

The left hand side of this equation has the same form as the original equation (2.5) so that the influence of the swell on the mean action spectral density is represented by the two new terms on the right. Now, to the first order, the wave-induced modulations N' are proportional to N (Wright et al 1980) and to the root-mean square slope of the long wave field, s are the local gradients with respect to x and k , so that the covariance terms are of order $\epsilon^2 \bar{N}$, where ϵ is the swell frequency. Their only effect, then, is to modify slightly (by order ϵ^2) the equilibrium mean spectral levels from that which would obtain in the absence of swell.

The fact that the swell can therefore be ignored in a consideration of the local mean back-scattering from short propagating waves is at first sight counter-intuitive, but the essence of the matter is that the modulation patterns at a fixed wave-number are periodic and non-cumulative provided the swell slope is sufficiently small that the dissipation response can be linearized.

4. Variations in N produced by surface currents.

The dynamical balance (2.5) can be written in terms of the degree of saturation B by substituting $N = g^{1/2} k^{-1/2} B(k)$ and the expression (2.18).

$$\begin{aligned} \frac{\partial B}{\partial t} + (C_j + U_j) \frac{\partial B}{\partial x_j} + \frac{g}{2} \frac{k_i k_j}{k^2} \frac{\partial U_i}{\partial x_j} B - k_j \frac{\partial U_i}{\partial x_i} \frac{\partial B}{\partial k_i} \\ = \sigma m \left(\frac{u_*}{c} \right)^2 \left\{ 1 - \left(\frac{B}{B_0} \right)^{n-1} \right\} B. \end{aligned} \quad (4.1)$$

If the magnitude of the current variations is represented by U_0 and the length scale over which they occur by L , then

$$U_i = U_0 f_i(x/L) = U_0 f_i(\xi), \text{ say}$$

Also, if $b(\xi) = B/B_0$, the local degree of saturation relative to its equilibrium level, then under steady conditions (4.1) can be written in dimensionless form as

$$\begin{aligned} \left(\frac{C_j}{c} + \frac{U_0}{c} f_j(\xi) \right) \frac{\partial b}{\partial \xi_j} + \frac{g}{2} \frac{U_0}{c} \frac{k_i k_j}{k^2} \frac{\partial f_i}{\partial \xi_j} b - \frac{U_0}{c} k_j \frac{\partial f_i}{\partial \xi_i} \frac{\partial b}{\partial k_i} \\ = \frac{m L \sigma}{c} \left(\frac{u_*}{c} \right)^2 \left\{ 1 - b^{n-1} \right\} b \\ = 2 \pi m \left\{ \frac{L}{\lambda} \left(\frac{u_*}{c} \right)^2 \right\} \left\{ 1 - b^{n-1} \right\} b \end{aligned}$$

where c represents the phase velocity and λ the (fixed) wavelength of the component considered.

It is interesting to note that this equation involves only two basic parameters, U_0/c expressing the strength of the current field and $(L/\lambda) (u_*/c)^2$ representing the combined influence of the wind, the scale of the current field and, implicitly, breaking. This second parameter can also be written as

$$2 \pi \frac{L u_*^2}{\lambda^2 g} \quad \text{or as} \quad \frac{1}{2 m} \left(\frac{L}{c} \right) \left\{ m \sigma \left(\frac{u_*}{c} \right)^2 \right\}$$

ORIGINAL PAGE IS
OF POOR QUALITY

where C is the group velocity. The latter form provides a useful physical interpretation of this parameter as proportional to the ratio of the time taken for an energy packet to move over one scale distance L to the characteristic growth time of the waves under the influence of the wind alone. If this parameter is large, re-adjustment of the waves is rapid in the time taken to traverse the current variation, so that the response in the relative degree of saturation is small. Small values of the parameter indicate situations where the re-adjustment time is long, so that one might expect a significant response.

For the sake of definiteness, suppose that the 1-direction in (4.2) is chosen as the direction of the wave-number being sampled. The middle term on the left-hand side then reduces to

$$\frac{a}{2} \frac{U_0}{c} \frac{\partial f}{\partial x_1} b$$

expressing the influence of convergence or divergence of the current field in this direction. The third term involves the variation with respect to magnitude and direction of the degree of saturation and must be considered when a current, varying in x , is in the transverse direction so that energy paths are deflected. Little is known (although much is speculated) about the angular distribution of the wave spectrum or b , so that in order to obtain a sense of the magnitude to be expected of the variations in the local degree of saturation relative to the background, we will neglect the variations of b with k and consider convergences or divergences only with $U_1 = U(x_1)$. In the flow over relatively shallow topography such as the Nantucket Shoals, both local convergences ($\partial U / \partial x < 0$) and divergences ($\partial U / \partial x > 0$) can be expected; under open sea conditions, divergences would be expected in regions of local upwelling while local convergences may be found along fronts, with one water mass overriding another, slightly denser.

With $\underline{f}(\underline{s}) = (f(r), 0, 0)$, say, equation (4.2) reduces to

$$\left(\frac{1}{2} + \frac{U_0}{c} f(r) \right) \frac{\partial b}{\partial x} + \frac{a}{2} \frac{U_0}{c} \frac{\partial f}{\partial x} b = 2\pi m S (1 - b^n) b, \quad (4.3)$$

where S is the parameter $(L/\lambda)(u_*/c)^2$. The value of the index n , although greater than 1, is not known at this time; for the purposes of these calculations n was taken as 3. A smaller value gives a more gradual onset of energy loss by breaking as b increases and so a larger response to convergences; a larger value reduces the response. This is shown explicitly below. The wind is supposed to act in the x direction also so that $m = 0.04$ and a current distribution of the form

$$f(s) = \frac{1}{2} \{ 1 + \tanh s \}$$

ORIGINAL PAGE IS
OF POOR QUALITY

was chosen. The equation (4.3) was integrated numerically with $b = 1$ at $\mathcal{F} = -2$ for various values of U_0/c and S , using an Apple II computer. When $U_0/c < 0.5$, equation (4.3) has a mathematical singularity at which the coefficient of the first term vanishes. In those cases, the integrations were performed following the direction of the wave energy flow, from $\mathcal{F} = -2$ to within one step of the singularity and then from $\mathcal{F} = +6$ back to the singularity since in this part of the physical domain, the backwards energy convection of the current overcomes the forwards propagation. If the waves on the far side of the convergence zone have had sufficient fetch and duration to achieve equilibrium, then $b = 1$ at $\mathcal{F} = 6$ also and it is found, somewhat surprisingly, that the two branches of the solution form a continuous curve across the singularity at which $(1/2 + (U_0/c) f(\mathcal{F})) = 0$. On the other hand, if the fetch or duration on the far side is limited, then b on the far side may be less than unity for these waves and a real, physical singularity will occur at this point. It seems that only in this case will an abrupt change in the return signal coincide with this singularity.

Some results of these calculations are illustrated in Figure 2. When the parameter S is of order 10 or more, the responses of b to the current field are small and limited essentially to the region of current shear. For smaller values of S , the magnitude of the response increases; in a convergence ($U_0/c < 0$) the region over which b is significantly greater than 1 remains limited to the convergence region because of the relatively rapid reduction in wave energy by breaking. In a divergence, however, the degree of saturation at a given k reduces as a result of two effects - the divergence spreads the action density out over a greater spatial interval and (more important) the energy packet at the wave number observed after divergence was, before the divergence, at a larger wave-number or smaller scale, so that its action density was less. At values of S less than about 4, the recovery distance of the wave field after suppression is significantly greater than L so that the waves remain unsaturated for a considerable distance.

In a convergence zone, the maximum degree of saturation relative to the background occurs close to the point of maximum strain rate, when $f(\mathcal{F}) = 1$. From (4.3) this occurs when

$$- \frac{9}{2} \frac{U_0}{c} = 2\pi n S (1 - b^n),$$

so that the maximum contrast is

$$b_{\max} = \left\{ 1 + \frac{9}{4\pi n} \frac{U_0}{c} \right\}^{1/(n-1)} \quad (4.4)$$

In the cases shown in Figure 2, n has been taken as 3; since the coefficient $9/4\pi n \approx 20$, b_{\max} varies approximately as $(U_0/c)^{1/2} S^{-1/2}$ for values of $S < 4 U_0/c$ or so. But the value of the index n in the representation (2.15) cannot be regarded as known and, in

ORIGINAL PAGE IS
OF POOR QUALITY

fact, the expression (4.4) may allow it to be determined by field measurements of the maximum contrast in the degree of saturation at a fixed k in convergence zones over a range of values of S and U_0/c , although if n is significantly greater than 1 (as expected), the dependence on n is rather weak.

A general conclusion from these computations is that if freely propagating waves under the influence of wind and breaking are to experience a significant variation in the degree of saturation at a fixed wavelength λ , then the second term in the bracket of (4.4), must be greater than unity, say, or that

$$\frac{U_0}{cS} > 0.05 \quad (4.5)$$

Expressed alternatively in terms of the strain rate in a convergence, a significant response requires

$$\frac{U_0}{L} \geq 0.12 \frac{u_*^2}{g^{1/2} \lambda^{3/2}} \quad (4.6)$$

For example, if $u_* = 20 \text{ cm/s}$ and $\lambda = 16 \text{ cm}$, then U_0/L must be greater than about $2 \times 10^{-2} \text{ sec}^{-1}$, which is a very large oceanic strain rate outside frontal regions. Light winds clearly favour a more sensitive response.

It should be noted, however, that for a given convergence field and wind stress, (4.4) can be written as

$$b_{\text{max}} = \left\{ 1 + \frac{g}{2} n^{-1} (2\pi)^{-2/2} \frac{U_0 g^{1/2} \lambda^{3/2}}{L u_*^2} \right\}^{1/(n-1)}; \quad (4.7)$$

the contrast in degree of saturation increases with wavelength, the smaller value of U_0/c being more than compensated by the increase in S^{-1} . Increased harmonic content of these longer waves and denser breaking patches may give enhanced Bragg and specular scattering that may possibly dominate the direct return from freely travelling waves at the wave-number sensed by Bragg scattering in the background.

In a region of surface divergence (and upwelling), when S is small the recovery of the wave field by the wind is slow over the scale of the divergence, and the reduction in b can be estimated by neglecting the wind input (and wave breaking) over this interval. With $U_0 f(\tau) = U(\tau)$, equation (4.3) reduces to

$$\left(\frac{1}{2} + \frac{U(\tau)}{c} \right) \frac{db}{d\tau} + \frac{g}{2} \frac{d}{d\tau} \left(\frac{U(\tau)}{c} \right) b = 0,$$

C-6

which integrates exactly to

$$b(f) = (1 + 2U(f)/c)^{-9/2}, \quad (4.8)$$

since $b = 1$ when $U = 0$. This reduction ($U(f) > 0$) at a fixed wave-number is, of course, greater than for an energy packet or wave train at a fixed apparent frequency, as calculated by Longuet-Higgins and Stewart (1960) since the waves elongated by the divergence to the wave-number k had a larger wave-number and smaller spectral density than the waves at wave-number k before the straining.

The SEASAT synthetic aperture radar imagery, such as that reproduced in the book by Beal et al (1981; see especially pp. 22 and 96), offers a number of examples that seem, in the light of these results, to be interpretable as lines of local convergence or divergence. There is unfortunately little independent information on the current field or the local wind stress so that attempts at a quantitative comparison must await imagery for which more complete documentation is available. However, these results do indicate the potential in synthetic aperture radar imagery for measuring rates of strain in oceanic fronts and rates of upwelling over a substantial spatial domain.

Acknowledgements It is a pleasure to acknowledge the support of NASA during the early stages of this investigation under contract NAGW-304. It was completed with the support of the Fluid Dynamics Branch of the Office of Naval Research under contract N00014-76-C-0184.

References

- Banner, M.L. (1984) A comparison of the wave-induced momentum flux to breaking and non-breaking waves, in Hasselmann and Phillips, op.cit.
- Banner, M.L. and W.K. Melville (1976) On the separation of air flow over water waves. J. Fluid Mech., 77, 825-42.
- Beal, R.C. (1981) Spatial evolution of ocean wave spectra. pp 110-127 of Beal, DeLeonibus and Katz. op.cit.
- Beal, R.C., P.S. DeLeonibus and I. Katz (eds) (1981) Spacebourne Synthetic Aperture Radar for Oceanography. pp 215., The Johns Hopkins University Press.
- Fox, M.J.H. (1976) On the nonlinear transfer of energy in the peak of a gravity wave spectrum, II. Proc.Roy.Soc. A, 348, 467-83
- Gent, P.R. and P.A. Taylor (1976) A numerical model of the air flow above water waves. J. Fluid Mech., 77, 105-28.
- Hasselmann, K. and O.M. Phillips (eds) (1984) Wave Dynamics and Radio Probing of the Ocean Surface. pp xxx N.Y.: Plenum Press.
- Keller, W.C. and J.W. Wright (1975) Microwave scattering and the straining of wind-generated waves, Radio. Sci., 10, 139-147.
- Kitaigorodskii, S.A. (1983) On the theory of the equilibrium range in the spectrum of wind-generated gravity waves. J. Phys.Oceanog., 13, 816-27.
- Longuet-Higgins, M.S. and R.W. Stewart (1960) Changes in the form of short gravity waves on long waves and tidal currents. J. Fluid Mech., 8, 565-83.
- Mitsuyasu, H. and T. Honda (1984) The effects of surfactant on certain air-sea interaction phenomena. In Hasselmann and Phillips, op.cit.
- Phillips, O.M. (1980) The Dynamics of the Upper Ocean. pp 336 Cambridge University press
- Phillips, O.M. (1958) The equilibrium range in the spectra of wind-generated waves. J. Fluid Mech., 4, 426-34.
- Phillips, O.M. and M.L. Banner (1974) Wave breaking in the presence of wind drift and swell. J. Fluid Mech., 66, 625-40.
- Plant, W.J. (1982) A relationship between wind stress and wave slope. J. Geophys. Res., 87, 1961-67.

References

- Toba, Y. and H. Kunishi (1970) Breaking of wind waves and the sea surface wind stress. J. Oceanog. Soc. Japan 26, 71-80.
- West, B.J. (1984) Statistical properties of water waves, Part IV. In Hasselmann and Phillips, op.cit.
- Wright, J.W., W.J. Plant, W.C. Keller and W.L. Jones (1980) Ocean wave-radar modulation transfer function from the West Coast experiment. J. Geophys. Res., 85, 4957-66.

ORIGINAL PAGE 19
OF POOR QUALITY

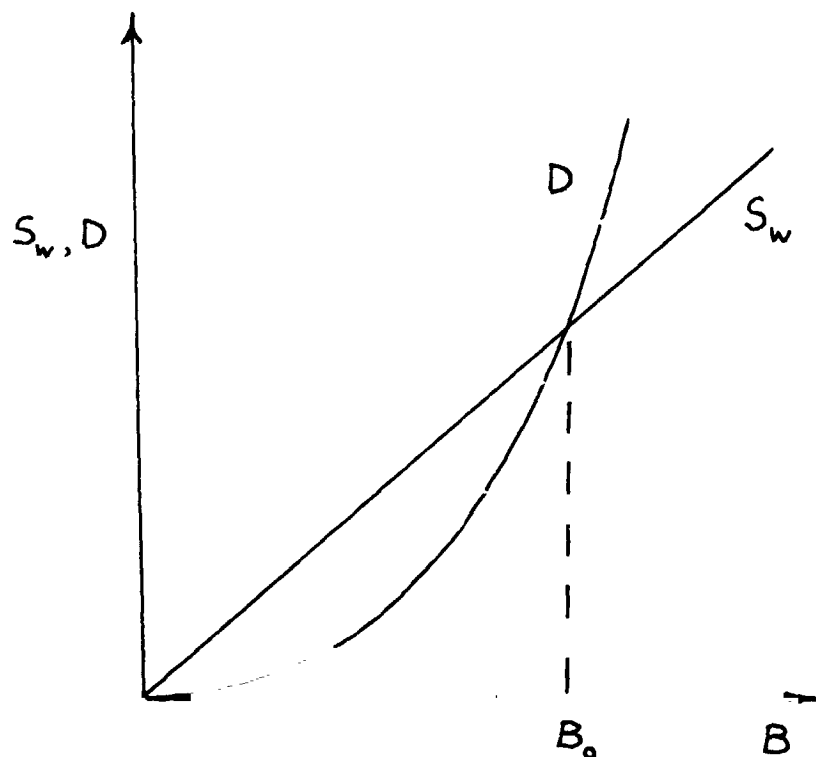


Figure 1: Input from the wind, S_w , and dissipation D of action spectral density as functions of the degree of saturation B . The intersection specifies B_0 , the high wave-number equilibrium value.

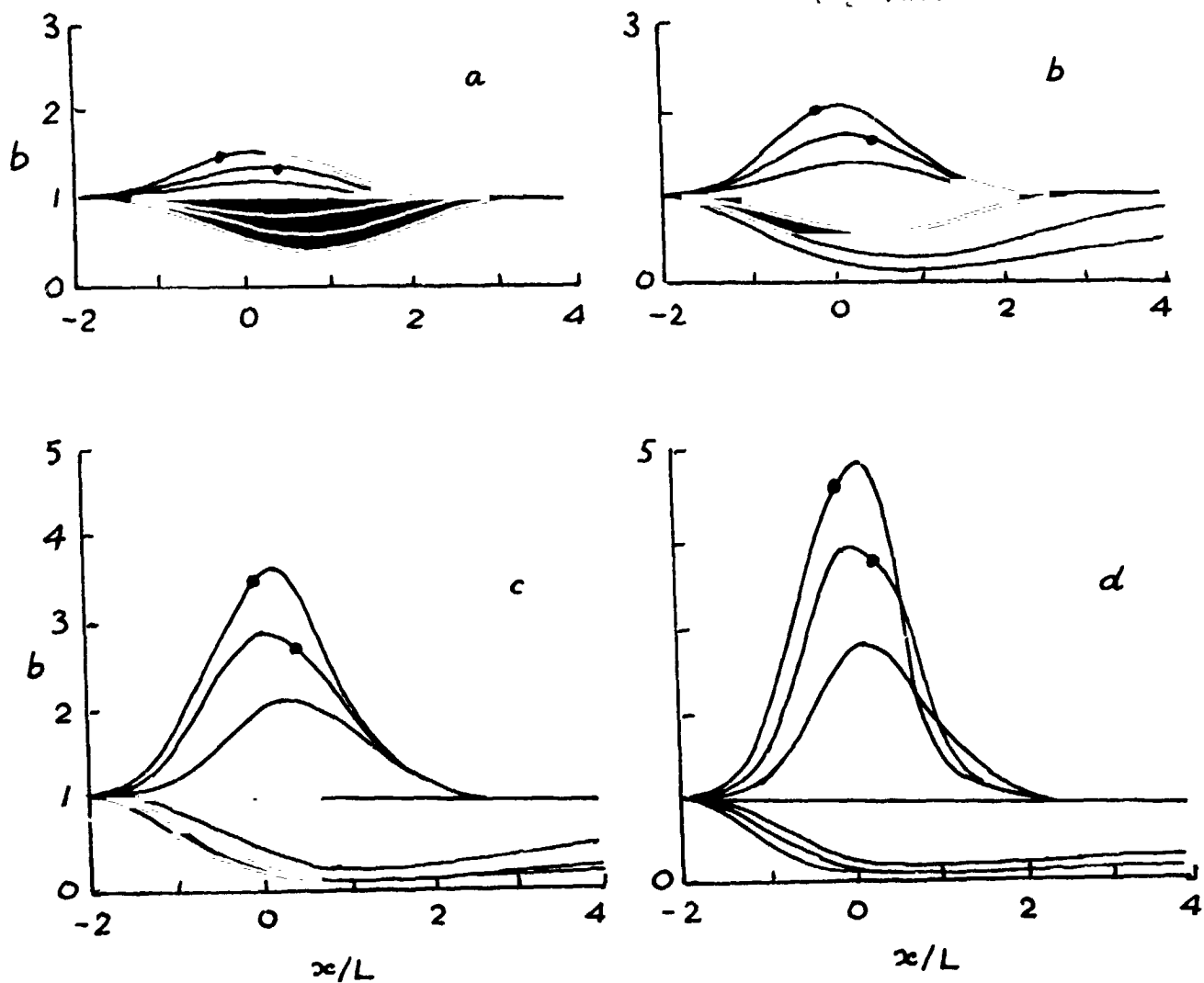


Figure 2: Relative degrees of saturation $b = B/B_0$ at a fixed wave-number as functions of position in a local convergence or divergence centered at $x = 0$. In Figure 2a, $(L/\lambda)(u_*/c)^2 = 12$; in 2b, 4; in 2c, 1 and in Figure 2d, 0.5. The three upper curves in each group represent the convergence cases with $U_0/c = -1.2, -0.8$ and -0.4 ; the three lower curves are for divergences with $U_0/c = 0.4, 0.8$ and 1.2 . The black dots represent positions where $U(x)/c = 0.5$.

VARIATIONS IN SURFACE CURRENT OFF THE COASTS OF CANADA
AS INFERRED FROM INFRARED SATELLITE IMAGERY

W.J. Emery, M. Ikeda, L.A. Mysak and P.H. LeBlond
Department of Oceanography
University of British Columbia
Vancouver, B.C. V6T 1W5, Canada

ABSTRACT

Infrared satellite images of sea surface temperature are used to infer changes in the surface currents off both the east and west coasts of Canada. Off the east coast summer infrared temperature patterns suggest a close connection between the location of the continental slope and the path of the Labrador Current as marked by a strong thermal front. Meanders and eddies appear to form where abrupt changes in the shape of the continental slope occur. In winter both infrared and visible imagery reveal the southward propagation of wavelike features in the ice patterns along the Labrador coast. A relatively large number of images from the Canadian west coast have been used to depict the evolution of surface temperature features associated with fluctuations in the corresponding current system. In winter and spring 150 km current meanders are fed energy by the baroclinic instability of the uniformly directed current which flows northwest in winter and southeast in spring. In summer the surface current is directed southeastward while below it an undercurrent flows to the northeast. Initiated by an interaction with the irregularities of the local continental slope 75 km current meanders begin to form. Energy is then fed non-linearly by baroclinic instability into longer scale 150 km meanders which eventually shed to form separate eddies.

INTRODUCTION

Infrared satellite imagery have often been used in oceanography to suggest the complexities of the ocean and to infer characteristics of surface currents possibly connected to the sea surface temperature patterns. By using a sequence or collection of such images it should be possible to examine both spatial and temporal changes in the infrared thermal patterns in an effort to better describe and understand the oceanographic mechanisms associated with these observed changes. In such a study it must be realized that while infrared satellite imagery has the limitation that it can only sense at the sea surface it also has the significant advantage that it can view a large part of the ocean in a truly synoptic fashion. Thus is provides oceanographers with a unique view of the ocean and studies using these images should focus on this advantage by looking for space and time scales clearly represented in the thermal imagery. In this way satellite infrared imagery can provide meaningful insight into ocean dynamics without the stringent requirements of providing precise and accurate surface temperature measurements.

ORIGINAL PAGE IS
OF POOR QUALITY

Unfortunately for this study only a very limited number of digital images were available for the Canadian east coast which restricts the type of study that can be carried out. We will therefore only look at a few examples of summer imagery that suggest some interesting relationships between surface temperature patterns and details in the coastal bottom topography. Winter ice patterns will also be examined which suggest the southward, along-coast propagation of wavelike features at the edge of the ice. An earlier study by LeBlond (1982) identified these features in a sequence of four visible satellite images. From changes in the patterns of the ice edge he inferred a southeastward phase speed of features with a 73 km wavelength. Similar features are evident in some of the 18 winter/spring images examined in this study.

A substantially larger number of images was used to study changes in infrared surface temperature patterns off the Canadian west coast. Starting in the spring of 1980 arrangements were made to receive digital AVHRR data from a receiving station in Edmonton, Alberta operated by the Canadian Atmospheric Environment Service (AES). Most of the AVHRR images discussed in this study are recorded at this facility. Recently, however, a receiving station has been set up and is operating at the Department of Oceanography at the University of British Columbia. The availability of digital data from this station has greatly increased the number of useful images being archived.

East Coast Imagery

As mentioned earlier a limited number of both summer and winter/spring images were available for the east coast. The primary region of main interest was selected as the Labrador coast between Cape Chidley and Hamilton Inlet along with the mouth of Hudson Strait and all of Ungava Bay. Off the Labrador coast the cold Labrador Current flows south carrying water from Davis Strait down to the coast of Newfoundland. Some of this water enters into Hudson Strait at the north while other water discharges from the Strait eastward to join the Labrador Current. These general flow patterns are clearly depicted in the 0/1000 db dynamic height contours drawn by Smith (1937) and presented here as Fig. 1. This mean flow pattern also shows how the discharge at the mouth of Hudson Strait separates into both off-shore and nearshore portions leaving part of the area just south of Cape Chidley without a strong mean flow. This will be seen in the infrared imagery as a region of complex temperature patterns representative of the small scale structure in this area between the two branches of the Labrador Current. As can also be seen in Fig. 1 these two current branches reunite just north of Hamilton Inlet where the current turns eastward along the geographic boundary. The union of these two current branches is also revealed by the satellite images which show cold coastal waters joining with the cold offshore portion of the Labrador Current. These patterns are also apparent in winter when the ice appears to frequently display a clear region in the region just southeast of Cape Chidley. Similarly the ice patterns appear to change just north of Hamilton Inlet with the wavelike features observed by LeBlond (1982) increasing in amplitude at this point.

ORIGINAL PAGE 18
OF POOR QUALITY

Returning to summer images the most striking characteristic of the image in Fig. 2a is the close correspondence between the position and shape of the interface between the cold and warm surface waters and the shape and location of the continental slope. In Fig. 2b this surface temperature boundary has been drawn schematically on a map of the coast which also shows the bottom topography. The similarity between the 2000 m contour and the surface temperature front suggests the topographic steering of the current associated with the temperature gradient. Of particular interest is the sharp seaward meander of the boundary over the small topographic ridge slightly northeast of Hamilton Inlet. This same image (Fig. 2a) also demonstrates how the current turns away from the coast at about 55°N as the current narrows to round the coast leaving a large patch of warm surface water nearest the coast off Hamilton Inlet. The outer boundary of the cold water also turns seaward following the path of the 2000 m contour. Relatively small patches of cold water farther offshore suggest that meanders of the cold current band may separate to form eddies. While these eddies appear cold at the surface their sense of rotation must be anti-cyclonic if formed as meanders of the southbound current. This and other images suggest by the shape of the features that they may be rotating clockwise consistent with this formation mechanism.

In Fig. 3a, another summer image collected on August 19, 1980, the outer boundary of the cold tongue again follows the continental slope lying between the 1500 and 2000 m depth contours. Unlike the image from July 1979 the cold core of the Labrador Current is quite narrow and highly meandered. The patch of warm water off Hopedale, north of Hamilton Inlet, is broken by tongues of cold water extending shoreward in from the cold core of the Labrador Current.

Just southwest of 57°N, 58°W a sharp "v" shaped meander marks a shoreward meander of the current. Oddly enough another image just one year earlier also exhibited a "v" shaped meander at about the same location. It is possible that the small topographic ridge at this position (Fig. 3b) is responsible for the quasi-permanence of this meander feature.

An interesting series of images from the summer of 1981 covers the region of Ungava Bay, the mouth of Hudson Strait and the northeast coast of Labrador. In an image from June 28 (Fig. 4), there is a concentration of warm water along the eastern boundary of Ungava Bay which extends northward in a 30 km band. This warm band narrows as it turns east to round Cape Chidley extending out to almost 62°W. From this image alone it is not clear if this warm water joins with that just to the southwest which separates the cold cores of the in and offshore branches of the Labrador Current.

It is interesting that just north of this warm water exiting Hudson Strait is a narrow band of cold water which also appears to originate within the Strait. This cold band is then separated from the cold waters which ring Resolution Island by warm water which seems to turn into the mouth of Hudson Strait from farther north. East of 63°W this warm water turns to cold which appears to be flowing south to connect with the offshore branch of the Labrador Current.

2)

About three weeks later a cloud-free image from July 15 (Fig. 5) reveals a somewhat different pattern. As on June 28 there is warm water in a band along the eastern boundary of Ungava Bay; at this later time the band reveals eddy-like patches in the south and a branch extending westward from 60°N , 66°W . This coastal warm band is again about 30 km wide but no longer extends eastward around the northern tip of Labrador. Instead cold water flows out of the central mouth of Hudson Strait to then split into a narrow coastal branch and a wider offshore branch of the Labrador Current. The warm water between these branches is highly meandered and eddied with filaments of warm and cold water marking both cyclonic and anticyclonic rotations. The nearshore portion of the coastal branch also appears meandered with small patches of warm water.

Finally on July 29 (Fig. 6) this pattern has been amplified with cold water coming out of Hudson Strait and clearly splitting just southeast of Cape Chidley into near and offshore cold bands representative of the branches of the Labrador Current. The warm water between these branches is similar in shape and location to its expression in the image two weeks earlier (Fig. 5). Again interesting is the warm tongue just north of 61°N which turns westward into the mouth of Hudson Strait. This warm tongue, and its connection to the warm water along 64°W , are seen in all three images. This separation strongly suggests that the coastal branch, of the Labrador Current, is fed by the discharge from Hudson Strait rather than from water flow south out of Davis Strait.

A late spring image from May 29, 1981 (Fig. 7) contains an open area southeast of Cape Chidley where the warm water was seen in summer. In this image the open water area is quite large and stretches south to about 59°N . Southward the ice is fairly broken up and fragmented with large open leads adjacent to the coast. Ungava Bay appears ice covered and some ice can be seen extending out through the mouth of Hudson Strait. The outer edge of this ice cover is just inside and roughly parallel to the 500 m bathymetric contour. Ice patterns similar to those discussed by LeBlond (1982) were observed as shown for example in Fig. 8, a visible image from April 18, 1982. In this image the area just southeast of Cape Chidley is once again clear of ice and a number of other open leads appear nearshore farther down the coast. The seaward edge of the pack ice is composed of offshore extending tongues of many different length scales. Some appear associated with definite cyclonic features while others are likely expressions of anticyclonic eddies. The most prominent feature is a warm patch with a cold center between 59 and 59°N along 61°W . This and many other features have size scales around 50-60 km similar to the 73 km wavelength inferred from visible satellite images by LeBlond (1982). Also consistent with LeBlond's study are the southeastward extending tongues of ice off Hopedale at the lower right of the image. As with the four visible images analyzed by LeBlond (1982) these tongues appear to grow in amplitude toward the south.

In summary both summer and winter images from the Canadian east coast have demonstrated the close correspondence between sea surface temperature expressions of the Labrador Current and the shape of the continental slope. The outer edge of the cold band marking the

Labrador Current appears to follow the outer portion of the slope running along the 2000 m depth contour. Smaller scale changes in the shape of the continental slope lead to meanders and eddy formation in the Current. In winter coastal pack ice cover also exhibits wavelike meanders which grow in amplitude towards the south. Just southeast of Cape Chidley the cold Labrador Current waters splits into coastal and offshore branches. Cold water discharged from Hudson Strait contributes to both of these current branches. The area between these two branches is usually warm in summer and ice free in winter/spring.

West Coast Imagery-Baroclinic Instability

Our study of infrared satellite imagery off the Canadian west coast has focused on the region off Vancouver Island and the northern part of Washington State as shown in Fig. 9. Earlier studies of this region (Mysak, 1977; Emery and Mysak, 1980) suggested that tongue-like meanders in the infrared sea surface temperature exhibited length scales and growth rates consistent with their formation through the mechanism of baroclinic instability. As first modelled by Mysak (1977) this instability transferred energy from the shear between a northwestward undercurrent flow, and a deeper layer at rest into these meanders. Later Wright (1980) added a third layer to this model and concluded that the energy transfer was from the shear between the southeastward surface current and the underlying northwestward undercurrent to the meanders. The presence of this undercurrent, called the California Undercurrent, as far north as Vancouver Island has been discussed by Hickey (1979).

All of these earlier studies looked at a very limited number of satellite images and thus relied primarily on analytical models to reveal characteristics of the instability mechanism and the associated flow system. In the present study we have used a large number of relatively cloud-free images from the period between 1980 and 1982. We have also been fortunate in having current meter data available for 1980 collected off the west coast of Vancouver Island by scientists at the Institute of Ocean Sciences at Patricia Bay, B.C. Temperature and salinity data, collected in conjunction with these current meter data, have also served to independently confirm our conclusions based on the satellite imagery and numerical modeling.

The best series of surface temperature images is from the summer of 1980. Starting on July 21 (Fig. 10) the image reveals a warm sea surface off the coast of Vancouver Island. The only exception in this image is a patch of cold water off the mouth of the Strait of Juan de Fuca. As discussed by Freeland and Denman (1983) this is the expression of a cold cyclonic eddy driven by the interaction between the undercurrent and the topographic irregularity of the Juan de Fuca Canyon (Fig. 9). In summer this cold patch is almost always present independent of whether or not wind-driven upwelling is occurring. In response to southeastward alongshore wind coastal upwelling produces a band of cold water off the coast of Vancouver Island (Fig. 11, July 28) which appears highly meandered with a relatively short spatial scale. Cold water can also be seen along the coast of Washington and in the Strait of Juan de Fuca. On August 24 (Fig. 12)

these meanders have developed into a series of six tongues spaced about 75 km apart. A sequence of six images documents the evolution of the surface temperature field between this August 25 image and Fig. 13 the image from September 14. Here only three tongues are apparent with a spacing of about 150 km. The largest of these is shaped somewhat like a "T" and is the expression of a pair of matched, counter-rotating eddies we called "dipole eddies". On October 2 (Fig. 14) the image records the separation of these tongues into a series of three distinct cold cyclonic eddies with the central feature being much larger than the eddies to the north and south. This pattern of surface temperature evolution is summarized in Fig. 15 where the reference line represents the position of the continental shelf break. Fourier spectral analyses of these images confirms the shift from both 75 and 150 km features in July and August to only 150 km features in September and October.

Linear instability theory, for the summer current conditions of a southward surface flow over a northward undercurrent, yields a fastest growing wavelength of about 100 km. This is between the 75 and 150 km wavelengths observed in the imagery from the summer of 1980. As a possible solution to this discrepancy non-linear numerical calculations were carried out for the summer conditions. The model used had four layers in the vertical and represented the flow seaward of the continental shelf-break as shown graphically in Fig. 16. Also shown here is the vertical mean current profile used in the model. This model was initiated with small amplitude 75 and 150 km scale meanders. As represented schematically in Fig. 17 the evolution of this model over a 44 day period demonstrates the early growth of the shorter scale meanders which then weaken to transition into the larger 150 km meanders which then form into discrete cold cyclonic eddies. During this evolution the formation of dipole eddies is evidenced about 30 days into the model run. Thus the non-linear numerical model correctly simulates the events inferred from the infrared satellite images and explains why the linear theory fails to predict the proper meander wavelength. This is quite reasonable since in the summer the very strong shear between the southward surface current and the northward undercurrent would lead to the increased influence of non-linear energy transfer mechanisms. An energy analysis of the numerical results reveals that while both barotropic and baroclinic instability mechanisms are operating the baroclinic instability accounts for more than 80% of the energy transfer. Looking at *in situ* oceanographic data from 1980 Thomson (1984) also concludes that baroclinic instability is primarily responsible for the formation of cyclonic eddy seen just off Vancouver Island in the same location as the northernmost meander and later eddy in Figs. 12 and 13.

In searching for an initial generating mechanism, for the smaller scale 75 km meanders, it was observed (Ikeda, et al., 1984a) that the continental slope off Vancouver Island contains variations with an alongshore scale of about 75 km (Fig. 9). To evaluate the possible role of these bottom topography variations another numerical simulation was run with no initial meanders but a bottom topography with topographic bumps that extended into the second or undercurrent layer (Fig. 18). Run over a time similar to that for the earlier model this simulation demonstrated the excitation of the

75 km meanders by the interaction of the undercurrent with the irregularities in the bottom. These short scale meanders grew initially and then transferred energy via a non-linear interaction into the large 150 km scale features which then shed independent cold eddies (Ikeda, et al., 1984b). Thus the summer evolution is a "red-cascade" from small scale 75 km meanders, started by an interaction with the bottom topography, to longer 150 km meanders which then shed cold cyclonic eddies in a period of a month to six weeks. This sequence of surface temperature features has also been observed in the infrared satellite imagery from the summer of 1982 (Ikeda, et al., 1984b).

In winter and spring the mean current (0-1000 m) off Vancouver Island is all directed northwest or southeast respectively. The absence of the undercurrent during these periods is discussed by Hickey (1979) and is clearly represented in the current meter records from the west coast discussed by Freeland, et al. (1984). Late fall and winter satellite images appear to contain only larger scale meander features with wavelengths of about 120 to 150 km, as shown for example in Fig. 19, an image from November 27, 1981. Interestingly linear instability theory predicts wavelengths of this magnitude for winter flow conditions.

In spring the uniformly flowing southward current also leads to longer scale features as predicted by the linear stability theory. Imagery from this season again exhibit larger scale features between 120 to 150 km consistent with the scales of linear theory. A sample spring image is shown in Fig. 20 for April 6, 1982. Here as in other images the cold/warm boundary has been outlined to better define the meanders revealed by the surface temperature patterns. It should be noted that while in summer the boundary is between cold, upwelled coastal water and warmer water offshore, in spring the boundary marks meanders as seaward extending tongues of warm water off of Vancouver Island. While this appears to contradict the geostrophic relationship it should be remembered that especially in spring salinity plays a significant role in establishing the coastal current (Tabata, 1976).

That this instability mechanism may be operating farther south along the west coast of North America is suggested by the marked tongue-like meanders in Fig. 21, a satellite image from the area off northern California and Oregon collected on September 13, 1982. Fourier analysis of this and other similar images suggests that again 150 km meanders dominate later in the summer. In these images, however, there is also a 200 km length scale which appears to be associated with the large horizontal scale of the topographic ridges in this region. Thus once again both bottom topography and non-linear interaction appear to influence the formation of current meanders as expressed in infrared satellite sea surface temperatures. As recently discussed by Mooers and Robinson (1984) meanders, eddies and even dipole eddies have been observed in hydrographic data collected in this region during summer. This provides independent evidence of the instability mechanism inferred from the infrared satellite imagery.

In summary surface temperature patterns, as revealed by infrared satellite imagery, contain large scale (120-150 km) meanders in spring and winter consistent with the length scales predicted by

linear instability theory for these seasons. In summer non-linear mechanisms are more important and a non-linear numerical model simulates the evolution of meanders from an initial scale of about 75 km to that of 150 km over a period of about 45 days as seen in series of summer infrared satellite images. In summer the meanders appear as cold tongues of upwelled water extending seaward from the continental shelf. Numerical simulation also documents the excitation of the initial 75 km meanders by similar sized variations in the bottom topography. In all cases the primary instability mechanism is a baroclinic transfer of energy from the mean shear into the meanders. In summer the large-scale meanders grow to eventually shed cold cyclonic eddies thus dissipating energy from the mean flow. Satellite images from northern California and Oregon also appear to exhibit surface temperature patterns consistent with this baroclinic instability mechanism.

CONCLUSION

Satellite infrared images from the Canadian east coast suggest a relationship between the path of the Labrador Current and the shape of the continental shelf break. Water from Hudson Strait is seen to contribute to both the near and offshore branches of the Labrador Current which is seen to separate just southeast of Cape Chidley. Between the current branches the ocean is relatively warm in summer and generally ice free in winter/spring. Also related to the shape of the continental shelf break, current meanders form off the Canadian west coast and appear as tongues of warm and cold water in infrared satellite images. Length scales of these meanders (120-150 km) are consistent with linear instability theory in spring and winter while non-linear numerical simulations correctly reproduce the summer/fall meander evolution from 75 to 150 km length scales. Baroclinic instability associated with the structure of the mean flow is responsible for the growth of these meanders and the subsequent shedding of cold, cyclonic eddies.

ACKNOWLEDGEMENTS

This research was supported by the Canadian Natural Sciences and Engineering Research Council, under their Strategic Grants Program for Oceans; this support is gratefully acknowledged.

REFERENCES

- Emery, W.J. and L.A. Mysak, 1980: Dynamical interpretation of satellite sensed thermal features off Vancouver Island. *J. Phys. Oceanogr.*, 10, 961-970.
- Freeland, H.J. and K.L. Denman, 1982: A topographically controlled upwelling centre off southern Vancouver Island. *J. Mar. Res.*, 40, 1069-1093.
- Hickey, B.M., 1979: The California Current system - hypothesis and fact. *Prog. in Oceanogr.*, 8, 191-273.
- Ikeda, M., L.A. Mysak and W.J. Emery, 1984: Observation and modeling of satellite-sensed meanders and eddies off Vancouver Island, *J. Phys. Oceanogr.* (in press).

- Ikeda, M., W.J. Emery and L.A. Mysak, 1984: Seasonal variability in meanders of the California Current system off Vancouver Island. J. Geophys. Res. (in press).
- LeBlond, P.H., 1982: Satellite observations of Labrador Current undulations. Atm. Ocean, 20, 129-142.
- Mooers, C.N.K. and A.R. Robinson, 1984: Turbulent jets and eddies in the California Current and inferred cross-shore transports submitted to Science.
- Mysak, L.A., 1977: On the stability of the California Undercurrent off Vancouver Island, J. Phys. Oceanogr., 7, 904-917.
- Smith, E.H., 1937: The Marion Expedition to Davis Strait and Baffin Bay. U.S. Treasury, U.S. Coast Guard Bull. 19, Part 2, Report of the International Ice Patrol Service in the North Atlantic Ocean, 259 pp.
- Tabata, S., 1976: The general circulation of the Pacific Ocean and a brief account of the oceanographic structure of the North Pacific Ocean. Part II - Thermal regime and influence on the climate. Atmosphere, 14, 1-27.
- Thomson, R.E., 1984: A cyclonic eddy over the continental margin of Vancouver Island: Evidence for dynamical instability (submitted to J. Phys. Oceanogr.).

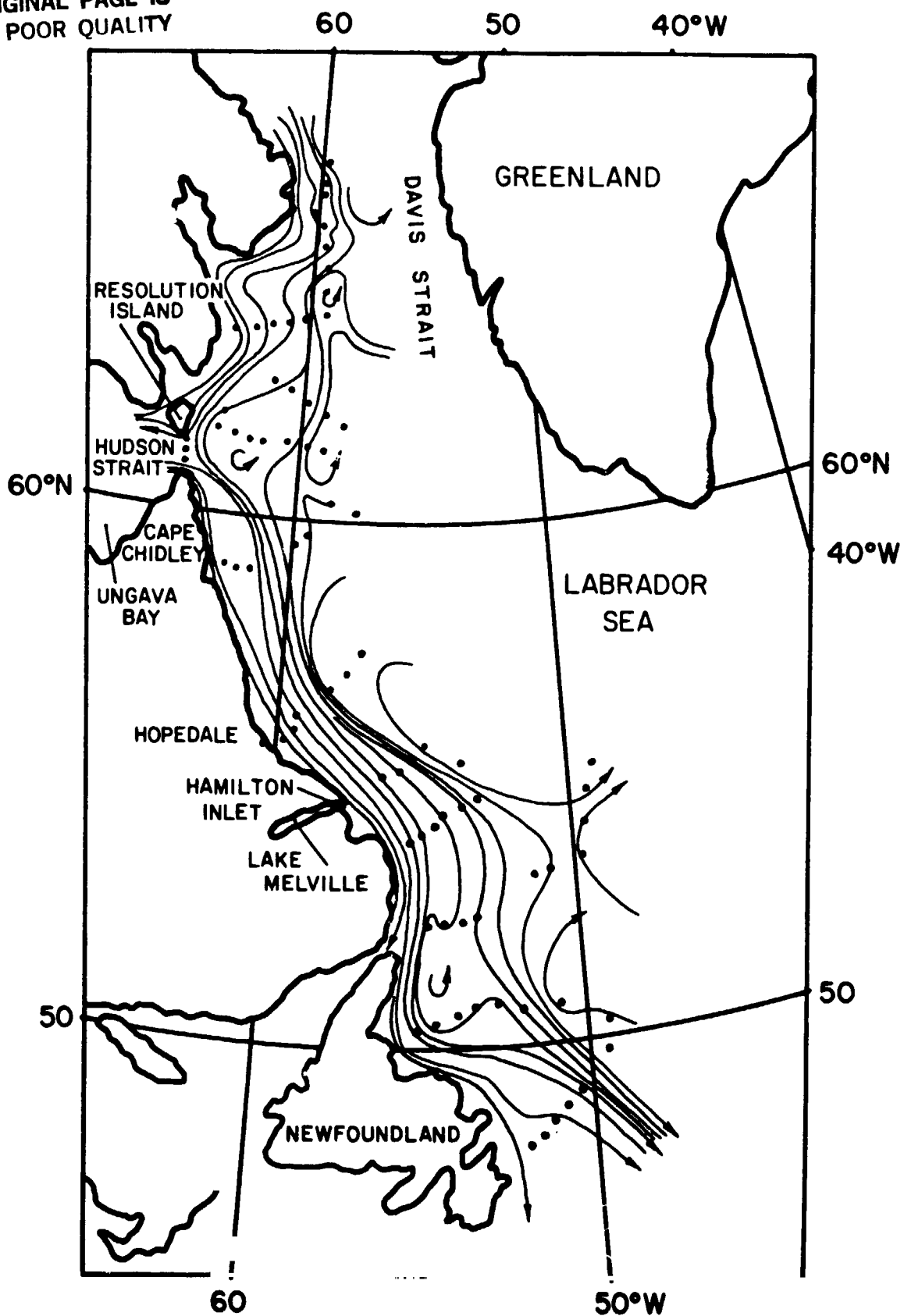
List of Figures

Fig.

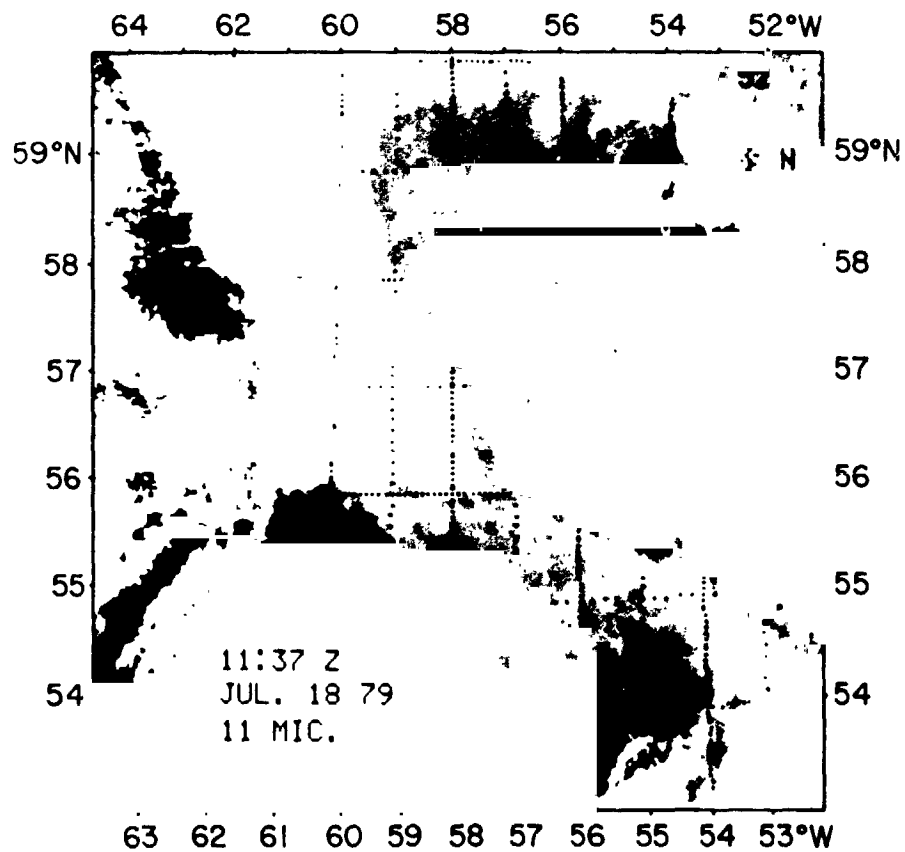
1. Station array and 0/1000db dynamic height streamlines off the Canadian east coast (from Smith, 1937).
2. a) Infrared ($10.3-11.3\mu$) image of the central Labrador Coast on July 18, 1979. Light tones represent cold sea surface temperatures.
b) Interpretative map of Fig.2a. Heavy dashed line represents the cold/warm boundary in Fig.2a. Cloudy areas are cross hatched. Bottom topography contours are in meters.
3. a) As in Fig.2a for Aug. 19, 1980;
b) Interpretation map of Fig. 3a. Conventions are the same as in Fig.2a.
4. Infrared image of the mouth of Hudson Strait from June 28, 1981.
5. As in Fig.4 for July 15, 1981.
6. As in Fig.4 for July 29, 1981.
7. As in Fig.4 for May 29, 1981.
8. Visible ($0.58-0.68\mu$) image of the Labrador Coast from April 18, 1981.
9. Reference map for the west coast. Dashed lines are the 200m and 500m depth contours while the "+" signs mark current meter locations. Boxes labelled A through G are portions of the numerical model domain.
10. Infrared image of the west coast of Vancouver Island from July 21, 1980. Heavy dashed line is an estimate of the surface current axis.
11. As in Fig.10 for July 28, 1980.
12. As in Fig.10 for Aug. 24, 1980.
13. As in Fig.10 for Sept. 14, 1980.
14. As in Fig.10 for Oct. 2, 1980.
15. Schematic time series evolution of the surface current axis relative to the baseline in Fig.9.

16. The four layer model used for linear stability theory and nonlinear numerical simulations.
17. Schematic time series evolution of the surface current axis from the numerical simulation. Numbers in parentheses refer to actual elapsed days.
18. Diagram of topographic obstructive used in the model along with a plan view of the numerical model domain.
19. As in Fig.10 for Nov. 27, 1981.
20. As in Fig.10 for April 6, 1982.
21. Infrared image from the west coasts of Oregon and northern California from Sept. 3, 1982.

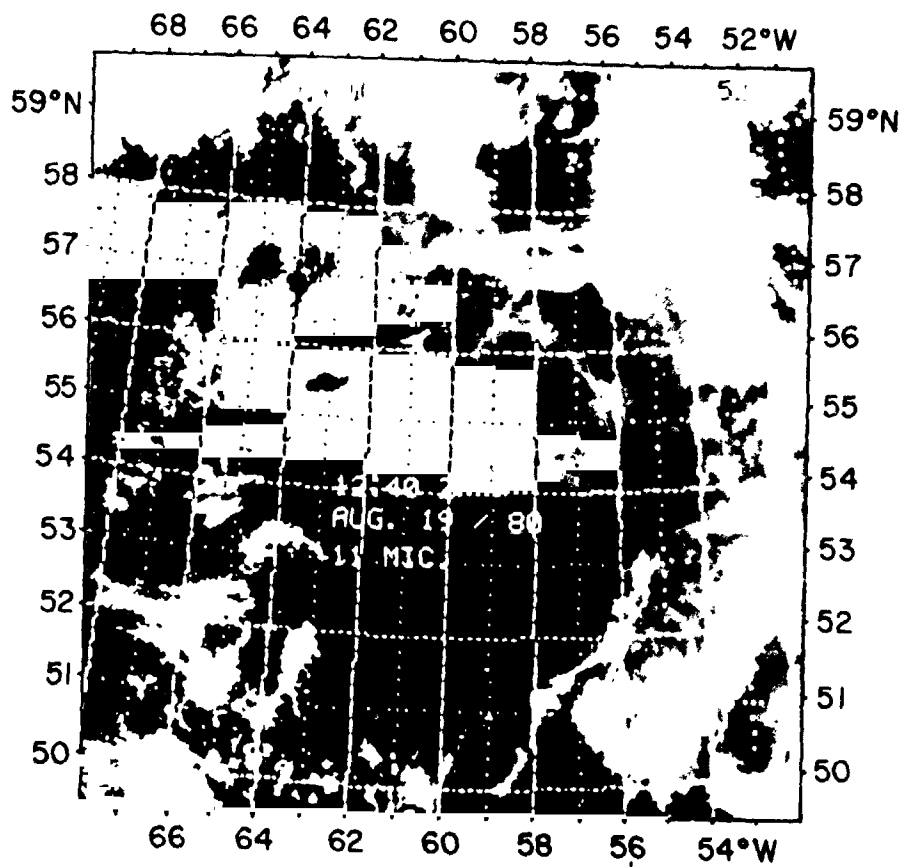
ORIGINAL PAGE 19
OF POOR QUALITY



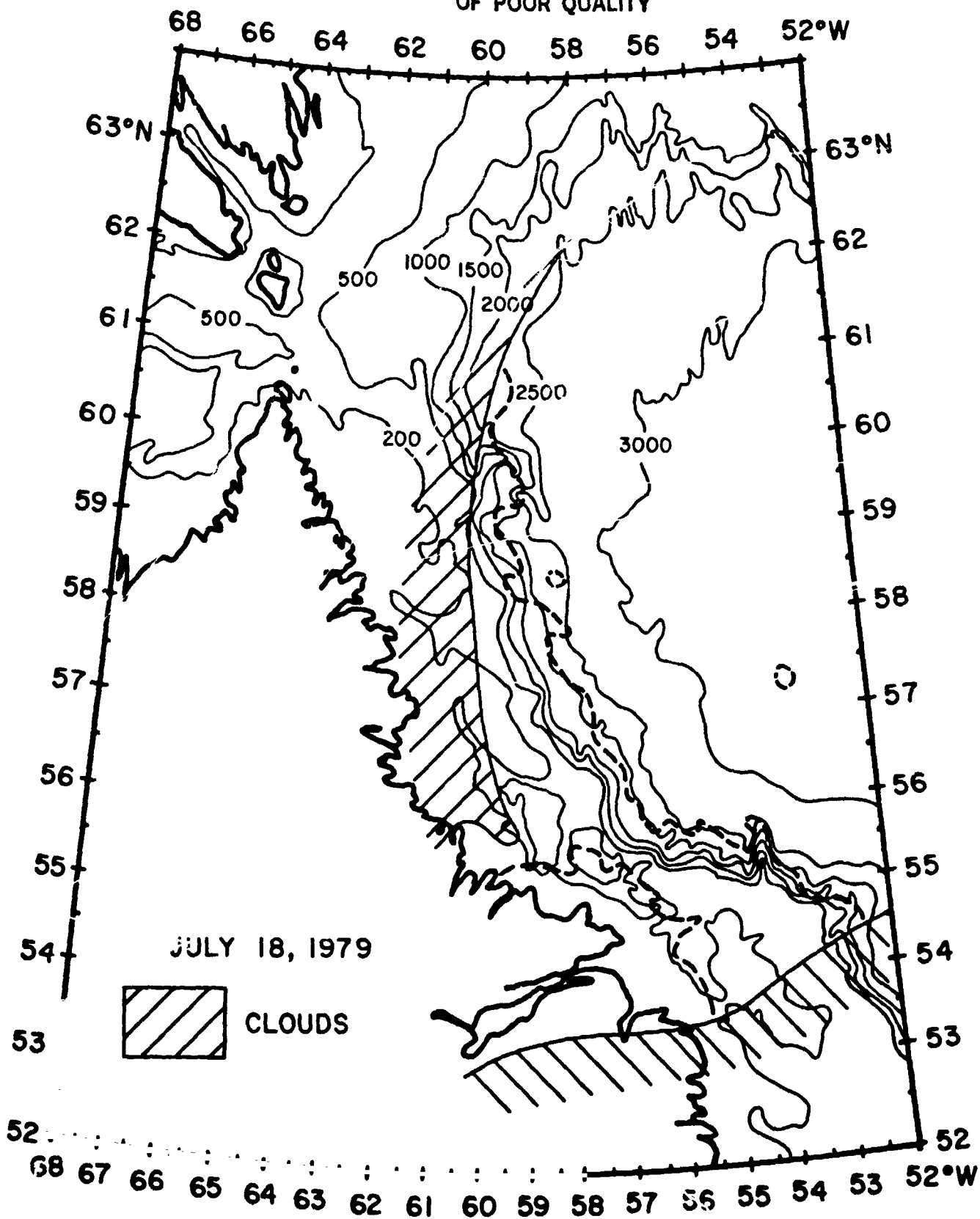
ORIGINAL PAGE 19
OF POOR QUALITY



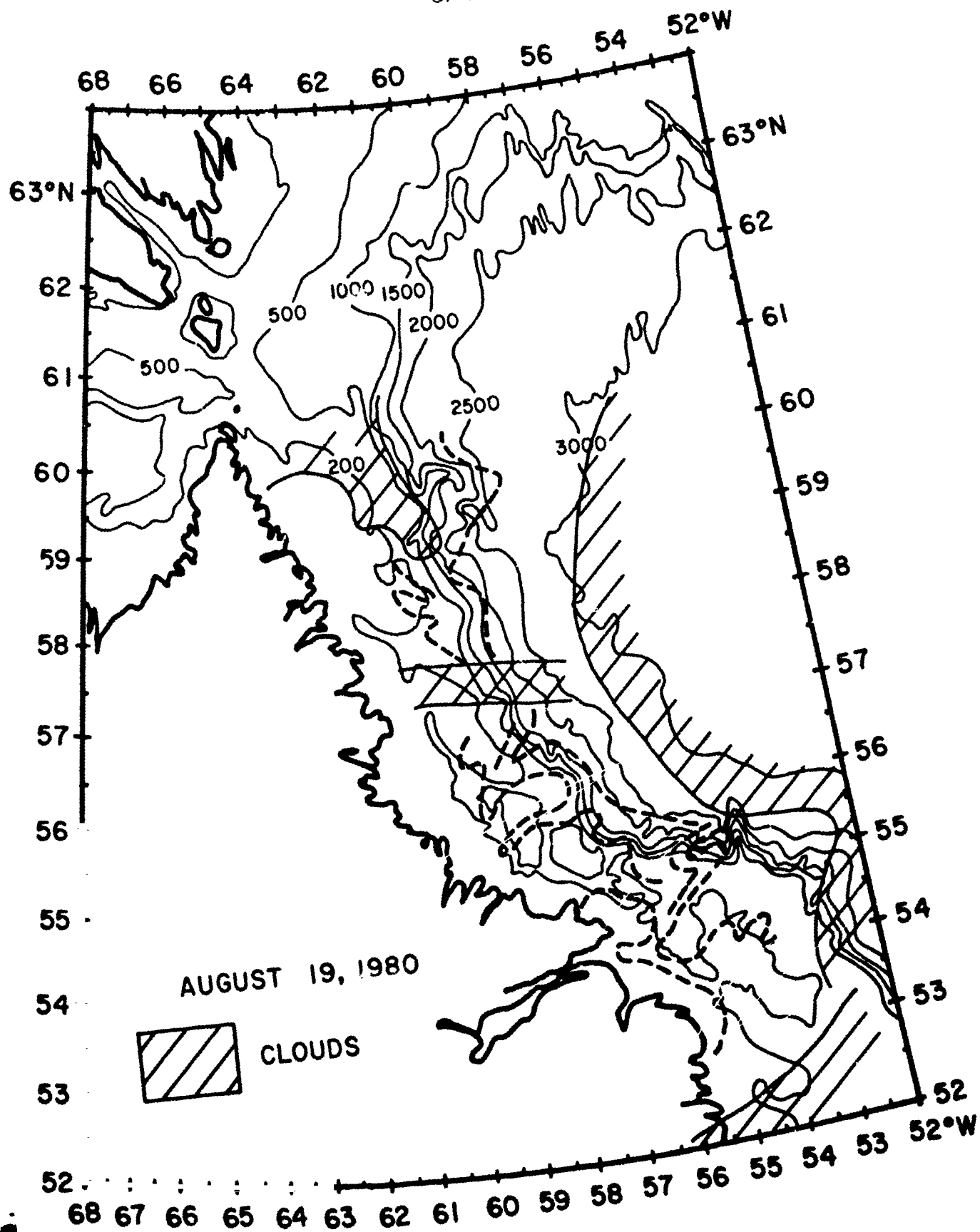
ORIGINAL PAGE 19
OF POOR QUALITY



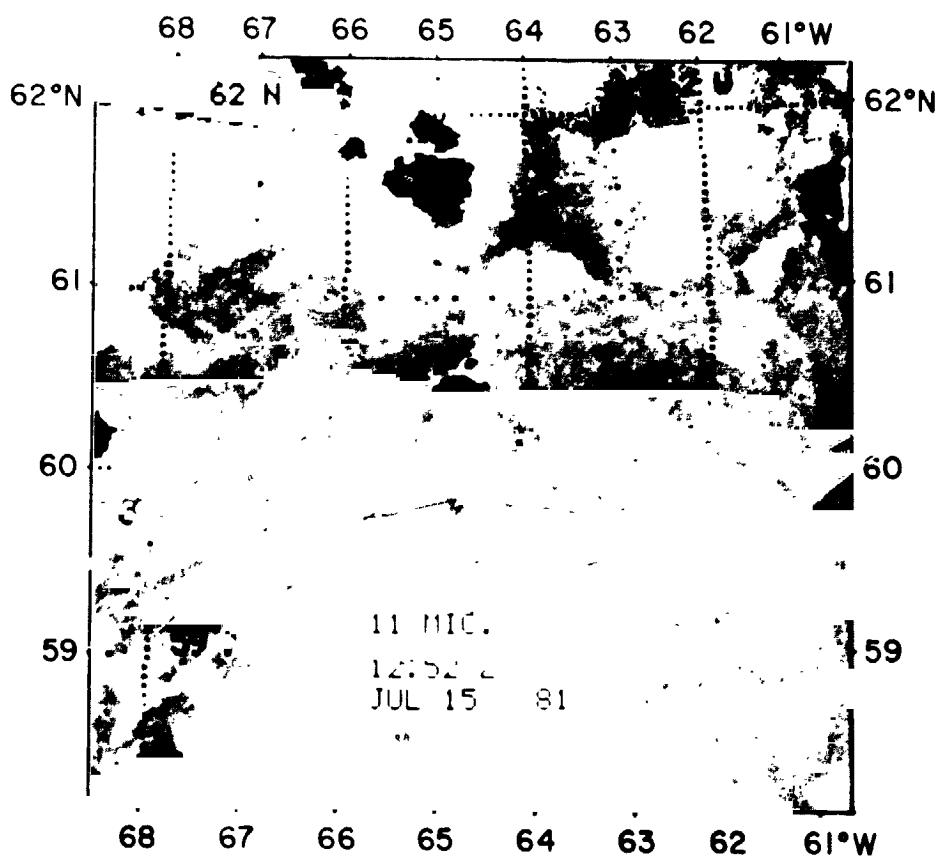
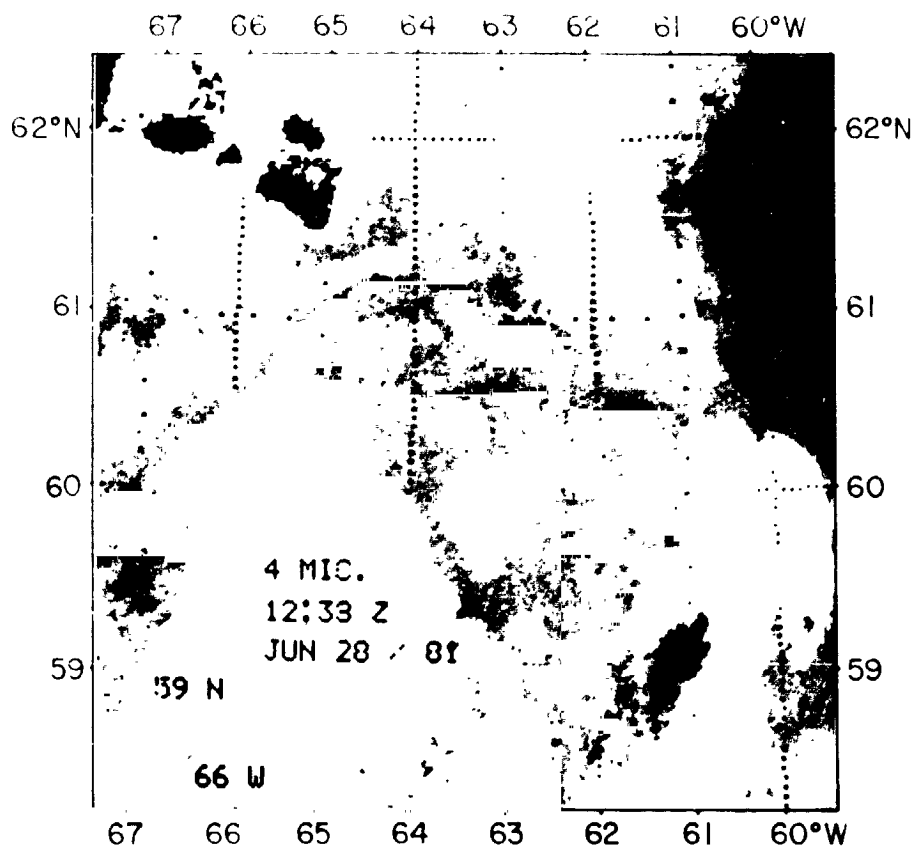
ORIGINAL PAGE 19
OF POOR QUALITY

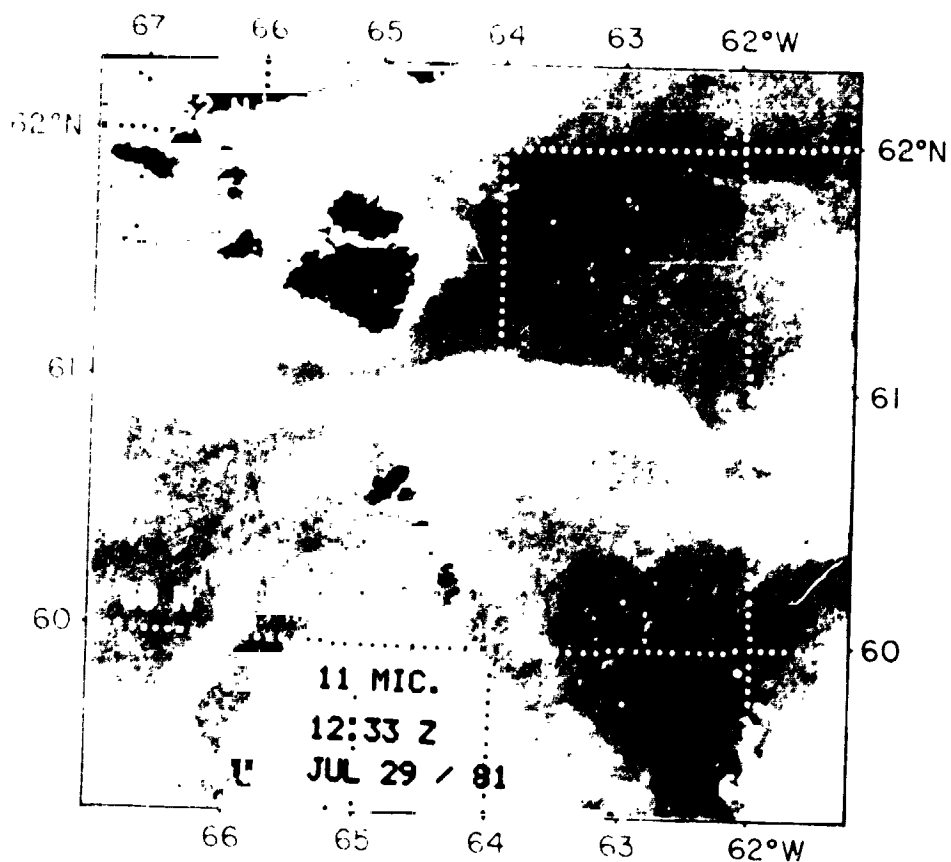


ORIGINAL PAGE 18
OF POOR QUALITY

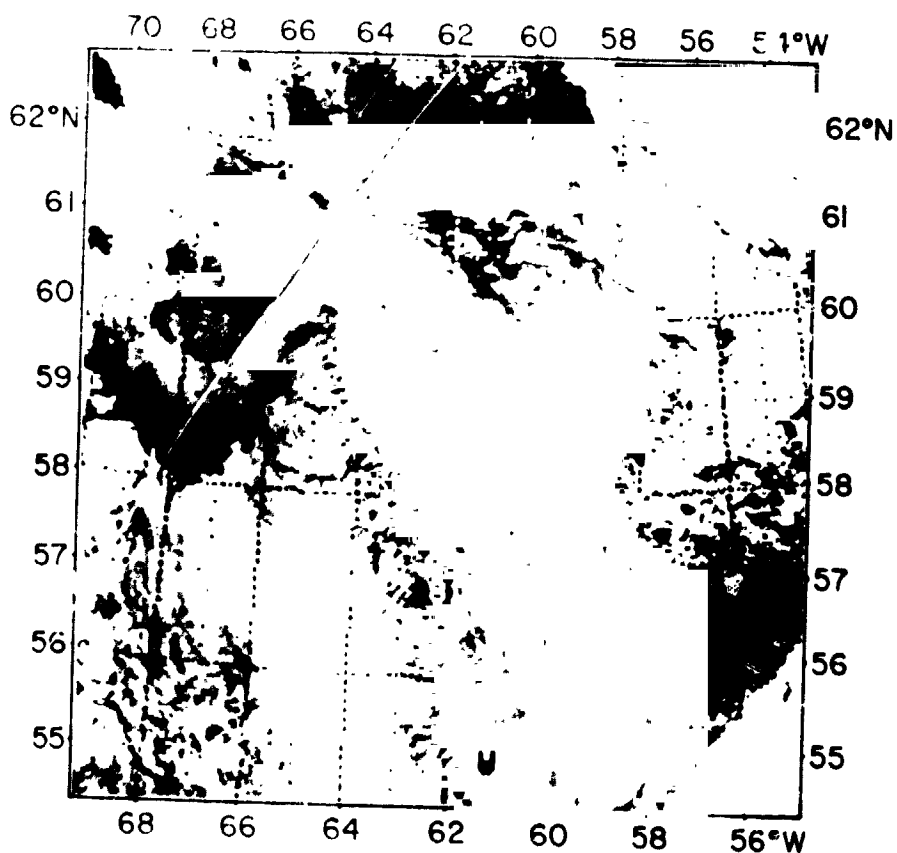


ORIGINAL PAGE IS
OF POOR QUALITY

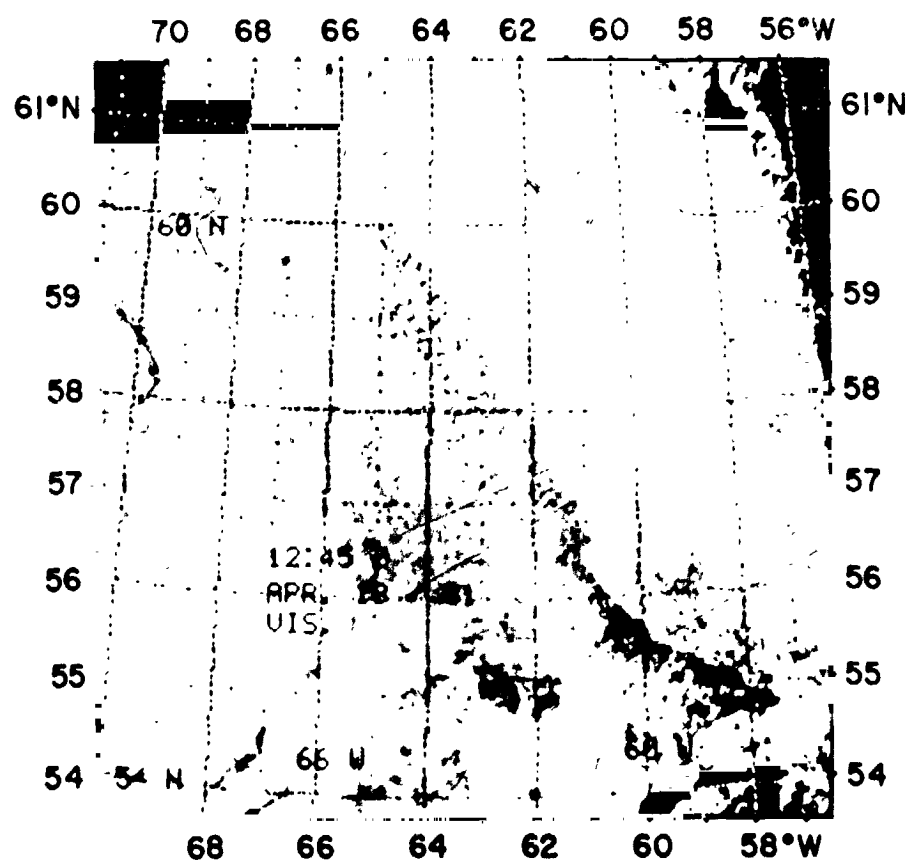




ORIGINAL PAGE IS
OF POOR QUALITY



ORIGINAL PAGE 19
OF POOR QUALITY



ORIGINAL PAGE 19
OF POOR QUALITY

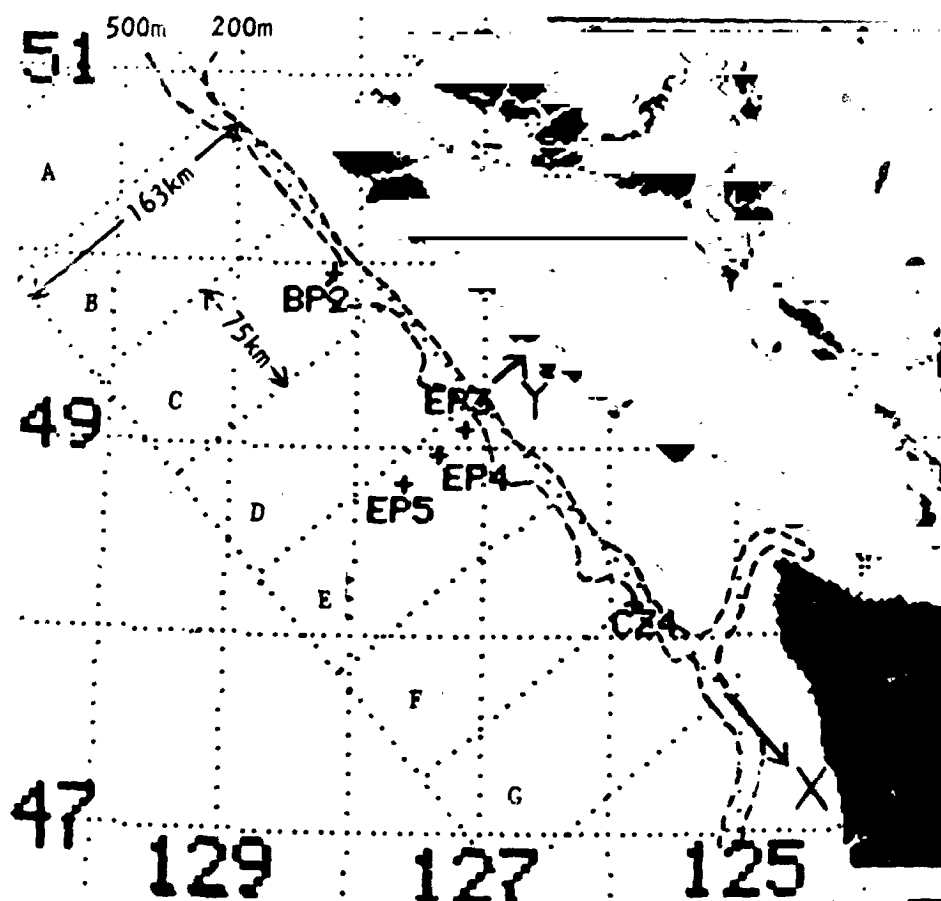
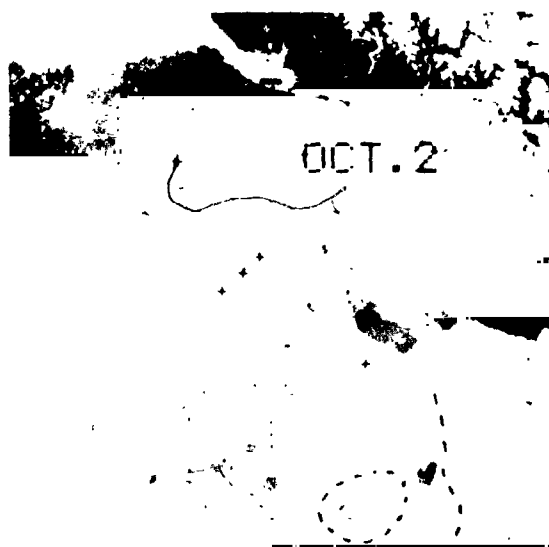
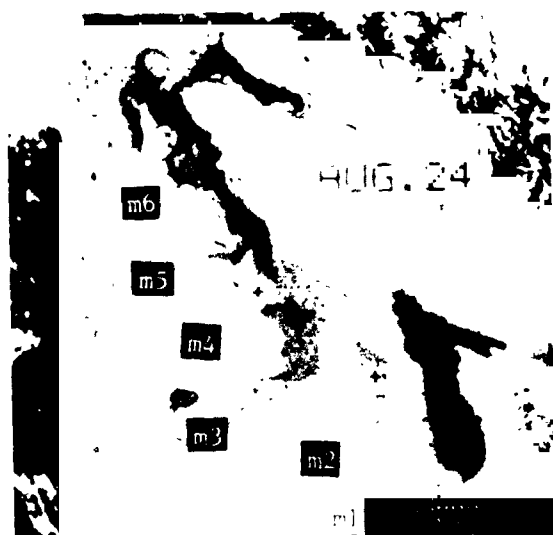
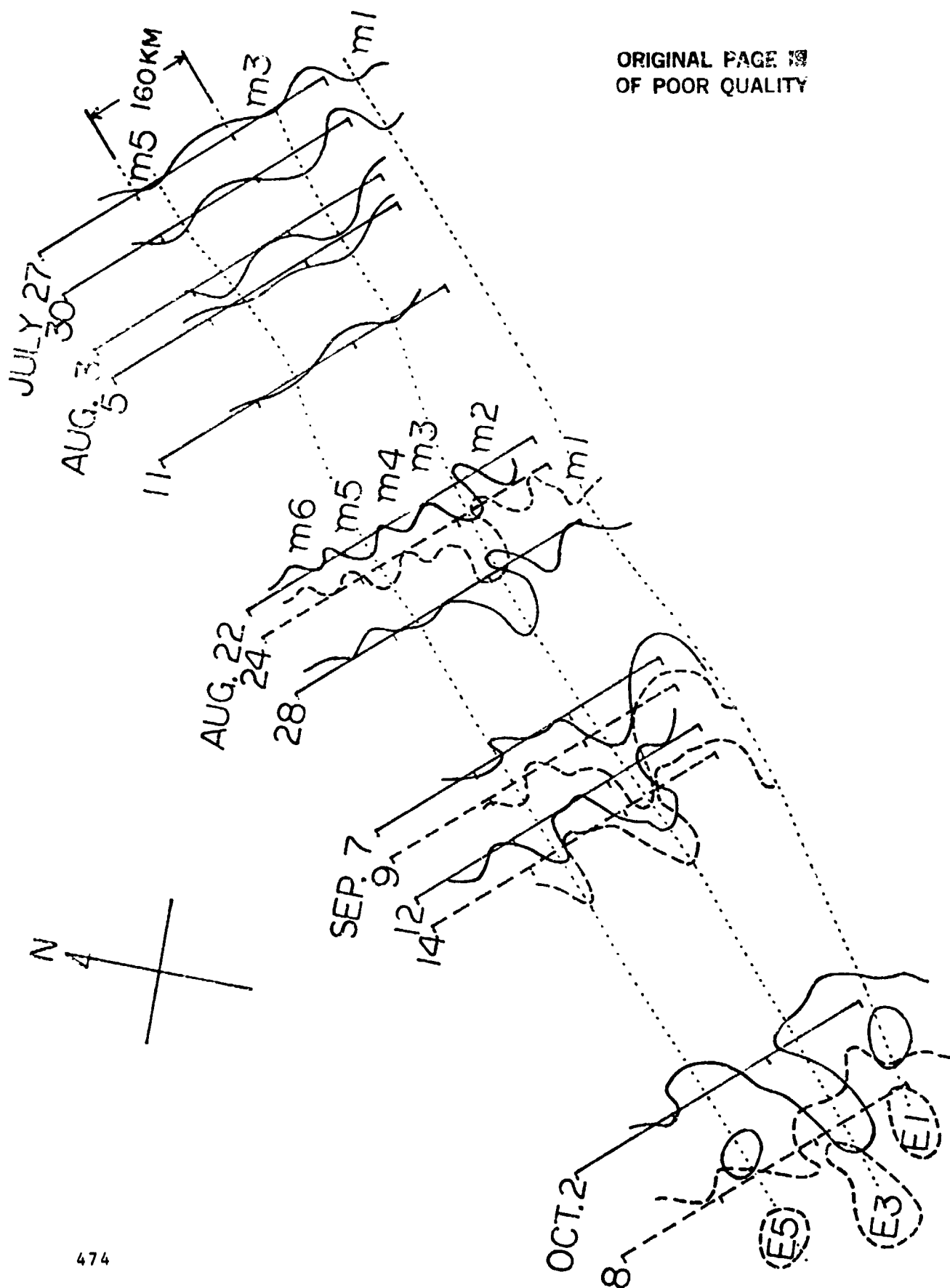


Figure 1 The area observed by satellite infrared images. Nearly vertical and horizontal dotted lines denote longitude and latitude, respectively. Five current meter mooring stations (BP2, EP3, EP4, EP5, CZ4) are indicated by +, 200 m and 500 m-isobaths by broken lines, and the domain of numerical calculations by a long rectangle divided into seven smaller rectangles.

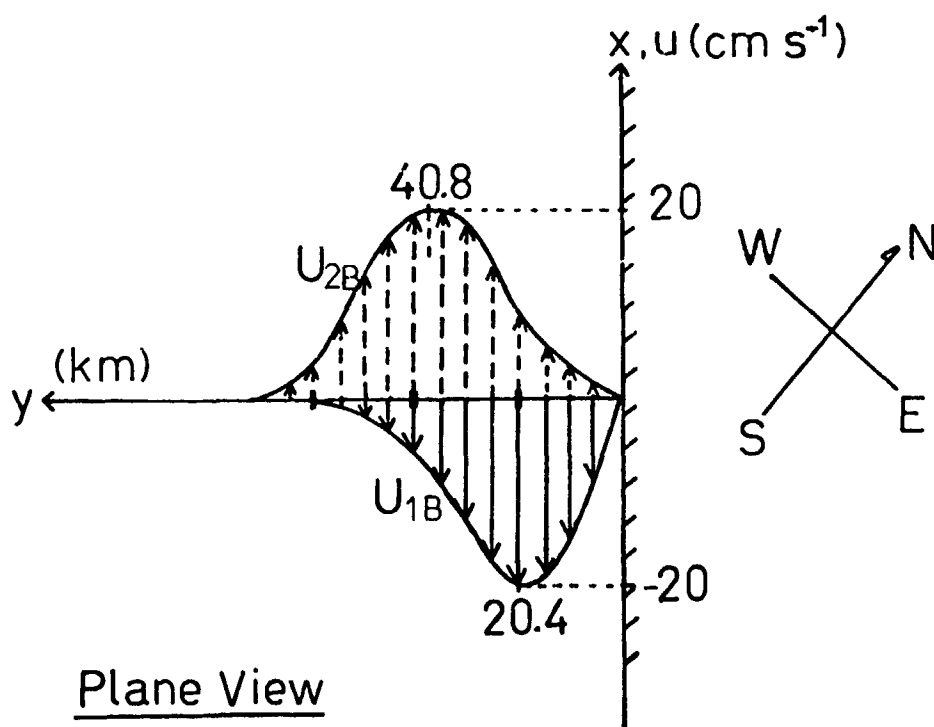
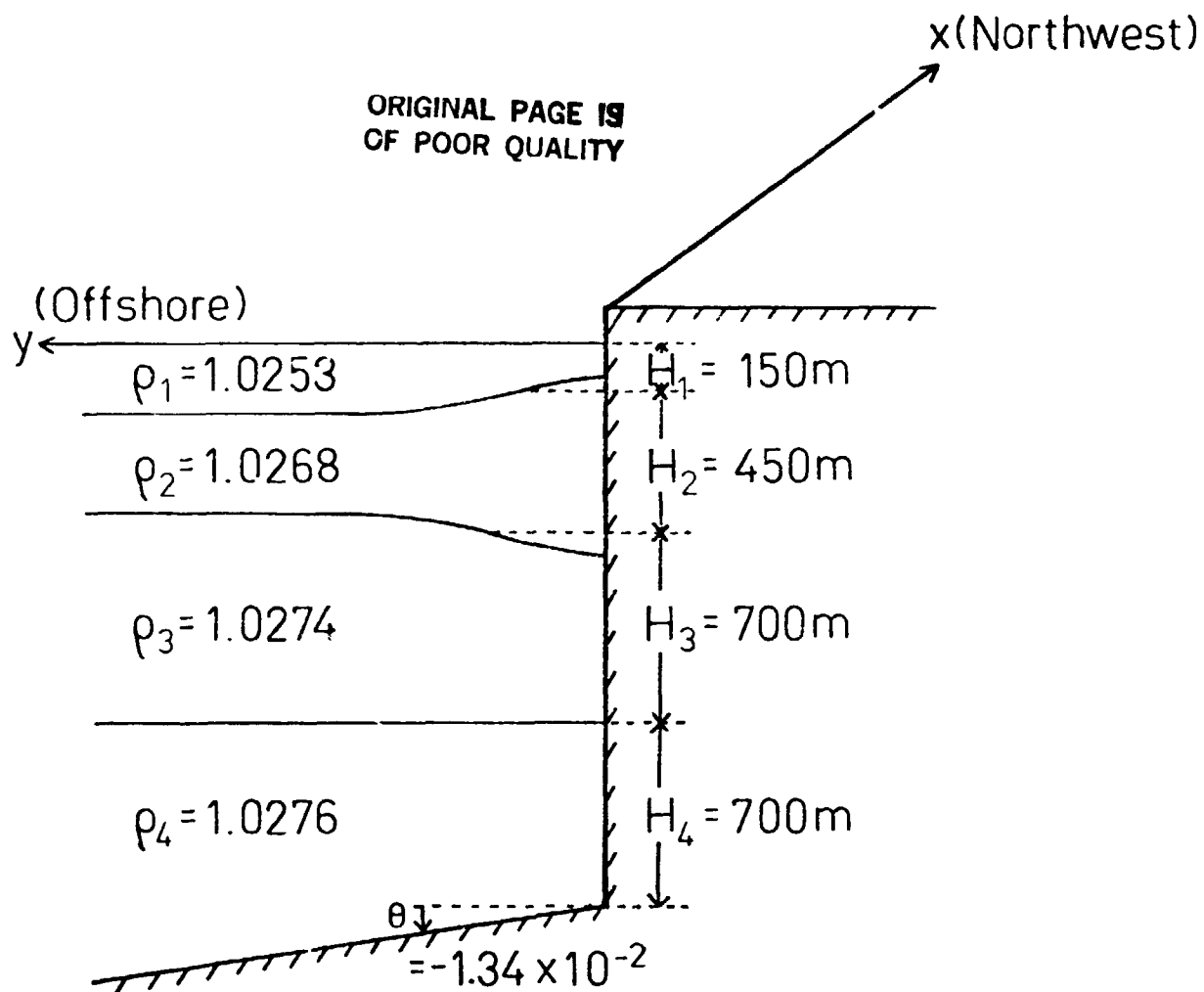
ORIGINAL PAGE 19
OF POOR QUALITY



ORIGINAL PAGE 19
OF POOR QUALITY

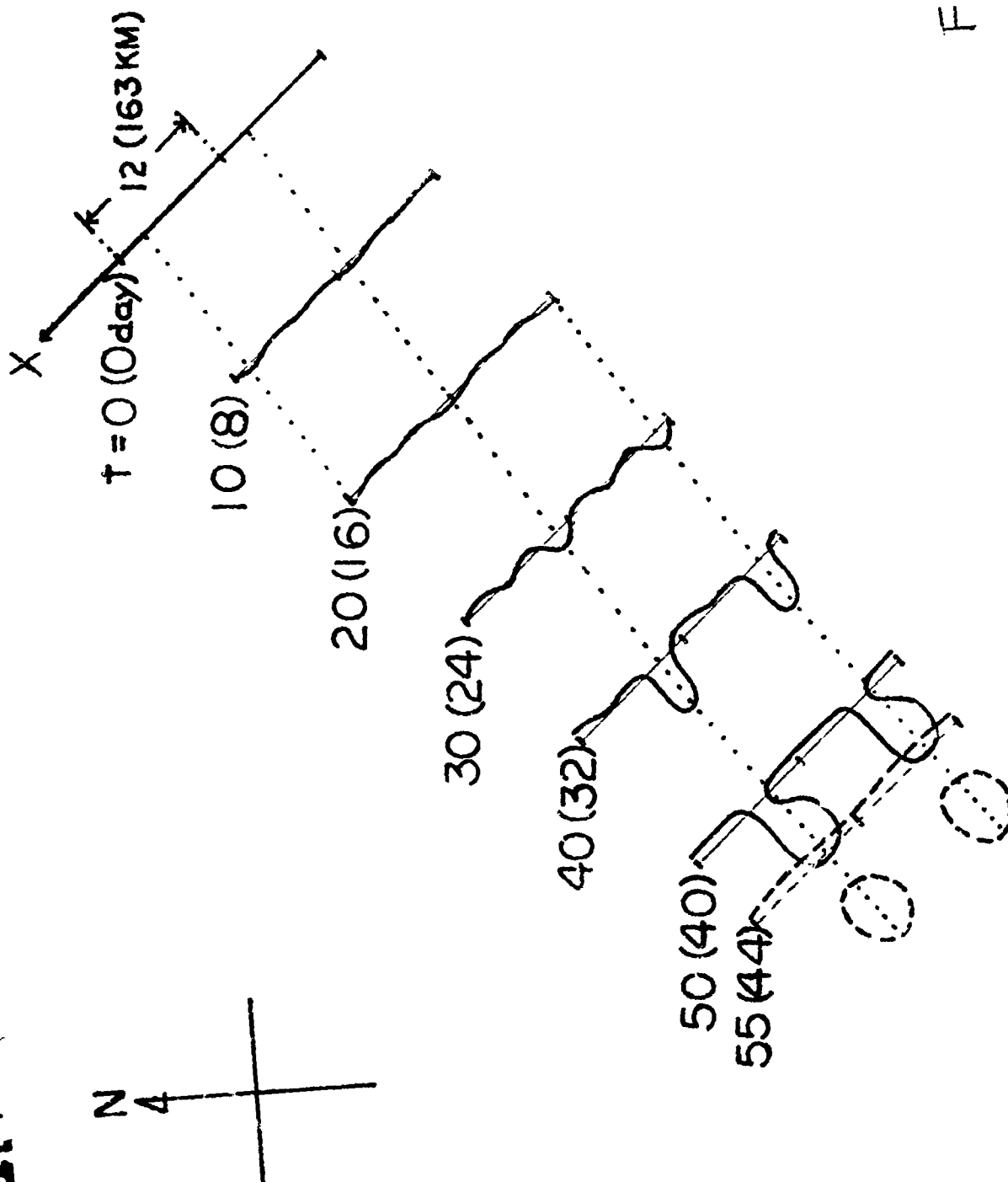


ORIGINAL PAGE IS
OF POOR QUALITY

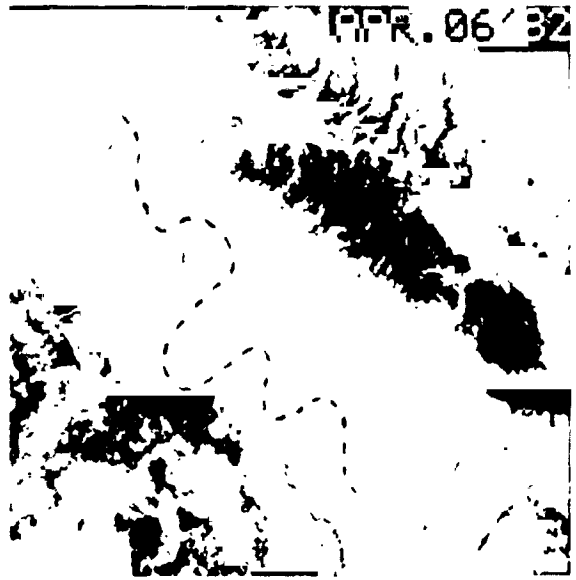


ORIGINAL PAGE IS
OF POOR QUALITY

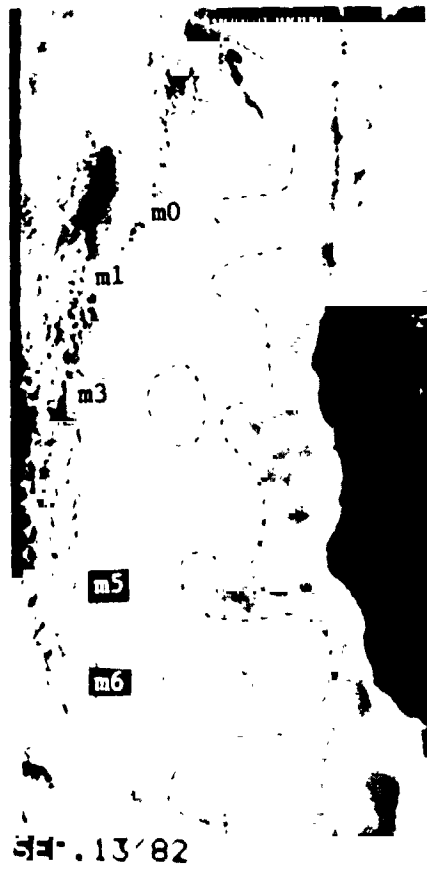
Fig. 17







ORIGINAL PAGE IS
OF POOR QUALITY



LN84 27306 4

THE DEPICTION OF THE ALBORAN SEA GYRE DURING DONDE VA?
USING REMOTE SENSING AND CONVENTIONAL DATA

Paul E. La Violette
Naval Ocean Research and Development Activity
NSTL, MS 39529 U.S.A.

ABSTRACT

Experienced oceanographic investigators have come to realize that remote sensing techniques are most successful when applied as part of programs of integrated measurements aimed at solving specific oceanographic problems. A good example of such integration occurred during the multi-platform international experiment, "Donde Va?" in the Alboran Sea during the period June through October, 1982. The objective of "Donde Va?" was to derive the interrelationship of the Atlantic waters entering the Mediterranean Sea and the Alboran Sea Gyre. The experimental plan conceived solely with this objective in mind consisted of a variety of remote sensing and conventional platforms: three ships, three aircraft, five current moorings, two satellites and a specialized beach radar (CODAR). Integrated analyses of these multiple-data sets are still being conducted. However, the initial results show detailed structure of the incoming Atlantic jet and Alboran Sea Gyre that would not have been possible by conventional means.

1. INTRODUCTION

In the past (and to a certain extent, at this writing) most ocean studies utilizing satellite imagery have been descriptive in nature. Normally, they implied that certain ocean events were taking place, based on a general knowledge of the regional oceanography, past experience with the phenomenon under discussion, and information on the meteorological conditions occurring at the time. Such descriptive studies have and will continue to be useful. There is no question that the broad synoptic views provided by satellite imagery provide valuable insights to the physical and biological events taking place in the ocean. Many of the studies now being conducted on fronts and eddies have evolved to their present state due to information provided by satellite imagery.

Technological advances in interactive computer systems, advanced satellite sensors with improved calibrations, and the development of more accurate sensor algorithms have allowed satellite data to shift from a purely descriptive tool of ocean research to one that is equally quantitative. As a result, experienced oceanographers have come to realize that satellite data are most useful when applied as an integral part of an ocean data set whose collection is aimed at solving specific oceanographic problems.

To be successful, such an approach requires that the investigator reexamine some of the basic concepts of his study field. The statement that the physical, chemical, and biological processes taking place in the ocean are normally interrelated is not a platitude. One must force oneself to remember that, although these relationships are not linear, a thorough understanding of the various processes taking place in any one discipline, quite often requires a broad understanding of the processes occurring in others. For example, a synoptic quantitative view of the spatial and temporal events taking place in and about the region of a front would be needed for a proper study of some particular single aspect of the front. To a limited degree, satellite (and aircraft) remote sensing techniques can now provide these synoptic and quantitative views.

The limitations are imposed by the fact that remote sensors have no direct connection with the ocean. Data collection using these techniques is, thus, limited to the utilization of the electromagnetic radiation of the ocean. However, the data blended within a strong integrated data collection program (i.e., remote sensed and in situ data) can be descriptively and quantitatively used to bring about a broad understanding of ocean processes.

A good example of such integration occurred during the multi-platform, international experiment, "Donde Va?" in the Alboran Sea during the period June through October, 1982. The objective of "Donde Va?" was to derive the interrelationship of the Atlantic waters entering the Mediterranean Sea and the Alboran Sea Gyre. The experimental plan, conceived solely with this objective in mind, consisted of a variety of remote sensing and conventional platforms: three ships, three aircraft, five current moorings, two satellites, and a specialized beach radar (CODAR) (La Violette, et al., 1982; Kinder, 1983). Integrated analyses of these multiple-data sets are still being conducted. However, the initial results show detailed structure of the inflowing Atlantic water and Alboran Sea Gyre that would not have been possible by conventional means. Portions of the results of this experiment are presented here to illustrate the philosophic remarks made above.

2. THE ALBORAN SEA

The Alboran Sea is the most western of the series of semi-enclosed, evaporative basins which form the Mediterranean Sea. As such, the Alboran Sea forms the first junction between the warm, highly saline waters of the Mediterranean and the colder, less-saline waters of the Atlantic. The circulation and physical properties of the waters in the Alboran Sea reflect this juncture. Atlantic water flows into the basin from the west through the narrow (20 km) and shallow (300 m) Strait of Gibraltar to form a 200 m surface layer (Lanoix, 1974). Mediterranean water (13.1°C and 38.4‰) entering the Alboran Sea through its broader eastern end, flows westward below the incoming Atlantic water continuing out of the Mediterranean through the Strait of Gibraltar. Mixing between the Atlantic and Mediterranean waters is continuously taking place in the Alboran Sea, and the vertical and horizontal variations of temperature and salinity that are found in the upper 300 meters are a result of this mixing.

The narrowness of the Strait of Gibraltar, the angle of the strait with respect to the Alboran Sea, and the effect of the earth's rotation control the mean positions of the two water masses in the sea (Preller and Hurlburt, 1982). Imposed on these mean conditions are the long-period changes created by year-to-year and seasonal variations in the rate of evaporation within the Mediterranean and the short-term changes caused by the tides and meteorological events (Frassetto, 1960; Peluchon and Donguy, 1962; and Crepon, 1965).

These physical controls force the Atlantic water to enter the Alboran Sea as a band less than 30 km wide and at a speed of greater than 100 cm/sec (Lacombe, 1961; Peluchon and Donguy, 1962; Lanoix, 1974; Cheney 1977; Cheney, 1978; Wannamaker, 1979; and La Violette, 1983). Once in the sea, the band of Atlantic inflow tends to bend southward to form a clockwise circulation system called the Alboran Sea Gyre which is a permanent feature occupying most of the basin west of Alboran Island. When the water of the gyre reaches the African coast west of Cape Tres Forcas, (normally around 3°30'W) it splits into two branches--one flows west along the coast toward the Strait of Gibraltar, and the other into the sea's eastern basin to form a series of less intense, smaller gyres that hug the African coast. A classic depiction of the gyre is shown by Lanoix (1974) who used ship data collected in July and August 1962 to form a chart of dynamic topography (Figure 1).

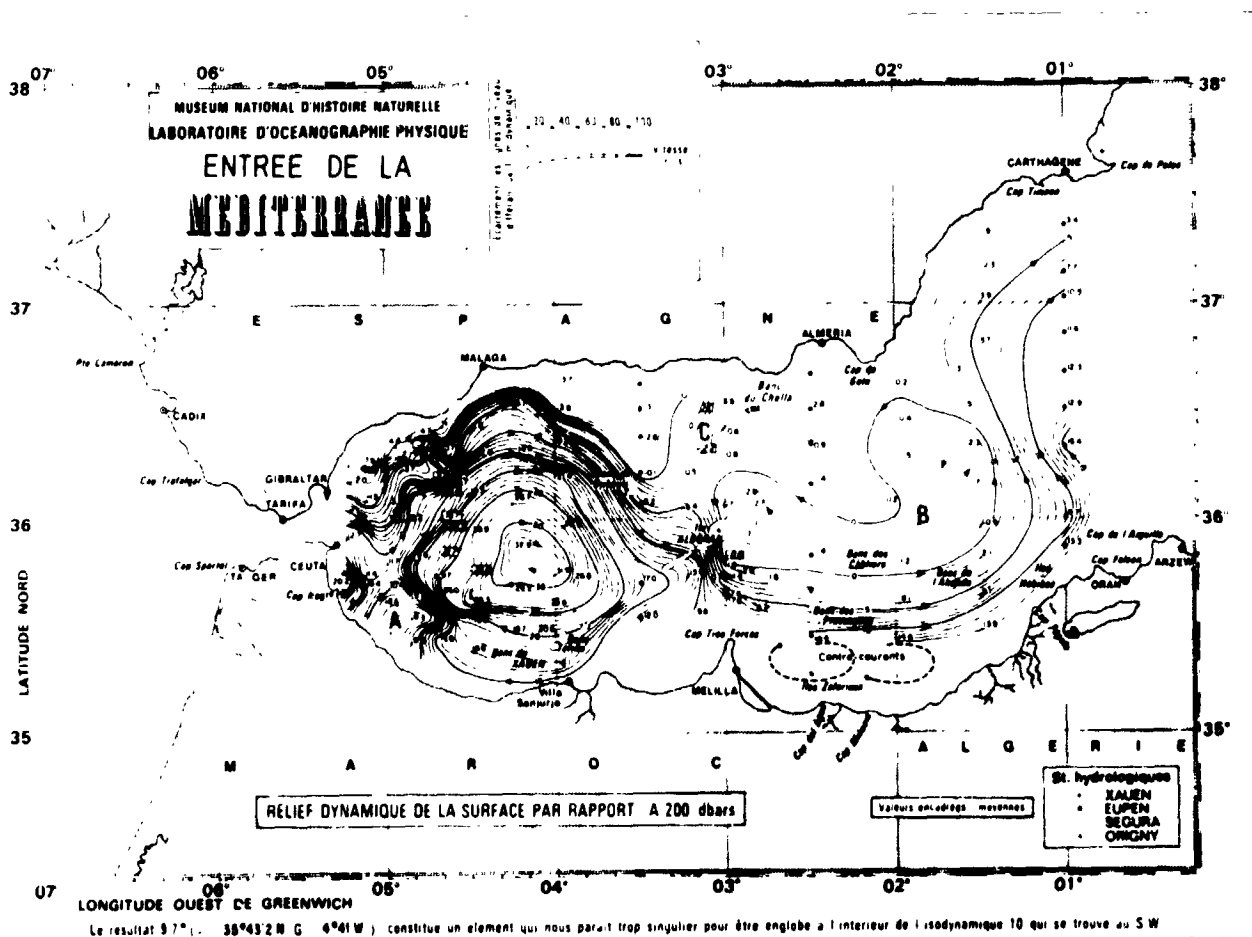


Figure 1. Dynamic topography for the surface based on 200 dbars for the period July and August 1962 (Lanoix, 1974).

(+)

For the purposes of this paper, it must be understood that the problem with studying the currents that constitute the Alboran Sea Gyre is the difficulty in quantitatively measuring the spatial changes that occur in time. An examination of satellite imagery shows that the surface thermal gradients associated with the Atlantic inflow have large spatial variations that occur over a few days. Although a number of investigators (Cheney, 1978; Cheney and Doblar, 1982; Wannamaker, 1979; Gallagher, et al., 1981a; Gallagher, et al., 1981b; Philippe and Harang, 1982) have used satellite imagery in their studies of the Alboran Sea, very little work has been done to quantitatively associate the surface radiation temperatures shown in the thermal imagery with either the subsurface temperatures or the regional flow.

If the large day-to-day horizontal temperature changes shown in the satellite infrared (IR) imagery reflect current variations, then compositing current-related measurements made over longer periods such as weeks, can mask critical movements in the current. For similar reasons, positioning long-period current moorings across the historical location of the axis of the Atlantic inflow can result in a deceptive data set. The thermal gradient changes shown by the satellite IR data indicate that the axis of the Atlantic inflow varies considerably from the historical mean. Thus, without simultaneous horizontal data to aid in the analyses, interpretation of the current mooring data by themselves could lead to erroneous conclusions. Similar remarks may be made concerning analyses of vertical sections of temperature or salinity that do not include coincident horizontal data.

In effect, to fully understand the conditions which create the Alboran Sea Gyre, data collections must be made that include horizontal, as well as vertical, data sets. With this methodology as a basis, the Donde Va? experiment was conducted in 1982, with the methodology of the data collection placing particular emphasis on measuring the Atlantic inflow.

3. THE SATELLITE AND IN SITU DATA

3.1 Satellite Data Registration:

Accurately locating the geographic position of dynamic ocean features seen in satellite imagery is a major problem. Good earth referencing is important, especially if satellite data are to be correlated with other satellite, ship, or aircraft data.

TIROS-N and post-TIROS-N satellite data (NOAA 6, 7 and 8) distributed in computer compatible tapes (CCT'S) by such satellite data distribution centers as NOAA/EDIS (U.S.) and CMS (France) have incorporated in their data geographic positions. Imagery constructed from these data have been shown to have standard deviations of 1.7 km about mean errors of 3.7 km (Clark and La Violette, 1980). This

accuracy allows the registration process to be taken one step further: i.e., to allow common map projections to be made, such as mercator or equal area projections. The method often used to warp NOAA type data to various standard map projections utilizes two-dimensional, third-order polynomials derived from the latitude/longitude data on the CCT. In the Mediterranean, with its easily identifiable landmarks and comparatively short fetches, these registrations can be improved upon and made extremely accurate. Figure 2 showing the Alboran Gyre is a good example. The results of such warping can be done with sufficient accuracy to produce time-lapse sequences (movie loops) of oceanographic features with no noticeable misregistration jitter.

3.2 Atmospheric Correction of Satellite Data:

In addition to the obvious interference of clouds, the more subtle degradation of infrared and visible satellite imagery by absorption and radiation of the atmosphere moisture and aerosols plays a large role in limiting the oceanographic use of imagery in these spectral ranges. These atmospheric constituents must be compensated for in order to quantitatively compare one day's images to another or to in situ data. This problem has several possible solutions.

To arrive at the absolute temperatures of the ocean, infrared imagery may be corrected by several methods. The one showing the most promise is the multichannel single-satellite approach (McClain, et al., 1982). The principle behind the multichannel correction is illustrated in Figure 3. The three IR channels of the Advanced Very High Resolution Radiometer (AVHRR) aboard the NOAA-7 satellites used in this study, cover spectral ranges respectively of 3.55-3.93 microns, 10.5-11.5 microns, 11.5-12.5 microns, referred to as the 3.7 micron, 11 micron, and 12 micron channels, fall within "atmospheric windows." These spectral bands thus, have relatively high transmittances with regard to middle- and far-infrared spectral range energy emitted by the ocean surface. The most significant atmospheric absorption constituents in these regions are water vapor and aerosols. However, the amount of absorption varies for each spectral region: the 3.7 micron channel has a transmittance of approximately 90%, the 11 micron channel has a transmittance of approximately 75%, and the 12 micron channel transmittance is approximately 80%. These variations in infrared transmittance for the same ocean scene allows an atmospheric moisture correction to be made that will result in absolute ocean temperatures. An empirical algorithm can be derived by subtracting the effects of one channel from another with the remainder being a factor of the amount of moisture present in the atmosphere.

Although limited to night use, one of the preferred channels to use (because of its high transmittance rate) is the 3.7 micron channel; however, high noise levels in this channel in the NOAA-7 and NOAA-8 satellites have, until very recently, precluded any real use of multichannel algorithms.



Figure 2. Satellite (a,b) and aircraft (c) sea surface temperatures for the Alboran Sea for 6 October 1982. To produce the thermal image the satellite data was registered to a mercator projection and then atmospherically corrected using an algorithm developed by McClain, et al., 1982. The correction leaves a systematic negative bias to the data of approximately 1°C. In this instance, a study of 76 aircraft XBTs dropped within three hours of the satellite overpass showed a bias of exactly 1°C with a standard deviation of 0.6°C. The isolines in (b) are computer smoothed outlines of the equivalent temperature values of the atmospherically corrected thermal image (La Violette, 1983).

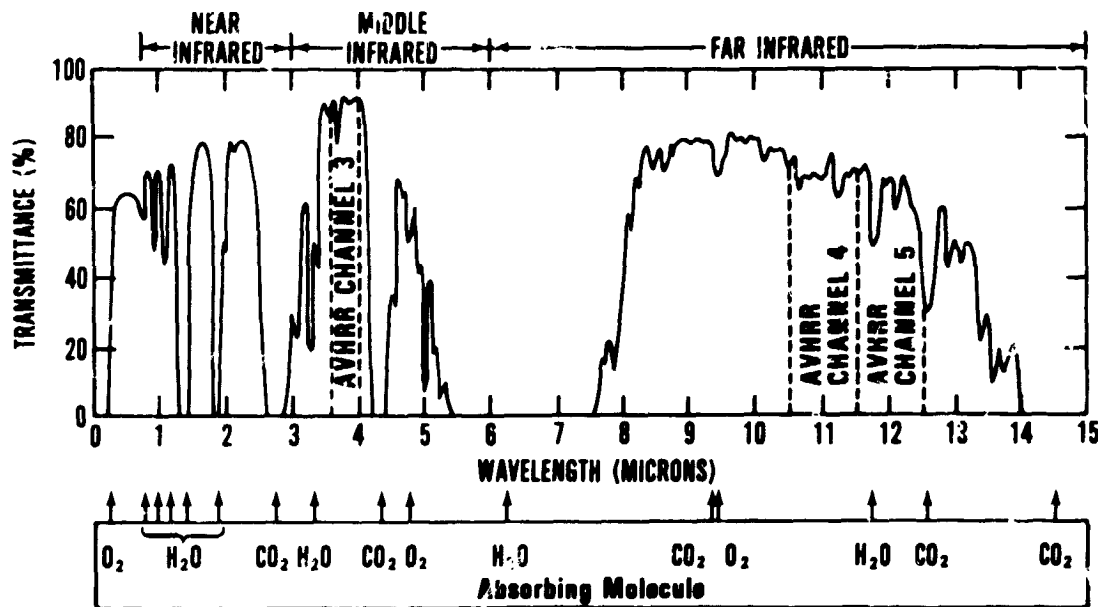


Figure 3. The wavelength of the three channels of the NOAA AVHRR as a function of transmittance for an atmospheric path containing 1.7 cm of precipitable water.

3.3 The Alboran Sea Satellite Data:

One of the primary satellite sensors used during Donde Va? is the AVHRR of NOAA-7. The 11 and 12 micron channels of this radiometer are the principal data sources. The NOAA satellite and the AVHRR are described by Schwalb (1978) and Hussy (1979).

During the period November 1981 through October 1982, NOAA-7 data of the Alboran Sea were collected and examined at the Centre de Meteorologie Spatiale (CMS) satellite data receiving station at Lanion, France. The data were used in the field to help operationally control the survey and retained for post-survey analyses. From these, 24 AVHRR tapes were selected for the period 6 through 20 October 1982 that were sufficiently cloud-free to use in the present analysis. These tapes were calibrated, atmospherically corrected and geometrically registered (to a mercator projection) using the Naval Ocean Research and Development Activity (NORDA) interactive computer system. The atmospheric-corrections were made using the split-window technique developed by McClain, et al., (1982).

In addition to the NOAA-7 AVHRR data, NIMBUS-7 Coastal Zone Color Scanner (CZCS) data are used. A description of the NIMBUS satellite and the CZCS can be found in Hovis, et al., 1980.

3.4 The Surface Data:

Most of the nonsatellite data used in this study were obtained from a United States Naval Oceanographic research aircraft. These data include both oceanographic and meteorological information. The aircraft made four mapping flights that collected continuous precision radiometric thermometer (PRT-5), airborne expendable bathythermograph (AXBT), and some buoy (drift) data over the Alboran Sea west of Alboran Island (since the incoming Atlantic water is restricted to the upper 200 m, these temperature data include all of the inflowing water). A full description of this aircraft's instrumentation during Donde Va?, as well as extensive analysis of the collected data can be found in La Violette (1983) and La Violette and Kerling (1983).

The remaining ocean data were collected by Donde Va? research vessels using conventional expendable bathythermographs (XBTs) and Conductivity/Temperature/Depth (CTD) profilers. These vessels also provided meteorological information for selected days and positions. Additional weather data were obtained from Spanish coastal meteorological stations, a special Spanish weather station established on Alboran Island, and from the Royal Air Force Meteorological Office, Gibraltar.

4. ANALYSIS AND DISCUSSION

The twice-daily passes of the NOAA-7 over the study area permitted almost continuous monitoring of the surface thermal changes that occurred in the Alboran Sea Gyre during the October period when intensive air and sea measurements were being conducted as part of Donde Va?. The NOAA-7 infrared imagery show that a number of submesoscale cold-water features were being advected about the gyre during that period. Although the present study is centered about the October 1982 movement of these cold-water features, the features are also visible in almost all of the satellite infrared imagery collected during the one year Donde Va? study period (November 1981 through October 1982). An examination on satellite imagery of other years also show these mesoscale cold-water features are normally present as part of the Alboran Sea Gyre. In fact, two features similar in appearance and location to the cold water features can be seen in the dynamic topography presentation by Lanoix (1974) in Figure 1.

Figure 4 shows two sequences of five images each spaced 12 hours apart starting on the afternoon of 6 October through the afternoon of 8 October, 1982 for one sequence and for the period from early morning 11 October through the afternoon of 13 October 1982 for the other sequence (the image from the morning pass for 13 October has been omitted from the second sequence because of clouds). The arrows, dots and

Figure 4. Registered and atmospherically corrected NOAA-7 infrared imagery of the Alboran Sea for the periods 6 through 8 October and 1 through 13 October 1982 (La Violette, 1984).

ORIGINAL PAGE IS
OF POOR QUALITY

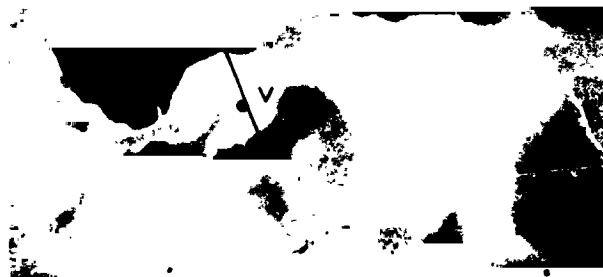
1432 GMT 6 OCTOBER



0256 GMT 7 OCTOBER



1422 GMT 7 OCTOBER



0244 GMT 8 OCTOBER

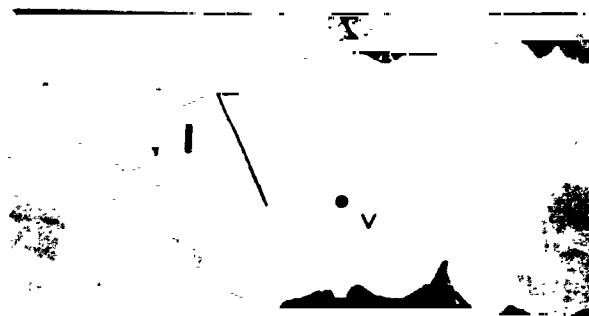


1408 GMT 8 OCTOBER



ORIGINAL PAGE 19
OF POOR QUALITY

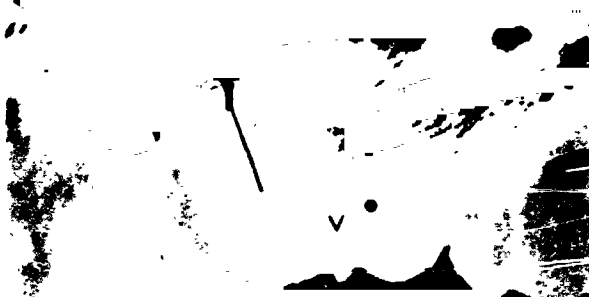
0349 GMT 11 OCTOBER 1982



1513 GMT 11 OCTOBER 1982



0337 GMT 12 OCTOBER 1982



1501 GMT 12 OCTOBER 1982



1449 GMT 13 OCTOBER 1982



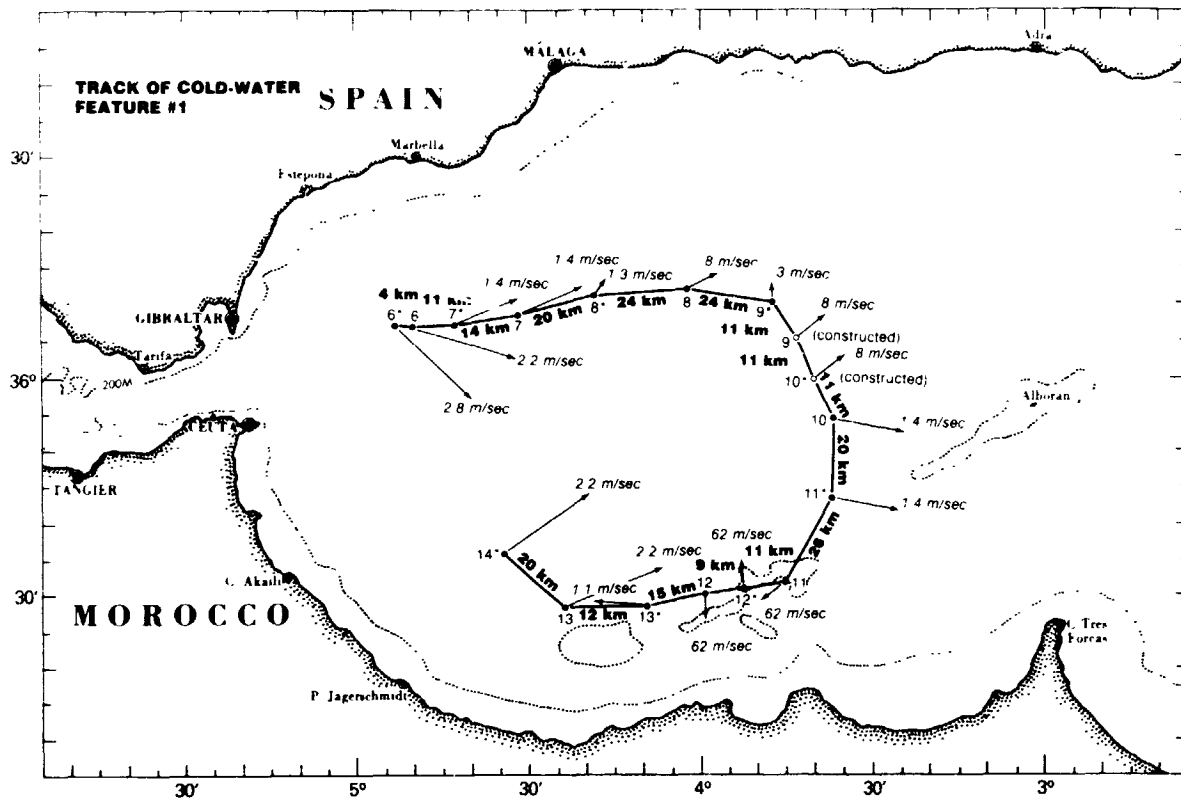


Figure 5. A plot of the complete track of the feature marked with a "bar" in Figure 4. The arrows represent the direction and speed of the wind at or near the time of the plotted position of the cold water feature (La Violette, 1984).

bars in each of the imagery trace the movement of two cold-water features from their apparent origin east of Gibraltar across the top of the gyre. The five-image sequence covers only portions of the features total movements. In Figure 5, a plot of positions taken from satellite data, shows the complete circuit of feature #6 (the bar in the second sequence) around the gyre until it became hidden by clouds on the afternoon of 14 October.

The vertical sections in Figure 6 constructed from AXBT data along 36°N latitude, shows the structure of three of the cold water features with depth. These sections show that generally the cold water in the area had upwelled from greater than 100 meters. In addition, data from the USNS BARTLETT for 7 October 1982, (CTD station 120--T. Kinder, personal communication) give salinity values of 36.73 ppt in the same area as the feature for 6 October. Comparison of these data with historical data (e.g., Lacombe and Tchernia, 1982) indicates the upwelled water is of Atlantic origin.

Note that in the second five-image sequence of Figure 4, another cold-water feature can be seen to develop on 12 October in the region east of Gibraltar. During the aircraft flights over the front, it was noted that sharp color changes were coincident with the thermal front. This effect suggested a method to derive the

ORIGINAL PAGE 19
OF POOR QUALITY

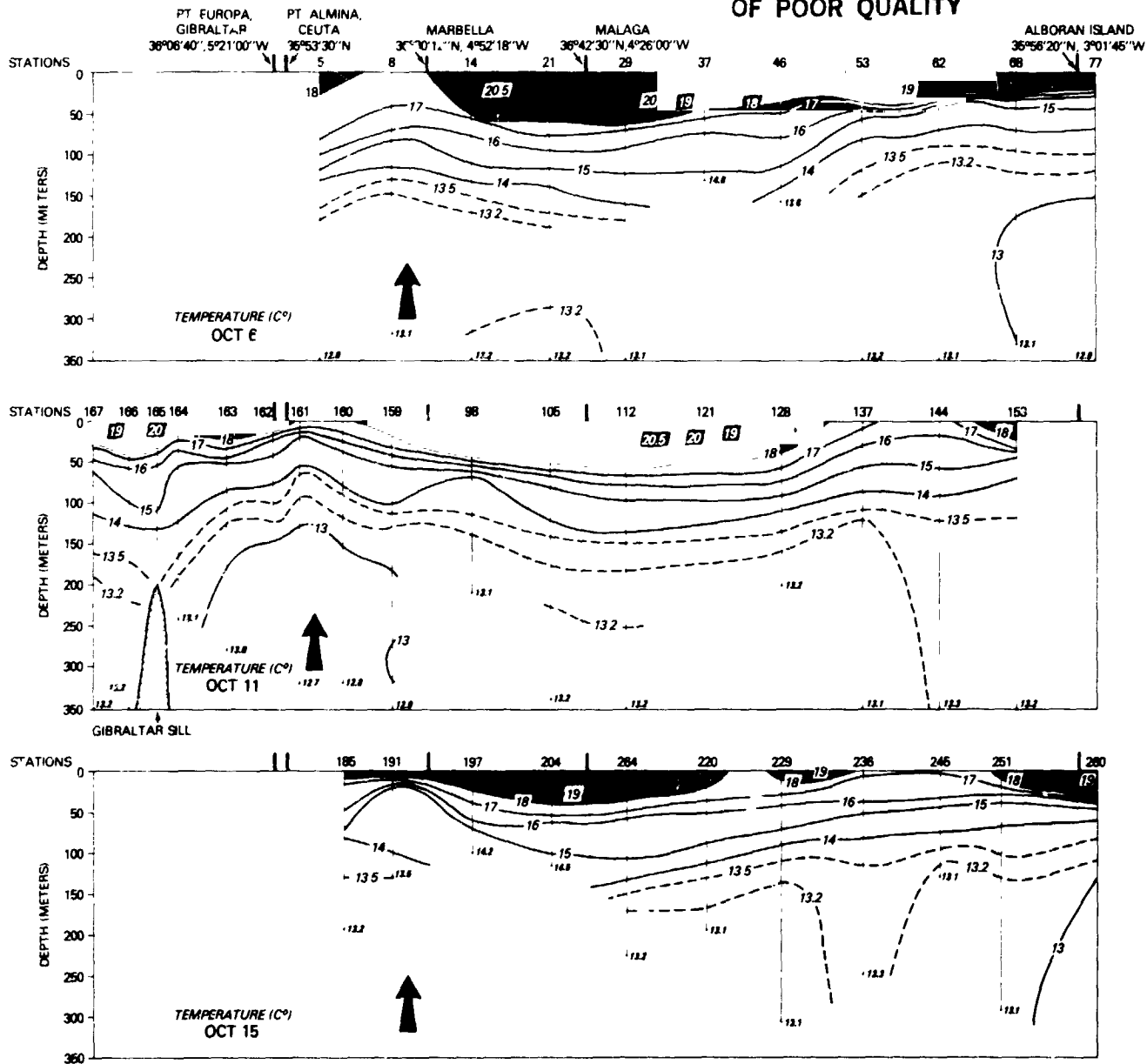


Figure 6. East-west vertical temperature sections taken along the 36° latitude (data based on aircraft XBTs). The arrows refer to cold water features found near the Strait of Gibraltar. The 6 October arrow refers to the "v's" in Figure 4, whereas the arrow on 11 October refers to the "bars" shown in the same figure (La Violette, 1984).

movement of the front for periods less than 12 hours. An enlargement of the IR image for the afternoon of 12 October (1501 hrs) is presented in Figure 7 together with NIMBUS-7 CZCS visible image of the same area for 1155 hrs of the same day. (The CZCS enhancement uses the principal component analysis method described in Holyer and La Violette, 1983. This particular enhancement is designed to show the distribution of chlorophyll). Examination of the NOAA imagery shows that the feature (called here feature #7) moved approximately 17 km in the 11 hours from the time of the morning NOAA IR image to the time of the afternoon NOAA IR image; or at an average speed of approximately 0.4 m/sec. The CZCS image indicates a movement of approximately 9 km

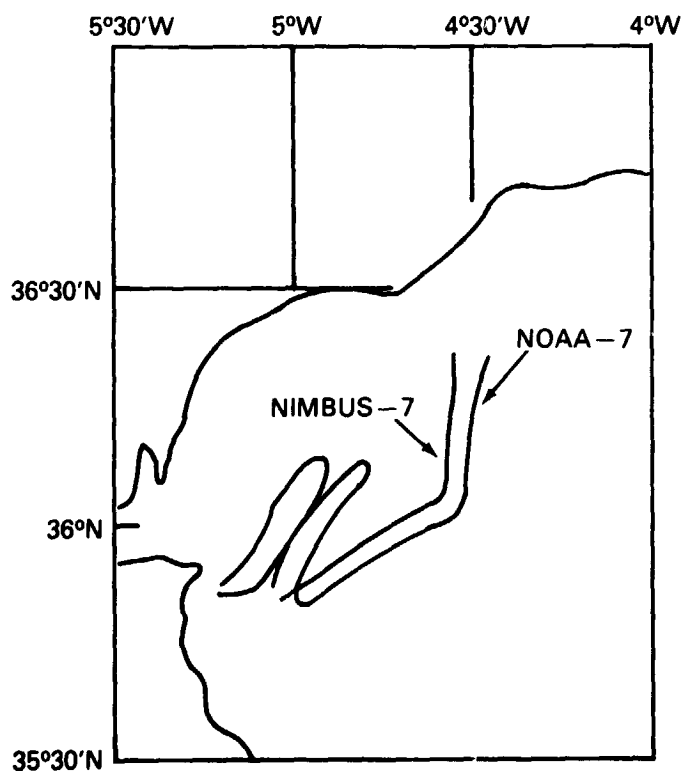
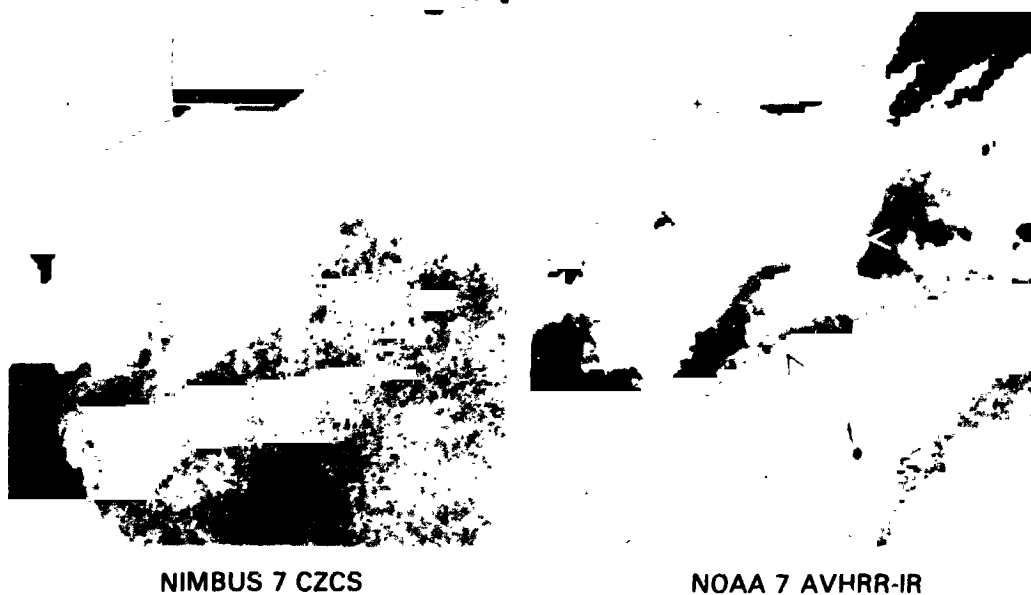


Figure 7. The short term movement of Feature #7 shown by Nimbus CZCS visible and NOAA-7 AVHRR infrared imagery. The movement amounting to approximately 9 km took place between 1155 (Nimbus) and 1501 (NOAA) hours GMT on 12 October 1982 (La Violette, 1984).

in the time between the Nimbus noon pass and NOAA afternoon pass (i.e., if one assumes that the sharpest gradient change in the CZCS image is directly associated with the sharpest thermal gradient in the NOAA imagery.). This equates to a movement of 0.8 m/sec or twice the rate of movement for the 11-hour period between the two NOAA imagery. The figure gives a graphic indication of how much movement can take place in four hours.

Figure 8 shows feature #8 as defined by the satellite and aircraft data. The aircraft PRT and AXBT data analysis shows the spatial continuity of the feature down to 350 m. However the vertical section in Figure 6 indicates the upwelling does not appear to go deeper than 75 m. Because of clouds, this feature was visible in only three of the IR imagery.

In comparing the different cold-water features, it is important to note that they are not equally distinguishable in the thermal imagery. In the fifteen-day period, only nine are distinct enough to be tracked for several days. In addition to thermal clarity, the times the features can be tracked are limited by cloud cover. The two five-image sequences presented here show that the advective movement of the features are easily followed (the author has made a loop-movie for the full fifteen days which shows this advection quite graphically). It is, however, more difficult to assign a particular point on any one feature and then precisely track that point from image-to-image as the feature moves about the gyre. Nevertheless, reasonable measurements of speeds may be made by marking the general leading edge of the feature with indicators such as the arrows in the first of the five-image sequences. Such measurements show that the advective speed of the features varied from day-to-day; ranging from 0.2 to 0.6 m/sec with the average speed being 0.4 m/sec.

In a study of the drift rate of sonobuoys dropped from the Navy aircraft during 9 through 18 October, La Violette (1983) shows that surface currents associated with the incoming Atlantic water flowed at speeds equal to or greater than 1.0 m/sec, and that on the average, the fastest speeds (i.e., speeds of ≥ 1.2 m/sec) were limited to a band less than 16 km wide centered approximately between the 17° and 18°C surface isotherm. Of interest is the fact that the band of fast moving surface water flowed just inside the periphery of the advected cold-water features shown in the satellite imagery. (The arrows in Figure 8 represent the sonobouy drift data analyses.)

Comparing the average drift speed of the sonobuoys (≥ 1.2 m/sec) at the periphery with the average advective speed of the cold-water feature (0.4 m/sec) gives an indication of the differences between the surface currents and the translation speed of the cold features in the area of the Marbella Lines. As the features were advected around the gyre, these differences were reduced. Examination of the sonobuoy-based current data dropped in the neighborhood of Alboran Island on 18 October and the advected speeds derived from the 18 and 19 October imagery reveals that while the sonobuoy drift speeds decreased sharply from the velocities found south of Marbella, the translation speed of the features remained essentially the same.

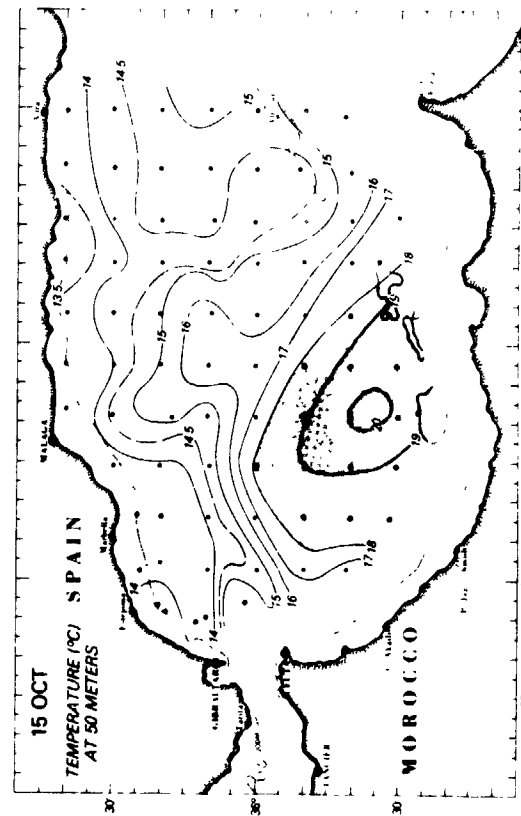
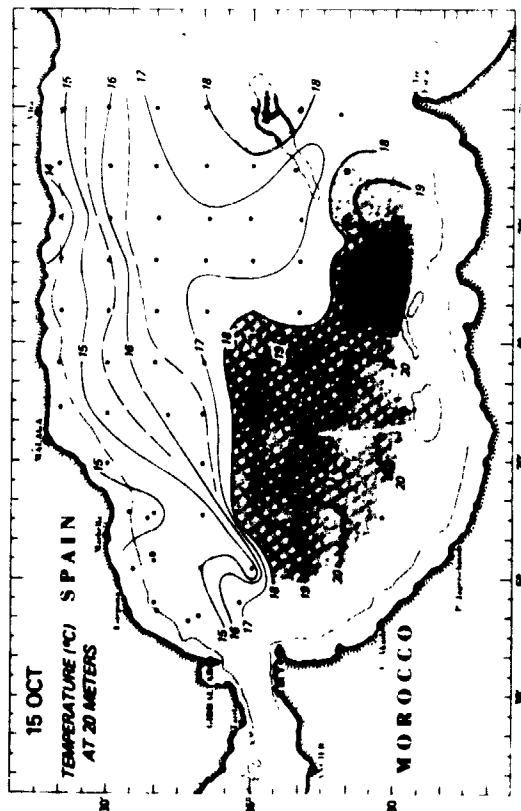
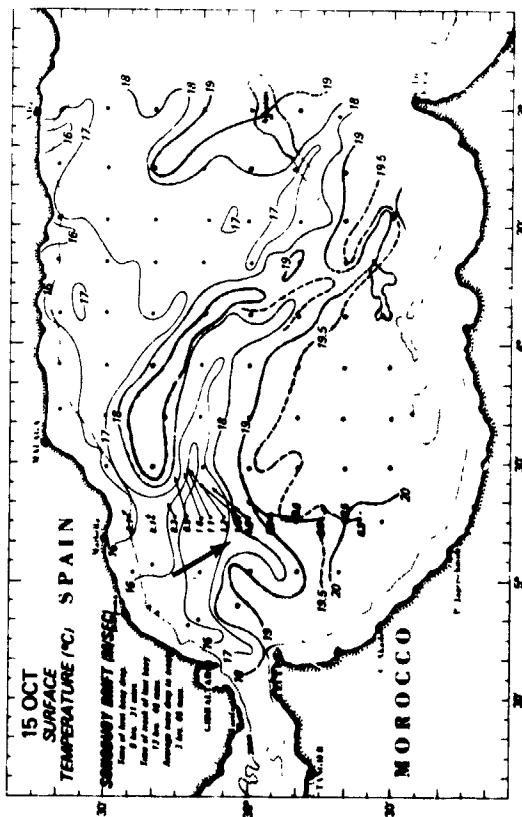


Figure 8. Aircraft data analysis for surface, 20, and 50 m and the morning NOAA-7 infrared imagery for 15 October. The surface aircraft data was derived from a precision radiation temperature sensor whereas the subsurface was derived from more widely spaced data obtained from aircraft expendable bathy thermographs. The arrows represent the initial drop position and drift rate and direction of sonobuoys dropped on 15 October. The large arrow marks the position of the cold water feature seen in both the PRT analysis and the satellite image (La Violette, 1984).

5. CONCLUSIONS

The above discussion and data analyses were liberally extracted from La Violette (1983) and La Violette (1984). It is suggested that the reader refer to these studies for a more extensive analysis. From the brief discussion presented here, it is shown by the satellite data that, rather than being a simple linear flow angled into the Alboran Sea from the Strait of Gibraltar, the incoming Atlantic water and the continuously generated cold-water features east of Gibraltar are linked.

The complexity of the data together with the rapid change in conditions show why any regional current study must be accompanied by horizontal and vertical data. In this study remote sensors aboard satellite and aircraft provided this data, with the aircraft XFT also providing temperature information down to 350 m. In comparison, the satellite and aircraft data show the close relationship of the surface and subsurface waters down to 20 m and greater (Figure 8). Thus, the data indicates that the structural displays of thermal gradients shown by the satellite imagery may be reliably used as indications of conditions in the near-surface layers.

The purpose of this paper is to show that satellite data may be used as a reliable, quantitative input to an integrated ocean data set. Emphasis has been placed on understanding the oceanography of the region and knowing the limitations of the satellite data. Other basic concepts such as computer techniques are required if the data are to be quantitatively used. Certainly, atmospheric corrections provide a reliability of the thermal values presented in the imagery. This, in turn, provides a continuity that can be expanded to thermal data from other sources. Proper registration is also extremely useful in allowing several days of data to be studied as a temporal continuity.

As the study presented has attempted to show, the exploitation of satellite imagery in conjunction with other data sources can provide an imaginative investigator with a powerful analytical tool to study the ocean.

6. REFERENCES

- Cheney, R. E. and R. A. Doblar, 1982. Structure and Variability of the Alboran Sea Frontal System. J. Geophys. Res. v. 87, n. C1, p. 585-594.
- Cheney, R. E., 1978. Recent Observations of the Alboran Sea Frontal System. J. Geophys. Res., v. 83, n. C9, p. 4593-4597.
- Cheney, R. E., 1977. Aerial Observations of Oceanic Fronts in the Western Mediterranean Sea. Technical Note 3700-69-77, U.S. Naval Oceanographic Office, Washington, D.C., July, 23 p.
- Clark, R. and P. E. La Violette, 1980. The Detection of Moving Oceanic Fronts Using Successive TIROS-N Imagery. Geo. Res. Lett., v. 8, n. 3, p. 229-232.

- Crepon, M., 1965. Influence de la pression atmospherique sur le niveau moyen de la Mediterranee occidentale et sur le flux a travers le detroit de Gibraltar. Presentation d'observations, Cah. Oceanogr. v. 17, n. 1, p. 14-32.
- Frassetto, R., 1960. A Preliminary Survey of Thermal Microstructure in the Strait of Gibraltar. Deep Sea Res. v. 7, n. 3, December, p. 152-162.
- Gallagher, J. J., M. Fecher and J. Gorman, 1981a. Project HUELVA - Oceanographic/Acoustic Investigation of the Western Alboran Sea. Naval Underwater Systems Center Technical Report 6023. 106 p.
- Gallagher, J. J., M. Philippe and B. Wannamaker, 1981b. Satellite Monitoring of Ocean Temperature Variability in the Mediterranean Sea. Oceanography from Space. J.F.R. Gower (Editor), Plenum Press, NY, p. 175-182.
- Holyer, R. J. and P. E. La Violette, 1983. The Use of Principal Components Analysis Techniques on Nimbus-7 Coastal Zone Color Scanner Data to Define Mesoscale Ocean Features through a Warm, Humid Atmosphere. Naval Ocean Research and Development Activity Report No. 60. (In preparation)
- Hovis, W. A., D. L. Clark, F. Anderson, R. W. Austin, W. H. Wilson, E. T. Baker, D. Ball, H. R. Gordon, and J. L. Mueller, 1980. Nimbus-7 CZCS: System Description and Initial Imagery. Science v. 210, p. 60-63.
- Hussey, W. J., 1979. The TIROS-N/NOAA Operational Satellite System. NOAA NESS Tech. Memo. 95, National Environmental Satellite Service/NOAA, Washington, D.C., 35 p.
- Kinder, T. H., 1983. Donde Va? An Oceanographic Experiment Near the Straits of Gibraltar. Proceedings of IAPSO/ONR/NFKO Workshop on Straits Inst. Phy. Ocean., Copenhagen, Den.
- Lacombe, H., 1961. Etude Hydrologique et Dynamique du Detroit de Gibraltar, Mai-Juin, 1961. Compte-Rendu Preliminaire. Cahiers v. 13, n. 7, July-August, p. 431.
- Lacombe, H. and P. Tchernia, 1971: Caracteres Hydrologiques et Circulation des Eaux a Mediterranean. The Mediterranean Sea: A Natural Sedimentation Laboratory, D. V. Stanley, (Editor), p. 25-36.
- Lanoix, F., 1974. Project Alboran. Etude Hydrologique et Dynamique de la Mer D'Alboran. NATO Technical Report 66, 39 p. and 32 figures.
- La Violette, P. E., 1983. Short-term Measurements of Surface Currents Associated with the Alboran Sea Gyre during Donde Va?. EOS, v. 64, n. 18, p. 248.

- La Violette, P. E., 1984. The Advection of Submesoscale Thermal Features in the Alboran Sea Gyre. JPO (In press)
- La Violette, P. E. and J. Keriing, 1983. An Analysis of Aircraft Data Collected in the Alboran Sea during Donde Va? 6 through 18 October 1982. NORDA Tech. Note 222.
- La Violette, P., T. H. Kinder, R. Preller, and H. E. Hurlburt, 1982. Donde Va?: A Mesoscale Flow Dynamics Experiment in the Straits of Gibraltar and Alboran Sea. XXVIIIth Congress and Plenary Assembly of ICSEM, Cannes, France, December 2-11, 1982. (In proceedings)
- McClain, E. P., W. G. Pichel, C. C. Walton, Z. Ahmad, and J. Sutton, 1982. Multi-channel Improvements to Satellite-Derived Global Sea Surface Temperatures. XXIV COSPAR Meeting, Ottawa, Canada, May 1982. (In proceedings)
- Peluchon, G. and J. R. Donguy, 1962. Travaux Oceanographiques de la 'ORIGNY' dans le Detroit de Gibraltar (Mai-Juin, 1961). Etude des Courants Superficiels dans le Detroit de Gibraltar en Relation Avec la Temperature de Surface. Cahiers Oceanographiques, v. 14, n. 9, November, p. 626-632.
- Philippe, M. and L. Harang, 1982. Surface Temperature Fronts in the Mediterranean Sea from Infrared Satellite Imagery. Hydrodynamics of Semi-enclosed Sea by J.C.J. Nihoul (Editor), Elsevier, Amsterdam, p. 91-128.
- Preller, R. and H. E. Hurlburt, 1982. A reduced gravity model of circulation in the Alboran Sea. In Hydrodynamics of Semi-enclosed Seas. J.C.J. Nihoul (editor), Elsevier, p. 75-90.
- Schwalb, A., 1978. The TIROS-N/NOAA A-G Satellite Series. National Environmental Satellite Service. NOAA, Washington, D.C., March, NOAA Tech. Memo. NESS 95, 75 p.
- Wannamaker, B., 1979. The Alboran Sea Gyre: Ship, satellite and historical data. SACLANT ASW Research Centre Report SR-30. 27 p.

IN 84 27307

SOMALI CURRENT STUDIED FROM SEASAT ALTIMETRY

C. Perigaud and J-F. Minster
Laboratoire de Physique et Chimie de l'Hydrosphere (LA 196)
Institut de Physique du Globe
75230 Paris cedex 05 - France

V. Zlotnicki
Department of Earth and Planetary Sciences
Massachusetts Institute of Technology
Cambridge, Massachusetts 02139

G. Balmino
Bureau Gravimetrique International
Centre National des Etudes Spatiales
18, avenue E. Belin
31055 Toulouse, France

ABSTRACT

Mesoscale variability has been obtained for the world ocean from satellite altimetry by using the repetitive tracks data of Seasat (Cheney, R., 1982; Menard, Y., 1982). No significant results were obtained for the Somali current area for two main reasons: the repetitive tracks are too sparse to cover the expected eddy pattern and these data were obtained in late September and early October when the current is strongly decaying. The non repetitive period of Seasat offers the possibility to study a dozen of tracks parallel to the eddy axis or crossing it. These are used here to deduce the dynamic topography of the Somali current.

The first part of this work consists in reducing the errors on the data. Bad data are eliminated when the wave height is smaller than 10 centimeters or when the absolute value of the altimetric height above the Marsh mean sea surface is greater than 8 meters. Tides and orbit corrections are performed by calculating a bias for each track in order to minimize the crossover RMS difference; this difference is reduced from 2.55 meters to 29 centimeters. Then, tracks are compared between them in order to detect the eddy signal: tracks separated by less than 10 km can be assumed close enough with regard to the scale of the oceanic dynamic topography for their differences to be a measure of its variability; the gravimetric, bathymetric and magnetic data in the area give reasons to believe that the geoid is smooth there, and that the differences between these track data cannot be due to the gravity field.

Furthermore, this variability compares well with that deduced from XBT data obtained at the same period along the Tanker sea lane (Swallow, J.E. and M. Fieux, 1982): this lane is quasi-parallel to and superimposed with three Seasat tracks. The variability profiles show the same extremes at the same locations, and follow the same evolution with time: the maximum slope differences appear from 7° to 10° between early and late July (the height difference is 49.5 cm for

the Tanker data and 55 cm for Seasat). It decreases in August (respectively, 41.5 and 47 cm).

Finally, we are building a local geoid using a collocation inverse method to combine surface gravity data (see map) and altimetry: the repetitive tracks show no variability (which confirms that the current is quasi-inexistent at that time) and can be used as data for the local geoid. This should provide a measure of the absolute dynamic topography of the Somali current.

ORIGINAL PAGE 19
OF POOR QUALITY



— Seasat tracks
— Gravimetric cruises

SATELLITE REMOTE SENSING OVER ICE

Robert H. Thomas

California Institute of Technology
Jet Propulsion Laboratory
4800 Oak Grove Drive
Pasadena, CA 91109

Abstract: Satellite remote sensing provides unique opportunities for observing ice-covered terrain. Passive-microwave data give information on snow extent on land, sea-ice extent and type, and zones of summer melting on the polar ice sheets, with the potential for estimating snow-accumulation rates on these ice sheets. All weather, high-resolution imagery of sea ice is obtained using synthetic aperture radars, and ice-movement vectors can be deduced by comparing sequential images of the same region. Radar-altimetry data provide highly detailed information on ice-sheet topography, with the potential for deducing thickening/thinning rates from repeat surveys. The coastline of Antarctica can be mapped accurately using altimetry data, and the size and spatial distribution of icebergs can be monitored. Altimetry data also distinguish open ocean from pack ice and they give an indication of sea-ice characteristics.

1. INTRODUCTION

Most of the world's ice and snow lies in the polar regions, an area of some fifty million square kilometers that is sparsely populated and, to this day, poorly explored. Weather can be severe at any time of the year, clouds predominate over vast areas and, for several months each winter, there is no sunlight. Under these conditions, in situ scientific measurements are time-consuming and expensive, and they tend to be concentrated in locations of logistic convenience, with little or no coverage between these locations. Indeed, most of Antarctica remained unvisited and unmapped until after the Second World War, when extensive airborne surveys charted much of the coastline and most of the rock outcrops. More recently, a multi-year program of airborne radio-echo sounding of the ice cap has yielded maps of bedrock topography beneath approximately half of the ice sheet. However, spacing between flight lines was 50 to 100 km, and information density is sparse. Moreover, navigation is poor on most airborne surveys in polar regions and, unless well-defined control points exist within the survey area, there are significant errors in both positions and elevations of mapped features. Thus, mapping of the Antarctic ice sheet is still at a rudimentary level, with position errors of several kilometers and surface elevation errors of tens to hundreds of meters.

For many years, the study of polar ice was a pursuit for the dilettante eager to enjoy the scenery. More recently, however, our increased awareness of the role of polar ice in modulating and responding to polar climate, in controlling sea level, and in modifying ocean properties has exposed our lack of understanding of ice behavior. We do not know whether the ice sheets of Greenland and Antarctica are growing or shrinking; we do not know how much snow falls on these ice sheets,

how much surface melting there is, nor how much ice flows into the ocean to form icebergs; we cannot calculate accurately the forces that drive ice motion; and we cannot assess how strongly sea ice affects heat transfer between the ocean and atmosphere and hence influences both ocean properties and climate. We do know, however, that the polar regions are not dormant and unchanging. Wherever detailed measurements have been made, the ice sheet locally is either thickening or thinning, and there are major year-to-year changes in sea-ice cover that may influence weather conditions in areas far removed from the poles. We also know that predictions from climate models are strongly dependent on how sea ice is incorporated within the models. Indeed, sea-ice cover is often used as an adjustable parameter to force model predictions into verisimilitude at lower latitudes. For predictions of global-climate change due to factors such as increased CO_2 , the climate models urgently need more realistic incorporation of sea-ice response.

Each of these problems can be addressed using data from satellite remote sensing. Indeed, these data provide our only source of synoptic observations over the polar regions. A major goal of the NASA research program in the polar regions is to improve our ability to convert satellite measurements into useful geophysical parameters. In this paper, I shall briefly review satellite remote-sensing techniques for observing ice cover, provide examples of derived products, and describe some of my own work on applications of altimetry data over ice.

2. REMOTE-SENSING TECHNIQUES

Until the advent of satellite observations, little was known about seasonal and year-to-year changes in sea-ice cover. Weather satellites of the National Oceanic and Atmospheric Administration (NOAA) still provide daily images of the polar regions with a spatial resolution of 1 to 4 km, and these are routinely used by the Navy/NOAA Joint Ice Center to provide weekly analyses of global sea-ice cover. Higher resolution imagery (tens of meters) is obtained by Landsat, but not on a regular basis; special arrangements must be made to obtain images over specific areas. Moreover, all visible and infrared imagery is severely limited by darkness and/or clouds. In order to overcome this problem, NASA has developed sensors to obtain microwave data, which provide information day and night in all weathers. Here, I shall focus attention on these microwave techniques.

Microwave radiometers

All matter radiates electromagnetic energy as a consequence of molecular interaction. The energy is emitted over a range of wavelengths, the precise mix being determined by viewing angle, molecular composition, temperature, and material structure. Ice and liquid water have very distinct emission signatures, primarily because of differences in the way molecules are arranged in each. Moreover, different ice samples can have distinct signatures, partly because of temperature differences and partly because of differences in texture and impurity content. Snow density, grain size, surface roughness, brine content, and the degree of wetness all influence the radiated energy, and they influence it differently at different wavelengths. Thus, by sampling an appropriate suite of wavelengths the ice cover can be distinguished from open water and classified according to its surface and near-surface characteristics.

For snow and ice on land, passive-microwave data potentially distinguish extent, water equivalent and onset of snow melt for seasonal snow cover (Kunzi et al., 1982) and the regions where summer melting occurs on the terrestrial ice sheets of Greenland and Antarctica (Zwally and Gloersen, 1977). Some of these applications are still research topics but they promise to become operational tools within the near future. In addition, it may be possible to deduce snow-accumulation rates over the polar ice sheets (Zwally, 1977; Rotman et al., 1982). Over sea ice, passive-microwave data can distinguish water from ice and characterize the major ice types: new ice, just a few cm thick; first-year ice, generally snow covered and up to 2 m thick; and old ice, which has survived at least one summer, has undergone deformation and cracking, and is of variable thickness with a comparatively hummocky surface. Old ice is also distinctive in having lower salinity than younger ice, and this gives it a distinctive microwave signature. In this paper, I shall refer to this old ice as "multiyear ice." In principle, the relative concentrations of water and each of the major ice types can be distinguished using passive-microwave data at appropriate wavelengths. Major problems occur, however, during the summer season when the existence of liquid water on the ice surface significantly affects the microwave emissions. This problem is currently under investigation by several NASA-funded researchers (Comiso, 1983 ; Comiso et al., 1984; Carsey, In press).

The spatial resolution of a microwave sensor increases as the wavelength decreases or as the antenna size increases. Thus, high resolution can readily be obtained in the visible and infrared, but these short-wavelength radiations are strongly affected by atmospheric conditions, particularly clouds. Microwave radiations lie in the frequency range of 1 - 300 GHz (wavelengths from about 1 mm to 37 cm). They penetrate clouds and can provide all-weather, day/night synoptic

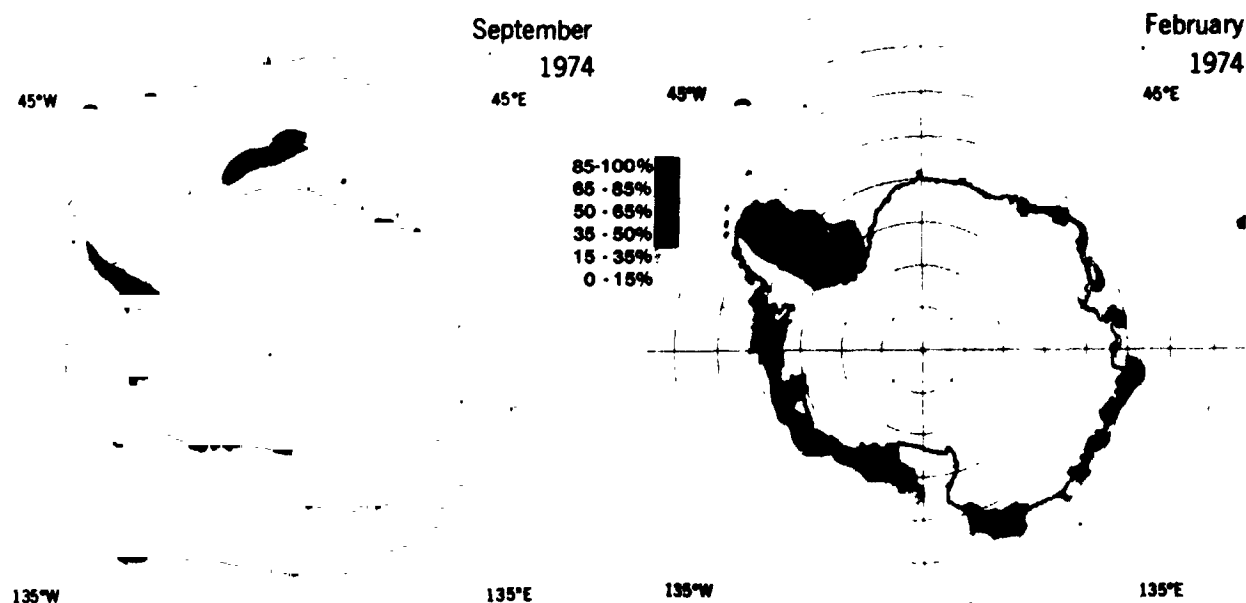


Figure 1. The contrast between winter maximum and summer minimum Antarctic sea-ice cover is clearly shown by these images obtained using ESMR data, with ice concentration depicted by different grey shades. From Zwally et al., 1983a.

ORIGINAL PAGE IS
OF POOR QUALITY

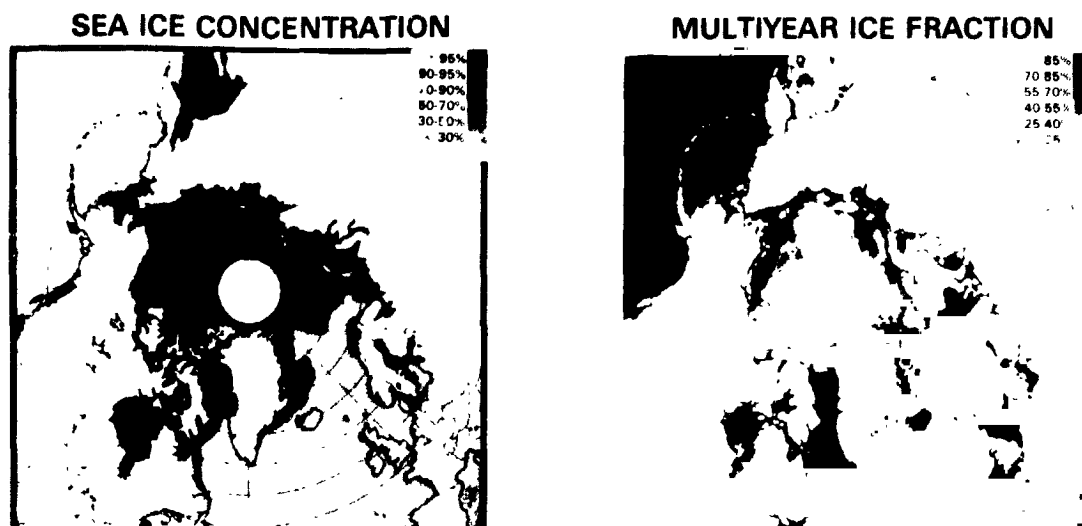


Figure 2. Arctic sea-ice concentrations and multiyear ice fractions for February 3-7, 1979, derived from SMMR data. From Cavalieri et al., In press, and included here by kind permission of D. Cavalieri.

measurements of several Earth-surface and atmospheric parameters (Njoku, 1982). The first satellite sensor to provide global information on ice extent was the Electrically Scanning Microwave Radiometer (ESMR), launched by NASA aboard Nimbus-5 in December 1972. It measured horizontally polarized radiation at 19.35 GHz with a spatial resolution of about 30 km, and useful swath width of 1400 km. Because measurements were made at only one frequency, there is ambiguity in data interpretation. However, estimates of ice concentration can be made to an accuracy of about $\pm 15\%$ in areas where the ice cover is more or less homogeneous. Antarctic sea ice fulfills these requirements, and ESMR data have been analyzed to give a time series of Antarctic sea-ice cover from 1973 through 1976 (Zwally et al., 1983a). Figure 1 shows the contrast between summer minimum and winter maximum ice cover for 1974. The open water "polynya" straddling the Greenwich meridian in the winter image was first detected in ESMR data. It does not form every winter, and why it forms is not fully understood. It may be initiated by wind action, but its survival through the winter must require major upwelling of warm ocean water.

The quality of ESMR data deteriorated after 1976, but they were still used for operational ice forecasting by the Navy/NOAA Joint Ice Center until 1983. In October, 1978, the Scanning Multichannel Microwave Radiometer (SMMR) was launched aboard Nimbus-7. It has provided excellent data since then and is expected to continue operating into the mid 80's. SMMR acquires data in both vertical and horizontal polarization at these five frequencies: 6.6, 10.7, 18, 21, and 37 GHz. Spatial resolution ranges from 30 to 150 km, depending on frequency, and swath width is 780 km. Data from the 18 and 37 GHz channels are used to obtain estimates of both total sea-ice concentration and how much multiyear ice there is (Cavalieri et al., in press). Figure 2 shows estimates of total ice concentration and multiyear fraction for Feb. 3-7, 1979.

Starting in 1985, a series of U.S. Defense Meteorological Satellite Program (DMSP) spacecraft will carry the Special Sensor Microwave/Imager (SSM/I), a scanning microwave radiometer that will collect data from a 1300 km swath in both vertical and horizontal polarization at 19.35, 37 and 85.5 GHz, and at 22.235 GHz in vertical polarization only. Spatial resolution will be between 12 and 50 km, depending on frequency. Sea-ice parameters will be obtained from the 19.35 and 37 GHz data and, potentially, from the 85.5 GHz data, which will provide better spatial resolution and may improve discrimination of ice types. NOAA plans to archive all SSM/I data, and NASA will process the data to higher-level products for research purposes.

Passive-microwave data provide excellent global synoptic coverage at low spatial resolution. Over the next decade, large-antenna radiometers will be developed, and resolution will improve to perhaps the 1 km level. Inevitably, data rates will increase and they will require improved techniques for processing and distribution.

Synthetic Aperature Radar (SAR)

The spatial resolution that can be achieved by a conventional radar is determined by radar frequency and antenna size. This imposes a practical limitation on the resolution. The SAR overcomes this by illuminating a swath off to the side of the spacecraft and discriminating individual resolution cells within the field of view according to range and Doppler shift in frequency due to spacecraft motion. The L-band SAR aboard NASA's Seasat, which operated from July to October, 1978, had a spatial resolution of 25 m and swath width of 100 km. Data were obtained at too high a rate (c. 100M bits per second) to be stored aboard the satellite, and they were transmitted in real time to appropriate receiving stations. A

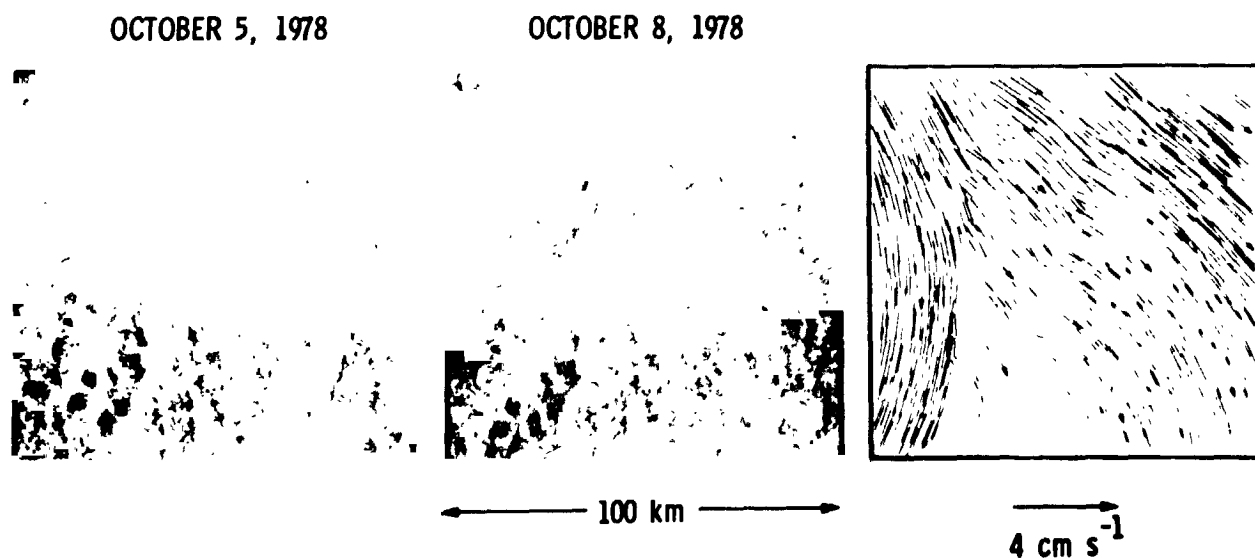


Figure 3. Seasat SAR images of Arctic pack ice taken 3 days apart, and velocity vectors obtained by comparing the positions of common floes in the two images. From Rothrock and Thorndike, In press, and included here by kind permission of D. Rothrock.

complex processing sequence yields a digital image of the illuminated swath with intensity proportional to radar backscatter, and an absolute position accuracy of about 100 m (Fu and Holt, 1982; Carsey et al., 1983).

Seasat clearly demonstrated the capability of using satellite SAR data to obtain all-weather, high-resolution imagery over sea ice. Figure 3 shows two SAR images of pack ice in the Beaufort Sea taken 3 days apart, with velocity vectors obtained by comparing positions of individual ice floes (Rothrock and Thorndike, In press). The images are filled with ice floes separated by dark areas of either open-water leads or very new ice. Many of the floes appear to be a patchwork of smaller units separated by light-shaded streaks, which may represent collision lines where ice has piled up to form ridges rising several meters above sea level. Current NASA research is focussed on developing automated techniques for analysing SAR sea-ice imagery to give ice-motion vectors and to characterize the ice by type.

Upcoming Space Shuttle missions will provide opportunities to acquire SAR data over sea ice for short periods and to test data-analysis techniques at different SAR frequencies. The next satellite SAR will operate at C-band aboard the European Space Agency's Remote Sensing Satellite (ERS-1), due to be launched in 1987/88. This should provide excellent sea-ice information, and NASA plans to establish a ground receiving station in Alaska to acquire ERS-1 SAR data over the Bering, Chukchi and Beaufort seas. There will also be ESA and Canadian receiving stations in Kiruna, Sweden and Prince Albert, Canada and, together with the NASA station, they will be capable of collecting data from most of the area covered by Arctic sea ice. Another satellite with the acronym ERS-1 will be launched by Japan in 1990, and this also will carry a SAR. Future prospects include acquisition of data over Antarctica, where the ice-sheet coastline could be mapped to an accuracy of about 100 m using SAR data.

Altimetry

Radar altimeters were carried aboard NASA's Geos-3 (April, 1975 to December, 1978) and Seasat (July to October, 1978). The Geos-3 orbit lay between latitudes 65°N and 65°S , and the data were used to improve significantly the surface-elevation map of the Greenland ice sheet (Brooks et al., 1978). Seasat extended coverage to 72° latitude and provided considerably greater accuracy. These altimeters were designed to measure ranges to the ocean surface by transmitting short radar pulses and measuring the time delay until receipt of the reflected pulse. Pulse rate was approximately 1000 per second and the altimeter was designed to track the half-power point on the leading edge of a composite return pulse formed by summing 50 consecutive received pulses. Summation took account of range changes between pulses by correcting delay times for range rate calculated from earlier measurements. In order to obtain high range resolution, return energy was measured only within a data-acquisition window of about 190 ns duration - equivalent to a range window 15 m above and below the measured surface.

The altimeters worked well over the oceans, where measured ranges change very slowly. But over sloping or undulating terrain, the servo-tracking circuit was not sufficiently agile to monitor rapidly changing ranges, and the altimeter frequently lost track of the return pulse. Although this resulted in short periods (usually a few seconds) when no useful data were obtained, the Seasat

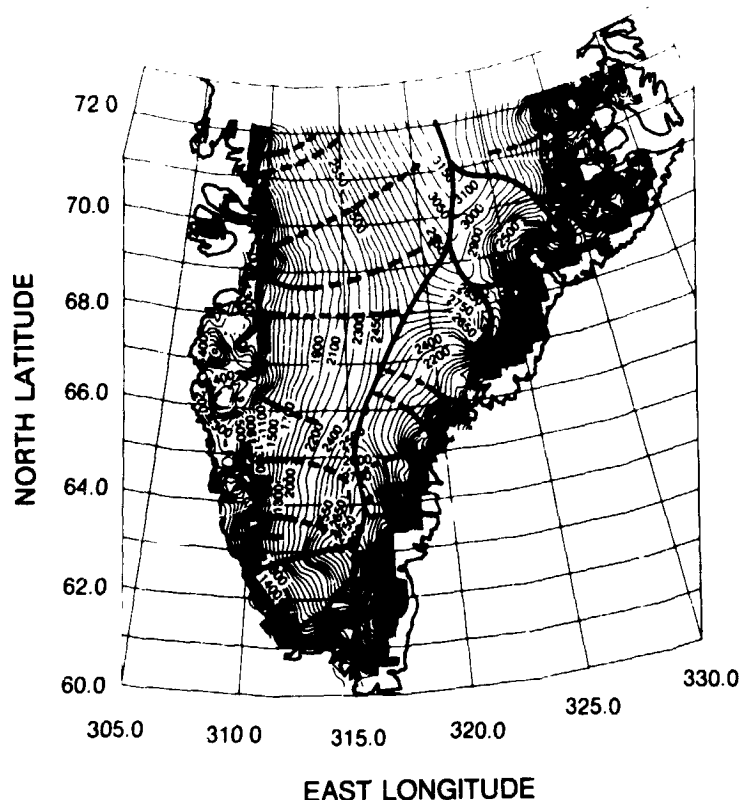


Figure 4. Ice surface topography over Greenland, derived from Seasat altimetry data. The heavy lines delineate drainage basins. From Bindschadler, In Press, and included here by kind permission of R. Bindschadler.

altimeter measured more than 600,000 useful elevations on the ice sheets of Greenland and Antarctica (Zwally et al., 1983b). It is important to note, however, the physical significance of these measured elevations. The radar beam produced a beam-limited footprint (BLF) of about 12 km radius, in contrast to the pulse-limited footprint (PLF) from which reflections comprising the leading edge of the return pulse were obtained. Over the ocean, the PLF had a radius between 1 and 5 km, depending on wave height, and measured ranges gave the average sea-surface elevation within the footprint. Over an ice sheet, however, spacing between surface undulations approaches the BLF radius, and the altimeter preferentially measured ranges to the closest undulation summits, averaging the effects of small-scale roughness, such as sastrugi. These summits were not necessarily directly beneath the satellite, leading to ambiguity when measured ranges are translated into surface elevations. Nevertheless, satellite radar altimeters provide the best available data for mapping ice-sheet topography over the vast areas of Greenland and Antarctica. The resulting surface represents a smoothed envelope biased slightly above the actual surface (Fig. 4). The smoothing distance is on the order of a few km, and the bias depends on local regional slope, undulation amplitude, and altimeter characteristics. To some extent, bias errors due to the regional slope can be corrected (Brenner et al., 1983).

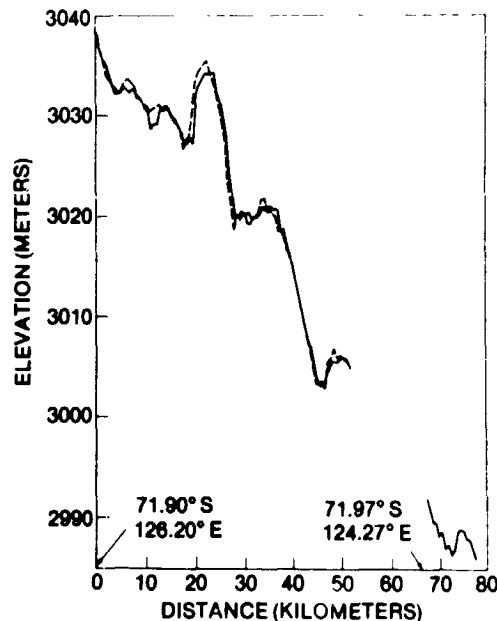


Figure 5. Two Seasat-altimetry profiles over the Antarctic ice sheet separated by about 40 m. From Zwally et al., 1983b.

The smoothed envelope obtained in this way is well suited to most glaciological requirements. Moreover, intercomparison of surfaces obtained from two altimetry missions a decade or so apart would provide clear indication of any regional changes in ice topography, since the local biases would be approximately the same for each survey. Here, however, it is important to note that altimeter design characteristics must be similar for both surveys. Figure 5 shows two sets of Seasat measurements along repeat tracks over Antarctica, and gives an indication of how well the altimeter performed over ice. Range accuracy over smoother portions of the ice sheet was ± 25 cm.

Return pulses over oceans and ice sheets generally have a similar shape, with a fairly sharp rise and a slow decay. But over sea ice, the return pulse has a much sharper rise followed by a quite rapid fall producing a spike characteristic of a specular reflection. In principle, the shape of this spike can give information on sea-ice characteristics, such as surface roughness, amount of open water within the footprint, and ocean swell within the pack ice. However, caution must be exercised in analysing existing altimetry data since significant range-rate errors over sea ice lead to appreciable broadening of the pulse shape in the Seasat data record, which was formed by summing two adjacent 50-pulse composites. Nevertheless, the altimetry data provide an accurate indication of the boundary between open ocean and sea ice.

Future altimetry missions will be flown aboard the U.S. Navy's Geosat (to be launched in 1984), ESA's ERS-1 (1987/8) and the U.S. Navy/NASA/NOAA joint mission NROSS (1989). Anticipated changes in altimeter design will probably yield significant improvements in performance over ice. Moreover, although Geosat will repeat approximately the Seasat coverage, ERS-1 and NROSS will provide data to 82° latitude.

3. MAPPING COASTAL ICE CLIFFS AND ICEBERGS FROM ALTIMETRY DATA

In a recent paper Thomas et al., (1983) showed how the coast of Antarctica could be mapped using satellite altimetry data. As it approached the continent from the ocean, the Seasat altimeter obtained strong reflections from sea ice even for a short time after passing over the ice front (Fig. 6). Measured ranges were oblique distances to the nearest portion of sea ice, yielding an apparent drop in surface elevation. The sequence of oblique ranges gives the position of the sea ice along a segment of the ice cliff that forms much of the Antarctic coastline. The entire Seasat data set provides an opportunity for mapping this coastline to an accuracy of $\pm (0.1 \text{ to } 1 \text{ km})$, representing a major improvement over existing surveys. Moreover, as the altimeter approached the ice cliff, the intensity of the radar signal arriving prior to the sea-ice reflection increased due to reflections from the ice surface inland from the ice cliff. This pre-pulse intensity reaches a maximum near the point where the satellite crossed over the ice cliff, and then diminishes. At the same time, the intensity of the sea-ice reflection decreases as the reflection becomes more oblique. This is well

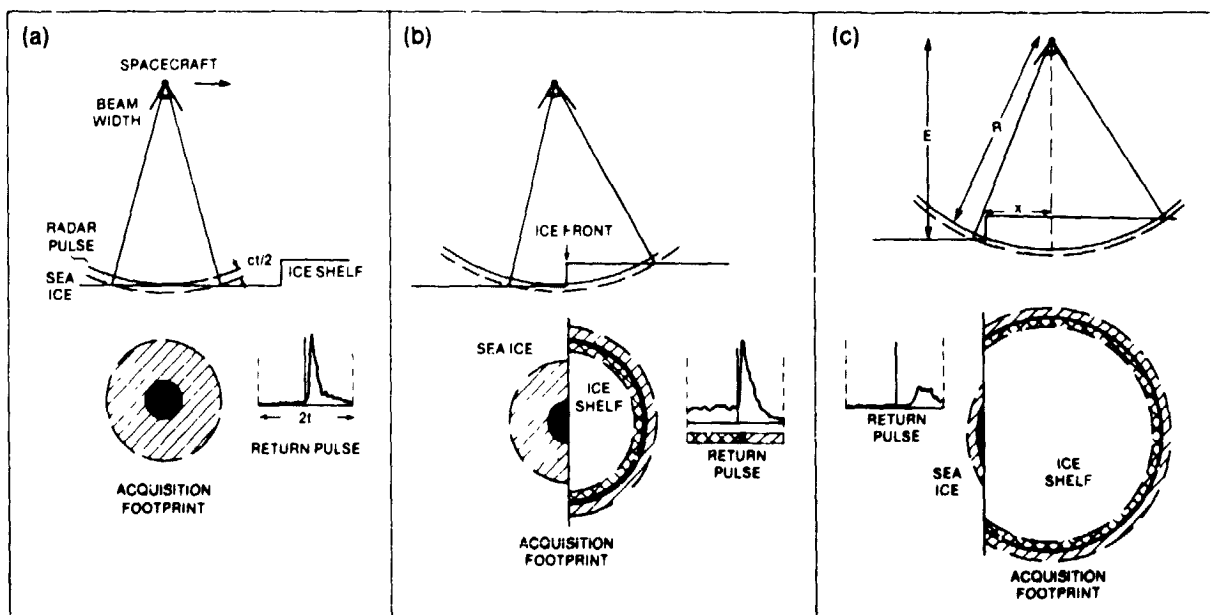


Figure 6. Radar altimeter approaching an ice shelf and continuing to measure ranges to nearby sea ice after crossing the ice front. The radar pulse is of very short duration and is represented by the solid line. The acquisition footprint (cross-hatched area in (a)) indicates the area from which reflections can be received during the data-acquisition window (of duration $2t$). The pulse-limited footprint (about 1 km radius) is the black area; the area from which reflections are received prior to the main return is double cross-hatched; the area contributing to the trailing edge of the return pulse is single cross-hatched. c is the velocity of light. From Thomas et al., 1983.

ORIGINAL PAGE IS
OF POOR QUALITY

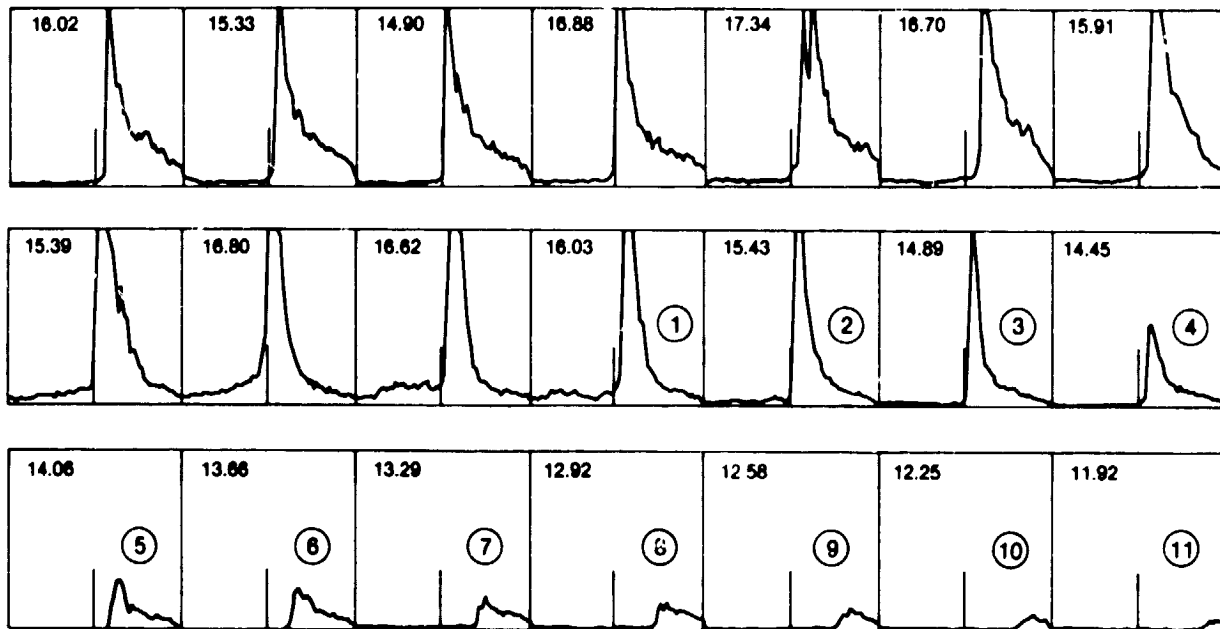


Figure 7. Reflected radar pulses obtained at intervals of 0.1 s by the Seasat altimeter as it approached from seaward, and then crossed Amery Ice Front. Each frame represents a time window of duration of about 188 ns, equivalent to an elevation difference of about 28 m. The numbers in each frame give the altimeter-derived surface elevation in meters above the ellipsoid. This elevation, before correction for lags in the tracking circuit, corresponds to the time of the short vertical line in the center of the window. Frames (1) to (11) represent oblique ranges to sea with the satellite over the ice shelf. From Thomas et al., 1983.

illustrated in Figure 7, where a sequence of reflected pulses are shown for a Seasat orbit approaching, and then passing over, the Amery Ice Shelf in Antarctica. Figure 8 shows the apparent surface elevation of the sea ice and the pre-pulse intensity plotted against distance along the subsatellite track.

Similar effects are noticed when the altimeter passed over icebergs. On each side of the iceberg there was a rise in pre-pulse intensity; over the iceberg, both the intensity of the sea-ice return and the measured surface elevation decreased. Figure 9 shows this sequence, obtained when Seasat passed over an iceberg near the Greenwich meridian off the coast of Antarctica. The Seasat data set contains many such examples, which we are currently analysing to obtain an estimate of iceberg sizes and distribution. Moreover, even icebergs that were not directly beneath the satellite left an imprint in the data record, since they elevated the pre-pulse intensity so long as they lay within the BLF. This provides a powerful technique for monitoring iceberg population in Antarctic waters, and indirectly obtaining an estimate of ice discharge from the continent.

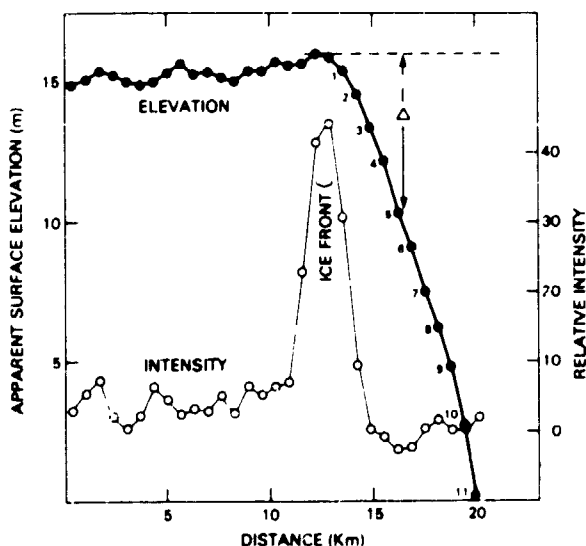


Figure 8. Apparent surface elevation versus distance along the subsatellite track for an orbit crossing Amery Ice Front. Also shown is the average intensity, in arbitrary units, of the pre-pulse radar reflection. From Thomas et al., 1983.

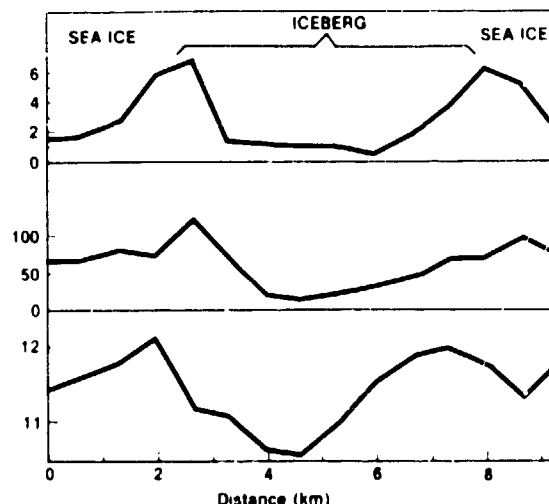


Figure 9. Measurements deduced from altimetry data obtained on 28 July, 1978, as Seasat passed over an iceberg surrounded by sea ice at 69.8°S , 2.4°W . The top plot shows pre-pulse intensity; the middle plot shows peak intensity of the main return; the lower plot shows apparent surface elevation derived from the altimetry data. Ordinates on the top and middle plots are arbitrary units, on the lower plot they are meters above the Earth ellipsoid. Abscissa is distance in km along the subsatellite track.

Acknowledgements: Most of the work reviewed here is being conducted by investigators funded by NASA's Oceanic Processes Branch, and I have benefitted particularly from numerous discussions with D. Cavalieri, J. Comiso and J. Zwally at Goddard Space Flight Center, F. Carsey at the Jet Propulsion Laboratory and D. Rothrock at the University of Washington.

REFERENCES

- Bindschadler, R. A., In press: Jacobshavn Glacier drainage basin: a balance assessment. *J. Geophys. Res.*
- Brenner, A. C., R. A. Bindschadler, R. H. Thomas, and H. J. Zwally, 1983: Slope-induced errors in radar altimetry over continental ice sheets. *J. Geophys. Res.*, 88, 1617-1623.
- Brooks, R. L., W. J. Campbell, R. O. Ramseyer, H. R. Stanley, and H. J. Zwally, 1978: Ice sheet topography by satellite altimetry. *Nature*, 274, 539-543.

- Cars F. D., In press: Summer Arctic sea ice character from satellite microwave data. *J. Geophys. Res.*
- Carsey, F. D., J. Curlander, B. Holt, and K. Hussey, 1983: Shear zone ice deformation using supervised analysis of Seasat data. AIAA 21st Aerospace Sciences Meeting, Reno, Nevada.
- Cavalieri, D. J., P. Gloersen, and W. J. Campbell. In press: Determination of sea ice parameters with the Nimbus-7 SMMR. *J. Geophys. Res.*
- Comiso, J. C., 1983: Sea ice effective microwave emissivities from satellite passive microwave and infrared observations. *J. Geophys. Res.*, 88, 7686-7704.
- Comiso, J. C., S. F. Ackley, and A. L. Gordon, 1984: Antarctic sea ice microwave signatures and their correlation with in situ ice observations. *J. Geophys. Res.*, 89, 662-672.
- Fu, L.-L. and B. Holt, 1982: Seasat views oceans and sea ice with synthetic-aperture radar. JPL Publication 81-120. Jet Propulsion Laboratory, Pasadena, California, 200p.
- Kunzi, K. F., S. Patil, and H. Rott, 1982: Snow-cover parameters retrieved from Nimbus-7 Scanning Multichannel Microwave Radiometer (SMMR) data. *IEEE Trans. Geosci. Remote Sensing*, GE-20, 452-467.
- Njoku, E. G., 1982: Passive microwave remote sensing of the Earth from space - a review. *Proc. IEEE.*, 70, 728-750.
- Rothrock, D. A. and A. S. Thorndike, In press: Measuring sea-ice floe size distribution. *J. Geophys. Res.*
- Rotman, S. R., A. D. Fisher, and D. H. Staelin, 1982: Inversion for physical characteristics of snow using passive radiometric observations. *J. Glaciol.*, 28, 179-185.
- Thomas, R. H., T. V. Martin, and H. J. Zwally, 1983: Mapping ice-sheet margins from radar altimetry data. *Annals of Glaciology*, 4, 283-288.
- Zwally, H. J., 1977: Microwave emissivity and accumulation rate of polar firn. *J. Glaciol.*, 18, 195-215.
- Zwally, H. J. and P. Gloersen, 1977: Passive microwave images of the polar regions and research applications. *Polar Record*, 18, 431-450.
- Zwally, H. J., J. C. Comiso, C. L. Parkinson, W. J. Campbell, F. D. Carsey, and P. Gloersen, 1983a: Antarctic sea ice, 1973-1976: satellite passive-microwave observations. NASA SP-459, NASA, Washington, D.C., 206p.
- Zwally, H. J., R. A. Bindshadler, A. C. Brenner, T. V. Martin, and R. H. Thomas, 1983b: Surface elevation contours of Greenland and Antarctic ice sheets. *J. Geophys. Res.*, 88, 1589-1596.

RADAR ALTIMETRY OVER SEA ICE

John Powell
Rutherford Appleton Laboratory
Science and Engineering Research Council
Chilton, Didcot,
Oxfordshire OX11 0QX

ABSTRACT

Variations of polar sea ice type and extent are of great importance for climatology and polar resource exploitation studies. This is particularly true of a region about 100 km wide around the ice edge where the open sea interacts with the ice. To study this region in the Bering and Greenland Seas a series of experimental campaigns, the Marginal Ice Zone Experiment (MIZEX) has been planned. A major objective of MIZEX is the development of a capability to relate the morphology and distribution of the sea ice to atmospheric and oceanographic parameters in an overall model.

A further capability, to infer and predict sea ice behaviour from remotely sensed satellite data, is also being studied. This will be particularly important if optimum use is to be made of the large quantities of microwave and infra-red data that will be collected in the polar regions towards the end of this decade by the European Remote Sensing satellite (ERS-1) and the American Defence Meteorological Satellite Programme (DMSP). ERS-1 will provide along-track measurements of surface altitude and roughness, wind speed and wave height (1.7 km footprint), wave spectra (5 km squares every 100 km), ocean surface wind velocity (50 km resolution, 400 km swath) surface temperature (0.5K, 1 km resolution, 500 km swath) and SAR imagery (30 metres resolution, 80 km swath). DMSP satellites will provide, among other measurements, microwave radiometric imagery at several frequencies (min spatial resolution 15 km in a 1,400 km swath).

In February 1983, during the first part of the MIZEX, a 13.7 GHz microwave radar altimeter/scatterometer having a pulse length of 16 nanoseconds was flown over the Bering Sea Marginal ice zone. On the same aircraft were the NASA GSFC 19 GHz Electronically Scanning Microwave Radiometer (ESMR), scanning radiometers at frequencies of 92 and 183 GHz and an infra-red, nadir pointing, temperature sounder. SLAR imagery and laser profilometry were collected in the same area from a NOAA aircraft and a large number of surface data were collected from two ships.

The altimeter/scatterometer was operated in nadir pointing and conically scanning (5-10° half angle) modes to collect measurements of reflectivity and pulse shapes. These will be related to sea-ice classifications, ocean wave spectra and coincident microwave and infra-red radiometric measurements and laser profilometer surface roughness estimates. The results of a preliminary study of the data collected by RAL during the MIZEX-WEST campaign will be presented together with plans for the 1984 Greenland Sea Campaign.

METHOD TO ESTIMATE DRAG COEFFICIENT AT THE
AIR/ICE INTERFACE OVER DRIFTING OPEN PACK ICE
FROM REMOTELY SENSED DATA

Uri Feldman

Department of Geography, Bar-Ilan University
Ramat-Gan 52100, Israel

ABSTRACT

A knowledge in near real time, of the surface drag coefficient for drifting pack ice is vital for predicting its motions. And since this is not routinely available from measurements it must be replaced by estimates. Hence, a method for estimating this variable, as well as the drag coefficient at the water/ice interface and the ice thickness, for drifting open pack ice was developed. These estimates were derived from three-day sequences of Landsat-1 MSS images and surface weather charts and from the observed minima and maxima of these variables. The method was tested with four data sets in the southeastern Beaufort sea. Acceptable results were obtained for three data sets. Routine application of the method depends on the availability of data from an all-weather air or spaceborne remote sensing system, producing images with high geometric fidelity and high resolution.

1. INTRODUCTION

The study of drifting pack ice depends on the knowledge of numerous parameters related to its motion (Feldman and Howarth, 1979). And since data vital for determining these parameters are not routinely available for the polar oceans they must be estimated (Feldman et al., 1979, 1982). The purpose of this study is to present a method for estimating ice thickness and drag coefficients at the air/ice and the water/ice interfaces for groups of detached ice floes. To this end, a reduced form of the general equation of motion for drifting pack ice was employed, assuming wind stress, water drag and Coriolis force to be at equilibrium.

Data were obtained from three sources:

- (1) Pack ice speed and direction of motion, which were measured from three-day sequences of sidelapping Landsat-1 multispectral scanner (MSS) images.
- (2) Surface wind speed and direction, at 10 m above the ice and air density, which were obtained from three-day sequences of surface weather charts, following the work by Feldman et al. (1979, 1981).
- (3) Minimum and maximum values of pack ice thickness and drag coefficients of its surface and subsurface, which were obtained from observations previously conducted in the Arctic ocean.

The method developed in this study is based upon employing three ratios between pairs of the unknown parameters, which could be calculated from the pack ice velocity vector and the wind field data, in conjunction with the known minima and maxima of the same parameters. The procedure to obtain the estimates was tested by four groups of open pack ice, consisting of three or four data sets within each group, which drifted in the Beaufort sea during October 1973, July and August 1974.

Acceptability of the results was determined from the corresponding values of the cross isobar angle.

2. PHYSICAL BACKGROUND

The general equation of motion for a unit area of drifting pack ice is given by Campbell (1965) as

$$\vec{\tau}_a + \vec{\tau}_w + \vec{C} + \vec{P} + \vec{I} = \rho_{ice} h d\vec{V}/dt \quad (1)$$

where $\vec{\tau}_a$ is the horizontal air stress at the air/ice interface, $\vec{\tau}_w$ is the horizontal water stress at the water/ice interface, \vec{C} is the horizontal Coriolis deflecting force, \vec{P} is the horizontal marine pressure gradient force, \vec{I} is the horizontal internal ice stress, ρ_{ice} is the ice density, h is ice thickness and $d\vec{V}/dt$ is the horizontal ice acceleration. Thorndike (1973) has shown that the horizontal acceleration term is usually much smaller than all other terms in equation (1). Therefore, a steady state drift can be assumed (Nansen, 1902; McPhee, 1982) and equation (1) can be rewritten as

$$\vec{\tau}_a + \vec{\tau}_w + \vec{C} + \vec{P} + \vec{I} = 0 \quad (2)$$

If this equation is applied to drifting open pack ice, consisting of detached ice floes, where internal ice stress cannot be transmitted among the floes (Hibler, 1979; McPhee, 1980) then equation (2) can be reduced to

$$\vec{\tau}_a + \vec{\tau}_w + \vec{C} + \vec{P} = 0 \quad (3)$$

Using data reported by Newton (1973, p.23) it can be shown that mean speed of ocean currents in the Beaufort sea is less than 2 m day^{-1} . In addition, Hibler and Tucker (1979) stated that geostrophic currents and ocean tilt have a negligible effect on short term, weekly drifts. Hence, it may be concluded that in the area of study motions of drifting open pack ice can be determined from a simple steady state equation, written as

$$\vec{\tau}_a + \vec{\tau}_w + \vec{C} = 0 \quad (4)$$

Nansen (1902), Sverdrup (1928), Shuleiken (1938), Fel'zenbaum (1958), Campbell (1965), Thorndike (1973), Neralla et al. (1980), Feldman et al. (1981) and McPhee (1982) applied equation (4) in their studies.

Under conditions of neutral equilibrium within the atmospheric boundary layer

$$\tau_a = \rho_a C_d^a U^2 \quad (5)$$

where ρ_a is the air density, C_d^a the drag coefficient at the air/ice interface

and U the horizontal surface wind speed at 10 m above the ice surface. Under similar conditions beneath the ice (Johannessen, 1970)

$$\tau_w = \rho_w C_d^w V^2 \quad (6)$$

where ρ_w is the ocean water density, C_d^w is the drag coefficient at the water/ice interface and V is the speed of the centre of gravity of a drifting group of ice floes. The Coriolis force may be derived from

$$C = \rho_{ice} f h V \quad (7)$$

where h is the ice thickness and $f (=2\omega \sin\phi)$ is the Coriolis parameter, ω ($=7.292 \cdot 10^{-5} \text{ s}^{-1}$) is the Earth's angular speed and ϕ is latitude.

Resolving the x and y components of $\vec{\tau}_a$, $\vec{\tau}_w$ and \vec{C} from equations (5), (6) and (7), allows equation (4) to be written as

$$\rho_a C_d^a U^2 \cos \Delta\gamma = \rho_w C_d^w V^2 \quad (8)$$

and

$$\rho_a C_d^a U^2 \sin \Delta\gamma = \rho_{ice} f h V \quad (9)$$

where $\Delta\gamma$, the angle of sea ice deflection (Feldman et al., 1981) is defined as

$$\Delta\gamma = \theta_{ice} - \theta_u \quad (10)$$

and θ_{ice} and θ_u are the directions of motion of the pack ice and the surface wind respectively.

The cross isobar angle, $\Delta\theta$ is defined as

$$\Delta\theta = \theta_G - \theta_u \quad (11)$$

where θ_G is the geostrophic wind direction. $\Delta\theta$ may be obtained from the difference between equations (11) and (10), written as

$$\Delta\theta = \Delta\gamma + \theta_G - \theta_{ice} \quad (12)$$

3. PACK ICE VELOCITY FROM LANDSAT MSS IMAGES

A number of techniques have been used to calculate the velocity of drifting pack ice from sequential Landsat MSS imagery (Crowder et al., 1973; Hibler et al., 1974; Wendler and Jayaweera, 1974; Nye and Thomas, 1974; Nye, 1975 and Sobczak, 1977). The orbits of Landsat converge in high latitude thereby producing sequences of four sidelapping images over the Beaufort sea. In this study, velocities of four groups of drifting ice floes were calculated over three-day sequences. A group could consist of any number of single ice floes in close proximity, but in

these cases they ranged from 3 to 26. To determine the velocity it is necessary to measure the co-ordinates of each ice floe in a group and to know the exact mean time of imaging, t_i , on each day. The co-ordinates, x_i ; y_i , of the ice floes were measured with a digitizer and were related to an origin and several control points located on land. The exact mean scanning time, t_i , was determined from the orbital information.

The area, A_i , of each floe was calculated from 1:250,000 scale enlargements of the images, using the dot grid method. The co-ordinates of the estimated centre of gravity of each group, X_{gr} ; Y_{gr} , were calculated from

$$X_{gr} = \sum A_i x_i / \sum A_i \quad (13) \quad \text{and} \quad Y_{gr} = \sum A_i y_i / \sum A_i \quad (14)$$

This procedure eliminated effects due to collisions which could occur within a group while in motion.

The component mean velocities of drifting centres of gravity, V_x ; V_y , were calculated for the intermediate scanning time, T_{11i+1} ($=t_{12}, t_{23}, t_{34}, \dots$) from

$$V_x = \Delta X_{gr} / \Delta t \quad (15) \quad \text{and} \quad V_y = \Delta Y_{gr} / \Delta t \quad (16)$$

where Δt is the time increment between sequential paths of Landsat-1 and ΔX_{gr} or ΔY_{gr} are the component distance increments during Δt .

4. RATIOS AND MEAN RATIOS BETWEEN ICE PARAMETERS

The first step towards estimating h , C_d^a and C_d^w consisted of determining the ratios M , N and B and their means \bar{M} , \bar{N} and \bar{B} . Values of M and N , defined as

$$M = h / C_d^a \quad (17) \quad \text{and} \quad N = C_d^w / C_d^a \quad (18)$$

were calculated from available data, for the four groups, at t_{11i+1} , by rewriting equations (17) and (18) from equations (9) and (8) respectively, as

$$M = (\rho_a U^2 \sin \Delta \gamma) / (\rho_{ice} f V) \quad \text{and} \quad (19)$$

$$N = (\rho_a U^2 \cos \Delta \gamma) / (\rho_w V^2) \quad (20)$$

The variable U was obtained from the geostrophic wind speed G by the formula

$$U = 0.54G + 1.68 \quad (21)$$

adopted by Feldman et al. (1979) from Hasse's (1974a, 1974b) work. G and ρ_a were derived from surface weather charts.

$\Delta\gamma$ was replaced by values of the mean angle of ice deflection $\overline{\Delta\gamma}$, defined and calculated by Feldman et al. (1981) in the area of study for t_{11i+1} . V was calculated from equations (15) and (16). Finally, the constants ϕ (required for calculating f in $f = 2 \omega \sin \phi$) ρ_w and ρ_{ice} were replaced by $\phi = 70^\circ$, $\rho_w = 1.03 \cdot 10^3 \text{ kg m}^{-3}$ and $\rho_{ice} = 0.91 \cdot 10^3 \text{ kg m}^{-3}$ respectively.

The means \overline{M} and \overline{N} were calculated for the four data sets at t_{12} & t_{23} , at t_{23} & t_{34} , at t_{12} & t_{34} and at t_{12} , t_{23} & t_{34} . Means of B , defined as

$$B = h/C_d^w \quad (22) \quad \text{were calculated from:} \quad B = M/N \quad (23)$$

by replacing M and N in equation (23) with \overline{M} and \overline{N} . Values of \overline{B} , \overline{M} and \overline{N} are presented in Table 1.

5. ACCEPTABILITY OF RESULTS FOR \overline{B} , \overline{M} AND \overline{N}

Results presented in Table 1 indicate that two fully acceptable ratio sets of \overline{B} , \overline{M} and \overline{N} are available for cycle 26a, as well as one for cycle 26b, one for cycle 41 and none for cycle 43. And although the acceptable ratio sets obtained are sufficient for deriving the estimates of h , C_d^a and C_d^w , for three out of the four cycles tested, it is evidently necessary to account for the frequent occurrence of ratio sets or ratios which were either not available or rejected in Table 1.

5.1 Availability of Landsat-1 MSS images

Ratio sets numbers 4.2, 4.3 and 4.4 could not be determined because the Landsat-1 image, required for obtaining the variables V and θ_{ice} for cycle 43 at t_4 , was not available. This might occur in cases where a dense cloud cover prevents identification of ice floes on an image or in cases where floes drift outside the area covered by the corresponding image.

5.2 Ratios rejected by $\overline{\Delta\theta}$

Ratio sets number 2.1, 2.2, 2.3, 3.2, 3.3 and 3.4 were rejected where values of $\overline{\Delta\theta}$, calculated from equation (12) were either less than 0° or greater than 60° . This range of $\overline{\Delta\theta}$ was chosen as the criterion of acceptability for the ratio sets, firstly because corresponding observed data, required for calculating M and N from equations (19) and (20) respectively, were not available for comparison and secondly, because this range, which was determined from observations, is relatively small. The limits of $\overline{\Delta\theta}$ (0° and 60°) were determined from studies by Gordon (1952), Reynolds (1956), Aagaard (1969), Hasse (1974a, 1974b) and Lavrov (1974) conducted over sea surfaces, which have drag coefficients similar to those over pack ice (Roll, 1965) and from studies by Smith et al. (1970), Banke and Smith (1973), Feldman et al. (1979) and Albright (1980) conducted over pack ice.

Data of V and θ_{ice} , used in this study, are considered to be highly accurate, because Landsat-1 MSS images are nearly free of distortions and because the technique employed to obtain these data produces accurate results. Hence, rejection

Table 1: Means of the Ratios, B, M and N

Data Set No.	Cycle No.	Date	Period	\bar{B} m	\bar{M} m	\bar{N}
1.1	26a	23/24 & 24/25.10.73	t_{12} & t_{23}	886.64	638.38	0.72
1.2	26a	24/25 & 25/26.10.73	t_{23} & t_{34}	970.94	980.65	1.01
1.3	26a	23/24 & 25/26.10.73	t_{12} & t_{34}	837.14	795.28	0.95
1.4	26a	23/24, 24/25 & 25/26.10.73	t_{12} , t_{23} & t_{34}	864.02	777.62	0.90
2.1	26b	25/26 & 26/27.10.73	t_{12} & t_{23}	262.46	1225.71	4.67
2.2	26b	26/27 & 27/28.10.73	t_{23} & t_{34}	*	*	*
2.3	26b	25/26 & 27/28.10.73	t_{12} & t_{34}	*	*	*
2.4	26b	25/26, 26/27 & 27/28.10.73	t_{12} , t_{23} & t_{34}	*	*	*
3.1	41	24/25 & 25/26.07.74	t_{12} & t_{23}	156.09	543.19	3.48
3.2	41	25/26 & 26/27.07.74	t_{23} & t_{34}	*	*	*
3.3	41	24/25 & 26/27.07.74	t_{12} & t_{34}	*	*	*
3.4	41	24/25, 25/26 & 26/27.07.74	t_{12} , t_{23} & t_{34}	*	*	*
4.1	43	24/25 & 25/26.08.74	t_{12} & t_{23}	127.10	7945.24	62.51
4.2	43	25/26 & — .08.74	t_{23} & —	(-)	(-)	(-)
4.3	43	24/25 & — .08.74	t_{12} & —	(-)	(-)	(-)
4.4	43	24, 25, 25/26 & — .08.74	t_{12} , t_{23} & —	(-)	(-)	(-)

0.72 Rejected ratios: Where \bar{B} , \bar{M} and \bar{N} are outside the acceptable range.

* Rejected ratios: Where the corresponding value of $\Delta\theta$ is outside the acceptable range.

(-) Ratios not given: Where data on pack ice velocity are not available.

ORIGINAL PAGE 12
OF POOR QUALITY

of a ratio may result either from errors in the variables $\overline{\Delta\gamma}$, ρ_a and U^2 (equations 19 and 20) and/or from errors in $\overline{\Delta\gamma}$ and $\overline{\theta_G}$ (equation 12). And since variations in $\overline{\Delta\gamma}$ (Feldman et al., 1981) and ρ_a are relatively small, and U is linearly related to G (equation 21), it follows that rejection of a ratio set is mainly due to errors in G^2 and/or $\overline{\theta_G}$. Employment of interpolated values of G and $\overline{\theta_G}$, which were needed to replace gaps in the data sequences obtained from the surface weather charts, could be the main source of error.

6. MINIMA AND MAXIMA OF RATIOS BETWEEN OBSERVED ICE PARAMETERS

The second step towards estimating h , C_d^a and C_d^w consisted of determining the observed minima and maxima B_o , M_o and N_o from the observed minima and maxima h_o , C_{do}^a and C_{do}^w , which had previously been measured in the Arctic ocean by other investigators. The ranges of h_o , C_{do}^a and C_{do}^w were summarized by Feldman et al. (1981) as

$$0.00 = h_o \text{ min} \leq h_o \leq h_o \text{ max} = 3.00 \text{ m} \quad (24)$$

$$0.95 = 10^3 C_{do \text{ min}}^a \leq 10^3 C_{do}^a \leq 10^3 C_{do \text{ max}}^a = 4.00 \quad \text{and} \quad (25)$$

$$3.32 = 10^3 C_{do \text{ min}}^w \leq 10^3 C_{do}^w \leq 10^3 C_{do \text{ max}}^w = 57.17 \quad (26)$$

Minima and maxima of B_o , M_o and N_o were determined by replacing h , C_d^a and C_d^w in equations (22), (17) and (18) with the observed minima and maxima of these parameters, given in equations (24), (25) and (26). These were

$$0.00 \leq B_o \leq 903.61 \text{ m} \quad (27)$$

$$0.00 \leq M_o \leq 3157.89 \text{ m} \quad \text{and} \quad (28)$$

$$0.83 \leq N_o \leq 60.18 \quad (29)$$

7. ESTIMATING ICE THICKNESS AND DRAG COEFFICIENTS

The final stage of estimating ice thickness and drag coefficients in the area during the period of study consisted of rewriting equations (22) and (17) for h , using the observed minima C_{do}^w , C_{do}^a and h_o from equations (26), (25) and (24), respectively, and the calculated means \overline{B} and \overline{M} , written as

$$h = C_{do}^w \overline{B} \geq 3.32 \cdot 10^{-3} \overline{B} \text{ m} \quad (30)$$

$$h = C_{do}^a \overline{M} \geq 0.95 \cdot 10^{-3} \overline{M} \text{ m} \quad \text{and} \quad (31)$$

$$h = h_o \geq 0.00 \text{ m} \quad (32)$$

hence

$$h \geq \max. \{3.32 \cdot 10^{-3} \overline{B}, 0.95 \cdot 10^{-3} \overline{M}, 0.00\} = h_{LL} \text{ m} \quad (33)$$

where h_{LL} , the lower limit of h , was given by the maximum (max.) among the three values of h in equation (33). In the same way h_{UL} , the upper limit of h was given by the minimum (min.) among the three values of h in equation (34).

$$h \leq \min. \{57.17 \cdot 10^{-3} \bar{B}, 4.00 \cdot 10^{-3} \bar{M}, 3.00\} = h_{UL} \text{ m} \quad (34)$$

The range of h was defined as

$$h_{LL} \leq h \leq h_{UL} \text{ m} \quad (35)$$

Ranges of h were determined for each data set from equations (33) and (34) with \bar{B} and \bar{M} from Table 1. Results are presented in Table 2.

Ranges of C_d^a and C_d^w were derived from (17) and (22) after replacing M and B by their means and h by its lower and upper limit, written as

$$h_{LL}/\bar{M} \leq C_d^a \leq h_{UL}/\bar{M} \quad (36) \quad \text{and} \quad h_{LL}/\bar{B} \leq C_d^w \leq h_{UL}/\bar{B} \quad (37)$$

Ranges of C_d^a and C_d^w were determined for each data set from equations (36) and (37) respectively with \bar{B} and \bar{M} from Table 1 and h_{LL} and h_{UL} from Table 2. The results were presented in Table 2.

8. EVALUATING THE ESTIMATES OF h , C_d^a AND C_d^w

When the calculated values \bar{B} , \bar{M} and \bar{N} (Table 1) are either less than the corresponding minimum or greater than the corresponding maximum of B_0 , M_0 and N_0 (equations 27, 28 and 29 respectively), then the estimated values of the lower limit of h , C_d^a and C_d^w are greater than the upper limit of these variables. In these cases the results are unacceptable as estimates for h , C_d^a and C_d^w . Hence, the results for cycle 43 in Table 2 were considered unacceptable.

The best results were those obtained for cycles 26b and 41, where \bar{B} , \bar{M} and \bar{N} (Table 1) are either greater than the minimum or less than the maximum of B_0 , M_0 and N_0 (equations 27, 28 and 29 respectively). For the same reasons the results for cycle 26a are partially acceptable (i.e., the results for t_{12} & t_{34} and for t_{12} , t_{23} & t_{34} are acceptable while those for t_{12} & t_{23} and for t_{23} & t_{34} are not).

The calculated values of the ranges of h obtained for cycles 26a and 26b do not agree with those measured at the nearest coastal stations (Table 2). Freeze up along the west coast of the Mackenzie bay occurred about 8 October 1973 (interpreted from Landsat-1 image 1442-20295) and at Tuktoyaktuk, N.W.T. on 9 October 1973 (AES, 1974). Since only 0.25 - 0.50 m of ice could be formed during a period of 2-3 weeks (Pounder, 1965), it was suggested that values of h , measured during cycles 26a and 26b, provide a better approximation to the actual values than the calculated one. The calculated value of h_{LL} for cycle 26b is less than h_{LL} for cycle 26a and provides, therefore, a better estimate for the actual value of h . The calculated values of h for cycle 41 were within the range of values measured at Sachs Harbour, N.W.T. (1.80 m) on 14 June 1974 and at Cape Parry, N.W.T. (1.07 m) on 5 July 1974 (AES, 1974).

Table 2: Estimates of Range and Mean Values of h , C_d^a and C_d^w for the Cycles

Data Set No.	Cycle No.	Date	Period	Thickness, h of Pack Ice and Fast Ice		Drag Coefficient at Surface $10^3 C_d$		at Subsurface $10^3 C_d^w$	
				Range, m	Mean, m	Range	Mean	Range	Mean
1.1	26a	23/24 & 24/25.10.73	t_{12} & t_{23}	2.93-2.55 (0.30-0.35)	2.74 (0.33)	4.58-4.00	4.29	3.32-2.90	3.11
1.2	26a	24/25 & 25/26.10.73	t_{23} & t_{34}	3.23-3.00 (0.30-0.35)	3.12 (0.33)	3.30-3.06	3.18	3.32-3.08	3.20
1.3	26a	23/24 & 25/26.10.73	t_{12} & t_{34}	2.78-3.00 (0.30-0.35)	2.89 (0.33)	3.49-3.77	3.63	3.32-3.59	3.46
1.4	26a	23/24, 24/25 & 25/26.10.73	t_{12}, t_{23} & t_{34}	2.87-3.00 (0.30-0.35)	2.94 (0.33)	3.69-3.86	3.78	3.32-3.47	3.40
2.1	26b	25/26 & 26/27.10.73	t_{12} & t_{23}	1.16-3.00 (0.30-0.35)	2.08 (0.33)	0.95-2.45	1.70	4.44-11.44	7.94
3.1	41	24/25 & 25/26.07.74	t_{12} & t_{23}	0.52-2.17 (1.07-1.80)	1.35 (1.44)	0.95-4.00	2.48	3.32-13.93	8.63
4.1	43	24/25 & 25/26.08.74	t_{12} & t_{23}	7.55-3.00 (--- - ---)	5.28 (---)	0.95-0.38	0.67	59.39-23.60	41.50

4.58 Rejected estimates, where their values are outside the corresponding observed ranges, h_o , C_{do}^a & C_{do}^w .
(0.30) Thickness of fast ice, measured at nearest coastal stations (AES, 1974)

9. CONCLUSIONS

It has been demonstrated that ice thickness and drag coefficients, associated with drifting open pack ice and vital for predicting its motions, which are not routinely available for the polar oceans, can be estimated from three-day sequences of satellite images and wind field data. Unfortunately, the method used could not be tested by a larger number of data sequences, since Landsat-1 has an 18 day repeat cycle and data recorded on cloudy days are useless.

Images recorded by weather satellites, within the visible or the thermal infrared regions of the electromagnetic spectrum were considered for application to this study. They were rejected because their images are geometrically distorted and have a relatively low resolution.

It is recommended that for a routine application of this method an all weather air or spaceborne remote sensing system, producing high geometric fidelity and high resolution images, should be employed.

10. ACKNOWLEDGEMENTS

The author would like to thank P.J. Howarth and J.A. Davies for their counsel during the preparation of the manuscript, to M.G. Sonis for his helpful comments and to Z. Drezner for his aid with the calculations. This work was supported by the Natural Science and Engineering Research Council, Canada and the Research Directorate, Atmospheric Environment Service, Canada.

11. REFERENCES

- Aagaard, K., 1969: Relationship between geostrophic and surface winds at weather ship M. J. Geophys. Res., 74, 3440-3442.
- AES, 1974: Ice thickness data for Canadian selected stations, freeze-up 1973 - break-up 1974. ICE 1-74. Atmos. Environ. Serv., Ottawa, Ont.
- Albright, M., 1980: Geostrophic wind calculations for AIDJEX. Sea Ice Processes and Models, 402-409, Univ. of Wash. Press, Seattle, WA.
- Banke, E.G. and S.D. Smith, 1973: Wind stress on arctic sea ice. J. Geophys. Res., 78, 7871-7883.
- Campbell, W.J., 1965: The wind driven circulation of ice and water in a polar ocean. J. Geophys. Res., 70, 3279-3301.
- Crowder, W.K., H.L. McKin, S.F. Ackley, W.D. Hibler III and D.M. Anderson, 1973: Mesoscale deformation of sea ice from satellite imagery. Advanced Concepts and Techniques in the Study of Snow and Ice Resources, 563-573, Nat. Acad. Sci., Washington, DC.
- Feldman, U. and P.J. Howarth, 1979: Predicting the motions of drifting open pack ice. J. Glaciol., 24, 501-502.
- Feldman, U., P.J. Howarth and J.A. Davies, 1979: Estimating the surface wind speed over drifting pack ice from surface weather charts. Boundary Layer Meteorol., 16, 421-428.
- Feldman, U., P.J. Howarth and J.A. Davies, 1981: Estimating surface wind direction over drifting open pack ice. J. Geophys. Res., 86, 8117-8120.

- Fel'zenbaum, A.I., 1958: The theory of steady drift of ice and the calculation of the long period drift in the central part of the Arctic basin. *Problemy Severa*, 2, 16-46. Translated from Russian in *Problems of the North*, 1961, 2, 13-44.
- Gordon, A.H., 1952: The relationship between the mean vector surface wind and the mean pressure gradient over the oceans. *Geofisica Pura e Applicata*, 21, 49-51.
- Hasse, L., 1974a: Note on the surface to geostrophic wind relationship from observations in the German bight. *Boundary Layer Meteorol.*, 6, 197-201.
- Hasse, L., 1974b: On the surface to geostrophic wind relationship at sea and the stability dependence of the resistance law. *Contrib. Atmos. Phys.*, 47, 45-55.
- Hibler, W.D. III, S.F. Ackley, W.K. Crowder, H.L. McKim and D.M. Anderson, 1974: Analysis of shear zone ice deformation in the Beaufort sea using satellite imagery. *The Coast and Shelf of the Beaufort Sea*, 285-296, Arctic Instit. N. Am., Arlington, VA.
- Hibler, W.D. III, 1979: A dynamic thermodynamic sea ice model. *J. Phys. Oceanogr.*, 9, 815-846.
- Hibler, W.D. III and W.B. Tucker III, 1979: Some results from a linear-viscous model of the Arctic ice cover. *J. Glaciol.*, 22, 293-304.
- Johannessen, O.M., 1970: Note on some vertical current profiles below ice floes in the gulf of St. Lawrence and near the North Pole. *J. Geophys. Res.*, 75, 2857-2862.
- Lavrov, N.A., 1974: Analysis of experimental data on the wind on the Baltic sea. *Meteorologiya i Gidrologiya*, 10, 102-104. Translated from Russian in *Meteorol. and Hydrol.*, 1974, 10, 130-133.
- McPhee, M.G., 1980: An analysis of pack ice drift in summer. *Sea Ice Processes and Models*, 62-75, Univ. of Wash. Press, Seattle, WA.
- McPhee, M.G., 1982: Sea ice drag laws and simple boundary layer concepts, including application to rapid melting. CRREL, Hanover, NH.
- Nansen, F., 1902: The currents of the north polar basin and the influence of the wind upon the drift of the north polar ice. *The Norwegian North Polar Expedition 1893-1896, Scientific Results*, Vol. 3, 357-386, Longmans, Green and Co., London, UK.
- Neralla, V.R., W.S. Liu, S. Venkatesh and M.B. Danard, 1980: Techniques for predicting sea ice motion. *Sea Ice Processes and Models*, 197-206, Univ. of Wash. Press, Seattle, WA.
- Newton, J.L., 1973: The Canada basin, mean circulation and intermediate scale flow features. Ph.D. thesis, Univ. of Wash., Seattle, WA.
- Nye, J.F. and D.R. Thomas, 1974: The use of satellite photographs to give the movement and deformation of sea ice. *AIDJEX Bull.*, 27, 1-21.
- Nye, J.F., 1975: The use of ERTS photographs to measure the movement and deformation of sea ice. *J. Glaciol.*, 15, 429-436.
- Pounder, E.R., 1965: *The Physics of Ice*. Pergamon Press, Oxford, UK.
- Reynolds, G., 1956: A wind analysis for the Northern Irish sea. *Quart. J. Roy. Meteorol. Soc.*, 82, 469-480.
- Roll, H.U., 1965: *Physics of the Marine Atmosphere*. Academic Press, New York, NY.
- Shuleikin, V.V., 1938: The drift of ice fields. *Comptes-Rendus (Doklady) de l'Academie des Sciences de l'URSS*, 19, 589-594.
- Smith, S.D., E.G. Banke and O.M. Johannessen, 1970: Wind stress and turbulence over ice in the gulf of St. Lawrence. *J. Geophys. Res.*, 75, 2803-2812.

- Sobczak, L.W., 1977: Ice movements in the Beaufort sea 1973-1975, determination by ERTS imagery. J. Geophys. Res., 82, 1413-1418.
- Sverdrup, H.U., 1928: The wind-drift of the ice on the north Siberian shelf. The Norwegian North Polar Expedition with the "Maud" 1918-1925, Scientific Results, Vol. 4, 1-46, John Grieg, Bergen, Norway.
- Thorndike, A.S., 1973: An integrated system for measuring ice motions. Ocean 73, 490-499. IEEE, New York, NY.
- Wendler, G. and K.C.L. F. Jayaweera, 1974: A technique to obtain ice movement. J. Geophys. Res., 79, 3478-3479.

OBSERVATIONS OF SEA ICE AND ICEBERGS FROM SATELLITE RADAR ALTIMETERS

C. G. Rapley,
Mullard Space Science Laboratory,
Department of Physics & Astronomy,
University College London,
Holmbury St. Mary,
Dorking, Surrey,
England

ABSTRACT

Satellite radar altimeters can make useful contributions to the study of sea ice both by enhancing observations from other instruments and by providing a unique probe of ocean-ice interaction in the Marginal Ice Zone (MIZ). The problems, results and future potential of such observations are discussed.

1. INTRODUCTION

Sea ice plays an important role in influencing high latitude weather and global climate through its effect on the ocean surface albedo and its modulation of exchanges of heat, moisture and momentum at the ocean-atmosphere interface. Systematic changes in sea ice extent may provide the first indications of climatic change. Indeed, the creation of an ice-free Arctic ocean may be one of the early dramatic consequences of even a modest atmospheric warming. Thus, global synoptic observations of the properties and behaviour of sea ice are of considerable importance to climatological research as well as being of direct interest to glaciologists and oceanographers. With growing activity in the exploitation of polar resources the applications value of the data is also significant.

However the geographic zones in which sea ice is to be found are extensive, remote and inhospitable. They experience long periods of darkness, and may often be cloud-covered. The advent of polar orbiting satellites carrying microwave instrumentation capable of making observations under any weather conditions and during the day or night thus represents a breakthrough in our ability to carry out global sea ice studies.

Until recently work has concentrated on the use of passive microwave radiometer systems to map the annual cycle and inter-annual variability of sea ice extent, concentration and type with rather coarse (30-100 km) spatial resolution (e.g. Svendsen et al., 1983). Studies of ice dynamics within certain selected areas have been carried out using high resolution (~25m) images from the Seasat Synthetic Aperture Radar (Leberl et al., 1983). However radar altimeter data gathered over sea ice by both GEOS-3 and Seasat have received comparatively little attention. This is surprising in view of the likelihood that the altimeter pulse waveforms contain useful, possibly unique, information on the nature of the ice pack. Also several studies based on airborne observations have indicated that improved discrimination of ice type under a wider variety of conditions of temperature and

surface state (melting/freezing, snow cover etc.) can be obtained by combining both active and passive microwave data (e.g. Livingstone et al., 1981).

In this paper we review the problems, results and potential of sea ice observations using pulse-limited altimeters, and identify several areas in which further research effort is urgently needed. We consider the likely impact of observations to be made from ESA's first remote sensing satellite ERS-1 and other forthcoming or proposed missions. Finally, we speculate on long term possibilities including the development of advanced beam-limited, multi-satellite systems.

2. OBSERVATIONAL OBJECTIVES

A comprehensive account of current priorities in ice research has recently been published by the US National Research Council (Polar Research Board, 1983). Here we shall restrict ourselves to considering those observational properties of sea ice which might be measurable using satellite altimeters, either alone or in combination with data from other microwave sensors. These include:-

- (i) Extent (defined as the zone with greater than 10-15% sea ice concentration)
- (ii) Concentration
- (iii) Floe size distribution
- (iv) Presence of major leads, polynyas
- (v) Type/Fraction
- (vi) Average freeboard
- (vii) Surface roughness (presence of pressure ridges)
- (viii) Surface condition (presence of snow, melt ponds)
- (ix) Sea state within pack
- (x) Sea state and surface wind speed adjacent to pack
- (xi) Iceberg concentrations, size distributions
- (xii) Antarctic tabular iceberg locations

Currently only (x) may be considered a demonstrated capability, with (i), (iv), and (ix) showing considerable promise as discussed below in section (5). All the remaining possibilities are more speculative, requiring further research (cf. section (6)).

3. SAMPLING AND COVERAGE

Significant variations of all the parameters listed in section (2) may take place locally on short (<1day) timescales. Thus temporal and spatial sampling requirements are an important consideration.

Figure 1 shows the Seasat ground track pattern in the vicinity of Antarctica at a time when the orbit was adjusted to repeat with a three day cycle. The Seasat orbital period was 100 minutes, giving 14.3 revolutions each day and 43 contiguous ground tracks over the full 3-day repeat cycle. Ground tracks in the figure are numbered according to a scheme in which the ascending node of rev 1 lies just east of Borneo. Also shown are the Antarctic coastline and the approximate location of the sea ice boundary at maximum winter extent. If it is assumed that at an arbitrary time of the year the sea ice limit lies approximately along a circle of latitude, the average spatial sampling interval at the boundary is given by:-

$$\Delta l = \frac{2\pi R \cos \theta}{\sin \alpha} \quad (1)$$

where θ is the latitude (>55), n is the number of revolutions in the cycle, R is the Earth's radius (~ 6360 km), and $1 < \alpha < 2$ depending on the disposition of the ice boundary with respect to the ground track pattern. Hence for the worst case, corresponding to the maximum winter extent and $\alpha = 1$, we have $\Delta l \sim 1700$ km for 1 day's data and $\Delta l \sim 450$ km for the full three day cycle. With a beam limited footprint of ~ 20 km and an ability to locate the ice boundary to much higher precision (cf. section 5) the altimeter spatial data is therefore severely undersampled.

Even so, the improved measurement precision relative to the passive microwave data is often referred to as a novel contribution of the altimeter to ice boundary monitoring. In practice it is difficult to take full advantage of this capability, since significant ice motion can take place on timescales short compared with the temporal sampling period. For example the average change in Antarctic ice boundary location at the time of maximum ice growth or decay may be ~ 10 km d^{-1} and localised variations of up to 50 km d^{-1} can take place at any time in response to storms. Thus for data collected on a 3-day repeat cycle spatial smoothing to ~ 30 km resolution is necessary in order to achieve some degree of self consistency. Although experience shows that even then inconsistencies in the boundary location can still occur. Since the ice boundary motion in a given region is rarely monotonic on timescales of order three days, interpolation schemes dealing separately with each ground track over several repeat cycles do not help.

ORIGINAL PAGE IS
OF POOR QUALITY

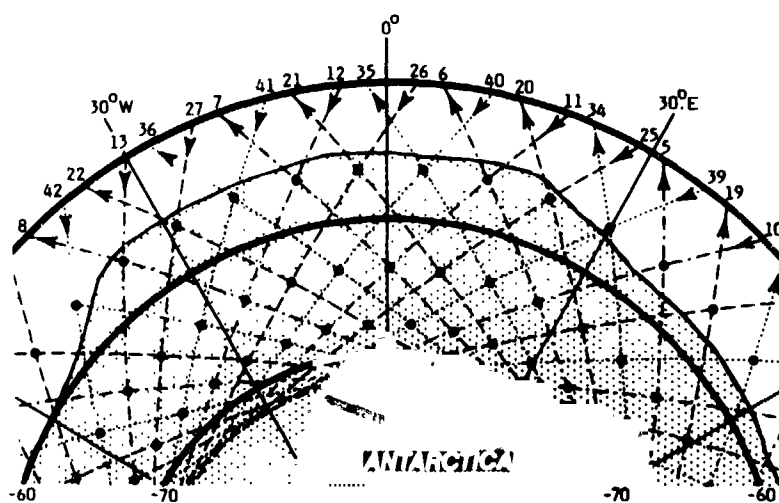


Figure 1: Seasat ground tracks in the vicinity of Antarctica for a 3-day orbit repeat cycle. Also shown are the Antarctic continent (dark dot) and the region covered by sea ice at the time of maximum winter extent (light dot).

Any attempt to overcome the temporal sampling problem by decreasing the period of the orbital repeat cycle merely worsens the degree of spatial undersampling. At the limit of a 1-day repeat cycle, smoothing to ~10 km resolution would be necessary to obtain reasonably self-consistent global sea ice maps (this may actually be quite acceptable since the ice edge is often difficult to define to better than ~10km) and sampling would be ~1700 km at the ice boundary. The inevitable conclusion is that a multi-satellite system is required if improved ice monitoring is to be achieved. For example a system of 5 satellites with orbits phased to provide the equivalent of five-day repeat cycle coverage each day would achieve usable ~10 km precision and 150-300 km spatial sampling (75 points) around the Antarctic ice boundary at maximum extent. (Note that for a single-satellite system a 3-day repeat cycle appears to be a near-optimum compromise.)

When considering the selection of orbital parameters the required latitude coverage must also be taken into account. For a nadir pointing, narrow swath instrument this is determined purely by the inclination of the satellite orbit. A low inclination is preferred for oceanographic missions in order to obtain approximately orthogonal ground track intersections over much of the globe since this is helpful in computing orbit error corrections. However an inclination of ~85° is necessary to achieve full coverage of Antarctic sea ice, and 90° is required if Arctic ice in the vicinity of the pole is not to be missed. (Note that for a 90° inclination orbit no ground track intersections occur except at the poles.) Once again it would appear that a multi-satellite system offers the only prospect of satisfying the conflicting requirements.

4. ALTIMETER OPERATION OVER SEA ICE

The action of a radar altimeter over a flat, horizontal, statistically homogeneous, rough surface such as the ocean surface is well understood. Two modes of operation are possible, the pulse limited mode and the beam limited mode (see Rapley et al., 1983). In the former case the use of a relatively broad beam results in an echo waveform with a time profile which corresponds to the height probability density function (pdf) of surface scatterers. Range estimates are made by timing to the 50% power point on the leading edge of the return pulse. For beam limited operation a narrow beam antenna is used and the echo waveform corresponds directly to the height pdf of scatterers. Range estimates are made to the 'centre of gravity' of the waveform. In both cases the use of an (effectively) short duration (~ nsec) transmitted pulse permits estimation of large (metre) scale surface roughness from detailed analysis of the waveform shape. Also the echo strength is related to the small scale (of order λ) surface roughness which for the ocean is determined by the surface wind.

Operation over a rough, flat surface which is not statistically homogeneous introduces certain fundamental difficulties. Firstly, the return waveform contains no information on the azimuthal direction of scatterers about the nadir. Also there exists an ambiguity between the height of a point scatterer relative to the mean surface and its radial distance from the nadir. Consequently it is impossible to unambiguously reconstruct surface details within the footprint from an analysis of individual waveforms. Furthermore, 'average' properties of the surface derived from individual echoes will be strongly biased by any highly reflecting zones within the beam limited footprint (BLF), particularly those with slant ranges similar in value to the vertical range to the nadir point. Even the additional information provided by systematic changes in waveform shape as a surface feature is traversed permit reconstruction of only very simple geometries such as discrete height transition or a single highly reflective point located at a known height or distance off-nadir.

Under these circumstances the beam limited mode offers some advantage since the potential for confusion is reduced by limiting the area from which echo signals can be received. Also the surface area sampled remains fixed in size, in contrast to the pulse limited case where it varies with surface roughness. However beam limited operation requires a large (>10m) antenna and a high-precision spacecraft pointing system, both of which imply greater cost. For this reason and because pulse limited operation is satisfactory for ocean observations, past and planned missions have adopted the pulse limited mode of operation exclusively.

Other problems are encountered when sea ice waveforms are presented to an altimeter's on-board processor. This unit carries out a number of functions including the summation of many individual return pulses in phase to reduce noise fluctuations, the tracking of the surface as range values vary, and the adjustment of the receiver gain to compensate for signal strength variations. It may also generate estimates of geophysical parameters such as mean surface height, roughness and backscatter coefficient for rapid dissemination and analysis on the ground. In executing these tasks the algorithms employed generally assume a standard ocean form for the pulse shape and are set up to accommodate only relatively slow variations in time. Over sea ice we may identify three areas of difficulty as follows:-

(i) Shape induced errors: The non-standard shapes of the return waveforms introduce systematic offsets of the range tracking point. For a peaked time profile typical of sea ice returns, the tracking point is displaced early where it becomes more susceptible to statistical noise. Tracker jitter is thus increased.

(ii) Dynamic lags and pulse blurring: Rapid variations of the return pulse shapes and strengths occur on timescales too short for the altimeter to follow. Dynamic lags are introduced and may be exacerbated by interaction amongst the processing loops. Resulting errors in the superposition of summed pulses will introduce 'blurring' of intrinsic pulse shapes.

(iii) 'Snagging': When passing over a transition from high to low reflectivity, the range tracker may remain locked on to the receding bright feature. Generally, after a modest excursion, the tracker recovers since the reflectivity of the feature decays rapidly as it is viewed increasingly far from normal incidence. Sometimes, however, the excursion may be sufficiently large to cause loss of track. Loop interactions cause all computed outputs to be in error during excursions. Note that the shortening of time constants to reduce dynamic lags will increase susceptibility to 'snagging'.

From the preceding discussion we may draw three broad conclusions:-

(a) The performance of an altimeter over sea ice will be less stable than over the ocean.

(b) On-board computed parameters suffer increased systematic and random errors, making ground analysis of the waveforms mandatory if the full potential of the data is to be obtained. The waveform data will be partly corrupted by blurring.

(c) Even with analysis of the waveform data there exists a fundamental limit on the spatial resolution achievable for all but the simplest of surface features. In general this corresponds to the beam limited footprint (~20 km) although transitions in surface properties might be located to 1/10 of this value.

ORIGINAL PAGE IS
OF POOR QUALITY

5. RESULTS FROM GEOS-3 AND SEASAT

Both GEOS-3 (inclination 65°) and Seasat (inclination 72°) carried pulse limited altimeters and obtained data over sea ice. Returns from first year ice were observed to be strongly peaked intense (peak power at least $\times 10$ that of ocean returns) and highly variable. Much deeper within the pack, possibly over multi-year ice or ice with a high concentration, return strengths could be as much as 8dB lower than for ocean returns. Brown (1982) has developed a model for near-normal incidence microwave scattering from first year ice which explains the main features observed in the GEOS-3 data. He suggests that the return waveform is dominated by power reflected from a population of smooth ice platelets all at the same height within the pack, corresponding to calm water or thin, smooth ice between the floes. The rapid fluctuations of the echo strength correspond to variations in the number of flat areas within the first few Fresnel zones as the footprint progresses across the pack. Robin, Drewry and Squire (1983), on the basis of a study of Seasat sea ice waveforms support Brown's general concept, pointing out that this may be described as a 'glistening' surface. They note that even if as little as 0.01% of the surface area contributes to the glistening component, it will dominate the diffuse echo from the tops of the floes.

Consequently we might expect the contrast in backscattering properties of first year ice and open water to provide a reliable means of locating the sea ice boundary. Dwyer and Godin (1980) exploited this technique using GEOS-3 data over the Bering sea, and carried out comparisons with cloud-free visible and infra-red images obtained from the DMSP satellites and TIROS-N. They were able to establish an 'ice index' which provided ice boundary discrimination in consistent agreement with the image data to an accuracy of a few km. They also noted qualitative correlations between their ice index and ice concentration and ice type, but did not pursue this result further.

Other uses of signal strength data have been as a means to eliminate 'ice-contaminated' results from ocean data (Marshall and Martin, 1982) and as a means to locate the Antarctic ice boundary and its variations over four of Seasat's 3-day repeat cycles in an analysis by Rapley (1984) described below (cf. Figure 2). However further intercomparisons of altimeter-deduced boundaries and estimates obtained independently by other means are certainly needed to validate properly the technique. For example, it is not at all clear that a criterion established for the location of first year ice boundaries will operate satisfactorily with multi-year ice or in regions where the ice concentration reaches a high value close to the ice edge.

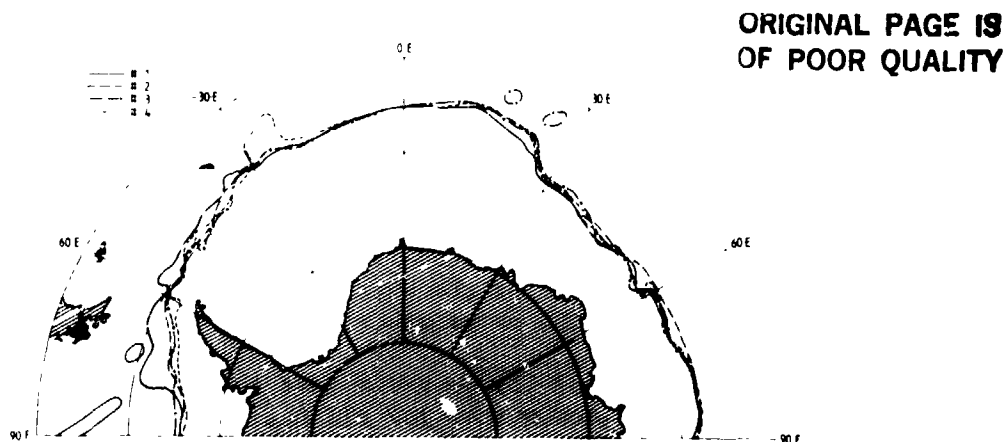
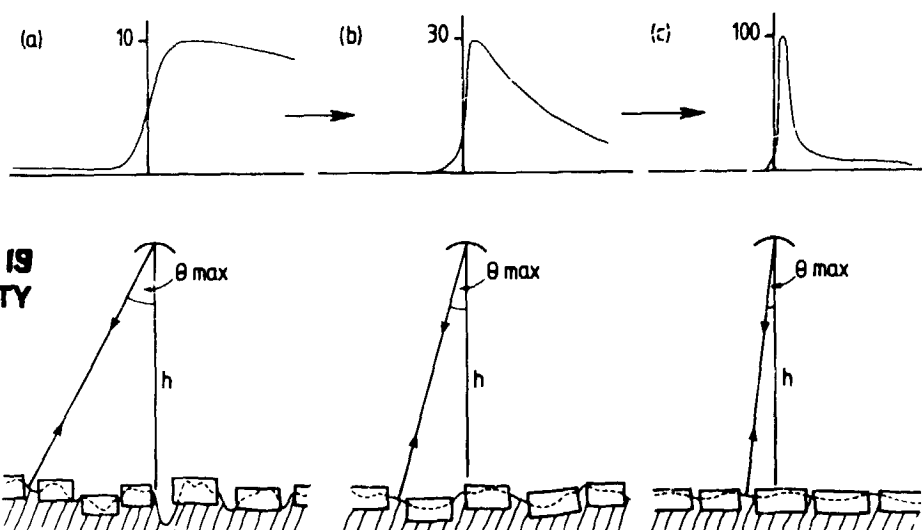


Figure 2: The Antarctic sea ice boundary and its variation over four of Seasat's 3-day repeat cycles as deduced from return echo strength (AGC) data (from Rapley, 1984).



ORIGINAL PAGE IS
OF POOR QUALITY

Figure 3: The evolution of waveform shape and strength as a function of increasing distance into the ice pack. Pulse falltimes are determined by the distribution of surface slopes as shown schematically in the lower panels. Pulse shape and strength change as ocean waves and swell are damped out by the action of ice floes within the pack.

Although ice boundary location is certainly a useful capability of the altimeter, the sampling problems discussed earlier make it clear that the altimeter data are unlikely to compete with the fully sampled global maps available from passive microwave imaging instruments such as the SMMR flown on NIMBUS-7. However a recent investigation by Rapley (1984) suggests that the altimeter can make a unique contribution to studies of the Marginal Ice Zone (MIZ) by monitoring the propagation of ocean swells within the ice. Figure 3 shows the typical evolution of return waveform shapes as the altimeter progresses from the ice edge into the pack. Initially the waveform is stronger but is of similar shape to nearby ocean returns. Subsequently the waveforms become increasingly peaked. Extending the concepts put forward by Brown and Robin, Drewry and Squire (as discussed above) Rapley suggests that the return pulse falltimes depend on the probability distribution of ocean surface slopes between the floes, as shown in the lower panels of Figure 3. The attenuation of ocean swell components by the floes is known to be exponential with an attenuation coefficient which depends strongly on the ice thickness and swell wavelength (e.g. see Squire and Moore, 1960). Thus an analysis of pulse falltimes using a modelled response could provide quantitative results from which estimates of ice and swell properties might be deduced. Such an analysis has not yet been completed. However the on-board computed values of Significant Wave Height (SWH) from the Seasat altimeter provide a crude measure of pulse peakiness and hence of ocean surface flatness amongst the floes. Figure 4 shows the behaviour of zones of apparent swell penetration within the Antarctic sea ice. The power of the altimeter to pursue this type of study is emphasised by its ability to monitor ocean swells in the vicinity of the ice using wind speed and sea state data and the method of Mognard (1983). Spatial and temporal correlations between the extent of the penetration zone and the presence of nearby ocean swell storms provide qualitative support for the suggestion that swell propagation is being monitored. Nevertheless, a more quantitative analysis modelling the Seasat waveform data is needed, as are comparisons of altimeter data with surface verification results, before the technique can be regarded as fully validated.

ORIGINAL PAGE IS
OF POOR QUALITY

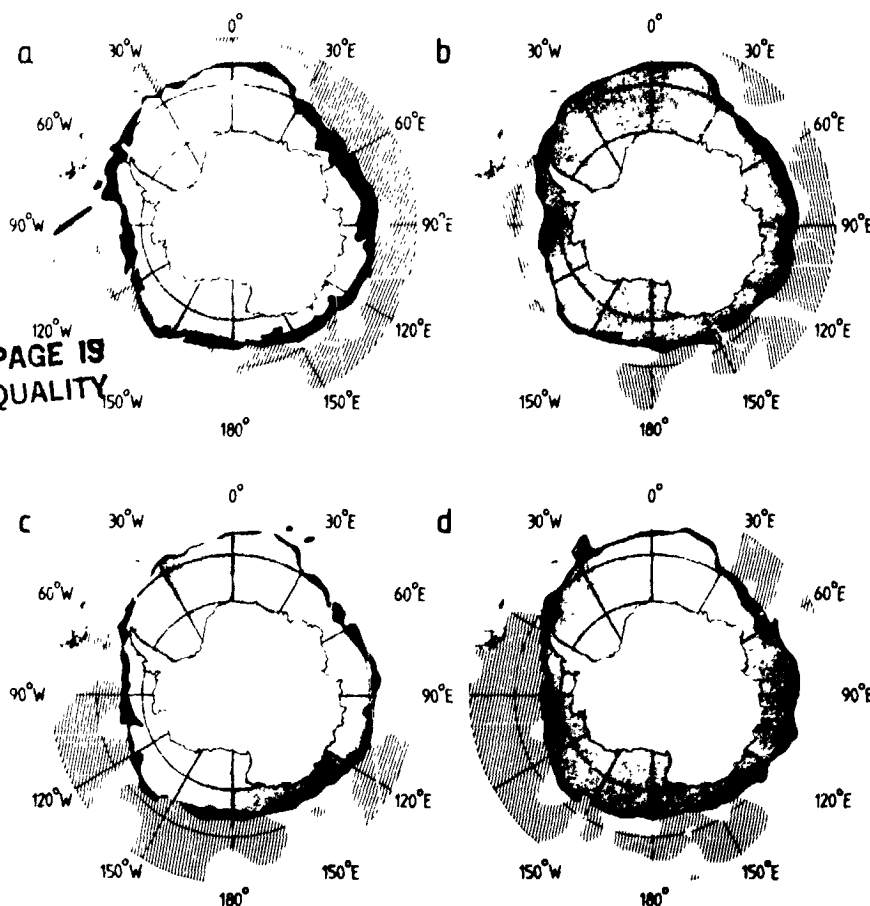


Figure 4: Four consecutive 3-day maps of Antarctic sea ice (shaded areas) and regions of ocean swell greater than 5m (cross-hatched areas) during September 1978. Zones of swell penetration into the ice (solid areas) derived from the Seasat SWH data contract and expand with the decline and subsequent growth of nearby ocean swell storms.

6. ADDITIONAL POSSIBILITIES

Of the observational objectives outlined in section (2) only the location of the ice boundary (and by analogy the presence of major leads and polynyas) and measurements of sea state adjacent to and within the MIZ have been addressed using actual satellite data. It has been stressed that even these capabilities require further validation. There is reason to believe that further studies of pulse strengths and shapes and the variability of both may permit others of the objectives to be achieved. However, the difficulty of obtaining adequate surface verification results for much of the GEOS-3 and Seasat data suggests that significant progress in these areas probably awaits future aircraft and satellite observations.

One area in which the usefulness of altimeter contributions seems dubious is that of providing locations of Antarctic tabular icebergs. Large icebergs may drift for many years in the Southern Ocean and have been monitored, albeit intermittently using visible and infrared images (e.g. McLain, 1978). In view of the small

likelihood of such an iceberg passing through the altimeter footprint it seems unreasonable to consider iceberg location as a major altimeter task. Nevertheless if such an event did occur and the altimeter locked on to the upper surface it would be possible to provide an accurate value for the iceberg's freeboard.

7. FORTHCOMING MISSIONS

In spite of wide interest in the use of altimeter data by climatological, oceanographic and glaciological scientists worldwide, the first satellite to carry an altimeter for non-military purposes following the early demise of Seasat in 1978 will be the European Space Agency's ERS-1 to be launched in 1988. The instrument will be very similar to the Seasat altimeter but will provide coverage up to $\pm 82^\circ$ with a lifetime initially of 2 years, extendible to 3 or more depending on spacecraft and instrument status. Thus full coverage of Antarctic sea ice and much improved coverage over the Arctic will be obtained for the first time over two full seasonal cycles. Plans are currently being formulated to ensure that adequate surface validation data including aircraft altimeter underflights will be obtained during the mission.

Other altimeter carrying satellites include the US Navy's GEOSAT due for launch in 1984 but with the possibility of restrictions on data access, the proposed US-French TOPEX mission and the French Poseidon, both likely to fly at the end of the decade. However TOPEX is primarily an ocean mission and will most probably be restricted to $\pm 62^\circ$ coverage. It will therefore not observe sea ice. Possibilities for the next decade include the provision of a UK altimeter for the Canadian Radarsat satellite, and a Japanese national mission. As yet no serious attempts have been made to coordinate international interest to achieve either the multi-satellite coverage discussed earlier in section 3 or continuity of observations over an extended period of many years, although coordination of this type would clearly be very beneficial.

As a final comment, it is worth recalling that the interpretation of altimeter waveform data over sea ice should be more straightforward for the case of beam-limited operation than for the currently universal pulse-limited mode. Interest in building a multi-beam, beam-limited instrument arises primarily from a desire to achieve much improved performance over topographic surfaces such as the continental ice sheets and land. Thus it seems likely that in the long term the technical and financial challenges of building instruments of this type will be tackled. Whether or not the advantages of a beam limited system will make a substantial impact on sea ice studies is currently impossible to predict without the benefit of considerable further effort on the analysis and interpretation of current and anticipated pulse limited data.

ORIGINAL PAGE IS
OF POOR QUALITY

8. REFERENCES

- Brown, G.S., 1982: Radio Sci., 17, 233-243.
- Dwyer, R.E. and Godin, R.H., 1980: NASA Contract Report, 156862.
- Leberl, F., Raggam, J., Elachi, C. and Campbell, W.J., 1983: J. Geophys. Res., 88, 1915.
- Livingstone, C.E., Hawkins, R.K., Gray, A.L., Arsenault, L.D., Oramoto, K., Wilkinson, T.L. and Pearson, D., 1981: CCRS Technical Report.
- Marsh, J.G., and Martin, T.V., 1982: J. Geophys. Res., 87, 3269-3280.
- McLain, E.P., 1978: Mariners' Weather Log, 22, 328-333.
- Mognard, N.M., 1983: in Satellite Microwave Remote Sensing, ed. T.D. Allan, Ellis Horwood Ltd., 425-438.
- Polar Research Board, 1983: "Snow and Ice Research, an assessment", Nat. Academy Press, Washington, DC.
- Rapley, C.G., Griffiths, H.D. Squire, V.A. Lefebvre, M., Birks, A.R. and 18 co-authors, 1983: ESA Contract Report, 5182/82/F/CG(SC).
- Rapley, C.G., 1984: Nature, 307, 150-152.
- Robin, G. de Q., Drewry, D.J. and Squire, V.A., 1983: Phil. Trans. R. Soc., A309, 447-463.
- Squire, V.A. and Moore, S.C., 1980: Nature, 283, 365-368.
- Svendsen, E., Kloster, K., Farrelly, B., Johannessen, O.M., Johannessen, J.A., Campbell, W.J., Gloersen, P., Cavalieri, D. and Matzler, C., 1983: J. Geophys. Res., 88, 2781.

SIMULATION AND ASSIMILATION OF SATELLITE ALTIMETER DATA AT THE OCEANIC
MESOSCALE

Pierre De Mey and Allan R. Robinson
Center for Earth and Planetary Physics
Harvard University, Cambridge, MA, 02138, USA

ABSTRACT

An improved Objective Analysis technique (Gandin, 1963) is used along with an altimeter signal statistical model, an altimeter noise statistical model, an orbital model, and synoptic surface current maps in the POLYMODE-SDE area, to evaluate the performance of various observational strategies in catching the mesoscale variability at mid-latitudes. In particular, simulated repetitive nominal orbits of ERS-1, TOPEX, and SPOT/POSEIDON are examined. Our statistical models are consistent with previous in-situ and remote-sensed results (Fu, 1983). Our own results show the critical importance of the existence of a subcycle, scanning in either direction. Moreover, long repeat cycles (>20 days) and short cross-track distances (<300 km) seem preferable, since they match mesoscale statistics. Another goal of our study is to prepare and discuss Sea-Surface Height assimilation in quasigeostrophic models. Our restored SSH maps are shown to meet that purpose, if an efficient extrapolation method or deep in-situ data (floats) are used on the vertical to start and update the model.

1. INTRODUCTION

Active and passive satellite-flown sensors have been extensively shown to open new perspectives in geophysical sciences; in particular, the altimeters of GEOS 3 and SEASAT are helping us in the study of the dynamics of mesoscale ocean currents. New products are now available, such as wavenumber spectra (Fu, 1983; Menard, 1983) or global maps of the statistics of the variability (Douglas et al., 1983; Cheney et al., 1983), and sample synoptic maps (Robinson et al., 1983) of which oceanographers have to take advantage. Three further altimeter missions which are currently planned include the European ERS-1, the American TOPEX, and the French SPOT (POSEIDON experiment). There are many ways to evaluate the altimeter missions of these satellites, and many parameters to optimize.

The direct measurement of sea surface height is an achievement of great scientific importance and the coverage provided by a satellite data base is unique in its space-time extent and along-track density. However, now and in the conceivable future, such data will be available only during a very few costly special missions. Moreover, a shortcoming of remotely sensed data to the deep sea oceanographer is the fact that only surface variables are measured. Thus every effort must be made to plan sampling strategies and analysis schemes to optimize the scientific utility of the observations. We are engaged in research to address several relevant questions along these lines. Our approach involves simulating the acquisition and analysis of altimetric data sets by performing operations on four-dimensional oceanic or oceanic-like fields. These fields are obtained by either i) combining existing real ocean data obtained from various in situ instruments or ii) using existing observations to drive a numerical ocean model (Robinson, 1984). In the first case we fly a simulated altimeter over historical data and in the second case we fly a simulated altimeter over simulated data. In our analysis we include the quantitative

investigation of the construction of deep ocean fields combined from both remotely sensed and in situ observations. Finally we mention our research on the assimilation of such observed fields in dynamical ocean models (Robinson & Leslie, 1984; Robinson et.al., 1984) for initialization and verification purposes and for dynamical interpolations and optimal estimates.

Here we describe preliminary experiments; firstly of observational network evaluation, i.e. optimization of sampling, in order to improve mesoscale mapping and statistics (Section 3), and secondly the construction of current maps (Sections 2 and 3) for the assimilation of the sea-surface height information in our quasigeostrophic model (Section 4).

2. SATELLITE ALTIMETER SIMULATIONS IN THE POLYMODE AREA

In order to sample Sea Surface Height (SSH) data as a satellite would do, an orbital model is needed. The requirements on this model are not very severe, since we only want to infer statistical conclusions on the coverage, and get synoptic mid-ocean maps of SSH. A simple circular orbit model has been used, along with accurate orbital parameters of future missions (ERS-1, TOPEX, SPOT). No atmospheric drag is involved. The repeat cycle, cross-track distance, inclination angle, and subcycles are adequately modelled. The numerical clock is accurate to 1 sec for more than 1 year, in order to ensure exact repetitiveness during long simulations. The altitude calculated by the model is accurate to 1%.

Linear optimal estimation is used to restore SSH maps. This is an 'intelligent' interpolation method, whose estimator is statistically data-adaptive. It allows the integration of other remote-sensed and in situ measurements, and is consistent with the data assimilation techniques currently in use at Harvard (e.g. Tu, 1981; Robinson, 1983). The estimation method is a space-time extension of the Gandin (1963) Objective Analysis method. Phase propagation is built into the signal correlation model. A limited set of influential points is selected at each interpolation point (Carter, 1983). An improved algorithm eliminates data points which are more correlated to each other than to the interpolation point. The need for such a stringent selection arises from the one-dimensional nature of the data.

Restored SSH maps can be used for operational system assessment, which is inferred from error estimates provided by Objective Analysis (see Section 3) or by initializing and updating the Harvard quasi-geostrophic baroclinic model (see Section 4).

We have used two different data sets to represent sea-truth. The first is a 1000 km simulation generated by the Harvard model using regionally tuned statistics in the POLYMODE-SDE region. The second sea-truth we have chosen is the 100 dbar level of the POLYMODE-SDE Mark II data set produced at Harvard. An interpolation scheme, similar to the one described above, has been used to combine POLYMODE-SDE Soviet current-meter moorings (1400-700 dbar) and XBTs (400-100 dbar), from Julian day 3345 (July 21, 1977) through Julian day 3725 (August 5, 1978). A mean salinity profile has been used to compute shallow geostrophic velocities relative to the 700 dbar absolute velocity level. The grid has 281.25 km long sides and is centered on 29.00 N, 70.00 W.

SSH is sampled from the sea-truth along arcs given by the orbital model. The streamfunction in the shallow level is interpreted in terms of pressure, which is converted into SSH by f_0/g . An overall mean is subtracted from the SSH time series

in the domain. Individual passes are assumed to be perfectly unbiased and detrended. As an illustration of the SSH variability in the whole POLYMODE-SDE Mark II data set, the following statistics are derived:

Mean elevation = 1.41 m (ref. to 700 dbar)
 Variance = 860 cm²
 Standard deviation = 29.33 cm
 Minimum (rel. to mean) = -28 cm
 Maximum (rel. to mean) = +33 cm
 Max. amplitude = 61 cm
 Data count (XBTs) = 1336

The variance above includes SSH variability at time scales much larger than the typical mesoscale time. Thus, the standard deviation order of magnitude of 10 cm has to be kept in mind.

A gaussian noise of 3 cm standard deviation is added to SSH time series.

The SSH correlations in the Mark II data set exhibit the following scales:

Space: SW-NE direction: 110 km Time: e-folding: 10-20 days
 SE-NW direction: 160 km

The space correlation scale is defined as the zero-crossing of the covariances.

In Section 3, an isotropic stationary signal correlation model has been used. It has the following analytical expression (see Fig. 1):

$$C(r,t) = (1 + ar - \frac{1}{3} a^3 r^3) e^{-(ar + t^2/R_{ct}^2)} \quad (1)$$

with:

$$\begin{aligned} a &= 2.1038/R_{cx} \\ R_{cx} &= \text{correlation scale} \\ R_{ct} &= \text{correlation time} \\ r &= ((x-c_x t)^2 + (y-c_y t)^2)^{1/2} \end{aligned}$$

Using this expression leads to a -2 power law for the kinetic energy spectrum. The following values have been used:

$$\begin{aligned} R_{cx} &= 150 \text{ km} \\ R_{ct} &= 13 \text{ days for 1000 km runs (error only)} \\ &\quad 20 \text{ days for 281.25 km runs (with sea truth)} \\ c_x &= 0 \\ c_y &= 0 \end{aligned}$$

Residual SSH power spectra, as obtained by Menard (1983) or Fu (1983), along repeat tracks of SEASAT altimeter data, can be used to calculate the signal correlation. If the along-track wavenumber spectrum is denoted by $E_1(k_1)$, the one-dimensional isotropic correlation function is written:

$$C(r) = \int_{-\infty}^{+\infty} E_1(k_1) \exp(2\pi i k_1 r) dk_1, \quad (2)$$

i.e. the Fourier transform of the spectrum. A typical correlation function for the mid-latitude south Atlantic is given on Fig. 2. For wavelengths shorter than 300 km,

the shape of this function shows good agreement with the shape of (1).

Clearly, the Objective Analysis technique cannot be more accurate than the statistics used to build the estimator. The question of confidence levels on variance and covariances is thus of critical importance. The availability of large data sets of SSH sampled on a homogeneous mesh on large space and time scales is a decisive advantage of satellites compared to in situ sensors: the statistics derived from remotely sensed data are likely to be much more reliable. In the POLYMODE-SDE area, estimates based upon GEOS 3 data (Douglas et al., 1983) and SEASAT data (Cheney et al., 1983) are available. The 3.5 year calculation of SSH variability from GEOS 3 (Fig. 3) yields a typical value of 10 cm. The 24 day calculation from SEASAT (Fig. 4) gives 5 cm. The discrepancy is due to considerable attenuation of the mesoscale signal (50-150 days) in the second case. The first value of 10 cm is more reliable, and in good agreement with the calculations from in situ measurements discussed above.

The noise level, denoted by E, has been set to 20% of the SSH variance. The residual noise in the altimeter data, using the repeat track method, is expected to be 5 cm at the mesoscale, or less, for SEASAT and future missions:

- Residual tropospheric error: 1-2 cm/50-500 km
(Rain and water vapor)
- Atmospheric loading: 3 cm/200-1000 km
(Inverse barometer effects)
- Residual geoid: a few centimeters/all scales
(Tracking errors)

Assuming the 10 cm variability of Douglas et al., we find that $E = 25\%$, which is likely to be pessimistic if the data have been correctly undersampled along passes.

3. TWO EXAMPLES: ERS-1 and SPOT

Figs 5 and 6 are RMS expected error maps for two 1000 km simulations carried out with regionally tuned statistics in the POLYMODE-SDE area, resp. with ERS-I and SPOT. The following orbital parameters are used:

- | | |
|----------|-----------------------------------|
| ERS-1: | $14 + \frac{1}{3}$ rotation/day |
| (Fig. 7) | repeat cycle: 3 days |
| | cross-track distance: 910 km |
| | inclination angle: 98.52° |
| SPOT: | $14 + \frac{5}{26}$ rotations/day |
| (Fig. 8) | repeat cycle: 26 days |
| | cross-track distance: 106 km |
| | inclination angle: 98.72° |

These two satellites stand for the two possible extremes as far as regional mid-latitude coverage is concerned. TOPEX (Fig. 9) is just in between (repeat cycle: 10 days). ERS-1 and SPOT are sun-synchronous: the angle between ascending and descending passes (respectively 24.85° and 25.33° at the equator) is sharper than for TOPEX (44.61° at the equator).

Let us define the overbar as the space and time average on the maps on an

ORIGINAL PAGE IS
OF POOR QUALITY

integer number of repeat cycles (6 for ERS-1 = 18 days, 1 for SPOT = 26 days), $\sigma^2(x,y,t)$ as the local expected error in terms of signal variance, v as the signal variance, $h(x,y,t)$ and $\hat{h}(x,y,t)$ as the actual and restored SSH. The following statistics are derived for a 1000 km domain:

	ERS-1	SPOT
Global RMS expected error = $\overline{\sigma^2}^{1/2}$:	71.90%	56.15% of st. dev.
Global MS expected error = $\overline{\sigma^2}$:	51.70%	31.50% of var.
Global average expected error (bias) :	0	0

ERS-1 exhibits an excellent localized resolution, and a high variance of error, due to the absence of a subcycle to scan between adjacent tracks. The inhomogeneity in resolution would probably result in improper model assimilation.

SPOT shows a good general resolution, and a low error variance. The minimum error (29%) is higher, but the global statistics are much better. The whole error field propagates with the subcycle, i.e. at 25.1 cm/s, westward. Scanning between two successive tracks, with a subcycle of 5 days, is responsible for the good behavior of SPOT. TOPEX has a subcycle of 3 days, scanning eastward at 122.2 cm/s. SPOT is probably better for longer periods and relatively slow-moving events, while TOPEX is likely to perform better for energetic, rapidly evolving events at the advective time scale. Besides, TOPEX is not sunsynchronous, thus releasing the constraint of an almost polar orbit. The angle between ascending and descending passes is more open, and the chances to catch a mesoscale event are higher.

Fig. 10 shows a 5-day sequence of SSH simulation and reconstruction, in the 281.25 km domain sampled by SPOT. Also shown are the actual error field and the expected error field, both expressed in signal variance units. The following overall statistics are derived from the 26-day simulation:

Mark-II domain	ERS-1
Global RMS expected error = $\overline{\sigma^2}^{1/2}$:	43.11% of st. dev.
Global MS expected error = $\overline{\sigma^2}$:	18.58% of variance
Global average expected error :	0
Global RMS actual error = $\overline{(h-\hat{h})^2}^{1/2} / v^{1/2}$:	40.18% of st. dev.
Global MS actual error = $\overline{(h-\hat{h})^2} / v$:	16.14% of variance
Global average actual error = $\overline{h-\hat{h}} / v^{1/2}$:	4.95% of st. dev.

The bias is clearly negligible. It is striking to see how close the expected and actual values are. Objective Analysis can thus be expected to be a good method to interpolate along-track data, and the altimeter to catch accurately the variance, even in this small domain.

The introduction of phase speeds in the correlations, and the use of a larger domain are both likely to lead to more definitive conclusions on the different sampling schemes.

4. ASSIMILATING SEA-SURFACE HEIGHTS IN QG MODELS

Considerable recent progress has been made in assimilating data into the Harvard QG open ocean model (Robinson and Leslie, 1984; Robinson et.al., 1984). Both barotropic and baroclinic experiments have been carried out in order to resolve questions as to the source(s) of accuracy and error in both the objective analysis and the dynamical forecast (for details of the model, see: Tu, 1981; Miller et.al., 1983). Figs. 11a-c show a barotropic experiment involving the assimilation of sea surface heights in the QG model. Fig. 11a is the model generated 'Veritas' data set at period 3.0. The objective analysis is performed on the 'Veritas' data sampled with the MODE-1 observational network (Fig. 11b) and with the MODE-1 network and a simulated satellite track 'cross' (Fig. 11c). The addition of the satellite track restores much of the missing structure of the 'Veritas' data. These SSH maps are used to initialize the model, which computes the evolution of streamfunction using the discretized QG equations. There is good agreement between sea-truth and the model outputs, and the westward propagation is restored.

Fig. 11d illustrates the results of a 17 day baroclinic forecast using real data. Note that forecast in this 144 km domain experiment maintains (with the exception of some spikes) a level of rms difference between forecast and data of less than 25%. The spikes have been attributed to 'unrepresentative' hydrocasts in the data set. This forecast experiment does not involve use of remotely sensed data or a satellite simulation. This remains as a next step for the POLYMODE-SDE region. The Harvard model has been initialized with Rossby waves, simulated data, simulated satellite observed sea-surface heights (barotropic), and real data and run over flat bottoms and real topography. 'This model is proving to be an efficient and accurate component in the prediction and description of fields in open ocean regions of various internal dynamics' (Robinson and Leslie, 1984).

In the summer of 1983 a significant step in data assimilation was accomplished by carrying out a real time forecast in the regime of turbulent jets and eddies in the California Current (Robinson et al. 1984). The dynamical model successfully predicted the appearance of a zonal jet in the center of the experimental region and also provided the means of identifying a major eddy-eddy interaction event. The implications of these results for the effective exploitation of satellite altimetric data for practical forecasts and scientific studies are substantial.

5. CONCLUSION

The analyses and simulations presented here show the ability of objective analysis to map along-track altimeter data in a suitable way for dynamical model initialization, and to evaluate sampling strategies. A set of global statistical parameters have been defined for that purpose. The two case studies on ERS-1 and SPOT show the great interest of the subcycle, which, as a matter of fact, doubles the capabilities of the instrument, by being tuned on two time scales (5 days and 26 days). Furthermore, it can be shown (Fig. 12) that the most economical way to set two tracks apart is to equal their distance to the horizontal correlation scale. This is also true in time with the repeat cycle and the correlation time. 5 days and 26 days stand approximately for the advective and linear time scales at mid-latitudes respectively. The SPOT observational strategy is thus regionally adapted, as far as sampling parameters are concerned. It is still unclear whether in situ data, along with altimeter data, are compulsory for assimilation. Different techniques of extrapolation on the vertical are currently tried in Harvard, in order to initialize and update properly the dynamical model for multi-level runs. The efficient use of these

techniques and of those described above can be considered an essential step towards our knowledge of the oceanic mesoscale on large space and time scales.

6. ACKNOWLEDGEMENTS

We wish to thank Dr. Melvin Marietta and Dr. E.S. Hertel of Sandia National Laboratories for the preparation of the 1000 km domain 'sea truth', and Mr. Wayne Leslie for his help in the preparation of this manuscript. The support of this work under a contract from the Office of Naval Research, N000 14-75-C-0225 and a fellowship from the European Space Agency, Paris, France, granted to Pierre De Mey is gratefully acknowledged.

FIGURE CAPTIONS

1. Correlation function for the objective analysis of altimeter data, as a function of distance. As an example, a 50km correlation radius has been chosen to draw this plot.
2. Average correlation function from a group of repeat tracks of SEASAT altimeter data in the SW Atlantic (from Fu, 1983).
3. Sea surface height variability in centimeters from GEOS-3 altimeter repeat pairs (from Douglas et al., 1983).
4. Sea surface height variability (contour interval = 1 cm) from repeat tracks of SEASAT altimeter data (from Cheney et al., 1983).
5. RMS expected error maps for a simulation of ERS-1 in a 1000 km square domain center on 29N, 70W (POLYMODE Soviet current meter array). Maps are shown for days 1,2,3,4. Contour interval is 0.08. The parameters of the analysis are given in the text.
6. RMS expected error maps for a simulation of SPOT in a 1000 km square domain centered on 29N, 70W. Maps are shown for days 0,5,10,15. Contour interval is 0.07. Note westward propagation. The parameters of the analysis are given in the text.
7. Global coverage of ERS-1 (from Tavernier, 1983).
8. Global coverage of SPOT (from Tavernier, 1983).
9. Global coverage of TOPEX (from Tavernier, 1983).
10. Sea-truth, restored sea-surface height, RMS actual error field and RMS expected error field for a simulation of SPOT in a 281.25 km square domain centered on 29N, 70W (Harvard POLYMODE SDE Mark II data set). Contour intervals are: 2 cm, 2 cm, 1% of st. dev. of SSH, 5% of st. dev. of SSH. The westward propagation of the southern eddy and the stationarity of the northern one are reproduced.
11. Sea-truth, restored sea-truth (without satellite track), restored sea-truth (with satellite track), and results of 17 day 144 km baroclinic forecast using real data.
12. RMS expected error vs. cross-track distance for an objective analysis of 2 parallel tracks. The correlation radius was 50.0 km. Note the first minimum. The upward slope after the second minimum is an artifact of the integration in a finite domain.

BIBLIOGRAPHY

- Carter, E.F., 1983: The statistics and dynamics of ocean eddies. Reports in Meteor. Oceanogr., 18, Harvard University.
- Cheney, R.E., J.G. Marsh and B.D. Beckley, 1983: Global mesoscale variability from collinear tracks of SEASAT altimeter data. J. Geophys. Res., 88(C7), 4343-4354.
- Douglas, B.C., R.E. Cheney and R.W. Agreen, 1983: Eddy energy of the northwest Atlantic and Gulf of Mexico determined from GEOS-3 altimetry. J. Geophys. Res., 88(C14), 9595-9603.
- Fu, L.L., 1983: On the wavenumber spectrum of oceanic mesoscale variability observed by the SEASAT altimeter. J. Geophys. Res., 88(C7), 4331-4342.
- Gandin, L.S., 1963: Objective Analysis of meteorological fields. Leningrad, Gidrometeorizdat, 266 pp.
- Menard, Y., 1983: Observation of eddy fields in the northwest Atlantic and northwest Pacific by SEASAT altimeter data. J. Geophys. Res., 88, 1853-1866.
- Miller R.N. and A.R. Robinson, 1983: Dynamical Forecast Experiments with a Baroclinic Quasigeostrophic Open Ocean Model, Proceedings of Conference on Predictability of Fluid Motion, La Jolla, Ca., G. Holloway, Editor (in press).
- Miller, R.N., A.R. Robinson and D.B. Haidvogel, 1983: A baroclinic quasigeostrophic open ocean model. J. Comp. Phys., 50, 38-70.
- Robinson, A.R., 1983: Description and prediction of oceanic fields: Data assimilation and optimal estimation. Proc. of COO/JOC (SCOR-WCRP) Study Conference on Large Scale Ocean Experiment in the World Climate Research Program, Tokyo, 1982.
- Robinson, A.R., J.A. Carton, C.N.K. Mooers, L.J. Walstad, E. F. Carter, M.M. Rienecker, J.A. Smith and W.G. Leslie, 1984: A real time dynamical forecast of ocean synoptic/mesoscale eddies, (submitted).
- Robinson, A.R., N.E. Huang, C.D. Leita and C.G. Parra, 1983: A study of the variability of ocean currents in the Northwestern Atlantic using satellite altimetry. J. Phys. Oceanogr., 13, 565-585.
- Robinson, A.R. and W.G. Leslie, 1984: Estimation and prediction of oceanic eddy fields, Prog. in Oceanogr., (In press).
- Tavernier, G., Projet POSEIDON: Echantillonnage spatio-temporel d'un satellite altimétrique pour la détermination des différentes composantes de la circulation océanique, ENSAE/GRGS, Toulouse, France, 1983.

Tu, K., 1981: A combined statistical and dynamical approach to regional forecast modelling of open ocean currents. Reports in Meteor. Oceanogr., 13, Harvard University.

ORIGINAL PAGE IS
OF POOR QUALITY

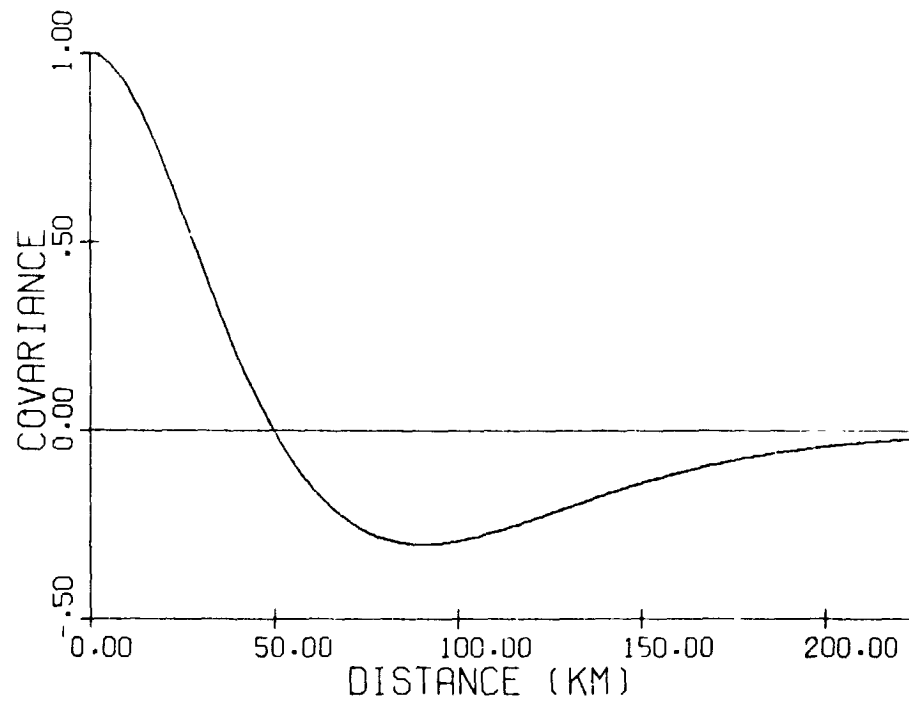


Figure 1

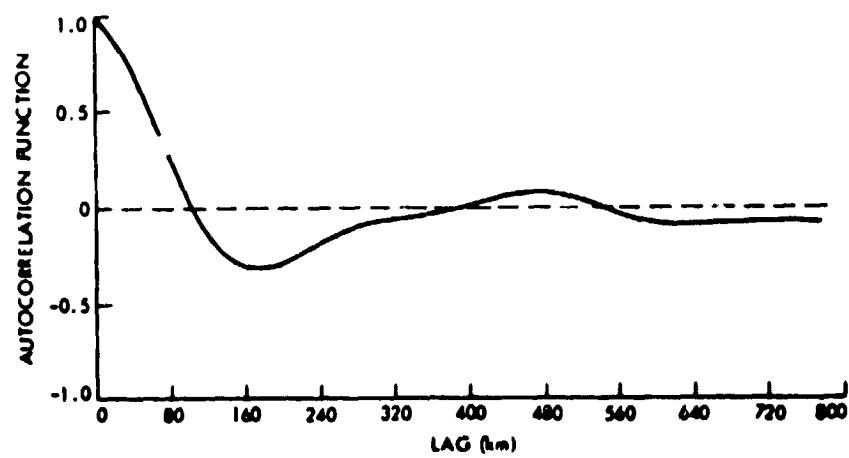


Figure 2

ORIGINAL PAGE 19
OF POOR QUALITY



Figure 3

ORIGINAL PAGE IS
OF POOR QUALITY

SEASAT ALTIMETER MESOSCALE VARIABILITY

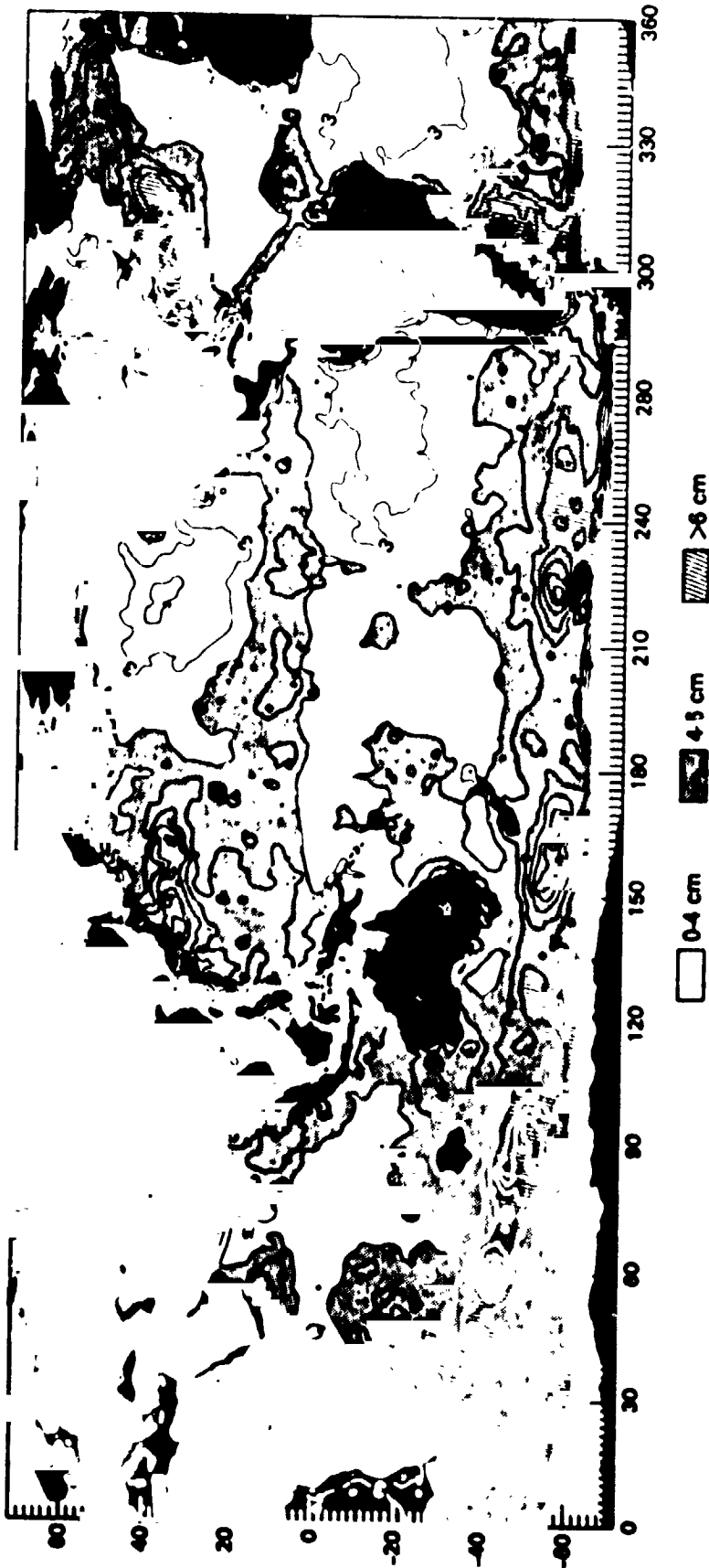


Figure 4

ORIGINAL PAGE 17
OF POOR QUALITY



Figure 5 (ERS-1)



Figure 6 (SPOT)

ORIGINAL COPY
OF PAPER QUALITY

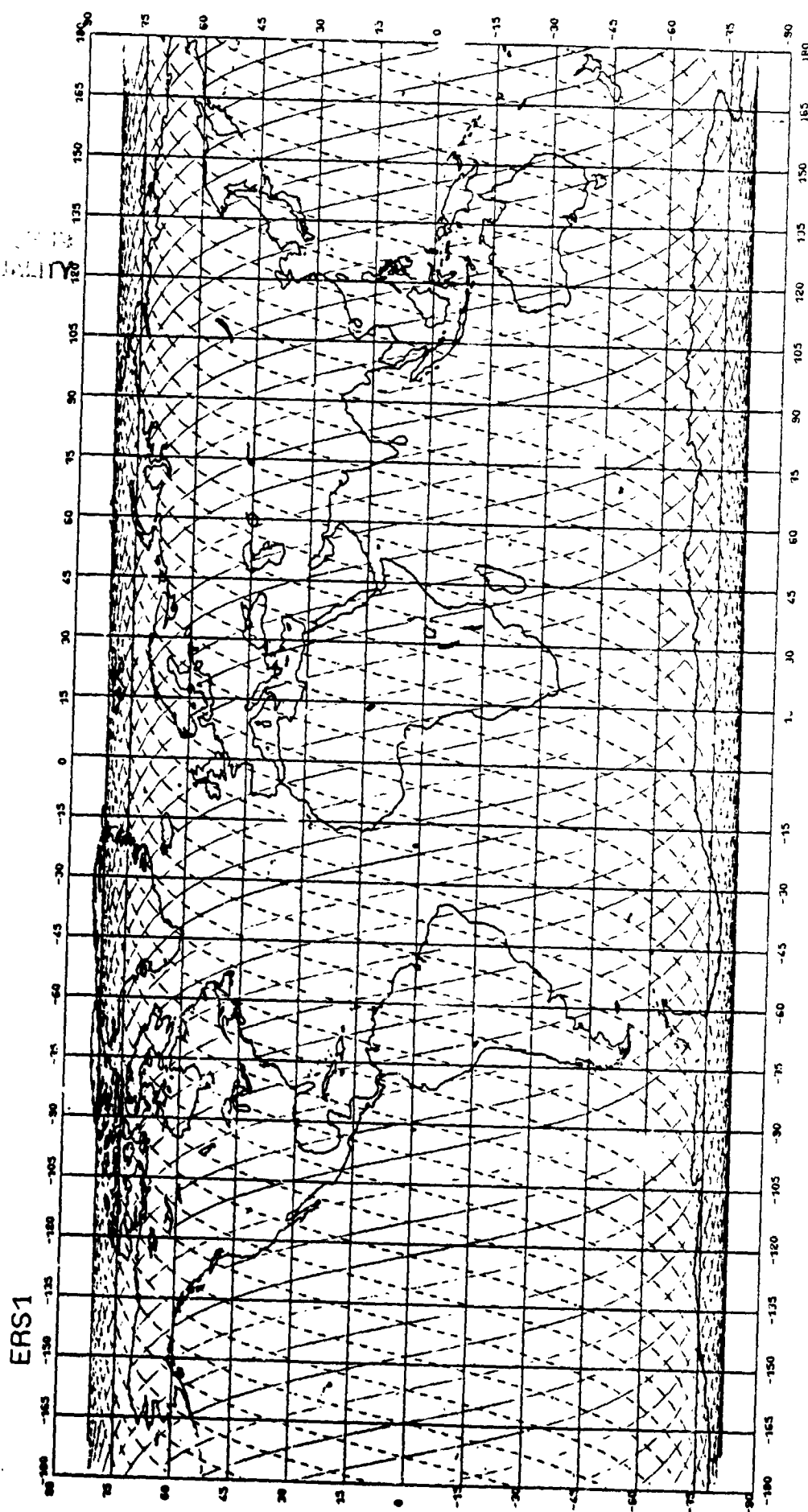
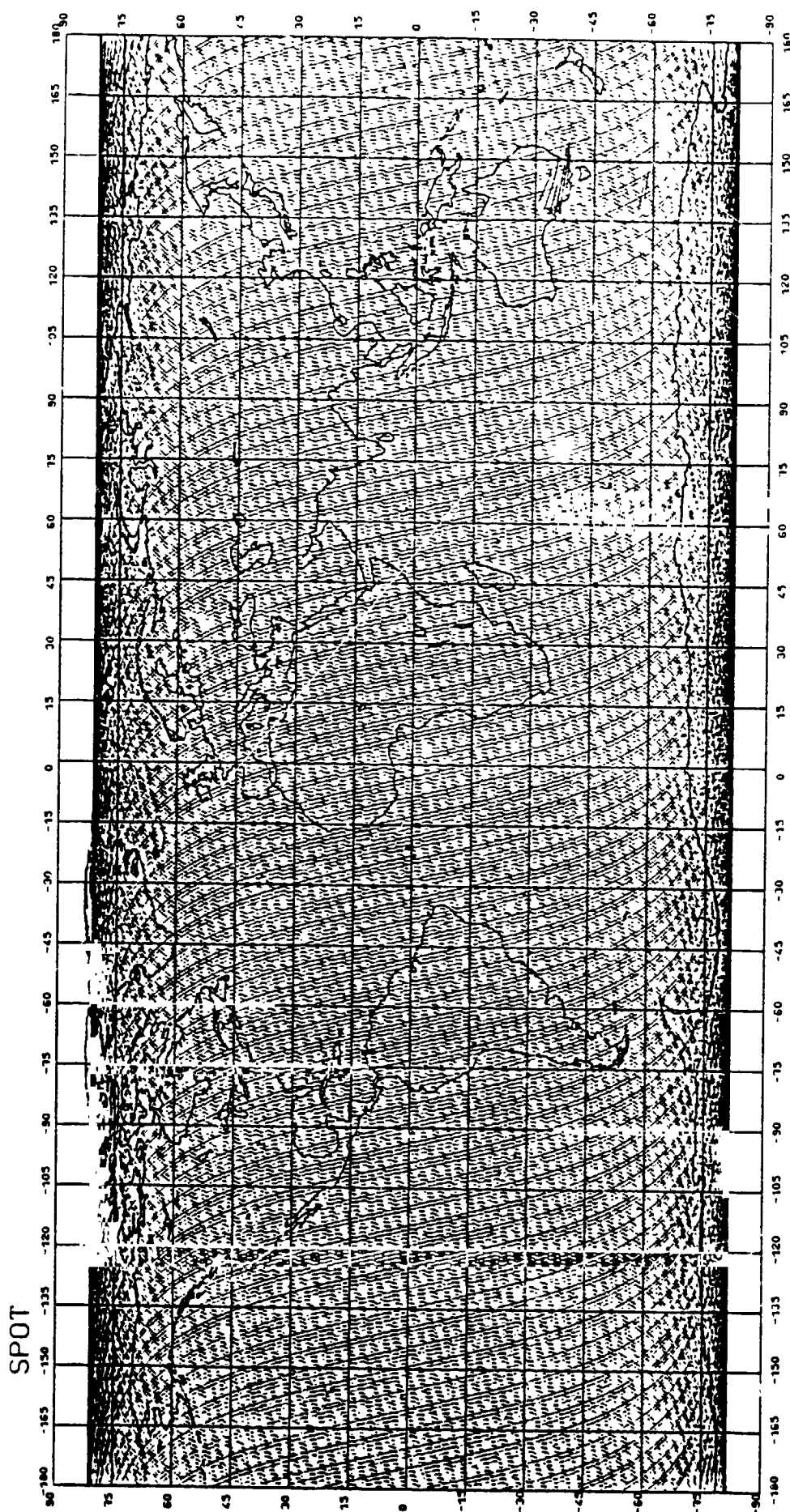


Figure 7



ORIGINAL PAGE IS
OF POOR QUALITY

Figure 8

ORIGINAL PAGE 13
OF POOR QUALITY

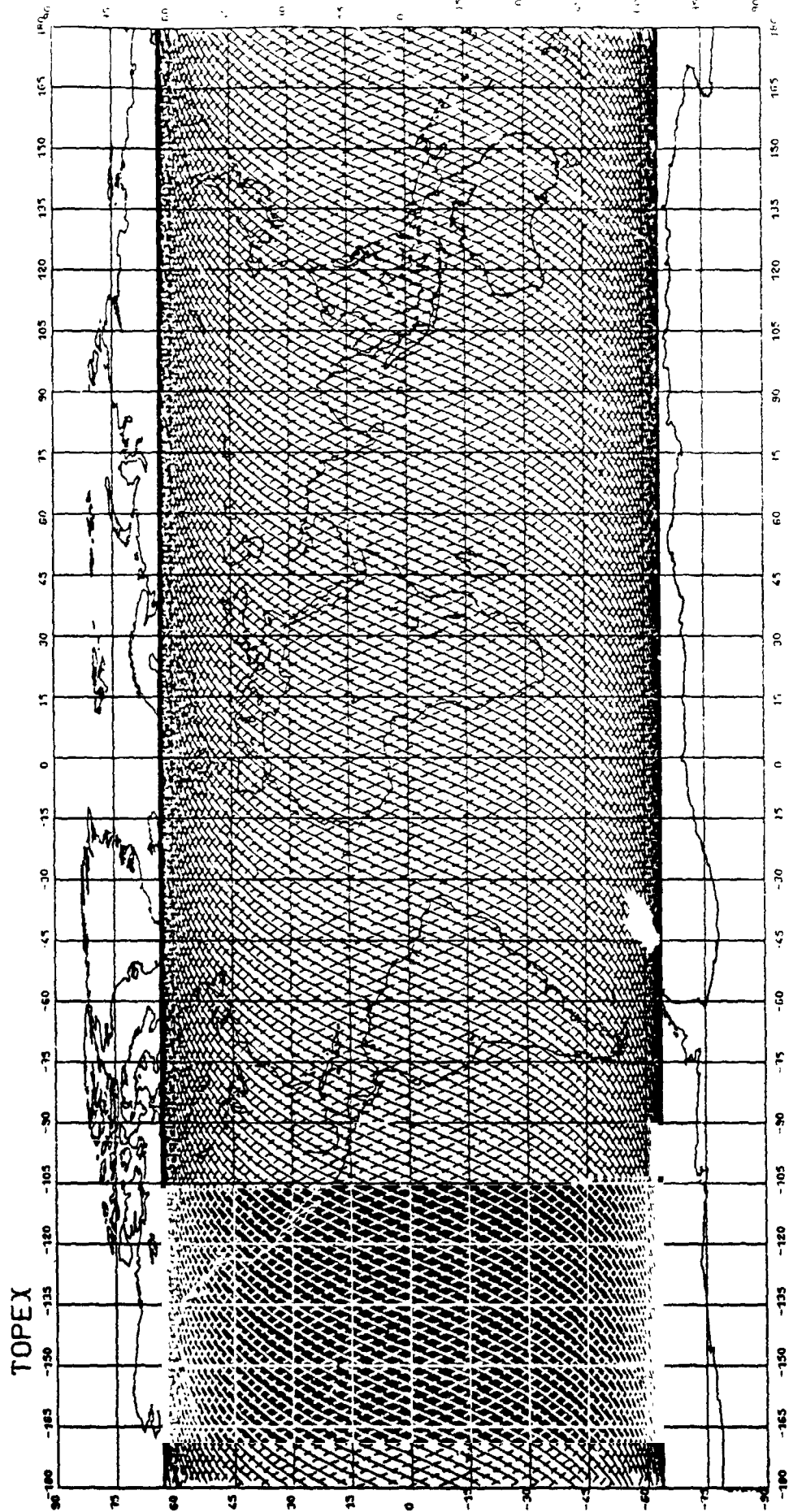
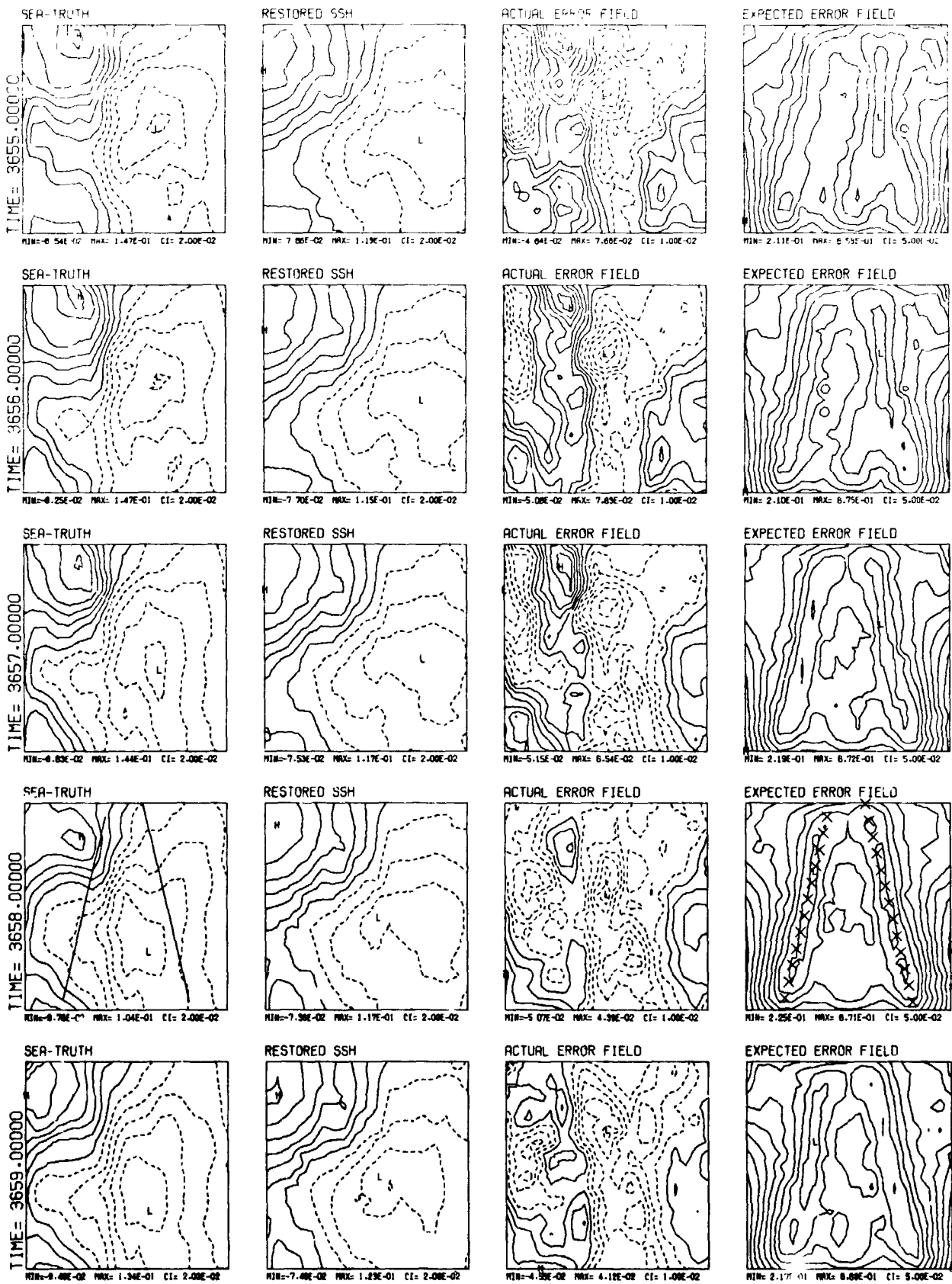
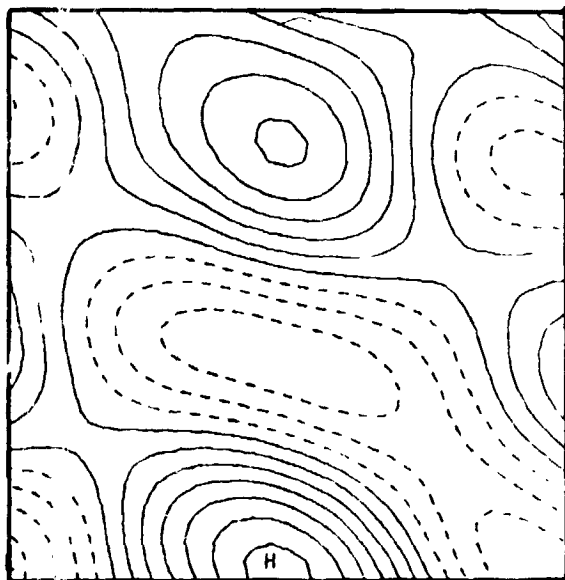


Figure 9

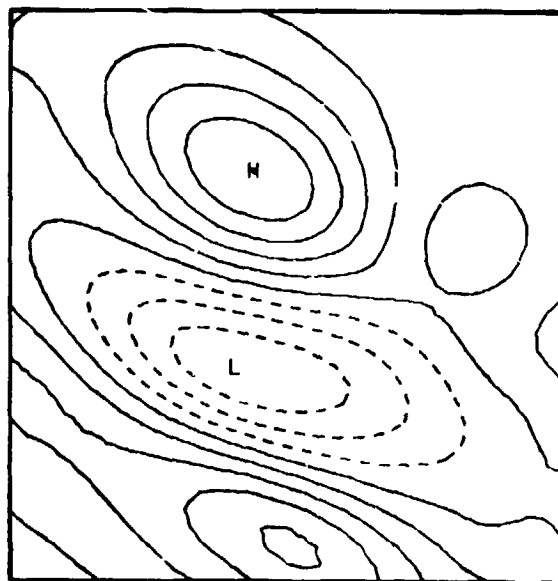
ORIGINAL PAGE IS OF POOR QUALITY



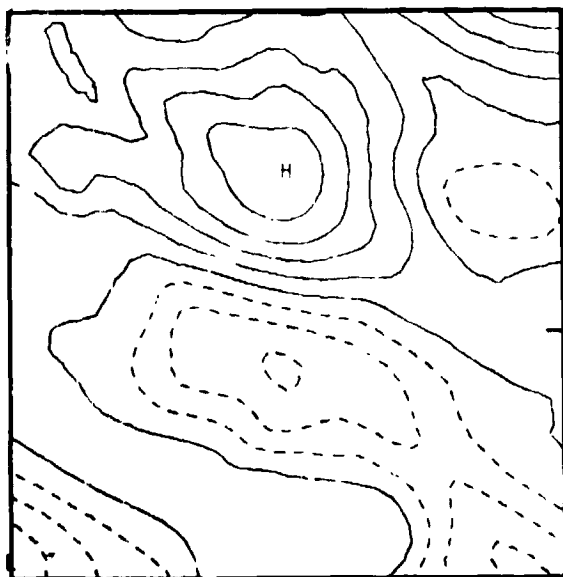
ORIGINAL PAGE IS
OF POOR QUALITY



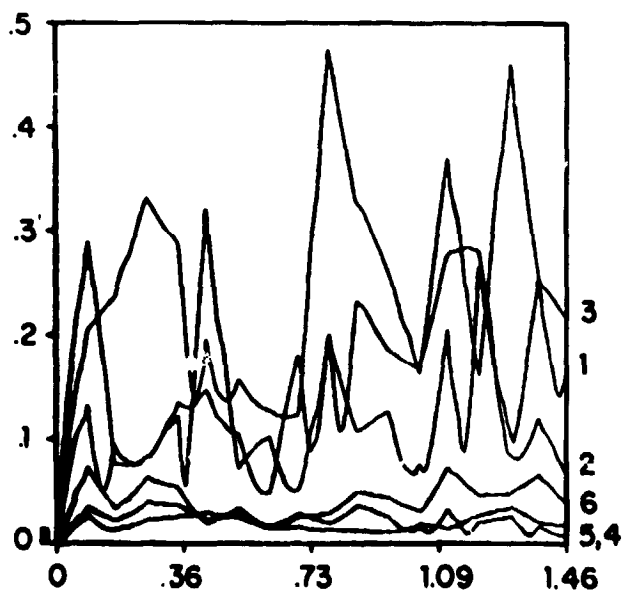
VERITAS PSI



OBJ ANAL PSI (without SAT)



OBJ ANAL PSI (with SAT)



17x17 BENCHMARK

RMS(DIFF(STFN))

Figure 11

ORIGINAL PAGE IS
OF POOR QUALITY

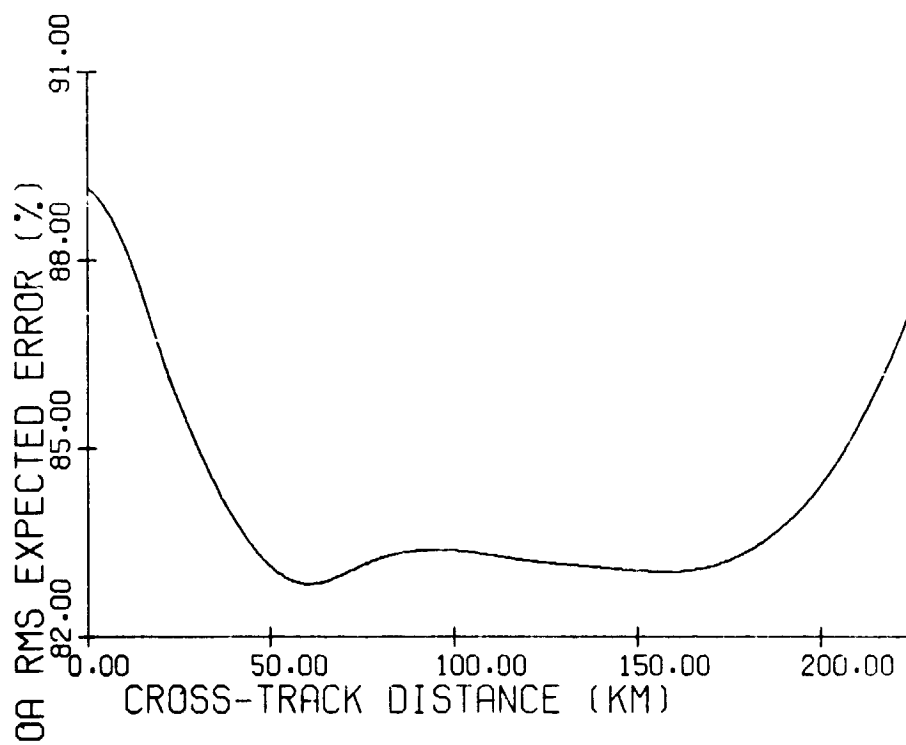


Figure 12

N84 27313

VECTOR WIND, HORIZONTAL DIVERGENCE, WIND STRESS AND WIND STRESS CURL FROM
SEASAT-SASS AT A ONE DEGREE RESOLUTION

By
Willard J. Pierson Jr.⁺, Winfield B. Sylvester⁺ and Robert E. Salfi^{*}

⁺The City College of New York, N. Y., N.Y. 10031

^{*}Present affiliation, Hofstra University, Hempstead, N.Y. 11550

ABSTRACT

Conventional data obtained in 1932 are contrasted with SEASAT-SASS and SMMR data to show how observations at a single station can be extended to an area of about 150,000 square km by means of remotely sensed data obtained in nine minutes. Superobservations at a one degree resolution for the vector winds are estimated along with estimates of their standard deviations. From these superobservations, the horizontal divergence, vector wind stress, and the curl of the wind stress can be found.

INTRODUCTION

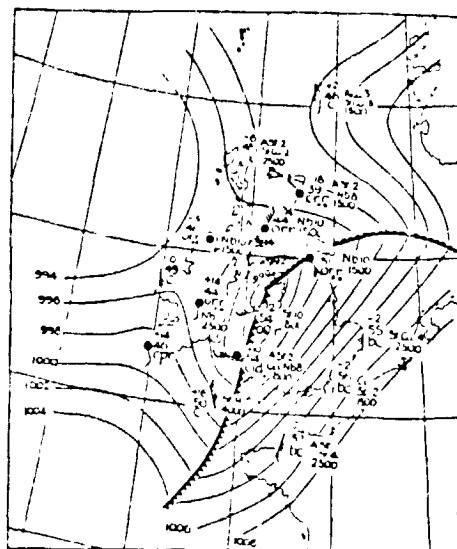
The basic tenets of those who believe that it is possible to predict the weather are three. These are (1) that the time evolution of the meteorological variables can be correctly described by appropriate equations, (2) that the initial conditions for the start of the prediction can be adequately specified and (3) that computers can be made with a large enough capacity and a fast enough speed to compute the evolution of the weather for the future. These tenets evolved with time from the days of Bjerknes (1904) who wrote that what was needed was "a sufficiently accurate knowledge of the state of the atmosphere at the initial time" and "a sufficiently accurate knowledge of the laws according to which one state of the atmosphere develops from another", through Richardson's (1922) "Weather Prediction by Numerical Process", on to the day when the authors of a recent paper wrote "The main reason we cannot tell the weather tomorrow is that we do not know the weather today".

These tenets are interdependent because improved computers provide higher resolution. Improved descriptions of the physics of the atmosphere require more data. The problem is to predict the synoptic scale meteorological evolution and to filter out the higher wavenumbers and frequencies. This is a corollary of the basic tenets and involves all aspects of turbulence, where much is yet to be learned.

Much of what has been learned in the past about the behaviour of weather systems has been lost because of present day computer constraints. To our knowledge, no operational hemispheric numerical model with a one degree by one degree resolution, and a corresponding vertical resolution, presently exists. With an adequate description of the physics of the atmosphere and of subgrid turbulence, including the possibility of transfer of energy from high to low wave numbers, a one degree, at least hemispheric model, is presently conceivable.

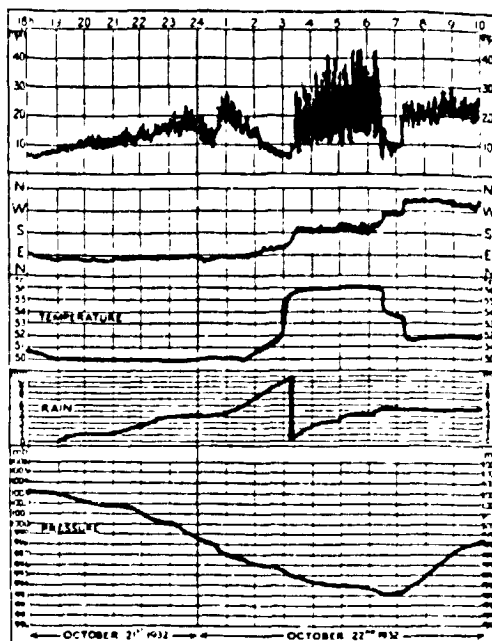
OCTOBER 21, AND 22, 1932 AT HOLYHEAD, ENGLAND

Before showing what can be achieved by means of remote sensing, it is useful to go back to a text by Brunt (1942). It is then possible to compare the results of the analysis of SEASAT data obtained in about 9 minutes with data obtained over a 16 hour period in England.



The Depression of October 22, 1932, at 7h

1 a



1 b

Fig. 1(a) Synoptic analysis for the weather on October 22, 1932 at 0700 for the British Isles and part of Europe and (b) time histories at Holyhead. Wind speed from 0 to 50 miles per hour; Direction, meteorological convention; Temperature, degrees Fahrenheit 50° to 58°; Integrated rainfall in millimeters, 0 to 10 mm; Sea level pressure, millibars, 990 to 1006. From Brunt (1942).

Fig. 1(a) shows the synoptic scale analysis for 07h Oct. 22, 1932, London time, for an area around the British Isles. Fig. 1(b) shows the time history of the evolution of winds, temperature, integrated rainfall and sea surface atmospheric pressure at Holyhead, England (approximately 52.5°N, 4.8°W) beginning on Oct. 21 at 18h and ending on Oct 22 at 10h (16 hours). Some data have probably been omitted for clarity in Fig. 1(a) but there are roughly four observations per 10 degree latitude by longitude "square" which permit an adequate analysis. The cold front of the open wave cyclone is in the process of passing Holyhead.

The anemometer had a rather short time constant so that mesoscale fluctuations of the wind were recorded. Even in 1932, it would have been obvious that a two minute average could give erroneous synoptic scale values as recently rediscovered by Pierson, et al. (1980) and made quantitative by Pierson (1983a).

If one imagines the wave cyclone to be moving without too much change in form along an appropriate track, the winds in advance of the warm sector were ENE for the first eight hours building from 6 or 7 miles per hour (2.24 mph equals 1 m/s) to 22 mph (with gusts to 29) followed by a decrease to 6 mph and a wind shift to the ESE. The wind shift to SSW occurred in about 20 minutes. The temperature rose slowly from about 1:40 to 3 AM then rapidly for 10 to 15 minutes with a $1 - \exp(-Bt)$ asymptotic approach to 56° F. The total warming was 6° F.

The winds in the warm sector were very gusty and turbulent with 40° fluctuations in direction and speeds that varied moment by moment from under 10 mph to nearly 45 mph. The average wind in the warm sector increased from about 20 mph to 25 mph before the cold front passage.

The cold front went by in two steps at about 6:30 and 7:20 with a wind shift to the WSW followed by the final one to the NW. The temperature dropped sharply twice in 2° F steps and settled down to a value of 52° F.

Light pre-warm front rain occurred from 1900 to 1930 and from 2050 to 2255. Heavier rain began after midnight and lasted steadily for more than two hours tapering off after the warm front passage and stopping at about 0620 at the first

passage of the cold front.

With modern communication systems, it would be possible, in principle, to obtain similar data with data buoys over the ocean and closely spaced land installations for pre processing locally to define the planetary boundary layer with sufficient accuracy at the synoptic scale and to collect and use the data in time for forecasts. The cost would be substantial. Over the oceans, remote sensing can provide a cost effective alternative.

THEORY

To predict the weather, meteorologists start with the hydrodynamic equations for a rotating Earth plus H_2O conservation equations, sources and sinks, plus radiation budget equations, plus whatever else might be needed and try to put them in a form that can be integrated forward by means of about 10 minute time steps so as to reach out to the future. The first difficulty is that the hydrodynamic equations are inappropriate. It is impossible to measure the various fields at the resolutions they need, and equally impossible to integrate them forward in time to make a forecast. The atmosphere is turbulent at scales that are, and always will be, unresolvable for such purposes. The equations that are actually used require time and space averaged values and therefore become strangely altered because they must account for the effects of fluctuations within the space and time average. A host of new terms such as $\langle u'w' \rangle$ arise because of nonlinearity that must be removed by means of an appropriate closure model. Just how this ought to be done is a matter for discussion as in Robinson (1978), among others.

To put things simply, the synoptic scale winds are needed for a numerical weather prediction as defined in a circular way by Pierson (1983a). Each SASS wind in a swath is defined by four numbers; they are the latitude, θ_i , longitude λ_i , wind speed at 19.5 meters for an effective neutral wind $|V|_i$, and the meteorological wind direction, χ_i , after the removal of ambiguities.

Each SASS wind in a data set departs from the desired synoptic scale value at θ_i , χ_i for two reasons (at least). The footprint (or cell) illuminated by the radar is analogous to a rather brief time average that would not quite recover the synoptic scale value. For a typical cell size and a synoptic scale wind of 15 m/s the variability due to this effect can, for example, be ± 0.38 m/s at one standard deviation. Other sources of error caused by the radar itself, and lumped into one term (Pierson(1983(a), 1983(b))), produce about an 0.6 m/s variation, but this can vary for various reasons as a function of the wind direction and incidence angle. For direction, the corresponding values are 1.2° and 6° for this example. The combined effect is about 0.71 m/s for speed and slightly over 6° for direction. These are representative conditions, but over a full swath these two effects can combine to give variations more than twice as large or less than half as much. They are inseparable after the vector wind is found. Neither effect is desirable for the purpose of synoptic scale analyses. Both are random from one measurement to another.

The data analysis procedure reduces these sources of variability and recovers a reliable estimate (in a statistical sense) of the synoptic scale wind at 19.5 m above the sea surface for a neutrally stratified atmosphere. For each integer value of latitude and longitude in the swath, say θ_0 , λ_0 , all SASS wind within the 2 by 2 degree "square" surrounding the target point were found. The average latitude and longitude of the SASS winds in this sample would not quite be at θ_0 , λ_0 and a few values were dropped from the sample at the outer edges to obtain an average latitude and longitude close to θ_0 , λ_0 . This slightly reduced sample was then processed as a superobservation to obtain synoptic scale fields with estimates of sampling variability effects at a one degree resolution by overlapping the 2 by 2 degree squares.

For each sample a mean direction can be found as in (1).

$$\bar{x} = \frac{1}{N} \sum x_i \quad (1)$$

Each SASS wind can be resolved into components parallel and normal to \bar{x} such as V_{pi} and V_{Ni} such that

$$\bar{v}_p = \frac{1}{N} \sum V_{pi} \quad (2)$$

and

$$\bar{v}_N = \frac{1}{N} \sum V_{Ni} \quad (3)$$

and their variances can be found as in (4) and (5). Also quantities such as $\sum(\theta_i - \theta_o) = \sum \Delta\theta_i$, $\theta_o + \Delta\theta$, $\lambda_o + \Delta\lambda$, $\text{VAR}(\Delta\theta)$, and so on, are needed because the winds are not exactly at λ_o , θ_o .

$$\text{VAR } \bar{v}_p = \frac{1}{N} \sum (V_{pi} - \bar{v}_p)^2 \quad (4)$$

$$\text{VAR } \bar{v}_N = \frac{1}{N} \sum (V_{Ni} - \bar{v}_N)^2 \quad (5)$$

From standard statistical theory, the expected value of the mean is the mean and the variance of the mean is the variance of the sample as in (4) and (5) times N^{-1} . The only difficulty is the presence of gradients in the winds over the swath which can overestimate the variances that are needed and the slight mis-location of the desired winds by $\Delta\theta$, $\Delta\lambda$.

Further data processing in terms of east-west components, U_λ and north-south components, V_θ , allows the effects of gradients to be removed to first order, the wind vector to be located at λ_o , θ_o , and the standard deviations of the mean east-west and north-south components to be found. The final results, with added complexities at the edges of the available data, were values for the vector components of the wind at each θ_o , λ_o that were much more accurate estimates of the synoptic scale wind with known effects of sampling variability as in equations (6) and (7). (We have simplified notation for this paper).

$$U_{\lambda_s} = \bar{U}_\lambda + t_1 \Delta U_1 + t_2 \Delta U_2 \quad (6)$$

$$V_{\theta_s} = \bar{V}_\theta + t_1 \Delta V_1 + t_2 \Delta V_2 \quad (7)$$

In (6) and (7), U_{λ_s} and V_{θ_s} are the desired, but always unknown, synoptic scale values, \bar{U}_λ and \bar{V}_θ are their superobservation estimates and ΔU_1 , ΔU_2 , ΔV_1 , ΔV_2 , express the reduced effects of the components of (4) and (5) after removing the contribution from gradients in the wind field and obtaining the appropriate vector components. The values of t_1 and t_2 near the middle of the swath where N can be above 30 are close to being values drawn at random from a zero mean unit variance normal probability density function.

As an example, at 54° N 209° W (for another SEASAT pass), the superobservation yielded a wind from 260° at 20.2 m/s. The other data obtained then gave (8) and (9) in m/s. From (8) and (9), as one of many examples that could be given, the uncertainty in wind speed is ± 0.17 m/s at one standard deviation and the uncertainty in direction is $\pm 2.75^\circ$. It will be a while before meteorologists will believe such results.

$$U_{\lambda_s} = 19.95 + t_1(0.17) + t_2(0.14) = 19.95 + t_1^*(0.22) \quad (8)$$

$$V_{\theta_s} = 0.156 + t_1(0.02) + t_2(-0.96) = 0.156 + t_2^*(0.96) \quad (9)$$

By these methods as an example for the REV to be studied, the original 1,081 SASS winds were reduced to 120 superobservation winds as in (6) and (7) with each wind accompanied by estimates of its sampling variability for a reduction to 11% of the original data for further processing.

For every point in the superobservation wind field that had four points around it, it was possible to estimate the horizontal field of divergence at 19.5 meters and to carry along the four terms in (6) and (7) so as to obtain the standard deviation of the estimate of the divergence. The appropriate equation is (10)

$$\text{div}_2 \vec{W}_h = \frac{1}{R \cos \theta} \left(\frac{\partial U_\lambda}{\partial \lambda} + \cos \theta \frac{\partial V_\theta}{\partial \theta} - V_\theta \sin \theta \right) \quad (10)$$

where R is the radius of the Earth.

The finite difference form is (11).

$$\begin{aligned} \text{div}_2 (\vec{W}_h(\theta_o, \lambda_o))_s = \frac{2.5 \cdot 10^{-6}}{\cos \theta} & \left\{ (U_{s\lambda}(\theta_o, \lambda_o+1) - U_{s\lambda}(\theta_o, \lambda_o-1)) \right. \\ & + \cos \theta_o (V_{s\theta}(\theta_o+1, \lambda_o) - V_{s\theta}(\theta_o-1, \lambda_o)) \\ & \left. - 0.0349065 \sin \theta_o V_{s\theta}(\theta_o, \lambda_o) \right\} \quad (11) \end{aligned}$$

Five different terms such as (8) and (9) are needed. The expected value of the 10 different t 's that enter is zero so that the expected value of the divergence can be found.

Also

$$E((\text{div}_2 \vec{W}_h(\theta_o, \lambda_o))_s - \text{div}_2(\vec{W}_h(\theta_o, \lambda_o)))^2 = \text{VAR}(\text{div}_2(\vec{W}_h(\theta_o, \lambda_o))) \quad (12)$$

can be found as a weighted sum of the squares of the ΔU_j and ΔV_j so that the standard deviation of the estimate of the divergence can also be estimated. The field of horizontal divergence is rarely calculated from conventional data because of large errors in measurement. The divergences that were found formed logical coherent patterns.

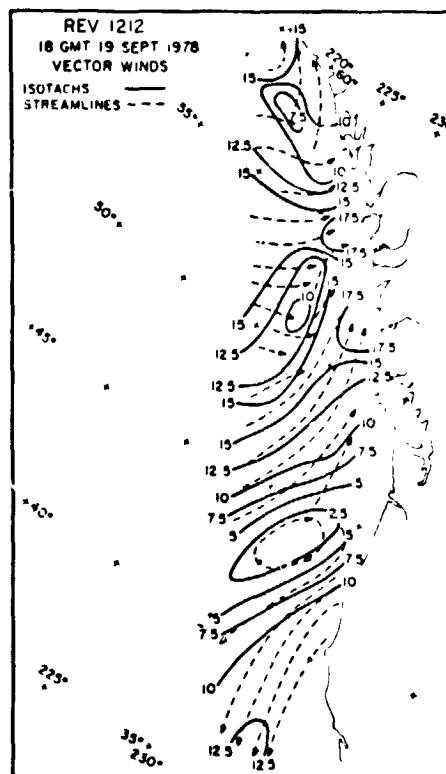
THE WESTERN NORTH PACIFIC FOR SEPTEMBER 19, 1978 AT ABOUT 1800 GMT

On this date, SEASAT crossed the Equator, on its 1212th revolution of the Earth in a retrograde circular orbit with a period of about 100 minutes at an altitude of 800 km., going north bound, a few seconds before 1754 GMT and obtained the data that were analysed for the following material between about 1803 and 1812 GMT from the SASS and the SMR. For details, see for example *IEEE J. Oceanic Eng.* Vol. OE-5 and *J. Geophys. Res.* Vol. 87, No. C5 and Vol. 88, No. C3. Further details on these particular results and for three additional weather patterns are given by Pierson, et al. (1983). During this 9 minute interval, the SASS found 1,081 values for the winds over an area about 600 km wide extending from 35° N to 60° N in a one side scanning mode. The SMR also obtained data over a slightly narrower swath. At nearly the same time, the GOES spacecraft obtained both visible and infrared imagery. The results for the synoptic scale wind field and the field of the horizontal divergence of the wind will be described. Fields for the wind stress, $(u_*)^2$, and the curl of the wind stress will be found by similar methods, also.

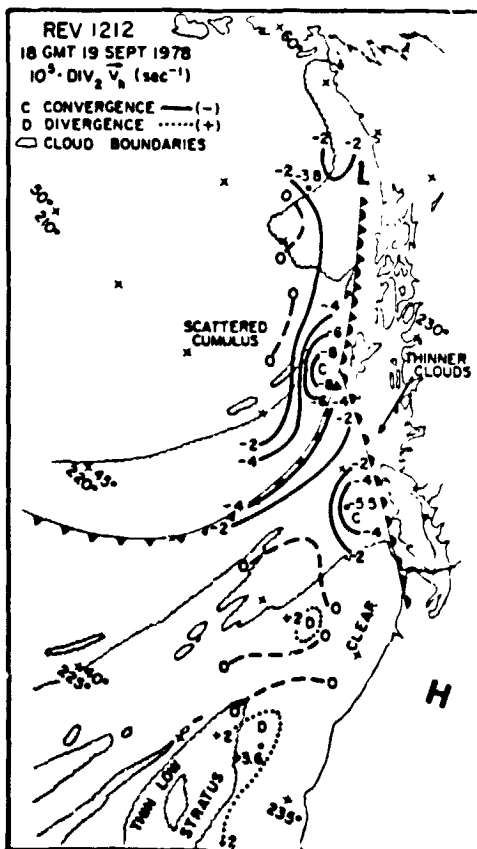
McMurdie and Katsaros (1983) have used the SMR data to obtain the values in Fig. 3 for this REV. Their results can be combined with the vector wind values and the divergence field to produce data over an area of roughly 150,000 square kilometers that are effectively the equivalent of having records similar to Fig. 1(b) from every one degree latitude longitude intersection in the swath for synoptically averaged winds and for the rainfall rates. Given the few ship reports of sea surface atmospheric pressure within the swath, it ought not to be unduly difficult to recover the sea surface pressure field within the swath. Air temperature just above the sea surface is still a problem for remote sensing, and the sparsity of conventional ship reports makes such data difficult to obtain.



2 a



2 b



2 c

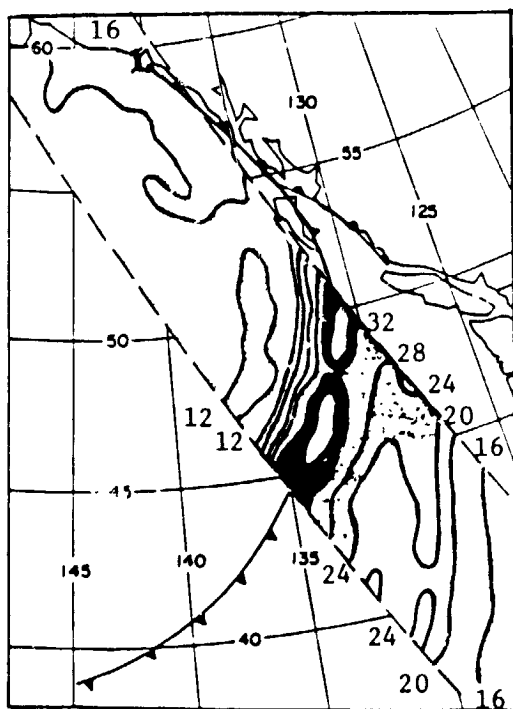
Fig. 2. (a) Geostationary cloud image of the extratropical cyclone for SEASAT REV 1212. (b) Streamline, isotach analysis of the superobservations. Speeds in meters per second. Data from the SEASAT A Scatterometer, (SASS). (c) Field of horizontal divergence computed from the superobservations. Fig. 2(a) is from Woiceshyn, et al. (1979).

The GOES cloud imagery, the SASS superobservation winds, and the divergence field computed therefrom plus the SMMR results provide a detailed meteorological description of an occluded cyclone approaching the west coast of North America. The GOES cloud image in Fig. 2(a) shows an occluded low crossing the west coast of North America. A long cold front trails to the south and west over the Pacific. The cloud shield extends well into Canada and covers Queen Charlotte Island and most of Vancouver.

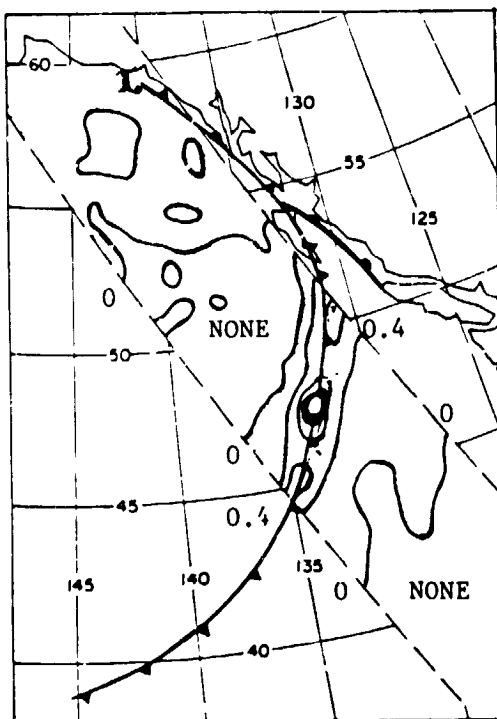
Streamlines and isotachs (m/s) are shown in Fig. 2(b). Strong warm air advection for the streamlines surrounded by the 15 m/s isotach and to the south to 10 m/s is shown. The wind shift in the general vicinity of the occlusion is shown.

Queen Charlotte Island is not shown for simplicity.

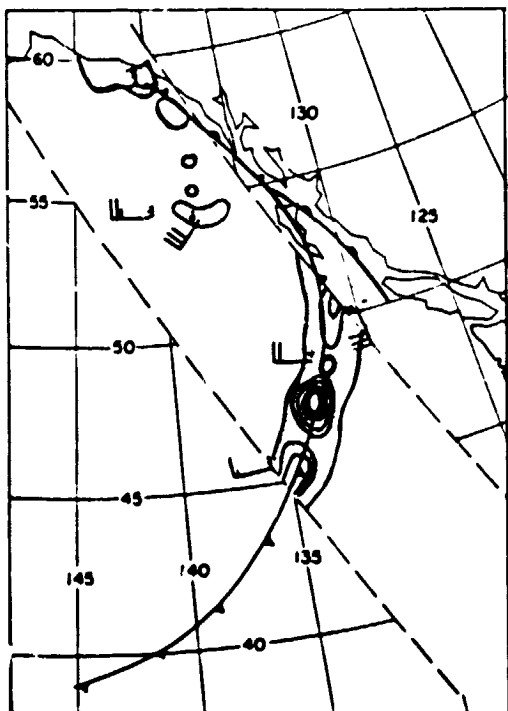
The field of divergence is shown in Fig. 2(c) based on 65 values as a composite with the frontal analysis based on conventional analysis plus a schematic of the cloud image shown in Fig. 2(a). Strong convergence is shown at the intersection of the cold and warm front with a band less than $-4 \times 10^{-5} \text{ sec}^{-1}$ extending over



3 a



3 b



3 c

Fig. 3. The integrated water vapor in kg/m^2 (a), the integrated liquid water in kg/m^2 (b), and the rainfall rate in mm/hr (c), found from the Scanning Multichannel Microwave Radiometer on SEASAT. In (a) the contours that parallel the cold front have values of 16, 20, 24 and 28. The dark area has values over 32 and the inner white area values over 40. In (b), the area in the center has values of 0.8, 1.2 and 1.6 with 1.6 in white. In (c), the rainfall rate contours are for 0.4, 0.8, 1.2 and 1.6 mm/hr . with the center white dot showing 1.6 mm/hr . From McMurdie and Katsaros (1983).

more than 5° of longitude. Convergence is also shown to the west of Vancouver in the warm air sector of the system. Divergence values as high as $(3.55 \pm 0.38) \times 10^{-5} \text{ sec}^{-1}$ and as low as $(-7.98 \pm 0.91) \times 10^{-5} \text{ sec}^{-1}$ were obtained. The standard deviations show that the first was surely positive and the second surely negative. Values of near zero divergence would be indicated if the estimate plus one standard deviation and the estimate minus one standard deviation changed sign. This happened six times.

The estimate was between $1 \times 10^{-5} \text{ sec}^{-1}$ and $1 \times 10^{-5} \text{ sec}^{-1}$ 28 times, suggesting areas of nearly nondivergent flow.

The higher convergence values would produce upward vertical velocities of 1.6 cm/sec at a height of 200 m. Air moving at 15 m/s will rise 57 m as it travels 54 km in one hour. Over a one degree square at 50° N about 400 cubic kilometers of air pass upward through the 200 meter level each hour in the area of strong convergence.

Figure 3 shows respectively the total mass of water vapor over each square meter of the sea surface in kg/m^2 , the total liquid water in kg/m^2 and the rainfall rate in mm/hr . The fronts in these figures are different from those in Fig. 2. The analyses involved were independent and need to be reconciled on the basis of more data and consistency checks.

These figures for REV 1212 provide valuable quantitative data on the properties of an extratropical cyclone. The winds are shown to be transporting warm moist air by means of a concentrated southerly flow in advance of the cold front. The moisture is concentrated by this flow in a narrow band along the surface front. The band of high water vapor content undoubtedly would continue beyond the swath following along the frontal system. The highest concentrations of liquid water in Fig. 3(b) are along the front and in the area of convergence of Fig. 2(b). The precipitation is patchy in small cells with values over 4 mm/hr . Were the pattern in Fig. 3(c) to be shifted north north westward, without change in form, past a point at about 49°N , 130°W , at, say, 15 or 20 m/s and the rainfall rate integrated with time, the result would be an integrated rainfall graph very similar to the one in Fig. 1(b). The cold front passage as in Fig. 1 would also appear as a time history at this and many other points properly located in time.

WIND STRESS AND WIND STRESS CURL

There are many different equations that have been proposed to relate the wind at 10 m to the wind stress defined either by

$$\vec{\tau}/\rho = u_*^2 = - \langle u'w' \rangle \quad (13)$$

or by $C_{10} = u_*^2 / \bar{U}(10)^2 \quad (14)$

as, for example, Large and Pond (1981). A completely new one based on data from three different sources was used in this study. Lots of questions in this problem area remain unsolved, but if the superobservation represents the synoptic scale wind at 19.5 meters, it can be related to the wind at 10 m by (15).

$$\bar{U}(19.5) = \bar{U}(10) + (u_* (\bar{U}(10)) \ln(19.5/10)) / \kappa \quad (15)$$

and by, in meters per second,

$$u_*^2 = 10^{-3} (2.717(U(10)) + 0.142(U(10))^2 + 0.0761(U(10))^3) \quad (16)$$

For selected values of $U(19.5)$ Table 1 can be obtained as examples and as detailed a table as desired can be constructed. There is a one to one relationship between the isotach values in Fig. 2(b) and u_*^2 values from the following table and the above equations except that u_*^2 is strongly concentrated in areas of high winds. As the wind varies by a factor of 5 the stress varies by a factor of 45.

TABLE 1 Values of $\bar{U}(19.5)$, $\bar{U}(10)$, u_*^2 and u_* in Meters per Second Except u_*^2 .

$\bar{U}(19.5)$	$\bar{U}(10)$	u_*^2	u_*
5	4.7	0.024	0.156
10	9.5	0.103	0.321
15	14.4	0.281	0.531
20	18.7	0.601	0.775
25	23.2	1.100	1.049

For an air density of 1.25 kg/m^3 , the vector value of $\vec{\tau}$ can be computed along with corresponding parallel and normal estimates of sampling variability.

The finite difference estimate of the curl is given by (17) in units of ((Newtons per square meter) per meter).

ORIGINAL FIGURE
OF POOR QUALITY

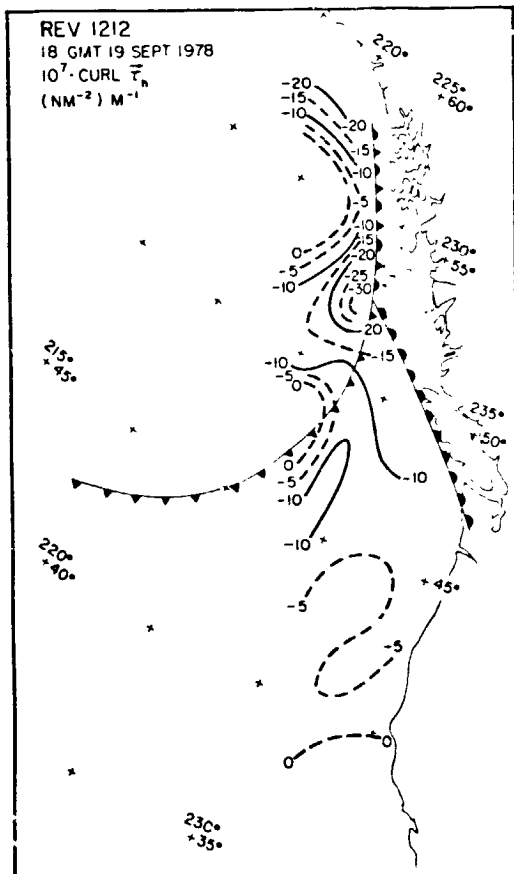


Fig. 4 The Curl of the Wind Stress for REV 1212. Values are in Newtons per Square Meter per Meter.

Fig. 4 shows the field of the curl of the wind stress within the swath for REV 1212. For the four REVS of Pierson, et al. (1983), this figure is typical. Both high wind stress values and high values of the curl are concentrated over relatively small areas of the ocean.

At the synoptic scale, the wind stress is large over relatively small areas and small over relatively large areas. Areas of large wind stress curl are concentrated over small areas. The erratic day to day motions of drogued buoys as studied by Kirwan, et al. (1978) in the North Pacific may eventually be explainable by such data.

DISCUSSION

The time is not too far off relative to a time scale beginning around 1900 and accelerating since Skylab in 1973 and SEASAT in 1978 to plans for several scatterometers, radiometers and altimeters in the late 1980's when analyses such as this one over the oceans will be global and used to prepare routine weather forecasts and to understand the ocean circulation. There are problems of four dimensional space time data assimilation still to be solved plus the need for better atmospheric models and improved representations for turbulence. It will not be possible to beg the question by arguing that the initial value specification is not good enough to yield a

correct forecast. It is already clear from the analysis of SEASAT products that the specification of wind fields over the oceans can, at times, be grossly in error when only conventional data are used.

$$\begin{aligned} \text{CURL}(\vec{\tau}_h)_s = \frac{4.5 \cdot 10^{-6}}{\cos \theta_o} & \left\{ (\tau_{s\theta}(\lambda_o + 1, \theta_o) - \tau_{s\theta}(\lambda_o - 1, \theta_o)) \right. \\ & - \cos \theta_o (\tau_{s\lambda}(\lambda_o, \theta_o + 1) - \tau_{s\lambda}(\lambda_o, \theta_o - 1)) \\ & \left. + 0.034905 \sin \theta_o \tau_{s\lambda}(\lambda_o, \theta_o) \right\} \end{aligned} \quad (17)$$

ACKNOWLEDGEMENTS

The research reported herein was supported by the National Aeronautics and Space Administration under Contract NAGW-266. We thank the many persons who have helped us as described in the more detailed paper on which this summary is based.

REFERENCES

- Bjerknes, V. 1904: Das Problem der Wettervorhersage Betrachtet vom Standpunkte der Mechanick and der Physik, Meteor. Z., Vol. 21, 1-7.
- Brunt, D. 1942: Weather Study. The Roland Press Co. 215 pp.
- Kirwan, A. D., G. J. McNally, E. Reyna and W. J. Merrell Jr. 1978: The Near Surface Circulation of the Eastern North Pacific. J. Phys. Oceanogr. Vol. 8, No. 6, 937-945.
- Large, W. G., and S. Pond 1981: Open Ocean Momentum Flux Measurements in Moderate to Strong Winds. J. Phys., Oceanogr. Vol. 11, 324-326.
- McMurdie, L. A., and K. B. Katsaros 1983: Locating Synoptic Fronts and Rain Areas Using the SEASAT Scanning Multichannel Microwave Radiometer. In Studies of Atmospheric Water with the SEASAT Scanning Multichannel Microwave Radiometer. Final Report to NOAA, Cont. Na-81-SAS-00756 U. of Wash. Seattle, Contribution No. 671.
- Pierson, W. J. 1983a: The Measurement of the Synoptic Scale Wind Over the Ocean. J. Geophys. Res. Vol. 88 No. C3. 1683-1708.
- Pierson, W. J. 1983b: Highlights of the SEASAT-SASS Program: A Review in Allan T. D., Satellite Microwave Remote Sensing. John Wiley and Sons. 69-86.
- Pierson, W. J., W. B. Sylvester and R. E. Salfi 1983: Synoptic Scale Wind Field Properties from the SEASAT-SASS. The City College, Tech. Rept. NASA Contract NAGW-266. 152 pp. Plus Appendicies.
- Pierson, W. J., S. Peteheych and J. C. Wilkerson 1980: The Winds of the Comparison Data Set for the SEAST Gulf of Alaska Experiment, IEEE J. Ocean. Eng. OE5(2), 169-176.
- Richardson, L. F. 1922: Weather Prediction by Numerical Process, London Cambridge University Press, (Reprinted Dover 1965), 236 pp.
- Robinson, G. D 1978: Weather and Climate Forecasting as Problems in Hydrodynamics. M. Weather Rev., Vol. 106, No. 4 448-457.
- Woiceshyn, P. M. ed 1979: SEASAT Gulf of Alaska Workshop Vol II Comparison Data Base: Conventional Marine Meteorological and Sea Surface Temperature Analysis. Appendice A and B. JPL Document 622-101. Jet Propul. Lab. Pasadena, Cal.

THE IMPACT OF SCATTEROMETER WIND DATA ON GLOBAL WEATHER FORECASTING

By

R. Atlas, W. E. Baker, E. Kalnay, M. Halem, P. Woiceshyn†, and S. Peteherych*
Goddard Laboratory for Atmospheric Sciences, NASA/Goddard Space Flight Center
Greenbelt, MD 20771

†Jet Propulsion Laboratory, 4800 Oak Grove Drive, Pasadena, CA 91109

*Atmospheric Environment Service, Downsview, Ontario M3H 5T4, CANADA

ABSTRACT

A series of experiments has been performed to assess the impact of Seasat-A scatterometer (SASS) winds on coarse resolution GLAS model forecasts. In general, the effect of objectively dealiased-SASS data is found to be negligible in the Northern Hemisphere. In the Southern Hemisphere the impact is larger and primarily beneficial when VTPR data is excluded. However, the inclusion of VTPR data eliminates the positive impact, indicating some redundancy between the two data sets.

1. INTRODUCTION

The Seasat-A satellite that flew for three months in 1978 provided a new source of data over the world's oceans for meteorological and oceanographic research. On board the satellite, an active microwave sensor known as the Seasat-A Satellite Scatterometer (SASS) measured capillary wave backscatter, which can be used to infer wind stress or surface wind velocity (Jones *et al.*, 1978). The scatterometer provides high resolution winds, but each wind can have up to four possible directions. One wind direction is correct, and the rest are ambiguous or "aliases". Consequently, before an analysis can be made with the SASS winds the aliases must be removed.

Until recently only a few limited studies had been conducted to evaluate the usefulness of SASS data for numerical weather prediction. In a simulation study, Cane *et al.* (1981) found an improvement in the surface pressure forecast over the extratropics with SASS winds. However, their results are probably too optimistic because the assimilated winds did not contain an alias and were inserted at the lowest model level (nominally 945 mb). This underestimated the typical errors made in obtaining a 945 mb wind field from the ambiguous surface winds.

In studies with actual SASS data, Yu and McPherson (1979) designed an iterative procedure for alias removal and analyzed the resolved SASS winds with a global optimum interpolation scheme (Bergman, 1979). They found the effect of the SASS winds on the surface pressure analysis to be negligible over areas where ship reports are plentiful. However, large effects were noted over areas where ship reports are sparse.

In a later study, Yu and McPherson (1981) used SASS winds directly in the lower tropospheric wind analysis. They found large differences in the SASS and NOSASS (without SASS winds) wind and height analyses in the Southern Hemisphere after 48 h of assimilation. The differences in the Northern Hemisphere were much smaller. Similarly, the 72 h forecast differences were significant in the Southern Hemisphere, but very small in the Northern Hemisphere.

Using a variational approach to remove the ambiguity of the SASS winds, Hoffman (1982) found the resulting analysis within the SASS data swath to be a reasonable representation of the surface wind. However, Hoffman noted some deficiencies particularly near circulation centers which could be corrected by subjective intervention.

In this study, we examine the impact of SASS data on the GLAS analysis/forecast system. In Section 2, the objective analysis and assimilation of SASS winds is discussed. A scheme developed to objectively dealias the SASS data is discussed in Section 3. Section 4 presents the results of some analysis and forecast experiments, and a summary follows in Section 5.

2. OBJECTIVE ANALYSIS AND ASSIMILATION OF SASS WIND DATA

In this section we describe the analysis system developed for the evaluation of the usefulness of Seasat data for numerical weather prediction. A similar version was utilized in the evaluation of data from the FGGE observing systems (Halem *et al.*, 1982).

2.1 Forecast Model

The forecast model is the 4° latitude by 5° longitude fourth order global general circulation model described by Kalnay-Rivas *et al.* (1977) and Kalnay-Rivas and Hoitsma (1979). It is based on an energy-conserving scheme in which all horizontal differences are computed with fourth-order accuracy. A two-dimensional (latitude and longitude) sixteenth order Shapiro (1970) filter is applied every 2 h on the sea level pressure, potential temperature, and wind fields. In this scheme, wavelengths longer than four grid lengths are resolved accurately without damping. Wavelengths shorter than four grid lengths, which would otherwise be grossly misrepresented by the finite differences, are filtered out while they are still infinitesimal.

2.2 Objectively Analysis Scheme

The objective analysis scheme, described in Baker (1983), employs a successive correction method (Cressman, 1959) utilizing the first guess provided by the model 6 h forecast from the previous analysis. Eastward and northward wind components, geopotential height, and relative humidity are analysed on mandatory pressure surfaces. Surface pressure and temperature are reduced to sea level and analyzed there. An intermittent analysis is performed every 6 h on batches of data grouped in a ± 3 h window about each synoptic time.

In the assimilation of the SASS wind data, the analysis procedure was modified from the way in which it was applied with the FGGE data (Halem *et al.*, 1982). The various steps in the assimilation of SASS data involve objective dealiasing, optional subjective enhancement, objective analysis of the final dataset, and adjustment of the sea level pressure field by the surface wind field using the linear balance equation on the wind increments introduced by the analysis. The model is then integrated either 6 h to provide a first guess for the next dealiasing or for a few days in order to conduct data impact studies.

3. OBJECTIVE DEALIASING OF THE SASS WIND FIELD

A three-pass procedure was developed to objectively dealias the SASS wind field. The guess for the first pass over the data is provided by a 6 h prediction from the previous analysis by the GLAS fourth order model. The SASS wind vector which is selected from the possible aliases is the one nearest in direction to the first guess vector obtained by a bilinear interpolation of the four surrounding first guess vectors. The least ambiguous data points (two aliases) are handled in the first pass, with the more ambiguous cases (three or four aliases) handled in the second or third pass. This approach was adopted because of our experience in subjectively dealiasing SASS data which indicated that a more accurate SASS wind field could be produced by using resolved SASS vectors from data points with lesser ambiguity in subsequent dealiasing passes over data points with more ambiguity.

After the first pass over the SASS data, the resolved SASS vectors and available ship winds are analyzed by a successive correction method (SCM). The resulting surface wind analysis is utilized in resolving the SASS wind vectors in the second pass. The resolved SASS winds from the first two passes and the ship data are then analyzed as before. This analysis is then utilized in the third pass in a similar manner.

4. RESULTS OF ANALYSIS/FORECAST EXPERIMENTS

In this section we present the results of some analysis/forecast experiments with the Seasat data. Four assimilation experiments have been conducted from 0000 GMT 7 September 1978 to 1200 GMT 13 September 1978. The experiments began from initial conditions provided by the global operational Hough analysis (Flattery, 1971) of the National Meteorological Center (NMC) for 0000 GMT 7 September 1978.

The four assimilation experiments differed only with respect to the use of objectively dealiased SASS wind data or satellite temperatures from the vertical temperature profile radiometer (VTPR) on board NOAA-4. All other available conventional and satellite cloud track wind data were included in each of the assimilation experiments. A total of 16 forecasts (four for each experiment) were generated from the initial conditions provided by the assimilation at 0000 GMT 9, 1200 GMT 13 September 1978. Extensions of these assimilation cycles and forecast cases as well as a fifth assimilation experiment using the subjectively enhanced SASS winds are planned for the near future.

The evaluation of SASS data impact concentrated on differences between the initial states which resulted from the assimilation of SASS winds and differences between numerical predictions made from these initial states. Initial state differences were evaluated by comparing pressure and wind field analyses produced with and without SASS data. Numerical predictions were evaluated objectively by S_1 scores and rms differences and by subjective comparisons.

4.1 Initial State Differences

For satellite observations of surface wind to have a significant impact on numerical weather prediction, substantial differences between the atmospheric state analyses produced with and without the data must occur. The surface wind observations should be consistent with the higher level analysis and low level

mass field, and the forecast model should be sensitive to the low level wind modifications. Assimilation of scatterometer data can work in two ways to modify the analysis. First, it can modify the wind field directly and the mass field indirectly through balance adjustments to the wind increments. Second, these differences may be amplified at the next analysis time due to their effects on the first guess fields used for that analysis.

The magnitude of the initial state differences depends strongly on the amount of available conventional and satellite data. Thus, larger differences would be expected in the Southern Hemisphere than in the Northern Hemisphere and in the assimilation without VTPR data.

Comparisons of analyses produced by the four assimilation experiments (not shown) for the most part confirm this expectation. In the Northern Hemisphere, with or without VTPR data, the assimilation of SASS winds produced only modest (generally $< 10 \text{ m sec}^{-1}$) vector wind differences from 1000-500 mb. Over most of the oceans there were negligible differences in sea level pressure and 500 mb geopotential height. Maximum 500 mb height differences of 64 m, covering not more than two model grid points were occasionally observed. On the average, the central pressure of cyclones at sea level differed by .5 mb. The maximum difference in central pressure was 5 mb.

In the Southern Hemisphere, more significant differences occurred. For the assimilations with VTPR data included, vector wind differences of 10-20 m sec^{-1} , sea level pressure differences of 8-16 mb and 500 mb height differences of 64-98 m covered large regions of the extratropical oceans. The average and maximum central pressure differences for cyclones at sea level were 3 mb and 15 mb respectively. For the assimilation with VTPR data excluded substantially larger differences were observed.

4.2 Prognostic Differences

Both objective scores and subjective comparisons were used to evaluate the impact of SASS data on GLAS model forecasts of sea level pressure and 500 mb height. S_1 scores and rms differences were calculated for each of the 72 h forecasts at 24 h intervals using the NMC objective analysis for the same time as verification. For reasons of brevity, only S_1 scores averaged over all forecasts for North America and Europe (Fig. 5) and for South America and Australia (Fig. 6) are presented here.

Fig. 5 shows the average effect of the SASS data to be insignificant over North America and Europe. With VTPR data excluded, the impact of SASS winds is very slightly positive from 24-48 h and very slightly negative at 72 h. The inclusion of VTPR data results in improved predictions at 24 h and 48 h at 500 mb but degrades the 24 h and 72 h forecast skill at sea level and the 72 h skill at 500 mb. This degradation is larger in the forecasts which also included SASS data. Thus, in the cases with VTPR data, the impact of SASS winds is slightly negative at sea level and negligible at 500 mb throughout the 72 h period.

Fig. 6 shows that the effect of SASS data on forecasts for South America and Australia is highly dependent upon whether or not VTPR soundings were assimilated over the Southern Hemisphere oceans. When VTPR data is excluded, the impact of SASS winds is increasingly positive from 24-72 h at sea level; at

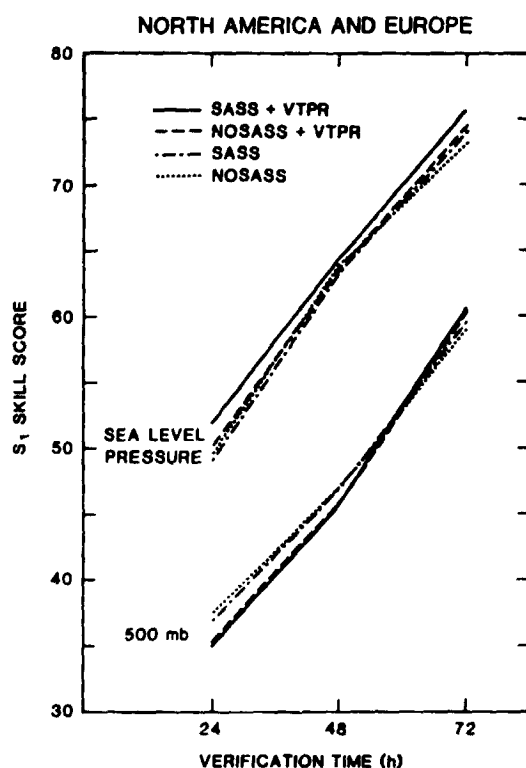


Fig. 1. S_1 scores for North America and Europe averaged over 4 forecasts.

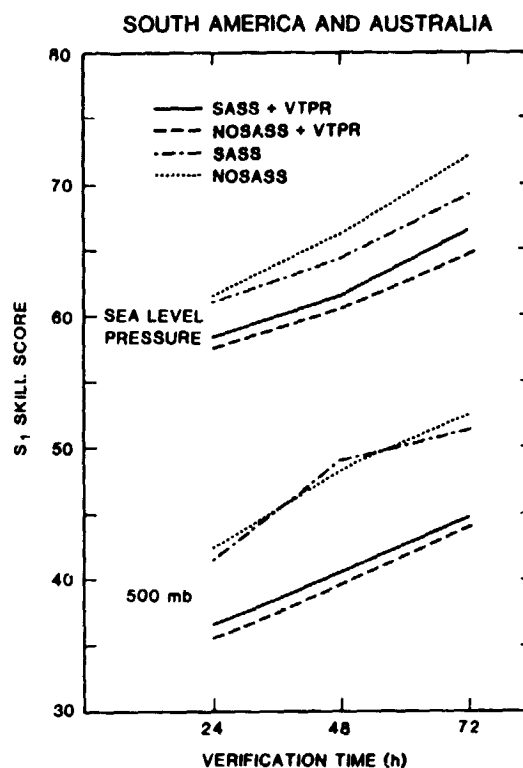


Fig. 2. Same as Fig. 1 for South America and Australia.

500 mb the effect is essentially negligible. It is very slightly positive at 24 h and 72 h and very slightly negative at 48 h. the inclusion of VTPR data in the Southern Hemisphere has a large beneficial effect. However, it improves the NOSASS predictions substantially more than the SASS forecasts. As a result, the impact of SASS winds is slightly negative at both sea level and 500 mb from 24-72 h.

For the subjective evaluation sea level pressure and 500 mb prognostic charts from the four experiments were compared with the NMC analysis over North America, Europe, South America and Australia. Comparisons were made at 12 h intervals and the SASS forecasts were classified as significantly better, slightly better, the same, slightly worse, or significantly worse following the procedures described by Atlas et al., (1982).

Table 1 presents a summary of the subjective ratings. These results confirm the generally insignificant effect of SASS data over North America and Europe with only one prognostic chart being classified as significantly worse due to the combined effect of SASS and VTPR data. For South America and Australia, the effect of SASS data is larger but inconsistent. Both positive and negative impacts occur. The impact is largest and most beneficial when VTPR soundings are not assimilated.

Table 1. Subjective Evaluation of SASS Impact For Sea Level Pressure and 500 mb Height.

SASS Prognostic Charts	North Amer. & Europe		South Amer. & Australia	
	W/VTPR	W/O VTPR	W/VTPR	W/O VTPR
Significantly Better	0	0	1	3
Slightly Better	0	0	0	10
Same	71	72	65	50
Slightly Worse	0	0	4	3
Significantly Worse	1	0	0	2

5. SUMMARY

A series of assimilation/forecast experiments has been performed to assess the impact of Seasat-A scatterometer (SASS) winds on GLAS model forecasts. Four assimilation cycles were conducted from 0000 GMT 7 September to 1200 GMT 13 September 1978 which differed only with respect to the inclusion or exclusion of objectively dealiased SASS winds or VTPR soundings. four forecasts winds or VTPR soundings. Four forecasts from each assimilation were evaluated by objective measures and subjective comparisons.

In general, the results of this evaluation show a negligible effect of the SASS data in the Northern Hemisphere. In the Southern Hemisphere the impact is larger and primarily beneficial when VTPR is excluded. However, the inclusion of VTPR data effectively eliminates this positive impact, indicating some redundancy between the two data sets.

This study was limited by the coarse resolution of the analysis and forecast model, the lack of a detailed planetary boundary layer formulation in the model, the use of only objective dealiased SASS winds, the small number of forecast cases and others. We plan to investigate the importance of each of these factors in the near future.

6. ACKNOWLEDGEMENTS

The SASS wind data fields, utilized in this study were obtained from the Atmospheric Environment Service (AES) of Canada, courtesy of S. Peteherych. Subjective dealiasing and subjective enhancement of objectively dealiased winds at GLAS are being performed in collaboration with P. Woiceshyn (JPL), M. Wurtele (UCLA) and S. Peteherych. (AES). The authors benefited from discussions with each of the above investigators as well as with R. Hoffman, M. Cane, T. Yu and R. McPherson. Excellent technical assistance with the data processing and assimilation were provided by D. Edelmann, A. Pursch and D. Wallace. S. Postman, H. Bloom, J. Badner and R. Laplante participated in the subjective evaluation. L. Thompson typed the manuscript and L. Rumburg drafted the figures.

7. REFERENCES

- Atlas, R., M. Halem, and M. Ghil, 1982: The effect of model resolution and satellite sounding data on GLAS model forecasts. *Mon. Wea. Rev.* 110, 662-682.
- Baker, W. E., 1982: Objective analysis and assimilation of observational data from FGGE. *Mon. Wea. Rev.*, 111. in press.
- Bergman, K. H., 1979: Multivariate analysis of temperatures and winds using optimum interpolation. *Mon. Wea. Rev.*, 107, 1423-1444.
- Boggs, D., 1981: The Seasat scatterometer model function: the genesis of SASS1. Jet Propulsion Laboratory, Pasadena, California, 44 pp., [NTIS PD 622-230].
- Cane, M. A., V. J. Cardone, M. Halem and I. Halberstam, 1981: On the sensitivity of numerical weather prediction to remotely sensed marine surface wind data: A simulation study. *J. Geophys. Res.*, 86, 8093-8106.
- Cressman, G. P., 1959: An operational objective analysis scheme. *Mon. Wea. Rev.*, 87, 367-374.
- Flattery, T., 1971: Spectral models for global analysis and forecasting. *Proc. Sixth AWS Technical Exchange Conference*, U. S. Naval Academy, Annapolis, Air Weather Service Tech. Rep. 242, 42-54.
- Halem, M. E., Kalnay, W. E. Baker and R. Atlas, 1982: An assessment of the FGGE satellite observing system during SOP-1. *Bull. Amer. Meteor. Soc.*, 63, 407-426.
- Hoffman, R. N., 1982: SASS wind ambiguity removal by direct minimization. *Mon. Wea. Rev.*, 110, 434-445.
- Jones, W. L., F. W. Wentz and L. C. Schroeder, 1978: Algorithm for inferring wind stress from Seasat-A. *J. Spacecraft and Rockets*, 15, 368-374.
- Kalnay-Rivas, E., A. Bayliss and J. Storch, 1977: The 4th order GISS model of the atmosphere. *Beitr. Phys. Atmos.*, 50, 299-311.
- Kalnay-Rivas, E. and D. Hoitsma, 1979: The effect of accuracy, conservation and filtering on numerical weather forecasting. *Preprints Fourth Conference on Numerical Weather Prediction* Silver Spring, Maryland, AMS, Boston, pp. 302-312.
- Yu, T. W. and R. D. McPherson, 1979: Surface pressure analysis using scatterometer derived wind data from the Seasat-A satellite. *Preprints Fourth Conference on Numerical Weather Prediction*, Silver Spring, Maryland, AMS, Boston, pp. 351-355.
- Yu, T. W. and R. D. McPherson, 1981: Global data assimilation experiments with scatterometer winds from Seasat-A. *Preprints Fifth Conference on Numerical Weather Prediction*, Monterey, California, AMS, Boston, pp. 9-13.

17-10
53
N84 27315

FIRST GLOBAL ANALYSIS OF SEASAT SCATTEROMETER WINDS AND POTENTIAL FOR
METEOROLOGICAL RESEARCH

Steven Peteherych

Atmospheric Environment Service, Downsview, Ontario M3H 5T4, Canada

Morton G. Wurtele

Department of Atmospheric Sciences, U.C.L.A., Los Angeles, CA 90024, USA

Peter M. Woiceshyn

Jet Propulsion Laboratory/California Institute of Technology, Pasadena, CA 91109, USA

Dale H. Boggs

dB Systems, Ltd., Inc., La Canada-Flintridge, CA 91011, USA

Robert R. Atlas

Goddard Laboratory of Atmospheric Sciences/NASA, Greenbelt, MD 20771, USA

1. ABSTRACT

The first global wind fields from Seasat scatterometer data have now been produced. Fifteen days (Sept. 6-20, 1978) of record are available on tape, with unique wind directions indicated for each observation. The methodology of the production of this data set is described, as well as the testing of its validity. A number of displays of the data, on large and small scales, analyzed and gridded, are provided.

2. INTRODUCTION

This paper is concerned with the production and scientific potential of global data sets from Seasat Scatterometer (SASS) data record. The validation of the individual wind vector observations is fully documented (Jones et al., 1982; Schroeder et al., 1982) and is here taken as established, although elsewhere in this volume (Woiceshyn et al., 1984), certain features of the geophysical algorithm are called into question. A number of interesting case studies using SASS data have demonstrated the capability of resolving features and patterns with significantly greater accuracy and resolution than is possible with conventional data (Peteherych et al., 1981; Pierson, Sylvester, and Salfi, 1984). However, the problems associated with the production of a global data set, and the research made possible through use of such sets, are different from those involved in case studies; and these aspects of SASS data are the ones treated herein.

As is well known, the Seasat Scatterometer, having two antennas on each side, produced a Geophysical Data Record (GDR) that is ambiguous as to wind direction, with two to four alternative directions associated with each pair of doppler cells. Figure 1 displays schematically the relation between the number and orientation of alternative wind directions and the direction of the satellite antennas. This relationship became crucial in the methodology of producing a set of unique wind vectors from the SASS data, as will be seen below.

Two major field programs, the Gulf of Alaska Experiment (GOASEX) and the Joint Air-Sea Interaction Experiment (JASIN) in the northeast Atlantic provided observational data against which the Seasat geophysical data, including those from SASS, could be compared and validated. The comparisons were carried out in three workshops organized for that purpose.

The process of selecting a single direction from among alternatives ("aliases") became known as "dealiasing," and partial regional data sets were dealised for the GOASEX and JASIN workshops. It was evident to meteorologists

that dealiasing could be achieved by that process of subjective pattern-recognition that is called meteorological analysis; and this procedure, as well as the SASS technology in producing wind measurements, was validated at the two workshops. The GOASEX workshop results were reported by Jones et al. (1979). The cover of the issue of *Science* containing the GOASEX reports was devoted to a dealiased SASS swath off the Canada/Alaska coast. Since that publication date, all available ship observations were collected and added to the figure to show the near-perfect agreement. This is here reproduced as Figure 2, with the ship winds drafted in heavier line than the SASS winds.

In the case of JASIN, two teams of analysts worked independently and without the aid of *in situ* observations or satellite imagery. Their final products agreed to an extent that was acceptable to the workshop scientists, and did not require alteration when the *in situ* data were made available. Details of this experiment are presented in the article by Wurtele et al. (1982), in which the fundamental kinematic patterns - common to all two-dimensional vector fields - are systematically described, and examples given illustrating the realization of these patterns in JASIN data.

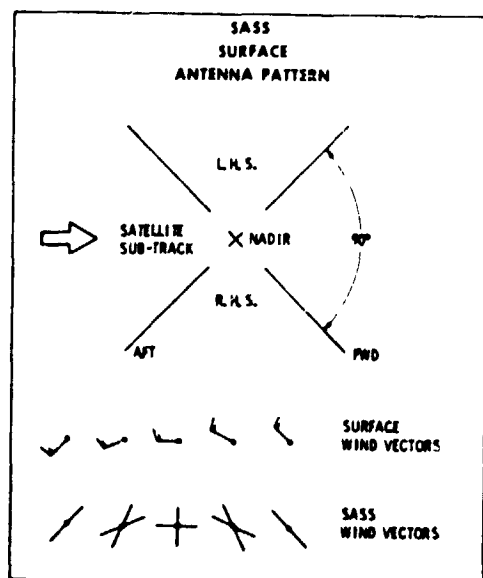


Figure 1. Schematic showing relation between wind direction, antenna orientation, and SASS reported directions.

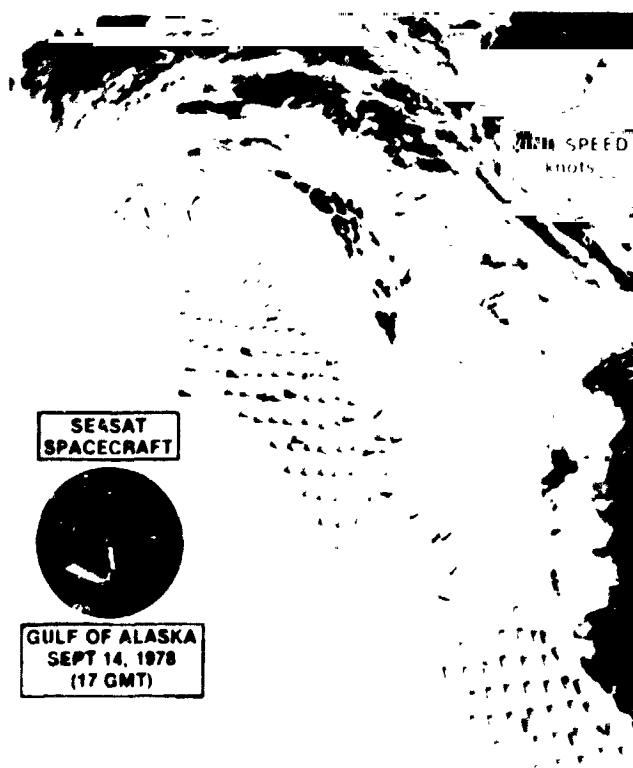


Figure 2. SASS Rev 1140 from GOASEX workshop, dealiased, with satellite imagery superimposed. Note 50-km resolution. Ship-observed winds have been added in heavy line drafting to compare with scatterometer data.

3. PRODUCTION OF THE DATA FILE

In July 1982 a cooperative project was begun to dealise a global data set. The participating institutions were Jet Propulsion Laboratory, Atmospheric Environment Service of Canada (AES), NASA Goddard, and U.C.L.A. (Meanwhile, objective dealiasing techniques had been under investigation at Goddard Laboratory of Atmospheric Science (Baker et al., 1984), and the two methodologies contributed to the development of each other.)

The official GDR was found less useful in the subjective dealising than the charts produced by AES, on which the SASS observations were plotted with 100 km-resolution at equal intervals and in rows normal to the satellite subtrack. In situ data from coastal stations and ships were plotted on charts with identical cartography. The analysts consulted also imagery from GOES East and West, DMSP, and Meteosat. (In fact, the analysts were quickly impressed by the extent to which the cloud patterns - at any height - could be associated with surface wind patterns.)

As with JASIN, the analysts worked in two teams, independently, one at AES, the other with JPL/UCLA. Various measures were recorded of the agreement of the wind-vector selections of the two teams; here it suffices to say that agreement without consultation was achieved in about 80 percent of the individual vectors. The areas of disagreement were discussed in workshops, and a "consensus" set of selected wind vectors was determined.

At this point, however, a severe data-handling problem arose, that had not been faced with the GOASEX and JASIN data. When the analysts had done their work, the consensus data existed only on the analysts' charts; it now had to become a part of the SASS data tape, that each SASS wind observation would have one of its alternatives designated as the "correct" direction. Each chart contained approximately 4500 wind observations, and each SASS-day required six charts.

The procedure finally adopted for this massive data handling constituted a semi-automated routine based on the characteristics of the SASS instrument represented in Figure 1. There, it will be noted, the true direction varies by no more than 90 degrees, and each SASS datum has one and only one direction in that quadrant. Thus a single designator, for the rear quadrant, can specify the correct selection from the aliases. Thus it is possible to delineate polygonal areas within a SASS swath - greater or lesser in extent - within which all "correct" wind directions fall within a single quadrant, relative to the satellite sub-track. The vertices of these polygons are identified and recorded on tape by a digitizer, together with the essential information, including, of course, the quadrant direction designator. An example of five SASS swaths divided among polygons is presented in Figure 3. The polygon file thus generated is merged with the original SASS data file to create a geophysical data record of unique marine wind vectors. (The alias directions are retained in the file for the benefit of scientists who prefer to do it themselves).

ORIGINAL PAGE IS
OF POOR QUALITY

QUADRANT POLYGONS DEFINING REGIONS AND
DIRECTIONS FOR CREATING DATA RECORD OF UNIQUE
SASS WIND DIRECTIONS BY BATCH PROCESSING

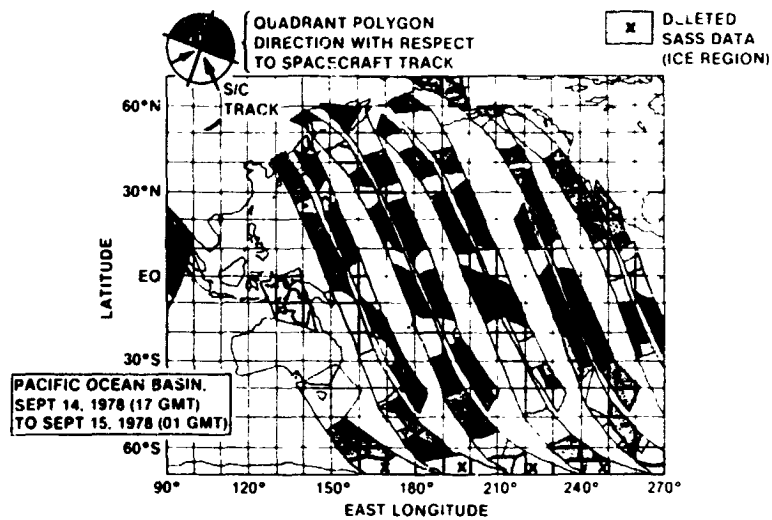
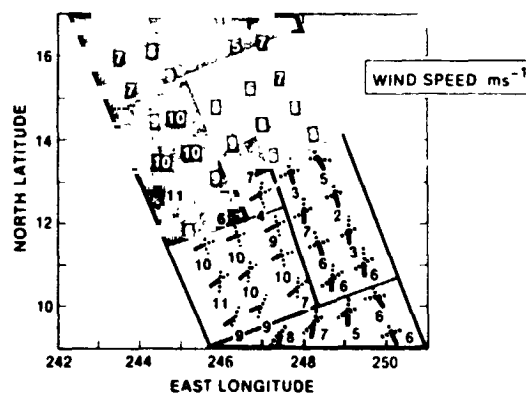


Figure 3. Polygons indicating wind direction for five SASS swaths.

DETAIL OF QUADRANT POLYGONS WITH SELECTED
WIND DIRECTION (BLACK)



ORIGINAL FILED IN
OF FOUR QUALITY

SEASAT SCATTEROMETER GLOBAL MARINE WIND ANALYSIS

STREAMLINES AND ISOTACHS

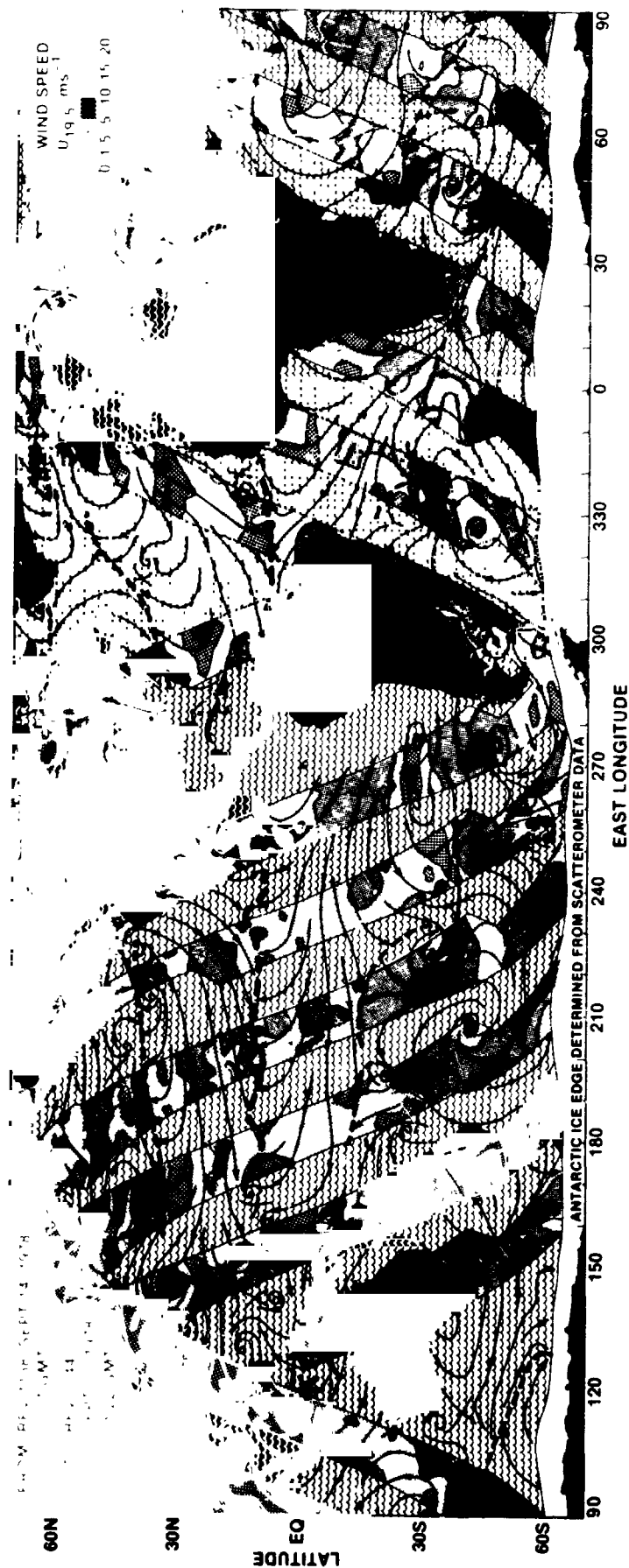


Figure 4. One global SASS day wind field, represented by streamlines (solid black, with arrows) and isotachs (code at upper right). ITCZ is heavy dashed line; fronts are light dashed lines. Wavy lines designate ocean between SASS swaths.

ORIGINAL PAGE IS
OF POOR QUALITY

4. GLOBAL DATA PRESENTATION

By the methods described, then, a total of 15 days of global SASS data has been dealiased, and is now available to scientists upon application to NASA Headquarters. Almost one-half million wind observations are recorded in this data set. There are more observations in some regions of the southern oceans than are represented in the total climatological history of these regions before Seasat. Visual presentation of these global data may be made in a number of ways, and we have chosen the following. Half the globe is plotted with descending orbital data, the other half with the corresponding ascending orbital data. Such a plot is presented in Figure 4. It is a mode of presentation unfamiliar to meteorologists accustomed to synoptic charts.

Consecutive parallel orbits are removed by 1.5 hours in time from each other. The two V-shaped configurations, where ascending and descending orbits meet, represent a 12-hour displacement in time. Between successive orbital swaths streamline interpolation is possible, and in any case, analyses may be checked against co-located data 12 hours earlier or later. Interpolation in the V-regions will constitute, in effect, a smoothing over a 12-hour period, and is therefore less reliable as representing momentary directions. The streamlines in Figure 4 are black lines with direction arrows. Speeds (not interpolated between swaths) are indicated according to the code in the upper right.

Such a global presentation, based on some 28,000 observations, is an exciting event to meteorologists. We note the greater wind speeds in the Southern Hemisphere; the monsoonal flow onto the Indian subcontinent and the African continent, east and west coasts; the two typhoons (Irma and Judy) on either side of the Japanese islands. The Antarctic ice is shown in white, the ice-edge itself having been identified from the SASS observations. The Intertropical Convergence Zone (ITCZ) - a heavy dashed black line - shows strongly in the eastern half of the Pacific and extends from Africa to Brazil in the Atlantic.

We may now look in higher resolution at one of the interesting features of the map, the ITCZ in the region of 220-260E. Figure 5 presents an analysis of this area, superimposed on the un-dealiased scatterometer observations. The storm-induced perturbations on the ITCZ are clearly delineated in the 100-km resolution

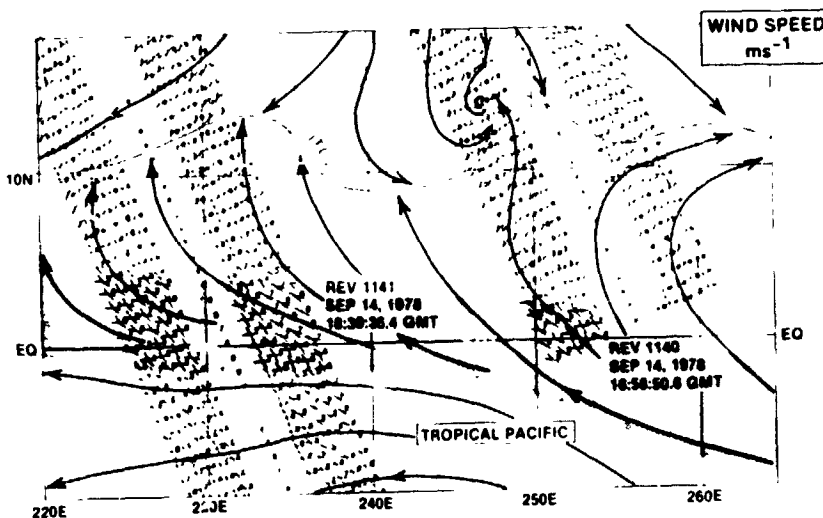


Figure 5. ITCZ area
220-260 E for 14
September.

wind data, and even more striking is the different westward flow pattern detected by the SASS data along the Equator, emphasized in the Figure by gray shading. This is not a unique occurrence of this phenomenon. Rather, the data set reveals that when tropical depressions on the ITCZ intensify, they tend to be associated with a zone of divergence along the Equator. The density and quality of the data permit the calculation of vorticity and divergence fields, for the entire global oceans, or for any area of interest. Figures 6 and 7 show, respectively, the contours of vorticity and divergence in the area covered by Figure 5. (Units for both are 10^{-6} s^{-1}). Maxima of vorticity appear at the perturbations of the ITCZ, with values of $4 \times 10^{-5} \text{ s}^{-1}$, and vorticity minima of about half the magnitude, are only four to six degrees to the south. Convergence and divergence maxima, however, are of about equal magnitude ($\pm 3 \times 10^{-5} \text{ s}^{-1}$), and are separated by ten degrees latitude, the divergence centers being, as anticipated very near the Equator. These surface flow patterns seem to suggest a meridional circulation, rising over the ITCZ and sinking at the equator.

5. GRIDDED FIELDS

For numerical manipulation, it is essential to connect the streamlines /isotach fields to digital (u,v) vector fields at regularly spaced grid points. This has been done by means of a three-point linear interpolation algorithm modified for the unique requirements of the present project. A display of gridded wind field data is of little interest in itself; but from such fields, with appropriate software, many interesting fields may be derived.

As an example, Figures 8 and 9 present, respectively, the mean eastward and mean northward velocity components for the entire 15-day data set, in the Pacific Ocean. Dashed light contours are for negative values, solid contours for positive, and the heavy solid lines if the zero contour. The huge area of easterly trades dominates Figure 8, with mean westerlies much stronger in the Southern Hemisphere. Figure 9 vividly illustrates the intensity of the ITCZ in the eastern Pacific, and the weakness in the western. Flow onto the Antarctic ice pre-dominates in the Pacific; off the ice, in the Atlantic (not shown). Wind climatologies exist for variety of oceanic regions, and a variety of periods of record. Meteorologists may be impressed to find a 15-day mean so similar in many features to the climatological September. Certainly the question of the time period necessary for averaging out various transient features is an important one in the theory of climate. A systematic discussion would require analysis in terms of empirical orthogonal functions.

Another statistical representation of the data set is contained in Figure 10. Here is contoured the difference between the magnitude of the vector mean wind and the standard deviation of the speed, with positive (dark) and negative areas only being shown for the sake of clarity. Thus a positive area indicates relative steadiness of both direction and speed. An outstanding feature is the steadiness of the Southern Hemisphere belt of westerlies, equally pronounced in Atlantic and Indian Oceans (not shown). Despite the sharp gradients of the north-south component (Figure 9), the region of the ITCZ in Figure 10 is seen to be one in which the standard deviation is greater than the mean, a situation arising from the relative small spatial scale perturbations of the ITCZ. The large positive areas are, of course, the trade wind regions.

Figure 6. Vorticity contours in area of Figure 5. Units: 10^{-6} s^{-1} .

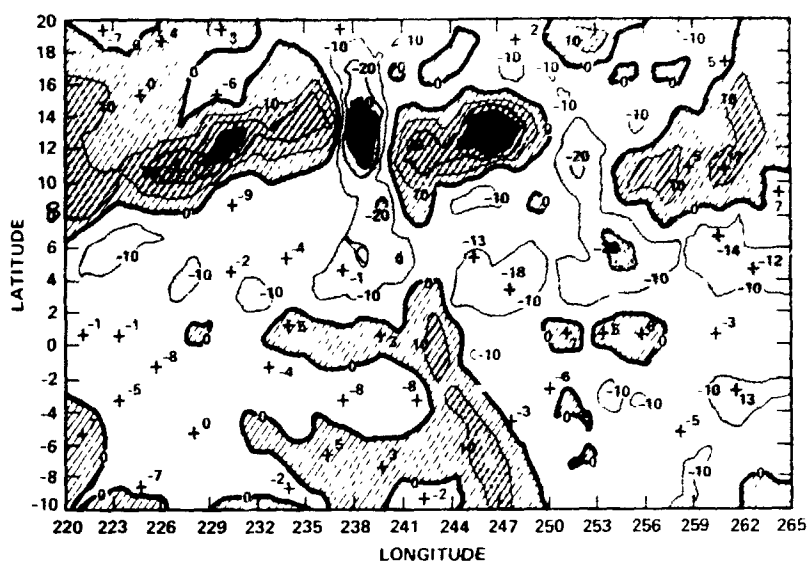
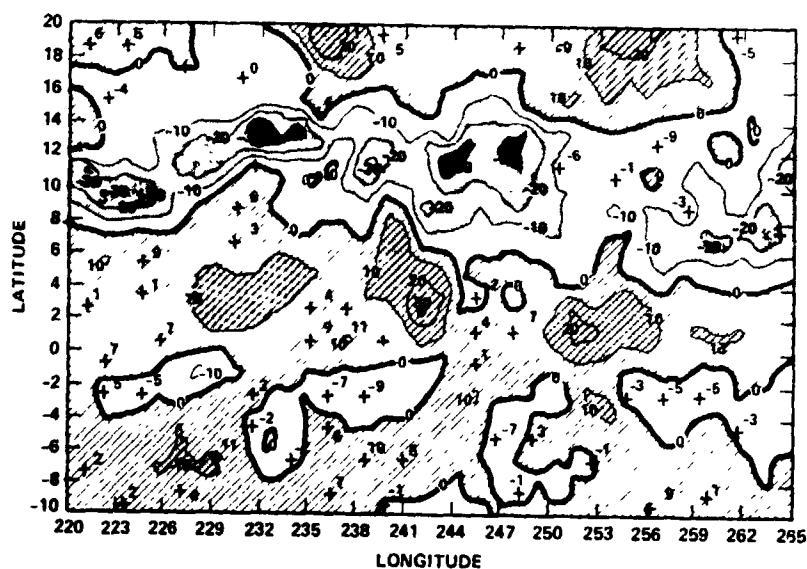


Figure 7. Divergence contours in area of Figure 5. Units: 10^{-6} s^{-1} .



ORIGINAL PAGE IS
OF POOR QUALITY

Figure 8. Mean west wind component for 15-day data set. Solid contours positive values.

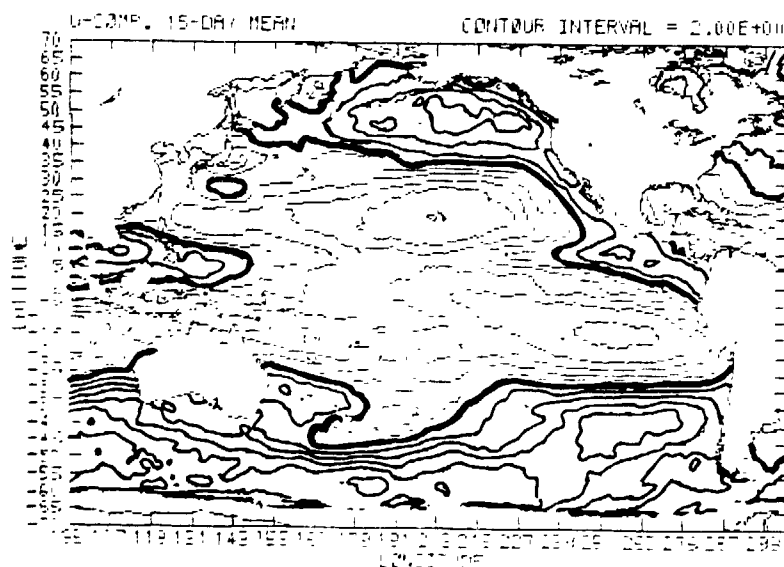


Figure 9. Same as Figure 8 for south wind components.

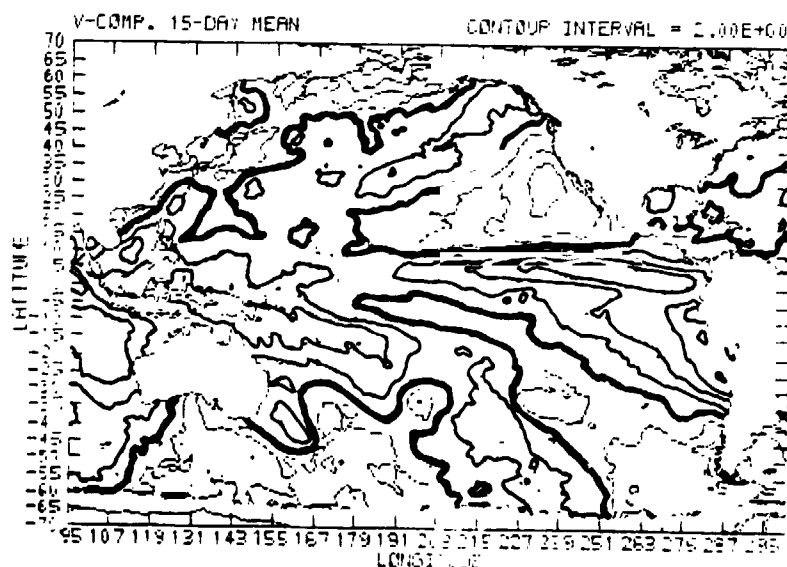
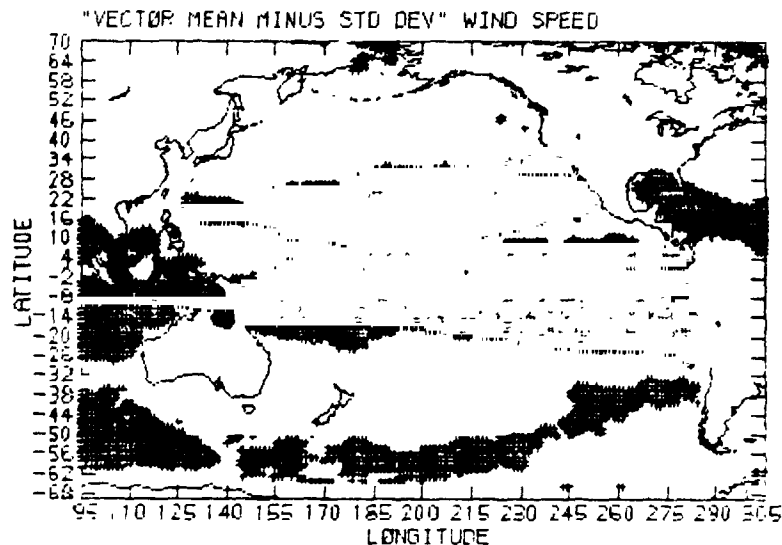


Figure 10. Magnitude of vector mean wind minus standard deviation of speed (15-day data set). White areas, positive; shaded areas, negative.



CONCLUSION

Methods have been developed for dealiasing the Seasat SASS data record and for producing a data tape in the same format, but with a unique selected wind direction associated with each observation. Fifteen days (Sept. 6-20, 1978) are now available for scientific use. The resulting global wind fields, as represented by streamlines and isotachs, provide a visualization of meteorological features of every scale upward from 100 km. The data may be interpolated onto a grid array and then handled numerically by conventional procedures.

The scientific opportunities offered by scatterometer data have yet to be systematically discussed, although some areas of especial interest are identified in the forthcoming science opportunities documented for the Navy Remote Oceanographic Satellite System (Freilich, 1984), scheduled for 1988-89 launch.

ACKNOWLEDGMENTS

The following meteorologists participated in the production of the data set: Mirek Borowsky, Glenn Cunningham, Al Davies, Gordon Muttit, Greg Pihos, Mike Presley.

The authors would like to express their gratitude to John Theon, Robert Curran, and Laurence McGoldrick for continued encouragement and counsel.

Part of this research was jointly supported by the Atmospheric and Oceanic Processes Branches at NASA Headquarters, and was partly conducted at the Jet Propulsion Laboratory/California Institute of Technology, under NASA Contract NAS 7-918.

ORIGINAL PAGE 19
OF POOR QUALITY

References

- Atlas, R., Petehrych, S., Woiceshyn, P., and Wurtele, M. G., 1982: Analysis of satellite scatterometer data and its impact on weather forecasting, Oceans, September 1982, 415-420.
- Baker, W. E., Atlas, R., Kalnay, E., Halem, M., Woiceshyn, P. M., Eddman, D., 1983: Large-scale analysis and forecast experiments with wind data from the Seasat-A scatterometer, to be published, J. Geophys. Res.
- Frellich, M., 1984: NROSS Scatterometer Science Opportunities, to be published by JPL, April, 1984.
- Halperman, Sol, and Rosenstein, M., 1983: Normal monthly windstress over the world oceans with error estimates, J. Phys. Ocean., 13, 1093-1104.
- Jones, W. L., Black, P. G., Boggs, D. M., Bracalente, E. M., Brown, R. A., Dome, G., Halberstam, I. M., Overland, J. E., Peteherysh, S., Pierson, W. J., Wentz, F. J., Woiceshyn, P. M., and Wurtele, M. G., 1979: Seasat scatterometer results for the Gulf of Alaska Workshop, Science, 204, 1413-1415.
- Jones, W. L., Schroeder, L. C., Boggs, D. H., Bracalente, E. N., Brown, R. A., Dome, G. J., Pierson, W. J., and Wentz, F. J., 1982: The Seasat A Satellite Scatterometer: the geophysical evaluation of remotely sensed wind vectors over the oceans, J. Geophys. Res., 87, 3297-3317.
- McDonald, W. F., 1938: Atlas of Climatic Charts of the Oceans, U. S. Weather Bureau No. 1247.
- Pierson, W. J., Sylvester, W. B., and Salfi, R. E., 1984: Vector wind, horizontal divergence, wind stress curl from Seasat-SASS at a one-degree resolution, These Proceedings.
- Peteherych, S., Woiceshyn, P. M., Appleby, W. A., Chu, L., and Spagnol, J., 1981: High resolution marine meteorological analysis using Seasat data, Oceanography from Space, Plenum Publishing Co., 581-588.
- Schroeder, L. E., Boggs, D. H., Dome, G., Halberstam, I. M., Jones, W. L., Pierson, W. J., and Wentz, F. W., 1982: The relationship between wind vector and normalized radar cross section and to derive Seasat A Satellite Scatterometer winds, J. Geophys. Res., 87, 3318-3336.
- Woiceshyn, P. M., Wurtele, M. G., McGoldrick, L. F., Boggs, D. H., and Peteherych, S., 1984: A new parameterization of the geophysical processes in wind/ocean scatterometry, these Proceedings.
- Wurtele, M. G., Woiceshyn, P. M., Peteherych, S., Borowski, M., and Appleby, W. S., 1982: Wind direction alias removal studies of Seasat Scatterometer-derived winds, J. Geophys. Res., 87, 3365-3377.

N84 27316

D58

THE IMPORTANCE OF ALTIMETER AND SCATTEROMETER
DATA FOR OCEAN PREDICTION

Harley E. Hurlburt
Naval Ocean Research and Development Activity
Code 324
NSTL, MS 39529 USA

ABSTRACT

The potential for ocean prediction within the next decade is discussed in terms of the crucial elements: data, computing power, and models. The paper outlines a strategy for a global ocean prediction system that is based on appropriate satellite data, Class 7 computers (~1 gigaflop and 32-128 million words), and eddy-resolving basin or global scale models. The paper is focused on the prediction of meandering currents, frontal positions, and eddies, but prediction of other oceanic phenomena is also surveyed.

1. INTRODUCTION

The next decade should be to numerical prediction of the ocean circulation what the 1950's and 1960's were to numerical weather prediction, a time when the essential elements came together to permit major advances in forecasting skill. These elements are 1) adequate data input, 2) adequate computing power, and 3) properly designed and adequately validated models for both data assimilation and forecasting. Ten years ago none of these requirements were satisfied for many aspects of ocean prediction. Meandering currents and eddies provide a notable example: (1) clear prospects for adequate data with high density and global coverage from satellite-borne instruments have become evident only in the last few years, (2) Class 7 computers with a sustainable speed of ~1 gigaflop and 32-128 M words of memory are required for eddy-resolving forecasts in major ocean basins, and (3) notable differences from meteorology are required in model design and in data assimilation.

The U.S. Navy has determined a requirement for an ocean prediction capability, and has established a research program to meet the requirement. This paper is an overview of the requirements for data and computing power, and the issues of model design and data assimilation primarily in the context of the effort at the Naval Ocean Research and Development Activity. It should be stressed that there are many types of ocean prediction aimed at different aspects of the motion, internal structure, and surface of the ocean. These provide several important roles for satellite data. This paper is focused on one important aspect of ocean prediction where altimeter data can play a central role. In particular, there will be a demonstration of the role that satellite altimeter data can play in detailed surface and subsurface forecasts of meandering currents, eddies, and frontal locations, forecasts that may extend up to several months.

2. DIFFERENT TYPES OF OCEAN PREDICTION

2.1 Classes of Response to Atmospheric Forcing

Before concentrating on a particular type of ocean prediction, it is useful to survey the scope of the problem. Table 1 from Hurlburt (1984) shows three classes of oceanic response to atmospheric forcing that cover many phenomena for

Table 1 *

Classes of oceanic response to atmospheric forcing where predictive skill is feasible.

Class	Implications	Examples
1. Strong, rapid (< 1 wk) and direct	<p>A. short-range forecasts limited by the time scale for atmospheric predictive skill</p> <p>B. less sensitive to errors in the initial state; more sensitive to errors in the forcing functions</p>	<p>surface mixed layers, surface and some internal waves, Ekman drift currents, some coastal and equatorial processes such as upwelling (in some cases), coastal storm surges, and the onset of some equatorial and coastal waves</p>
2. Slow (weeks to months) and indirect	<p>A. long-range forecasts (potentially a month or more)</p> <p>B. more sensitive to errors in the initial state, less sensitive to errors in the forcing functions</p> <p>C. statistical properties of features and ensembles may be predicted by skillful simulation</p> <p>D. prediction of individual features requires oceanographic data. Altimeter data are the most promising operational source now on the horizon</p>	<p>mesoscale eddies, meandering currents, some frontal positions, features caused by mesoscale flow instabilities.</p>
3. Slow (weeks to years) but direct (i.e. integrated response)	<p>A. long-range forecasts</p> <p>B. sensitive to errors in atmospheric forcing functions on long time scales (e.g. monthly means); but less sensitive to errors on short time scales (e.g. daily fluctuations)</p> <p>C. nowcasting and forecasting are potentially feasible without good oceanic data by means of simulations that use appropriate ocean circulation models</p>	<p>El Nino, much of the tropical ocean circulation (in the Atlantic, Pacific, and Indian Oceans), equatorial waves, part of the large-scale ocean circulation, features such as gyres directly driven by persistent or repeated patterns in the wind, often in conjunction with geometric constraints, e.g. most of the circulation features in the Mediterranean Sea with scales > 100 km.</p>

*From Hurlburt (1984)

which prediction appears to be feasible and useful. It is not all-encompassing (e.g. tides and tsunamis are omitted), but it is intended to help put the multifaceted problem of ocean prediction into perspective, identify phenomena where predictive skill is feasible, clarify the potential roles of satellite data, and to define the focus of the paper, which is primarily on Class 2. Fortunately, many phenomena are sufficiently decoupled that it is possible to design forecast models that can simulate and predict certain phenomena while suppressing or parameterizing the statistical effects of the remainder.

2.2 Nowcasting

"Nowcasting" is important in all three classes. To nowcast the models are integrated forward in time while driven by new atmospheric forcing functions and assimilating appropriate new ocean data as they become available. This allows the models to

- a. Fill in temporal gaps in the data by using their predictive skill.
- b. Convert better observed surface fields into subsurface structure,
- c. Convert better observed atmospheric forcing functions into oceanic information.

2.3 Class 1: Strong, Rapid, and Direct

Until now ocean prediction efforts have concentrated primarily on tides and certain phenomena in Class 1, a class which to some extent includes the cumulative effects of fine scale phenomena that are predicted via empirical or semi-empirical parameterizations. Storm surges have received the most attention (Welander, 1961; Jelesnianski, 1967; Crawford, 1979), but recently the U.S. Navy has initiated hemispheric forecasts of surface waves (Pierson, 1982) and the upper mixed layer (Clancy and Martin, 1981; Clancy and Pollak, 1983).

The output from atmospheric prediction models and satellite-borne instruments measuring surface wind speed and direction (scatterometer) or even wind speed alone (scanning multi-frequency microwave radiometer (SMMR)) show great promise in facilitating predictions in Class 1 and Class 3. Scatterometers and microwave radiometers can provide adequate coverage, accuracy, and spatial and temporal resolution except for coverage near coastal boundaries (Jones et al, 1982; Wentz et al, 1982; Lipes, 1982; Satellite Surface Stress Working Group, 1982; Mueller, 1982). For mixed layer forecasting, measurements of sea surface temperature (SST) (multi-channel infrared and microwave radiometers) would be of value. Some work has also been done on satellite measurement of latent heat flux (Liu, 1984) and incident solar radiation at the surface (Gautier, 1981), the two heat fluxes that are usually the largest at the air-sea interface.

Although a satellite altimeter can measure surface wind speed and significant wave height in addition to sea surface elevation (Fedor and Brown, 1982), the value of a single altimeter with only a nadir beam is severely degraded when applied to prediction of phenomena in Class 1. This is due to the inverse relation between spatial and temporal resolution that prevents adequate resolution for these phenomena in both space and time simultaneously. However, the altimeter can be useful in constructing climatologies of wind speed and significant wave height (Chelton et al., 1981; Wentz et al., 1982; Mognard et al., 1983), in validation and tuning of certain models and in some research problems involving these quantities. Because tides are repetitive with known periods, the altimeter should be important in refining the global knowledge of tidal phase and amplitude (Cartwright and Alcock, 1981; Brown and Hutchinson, 1981; Diamante and Nee, 1981; Mazzega, 1983).

2.4 Class 2: Slow and Indirect

The prediction of mesoscale (~50-500 km) eddies, meandering currents, and frontal positions (phenomena in Class 2) is the focus of this paper. It poses a problem where altimeter data should play a central role. This is because (1) individual mesoscale eddies and current meanders are often not driven directly by the wind or by any other external forcing function, and (2) eddies can persist for more than a year after their initial generation (Lai and Richardson, 1977). Thus, oceanic data are crucial for reliable prediction of individual eddies and current meanders. With sufficient oceanic data, we anticipate that the prediction of these features can be treated as an initial value problem in which the future forcing functions are representative but not accurate on time scales greater than a few days. Without oceanic data input, simulation can be used to predict the statistical properties of features and ensembles, but usually not the evolution and movement of individual features.

There has been little work on the prediction of Class 2 phenomena except for the work on prediction of mesoscale eddies, using limited-area models, by A.R. Robinson's group at Harvard (Robinson and Halvøgel, 1980; Robinson and Tu, 1982; Miller and Robinson, 1983). However, there is a substantial body of literature on the simulation and ocean dynamics of Class 2 phenomena which is very useful in the design of ocean circulation prediction models (Holland and Lin, 1975; Rhines, 1977; Semtner and Mintz, 1977; Holland, 1978, 1982; McWilliams and Flierl, 1979; Cox, 1979; Hurlburt and Thompson, 1980, 1982; Lin and Hurlburt, 1981; Schmitz and Holland, 1982; Heburn et al., 1982). Many of these have simulated some features of the ocean circulation with substantial success using simple models, rectangular domains, and simple steady forcing functions. This is an indication of potential predictive skill, but one largely unverified at this time.

As an example, Figure 1 illustrates model simulation skill for a Class 2 phenomenon in the Gulf of Mexico. The model has two active layers, realistic geometry and bottom topography, and horizontal resolution sufficient for major current systems and eddies. Surprisingly, no eddy-resolving ocean modeling study published to date has included all of these features in a deep ocean basin where planetary vorticity advection was important and the model was integrated to statistical equilibrium. This calculation was performed by A. Wallcraft (personal communication) using the model of Hurlburt and Thompson (1980). The ability to handle detailed coastline geometry was added by Wallcraft. The model was driven from rest to statistical equilibrium solely by a steady inflow through the Yucatan Straits between Cuba and Mexico which was compensated by outflow through the Florida Straits.

Figure 1 compares "instantaneous" upper ocean flow patterns (a) from the numerical model and (b) from observations by Leipper (1970). The Loop Current is the major current system depicted. At this point it is about to shed an eddy. The Loop Current is observed to penetrate into the Gulf, bend westward, and to shed an eddy with a period of approximately one year. This "annual" cycle was long thought to be due to seasonal variations in the flow through the Yucatan Straits (Cochrane, 1965). However, the model Loop Current exhibits an approximately annual eddy-shedding period when the inflow is steady, contradicting the earlier hypothesis. Although time variations are not essential, they can still play a significant role in the eddy shedding (Hurlburt and Thompson, 1980). The model Loop Current also spontaneously shed eddies with realistic diameters, amplitudes, and westward propagation speeds. The dynamical basis for the agreement between the observations and a circulation model with low vertical resolution is discussed by Hurlburt and Thompson (1980, 1982). Additional information on the simulation in Figure 1 is found in Hurlburt (1984), including the spontaneous generation of a

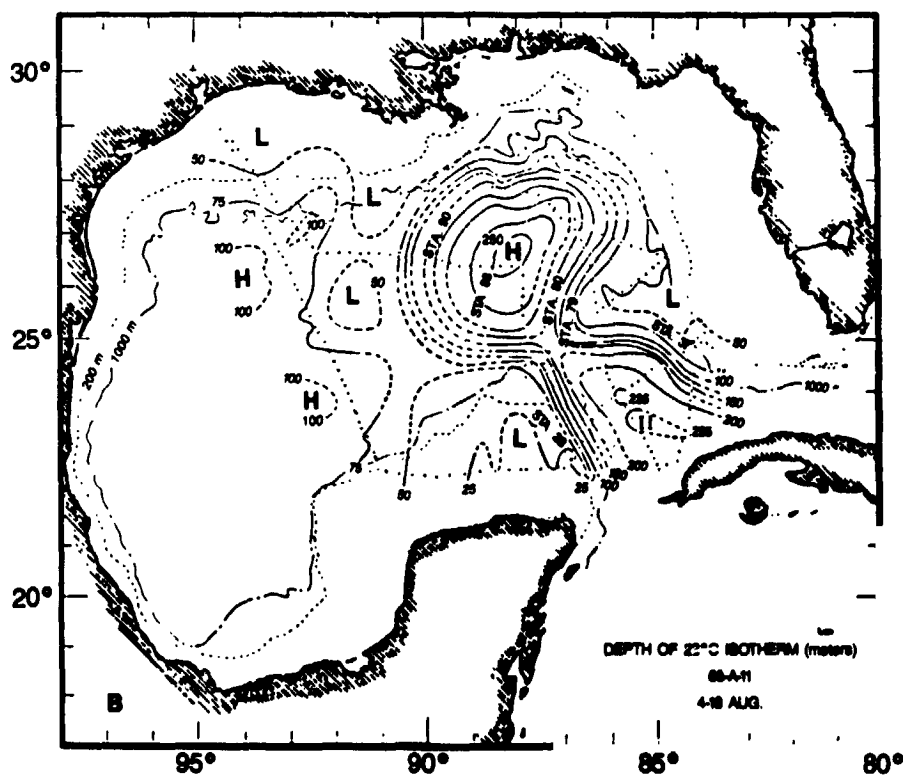
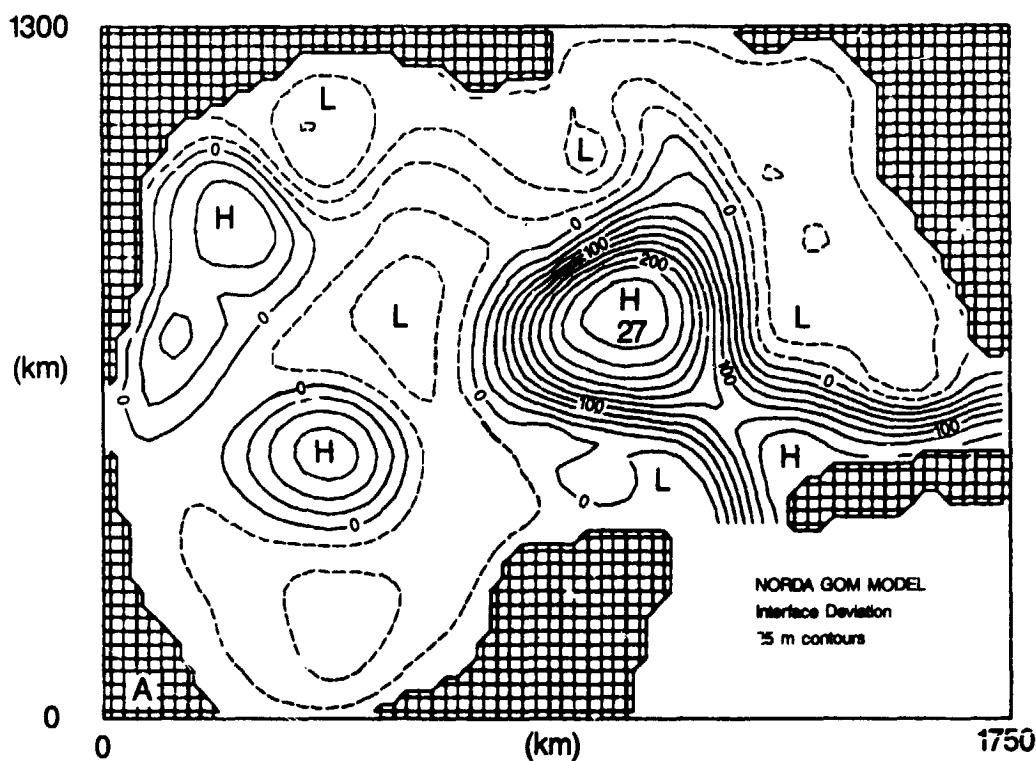


Figure 1. (a) Instantaneous view of the interface deviation in a two-layer simulation of the Gulf of Mexico driven from rest to statistical equilibrium solely by inflow through the Yucatan Straits. The contour interval is 25 m with solid contours representing downward deviations. (b) Depth of the 22°C isothermal surface, 4-18 Aug 1966 (Alimos cruise 66-A-11) from Leipper (1970). The contour interval is 25 m. (From Hurlburt, 1984)

counter-rotating vortex pair as the eddy propagates westward. Such a feature has been observed repeatedly in the western Gulf of Mexico.

2.5 Class 3: Slow and Direct

Phenomena in Class 3 are a direct response to atmospheric forcing, but on much longer time scales than those in Class 1. Because they are a much more integrated response to the wind, the requirements for temporal resolution and accurate depiction of daily atmospheric fluctuations are not as stringent as in Class 1. This should permit forecasts on time scales greater than the few-day time scale for atmospheric predictability. In Class 3 "nowcasting" and forecasting may be feasible by using new atmospheric forcing functions without new oceanic data. The addition of altimeter-derived sea surface elevation accurate on the scales of major ocean basins as well as on mesoscales would reduce the burden on the simulation skill of the model. Examples of Class 3 simulation and prediction studies include the work by Haney (1980) on predicting large-scale anomalies in the North Pacific, by Busalacchi et al (1983) on the tropical Pacific, and by Preller and Heburn (1983) on the western Mediterranean Sea.

3. RESOLUTION REQUIREMENTS FOR ALTIMETER AND SCATTEROMETER DATA

The horizontal and temporal resolution required for the forcing functions is dictated primarily by the space and time scales of the atmosphere. Thus, scatterometer-derived wind stress data would be needed on a daily basis to resolve the evolution of atmospheric storm systems. The spatial resolution of the wind stress data should be sufficient (~ 50 km) to resolve the wind stress curl associated with atmospheric cyclones, anti-cyclones and fronts. Winds as close to coastlines as possible are highly desirable. In these regions horizontal resolution should be 20 km or better. Since a satellite scatterometer with an orbit altitude of about 850 km has about a 1500 km swath width (with gaps), a single satellite in conjunction with atmospheric models and the existing data base could meet these requirements adequately (Satellite Surface Stress Working Group, 1982).

Altimeter data is essential for global prediction and representation of individual current meanders and eddies. Cheney and Marsh (1981) have already demonstrated the ability of the SEASAT altimeter to detect the Gulf Stream and mesoscale eddies when using either repeat tracks or a geoid, and Cheney et al (1983) have used nine sets of 3-day repeat tracks from SEASAT to produce a global map depicting the RMS mesoscale variability of the sea surface elevation during Sep - Oct, 1978. Tapley et al (1982) and Wunsch and Gaposhkin (1980) review the problem of obtaining accurate measurements of current-related variations in the sea surface elevation from a satellite altimeter and the success achieved with SEASAT. To be useful in ocean circulation prediction, the altimeter data must, of course, resolve major current systems and eddies in time, amplitude, and horizontal dimension. However, the amplitude dependence on horizontal scale should also be noted. For currents in geostrophic balance

$$\hat{k} \times f \vec{v}_g = -g \nabla \eta$$

where f is the Coriolis parameter, \vec{v}_g is the velocity of the geostrophic surface current, g is the acceleration due to gravity, and η is the sea surface elevation above the geoid related to oceanic surface currents. The maximum velocity (V) for typical, significant, persistent, mesoscale (~ 50 to 500 km) features in the ocean ranges from about 10 cm/sec to 1 m/sec. Up to 2 m/sec is not uncommon in the stronger currents. For an altimeter which can usefully measure oceanographic features with a minimum amplitude of $\eta = 10$ cm, the minimum radius of an eddy or half-width of a current (L) with $V = 10$ cm/sec is $L = 100$ km at 42° Lat and $L = 150$

km at 27° Lat. For $V = 100$ cm/sec, $L = 10$ km at 42° Lat, and the Rossby number, $R_0 = V/fL = 1$. For $R_0 \ll 1$ the flow is geostrophically balanced. For $R_0 \gg 1$ vortices can develop cyclostrophic balance,

$$\frac{v_\theta^2}{r} = -g \frac{\partial \eta}{\partial r}$$

where v_θ is the tangential velocity and r is the radius of curvature. In this case the amplitude of η associated with the vortex is dependent on v^2 but is nearly independent of the scale of the vortex. However, a velocity scale > 2 m/s is required for a signal in the sea surface elevation > 10 cm.

From this we conclude that a satellite altimeter able to measure variations in the sea surface elevation > 5 cm, which are associated with oceanic currents, should provide usable information for the more significant currents and eddies with scales greater than a few tens of kilometers. This accuracy is feasible with current technology (TOPEX Science Working Group, 1981). Altimeter track spacing of about 30 km and at most 50 km at mid-latitudes is needed for horizontal resolution of most detectable eddies. Experiments by J. Kindle at NORDA have shown that three ascending or descending tracks with error-free data are sufficient to adequately map an eddy with a nearly circular shape. Repeat intervals up to a month should provide adequate temporal resolution for most mesoscale features, particularly with the aid of predictive models to fill in the temporal gaps. To minimize the time required for altimeter tracks to span a given eddy, the orbit should be chosen so that adjacent tracks are one day apart. This requirement should override any concern about tidal aliasing, since the tides are relatively large scale and because removal of the tidal contributions to the sea surface elevation appears feasible (Schwiderski, 1980; Cartwright and Alcock, 1981; Brown and Hutchinson, 1981; Diamante and Nee, 1981; Mazzega, 1983). However, as noted in some of the preceding references, accurate determination of the tidal phases and amplitudes would be facilitated by at least once having an altimeter in an orbit relatively free of tidal aliases with long periods.

A single satellite in a 20-day repeat orbit which carried a multi-beam altimeter (Bush et al, 1984) could easily meet the preceding requirements. Minimal satisfaction of the requirements could be achieved by using a single satellite with a nadir beam altimeter in a 40-day repeat orbit, if a numerical model was able to bridge the temporal gaps. In the absence of an adequate geoid, it would be necessary to use a mean sea surface, so that only deviations from the mean would be available to the model. In that case the model could obtain the mean from its own or observed climatology. Bandpass filtering could be required to remove short ($< 0(10$ km)) and long wave ($> a$ few thousand km) errors, the scales with the greatest errors (TOPEX Science Working Group, 1981).

4. STRATEGY FOR OCEAN PREDICTION

Highly efficient models with low vertical resolution have demonstrated a remarkable ability to simulate meandering currents and eddies, but high horizontal resolution (~ 10 km) is required to resolve them. To avoid serious limitations on data assimilation and predictive skill, it is advantageous to use domains which cover major ocean basins or semi-enclosed seas where the phenomena of interest are generated within the domain, and where the open boundary segments are either small (such as flow through a strait) or very distant from the region of interest.

Circulation models on subdomains of major ocean basins which have extensive open ocean boundaries are extremely dependent on some source like a large-scale model for boundary conditions during both the data assimilation and prediction phases (Miller and Robinson, 1983). To provide useful boundary conditions, the large-scale model must also have resolution sufficient for the currents and eddies. To model major ocean basins with high horizontal resolution and low vertical resolution, a Class 7 computer (~ 1 Giga-flop and 32M to 128M words) is required. The introduction of Class 7 computers is anticipated in the middle and late 1980's.

Currently, satellites and atmospheric forecast models provide the only real prospects for oceanic data and forcing functions with global coverage and resolution adequate for use in ocean circulation models. For this purpose, the fields of greatest value, which are observable from satellites, are altimeter-derived sea surface elevation, scatterometer-derived wind stress, and heat fluxes. Successful ocean prediction appears feasible without extensive subsurface data collection by using the simulation skill of the model to convert the potentially well-observed fields at the surface into subsurface information. This looks more promising than attempting to assimilate the extremely sparse subsurface data, a process likely to do more harm than good. Where eddy-resolving subsurface data with useful coverage is available (nowhere at present), it should, of course, be used, especially if it is available on a regular basis and its statistical properties are well known. In the long term, acoustic tomography shows promise in this area (Munk and Wunsch, 1982), but we anticipate that subsurface data acquisition adequate for prediction of mesoscale features will, at best, be limited in coverage for at least the next decade. Some subsurface data and major field programs are essential for the local and regional subsurface validation of the forecast models.

The surface to subsurface data conversion process would be accomplished by using both the altimeter data and the atmospheric data as forcing functions. Although this is an untested hypothesis at this time and the assimilation of the altimeter data could be troublesome, the potential for surface to subsurface conversion is enhanced by noting that (1) a single internal vertical mode explains much of the oceanic variability (Richman et al, 1977; Flierl, 1978), (2) in a layered circulation model with a single internal mode there is a one-to-one correspondence between variations in the sea surface elevation and variations in the depth of the pycnocline, (3) such a model can be initialized by altimeter data alone, except near the equator where wind stress is necessary, and (4) such models have demonstrated remarkable simulation skill in certain situations (Busalacchi et al, 1983; Lin and Hurlburt, 1981; Hurlburt and Thompson, 1980, 1982), although they miss the sometimes important effects of topography and baroclinic instability (Holland and Lin, 1975; McWilliams et al, 1978; Hurlburt and Thompson, 1983). These require at least one additional vertical mode and we recommend no less than three in an operational forecast model. High vertical resolution can be obtained by coupling the circulation model with low vertical resolution to an array of one-dimensional mixed layer models with high vertical resolution. A hemispheric array makes up the mixed-layer forecasts by the U. S. Navy (Clancy and Martin, 1981).

Among the ideas proposed for application to ocean prediction, some that show promise are 1) the use of satellite altimeter and scatterometer data, 2) the conversion of surface into subsurface information, 3) the partial decoupling of the ocean circulation problem from the turbulent thermodynamic mixed layer problem, 4) eddy-resolving circulation models with low vertical resolution and basin or global-scale domains, and 5) Class 7 computers. Some that are not

promising (at least within the next decade or more) are 1) eddy-resolving models for major ocean basins with many fixed levels in the vertical, 2) the inclusion of sophisticated mixed layer physics in eddy-resolving circulation models covering major ocean basins, 3) the assimilation of sparse in situ data by ocean circulation models, 4) coarse grid, non-eddy-resolving prediction models for the ocean circulation, and 5) sub-basin-scale models with extensive open boundaries except when they can obtain boundary conditions from an eddy-resolving basin scale model. "Nowcasts" and short-range forecasts (a few days) from stand-alone limited-area models appear feasible in regions with adequate subsurface sampling (none at present). The first two ideas lack promise only because of the anticipated computing power within the next decade or more.

Within the next decade the appropriate satellite data, Class 7 computers, and eddy-resolving basin or global-scale models should become available, and they should be used to form the heart of a global ocean prediction system. In the meantime, alternate methods can provide a more limited capability which is applicable in some situations. Forcing functions from atmospheric models should permit useful nowcasting and predictive skill for Class 1 and Class 3 phenomena listed in Table 1 prior to the availability of satellite altimeter and scatterometer data.

ACKNOWLEDGEMENTS

Funding is from the Office of Naval Research under the Special Focus Program, "Ocean dynamics from GEOSAT". This paper is a condensation of Hurlburt (1984). The manuscript was typed by Charlene Parker.

REFERENCES

- Brown, R. D., and M. K. Hutchinson, 1981: Ocean tide determination from satellite altimetry. Oceanography from Space. J. F. R. Gower, Ed. Plenum Press, New York, 897-906.
- Busalacchi, A. J., K. Takeuchi, and J. J. O'Brien, 1983: On the interannual wind-driven response of the tropical Pacific Ocean. Hydrodynamics of the Equatorial Ocean, J. C. J. Nihoul, Ed., Elsevier Science Publishers, Amsterdam, 155-195.
- Bush, G. B., E. B. Dobson, R. Matyskiela, C. C. Kilgus, and E. J. Walsh, 1984: An analysis of a multibeam altimeter. Marine Geodesy (in press).
- Cartwright, D. E. and G. A. Alcock, 1981: On the precision of sea surface elevation and slopes from SEASAT altimetry of the northeast Atlantic Ocean. Oceanography from Space, J. F. R. Gower, Ed., Plenum Press, New York, 885-895.
- Chelton, D. B., K. J. Hussey, and M. E. Parke, 1981: Global satellite measurements of water vapour, wind speed and wave height. Nature, 294, 529-532.
- Cheney, R. E. and J. G. Marsh, 1981: SEASAT altimeter observations of dynamic topography in the Gulf Stream region. J. Geophys. Res., 86, 473-483.
- Cheney, R. E., J. G. Marsh, and B. D. Beckley, 1983: Global mesoscale variability from collinear tracks of SEASAT altimeter data. J. Geophys. Res., 88, 4343-4354.
- Clancy, R. M. and P. J. Martin, 1981: Synoptic forecasting of the oceanic mixed layer using the Navy's operational environmental data base: present capabilities and future applications. Bull. Am. Meteorol. Soc., 62, 770-784.
- Clancy, R. M. and K. D. Pollak, 1983: A real-time synoptic ocean thermal analysis/forecast system. Prog. Oceanogr., 12, 383-424.
- Cochrane, J. D., 1965: The Yucatan Current and equatorial currents of the western Atlantic. Unpublished report, Dept. of Oceanography, Texas A&M University, Ref. (65-17T), 20-27.
- Cox, M. D., 1979: A numerical study of Somali Current eddies. J. Phys. Oceanogr 9, 311-326.
- Crawford, K. C., 1979: Hurricane surge potentials over southeast Louisiana as revealed by a storm-surge forecast model: a preliminary study. Bull. Am. Met. Soc., 60, 422-429.
- Diamante, J. M. and T. S. Nee, 1981: Application of satellite radar altimeter data to the determination of regional tidal constituents and the mean sea surface. Oceanography from Space, J. F. R. Gower, Ed., Plenum Press, New York, 907-918.
- Fedor, L. S. and G. S. Brown, 1982: Waveheight and wind speed measurements from the SEASAT radar altimeter. J. Geophys. Res., 87, 3254-3260.

- Flierl, G. R., 1978: Models of vertical structure and the calibration of two-layer models. Dyn. Atmos. Oceans, 2, 341-381.
- Gautier, C., 1981: Daily shortwave energy budget over the ocean from geostationary satellite measurements. Oceanography from Space, J. F. R. Gower, Ed., Plenum Press, New York, 201-206.
- Haney, R. L., 1980: A numerical case study of the development of large-scale thermal anomalies in the Central North Pacific Ocean. J. Phys. Oceanogr., 10, 541-556.
- Heburn, G. W., T. H. Kinder, J. H. Allender, and H. E. Hurlburt, 1982: A numerical model of eddy generation in the southeastern Caribbean Sea. Hydrodynamics of Semi-enclosed Seas, J. C. J. Nihoul, Ed., Elsevier Scientific Publishing Company, Amsterdam, 299-327.
- Holland, W. R., 1978: The role of mesoscale eddies in the general circulation of the ocean - numerical experiments using a wind-driven quasi-geostrophic model. J. Phys. Oceanogr., 8, 363-392.
- Holland, W. R., 1982: Simulation of North Atlantic variability. Proceedings of the Workshop on Gulf Stream Structure and Variability, J. M. Bane, Jr., Ed., Sponsored by U. S. Office of Naval Research, 114-126.
- Holland, W. R. and L. B. Lin, 1975: On the generation of mesoscale eddies and their contribution to the oceanic general circulation. J. Phys. Oceanogr., 5, 642-669.
- Hurlburt, H. E., 1984: The potential for ocean prediction and the role of altimeter data. Marine Geodesy (in press).
- Hurlburt, H. E. and J. D. Thompson, 1980: A numerical study of Loop Current intrusions and eddy shedding. J. Phys. Oceanogr., 10, 1611-1651.
- Hurlburt, H. E. and J. D. Thompson, 1982: The dynamics of the Loop Current and shed eddies in a numerical model of the Gulf of Mexico. Hydrodynamics of Semi-enclosed Seas, J. C. J. Nihoul, ed., Elsevier Scientific Publishing Company, Amsterdam, 243-297.
- Hurlburt, H. E. and J. D. Thompson, 1983: Preliminary results from a numerical study of the New England Seamount Chain influence on the Gulf Stream. Predictability of Fluid Motions, G. Holloway and B. J. West, Eds., American Institute of Physics, New York, 489-504.
- Jelesnianski, C. P., 1967: Numerical computations of storm surges with bottom stress. Mon. Wea. Rev., 95, 740-756.
- Jones, W. L., L. C. Schroeder, D. H. Boggs, E. M. Bracalente, R. A. Brown, G. J. Dame, W. J. Pierson, and F. J. Wentz, 1982: The SEASAT-A satellite scatterometer: the geophysical evaluation of remotely sensed wind vectors over the ocean. J. Geophys. Res., 87, 3297-3317.
- Lai, D. Y. and P. L. Richardson, 1977: Distribution and movement of Gulf Stream rings. J. Phys. Oceanogr., 7, 670-683.

- Leipper, D. F., 1970: A sequence of current patterns in the Gulf of Mexico. J. Geophys. Res., 75, 637-657.
- Lin, L. B. and H. E. Hurlburt, 1981: Maximum simplification of nonlinear Somali Current dynamics. Monsoon Dynamics, M. J. Lighthill and R. P. Pearce, eds., Cambridge University Press, 541-555.
- Lipes, R. G., 1982: Description of SEASAT radiometer status and results. J. Geophys. Res., 87, 3385-3395.
- Liu, W. T., 1984: Estimation of latent heat flux with SEASAT SMMR, a case study in the North Atlantic. Large Scale Experiments and Satellites, C. Gautier and M. Fieux, Eds., Reidel Press, Boston (in press).
- Mazzega, P., 1983: The M2 oceanic tide recovered from SEASAT altimetry in the Indian Ocean. Nature, 302, 514-516.
- McWilliams, J. C. and G. R. Flierl, 1979: On the evolution of isolated, nonlinear vortices. J. Phys. Oceanogr., 9, 1155-1182.
- McWilliams, J. C., W. R. Holland, and J. H. S. Chow, 1978: A description of numerical Antarctic Circumpolar Currents. Dyn. Atmos. Oceans, 2, 213-291.
- Miller, R. N. and A. R. Robinson, 1983: Dynamical forecast experiments with a baroclinic quasi geostrophic open ocean model. Predictability of Fluid Motions, G. Holloway and B. J. West, Eds., American Institute of Physics, New York, 457-472.
- Mognard, N. M., W. J. Campbell, R. E. Cheney, and J. G. Marsh, 1983: Southern ocean mean monthly waves and surface winds for winter 1978 by SEASAT radar altimeter. J. Geophys. Res., 88, 1736-1744.
- Mueller, J. L., 1982: Analysis of satellite remote sensing systems. Proceedings of the Ocean Prediction Workshop. C. N. K. Mooers, S. A. Piacsek, and A. R. Robinson, Eds. Sponsored by the Oceanographer of the Navy and the Office of Naval Research, 292-307.
- Munk, W. and C. Wunsch, 1982 : Observing the ocean in the 1990's. Phil. Trans. R. Soc. Lond., A, 307, 439-464.
- Pierson, W. J. 1982: Spectral Ocean Wave Model (SOWM), a northern hemisphere computer model for specifying and forecasting ocean wave spectra. Tech. Report, DTNSRDC-82/011. David Taylor Naval Ship Research and Development Center, Bethesda, MD 186 pp.
- Preller, R. H. and G. W. Heburn, 1983: A simple numerical model of circulation in the western Mediterranean Sea. (Submitted to Oceanologica Acta).
- Rhines, P. B., 1977: The dynamics of unsteady currents. The Sea, Vol. 6, E. D. Goldberg, I. N. McCave, J. J. O'Brien and J. H. Steele, Eds., Wiley Interscience, 189-318.
- Richman, J. G., C. Wunsch, and N. G. Hogg, 1977: Space and time scales of mesoscale motion in the western North Atlantic. Rev. of Geophys. and Space Phys., 15, 385-420.

- Robinson, A. R. and D. B. Haidvogel, 1980: Dynamical forecast experiments with a barotropic open ocean model. J. Phys. Oceanogr., 10, 1909-1928.
- Robinson, A. R. and K. Tu, 1982: A combined statistical/dynamical approach to regional forecast modeling of open ocean currents. Proceedings of the Ocean Prediction Workshop, C. N. K. Mooers, S. A. Piacsek, and A. R. Robinson, Eds. Sponsored by the Oceanographer of the Navy and the Office of Naval Research, 114-141.
- Satellite Surface Stress Working Group, 1982: Science Opportunities Using Satellite Wind Stress Measurements over the Ocean. J. J. O'Brien, Chairman. Prepared for: National Aeronautics and Space Administration, 153 pp.
- Schmitz, W. J., Jr. and W. R. Holland, 1982: A preliminary comparison of selected numerical eddy-resolving general circulation experiments with observations, J. Mar. Res., 40, 75-117.
- Schwiderski, E. W., 1980: On charting global tides. Rev. of Geophys. and Space Phys., 18, 243-268.
- Semtner, A. J., Jr. and Y. Mintz, 1977: Numerical simulation of the Gulf Stream and mid-ocean eddies, J. Phys. Oceanogr., 7, 208-230.
- Tapley, B. D., G. H. Born, and M. E. Parke, 1982: The SEASAT altimeter data and its accuracy assessment. J. Geophys. Res., 87, 3179-3188.
- TOPEX Science Working Group, 1981: Satellite altimetric measurements of the ocean. C. Wunsch, Chairman. Report issued by NASA and JPL, 78 pp.
- Welander, P., 1961: Numerical prediction of storm surges, Advances in Geophysics, 8, 315-379.
- Wentz, F. J., V. J. Cardone, and L. S. Fedor, 1982: Intercomparison of wind speeds inferred by the SASS, Altimeter and SMMR. J. Geophys. Res., 87, 3378-3384.
- Wunsch, C. and E. M. Gaposkin, 1980: On using satellite altimetry to determine the general circulation of the oceans with application to geoid improvement. Rev. of Geophys. and Space Phys., 18, 725-745.

N84 27317

SAMPLING STRATEGIES AND FOUR-DIMENSIONAL ASSIMILATION OF ALTIMETRIC DATA
FOR OCEAN MONITORING AND PREDICTION

John C. Kindle
J. Dana Thompson
and H. E. Hurlburt

Dynamical Ocean Forecasting Branch
Code 324
Naval Ocean Research and Development Activity
NSTL, MS 39529

ABSTRACT

Numerical experiments using simulated altimeter data are conducted in order to examine the assimilation of altimeter-derived sea surface heights into numerical ocean circulation models. A reduced-gravity, primitive equation circulation model of the Gulf of Mexico is utilized; the Gulf of Mexico is chosen because of its amenability to modeling and the ability of low vertical-mode models to reproduce the observed dynamical features of the Gulf circulation. The simulated data are obtained by flying an imaginary altimeter over the model ocean and sampling the model sea surface just as a real altimeter would observe the true ocean. The data are used to initialize the numerical model and the subsequent forecast is compared to the true numerical solution. Results indicate that for a stationary, circular eddy, approximately 3-4 tracks (either ascending or descending) across the eddy are sufficient to ensure adequate spatial resolution.

1. INTRODUCTION

The satellite radar altimeter offers the most promising capability of routinely providing global, timely observations suitable for initializing an ocean circulation forecasting model. The inability, though, of a single nadir-beam altimeter to provide a truly synoptic measurement which adequately resolves the mesoscale eddy field, major current systems and fronts poses a serious obstacle to the development of a skillful forecasting ability. A balance between track spacing and period of the repeat tracks is necessitated. Hence, in addition to the observational accuracy requirements, a viable oceanic forecast will also depend on an innovative development of sampling strategies, four-dimensional data assimilation techniques and initialization methods. The thrust of this report is an examination of sampling strategies which optimize the usefulness of altimeter derived sea-surface heights in ocean monitoring and prediction. In particular, we will attempt to determine the minimum track spacing which adequately resolves the detectable meandering current systems and eddies and to investigate the ability of numerical circulation prediction models to fill in the resulting temporal gaps.

In addition to assimilating altimetric data, numerical ocean models are useful in simulation mode for generating "synthetic" sea surface heights to investigate optimum sampling and initialization strategies and for comparison with actual altimeter data (Thompson et al., 1983). A reduced-gravity, primitive equation circulation model of the Gulf of Mexico (Hurlburt and Thompson, 1980) is utilized in order to examine the methodology of incorporating satellite altimeter data into ocean forecasting models. Simulated altimeter measurements of sea surface height are obtained by: 1) integrating the model to statistical

equilibrium, 2) flying an imaginary altimeter over the model ocean, 3) objectively mapping the perfect (i.e., uncontaminated by geoid, tide or noise) sampled data onto a numerical grid. The model is initialized and restarted using the "observed" field, and the subsequent forecast (up to several months) is compared to the true solution. This approach allows us to investigate the maximum ratio of track spacing to eddy diameter for adequate mesoscale mapping, the optimum sampling period/track spacing for repeat orbits, four-dimensional data assimilation methods, initialization schemes and techniques for updating the forecast. This, admittedly, antiseptic approach to studying the assimilation problem is intended as a first step. Experiments with contaminated data are also being conducted in order to assess the accuracy requirements of altimeter data for use in ocean forecasting. The results of these experiments will be reported elsewhere.

2. THE GULF OF MEXICO MODEL

The Gulf of Mexico has been chosen for this study for several reasons. As a semi-enclosed sea with well defined inflow and outflow ports, it is highly amenable to modeling. The size of the basin is small enough to permit a relatively large number of experiments with fine resolution, and is sufficiently large so that the dynamical features possess many similarities to those found in larger ocean basins. The primary forcing in the Gulf is the intense Loop Current which enters through the Yucatan Straits and exits through the Florida Straits. Approximately once per year, the Loop Current sheds an anti-cyclonic eddy which propagates westward. Both the Loop Current and the associated eddies have large sea-surface signatures (~ 30 - 50 cm). Additionally, the eddies propagate slowly (~ 3 cm/sec) and have large horizontal scales (300-500 km in diameter). Also, during a portion of the GEOSAT (a U. S. Navy spacecraft whose primary altimetric purpose is geodetic) mission there is a proposed field experiment capable of providing verification data for the numerical forecast experiments.

The numerical simulations use the one-layer reduced-gravity version of the Hurlburt and Thompson (1980) model of the Gulf of Mexico circulation. This formulation represents the ocean as two incompressible, homogeneous layers. The lower layer is motionless because the pressure gradient generated by the slope of the interface exactly balances that due to the surface slope. Hence, the interface (model pycnocline) slope is an inverted representation of the surface height field. This is an advantageous formulation for altimeter applications because the internal pressure field is uniquely determined by the sea-surface height variations. In spite of its simplicity, the model has demonstrated a remarkable ability to reproduce such observed features as the shedding of eddies from the Loop Current with realistic diameters, amplitudes and westward propagation speeds (Hurlburt and Thompson, 1980). In addition, the two layer version of the model was used in the study by Thompson et al. (1983) as an aid in identifying the Loop Current system from collinear-track altimetry from SEASAT.

3. EXPERIMENT DESIGN AND RESULTS

The simulation experiments described herein are motivated by a NORDA research program to study ocean dynamics using the altimeter derived sea-surface heights acquired during the GEOSAT mission. The satellite track sequence during the first 18 months of GEOSAT is shown in Fig. 1. This pattern produces an equatorial track separation of 40 km with global coverage in approximately 70 days. The tracks, however, do not repeat and, hence, may be only marginally

ORIGINAL PAGE IS
OF POOR QUALITY

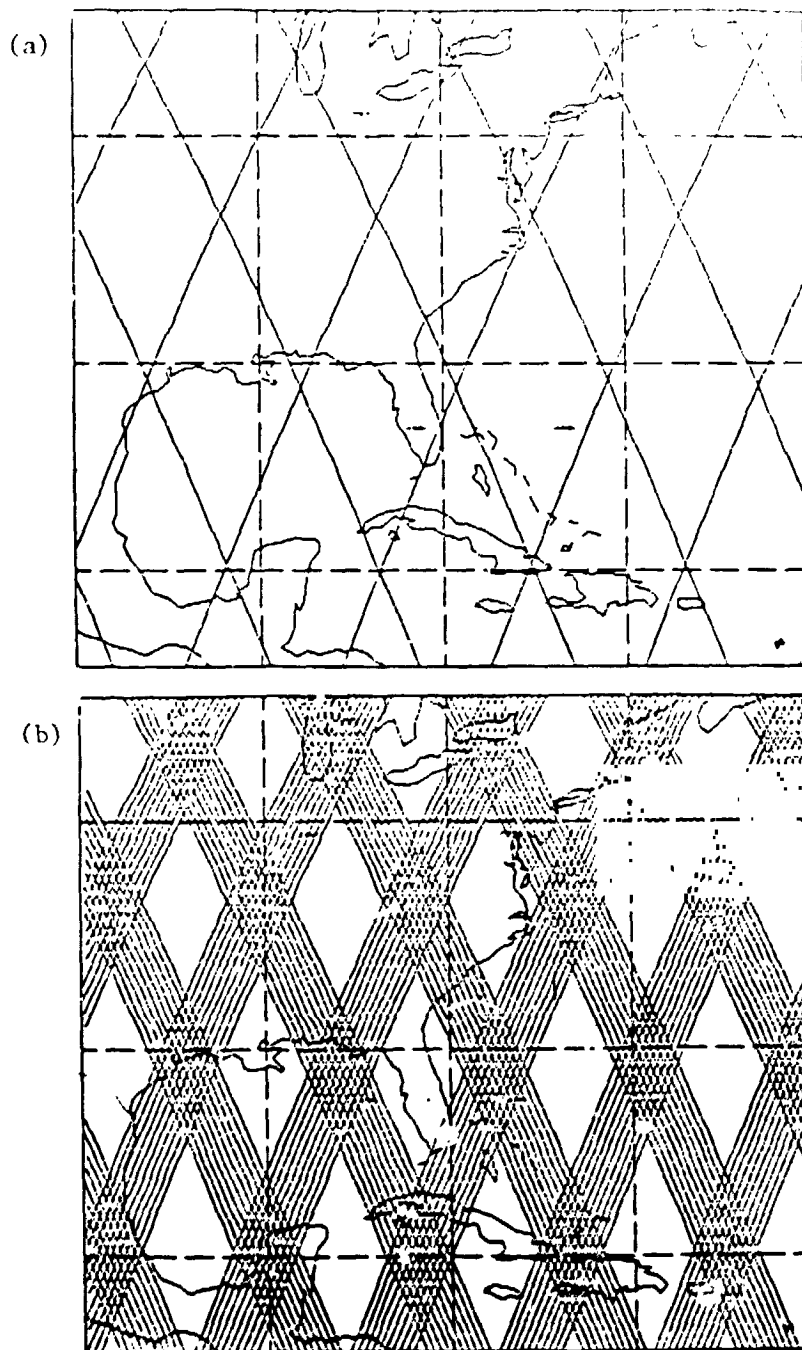


Figure 1. Ascending and descending tracks during the nominal geodetic mission of GEOSAT. (a) Coverage after 3 days. At this point, adjacent tracks in the Gulf of Mexico are 1 day apart and separated by approximately 900 km. (b) Track pattern after 30 days. The tracks fill the open regions from left to right. Adjacent tracks are 3 days apart and separated by approximately 36 km in the Gulf of Mexico. About 70 days are required for the entire pattern to fill in. (Courtesy of Dr. Z. Hallock, NORDA).

useful for mesoscale modeling. The geodetic portion of GEOSAT may be followed by an extended mission with exactly repeating tracks and a shorter repeat track period.

As a first step in designing an optimum sampling strategy for mesoscale modeling and forecasting, the track spacing required to resolve adequately a stationary eddy is examined. Figure 2(a) depicts the ascending and descending tracks with a separation of 100 km superimposed on the numerical solution at Day 1120. The values of the model pycnocline depth are sampled every 20 km along the tracks. Because, in general, the location of the observation points do not coincide with the model grid points, the observation is an interpolated value from the numerical solution. The 'observed' data are mapped back to the numerical grid in order to reconstruct the solution (Fig. 2(b)). The RMS error difference between the true solution and the observed values is determined; the error is calculated only within a square circumscribing the eddy and is normalized by the standard deviation of the true solution within the square. For each value of track separation, two values of the RMS error are calculated: a) only one set of tracks (i.e. ascending or descending are used in the analysis and b) both ascending and descending tracks are used to reconstruct the height field. The results (Fig. 3) reveal that if data from both tracks are used, track separation as large as an eddy radius adequately resolves the features. Additional tracks yield only a slightly improved representation. For cases in which the ascending and descending tracks sample the eddy at significantly different times, it may be advantageous to assimilate the observations from only one set of tracks. In such instances, Fig. 3 suggests that 3-4 tracks per eddy are required.

The non-stationarity of the ocean adds a frustrating complexity to the sampling problem. The inverse relationship between repeat track period and track separation for a single, nadir-beam altimeter demands a prudent sampling and four-dimensional assimilation strategy for optimum results. If the dynamical features of interest necessitate narrow track spacing, the temporal resolution may be inadequate unless a numerical model is able to fill in the temporal gaps. This problem is illustrated by Fig. 4 in which the interpolated Gulf of Mexico height field is shown for both a 72-day and a 39-day repeat track period. The model ocean is sampled during the repeat period just as a real altimeter would observe the true ocean. The 72-day sampling period grossly distorts the westward propagating eddy. The deformation is substantially reduced in the 39-day repeat period case; the 21-day repeat period sampling (not shown) exhibits very little distortion of the eddy.

The 'observed' data are used to initialize a forecast of the Gulf of Mexico circulation in order to measure the skill of a particular sampling strategy. The forecast begins on day 1200 of the numerical simulation and continues for 180 days. Initial conditions for the forecast are obtained by sampling the model ocean with an imaginary altimeter for a duration nearly equal to the repeat track period. This insures complete coverage of the basin. In each case, the last observation occurs on day 1200. Hence, the 21-day repeat period case samples the model ocean from day 1182 to day 1200 while the 72-day case 'observes' the ocean from day 1131 to day 1200. The height field is interpolated to the numerical grid and treated as a synoptic data set. The results described below are based on techniques which exclude both four-dimensional assimilation and updating of the forecast; future experiments will include these important aspects of the assimilation problem. The initial height fields are somewhat smoother than those shown in Fig. 4 due to the incorporation of data from both ascending and descending tracks. The initial velocity field is determined from the geostrophic approximation; the initial conditions are assumed to be valid at approximately the mid-

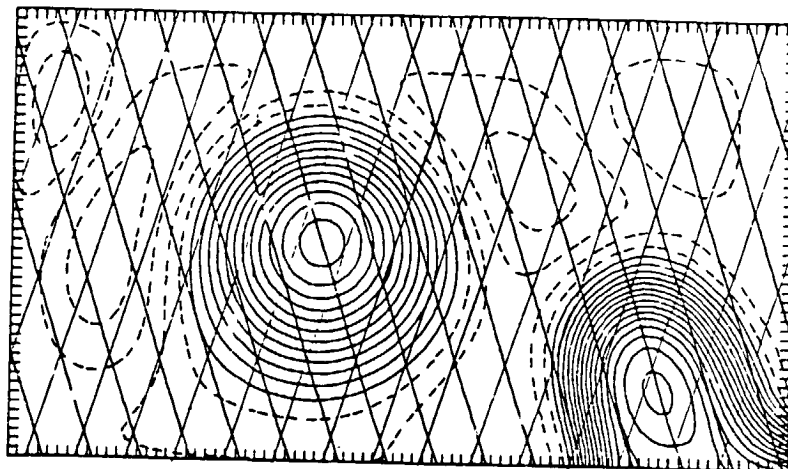
ORIGINAL PAGE IS
OF POOR QUALITY

(a)

ORIGINAL H-FIELD WITH TRACKS

DAY 1120.

DX1=100.0



INTERPOLATED H-FIELD (ALL TRACKS)

DAY 1120.

ANGL(1)= 72.0 ANGL(2)=108.0 DX1=100.0

MIN = -7978.5

MAX = 14246.5

(b)

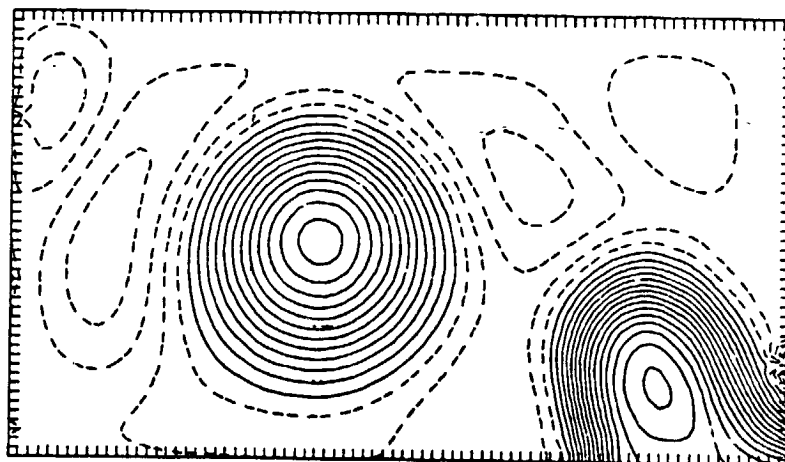


Figure 2. a) Ascending and descending tracks (separation equals 100 km) of an imaginary altimeter superimposed on the numerical solution of the Gulf of Mexico. The contours are the model interface deviation from its initial flat position. The contour interval is 10 m. Solid lines denote a deepening of the pycnocline while dashed lines represent shoaling. The model is sampled every 20 km along each track. The solution is stationary during the sampling process. b) A reconstruction of the numerical solution at Day 1120 from the values sampled along the tracks in (a). Experiment RG8 from Hurlburt and Thompson (1980) is the base experiment.

ORIGINAL PAGE 19
OF POOR QUALITY

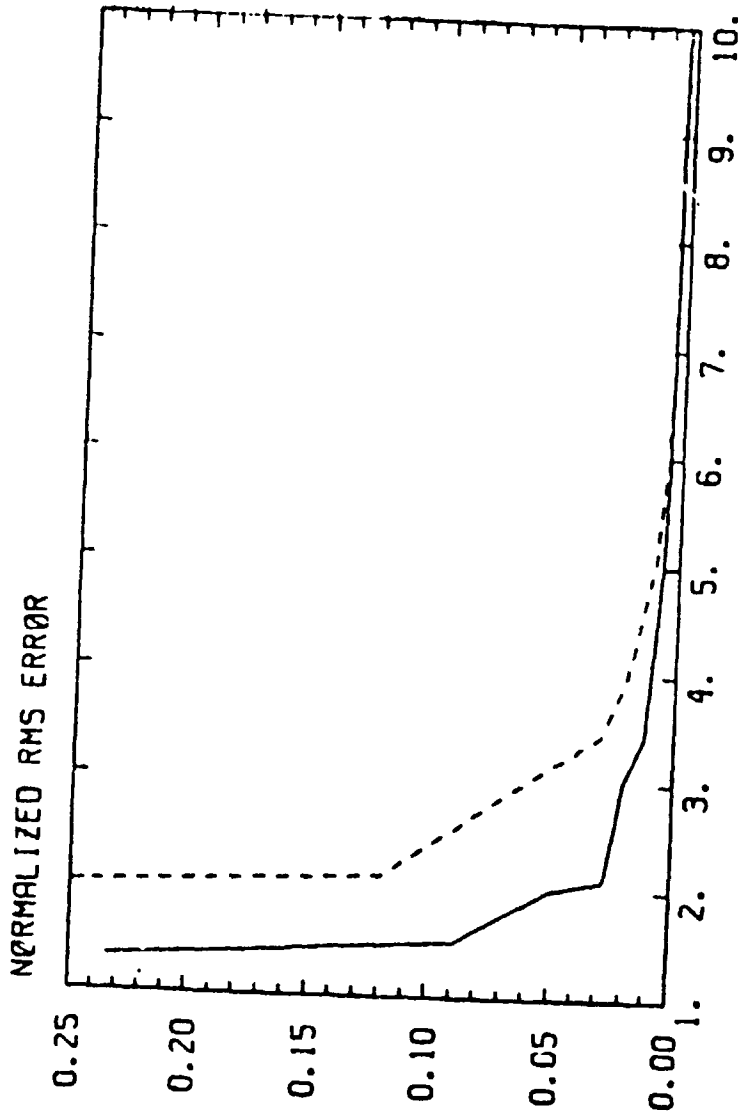


Figure 3. The RMS error difference between the interpolated field and the true numerical solution of an isolated, stationary eddy as a function of the ratio of eddy diameter to track separation. The solid line is the RMS error when both ascending and descending tracks are used whereas the dashed line is the same calculation utilizing only ascending or descending tracks. The RMS error is normalized by the standard deviation of the true solution.

ORIGINAL PAGE IS
OF POOR QUALITY

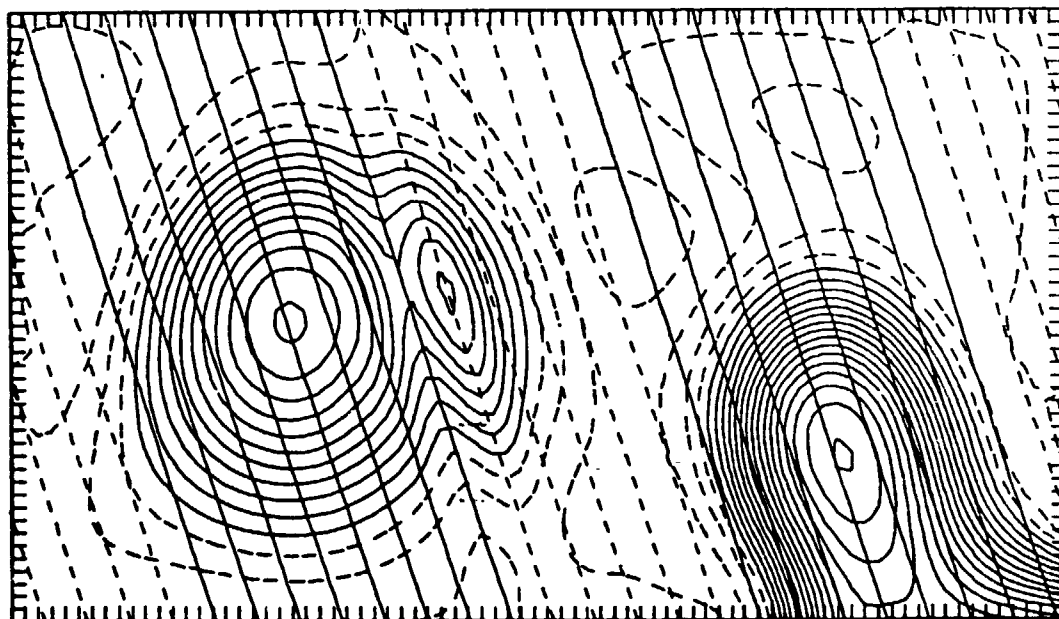
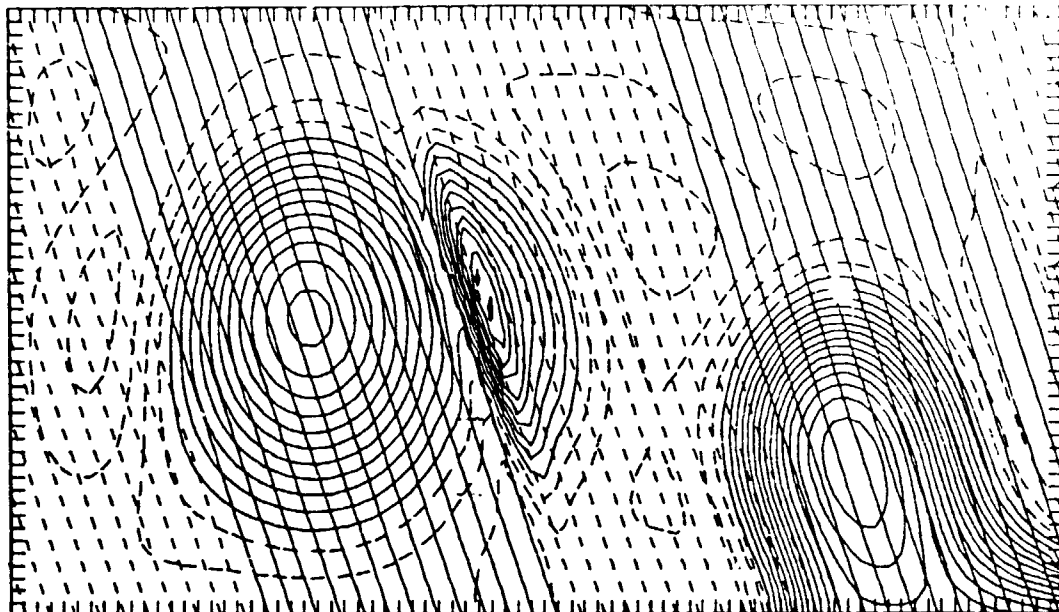


Figure 4. The ascending tracks of an imaginary altimeter superimposed on the interpolated height field. The values of the pycnocline height anomaly were determined by sampling the numerical model every 20 km along the tracks. The dashed track lines denote where the model was sampled during the first half of the repeat track period and the solid tracks depict where the model was sampled during the latter half. Adjacent tracks sampled the model three days apart. The most recent track (i.e. at Day 1200) is a solid track just to the left of an adjacent dashed track. a) 72-day repeat track period. The model was observed from Day 1131 to Day 1200. The distortion of the eddy is caused by westward propagation during the sampling period. The eddy is most distorted where two adjacent tracks differ by 69 days. b) 39-day repeat track period. The model is sampled from Day 1164 to Day 1200. The distortion of the eddy is not as large as in (a) because the most recent and oldest tracks only differ by 36 days.

point of the sampling period. The skill of the forecast is determined by calculating the RMS error difference between the predicted pycnocline depth and the numerical solution throughout the basin. The results for three cases are shown in Fig. 5. For the Gulf of Mexico simulation, the 21-day repeat track case offers the best compromise between track separation and repeat period.

As a more stringent test of the optimum sampling strategy for the Gulf, the experiments are repeated with a very fine-resolution Gulf of Mexico simulation. The grid spacing and eddy viscosity are reduced from 20 km and 300 m²/sec to 10 km and 100 m²/sec, respectively. Although the essential elements of the Gulf circulation are still present, the fine scale solution is also characterized by a larger number of eddies exhibiting a wide range of shape, amplitude and horizontal scale. Moreover, the dynamical features behave in a much more irregular manner.

The methodology of the forecast is identical to the process described above except that the prediction begins on day 1530 instead of day 1200. This is due to the longer spin-up time of the fine-scale simulation. Forecasts are again performed for the 21, 39 and 72-day repeat periods. In addition, a 40-day repeat track case is conducted in which the adjacent tracks are laid down one day apart instead of three days. For a given track separation, this scheme has the advantage of sampling a given feature in the shortest time. A comparison of the true solution and the forecast initialized from the 40-day repeat period case is shown in Fig. 6. The RMS error plots of the forecasts are given in Fig. 7. Clearly, the 72-day repeat track period is inadequate. The relatively minor differences between the other cases is supported by Fig. 3. The track separation of the 21-day repeat period (~ 120 km) is sufficient to resolve the primary dynamical features. Hence, additional tracks do not significantly improve the spatial error of the measurement. The propagation speed of the eddies is slow enough that the 39 and 40 day repeat periods yield reasonably synoptic observations.

4. CONCLUSIONS

Simulated altimeter data have been incorporated into numerical ocean circulation models in order to examine optimum sampling strategies of a single nadir-beam altimeter. The numerical experiments suggest that approximately 3-4 tracks (either ascending or descending) across an eddy provide adequate resolution. For the Gulf of Mexico the track separation of the 20-day repeat period resolves the Loop Current and the westward propagating anti-cyclonic eddies. Sampling with a smaller track separation does not improve the forecast. In other oceanic regions, however, the 20-day repeat period yields a track separation unable to resolve the energetic mesoscale field. In western boundary systems, where eddies have smaller horizontal scales and propagate more rapidly, simultaneously obtaining adequate spatial and temporal resolution is more difficult. As part of this research program, numerical experiments using simulated altimeter data will also be conducted for the Gulf Stream region.

The experiments described in this report are merely a first step towards the development of a methodology for assimilating altimeter data into ocean forecast models. The utilization of contaminated data, optimal interpolation and initialization schemes, forecast updating methods and multi-layer models need to be examined. These studies may substantially alter any quantitative conclusions which might be derived from the results presented here.

ORIGINAL PAGE IS
OF POOR QUALITY

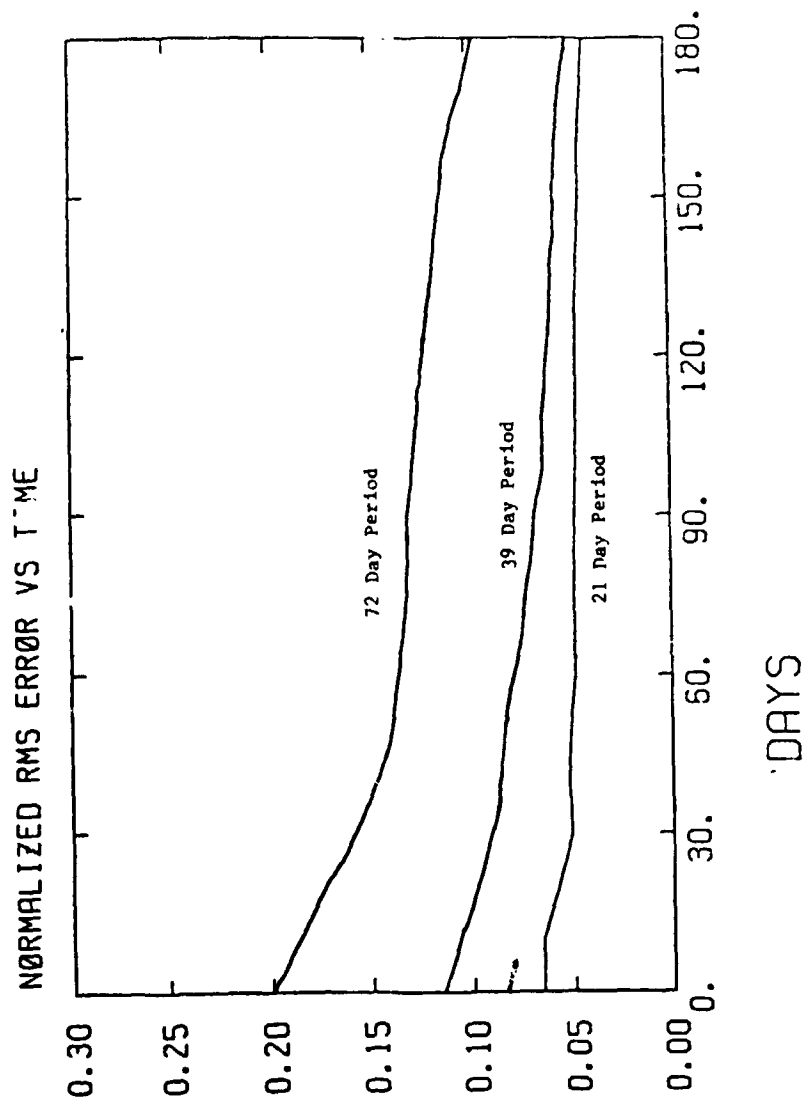


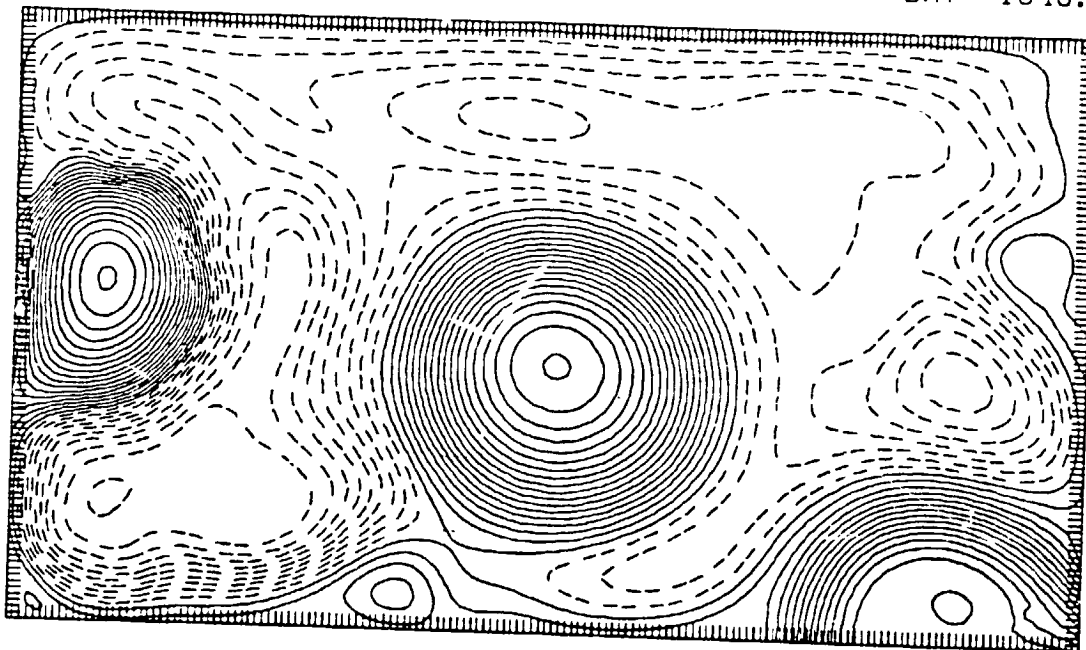
Figure 5. Normalized RMS error of forecast for the 21, 39, and 72-day repeat track periods. The error is the RMS difference between the forecast and the true solution normalized by the standard deviation of the true solution.

ORIGINAL PAGE IS
OF POOR QUALITY

TRUE FIELD

DAY 1640.

(a)



FORECAST FIELD

DAY 1640.

(b)

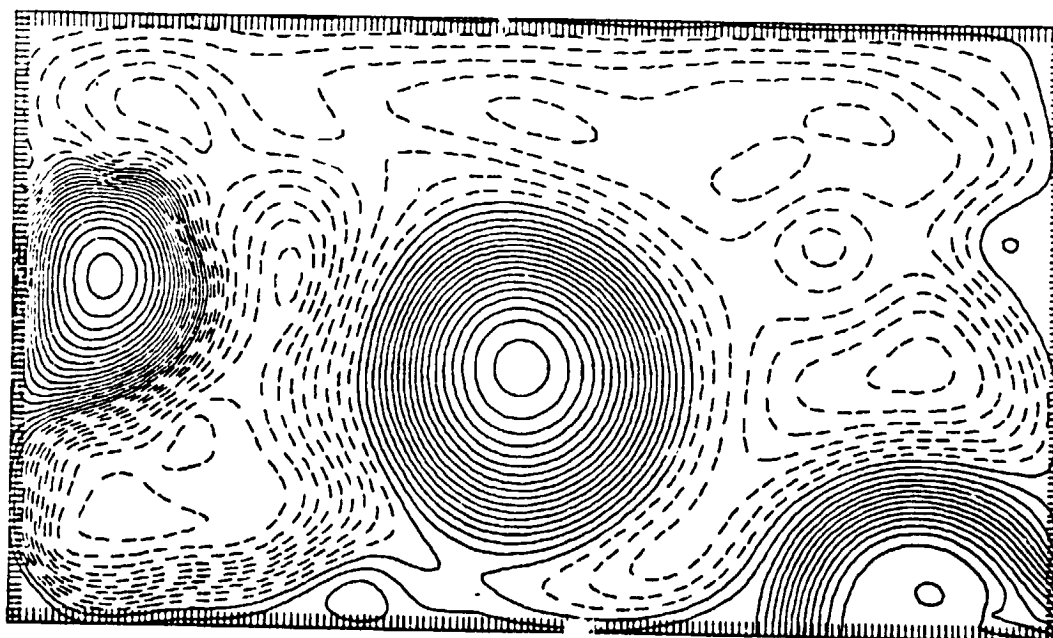


Figure 6. a) Contours of pycnocline height anomaly for the fine scale numerical simulation of the Gulf of Mexico circulation. b) Forecast of PHA in which simulated altimeter data are used to initialize the model. The forecast, which begins on Day 1530, is for the 40-day repeat track period case.

ORIGINAL PAGE 19
OF POOR QUALITY

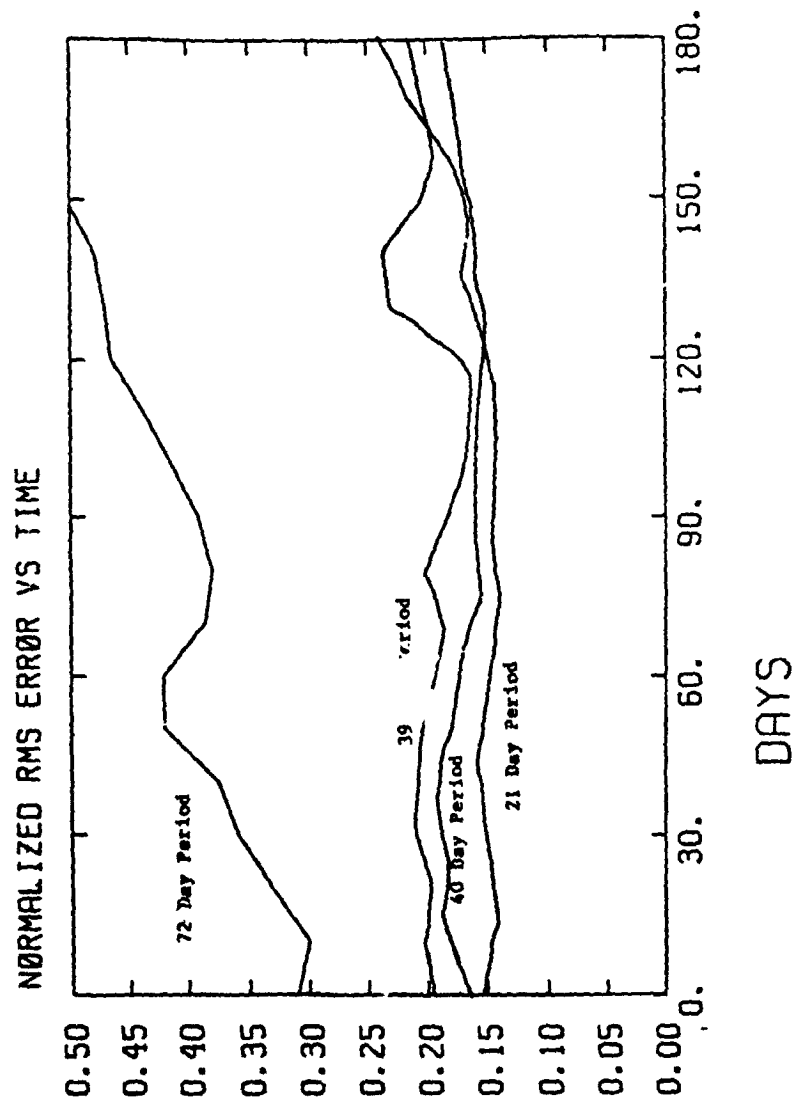


Figure 7. Normalized RMS error of the fine resolution forecast for the 21, 39, 40 and 72-day repeat track periods. Adjacent tracks for the 40-day period are one day apart instead of three.

ACKNOWLEDGEMENTS

Funding is from the Office of Naval Research under the Special Focus Program, "Ocean Dynamics for GEOSAT". The computations were performed on the Texas Instruments Advanced Scientific Computer at the Naval Research Laboratory in Washington, D.C. The authors are grateful for the technical assistance provided by Monty Peffley. Thanks are also due to Charlene Parker for typing the manuscript.

REFERENCES

- Hurlburt, H. E. and J. D. Thompson, 1980: A numerical study of Loop Current intrusions and eddy shedding. J. Phys. Oceanogr., 10, 1611-1651.
- Thompson, J. D., G. H. Born and G. A. Maul, 1983: Collinear-Track Altimetry in the Gulf of Mexico from SEASAT: measurements, models and surface truth. Geophys. Res., 88, 1625-1636.

THE INFLUENCE OF ACTUAL AND APPARENT GEOID ERROR
ON OCEAN ANALYSIS AND PREDICTION

by

J. Dana Thompson

Dynamic Ocean Forecasting Branch, Code 324
Naval Ocean Research and Development Activity
National Space Technology Laboratory
NSTL, MS 39529

ABSTRACT

The radar altimeter is the only satellite remote sensor with a proven capability for synoptically measuring an integral property of the dynamic ocean on a near-global, all-weather basis. Because acquisition of global, in-situ ocean data with space/time resolution adequate to describe dynamically important ocean features is practically impossible, any attempt to develop a global ocean monitoring and forecasting system will rely heavily on altimetric data for initialization and updating. Maximizing useful information from the altimeter while minimizing error sources and developing methods for assimilating altimeter data into dynamical models are, therefore, vital areas for research and development.

In addition to assimilating altimetric data, numerical ocean models are useful in simulation mode for generating "synthetic" sea surface heights to (1) assess the influence of sea surface height estimation error on predictability, (2) investigate optimum sampling and initialization strategies, and (3) compare with actual altimeter data associated with specific phenomena (Thompson et al., 1983). Because many applications of satellite altimetry require that we "know" the geoid, it is vital that we determine acceptable limits for geoid errors, especially in the vicinity of strong topographic variability where oceanographic processes may be especially active and where geoid error may be exceptionally high. This paper focuses on (1) with emphasis on limits to predictability introduced solely by errors in the geoid or apparent errors associated with ground track variations under "exactly repeating" orbits in the vicinity of strong geopotential gradients.

A two-layer primitive equation ocean model (Hurlburt and Thompson, 1980) which retains sea surface height as a prognostic variable is used to simulate the circulation in two regions of the Gulf Stream system: the Gulf of Mexico and the Gulf Stream north of Charleston. The model successfully simulates many of the observed features of these regions, including the penetration of the Loop Current and the shedding of large anticyclones from the Loop in the Gulf of Mexico and the development of realistic Gulf Stream meanders and warm and cold core Gulf Stream rings in the western Atlantic (Hurlburt and Thompson, 1983). Because these are regions of significant topographic variability, where geoid errors are likely to be greatest, the model serves as a representative test bed for these first predictability experiments.

The experiments typically have the following sequence: The model is integrated from rest to statistical equilibrium. Model forecasts are stored on a history tape at regular intervals. Some time after equilibrium has been reached the perfect (uncontaminated by tides, altimeter measurement error or

geoid errors) sea surface height data is corrupted with geoid error. To a first approximation the geoid error is assumed proportional to a linear combination of local bottom depth and topographic gradient. Using the corrupted sea surface heights, an associated current field (typically determined from the geostrophic approximation) is calculated. The model is then initialized with the contaminated data at every grid point and integrated forward in time. Model forecasts are then compared with the "true" fields from the original integration and error statistics are calculated. Because model data is used at every grid point in these experiments we have isolated the geoid error from sampling errors associated with track spacing, repeat period, and particular objective analysis schemes. Thus, the predictability limits found in these investigations may be considered upper limits to those found in such studies.

REFERENCES

- Hurlburt, H. E. and J. D. Thompson, 1980: A numerical study of Loop Current intrusions and eddy-shedding. J. Phys. Oceanogr., 10, 1611-1651.
- Hurlburt, H. E. and J. D. Thompson, 1983: Preliminary results from a numerical study of the New England Seamount Chain on the Gulf Stream. Predictability of Fluid Motions, G. Holloway and B. J. West, eds., American Institute of Physics; New York, 489-504.
- Thompson, J. D., G. H. Born, and G. A. Maul, 1983: Collinear Track Altimetry in the Gulf of Mexico from SEASAT: Measurements, Models, and Surface Truth. J. Geophys. Res., 88, pp. 1625-1636.

Author and Coauthor/Page Index

Alpers, W.,	403
Alperson, Z.,	337, 345
Atlas, D.,	41
Atlas, R.,	567, 575
Bahar, E.,	149
Baker, W.E.,	567
Balmino, G.,	497
Barrick, D.E.,	149
Beal, R.C.,	19, 159
Ben-Amram, T.,	337
Black, H.D.,	327
Black, P.G.,	281
Boggs, D.H.,	57, 575
Brodrick, H.,	345
Brown, R.A.,	51
Chang, J-T.,	345
Chien, J-Z.,	281
DeHority, D.C.,	281
De Mey, P.,	537
Donelan, M.A.,	75
Druyan, L.M.,	337
Durden, S.L.,	137
Eisner, A.,	327
Emery, W.J.,	453
Eng., W.P.,	199
Fedor, L.S.,	391
Feldman, U.,	515
Fitzwater, M.A.,	14
Gjessing, D.T.,	179
Goldfinger, A.D.,	159
Goldhirsh, J.,	287, 297
Grassl, H.,	317
Gruber, A.,	345
Guissard, A.,	257
Halem, M.,	568
Halpern, D.,	357
Hans, P.,	115
Hildebrand, P.H.,	271
Hjelmstad, J.,	179
Huang, N.E.,	247
Hurlburt, H.E.,	587, 601
Ikeda, M.,	453
Jackson, F.C.,	233
Johnson, J.W.,	215
Kalnay, E.,	567
Kasischke, E.S.,	415
Katsaros, K.B.,	307
Kindle, J.C.,	601
Kirimoto, T.,	89
Kozman, A.,	415
La Violette, P.E.,	479
LeBlond, P.H.,	453

Author and Coauthor/Page Index

Lewis, R.M.,	307
Lyzenga, D.R.,	.169, 415
Maccoll, D.,	11
Maxwell, M.S.,	29
McClain, E.P.,	367
McGoldrick, L.F.,	1, 57
Minster, J-F.,	497
Mitchell, J.L.,	389
Mollo-Christensen, E.,	41
Monaldo, F.M.,	159, 287, 297
Moore, R.K.,	89
Mueller, C.K.,	271
Mysak, L.A.,	453
Napolitano, D.A.,	137
Ohring, G.,	345
Petigaud, C.,	497
Peterherych, S.,	57, 105, 567, 575
Phillips, B.B.,	259
Phillips, O.M.,	433
Pierson, W.J.,	75, 557
Pisacane, V.L.,	367
Plant, W.J.,	193
Powell, J.,	513
Raney, R.K.,	123
Rapley, C.G.,	527
Reeves, A.B.,	193
Robinson, A.R.,	537
Rosenberg, N.,	431
Rufenach, C.L.,	.149, 169
Salfi, R.E.,	557
Serafin, R.J.,	259
Schlussel, P.,	317
Schuessler, H.,	115
Schuler, D.L.,	199
Shuchman, R.A.,	.169, 415
Smith, M.P.,	137
Sobieski, P.,	257
Swift, C.T.,	281
Sylvester, W.B.,	557
Szejwach, G.,	259
Tilley, D.G.,	159
Thomas, R.H.,	501
Thomasell, A.,	345
Thompson, J.D.,	.601, 613
Vesecky, J.F.,	137
Walsh, E.J.,	.287, 391
Weissman, D.E.,	215
Wentz, F.J.,	105
Woiceshyn, P.M.,	.57, 567, 575
Wolfson, N.,	345
Wurtele, M.G.,	.57, 575
Zlotnicki, V.,	497

Appendix B

First Author Affiliations

Dr. Werner Alpers
Max Planck Institut für Meteorologie
Bundesstr. 55
2 Hamburg 13, W. Germany

Dr. David Atlas
Laboratory for Atmospheric Sciences
NASA/Goddard Space Flight Center
Greenbelt, Maryland 20771

Dr. Robert Atlas
Laboratory for Atmospheric Sciences
NASA/Goddard Space Flight Center
Greenbelt, Maryland 20771

Dr. Ezekiel Bahar
Electrical Engineering Department
University of Nebraska-Lincoln
Lincoln, Nebraska 68588-0511

Mr. Robert C. Beal
Applied Physics Laboratory
Johns Hopkins University
Johns Hopkins Road
Laurel, Maryland 20707

Dr. Harold D. Black
Applied Physics Laboratory
The Johns Hopkins University
Johns Hopkins Road
Laurel, Maryland 20707

Dr. Robert A. Brown
Department of Atmospheric Sciences
Polar Science Center
University of Washington JC-10
Seattle, Washington 98105

Dr. Mark A. Donelan
Canada Centre for Inland Waters
867 Lakeshore Road
Burlington, Ontario L7R 4A6, Canada

Dr. Leonard M. Druyan
Department of Geography
Bar Ilan University
Ramat Gan, Israel 52100

First Author Affiliations

Dr. William J. Emery
Department of Oceanography
University of British Columbia
Vancouver, B.C. V6T 1W5, Canada

Dr. Leonard S. Fedor
NOAA/Wave Propagation Laboratory
325 Broadway
Boulder, Colorado 80303

Dr. Uri Feldman
Department of Geography
Bar-Ilan University
Ramat-Gan 52100, Israel

Dr. Dag T. Gjessing
Royal Norwegian Council for Scientific
& Industrial Research
Environmental Surveillance Technology Programme
P.O. Box 25
N-2007 Kjeller, Norway

Dr. Andrew D. Goldfinger
Applied Physics Laboratory
The Johns Hopkins University
Johns Hopkins Road
Laurel, Maryland 20707

Dr. Julius Goldhirsh
Applied Physics Laboratory
The Johns Hopkins University
Johns Hopkins Road
Laurel, Maryland 20707

Dr. Hartmut Grassl
Institut für Meereskunde
Dusternbrooker Weg 20
D-2300 Kiel 1, FRG

Prof. A. Guissard
Faculte des Sciences Appliquees
Laboratoire de Telecommunications
et d'Hyperfréquences
Batiment Maxwell, Place Du Levant 3
B-1348, Louvain-La-Neuve, Belgium

Dr. David Halpern
NOAA/Pacific Marine Environmental Lab.
7600 Sand Point Way NE
Seattle, Washington 98115

First Author Affiliations

Dr. Peter Hans
Space Programme Department
Dornier System GmbH
P.O. Box 1360
7990 Friedrichshafen, W. Germany

Dr. Peter H. Hildebrand
National Center for Atmospheric Research
P.O. Box 3000
Boulder, Colorado 80307

Dr. Norden E. Huang
NASA/Goddard Space Flight Center
Code 912
Greenbelt, Maryland 20771

Dr. Harley E. Hurlburt
Naval Ocean Research & Development Act.
Code 324
NSTL, Mississippi 39529

Dr. Fred C. Jackson
NASA/Goddard Space Flight Center
Laboratory for Atmospheric Sciences
Greenbelt, Maryland 20771

Prof. Kristina B. Katsaros
Department of Atmospheric Sciences
University of Washington, AK-40
Seattle, Washington 98195

Dr. John C. Kindle
Dynamical Ocean Forecasting Branch
NORDA, Code 324
NSTL, Mississippi 39529

Dr. T. Kirimoto
University of Kansas Center for Research
Remote Sensing Laboratory
Lawrence, Kansas 66045-2969

Dr. Paul E. La Violette
Remote Sensing Branch
Oceanography Division
Naval Ocean Research & Development Act.
NSTL, Mississippi 39529

Dr. Douglas Maccoll
European Space and Technology Centre
Postbus 299 - 2200 AG Noordwijk zh
The Netherlands

Dr. Marvin S. Maxwell
NASA/Goddard Space Flight Center
Code 920
Greenbelt, Maryland 20771

First Author Affiliations

Dr. E. Paul McClain
National Environmental Satellite, Data,
and Information Service, NOAA
Federal Building 4
Washington, D.C. 20233

Dr. Lawrence F. McGoldrick
Applied Physics Laboratory
The Johns Hopkins University
Johns Hopkins Road
Laurel, Maryland 20707

Dr. Jim L. Mitchell
Department of the Navy
Naval Ocean Research & Development Act.
NSTL, Mississippi 39529

Mr. Francis M. Monaldo
Applied Physics Laboratory
The Johns Hopkins University
Johns Hopkins Road
Laurel, Maryland 20707

Dr. C. Perigaud
Laboratoire de Physique et Chimie
de l'Hydrosphere (LA 196)
Institut de Physique du Globe
75230 Paris cedex 05, France

Dr. Steven Peteherych
Atmospheric Environment Service
4904 Dufferin Street
Downsview, Ontario M3H 5T4, Canada

Prof. Owen M. Phillips
Dept. of Earth & Planetary Sciences
The Johns Hopkins University
34th & Charles Street
Baltimore, Maryland 21218

Dr. Willard J. Pierson, Jr.
The City College of New York
Convent Ave. at 138th Street
New York, New York 10021

Dr. Vincent L. Pisacane
Applied Physics Laboratory
The Johns Hopkins University
Johns Hopkins Road
Laurel, Maryland 20707

Dr. William J. Plant
Naval Research Laboratory
Code 7913P
Washington, D.C. 20375

First Author Affiliations

Dr. John Powell
Science and Engineering Research Council
Rutherford Appleton Laboratory
Chilton, Didcot
Oxfordshire OX11 0QX, England

Dr. P. Keith Raney
RADARSAT
110 O'Connor Street
Ottawa, Ontario K1P 5M9, Canada

Dr. Chris G. Rapley
Mullard Space Science Laboratory
Department of Physics & Astronomy
University College London
Holmbury St. Mary,
Dorking, Surrey, England

Dr. Allan R. Robinson
Center for Earth & Planetary Physics
Division of Applied Sciences
Pierce Hall
Cambridge, Massachusetts 02138

Dr. Norman Rosenberg
Faculty of Engineering
Tel Aviv University
Ramat Aviv, Israel

Dr. Clifford L. Rufenach
NOAA/ERL/Wave Propagation Laboratory
325 Broadway
Boulder, Colorado 80303

Dr. Robert J. Serafin
National Center for Atmospheric Research
P.O. Box 3000
Boulder, Colorado 80307

Dr. Dale L. Schuler
Naval Research Laboratory
Code 7913S
Washington, D.C. 20375

Dr. Robert A. Shuchman
Radar Division, ERIM
P.O. Box 8618
Ann Arbor, Michigan 48107

First Author Affiliations

Dr. Calvin T. Swift
University of Massachusetts
Department of Electrical and Computer
Engineering
Amherst, Massachusetts 01003

Dr. Robert H. Thomas
Code EE-8
NASA Headquarters
Washington, D.C. 20546

Dr. J. Dana Thompson
Dynamic Ocean Forecasting Branch
NORDA, Code 324
NSTL, Mississippi 39529

Dr. John F. Vesecky
Stanford Center for Radar Astronomy
Stanford University
Stanford, California 94305

Dr. David E. Weissman
Hofstra University
Department of Engineering Science
Hempstead, New York 11550

Dr. Frank J. Wentz
Remote Sensing Systems
475 Gate Five Road
Sausalito, California 94965

Dr. Peter M. Woiceshyn
Jet Propulsion Laboratory
4800 Oak Grove Drive
Pasadena, California 91109

Dr. Noah Wolfson
National Environmental Satellite, Data,
and Information Service, NOAA
Washington, D.C. 20233

Dr. Morton G. Wurtele
Department of Atmospheric Sciences
University of California
Los Angeles, California 90024